Nanomaterials for the Life Sciences

Edited by Challa Kumar

WILEY-VCH

Magnetic Nanomaterials

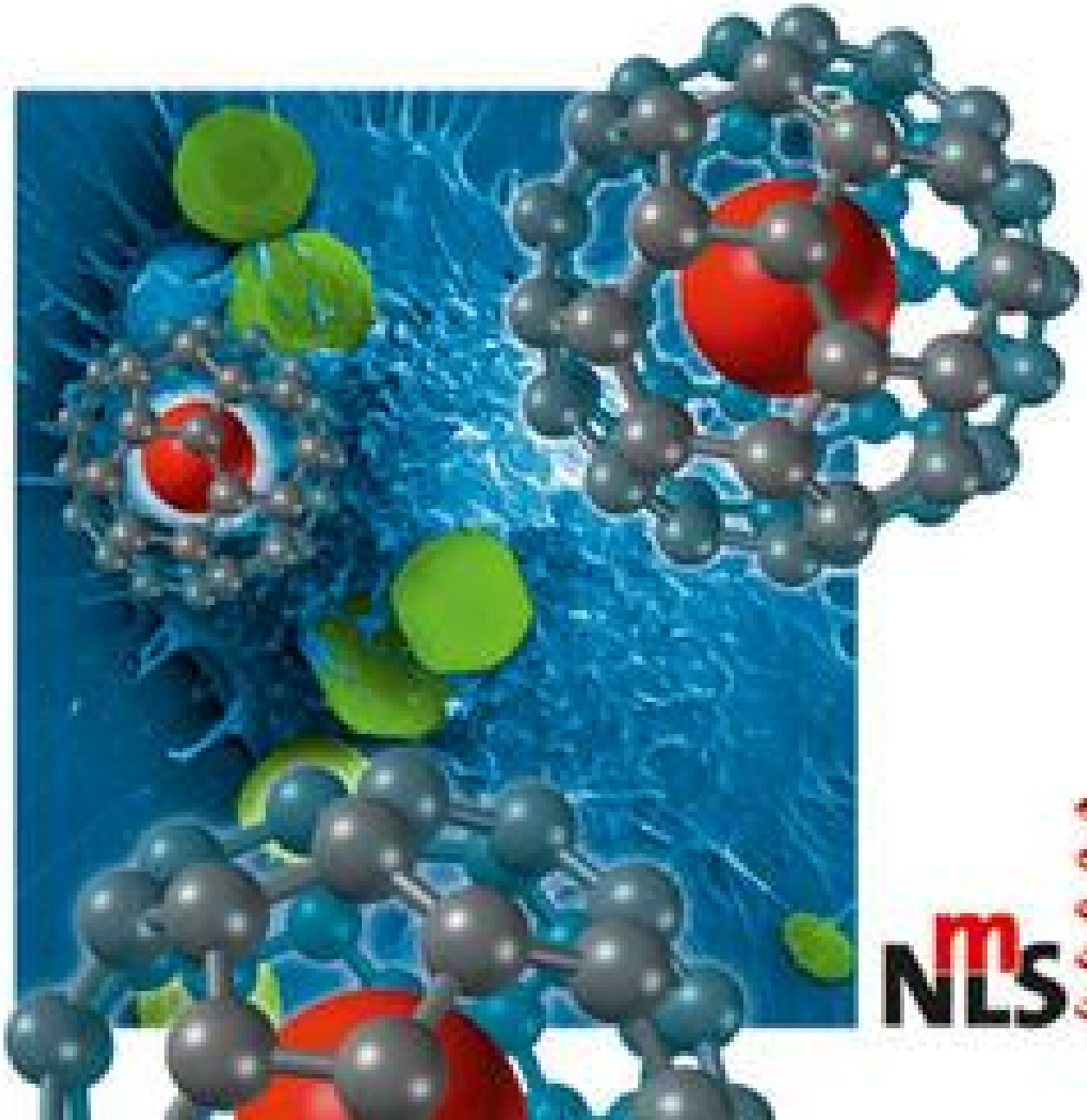

Contents

Nanomaterials for the Life Sciences Vol. 4: Magnetic Nanomaterials. Edited by Challa S. S. R. Kumar

ISBN: 978-3-527-32154-4

1
Nanomaterials-Based Magnetic Relaxation Switch Biosensors

Tom Lowery

1.1
Introduction

Magnetic nanoparticles or microparticles can serve as magnetic relaxation switches (MRSws) when they react with molecular targets and undergo changes in aggregation state that affect solvent magnetic resonance relaxation. Coupling this target-mediated aggregation with an appropriate detection device yields a reagent–instrument biosensor system for detecting target analytes. Since their introduction in 2001 [1], MRSw biosensors have been the subject of over 40 reports demonstrating their capability of detecting virtually any analyte in a variety of dirty, opaque samples. MRSws have been shown capable of detecting nucleic acids, proteins, enzymes, small molecules, ions, viruses and cells in solutions such as water, blood, cell lysate, urine, plasma, and serum. Due to the broad range of possible target analytes, and the capability of obtaining measurements without sample preparation, MRSw technology has remarkable potential to change the paradigm of solution-based biosensing, and thus to impact greatly on several fields of application, including medical diagnostics, environmental sensing, and homeland security.

The MRSw technology draws on the unique combination of scientific fields of nanotechnology, biochemistry, and nuclear magnetic resonance (NMR). To date, only one brief review has been published, relatively early during the development of this technology [2]. Due to the rapidly growing body of these investigations, and the interdisciplinary nature of MRSws, there is a need for a comprehensive description of the technology and summary of recent progress. To this end, this chapter provides an introduction to the relevant nanomaterials, an explanation of relevant NMR measurement techniques, a summary of the underlying theoretical physics behind nanoparticle clustering, an overview of the published MRSw research articles, and a description of portable and miniaturized magnetic resonance instrumentation. Although a sizeable body of work exists using other types of magnetic resonance contrast agents for molecular detection [3–12], this chapter will focus exclusively on MRSw biosensors.

Nanomaterials for the Life Sciences Vol. 4: Magnetic Nanomaterials. Edited by Challa S. S. R. Kumar

ISBN: 978-3-527-32154-4

1.2 Superparamagnetic Nanoparticles

The properties of nanoparticle reagents make possible the unique characteristics of MRSw biosensing. To date, all MRSw demonstrations have used some type of superparamagnetic iron oxide (SPIO) particle. The earliest iron oxide particles were utilized for localized lymph node heating over 45 years ago [13]. SPIO nanoparticles contain one or more superparamagnetic iron oxide cores composed of a mixture of magnetite (Fe_3O_4) and maghemite (γ-Fe_2O_3), which have similar magnetic properties. These iron oxide cores, which typically are less than 14 nm in diameter, are encapsulated in a hydrophilic monomer or polymer coating so as to endow water solubility [14]. When magnetite crystals are oxidized, the crystal lattice changes from the inverse spinel of magnetite to the cubic Fe(III) oxide lattice of maghemite [14]. SPIO particles are distinguished from paramagnetic particles in that their small iron oxide cores are comprised of single-domain magnetic crystals, the magnetic moments of which readily align with an external magnetic field, and this results in a microscopic dipolar magnetic field surrounding the iron crystal. Upon removal of the external magnetic field, the magnetic moments of these cores randomize, leading to a complete dissipation of the induced magnetic field [14, 15]. The magnetization and magnetic susceptibility of SPIO nanoparticles are much larger than that of paramagnetic ions and bioinorganic complexes of iron, such as ferritin [16].

Depending on the method of synthesis, SPIO particles can range in size from ~2 nm (citrate-inhibited growth), tens of nanometers (polymer-coated), to micrometers [14]. SPIO are typically categorized based on their overall diameter, which includes the metal core and organic coating [14]. SPIO particles between 300 nm and 3.5 μm are referred to as oral-SPIO because they were first used for *in vivo* imaging via oral delivery, such as the silane-coated contrast agent ferumoxsil (trade name GastroMARK®) [17]. Like most particles larger than 50 nm, oral-SPIOs contain more than one iron core per particle. Over a matter of minutes, however, a solution of oral-SPIO particles can settle due to their large size [18], which complicates their use for the aggregation-based sensing used by MRSws. In order to circumvent this, MRSw applications using oral-SPIOs have utilized surface treatments to provide adequate buoyancy to the particles, such that they do not settle. In addition, timed mixing steps with rapid measurements have been used to ensure a reproducible suspension of the particles during measurement [19, 20].

Particles which are slightly smaller than oral-SPIO particles are referred to as standard SPIO (SSPIO) nanoparticles, and have hydrated diameters of 60–150 nm. As with oral-SPIO, these particles contain more than one iron core per particle. A solution of these particles does not settle, although under certain conditions they may aggregate when placed in a magnetic field [18]—a property which is used for magnetic separations by SSPIO (examples include those produced by companies such as Miltenyi Biotech). A similar, field-dependent aggregation has also been observed for oral-SPIO [21–23], and can be used for the sensitivity enhancement of MRSw biosensors [19]. However, the application of these particles to MRSw

biosensors must be accompanied by proper controls to ensure that the observed change in signal is the result of target binding and not simply field-induced clustering.

Particles smaller than ~50 nm are known as ultrasmall SPIO (USSPIO), some of which have been developed to produce *in vivo* contrast agents such as ferumoxide (Feridex®) and ferumoxtran (Combidex®) [24–27]. Although their density is greater than that of water, their size is sufficiently small that Brownian motion keeps them suspended in solution [18, 20]. The subjection of these solutions to a magnetic field gradient does not lead to separation from solution, as it does for larger SPIO particles [18, 20, 28, 29]. Instead, the suspended particle solution behaves like a homogeneous magnetic colloid, or ferrofluid [18]. A subset of USSPIO is those that have single monocrystalline cores. Monocrystalline iron oxide nanoparticles (MIONs) typically have hydrated diameters of 10–30 nm, which are too small for magnetic grid purification.

As will be discussed below, a variety of SPIO particle sizes and particle materials have been used for MRSw assays, ranging from USSPIO to micron-sized oral-SPIO. MRSw technology was pioneered using a variant of MION [24, 30] known as crosslinked iron oxide (CLIO) nanoparticles. CLIO nanoparticles are MION nanoparticles, the polysaccharide coating of which has been crosslinked to endow a greater stability upon the particle. As with MION, CLIO nanoparticles have iron oxide cores which are between 3 and 5 nm in size, with a crystal structure of inverse spinel structure (cubic close-packed) of $(Fe_2O_3)_n(Fe_2O_4)_m$. They are surrounded by 10 kDa crosslinked dextran polysaccharide that is approximately 10 nm thick, to result in a total particle diameter of 25–30 nm [2].

One of the earliest characterizations of USSPIO nanoparticles was reported by a team led by T. Shen in the Weissleder group at the Massachusetts General Hospital (MGH), and also by a team led by C. Jung at Advanced Magnetics [17, 24, 25, 30]. The properties determined by these studies were typical of the MION nanoparticles used to create targeted CLIO nanoparticles for subsequent MRSw studies at MGH. The MION particle characterized in the original studies has been the parent particle for several different magnetic resonance imaging (MRI) contrast agent applications, including Combidex [17, 24, 25, 31–33] and many MRSw biosensors. The sizes of MION and other USSPIO iron oxide cores were measured, using transmission electron microscopy (TEM) and X-ray diffraction (XRD), as ranging between 4 nm and 10 nm, depending on the method of preparation [24, 25, 30]. A hexagonal crystal shape was also reported, which was consistent with the inverse spinel crystal structure typical of magnetite and the results of x-ray powder diffraction studies. The magnetization of these particles was 68 emu g^{-1} at room temperature and with an external field of 1.5 T. Magnetization of these particles saturated around 50 000 gauss, or 5 T; consequently, at 0.5 T the magnetization was ~60% saturated [24, 30]. When the magnetic field was switched off, no remnant field was measured from the MION, which was indicative of their superparamagnetic nature. Shen *et al.* measured the fractional weight content of iron and dextran on MION to deduce an 80 : 1 iron : dextran molar ratio, although this value would, of course, depend on the specific preparation of the MION. Both,

iron and dextran content were determined by chemical pretreatment and spectrophotometry. In solution, the MION were unimodal, with an average hydrodynamic radius of 20 nm, as determined by laser light scattering [24, 30]. When MION were placed in nonaqueous micelles, their overall diameter decreased to 8 nm, underlining the porous nature of the dextran polymer layer. Based on the crystal structure and TEM measurements of the iron core, each iron core was calculated to contain 2064 iron atoms. Accordingly, each core was calculated to have 25 ± 6 dextran molecules (10 kDa) attached [30].

Many different synthetic methods have been introduced for synthesizing superparamagnetic nanoparticles, and the reader is referred to pertinent reviews for further details [34–39]. Water-soluble CLIO nanoparticles can be synthesized using a two-step method, involving the base-induced crystallization of iron salts in the presence of a polysaccharide to form MION, with subsequent crosslinking to form CLIO [30, 32, 33]. In this method, ferric salts were stirred overnight in an acidic aqueous solution at 4 °C in the presence of dextran, which is a highly soluble, linear polysaccharide composed of D-glucose. Following the addition of ferrous salt and titrating with ammonium hydroxide to form a basic mixture, the temperature was increased to 80 °C, at which point precipitation of the MION nanoparticles occurred. Any unreacted dextran was then removed by filtration, and the dextran coating crosslinked by the addition of epichlorohydrin and aminated by reaction with ammonia [40, 41]. These series of reactions resulted in a MION particle that was coated with aminated, crosslinked dextran, referred to as an amino-CLIO. Amino-CLIO nanoparticles have an iron core diameter of 5 nm and a hydrated diameter of 25–30 nm, which is equivalent in size to a globular protein between 750–1200 kDa [2]. The surface amino-CLIO can be functionalized by attaching appropriate targeting moieties to amino groups, such as antibodies or binding proteins, using standard bioconjugation chemistry techniques.

1.3 Agglomeration-Based Sensing

The fundamental means by which magnetic relaxation switch biosensors detect the presence of an analyte is analogous to agglutination-based immunoassays. Agglutination immunoassays, which were first conceived over 50 years ago [42], detect the presence of a target analyte by using microparticles (often latex) decorated with a selective binding agent, such as an antibody. On addition of the target analyte, the functionalized microparticles undergo a transition from dispersed to agglomerated that is often detected by a change in the optical density of the solution [42, 43]. The limitations of this approach include the need to obtain a transparent sample for optical detection of the agglutination phenomenon, and low sensitivity and high interference rates due to nonspecific binding to the microparticle surfaces. For this reason, many applications that require higher sensitivity and selectivity require multiple washing steps to remove high-concentration interferents that bind, nonspecifically, any low-affinity particles [43, 44]. Unlike standard agglutination-based

assays, MRSw biosensors can be measured in opaque samples, and do not experience the same level of nonspecific binding to particle surfaces. These two distinguishing attributes arise from the advantages of the nanoparticle reagents and the non-optical magnetic resonance measurement approach; therefore, MRSw biosensor measurements can be conducted in relatively "dirty" samples, and with very few fluidic pre-processing steps [1, 2, 45–49].

A selective binding sensitivity of a nanoparticle for a desired molecular target can be achieved by the attachment of binding groups, such as antibodies or oligonucleotides, to the nanoparticle. If the binding group can bind to more than one site on a given analyte, and there are multiple binding sites per nanoparticle, the addition of an analyte to target-sensitized nanoparticles leads to a self assembly of the nanoparticles and target analytes into what has been termed nanoaggregates (Figure 1.1). In this manner, nanoparticles can be configured to switch from a dispersed state to an aggregated state due to the presence of an analyte. The basis of this transition is the tailored affinity of nanoparticle surface groups for a specific analyte. Similarly, nanoparticles can be configured to switch from aggregated to dispersed states due to the presence of analyte. As will be discussed below, a wide range of strategies have been employed by research groups to effect a transition between clustered and dispersed nanoparticles.

The transition of nanoparticles from dispersed to clusters can be quantitatively detected by measuring a change in a magnetic resonance signal, called "T_2", from surrounding water molecules. Because of the nature of the T_2 signal sensitivity, changes in the fraction of clustered nanoparticles can be detected without the separation of target-free from target-bound nanoparticles. The capability of measuring a binding phenomenon without a washing step represents a powerful advantage of MRSws over other technologies. This greatly simplifies sample handing and measurement steps, and also enables the use of extremely simple and rapid test formats.

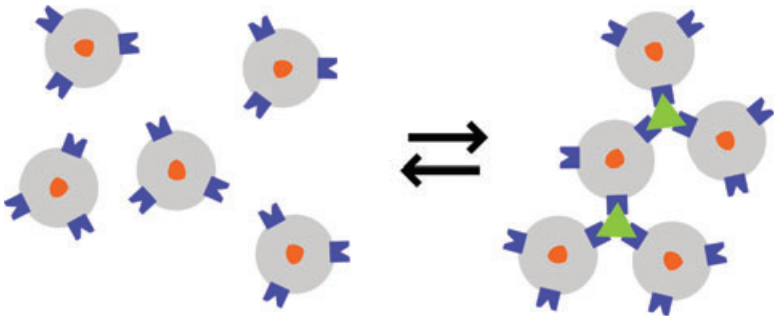

Figure 1.1 Magnetic relaxation switch biosensors are based on the magnetic resonance detection of the transition of dispersed and clustered populations of targeted nanoparticles. The targeted nanoparticles consist of a superparamagnetic iron oxide core (orange), a polymer coating (gray), and selective binding agents (blue). For one biosensor configuration, the addition of an analyte (green) leads to nanoparticle self-assembly to form nanoparticle–analyte aggregates.

1.4
T_2 Sensitivity of MRSW Particles

Understanding the connection between the T_2 signal and the agglomeration state of the nanoparticles is critical for designing MRSw systems. In the following sections, both the mechanism and measurement of T_2, and the connection between nanoparticle agglomeration and T_2, are described. This aim of this section is to introduce investigators to the fundamentals of the magnetic resonance measurement of MRSw assays, so as to better enable biosensor development and optimization.

1.4.1
Fundamentals of T_2 Relaxation

Magnetic relaxation switch biosensors require measurement of the magnetic resonance T_2 relaxation parameter of bulk water. The T_2 relaxation measurement can be used to determine the extent of particle agglomeration, and thereby the amount of analyte present in a sample. This explanation is one model for the T_2-sensitivity of water protons to the microscopic field nonuniformities created by SPIO nanoparticles. Other mechanisms, such as particle motion, also lead to spin dephasing. The results from a more complete theoretical model are presented below.

Magnetic resonance signals arise from the nuclei of water hydrogen atoms. According to the classical description of NMR, these nuclei can be thought of as having tiny spins that precess in the presence of an external magnetic field, such as that provided by a permanent magnet inside a relaxometer. The rate of precession of the nuclear spins is directly proportional to the strength of the magnetic field, by the equation:

$$\omega_0 = (1/2\pi)\gamma B_0 \tag{1.1}$$

where ω_o is the proton precession frequency (Lamour frequency) in Hz (20 MHz for 0.47 T), γ is the gyromagnetic ratio of protons (2.675×10^8 rad s^{-1} T^{-1} for protons), and B_o is the strength of the applied magnetic field. An ensemble of nuclear spins inside a magnetic field arranges into two quantum spin states of different energies. The higher energy state corresponds to spins that align against the applied magnetic field, while the lower energy state corresponds to spins that align with the applied field. As the lower energy state has a slightly higher population ($<1 \times 10^{-6}$), there is a net nuclear magnetization that points in the same direction as the magnetic field (Figure 1.2a). To detect the spins, the magnetization vectors are "tipped" into the x–y plane (Figure 1.2b), also called the "transverse plane", by means of a transient magnetic field, B_1, which is perpendicular to and smaller than the main B_o field. Such transient B_1 fields are generated by radiofrequency (RF) pulses from specialized antennae, typically called coils. Once in the transverse plane, the ensemble of spins oscillate about the B_o field (Figure 1.2c); indeed, it is this oscil-

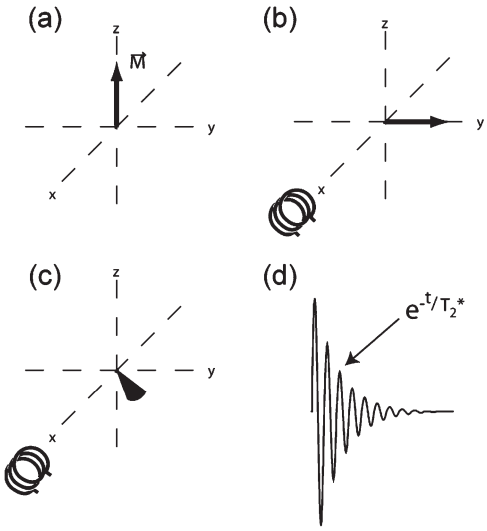

Figure 1.2 A series of schematics explaining nuclear magnetic resonance detection according to classical physics. (a) When nuclear spins are in the presence of a magnetic field, a bulk magnetization vector is present from the majority of the spins aligning with the field direction; (b) This magnetization can be detected by subjecting the sample to a radiofrequency pulse that tips the bulk magnetization vector into the x–y plane; (c) As this vector oscillates in transverse plan it decays according to T_2^* relaxation. This decay is called "spin dephasing", which is depicted by the vector fanning out; (d) Detection of the oscillating magnetic vector yields an oscillating signal that decays with a time constant of T_2^*.

lation which is detected by the RF detection coil, which is typically the same coil as that used to generate the RF pulse.

Once generated, the magnitude of the oscillating signal decays according to spin–spin relaxation, which occurs when a given ensemble of oscillating spins lose coherence, or synchronicity. This can be depicted by an oscillating vector "fanning out" over time (Figure 1.2c). A loss of spin coherence leads to a decay in the oscillating signal. A measure of the magnitude of this decay is the time constant T_2^* (Figure 1.2d).

A loss of spin coherence occurs when the spins within an ensemble experience variations in their Lamour frequencies, ω_o, during oscillation in the transverse plane. Such variations are caused not only by macroscopic inhomogeneities but also by microscopic fluctuations in the local B_o field. The contribution of macroscopic and microscopic B_o variations to T_2^* relaxation can be differentiated by specific detection sequences, as will be discussed below.

In both USPIO and SSPIO samples, microscopic variations in B_o are dominated by the agglomeration state of the particles. Measuring this contribution to T_2^* is critical for detecting the agglomeration state of particles. Because of their magnetic properties, superparamagnetic particles create local magnetic fields when in the presence of a B_o field; this in turn creates a local field "gradient", or a spatially

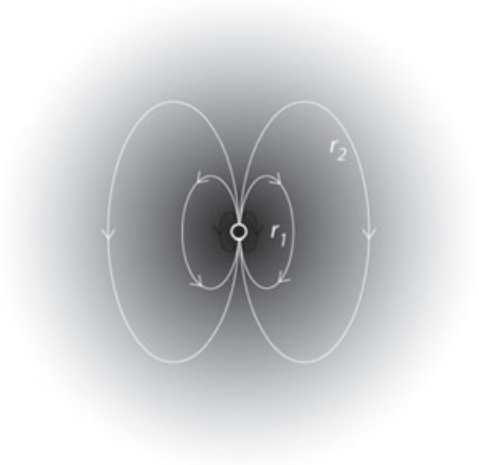

Figure 1.3 When inside a magnetic field, superparamagnetic particles generate local fields. The strength of the generated fields decreases as a function of distance from the particle, as indicated here by the spacing of the white field lines and the shading.

changing magnetic field, directly around each particle. The shape of this gradient is much like that generated by a simple bar magnet (Figure 1.3). The B_o field experienced by a given spin is the sum of the applied field and the local field generated by a particle (Equation 1.1). Spins that are near the particle, r_1, and those that are far away from the particle, r_2, precess at different frequencies, ω_1 and ω_2, respectively (Figure 1.3). Because water molecules are constantly diffusing, spins at r_1 and oscillating at ω_1 can move to r_2 and oscillate at ω_2 over the time course of signal detection. Such changes in ω_o lead to a loss of coherence, or synchronicity, between the spins within an ensemble.

The loss of spin coherence due to diffusion can be understood in terms of the property called phase. Phase corresponds to the relative positions of the magnetization vectors of spins in an ensemble. Figure 1.4a shows the magnetization vectors for two spins in the presence of the same magnetic field, such as at position r_2 (see Figure 1.3). When one of the spins transiently experiences a different magnetic field, such as diffusing from r_2 to r_1 and back to r_2 (Figure 1.3), then it undergoes a change in phase, as shown in Figure 1.4b. This change in phase arises from spins transiently oscillating at different frequencies due to changes in B_o field strengths. Because all spins in the sample are rapidly diffusing, the magnetization vectors of all spins undergo different phase shifts, leading to loss of spin coherence over time; this phenomenon is also called spin dephasing.

Spin dephasing occurs during signal acquisition, and affects the measurement (as shown in Figure 1.5). The NMR detector detects the bulk magnetization, or the sum of the magnetization vectors of each spin. When a population of spins

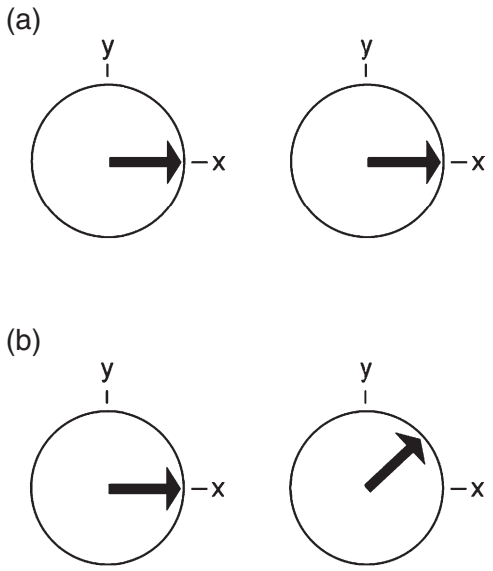

Figure 1.4 A schematic explaining the phenomenon of dephasing, or loss of phase coherence. (a) Snapshot of magnetization vectors for two spins that are oscillating at the same frequency because they are experiencing the same magnetic field. These two spins have the same phase; (b) A snapshot of these two spins after one spin has experienced a stronger field for a short time. They are still oscillating at the same frequency, but one spin has acquired a phase shift due to temporarily experiencing a different magnetic field, such as that experienced by a water molecule that has diffused past a superparamagnetic particle.

dephase, the bulk magnetization vector "fans out", decreasing the observed signal as a function of time (Figure 1.5a). However, if a sample experiences greater magnetic field variations (Figure 1.5b), then the observed magnetization vector will dephase (fan out) more rapidly, leading to a more rapid decay in the observed signal (Figure 1.5b).

1.4.2 Detecting T_2 Relaxation

Magnetic resonance signals are measured by pulse sequences, which are so named because they consist of a series of RF pulses separated by specific delays for spin evolution and signal detection. An RF pulse generates a transient magnetic field, B_1, that is perpendicular to the main magnetic field, B_o, as mentioned above ($B_1 << B_o$). The power and length of an RF pulse is tuned to rotate the bulk magnetic moment of the nuclear spins a given amount, such as 90° or 180°. The most simple pulse sequence consists of a pulse that rotates the magnetic field into the transverse plane for detection (see Figure 1.2); this is commonly referred to as a "90° pulse–detect measurement".

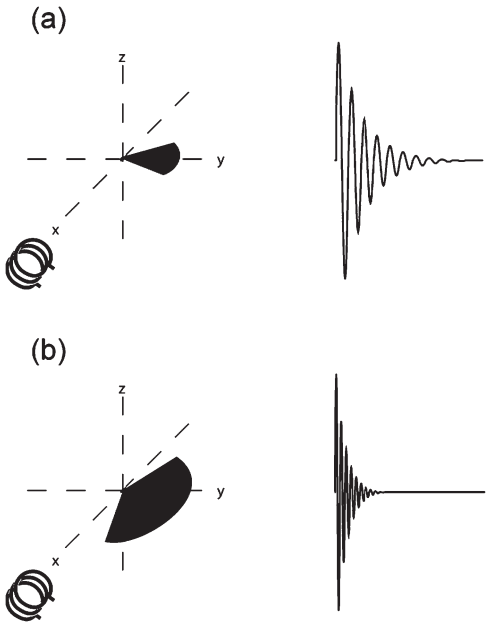

Figure 1.5 NMR signal acquisition from two samples that have (a) a long T_2 value; and (b) a short T_2 value. These two samples could be a sample of (a) disperse and (b) agglomerated MRSW particles. When the spin dephasing is more pronounced (b), the NMR signal decays more rapidly, corresponding to a lower T_2 value.

The simple 90° pulse–detect measurement can be used to measure T_2^*. As discussed above, magnetic field nonuniformities lead to nuclear spin dephasing. The amplitude of spin dephasing can be measured by determining the decay constant of the oscillating signal in the transverse plane, T_2^*, as shown in Figure 1.2d. For magnets used in most bench-top and portable relaxometers, T_2^* is dominated by variations in the applied magnetic field across the sample, which are also known as magnetic field inhomogeneities. The inhomogeneities of a magnetic field can be reported in terms of ppm, as calculated by the equation:

$$\Delta\omega_0(ppm) = \frac{1}{\left(\omega_0 T_2^*\right)} \tag{1.2}$$

where $\Delta\omega_o(ppm)$ is a measure of the inhomogeneity of the magnetic field, or relative change in homogeneity across a specific volume, ω_o is the Lamour frequency (in MHz), and T_2^* is the exponential decay rate in seconds of the magnetic resonance signal after a single 90° pulse–detect sequence. If one wishes to use T_2^* as a means to measure systems with long effective T_2 values, such as MRSw solutions, then magnets with high homogeneities (<0.1 ppm) must be used, such as

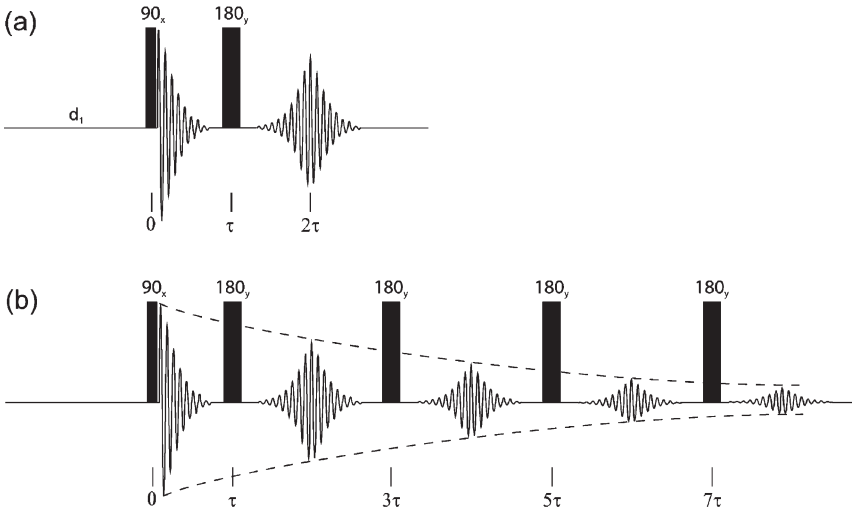

Figure 1.6 Two different MR pulse sequences for measuring T_2. (a) A spin echo sequence consists of two radiofrequency (RF) pulses: a 90° *x* phase, and a 180° *y* phase, separated by a delay τ. The echo signal appears at time 2τ. T_2 is measured by obtaining the echo signal from successive cycles using incremental values of τ. The recycle delay, d_1, is typically 1–3 s; (b) A CPMG sequence allows for much faster T_2 measurements because multiple echos are acquired in rapid succession by a series of 180° *y* phase RF pulses and signal acquisitions. T_2 measurements acquired with a CPMG sequence avoids diffusion artifacts because of the short time over which the measurement occurs.

those found in high-field superconducting magnets or large nonportable permanent magnets.

More sophisticated pulse sequences allow for the measurement of T_2 relaxation in the presence of a relatively inhomogeneous magnetic field. To do this, the contribution of magnetic field inhomogeneities to signal decay must be removed, which can be achieved using "spin echoes". The phenomenon and use of spin echos were discovered early during the development of magnetic resonance by Erwin Hahn, and later refined for rapid T_2 measurements by H.Y. Carr, E.M. Purcell, S. Meiboom and D. Gill to yield the so-called CPMG sequence [50–52]. A spin echo sequence is composed of two pulses; the first pulse rotates the spins 90°, and the second 180°. After the first pulse, the spins oscillate in the transverse plane and begin to dephase, as shown in Figure 1.5. After time τ, the fastest oscillating spins are on the leading edge of the "fan", while the slowest oscillating spins are at the lagging edge of the fan. A 180° pulse flips the spins in the transverse plane to the opposite side of the *z*-axis, switching the relative positions of the fastest and slowest spins. After time 2τ, the fastest spins catch up with the slowest, thus refocusing the magnetization vectors and the observed signal (Figure 1.6a). In order to obtain a measure of the decay constant that results from microscopic magnetic field fluctuations, or T_2, a series of spin echo sequences are run with incremented delay times, τ(typically milliseconds). Sequential scans must be

separated by a recycle delay, d_1, to allow the system to return to equilibrium as dictated by the spin-lattice relaxation time T_1 (typically 1–5 s). Fitting a plot of the maximal echo signal as a function of τ yields the time constant, T_2.

Using the spin echo sequence to measure T_2 values has two limitations. The first limitation is that any diffusion of spins during the long d_1 delay time between experiments can decrease the observed T_2 values. The second limitation is the long delay time, d_1. Because at least five datum points are necessary for a data fit, spin echo sequences can require over 20 s for the measurement of one T_2 value. A much faster and more efficient means of measuring T_2 is the CPMG pulse sequence, in which additional 180° RF pulses spaced by time 2τ are included to provide for the repeated refocusing of the echo signal. The amplitude of the echos measured between the pulses decays with the time constant T_2 (Figure 1.6b). As the time constant τ is typically less than a few milliseconds, a single T_2 measurement of several hundred echos can be completed in less than 1 s. However, one must be aware that CPMG and spin echo measurements can yield different T_2 values for some systems. Typically, CPMG sequences are sensitive to magnetic field variations that occur over periods of time less than hundreds of milliseconds, whereas spin echoes are sensitive to variations that occur over periods of time of less than seconds. One result of this difference is that CPMG T_2 measurements are independent of diffusion phenomena, while spin echo T_2 measurements are heavily dependent on diffusion, and this difference must be borne in mind when comparing T_2 values obtained by the two methods. In addition, CPMG T_2 measurements can exhibit a heavy dependence on the inter-echo delay time, 2τ. However, as will be described below, this dependence may be very useful for MRSw characterization and optimization.

1.4.3
Theoretical Model for T_2 and Nanoparticle Size

Although the use of MRSw biosensors was first demonstrated in 2001 [1], the theoretical foundation for how superparamagnetic nanoparticles affect measured T_2 relaxation rates began to take shape as early as 1991 [53]. These theory-based investigations were made possible by the early experimental observations that solvent relaxivity was a function of SPIO particle size [18]. In this early study, SPIO particles of various sizes were prepared by varying the number of iron oxide cores per particle, and the effect of ferromagnetic, paramagnetic, and superparamagnetic iron oxide particles on the longitudinal and transverse relaxivity, $R_1 = 1/T_1$ and $R_2 = 1/T_2$, respectively, was reported [18]. Subsequently, a group of theoreticians in Belgium, including Robert Muller, Pierre Gillis, Rodney Brooks, and Alan Roch, began exploring the underpinnings of magnetic, paramagnetic, and superparamagnetic particles that were used as contrast agents for MRI. The initial studies demonstrated that Monte Carlo numerical simulations of a distribution of magnetic particles surrounding by hydrogen nuclei could be used to accurately reproduce the observed dependence of R_2 on the size of iron oxide micro and nanoparticles [53, 54]. Simulations and experimental data showed that both R_2

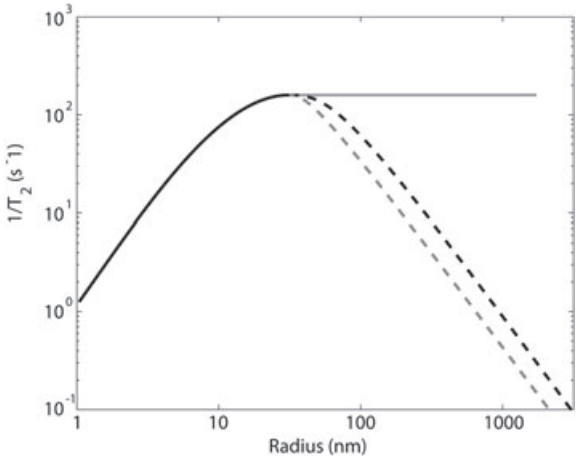

Figure 1.7 Sketch of the relationship between R_2 ($1/T_2$) and SPIO radius. In the motional averaging regime (solid dark line), R_2 increases with nanoparticle size, while in the visit-limited regime R_2 decreases with nanoparticle size (dashed lines). In the motional averaging regime, R_2 is equal to R_2^*, whereas in the visit-limited regime (also termed the static dephasing regime) R_2 no longer equals R_2^* (gray solid line). The static dephasing regime does not apply to most permanent magnet systems because R_2^* is dominated by their magnetic field nonuniformity; therefore, for portable systems R_2^* is always much larger than R_2. A unique property of the visit-limited regime is that R_2 exhibits a dependence on the inter-echo delay. The appropriate regime for a given SPIO system can be determined experimentally by measuring the R_2 and R_2^*, if using a high-field homogeneous magnet, or by measuring R_2 as a function of different inter-echo delays. These curves are a representative sketch of curves shown in Refs. [53] and [56], respectively. The exact position and curvature of the plots depends on the conditions used to generate the original curves.

and $R_2^*\left(R_2^* = 1/\mathrm{T}_2^*\right)$ increased with particle diameter until ~50 nm, whereas R_2 measured with spin echos decreased with increasing particle size, and R_2^* measured with a 90° pulse-detect reached a plateau (Figure 1.7). Subsequent experimental studies and computer simulations explored the dependence of R_2 on the concentration of dissolved iron, magnetic susceptibility, and temperature [54]. These early investigations laid the foundations for the development of a set of analytical models that accurately reproduced the dependence of transverse relaxivity on particle size, magnetization, iron concentration, temperature, and inter-echo delay for both strongly [55–57] and weakly magnetized nanoparticles [58].

According to developed theory, superparamagnetic nanoparticles are divided into categories of strongly magnetized and weakly magnetized. The boundaries between these two regimes depends on the relative magnitude of the frequency difference between nuclei at the surface of the nanoparticle and nuclei distant from the nanoparticle, $\Delta\omega$, and the inter-echo delay used in the CPMG detection sequence, τ_{CP}. $\Delta\omega$ is essentially a relative measure of the effect of the dipolar

magnetic field generated by a superparamagnetic particle on the resonant frequency of hydrogen nuclei in adjacent water molecules. When $\Delta\omega\tau_{CP} > 1$, then the particles are termed "strongly" magnetized, but when $\Delta\omega\tau_{CP} < 1$ the particles are termed "weakly" magnetized. Since, for a typical relaxometer, τ_{CP} is no shorter than tens of microseconds, $\Delta\omega$ must be less than 10^5 for the particles to be within the weakly magnetized regime. Therefore, most superparamagnetic nanoparticles used for magnetic relaxation assays are in the strongly magnetized theoretical region because $\Delta\omega$ ($\sim 1 \times 10^7$) is large compared to the inverse of achievable echo times ($1/\tau_{CP} = 10^3$). This means that the inter-echo delay is always longer than the amount of dephasing that occurs at the surface of a particle. Particles with weaker magnetizations ($\Delta\omega \sim 10^3$) induce less dephasing and are, within the theoretical regime, referred to as "weakly" magnetized.

Another characteristic of superparamagnetic nanoparticle solutions that is used to differentiate physical behavior is the diffusion time, or travel time, of water (τ_D) relative to the inter-echo time of the pulse sequence, τ_{CP}. Nanoparticle solutions are in the long echo limit when the τ_D is significantly less than τ_{CP}. τ_D can be determined by the relationship:

$$\tau_D = \frac{R^2}{D} \tag{1.3}$$

where τ_D is the time taken for a water molecule to diffuse the distance of a nanoparticle radius, R, and D is the diffusion constant of water ($10^{-9}\,m^2\,s^{-1}$). Here, τ_D can be thought of as the time taken for a water molecule to pass a hemisphere of a nanoparticle, or a "flyby" time. When τ_D is much larger than τ_{CP}, then the nanoparticle system is within the short echo limit. Typical CPMG sequences have echo times on the order of hundreds of microseconds to several milliseconds, and therefore the short echo limit cannot be approached unless the nanoparticle diameter approaches 1000 nm. The most common MRSw biosensors are within the "long echo limit" because the length of the inter-echo delays ($\tau_{CP} > 0.25$ ms) is longer than the time taken for a water molecule to diffuse pass the hemisphere of a nanoparticle (0.2–100 μs).

As the particle size of a solution of superparamagnetic particles at fixed iron concentration is increased, there is an initial increase in R_2, followed by a plateau and a later decrease (Figure 1.7). The regime on the left-hand side of the curve has been termed the motional averaging regime, the regime in the middle the static dephasing regime, and the regime on the right the visit-limited, or slow-motion regime [57]. The boundaries between the motional averaging and visit-limited regimes can be determined by generating plots such as that shown in Figure 1.7, or they can be determined by the relationship between $\Delta\omega$ and τ_D. If $\Delta\omega\tau_D < 1$, then the system is in the motional averaging regime, but if $\Delta\omega\tau_D > 1$ then the system is in the visit-limited regime. As the diameter of the particles increase in the motional averaging regime, the refocusing echos in the CPMG pulse sequence (used to measure T_2) cannot efficiently refocus the magnetization that has been dephased by the nanoparticles – hence the increase in R_2 (or decrease

in T_2). In other words, the refocusing pulses cannot compensate for increased dephasing by larger nanoparticles. The flat region of the static dephasing regime is due to R_2 being limited by R_2^*. The decreasing R_2 with increasing diameter in the visit-limited regime results in the refocusing pulses being able to refocus the dephasing caused by the nanoparticles. Also apparent in Figure 1.7 is that R_2 in the slow-motion regime exhibits a dependence on the inter-echo delay of the spin echo sequence [53].

In a homogeneous magnetic field, it is possible to determine which regime applies to a sample by comparing R_2 to R_2^*. If these values are identical, then one is in the motional averaging or static dephasing regime, but if they are different then one is in the visit-limited regime [53, 54]. This approach has been employed for determining the physical characteristics of MRSw biosensor systems [59–61]. However, as discussed above, the T_2^* of bench-top relaxometers is rarely larger than 5 ms, resulting in a lower limit for R_2^* of 200 s^{-1}. This means that, on bench-top relaxometers, R_2 will never be equivalent to R_2^* except at extremely high iron concentrations. For example, a typical solution of nanoparticles such as CLIO-47 has an R_2 of 40 $mM^{-1}s^{-1}$, so for R_2^* to equal R_2 the concentration of iron would need to exceed 5 m*M*, which is 50-fold higher than typical iron conditions. The relationship between R_2^* and field homogeneity is important to bear in mind when selecting instruments for characterizing MRSws. Fortunately, the echo time dependence of R_2 allows an easy method for determining whether one is in the motional averaging or visit-limited regime.

The conditions used to generate the analytical models that explain the dependence of R_2 on particle size were similar to the conditions used for MRSw assays. That is, the concentration of iron was held constant while R_2 was monitored as a function of nanoparticle diameter. The analytical models have been shown to accurately predict the dependence of R_2 on parameters that a biosensor designer can control, such as iron concentration, temperature, magnetic susceptibility, particle size, and particle size [54]. Interestingly, all of these parameters remain relatively constant for a given MRSw in comparison to particle size, which dominates the change in R_2. The same group which developed the analytical models was the first to demonstrate that these models could be used to explain the behavior of a system of clustering superparamagnetic particles [62]. Their experimental system consisted of superparamagnetic nanoparticles that clustered due to a change in the pH of the solution. After an initial phase that was attributed to a stabilization of the dispersed particles, R_2 was seen to increase with agglomeration until a plateau was reached prior to a decrease in R_2 with agglomeration. The shape of the R_2 response as the particles agglomerated generally matched the expected trend for the increase in average nanoparticle size, which was similar to the shape of both dashed lines in Figure 1.7. Additionally, Roch *et al*. demonstrated a general quantitative agreement between the measured and expected R_2 values. Similar exercises have since been carried out by subsequent authors to validate the qualitative nature of the T_2 response they were observing, and to determine which regime their nanoparticle assays fell within [20, 59, 61].

The similarity between the R_2 of particle agglomerates and that of spherical nanoparticles suggests that one can equate nanoparticle aggregates and spherical shapes. Even though this assumption may seem to be in contradiction with the fractal nature of nanoparticle agglomerates, the shape of the nanoparticle aggregates observed by with magnetic resonance measurements is determined by the ensemble of diffusing water molecules in solution, which can be approximated by the radius of hydration measured by light scattering. Recent studies by the group of A. Jasanoff at the Massachusetts Institute of Technology demonstrated an extension of the original outer sphere theory to nanoparticle aggregates by outlining the relationship between the parameters of the outer sphere theory and the fractal nature of nanoparticle aggregates [59]. These studies were subsequently extended by the research group at MGH, who showed that nanoparticle cluster size was inversely related to the T_2 of clusters in the motional averaging regime [61], and linearly related to the T_2 of clusters in the visit-limited regime [20], thus validating application of the outer-sphere theory to MRSws. Additionally, because the fractal dimension of nanoparticle clusters is approximately 2, the number of nanoparticles in an aggregate has been shown to be linearly related to the measured T_2 value for particles and clusters in the visit-limited regime. These observations indicate that application of the outer-sphere theory can provide useful insight on at least a semi-quantitative level into understanding and designing MRSw biosensors.

1.5 Kinetics of Magnetic Relaxation Switch Biosensors

Rapid measurements are often critical for biosensor performance and application. For MRSws, the rate of the transition between dispersed and clustered nanoparticles depends on various parameters that can be controlled for a specific set of biosensor conditions. T_2 measurements can be measured in real-time during the analyte-induced response, or at the end point of the clustering reaction. For the former case, T_2 changes as a function of measurement time and the rate of T_2 change can be correlated to a quantitative amount of analyte; for the latter case, after an incubation time T_2 remains constant as a function of measurement time, and the magnitude of T_2 can be correlated to a quantitative amount of analyte. Both measurement approaches have been used for MRSw biosensors to date.

Sample mixing and loading, as well as T_2 measurements, can be completed in tens of seconds, making sample incubation the rate-limiting step for MRSw measurements. To date, incubation times have ranged between 0 and 120 min. Although several studies have demonstrated real-time T_2 measurements immediately after sample mixing [1, 45, 63, 64], most quantitative data acquired to date has used end-point readings. In some cases, faster kinetics can be achieved by using systems that transition from clustered nanoparticles to dispersed nanoparticles [63–65]. However, for both types of assay design a significant variation in

reaction rates has been observed. A recent theoretical study conducted in the laboratory of A. Jasanoff suggested how several parameters, including particle concentration, functional group density, and ratio of particle types, can be optimized to achieve reaction rates on the order of seconds [59]. The group's simulations predicted that reaction rates could vary over three orders of magnitude within reasonable activation kinetics, biomolecular on and off rates, particle concentrations, and functionalization levels.

Shapiro *et al*. have proposed a two-step model for MRSw agglomeration, with the first step consisting of an activation of both species of nanoparticles due to the presence of an analyte [59]. Such activation results from the analyte binding to or analyte-induced modification of the particle surface. The second step consisted of agglomeration of the activated nanoparticles. These two steps are shown in Equation 1.4:

$$A + B \rightarrow A^* + B^* \rightarrow \sum A_j^* B_j^* \tag{1.4}$$

where A and B denote nanoparticles of two different functionalities, A* and B* represent activated A and B particles, respectively, and $A_i^* B_j^*$ represent an aggregate composed of *i* A particles and *j* B particles [59]. These authors assumed that the rate of the first step was much faster than that of the second step, thus causing agglomeration to be the rate-limiting step. Interestingly, for sensors that are based on nanoparticle dispersion, deactivation and dispersion are likely both to be fast steps, which explains why for some sensors much faster rates are observed for nanoparticle dispersion. Because T_2 measurements made by CPMG echos can be less than seconds, the signal acquisition is rapid compared to the first two steps, and will not significantly influence most observed reaction rates.

This two-step model was used to predict how changes in particle concentration, the number of functional groups per particle, and also the ratio between particle types, could influence the observed binding kinetics and particle size. Reaction rates for different conditions were compared in terms of an observed time constant (T_{obs}). T_{obs} is the time required for the reaction to reach 63% completion (one exponential unit). A reaction following first-order kinetics is 95% complete after $3 \times T_{obs}$, and 99% complete after $5 \times T_{obs}$. Particle concentrations of 23 n*M* (iron content 10 μg ml^{-1}), which are similar to those used for most MRSw studies, have a predicted T_{obs} value of <100 s. This suggests that these reactions should be complete in less than 10 min, which is faster than many observed reaction times. This discrepancy may arise from the number of functional groups for the experimental results being much lower than those used for the simulations. Particle concentrations as low as ~10 p*M* have predicted T_{obs} values longer than 1000 s, while concentrations as high as 0.1 μ*M* and 60 functional groups per particle have predicted T_{obs} values of 2 s. Under all reaction conditions, the optimal ratio of particle types A and B was predicted to be 1 : 1. According to these theoretical results, relatively fast reaction times should be observed for particles at concentrations >50 n*M* that have been decorated with a high number of functional groups (>50). Many MRSw nanoparticles have had much fewer functional groups on their surface, corresponding with

reaction rates on the order of several minutes. These simulations can serve as general guidelines for navigating the parameter space of MRSw biosensor design. The results of studies conducted by Shapiro *et al*. have indicated that a measurement time of less than 10 min can be achieved for most nanoparticle preparations, and that that optimized sensors may allow for single-second measurement times.

1.6 Demonstrations of Magnetic Relaxation Switch Biosensors

The two most distinguishing properties of MRSws is their breadth of application and capability to detect target analytes in opaque samples. To date, MRSws have been used to detect DNA, RNA, proteins, enzymes, small molecules, hormones, bacterial cells, ions, eukaryotic cells, viruses, and antibodies (Table 1.1). Demonstrated sample matrices include whole-cell lysates, whole blood, serum, plasma, and urine (Table 1.2). The high tolerance for opaque samples and large amounts of background substances stems from the nonoptical nature of the magnetic resonance measurement and the properties of the superparamagnetic nanoparticles. For most other biosensor methods, nonspecific binding and other surface-mediated effects lead to background interference and necessitate a washing step. The breadth of application and high background tolerance of MRSws is unprecedented among biosensor technologies.

The following sections describe the variety of examples of magnetic relaxation switch biosensor technology. The examples have been roughly grouped by analyte type, with each being described in terms of the biosensor design, reported observa-

Table 1.1 Classes of analyte detected with MRSw assay technology.

Analyte	Reference(s)
Virus	[46]
Small molecules, peptides	[23, 63, 65]
DNA, mRNA	[1, 45, 46, 66, 67]
Peroxidases	[48]
Proteases	[45, 47, 68]
Telomerase	[66]
Methylase	[46]
Hormone	[69, 70]
Ions	[60, 71, 72]
Bacterial cells	[23, 48]
Proteins	[23, 45, 49, 61, 69]
Immunoglobulins	[19]
Eukaryotic cells	[23]

Table 1.2 Conduction of MRSw assays in various media to validate potential for minimal sample processing and measurement in dirty samples.

Specimen	Analyte	Reference
Whole-cell lysates	Nucleic acids	[45]
Cell culture media	Enzyme	[47]
10% blood	Bacterial cells	[48]
2% whole blood	Enzyme	[47]
Serum	Virus	[46]
50% whole blood	Protein	[73]
50% serum	Protein	[73]
50% plasma	Protein	[73]
50% urine	Protein	[73]

tions and conclusions, and likely future directions. In all cases, the reader is encouraged to investigate the primary literature for more detail.

1.6.1 Detecting Nucleic Acids

Magnetic relaxation switch biosensor technology was invented by a team led by Lee Josephson and Ralph Weissleder at the Center for Molecular Imaging Research at MGH. In a first report, the group presented details of a biosensor that was sensitive to the presence of a 24-base pair (bp) synthetic oligonucleotide sequence [1]. The biosensor design consisted of a solution composed of a 1 : 1 mixture of two types of CLIO that differed only by the sequence of the 36-bp oligonucleotides attached to the particle surface. An average of three synthetic oligonucleotides was attached to the nanoparticles by a standard heterobifunctional crosslinker reactive with the thiol-functionalized oligonucleotide and the amino-CLIO. When the target sequence was added to this solution, a change in turbidity was observed after 3 h, and a visible brown precipitate after 16 h. The T_2 relaxation rate, measured as a function of time, was shown to have decreased from 63 ms to 45 ms within 20 min of adding the target sequence (Figure 1.8). This change in T_2 was accompanied by a change in the size of suspended particles, from 53 ± 11 nm to 215 ± 19 nm, as measured by light scattering. As with most sizing data reported for MRSws, these data were measured using photon correlation light scattering. The change in particle size and T_2 was confirmed to be a result of the specific interaction between the target DNA sequence and the nanoparticle-bound oligonucleotides by adding non-complementary oligonucleotides, which resulted in no nanoparticle clustering nor any change in T_2; by gel electrophoresis, which showed no free DNA under nondenaturing conditions; and by temperature cycling, which showed that the nanoparticle clustering was reversible upon DNA melting and annealing [1].

One common means of characterizing the transverse relaxivity of SPIO is to report R_1 and R_2. For these particles, the addition of a complementary target DNA sequence led to a change in R_2, from 75 s^{-1} mM^{-1} to 128 s^{-1} mM^{-1}, but no change in the R_1 of 27 s^{-1} mM^{-1}. A linear dependence of measured T_2 values on the amount of nucleic acid analyte was reported (Figure 1.8), which was consistent with the above-discussed observations of particle size and relaxivity [20, 61]. Josephson *et al.* were able to detect tens of femtomoles of DNA in 1 ml, and suggested that amounts as low even as attomoles might be detected. This sensitivity was realized three years later when by tens of attomoles of DNA oligonucleotides were detected in a volume of 50 µl (0.2 p*M* concentration) after a incubation time of 40–60 min and a change in T_2 of 30 ms [66]. Grimm *et al.* compared the sensitivity and dose response of their MRSws to a standard telomeric repeat hybridization assay, which was a PCR-dependent, ELISA-based photometric assay. For their 54-mer telomeric repeat test sequence, these authors showed a very tight correlation (r^2 = 0.99) and equivalent sensitivity between the two methods. Grimm *et al.* concluded that the performance of MRSws matched that of PCR-independent assays, and was within the upper range of PCR-based assays. Additionally, MRSws have advantages over other DNA assays in that they are inherently quantitative, quick and simple to run, have no requirement for a solid phase, and inherently lack the PCR-related artifacts [66].

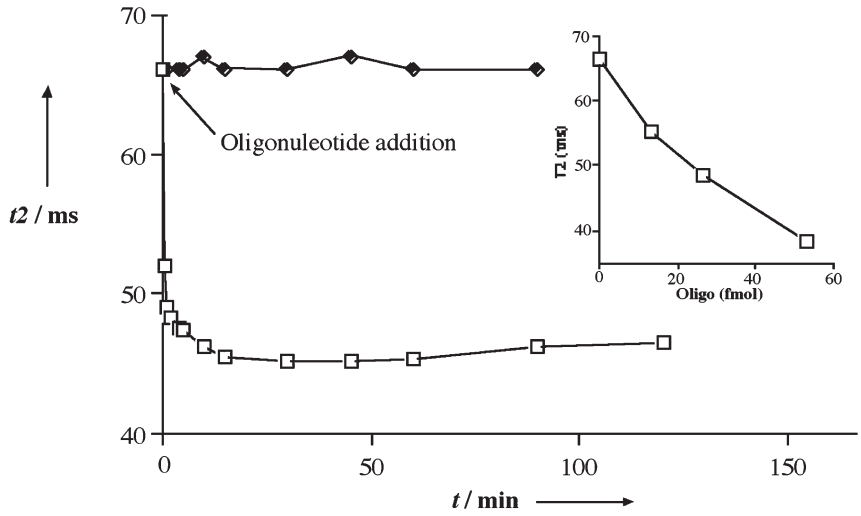

Figure 1.8 First demonstration of a magnetic relaxation switch biosensor. On the addition of femtomoles of single-stranded oligonucleotide the T_2 value was decreased by 20 ms due to nanoparticle clustering (□). No change in T2 was observed in the absence of complementary oligonucleotide (◆). T_2 values responded linearly with increasing amounts of analyte (inset). Original figure provided by Dr Lee Josephson, Center for Molecule Imaging Research, Massachusetts General Hospital, Boston, MA. Reproduced with permission from Ref. [1]; © 2001, Wiley-VCH Verlag GmbH & Co. KGaA.

Much of the early development of MRSw biosensors was pioneered by J. Manual Perez, while working in the groups of Lee Josephson and Ralph Weissleder. A follow-up study of the first report introducing the DNA MRSw sensor further demonstrated the potential for nucleic acid sensing, and also introduced the capability to detect single-base pair mismatches [45]. The DNA-functionalized nanoparticle sensors in this study transitioned from 45 nm diameter particles to 140 nm diameter clusters upon addition of complementary mRNA, with an accompanying change in T_2 of 20 ms. The change in T_2 was shown to be sensitive to single base insertions and mismatches, and to be completely eliminated for double base insertions or mismatches [45].

Perez *et al*. also demonstrated the detection of a target mRNA from a transfected green fluorescent protein (GFP) gene in various eukaryotic cell lines [45]. T_2-based measurements were shown to correlate with GFP activity for both extracted GFP mRNA and GFP mRNA directly in cell lysate after overnight incubation with the MRSw nanoparticles. The mRNA sensors were configured similarly to those previously used for DNA sensing. Two different 12 bp, thiolated oligonucleotides were attached to two different batches of nanoparticles. The target mRNA bridged the multivalent nanoparticles to induce nanoparticle assembly into clusters [45].

These initial reports on DNA-based sensing demonstrated that the addition of a bivalent biomolecular target to trivalent DNA–nanoparticle conjugates could induce nanoparticle clustering such that a change in T_2 corresponded linearly to the amount of added analyte. These initial studies also demonstrated that light-impermeable samples could be measured, and that the assay was homogeneous because it did not require a washing step.

A recent study conducted by the group of S. Pun at the University of Washington demonstrated the use of USSPIO for gene delivery [67]. These authors functionalized 10 nm USSPIO with polyethylenimine to form positively charged USSPIO that were ~24 nm in diameter. The addition of plasmid DNA led to the formation of 100 nm complexes and an increase in the T_2 relaxation time, from 600 ms to 1400 ms. The USSPIO complexation by plasmid DNA was shown to be inhibited by the addition of high salt concentrations, which disrupted the electrostatic interactions between the negatively charged DNA and positively charged nanoparticles. In this study, all measurements were obtained on a 3 T MRI scanner with a multi-spin echo pulse sequence [67]. Based on the outer sphere theory and the particle sizes, it would be expected that these particles would undergo a decrease in T_2 upon plasmid DNA complex formation; however, the nanoparticle concentration, magnetization, solution viscosity, and external magnetic field must have been such that the nanoparticles were in the visit-limited regime (Figure 1.7). The authors could have determined the cause of their increase in T_2 by obtaining T_2^* measurements of their nanoparticle solutions or T_2 measurements using different inter-echo delays. If T_2^* had been different than T_2, or if T_2 would have changed with inter-echo delay, then the visit-limited regime would have been confirmed. The USSPIO nanoparticles used by Park *et al*. were synthesized by a new formulation [36], which might also explain their unique behavior. The further characterization

of these nanoparticles, in terms of magnetic relaxation biosensing, will clarify the apparent discrepancy in the observed change in T_2.

1.6.2 Detecting Proteins

The general applicability of MRSw design introduced with DNA detection was quickly demonstrated for other types of analyte. A team led by J. M. Perez, whilst at MGH, demonstrated the capability of MRSws for measuring proteins by attaching biotinylated anti-GFP polyclonal antibodies to the surface of avidin-functionalized, dextran-coated SPIO nanoparticles. When GFP was introduced to a solution of anti-GFP decorated nanoparticles (45 nm diameter), there was a time- and dose-dependent response in the measured T_2 values. After about 30 min, however, the T_2 signal stabilized, indicating that the clustering reaction had reached completion. Concentrations of GFP as low as single nanomolar were detected with T_2 changes on the order of 10–20 ms [45].

Subsequent studies led by S. Taktak at MGH demonstrated that proteins could be detected by decorating the nanoparticles with a ligand for which a multivalent protein target had a selective binding affinity. This biosensor was created by functionalizing superparamagnetic nanoparticles with the ligand biotin, such that there were ~70 biotins per nanoparticle [61]. Addition of the tetravalent protein avidin led to nanoparticle clustering and a change in average particle size, from 30 nm to 150 nm. There was a concomitant increase in R_2, from 37 mM^{-1} s^{-1} to 132 mM^{-1} s^{-1}, which corresponded to a decrease in T_2 of 135 ms to 38 ms at an iron concentration of 0.2 mM. Taktak *et al.* extensively characterized the biophysical characteristics of their avidin MRSw system by introducing the concept of reporting analyte titrations in terms of the ratio of moles of analyte to moles of nanoparticles. According to their observations, the linear T_2 response for avidin spanned 0.4 and 1.2 avidin per nanoparticle equivalent. This approach, which relies on knowing the moles of iron atoms per nanoparticle, has been shown to be particularly useful for determining the point at which cluster formation leads to unstable aggregates [61, 69].

Taktak *et al.* reported T_2 and T_2^* measurements at 1.5 T, 4.7 T, and 9.4 T to confirm that their system was in the motional averaging regime, which was consistent with the linear dependence of R_2 on average particle size (Figure 1.7). From these data and the available theory, the group predicted that there was a decrease in cluster magnetization as the cluster size increased, and an accompanying increase in volume fraction of the clusters during agglomeration. These results were consistent with the clusters being porous fractal aggregates, as determined by other theoretical and experimental observations [59, 61]. The use of this avidin MRSw sensor for the development of new sensitivity enhancement methods is discussed in greater detail below.

The protein hormone human chorionic gonadotropin (hCG) was detected by antibody-decorated nanoparticles by a team in Michael Cima's laboratory at the MIT [69]. hCG functions as a clinical pregnancy marker, and is also overexpressed

by certain types of malignant cancers. G. Kim and coworkers used two monoclonal antibodies to generate a sandwich assay MRSw which consisted of two types of nanoparticle, each decorated with a different monoclonal antibody, mixed in a 1 : 1 ratio. The two monovalent antibodies bound to nonoverlapping epitopes on the hCG protein. Antibody–nanoparticle coupling was then conducted such that, on average, there were between 2 and 4.5 antibodies per nanoparticle. The addition of hCG to a 1 : 1 mixture of nanoparticles led to an increase in particle size as well as to a decrease in T_2. The limit of detection for this biosensor was 3.6 n*M* hCG, or 0.1 molecules of analyte per nanoparticle, after a 1 h incubation at 40 °C. As predicted by theoretical modeling [59], the nanoparticles with higher a antibody valency demonstrated greater sensitivity. These nanoparticle reagents also exhibited a time-dependent instability manifest by micron-sized cluster formation and precipitation. Interestingly, this instability was also greater at a higher antibody functionality. This same MRSw system was used to demonstrate detection of the multivalent protein A, for which there was a limit of detection of 1 μg ml^{-1} protein A, with an incubation time of 1 h at 40 °C. The limit of detection in terms of target molecules per nanoparticle was on the order of 0.1 to 1 for both hCG and protein A [69].

T2 Biosystems has demonstrated the potential for enhancing the sensitivity of a protein assay by using the hCG assay introduced by Kim *et al*. and improving its limit of detection to beyond that offered by commercial hCG diagnostic assays. Efforts aided by a fundamental theoretical understanding of agglomerative-based assays and novel signal enhancement methods provided a 3000-fold improvement in sensitivity over that reported by Kim *et al*. [74].

The demonstrations of protein detection with MRSws extended their range of application to include any biomolecular target for which an antibody is available. Because of the long history of commercial immunoassays, antibodies are available for thousands of medically relevant targets. The adaptability of MRSws to the immunoassay format will most likely enable new applications that rely on speed to obtain results, on simple sample processing, and also portability to the field of *in vitro* medical diagnostics.

1.6.3 Detecting Enzymes

Both, nucleic acid and protein sensing require a molecular binding step between the nanoparticle reagent and analyte. At an early stage of MRSw research, the range of application was extended to detect enzymatic targets, which cannot be sensed via molecular binding interactions.

The first demonstration of enzyme sensing with MRSw biosensors was made shortly after their first being reported. These studies, led by J. M. Perez, utilized two different nanoparticle–oligonucleotide conjugates which were created by functionalizing a monodisperse solution of nanoparticles with one of two complementary 18 bp strands of DNA [64]. When these two types of nanoparticle were mixed in an equimolar ratio, their oligonucleotides hybridized to create nanoparticle agglomerates that were crosslinked via double-stranded DNA (dsDNA). By design,

the crosslinking dsDNA contained a GATC sequence that could be selectively cleaved by *Bam*H1 endonuclease; indeed, the addition of *Bam*H1 to these nanoparticle clusters led to a change in T_2 from 32.3 ± 0.6 ms to 59.4 ± 0.4 ms as the nanoparticles transitioned from a clustered to a dispersed state. The increase in T_2 arose from the nanoparticles transitioning from ~350 nm clusters to ~55 nm dispersed particles [64]. This diameter-dependent T_2 response corresponded to the motional averaging regime (Figure 1.7), and has been termed a dispersive assay because analyte addition leads to agglomerate dispersion. This restriction endonuclease sensor introduced by Perez *et al.* represents the first reported dispersive MRSw assay. *Bam*H1 activity was confirmed as the source of this change in T_2 by means of gel electrophoresis on the nanoparticle reagents, and also by observing no change in T_2 when endonucleases with different selectivities were added. These results showed that, in cases where a chemical moiety exists that can be cleaved by an enzyme, that enzyme could be sensed by appropriately crosslinking nanoparticle clusters [64].

Perez *et al.* subsequently demonstrated how a simple enzyme sensor could be configured to detect other enzymatic targets, given the correct biochemical relationship. In these studies, the DNA involved in crosslinking the nanoparticles was methylated by the addition of dam methylase. The addition of a methylated-DNA-selective GATC endonuclease, *Dpn*1, then resulted in a T_2 change only when the sensor had been exposed to active dam methylase. Figure 1.9 shows that there was

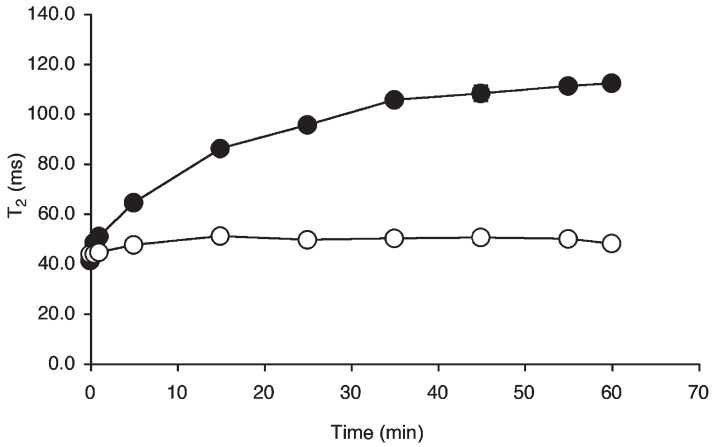

Figure 1.9 Demonstration of MRSw enzyme detection. SPIO nanoparticles were crosslinked via DNA hybridization to form nanoparticle aggregates. Aggregates that had been pretreated with methylase (●) exhibited an increase in T_2 over time after exposure to the endonuclease *Dpn*I, which selectively cleaves methylated double-stranded DNA. The increase in T_2 arose from nanoparticle dispersion. Untreated nanoparticle clusters (○) were not affected by the presence of *Dpn*I, and no change in T_2 was observed [64]. Original figure provided by Dr Lee Josephson, Center for Molecule Imaging Research, Massachusetts General Hospital, Boston, MA. Reproduced with permission from Ref. [64]; © 2002, American Chemical Society.

a change in T_2 from ~40 ms to ~120 ms over 1 h only for those nanoassemblies that had been methylated, thus demonstrating that dam methylase activity could be monitored via these nanoassemblies and *Dpn*1 [64]. Although no dose–response curve was reported for dam methylase activity, these results showed that MRSws could be configured to monitor enzymatic activity in both a direct and an indirect manner. This approach expands the types of target enzyme beyond those that can cut or cleave a crosslinking moiety. It also indicates that MRSws can be configured with coupled enzyme assays to further expand the types of enzyme and analyte that can be detected. These results also demonstrated that the internal architecture of nanoparticle clusters could be accessed by enzymes.

Shortly after the sensitivity of MRSw biosensors to endonuclease and methylase activities were reported, an analogous architecture was used to demonstrate protease detection. The same nanoparticle scaffold was decorated with either a biotinylated peptide containing the DEVD amino acid sequence, or with the protein avidin. A combination of these two types of particle led to cluster formation. Addition of the protease Caspase 3 to these clustered nanoparticles led to an increase in T_2, from 27 ms to 80 ms within 15 min [45]. In the presence of a Caspase 3 inhibitor, however, no change in T_2 was observed, thus validating the Caspase-specific T_2 response. These data further demonstrated that an enzyme activity-dependent T_2 signal could be generated by appropriately designed nanoparticle reagents [45].

Achieving true enzyme activity measurements requires a calibration curve to be obtained for a fixed reaction conditions and increasing amounts of protease. Another team at MGH, led by M. Zhao, achieved this goal and benchmarked their protease biosensor against fluorescence resonance energy transfer (FRET). Unlike the previous single-step methods, Zhao *et al*. used a two-step method for measuring protease activity [47]. The first step consisted of adding the protease of interest to a bi-biotinylated peptide that contained a cleavable amino acid sequence. After incubation at room temperature for 1 h, the second step was completed by adding the incubated sample to a solution of monodisperse avidin-coated nanoparticles. As the amount of intact bi-biotinylated peptide was inversely proportional to the protease activity, the extent of agglomeration and concomitant decrease in T_2 was, therefore, proportional to the protease activity. For the clinically relevant renin protease this assay had a similar limit of detection (69 ng ml^{-1} h^{-1} or 31 n*M* h^{-1} substrate hydrolyzed) to FRET, and had an approximately linear correlation plot with FRET over the 170 ms sampled by the T_2 measurement. If mouse whole blood was added to a volume fraction of 2% prior to signal readout, the FRET signal was completely lost, but the T_2 signal was unaffected. This demonstrated the capability for such measurements to be conducted in complex, opaque samples, and was the first reported example of a MRSw biosensor being used in diluted whole blood [47]. The fact that this two-step format did not require the direct conjugation of the peptide to the nanoparticles allowed much simplification of the reagent preparation, which in turn allowed the application of a single set of nanoparticle reagents to a broader range of protease targets.

The same two-step format was used to measure the trypsin and matrix metalloproteinase 2 (MMP-2) proteases, with limits of detection as low as $0.05\,\mu g\,ml^{-1}$ being demonstrated for trypsin. MMP-2 protease activity, which has been linked to metastasis and tumor angiogenesis, was successfully measured, using MRSws, in unpurified fibrosarcoma cell growth supernatant – conditions under which the standard MMP-2 fluorescence assay could not function [47]. This is a further example of the ability of MRSws to sample complex, turbid sample environments.

Another enzyme disease biomarker targeted by MRSw was telomerase, the activity of which may be elevated in tumor malignancies [66]. Magnetic relaxation switches were configured to monitor telomerase activity by decorating the nanoparticles with oligonucleotides that hybridized to the TTAGGG repeats synthesized by telomerase. After coupling four oligonucleotides per nanoparticle, the average nanoparticle diameter was 45 ± 4 nm. Addition of these nanoparticles to solutions containing telomeric repeats resulted in a biphasic change in T_2, with the rapid phase complete within 30 s, and the slow phase within 40–60 min. Although the exact mechanism that caused the biphasic change in T_2 was not fully characterized, the authors suggested that the nanoparticles might form pseudo-linear agglomerates along the telomeric repeats. Grimm *et al*. characterized this sensor in terms of a nucleic acid sensor that could also monitor telomerase activity [66] and, accordingly, the design provided an indirect means of measuring enzyme activity.

On realizing that enzyme activity could also be sensed by means of activating surface groups on nanoparticles to facilitate particle agglomeration, two different groups took this approach for measuring enzymes. In the first report, made by J. M. Perez at MGH, the activities of two different peroxidases – horseradish peroxidase (HRP) and myeloperoxidase (MPO) – were measured. The latter of these peroxidases has been shown to play a role in atherosclerosis and inflammation [75]. In order to detect these enzymes, either dopamine (for HRP) or serotonin (for MPO) was attached to create SPIO nanoparticles that could act as electron donors to the enzyme-catalyzed reduction of H_2O_2. After functionalizing the SPIO, each solution of nanoparticle reagent was monodisperse with a diameter of 50 nm and a ratio of ~40 reactive groups per particle. The reported R_1 was $25.8\,mM^{-1}\,s^{-1}$, and R_2 $67\,mM^{-1}\,s^{-1}$. In both cases, the peroxidase-catalyzed reduction of H_2O_2 converted the phenol group on dopamine or serotonin to a radical, which led to a radical-based crosslinking of the nanoparticles and the formation of nanoassemblies. Incubation with $0.9\,units\,\mu l^{-1}$ HRP for 2 h resulted in an increase in the diameter of dopamine-coated nanoparticles, from 50 nm to 440 nm, and a concomitant change in T_2 by 30 ms in a dose-dependent manner at 1.5 T. The MPO concentrations, which were as low as $0.003\,U\,\mu l^{-1}$, were measured in a MPO titration over one order of magnitude enzyme concentration and a range of change in T_2 between 20 ms to 300 ms at 1.5 T. At 0.5 T, the HRP sensor had a limit of detection of $0.1\,U\,ml^{-1}$, and a change in T_2 of 32 ms after a 2 h incubation at 4 °C. When H_2O_2 was not present, or a peroxidase inhibitor was added, there was no change in T_2 or nanoparticle cluster size, which indicated that the aggregate formation

was indeed due to peroxidase activity [75]. These two MRSw sensors represented the first example of agglomerative format sensing enzyme activity, and the first example of a covalently crosslinked nanoparticle assembly.

A similar approach was used by a collaborative group at MIT, the Brigham & Women's Hospital in Boston, the University of California at San Diego, and the Burnham Institute. This group, which was led by Todd Harris of the MIT, used an approach which differed from that of Zhao *et al.* to measure MMP-2 activity [68]. Rather than detecting MMP-2 by monitoring its proteolysis of a divalent peptide that has been activated to enable nanoparticle crosslinking, Harris *et al.* decorated two types of nanoparticle coated with biotin or avidin with a cleavable peptide attached to polyethyleneglycol (PEG). The bulky PEG groups inhibited binding between the biotin and streptavidin. The addition of MMP-2 led to cleavage of the peptide linker that attached PEG to the nanoparticles, thus exposing the biotin and avidin coatings so that the nanoparticles could self-assemble into clusters [68]. This indirect agglomeration approach was analogous to that used for detecting peroxidases, namely that the nanoparticle surface groups are activated by the presence of a target enzyme to facilitate particle agglomeration. Harris *et al.* reported a limit of detection of 170 ng ml^{-1} (9.4 U ml^{-1}) and a T_2 change of 150 ms at 4.7 T after a 3 h incubation. Their dispersed nanoparticles were 50 nm in diameter prior to coating with the PEG-peptide, and could be separated magnetically, which indicated that they were indeed different in nature to those used by Zhao *et al.* The MMP-2 cleavable peptide was eight residues long, and PEG chains of 2 kDa, 5 kDa, 10 kDa, and 20 kDa were tested. PEG sizes below 10 kDa did not inhibit biotin–avidin-mediated particle agglomeration in the absence of MMP-2 [68]. The sensitivity of this sensor was within the concentration range of MMP-2 typically found in tumor cells.

These demonstrations of enzyme detection showed not only the feasibility of detecting enzyme activity in both direct and indirect ways, but also the architectural flexibility of MRSws that would in turn allow designers to tailor these nanoparticle assays in a specific manner. Although, to date such flexibility has enabled the broad application of MRSws, as their development continues it is most likely that such flexibility that will lead to not only a wide range of applications but also excellent performance and sensitivity.

1.6.4
Detecting Viruses

One of the most impressive applications of MRSws has been the detection of the herpes simplex virus (HSV-1) and adenovirus (ADV) [46]. Due to the multivalent nature of these analytes, extremely low concentrations of virus could be detected in serum; in fact, a limit of detection as low as five viral particles in 10 µl was achieved, which is subattomolar in terms of viral concentration. These viral sensors were constructed by decorating superparamagnetic nanoparticles with monoclonal antibodies by means of a protein G coupling method. The monovalent antibodies bound selectively to coat proteins on the surface of either HSV-1 or ADV. The

addition of virus lead to a change in particle dispersity and size, from a monodisperse solution of nanoparticles with 46 nm diameter to a polydisperse solution containing both 46 nm particles and particles of up to 550 nm, as measured by light scattering. The aggregate size of 550 nm was consistent with a superassembly of nanoparticles and HSV or ADV viruses, as the ADV virus is ~80 nm in diameter [76] and the HSV-1 virus ~125 nm in diameter [77]; large aggregates were observed using atomic force microscopy (AFM) [46]. The addition of virus to the nanoparticle sensors led to a change in T_2 of up to 45 ms over the course of 100 min. For HSV-1, the limit of detection was 100 viral particles per 100 µl, and for ADV it was five viral particles per 10 µl. In both cases, the T_2 values were measured at 1.5 T. On a commercial instrument at 0.47 T, a similar dose and time-dependent response in T_2 was observed following the addition of viral particles [46].

In their report, Perez *et al.* noted that MRSw biosensors offered several advantages over current PCR-based viral detection methods. These included speed of obtaining results, ease of use, no requirement for enzymatic amplification, and a greater robustness. These attributes of MRSw biosensors distinguish them from many diagnostic and biosensing technologies. The most significant conclusion of the viral-based sensors has been that an increased target valency can provide greater sensitivity, a hypothesis which was later expanded upon by Hong *et al.* at MGH to provide means of increased sensitivity [20].

1.6.5 Detecting Small Molecules

Although the multivalency of viral targets provided an extremely high sensitivity for target quantification, small-molecule targets – unlike viral targets – are not multivalent. In fact, a major challenge exists to design molecule-affinity agents (e.g., antibodies) to attach in even a bivalent fashion to many small molecules. Despite this limitation, agglomeration-based assays can be configured to detect monovalent analytes by means of a competitive–dispersive format. In this case, a bivalent or multivalent binding agent is used to cluster nanoparticles that have been decorated with a derivative of the target small molecule. If the desired small molecule is present in the sample, it will compete with the modified nanoparticles from the multivalent binding agent, leading to dispersion of the nanoparticles in an amount which is proportional to the concentration of the target.

The first demonstration of a MRSw capable of detecting small molecules was made by Tsourkas *et al.*, where the D stereoisomer of phenylalanine (D-Phe) was selectively detected with background L phenylalanine (L-Phe) [63]. This report was also the first example of a nonenzymatic dispersive MRSw biosensor assay. The biosensor was capable not only of detecting a small molecule but could do so in a stereoselective manner; that is, it could distinguish D-Phe from L-Phe. Tsourkas *et al.* accomplished this by decorating superparamagnetic nanoparticles with a derivative of D-Phe in a manner that conserved the stereochemistry of D-Phe, and loaded the particles with 15 D-Phe per nanoparticle [63]. The addition of a bivalent antibody that binds D-amino acids (anti-D-AA) led to nanoparticle clustering. The

subsequent introduction of free D-Phe led to displacement of the antibody–nanoparticle complex and a dispersion of the clustered nanoparticles. For the conditions sampled, the T_2 changed by more than 100 ms for 500 μ*M* D-Phe and by about 10 ms for 5 μ*M* D-Phe. The group reported a limit of detection of 0.1 μ*M* and a coefficient of variation (CV) of <5% [63]. The kinetics of this sensor was relatively rapid (Figure 1.10), which was in general agreement with kinetic theory for dispersive assays [59]. Figure 1.10 also shows that almost two orders of magnitude in dynamic range were achieved for this MRSw. Additionally, interference studies showed that the cross-reactivity to L-Phe was 0.075% [63]. As with all MRSw biosensors, the selectivity of the MRSw was determined by the selectivity of the binding agent, which was anti-D-AA antibody in this case.

The competitive–dispersive format was used for three other small-molecule MRSws used to measure glucose, the hemagglutinin (HA) peptide, and folic acid [65]. For glucose, the nanoparticles were decorated with two glucosamine hydrochlorides and pre-complexed with the glucose-binding protein, concanavalin A. The addition of glucose led to a quantitative change in T_2 of over 40 ms within 50 min, using a kinetic reading, and a limit of detection of <50 mg dl^{-1} for glucose. For the detection of the influenza HA peptide, the nanoparticles were functionalized with HA peptide and pre-clustered with anti-HA antibody. This sensor had a T_2 change of >150 ms over a time of 100 min, and a limit of detection of <50 n*M* HA. The folic acid biosensor consisted of nanoparticles decorated with folic acid, and an anti-folic acid antibody that pre-clustered the nanoparticles. The addition of folic acid led to T_2 changes over 120 ms with reaction completion times of almost 20 min and a limit of detection of <3 n*M* [65].

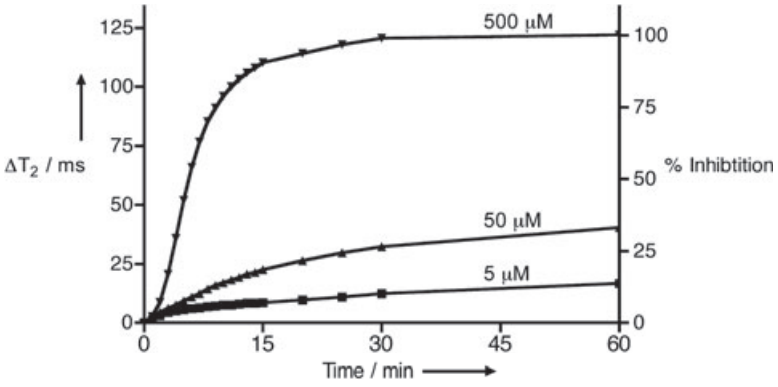

Figure 1.10 A stereoselective, small-molecule, dispersive magnetic relaxation switch biosensor. The addition of D-Phe to a solution of D-Phe-functionalized CLIO nanoparticles and antibody that binds D amino acids (anti-D-AA) led to a dispersion of the antibody–nanoparticle complex as a function of time. The rate and magnitude of the change in T_2 increased with increasing amounts of D-Phe [63]. Original figure provided by Dr Lee Josephson, Center for Molecule Imaging Research, Massachusetts General Hospital, Boston, MA. Reproduced with permission from Ref. [63]; 2004, © Wiley-VCH Verlag GmbH & Co. KGaA.

A comparison of these three small-molecule assays demonstrates the wide range of assay performance that can be achieved with MRSw biosensors. The HA assay was 80-fold more sensitive than the glucose assay, while the folic acid assay was 1000-fold more sensitive than the glucose assay [65]. Although these authors did not offer any explanation for these differences in assay performance, the variation further confirmed that the flexibility in MRSw design could be used to tailor biosensors for specific diagnostic applications. The characteristics of the folic assay were surprisingly similar to the commercial diagnostic assay for folic assay, thus validating the capabilities of this technology to meet commercial specifications [78].

The primary motivation of Sun *et al.* was to demonstrate the reversible nature of MRSws. This was achieved by containing the nanoparticle sensor solution inside semipermeable Spectra/Por tubing. Increasing and decreasing the amount of analyte, by altering its concentration in the surrounding solution, led to a corresponding change in the nanoparticle agglomeration state. Due to the membrane pore size, the nanoparticles could not diffuse across the membrane, whereas the small-molecule analytes could diffuse. In the case of the glucose sensor, the concentration of glucose was cycled six times, and this was reflected in the corresponding changes in T_2 values [65]. The reversible nature of these three sensors was made possible by the equilibrium that can exist between the dispersed and clustered nanoparticles, due to the binding characteristics of the functionalized nanoparticles and binding protein or antibodies.

These types of sensor show great promise for applications that require the continuous monitoring of target analyte levels, such as real-time environmental sensors or implantable sensors [65]. The potential for reversible sensing for implantable MRSws was introduced by the laboratories of Michael Cima and Robert Langer, using the protein biosensor for hCG and a polydimethylsiloxane (PDMS) device. The PDMS unit was designed to contain the nanoparticle reagents between two polycarbonate membranes, each of which had 10 nm pores that allowed passage of the hCG target but contained the nanoparticle reagents. The feasibility of this device for real-time sensing was confirmed by observing changes in T_2 inside the reservoirs due to changes in hCG levels in the surrounding solution, by means of MRI [70]. Subsequent studies with this device should demonstrate its use for detecting *in vivo* circulating biomarkers. In this respect, studies conducted by Daniel and coworkers have demonstrated the unique potential of MRSws in applications that require continuous monitoring. Given the appropriate instrumentation, applications can be envisioned where implanted MRSw devices are measured in a simple, portable format. Indeed, such instrumentation and applications are currently under development at T2 Biosystems and in the laboratories of both Michael Cima and Robert Langer.

1.6.6
Detecting Ions

The capability of extending the possible target analytes for MRSw biosensors to ions has been demonstrated by two ingenious experiments, both of which have

used the same general approach. This consisted of separating selective ion-binding moieties between separate nanoparticles, such that the presence of the target ion led to self-assembly of the ion-binding groups and concomitant nanoparticle agglomeration.

The first demonstration of ion detection was made by a team at the MIT in Alan Jasanoff's laboratory, led by T. Atanasijevic [60, 71]. Atanasijevic and colleagues used the reversible calcium-dependent protein–peptide interaction of the calmodulin protein and a calmodulin-binding peptide to endow calcium-dependent agglomeration upon superparamagnetic iron oxide nanoparticles. Streptavidin-coated nanoparticles (from Miltenyi Biotech) were decorated with either the calmodulin protein or with one of the two calmodulin-binding peptides, the kinase M13 peptide or kinase RS20 peptide. These nanoparticles were significantly different in terms of size and relaxivity from those used by the teams at MGH, having an iron oxide core size of 10 nm, a Fe_2O_3 content of 50% prior to protein conjugation, and with a distribution of average diameter of between 20 nm and 100 nm after conjugation to the targeting groups. In addition, because of their larger size and iron content, their R_2 was much higher at $410\,\mathrm{m}M^{-1}\,\mathrm{s}^{-1}$ [60, 71].

The addition of calcium to a mixture of the calmodulin-functionalized nanoparticles and kinase-peptide-functionalized nanoparticles led to an increase in the average nanoparticle diameter by a factor of two, and an increase in T_2 from 27 ms to 50 ms [60]. The increase in T_2 upon cluster formation arose from the bulk of the nanoparticles being in the visit-limited regime, or the right-hand side of the T_2 versus diameter curve in Figure 1.7. This was supported by the observation of echo-time dependence of the measured T_2 values and by the authors' calculations [60].

The addition of a calcium chelator (e.g., EDTA) reversed the biosensor reaction and caused the calcium-clustered nanoparticles to disperse. As expected, reaction rates for nanoparticle dispersion were much faster than those for nanoparticle agglomeration, the latter requiring an incubation time of up to 60 min [60, 71]. The team led by T. Atanasijevic elegantly showed that the calcium concentration range over which the sensor responded could be tuned by altering the affinity of the particle-attached binding groups. The mid-point of the response curve, or EC_{50}, for wild-type calmodulin was $1.4\,\mu M$, while that for a variant of calmodulin was $10\,\mu M$. The total response range for the former was $0.1–1.0\,\mu M$, which spans typical *in vivo* calcium concentrations, and that for the latter was $1–100\,\mu M$. These two sensors could be combined to achieve an optimal dynamic range, sensitivity, and selectivity for a given application [60, 71].

A more general approach for ion detection with nanoparticles was introduced by S. Taktak in the Josephson laboratory at MGH [72]. Taktak *et al.* showed that the surface chemistry used for ion-selective electrodes could be adapted for use with MRSw biosensors. The group targeted CLIO nanoparticles by functionalization with diglycolic anhydride, which complexes Ca^{2+} at molar ratios of 2 : 1 and 3 : 1. Because calcium can induce the self-assembly of multiple diglycolic anhydride moieties, the addition of Ca^{2+} to the targeted nanoparticles led to cluster formation and a decrease in T_2, from 200 ms to 50 ms for the lowest concentration

of nanoparticles used by Taktak *et al.* As has been shown for the avidin protein biosensor, the calcium concentration range over which there was a T_2 response could be tuned by changing the concentration of nanoparticles. The addition of K^+, Li^{2+} and NH^{4+} did not elicit a change in T_2, but the addition of Mg^{2+} led to a change in T_2 which was similar to that for Ca^{2+}. This was a result of the cross-reactivity of the chelating group attached to the nanoparticles. When Ca^{2+} was added to the targeted nanoparticles in the presence of EDTA, no change in T_2 was observed, consistent with a Ca^{2+}-dependent T_2 response. The addition of EDTA to Ca^{2+}-induced clusters led to a dispersion of the clusters, and exhibited the reversible nature of this assay system. Taktak *et al.* suggested a range of chelating groups used by ion-selective electrodes that could be adapted in a similar manner to create MRSw biosensors that were sensitive to magnesium and copper [72]. This approach to ion sensor design greatly expands the range of possible target ions for MRSw biosensors due to the available chemistries used for electrochemical ion detection. Despite the commercial availability of many ion-detection technologies, the ability to detect ions with MRSw not only enables the creation of more sophisticated *in vivo* biosensors [72] but also expands the available test menu for *in vitro* biosensing.

1.6.7 Detecting Cells

One of the most recent developments in MRSw technology has been the demonstration of a capability for cell detection. This can be achieved either via indirect means, such as detecting nucleic acids or excreted biomarkers which are associated with the presence of a cell type, or by direct means, such as cell staining. Many indirect cell detection methods, including molecular testing such as PCR and immunoassays, have moderate turn-around times and costs. In contrast, direct cell detection methods, such as cell culture or cell sorting, may have slow turn-around times and high costs [79]. MRSw-based indirect and direct cell detection would allow for a low-cost, rapid turn-around time quantitative cellular testing. Whilst indirect cell detection could be achieved using many of the assays discussed above, two different groups have recently extended the use of MRSws to direct cell detection. In both cases, biomarkers expressed on the surface of the desired cell were targeted with appropriately decorated superparamagnetic nanoparticles.

The first group to report cell detection was that of J.M. Perez, at the University of Central Florida. In these studies, the group targeted the organism *Mycobacterium avium paratuberculosis* (MAP) by conjugating anti-MAP antibodies to the surface of superparamagnetic nanoparticles that were 70 nm in diameter, and had an R_2 of 320 $mM^{-1}s^{-1}$ [48]. These characteristics were much more similar to those employed by A. Jasanoff's group than by the Josephson and Weissleder groups at MGH. The titration of these particles with MAP cells led to larger changes in T_2 at lower MAP concentrations than at higher MAP concentrations. The maximum observed change in T_2 occurred at 6–8 ms after incubation times of 30–60 min at 37 °C. Although this change in T_2 approaches the run-to-run precision limit

observed by another research group [19], the reported limit of detection was 40 colony-forming units (CFU) in 10 µl of milk, and 40 CFU in 20 µl of blood [48].

The nature of the response curve observed by the authors was unlike any previously reported response curves. MRSw response curves typically approach a change in T_2 of zero as the concentration of the target decreases. For this sensor, the change in T_2 approached a maximum as the concentration of analyte approached zero. In order to explain this abnormal binding curve, the authors hypothesized that the change in T_2 was derived from a mechanism which was different than that of nanoparticle agglomeration. According to their hypothesis, the change in T_2 was a function of the proximity between superparamagnetic nanoparticles on the surface of the target cells. Accordingly, at high cell concentrations, the nanoparticles were distributed between many cells, thereby having a more distant inter-particle proximity. In addition, at low cell concentrations the nanoparticles were distributed between only a few cells, and thus had a close inter-particle proximity. Although the group validated the specificity of their observed T_2 response to the desired target cell, they failed to conduct any independent tests and controls to validate their proposed mechanism for cell detection. Consequently, further investigations will be required to confirm the source of these unprecedented T_2 response curves.

More recently, a group in the Weissleder laboratory reported the detection of intact whole cells with MRSw biosensors; these included bacterial cells from *Staphylococcus aureus* and a variety of mammalian cells. The detection of *S. aureus* was achieved by derivatizing nanoparticles with vancomycin, which binds to peptide moieties on the bacterial cell wall. Following a 15 min incubation of the vancomycin–nanoparticles with increasing amounts of *S. aureus* (from 10^0 to 10^3 cells), a linear dose–response curve with a change in T_2 of 30 ms was observed [23]. The group also reported a limit of detection of 10 CFU in 10 µl, and verified that the nanoparticles were indeed attaching to the cell surface by using TEM and energy dispersive X-ray spectrometry (EDS). This observation, in combination with a fairly extensive set of controls, indicated that the T_2 sensitivity arose from a vancomycin-dependent interaction between the nanoparticles and the cell surfaces [23].

Lee *et al.* also demonstrated the detection of mammalian cells and cell biomarker profiling. For this, mouse macrophages were detected via a multistep method that consisted of incubating the cells with fluorescein-conjugated, dextran-coated nanoparticles. Following a 3 h incubation at 37 °C to allow the macrophages to take up the dextran-coated nanoparticles, the nanoparticle-labeled cells were separated from any unbound nanoparticles by multiple washing. The resultant solution, after calibration with a hemocytometer, was used to determine the limit of detection for nanoparticle-labeled mouse macrophages; this proved to be a single cell in 10 µl, or 100 cells per ml. This multistep approach differed from the method used to detect *S. aureus*, in that the unbound nanoparticles were separated from the cell-immobilized nanoparticles. A similar multistep approach was used to profile different types of cancer cell by means of various antibody-targeted nanoparticles [23]. Although mammalian cell detection required the inclusion of washing

steps to remove any free magnetic nanoparticles, the application of tailored fluidic and separation methods will probably permit the necessary washing steps required for apparent single-step mammalian cell detection.

Although cells can be detected with MRSws via many secondary markers, cell detection via direct surface binding will undoubtedly broaden the "menu" of available tests so as to include very powerful methods such as profiling cellular expression pathways. Ultimately, many of these should enable the use of low-cost and portable applications for circulating tumor cell analysis, as well as other diagnoses that currently are possible only by utilizing cell-sorting technologies.

1.7 Methods Development

Although much of the available MRSw-related literature has demonstrated the versatility of the technology in detecting a wide range of analytes in many sample types, a subset has introduced new methods of reagent preparation and characterization, biosensor configuration, and relaxation rate measurements; these various methods are detailed in the following sections.

1.7.1 Reagent Synthesis, Preparation, and Characterization

An understanding of the physical characteristics of a nanoparticle system can be critical for the successful design of an MRSw system. During their early studies, both Shen and Jung and the coworkers relied on TEM measurements and knowledge of the iron oxide crystal form in order to determine the number of iron atoms per nanoparticle iron core (this is also referred to as the nanoparticle core weight) [17, 24, 25, 30]. Later studies performed by F. Reynolds at MGH led to the introduction of a simpler method for determining the nanoparticle core weight which used viscosity measurements and light scattering. Four parameters were used to determine nanoparticle core weight:

- The partial specific volume, as determined by a range of viscosity measurements.
- The volume of a single nanoparticle, as determined by diameter measurements with light scattering.
- The weight per volume of nanoparticles.
- The weight per volume of iron [80].

This method was easier to implement than TEM due to its use of more common laboratory equipment and faster turn-around time. Because the CLIO core weight depends on the conditions used in nanoparticle synthesis, it is important to determine the core size for new nanoparticle formulations. Knowledge of the nanoparticle core weight is necessary when calculating the average number of functional groups per nanoparticle, with cores sizes of 2000 and 8000 irons atoms per core having been reported [30, 80].

Another essential component when designing MRSws is the attachment of an appropriate targeting group, so as to endow proper binding selectivity and sensitivity upon the nanoparticles. Because the iron oxide nanocrystal is entrapped within an aminated polysaccharide coating, many common chemical crosslinking strategies can be employed. However, a specific bioconjugation method has been shown to greatly influence the performance of targeted SPIO nanosensors by altering the number and nature of the targeting groups per nanoparticle [81]. Several different types of bioconjugation strategies have been used to activate the nanoparticles. For example, a team led by E. Y. Sun demonstrated the use a CLIO variant termed a magnetofluorescent nanoparticle, which consisted of two fluorescein isothiocyanate (FITC) molecules attached to amino-CLIO nanoparticles, to demonstrate the rapid development of nanoparticle libraries. For these particles, the R_1 was $21\,mM^{-1}s^{-1}$ and R_2 $62\,mM^{-1}s^{-1}$, while the FITC absorbed at 494 nm with an extinction coefficient of $73\,mM^{-1}cm^{-1}$ [82]. Small molecules were attached via a variety of reactive handles to the ~62 free amines per nanoparticle. The small-molecule reactive handles included anhydride, amino, hydroxyl, carboxyl, thiol, and epoxy. Each of the resulting conjugates had unique functionality in terms of MRSw biosensor response and macrophage uptake, demonstrating that the specificity and selectivity of a nanoparticle conjugate is determined by the surface functionality [82]. Other crosslinkers that have been to date used include Pierce Biotech (Rockford, IL, USA) heterobifunctional crosslinking agents such as *N*-succinimidyl 3-(2-pyridyldithio)-propionate (SPDP) and *N*-succinimidyl-*S*-acetylthioacetate (SATA), generic activating and crosslinking agents such as succinimidyl iodoacetate, 1-ethyl-3-[3-dimethylaminopropyl]carbodiimide hydrochloride (EDC or EDAC), *N*-hydroxysulfosuccinimide (Sulfo-NHS), and antibody-specific coupling reagents such as protein G. In another series of studies, a team led by E.Y. Sun demonstrated the use of azide-alkyne reactions (known as "click chemistry") for the attachment of targeting groups. Sun's group demonstrated that stable alkyne- or azido-functionalized CLIO nanoparticles could be generated for click chemistry attachment to a variety of appropriately functionalized small molecules [83]. Unfortunately, the details of bioconjugation methods are beyond the scope of this chapter; thus, the reader is referred to the original data (as cited) and to more comprehensive sources [84].

Regardless of the specific coupling method used, a number of critical issues must be considered in particle design. These include the activity and number of targeting groups attached on each nanoparticle – an issue was explored by a team led by D. Hogeman at MGH. In these studies, it was shown that nonselective oxidative coupling of the protein transferrin led to an inferior biosensor performance when compared to that coupled with the heterobifunctional linker, SPDP [81]. The SPDP linker led to a fourfold increase in the number of transferrin molecules per nanoparticle, and also preserved the activity of the transferrin protein, leading to an increased binding affinity for their cellular target. The reduced affinity of transferrin when coupled to nanoparticles via oxidative coupling most likely arose from the nonselective nature of the coupling, which may

lead to cross-reactions. Directed coupling with SPDP led to increased affinities and increased binding densities, as had been shown previously for other applications [81]. The increased affinity and valency of the particles led to a 16-fold increase in the performance of the nanoparticle sensor for cell internalization. Although these studies focused on targeting superparamagnetic nanoparticles for cell encapsulation with endosomes, the dependence of performance on the bioconjugation method may be generalized for nanoparticle-based sensors [81]. Similar observations were made for a cell-targeted biosensor that used multivalent-RGD-decorated nanoparticles to bind cell-surface integrin proteins [85].

Several other reports have been made of the methods used for coupling targeting groups to polymer-coated, superparamagnetic nanoparticles. Some of these have utilized bifunctional nanoparticles, such as fluorescently labeled CLIO nanoparticles, to conduct parallel synthesis and high-throughput screening (HTS) on large numbers of nanoparticles for cell recognition applications [86]. Robotic systems have also been used to conjugate 146 different small molecules (<500 Da) to fluorescently functionalized CLIO nanoparticles [87], with the average coupling ratios being 60 small molecules per nanoparticle. These nanoparticle conjugates were also screened for eukaryotic cellular uptake, thus demonstrating that nanoparticle surface modification can target nanoparticles not only to different cell types but also to different physiological states of the same cell type [88].

1.7.2 Measurement and Sensitivity Enhancement Methods

A variety of reports have introduced new methods for measuring MRSw assays to improve measurement accuracy and sensitivity. One such report, made by a team led by S. Taktak, utilized a biotin–avidin model system to examine the physical characteristics of the MRSw biosensor system [61]. The model system was created from biotinylated nanoparticles that agglomerated in the presence of the tetrameric protein avidin. Upon the addition of avidin, the T_2 changed from 100 ms to 40 ms after incubation at room temperature for 1 h. Taktak *et al.* showed that the overall average cluster size increased linearly with the addition of avidin, and that the observed R_2 depended linearly on the average particle size [61]; these findings were similar to previous results which demonstrated avidin-coated particles and a bi-biotinylated peptide [47]. This relationship corresponded to these nanoparticles being within the motional averaging regime (i.e., on the left side of the curve in Figure 1.7). This correlated well with observations for other MRSw systems [69], and the proposed porous fractal nature of nanoparticle aggregates [60, 61]. Based on these observations, Taktak *et al.* predicted that, as cluster size increases there should be a decrease in the cluster magnetization and increases in the cluster volume fraction [61].

In addition to exploring the fundamental physics that underlie MRSw, Taktak *et al.* introduced some new methods for improving assay performance. The first method consisted of tuning the dynamic range and sensitivity of the assay by

changing the concentration of nanoparticles in solution. For the avidin biosensor, the sensitivity of the T_2 response increased and dynamic range, or the target concentration range over which the biosensor was responsive, decreased at lower nanoparticle concentrations. Conversely, at higher nanoparticle concentrations the sensitivity decreased and the dynamic range increased. This observation indicated that the dynamic range and sensitivity of an assay could be tuned by means of the nanoparticle concentration [61].

The second method introduced by Taktak *et al.* provided a means for controlling nanoparticle precipitation. As discussed in the present and subsequent reports, under certain conditions nanoparticle clusters can become unstable in solution and precipitate [49, 61, 69]. Precipitation, which leads to an increase in T_2, is most often caused by the over-titration of analyte, which leads to extremely large clusters [61, 69]. This may be detrimental to MRSw measurements because, in this case, it leads to a different change in T_2 than would be expected for target-induced clustering. Fortunately, T_1 can be used as an independent marker for particle precipitation, because T_1 depends only on the total amount of soluble iron in solution, and not on the clustering state of the nanoparticles [61]. Taktak *et al.* demonstrated that T_1 remained constant when T_2 changed from analyte-induced nanoparticle clustering, a similar observation to that made for the first MRSw biosensor [1]. Upon over-titration, both the T_2 and T_1 increased, indicating a loss of iron from solution and a shift of the assay conditions to outside the linear response curve. Taktak and coworkers subsequently recommend a workflow to validate that an assay is within the linear response curve by taking both T_2 and T_1 measurements [61]. Although this workflow was initially intended for manual sample preparation, it could be integrated into an automated fluidic handling system for applications that require minimal user interaction.

A third method introduced by Taktak *et al.* was to monitor the coefficient of variation between multiple T_2 measurements, and thus to determine if the biosensor solution was within the linear response range, or if the reagents had precipitated or degraded in some way. It was shown that, when three T_2 measurements were obtained within several minutes, the coefficient of variation between measurements was increased dramatically when particle precipitation or instability had occurred. The utility of this approach was analogous to that of the T_1 measurement system, in that it allowed for an independent verification that the measured T_2 value could be used to obtain the concentration of target via a calibration curve [61]. These methods are important when independently validating the integrity of biosensor measurements.

The methods introduced by Taktak *et al.* were later extended at T2 Biosystems to demonstrate how splitting a sample between multiple nanoparticle reagent chambers could provide validated results, and also expand the biosensor dynamic range [49]. These methods were demonstrated with the same avidin-sensitive biotinylated MRSw architecture. The addition of avidin led to nanoparticle clustering and a change in T_2 from 350 ms to 175 ms. The methods introduced by Taktak *et al.* were extended to include a control for variations in the background T_2, which can be observed in complex samples such as blood due to variations in the

physico-chemical properties that may affect T_2, such as hemoglobin content and viscosity. Sample-to-sample variations could be controlled by splitting the sample between two nanoparticle reagent chambers, such that the detection chamber contained nanoparticles sensitized to the target analyte, while the reference chamber contained identical nanoparticles that were not sensitized to the target analyte. The addition of a sample would then lead to a difference in T_2 between the two chambers only when the analyte was present (Figure 1.11). Accordingly, the calibration curve would be determined from the difference in T_2 between the sample and control chambers [49].

Splitting the sample between multiple chambers can also be used to expand the dynamic range by preloading chambers with different concentrations of nanoparticles. This would allow for higher sensitivity measurements at low target concentrations, and simultaneous lower sensitivity measurements over a much wider dynamic range. In time, this approach will most likely diminish the proportion of inaccurate readings due to biosensor prozoning, and also avoid the user having to prepare sequential dilutions of the sample [49].

These approaches for validating acquired T_2 values can be applied by measuring multiple samples sequentially with a single detector [61], or by acquiring T_2 measurements from two samples simultaneously with a single detector [49]. The T2 Biosystems team demonstrated that a single detection coil could be used to measure the T_2 of two samples at the same time by means of a tailored bi-exponential fit method. This method was shown to accurately measure two T_2 values as long as they were at least 21% different. This approach can also expand the number of simultaneous measurements from a single detection coil, thus increasing the number of possible tests on a given hardware system [49]. However, the

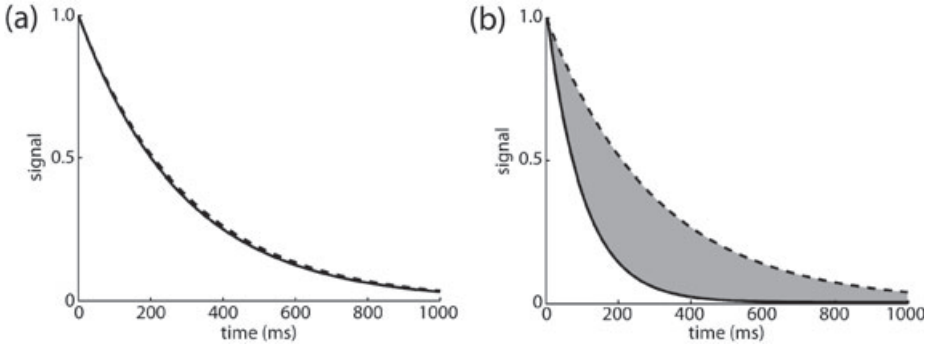

Figure 1.11 Background variations in T_2 can be controlled by splitting the sample between two chambers: one chamber that contains particles sensitized to the target analyte (solid line), and one that contains particles *not* sensitized to the target analyte (dashed line). (a) In the absence of analyte, the two chambers will have identical relaxation curves and no change in T_2 will be reported; (b) In the presence of analyte, the chamber with sensitized nanoparticles will have a different T_2 from that of the reference chamber (shaded area). The quantitative change in T_2 can be obtained by curve fitting [49].

methods for addressing background variations in T_2 and expanding the dynamic range can be applied in a variety of detection coil configurations, including the multiplexed detection hardware introduced by H. Lee in the Weissleder group, which will be discussed in greater detail below [23].

A team led by I. Koh in the Josephson laboratory at MGH has demonstrated that a combination of methods can be used to increase the projected sensitivity of a MRSw assay by five orders of magnitude [19]. The model system used to demonstrate these methods consisted of superparamagnetic nanoparticles or microparticles decorated with the Tag peptide, which is from the HA of the human influenza virus. The addition of an anti-Tag antibody led to clustering of the peptide-decorated particles. The method employed CLIO nanoparticles that were 30 nm in diameter, did not settle, had 20–30 attached peptides per nanoparticles, an R_2 of $50\,s^{-1}\,mM^{-1}$, a magnetization of 86.6 emu g^{-1} Fe, with 8000 iron atoms per nanoparticle, and a concentration of 2.8×10^{-9} for a T_2 of 100 ms. The microparticles used were 1000 nm in diameter, settled less than 5% in aqueous solution [20], had 3×10^5 peptides per particle, an R_2 of $43\,s^{-1}\,mM^{-1}$, a magnetization of $105\,emu\,g^{-1}$ Fe, 2.8×10^9 Fe atoms per particle, and a concentration of 5.1×10^{-15} for a measured T_2 of 100 ms. Koh *et al.* characterized the performance of these nanoparticles in terms of EC_{50} and projected sensitivity. For simplicity, the projected sensitivity will be discussed at this point [19].

When the nanoparticles (NP) and microparticles (MP) were titrated with anti-Tag antibody, the T_2 values decreased for the NP and increased for the MP, which corresponded to the NP being within the motional averaging regime and the MP being within the visit-limited regime [19]. The NP and MP exhibited projected sensitivities of 26 n*M* and 0.41 n*M*, respectively. The >60-fold increase in sensitivity for MP arose from the larger mass of iron per unit conjugated peptide that corresponded to a much larger R_2 relaxivity on a per particle basis [19, 20]. Previous studies with viral targets have suggested that crosslinking agents with a greater binding valency could lead to increased sensitivity [46], and this was confirmed by Koh *et al.*, who increased the valency of their bivalent antibody target to a tetravalent target with the addition of an antibody that selectively bound the Fc region of the anti-Tag antibody. This increased the projected sensitivity for the MP to 0.0002 n*M*, or by a factor of 2000 [19].

The use of MP allows for an additional method for sensitivity enhancement. Investigations conducted by Baudry and coworkers in Paris showed that the reaction rate between reactive groups on magnetic MP could be greatly accelerated by magnetic field-induced self-assembly of the MP into linear chains [21–23] or fractal agglomerates [20]. For Koh *et al.*, an alignment of the magnetic dipoles of individual MP during incubation in a 0.47 T bench-top magnet led to spatial confinement of the MP and increased reaction kinetics. During incubation in the magnet, the T_2 increased due to the linear self-assembly of the MP. In order to distinguish the magnetic-field induced T_2 changes from analyte-induced T_2 changes, the sample was removed from the magnet for a few minutes prior to T_2 measurement. If analyte was present, the MP remained clustered, but if no analyte was present then the MP would disperse due to Brownian motion. This method, termed

magnetic aggregation, resulted in seven- and two-fold increases in projected sensitivity when used with and without valency enhancement, respectively. Magnetic aggregation cannot be applied to NP-based assays due to the attractive forces between the magnetic dipoles of individual NP being much smaller than the forces of Brownian motion [20]. Although it has not been exactly determined, the increase in sensitivity for MP-based assays from magnetic aggregation most likely arose from the more rapid kinetics due to the confinement and resultant close proximity of reactive surfaces. The method of magnetic aggregation has also been applied to solution viscosity measurements by monitoring the rate of change in T_2 over the course of MP aggregation and dispersion phenomena [20].

The most important lesson derived from the findings of Koh *et al*. was that many different methods can be used to increase MRSw sensitivity. For example, Koh *et al*. reported a sensitivity enhancement over the basic NP biosensor configuration of 10^5 due to the use of MP, valency enhancement, and magnetic aggregation. As they showed, many sensitivity enhancement methods are multiplicative in their effect, providing for highly sensitive, tailored results for a given assay. The ideal combination of methods will depend on the particular requirements for a biosensing application, which include reagent stability, time to results, dynamic range, and sensitivity.

1.8 Micro-NMR of Magnetic Relaxation Switch Biosensors

A key component to enabling the successful application of magnetic relaxation switch biosensors is to tailor, in appropriate fashion, the detection platform to the setting in which it will be used. A variety of settings would greatly benefit from a universal detection technology such as MRSw biosensors. These include applications such as biowarfare first responders and home testing, both of which require highly mobile, robust, and perhaps handheld, instruments; applications such as biomarker discovery, which require automation and high throughput; and applications such as health clinics or doctor's offices, which require a compact, user-friendly bench-top unit. Although the majority of commercial magnetic resonance detection instruments are very large, recent progress in magnetic resonance technology engineering has demonstrated scalability and portability. In this section, we will introduce the magnetic readers that have been used to obtain MRSw biosensor measurements, summarize the recent progress in magnetic resonance instrumentation that has enabled the development of miniaturized detectors for biosensor applications, and also provide an update on progress towards developing portable MRSw biosensor readers.

An alternative measurement approach has been proposed to circumvent the low sample measurement throughput of current bench-top systems by a team at MGH, led by D. Hogemann. This group demonstrated the use of a 1.5 T magnetic resonance scanner and T_2-weighted magnetic resonance images to provide HTS for nanoparticle-based reagents. By using this method, up to 1920 samples could be

measured in 50 min by obtaining T_2-weighted spin echo images from each sample in six 384-well plates (only 320 samples per plate were measured due to the limited field of view of the detection coil) [89]. Although other research groups have used this approach to characterize MRSw biosensors, the associated cost for scanner time and challenges in quantitatively relating the T_2 values obtained at 1.5 T to those measured at lower fields will likely limit the widespread use of this approach. A possible high-throughput development platform for MRSw biosensors would consist of a bench-top unit with a throughput of between tens and thousands of samples per hour. This would enable T_2 measurements to be obtained with detector specifications that matched those of portable readers, and also to reduce the associated cost to the level of other bench-top analytical instrumentation.

Recent advances in the field of portable and micro NMR have provided the technological breakthroughs in miniaturized magnetic resonance detectors and magnets for developing truly portable and integrated diagnostic measurement devices. These breakthroughs have included new types of detection coil fabrication methods that allow for submicroliter detection volumes and submillimeter sizes in selenoidal coils that are either hand-wound [90–92] or machine-wound [93, 94]; alternatively, planar detection coils would allow straightforward integration with silicon microchannels [95, 96] and microfluidic systems [97, 98]. Additional breakthroughs have demonstrated that nanoliter volumes can be detected with high sensitivity using microfabricated coils [99–101], and high-sensitivity micro-coils of novel architectures [102].

These advances in miniaturized detection coil design and fabrication have been applied to magnetic resonance instruments with permanent magnets at fields near 0.5 T [103, 104]. Recently, a group at the University of New Mexico and Sandia National Laboratories, led by L. Sillerud, demonstrated the use of a microfabricated detection coil and permanent magnet system for the detection of iron oxide MP [105]. Sillerud *et al*. demonstrated the use of a 550 µm outer diameter solenoidal microcoil (264 nl) in combination with a highly homogeneous (0.06 ppm) 1.04 T permanent magnet (weight > 50 kg) to detect the presence of micron-sized superparamagnetic iron oxide nanoparticles, which are similar to oral-SPIO that are routinely used for magnetic separations. The presence of magnetic particles was detected by detecting a change in the T_2^*, which can be measured via the decay rate of the time domain signal, or by a change in the linewidth of the frequency domain signal [105]. Although the detection of analyte was not demonstrated, it is likely that such systems will be developed for detecting cells that have been tagged with superparamagnetic microparticles. The ultimate aim would be to attain single cell sensitivity by decreasing the size of the detection coil.

A much smaller magnet than that used in the above-described study is currently under development [106], although the use of a CPMG pulse sequence to measure T_2, rather than measuring T_2^*, would inherently allow for measurements in a less uniform magnet, which would be smaller and less expensive. The application of pulse sequences such as CPMG, which enable accurate measurements to be made in highly inhomogeneous magnetic fields, will be critical in allowing magnetic resonance to enter the filed of applications that require low cost and portability.

Recent improvements and optimizations of the CPMG sequence have permitted perhaps the most extreme example of magnetic resonance relaxation measurements in inhomogeneous fields, namely oil well logging, which involves obtaining measurements external to a single-sided magnet and planar detection coil inserted deep within an oil well [107].

In recent years, magnet design technology has progressed to move magnetic resonance measurements outside of the conventional high-field magnet laboratory by creating customized, portable magnets. Many of the current developments in magnetic resonance hardware and methods have been directed towards spectroscopic and imaging measurements that require much higher magnetic field uniformities than the relaxation measurements used for MRSw. The technical advances that result from efforts towards creating portable magnetic resonance spectroscopy and imaging systems will directly benefit MRSws. Other applications that have benefited from such progress include on-site materials characterization [108–114], oil well logging [107], foods analyses [115, 116], portable tendon injury scanning [117], imaging [118–121], and magnetic resonance spectroscopy [122–124] and relaxometry measurements outside of enclosed permanent magnet systems (often referred to as "ex-situ NMR"). Many of these advances have been made with single-sided magnets for the measurement of bulky samples that cannot be fitted within an enclosed permanent magnet assembly [106, 109, 113, 115, 121]. Although such architectures are not directly relevant to most MRSw applications, the fabrication and measurement methods pioneered for these applications will undoubtedly become essential in the design of miniature magnets for diagnostic readers. One example of these advances in magnet hardware, which has directly benefited the development of smaller magnetic resonance instruments, is that of Halbach magnet design [125]. Halbach magnets for magnetic resonance usually consist of multiply oriented discrete magnetic blocks that are used to achieve a single homogeneous "sweet spot" at the region of the magnet occupied by the detection coil. These magnets have been used for both bench-top, single-sided [113, 126] and enclosed [104, 127, 128] magnetic resonance applications.

A team in the Weissleder group has recently demonstrated the use of a downsized magnet, downsized detection coils, and downsized spectrometer components for the detection of MRSws. This team, led by H. Lee, built a 0.49 T relaxometer from a palm-sized magnet and planar microcoils [23], with some of the spectrometer components being integrated onto a printed circuit board (PCB). When using this system, the authors reported an 80-fold increase in mass sensitivity for a MRSw model system. In accordance with microcoil NMR sensitivity improvements of mass-limited samples, this increase in mass sensitivity arose almost entirely from the decrease in detection volume (from ~300 µl to ~5 µl). The absolute sensitivity of the microcoils in terms of the signal-to-noise ratio of the water signal was ~10 after 64 scans, which was much lower than that of commercial bench-top systems [23]. This decreased performance most likely arose from the less efficient planar microcoil detector and less homogeneous magnetic field used in the miniaturized system; by comparison, the commercial bench-top system had a much more sensitive solenoid coil and a more homogeneous magnet.

However, for a given amount of sample, there is an optimal RF microcoil geometry for maximum sensitivity, the optimization of which will most likely allow for these microcoil sensitivity limitations to be overcome. Most importantly, the system built by Lee *et al*. proved to be a powerful demonstration of the portability and ease of use available to MRSw applications.

An additional benefit of miniaturizing the magnetic resonance detection system is a greater multiplexing capability. Because the homogeneous region of a magnet is limited, the smaller volume occupied by microcoils can allow for multiple detection coils within a single magnet. Lee *et al*. utilized this approach by constructing an array of eight microfabricated planar detection coils for their miniaturized magnetic resonance instrument (Figure 1.12a). The eight coils were connected to a single-channel spectrometer by means of a multiplexer switch, and the system was used to detect eight biomarkers from single samples in parallel for both diabetes and cancer biomarker panels (Figure 1.12) [12]. These studies represented a powerful demonstration of how MRSw might provide users with readings for a panel of biomarkers relevant to a specific diagnostic condition, such as cancer. Because of the breadth of the demonstrated target analytes for MRSw, such panels would be capable of spanning an unprecedented range of analyte classes (e.g., cellular, protein, molecular, protein, enzymatic, and therapeutic, etc.), thus yielding a virtually limitless set of test menus for specific applications.

Whilst the studies of H. Lee elegantly demonstrated the potential for downsized detection coils and magnets for MRSw biosensors [23], a subsequent and complementary effort by the team of Y. Liu *et al*. at Harvard, in the laboratory of Donhee

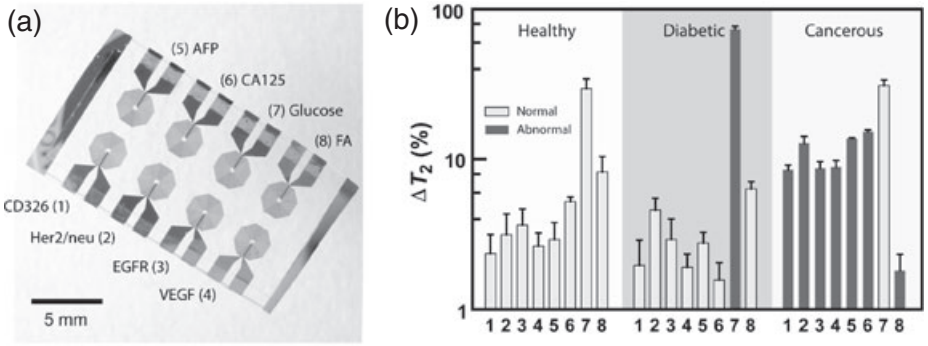

Figure 1.12 Demonstration of MRSw multiplexing by means of microcoils. (a) A planar microcoil array of eight detection coils fabricated from electroplated copper on a glass substrate. Each microcoil was positioned under a sample well containing nanoparticles sensitized to a different analyte; (b) Spiked serum samples representing diabetic or cancer sera were analyzed by aliquoting the sample between the detection coils and measuring the change in T_2 relative to normal sera. This approach demonstrated the potential of MRSw for monitoring multiple biomarkers from a single sample simultaneously [23]. This figure was a generous gift from Dr Hakho Lee, Center for Systems Biology, Massachusetts General Hospital, Boston, MA.

Ham, demonstrated the capability of significantly downsizing the spectrometer. Although, prior to the studies of Y. Liu *et al*., single PCB spectrometers had been demonstrated [129–131], in order for MRSw biosensor detectors to achieve the size, cost, and range of applications of conventional portable electronics, it was necessary to downsize the entire magnetic resonance spectrometer to the scale of an integrated circuit (IC). The studies of Liu *et al*. represented the most significant steps towards achieving this, by showing that the heart of a spectrometer – the transceiver – could be hosted on an IC. The CMOS design of Liu *et al*. was able to transmit and receive RF pulses to and from a detection coil [132], although a similar performance was reported (in terms of sensitivity) to that achieved by Lee *et al*. with a transceiver built from off-the-shelf, discrete components. The RF transceiver of Liu *et al*. has proved to be one of the smallest transceiver units reported to date [132]. The integration of other spectrometer components should enable an extremely small complete magnetic resonance spectrometer.

These breakthroughs in magnetic resonance detection instrumentation suggest that this technology can be tailored to biosensor applications that require downsized and portable readers. In fact, efforts are currently under way at T2 Biosystems to produce completely integrated, portable MRSw biosensor readers that would most likely consist of a relaxometer (magnet, detection coil, and spectrometer) as well as a user interface, power source, and connection to external data networks. Depending on the application, the MRSw biosensor reader may also provide sample incubation, disposable cartridge reading and handling, and fluidics actuation. Recently, a team from T2 Biosystems, led by P. Prado, introduced a shoebox-sized, fully integrated relaxometer that weighs less than 4 kg [73], and consists of a 0.5 T magnet, spectrometer, operating system, touchscreen user interface, and DC power input. Additional investigations at T2 Biosystems have demonstrated the capability of further downsizing a 0.5 T magnet unit to be 10 000-fold smaller than a commercial bench-top magnet and probehead units [73], by means of an extremely low-cost magnet and coil architecture. Moreover, when using this prototype magnet and microcoil, MRSw biosensor-mediated measurements of hCG protein were conducted at femtomolar levels, in nanoliter sample volumes. Due to the range of application of these MRSw biosensor tests, and the recent and ongoing breakthroughs in the downsizing of instruments, continued development will in time surely enable the deployment of MRSw biosensors within virtually any setting, and for virtually any target.

Acknowledgments

The author acknowledges the T2 Biosystems team and expresses his gratitude to those who provided helpful feedback for this chapter, including Lee Josephson, Sonia Taktak, Hakho Lee, Pablo Prado, Vicky Demas, Kim Foster, and Sonia Kumar. The author also acknowledges the many hours of relinquished time from Sherri, Sophia, and Henry Lowery.

References

1 Josephson, L., Perez, J.M. and Weissleder, R. (2001) Magnetic nanosensors for the detection of oligonucleotide sequences. *Angewandte Chemie, International Edition in English*, **40**, 3204–6.

2 Perez, J.M., Josephson, L. and Weissleder, R. (2004) Use of magnetic nanoparticles as nanosensors to probe for molecular interactions. *Chembiochem*, **5**, 261–4.

3 Li, W.-H., Fraser, S.E. and Meade, T.J. (1999) A calcium-sensitive magnetic resonance imaging contrast agent. *Journal of the American Chemical Society*, **121**, 1413–14.

4 Loui, A.Y., Huber, M.M., Ahrens, E.T., Rothbacher, U., Moats, R., Jacobs, R., Fraser, S.E. and Meade, T.J. (2000) In vivo visualization of gene expression using magnetic resonance imaging. *Nature Biotechnology*, **18**, 321–5.

5 Aime, S., Botta, M., Eliana, G. and Terreno, E. (2000) A p(O2)-responsive MRI contrast agent based on the redox switch of manganese(II/III)-porphyrin complexes. *Angewandte Chemie, International Edition in English*, **39**, 747–50.

6 Nivorozhkin, A.L., Kolodzieg, A.F., Caravan, P., Greenfield, M.T., Lauffer, R.B. and McMurry, T.J. (2001) Enzyme-activated Gd^{3+} magnetic resonance imaging contrast agents with a prominent receptor-induced magnetization enhancement. *Angewandte Chemie, International Edition in English*, **40**, 2903–6.

7 Hanaoka, K., Kikuchi, K., Urano, Y., Narazaki, M., Yokawa, T., Sakamoto, S., Yamaguchi, K. and Nagano, T. (2002) Design and synthesis of a novel magnetic resonance imaging contrast agent for selective sensing of zinc ion. *Chemistry & Biology*, **9**, 1027–32.

8 Aime, S., Castelli, D.D. and Terreno, E. (2002) Novel pH-reporter MRI contrast agents. *Angewandte Chemie, International Edition in English*, **41**, 4334–6.

9 Aime, S., Castelli, D.D., Fedeli, F. and Terreno, E. (2002) A paramagnetic MRI-CEST agent responsive to lactate concentration. *Journal of the American Chemical Society*, **124**, 9364–5.

10 De Leon-Rodriguez, L.M., Ortiz, A., Weiner, A.L., Zhang, S., Kovacs, Z., Kodadeck, T. and Sherry, A.D. (2002) Magnetic resonance imaging detects a specific peptide-protein binding agent. *Journal of the American Chemical Society*, **124**, 3514–15.

11 Lowery, T.J., Rubin, S.M., Ruiz, E.J., Spence, M.M., Winssinger, N., Schultz, P.G., Pines, A. and Wemmer, D.E. (2003) Applications of laser-polarized ^{129}Xe to biomolecular assays. *Magnetic Resonance Imaging*, **21**, 1235–9.

12 Schroeder, L., Lowery, T.J., Hilty, C., Wemmer, D.E. and Pines, A. (2006) Molecular imaging using a targeted magnetic resonance hyperpolarized biosensor. *Science*, **314**, 446–9.

13 Gilchrist, R.K., Medal, R., Shorey, W.D., Hanselman, R.C., Parrott, J.C. and Taylor, C.B. (1957) Selective inductive heating of lymph nodes. *Annals of Surgery*, **146**, 596–606.

14 Thorek, D.L., Chen, A.K., Czupryna, J. and Tsourkas, A. (2006) Superparamagnetic iron oxide nanoparticle probes for molecular imaging. *Annals of Biomedical Engineering*, **34**, 23–8.

15 Pankhurst, Q.A., Conolly, J., Jones, S.K. and Dobson, J. (2003) Applications of magnetic nanoparticles in biomedicine. *Journal of Physics D: Applied Physics*, **36**, R167–81.

16 Josephson, L., Bigler, J. and White, D. (1991) The magnetic properties of some materials affecting MR images. *Magnetic Resonance in Medicine*, **22**, 204–8.

17 Jung, C.W. (1995) Surface properties of superparamagnetic iron oxide MR contrast agents: ferumoxides, ferumoxtran, ferumoxsil. *Magnetic Resonance Imaging*, **13**, 675–91.

18 Josephson, L., Lewis, J., Jacobs, P., Hahn, P.F. and Stark, D.D. (1988) The effects of iron oxides on proton relaxivity. *Magnetic Resonance Imaging*, **6**, 647–53.

19 Koh, I., Hong, R., Weissleder, R. and Josephson, L. (2008) Sensitive NMR sensors detect antibodies to influenza. *Angewandte Chemie, International Edition in English*, **47**, 4119–21.

20 Hong, R., Cima, M.J., Weissleder, R. and Josephson, L. (2008) Magnetic microparticle aggregation for viscosity determination by MR. *Magnetic Resonance in Medicine*, **59**, 515–20.

21 Baudry, J., Rouzeau, C., Goubault, C., Robic, C., Cohen-Tannoudji, L., Koenig, A., Bertrand, E. and Bibette, J. (2006) Acceleration of the recognition rate between grafted ligands and receptors with magnetic forces. *Proceedings of the National Academy of Sciences of the United States of America*, **103**, 16076–8.

22 Cohen-Tannoudji, L., Bertrand, E., Baudry, J., Robic, C., Goubault, C., Pellissier, M., Johner, A., Thalmann, F., Lee, N.K., Marques, C.M. and Bibette, J. (2008) Measuring the kinetics of biomolecular recognition with magnetic colloids. *Physical Review Letters*, **100**, 108301.

23 Lee, H., Sun, E., Ham, D. and Weissleder, R. (2008) Chip-NMR biosensor for detection and molecular analysis of cells. *Nature Medicine*, **14**, 869–74.

24 Jung, C.W., Weissleder, R., Josesphson, L., Bengele, H. and Brady, T.J. (1996) Physical properties of MION-46 and AMI-27, Presented at the Society of Magnetic Resonance Fourth Scientific Meeting, New York, 1996.

25 Jung, C.W. and Jacobs, P. (1995) Physical and chemical properties of superparamagnetic iron oxide MR contrast agents: ferumoxides, ferumoxtran, ferumoxsil. *Magnetic Resonance Imaging*, **13**, 661–74.

26 Josephson, L., Groman, E.V., Menz, E., Lewis, J.M. and Bengele, H. (1990) A functionalized superparamagnetic iron oxide colloid as a receptor directed MR contrast agent. *Magnetic Resonance Imaging*, **8**, 637–46.

27 Weissleder, R., Elizondo, G., Wittenburg, J., Rabito, C.A., Bengele, H.H. and Josephson, L. (1990) Ultrasmall superparamagnetic iron oxide: characterization of a new class of contrast agents for MR imaging. *Radiology*, **175**, 489–93.

28 Whitesides, G.M., Kazlauskas, R.J. and Josephson, L. (1983) Magnetic separations in biology. *Trends in Biotechnology*, **1**, 144–8.

29 Franzred, M., Siemann-Herzberg, M., Hobley, T.J. and Thomas, O.R. (2006) Protein purification using magnetic adsorbent particles. *Applied Microbiology and Biotechnology*, **70**, 505–16.

30 Shen, T., Weissleder, R., Papisov, M., Bogdanov, A. and Brady, T.J. (1993) Monocrystalline iron oxide nanocompounds (MION): physiochemical properties. *Magnetic Resonance in Medicine*, **29**, 599–604.

31 Weissleder, R., Lee, A.S., Fischman, A.J., Reimer, P., Tueng, S., Wilkinson, R., Callahan, R. and Brady, T.J. (1991) MR antibody imaging: polyclonal human IgG labelled with polymeric iron oxide. *Radiology*, **181**, 245–9.

32 Weissleder, R., Bogdanov, A. and Papisov, M. (1992) Drug targeting in magnetic resonance imaging. *Magnetic Resonance Quarterly*, **8**, 55–63.

33 Weissleder, R., Lee, A.S., Khaw, A., Shen, T. and Brady, T.J. (1992) Antimyosin-labeled monocrystalline iron oxide allows detection of myocardial infarct: MR antibody imaging. *Radiology*, **182**, 381–5.

34 Tartaj, P., Morales, M.D.P., Veintemillas-Verdaguer, S., Gonzalez-Carreno, T. and Serna, C.J. (2003) The preparation of magnetic nanoparticles for applications in biomedicine. *Journal of Physics D: Applied Physics*, **36**, R182–97.

35 Jun, Y.-W., Lee, J.-H. and Cheon, J. (2008) Chemical design of nanoparticle probes for high-performance magnetic resonance imaging. *Angewandte Chemie, International Edition in English*, **47**, 5122–35.

36 Park, J., An, K., Hwang, Y., Park, J.-G., Noh, H.-J., Kim, J.-Y., Park, J.-H., Hwang, N.-M. and Hyeon, T. (2004) Ultra-large-scale synthesis of monodisperse nanocrystals. *Nature Materials*, **3**, 891–5.

37 Laurent, S., Forge, D., Port, M., Roch, A., Robic, C., Van der Elst, L. and Muller, R.N. (2008) Magnetic iron oxide nanoparticles: synthesis, stabilization, vectorization, physiochemical characterizations, and biological applications. *Chemical Reviews*, **108**, 2064–110.

38 Gupta, A.K. and Gupta, M. (2005) Synthesis and surface engineering of iron oxide nanoparticles for biomedical applications. *Biomaterials*, **26**, 3995–4021.

39 Petri-Fink, A. and Hofmann, H. (2007) Superparamagnetic iron oxide nanoparticles (SPIONs): from synthesis to in vivo studies–a summary of the synthesis, characterization, in vitro, and in vivo investigations of SPIONs with particular focus on surface and colloidal properties. *IEEE Transactions on Nanobioscience*, **6**, 289–97.

40 Wunderbaldinger, P., Josephson, L. and Weissleder, R. (2002) Crosslinked iron oxides (CLIO): a new platform for the development of targeted MR contrast agents. *Academic Radiology*, **9** (Suppl. 2), S304–6.

41 Josephson, L., Tung, C.-H., Moore, A. and Weissleder, R. (1999) High-efficiency intracellular magnetic labeling with novel superparamagnetic-tat peptide conjugates. *Bioconjugate Chemistry*, **10**, 186–91.

42 Singer, J.M. and Plotz, C.M. (1956) The latex fixation test. I. Application to the serologic diagnosis of rheumatoid arthritis. *The American Journal of Medicine*, **21**, 888–92.

43 Price, C.P. and Newman, D.J. (1997) *Principles and Practice of Immunoassay*, MacMillan Reference, London.

44 Van Weemen, B.K. and Shuurs, A.H.W. (1971) Immunoassay using antigen-enzyme conjugates. *FEBS Letters*, **15**, 232–6.

45 Perez, J.M., Josephson, L., O'Loughlin, T., Högemann, D. and Weissleder, R. (2002) Magnetic relaxation switches capable of sensing molecular interactions. *Nature Biotechnology*, **20**, 816–20.

46 Perez, J.M., Simeone, F.J., Saeki, Y., Josephson, L. and Weissleder, R. (2003) Viral-induced self-assembly of magnetic nanoparticles allows the detection of viral particles in biological media. *Journal of the American Chemical Society*, **125**, 10192–3.

47 Zhao, M., Josephson, L., Tang, Y. and Weissleder, R. (2003) Magnetic sensors for protease assays. *Angewandte Chemie, International Edition in English*, **42**, 1375–8.

48 Kaittanis, C., Naser, S.A. and Perez, J.M. (2007) One-step, nanoparticle-mediated bacterial detection with magnetic relaxation. *Nano Letters*, **7**, 380–3.

49 Lowery, T.J., Palazzolo, R., Wong, S.M., Prado, P.J. and Taktak, S. (2008) Single-coil, multisample, proton relaxation method for magnetic relaxation switch assays. *Analytical Chemistry*, **80**, 1118–23.

50 Hahn, E.L. (1950) Nuclear induction due to free Lamour precession. *Physical Review*, **77**, 297–8.

51 Carr, H.Y. and Purcell, E.M. (1954) Effects of diffusion on free precession in nuclear magnetic resonance experiments. *Physical Review*, **94**, 630–8.

52 Meiboom, S. and Gill, D. (1958) Modified spin-echo method for measuring nuclear relaxation times. *Review of Scientific Instruments*, **29**, 688–91.

53 Muller, R.N., Gillis, P., Moiny, F. and Roch, A. (1991) Transverse relaxivity of particulate MRI contrast media: from theories to experiments. *Magnetic Resonance in Medicine*, **22**, 178–82.

54 Weisskoff, R.M., Zuo, C.S., Boxerman, J.L. and Rosen, B.R. (1994) Microscopic susceptibility variation and transverse relaxation: theory and experiment. *Magnetic Resonance in Medicine*, **31**, 601–10.

55 Bulte, J.W.M., Brooks, R.A., Moskowitz, B.M., Bryant, L.H. and Franck, J.A. (1998) T1 and T2 relaxometry of monocrystalline iron oxide nanoparticles (MION-46L): theory and experiment. *Academic Radiology*, **5** (Suppl. 1), S137–40.

56 Brooks, R.A. (2002) T2-shortening by strongly magnetized spheres: a chemical exchange model. *Magnetic Resonance in Medicine*, **47**, 388–91.

57 Gillis, P., Moiny, F. and Brooks, R.A. (2002) On T2-shortening by strongly magnetized sphere: a partial refocusing model. *Magnetic Resonance in Medicine*, **47**, 257–63.

58 Brooks, R.A., Moiny, F. and Gillis, P. (2001) On T2-shortening by weakly magnetized particles: the chemical exchange model. *Magnetic Resonance in Medicine*, **45**, 1014–20.

59 Shapiro, M.G., Atanasijevic, T., Faas, H., Westmeyer, G.G. and Jasanoff, A. (2006) Dynamic imaging with MRI contrast agents: quantitative considerations. *Magnetic Resonance Imaging*, **24**, 449–62.

60 Atanasijevic, T., Shusteff, M., Fam, P. and Jasanoff, A. (2006) Calcium-sensitive MRI contrast agents based on superparamagnetic iron oxide nanoparticles and calmodulin. *Proceedings of the National Academy of Sciences of the United States of America*, **103**, 14707–12.

61 Taktak, S., Sosnovik, D., Cima, M.J., Weissleder, R. and Josephson, L. (2007) Multiparameter magnetic relaxation switch assays. *Analytical Chemistry*, **79**, 8863–9.

62 Roch, A., Gossuin, Y., Muller, R.N. and Gillis, P. (2005) Superparamagnetic colloid suspensions: water magnetic relaxation and clustering. *Journal of Magnetism and Magnetic Materials*, **293**, 532–9.

63 Tsourkas, A., Hofstetter, O., Hofstetter, H., Weissleder, R. and Josephson, L. (2004) Magnetic relaxation switch immunosensors detect enantiomeric impurities. *Angewandte Chemie, International Edition in English*, **43**, 2395–9.

64 Perez, J.M., O'Loughlin, T., Simeone, F.J., Weissleder, R. and Josephson, L. (2002) DNA-based magnetic nanoparticle assembly acts as a magnetic relaxation nanoswitch allowing screening of DNA-cleaving agents. *Journal of the American Chemical Society*, **124**, 2856–7.

65 Sun, E.Y., Weissleder, R. and Josephson, L. (2006) Continuous analyte sensing with magnetic nanoswitches. *Small*, **2**, 1144–7.

66 Grimm, J., Perez, J.M., Josephson, L. and Weissleder, R. (2004) Novel nanosensors for rapid analysis of telomerase activity. *Cancer Research*, **64**, 639–43.

67 Park, I.-K., Ng, C.-P., Wang, J., Chu, B., Yuan, C., Zhang, S. and Pun, S.H. (2008) Determination of nanoparticle vehicle unpackaging by MR imaging of a T2 magnetic relaxation switch. *Biomaterials*, **29**, 724–32.

68 Harris, T.J., von Maltzahn, G., Derfus, A.M., Ruoslahti, E. and Bhatia, S.N. (2006) Proteolytic actuation of nanoparticle self-assembly. *Angewandte Chemie, International Edition in English*, **45**, 3161–5.

69 Kim, G.Y., Josephson, L., Langer, R. and Cima, M.J. (2007) Magnetic relaxation switch detection of human chorionic gonadotrophin. *Bioconjugate Chemistry*, **18**, 2024–8.

70 Daniel, K.D., Kim, G.Y., Vassiliou, C.C., Jalili-Yazdi, F., Langer, R. and Cima, M.J. (2007) Multi-reservoir device for detecting a soluble cancer biomarker. *Lab on a Chip*, **7**, 1288–93.

71 Atanasijevic, T. and Jasanoff, A. (2008) Preparation of iron oxide-based calcium sensors for MRI. *Nature Protocols*, **2**, 2582–9.

72 Taktak, S., Weissleder, R. and Josephson, L. (2008) Electrode chemistry yields a nanoparticle-based sensor for calcium. *Langmuir*, **24**, 7596–8.

73 Lowery, T.J., Demas, V. and Prado, P.J. (2008) Portable and implantable magnetic resonance based molecular diagnostics, oral presentation 49th ENC 2008, March, 9–14, Pacific Grove, CA.

74 Kumar, S., Mozeleski, B., Wong, S., Taktak, S., Lowery, T.J. and Foster, K. Particles 2008. Magnetic relaxation diagnostics using superparamagnetic nanoparticles, May 2008, Orlando, FL. Available at: http://www.nanoparticles.org/Particles2008/.

75 Perez, J.M., Simeone, F.J., Tsourkas, A., Josephson, L. and Weissleder, R. (2004)

Peroxidase substrate nanosensors for MR imaging. *Nano Letters*, **4**, 119–22.

76 Bil, I., Rybka, B. and Wozniak, M. (2008) Adenoviral infection–pathomechanism and diagnostics. *Advances in Clinical and Experimental Medicine*, **17**, 91–9.

77 Spencer, J.V., Newcomb, W.W., Thomsen, D.R., Homa, F.L. and Brown, J.C. (1998) Assembly of the herpes simplex virus capsid: preformed triplexes bind to the nascent capsid. *Journal of Virology*, **72**, 3944–51.

78 Olson, J., Ishikawa, F., Rowan, M. and Sallinen, J. (2006) Performance of the anemia panel assays (ferritin, folate and vitamin B12) on the Abbott AxSYM® instrument. American Association of Clinical Chemistry meeting, July 23–27, Chicago, Illinois. Available at: http://www.abbottdiagnostics.es/ciencia/pdf/18.pdf.

79 Moss, M.W., Carella, A.V., Provost, V. and Quinn, T.C. (1996) Comparison of absolute CD4+ lymphocyte counts determined by enzyme immunoassay (TRAx CD4 test kit) and flow cytometry. *Clinical and Diagnostic Laboratory Immunology*, **3**, 371–3.

80 Reynolds, F., O'Loughlin, T., Weissleder, R. and Josephson, L. (2005) Method of determining nanoparticle core weight. *Analytical Chemistry*, **77**, 814–17.

81 Högemann, D., Josephson, L., Weissleder, R. and Basilon, J.P. (2000) Improvement of MRI probes to allow efficient detection of gene expression. *Bioconjugate Chemistry*, **11**, 941–6.

82 Sun, E.Y., Josephson, L., Kelly, K.A. and Weissleder, R. (2006) Development of nanoparticle libraries for biosensing. *Bioconjugate Chemistry*, **17**, 109–13.

83 Sun, E.Y., Josephson, L. and Weissleder, R. (2006) "Clickable" nanoparticles for targeted imaging. *Molecular Imaging*, **5**, 122–8.

84 Hermanson, G.T. (1996) *Bioconjugate Techniques*, Academic Press, San Diego.

85 Montet, X., Funovics, M., Montet-Abou, K., Weissleder, R. and Josephson, L. (2006) Multivalent effects of RGD peptides obtained by nanoparticle display. *Journal of Medicinal Chemistry*, **49**, 6087–93.

86 Schellenberger, E.A., Reynolds, F., Weissleder, R. and Josephson, L. (2004) Surface-functionalized nanoparticle library yields probes for apoptotic cells. *ChemBioChem*, **5**, 275–9.

87 Weissleder, R., Kelly, K., Sun, E.Y., Shtatland, T. and Josephson, L. (2005) Cell-specific targeting of nanoparticles by multivalent attachment of small molecules. *Nature Biotechnology*, **23**, 1418–23.

88 Weissleder, R., Moore, A., Mahmood, U., Bhorade, R., Benveniste, H., Chiocca, E.A. and Basilon, J.P. (2000) In vivo MR imaging of transgene expression. *Nature Medicine*, **6**, 351–5.

89 Högemann, D., Ntziachristos, V., Josephson, L. and Weissleder, R. (2002) High throughput magnetic resonance imaging for evaluating targeted nanoparticle probes. *Bioconjugate Chemistry*, **13**, 116–21.

90 Wu, N., Peck, T.L., Webb, A.G. and Sweedler, J. (1994) 1H NMR spectroscopy on the nanoliter scale for static and on-line measurements. *Analytical Chemistry*, **66**, 3849–57.

91 Wu, N., Peck, T.L., Webb, A.G., Magin, R.L. and Sweedler, J. (1994) Nanoliter volume sample cells for 1H NMR: application to on-line detection in capillary electrophoresis. *Journal of the American Chemical Society*, **116**, 7929–30.

92 Olson, D.L., Lacey, M.E., Webb, A.G. and Sweedler, J. (1999) Nanoliter-volume 1H NMR detection using periodic stopped-flow capillary electrophoresis. *Analytical Chemistry*, **71**, 3070–6.

93 Olson, D.L., Peck, T.L., Webb, A.G., Magin, R.L. and Sweedler, J.V. (1995) High-resolution microcoil 1H-NMR for mass-limited, nanoliter-volume samples. *Science*, **270**, 1967–70.

94 Seeber, D.A., Hoftiezer, J.H., Daniel, W.B., Rutgers, M.A. and Pennington, C.H. (2000) Triaxial magnetic field gradient system for microcoil magnetic resonance imaging. *Review of Scientific Instruments*, **71**, 4263.

95 Massin, C., Vincent, F., Homsy, A., Ehrmann, K., Boero, G., Besse, P.-A.,

Daridon, A., Verpoorte, E., de Rooij, N.F. and Popovic, R.S. (2003) Planar microcoil-based microfluidic NMR probes. *Journal of Magnetic Resonance*, **164**, 242–55.

96 Sorli, B., Chateaux, J.F., Pitaval, M., Chahboune, H., Favre, B., Briguet, A. and Morin, P. (2004) Micro-spectrometer for NMR: analysis of small quantities in vitro. *Measurement Science and Technology*, **15**, 877–80.

97 Trumbull, J.D., Glasgow, I.K. and Beebe, D.J. (2000) Integrating microfabricated fluidic systems and NMR spectroscopy. *IEEE Transactions on Biomedical Engineering*, **47**, 3–7.

98 Wensink, H., Hermes, D.C. and van den Berg, A. (2004) High signal to noise ratio in low field NMR on chip, simulations and experimental results. 17th IEEE International Conference on Micro Electro Mechanical Systems, Maastricht, Netherlands, January 25–29, pp. 407–10.

99 Peck, T.L., Magin, R.L., Kruse, J. and Feng, M. (1994) NMR microspectroscopy using 100 μm planar RF coils fabricated on gallium arsenide substrates. *IEEE Transactions on Biomedical Engineering*, **41**, 706–9.

100 Stocker, J.E., Peck, T.L. and Webb, A.G. (1997) Nanoliter volume, high-resolution NMR microspectroscopy using a 60-μm planar microcoil. *IEEE Transactions of Biomedical Engineering*, **44**, 1122–7.

101 Massin, C., Boero, G., Vincent, F., Abenhaim, J., Besse, P.-A. and Popovic, R.S. (2002) High-Q factor RF planar microcoils for micro-scale NMR spectroscopy. *Sensors and Actuators A*, **A97–A98**, 280–8.

102 Walton, J.H., de Ropp, J.S., Shotov, M.V., Goloshevsky, A.G., McCarthy, M.J., Smith, R.L. and Collins, S.D. (2003) A micromachined double-tuned NMR Microprobe. *Analytical Chemistry*, **75**, 5030–6.

103 Goloshevsky, A.G., Walton, J.H., Shutov, M.V., de Ropp, J.S., Collins, S.D. and McCarthy, M.J. (2005) Development of low field nuclear magnetic resonance microcoils. *Review of Scientific Instruments*, **76**, 024101.

104 Demas, V., Herberg, J.L., Malba, V., Bernhardt, A., Evans, L., Harvey, C., Chinn, S., Maxwell, R. and Reimer, J. (2007) Portable, low-cost NMR with laser-lathe lithography produced microcoils. *Journal of Magnetic Resonance*, **189** (1), 121–9.

105 Sillerud, L.O., McDowell, A.F., Adolphi, N.L., Serda, R.E., Adams, D.P., Vasile, M.J. and Alam, T.M. (2006) 1H NMR Detection of superparamagnetic nanoparticles at 1 T using a microcoil and novel tuning circuit. *Journal of Magnetic Resonance*, **181**, 181–90.

106 Demas, V., Herberg, J.L., Malba, V., Bernhardt, A., Evans, L., Harvey, C., Chinn, S., Maxwell, R., Franck, J., Reimer, J. and Pines, A. (2008) Ex Situ NMR with microcoils, poster presentation 49th ENC March 9–14, 2008, Pacific Grove, CA.

107 Allen, D., Flaum, C., Ramakrishnan, T.S., Fairhurst, D., Pritchard, T., Bedford, J., Gubelin, G., Heaton, N., Minh, C.C., Ramamoorthy, R., Castelijns, K., Norville, M.A. and Seim, M.R. (2000) Trends in NMR logging. *Oilfield Review*, **12**, 2–19.

108 Blümich, B., Blümler, P., Eidmann, G., Guthausen, A., Haken, R., Schmitz, U., Saito, K. and Zimmer, G. (1998) The NMR-mouse: construction, excitation, and applications. *Magnetic Resonance Imaging*, **16**, 479–84.

109 Eidmann, G., Savelsberg, R., Bluemler, P. and Bluemich, B. (1996) The NMR MOUSE, a mobile universal surface explorer. *Journal of Magnetic Resonance, Series A*, **122**, 104–9.

110 Marko, A., Wolter, B. and Arnold, W. (2007) Application of a portable nuclear magnetic resonance surface probe to porous media. *Journal of Magnetic Resonance*, **185**, 19–27.

111 McDonald, P.J., Aptaker, P.S., Mitchell, J. and Mulheron, M. (2007) A unilateral NMR magnet for sub-structure analysis in the built environment: the surface GARField. *Journal of Magnetic Resonance*, **185**, 1–11.

112 Glover, P.M., Aptaker, P.S., Bowler, J.R., Ciampi, E. and McDonald, P.J. (1999) A novel high-gradient permanent magnet

for the profiling of planar films and coatings. *Journal of Magnetic Resonance*, **139**, 90–7.

113 Prado, P.J. (2001) NMR hand-held moisture sensor. *Magnetic Resonance Imaging*, **19**, 505–8.

114 Manz, B., Coy, A., Dykstra, R., Eccles, C.D., Hunter, M.W., Parkinson, B.J. and Callaghan, P.T. (2006) A mobile one-sided NMR sensor with a homogeneous magnetic field: the NMR-MOLE. *Journal of Magnetic Resonance*, **183**, 25–31.

115 Martin, D.R., Ablett, S., Pedersen, H.T. and Mallett, M.J.D. (2002) The NMR MOUSE: its applications to food science. Special Publication – Royal Society of Chemistry, Magnetic Resonance in Food Science, Vol. **286**, pp. 54–61.

116 Nordon, A., McGill, C.A. and Littlejohn, D. (2001) Process NMR spectrometry. *Analyst*, **126**, 260–72.

117 Haken, R. and Blumich, B. (2000) Anisotropy in tendon investigated in vivo by a portable NMR scanner, the NMR-MOUSE. *Journal of Magnetic Resonance*, **144** (2), 195–9.

118 Rahmatallah, S., Li, Y., Seton, H.C., Mackenzie, I.S., Gregory, J.S. and Aspden, R.M. (2005) NMR detection and one-dimensional imaging using the inhomogeneous magnetic field of a portable single-sided magnet. *Journal of Magnetic Resonance*, **173**, 23–8.

119 Casanova, F., Robert, H., Perlo, J. and Pusiol, D. (2003) Echo-planar rotating-frame imaging. *Journal of Magnetic Resonance*, **162**, 396–401.

120 Rokitta, M., Rommel, E., Zimmermann, U. and Haase, A. (2000) Portable nuclear magnetic resonance imaging system. *Review of Scientific Instruments*, **71**, 4257–62.

121 Prado, P.J. (2003) Single sided imaging sensor. *Magnetic Resonance Imaging*, **21**, 397–400.

122 Perlo, J., Demas, V., Casanova, F., Meriles, C.A., Reimer, J., Pines, A. and Bluemich, B. (2005) High-resolution NMR spectroscopy with a portable single-sided sensor. *Science*, **308**, 1279.

123 Perlo, J., Casanova, F. and Blümich, B. (2007) Ex situ NMR in highly homogeneous fields: 1H spectroscopy. *Science*, **315**, 1110–12.

124 Meriles, C., Sakellariou, D., Henrike, H., Moule, A.J. and Pines, A. (2001) Approach to high-resolution ex situ NMR spectroscopy. *Science*, **293**, 82–5.

125 Halbach, K. (1980) Design of permanent multipole magnets with oriented rare earth cobalt material. *Nuclear Instruments and Methods*, **169**, 1–10.

126 Marble, A.E., Mastikhin, I.V., Colpitts, B.G. and Balcom, B.J. (2007) A compact permanent magnet array with a remote homogenous field. *Journal of Magnetic Resonance*, **186**, 100–4.

127 Moresi, G. and Magin, R. (2003) Miniature permanent magnet for table-top NMR. *Concepts in Magnetic Resonance Part B (Magnetic Resonance Engineering)*, **19B** (1), 35–43.

128 Hills, B.P., Wright, K.M. and Gillies, D.G. (2003) A low-field, low-cost Halbach magnet array for open-access NMR. *Journal of Magnetic Resonance*, **175**, 336–9.

129 Takeda, K. (2008) OPENCORE NMR: open-source core modules for implementing an integrated FPGA-based NMR spectrometer. *Journal of Magnetic Resonance*, **192**, 218–29.

130 Takeda, K. (2007) A highly integrated FPGA-based nuclear magnetic resonance spectrometer. *Review of Scientific Instruments*, **78**, 033103.

131 Job, C., Pearson, R.M. and Brown, M. (1994) A personal computer-based nuclear magnetic resonance spectrometer. *Review of Scientific Instruments*, **65**, 3354–62.

132 Liu, Y., Sun, N., Lee, H., Weissleder, R. and Ham, D. (2008) CMOS mini nuclear magnetic resonance system and its application for biomolecular sensing. *IEEE International Solid-State Circuits Conference*, **7** (3), 140.

Keywords

nanoparticles; superparamagnetism; diagnostics; biosensor; nuclear magnetic resonance; portable detectors

2
Multiplexed Detection with Magnetic Nanoparticles

Robert Wilson

2.1
Introduction

Although, during the early stages of their evolution, detection methods were designed to detect a single analyte in a large volume of sample, two trends have subsequently emerged. In one trend, the sample volume has been decreased with the aid of improved sample processing techniques and more sensitive detection methods, whilst in the other trend the number of analytes that are detected in the same sample has been increased. These trends of increasing numbers and smaller size are analogous to what has occurred in the semiconductor industry, where an increasing number of electronic components have been compressed into a shrinking volume of hardware. Thus, today, multiple tests can be carried out on the same small volume of sample by techniques that are collectively known as multiplexed detection. Over time, however, this term has acquired several different meanings. In this chapter, it is defined as the detection of multiple analyte (target) molecules in the same undivided volume (aliquot) of sample, at the same time. For biomolecular assays, two main platforms are used for multiplexed detection; in one platform the sample is interrogated with a two-dimensional (2-D) array of probe molecules (Figure 2.1a) [1–3], while in the other platform the probe molecules are attached (conjugated) to encoded particles and added to the sample (Figure 2.1b). The latter will henceforth be referred to as suspension arrays [4–6]. Each of these alternatives has its own advantages: in general, 2-D arrays allow many more analytes to be interrogated in the same sample, but suspension arrays are less expensive and have shorter sample to answer times. Magnetic nanoparticles – either on their own or as constituents of magnetic microspheres – are used in both procedures.

Nanomaterials for the Life Sciences Vol. 4: Magnetic Nanomaterials. Edited by Challa S. S. R. Kumar

ISBN: 978-3-527-32154-4

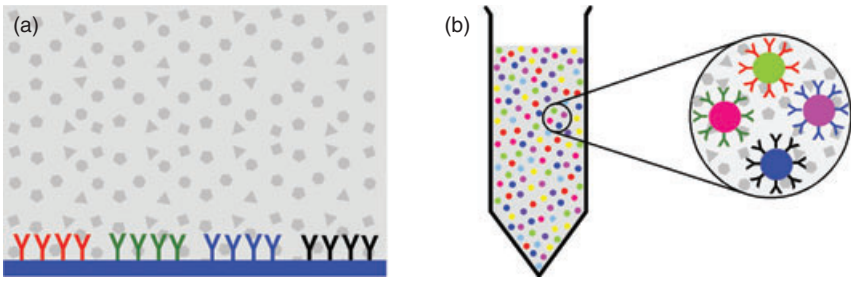

Figure 2.1 (a) Two-dimensional array consisting of a planar grid of probe molecules in which each test is confined to different locations; (b) Suspension array consisting of a mixture of encoded particles in which each test is confined to a different encoded particle.

2.2
Magnetism and Magnetic Particles

Magnetism derives from the spin and orbital behavior of electrons. Materials with filled electron shells in which all electrons are paired are said to be diamagnetic; thus, the magnetic dipoles of their individual electrons cancel out and they exhibit a low negative susceptibility (weak repulsion) in a magnetic field. Examples of diamagnetic materials are copper, gold, and silver. Materials with unpaired electrons in which the magnetic dipoles are orientated in random directions at normal temperatures are said to be paramagnetic. Some of these single-electron dipoles line up with an applied magnetic field, and therefore paramagnetic materials display a low positive susceptibility (weak attraction) in a magnetic field; however, they do not remain magnetic when the field is removed, because the ambient thermal energy is sufficient to reorientate the dipoles in random directions. Both, ferromagnetic and ferrimagnetic materials also contain unpaired electrons although, unlike the unpaired electrons in paramagnetic materials, these are organized into domains comprising the electrons of many atoms or ions. Each domain is a single magnetic dipole that typically has dimensions of less than 100 nm. In an equilibrated ferromagnetic or ferrimagnetic material the magnetic dipoles are organized in random directions; however, when a magnetic field is applied they align with the field, and remain aligned even when the field is removed because the ambient thermal energy is insufficient to reorientate them. All "permanent" magnets are made from ferromagnetic or ferrimagnetic materials; examples include iron, cobalt, nickel, and magnetite (iron oxide). Materials in which single electron magnetic dipoles are aligned in a regular pattern, and in which the neighboring dipoles cancel out, are classified as antiferromagnetic. When a ferromagnetic film is grown on or annealed to an antiferromagnetic material in an aligning magnetic field, the direction of magnetization in the ferromagnetic layer remains pinned in this direction when the magnetic field has been removed. Typical examples of antiferromagnetic materials are chromium and nickel oxide.

Because both ferromagnetic and ferrimagnetic materials depend on their domain structure in order to remain magnetic in the absence of an applied field, their properties undergo an important change when their dimensions are decreased to less than domain size. Particles of this size are said to be superparamagnetic because, although their dipoles line up parallel to an applied magnetic field, the ambient thermal energy is sufficient to spontaneously disorganize the direction of their magnetization when the field is no longer applied. This is important for biotechnology applications, because it would not be possible to resuspend magnetic particles in solution following a magnetic separation due to mutual attraction if they remained magnetic. The force (magnetic moment) experienced by a particle depends on the strength of the applied field and the size and composition of the particle. Because of their small sizes, individual superparamagnetic nanoparticles (Figure 2.2a) respond relatively slowly to an applied magnetic field. The makers of large magnetic microspheres overcome this problem by dispersing large numbers of superparamagnetic nanoparticles in an organic or silica matrix, as shown in Figure 2.2b. The core of the particle shown is packed with 17% (by weight) of ~7.5 nm diameter magnetite nanoparticles. Because the nanoparticles are present in such large numbers, the microspheres respond rapidly to an applied field, but because each individual nanoparticle is so small the ambient thermal energy is sufficient to disorganize their dipoles as soon as the applied field is removed. Magnetic microspheres are available from companies such as Dynal (now part of Invitrogen), Bangs Laboratories, Micromod, Seradyne, Polysciences and Estapor, in sizes ranging from 0.3 to 25 μm, and with a wide range of surface chemistries for easy conjugation to biological and other molecules. Magnetic nanoparticles are available from Micromod and Microspheres-Nanospheres; however, the development of new particles and surface chemistries is at present a highly active area of research [8].

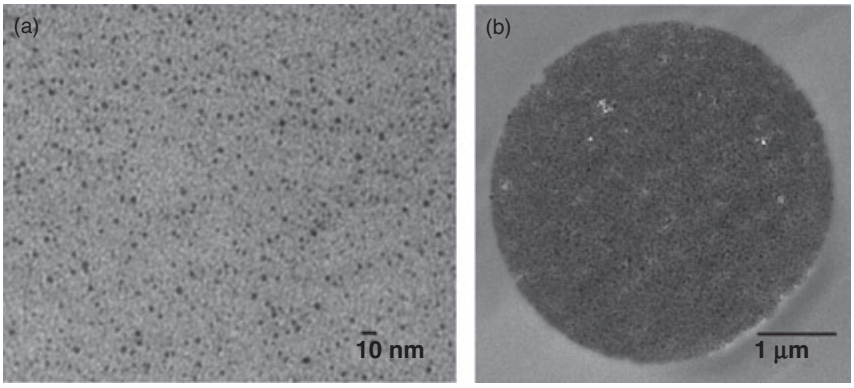

Figure 2.2 (a) Transmission electron microscopy (TEM) image of water-soluble superparamagnetic colbalt nanoparticles. Reproduced from Ref. [7] (http://dx.doi.org/10.1039/b713528a), with permission from The Royal Society of Chemistry; (b) TEM image of a thin section through a magnetic microsphere; the lighter areas correspond to the polymer matrix, and the dark specks are superparamagnetic iron oxide nanoparticles.

2.2.1 Separating and Mixing Magnetic Particles

The main reason why magnetic particles are used in biological applications is because they are easily separated from ambient matrices under mild conditions, with the use of simple and inexpensive equipment. Magnetic separation may be as simple as applying a permanent magnet to the outside of a container; such an approach is used in commercial separators that allow magnetic particles to be retained while supernatant volumes of between 10 µl and 50 ml are removed manually. Automated versions that allow multiple samples to be processed in parallel are also available. Until recently, magnetic separations have been mainly been confined to small volumes of up to a few milliliters, although equipment capable of performing separations on larger volumes, of up to several liters, is now available from companies such as Dexter Magnetic Technologies, IL, USA. In this equipment, the magnets are positioned all around the sample container rather than on only one of its sides. As magnetic microspheres will eventually precipitate under the influence of gravity, some form of forced mixing will be required to maintain them in suspension. Because the solution volumes used in biomolecular assays are usually very small, traditional stirring is impractical and for most purposes a plate shaker or slow-tilt rotation is sufficient to maintain the particles in suspension. Equipment for slow-tilt rotation is available from Dynal-Invitrogen.

2.3 Planar Arrays

In addition to their use in positioning and separating biological and other molecules, magnetic particles can be used as labels in magnetometric assays. In this role they have several advantages over alternative labels, including long-term stability and high sensitivity due to the low background signals that are present in most biological matrices. Detection technologies include superconducting quantum interference devices (SQUIDs) [9, 10], cantilever arrays [11], magnetoresistive sensors [12–14], induction devices [15, 16], and Hall sensors [17, 18], although not all of these can be configured to interrogate 2-D arrays of probe molecules. The most recent attention has focused on magnetoresistive sensors [giant magnetoresistive (GMR) sensors and spin valves) and planar Hall sensors, mainly because of the possibility of fabricating arrays of micrometer-sized sensing elements by standard semiconductor manufacturing techniques and interfacing them with arrays of probe molecules (as shown in Figure 2.3a). Magnetoresistive sensors are based on the GMR effect, which occurs when thin films of ferromagnetic material are separated by thin films of a nonmagnetic metal. A section through a single sensing element in an array of GMR sensors is shown in Figure 2.3b. Here, the sensing resistor is connected to an on-chip reference resistor that compensates for variations in temperature, and two off-chip resistors. Together, these resistors form a Wheatstone bridge circuit. When the magnetic labels have

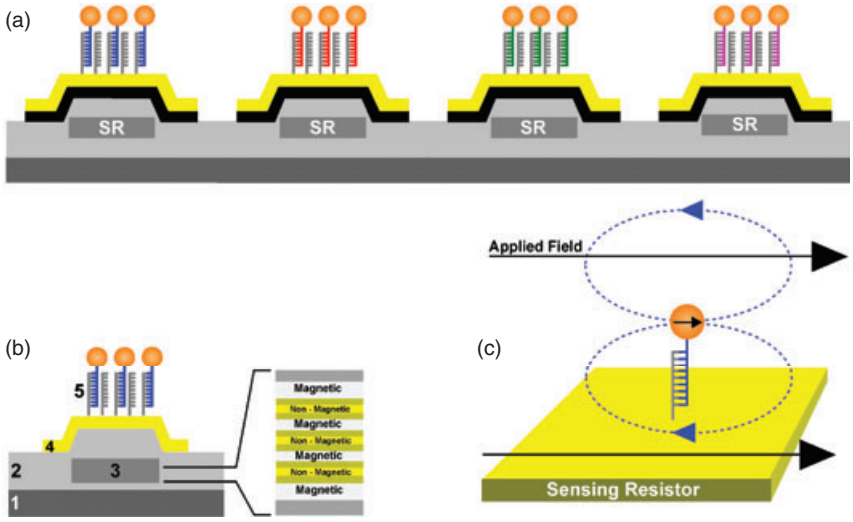

Figure 2.3 (a) Section through a two-dimensional array of magnetoresistive sensing elements. Each sensing resistor (SR) is located under one spot of probe molecules in the array; (b) Section through individual sensing element in a giant magnetoresistive (GMR) array. Key: 1 = silicon substrate; 2 = silicon nitride buffer; 3 = sensing resistor; 4 = gold film for anchoring probe molecules; 5 = sensing surface with probe molecules bound to magnetic labels. The inset shows an enlarged section through the multilayer structure of the sensing resistor; (c) Scheme showing how the direction of the induced dipole field surrounding a magnetic label (broken blue lines) opposes the applied field in the region where it interacts with the sensing resistor. The resultant decrease in field strength experienced by the sensing resistor leads to a decrease in electrical resistance.

been captured by the sensing surface, a small sensing current is passed through the resistor and an alternating magnetic field applied in a direction perpendicular to the surface. The latter magnetizes any bound superparamagnetic labels and induces a dipole field in their vicinity (Figure 2.3c); this in turn causes the direction of the magnetization in the ferromagnetic layers to rotate and to become more aligned. This leads to a decrease in resistance which is proportional to the number of magnetic labels captured by the sensing surface. The possibility of using the GMR effect for detecting magnetic labels was first described by Baselt and colleagues in 1998 [19], and subsequently the concept has been developed by other research groups, notably at the Naval Research Laboratory in Washington DC, where arrays of GMR sensors have been fabricated and used for multiplexed immunoassays and nucleic acid assays [20, 21].

Spin valve sensors are also based on the GMR effect, but in this case each sensing resistor is composed of only two ferromagnetic layers, separated by a nonmagnetic metallic layer. The direction of the magnetization in the magnetic layer furthest from the sensing surface is pinned by interfacing it with a strong antiferromagnetic material. When magnetic labels bind to the sensing surface they cause the

direction magnetization in the unpinned magnetic layer to rotate, which induces a decrease in electrical resistance. A number of reports have described how spin valves can be used to detect low numbers of magnetic particles, and Graham and colleagues have used them to detect streptavidin–biotin interactions and DNA hybridization [22, 23]. Because spin valves are sensitive to the direction of the local magnetic field as well as its strength, the effect of magnetic labels interacting with opposite sides of a sensing resistor can cancel out, leading to a reduction in sensitivity. Research groups at Philips Research (Eindhoven, The Netherlands) overcame this problem by immobilizing probe molecules in the region between two neighboring spin valves [24], while Wirix-Speetjens and colleagues avoided it by releasing bound labels from the sensing surface and detecting them after they had become aligned along one edge of a spin valve [25]. The latter group also compared the performance of magnetic labels with diameters of 1 μm and 300 nm in immunoassays, and found the latter to produce a lower limit of detection and a broader dynamic range. More recently, the teams at Philips Research have carried out immunoassays with spin valve sensors located in close proximity to current-carrying conductors integrated on the same chip [26]. These conductors generate high-frequency magnetic fields that excite those magnetic labels bound to the sensing surface. Each chip is embodied in a disposable microfluidic cartridge that inserts into an electronic reader, with potential for miniaturization into a handheld instrument. Hall sensors are based on the Hall effect, whereby when a magnetic field is applied at right-angles to the movement of charged particles in a conducting material, a voltage is developed at right-angles to the directions of their movement and the applied field. For sensing purposes, a small current is passed through the conductor, after which an alternating magnetic field is applied along the same axis as the direction of current flow and a unidirectional magnetic field is pulsed on and off at right-angles to it. In the absence of any magnetic labels bound to the sensing surface, the latter induces a stable Hall voltage; however, when bound magnetic labels are present, the alternation of their dipole field superimposes an alternating component on the Hall voltage, which can be detected by lock-in electronics. Besse and colleagues have demonstrated the detection of single magnetic microspheres with a Hall sensor [17], while others have used them to detect DNA [18, 27].

There are a several problems that must be overcome before arrays of magnetic sensing elements can be used for multiplexed detection. In common with other detection methods that seek to interface arrays of sensing elements with arrays of probe molecules, it is necessary to ensure that the latter are immobilized at the same location as former. Some probe molecules (e.g., oligonucleotides) can be synthesized *in situ* by employing photolithographic methods similar to those used to fabricate the sensing elements, although other probe molecules (e.g., antibodies) must be immobilized directly onto the sensing elements. This inevitably becomes more difficult as the dimensions of the sensing elements become smaller. A possible solution to this problem would be a version of the immobilization technique developed by Nanogen (San Diego), in which probe molecules are directed to individual sensing elements by on-chip electric fields. Alternatively, the

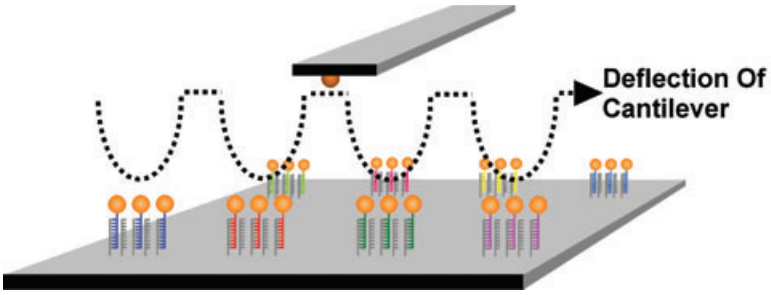

Figure 2.4 The deflection of a scanning cantilever tipped with a ferromagnetic particle can be used to detect magnetic labels bound to an array of probe molecules (although in practice this would be very slow). A faster interrogation could be achieved by scanning with 2-D arrays of cantilevers, as described for dip-pen lithography in Ref. [28].

sensing element(s) can be scanned over the probe molecules in much the same way as an atomic force microscopy (AFM) tip is scanned over a substrate (as shown in Figure 2.4). Although this concept is used in magnetic force microscopy [29], Rudnitsky and colleagues have suggested its use also for the detection of magnetic labels bound to very high-density arrays of probe molecules [11]. The idea of using a scanning probe rather than a fixed array of sensing elements could also be extended to other detection methods, as recently reported by Kazakova and colleagues, who used a scanning Hall microscope to detect individual magnetic particles distributed on a planar substrate [30].

Most of the studies that have been carried out with magnetic sensors have emphasized their potential sensitivity by detecting very low numbers of magnetic particles; however, very few studies have extended to the detection of actual analyte molecules, let alone such molecules in real samples. At some point in any real detection protocol the analyte molecules must be concentrated at the sensing site. In a simple sandwich assay, this is normally achieved by binding the analyte molecules directly to surface-immobilized probe molecules, but when magnetic labels are used they can also be concentrated by binding to the reporter molecules in solution. One advantage of this alternative approach is that the initial binding events take place under conditions where they are favored by faster kinetics. The magnetic labels can then be concentrated into a much smaller volume, as shown schematically in Figure 2.5a, and even focused at particular sensing sites by the application of one or more magnetic field gradients. Graham and colleagues have demonstrated how magnetic particles can be concentrated on spin valve sensors using the magnetic field of adjacent current carrying conductors [31], while Sandhu and colleagues have used a similar approach to concentrate magnetic particles on Hall sensors [32]. Lee and coworkers have demonstrated the microscale manipulation of magnetic particles with 2-D grids of current-carrying wires [33], and Graham and colleagues have shown how on-chip current-carrying wires can be

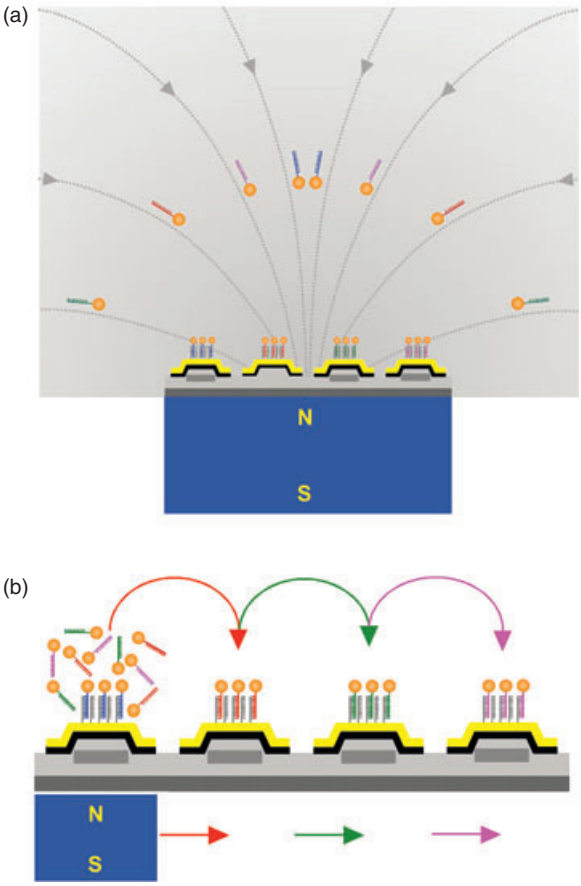

Figure 2.5 (a) An advantage of magnetic labels is that, subsequent to interrogating a large sample volume, they can be concentrated onto a small sensing surface; (b) By moving the applied magnetic field from site to site in the direction of the colored arrows, the magnetic labels can also be concentrated on each individual sensing spot in series, but the time required for binding at each site makes this impractical for multiplexed detection.

used to focus magnetically labeled nucleic acid sequences onto spin valve sensors for hybridization with the corresponding probe sequence [23]. One problem with this approach is that, for maximum sensitivity, it would be necessary to concentrate all magnetic labels on one sensing site before moving on to the next, as shown in Figure 2.5b. In multiplexed detection, where there would be multiple sensing sites, the total time required would be equal to the number of sensing sites, multiplied by the time taken to complete the process of concentration and hybridization at each individual sensing site. Given that the latter takes at least 30 min, it can easily be understood that the concentration at individual sensor sites would not be practical for multiplexed detection.

2.4
Rotating Discs

In many cases, methods that allow magnetic labels to be detected with great sensitivity cannot be configured to interrogate even low-density 2-D arrays of probe molecules, because of their size. SQUID sensors consist of two Josephson tunnel junctions in parallel, in association with a pick-up coil (antenna) that focuses the signal from the magnetic labels onto them. Small currents are able to pass through the junctions without developing a voltage, but when the current exceeds a certain critical value then a voltage is developed. The magnitude of this critical current depends on the ambient magnetic field in a way that allows trace amounts of magnetic label to be detected, although in order to operate the SQUID sensors must be cooled with liquid nitrogen. The size of the cooling apparatus, and the need to insulate biological molecules from contact with very low temperatures, make it impractical to interface SQUID sensors directly with each individual spot in a 2-D array. Nonetheless, Tsukamoto and colleagues overcame this problem by locating individual tests around the perimeter of a rotating disc, as shown in Figure 2.6 [34]. A magnetic field was applied to samples outside the magnetic shield, and the residual magnetism of the labels was detected as they passed over the SQUID. This allowed the bound labels to be distinguished from the unbound

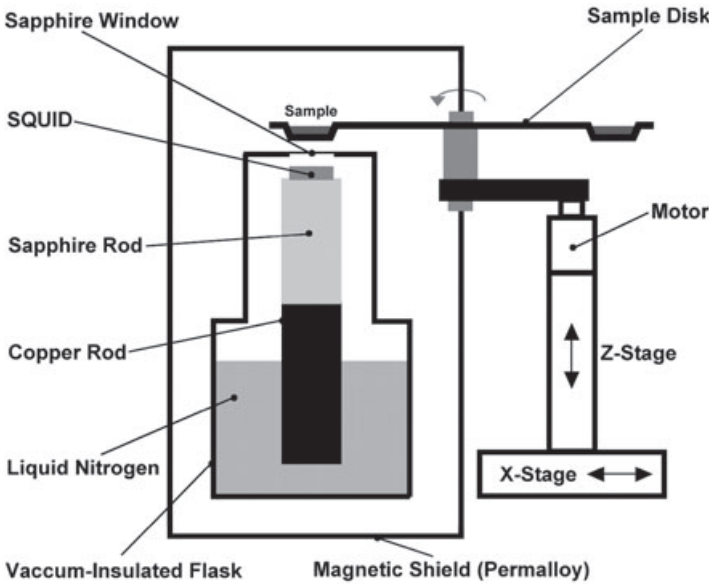

Figure 2.6 Schematic representation showing how liquid samples organized around the rim of a disk are rotated (in the direction of the red arrow) to locate individual samples in close proximity to a high-temperature SQUID sensor.

labels, without a separation step. A similar method of detection is currently being developed by MagneSensors (San Diego, CA, USA; http://home.san.rr.com/magnesensors/) in which attomolar sensitivity is achieved by bringing the sample to within less than 1 mm of the SQUID sensor.

2.5 Diagnostic Devices

Today, lateral flow devices are one of the most important products of the *in vitro* diagnostics industry. In their simplest form they consist of a rectangular strip of plastic-backed porous material which is striped with lines of immobilized probe molecules, and fitted with a conjugate release and wicking pads (as shown in Figure 2.7a). When a device is inserted into the sample, liquid migrates along the strip and releases labeled capture molecules from the conjugate release pad. These bind to analyte molecules present in the sample and develop a signal when they interact with immobilized probe molecules at the test line. The lateral flow devices are completely self-contained, and can be stored in dry form without refrigeration for many months. Existing devices, based mainly on dyed latex particle or gold nanoparticles, at-best produce semi-quantitative results that must often be interpreted by the user without additional equipment. However, demands for improved sensitivity, numerical outputs and multiplexed detection are driving development in the direction of devices that can be interfaced with inexpensive field-portable detectors. MagnaBioSciences (San Diego, CA, USA; http://www.qdusa.com/biotech06/index.html) [35] and Magnasense (Finland; magnasense.com) have both developed lateral flow device readers based on electromagnetic induction. This penetrates further from the sensing interface than the GMR and Hall effects, and is therefore better able to interrogate the entire thickness of a lateral flow strip. In these readers the device is placed in a strong magnetic field in close proximity to an array of planar coils (Figure 2.7b). The array is designed such that the net current induced in the coils is zero, unless magnetic particles are present. When these particles accumulate at the test line they distort the magnetic field and induce a net voltage which is proportional to number of particles, and hence to the amount of analyte in the sample. Sensitivity is said to range from 10- to 1000-fold greater than traditional lateral flow devices, and MagnaBioSciences have claimed that their preliminary work have shown the technology capable of being adapted for use with planar arrays. Magnisense (France; www.magnisense.com) has developed an improved detection technology based on the nonlinear magnetization of superparamagnetic particles [36, 37]. In this method, the particles are subjected to an alternating magnetic field that has two components: a high-amplitude, low-frequency component capable of switching off further magnetization of the particles; and a low-amplitude, high-frequency component that contributes to the resulting induction signal. This promotes high sensitivity because it permits the signal from superparamagnetic labels to be discriminated from background signals derived from paramagnetic sources. The improved method has been incor-

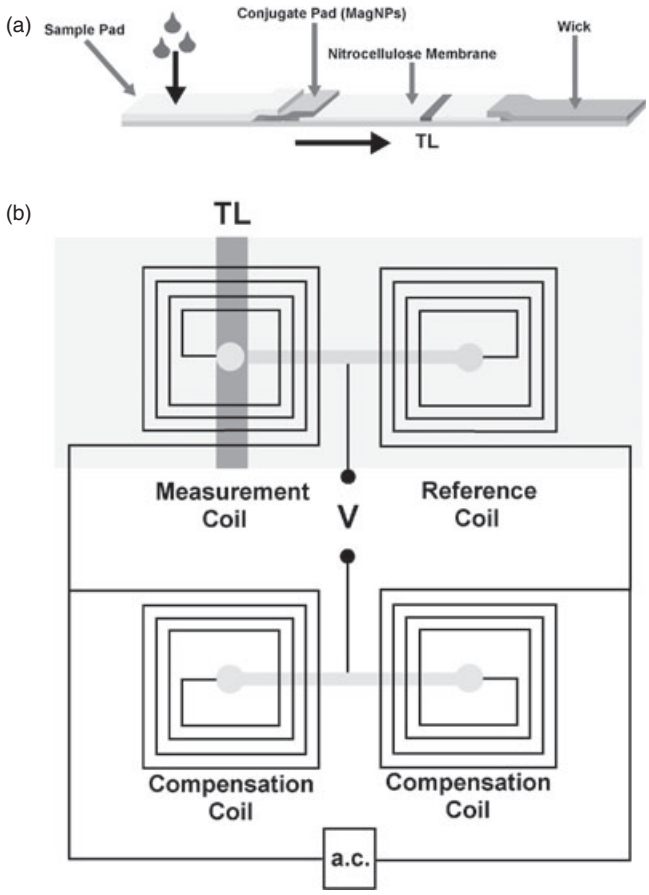

Figure 2.7 (a) A lateral flow device. The liquid sample (drops) releases magnetic labels from the conjugate pad, after which the analyte molecules bind to the labels as they migrate (in the direction of the arrow) towards the test line (TL). At the TL, the labels bind to capture molecules in proportion to the amount of analyte in the sample. The device is then inserted into a reader; (b) A plan-view showing part of lateral flow device located above an array of coils (impedance bridge) in the reader developed by Magnasense. Magnetic labels bound to the test line unbalance the impedance bridge, leading to a change in the output voltage (V). The reader developed by MagnaBioSciences is based on a different approach, in which the lateral flow device is located in a uniform magnetic field above an array of coils.

porated into a lateral flow device reader based on electromagnetic induction, but it also has the potential to improve the sensitivity of Hall, GMR, and other sensors. Diagnostic Biosensors (Minneapolis, USA; www.diagnosticbiosensors.com) is currently developing arrays of GMR sensors for use with lateral flow and microfluidic devices. One problem with GMR as a means of interrogating lateral flow strips is that the sensitivity to the presence of magnetic particles decreases according to

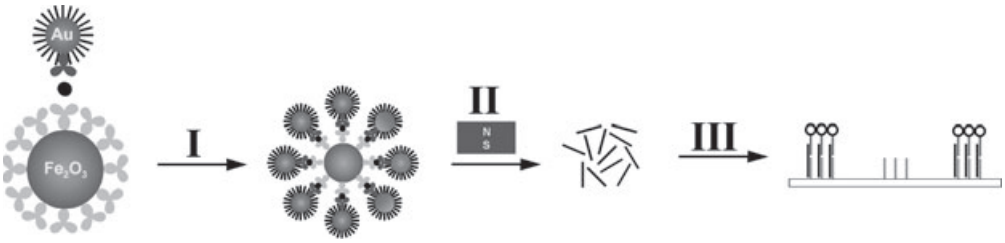

Figure 2.8 Scheme of the bio-barcode assay. Stage I: Analyte molecules are sandwiched between magnetic microspheres and bio-barcodes (gold nanoparticles conjugated to antibodies and DNA barcodes); Stage II: the microspheres are magnetically precipitated; Stage III: the DNA barcodes precipitated in Stage II are released and detected by hybridization to a 2-D array.

the inverse cube of the distance between the particles and the sensing resistor. Thus, sensitivity to labels located on the far side of the plastic backing support of a lateral flow device would be low. In order to overcome this problem, Tondra has suggested that sensing elements could be fabricated directly onto the backing material, thereby placing them in closer proximity to magnetic labels in the porous membrane [38].

2.6
Bio-Barcode Assays Based on Magnetic Microspheres

In its most common embodiment, the bio-barcode approach uses magnetic separation to carry out multiplexed nucleic acid assays and immunoassays [39, 40]. Bio-barcodes are gold nanoparticles conjugated to recognition molecules and DNA barcodes. In multiplexed assays, target molecules are sandwiched between capture probe molecules conjugated to magnetic microspheres and bio-barcodes, as shown in Figure 2.8. The magnetic microspheres, and the bio-barcodes bound to them, are magnetically separated and washed, after which the barcodes are released and detected by hybridization to a 2-D array. Multiplexed assays for both antigenic and nucleic acid target molecules have been reported in which released barcodes are detected by sandwiching them between arrays of capture probes and reporter probes. In most cases, the reporter probes are labeled with gold nanoparticles that are detected after silver enhancement.

2.7
Spectrally Encoded Suspension Arrays of Magnetic Microspheres

The first suspension arrays to be introduced were based on nonmagnetic microspheres encoded with fluorescent dyes [6, 41]. For this method of encoding, the

microspheres are swollen in a solution of the dyes in a nonpolar solvent. The dyes are able to partition into the microspheres which, on being transferred to a polar solvent, will shrink such that the dyes become entrapped. This method is used to encode microspheres for use in the commercial suspension arrays, although the number of codes that can be prepared is limited by the properties of the fluorescent dyes.

Many of the limitations imposed by fluorescent dyes can be eliminated, however, by using semiconductor quantum dots (QDs) [42–44]. These photoluminescent nanoparticles have narrow, size-tunable emission spectra, and many colors can be excited at a single wavelength far removed (>100 nm) from their emission wavelengths. In theory, up to eight different colors of QDs can be resolved in the visible/near-infra-red region of the spectrum, with acceptable spectral overlap. Nie and colleagues conferred both a spectral code and magnetic properties on porous silica microspheres by doping them with CdSe@ZnS QDs and iron oxide nanoparticles capped with hydrophobic ligands [45]. The microspheres had a diameter of 3–5 μm and a mean pore size of 30 nm, and all surfaces – both internal and external – were functionalized with hydrophobic octadecyl silane. For encoding purposes, the microspheres were first mixed with the nanoparticles in butanol. Then, after allowing time for the particles to partition into the pores, the microspheres were washed with ethanol and then rendered hydrophilic by coating them with amphiphilic poly(acrylic acid) functionalized with octylamine. One potential problem with this method is that iron oxide nanoparticles significantly reduce the photoluminescence intensities of the QDs because of their broad absorbance spectrum, which interferes with both excitation and emission. Some commercial microspheres have structures which comprise a core containing iron oxide nanoparticles that does not swell in nonpolar solvents, but is surrounded by a shell that does. Whitman and colleagues used solvent swelling to incorporate either fluorescent dyes or QDs into the shells of microspheres with this structure, and then used these in immunoassays for *Bacillus anthracis* spores [46]. In these immunoassays, an applied magnetic field was used to remove any microspheres bound to the substrate by weak nonspecific interactions, thereby reducing the background and increasing sensitivity.

One problem with solvent swelling as a means of encoding microspheres is that all dyes must be incorporated at the same time, but this becomes increasingly imprecise as the number of dyes and their concentrations are increased. Layer-by-layer (LBL) self-assembly is a technique in which materials are assembled in sequence by virtue of their mutual attraction [47]. As a method of encoding microspheres, this imposes a high degree of control over the amount of photoluminescent polymers or nanoparticles that can be deposited on the microsphere cores. Provided that the encoding elements are in excess, the amount assembled will depend only on the surface area of the microspheres, and therefore precise control over their concentrations is unnecessary. A number of reports have been produced describing the LBL assembly of QDs on nonmagnetic microspheres [48–51], most of which have involved iterative cycles of assembly and washing, with the latter generally being carried out by either centrifugal precipitation [48–51] or filtration

[50]. Unfortunately, this is a time-consuming procedure, and results in a progressive loss of microsphere cores as more layers are assembled. In one study, 80% of the microspheres were found to be lost when centrifugal washing was used during the assembly of 20 polyelectrolyte layers on nonmagnetic microspheres [51]. However, Wilson and colleagues overcame this problem by using magnetic separation to perform the washing steps, as shown in Figure 2.9a [52, 53], as this allows many layers of QDs to be assembled on magnetic cores, without any significant loss of microspheres and in less than one-quarter of the time required when centrifugal precipitation is used. Because the QDs are assembled in a shell

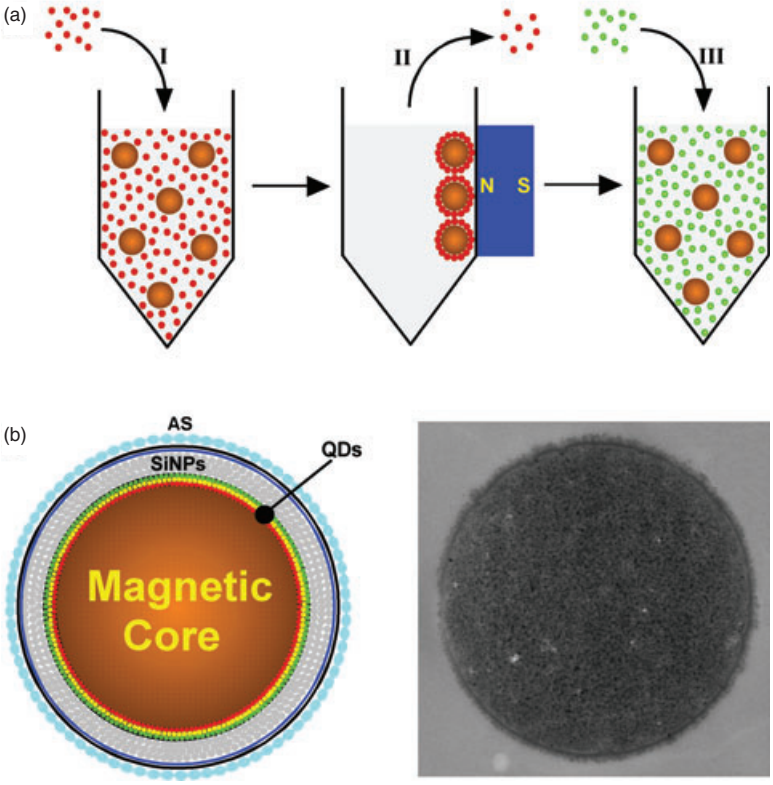

Figure 2.9 (a) Simplified scheme of LBL self-assembly of photoluminescent QDs on magnetic cores. Step I, mix magnetic particles and QDs; Step II, precipitate magnetic particles and remove excess QDs; Step III, assemble new layer of QDs; (b) By combining LBL self-assembly and magnetic separation, sophisticated nanoscale architectures can be constructed. In the scheme on the left, a magnetic core is surrounded by an inner shell of QDs and an outer shell of silica nanoparticles (SiNPs). The latter is functionalized with an immunosorbent antigenic surface (AS) for use in multiplexed immunoassays. The TEM image on the right shows a thin section though a magnetic microsphere, with the architecture shown in the scheme on the left. The encoding QDs are visible as a dark line between the magnetic core and outer shell of SiNPs. The TEM image was reproduced from Ref. [53]; © American Chemical Society.

surrounding the magnetic core, their photoluminescence is not quenched by the iron oxide nanoparticles. In one example, three colors of QDs were assembled on paramagnetic microspheres, followed by an outer shell of silica nanoparticles, as shown in Figure 2.9b. The latter – which are completely transparent at all excitation and emission wavelengths – were subsequently silanized and functionalized with an antigenic surface for use in multiplexed immunoassays for serum proteins. In these immunoassays, three sets of microspheres were incubated with the sample (as shown in Figure 2.10a), and results were determined by decoding the particles and detecting molecules bound to them with a fluorescence reader (Figure 2.10b). By combining solution-phase kinetics and magnetic separation the immunoassays could be completed in less than 30 min.

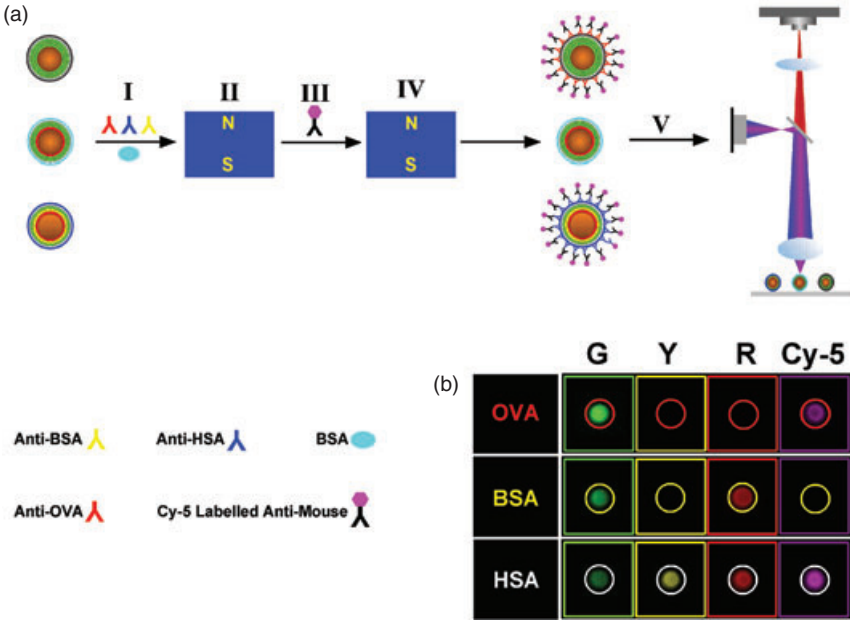

Figure 2.10 (a) Scheme of multiplexed competitive immunoassay for serum proteins. Stage I, three sets of magnetic particles, each with a different color code and a different antigenic surface, are incubated with the corresponding antibodies and the sample; in this example the sample contains bovine serum albumin (BSA); Stage II, the magnetic particles are precipitated and the sample is removed; Stage III, the magnetic particles are incubated with fluorescent Cy-5-labeled antibodies; Stage IV, the particles are precipitated and washed; Stage V, the particles are imaged with a fluorescence reader; (b) Fluorescence images showing colors of the encoding QDs and Cy-5 fluorescence, for one particle from each set at the end of the immunoassay. Particles with a code of red and green QDs are not fluorescent in the Cy-5 (cyanine-5) window because BSA was present in the sample. However, particles with other codes are fluorescent because OVA (ovalbumin) and HSA (human serum albumin) were not present in the sample. Reproduced with permission from Ref. [53]; © American Chemical Society.

The Quantum Dot Corporation (now part of Invitrogen) has also developed magnetic microspheres encoded by what appears to be some form of LBL process, although insufficient details have been revealed to be certain of this [44]. The microspheres have a diameter of 8 μm and are encoded with up to four colors of QDs at 12 different intensity levels; in theory, this could yield up to 455 spectral codes. The encoding QDs had emission peaks at 525, 545, 565, and 585 nm, while a fifth QD conjugated to streptavidin with an emission peak at a longer wavelength was used as a reporter label. The encoded microspheres were used for the multiplexed gene expression profiling of 100 cRNA sequences and 20 calibrator sequences. The results clearly demonstrated the advantages of performing multiplexed detection with suspension arrays combining QD encoding and magnetic separation. In comparison with microarrays, the duration of the assay was an order of magnitude faster, the dynamic range was 2–3 log units broader; the sensitivity was an order of magnitude better, and reproducibility approached that of an Affymetrix GeneChip microarray. Moreover, quality control was straightforward because encoded microspheres can be prepared in gram-sized batches, with each gram being sufficient to perform at least 10^9 assays.

2.7.1 Magnetically Encoded Suspension Arrays

The possibility of encoding suspension arrays with a combination of luminescent and magnetic entities has been described elsewhere [54]. The maximum number of spectral codes that can be resolved by fluorescence alone is ultimately limited by the ability of the detector to distinguish between different colors and intensities. The number of resolvable codes can be doubled by the simple expedient of incorporating additional magnetic encoding elements into some of the fluorescent particles. Two suspension arrays with identical spectral codes are prepared, with the single difference that one of them is based on magnetic particles; the arrays can therefore be separated by the application of a magnetic field gradient before reading the spectral code. In a variation on this idea, Kim and Park carried out dual analyte sandwich immunoassays in which the identity of captured analyte molecules was indicated by the fluorescence code of the microsphere, and the amount of target molecule captured by them was determined from their velocity in an applied magnetic field [55]. Particles in a suspension array can also be identified by means of magnetic codes alone. The force on a magnetic particle in a magnetic field depends on its size and composition; thus, particles in a suspension arrays could in theory be separated and identified on the basis of their magnetic content. The separation of particles in a magnetic field, which is known as magnetophoresis or magnetic spectrometry, has been used to separate populations of cells labeled with antibodies conjugated to magnetic nanoparticles [56, 57], and more recently to separate particles on the basis of their size and magnetic moment. In one of these reports, magnetic particles were injected into a planar flow cell and separated into eight outlet bins by the application of a magnetic field gradient at right-angles to the direction of flow (see Figure 2.11) [58]; similar separations

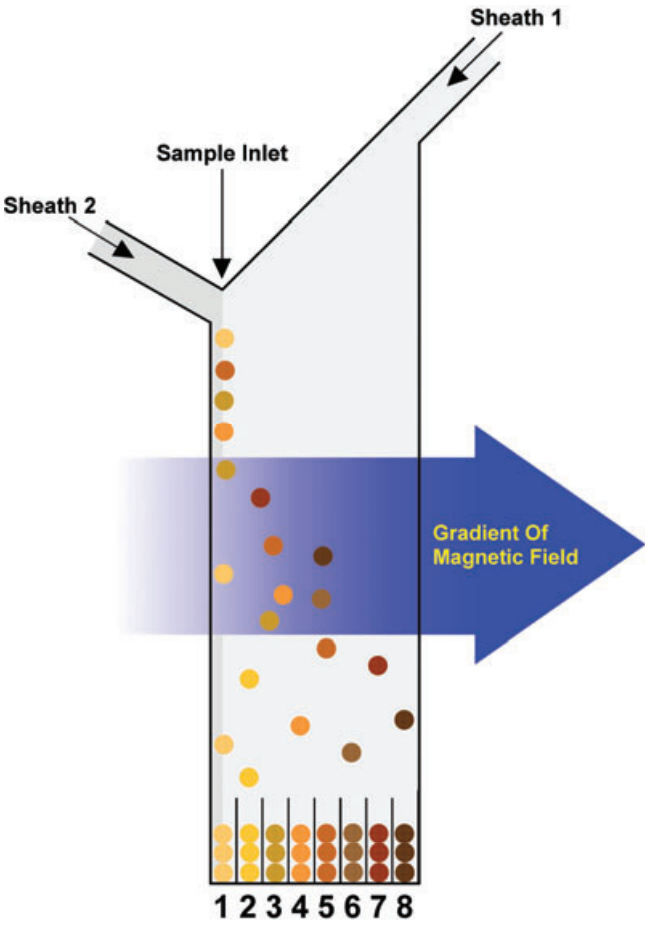

Figure 2.11 Particles encoded with different amounts of magnetic material in a flowing stream can be resolved by applying a magnetic field at right-angles to the direction of flow. In this scheme, particles with a higher magnetic content are indicated by circles of a darker color; the higher the magnetic content of the particles, the more they are deflected by the magnetic field.

have been carried out in microfluidic devices [59]. At present, the main barrier to further progress in this area is that most existing particles vary widely in their magnetic moments. Baselt and colleagues, for example, found that microspheres in the same batch of M-280 Dynabeads (2.8 μm diameter) had a relative standard deviation of 72% [19]. Recently, Wang and colleagues have synthesized nanoparticles with a multiplayer structure that promotes low magnetic remanence and allows the magnetic moment of particles to be tuned [60]. Particles such as these should prove to be useful for investigating the potential of magnetic encoding,

although because of the way in which they are made it would not be possible to produce them in sufficient numbers to offer a practical alternative to suspension arrays based on spectrally encoded microspheres.

2.8 Summary and Conclusions

Magnetic nanoparticles, either on their own or embedded in microspheres, are used in multiplexed assays based on both planar and suspension arrays. Two-dimensional arrays of sensing elements for magnetometric assays can be made and integrated into the requisite circuitry by standard semiconductor manufacturing techniques, although difficulties exist in locating probe molecules at precisely the same sites as the sensing elements. It may be possible to overcome this problem by directing probe molecules to the desired location with on-chip electric or magnetic fields, but the ancillary components necessary to do this would themselves occupy space. Because of these limitations, it is likely that arrays of magnetic sensing elements will be limited to low- and medium-density arrays, such as those used in field-portable, point-of-use devices. Although the use of microspheres containing magnetic nanoparticles in suspension arrays for separation purposes is well established, the possibility of using magnetic nanoparticles as encoding elements has recently been explored. At present, a lack of microspheres with well-defined magnetic moments is said to be delaying advances in this area, but presumably these could be prepared in relatively large numbers using the same LBL techniques that have been used to assemble magnetic and other nanoparticles on nonmagnetic microspheres. Even when suitable microspheres become available, however, it is unlikely that a purely magnetic-based method of encoding would yield the same number of codes as would fluorescent dyes or luminescent nanoparticles. A more realistic prospect is that a combination of luminescent and magnetic encoding could be used to achieve significantly higher levels of multiplexing than is currently possible with luminescence encoding alone. During the past few years, Chen and colleagues have described suspension arrays composed of at least 100 different codes based on QDs [44], while Carr and colleagues have shown how microspheres can be separated into eight different sets in a magnetic field gradient [58]. A combination of these approaches would yield at least 800 resolvable codes, without losing any of the advantages that have contributed to the success of suspension arrays.

References

1 Schena, M., Heller, R.A., Theriault, T.P., Konrad, K., Lachenmeier, E. and Davis, R.W. (1998) Microarrays: biotechnology's discovery platform for functional genomics. *Trends in Biotechnology*, **16**, 301–6.

2 Bowtell, D.D.L. (1999) Options available – from start to finish – for

obtaining expression data by microarray. *Nature Genetics*, **21**, 25–32.
3 La Fratta, C.N. and Walt, D.R. (2008) Very high density sensing arrays. *Chemical Reviews*, **108**, 614–37.
4 Braeckmans, K., De Smedt, S.C., Leblans, M., Pauwels, R. and Demeester, J. (2002) Encoding microcarriers: present and future technologies. *Nature Reviews Drug Discovery*, **1**, 447–56.
5 Finkel, N.H., Lou, X.H., Wang, C.Y. and He, L. (2004) Barcoding the microworld. *Analytical Chemistry*, **76**, 353A–9A.
6 Wilson, R., Cossins, A.R. and Spiller, D.G. (2006) Encoded microcarriers for high-throughput multiplexed detection. *Angewandte Chemie, International Edition in English*, **45**, 6104–17.
7 Lu, L.T., Tung, L.D., Robinson, I., Ung, D., Tan, B., Long, J., Cooper, A.I., Fernig, D.G. and Thanh, N.T.K. (2008) Size and shape control for water-soluble magnetic cobalt nanoparticles using polymer ligands. *Journal of Materials Chemistry*, **18**, 2453–8.
8 Thanh, N.T.K., Robinson, I. and Tung, L.D. (2007) Magnetic nanoparticles: synthesis, characterisation and biomedical applications, in *The Dekker Encyclopedia of Nanoscience and Nanotechnology*, Vol. **1** (eds J.A. Schwarz, C. Contescu and K.P. April), Taylor and Francis, New York, pp. 1–10.
9 Carr, C., Matlachov, A.N., Sandin, H., Espy, M.A. and Kraus, R.H. (2007) Magnetic sensors for bioassay: HTS SQUIDs or GMRs? *IEEE Transactions on Applied Superconductivity*, **17**, 808–11.
10 Tsukamoto, A., Saitoh, K., Suzuki, D., Sugita, N., Seki, Y., Kandori, A., Tsukada, K., Sugiura, Y., Hamaoka, S., Kuma, H., Hamasaki, N. and Enpuku, K. (2005) Development of multisample biological immunoassay system using HTS SQUID and magnetic nanoparticles. *IEEE Transactions on Applied Superconductivity*, **15**, 656–9.
11 Rudnitsky, R.G., Chow, E.M. and Kenny, T.W. (2000) Rapid biochemical detection and differentiation with magnetic force microscope cantilever arrays. *Sensors and Actuators A*, **83**, 256–62.
12 Graham, D.L., Ferreira, H.A. and Freitas, P.P. (2004) Magnetoresistive-based biosensors and biochips. *Trends in Biotechnology*, **22**, 454–62.
13 Wirix-Speetjens, R. and De Boeck, J. (2006) Magnetic sensor based biosensors, in *Encyclopedia of Sensors*, Vol. **5** (eds C.A. Grimes, E.C. Dickey and M.V. Pishko), American Scientific Publishers, CA, pp. 403–14.
14 Megens, M. and Prins, M. (2005) Magnetic biochips: a new option for sensitive diagnostics. *Journal of Magnetism and Magnetic Materials*, **293**, 702–8.
15 Richardson, J., Hill, A., Luxton, R. and Hawkins, P. (2001) A novel measuring system for the determination of paramagnetic particle labels for use in magneto-immunoassays. *Biosensors and Bioelectronics*, **16**, 1127–32.
16 Lany, M., Boero, G. and Popovic, R.S. (2005) Superparamagnetic microbead inductive detector. *Review of Scientific Instruments*, **76**, article 084301.
17 Besse, P.A., Boero, G., Demierre, M., Pott, V. and Popovic, R. (2002) Detection of a single magnetic microbead using a miniaturized silicon Hall sensor. *Applied Physics Letters*, **80**, 4199–201.
18 Ejsing, L., Hansen, M.F., Menon, A.K., Ferreira, H.A., Graham, D.L. and Freitas, P.P. (2005) Magnetic microbead detection using the planar Hall effect. *Journal of Magnetism and Magnetic Materials*, **293**, 677–84.
19 Baselt, D.R., Lee, G.U., Natesan, M., Metzger, S.W., Sheehan, P.E. and Colton, R.J. (1998) A biosensor based on magnetoresistance technology. *Biosensors and Bioelectronics*, **13**, 731–9.
20 Rife, J.C., Miller, M.M., Sheehan, P.E., Tamanaha, C.R., Tondra, M. and Whitman, L.J. (2003) Design performance of GMR sensors for the detection of magnetic microbeads in biosensors. *Sensors and Actuators A*, **107**, 209–18.
21 Mulvaney, S.P., Cole, C.L., Kniller, M.D., Malito, M., Tamanaha, C.R., Rife, J.C., Stanton, M.W. and Whitman, L.J. (2007) Rapid, femtomolar bioassays in complex matrices combining microfluidics and magnetoelectronics. *Biosensors and Bioelectronics*, **23**, 191–200.

22 Ferreira, H.A., Graham, D.L., Freitas, P.P. and Cabral, J.M.S. (2003) Biodetection using magnetically labeled biomolecules and arrays of spin valve sensors (invited). *Journal of Applied Physics*, **93**, 7281–6.

23 Graham, D.L., Ferreira, H.A., Feliciano, N., Freitas, P.P., Clarke, L.A. and Amaral, M.D. (2005) Magnetic field-assisted DNA hybridisation and simultaneous detection using micron-sized spin-valve sensors and magnetic nanoparticles. *Sensors and Actuators B*, **107**, 936–44.

24 De Boer, B.M., Kahlman, J.A.H.M., Jansen, T.P.G.H., Duric, H. and Veen, J. (2007) An integrated and sensitive detection platform for magneto-resistive biosensors. *Biosensors and Bioelectronics*, **22**, 2366–70.

25 De Palma, R., Reekmans, G., Liu, C.X., Wirix-Speetjens, R., Laureyn, W., Nilsson, O. and Lagae, L. (2007) Magnetic bead sensing platform for the detection of proteins. *Analytical Chemistry*, **79**, 8669–77.

26 Sandhu, A., Kumagai, Y., Lapicki, A., Sakamoto, S., Abe, M. and Handa, H. (2007) High efficiency Hall effect micro-biosensor platform for detection of magnetically labeled biomolecules. *Biosensors and Bioelectronics*, **22**, 2115–20.

27 Wang, S.X., Bae, S.Y., Li, G.X., Sun, S.H., White, R.L., Kemp, J.T. and Webb, C.D. (2005) Towards a magnetic microarray for sensitive diagnostics. *Journal of Magnetism and Magnetic Materials*, **293**, 731–6.

28 Salaita, K., Wang, Y.H. and Mirkin, C.A. (2007) Applications of dip-pen nanolithography. *Nature Nanotechnology*, **207** (2), 145–55.

29 Schreiber, S., Savla, M., Pelekhov, D.V., Iscru, D.F., Selcu, C., Hammel, P.C. and Agarwal, G. (2008) Magnetic force microscopy of superparamagnetic nanoparticles. *Small*, **4**, 270–8.

30 Kazakova, O., Gallop, J., Perkins, G. and Cohen, L. (2007) Scanned micro-Hall microscope for detection of biofunctionalized magnetic beads. *Applied Physics Letters*, **90**, article 162505.

31 Graham, D.L., Ferreira, H., Bernardo, J., Freitas, P.P. and Cabral, J.M.S. (2002) Single magnetic microsphere placement and detection on-chip using current line designs with integrated spin valve sensors: biotechnological applications. *Journal of Applied Physics*, **91**, 7786–8.

32 Kumagai, Y., Togawa, K., Sakamoto, S., Abe, M., Handa, H. and Sandhu, A. (2006) Hall biosensor with integrated current microstrips for control of magnetic beads. *IEEE Transactions on Magnetics*, **42**, 3893–5.

33 Lee, C.S., Lee, H. and Westervelt, H.R.M. (2001) Microelectromagnets for the control of magnetic nanoparticles. *Applied Physics Letters*, **79**, 3308–10.

34 Tsukamoto, A., Saitoh, K., Suzuki, D., Sugita, N., Seki, Y., Kandori, A., Tsukada, K., Sugiura, Y., Hamaoka, S., Kuma, H., Hamasaki, N. and Enpuku, K. (2005) Development of multisample biological immunoassay system using HTS SQUID and magnetic nanoparticles. *IEEE Transactions on Applied Superconductivity*, **15**, 656–9.

35 La Borde, R.T. and O'Farrell, B. (2002) Paramagnetic-particle detection in lateral flow assays. *IVD Technology*, **8**, 36–41.

36 Nikitin, P.I., Vetoshko, P.M. and Ksenevich, T.I. (2007) Magnetic immunoassays. *Sensor Letters*, **5**, 296–9.

37 Nikitin, P.I., Vetoshko, P.M. and Ksenevich, T.I. (2007) New type of biosensor based on magnetic nanoparticle detection. *Journal of Magnetism and Magnetic Materials*, **311**, 445–9.

38 Tondra, M. (2007) Using integrated magnetic microchip devices in IVDs. *IVD Technology*, **5**, 31–8.

39 Stoeva, S.I., Lee, J.S., Thaxton, C.S. and Mirkin, C.A. (2006) Multiplexed DNA detection with biobarcoded nanoparticle probes. *Angewandte Chemie, International Edition in English*, **45**, 3303–6.

40 Stoeva, S.I., Lee, J.S., Smith, J.E., Rosen, S.T. and Mirkin, C.A. (2006) Multiplexed detection of protein cancer markers with biobarcoded nanoparticle probes. *Journal of the American Chemical Society*, **128**, 8378–9.

41 Kellar, K.L. and Douglass, J.P. (2003) Multiplexed microsphere-based flow cytometric immunoassays for human cytokines. *Journal of Immunological Methods*, **279**, 277–85.

42 Han, M.Y., Gao, X.H., Su, J.Z. and Nie, S.M. (2001) Quantum-dot-tagged microbeads for multiplexed optical coding of biomolecules. *Nature Biotechnology*, **19**, 631–5.

43 Gao, X.H., Chan, W.C.W. and Nie, S.M. (2002) Quantum-dot nanocrystals for ultrasensitive biological labeling and multicolor optical encoding. *Journal of Biomedical Optics*, **7**, 532–7.

44 Eastman, P.S., Ruan, W.M., Doctolero, M., Nuttall, R., De Feo, G., Park, J.S., Chu, J.S.F., Cooke, P., Gray, J.W., Li, S. and Chen, F.Q.F. (2006) Qdot nanobarcodes for multiplexed gene expression analysis. *Nano Letters*, **6**, 1059–64.

45 Sathe, T.R., Agrawal, A. and Nie, S.M. (2006) Mesoporous silica beads embedded with semiconductor quantum dots and iron oxide nanocrystals: dual-function microcarriers for optical encoding and magnetic separation. *Analytical Chemistry*, **78**, 5627–32.

46 Mulvaney, S.P., Mattoussi, H.M. and Whitman, L.J. (2004) Incorporating fluorescent dyes and quantum dots into magnetic microbeads for immunoassays. *Biotechniques*, **36**, 602–9.

47 Decher, G. and Schlenhoff, J.B. (2003) *Multilayer Thin Films*, Wiley-VCH Verlag GmbH, Weinheim, Germany.

48 Yang, W.J., Trau, D., Renneberg, R., Yu, N.T. and Caruso, F. (2001) Layer-by-layer construction of novel biofunctional fluorescent microparticles for immunoassay applications. *Journal of Colloid and Interface Science*, **234**, 356–62.

49 Wang, D.Y., Rogach, A.L. and Caruso, F. (2002) Semiconductor quantum dot-labeled microsphere bioconjugates prepared by stepwise self-assembly. *Nano Letters*, **2**, 857–61.

50 Caruso, F., Caruso, R.A. and Möhwald, H. (1998) Nanoengineering of inorganic and hybrid hollow spheres by colloidal templating. *Science*, **282**, 1111–14.

51 Sukhorukov, G.B., Donath, E., Lichtenfeld, H., Knippel, E., Knippel, M., Budde, A. and Möhwald, H. (1998) Layer-by-layer self assembly of polyelectrolytes on colloidal particles. *Colloids and Surfaces A – Physicochemical and Engineering Aspects*, **137**, 253–66.

52 Wilson, R., Spiller, D.G., Prior, I.A., Bhatt, R. and Hutchinson, A. (2007) Magnetic microspheres encoded with photoluminescent quantum dots for multiplexed detection. *Journal of Materials Chemistry*, **41**, 4400–6.

53 Wilson, R., Spiller, D.G., Prior, I.A., Veltkamp, K.J. and Hutchinson, A. (2007) A simple method for preparing spectrally encoded magnetic beads for multiplexed detection. *ACS Nano*, **1**, 487–93.

54 Bobrow, M.N., Adler, K.E. and Schermer, M.J. (2006) WO/2007/075891.

55 Kim, K.S. and Park, J.K. (2005) Magnetic force-based multiplexed immunoassay using superparamagnetic nanoparticles in microfluidic channel. *Lab on a Chip*, **5**, 657–64.

56 Schneider, T., Moore, L.R., Jing, Y., Haam, S., Williams, P.S., Fleischman, A.J., Roy, S., Chalmers, J.J. and Zborowski, M. (2006) Continuous flow magnetic cell fractionation based on antigen expression level. *Journal of Biochemical and Biophysical Methods*, **68**, 1–21.

57 Chalmers, J.J., Zborowski, M., Sun, L.P. and Moore, L. (1998) Flow through, immunomagnetic cell separation. *Biotechnology Progress*, **14**, 141–8.

58 Espy, M.A., Sandin, H., Carr, C., Hanson, C.J., Ward, M.D. and Kraus, R.H. (2006) An instrument for sorting of magnetic microparticles in a magnetic field gradient. *Cytometry Part A*, **69A**, 1132–42.

59 Pamme, N. and Manz, A. (2004) On-chip free-flow magnetophoresis: continuous flow separation of magnetic particles and agglomerates. *Analytical Chemistry*, **76**, 7250–6.

60 Hu, W., Wilson, R.J., Koh, A., Fu, A., Faranesh, A.Z., Earhart, C.M., Osterfeld, S.J., Han, S.J., Xu, L., Guccione, S., Sinclair, R. and Wang, S.X. (2008) High-moment antiferromagnetic nanoparticles with tunable magnetic properties. *Advanced Materials*, **20**, 1479–83.

Keywords

multi-analyte; arrays; sensors; giant magnetoresistive; Hall; SQUID; encoded; microspheres

3
Magnetophoretic Biosensing and Separation Using Magnetic Nanomaterials

Joo H. Kang, Young Ki Hahn, Kyu Sung Kim, and Je-Kyun Park

3.1
Introduction

Nanomaterials have shown, and continue to show, considerable promise for the detection and separation of objects of interest, and in this context have been widely used in biology and medicine for over 50 years [1, 2]. Today, many advanced techniques have been devised for the straightforward production of homogeneous nanomaterials, which involve: first, the reaction of a gaseous mixture at a hot surface; second, a cooling of the mixture from a hot gas or plasma; and third, the formation of intermolecular forces during the self-assembly of individual components [3]. Consequently, nanomaterials continue to attract a great deal of attention because, by using these new techniques, their application can be easily and extensively controlled and tuned.

Among currently available nanomaterials, magnetic variants are used in a wide range of research areas, including catalysis, biomedicine, and magnetic resonance imaging (MRI), generally on the basis of their functional versatility [4–10]. In particular, magnetic nanomaterials have the potential to create a sensation among current clinical diagnostics, biosensors, separations, and drug delivery applications, based on not only their unique physical properties but also their ability to function at the cellular and molecular level in biological interactions. Most often, magnetic nanomaterials consist of magnetic elements such as iron, nickel, cobalt and manganese (and chemical compounds thereof), and so may be easily provided with a biocompatible surface coating that endows them with great stability under physiological conditions. It is on account of these properties that the use of magnetic nanomaterials in biological detections and separations leads not only to an enhancement of the sensor's signal sensitivity but also to a reduction in the physical size of the detection and separation systems.

Magnetophoresis is a phenomenon which describes the particle migration that occurs when a magnetic force is exerted on a particle. The magnetic force induced by an external magnetic field causes an object to move towards a denser or more sparse magnetic field. Whilst all particles exhibit their own magnetic properties,

Nanomaterials for the Life Sciences Vol. 4: Magnetic Nanomaterials. Edited by Challa S. S. R. Kumar

ISBN: 978-3-527-32154-4

according to their chemical compositions, the intensity of the magnetic force – and its direction – depend on the magnetic properties of the materials and also on their surroundings, including their diamagnetism and paramagnetism. The principle of magnetophoresis was recently applied to magnetic biosensors, in which magnetic microbeads and nanoparticles were used as a solid support and a labeling, respectively [11–15]. Originally, the role of magnetic microbeads in magnetic biosensors was linked with the function of separation, because they provided biomolecules of interest which not only had a reaction space but could also be used to separate the biomolecules. The same strategy has also been adapted to other detection methods, but based on principles of fluorescence and electrochemistry [16–18]. While magnetic microbeads are generally used for the separation of target materials, magnetic nanoparticles can be used directly for magnetophoretic sensing in biosensors, these actions being based on the detection of biologically functionalized magnetic labels of cells or microbeads in a magnetic field-induced microchannel with high sensitivity. Recently, a number of magnetophoretic biosensors using magnetic nanoparticles as labels have been developed [19, 20] and applied to the analysis of biomolecule concentrations. This approach employs the magnetophoretic mobility of a microbead, and depends on the amount of associated superparamagnetic nanoparticles under a magnetic field gradient in a microfluidic channel. By measuring the magnetophoretic deflection velocity of microbeads as a signal for the presence of analytes, it was possible to quantify multiple analytes, in simultaneous fashion, by using conjugated nanoparticles as labels.

Magnetic microparticles and nanoparticles have long been used for the separation of biomolecules [21], and among the various separation applications [22] can be included the immunomagnetic separation of cells. Such separation has been especially important in cell biology and medicine, where magnetic-activated cell sorting (MACS) has provided the means to separate cells of interest from mixed-cell populations [17, 23–27]. In MACS, magnetic microparticles and nanoparticles are first conjugated with antibodies specific to the cell membrane protein of interest. Subsequently, when the magnetic particle-bound cells are maintained in a strong magnetic field, the target cells will be separated from any untreated samples containing impurities.

In general, two cell separation methods are used, namely direct and indirect [28]:

- In the *direct method*, magnetic nanoparticles with appropriate affinity ligands are applied directly to the target cells. When the magnetic nanoparticles have become bound to the target cells, the solution containing the complexes is allowed to flow through a separating column to which is applied a magnetic field.

- In the *indirect method*, a free affinity ligand (in most cases an appropriate antibody, which often is biotinylated) is first added to the cell suspension, after which the labeled cells are captured by magnetic nanoparticles bearing an affinity ligand against the primary label (e.g., secondary antibodies or

streptavidin). As with the direct method, the resultant magnetic complex can be separated by using an appropriate magnetic separator.

The magnetic nanoparticles which are used to label the cells have no negative effect on cell viability, and the isolated cells will remain unaffected. The extremely small size of the magnetic nanoparticles also means that the cells avoid mechanical stress, and that the incubation time will be short and the processing rapid. The nanoparticles form a stable colloidal suspension, and neither sediment nor aggregate in the magnetic field. Their size and composition would normally render the particles biodegradable, but typically they neither activate the cells nor influence cell function and viability. Accordingly, the cells are able to retain their physiological function during the separation process [29].

In this chapter, we describe both existing and emerging magnetophoretic biosensors and separation applications using magnetic nanomaterials, the aim being to outline the basic principles and major issues that arise within each technology. The concepts of the magnetic properties of a material, magnetophoresis and high-gradient magnetic separation (HGMS) are first outlined, after which the details of magnetophoresis in a microfluidic system, including the microfabrication of microfluidic devices and measurement/analysis, are addressed. Biosensing and separation applications using magnetophoresis are then described, and some conclusions and possible future research directions proposed.

3.2 Theory

3.2.1 Magnetic Properties of a Material

The classification of a material's magnetic properties is based on its magnetic susceptibility (χ), which is defined by the ratio of the induced magnetization (M) to the applied magnetic field (H). In diamagnetic materials, the magnetic moment is antiparallel to H, resulting in very small and negative susceptibilities (-10^{-6} to -10^{-3}). Diamagnetic materials do not retain magnetic properties when the external field is removed; likewise, they have no unpaired electrons and tend to be repelled from the magnetic field. By contrast, magnetic materials show magnetic properties even if no external magnetic field is present. Magnetic materials may be divided broadly into three classes; paramagnetic; ferromagnetic; and superparamagnetic.

- Materials with magnetic moments aligned parallel to H and susceptibilities on the order of 10^{-6} to 10^{-1} are described as *paramagnetic*, in which they show magnetism only in the presence of an externally applied magnetic field. They have induced magnetic forces which respond linearly to the applied magnetic field and tend to be attracted to the external magnetic field.

- In *ferromagnetic* materials, the magnetic moments also align parallel to H, coupling interactions between the electrons of the material result in ordered magnetic states, that is, magnetic domains, and large spontaneous magnetization. Therefore, they can become saturated with a strong magnetic force and a residual magnetism exists when the applied magnetic field is removed. They are permanently magnetized when exposed to the external magnetic field. The susceptibilities of these materials depend on their atomic structures, temperature, and the external magnetic field, H.
- If the ferromagnetic materials are of a smaller size (on the order of tens of nanometers), they become a single magnetic domain and therefore maintain one large magnetic moment; they are then known as *superparamagnetic* materials. Superparamagnetic materials have lost their net magnetization in the absence of an external field at sufficiently high temperatures because the magnetic dipole–dipole interaction energy is weaker than thermal energy. This superparamagnetic property enables the particles to maintain their colloidal stability and to avoid aggregation, which makes their use feasible in biomedical applications. Furthermore, the coupling interactions within these single magnetic domains result in much higher magnetic susceptibilities than for paramagnetic materials. Due to these properties of superparamagnetic materials, magnetic nanomaterials have been used in biosensors which require a high sensitivity and biomolecular separation systems, although ferromagnetic materials may be used in certain systems.

3.2.2 Magnetophoresis

The force on a magnetic particle (F_m) in a magnetic field can be controlled with the volume of the particle, the difference in magnetic susceptibility, and the strength and gradient of the applied magnetic field. F_m is given by:

$$F_{tsm} = \frac{1}{2\mu_0} \Delta\chi V_m \nabla B^2 \tag{3.1}$$

where μ_0 is the magnetic permeability of free space, $\Delta\chi$ is the difference ($\Delta\chi = \chi_p - \chi_m$) in magnetic susceptibility between the magnetic material (χ_p) and the surrounding medium (χ_m), V_m is the volume of magnetic material, and B is the magnetic flux density.

As mentioned in Section 3.1, nanoparticles are used for magnetophoretic biosensing and separation. When the magnetic nanoparticles are conjugated with a cell or a microbead, the applied magnetic field will induce the magnetic force on them. The total magnetic force (F_{tm}) of the magnetic nanoparticles on the cell or microbead is the sum of the magnetic forces acting on each magnetic nanoparticle. F_{tm} is described by:

$$F_{tm} = N_m F_m = \frac{1}{2\mu_0} N_m \Delta\chi V_m \nabla B^2 \tag{3.2}$$

where N_m is the number of the magnetic nanoparticles conjugated with a cell or a microbead. In a microfluidic channel, the fluid generates a laminar rather than a turbulent flow. While the Reynolds number is <0.1, it can be assumed that drag forces follow Stokes' equation, and thus F_d is defined as:

$$F_d = -6\pi R_m \eta v \tag{3.3}$$

where R_m is the radius of the cell or microbead, η is the viscosity of the aqueous medium, and v is the velocity of the cell or microbead. The force balance on the cell or microbead can be written as:

$$F = m \cdot a = F_{tm} + F_d + F_g + F_{bou} \tag{3.4}$$

where F_g is the gravity force and F_{bou} the buoyancy force. For micrometer-scale materials, the term on the left-hand side of Equation 3.4 is much smaller than those of the magnetic and drag forces of fast-moving particles. Accordingly, the left-hand side of Equation 3.4 can be assumed to zero [30]. As the direction of the magnetic force is perpendicular to the fluid flow and gravity, we are only interested in the horizontal movement of the cell or microbead through the fluid. Based on this fact, Equation 3.4 is rewritten as:

$$0 = F_{tm} + F_d \tag{3.5}$$

Substituting Equations 3.2 and 3.3 into Equation 3.5, the velocity of the cell or microbead conjugated with magnetic nanoparticles in the microfluidic channel is represented by:

$$v = \frac{N_m V_m \Delta\chi}{12\pi R_m \eta \mu_0} \nabla B^2 \tag{3.6}$$

Equation 3.6 describes the magnetophoretic mobility of cells or microbeads conjugated with magnetic nanoparticles. If the sizes of the magnetic nanoparticles (V_m) and cells or microbeads (R_m) are assumed to be uniform, then their velocities are affected by the number of magnetic nanoparticles conjugated on the cell or microbead (N_m) and the magnetic field gradient and intensity. From this viewpoint, the principle of magnetophoresis can be applied to applications such as biosensing, in which the presence of a target biomolecule is detected and analyzed quantitatively, and separation techniques, where the cells or materials of interest are sorted from various mixtures.

3.2.3
High-Gradient Magnetic Separation

For applications using magnetic forces, two types of magnetic field are available: a homogeneous magnetic field and an inhomogeneous magnetic field. In a homogeneous magnetic field, there is no gradient in the magnetic field because the

magnetic flux density is constant over a distance. Thus, this field is unable to either attract or repel magnetic materials. In an inhomogeneous magnetic field, however, there exists a gradient in the magnetic flux density. In magnetophoresis applications, an inhomogeneous magnetic field is required to trap materials with magnetic properties and to manipulate cells using magnetic nanoparticles. In addition, the steeper the slope of the gradient in a magnetic field, the more profitable it is in magnetophoresis. To this end, microscale ferromagnetic materials are used to enhance the magnetic field gradient in microfluidic applications.

In HGMS, ferromagnetic materials are used to concentrate the external magnetic field so that the magnetic field gradient is larger and the magnetic force becomes stronger [21, 31]. The magnetic field gradient in HGMS is usually obtained by placing ferromagnetic wire into the magnetic field; this causes the ferromagnetic materials to become magnetically saturated, such that a gradient using only external magnetic field (e.g., a permanent magnet) cannot be increased by increasing the field. In HGMS, the direction of the external magnetic field and the orientation of the ferromagnetic wire can have important effects on the separation [32, 33]. According to the direction of the external magnetic field relative to the ferromagnetic wire – that is, perpendicular or horizontal – the magnetized wire can attract paramagnetic particles to part of its surface while repelling the same particles at other locations (Figure 3.1). Thus, it is possible to manipulate diamagnetic objects with magnetic fields. Such objects experience a force towards magnetic field minima, allowing for levitation

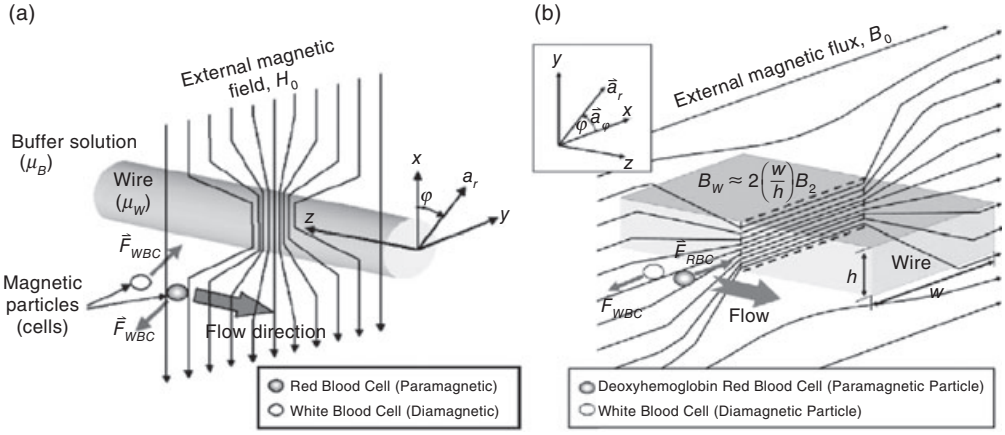

Figure 3.1 The principle of high-gradient magnetic separation (HGMS). A ferromagnetic wire in a uniform external magnetic flux concentrates the external magnetic field towards itself, so that the magnetic field deforms near the ferromagnetic wire and a high gradient magnetic field is generated. (a) The case of a magnetic field applied in a perpendicular direction to the ferromagnetic wire. Reprinted with permission from Ref. [32]; © 2004, American Institute of Physics; (b) The case of a magnetic field applied in a horizontal direction to the ferromagnetic wire. Reproduced with permission from Ref. [33]; © 2006, The Royal Society of Chemistry.

and trapping. It may also be very easy to separate and purify target materials such as mammalian cells, red blood cells (RBCs) and carbon nanotubes (CNTs) with high precision by arranging the ferromagnetic materials in a variety of structures [34–37].

Because a microchannel in which the fluid containing the cells or microbeads flows is located beside the wire, attention will be focused on the magnetic field gradient alongside the ferromagnetic wire. When applied in a perpendicular direction to the ferromagnetic wire, the magnetic field is relatively more sparse alongside the wire than at more distant regions. As shown in Figure 3.1a, the RBCs will be repelled from a magnetized wire, despite their having natural magnetic properties. In contrast, the white blood cells (WBCs), which have diamagnetic properties, are attracted to the magnetized wire. When the magnetic field is applied in a horizontal direction to the ferromagnetic wire, the field will be more dense alongside the wire; consequently, any paramagnetic particles (RBCs) will be attracted to the magnetized wire, whereas any diamagnetic particles (WBCs) will be forced away to the sparse magnetic field (Figure 3.1b).

3.3
Magnetophoresis in Microfluidic Devices

3.3.1
Design and Microfabrication Processes

The microfluidic device for magnetophoresis generally requires several components for the microchannels and the magnetic energy source. The most popular fabrication methods for microfluidic channels include the poly(dimethylsiloxane) (PDMS) micromolding process and Si-wafer micromachining. Other fabrication processes, such as hot embossing and injection molding, can provide low-cost and single-use plastic chips for magnetophoresis. However, when considering the applications and integration of microchannels with a magnetic energy source, there will be a restriction in the choice of available microfabrication process. In general, magnetic energy sources are provided either by an electromagnet or a permanent magnet. As shown in Table 3.1, the electromagnetic system [38] is advantageous for controlling magnetic forces on substances in the microchannel, although several problems may arise due to Joule heating and complicated fabrication processes.

A permanent magnet system is preferable in microfluidic magnetophoresis, because present-day, laboratory-based research investigations require simple and easy accessibility rather than the complicated, on-chip integration used in a commercial set-up [39]. In the case of the permanent magnetic system, several approaches have been shown to improve the magnetic flux density gradient across the microfluidic channel, using ferromagnetic microstructures [33, 40–42]. As described in Section 3.2.2, the magnetic force acting on a particle is proportional to the magnetic flux density gradient (dB/dx), and this is rapidly reduced

Table 3.1 Comparison of magnetic energy sources.

Magnetic energy source	Advantages	Disadvantages
Electromagnet	On-chip integration Magnetic field switching Reliable	Joule heating Energy consumption Limited field strength Nonuniform magnetic field Complicated fabrication
Permanent magnet	Inexpensive No power consumption Confined fringe field Easy accessibility	Limited field strength Limited field uniformity Temperature sensitivity Weight

with distance from the magnetic energy source. Therefore, when designing the microfluidic device it is critical that the microchannel is adjacent either to the magnetic energy source or to the magnetic field-applied ferromagnetic microstructure. Because the magnetic flux lines diverge from, and converge into, the corner of the permanent magnet (which results in a high magnetic flux density gradient in the region of the corner), it is advantageous to use the edge of the magnet adjacent to the microchannels in order to obtain an enhanced magnetic force. Unfortunately, a potential problem may arise when using an enhanced magnetic field at the edge that provides nonuniform directions of the magnetic flux lines, as this may result in magnetic forces acting on the particle, as shown in Figure 3.2.

In the past, nickel has often been used as a ferromagnetic material to enhance the magnetic flux density gradient, mainly because nickel microstructures can be obtained relatively easily by using conventional electroplating processes. Details of the microfabrication and of the microfluidic PDMS device are shown in Figures 3.3 and 3.4. Although not described in detail, the remaining PDMS film (ca. $<10\,\mu m$) at the thermal compression method (stage A5 in Figure 3.3) plays a crucial role in the prevention of fluid leakage at the interface between the microchannel and nickel microstructures. Because the deposition rate in electroplating is dependent on the current density within the electroplating seed layer, the thickness of the nickel microstructures is not uniform; consequently, a chemical mechanical polishing (CMP) process should be followed to obtain an even height of the microstructure. An alternative approach would be to use a permanent magnet to deposit a thick film of the permanent magnet (e.g., NdFeB), using triode sputtering (see Figure 3.5); this method is often used for integrated microscaled rather than macroscaled permanent magnets [43]. The same method is also useful for producing integrated microfluidic devices for magnetophoresis, although it does not allow the magnetic field to be switched on and off.

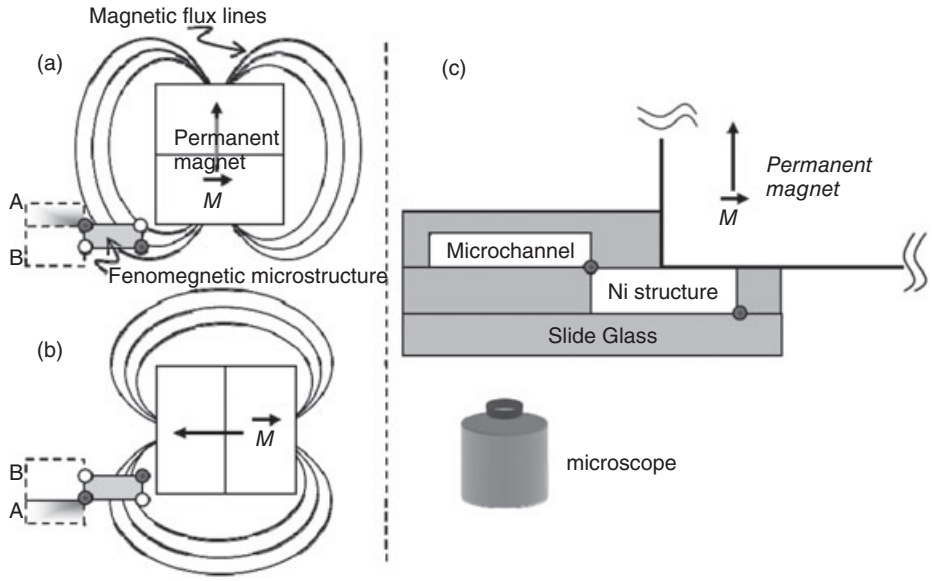

Figure 3.2 (a, b) Schematic view of the relationship between a permanent magnet and a ferromagnetic microstructure positioned near a permanent magnet. According to the magnetization direction of the magnet, magnetic-field generation appears in different shapes. Because of the ferromagnetic structure located around the edge of the magnet, a magnetic flux-density gradient is generated in a slanted direction, rather than horizontal to the sidewall of the ferromagnetic structure. In order to effectively exploit the enhanced magnetic flux-density gradient, microchannels must be located in area A rather than area B, in (a) and (b), respectively; (c) Experimental set-up of a microfluidic device and a permanent magnet and an inverted microscope. The dark-circled edges of ferromagnetic structures in (a–c) depict highly converged points of magnetic flux lines; while the open circles represent a depletion of the flux lines. Reproduced with permission from Ref. [41]; © 2007, Wiley-VCH Verlag GmbH & Co. KGaA.

3.3.2 Experimental Set-Up

Measurements for magnetophoretic biosensing and separation in microfluidic devices are carried out using a charge-coupled device (CCD)-mounted microscopic system. If the materials used to create the device are transparent (e.g., glass or PDMS), it is possible to use an inverted microscope; however, if the materials are opaque (e.g., Si wafers or metal layers), then a reflecting microscope should be used. As shown in Figure 3.6, the inverted microscopic system is generally employed for PDMS-based microfluidic devices, with the images being captured simultaneously by a CCD camera linked to a computer. Aqueous solutions injected into the microfluidic devices are manipulated precisely with syringe pumps, with the syringes and devices being connected by silicone tubes. When a permanent magnet which is several tens of millimeters in size is used, care must be taken to

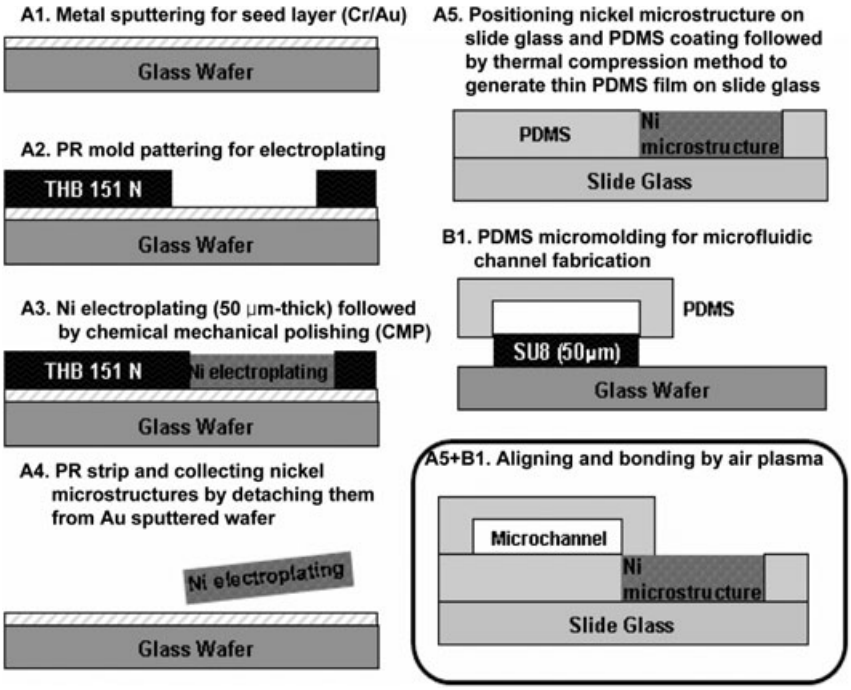

Figure 3.3 Fabrication process of a microfluidic device for magnetophoresis. The microfabrication process consists of PDMS micromolding and nickel electroplating. In the nickel electroplating step (A3), a CMP process ensures the even height of the nickel structures. After air plasma treatment of PDMS substrates, the microfluidic devices were achieved by an alignment between the microchannels and the nickel microstructures. Reproduced with permission from Ref. [41]; © 2007, Wiley-VCH Verlag GmbH & Co. KGaA.

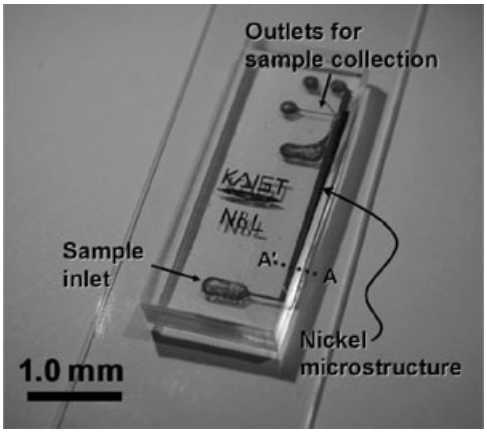

Figure 3.4 The microfluidic PDMS device fabricated by the processes described in Figure 3.3.

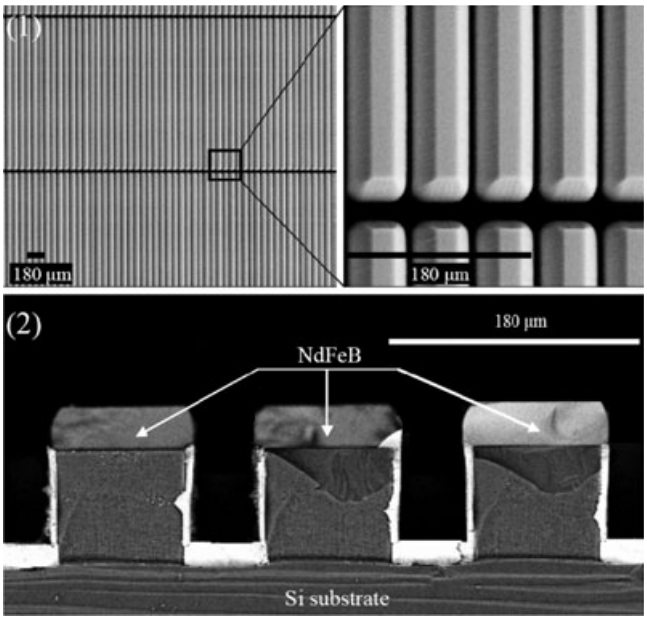

Figure 3.5 Scanning electron microscopy images of 30 μm-thick NdFeB micro-magnets. 1, top view; 2, cross-sectional view. Reproduced with permission from Ref. [43]; © 2007, IEEE-Copyrighted Material.

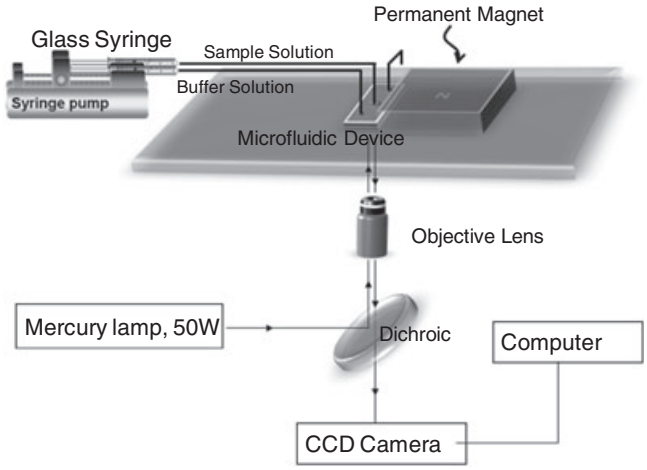

Figure 3.6 Experimental set-up for microfluidic magnetophoresis. The microfluidic device is mounted on an inverted microscope and a permanent magnet is located near the device. The aqueous samples are injected by syringe pumps, and the movements of particles, including cells, are observed with a CCD camera.

prevent the magnet from suddenly moving to the ferromagnetic compartments of the microscope. The surroundings of the microfluidic device and permanent magnet (objective lens, stages, microscope frame) should not contain any ferromagnetic materials such as nickel, iron, cobalt, nor alloys of them, because these can affect and reduce the magnetic field around the microfluidic channels. The magnetic field intensity can be modulated in a permanent magnet system, where the distance between the permanent magnet and the device can be manipulated by using a linear moving stage (M-460A-XYZ; Newport Corporation, CA, USA) to modulate the magnetic field intensity acting on the microfluidic channel [19].

3.3.3
Measurement and Analysis

Microscaled particles (e.g., polystyrene particles) and cells can be observed by the CCD camera, and their movement traced by using either commercialized software (e.g., i-Solution; IMT i-Solution Inc., Vancouver, Canada) or custom-made programs coded by Matlab® and C++. The positions of the fluorescent particles can be easily measured using fluorescence microscopy, and analyzed with an image analysis program. However, those particles which do not contain fluorescent dyes cannot be simply distinguished from the background images, and their positions (x-y coordinates) are rarely detectable via any automatic acquisition mode of the software. Several steps of image processing, followed by image capture, can be used to improve image quality and assist in the automatic measurement of the particle positions determined by the software. If the automatic image program for the particle position measurement is not available due to the background noise of the images, then each image containing the particles should be analyzed manually using programs such as ImageJ (W. Rasband, ImageJ 1.29, freeware, http://rsb.info.nih.gov/ij/) and i-Solution.

Nanoscale particles, such as CNTs and magnetic nanoparticles, are rarely detectable by using a conventional CCD camera, due to their inherent small size. Consequently, a variety of alternative analytical procedures should be applied to determine magnetophoretic separation, including energy-dispersive X-ray spectroscopy (EDS), scanning electron microscopy (SEM), transmission electron microscopy (TEM), thermogravimetric analysis (TGA), superconducting quantum interference devices (SQUID), and Raman spectroscopy [41]. Magnetophoretic separation can be evaluated either by an *in situ* analysis in the microfluidic channel, using microscopic tools (CRAIC Technologies, Inc., www.microspectra.com, San Dimas, CA, USA), or by analyzing samples collected from the microfluidic devices, using the above-described techniques.

3.4
Magnetophoretic Biosensing

Among biosensor applications, a variety of sensing principles, such as detecting the magnetic properties of target materials and/or of the magnetic micro/

nanoparticles conjugated to them, have been widely used over the past few decades. In general, biosensors using magnetic materials measure the permeability and/or susceptibility of target molecules or magnetic micro/nanoparticles, allowing not only their presence to be determined but also their quantitation [11, 44–48]. In addition to these principles, methods which measure changes in the resonant frequency of a coil of wire when magnetic micro/nanoparticles are placed, or when biomolecules are captured on the substrate inside the coil, have also been developed [49–52]. Although these methods show excellent sensitivity, they also incorporate several disadvantages, notably a requirement for complex and expensive equipment that is also difficult to miniaturize. More recently, new magnetophoretic principles for biomolecular sensing have also been investigated [19, 20, 53, 54] that provide an improved sensitivity and allow the system to be miniaturized. Such advances would indeed open the door to point-of-care (POC) systems.

3.4.1 Magnetophoretic Sandwich Immunoassay

Today, immunoassay is a universal method applied to both routine analyses and research investigations in biological and medical sciences, with sandwich immunoassays using labeled materials for fluorescent, electrochemical and magnetic detection being used extensively. Among these variations, immunoassays employing magnetic labels have been especially effective due to their high sensitivity and convenience of detection. Recently, Park and coworkers have developed a new series of magnetophoretic immunoassay principles [19], having described a microfluidic immunoassay which utilizes the binding of superparamagnetic nanoparticles (SMNPs) to microbeads and the subsequent deflection of microbeads in a magnetic field as the signal for measuring the presence of an analyte. In this procedure, the 50 nm SMNPs and 1 μm fluorescent polystyrene microbeads are immobilized with specific antibodies. Subsequently, when the target analytes react with the microbeads and SMNPs simultaneously, the latter become attached to the microbeads via an antigen–antibody complex. As a result, within the PDMS microfluidic channel, only those microbeads which are conjugated to SMNPs by analytes can move to the high-gradient magnetic field under the applied magnetic field. In addition, it is possible to perform a quantitative analysis of the analytes, because the amount of SMNPs conjugated to a microbead will differ according to the concentration of the analytes. If the concentration of SMNPs on a microbead increases, then the velocity of a microbead will be increased, since this is proportional to the total volume of magnetic nanoparticles on a microbead and the magnetic field gradient [55]. Consequently, the concentration of target biomolecules can be analyzed simply by measuring the velocity of the microbeads. This new magnetophoretic immunoassay was verified in the microfluidic device shown in Figure 3.7. Here, the buffer and sample solutions containing the microbead–magnetic nanoparticle complexes is injected into each side of the inlets. The microbeads are hydrodynamically focused at the junction part of two inlets (Figure 3.7b), after which the hydrodynamically focused sample solutions may flow

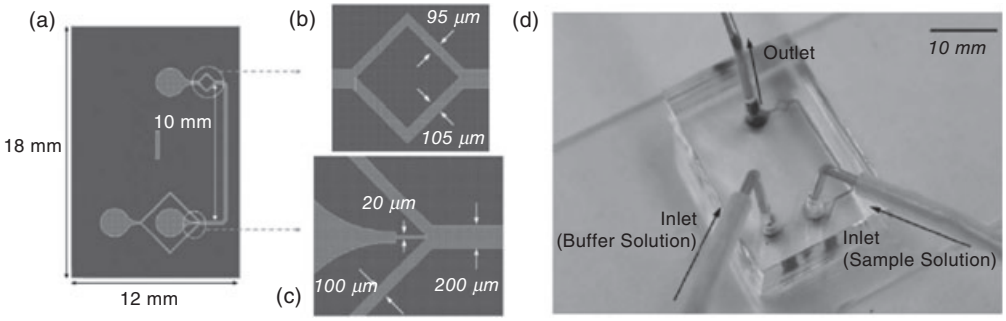

Figure 3.7 (a) Layout of the device which has two inlets and one outlet; (b) At the part of the inlet, sample solution was hydrodynamically focused; (c) The focused sample solution flowed through the 105 μm-wide channel before the outlet; (d) A photograph of the fabricated device. Reproduced with permission from Ref. [19]; © 2005, The Royal Society of Chemistry.

through a 10 mm-long microchannel, to the right-hand side of which is located a permanent magnet.

In these studies, the magnetic force-based microfluidic immunoassay was successfully applied to detect rabbit immunoglobulin G (IgG) and mouse IgG as model analytes. For this, a sandwich immunoassay was performed using the yellow-green-fluorescent microbeads immobilized with goat anti mouse IgG, and red-fluorescent microbeads immobilized with goat anti rabbit IgG. The concentration of the red-fluorescent microbeads was 2.55×10^5 microbeads in 70 μl of buffer solution, while the antigen solution (10 μl) contained rabbit IgG at different concentrations. A control experiment was carried out with 10 ml of 0.1% bovine serum albumin in phosphate-buffered saline, instead of rabbit IgG. A background velocity, which was defined as the velocity of the microbead without attached SMNPs, was not observed, except for the oscillation due to the diffusion effect. The background velocity was $<0.05\,\mu m\,s^{-1}$. In contrast, the mean velocity at a concentration of $250\,ng\,ml^{-1}$ rabbit IgG was $2.39 \pm 0.3\,\mu m\,s^{-1}$ (Figure 3.8a). As shown in the figure, the velocities of the microbeads were measured over a range of concentrations of rabbit IgG, from $1\,ng\,ml^{-1}$ to $1\,\mu g\,ml^{-1}$. When subsequently, and under the same experimental conditions, a quantitative analysis of mouse IgG was performed (Figure 3.8b), the velocities of both rabbit and mouse IgGs were almost saturated at approximately $1\,\mu g\,ml^{-1}$ and $2\,\mu g\,ml^{-1}$, respectively. The reason for this saturated velocity can be explained by the limited binding capacity of the microbead surface, with the lowest concentrations of rabbit and mouse IgG measured over the background being $244\,pg\,ml^{-1}$ and $15.6\,ng\,ml^{-1}$, respectively. The velocities of microbeads conjugated with SMNPs may be demonstrated by magnetic field gradients in microfluidic channels.

In this magnetophoretic assay system, the dynamic range was shown to be controlled by the area on which the reactions between the two proteins were

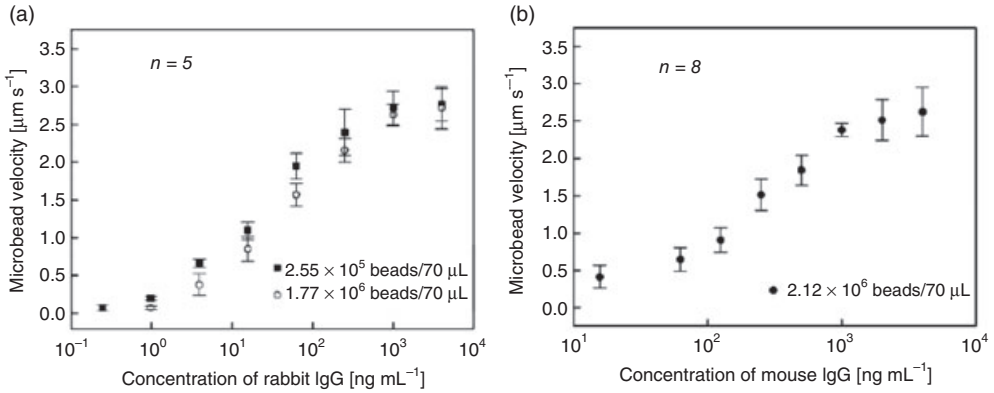

Figure 3.8 (a) Results of magnetic force-based microfluidic sandwich immunoassay for detection of rabbit IgG. Detection was feasible over a concentration range from 1 ng ml^{-1} to 1 μg ml^{-1}; (b) The dynamic range of mouse IgG was 62.5 ng ml^{-1} to 2 μg ml^{-1}. Reproduced with permission from Ref. [19]; © 2005, The Royal Society of Chemistry.

carried out. The experiment was then repeated by assaying rabbit IgG under the same conditions, but with a different concentration of microbeads, namely sevenfold (1.77×10^6 microbeads in 70 μl). As shown in Figure 3.8a, the range of detectable concentrations was shifted to the right compared to the above experiment, which used different concentrations of microbeads (2.55×10^5 microbeads in 70 μl). This shift was mainly due to the increased total surface area of the microbeads. Based on these results, it appears that the detection ranges can be adjusted by changing the concentration of the microbeads.

This system enabled the detection of dual analytes within a single reaction, using fluorescent-encoded microbeads in the microfluidic device. This magnetophoretic assay system was also shown to be capable of controlling the detectable range of analytes by adjusting the magnetic field (by altering the location of the permanent magnet). All of these procedures and reactions were performed in one tube, with the reacted microbeads outside the magnetic field gradient flowing along their own focused line (Figure 3.9a), and thus maintaining their flow path. However, when the magnet was placed 4 mm away from the microchannel, the flow path of red-fluorescent microbeads was shifted such that they flowed through the upward channel; however, the yellow-green-fluorescent microbeads were restricted to their own flow path (see Figure 3.9b). However, when the magnet was adjusted to be only 2 mm away from the microchannel, the flow paths of both red- and yellow-green-fluorescent microbeads were switched to the upward channel (Figure 3.9c).

This magnetophoretic assay system differs from any previous assay systems using magnetic micro/nanoparticles, in that the magnetic nanoparticles function not as a label for direct detection (e.g., via permeability or susceptibility), but rather as an epochal tool, without complex measurement equipment. As mentioned

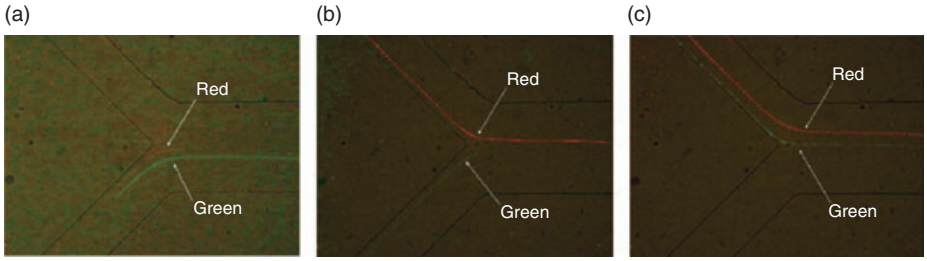

Figure 3.9 CCD images of fluorescent microbeads. The original background images of fluorescent microbeads were dark, but a microchannel image on the same place was folded on the original images in order to show the trace of the microbeads. (a) The trace of the microbeads without a permanent magnet; (b) The trace of the microbeads with a permanent magnet which was 4 mm away from the microbeads; (c) The trace of the microbeads with a permanent magnet 2 mm away from the microbeads. Reproduced with permission from Ref. [19]; © 2005, The Royal Society of Chemistry.

above, the dynamic range and detection limit can be easily adjusted via the microbead concentration and a higher magnetic field gradient. In addition, the magnetic force detection scheme may possibly be utilized in multiplexed biological assays.

3.4.2 Highly Sensitive Biosensors Using HGMS

In biosensor applications, the detection limit represents a crucial factor, especially when infinitesimally small biomolecules are to be analyzed for the early diagnosis of cancer and the detection of specific proteins. In the case of a magnetophoretic assay system, the most effective approach is to enhance the magnetic field gradient and, for this purpose (see Section 3.2.3), ferromagnetic materials are often used to concentrate the magnetic field. If ferromagnetic materials are introduced into a microfluidic device, it is possible to detect materials with low paramagnetic properties, for example RBCs which contain high concentrations of paramagnetic hemoglobin, and/or magnetotactic bacteria which contain small magnetic particles within their cells [28]. It is also possible to separate diamagnetic and paramagnetic materials relatively easily, such that the ferromagnetic material will provide a sensor with better sensitivity and resolution [56]. Moreover, if the ferromagnetic material is arranged in a variety of dispositions, the analytes can be detected in a desirable region, without the need for a complex magnetic field [35–37].

The effect of a ferromagnetic material in a magnetic field gradient was calculated and compared with the case of a permanent magnet [20]. As the magnetophoretic drag velocity is proportional to the analyte concentration and magnetic field gradient, the detection limit can be improved by increasing the velocity under a higher magnetic field gradient. To confirm this effect, the magnetic flux density gradient of a permanent magnet and that of a Ni microstructure under an external magnetic field were simulated by using a FEMM program. Both, the simulation and

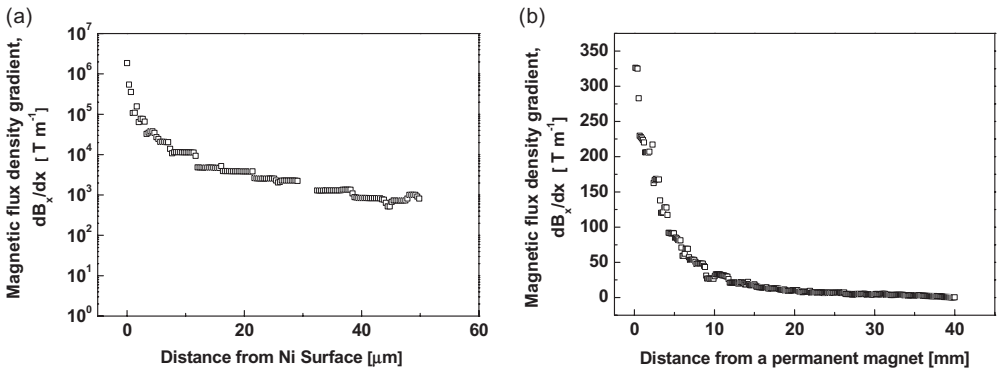

Figure 3.10 Comparison of simulated results between a permanent magnet and a Ni microstructure under external magnetic field: profiles of simulated magnetic field gradient (a) with a Ni microstructure under external magnetic field and (b) with a permanent magnet only. Reproduced with permission from Ref. [20]; © 2007, American Chemical Society.

experimental conditions were identical. The height, width, and length of the permanent magnet were 10, 25, and 50 mm, respectively, while the height and width of the Ni microstructure were 50 μm and 50 μm, respectively. The distance between the permanent magnet and the Ni microstructure was 2 mm. The properties of the permanent magnet were as follows: relative recoil permeability, 1.05; density, 7.4 g cm^{-3}; and specific resistivity, 144 μΩ · cm. Figures 3.10a and b show the simulated results with a Ni microstructure under the external magnetic field and a permanent magnet only, respectively. The simulated magnetic field gradient of a permanent magnet was approximately 200 T m^{-1} in the region concerned, which was approximately 2 mm away from the permanent magnet. By contrast, the Ni microstructure under the external magnetic field exhibited about a 50-fold enhanced gradient (~10^4 T m^{-1}) compared to the permanent magnet, thus confirming that the ferromagnetic material had concentrated the magnetic flux density. On the basis of this expectation, the effect of ferromagnetic material in the biosensor was evaluated [53]. When compared with previous results [19], this case increased the sensitivity about 250-fold, as shown in Figure 3.11. Whereas, the detection limit of the permanent magnet alone was 244 pg ml^{-1}, that of the ferromagnetic material was 1 pg ml^{-1}. It appears, therefore, that the detection sensitivity of this assay system can be improved to cover femtomolar concentrations.

3.4.3
Disease Diagnosis Using Magnetophoretic Assay Systems

Diagnosis represents a highly important process in evaluating the condition of a person and the type of disease(s) that might be present. Often, there is a

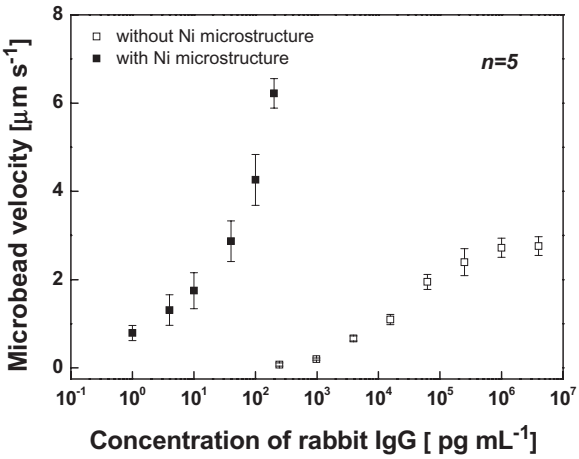

Figure 3.11 Results of detection for IgG using the microfluidic devices with and without the Ni microstructure.

requirement to monitor the infinitesimally small levels of specific proteins in a patient's serum in order to achieve an early diagnosis of a disease. The need for a highly sensitive biosensor is a particular diagnostic requirement for the biomarkers of cancer, and also of the serum levels of immunoglobulin E (IgE) as a criterion of an allergic response. Based on these needs, a magnetophoretic biosensor for the diagnosis of allergies was recently developed [20] which incorporated a magnetophoretic immunoassay of allergen-specific IgEs. This was based on the magnetophoretic deflection velocity of a microbead associated with magnetic nanoparticles under an enhanced magnetic field gradient in a microfluidic channel. In this detection scheme, two types of house dust mite, *Dermatophagoides farinae* and *Dermatophagoides pteronyssinus*, were used for the diagnosis of allergy. Polystyrene microbeads conjugated with each of the mite extracts were incubated with serum samples, and the resultant mixtures reacted with magnetic nanoparticle-conjugated anti-human IgE, in order to detect allergen-specific IgEs by using sandwich immunoreactions. Following the creation of a standard curve for the diagnosis system, unknown samples were subjected to a "blind" test and compared with a conventional test kit (CAP system), the aim being to evaluate the reproducibility and accuracy of the newly developed magnetophoretic immunoassay system.

To prepare a standard curve for the diagnosis system, pooled serum samples were used from 44 patients (aged from 2 to 62 years) [20]. It has been reported that the sera of patients with different allergies demonstrate different IgE reactivity profiles from those of house mite allergens [57, 58]. In order to minimize the effect of such differences on IgE reactivity profiles in the standard curve and in sample-to-sample variation of their protein contents, four or five serum samples from patients were pooled with the same volume for *D. farinae* and *D. pteronyssinus*, respectively. Mite allergen-specific IgE levels in the pooled serum were then determined using a commercial diagnostic kit (CAP system).

When the magnetophoretic velocities of microbeads were measured in a microfluidic channel under an enhanced magnetic field using a ferromagnetic material, the deflection velocity of a SMNP-associated microbead was shown to depend on the number of associated SMNPs, as reported previously [19, 53]. For the background experiment, the velocity of a microbead for the allergen of *D. farinae* was shown to be approximately $0.3 \pm 0.16\,\mu m\,s^{-1}$ (Figure 3.12a). However, for the negative control experiment, whereby $1\,\mu g\,ml^{-1}$ of purified human IgE was added to a reaction mixture, the velocity of a microbead was estimated as $0.65 \pm 0.36\,\mu m\,s^{-1}$ (Figure 3.12b). The deflection velocity of a microbead in the negative control experiment was generally within the range of background level, despite the concentration of purified IgE used being much higher than the maximum concentration of allergen-specific IgE in the *D. farinae* experiment. These results indicated that there was a negligible cross-reactivity between *D. farinae* allergen-specific human IgEs and other human IgEs in this detection system.

The mite allergen-specific human IgEs in serum were measured using the system developed for pooled sera. As a result, the velocity of a microbead

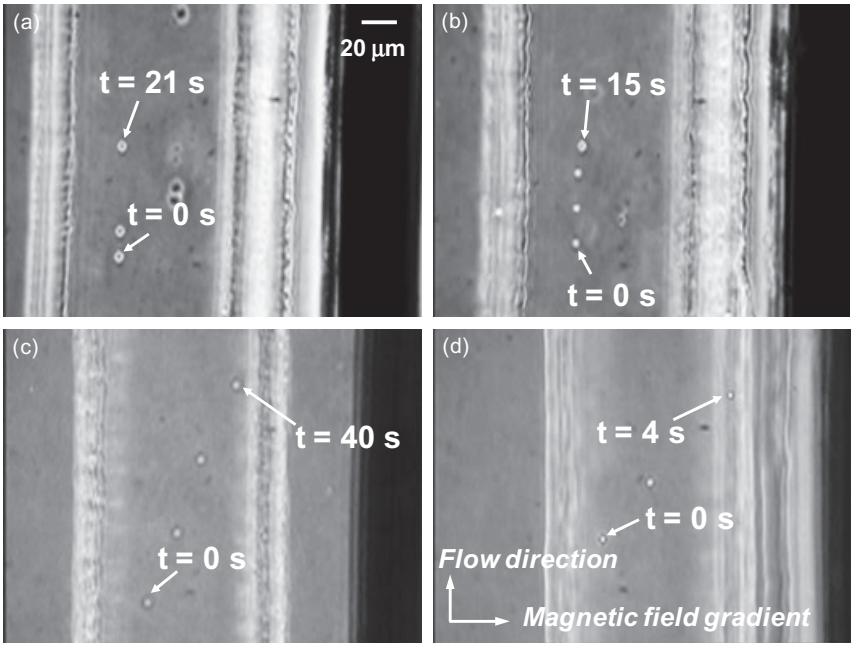

Figure 3.12 CCD images showing the movement of *D. farinae* allergen-conjugated microbeads at different time intervals for various concentrations of analyte. (a) Background control (analyte: 10 μl of phosphate-buffered saline); (b) A negative control (analyte: 10 μl of 190 μ*M* purified human IgE containing no mite allergen-specific human IgE); (c) Injection of 547 f*M* *D. farinae* allergen-specific human IgE; (d) Loading of 102.5 p*M* *D. farinae* allergen-specific human IgE. Reproduced with permission from Ref. [20]; © 2007, American Chemical Society.

conjugated with allergen from *D. farinae* increased with the increasing concentration of *D. farinae* allergen-specific human IgE, ranging from 547 f*M* to 102.5 p*M*. The lowest concentration of human IgE measured over the background level was about 547 f*M*, while the mean velocity at the lowest concentration (547 f*M*) of human IgE was $1.78 \pm 0.36\,\mu m\,s^{-1}$ (see Figure 3.12c). With 102.5 p*M* human IgE, the velocity was estimated as $14.58 \pm 0.81\,\mu m\,s^{-1}$ (Figure 3.12d). In a similar experiment conducted with the *D. pteronyssinus* allergen, the velocities in the background and negative control experiments were determined as $0.11 \pm 0.09\,\mu m\,s^{-1}$ and $0.36 \pm 0.07\,\mu m\,s^{-1}$, respectively. The velocity of a microbead was measured for concentrations of *D. pteronyssinus* allergen-specific human IgEs ranging from 795 f*M* to 56.2 p*M*. The lowest concentration of human IgE measured over the background was approximately 795 f*M*, and the mean velocity at the lowest concentration (795 f*M*) of human IgE was $1.0 \pm 0.48\,\mu m\,s^{-1}$. In the presence of 56.2 p*M* human IgE the velocity was $10.0 \pm 0.33\,\mu m\,s^{-1}$. Based on these measured velocities, standard calibration curves for the two allergen-specific human IgEs were developed (see Figure 3.13).

In order to evaluate the developed magnetophoretic immunoassay system, unknown samples were subjected to blind testing and compared with the results obtained with a conventional test kit (Table 3.2). Eight patient sera were used for the diagnosis of *D. farinae* and *D. pteronyssinus* allergens, respectively. Based on the measured velocity of a microbead, and using the same procedure, the concentration of mite allergen-specific human IgE in serum was determined from the respective calibration curve shown in Figure 3.8. As with samples of *D. farinae*,

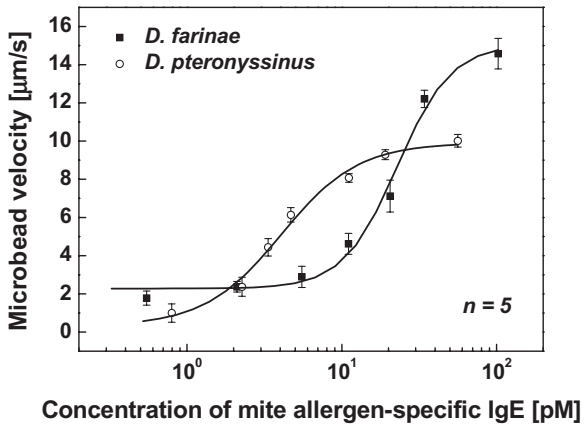

Figure 3.13 Deflection velocities of microbeads with respect to the concentrations of *D. farinae* and *D. pteronyssinus* allergen-specific human IgEs, respectively. The velocities of five microbeads were independently determined. Error bars indicate the means and standard deviations of measurements. Reproduced with permission from Ref. [20]; © 2007, American Chemical Society.

Table 3.2 Blind tests of unknown sera samples, and comparison with a CAP system.

Source of allergen	Patient number	Microbead velocity[a] ($\mu m\,s^{-1}$)	IgE concentration		
			From standard curve (p*M*)	From standard curve ($IU\,ml^{-1}$)	From CAP system ($IU\,ml^{-1}$)
D. farinae	B-1	2.531 ± 0.33	4.89 ± 0.95	0.388	0.37
	B-2	2.64 ± 0.34	5.63 ± 2.42	0.446	0.5
	B-3	8.215 ± 0.79	21.4 ± 2.16	1.7	1.74
	B-4	14.488 ± 0.948	76.3 ± 13.4	6.17	6.33
D. pteronyssinus	B-5	1.947 ± 0.35	1.66 ± 0.237	0.13	<0.35
	B-6	6.01 ± 0.49	5.0 ± 0.579	0.396	0.38
	B-7	7.815 ± 0.82	8.26 ± 2.53	0.65	0.85
	B-8	9.683 ± 0.42	33.8 ± 8.05	2.68	2.83

a Five microbeads were used for determination of the average velocity.
Reproduced with permission from Ref. [20]; © 2007, American Chemical Society.

the concentrations of IgEs in the B-1, B-2, B-3, and B-4 samples were determined as 4.89, 5.63, 21.4, and 76.3 p*M*, respectively, and coincided well with data acquired with the CAP system. In a similar manner, the concentrations of IgEs for *D. pteronyssinus* in four serum samples also correlated well with data provided by the CAP system. Blind testing using a magnetophoretic immunoassay revealed a good correlation with the CAP system, with an R^2 value of 0.9989. The coefficient of variance (CV) of the magnetophoretic immunoassay system was calculated as 10.2% (range: 4.1–17.5%), and comparable with that for the CAP system (10.3%; range: 6–14%) [59].

Based on these results, magnetophoretic immunoassay system has been verified as effective for the diagnosis of mite allergy, with a good reliability. In addition, the detection limits for *D. farinae* and *D. pteronyssinus* were estimated as 565 f*M* ($0.045\,IU\,ml^{-1}$) and 268 f*M* ($0.021\,IU\,ml^{-1}$), respectively, these levels being about one order of magnitude lower than those determined with a conventional CAP system ($0.35\,IU\,ml^{-1}$). Unfortunately, however, the magnetophoretic assay system showed one disadvantage in that it was vulnerable to multiplexing and, consequently, it is imperative that a multiplexed assay system for the biosensor be developed. For the purpose of multiplexing, several such assay systems with various detection principles have recently been developed (see Section 3.4.4).

3.4.4
Multiplexed Magnetophoretic Immunoassay

Although the demand for multiplexed assays of important target analytes continues to be high, the procedure has attracted much attention in the recent past [60–63]. A multiplexed assay can provide quantitative information on target

analytes of major physiological significance in a high-throughput manner, thus accelerating both disease diagnosis and biomedical studies, and also permitting the screening of biomolecules of interest. In the case of multiplexed assays, several research groups have focused on microsphere-based suspension arrays, based on their high flexibility for target selection, fast binding kinetics, good reproducibility, and easily controlled binding conditions [64, 65]. Recently, multiplexed microsphere-based suspension arrays have been reported which employ fluorescent molecules, quantum dots, photonic crystals and radiofrequency as encoding tools [66–69]. Among these diverse detection methods, fluorescent dyes are used almost universally for the encoding of target analytes [70–72]. However, microspheres with fluorescent dyes are sensitive, because the dyes tend to be either quenched or bleached, while their broad emission bands can make the simultaneous evaluation of multiple probes difficult due to spectral cross-talk [73–75].

In seeking to substitute the fluorescent encoding method, a wide variety of principles has been investigated, including graphical encoding, physical encoding, and colored microspheres or nanoparticles [76–87]. Notably, those methods which use colored microspheres or nanoparticles are more suitable than others, in that they require no complex detection equipment and are easily applied to microfluidic devices than are other methods. The advantage of colored microspheres was recently utilized in the development of a magnetophoretic multiplexed assay system [88], with colored microspheres being used as an encoding tool in a microchannel. The colored microspheres were conjugated with respective capture molecules and then incubated with a mixture of target analytes; this was followed by a reaction with the probe molecules which had been conjugated with SMNPs (Figure 3.14). Under the magnetic field gradient, the resultant microspheres were deflected from their focused streamlines in a microchannel, and the respective colored microspheres detected by using CCD in a specific detection region of the microchannel. By using this system, it was possible to analyze simultaneously three types of biotinylated IgG (e.g., goat, rabbit and mouse), using colored microspheres (red, yellow, and blue, respectively). Here, the corresponding anti-IgGs were employed as the capture molecules, and the target analytes probed by using streptavidin-modified SMNPs.

The color and position of the respective colored microsphere were automatically decoded and analyzed by the Matlab program, and their positions correlated with the concentrations of corresponding target analytes [88]. The program for the microsphere analysis was composed of four steps. First, the program selected the captured images which contained microspheres, recognized the colored microspheres from background of the selected images, measured the positions of deflected colored microspheres, and finally determined their color. The positions of microspheres were measured by pinpointing the darkest pixels of images when the captured images were converted into gray scale. Because it is very important to detect the center of mass of a microsphere for an exact color determination, 17 pixels in long and wide small regions around the darkest pixels were selected. In these regions, those pixels with a brightness greater than predefined values were selected, after which the center of mass of selected pixels was calculated. Based

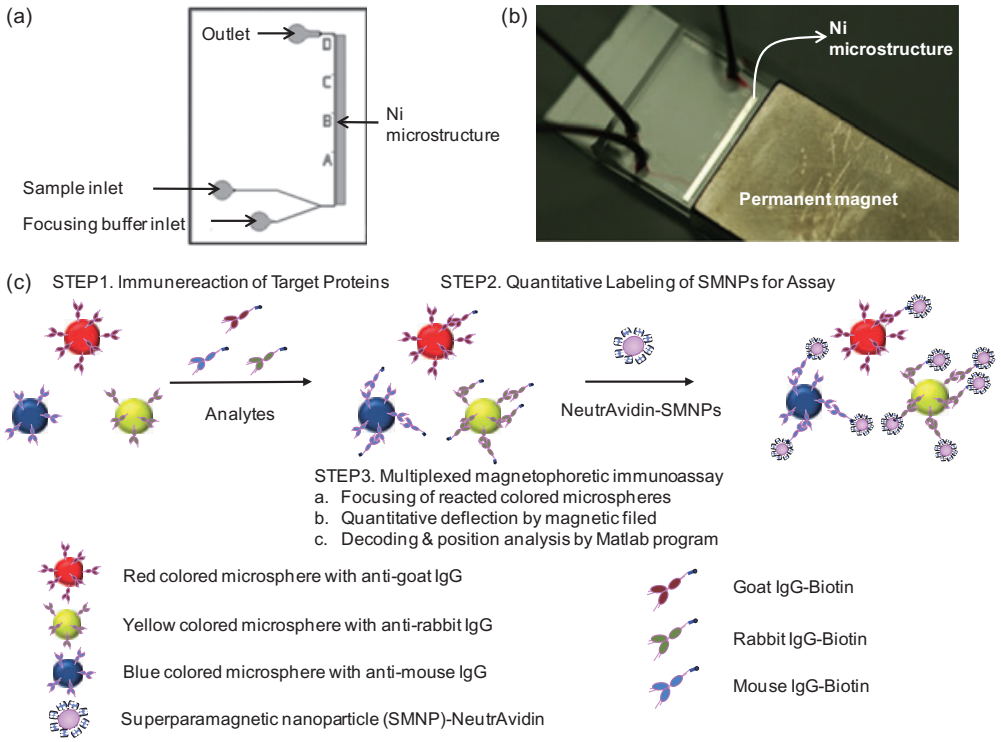

Figure 3.14 Schematic of magnetophoretic multiplexed immunoassays using colored microspheres. (a) Design of a magnetophoretic chip which comprises four detection zones, A-D. The first detection zone A was used to obtain a calibration curve by magnetophoretic assay; (b) A photograph of the fabricated magnetophoretic chip; (c) Procedure of magnetophoretic immunoassay using colored microspheres. No washing steps were required in this assay. Reproduced with permission from Ref. [88]; © 2008, Elsevier Ltd.

on this program, the colored microspheres of known colors were confirmed. This decoding program showed an accuracy of 92.6%, 96.7%, and 98.9% for red, yellow, and blue microspheres, respectively.

This magnetophoretic multiplexed system was used to determine analyte concentrations by measuring the positions of colored microspheres conjugated with SMNPs within a microchannel. Thus, focusing of the microspheres which flow through the inlet is important. By using hydrodynamic focusing, the microspheres could be focused at a location $3.46 \pm 1.89\,\mu m$ from the left wall of the microchannel, at a flow rate of $3\,\mu l\,h^{-1}$. However, when the flow rate was faster, the results of the focusing were below this value. Based on this reference, a standard curve of the magnetophoretic multiplexed system, at a flow rate of $3\,\mu l\,h^{-1}$, is shown in Figure 3.15. The positions of the respective colored microspheres were measured over ranges of concentration of goat IgG-biotin and mouse IgG-biotin from 6.7 to 666.0 f*M*, and of rabbit IgG-biotin from 26.6 to 799.2 f*M*. In the case of goat

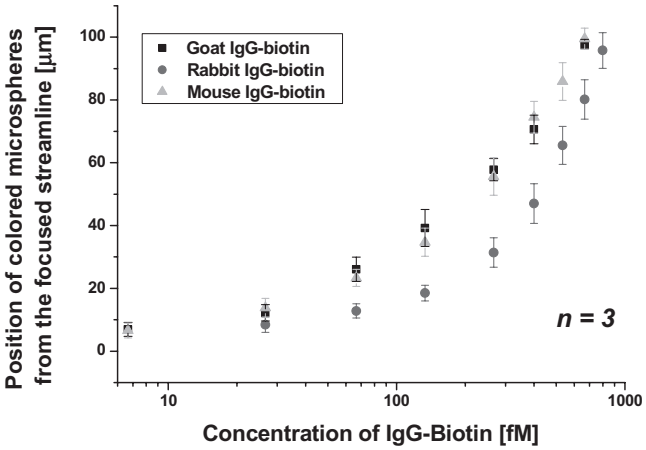

Figure 3.15 Standard curves for three types of IgG by magnetophoretic immunoassay. The standard curves were obtained at the first detection zone A and a flow rate of $3\,\mu l\,h^{-1}$. Reproduced with permission from Ref. [88]; © 2008, Elsevier Ltd.

IgG-biotin, the lowest concentration measured over background was 6.7 f*M*, and the corresponding position of the red-colored microspheres was 6.92 ± 2.22 μm. The lowest concentrations of rabbit IgG-biotin and mouse IgG-biotin were 26.6 f*M* and 6.7 f*M*, respectively, which corresponded to 8.40 ± 2.46 μm and 6.58 ± 2.35 μm, respectively. The positions of the reacted colored microspheres were found to be accordingly higher, as the concentrations of analytes were higher. The detection limits for goat IgG-biotin, rabbit IgG-biotin and mouse IgG-biotin were 10.9, 30.6 and 12.1 f*M*, respectively. When this system was applied to analyze the concentration and types of respective proteins, known concentrations of three types of IgG-biotin were assayed so that the corresponding positions were measured. With these results of positions, the concentrations of analytes to be analyzed were re-estimated from the respective standard curves, in reversible fashion. Finally, known analyte concentrations were compared with values estimated from standard curves and, as a result, concentrations estimated from three assays corresponded well with the known concentrations, within an acceptable error range (Table 3.3). Here, in assay 1 the number of colored microspheres analyzed was 47, and all microspheres were decoded to the correct color. In assays 2 and 3, 30 and 73 of the colored microspheres were detected, and only two and five of the colored microspheres, respectively, were decoded incorrectly. Accordingly, the accuracy for the decoding of colored microspheres was shown to be 100% in assay 1, and 93% in assays 2 and 3.

In addition, by adjusting the flow rate and detection zone, the dynamic range of the system can be controlled by more than one order of magnitude. The effect of flow rate is presented in Figure 3.16a, where the positions of reacted red

Table 3.3 Reproducibility of magnetophoretic multiplexed immunoassays.

Immunoassay	Goat IgG-biotin	Rabbit IgG-biotin	Mouse IgG-biotin
Assay 1			
Concentration (f*M*)	26.6	799.2	266.4
Multiplexed immunoassay (μm)	17.00 ± 3.00	96.45 ± 5.09	59.44 ± 5.48
Fitting into the standard curve (f*M*)	37.8 ± 11.2	795.6 ± 41.0	285.7 ± 40.6
Assay 2			
Concentration (f*M*)	666.0	399.6	6.7
Multiplexed immunoassay (μm)	99.60 ± 0.91	45.50 ± 4.42	6.00
Fitting into the standard curve (f*M*)	682.6 ± 11.8	381.2 ± 37.2	4.5
Assay 3			
Concentration (f*M*)	266.4	26.6	666
Multiplexed immunoassay (μm)	56.80 ± 5.97	9.10 ± 3.00	98.70 ± 3.46
Fitting into the standard curve (f*M*)	258.3 ± 44.0	28.10 ± 9.80	654.5 ± 41.4

Accuracy of decoding–Assay 1: 100%, Assay 2: 93%, Assay 3: 93%.
No. of microspheres analyzed–Assay 1: 47, Assay 2: 30, Assay 3: 73.
Reproduced with permission from Ref. [88].; © 2008, Elsevier Ltd.

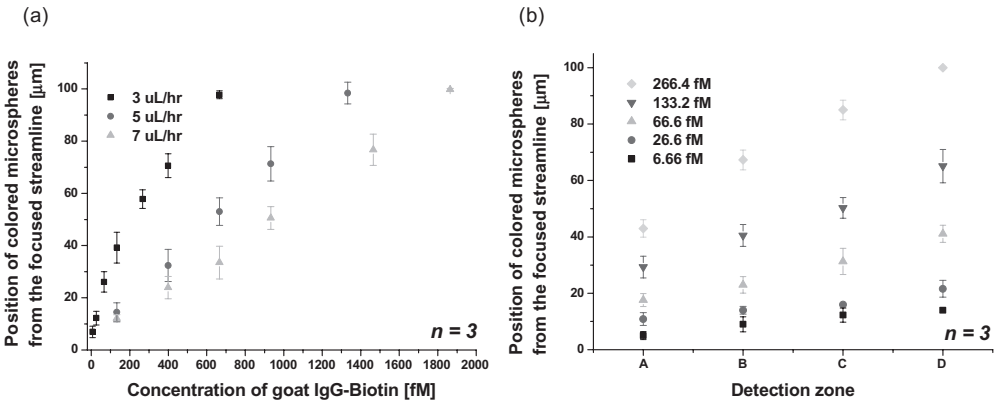

Figure 3.16 (a) Effect of flow rate on the dynamic range. Goat IgG-biotin was used, and red microspheres that had been reacted with goat IgG-biotin were detected at the detection zone A; (b) Effect of the detection zone on the dynamic range. Blue microspheres that had been conjugated with mouse IgG-biotin were measured at various detection zones at a fixed flow rate of $3\,\mu l\,h^{-1}$. Four different detection zones were used; the distance between the detection zones was ca. 4 mm. Reproduced with permission from Ref. [88]; © 2008, Elsevier Ltd.

microspheres were measured through the first detection zone A of Figure 3.14a and the flow rates were changed from 3 to 7 $\mu l\,h^{-1}$. As shown in Figure 3.16a, the dynamic range was shifted to a higher concentration as the flow rate increased. At a flow rate of 3 $\mu l\,h^{-1}$, the dynamic range of goat IgG-biotin was 6.7 to 666.0 f*M*. Meanwhile, the dynamic range at a flow rate of 7 $\mu l\,h^{-1}$ was shown to be 133.2 f*M* to 1.9 p*M*. As the flow rate became higher, the microsphere would become exposed to the magnetic field gradient for a shorter time, and consequently the dynamic range at a faster flow rate would be extended to a broader range of analyte concentration. However, the calibration sensitivity – which is defined as the ratio of channel width to maximum detectable concentration – was decreased. In addition, the microsphere at the faster flow rate was detected at a lower position, even for the same concentration of analyte.

Finally, this system was applied to adjust the dynamic range by changing the detection zone at a flow rate of 3 $\mu l\,h^{-1}$ (Figure 3.16b). The blue microspheres which reacted with mouse IgG-biotins were analyzed at the four detection zones (A, B, C, and D), the difference in the detection zones being marginal at the low concentration range of the analyte. However, a higher concentration of analyte gave rise to a steeper slope in the graph; this occurred because the reacted microspheres were deflected more as the microspheres became exposed to the magnetic field gradient for a longer time – in other words, as the detection zone changed from A to D. In the first detection zone, A, the position detection showed a higher dynamic range (up to 655.8 f*M*) than that of other detection zones. Meanwhile, although the position detection showed a low dynamic range (up to 266.4 f*M*) in the last detection zone, D, a higher calibration sensitivity (0.33 $\mu m\ fM^{-1}$ at detection zone D) could be achieved than for other detection zones (e.g., 0.14 $\mu m\ fM^{-1}$ at detection zone A). Based on these results, an improved detectable concentration range and sensitivity for a target analyte could be expected by simply adjusting the detection zone in a microchannel.

As explained above, the multiplexed assay system using magnetophoresis is suitable for the diagnosis of diseases such as cancer and allergy, the various biomarkers and proteins of which may be detected and quantified simultaneously. As the principle of magnetophoresis does not require complex and expensive detection equipment, and has a high sensitivity, it has much potential as a biosensor in comparison with other technologies. Based on these merits, further research in the field of biosensors will undoubtedly be conducted in the future.

3.5 Magnetophoretic Separation

3.5.1 Cell Separation and Analysis

Among microtechnologies dedicated to particle (or cell) separation (see Figure 3.17), magnetophoresis provides several advantages over other methods, in that it

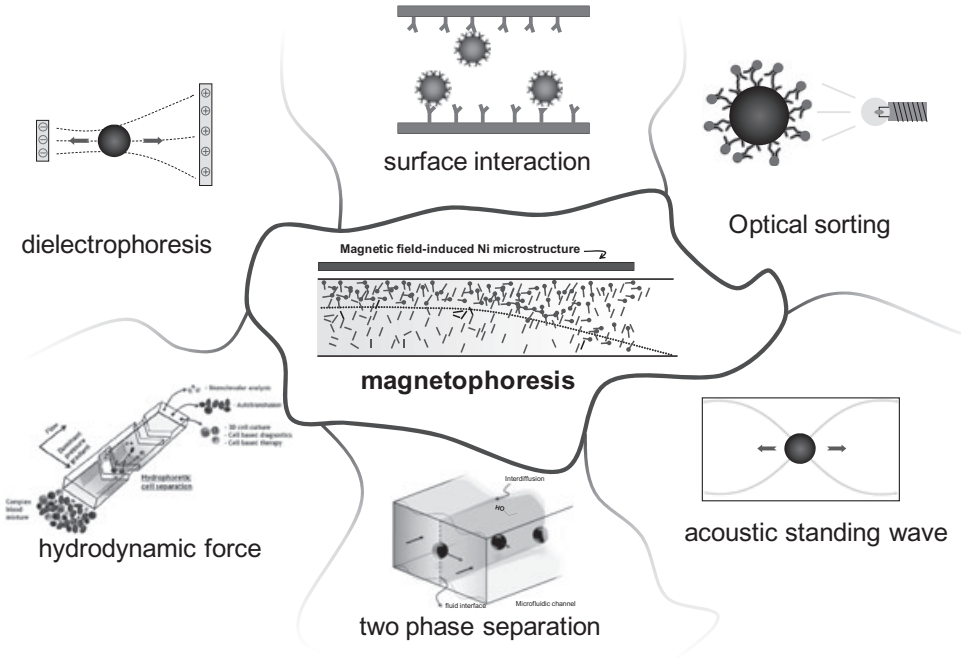

Figure 3.17 Various principles for particle sorting, as demonstrated by microfluidic technology.

allows high selectivity (immunemagnetic), strong force, easy accessibility, minimal energy consumption (permanent magnet), and low cost. As magnetic separation has been shown frequently as one of the most useful tools in biotechnology, separation techniques based on magnetism have been investigated and developed by many research groups. Among conventional methods, Zborowski and coworkers have reported several cell separation results using magnetic particles [24, 30, 55, 89–96]. Although infrequently used, those microfabrication methods for preparing devices have employed many physical approaches, including magnetic susceptibility [30, 91, 94], binding capacity [24, 93, 97], and separation using real cell samples [94, 95]. Yet, despite these previous reports, magnetic cell separation combined with microfabrication techniques has achieved very few results [32, 35, 98]; studies conducted by Han *et al.* [33] and by the Reich group [98] have involved non-immunological magnetic separation using the inherent paramagnetic properties of RBCs and nanowire-bound cells, respectively.

The method of magnetophoretic cell separation can be applied via two approaches: (i) an immunomagnetic separation using magnetic particles; and (ii) a non-immunomagnetic separation based on the inherent magnetic susceptibility of the cells. The immunomagnetic cell-sorting method is advantageous for separating cells of interest from mixed cell populations, such as peripheral whole blood. This approach uses magnetic microparticles and nanoparticles [99, 100]

conjugated with antibody proteins that are specific to the cell membrane protein of interest; the magnetic particle-bound cells are attracted by the highly enhanced magnetic force such that, finally, the cells change their pathway. Non-bound cells, however, have no influence on the magnetic field and maintain their pathways. Recently, Pamme *et al*. reported the details of an immunomagnetic cell sorting technique using microfluidic devices for separating mouse macrophages and human ovarian cancer (HeLa) cells [26]. Likewise, Xia *et al*. reported an integrated microfluidic device for removing *Escherichia coli* bound to magnetic nanoparticles from flowing solutions [101]. For this, the authors used ferromagnetic microstructures integrated into the microfluidic device, which was similar to the scheme of the device reported by Kang *et al*. [41, 42] Subsequently, Inglis *et al*. reported the details of a microfluidic device for the immunomagnetic separation of blood cells, by exploited ferromagnetic wires embedded in the bottom glass substrate [102]. The use of magnetic microparticles is preferred in conventional macroscale cell separations, because they offer a high magnetic mobility when bound to the cell surfaces, whereas the magnetic nanoparticles provide much less magnetic mobility than do microparticles. However, within the microfluidic environment, the microparticles used for immunomagnetic cell sorting may be inadequate due to their high magnetic susceptibility, which consequently results in a high magnetic force acting on the cells. This leads to the cell–magnetic particle complexes becoming trapped in the microfluidic channels, and causes microchannel clogging. In addition, the fast drag velocity of the magnetic microparticle-bound cells restricts the magnetophoretic analysis for the cell-surface protein-binding capacities [97].

3.5.2 Separation of Nanomaterials

Magnetophoresis assisted by microfluidic techniques can be applied to the separation of magnetic nanoparticles suspended in aqueous solution. Recently, the magnetophoretic continuous separation of nanoparticles attracted interest and was demonstrated in a microfluidic device (Figure 3.18) [41]. These authors had previously reported a microfluidic purification method using single-walled carbon nanotubes (SWCNTs), which attracted much attention and promised a wide range of applications [103, 104]. Unfortunately, SWCNTs are synthesized using metal catalysts such as Fe, Ni, and Co, and these must be removed from the pure SWCNTs in order for the latter to achieve many potential applications. Despite various successful reports regarding SWCNT purification, including gas-phase oxidation, wet-chemical and thermal treatments, microwave-assisted methods, and combined multistep purification platforms [105, 106], the current purification methods, mainly using chemical, thermal, and ultrasonic treatments, have resulted in structural defects or the surface modification of the SWCNTs [106]. Because most metal catalysts used in SWCNT synthesis are superparamagnetic [107], several approaches for the magnetic purification of SWCNTs have been demonstrated, using magnetic-trapping methods [108–110]. Unfortunately, however, these (largely macroscale) purification schemes have been limited to obtaining

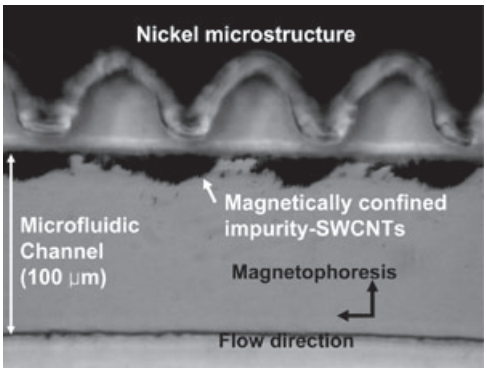

Figure 3.18 Magnetically confined impurity-containing SWCNTs on the sidewall of the saw-tooth nickel microstructure induced by a permanent magnet. Locally confined impure SWCNTs were repeatedly concentrated in the regions of highest magnetic-flux density. Reproduced with permission from Ref. [41]; © 2007, Wiley-VCH Verlag GmbH & Co. KGaA.

high-purity SWCNTs, due to the relatively low magnetic field intensity employed and crude control of the SWCNT solutions. Consequently, a microfluidic device for magnetophoresis was used for the purification of SWCNTs, with highly enhanced magnetic flux density gradient and precise fluidic controls assisted by microfluidic manipulation techniques.

In Figure 3.18, SWCNTs containing the metal catalysts are shown trapped by the highly enhanced magnetic flux density gradient across the microfluidic channel. Because the SWCNTs are too small to be visualized with conventional microscopy, the analysis of SWCNT purification should be assessed with indirect methods such as TGA, TEM, SEM, and SQUID. Figure 3.19 shows two TEM images of SWCNTs collected from the device, supporting the purified SWCNTs after a single-round purification process of the microfluidic magnetophoresis. The relationship between the mass of the superparamagnetic materials and magnetized moments [107] allows an evaluation of the purified SWCNTs compared to the unpurified samples [41]. As shown in Figure 3.20, the M–H curves of as-prepared and purified SWCNTs (ca. 10.0 mg) were measured using SQUID magnetometry at 300 K, and support the fact that purified SWCNTs rarely contain metal impurities. In these results, the saturation magnetic moment (M_S) should be calibrated to the net weight of SWCNTs because the purified SWCNTs are mixed with surfactant. The measured moment was 8.37×10^{-4} emu, where the sample weight was 11.9 mg. The calibrated M_S (0.42 emu g^{-1}) was rather smaller than that of the SWCNTs, albeit with 98.47 ± 0.33% purity [107]. The practical M_S may be smaller than as-calibrated, since the dilution factor (1/6) increases if the collected SWCNTs are washed with methanol. When comparing these results with previously published data [107], the purity of the purified SWCNTs can be estimated as

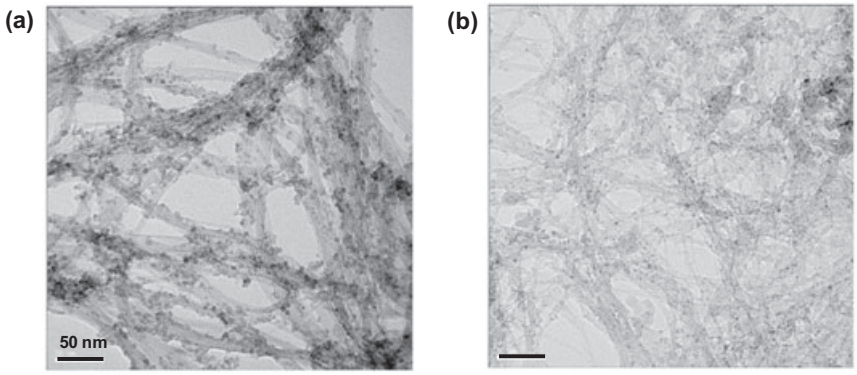

Figure 3.19 Transmission electron microscopy images of (a) as-dispersed and (b) magnetophoretically purified SWCNTs. Reproduced with permission from Ref. [41]; © 2007, Wiley-VCH Verlag GmbH & Co. KGaA.

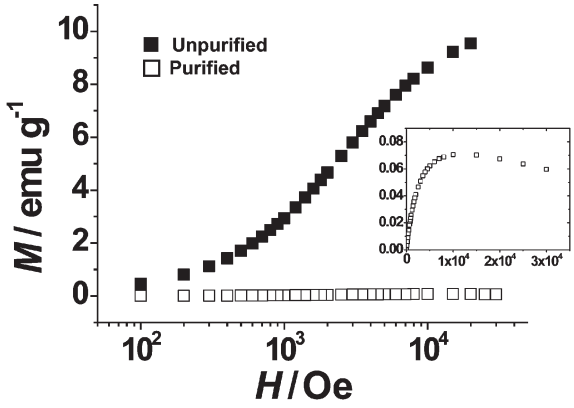

Figure 3.20 *M–H* curve of SWCNTs measured at 300 K using SQUID magnetometry, proving that magnetically purified SWCNTs have a remarkably reduced iron content, and showing the decreased magnetic susceptibility. The inset shows a magnified graph of purified SWCNTs below 0.1 emu g^{-1} of magnetization. Reproduced with permission from Ref. [41]; © 2007, Wiley-VCH Verlag GmbH & Co. KGaA.

approximately 98–99%. During the analysis of magnetic nanoparticles using various analytical tools, such as EDS and TGA, analytical errors often arise from those impurities contained not by the nanomaterials but rather by the surfactant. In order to dissolve the nanoparticles in aqueous solution, surfactants are generally used to modify the surface properties of the nanomaterials. However, if the

surfactant contains its own impurities, this will prevent an accurate analysis and result in analytical errors [41]. Therefore, multiple analytical results using a variety of tools should be sought when separating nanomaterials in microfluidic devices.

3.5.3 Isomagnetophoresis (IMP)

Since the magnetic susceptibility of a material is determined by a combination of constituent elements, electrons, chemical bond, and bond–bond interaction [111], thereby revealing information about a molecule's properties and composition, this characteristic has been widely studied in several research fields, including materials science [112] and biomedical research [113, 114]. As a novel principle, isoelectrophoresis (IEP), which has been widely used in molecular biology and analytical biochemistry, can be dedicated to improvements of the current magnetophoretic analysis techniques. On the other hand, isomagnetophoresis (IMP) can be demonstrated by generating the magnetic susceptibility gradient across the microfluidic channel, where the magnetic flux density gradient also exists. As shown in Figure 3.21, IMP enables one to discriminate the subtle difference in the magnetic susceptibility, which cannot be distinguished by using conventional

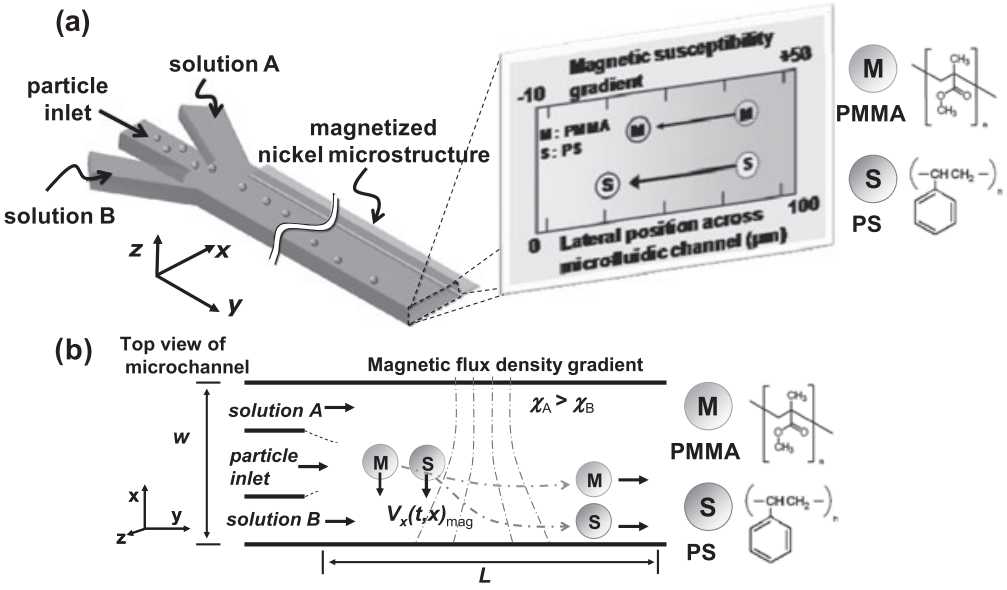

Figure 3.21 Schematic of isomagnetophoretic discrimination process of particles having subtle difference of magnetic susceptibility ($\Delta\chi$) in a microfluidic channel. Reproduced with permission from Ref. [42]; © 2008, American Chemical Society.

magnetophoresis methods. Recently, Kang *et al*. demonstrated a discrimination between the polymer particles of polystyrene (PS), poly(methyl methacrylate) (PMMA), and borosilicate (BS), by using IMP in the microfluidic channel [42]. As the following experimental results and numerical estimation indicate, whilst the polymer particles of PS and PMMA cannot be discerned with conventional magnetophoresis, IMP is indeed able to discriminate the subtle differences in the magnetic susceptibilities of these materials. Although these present demonstrations of IMP have not included any separations using nanomagnetic materials, the method is described here because it will surely encourage great advances on conventional magnetophoretic analysis, and may even be extended to magnetic nanomaterials in further studies.

In order to verify the theoretical hypothesis, an analytical model has been established by composing several functions of magnetic drag velocity, $V_x(t,x)$, the magnetic susceptibility gradient, $K(t,x)$, magnetic flux density gradient $B(x)$, and particle velocity driven by the parabolic flow profile, $V_y(x)$ (Equation 3.10). $K(t,x)$ is obtained from the concentration gradient, $C(t,x)$ (Equation 3.9), generated across the microfluidic channel in accordance with Wiedemann's additivity law (Equation 3.11) [115]:

$$V_x(t,x) = -\frac{2R^2(\chi_p - K(t,x))B(x)}{9\mu_0\eta} \tag{3.7}$$

$$B(x) = -2.466(100 - x) + 378.68 \tag{3.8}$$

$$C(t,x) = \frac{1}{2}C_0\sum_{n=-\infty}^{\infty}\left\{erf\frac{h+2nw-x}{2\sqrt{Dt}} + erf\frac{h-2nw+x}{2\sqrt{Dt}}\right\} \tag{3.9}$$

$$V_y(x) = \frac{3}{2}v_0\left(1 - \frac{4(50-x)^2}{w^2}\right) \tag{3.10}$$

$$\chi(mixture) = \sum_{i=1}^{N} V_i\chi_i \Big/ \sum_{i=1}^{N} V_i \tag{3.11}$$

$$K(t,x) = C_{Gd-DTPA}(t,x)\chi_{Gd-DTPA} + (1 - C_{Gd-DTPA}(t,x))\chi_{D-glucose} \tag{3.12}$$

where $V_x(t, x)$ is the magnetophoretic velocity at time, t (*s*) at position of x, R is the radius of a particle (ca. 7.5 μm), χ_p and $K(t,x)$ are the volumetric magnetic susceptibility of a particle and fluid, respectively, $B(x)$ is the magnetic flux density gradient (T^2m^{-1}), μ_0 is vacuum permeability, η dynamic viscosity of fluid (Pa s), C_0 the initial concentration, h is the width of the initial distribution (50 μm), w is the width of the channel (100 μm), D is the diffusion coefficient of Gd-DTPA (2.3×10^{-6} cm^2s^{-1}) [116], and v_0 is the average fluid velocity in the channel (mm s^{-1}). The magnetic susceptibility of Gd-DTPA and D-glucose was obtained from published reports [117, 118]. The finite element method magnetic (FEMM) program can be used to estimate the magnetic flux density gradient across the microchannel, $B(x)$, and the magnetic permeability of nickel can be obtained from published

data [119]. As presented in Section 3.3.1, because the microfluidic channel is placed near the edge of a permanent magnet (NdFeB35; 50 mm × 25 mm × 10 mm; Magtopia, Korea) and the nickel microstructures were positioned between the permanent magnet and microfluidic channel, it was difficult to estimate the magnetic flux density around the microchannels using a numerical equation. Fortunately, the width of the microchannel is narrow enough (100 μm) to make a rough assumption that dB/dx has a linear relationship with the cross-sectional distance of the microchannel. Therefore, Equation 3.8 can be used to estimate the magnetophoretic velocity, $V_x(t, x)$.

In order to compare the numerical estimation with the experimental results, the magnetophoretic and isomagnetophoretic analysis was assessed in the microchannels. In Figure 3.22a, the lateral positions (18.52 ± 1.58 μm, n = 247; 18.20 ± 6.61 μm, n = 802, respectively) of the PS and PMMA particles are overlapped so that the two types of material cannot be distinguished one from another. A broad deviation of the lateral position (PMMA and BS; 52.13 ± 5.33 μm, n = 1097) also results from a large size variation of the particles, its deviation being proportional to the size variation as described in Equation 3.7. Isomagnetophoresis, however, in Figure 3.22b exhibits the large difference of the lateral position of PS (17.68 ± 1.62 μm. n = 576) and PMMA (30.44 ± 3.48 μm, n = 406) particles providing the enhanced discernible capability. Furthermore, it remarkably reduces the deviation width of the particle position for all types of particle because the isomagnetophoretic migration is attenuated by the isopoint of χ and the particles stands in the vicinity of the their isopoint, without regard for the particle size.

By combining the equation stated above, it is possible to predict the particle traces in conventional magnetophoresis and new IMP. In the analytical model, the microparticle positions in the microchannel are considered as a point in a

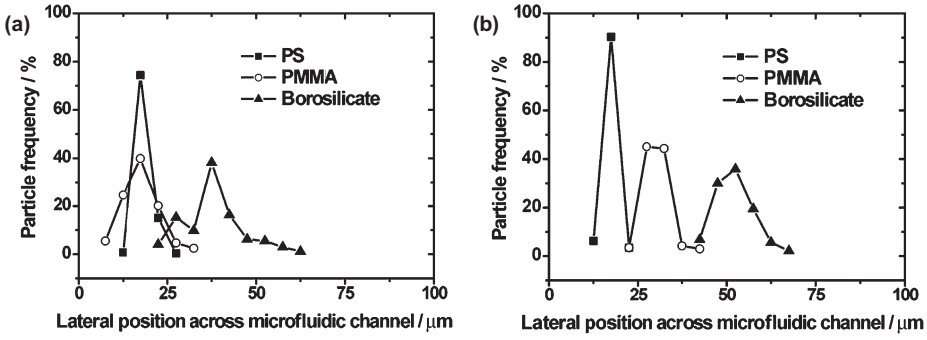

Figure 3.22 Measured particle positions of PS, PMMA, and borosilicate in conventional magnetophoresis (a) and isomagnetophoresis (b). Subtle difference in magnetic susceptibility between PS and PMMA was pre-eminently discriminated in isomagnetophoretic displacement (b). Reproduced with permission from Ref. [42]; © 2008, American Chemical Society.

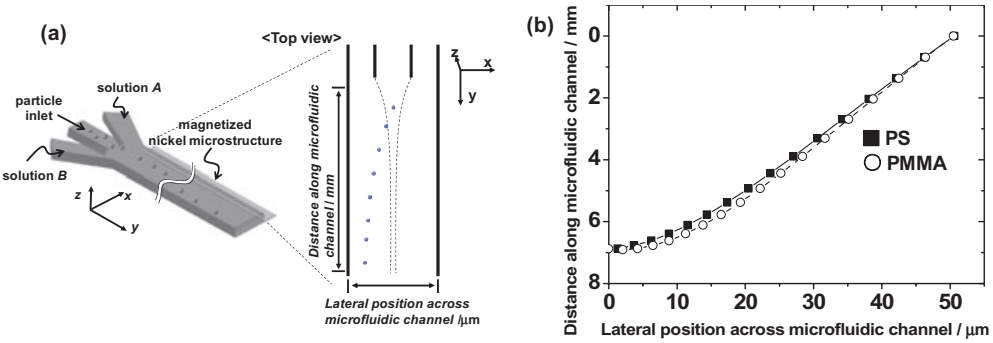

Figure 3.23 (a) Theoretical estimation of the microparticle displacement in the microfluidic channels under conventional magnetophoresis; (b) Particle traces of the PS and PMMA particles, supporting the experimental results as described in Figure 3.22. The plot presents the theoretical particle traces without particle size deviation. Considering the practical particle size deviation, the lateral positions of PS and PMMA particles in the outlet port become indiscernible. Reproduced with permission from Ref. [42]; © 2008, American Chemical Society.

Cartesian coordinate system, assuming that all parts of a microsphere (polymer particle) are exerted by the uniform magnetic force. Then, the composite function (V_x and V_y) is iterated by increasing the time (from $t = 0$) until the y reaches 11 mm (distance along the microfluidic channel) (Figure 3.23).

The ideal condition for IMP requires the static gradient of χ_{fluid} over the microfluidic channels, but the present device scheme does not generate the stationary χ_{fluid} profiles across the microfluidic channel because of diffusion. Therefore, for a theoretical consideration of the present quasi-isomagnetophoretic displacement (due to transition of the χ_{fluid} gradient in accordance with time and particle position in y-axis), $V_x(t,x)$ and $V_y(x)$ are employed to estimate the particle displacement at time, t. By using this model and the experimental data above, χ_{PS}, χ_{PMMA} and χ_{BS} are discriminated to be -8.75×10^{-6}, -5.40×10^{-6}, and -2.10×10^{-6}, respectively, which are comparable with published values [120]. Figure 3.24a presents a theoretical prediction of PS and PMMA particles, which shows a clear correlation with the experimental data, comparing the magnetophoretic prediction (Figure 3.24b). For the apparent verification of IMP compared to magnetophoresis, the (iso)magnetophoretic distinction coefficient in the microfluidic devices, $D = \Delta x/\Delta\chi_{particle}$, has been newly defined, where Δx (10^{-6} m) and $\Delta\chi_{particle}$ are the difference in the lateral positions of certain types of two particles at the outlet (P and Q, $\Delta x = x_P - x_Q$) and in magnetic susceptibility ($\Delta\chi_{particle} = \chi_P - \chi_Q$), respectively. We can estimate D_{mag} and D_{iso}, by considering if the particle, P, is polystyrene and χ_Q varies from -0.75×10^{-6} to -15.75×10^{-6}. As reported in Figure 3.24b,c, IMP provides a larger D_{iso}(3.89) compared to D_{mag}(1.41) and, in addition, it reduces the errors caused by size deviation of the particles, thus supporting the results of Figure 3.22. The dotted-lines (upper and lower) in Figure 3.24b and c are the plotted results when the particle size of P is 15.0 μm, and the particle sizes of Q are 16.0 μm and 14.0 μm, respectively.

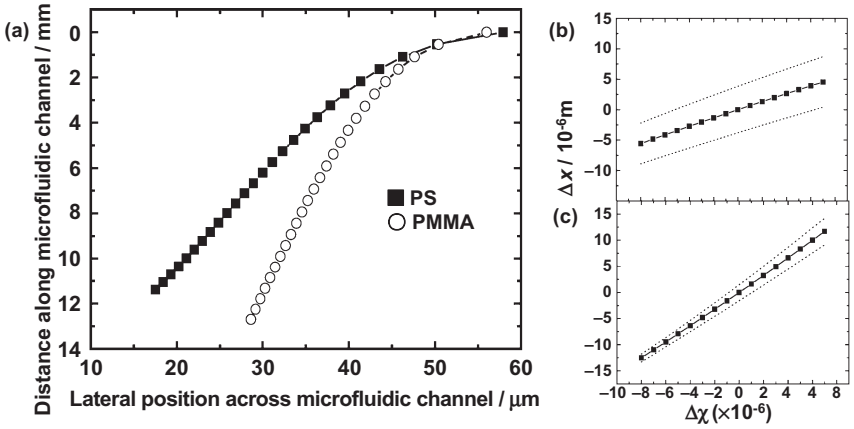

Figure 3.24 Theoretical estimation of particle displacement in the microchannels. (a) Particle traces of PS and PMMA particles diverged along the microchannels under isomagnetophoresis. The data points in (a) are the particle position over the microchannel in the *x*-*y* coordinate system. The magnetophoretic distinction coefficient of isomagnetophoresis (c) is greater than that of conventional magnetophoresis (b). The dotted lines in (b) and (c) are expected errors caused by particle size deviation (±1.0 μm). Reproduced with permission from Ref. [42]; © 2008, American Chemical Society.

Although IMP as described in this chapter does not present the microfluidic separation using magnetic nanomaterials, it can be expected that this method will enable an enhanced separation and biosensing ability in microfluidic environments using this platform. It will also pave the way for the improved magnetic manipulation and sorting of various materials, including cancer cells, nucleic acids, proteins, and CNTs [41, 120], by discerning the subtle difference in orientation-averaged magnetic susceptibility as we modulate the magnetic susceptibility of the injected solutions and optimize the experimental conditions by using the analytical model.

3.6 Concluding Remarks

In this chapter we have summarized magnetophoretic biosensing technologies and also separation results, notably those developed using microfluidic techniques. Although the approaches towards magnetophoretic analysis assisted by microfluidics are restricted to within the nanoliter scale, they offer a variety of advantages, including high efficiency, low cost, high purity, and enhanced sensitivity. In addition, IMP, a novel analytical method, is expected to improve the conventional magnetophoretic analysis tools by increasing discriminatory ability in biosensing and separation fields, if the current technical problems of optimization, such as

the magnetic susceptibility gradient conditions, can be addressed. The various studies of novel magnetic nanomaterials, such as SMNPs, are crucial to improve magnetophoretic efficiency as well to develop device fabrication technology and new physical principles. By combining the magnetophoretic biosensing and IMP, it is to be expected that an ultrasensitive isomagnetophoretic immunoassay platform could be developed for the detection of tiny quantities of biomolecules, not only in the diagnosis of disease but also for environmental monitoring.

Acknowledgments

These studies were supported by the Korea Science and Engineering Foundation (KOSEF) NRL Program grant funded by the Korea government (MEST) (R0A-2008-000-20109-0). The authors also thank the Chung Moon Soul Center for BioInformation and BioElectronics, KAIST.

References

1 West, J.L. and Halas, N.J. (2003) Engineered nanomaterials for biophotonics applications: improving sensing, imaging, and therapeutics. *Annual Review of Biomedical Engineering*, **5**, 285–92.

2 De, M., Ghosh, P.S. and Rotello, V.M. (2008) Applications of nanoparticles in biology. *Advanced Materials*, **20**, 1–17.

3 Fortina, P., Kricka, L.J., Graves, D.J., Park, J., Hyslop, T., Tam, F., Halas, N., Surrey, S. and Waldman, S.A. (2007) Applications of nanoparticles to diagnostics and therapeutics in colorectal cancer. *Trends in Biotechnology*, **25**, 145–52.

4 Ballesteros, B.N., Tobias, G., Shao, L., Pellicer, E., Nogués, J., Mendoza, E. and Green, M.L.H. (2008) Steam purification for the removal of graphitic shells coating catalytic particles and the shortening of single-walled carbon nanotubes. *Small*, **4**, 1501–6.

5 Sun, C., Lee, J.S.H. and Zhang, M. (2008) Magnetic nanoparticles in MR imaging and drug delivery. *Advanced Drug Delivery Reviews*, **60**, 1252–65.

6 Plank, C. (2008) Nanomagnetosols: magnetism opens up new perspectives for targeted aerosol delivery to the lung. *Trends in Biotechnology*, **26**, 59–63.

7 Mornet, S., Vasseur, S., Grasset, F., Veverka, P., Goglio, G., Demourgues, A., Portier, J., Pollert, E. and Duguet, E. (2006) Magnetic nanoparticle design for medical applications. *Progress in Solid State Chemistry*, **34**, 237–47.

8 Ferrari, M. (2005) Cancer nanotechnology: opportunities and challenges. *Nature Reviews. Cancer*, **5**, 161–71.

9 Pisanic, T.R., Blackwell, J.D., Shubayev, V.I., Ones, R.R.F. and Jin, S. (2007) Nanotoxicity of iron oxide nanoparticle internalization in growing neurons. *Biomaterials*, **28**, 2572–81.

10 Derfus, A.M., Maltzahn, G.V., Harris, T.J., Duza, T., Vecchio, K.S., Ruoslahti, E. and Bhatia, S.N. (2007) Remotely triggered release from magnetic nanoparticles. *Advanced Materials*, **19**, 3932–6.

11 Edelstein, R.L., Tamanaha, C.R., Sheehan, P.E., Miller, M.M., Baselt, D.R., Whitman, L.J. and Colton, R.J. (2000) The BARC biosensor applied to the detection of biological warfare agents. *Biosensors and Bioelectronics*, **14**, 805–13.

12 Enpuku, K., Kuroda, D., Ohba, A., Yang, T.Q., Yoshinaga, K., Nakahara, T., Kuma, H. and Hamasaki, N. (2003)

Biological immunoassay utilizing magnetic marker and high Tc superconducting quantum interference device magnetometer. *Japanese Journal of Applied Physics*, **42**, L1436–8.

13 Graham, D.L., Ferreira, H.A. and Freitas, P.P. (2004) Magnetoresistive-based biosensors and biochips. *Trends in Biotechnology*, **22**, 455–62.

14 Mulvaney, S.P., Cole, C.L., Kniller, M.D., Malito, M., Tamanaha, C.R., Rife, J.C., Stanton, M.W. and Whitman, L.J. (2007) Rapid, femtomolar bioassays in complex matrices combining microfluidics and magnetoelectronics. *Biosensors and Bioelectronics*, **23**, 191–200.

15 Rife, J.C., Miller, M.M., Sheehan, P.E., Tamanaha, C.R., Tondra, M. and Whitman, L.J. (2003) Design and performance of GMR sensors for the detection of magnetic microbeads in biosensors. *Sensors and Actuators. A, Physical*, **107**, 209–18.

16 Hayes, M.A., Polson, N.A., Phayre, A.N. and Garcia, A.A. (2001) Flow-based microimmunoassay. *Analytical Chemistry*, **73**, 5896–902.

17 Choi, J.-W., Oh, K.W., Thomas, J.H., Heineman, W.R., Halsall, H.B., Nevin, J.H., Helmicki, A.J., Henderson, H.T. and Ahn, C.H. (2002) An integrated microfluidic biochemical detection system for protein analysis with magnetic bead-based sampling capabilities. *Lab on a Chip*, **2**, 27–30.

18 Nam, J.-M., Thaxton, C.S. and Mirkin, C.A. (2003) Nanoparticle-based bio-bar codes for the ultrasensitive detection of proteins. *Science*, **301**, 1884–6.

19 Kim, K.S. and Park, J.-K. (2005) Magnetic force-based multiplexed immunoassay using superparamagnetic nanoparticles in microfluidic channel. *Lab on a Chip*, **5**, 657–64.

20 Hahn, Y.K., Jin, Z., Kang, J.H., Oh, E., Han, M.K., Kim, H.S., Jang, J.T., Lee, J.H., Cheon, J., Kim, S.H., Park, H.S. and Park, J.K. (2007) Magnetophoretic immunoassay of allergen-specific IgE in an enhanced magnetic field gradient. *Analytical Chemistry*, **79**, 2214–20.

21 Dunlop, E.H., Feiler, W.A. and Mattione, M.J. (1984) Magnetic separation in biotechnology. *Biotechnology Advances*, **2**, 63–74.

22 Kang, J.H. and Park, J.-K. (2005) Technical paper on microfluidic devices – cell separation technology, *Asia Pacific Biotech News*, **9**, 1135–46.

23 Furdui, V.I. and Harrison, D.J. (2004) Immunomagnetic T cell capture from blood for PCR analysis using microfluidic systems. *Lab on a Chip*, **4**, 614–18.

24 McCloskey, K.E., Chalmers, J.J. and Zborowski, M. (2003) Magnetic cell separation: characterization of magnetophoretic mobility. *Analytical Chemistry*, **75**, 6868–74.

25 Lermo, A., Campoy, S., Barbé, J., Hernández, S., Alegret, S. and Pividori, M.I. (2007) In situ DNA amplification with magnetic primers for the electrochemical detection of food pathogens. *Biosensors and Bioelectronics*, **22**, 2010–17.

26 Pamme, N. and Wilhelm, C. (2006) Continuous sorting of magnetic cells via on-chip free-flow magnetophoresis. *Lab on a Chip*, **6**, 974–80.

27 Tsai, H., Lin, Y., Chang, H.W. and Fuh, C.B. (2008) Integrating the QCM detection with magnetic separation for on-line analysis. *Biosensors and Bioelectronics*, **24**, 485–8.

28 Šafařík, I. and Šafaříková, M. (1999) Use of magnetic techniques for the isolation of cells. *Journal of Chromatography B*, **722**, 33–53.

29 Šafařík, I. and Šafaříková, M. (2002) Magnetic nanoparticles and biosciences. *Monatshefte für Chemie*, **133**, 737–59.

30 Reddy, S., Moore, L.R., Sun, L., Zborowski, M.J. and Chalmers, J.J. (1996) Determination of the magnetic susceptibility of labeled particles by video imaging. *Chemical Engineering Science*, **51**, 947–56.

31 Delatour, C., Schmitz, G., Maxwell, E. and Kelland, D. (1983) Designing HGMS matrix arrays for selective filtration. *IEEE Transactions on Magnetics*, **Mag**-19, 2127–9.

32 Han, K.-H. and Frazier, A.B. (2004) Continuous magnetophoretic separation

of blood cells in microdevice format. *Journal of Applied Physics*, **96**, 5797–802.
33 Han, K.-H. and Frazier, A.B. (2006) Paramagnetic capture mode magnetophoretic microseparator for high efficiency blood cell separations. *Lab on a Chip*, **6**, 265–73.
34 Tanase, M., Felton, E.J., Gray, D.S., Hultgren, A., Chen, C.S. and Reich, D.H. (2005) Assembly of multicellular constructs and microarrays of cells using magnetic nanowires. *Lab on a Chip*, **5**, 598–605.
35 Berger, M., Castelino, J., Huang, R., Shah, M. and Austin, R.H. (2001) Design of a microfabricated magnetic cell separator. *Electrophoresis*, **22**, 3883–92.
36 Inglis, D.W., Riehn, R., Austin, R.H. and Sturm, J.C. (2004) Continuous microfluidic immunomagnetic cell separation. *Applied Physics Letters*, **85**, 5093–5.
37 Oh, S.-H., Singh, A.K., Bessette, P.H., Kenrick, S.A., Rice, J.J., Qian, J., Daugherty, P.S. and Soh, H.T. (2006) Screening of molecular libraries using the continuous-flow, micro-magnetic cell sorter. Proceedings of Micro Total Analysis Systems 2006 Conference, November 5–9, Tokyo, Japan, Society for Chemistry and Micro-Nano Systems, pp. 975–7.
38 Siegel, A.C., Shevkoplyas, S.S., Weibel, D.B., Bruzewicz, D.A., Martinez, A.W. and Whitesides, G.M. (2006) Cofabrication of electromagnets and microfluidic systems in poly(dimethylsiloxane). *Angewandte Chemie International Edition in English*, **45**, 1–6.
39 Pamme, N. (2006) Magnetism and microfluidics. *Lab on a Chip*, **6**, 24–38.
40 Deng, T., Prentiss, M. and Whitesides, G.M. (2003) Fabrication of magnetic microfiltration systems using soft lithography. *Applied Physics Letters*, **80**, 461–3.
41 Kang, J.H. and Park, J.-K. (2007) Magnetophoretic continuous purification of single-walled carbon nanotubes from catalytic impurities in a microfluidic device. *Small*, **3**, 1784–91.
42 Kang, J.H., Choi, S., Lee, W. and Park, J.-K. (2008) Isomagnetophoresis to discriminate subtle difference in magnetic susceptibility. *Journal of the American Chemical Society*, **130**, 396–7.
43 Chetouani, H., Haguet, V., Jeandey, C., Pigot, C., Walther, A., Dempsey, N.M., Chatelain, F., Delinchant, B. and Reyne, G. (2007) Diamagnetic levitation of beads and cells above permanent magnets, in The 14th International Conference on Solid-State Sensors, Actuators and Microsystems, IEEE, Lyon, France, June 10–14, 2007, pp. 715–18.
44 Kriz, C.B., Radevik, K. and Kriz, D. (1996) Magnetic permeability measurements in bioanalysis and biosensors. *Analytical Chemistry*, **68**, 1966–70.
45 Kriz, K., Ibraimi, F., Lu, M., Hansson, L.-O. and Kriz, D. (2005) Detection of C-reactive protein utilizing magnetic permeability detection based immunoassays. *Analytical Chemistry*, **77**, 5920–4.
46 Enpuku, K., Inoue, K., Soejima, K., Yoshinaga, K., Kuma, H. and Hamasaki, N. (2005) Magnetic immunoassays utilizing magnetic markers and a high-T_c squid. *IEEE Transactions on Applied Superconductivity*, **15**, 660–3.
47 Li, G., Sun, S., Wilson, R.J., White, R.L., Pourmand, N. and Wang, S.X. (2006) Spin valve sensors for ultrasensitive detection of superparamagnetic nanoparticles for biological applications. *Sensors and Actuators. A, Physical*, **126**, 98–106.
48 Enpuku, K., Soejima, K., Nishimoto, T., Matsuda, T., Tokumitsu, H., Tanaka, T., Yoshinaga, K., Kuma, H. and Hamasaki, N. (2007) Biological immunoassays without bound/free separation utilizing magnetic marker and HTS SQUID. *IEEE Transactions on Applied Superconductivity*, **17**, 816–19.
49 Richardson, J., Hill, A., Luxton, R. and Hawkins, P. (2001) A novel measuring system for the determination of paramagnetic particle labels for use in magneto-immunoassays. *Biosensors and Bioelectronics*, **16**, 1127–32.

50 Kiely, J., Hawkins, P., Wraith, P. and Luxton, R. (2007) Paramagnetic particle detection for use with an immunoassay based biosensor. *IET Science, Measurement & Technology*, **1**, 270–5.

51 Xiao, X., Guo, M., Li, Q., Cai, Q., Yao, S. and Grimes, C.A. (2008) In-situ monitoring of breast cancer cell (MCF-7) growth and quantification of the cytotoxicity of anticancer drugs fluorouracil and cisplatin. *Biosensors and Bioelectronics*, **24**, 247–52.

52 Tamanaha, C.R., Mulvaney, S.P., Rife, J.C. and Whitman, L.J. (2008) Magnetic labeling, detection, and system integration. *Biosensors and Bioelectronics*, **24**, 1–13.

53 Kang, J.H., Hahn, Y.K., Kim, K.S. and Park, J.-K. (2005) Microfluidic sandwich immunoassays for sub-femtomole detection using magnetic field-induced nanoparticles. Proceedings of the Micro Total Analysis Systems 2005 Conference, October 9–13, Boston, The Transducer Research Foundation, Inc., vol. 1, pp. 25–7.

54 Hahn, Y.K., Jin, Z., Kang, J.H., Oh, E., Kim, H.-S., Jang, J.-T., Cheon, J., Park, H.-S. and Park, J.-K. (2006) Magnetophoretic immunoassay for allergen-specific immunoglobulin E (IgE) in patient samples. Proceedings of the Micro Total Analysis Systems 2006 Conference, November 5–9, Tokyo, Japan, Society for Chemistry and Micro-Nano Systems, pp. 320–2.

55 Zborowski, M., Fuh, C.B., Green, R., Sun, L. and Chalmer, J.J. (1995) Analytical magnetophoresis of ferritin-labeled lymphocytes. *Analytical Chemistry*, **67**, 3702–12.

56 Han, K.-H., Han, A. and Frazier, A.B. (2006) Microsystems for isolation and electrophysiological analysis of breast cancer cells from blood. *Biosensors and Bioelectronics*, **21**, 1907–14.

57 Pierson-Mullany, L.K., Jackola, D.R., Blumenthal, M.N. and Rosenberg, A. (2002) Evidence of an affinity threshold for IgE-allergen binding in the percutaneous skin test reaction. *Clinical and Experimental Allergy*, **32**, 107–16.

58 Weghofer, M., Thomas, W.R., Pittner, G., Horakz, F., Valenta, R. and Vrtala, S. (2005) Comparison of purified *Dermatophagoides pteronyssinus* allergens and extract by two-dimensional immunoblotting and quantitative immunoglobulin E inhibitions. *Clinical and Experimental Allergy*, **35**, 1384–91.

59 Williams, P.B., Barnes, J.H., Szeinbach, S.L. and Sullivan, T.J. (2000) Analytic precision and accuracy of commercial immunoassays for specific IgE: establishing a standard. *Journal of Allergy and Clinical Immunology*, **105**, 1221–30.

60 Plowman, T.E., Durstchi, J.D., Wang, H.K., Christensen, D.A., Herron, J.N. and Reichert, W.M. (1999) Multiple-analyte fluoroimmunoassay using an integrated optical waveguide sensor. *Analytical Chemistry*, **71**, 4344–52.

61 Eriksson, S., Vehniäinen, M., Jansén, T., Meretoja, V., Saviranta, P., Pettersson, K. and Lövgren, T. (2000) Dual-label time-resolved immunofluorometric assay of free and total prostate-specific antigen based on recombinant Fab fragments. *Clinical Chemistry*, **46**, 658–66.

62 Ferguson, J.A., Steemers, F.J. and Walt, D.R. (2000) High-density fiber-optic DNA random microsphere array. *Analytical Chemistry*, **72**, 5618–24.

63 Mcbride, M.T., Gammon, S., Pitesky, M., O'Brien, T.W., Smith, T., Aldrich, J., Langlois, R.G., Colston, B. and Venkateswaran, K.S. (2003) Multiplexed liquid arrays for simultaneous detection of simulants of biological warfare agents. *Analytical Chemistry*, **75**, 1924–30.

64 Trau, M. and Battersby, B.J. (2001) Novel colloidal materials for high-throughput screening applications in drug discovery and genomics. *Advanced Materials*, **13**, 975–9.

65 Nolan, J.P. and Sklar, L.A. (2002) Suspension array technology: evolution of the flat-array paradigm. *Trends in Biotechnology*, **20**, 9–12.

66 Moran, E.J., Sarshar, S., Cargill, J.F., Shahbaz, M.M., Lio, A., Mjalli, A.M.M. and Armstrong, R.W. (1995) Radio frequency tag encoded combinatorial library method for the discovery of tripeptide-substituted cinnamic acid

inhibitors of the protein tyrosine phosphatase PTP1B. *Journal of the American Chemical Society*, **117**, 10787–8.

67 Fenniri, H., Hedderich, H.G., Haber, K.S., Achkar, J., Taylor, B. and Ben-Amotz, D. (2000) Towards the DRED of resin-supported combinatorial libraries: a non-invasive methodology based on bead self-encoding and multispectral imaging. *Angewandte Chemie International Edition in English*, **39**, 4483–5.

68 Medintz, I.L., Uyeda, H.T., Goldman, E.R. and Mattoussi, H. (2005) Quantum dot bioconjugates for imaging, labelling and sensing. *Nature Materials*, **4**, 435–46.

69 Kuang, M., Wang, D., Bao, H., Gao, M., Möhwald, H. and Jiang, M. (2005) Fabrication of multicolor-encoded microspheres by tagging semiconductor nanocrystals to hydrogel spheres. *Advanced Materials*, **17**, 267–70.

70 Fulton, R.J., McDade, R.L., Smith, P.L., Kienker, L.J. and Kettman, J.R., Jr (1997) Advanced multiplexed analysis with the Flowmetrix™ system. *Clinical Chemistry*, **43**, 1749–56.

71 Egner, B.J., Rana, S., Smith, H., Bouloc, N., Frey, J.G., Brocklesby, W.S. and Bradley, M. (1997) Tagging in combinatorial chemistry: the use of coloured and fluorescent beads. *Chemical Communications*, **8**, 735–6.

72 Battersby, B.J., Bryant, D., Meutermans, W., Matthews, D., Smythe, M.L. and Trau, M. (2000) Toward larger chemical libraries: encoding with fluorescent colloids in combinatorial chemistry. *Journal of the American Chemical Society*, **122**, 2138–9.

73 Cunin, F., Schmedake, T.A., Link, J.R., Li, Y.Y., Koh, J., Bhatia, S.N. and Sailor, M.J. (2002) Biomolecular screening with encoded porous-silicon photonic crystals. *Nature Materials*, **1**, 39–41.

74 Stoermer, R.L., Sioss, J.A. and Keating, C.D. (2005) Stabilization of silver metal in citrate buffer: barcoded nanowires and their bioconjugates. *Chemistry of Materials*, **17**, 4356–61.

75 Zhou, H., Roy, S., Schulman, H. and Natan, M.J. (2001) Solution and chip arrays in protein profiling. *Trends in Biotechnology*, **19**, S34–S39.

76 Zhi, Z.-L., Morita, Y., Hasan, Q. and Tamiya, E. (2003) Micromachining microcarrier-based biomolecular encoding for miniaturized and multiplexed immunoassay. *Analytical Chemistry*, **75**, 4125–31.

77 Evans, M., Sewter, C. and Hill, E. (2003) An encoded particle array tool for multiplex bioassays. *Assay and Drug Development Technologies*, **1**, 199–207.

78 Sha, M.Y., Walton, I.D., Norton, S.M., Taylor, M., Yamanaka, M., Natan, M.J., Xu, C., Drmanac, S., Huang, S., Borcherding, A., Drmanac, R. and Penn, S.G. (2006) Multiplexed SNP genotyping using nanobarcode particle technology. *Analytical and Bioanalytical Chemistry*, **384**, 658–66.

79 Pregibon, D.C., Toner, M. and Doyle, P.S. (2007) Multifunctional encoded particles for high-throughput biomolecule analysis. *Science*, **315**, 1393–6.

80 Vaino, A.R. and Janda, K.D. (2000) Euclidean shape-encoded combinatorial chemical libraries. *Proceedings of the National Academy of Sciences of the United States of America*, **97**, 7692–6.

81 Dendukuri, D., Pregibon, D.C., Collins, J., Hatton, T.A. and Doyle, P.S. (2006) Continuous-flow lithography for high-throughput microparticle synthesis. *Nature Materials*, **5**, 365–9.

82 Chung, S.E., Park, W., Park, H., Yu, K., Park, N. and Kwon, S. (2007) Optofluidic maskless lithography system for real-time synthesis of photopolymerized microstructures in microfluidic channels. *Applied Physics Letters*, **91**, 041106.

83 Schultz, S., Smith, D.R., Mock, J.J. and Schultz, D.A. (2000) Single-target molecule detection with nonbleaching multicolor optical immunolabels. *Proceedings of the National Academy of Sciences of the United States of America*, **97**, 996–1001.

84 Schuetz, P. and Caruso, F. (2002) Electrostatically assembled fluorescent thin films of rare-earth-doped lanthanum

phosphate nanoparticles. *Chemistry of Materials*, **14**, 4509–16.
85 Lim, Y.T., Kim, J.K., Shin, Y.B. and Chung, B.H. (2006) Wavelength and intensity multiplexing of metal nanoparticles for the fabrication of multicolored micro- and nanospheres. *Advanced Functional Materials*, **16**, 1015–21.
86 Matsubara, K., Watanabe, M. and Takeoka, Y. (2007) A thermally adjustable multicolor photochromic hydrogel. *Angewandte Chemie International Edition in English*, **46**, 1688–92.
87 Gao, R., Zhang, Y. and Gopalakrishnakone, P. (2008) Single-bead-based immunofluorescence assay for snake venom detection. *Biotechnology Progress*, **24**, 245–9.
88 Hahn, Y.K., Chang, J.-B., Jin, Z., Kim, H.-S. and Park, J.-K. (2009) Magnetophoretic position detection for multiplexed immunoassays using colored microspheres in a microchannel. *Biosensors and Bioelectronics*, **24**, 1870–76.
89 Liping Sun, M.Z., Moore, L.R. and Chalmers, J.J. (1998) Continuous, flow-through immunomagnetic cell sorting in a quadrupole field. *Cytometry*, **33**, 469–75.
90 Chalmers, J.J., Haam, S., Zhao, Y., McCloskey, K., Moore, L., Zborowski, M. and Williams, P.S. (1999) Quantification of cellular properties from external fields and resulting induced velocity: cellular hydrodynamic diameter. *Biotechnology and Bioengineering*, **64**, 509–18.
91 Chalmers, J.J., Haam, S., Zhao, Y., McCloskey, K., Moore, L., Zborowski, M. and Williams, P.S. (1999) Quantification of cellular properties from external fields and resulting induced velocity: magnetic susceptibility. *Biotechnology and Bioengineering*, **64**, 519–26.
92 Chalmers, J.J., Zhao, Y., Nakamura, M., Melnik, K., Lasky, L., Moore, L. and Zborowski, M. (1999) An instrument to determine the magnetophoretic mobility of labeled, biological cells and paramagnetic particles. *Journal of Magnetism and Magnetic Materials*, **194**, 231–41.
93 Chalmers, J.J., Zborowski, M., Moore, L., Mandal, S., Fang, B. and Sun, L. (1998) Theoretical analysis of cell separation based on cell surface marker density. *Biotechnology and Bioengineering*, **59**, 10–20.
94 Zborowski, M., Ostera, G.R., Moore, L.R., Milliron, S., Chalmers, J.J. and Schechtery, A.N. (2003) Red blood cell magnetophoresis. *Biophysical Journal*, **84**, 2638–45.
95 Nakamura, M., Decker, K., Chosy, J., Comella, K., Melnik, K., Moore, L., Lasky, L.C., Zborowski, M. and Chalmers, J.J. (2001) Separation of a breast cancer cell line from human blood using a quadrupole magnetic flow sorter. *Biotechnology Progress*, **17**, 1145–55.
96 Williams, P.S., Zborowski, M. and Chalmers, J.J. (1999) Flow rate optimization for the quadrupole magnetic cell sorter. *Analytical Chemistry*, **71**, 3799–807.
97 McCloskey, K.E., Chalmers, J.J. and Zborowski, M. (2000) Magnetophoretic mobilities correlate to antibody binding capacities. *Cytometry*, **40**, 307–15.
98 Hultgren, A., Tanase, M., Felton, E.J., Bhadriraju, K., Salem, A.K., Chen, C.S. and Reich, D.H. (2005) Optimization of yield in magnetic cell separations using nickel nanowires of different lengths. *Biotechnology Progress*, **21**, 509–15.
99 MiltenyiBiotec GmbH, Germany, www.miltenyibiotec.com/.
100 Dynal Biotech AS, Oslo, Norway, www.dynalbiotech.com/.
101 Xia, N., Hunt, T.P., Mayers, B.T., Alsberg, E., Whitesides, G.M., Westervelt, R.M. and Ingber, D.E. (2006) Combined microfluidic-micromagnetic separation of living cells in continuous flow. *Biomedical Microdevices*, **8**, 299–308.
102 Inglis, D.W., Riehn, R., Sturm, J.C. and Austin, R.H. (2006) Microfluidic high gradient magnetic cell separation. *Journal of Applied Physics*, **99**, 08K101.
103 Wang, K., Fishman, H.A., Dai, H. and Harris, J.S. (2006) Neural stimulation

with a carbon nanotube microelectrode array. *Nano Letters*, **6**, 2043–8.

104 Chen, Z., Appenzeller, J., Lin, Y.-M., Sippel-Oakley, J., Rinzler, A.G., Tang, J., Wind, S.J., Solomon, P.M. and Avouris, P. (2006) An integrated logic circuit assembled on a single carbon nanotube. *Science*, **311**, 1735.

105 Xu, Y.-Q., Peng, H., Hauge, R.H. and Smalley, R.E. (2005) Controlled multistep purification of single-walled carbon nanotubes. *Nano Letters*, **5**, 163–8.

106 Vivekchand, S.R.C., Jayakanth, R., Govindaraj, A. and Rao, C.N.R. (2005) The problem of purifying single-walled carbon nanotubes. *Small*, **1**, 920–3.

107 Chen, F., Xue, Y., Hadjiev, V.G., Chu, C.W., Nikolaev, P. and Arepalli, S. (2003) Fast characterization of magnetic impurities in single-walled carbon nanotubes. *Applied Physics Letters*, **83**, 4601–3.

108 Kim, Y. and Luzzi, D.E. (2005) Purification of pulsed laser synthesized single wall carbon nanotubes by magnetic filtration. *Journal of Physical Chemistry B*, **109**, 16636–43.

109 Thiên-Nga, L., Hernadi, K., Ljubović , E., Garaj, S. and Forró, L.Z. (2002) Mechanical purification of single-walled carbon nanotube bundles from catalytic particles. *Nano Letters*, **2**, 1349–52.

110 Johnston, D.E., Islam, M.F., Yodh, A.G. and Johnson, A.T. (2005) Electronic devices based on purified carbon nanotubes grown by high-pressure decomposition of carbon monoxide. *Nature Materials*, **4**, 589–92.

111 Haberditzl, W. (1966) Advances in molecular diamagnetism. *Angewandte Chemie International Edition in English*, **5**, 288–98.

112 Haddon, R.C., Schneemeyer, L.F., Waszczak, J.V., Glarum, S.H., Tycko, R., Dabbagh, G., Kortan, A.R., Muller, A.J., Mujsce, A.M., Rosseinsky, M.J., Zahurak, S.M., Makhija, A.V., Thiel, F.A., Raghavachari, K., Cockayne, E. and Elser, V. (1991) Experimental and theoretical determination of the magnetic susceptibility of C_{60} and C_{70}. *Nature*, **350**, 46–7.

113 Wallmann, J.C., Cunningham, B.B. and Calvin, M. (1951) The magnetic susceptibility of vitamin B_{12} and B_{12b}. *Science*, **113**, 55–6.

114 Cerdonio, M., Congiu-Castellano, A., Mogno, F., Pispisa, B., Romani, G.L. and Vitale, S. (1977) Magnetic properties of oxyhemoglobin. *Proceedings of the National Academy of Sciences of the United States of America*, **74**, 398–400.

115 Kuchel, P.W., Chapman, B.E., Bubb, W.A., Hansen, P.E., Durrant, C.J. and Hertzberg, M.P. (2003) Magnetic susceptibility: solutions, emulsions, and cells. *Concepts in Magnetic Resonance Part A*, **18A**, 56–71.

116 Gordon, M.J., Chu, K.C., Margaritis, A., Martin, A.J., Ethier, C.R. and Rutt, B.K. (1999) Measurement of Gd-DTPA diffusion through PVA hydrogel using a novel magnetic resonance imaging method. *Biotechnology and Bioengineering*, **65**, 459–67.

117 Zhang, H., Moore, L.R., Zborowski, M., Williams, P.S., Margel, S. and Chalmers, J.J. (2005) Establishment and implications of a characterization method for magnetic nanoparticle using cell tracking velocimetry and magnetic susceptibility modified solutions. *Analyst*, **130**, 514–27.

118 Winkleman, A., Gudiksen, K.L., Ryan, D., Whitesides, G.M., Greenfield, D. and Prentiss, M. (2004) A magnetic trap for living cells suspended in a paramagnetic buffer. *Applied Physics Letters*, **85**, 2411–13.

119 Suzuki, T., Baba, H. and Matsumoto, E. (2001) Stress effect on hysteretic magnetization curve of nickel. *International Journal of Applied Electromagnetics and Mechanics*, **13**, 307–10.

120 Watarai, H. and Namba, M. (2001) Magnetophoretic behavior of single polystyrene particles in aqueous manganese(ii) chloride. *Analytical Sciences*, **17**, 1233–6.

Keywords

magnetic nanomaterials; microfluidic device; magnetophoresis; nanobiosensor; immunoassays; magnetophoretic separation; isomagnetophoresis

4
Magnetic Nanomaterials as MRI Contrast Agents

Yurii K. Gun'ko and Dermot F. Brougham

4.1
Introduction

The application of nanomaterials and nanotechnological approaches in medicine has opened up new possibilities in both medical diagnostics and therapeutics. Because their properties differ from those of their bulk counterparts, and can be selected through the control of particle size and architecture, nanoparticulate materials offer a wide range of potential applications. Developments in magnetic nanomaterials have had an enormous impact on modern science, technology and in biomedicine [1–3]. For example, magnetic particles can be utilized as drug delivery agents, which can be localized in the body at a site of interest using an external magnetic field. When exposed to an alternating magnetic field, magnetic nanoparticles can serve as powerful heat sources, and hence can be used in hyperthermia therapy for cancer. Magnetic fluids based on aqueous dispersions of small-sized, or superparamagnetic, nanoparticles have also been utilized as contrast agents for magnetic resonance imaging (MRI). The latter technique has proven to be one of the useful modern diagnostic methods in biomedical research and clinical medicine, and is perhaps also the technique with the greatest potential for further development.

The primary advantage of MRI over other instrumental diagnostic methods, is that it provides detailed images of soft tissues *in vivo*. Most imaging techniques offer a single contrast mechanism, for instance based on the differences in tissue density and atomic number (X-ray techniques), or acoustic impedance (ultrasound). In MRI, however, the contrast arises from the detailed physico-chemical environment of water in the tissues; hence, the procedure is sensitive not only to water binding, to the concentration of macromolecules in the tissue, and to the concentration of iron-containing or other paramagnetic species in the tissues, but also to many other parameters, most of which offer the potential for generating useful image contrast.

The second advantage of MRI is that it is a *functional* imaging modality whereby the image contrast can, under certain circumstances, be directly correlated with

Nanomaterials for the Life Sciences Vol. 4: Magnetic Nanomaterials. Edited by Challa S. S. R. Kumar

ISBN: 978-3-527-32154-4

local biochemical processes or metabolic activity. For instance, MRI can be used to measure blood flow in vessels or during tissue perfusion, as well as changes in blood oxygenation. This facility also serves as the basis for functional MRI (f-MRI) of the brain, which is currently revolutionizing the neuropsychology.

A third advantage of MRI is its *dynamic* imaging modality. As the technique is apparently safe, images can be acquired continuously and this, in principle, allows dynamic studies to be performed. Examples include imaging of the beating heart, transport in the vascular system, the movement of joints, or the response of the central nervous system (CNS) to external stimuli [3].

The enormous versatility and flexibility of MRI, combined with its relative safety and noninvasive nature, has led to a huge increase in demand for clinical scans over the past decade. In fact, today's MRI scanner manufacturers are investing heavily in the development of new diagnostics, with a view to opening up the market to sell more scanners. The same advantages have a powerful influence on the direction of academic research, where methods for the controlled growth, stabilization and functionalization of nanostructures have been imported from across the nanotechnology sector to produce a wide range of responsive and smart MRI-detected agents that can be applied to the biomedical field.

MRI contrast agents act to improve image quality by altering the magnetic resonance relaxation times of water in the tissues surrounding the agent, and hence cause a change in the intensity of the water signal in these tissues. Most MRI techniques utilize gadolinium complexes as contrast agents, which provide good positive contrast, or signal enhancement. However, compared with gadolinium chelates such as diethylenetriaminopenta-acetic acid (Gd-DTPA), magnetic nanoparticles are far more efficient as relaxation enhancers – that is, they exhibit a higher relaxivity and, in particular, a good negative contrast or signal suppression. Their effect on the relaxation time of water is measurable even at nanomolar concentrations and, as a result, the nanoparticulate agents are in many ways complementary to the gadolinium agents. Nanoparticulate agents also have advantages with respect to biocompatibility, selective uptake, targeted delivery, and removal from the body, which can be relatively easily tuned by changing the size and the nature of the surface coating of nanoparticles. These factors are extremely important for *in vivo* medical applications [2]. One very attractive feature of magnetic nanoparticles is the fact that they can be relatively easily functionalized with molecules, thus bestowing new properties on the particles. Aside from a range of hydrophobic and hydrophilic coatings, which themselves may influence biodistribution, the molecules that can be used in this role include a wide range of drugs and fluorescent compounds, all of which can be targeted to a specific area or tissue. For example, by attaching targeting molecules such as proteins or antibodies to the surfaces of the particles, the latter may be directed not only to molecules but also to any cell, tissue, or tumor in the body [4]. Added to this is the extra potential offered by the *magnetic moments*; this means that external magnetic fields can be applied to guide and trap the nanoparticles at the target site, where they may be used to effect a hyperthermic response. In particular, significant efforts have been directed at producing "smart" contrast agents, which could allow the very early

detection of various pathologies and also serve as presymptomatic diagnostics, and which could – at least potentially – be coupled with highly effective targeted therapy [4–7].

Despite these great successes, some very real challenges remain before the potential of magnetic nanocomposites as MRI contrast agents can be fully realized. One of the main, and most obvious, problems is the complexity in the preparation and functionalization of these nanocomposites, which frequently involves a multistep synthesis and many purification stages. Another typical problem is related to the instability and aggregation of these nanocomposites in solutions. Aggregation can be caused by magnetic, electrostatic or chemical interactions between particles, and therefore careful design and an extremely accurate synthesis methodology are required to develop magnetic nanocomposites while avoiding their aggregation and precipitation. Another drawback is the problem of avoiding rapid opsonization, and removal from the bloodstream, by the reticuloendothelial system (RES). For example, iron oxide-based nanoparticles normally demonstrate very good biocompatibility, with no adverse effects detectable from longitudinal histological analyses of the liver, spleen, and kidney [8]. However, the potential for nanotoxicity arising from the assembly of nanomaterials must be considered in each case [1], and therefore detailed studies of the biodistribution, clearance, and biocompatibility of any potential magnetic nanoparticle system for *in vivo* biomedical applications are necessary prior to their being promoted towards clinical use [6, 8].

The main aim of this chapter is to present an overview of those magnetic nanocomposite materials which are utilized as contrast agents for MRI. Hence, the various types of nanomaterials will be discussed, together with details of the main strategies for the specific functionalization of magnetic materials for MRI applications, and their properties and characterization. Current and potential clinical MRI uses, including cell labeling and molecular *in vivo* and *in vitro* imaging, will also be discussed.

4.2
Classification of Magnetic Nanomaterials Used for MRI Applications

The study of magnetic nanocomposites is a very rapidly developing field, which makes the classification of these materials quite difficult and sometimes arbitrary. In terms of contrast, MRI agents are traditionally classified as T_1-, or T_2- type. T_1, or *positive-contrast* agents reduce the spin-lattice relaxation times of the surrounding water; that is, they have a high spin-lattice relaxivity, or r_1 value. The relaxivity is defined as the relaxation rate enhancement per millimole of iron, and thus has units of $s^{-1}\,mM^{-1}$. If the imaging sequence is appropriately weighted, by reducing the recycle delay between sequence repetitions, and usually also the echo time, those tissues which contain the agent will show up brightly in the image. T_2, or *negative-contrast* agents reduce the spin-spin relaxation times of the surrounding water. By increasing the recycle delay between sequence repetitions, and the echo

time, those tissues which contain the agent will show up as dark in the image, when compared to adjacent tissues. Thus, negative agents have a high spin-spin relaxivity, or r_2 value, although more usually their efficacy is quantified by high values of the r_2/r_1 ratio. Typical examples of T_1-agents are molecular gadolinium chelates, while superparamagnetic ferrite-based particles represent T_2-agents [5, 7].

Based on the chemical nature of nanomaterials, the magnetic nanocomposites utilized in various MRI applications can be roughly grouped into three main classes: (i) magnetic oxide-based nanoparticles; (ii) metal- and metal alloy-based nanoparticles; and (iii) rare earth (Gd or Dy) chelate-loaded nanocomposites.

4.2.1 Magnetic Oxide-Based Nanoparticles

Typical examples of magnetic iron oxide-based nanoparticles are magnetite (Fe_3O_4) and maghemite (γ-Fe_2O_3), both of which are members of the ferrites family [9]. Ferrimagnetic oxides are ionic materials, consisting of arrays of positively charged iron ions and negatively charged oxide ions. Ferrites adopt a spinel structure based on a cubic close-packed (ccp) array of oxide ions. If the magnetic particles are of very small sizes (of the order of 10 nm), they can demonstrate superparamagnetic behavior [10]. Superparamagnetic particles consist of a single magnetic domain where the particle is in a state of uniform magnetization at any field. Superparamagnetism arises when the magnetic moments of the particles are thermodynamically independent. It is found that if the sample is composed of smaller particles, then the total magnetization will decrease with decreasing particle size.

For MRI applications, superparamagnetic iron oxide nanoparticles (SPIONs) have attracted much interest as they are relatively easy to form, have a low toxicity [11, 12], and the superparamagnetism increases the colloidal stability. The iron oxide-based nanoparticulate agents have been classified as ultra small particles of iron oxide (USPIOs), small particles of iron oxide (SPIOs), and oral (large) particles.

USPIOs have diameters ranging between 10 and 40 nm, and can be further subdivided into crosslinked iron oxide nanoparticles (CLIONs) and monocrystalline iron oxide nanoparticles (MIONs) [7, 8, 13]. USPIOs are dispersions of stabilized nanocrystals or small clusters of such particles which can have a strong T_1 (positive) contrast when an appropriate imaging pulse sequence is used [14]. The coatings surrounding the USPIO's inorganic core play a major role in both the *in vitro* stability and, overall, in the fate of USPIOs *in vivo* [15]. An example of a commercially available USPIO is Ferumoxtran-10, which is useful as a contrast material in MRI for the diagnosis of inflammatory and degenerative disorders associated with high macrophage activity [16–18]. SPIOs (see Section 4.5 and Table 4.1) are selected for lymph node imaging (AMI-227; i.e., Sinerem® and Combidex®; diameters 20–40 nm), bone marrow imaging (AMI-227), perfusion imaging (NC100150; i.e., Clariscan®; mean diameter 20 nm), and MR

Table 4.1 Nanoparticulate agents approved for clinical applications or clinically tested.

Agent name	Company	Coating agent	Relaxomic properties, 1.5 T ($mM^{-1}s^{-1}$)	Hydrodynamic size (nm)	Applications	Reference(s)
Ferumoxides AMI-25, Endorem®/ Feridex®	Guerbet, Advanced Magnetics	Dextran T10	$r_1 = 10.1$ $r_2 = 120$	120–180	Liver imaging; cellular labeling	[17]
Ferumoxtran-10 AMI-227 BMS-180549 Sinerem®/ Combidex®	Guerbet, Advanced Magnetics	Dextran T10, T1	$r_1 = 9.9$ $r_2 = 65$	15–30	Metastatic lymph node and macrophage imaging; blood pool agents; cellular labeling	[18, 17]
Ferumoxytol Code 7228	Advanced Magnetics	Carboxyl-methyl-dextran	$r_1 = 15$ $r_2 = 89$	30	Macrophage imaging; blood pool agent; cellular labeling	[193]
Ferumoxsil AMI-121 Lumirem®/ GastroMARK®	Guerbet, Advanced Magnetics	Silica	n.a.	300	Oral GIT imaging	[17, 141]
Ferucarbotran SHU-555A Resovis®	Schering	Carboxy-dextran	$r_1 = 9.7$ $r_2 = 189$	60	Liver imaging; cellular labeling	[83]
SHU-555C Supravist®	Schering	Carboxy-dextran	$r_1 = 10.7$ $r_2 = 38$	21	Blood pool agent; cellular labeling	[194]
Feruglose NC100150 Clariscan®	GE-Healthcare (abandoned)	PEG-ylated starch	n.a.	20	Blood pool agent	[19, 20]
Ferristene® Abdoscan®	GE-Healthcare	Sulfonated styrene-divinyl-benzene copolymer	n.a.	20	Oral GIT imaging	[192]
VSOP-C184	Ferropharm	Citrate	$r_1 = 14$ $r_2 = 33.4$	7	Blood pool agent; cellular labeling	[21]

GIT = gastrointestinal tract; n.a. = not applicable.
Reproduced from Ref. [6].

angiography (NC100150). Even smaller monocrystalline iron oxide nanoparticles are under research for receptor-directed MRI and magnetically labeled cell probe MRI [8].

SPIOs are suspensions of larger objects, with hydrodynamic diameters D_{hyd} >60 nm (normally 60–200 nm), containing multiple nanocrystals within a water-permeable shell, often composed of dextran or carboxydextran, and usually generate a strong T_2 (negative) contrast. Among the nanoparticulate contrast agents which are currently in use, or are in the later stages of clinical investigation, all are based on suspensions of magnetic iron oxide. These include Endorem® (Guebert) [17], a SPIO which incorporates multiple 5 nm magnetic iron oxide cores in a larger dextran particle, although the size distribution is very broad (D_{hyd} 120–180 nm). Endorem® is a negative-contrast agent ($r_2/r_1 \sim 12$) which is used primarily for liver imaging. Sinerem (also from Guebert) has a cluster size of 50 nm and is formed by fractioning Endorem® suspensions. Although it is still a negative-contrast agent ($r_2/r_1 \sim 6.6$), the improvement in size facilitates the application of Sinerem – which is usually classified as a USPIO – in staging metastatic lymph nodes and in blood pool imaging (see Section 4.5 and Table 4.1). Resovist®, a carboxydextran-stabilized USPIO produced by Schering AG, has a hydrodynamic size of 60 nm and is also used in liver imaging ($r_2/r_1 \sim 19.5$) [6].

Large (or Oral) particles of iron oxide (diameter between 300 nm and 3.5 μm) are not suitable for intravenous administration, but may be administered orally for gastrointestinal imaging. Examples include AMI-121 (Lumirem® and GastroMARK®) [17], which are used for bowel contrast, and OMP (i.e., Abdoscan®) [19, 20], which is used in liver/spleen imaging (see Section 4.5).

From a practical perspective, when examining an image it is easier to identify smaller, positively labeled regions than negatively labeled areas, and consequently there is ongoing interest in producing positive-contrast nanoparticulate agents. This represents a major challenge in colloidal chemistry as the agents must remain dispersed during storage, and also for a significant time under physiological conditions, as any aggregation will lead to an increase in r_2. Among the more interesting newly developed agents is VSOP-C184 [21] from Ferropharm which, with a hydrodynamic size of 7 nm, is among the smallest, and where the dispersed particles are stabilized with citrate. The absence of a polysaccharide shell reduces any targeting of the particles by the macrophages of the RES, which otherwise would result in a rapid accumulation of iron oxide in the liver. In addition, the small particle size and good dispersity improve the blood circulation life-time and generate positive contrast. These characteristics – and in particular the extended circulation times – mean that the agent has potential in blood pool imaging, where it may compete with the current industry standard Magnevist®, a gadolinium-based agent [22].

There are, however, still some drawbacks associated with nanoparticulate iron oxide-based contrast agents. Occasionally, they demonstrate unusual magnetic susceptibility artifacts which produce dark signals that may not only be misleading but also result in an incorrect interpretation of the T_2-weighted MR images. These dark areas can be confused with signals from bleeding, calcification, or metal

deposits, while the susceptibility artifacts also distort the background image [23, 24].

Consequently, significant efforts have recently been made on the development of T_1 MRI contrast agents based on magnetic nanoparticles of other metal oxides. These involve mostly manganese and rare earth-based oxides. For example, T_1 MRI contrast agents based on biocompatible MnO nanoparticles have recently been reported by Hyeon *et al.* [24]. This material facilitated the acquisition of good-quality T_1-weighted MR images of the brain, liver, kidney, and spinal cord, showing very fine anatomic structure in animal models. It was also noted that the MnO nanoparticles could be easily conjugated with a tumor-specific antibody and hence utilized for selective tumor imaging.

Small rare earth (Gd or Dy) oxide nanocrystals have also shown great promise as contrast agents for MRI, because they can provide a large number of unpaired electrons per unit of contrast agent, as well as the small particle size required for low r_2/r_1 values. Typically, small gadolinium oxide (Gd_2O_3) nanocrystals can be prepared via the polyol route by thermal decomposition of, for example, $Gd(NO_3)_3$ in the presence of diethylene glycol [25–27]. Diethylene glycol-capped Gd_2O_3 nanoparticles have been shown to demonstrate both r_1 and r_2 relaxivities almost twice as high as the corresponding Gd-chelate-based agents in aqueous solutions [27]. Similar solution-based thermal decomposition methods were employed to prepare nanocrystalline $Gd_2O(CO_3)_2{*}H_2O$ and Gd_2O_3 particles, which have also shown promising positive- and negative-contrast effects [28, 29]. However, rare earth oxides are highly reactive and must be coated with an appropriate shell in order to be utilized in physiological media. For example, when paramagnetic Gd_2O_3 cores were protected and stabilized by encapsulation within a polysiloxane shell, the r_1 values of these materials were found to be higher than those of positive contrast agents based on gadolinium chelates [30]. In another approach to improve stability and biocompatibility, gadolinium oxide nanoparticles were embedded in albumin microspheres and used as prototype contrast agents for multimodal X-ray and MRI studies [31].

4.2.2
Magnetic Metal- and Alloy-Based Nanoparticles as Contrast Agents

Transition metal nanoparticles such as pure Fe and Co, or metallic alloys such as FeCo, have been envisaged as potentially promising T_1 and T_2 contrast agents. These metallic nanoparticles tend to have a larger magnetic moment than their iron oxide counterparts [32].

Typical examples of metal alloy-based nanoparticles are face-centered cubic (fcc) FePt nanoparticles, which can be synthesized via the pyrolysis of iron(III) ethoxide and platinum(II) acetylacetonate. Relaxometry studies have shown that FePt particles have a higher T_2 effect than superparamagnetic iron oxide, indicating that the former might serve as superior negative contrast agents for MRI [33].

Iron metal-based nanoparticles can also be prepared by the laser-induced pyrolysis of iron carbonyl ($Fe(CO)_5$) vapors, the process resulting in the partial oxidation

of iron, and a thin iron oxide shell that stabilizes the iron nanoparticles. Typically, these particles can be coated with dextran and suspended in water, so as to produce strong positive contrast at low applied magnetic fields, and a stronger increase in negative contrast at higher fields, as compared to similar iron oxide nanoparticles [34, 35]. Thus, colloidal iron suspensions have potential applications as both T_1 and T_2 contrast agents.

Recently, much interest has been expressed in the development of stable, iron-containing core–shell nanostructures (see Section 4.2.3). For example, when iron(Fe)/gold(Au) core–shell nanoparticles were prepared using a reverse-micelle method, the nanomaterials demonstrated a high saturation magnetization and potential as T_1 agents [36]. Another example is that of Au_3Cu (gold and copper) nanoshell structures, which demonstrated promising MR contrast properties but with a degree of toxicity that called into question their suitability for *in vivo* applications [37].

4.2.3
Rare Earth Metal-Loaded Nanoparticulate Contrast Agents

As mentioned above, molecular gadolinium and dysprosium complexes are quite commonly used as MRI contrast agents. Unfortunately, however, these rare earth chelates demonstrate toxicity, fast diffusion and sometimes also a low contrast signal – all of which are serious drawbacks in many contrast agent applications. The main strategy used to avoid these problems is to incorporate paramagnetic rare earth molecular species into the nanoparticles; this allows improvements in relaxivity, by increasing the loading of paramagnetic ions and increasing the rotational correlation time of the nanosized particles [38]. Such a strategy can also enable the specific targeting of contrast agents to different tissues and organs by a further functionalization and vectorization of nanoparticles. The design and fabrication of rare earth-containing nanoparticles have been the subjects of several reviews [5, 38, 39].

A large proportion of recent research effort has focused on the development of nanoparticles that are labeled, or loaded, with Gd(III) or Dy(III) chelates, using a variety of different binding techniques [38]. These nanocomposites include rare earth-loaded polymer (or macromolecule) nanoparticles and rare earth-loaded oxide nanoparticles (e.g., SiO_2, Al_2O_3). The main approaches for the fabrication of rare earth metal nanocomposites involve the noncovalent or covalent binding of high-spin paramagnetic gadolinium chelates to macromolecules and polymers, or the grafting of chelates onto oxide and hydroxide nanoparticles [40].

Many examples have been described of polymer nanoparticles functionalized with gadolinium chelates. One of the most promising strategies is the conjugation of Gd-based chelates to biomacromolecules and protein nanoparticles. For example, Gd(III)-based MR contrast agents were conjugated to polyarginine oligomers, with the resultant nanocomposites being able to permeate cell membranes [41, 42]. In another report, when amphiphilic gadolinium Gd-DTPA chelates were incorporated into low-density lipoprotein nanoparticles (22 nm diameter), a

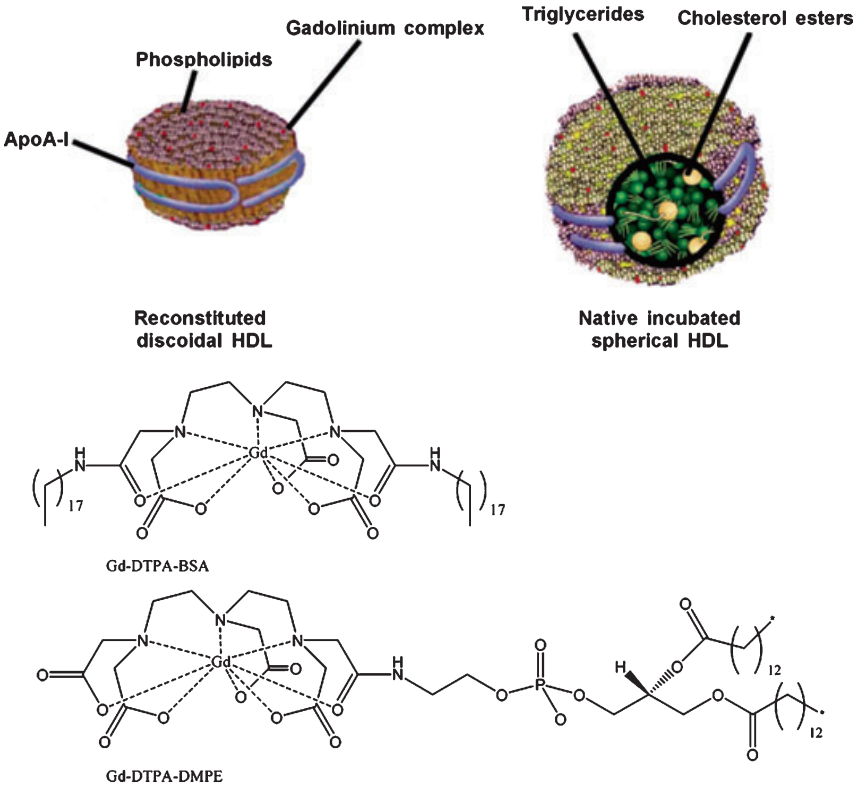

Figure 4.1 Different types of lipoprotein nanoparticle-based contrast agent, and the gadolinium complexes used in their preparation. Reproduced from Ref. [45].

significant contrast enhancement was provided [43]. Several similar Gd-chelate-loaded, low- or high-density lipoprotein particles (Figure 4.1) have also been recently reported [44, 45]. Another interesting development involves the synthesis of peptide-derivatized shell-crosslinked nanoparticles, which were functionalized with gadolinium chelates and studied as robust MRI agents. The highly hydrated nature of the shell layer, in which the Gd was located, coupled with the hydrodynamic diameter of 40 ± 3 nm, allowed for a rapid water exchange, and the resulting material demonstrated both large ionic and molecular relaxivities [46, 47].

Small particles of various biocompatible polymers have also been used for the fabrication of Gd-loaded paramagnetic nanostructured contrast agents. New 200 nm-diameter nanoparticles, which are composed of a noncovalent adduct between a gadolinium complex, a polymer of P-cyclodextrin, and dextran grafted with alkyl chains have been recently reported. These nanocomposites demonstrated a great relaxivity enhancement ($48.4\,mM^{-1}s^{-1}$, at 20 MHz and 37 °C) compared to a value of $5.2\,mM^{-1}s^{-1}$ for the Gd-III chelate itself [48]. Latex nanoparticles of 100, 400 and 900 nm diameter were doubly derivatized, first with tomato lectin

and then with Gd-DTPA to target them to epithelial and endothelial glycocalyceal N-glycans and to generate contrast enhancement in MRI [49].

Lipophilic paramagnetic Gd-chelates have also been incorporated into perfluorocarbon nanoparticles, resulting in materials which have up to 55% higher relaxivity than the corresponding free Gd-chelate [50]. These Gd-loaded perfluorocarbon nanoparticles could be easily conjugated to antibodies to achieve specific localization and imaging [51].

Another group of Gd-based nanoparticulate contrast agents are oxides loaded with rare earth metals, the most commonly used examples being rare earth-doped silica nanoparticles. For example, silica-Gd core–shell particles with a size of 71 nm were prepared by homogeneous precipitation from a water/propanol solution of $Gd(NO_3)_3$, urea and polyvinylpyrrolidone (PVP) in the presence of a suspension of the silica particles, followed by successive silica-coating using tetraethoxysilane (TEOS). These particles demonstrated relaxation enhancements under MRI conditions [52]. Mesoporous silica nanorods have been fabricated via surfactant-templated self-assembly under basic conditions, and subsequent mixing with solutions of $GdCl_3$ salt and Dye@MSN-R produced novel fluorescent and paramagnetic potential contrast materials [53].

Gd-DTPA chelates were intercalated into Mg- and Al-based layered double hydroxide (LDH) nanomaterials by anionic exchange. These novel paramagnetic bar-like nanomaterials, which had widths of 30–60 nm and lengths 50–150 nm, demonstrated fourfold and 12 fold increases in r_1 and r_2, respectively, as compared to free Gd(DTPA) chelates in solution under the same reaction conditions [54].

In another study, semiconducting nanoparticles (quantum dots) or colloidal metal (Au) nanoparticles were coated with thin silica shells, and covalently linked to appropriate gadolinium chelates; the result was a series of nanocomposites of 8–15 nm diameter, which demonstrated high relaxivities [55]. Gold nanoparticles encapsulated by a multilayered organic shell composed of gadolinium chelates, bound to each other through disulfide bonds, have also been reported [56, 57].

Finally, new ultrasensitive pH-smart probes (so-called gadonanotubes) have been prepared by incorporating nanoscale, superparamagnetic Gd^{3+}-ion clusters within single-walled carbon nanotubes (SWCNTs). These nanocomposites demonstrated a high performance as T_1-agents for MRI, with $r_1 \sim 180\,\mathrm{m}M^{-1}\,\mathrm{s}^{-1}$, which is about 40-fold greater than that of any current Gd^{3+} ion-based clinical agent [58, 59].

Traditional synthetic methods for the fabrication of magnetic nanomaterials include coprecipitation, hydrothermal and high-temperature processing, sol–gel processing, microemulsion methods, flow injection syntheses, sonolysis and electrospray synthesis, among others. These techniques are well established and have been considered in other chapters of this Handbook, and also in several recent reviews [7, 60–62]. In the following section, we present an overview of the methods used for coating and surface functionalization, to produce stable and biocompatible aqueous magnetic nanocomposite suspensions.

4.3
Coating and Surface Functionalization of Magnetic Nanoparticles

As the stability of magnetic fluids is crucial to their performance for any application, the factors that determine their stability have attracted a great deal of research activity. For MRI applications, stability in aqueous suspension, or under approximately physiological conditions (e.g., in phosphate-buffered saline at 37 °C), is also critical for assessing the shelf life of suspensions, and also provides a reasonable indication of their initial stability on introduction (usually by intravenous injection) into the bloodstream. The stability of suspensions on the bench – that is, their stability with respect to self-aggregation – is determined in the first instance by the nature of the surface of the nanoparticles or nanoparticle clusters. The stability of magnetic nanosuspensions as MRI contrast agents is, therefore, defined by the nature of surface capping stabilizers, which can be chemically linked with or physically adsorbed onto magnetic nanoparticles, so as to prevent their aggregation and/or precipitation. Magnetic nanoparticles can be coated either during (*in situ*) or after the synthesis, with the selection of coating frequently depending on the final application of the particles. Three main types of coatings can be used to stabilize nanoparticles in aqueous solutions, namely monomeric organic stabilizers, polymeric stabilizers, and inorganic coatings [7, 61, 62].

4.3.1
Surface Modification with Monomeric Stabilizers

Organic surfactants are frequently employed for the stabilization and coating of magnetic nanoparticles. One common and traditional approach is to use fatty acids (e.g., oleic or stearic acid) to stabilize the aqueous magnetic fluids, by the formation of a surface bilayer [63] with a chemisorbed fatty acid primary layer and an interpenetrating second layer; the latter is physisorbed onto the primary layer, with the hydrophilic head-groups pointing outwards. The structure and stability of the resultant nanoparticle clusters (ca. 100 nm) formed from the particles (ca. 10 nm) in suspension have been studied using both light-scattering and cryo-transmission electron microscopy (TEM) [64]. In aqueous suspension, the densely packed clusters were formed and shown to have a fractal dimension (as estimated by light-scattering) of 2.52. The same research group also reported a gradual increase in the hydrodynamic size on diluting the particles with water, this being due to a partial desorption of the second layer, destabilizing the colloid. Fatty acid-stabilized particles represent interesting model colloidal systems, as they are easy to produce and in general show good biocompatibility. However, this example illustrates the critical nature of the suspension's stability for real applications.

Both, dicarboxylic and tricarboxylic acids are also frequently utilized for the surface functionalization and stabilization of iron oxide-based nanoparticles in solution. In the case of these acids, some of the functional groups can bind to the surface of the metal oxide, while the remaining carboxylate groups provide a negative charge (depending on the pH) and improve the hydrophilicity of the particle

surface. This allows for a good stability of metal oxide-based nanoparticles in aqueous solutions. Among the acids most often used to stabilize magnetic iron oxide-based particle suspensions are citric, tartaric, and dimercaptosuccinic acids [65–67]. When monomeric anionic stabilizers are used for stabilization purposes, one critical factor which influences stability is the zeta-potential (ζ), which is the surface charge at the slipping plane. Thus, charged particles will repel each other (double-layer repulsion) and produce stable suspensions. Particles with $-30\,\text{mV} < \zeta < +30\,\text{mV}$, at a given pH, are generally found to be stable. For example, citrate-stabilized 7 nm-diameter iron oxide particles (VSOP-C184 [22]) have sufficient stability – both prior to and on injection – to be used as positive contrast agents for MRI angiography. As noted previously, however, this application is dependent on the nanoparticles remaining dispersed, as even a small amount of aggregation will significantly increase the negative contrast.

4.3.2 Modification Using Polymeric Stabilizers

Most potential nanoparticulate MRI contrast agents are stabilized by polymers which contain a variety of functional groups, including carboxylic acids, hydroxyls, phosphates, and sulfates [61]. In this case, the stabilization of nanoparticles can be achieved due to a group of interactions that are collectively termed steric forces [68, 69]. Aside from the magnetic interactions, in most cases attractive van der Waals' forces occur between the polymeric chains, although repulsive contributions also exist from the osmotic and elastic forces. The former arise from the unfavorable exclusion of solvent molecules from the interparticle space of two approaching particles, while the latter is due to the entropic penalty associated with reduced conformational mobility of the compressed or interdigitated chains of stabilizer molecules on adjacent particles; hence, this effect operates only at very short approach distances. In practice, the total force is usually repulsive, and this results in a stabilization of the particles. When modeling the surface interactions, the interaction potential is usually expressed as a sum of the three contributions integrated over the surfaces of the nanoparticles. Usually, the double-layer repulsion, which is described by the Derjaguin, Landau, Verwey, and Overbeek (DLVO) model, is not included [70, 71].

Due to their good solubility in water, biocompatibility, and also permeability, polysaccharides such as dextran or carboxydextran are among the most popular polymer coatings used for the stabilization of magnetic nanoparticles. Dextran-stabilized magnetic nanoparticles can be prepared using a coprecipitation method, with *in situ* coating by polysacchatide [72]. The most likely mechanism of dextran adsorption, however, involves collective hydrogen bonding between the dextran hydroxyl groups and the iron oxide particle surface [73].

Partially oxidized dextran can also be covalently linked to the amino groups of aminopropylsilane-coated magnetic nanoparticles via the formation of a Schiff's base bond [74]. One of the commercially available dextran-stabilized magnetic fluids, Ferumoxtran-10 (also known as AMI 227; Sinerem® and Combidex®), consists of superparamagnetic magnetite cores approximately 5 nm in diameter

which are coated with a dextran layer; the result is a hydrodynamic diameter of normally ranging between 15 and 30 nm. These particles demonstrate a prolonged blood residence time, excellent biocompatibility, and a high relaxivity, which makes them excellent MRI contrast agents [8, 22]. It has also been reported that dextran-coated nanoparticles can form larger aggregates with a hydrodynamic diameter of approximately 50 nm. It has been observed that increases occurred in the saturation magnetization, total susceptibility, and both the r_1 and r_2 relaxivities of the nanoparticle suspensions with an increase in nanocrystal size [75]. A new ferrofluid based on dextran-coated iron metal particles with aggregate sizes close to 50 nm has also been reported. These materials were found to demonstrate a higher saturation magnetization, magnetic susceptibility and r_2 relaxivity than similar iron oxide-based nanoparticles [76]. Dextran-coated superparamagnetic iron oxide particles can also form stable complexes with transfection agents. Moreover, such complexes can be internalized by endosomes/lysosomes, and have been utilized for cell labeling and *in vivo* MRI cell tracking [77]. One other polysaccharide which has been used for the coating and stabilization of magnetic nanoparticles is *alginate* [78–80].

Chitosan is a biocompatible and biodegradable polymer, and is of particular interest for coating magnetic nanoparticles [81, 82]. It has been reported that oleic acid-coated SPIONs can be easily dispersed in chitosan, producing stable ferrofluids with a typical hydrodynamic diameter of approximately 65 nm. The MRI properties of these ferrofluids were found to be similar to those of Resovist® (see Table 4.1), which is based on carboxydextran-coated iron oxide nanoparticles [83].

Polylactic acid, another biodegradable polymer, has been used to prepare stable biocompatible ferrofluids with varying ferromagnetic particle sizes, ranging from 10 to 180 nm [84]. Polylactic acid-coated nanoparticles can also be loaded with anticancer drugs (e.g., tamoxifen), which allows their use in simultaneous tumor imaging, drug delivery and the real-time monitoring of therapeutic effects [85]. Similar biocompatible nanoparticles have also been prepared via an *in situ*-controlled coprecipitation of magnetite from aqueous solutions containing suitable Fe^{2+} and Fe^{3+} salts, in a polymeric starch matrix. This process resulted in starch-coated SPIONs that demonstrated good potential for the imaging of nerve cells and the brain [86].

One very successful strategy for the preparation of stable and biocompatible nanoparticles is to graft polyethylene glycol (PEG) onto the surface (a process known as PEGylation). PEG is not only biocompatible but also has favorable chemical properties and solubility. In this situation, the stabilization is due primarily to steric interactions, while PEGylation can be used to further enhance the pharmacokinetic properties and improve the blood circulation times [87, 88]. This so-called "stealth technology" is used very widely across pharmacology, with various PEG-containing block copolymers having been developed and employed to coat magnetic nanoparticles for MRI, among many other biomedical applications [88–97]. For example, an increased image contrast in MRI was achieved by using polymeric micelles formed from SPIONs encapsulated in biocompatible, biodegradable poly(ε-caprolactone)-*b*-PEG copolymers. These materials have demonstrated significantly improved r_2 relaxivities and an ultra-sensitive MRI detection [92].

Gadolinium oxide nanocrystals may also be coated using PEG-silane derivatives, with such treatment resulting in an enhanced relaxivity whilst preventing aggregation of the oxide cores [26]. A dopamine-PEG-based ligand was synthesized and used to coat 9 nm magnetite nanoparticles under physiological conditions; this resulted in the formation of a stable ferrofluid (Figure 4.2), which was found subsequently to be a promising contrast agent for MRI [95]. In another study, trifluoroethylester-terminal-PEG-silane was self-assembled on iron oxide nanoparticles, allowing subsequent conjugation with cell-targeting agents (in this case, folic acid) via carboxylic or amine terminal groups [91]. Folic acid was also conjugated to bifunctional PEG coatings on SPIONs; this resulted in nanoconjugates that could serve as MRI contrast agents targeted at the detection of cancer cells that overexpressed the folate receptor [94]. New antibiofouling polymer-coated iron oxide nanoparticles have been developed using a copolymeric system comprising a "surface anchoring moiety" (silane group) and a "protein-resistant moiety" (PEG), denoted as poly-(TMSMA-r-PEGMA). These nanomaterials demonstrated good potential as MRI contrast agents for tumor detection [98]. Other PEG block copolymers used to stabilize magnetic nanoparticles for MRI applications include poly(poly(ethyleneglycol) monomethacrylate) [96] and poly(ethylene oxide)-block-poly(glutamic acid) [99].

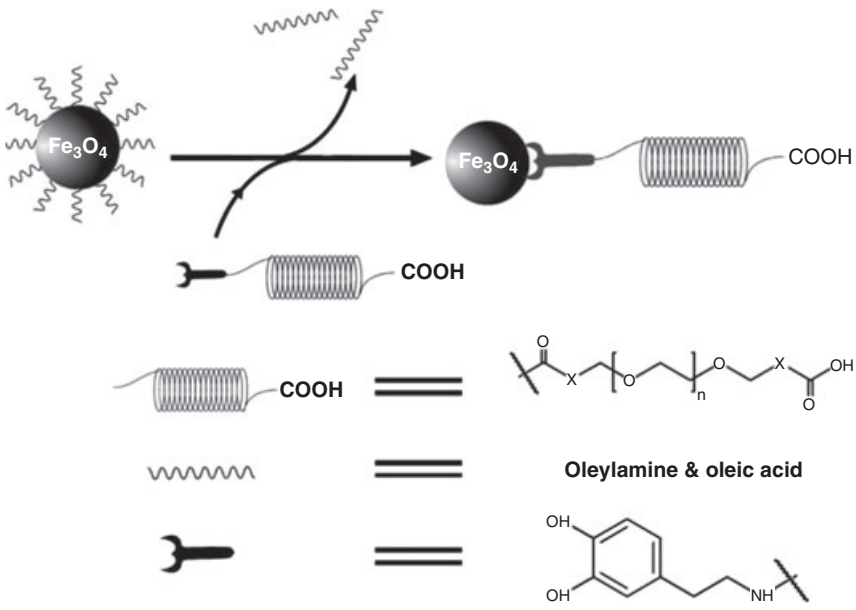

Figure 4.2 Surface modification of Fe_3O_4 nanoparticles via DPA-PEG-COOH. X = $CH_2NHCOCH_2CH_2$ for PEG3000, PEG6000, PEG20000. X is not present in PEG600; the bonds on both sides of the X are directly linked. Reproduced from Ref. [95].

Aside from the extended blood half-life that it can provide, one of the great advantages of PEG coating is that it can also be easily conjugated to antibodies or other biomolecules so as to achieve a specific targeted delivery. For example, in a recent report, biocompatible water-soluble magnetite nanocrystals were fabricated via the thermal decomposition of ferric triacetylacetonate in 2-pyrrolidone in the presence of monocarboxyl-terminated PEG (MPEG-COOH) [93]. The carboxylic acid groups on the surface of the particles were conjugated with a cancer-targeting anti-carcinoembryonic antigen (CEA) monoclonal antibody, via a carbodiimide coupling reaction. The resultant materials were assessed for their ability to label cancer tissues *in vivo*, for subsequent MRI detection [100]. PEG-coated iron oxide nanoparticles may also be conjugated to specific targeting peptides and receptors such as chlorotoxin [101], transactivator protein (Tat) of HIV-1 [102–104], and integrins [105, 106].

The coating of magnetic nanoparticles with PEG-modified phospholipids, which often are introduced as micelles during the synthesis, produces highly biocompatible and water-stable "magnetoliposomes" [107–109]. Such liposome encapsulation delays the natural dilution of the contrast agents, and limits their interactions with biological media. In addition, this approach may enable the simultaneous combination of diagnosis and therapeutic action by encapsulating a MRI contrast agent and a drug together [110].

Other polymers and copolymers, which have been used to coat magnetic nanoparticles, include PVP) [111–113], polyethylenimine (PEI) [114], polyvinyl alcohol (PVA) [115–117], polysodium-4-styrene sulfonate [118], poly(trimethylammonium ethylacrylate methyl sulfate)-poly-(acrylamide) [119], polyvinylbenzyl-*O*-beta-D-galactopyranosyl-D-gluconamide (PVLA) [120], polycaprolactone [121], and gummic acid [122]. In addition, several stable and biocompatible magnetic fluids have been prepared by coating magnetic nanoparticles with proteins, such as human serum albumin (HSA) [123], avidin [124], and Annexin A5 (anxA5)-VSOP [125].

Finally, both double- and single-stranded DNA have been shown to be very good stabilizers for magnetic iron oxide nanoparticles, allowing the preparation of highly stable magnetic fluids that have exhibited unprecedented high relaxivities and also show a good potential for MRI [126].

4.3.3
Modification Using Inorganic Coatings

Inorganic coatings for magnetic nanoparticles include silica, carbon, precious metals (e.g., Ag and Au), or metal oxides [61].

Silica coating represents one of the most frequently used inorganic coatings, for several reasons. The silica coating significantly improves the stability of magnetic nanoparticles, protecting them from oxidation, and it may also reduce any potential toxic effects of the nanoparticles [127]. Such coating also helps to prevent particle aggregation and to increase particle stability in solution. As the isoelectric point of magnetite is pH 7, it is necessary to further coat the particles in order to

stabilize them in the region of pH 6–10. The application of a thin layer of silica lowers this isoelectric point to approximately pH 3, which in turn increases the stability when approaching neutral pH [128]. Another important advantage of silica coating, over the traditional organic monomeric surfactants such as stearic or oleic acid considered above, is that there is no possibility of desorption of the strongly covalently bound silica shells. Finally, the silica surface can be easily functionalized, enabling the chemical bonding of various biological molecular species to the surface for site-specific targeted delivery [7, 129, 130]. Silica coating on magnetic nanoparticles can be achieved by using several different approaches, one of the most popular being sol–gel processing using tetraethyl orthosilicate (TEOS) (the Stöber method) [128, 131–134]. Here, silica shell formation is achieved by the hydrolysis of TEOS in the presence of ammonia and magnetic nanoparticles, while the thickness of the silica coating can be controlled by varying the concentration of ammonium and the ratio of TEOS to water. This technique can be used for the direct coating of commercially available, water-based ferrofluids (e.g. EMG 340) [132]. Some representative TEM images of iron oxide nanoparticles coated with silica shells of various thicknesses are shown in Figure 4.3. Such silica-coated

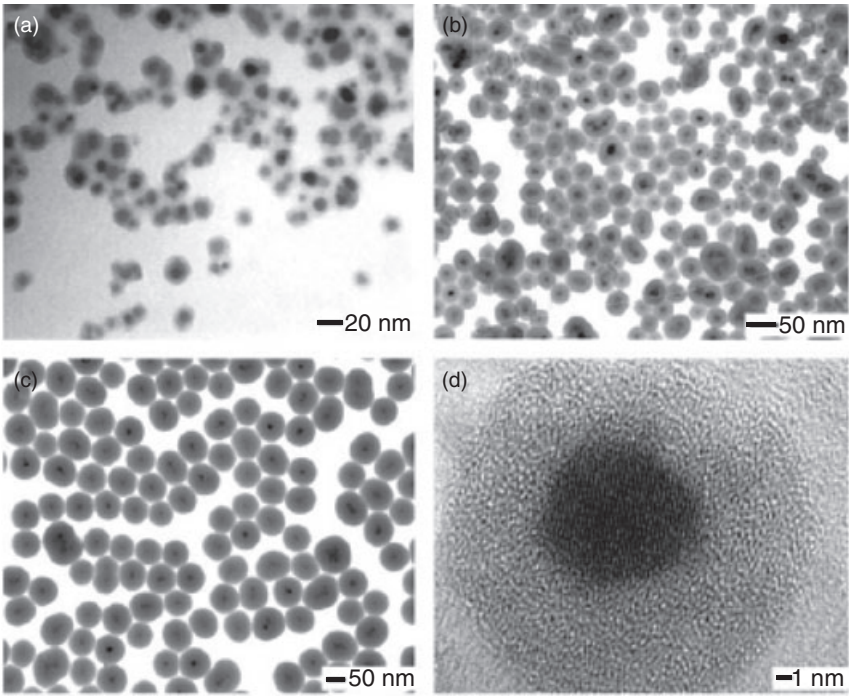

Figure 4.3 Transmission electron microscopy (TEM) images of iron oxide nanoparticles coated with silica shells of various thicknesses. The thickness of the silica coating was adjusted by controlling the amount of precursor added to the solution: (a) 10; (b) 60; and (c) 1000 mg of TEOS; (d) High-resolution TEM image of the iron oxide nanoparticle uniformly coated with a 6 nm-thick amorphous silica shell. Reproduced from Ref. [132].

nanoparticles can be redispersed in water, without the need for further surfactants, to produce stable magnetic fluids [61, 132].

Another approach to silica coating is that of microemulsion [135–137], when micelles or inverse micelles are used to deposit and control the coating. Water-in-oil microemulsions require three components, namely water, oil, and amphiphilic surfactant molecules. During the process, the surfactant lowers the interfacial tension between the water and oil, which results in the formation of a transparent solution. In this case, the water nanodroplets present in the bulk oil phase serve as nanoreactors for the synthesis and coating of nanoparticles. As an example, Tan *et al*. reported the preparation of iron oxide nanoparticles with a uniform silica coating as thin as 1 nm, by using a base-catalyzed hydrolysis and the polymerization reaction of TEOS in a microemulsion [135]. One advantage of the microemulsion method is that it also facilitates the incorporation of biological macromolecules, since the nanocomposites formed are porous [138]. A number of interesting iron oxide-based magnetic nanocomposites with silica-enriched surface layers have been prepared using a modified microemulsion technique, which involved the aerosol pyrolysis of an iron ammonium citrate/TEOS solution. This approach led to the production of hollow magnetic spheres and nanomagnets, dispersed in dense submicrospherical silica cages [139, 140].

Finally, one quite successful approach to coating is based on the deposition of silica from silicic acid solutions. This technique is relatively easy to apply, and also allows the thickness of the silica coating to be controlled by changing the ratio of SiO_2/Fe_3O_4, or by repeating the coating procedure when necessary [128, 140]. One of the earliest reports on this method was made by Philipse *et al*., who dispersed the bare magnetic nanoparticles by using tetramethylammonium hydroxide to form a stable magnetic fluid that was subsequently treated with sodium silicate [128].

Ferumoxsil [17], a well-known, orally administered clinical contrast agent (see Section 4.5) is based on silica-coated magnetite particles, which are functionalized with [3-(2 aminoethylamino)propyl]trimethoxysilane [141, 142]. Amino-silane-functionalized silica-coated nanoparticles can be quite easily further functionalized. As an example, in one report amino-silane coatings on magnetic nanoparticles were activated using glutaraldehyde, which served as a linker for the binding of Hepama-1, a humanized monoclonal antibody directed against liver cancer, This process resulted in new immunomagnetic nanoparticles for the targeted MRI of liver cancer [130].

Thus, whilst silica coating represents a very convenient and widely used approach for the protection and stabilization of magnetic nanoparticles, it does have certain drawbacks. For example, silica is not stable under basic conditions and is usually porous; consequently, oxygen and other species may be able to diffuse through the materials, with the resultant oxidation and deterioration of the magnetic core.

Coating with inert precious metals represents another effective means to protect the magnetic cores against oxidation and to stabilize the aqueous solutions, and several such methods have been reported. Reverse micelle (microemulsion) methods can be used to deposit a gold coating on iron nanoparticles [36, 143–145]; in one example, a series of iron nanoparticles coated with gold of varying shell

thicknesses was synthesized using reverse micelles as nanoreactors [143]. Redox transmetallation is another approach used to fabricate various "core–shell" types of Co–Pt nanoalloys with particle sizes <10 nm, this being achieved by the reaction of Co nanoparticles with Pt(hexafluoroacetyl-acetonate)$_2$ in solution. In this procedure, the composition of the nanoalloys could be controlled by the ratio of the reactants [146]. A redox approach has also been used for the synthesis of Au-coated magnetic Fe nanoparticles, these core–shell nanostructures were formed by a partial replacement reaction in 1-methyl-2-pyrrolidinone, using sodium naphthalide as a reducing agent [147].

Au-coated magnetic iron oxide nanoparticles have also been fabricated by the reduction of Au(III) species onto the surfaces of superparamagnetic maghemite or magnetite nanoparticles, via hydroxylamine seeding [148]. Elsewhere, multifunctional magnetic nanocomposites have been prepared by coating silica spheres with gold nanoshells embedded with Fe_3O_4 nanoparticles (Figure 4.4). These superparamagnetic gold nanoshells demonstrated a good potential as agents for both MRI and photothermal therapy [149].

Finally, the coating/protection of magnetic nanoparticles with carbon is a rapidly developing area, since carbon offers not only very high chemical and thermal stabilities but also an improved biocompatibility. Carbon-coated nanoparticles are generally present in the metallic state, and therefore will have a higher magnetic moment than the corresponding oxides [61, 150, 151].

Although, following their coating and stabilization, magnetic nanoparticles can be employed as MRI contrast agents, the further functionalization and targeted vectorization of the particles remains the subject of much interest. This applies in

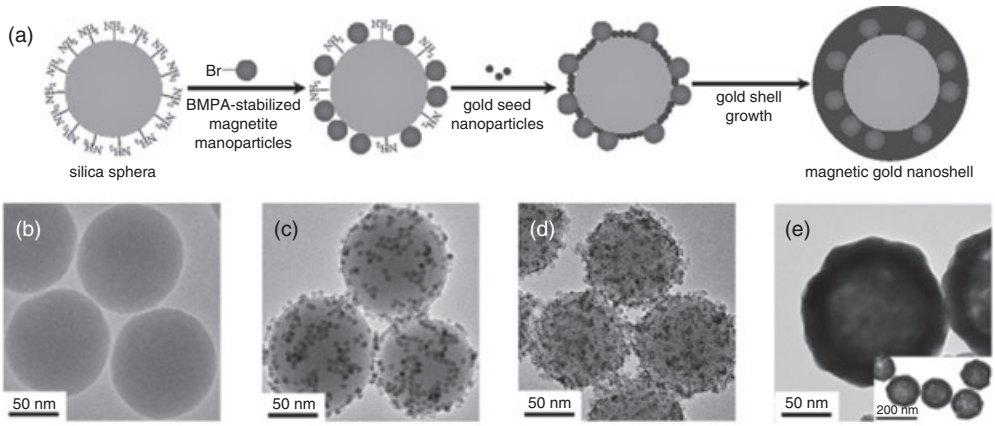

Figure 4.4 (a) Synthesis of the magnetic gold nanoshells (Mag-GNS). TEM images of: (b) amino-modified silica spheres; (c) silica spheres with Fe_3O_4 (magnetite) nanoparticles immobilized on their surfaces; (d) silica spheres with Fe_3O_4 and gold nanoparticles immobilized on their surfaces; and (e) the Mag-GNS. Reproduced from Ref. [149].

particular to improving the nanoparticles' performance not only for biomedical applications but also for specific cellular and molecular imaging.

4.3.4
Vectorization of Magnetic Nanomaterials for Targeted Imaging

Targeted cellular labeling and molecular imaging require further functionalization in order to provide molecular recognition for specific biological sites. Vectorization is also critical for the further stabilization of nanoparticles, to improve their biocompatibility, and to reduce their potential toxicity. The main vectorization strategies include: (i) the noncovalent grafting of biomolecules (e.g., antibodies or proteins) via ionic bonding or adsorption; and (ii) the covalent conjugation of biomolecules via strong chemical bonding [7].

Typical examples of the noncovalent approach include the preparation of streptavidin-coated iron oxide nanoparticles [152–154]. Although the noncovalent methods are relatively easy to undertake, the results are very often not reproducible and the response of the materials may be very difficult to control. In addition, noncovalently functionalized nanocomposites are sometimes unstable in variable biological media, and may lose their biological coating and undergo precipitation. Therefore the development of a covalent approach has attracted much more attention during recent years.

One of the frequently used covalent techniques is that of oxidative conjugation. This strategy is based on the periodate oxidation of a carbohydrate coating (e.g., a dextran or a carboxydextran) on nanoparticles to aldehydes, which may then be linked to biomolecules through the formation of a Schiff base. This method has been used for the covalent conjugation of dextran- and carbodextran-coated magnetic nanoparticles with a range of peptides [155], proteins [156, 157], monoclonal antibodies [158–161], agglutinin [162], and folic acid [74]. One of the strategies involving oxidative conjugation for the covalent grafting of folic acid to dextran-coated maghemite nanoparticles is presented in Figure 4.5 [74].

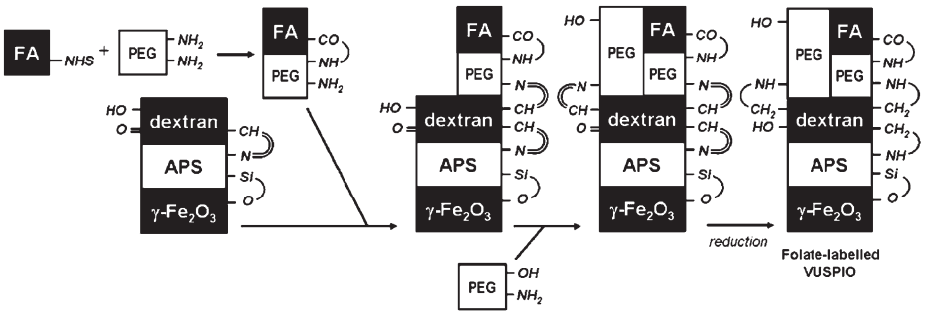

Figure 4.5 Multistep functionalization of maghemite nanoparticles (USPIO) by folic acid (FA). Folic acid was used in the form of its *N*-hydroxysuccinimide ester derivative. Reproduced from Ref. [74].

Another covalent approach is based on amine-terminated CLIO nanoparticles, which can be prepared from dextran-coated nanoparticles by crosslinking using epichlorohydrin and ammonia. The amine-terminated CLIO particles can subsequently be covalently conjugated to a range of target biomolecules by using standard organic chemistry methods. These include reactions that result in the formation of disulfide, carbon–thiol, and amide bonds [6, 7]. Such approaches have been applied to produce a library of 146 different biofunctionalized nanoparticle suspensions, all of which can be used for apoptotic cell recognition [23].

Another method involves 3-aminopropyltrimethoxysilane functionalized silica-coated magnetic nanoparticles, which can be covalently bound to the carboxylic acid functionalities available on target biomolecules, by using a carbodiimide (1-ethyl-3-(3-dimethylaminopropyl)-carbodiimide; EDC) coupling [5]. Overall, the surface chemistry involving reactions with alkyltrialkoxysilane or trichloroalkylsilane derivatives represents a good approach to the grafting of various molecules [163]. In the so-called "DMSA techniques" 2,3-dimercaptosuccinic acid (DMSA) -coated magnetic nanoparticles can be covalently linked to a variety of biomolecules via S–S bonds using *N*-succinimidyl 3-(2-pyridyldithio)propionate (SPDP) as a coupling agent [164]. This approach has been used to couple antibodies, lectins and annexin V to DMSA-coated magnetic nanoparticles [165–167]. Finally, the recently developed "click" chemistry, based on the azide–alkyne reaction, has been applied to the functionalization of iron oxide nanoparticles [168], and allows the relatively simple synthesis of azido- or alkyne-functionalized nanoparticles, which then can be linked to appropriate target molecules.

4.4 Properties and Characterization of Magnetic Nanoparticle Suspensions

The high relaxivity of magnetic nanoparticle suspensions arises from the particles' magnetic properties, by processes that are very well understood in the case of fully dispersed nanoparticles, and in broad terms for aggregates, or assemblies, of such particles. The relevant iron-oxide phases of magnetite (Fe_3O_4) and maghemite (γ-Fe_2O_3) are favored, as sub-20 nm particles of these oxides are superparamagnetic at room temperature and have a high saturation magnetization, M_s, that is somewhat reduced from the bulk values. Previously, M_s has been shown to be heavily dependent on nanoparticle size for sub-7 nm crystals, due to surface effects [169]. Thus, the optimal range for MRI applications can be estimated as 7 to 20 nm, within which range nanocrystals will have a magnetocrystalline anisotropy energy, ΔE_{anis}, in the low GHz range [170] (note that, by convention, this parameter is expressed in frequency units). The presence of a large magnetic moment on each particle, associated with the super-spin, results in high relaxivity of the suspending water. As the emergent magnetic resonance properties are highly sensitive to particle size, shape and aggregation, the monitoring and control of these factors is critical to producing agents with good and well-defined nuclear magnetic resonance (NMR) characteristics.

4.4.1 Characterizing the Suspensions

With a detailed physico-chemical characterization of magnetic suspensions being central to this field of research, a vast range of techniques can be applied to the problem, including electron microscopy, NMR relaxation time analysis, X-ray diffraction (XRD), Mössbauer spectroscopy, zeta-potential measurements, and atomic force microscopy (AFM). Here, attention will be focused on those methods most commonly used to assess the size, shape, and magnetism of the suspended particles, and how these properties change with time.

4.4.1.1 Nanoparticle Size: Transmission Electron Microscopy

Electron microscopy, and in particular TEM, remains the method of choice for measuring the size, shape, and size-dispersity of nanoparticles. Iron provides a reasonable z-contrast, and it is relatively easy to resolve the particle boundaries from the surrounding stabilizing materials, which are usually carbon-based. Particle size analyses based on two or three images for a given sample on a standard TEM grid are generally taken to be an acceptable level of core size analysis. A statistical analysis to yield d_{TEM} and σ_{TEM} values, based on a minimum of 100 particles, is performed usually by applying the log-normal approach [171], as this avoids the possibility of a nonzero probability distribution for negative particles sizes. This can be an issue when Gaussian distributions are used for the analysis of data for smaller magnetic nanoparticles, produced by the nonpolar synthetic routes [172].

The interpretation of any larger scale structures – for example, the presence and size of aggregates – from the analysis of TEM images is problematic. The observation of such structures can be very informative and the size of the structure may be representative of the size of bodies in the suspension. However, it is important to bear in mind the fact that the aggregates may have formed during the drying process. This is not only the case at high particle concentrations, because during the drying process the local concentration of suspended material can increase dramatically as a solvent front retreats across the grid. The possibility of producing aggregates during drying is somewhat reduced at lower concentration, and such a possibility can usually be excluded if the aggregates are dispersed across the grids. However, if much importance is to be attached to such structures, their presence should be confirmed by analysis of the suspensions themselves, for example by using photon correlation spectroscopy (see below).

4.4.1.2 Magnetic Properties: Magnetometry

Characterization by magnetometry, with measurements of sample magnetization as a function of applied field, is the most direct method for determining the magnetic properties of iron oxide suspensions. In particular, the absence of magnetic hysteresis, as manifest by a coercive field (the magnetic field required to reduce the sample magnetization to zero) and remanence magnetization (magnetization

at zero applied field) of close to zero, confirm the superparamagnetism of the suspensions. For superparamagnetic suspensions, the magnetic saturation of the sample can usually be observed at higher fields, yielding the sample saturation magnetization values, M_s. Information about the core size can also be obtained by analysis of the data using the Langevin function.

4.4.1.3 Hydrodynamic Size: Photon Correlation Spectroscopy

The method of choice for measuring the particle size in suspension (i.e., the hydrodynamic size, d_{hyd}), is photon correlation spectroscopy (PCS), which is also known as dynamic light scattering (DLS). In PCS, time-dependent fluctuations in the intensity of light, scattered by the suspended particles, are measured, the timescale of which depends on the particle size [173]. The experimental scattering time autocorrelation function is directly obtained from the measurement. All reliable methods for interpreting this function are based on the assumption that the particles under consideration are spherical, that they diffuse freely, and that there is single photon scattering only. Thus, despite technical innovations to overcome these problems, PCS is most reliable when used for dilute samples. For stable magnetic nanoparticle suspensions, which are usually in the millimolar concentration range for Fe, these criteria are usually satisfied.

The main advantage of PCS is that it is a nondestructive method, and can be used to rapidly measure *in situ* average hydrodynamic size [174], from ~1 nm up to the micrometer range. This offers the possibility of monitoring the stability, or the process of destabilization of, the suspensions. In addition to providing information on the average hydrodynamic diameter, many commercial PCS systems also provide a measure of the width of the size distribution, referred to as the polydispersity index (PDI) from a cumulants analysis. This index, unlike the classical polydispersity in polymer science, is usually close to zero for monodisperse suspensions, and to unity for polydisperse suspensions. The cumulants approach in effect describes the suspended size distribution with two numbers; d_{hyd} and PDI. Alternatively, particle size distributions can be produced from fits to the correlation function, although these do not necessarily contain any more information.

PCS can produce a systematically high estimate of the hydrodynamic size for real samples which, inevitably, exhibit some polydispersity. This is because larger particles scatter light more strongly than smaller particles, so the upper end of the PCS size distribution can contribute strongly to the scattering. This problem becomes more severe for wide, or bimodal, size distributions. For such suspensions it is important to be cautious in the interpretation of d_{hyd} values obtained from PCS, as they will usually not represent a reliable number average of the suspended population. The particle size distributions obtained for polydisperse samples present a significant amount of information. However, this information is not necessarily reliable, nor even reproducible from experiment to experiment on the same sample, as in such cases the fits obtained become highly sensitive to minor differences in the PCS data – that is, in the correlation function.

4.4.1.4 Magnetic Resonance Properties: Nuclear Magnetic Resonance Dispersion

The magnetic field dependence of the relaxation rate can be measured in the range 0.25 mT to 1 T, which is equivalent to a resonance frequency of 0.01 to 40 MHz for ^{1}H, using the technique of nuclear magnetic resonance dispersion (NMRD). In addition to allowing the measurement of r_1, the NMRD profiles obtained are commonly used to investigate the properties of magnetic colloidal dispersions, which are known to determine the MRI response [175].

In the NMRD technique [176], a fast-switching electromagnet is used to measure the spin-lattice relaxation time (T_1) as a function of the NMR frequency. Briefly, the sample magnetism is polarized in a magnetic field with a flux density, B_{pol}, which is as high as possible. The relaxation process subsequently occurs in a second (usually lower) field, B_{rlx}, which is maintained for a variable time, τ. The magnetism remaining after this interval is measured at a third, fixed field, B_{acq}, by applying a single radiofrequency (RF) pulse on-resonance to generate a free induction decay (FID). There is then an extended time delay at an external field of zero, for the restoration of thermal equilibrium prior to the next field cycle. By varying the value of τ, the spin-lattice magnetization recovery curve at the chosen field, B_{rlx}, can be obtained. By then repeating the measurement at different values of B_{rlx}, the frequency dependence of the spin-lattice relaxation can be obtained, as $\nu_L = \gamma^H B/2\pi$, where γ^H is the ^{1}H gyromagnetic ratio. Critical to the method is rapid field-switching, compared to the relevant T_1 value, so the sample is not exposed to intermediate values of the magnetic field during the time τ. A commercial field cycling system (Stelar SRL, Mede, Italy) is available up to approximately 40 MHz, that is, into the lower end of the clinical MRI range. Permanent magnet systems are often used to increase the frequency range, and these have traditionally been a good option as they also allow the measurement of T_2 in the clinical range. However, recent improvements in the Stelar system have offered further increases in the maximum field and may permit the measurement of T_2 with field-cycling. Both of these developments reduce the need for fixed-field systems. As mentioned previously, the frequency dependence of r_2, r_1, and the r_2/r_1 ratio, can be of interest in designing improved agents.

The NMRD profiles of SPIO dispersions exhibit a plateau in r_1 at low frequency, a maximum in the low MHz range, and a strongly decreasing relaxivity at higher frequency (see Figure 4.6). The shape of the profile is sensitive to the magnetic properties of the suspension.

4.4.2 NMR Relaxation in the Presence of Superparamagnetic Nanoparticles

The generally accepted theory for water relaxation due to the presence of dispersed (i.e., physically separated) superparamagnetic (SPM) nanoparticles in suspension (SPM theory) was developed by Muller and coworkers [170]. The theory is based on the classical outer-sphere theory of relaxation, but extended to include the presence of a high Curie component, even at moderate fields, and the presence of strong magnetocrystalline anisotropy. The high field relaxation is driven by

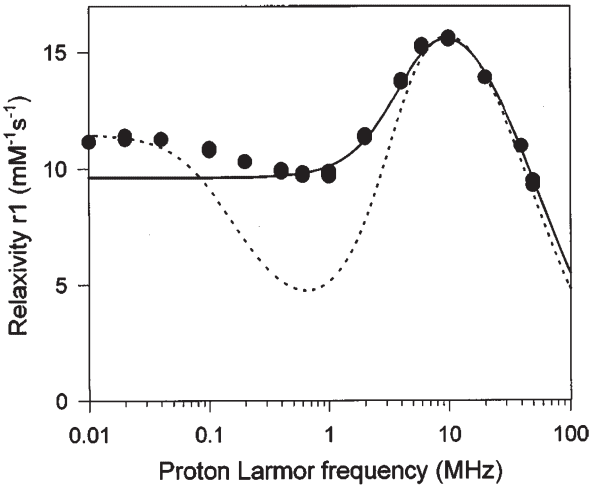

Figure 4.6 The nuclear magnetic resonance dispersion (NMRD) profile of typical SPIO, AMI25 (Advanced Magnetics, Cambridge, MA, USA) at T = 310 K. Reproduced from Ref. [170].

diffusion of water, with the position of the r_1 maximum determined by the characteristic diffusion time, $\tau_D = d^2/(4D)$, where d is the particle diameter and D is the diffusion coefficient. The low-field relaxation is due to fluctuations in the particles moment – that is, the Néel process. Muller's theory is only strictly applicable to monodispersed suspensions of sub-20 nm particles. However, by using physically acceptable values for the critical parameters – that is, the particle size, Néel correlation time τ_N, saturation magnetization M_s and anisotropy energy ΔE_{anis} – the theory produces a good agreement with the measured profiles of USPIO suspensions. Among the assumptions of the model are that the magnetocrystalline anisotropy is uniaxial, which corresponds to a single direction for the easy-axis. For dispersed superparamagnetic nanoparticles, the magnetic anisotropy is usually of the order of 0.2–2.0 GHz. However, surface anisotropy and the mutual anisotropy due to dipolar coupling between nearby crystals can complicate the issue for USPIO and SPIO dispersions, respectively. These contributing factors may be grouped together and referred to as the effective anisotropy energy. A detailed analysis of the performance of the theory has also been restricted by the polydispersity of the aqueous nanoparticle suspensions. The influence of the magnetic parameters on the shape of the NMRD profiles has recently been discussed in detail [7].

In summary, for disperse suspensions the high-frequency inflection point is determined by τ_D, and the position of the maximum is sensitive to the particle size, through its effect on τ_D. The value of the low-field r_1 plateau is determined by the anisotropy energy. In cases of low anisotropy, a weak

minimum can be observed in the low MHz range – an effect that is often observed for USPIOs, but usually not in SPIOs due to the presence of inter-core interactions.

4.4.3 SPM Theory Applied to Suspensions of Nanoparticle Clusters

The exposure of nanodispersions to biological environments often leads to the irreversible aggregation/ precipitation of the particles. Nanoclusters of superparamagnetic particles that may remain stable within the body for extended periods are therefore of interest in MRI and drug delivery. Berret and coworkers [177] have recently reported the controlled preparation of clusters of superparamagnetic γ-Fe_2O_3 nanoparticles with cationic-neutral copolymers, and have assessed their potential as negative contrast agents. Typically, the r_2/r_1 values obtained for these suspensions ranged from 3 to 9, depending on the polymer; hence, they are more suitable as T_2 agents.

SPM theory has been extended to include magnetic clusters of superparamagnetic iron oxide [178], by considering the relaxation of the water ^1H nuclei on passing into the cluster. The relaxation contribution from any given core within the agglomerate is taken to be superparamagnetic, and the familiar chemical exchange formalism is applied. This approach has been shown to reproduce the changes in spin-lattice relaxivity observed for the chemically induced flocculation of commercial SPIO dispersions (dextran-stabilized). Aggregates of hydrodynamic diameter ranging from 50 to 420 nm were grown by the addition of calcium ions, and progressive aggregation resulted in a gradual broadening and suppression of the r_1 maximum. This situation is consistent with increased water residence times in the larger clusters; moreover, this model is applicable to particle clusters with relatively weak intercore interactions.

The nature of the aggregates formed has a strong influence on the magnetic resonance properties of the suspension. This is largely due to changes in the effective magnetic anisotropy energy which arises from the inherent anisotropy of the cores, and from anisotropic interparticle interactions. In the case of *in situ* growth and the stabilization of iron oxide nanocomposites, by the reaction of Fe with polysodium-4-styrene sulfonate, Corr *et al.* [118] have recently shown that by controlling the ratio of Fe to polyelectrolyte used, superparamagnetic or partially magnetically blocked iron oxide nanocomposite suspensions could be prepared. By controlling the iron and polymer concentrations, it was possible to produce suspensions with progressively higher low-frequency spin-lattice relaxivity, which contrasted with the situation described above [178]. In some cases, the NMRD profiles of the PSSS-stabilized suspensions could be interpreted using the original version of SPM theory, but higher effective anisotropy energies were required than would normally be expected for dispersed particles in the 12–16 nm size range; this confirmed the presence of strong interparticle interactions. Depending on the reaction conditions used, stable suspensions could be produced which could not be modeled with SPM theory, due to the presence of very strong interactions. With

the potential of low-field MRI now beginning to be realized [179], it is possible that materials with high relaxivity at low field will be used to generate contrast in the micro-Tesla (μT) field range.

More substantial deviations from standard SPM theory, marked by an increase in the low-frequency relaxivity and the absence of a mid-frequency maximum, have also been observed for other complex aggregated magnetic materials, such as core–shell iron–iron oxide nanoparticle clusters [34]. These observations have been interpreted in terms of an increased magnetocrystalline anisotropy energy associated with inter-particle interactions within the aggregates, as in the case of magnetic nanoparticle clusters formed from synthetic polyelectrolytes [118], or long-chain DNA [126].

Corti and coworkers [180] have recently reported the preparation of spherical and tetrapod-like particles, via the phase transfer of particles produced by a non-polar route, into an aqueous solution on coating with amphiphilic polymers. Relaxivity measurements as a function of magnetic field in the clinical range (0.15–5 T; 5–212 MHz) were used to provide an insight into the contribution of primary particle size and shape to the surface and interparticle anisotropic interactions. This is a good example of a problem that could benefit from the extra information that the low-frequency relaxation behavior, which can be assessed using NMRD, provides. A similar observation could be applied to other interesting findings recently reported by the same group [181], where PEI-coated superparamagnetic nanoparticle aggregates were studied.

4.4.4 General Application of Relaxation Time Measurements

Many reports have been made over the past ten years where relaxivity (r_1 and r_2), measurements at single applied magnetic fields were used to characterize potential nanoparticulate contrast agents. Usually, the materials characterization in these studies is completed by other methods, such as magnetometry or the MRI imaging of phantoms, cells, or animals. The results of some representative studies are outlined here.

Recently, Wan and coworkers [182] reported a simple method for the production of monodisperse (16.5 ± 3.5 nm), triethylene glycol-stabilized, magnetite nanoparticles via an aqueous route, with relaxivity values of 14.14 and 82.7 $s^{-1}\,mM^{-1}$ for r_1 and r_2, respectively, being reported. The r_2/r_1 ratio of 5.85 indicated that the agents could have potential as negative contrast agents. Optical staining of normal rat and C6 glioma cells showed a preferential uptake of the particles into the cancer cells; hence, these materials might have potential applications for cellular imaging.

Qin and coworkers [183] recently reported the stabilization of iron oxide nanoparticles in aqueous solution with pluronic copolymers (PF127). Both, magnetometry and TEM were used to demonstrate that the primary particles were monodisperse and superparamagnetic, with a core size of 20 nm. The hierarchical structure of the coating resulted in stable, dispersed 71 nm composites which showed a very

strong T_2-effect. Relaxivity values of 0.311 and 71.3 $s^{-1} mM^{-1}$ were reported at 60 MHz for r_1 and r_2, respectively. The corresponding r_2/r_1 ratio was 229, far greater than in the commercially available nanoparticulate agents.

Morales and coworkers [75] presented their results of studies with dextran-stabilized iron oxide nanoparticle cluster suspensions, where the primary particle core (produced by the laser-induced pyrolysis of iron pentacarbonyl vapors) was varied in size. The clusters were typically 50–100 nm in size, but the strongest determinant of an increased r_2/r_1 ratio was found to be the primary particle size. It was suggested that this was due to an increased saturation magnetization of the cores, which manifested as a higher global moment of the cluster, and resulted in a greater field gradient which the diffusing water molecules could pass through; in other words, the relaxation was due to outer sphere effects.

4.5 Application of Magnetic Nanomaterials in MRI

Magnetic nanomaterials have numerous current and potential clinical applications as MRI contrast agents, and some of these will be considered below. In contrast, nonclinical applications of superparamagnetic nanoparticles are currently very limited in number, with most involving the biosensing [184, 185] and imaging of proteins or peptide assemblies [186, 187]. Such applications will not be discussed in this chapter.

4.5.1 Current Clinical Applications

At present, only limited SPIO- and USPIO-type magnetic nanoparticle-based contrast agents have been used in human clinical applications. Selected nanoparticulate agents, which have been approved for clinical applications or clinically tested are listed in Table 4.1.

Clinical applications for MRI of the liver, spleen, lymph nodes, bone marrow, kidneys and atherosclerotic plaques are based on accumulation of nanoparticles in the RES cells (e.g., macrophages); that is, an indication of the extent of cell labeling.

4.5.1.1 Gastrointestinal Tract and Bowel Imaging

MRI with fast-imaging sequences, which provide the ability to acquire motion-free T_1- and T_2-weighted images of static fluids, have opened up new developments in imaging and diagnostics of the gastrointestinal tract (GIT) [188]. Overall, MRI can successfully compete with computed tomography (CT) in both GIT and bowel imaging [189]. According to earlier reports, oral contrast-enhanced CT has a higher sensitivity (83%) than MRI, using superparamagnetic iron oxide particles (67%) in the detection of GIT pathologies. However, the specificity for CT was only 68% compared to 89% for MRI. Thus, SPIO MRI is more specific than CT [190].

In general, negative-contrast agents used for the bowel produce less noisy images with fewer motion artifacts than do positive-contrast agents [8]. Therefore, negative-contrast agents based on superparamagnetic iron oxide particles are frequently utilized in MRI of the GIT and bowel. For example, good or excellent small-bowel filling and distention was reported in 17 patients (63%) receiving a positive agent, and in 26 patients (87%) receiving a negative agent. However, normal and pathological structures were better delineated with the negative agent [191]. The best-known commercially available clinical oral GIT contrast SPIO imaging agents are Ferumoxsil (AMI-1210) [17, 141] and Ferristene (Abdoscan®; GE-Healthcare) [192]. Ferristene is based on polystyrene-coated superparamagnetic iron oxide nanoparticles, and in clinical studies was evaluated as an MRI contrast agent for abdominal imaging in 277 patients. Ferristene was shown to provide increased diagnostic information in 50.9% of patients, notably in those with abdominal masses, lymphoma, or pancreatic disease. Moreover, the agent was also well tolerated by the patients [192] (Table 4.1).

4.5.1.2 Liver and Spleen Imaging

Imaging of the liver and spleen was one of the first clinical applications of magnetic nanoparticle-based contrast agents. Following their intravenous administration, superparamagnetic nanoparticles are taken up by RES cells, such as hepatic macrophages or Kupffer cells of the liver and spleen [6, 8, 195, 196]. The accumulation of iron oxide-based SPIO T_2 contrast agents in liver and spleen normally results in a strong decrease in signal intensity. As Kupffer cells are located only in the healthy hepatic parenchyma of the liver and spleen, an uptake of magnetic nanoparticles will result in a significant increase in MR contrast between healthy tissue and the diseased tissue, which does not contain Kupffer cells. Consequently, a signal decrease of a benign lesion would normally be proportional to the Kupffer cell activity or tumor vascularity [197]. Dextran-coated magnetite nanoparticles (ferumoxides) demonstrated up to 95% sensitivity for metastatic lesion detection, and provided an excellent tumor-to-liver contrast in T_2-weighted images [8]. The use of these SPIO contrast agents allows the detection of liver tumors or metastases as small as 2–3 mm [6].

The T_1 effects of superparamagnetic iron oxide nanoparticles have also been utilized for liver imaging [8, 197, 198]. As an example, both iron oxide-based SPIO (with a high r_2/r_1 relaxivity ratio and short blood half-life; contrast agent SHU 555 A) and USPIOs (with a lower r_2/r_1 relaxivity ratio and longer blood half-life; e.g., contrast agent AMI-227) demonstrated a ring enhancement of malignant lesions in T_1-weighted images. Thus, iron oxide nanoparticles can be used to improve the quality of MR angiography of the hepatic artery and portal venous system by reducing the background signal (for liver tissue) and increasing intravascular signals [197].

The iron oxide-based contrast agent SHU 555A was also used to demonstrate temporal changes in signal intensity of liver, spleen, abdominal vessels, and focal liver lesions after an intravenous bolus injection. Interestingly, malignant liver lesions showed no significant changes in signal enhancement in T_1 images, while

hemangiomas demonstrated a peripheral-nodular signal enhancement [199]. In other clinical studies, 12 patients with liver hemangiomas were examined by MRI before and after the intravenous administration of iron oxide-based SPIO particles. Subsequently, the postcontrast T_2-weighted images of the hemangiomas showed, on average, a signal drop of 49% (second echo), although the signal enhancement was observed in liver hemangiomas on T_1 postcontrast images [198]. Similar observations have also been reported for clinically tested Code-7227 [200] and AMI-227 [201] iron oxide-based magnetic contrast agents. The results of all these studies show clearly that superparamagnetic iron oxide nanoparticles can serve as very useful diagnostic tools, allowing hemangiomas not only to be characterized but also to be differentiated from other liver tumors.

4.5.1.3 Lymph Node Imaging

As many primary malignancies spread through lymphatic dissemination, an effective visualization of the metastatic lymph nodes is extremely important in cancer diagnostics, and also for mesorectal transection at surgery [202–204]. Lymph node MRI without using a contrast agent is extremely difficult, because the signal intensities of both metastatic and normal nodes are generally similar; hence, the use of a contrast agent is crucial in such investigations [8]. Magnetic nanoparticle-based contrast agents are particularly useful for imaging lymph node metastases in cancer patients, using nanoparticle-enhanced lymphotropic magnetic resonance imaging (LMRI) or MR lymphography [202, 205]. Following their intravenous injection, the SPIONs are taken up by, and accumulated in, the macrophages of the lymph nodes. As result, in normally functioning nodes the nanoparticles will cause a reduction in signal intensity on postcontrast T_2- and T_2^*-weighted images. However, the picture is different in metastatic nodes, where the tumor has replaced the normal tissue and macrophages, such that the phagocytic activity is much lower. As a result, the metastatic nodes cannot take up the magnetic nanoparticles and so show no change in signal intensity on postdose imaging. This allows the micrometastases to be detected at a very early stage of the disease, even in normal-sized nodes [6, 8, 204–206].

In earlier studies, the intravenous administration of dextran-coated superparamagnetic iron oxide particles (BMS 180549) to healthy humans was shown to cause a dramatic decrease in the signal intensity of normal neck lymph nodes and the adjacent muscle in T_2^*-weighted gradient echo and T_2-weighted spin echo MR images [207]. Based on these findings, magnetic nanoparticle-based contrast agents were shown to be very practical for revealing metastatic lymph nodes in patients with head and neck cancer, by using MRI. As an example, dextran-coated SPIONs showed a 95% sensitivity and 84% specific differentiation in the MRI-mediated detection of metastatic nodes after intravenous administration [208]. An investigation with the superparamagnetic iron oxide-based agent ferumoxtran-10 (Combidex®) in healthy volunteers who underwent neck MRI showed the agent to be both effective and safe for lymph node evaluation, with the best signal intensity and specificity in T_2- and T_2^*-weighted sequences for normal nodes being achieved at 24 or 36 h after the administration of 2.6 or 3.4 mg Fe kg^{-1} [209]. Further studies

have demonstrated a very high efficacy of ferumoxtran-10-enhanced MRI in the detection of lymph node metastases for a variety of tumors [202, 210]. For example, Nishimura *et al.* reported an accurate detection of metastases to lymph nodes in patients with esophageal cancer by using MRI with ferumoxtran-10. In this study, the authors achieved an astonishing 100% sensitivity, 95.4% specificity, and 96.2% accuracy for lymph node metastases at 24 h after intravenous administration of the agent [211]. The same USPIO contrast agent was also used to detect pelvic lymph nodes in patients with primary urologic and pelvic cancers [212, 213], as well as in nodal staging in patients with breast [214], urinary bladder [202], and rectal cancer [215]. In addition, ferumoxtran-10 showed excellent sensitivity for measuring the magnetic tissue parameters of cancer metastases and normal unmatched lymph nodes in various types of cancer, using the LMRI technique. The use of ferumoxtran-10 permitted metastatic nodes to be distinguished from normal nodes, with an overall sensitivity of 98% and specificity of 92%. Most importantly, these parameters could be applied to datasets in a semi-automated fashion, allowing a three-dimensional reconstruction of complete nodal anatomy for different primary cancers. An example of breast cancer mapping is shown in Figure 4.7 [216].

4.5.1.4 **Bone Marrow Imaging**

The main role of the bone marrow is to provide erythrocytes, leukocytes and platelets in order to maintain the oxygenation, immune function and auto-restoration of the body. MRI is a very sensitive technique for the detection of marrow lesions [8], especially when monitoring bone marrow pathologies in patients following radiotherapy and chemotherapy [217].

The concept of bone marrow MRI using nanoparticle-based T_2 contrast agents is similar to that used when imaging the liver. USPIO contrast agents are taken up extensively by macrophages in normal bone marrow (via the process of phagocytosis), where they induce a T_2-shortening effect, but not by neoplastic marrow infiltrates, which do not contain macrophages. This allows a distinction to be made between hypercellular normal and neoplastic marrow [217–219].

Ferumoxtran-10 (Sinerem/Combidex) is the main USPIO to be used for bone morrow imaging [220–222]. The intravenous injection of this contrast agent in patients with cancer of the hematopoietic system (non-Hodgkin lymphoma) allowed an increase in the bone marrow-to-tumor contrast and the consequent differentiation between normal, hypercellular, and neoplastic bone marrow from T_1- and T_2-weighted MR images taken before and after ferumoxtran administration [218, 220, 221]. In another study, Metz *et al.* used ferumoxtran-10 for bone marrow imaging in patients with malignant non-Hodgkin lymphoma before and after conditioning therapy to quantify permeability changes of the blood–bone marrow barrier (BMB), and also to detect malignant bone marrow infiltrations. The identification of focal bone marrow lesions (<1 cm) in patients with lymphoproliferative disorders after the administration of USPIOs was significantly higher than in non-enhanced scans [222].

Other USPIO-based MRI contrast agents (Table 4.1) currently in different stages of preclinical and clinical trials include ferumoxides (Endorem®) [218], SHU555C/

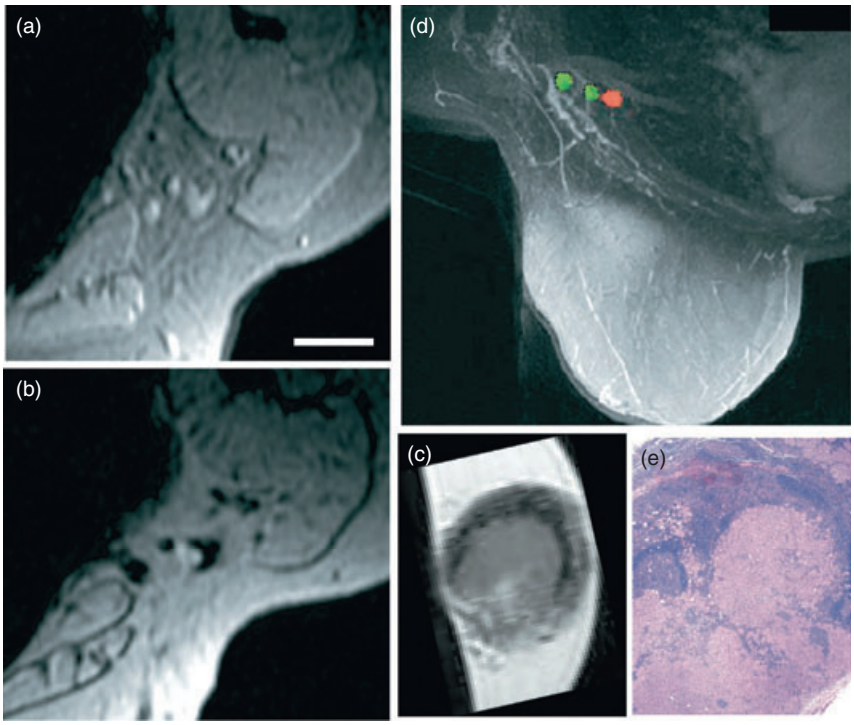

Figure 4.7 Breast cancer mapping of patient with breast cancer prior to sentinel lymph node biopsy. (a) Conventional axillary MRI shows nonenlarged lymph nodes that do not meet the size criteria of malignancy (scale bar = 5 mm); (b) Following the intravenous administration of nanoparticles, a single 3-mm intranodal metastasis was correctly identified; (c) *Ex vivo* MRI of sentinel node specimen confirms metastasis; (d) Semiautomated nodal analysis and reconstruction correctly juxtaposed solitary lymph node metastases adjacent to two normal lymph nodes; (e) Correlative histopathology confirms the diagnosis. Reproduced from Ref. [216].

Resovist S (Schering), Code 7228 (Advanced Magnetics), VSOP (Ferropharm), and Clariscan® (Amersham/GE) [217].

4.5.1.5 **Brain Imaging**

It has been established that brain inflammation contributes to the pathogenesis of neurodegeneration in common neurological diseases such as stroke and Alzheimer's disease [223]. It was noted above that superparamagnetic nanoparticles can easily be taken up by macrophages and, as macrophages prevail in inflammatory cell populations in stroke lesions, they can be visualized by using iron oxide-based USPIOs [224].

Ferumoxtran (AMI-227, Sinerem) has undergone clinical Phase II studies for head MRI in neurological in patients with typical clinical signs of stroke. Although, the contrast agent demonstrated a signal loss on T_2/T_2^*-weighted images associated with blood vessels, there was parenchymal enhancement in T_1-weighted

images which increased over time, which matched with the expected distribution of macrophages. This was a strong indication of brain infiltration by USPIO-laden macrophages. Importantly, the USPIO-induced signal alterations were different from the signatures of conventional gadolinium-enhanced MRI. Thus, USPIO-enhancement does not simply reflect blood–brain barrier (BBB) disruption as a nonspecific epiphenomenon of ischemic tissue damage, but provides additional pathophysiological information [224].

Ferumoxtran (Sinerem) was also used as a contrast agent for MRI of patients with multiple sclerosis during acute relapses [225]. These studies demonstrated, for the first time, the *in vivo* detection of monocyte/macrophage infiltration in inflammatory multiple sclerosis brain lesions using USPIO-enhanced MRI. The use of both gadolinium chelates and USPIOs allowed the lesions to be identified as high signal intensities on T_1-weighted images and low signal intensities on T_2-weighted images (Figure 4.8). These investigations provided *in vivo* evidence of

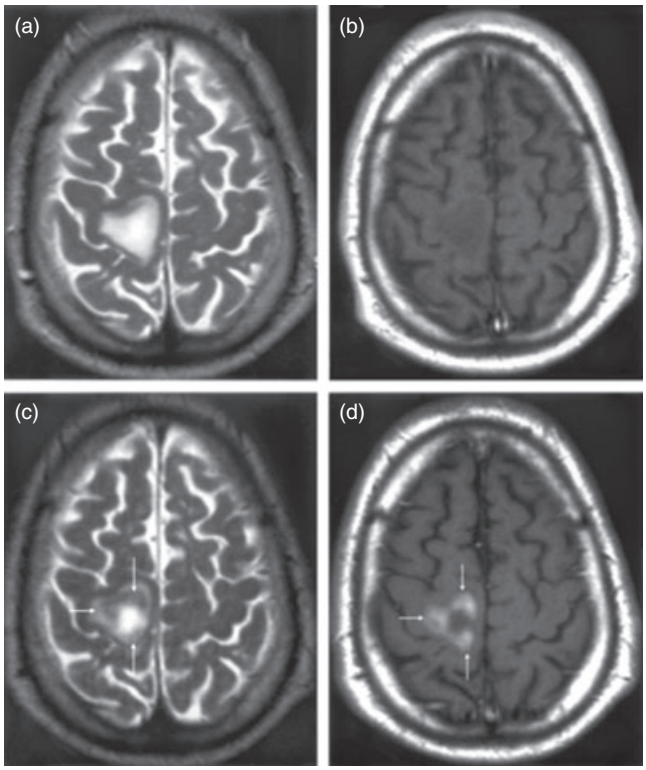

Figure 4.8 Mismatch of contrast agent uptake in USPIO-enhanced acute multiple sclerosis (MS) plaque. MR imaging of T_2-weighted (a) and T_1-weighted postgadolinium images (b) shows a large MS lesion that was not enhanced by gadolinium. MR imaging shows USPIO uptake at the periphery of the lesion (arrows), seen as a decreased signal intensity on T_2-weighted images (c) and a high signal intensity on T_1-weighted images (d). Reproduced from Ref. [225].

the regional infiltration of inflammatory cells in the presence or absence of increased BBB permeability.

In another study, ferumoxtran-10 was compared with standard gadolinium chelate-enhanced MRI in the evaluation of various CNS lesions, including lymphoma, multiple sclerosis, acute disseminated encephalomyelitis, and vascular lesions. Here, the USPIOs showed quite different enhancement patterns among the different lesions with inflammatory components in comparison to gadolinium chelate-based contrast agents. Hence, these two contrast agents might be complementary in MRI-based diagnoses of the CNS [226].

A few reports have also been made on the use of ferumoxides and ferumoxtran for brain MRI in patients with primary and metastatic intracranial tumors [227, 228]. Histological examinations revealed the iron nanoparticles to be localized mainly at the periphery of the lesions, with only minor iron staining of the tumor [227]. Whilst, in comparison with gadolinium, the pattern of USPIO enhancement was heterogeneous and variable, the USPIO agents seemed to enhance the delineation of neovascularization. It was concluded that USPIO agents would not replace gadolinium in brain tumor imaging, but might offer complementary information to permit the differentiation between brain tumors and areas of radiation necrosis [228].

Recently, new clinical applications have emerged for magnetic nanoparticles. Maier-Hauff *et al*. reported the details of clinical studies of thermotherapy using aminosilane-coated iron oxide nanoparticles in patients with glioblastoma multiforme (an aggressive type of primary brain tumor). For this, magnetic nanoparticles were injected into the tumor and the patients then exposed to an alternating magnetic field so as to induce particle heating. The process was monitored using MRI, which allowed the calculation of the expected heat distribution within the tumor, which depended on the magnetic field strength. The study results showed that MRI-controlled cranial thermotherapy using magnetic nanoparticles could be safely applied to glioblastoma multiforme patients [229].

4.5.1.6 **Blood Pool Imaging and MR Angiography**

Blood pool contrast agents normally remain in the blood for a prolonged time, and have longer half-lives and high relaxivities. High relaxivity is required to obtain a stronger blood signal in MRI, and in turn improves the spatial resolution, while a longer plasma half-life enables longer scan times and repetitive imaging to be achieved. Each of these factors is very important in MR angiography (MRA), which is used to examine blood vessels in various tissues and areas of the body [201, 230]. Blood pool contrast agents based on USPIO nanoparticles have found application in the cardiovascular system and myocardial perfusion imaging [191, 231], in assessments of the patient's inflammatory status [232], and even in cerebral blood volume imaging [233].

Ferumoxtran, a superparamagnetic iron oxide-based blood pool imaging contrast agent, has been shown to significantly enhance (on average by 128%) the image intensity gradients at the myocardial/blood pool interface [234]. Ferumoxtran-10 (AMI 227) has also been used to visualize and measure the

lengths of the renal arteries, using MRA; this allowed an increase in the signal-to-noise and contrast-to-noise ratios in the right coronary artery by an average of 80% ($p = 0.008$) and 109% ($p = 0.007$), respectively [235]. Contrast agent AMI 227 has also been used in MRA to visualize the aorta, the inferior vena cava, the portal vein, and muscle in patients, with all blood vessels showing significant enhancement at 45 min after intravenous injection of the agent [236].

A further example of iron oxide nanoparticle-based blood pool contrast agent is that of SHU 555, which has been used for chest MRA and cardiac perfusion. In these studies, a clear dose-dependent increase in signal intensity was demonstrated in the vessels, cardiac chambers and myocardium during both first-pass and equilibrium phases [237].

4.5.1.7 **Atherosclerosis Imaging**

Many cardiovascular diseases, such as myocardial infarction, stroke, and peripheral vascular disease, are strongly related to atherosclerosis. Therefore, earlier non-invasive imaging of atherosclerotic plaques is extremely important [238]. MRI has great potential for the effective visualization and localization of plaques in the vasculature, but current clinical studies involving MRI of atherosclerosis remain few in number. Contrast agent-enhanced MRI of atherosclerosis is based on the selective uptake of magnetic nanoparticles by macrophages in the macrophage-rich atherosclerotic plaques. To date, only ferumoxtran-10 (Sinerem) has been tested clinically in symptomatic patients scheduled for carotid endarterectomy. The results of this study highlighted an accumulation of magnetic nanoparticles in macrophages in predominantly ruptured and rupture-prone human atherosclerotic lesions, which in turn caused a signal decrease (95%) in the *in vivo* MR images after 24 h [239]. USPIO-enhanced MRI was also successfully utilized for the noninvasive determination of macrophage burden in asymptomatic carotid atheroma plaques [240, 241].

4.5.2 **Potential Clinical Applications**

Much of the potential clinical research with these contrast agents involves *in vitro* cellular imaging, the imaging of phantoms, and the *in vivo* imaging of animal models. Targeted cellular labeling and molecular imaging represent the main modern developments for the application of nanomaterials in MRI.

4.5.2.1 **Cellular Labeling and Tracking**

Today, research into stem cells and cell transplantation is a rapidly developing area which is expected to result in important clinical applications. Typical subjects include diagnostics and the treatment of spinal cord injury, Parkinson's disease, myelin disorders, Huntington's disease, and cardiovascular, renal and hepatic diseases. MRI is currently one of the best techniques for tracking magnetically labelled cells, as its resolution approaches the size of the cell itself [7]. In fact, MRI can be used to visualize and track transplanted stem cells labelled with magnetic

imaging contrast agents, both *in vitro* and *vivo* [6, 242–244]. Examples have also been described of single cell detection in small animals, using MRI [245].

It was noted above that a number of clinical MRI applications are based on the uptake of standard nanoparticulate MRI agents by the cells of the RES (e.g., macrophages). Consequently, a significant amount of research has been focused on the investigation of various commercially available USPIO and SPIO contrast agents in macrophages, glioma cells, leukocytes, and lymphocytes [246–250]. Numerous reports have also been made on the labeling of mesenchymal stem cells with various superparamagnetic nanoparticles, and their subsequent *in vitro* and *in vivo* tracking by MRI [251–260]. It has been shown that nanoparticle-labeled human CNS stem cells can survive over the long term and differentiate in a site-specific manner identical to that seen for transplants of unlabeled cells [261]. This has enabled a series of important studies to be performed *in vivo* using nanoparticle-labeled cells. For example, embryonic stem cells were labeled with a USPIO MRI contrast agent, using a lipofection procedure, and implanted into rat brains. Subsequently, it was found that, over a certain period of time, the cells migrated and massively populated the border zone of the damaged brain tissue on the hemisphere opposite to the implantation sites. In these studies, MRI demonstrated an excellent capability for the noninvasive observation of cell migration, engraftment, and morphological differentiation, with high spatial and temporal resolution [262].

Reports have also been made on the use of commercially available SPIO and USPIO magnetic labeling of human dermal fibroblasts [263, 264], HeLa cells [265], dendritic cells [266, 267], and human umbilical vein endothelial cells (HUVECs) [268].

Unfortunately, most of the above-described approaches are passive and rely entirely on the endocytosis of commercially available magnetic nanoparticles – which occasionally do not demonstrate sufficient cellular uptake. In order to increase the uptake of magnetic nanoparticles and provide specific targeting, the nanoparticles must be functionalized (or vectorized) with appropriate peptides, monoclonal antibodies, or proteins [157, 269–271].

In some cases, the cellular uptake of commercial nanoparticulate contrast agents (e.g., ferumoxides) can be improved by simply mixing the nanoparticles with appropriate transfection agents, such as dendrimers, high-molecular-weight poly-L-lysine, lipofectamine, or protamine sulfate [6, 199, 243, 247].

Several covalent approaches have been employed to improve particle uptake, depending on the cell type and structure. Significant efforts have also been focused on the specific targeting of cancer cells. For example, the conjugation of magnetic nanocrystals to a cancer-targeting antibody (herceptin) has allowed the specific labeling of human cancer cells and their *in vivo* monitoring in live mice by MRI [167]. Several reports also exist on the conjugation of magnetic nanoparticles to a peptide sequence from the transactivator protein (Tat) of HIV-1 [102–104, 272], and their investigation in T cells both *in vitro* and *in vivo* in live mice. In another study, magnetic nanoparticles were coupled to anti-Her-2/neu antibodies or gamma globulin IgG and used for the detection of Her-2/neu-expressing tumor cells *in vitro*

and in animal tumor models, and this in turn allowed the recognition of a distinct decrease in the normalized MR signal ratio between the tumor and a reference area [273]. The conjugation of magnetic nanoparticles to folic acid for targeting specific folate receptors in cancer cells has also been reported [74, 94, 274, 275]. One interesting new approach was that reported by Kohler *et al.* [276], who developed conjugates of iron oxide nanoparticles and methotrexate (a chemotherapeutic drug). These conjugates could be used as both contrast agents for diagnostics and as drug delivery systems for cancer therapy. Other studies have involved the targeting and *in vivo* tracking of cancer cells using ovalbumin-specific splenocytes (OT-1) labeled with magnetic nanoparticles [277], and also lymphocytes and 9L rat gliosarcoma labeled with a ferumoxide–protamine sulfate complex [278].

4.5.2.2 **Molecular Imaging**

In general, "molecular imaging" refers to the *in vivo* noninvasive imaging of targeted biomolecules or targeted cells and biological processes in living organisms [6, 279, 280]. For molecular imaging, MRI is one of the best available techniques, with the imaging agents being based on the recognition of unique cell-surface biochemical signatures. In this case, the use of magnetic nanoparticulate MRI agents can offer the opportunity not only for targeted diagnostic studies but also for image-monitored, site-specific therapeutic delivery, much like the "magic bullet". This combination of rational targeted diagnostic and therapy is expected to result in new clinical approaches to the treatment of many diseases [279].

Nanoparticulate contrast agents can be accumulated within a biological site by either passive or active targeting mechanisms.

- *Passive targeting* contrast agents concentrate in the phagocytic cells (e.g., macrophages, Kupffer's cells) and corresponding organs (liver, spleen, lymph nodes, etc.) that are responsible for particle clearance from the body. Passive targeting using commercially available nanoparticulate MR contrast agents (see Table 4.1) has mostly been considered above in clinical applications.
- *Active targeting* contrast agents require conjugation to specific ligands (pharmacophores), which then enables a targeted, site-specific accumulation of the agents. Typical ligands for targeting include antibodies, peptides, polysaccharides, aptamers, and drugs. As discussed above for vectorization, these ligands can be linked to magnetic nanoparticles either covalently or noncovalently.

To date, most MR contrast agent applications have been based on passive targeting. However, intensive research is currently being undertaken on the development of targeted magnetic nanoparticles, which have been evaluated in animal models, both *in vitro* and *in vivo*.

A large proportion of this research has been focused on the use of magnetic nanoparticle conjugates in targeted cancer imaging. For example, $\alpha_v\beta_3$ integrin-targeted magnetic nanoparticles have been used for the specific ultrasensitive MRI detection of small regions of angiogenesis associated with minute solid tumors

(e.g., malignant melanoma) [105, 281, 282]. (RGDyK) peptide-coated magnetite nanoparticles have also been shown to accumulate preferentially in the integrin $\alpha_v\beta_3$-rich tumor area [283].

Antibodies directed against several types of cancer marker have been conjugated to magnetic nanoparticles, and the conjugates used as MRI contrast agents *in vitro* and *in vivo* [100, 284–287]. The use of superparamagnetite particles coated with monoclonal antibodies directed against epidermal growth factor receptors (EGFRs), has allowed the high-contrast MRI imaging and diagnosis of squamous cell carcinoma of the esophagus [285]. MRI using contrast agents based on magnetic nanoparticles coated with polypeptide functionalized with monoclonal antibodies specific to carcinoembryonic antigen [287] and the therapeutic antibody Erbitux [286] have also been reported. Several biofunctionalized PEG-coated magnetic nanoparticles (including magnetic liposomes) have been successfully employed as contrast agents for cancer MRI [98, 100, 288]. For example, PEG-coated magnetite nanocrystals, which were functionalized with a specific cancer-targeting antibody, have been used as contrast agents for tumor detection in live mice by MRI (Figure 4.9) [100].

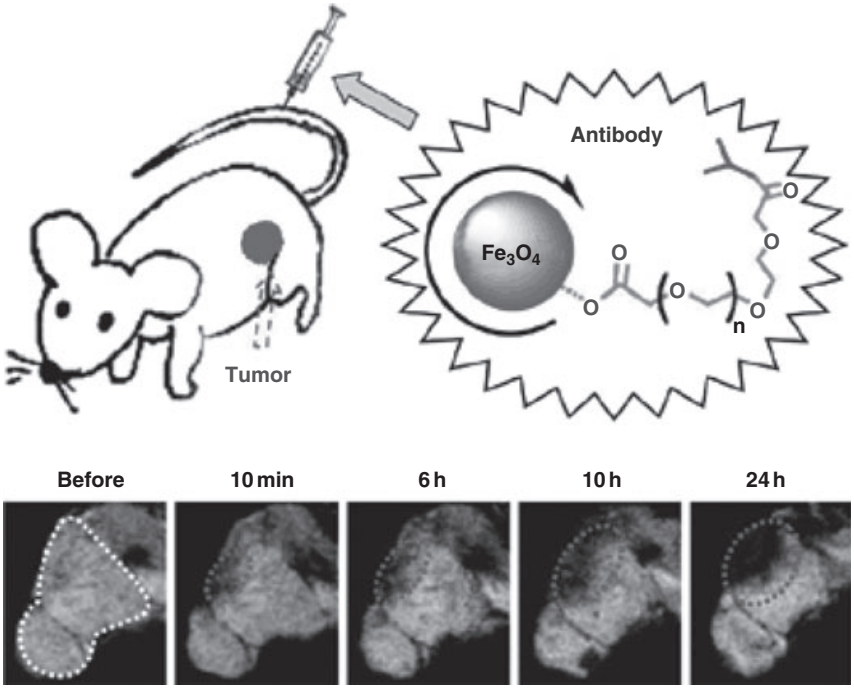

Figure 4.9 PEG-coated antibody-functionalized magnetic nanoparticles as MRI contrast agents for cancer detection (top). T_2^*-weighted MR images acquired before and at different times after injection of Fe_3O_4-(rch 24 mAb) conjugates (bottom). Reproduced from Ref. [100].

Other studies have involved targeted cancer MRI using paramagnetic polyamidoamine dendrimer–Gd chelate conjugates [289], and diarrheagenic bacterial peptide enterotoxin functionalized iron oxide nanoparticles [290].

Some interesting magnetic nanoparticle Hydro-Gel (MagNaGeI™) drug-device hybrids, which consisted of chemotherapeutic agents, iron oxide particles and targeting ligands, have been reported. These new nanomaterials can potentially serve both for cancer-targeted diagnostics and therapy, when used in conjunction with MRI and inductive heating [291].

Quite significant efforts have been focused on the development of MR contrast agents for cardiovascular molecular imaging [292], with several reports having been made on the use of magnetic nanoparticles for the molecular imaging of atherosclerotic lesions and myocardial injuries [45, 238, 246, 293–295]. For example, biochemically derivatized annexin V superparamagnetic iron oxide particles were used for imaging in rabbit models of human atherosclerosis. These targeted nanoparticles were found to produce high-negative-contrast images at 2000-fold lower doses than those reported for nonspecific atheroma uptake of untargeted superparamagnetic nanoparticles in the same animal model [238]. In another study, the use $\alpha_v\beta_3$ integrin-targeted paramagnetic nanoparticles allowed specific detection of the neovasculature within 2 h, providing an approximate 47% enhancement in MRI signal when averaged throughout the abdominal aortic wall in rabbits [296].

Interesting results were obtained using fibrin-targeted magnetic nanoparticles, which can specifically adhere to the fibrin clot surface. Biotinylated perfluorocarbon gadolinium-rich nanoparticles have been used as a new MR contrast agent, and have enhanced the detection of intravascular clots and minute thrombi within fissures of active vulnerable plaques (Figure 4.10). This technology has

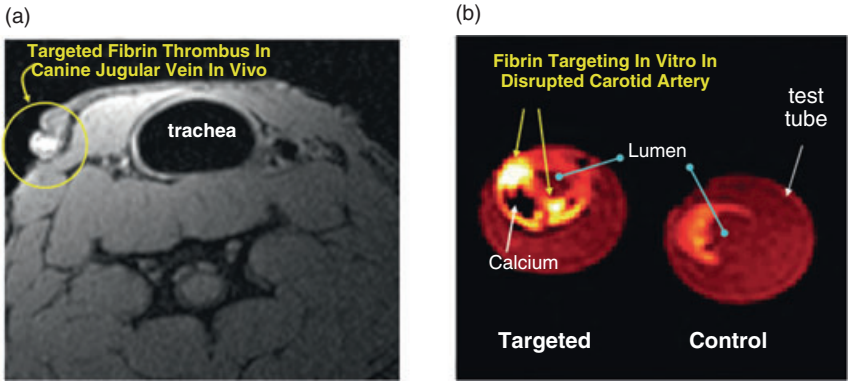

Figure 4.10 MR image of thrombi with paramagnetic nanoparticles targeted to fibrin. (a) Thrombus formed *in vivo* in a canine jugular vein imaged at 1.5 T. Note the "hot spot" at the site of nanoparticle binding; (b) "Disrupted" carotid endarterectomy specimens incubated with fibrin-targeted nanoparticles binding to small amounts of fibrin at the shoulder regions (note the "hotspots" indicated by yellow arrows) of the ruptured plaque cap, imaged *ex vivo* at 1.5 T. Reproduced from Ref. [298].

good potential for the early direct diagnosis of impending stroke or infarction [279, 297, 298].

Reports have also been made on the use of Tat-peptide-modified [299], antibody-conjugated streptavidinylated [300], trypsin-conjugated [301] and polyvinylpyrrolidone (PVP)-coated [111] iron oxide superparamagnetic nanoparticles for *in vivo* MRI of liver. Lymphocyte-homing magnetic nanoparticles have been used for the MRI monitoring of trafficking patterns of adoptively transferred leukocyte subsets in nonhuman primate models of AIDS [302].

Finally, the development of magnetic nanoparticles for CNS imaging has attracted considerable attention [118, 303, 304], with solid lipid magnetic nanoparticles having been found to overcome the BBB and to demonstrate great potential for brain MRI [305]. Superparamagnetic nanoparticles can also be trapped by the BBB allowing the observation of impaired BBB areas [306]. The T_2-weighted targeted MRI of glial brain tumor in rats was achieved after hyperosmotic BBB disruption and the injection of magnetite–dextran nanoparticles into the carotid artery [307]. Polyelectrolyte-stabilized magnetite nanoparticles with controlled relaxivities have been used to study the hippocampus and brain vasculature in live rats. These new magnetic fluids have demonstrated good biocompatibility and potential for *in vivo* MRI diagnostics [118].

Some selected examples of targeted magnetic nanoparticles for molecular and cellular imaging are listed in Table 4.2.

Table 4.2 Selected examples of targeted magnetic nanoparticles for molecular and cellular imaging.

Targeted contrast media	Coating agent	Characteristics	Pharmacophore	Biological target	Reference(s)
USPIO-antibody	PEG	D_h = 20.1 nm (DLS)	Anti-carcinoembryonic antigen (anti-CEA) monoclonal antibody rch 24	Human colon carcinoma	[100]
SPIO-antibody	Dextran	ND	Monoclonal antibody Mab A7	Colorectal tumor	[159]
CLIO-Cy5.5-bombesin	CLIO-NH_2	D_h = 35 nm	Bombesin peptide	Pancreatic ductal adenocarcinoma	[308]
CLIO-small molecule	CLIO-NH_2	ND	Small carboxylic molecules	Pancreatic cancer, macrophages	[23]
CLIO-Cy5.5	CLIO-NH_2	D_h = 32 nm	Cy5.5	Delineation of brain tumors	[270]

Table 4.2 *Continued*

Targeted contrast media	Coating agent	Characteristics	Pharmacophore	Biological target	Reference(s)
MION-antibody	Dextran	D = 8.3, r_2 = 24–29 $mM^{-1}s^{-1}$, 1.5 T	Monoclonal antibody anti-Her2/neu	Her2/neu receptors in tumors	[161]
MION-antimyosin	Dextran	r_1 = 10.1 and r_2 = 120 $mM^{-1}s^{-1}$ 0.47 T	Monoclonal antibody Antimyosin Fab ($R_{11}D_{10}$)	Myocardial infarction	[293]
SPIO-annexin V	Dextran	D_h = 100 nm	Annexin V	Atherosclerotic plaque	[238]
USPIO-RGD	Carbohydrate	ND	Cyclic RGD peptide	$\alpha_{IIB}\beta_3$-, thrombus imaging	[155]
USPIO Fe_3O_4/trypsin	Amino-groups	r_1 = 6.31 and r_2 = 8.33 $mM^{-1}s^{-1}$ 9.4 T	Oligonucleotides and trypsin	Kupffer cells and liver	[111]
CLIO-SC-Tf	CLIO-NH_2	r_1 = 32 and r_2 = 144 $mM^{-1}s^{-1}$ 0.47 T	Transferrin	Transferrin receptors	[309]
CLIO-Tat	CLIO-NH_2	r_1 = 22 and r_2 = 72 $mM^{-1}s^{-1}$ 0.47 T, D_h = 42	Tat peptide	Lymphocyte uptake	[272]
CLIO-antibody	CLIO-NH_2	D_h = 40 nm	Mouse-anti-human E selectin antibody fragment	Inflammation	[310]
CLIO-Cy5.5-cRGD	CLIO-Cy5.5-NH_2	D_h = 29–39 nm	Cyclic RGD peptide	$\alpha_v\beta_3$ integrin	[311, 312]
CLIO-SC-R4Cy5.5	CLIO-NH_2	r_1 = 29.9 and r_2 = 92.5 $mM^{-1}s^{-1}$ 0.47 T, D_h =62 ± 7 nm	RRRRGC peptide and Cy5.5	Cathepsin B	[313]
USPIO-folate	Silane-PEG-trifluoroethyl-ester	D = 9–11 nm (TEM)	Folic acid	Folate receptor	[94]

Overall, magnetic nanomaterials have a combination of unique properties, such as sensitivity in the nanomolar range, an ability to penetrate to the most unreachable remote parts of the tissue, and to be manipulated by an external magnetic field. This may, in time, open the door not only for advanced MRI but also for other biomedical applications, such as cancer hyperthermia therapy, the imaging and treatment of strokes, the detection and cleaning of blocked blood vessels, as well as micro – and even nano – surgery. All of these aspects will undoubtedly have great value in the further development of nanomedicine.

4.6
Summary and Future Outlook

In this chapter, we have outlined the depth and breadth of current research into the synthesis, stabilization and functionalization of aqueous magnetic nanoparticle and nanocomposite suspensions, although the survey was far from exhaustive. An outline has also been provided of the methods currently used by the materials research community in the development of these novel materials, and of the major issues facing the imaging community. The next challenge for these two communities is to exploit the potential of novel magnetic materials for biomedical applications. In the first instance, the focus is likely to be on the development of new magnetic materials to analyze the fate of biological markers in tissues, and even at a cellular level, in model systems. These methods will be critical to biologists, pharmacologists, and clinicians in the development of new therapeutic interventions.

The future of clinical MRI is, in part, dependent on the development of new contrast media. Whilst all indications suggest that nanoparticulate agents will continue to be important; there is a strong belief that their potential has only been partially realized. Among the applications with strong potential that have received huge attention are the use of particles in dynamic (or time-resolved) imaging and the development of smart and/or multifunctional agents. The latter are materials for which the magnetic properties depend on their biological environment, and which may combine multiple diagnostic functionalities and drug delivery capability.

There are, in principle, three ways to improve the performance of an agent in providing image contrast: (i) to improve the imaging hardware; (ii) to introduce new experiments and pulse sequences to exploit the properties of the agents; and (iii) to improve the characteristics and functionality of the agent itself. In the sections below, we will provide some brief examples of the first two types of innovation, before concentrating on new agents. The future of this research remains very open to unforeseen changes, while even the division of likely innovations into these approaches is arbitrary, as new applications may well embody some aspects of all three. Nonetheless, it is useful to survey relevant current research, as it may be indicative of the future direction of contrast agent development.

4.6.1 Improved Imaging Methods

Dynamic, or time-resolved, MRI imaging has already been explored to some extent, for example in pH sensing using a lanthanide chemical exchange saturation transfer (CEST) agent [314], and in the detection of apoptotic cells (effectively detecting gene-expression) using protein-conjugated magnetic nanoparticles [157]. The potential of dynamic MRI imaging using contrast agents has been recently assessed [315]. By assuming a 5% change in signal to be sufficient to detect an agent's response within a dynamic environment, simulations were generated for the major types of agent currently undergoing evaluation. For this, the Smoluchowski model was applied, using as inputs the inherent contrast and known clearance properties. Among the conclusions drawn was that nanoparticulate T_2 agents, because of their very low limits of detection [316], could be used for dynamic imaging in humans at concentrations several orders of magnitude lower than is possible with any of the alternatives, including gadolinium and the new generation of CEST agents. However, as the temporal limit is probably about 1 s this will limit the applications although, as in the case of conventional static imaging, nanoparticulate agents occupy a separate part of the clinically relevant parameter space and so have potential for as yet unidentifying applications.

As discussed above, magnetic nanoparticle suspensions usually function as either negative- or T_2-contrast agents. The strong local field generated by the high susceptibility of these agents results in a shift in the resonance frequency, as well as an easily detectable decrease in the (spin-spin) relaxation times, of water molecules in close proximity to the nanoparticles. The downside of these agents, arising from the large susceptibility artifacts, include difficulties in: the quantification of particle concentrations; the detection of particles in regions with intrinsically low signal-to-noise ratios; and distinguishing from the susceptibility changes at tissue interfaces. The long echo times (TE values) required limit the applications in dynamic imaging, as noted above. Significant efforts have been made, therefore, to develop techniques which generate positive-contrast from magnetic nanoparticles, particularly with a view to quantifying the nanoparticle concentration for tracking studies. In this respect, three approaches have been attempted: (i) gradient-dephasing-based imaging; (ii) off-resonance imaging (ORI); and (iii) off-resonance saturation. For the purpose of illustration, ORI makes use of the induced resonance frequency shifts, which can be in excess of 100 Hz at typical concentrations. It involves the use of a spectrally shifted ("off-resonance") RF pulse to selectively irradiate the shifted water signals only. This has been shown to be effective, particularly at lower end of the clinical field range due to the narrower water resonance lines (15 Hz at 4.7 T versus 45 Hz at 14 T), and for nanoparticle concentrations in excess of 150 μg Fe ml^{-1} [317], which was found to be sufficient to detect the accumulation of iron oxide nanoparticles in macrophages which had infiltrated healing myocardial infarcts.

4.6.2
Improved Imaging Hardware

Possibly the greatest barrier to the development of MRI is the requirement for high-field superconducting magnets, which in turn arises from the need to maximize signal intensity while maintaining high-field homogeneity. Apart from the high cost, superconducting magnets place physical constraints on the application of imaging in clinical medicine. For instance, access to the subject is severely restricted and the presence of metal-containing components, such as pacemakers, is prohibited. The development of ultralow-field imaging (ULF MRI) is being led by a few pioneering groups around the world, particularly Alexander Pines and coworkers at Berkeley [318]. Here, the central idea is to physically separate the polarization and detection fields; the sample magnetization is first polarized in a relatively strong but inhomogeneous field, which is usually in the mT range. The imaging experiment is subsequently performed at a lower field, which is usually in the range of hundreds of μT, which corresponds to Lamor frequencies in the low kHz range. Signal detection is with an array of high-sensitivity SQUID devices. The advantages of the system are that: (i) it is an inexpensive, portable, open-geometry approach; (ii) it does not require high fields; and (iii) the potential for T_1-weighted contrast due to natural effects, for example, due to complex slow-motions in cellular environments, or arising from the introduction of an agent, is generally higher at low fields. Recent innovations [319] in this field have included the combination of μT MRI with simultaneous magnetoencephalography (MEG) for imaging the human brain. This may open up new possibilities for neurobiology, with the direct measurement of neural currents [320].

4.6.3
Improved Contrast Agents

Enormous interest has also been expressed in recent years in the development of "smart" or responsive nanoparticulate contrast agents. For instance, there has been a strong focus on the development of MRI sensors for determining local concentrations of analytes of biological interest *in vivo*. In fact, a bewildering number of reports has been made in this field. An excellent example was recently reported by the Jasanoff group [184] of general methods for the preparation of MRI calcium indicators based on calmodulin-dependent protein–protein interactions, which produce large changes in T_2. The agents consisted of interacting polypeptides which were biotinylated and then conjugated to streptavidin-coated iron oxide nanoparticles. This approach was found to be sensitive to changes in calcium concentration of ~1 μ*M, in vitro*, while the materials could be prepared in approximately 12 h.

In general, research into smart contrast agents has mirrored developments in other fields of nanotechnology, where the development of multiple functionality has been a strong theme. In the case of MRI, this tendency becomes even more

exaggerated due to the potential offered by the presence of a strong magnetic moment, associated with the super-spin of the nanoparticle. Thus, it is possible to imagine, in a suggested order of complexity: (i) magnetic-fluorescent nanoparticles for dual MRI-optical detection; (ii) magnetic nanoparticles or nanoparticle clusters for MRI imaging and RF hyperthermia; and (iii) drug-loaded, magnetic-polymer nanocomposites and magnetoliposomes, or nanoparticles grafted with drug molecules. These have potentially favorable biodistribution and pharmacokinetics, which could be enhanced by magnetic positioning at the site of action on the application of a static magnetic field.

Recent progress in both optical and magnetic detection has suggested a strong future for this type of particulate agent in tracking experiments that may improve our understanding of cellular recognition events, and may even help develop new methods for assessing biodistribution and even screening for future therapeutics. For instance, magneto-optical nanocomposites have been used for tracking stem cells [321, 322], for imaging the macrophage infiltration of tissue [323], and for detecting specific molecular targets that are weakly expressed [324].

A related field of interest is in the development of multiple, simultaneous detection of different MRI stimuli, or analytes. This is analogous to the recent development of ranges of nanoparticles (and quantum dots) with optically distinguishable signatures which enable the tracking of many biological indicators. Thus, much interest has been expressed in developing multiplexed MRI sensors, which could be fabricated to be small enough for use as contrast agents in man [118]. A good recent example of this has been provided by Zabow and coworkers [325], who reported the fabrication of structures where ^{1}H frequency shifts and sensitivity enhancements were determined by the local geometry within a magnetic microstructure. This approach immediately offers multiplexing capability and may become the method of choice, given the advanced state of modern fabrication technology, once these structures have been scaled down towards, or even below, the 100 nm range.

A significant number of reports have also been made where the potential of magnetic nanoparticle suspensions for dual diagnostic and therapeutic (termed "theranostic") applications has been realized. The development of magnetic nanoparticle suspensions as dual contrast agents and hyperthermia mediators has been described. These applications are feasible, as nanoparticulate iron oxide has favorable MRI properties (as discussed earlier), and also has good RF energy-specific absorption rate (SAR) values [5]. Hyperthermia using superparamagnetic iron oxide has been investigated for many years as a potential treatment for solid tumors in particular [326].

A second, indirect, form of hyperthermia involves the use of alternate current field heating to deliver a therapeutic molecule from a carrier, such as a liposome or a polymer/nanoparticle composite. Examples of this approach have been reported for a range of carriers, including magnetic iron oxide liposomes for delivering 5-fluorouracil [327] and dextran-stabilized contrast agents combined

with melphalan [328]. In the latter case, the resultant "magnetohydrodynamic thermochemotherapy" produced a 30% regression of nonmetastatic tumors in mice, with a resulting increase in the life-span of 290%.

A large number of studies into the application of static magnetic fields for positioning magnetic nanoparticles at the required site of action have been undertaken. Most of these investigations have involved either the targeting of cells in culture, or feasibility studies in animal models. A good example of targeting in tumor models was recently reported [329] where MRI was used to confirm the migration of nanoparticles towards NdFeB magnets placed outside the peritoneal cavity, above grafts of a human ovarian carcinoma. An excellent demonstration of targeting in culture was provided by the group of Hyeon [330], where the uptake of polymer nanoparticles was enhanced by the application of a magnetic field, when clusters of Fe_3O_4 nanoparticles were loaded in doxorubicin-loaded polymer nanoparticles. The polymer particles were composed of biodegradable poly(lactic-*co*-glycolic acid) (PLGA), surface-coated with PEGylated folate for the active targeting of cancer cells. Interest in these targeting applications also arises from the possibility of detecting the particles after treatment, by MRI, and correlating the results with any histological findings [331].

In fact, polymer/iron oxide composites are the most commonly reported magnetic theranostic nanoparticles. A good recently described example [332] was the development of functionalized linkers to couple to amino-polyvinyl alcohol (aminoPVA), by amide linkages, to produce drug-functionalized-aminoPVA-iron oxide nanocomposites, as vectors for drug delivery. Linkers were developed to which the anti-cancer drugs 5-fluorouridine and doxorubicin were attached as biologically labile esters or peptides, respectively. The former proved to be viable delivery vehicles when tested using human melanoma cells in culture, as they were taken up by the cells and proved to be efficient anti-tumor agents.

A final class of therapeutic molecular/iron oxide composite involves the direct binding of a molecule of interest to the nanoparticle. A prominent example here [333] is the covalent linking of siRNA to magnetic nanoparticles labeled with a near-infrared dye. This strategy has been shown to be feasible for monitoring the efficiency of siRNA delivery and silencing, which is a current requirement in the development of cancer therapeutics.

Unfortunately, despite the obvious potential of a great many of these agents, the vast majority will be applied only in drug development and basic research, or will remain of academic interest only. Even with credible demonstrations of efficacy, in cellular or animal models, the pathway to use in humans is very long and expensive. A premium is placed by industry on producing simple, easily scaleable processes that are likely to result in new mass applications in medicine. Any technology that fails by these demanding measures is unlikely to progress very far, through the clinical and regulatory processes. It is likely, therefore, that convergent approaches – developed by adopting standardized and perhaps regulatory approved building blocks – could represent a shorter route to the clinic.

References

1 Jun, Y.W., Jang, J.T. and Cheon, J. (2007) Magnetic nanoparticle assisted molecular MR imaging, in *Bio-Applications of Nanoparticles*, Vol. 620, Springer, pp. 85–106.

2 Alexiou, C., Jurgons, R., Seliger, G. and Iro, H. (2006) Medical applications of magnetic nanoparticles. *Journal of Nanoscience and Nanotechnology*, **6** (9–10), 2762–8.

3 Pankhurst, Q.A., Connolly, J., Jones, S.K. and Dobson, J. (2003) Applications of magnetic nanoparticles in biomedicine. *Journal of Physics D*, **36** (13), R167–81.

4 Gupta, A.K., Naregalkar, R.R., Vaidya, V.D. and Gupta, M. (2007) Recent advances on surface engineering of magnetic iron oxide nanoparticles and their biomedical applications. *Nanomedicine*, **2** (1), 23–39.

5 Mornet, S., Vasseur, S., Grasset, F. and Duguet, E. (2004) Magnetic nanoparticle design for medical diagnosis and therapy. *Journal of Materials Chemistry*, **14** (14), 2161–75.

6 Corot, C., Robert, P., Idee, J.M. and Port, M. (2006) Recent advances in iron oxide nanocrystal technology for medical imaging. *Advanced Drug Delivery Reviews*, **58** (14), 1471–504.

7 Laurent, S., Forge, D., Port, M., Roch, A., Robic, C., Elst, L.V. and Muller, R.N. (2008) Magnetic iron oxide nanoparticles: synthesis, stabilization, vectorization, physicochemical characterizations, and biological applications. *Chemical Reviews*, **108** (6), 2064–110.

8 Wang, Y.X.J., Hussain, S.M. and Krestin, G.P. (2001) Superparamagnetic iron oxide contrast agents: physicochemical characteristics and applications in MR imaging. *European Radiology*, **11** (11), 2319–31.

9 Lu, J., Yang, S.H., Ng, K.M., Su, C.H., Yeh, C.S., Wu, Y.N. and Shieh, D.B. (2006) Solid-state synthesis of monocrystalline iron oxide nanoparticle based ferrofluid suitable for magnetic resonance imaging contrast application. *Nanotechnology*, **17** (23), 5812–20.

10 Bonnemain, B. (1998) Superparamagnetic agents in magnetic resonance imaging: physicochemical characteristics and clinical applications – a review. *Journal of Drug Targeting*, **6** (3), 167–74.

11 Marchal, G., Van Hecke, P., Demaerel, P., Decrop, E., Kennis, C., Baert, A.L. and van der Schueren, E. (1989) Detection of liver metastases with superparamagnetic iron oxide in 15 patients: results in MR imaging at 1.5 T. *American Journal of Roentgenology*, **152**, 771–5.

12 Weissleder, R., Stark, D.D., Engelstad, B.L., Bacon, B.R., Compton, C.C., White, D.L., Jacobs, P. and Lewis, J. (1989) Superparamagnetic iron oxide: pharmacokinetics and toxicity. *American Journal of Roentgenology*, **152**, 167–73.

13 Muller, R.N., Roch, A., Colet, J.-M., Ouakssim, A. and Gillis, P. (2001) *The Chemistry of Contrast Agents in Medical Magnetic Resonance Imaging*, John Wiley & Sons, Ltd, pp. 417–35.

14 Cunningham, C.H., Arai, T., Yang, P.C., McConnell, M.V., Pauly, J.M. and Conolly, S.M. (2005) Positive contrast magnetic resonance imaging of cells labeled with magnetic nanoparticles. *Magnetic Resonance in Medicine*, **53** (5), 999–1005.

15 Di Marco, M., Sadun, C., Port, M., Guilbert, I., Couvreur, P. and Dubernet, C. (2007) Physicochemical characterization of ultrasmall superparamagnetic iron oxide particles (USPIO) for biomedical application as MRI contrast agents. *International Journal of Nanomedicine*, **2** (4), 609–22.

16 Muller, K., Skepper, J.N., Tang, T.Y., Graves, M.J., Patterson, A.J., Corot, C., Lancelot, E., Thompson, P.W., Brown, A.P. and Gillard, J.H. (2008) Atorvastatin and uptake of ultrasmall superparamagnetic iron oxide nanoparticles (Ferumoxtran-10) in human monocyte-macrophages:

implications for magnetic resonance imaging. *Biomaterials*, **29** (17), 2656–62.

17 Jung, C.W. and Jacobs, P. (1995) Physical and chemical-properties of superparamagnetic iron-oxide MR contrast agents – ferumoxides, ferumoxtran, ferumoxsil. *Magnetic Resonance Imaging*, **13** (5), 661–74.

18 McLachlan, S.J., Morris, M.R., Lucas, M.A., Fisco, R.A., Eakins, M.N., Fowler, D.R., Scheetz, R.B. and Olukotun, A.Y. (1994) Phase-I clinical-evaluation of a new iron-oxide MR contrast agent. *Journal of Magnetic Resonance Imaging*, **4** (3), 301–7.

19 Kellar, K.E., Fujii, D.K., Gunther, W.H.H., Briley-Saebo, K., Bjornerud, A., Spiller, M. and Koenig, S.H. (2000) NC100150 injection, a preparation of optimized iron oxide nanoparticles for positive-contrast MR angiography. *Journal of Magnetic Resonance Imaging*, **11** (5), 488–94.

20 Daldrup-Link, H.E., Kaiser, A., Helbich, T., Werner, M., Bjornerud, A., Link, T.M. and Rummeny, E.J. (2003) Macromolecular contrast medium (feruglose) versus small molecular contrast medium (gadopentetate) enhanced magnetic resonance imaging: differentiation of benign and malignant breast lesions. *Academic Radiology*, **10** (11), 1237–46.

21 Taupitz, M., Wagner, S., Schnorr, J., Kravec, I., Pilgrimm, H., Bergmann-Fritsch, H. and Hamm, B. (2004) Phase I clinical evaluation of citrate-coated monocrystalline very small superparamagnetic iron oxide particles as a new contrast medium for magnetic resonance imaging. *Investigative Radiology*, **39** (7), 394–405.

22 Kaufels, N., Wagner, S., Schink, T., Hamm, B., Taupitz, M. and Schnorr, J. (2008) Magnetic resonance imaging of liver metastases: experimental comparison of anionic and conventional superparamagnetic iron oxide particles with a hepatobiliary contrast medium during dynamic and uptake phases. *Investigative Radiology*, **43** (7), 496–503.

23 Weissleder, R., Kelly, K., Sun, E.Y., Shtatland, T. and Josephson, L. (2005) Cell-specific targeting of nanoparticles by multivalent attachment of small molecules. *Nature Biotechnology*, **23** (11), 1418–23.

24 Na, H.B., Lee, J.H., An, K.J., Park, Y.I., Park, M., Lee, I.S., Nam, D.H., Kim, S.T., Kim, S.H., Kim, S.W., Lim, K.H., Kim, K.S., Kim, S.O. and Hyeon, T. (2007) Development of a T-1 contrast agent for magnetic resonance imaging using MnO nanoparticles. *Angewandte Chemie, International Edition in English*, **46** (28), 5397–401.

25 Soderlind, F., Pedersen, H., Petoral, R.M., Kall, P.O. and Uvdal, K. (2005) Synthesis and characterisation of Gd_2O_3 nanocrystals functionalised by organic acids. *Journal of Colloid and Interface Science*, **288** (1), 140–8.

26 Fortin, M.A., Petoral, R.M., Soderlind, F., Klasson, A., Engstrom, M., Veres, T., Kall, P.O. and Uvdal, K. (2007) Polyethylene glycol-covered ultra-small Gd_2O_3 nanoparticles for positive contrast at 1.5 T magnetic resonance clinical scanning. *Nanotechnology*, **18** (39), article 395501.

27 Engstrom, M., Klasson, A., Pedersen, H., Vahlberg, C., Kall, P.O. and Uvdal, K. (2006) High proton relaxivity for gadolinium oxide nanoparticles. *Magnetic Resonance Materials in Physics, Biology and Medicine*, **19** (4), 180–6.

28 Li, I.F., Su, C.H., Sheu, H.S., Chiu, H.C., Lo, Y.W., Lin, W.T., Chen, J.H. and Yeh, C.S. (2008) $Gd_2O(CO_3)_2$ center dot H_2O particles and the corresponding Gd_2O_3: synthesis and applications of magnetic resonance contrast agents and template particles for hollow spheres and hybrid composites. *Advanced Functional Materials*, **18** (5), 766–76.

29 Klasson, A., Ahren, M., Hellqvist, E., Soderlind, F., Rosen, A., Kall, P.O., Uvdal, K. and Engstrom, M. (2008) Positive MRI contrast enhancement in THP-1 cells with Gd_2O_3 nanoparticles. *Contrast Media and Molecular Imaging*, **3** (3), 106–11.

30 Bridot, J.L., Faure, A.C., Laurent, S., Riviere, C., Billotey, C., Hiba, B., Janier, M., Josserand, V., Coll, J.L., Van der Elst, L., Muller, R., Roux, S., Perriat, P.

and Tillement, O. (2007) Hybrid gadolinium oxide nanoparticles: multimodal contrast agents for in vivo imaging. *Journal of the American Chemical Society*, **129** (16), 5076–84.

31 McDonald, M.A. and Watkin, K.L. (2006) Investigations into the physicochemical properties of dextran small particulate gadolinium oxide nanoparticles. *Academic Radiology*, **13** (4), 421–7.

32 Gould, P. (2006) Nanomagnetism shows in vivo potential. *Nano Today*, **1** (4), 34–9.

33 Maenosono, S., Suzuki, T. and Saita, S. (2008) Superparamagnetic FePt nanoparticles as excellent MRI contrast agents. *Journal of Magnetism and Magnetic Materials*, **320** (9), L79–83.

34 Miguel, O.B., Gossuin, Y., Morales, M.P., Gillis, P., Muller, R.N. and Veintemillas-Verdaguer, S. (2007) Comparative analysis of the H-1 NMR relaxation enhancement produced by iron oxide and core-shell iron-iron oxide nanoparticles. *Magnetic Resonance Imaging*, **25** (10), 1437–41.

35 Bomati-Miguel, O., Morales, M.P., Tartaj, P., Ruiz-Cabello, J., Bonville, P., Santos, M., Zhao, X.Q. and Veintemillas-Verdaguer, S. (2005) Fe-based nanoparticulate metallic alloys as contrast agents for magnetic resonance imaging. *Biomaterials*, **26** (28), 5695–703.

36 Cho, S.J., Jarrett, B.R., Louie, A.Y. and Kauzlarich, S.M. (2006) Gold-coated iron nanoparticles: a novel magnetic resonance agent for T-1 and T-2 weighted imaging. *Nanotechnology*, **17** (3), 640–4.

37 Su, C.H., Sheu, H.S., Lin, C.Y., Huang, C.C., Lo, Y.W., Pu, Y.C., Weng, J.C., Shieh, D.B., Chen, J.H. and Yeh, C.S. (2007) Nanoshell magnetic resonance imaging contrast agents. *Journal of the American Chemical Society*, **129** (7), 2139–46.

38 Bottrill, M., Nicholas, L.K. and Long, N.J. (2006) Lanthanides in magnetic resonance imaging. *Chemical Society Reviews*, **35** (6), 557–71.

39 Sharma, P., Brown, S.C., Walter, G., Santra, S., Scott, E., Ichikawa, H., Fukumori, Y. and Moudgil, B.M. (2007) Gd nanoparticulates: from magnetic resonance imaging to neutron capture therapy. *Advanced Powder Technology*, **18** (6), 663–98.

40 Voisin, P., Ribot, E.J., Miraux, S., Bouzier-Sore, A.K., Lahitte, J.F., Bouchaud, V., Mornet, S., Thiaudiere, E., Franconi, J.M., Raison, L., Labrugere, C. and Delville, M.H. (2007) Use of lanthanide-grafted inorganic nanoparticles as effective contrast agents for cellular uptake imaging. *Bioconjugate Chemistry*, **18** (4), 1053–63.

41 Allen, M.J. and Meade, T.J. (2003) Synthesis and visualization of a membrane-permeable MRI contrast agent. *Journal of Biological Inorganic Chemistry*, **8** (7), 746–50.

42 Allen, M.J., MacRenaris, K.W., Venkatasubramanian, P.N. and Meade, T.J. (2004) Cellular delivery of MRI contrast agents. *Chemistry and Biology*, **11** (3), 301–7.

43 Corbin, I.R., Li, H., Chen, J., Lund-Katz, S., Zhou, R., Glickson, J.D. and Zheng, G. (2006) Low-density lipoprotein nanoparticles as magnetic resonance imaging contrast agents. *Neoplasia*, **8** (6), 488–98.

44 Crich, S.G., Lanzardo, S., Alberti, D., Belfiore, S., Ciampa, A., Giovenzanaz, G.B., Lovazzano, C., Pagliarin, R. and Aime, S. (2007) Magnetic resonance imaging detection of tumor cells by targeting low-density lipoprotein receptors with Gd-loaded low-density lipoprotein particles. *Neoplasia*, **9** (12), 1046–56.

45 Frias, J.C., Ma, Y.Q., Williams, K.J., Fayad, Z.A. and Fisher, E.A. (2006) Properties of a versatile nanoparticle platform contrast agent to image and characterize atherosclerotic plaques by magnetic resonance imaging. *Nano Letters*, **6** (10), 2220–4.

46 Becker, M.L., Bailey, L.O. and Wooley, K.L. (2004) Peptide-derivatized shell-cross-linked nanoparticles. 2. Biocompatibility evaluation. *Bioconjugate Chemistry*, **15** (4), 710–17.

47 Turner, J.L., Pan, D.P.J., Plummer, R., Chen, Z.Y., Whittaker, A.K. and Wooley, K.L. (2005) Synthesis of gadolinium-

labeled shell-crosslinked nanoparticles for magnetic resonance imaging applications. *Advanced Functional Materials*, **15** (8), 1248–54.

48 Battistini, E., Gianolio, E., Gref, R., Couvreur, P., Fuzerova, S., Othman, M., Aime, S., Badet, B. and Durand, P. (2008) High-relaxivity magnetic resonance imaging (MRI) contrast agent based on supramolecular assembly between a gadolinium chelate, a modified dextran, and poly-beta-cyclodextrin. *Chemistry–A European Journal*, **14** (15), 4551–61.

49 Paschkunova-Martic, I., Kremser, C., Mistlberger, K., Shcherbakova, N., Dietrich, H., Talasz, H., Zou, Y.P., Hugl, B., Galanski, M., Solder, E., Pfaller, K., Holiner, I., Buchberger, W., Keppler, B. and Debbage, P. (2005) Design, synthesis, physical and chemical characterisation, and biological interactions of lectin-targeted latex nanoparticles bearing Gd-DTPA chelates: an exploration of magnetic resonance molecular imaging (MRMI). *Histochemistry and Cell Biology*, **123** (3), 283–301.

50 Winter, P., Athey, P., Kiefer, G., Gulyas, G., Frank, K., Fuhrhop, R., Robertson, D., Wickline, S. and Lanza, G. (2005) Improved paramagnetic chelate for molecular imaging with MRI. *Journal of Magnetism and Magnetic Materials*, **293** (1), 540–5.

51 Anderson, S.A., Rader, R.K., Westlin, W.F., Null, C., Jackson, D., Lanza, C.M., Wickline, S.A. and Kotyk, J.J. (2000) Magnetic resonance contrast enhancement of neovasculature with alpha(v)beta(3)-targeted nanoparticles. *Magnetic Resonance in Medicine*, **44** (3), 433–9.

52 Kobayashi, Y., Imai, J., Nagao, D., Takeda, M., Ohuchi, N., Kasuya, A. and Konno, M. (2007) Preparation of multilayered silica-Gd-silica core-shell particles and their magnetic resonance images. *Colloids and Surfaces A: Physicochemical and Engineering Aspects*, **308** (1–3), 14–19.

53 Tsai, C.P., Hung, Y., Chou, Y.H., Huang, D.M., Hsiao, J.K., Chang, C., Chen, Y.C. and Mou, C.Y. (2008) High-contrast paramagnetic fluorescent mesoporous silica nanorods as a multifunctional cell-imaging probe. *Small*, **4** (2), 186–91.

54 Xu, Z.P., Kurniawan, N.D., Bartlett, P.F. and Lu, G.Q. (2007) Enhancement of relaxivity rates of Gd-DTPA complexes by intercalation into layered double hydroxide nanoparticles. *Chemistry–A European Journal*, **13** (10), 2824–30.

55 Gerion, D., Herberg, J., Bok, R., Gjersing, E., Ramon, E., Maxwell, R., Kurhanewicz, J., Budinger, T.F., Gray, J.W., Shuman, M.A. and Chen, F.F. (2007) Paramagnetic silica-coated nanocrystals as an advanced MRI contrast agent. *The Journal of Physical Chemistry C*, **111** (34), 12542–51.

56 Alric, C., Taleb, J., Le Duc, G., Mandon, C., Billotey, C., Le Meur-Herland, A., Brochard, T., Vocanson, F., Janier, M., Perriat, P., Roux, S. and Tillement, O. (2008) Gadolinium chelate coated gold nanoparticles as contrast agents for both X-ray computed tomography and magnetic resonance imaging. *Journal of the American Chemical Society*, **130** (18), 5908–15.

57 Debouttiere, P.J., Roux, S., Vocanson, F., Billotey, C., Beuf, O., Favre-Reguillon, A., Lin, Y., Pellet-Rostaing, S., Lamartine, R., Perriat, P. and Tillement, O. (2006) Design of gold nanoparticles for magnetic resonance imaging. *Advanced Functional Materials*, **16** (18), 2330–9.

58 Sitharaman, B., Kissell, K.R., Hartman, K.B., Tran, L.A., Baikalov, A., Rusakova, I., Sun, Y., Khant, H.A., Ludtke, S.J., Chiu, W., Laus, S., Toth, E., Helm, L., Merbach, A.E. and Wilson, L.J. (2005) Superparamagnetic gadonanotubes are high-performance MRI contrast agents. *Chemical Communications*, (**31**), 3915–17.

59 Hartman, K.B., Laus, S., Bolskar, R.D., Muthupillai, R., Helm, L., Toth, E., Merbach, A.E. and Wilson, L.J. (2008) Gadonanotubes as ultrasensitive pH-smart probes for magnetic resonance imaging. *Nano Letters*, **8** (2), 415–19.

60 Masala, O. and Seshadri, R. (2004) Synthesis routes for large volumes of

nanoparticles. *Annual Review of Materials Research*, **34**, 41–81.

61 Lu, A.H., Salabas, E.L. and Schuth, F. (2007) Magnetic nanoparticles: synthesis, protection, functionalization, and application. *Angewandte Chemie, International Edition in English*, **46** (8), 1222–44.

62 Gupta, A.K. and Gupta, M. (2005) Synthesis and surface engineering of iron oxide nanoparticles for biomedical applications. *Biomaterials*, **26** (18), 3995–4021.

63 Shen, L., Laibinis, P.E. and Hatton, T.A. (1999) Bilayer surfactant stabilized magnetic fluids: synthesis and interactions at interfaces. *Langmuir*, **15**, 447–53.

64 Shen, L., Stachowiak, A., Fateen, S.-E.K., Laibinis, P.E., and Hatton, T.A. (2001) Structure of alkanoic acid stabilized magnetic fluids. A small-angle neutron and light scattering analysis. *Langmuir*, **17** (2), 288–99.

65 Racuciu, M., Creanga, D.E. and Calugaru, G. (2005) Synthesis and rheological properties of an aqueous ferrofluid. *Journal of Optoelectronics and Advanced Materials*, **7** (6), 2859–64.

66 Racuciu, M., Creanga, D.E. and Airinei, A. (2006) Citric-acid-coated magnetite nanoparticles for biological applications. *The European Physical Journal. E, Soft Matter*, **21** (2), 117–21.

67 Hodenius, M.A.J., Niendorf, T., Krombach, G.A., Richtering, W., Eckert, T., Lueken, H., Speldrich, M., Gunther, R.W., Baumann, M., Soenen, S.J.H., De Cuyper, M. and Schmitz-Rode, T. (2008) Synthesis, physicochemical characterization and MR relaxometry of aqueous ferrofluids. *Journal of Nanoscience and Nanotechnology*, **8** (5), 2399–409.

68 Smitham, J.B., Evans, R. and Napper, D.H. (1975) Analytical theories of steric stabilization of colloidal dispersions. *Journal of the Chemical Society, Faraday Transactions I*, **71** (2), 285–97.

69 Evans, R. and Napper, D.H. (1977) Perturbation method for incorporating concentration-dependence of Flory-Huggins parameter in the theory of steric stabilization. *Journal of the Chemical Society, Faraday Transactions*, **73**, 1377–85.

70 Kitchens, C.L., Chandler McLeod, M. and Roberts, C.B. (2003) Solvent effects on the growth and steric stabilization of copper metallic nanoparticles in AOT reverse micelle systems. *The Journal of Physical Chemistry B*, **107**, 11331–8.

71 Shah, P.S., Holmes, J.D., Johnston, K.P. and Korgel, B.A. (2005) Size-selective dispersion of dodecanethiol-coated nanocrystals in liquid and supercritical ethane by density tuning. *The Journal of Physical Chemistry B*, **106**, 2545–51.

72 Molday, R.S. and Mackenzie, D. (1982) Immunospecific ferromagnetic iron-dextran reagents for the labeling and magnetic separation of cells. *Journal of Immunological Methods*, **52** (3), 353–67.

73 Bautista, M.C., Bomati-Miguel, O., Morales, M.D., Serna, C.J. and Veintemillas-Verdaguer, S. (2005) Surface characterisation of dextran-coated iron oxide nanoparticles prepared by laser pyrolysis and coprecipitation. *Journal of Magnetism and Magnetic Materials*, **293** (1), 20–7.

74 Duguet, E., Vasseur, S., Mornet, S., Goglio, G., Demourgues, A., Portier, J., Grasset, F., Veverka, P. and Pollert, E. (2006) Towards a versatile platform based on magnetic nanoparticles for in vivo applications. *Bulletin of Materials Science*, **29** (6), 581–6.

75 Morales, M.P., Bomati-Miguel, O., de Alejo, R.P., Ruiz-Cabello, J., Veintemillas-Verdaguer, S. and O'Grady, K. (2003) Contrast agents for MRI based on iron oxide nanoparticles prepared by laser pyrolysis. *Journal of Magnetism and Magnetic Materials*, **266** (1–2), 102–9.

76 Bautista, M.C., Bomati-Miguel, O., Zhao, X., Morales, M.P., Gonzalez-Carreno, T., de Alejo, R.P., Ruiz-Cabello, J. and Veintemillas-Verdaguer, S. (2004) Comparative study of ferrofluids based on dextran-coated iron oxide and metal nanoparticles for contrast agents in magnetic resonance imaging. *Nanotechnology*, **15** (4), S154–9.

77 Arbab, A.S., Wilson, L.B., Ashari, P., Jordan, E.K., Lewis, B.K. and Frank, J.A.

(2005) A model of lysosomal metabolism of dextran coated superparamagnetic iron oxide (SPIO) nanoparticles: implications for cellular magnetic resonance imaging. *NMR in Biomedicine*, **18** (6), 383–9.

78 Kroll, E., Winnik, F.M. and Ziolo, R.F. (1996) In situ preparation of nanocrystalline gamma-Fe_2O_3 in iron(II) cross-linked alginate gels. *Chemistry of Materials*, **8** (8), 1594–6.

79 Nishio, Y., Yamada, A., Ezaki, K., Miyashita, Y., Furukawa, H. and Horie, K. (2004) Preparation and magnetometric characterization of iron oxide-containing alginate/poly(vinyl alcohol) networks. *Polymer*, **45** (21), 7129–36.

80 Morales, M.A., Finotelli, P.V., Coaquira, J.A.H., Rocha-Leao, M.H.M., Diaz-Aguila, C., Baggio-Saitovitch, E.M. and Rossi, A.M. (2008) In situ synthesis and magnetic studies of iron oxide nanoparticles in calcium-alginate matrix for biomedical applications. *Materials Science and Engineering. C, Biomimetic Materials, Sensors and Systems*, **28** (2), 253–7.

81 Lee, H.S., Kim, E.H., Shao, H.P. and Kwak, B.K. (2005) Synthesis of SPIO-chitosan microspheres for MRI-detectable embolotherapy. *Journal of Magnetism and Magnetic Materials*, **293** (1), 102–5.

82 Lee, H., Shao, H.P., Huang, Y.Q. and Kwak, B. (2005) Synthesis of MRI contrast agent by coating superparamagnetic iron oxide with chitosan. *IEEE Transactions on Magnetics*, **41** (10), 4102–4.

83 Reimer, P., Marx, C., Rummeny, E.J., Muller, M., Lentschig, M., Balzer, T., Dietl, K.H., Sulkowski, U., Berns, T., Shamsi, K. and Peters, P.E. (1997) SPIO-enhanced 2D-TOF MR angiography of the portal venous system: results of an intraindividual comparison. *Journal of Magnetic Resonance Imaging*, **7** (6), 945–9.

84 Lee, S.J., Jeong, J.R., Shin, S.C., Kim, J.C., Chang, Y.H., Chang, Y.M. and Kim, J.D. (2004) Nanoparticles of magnetic ferric oxides encapsulated with poly(D,L latide-*co*-glycolide) and their applications to magnetic resonance imaging contrast agent. *Journal of Magnetism and Magnetic Materials*, **272**–276, 2432–3.

85 Hu, F.X., Neoh, K.G. and Kang, E.T. (2006) Synthesis and in vitro anti-cancer evaluation of tamoxifen-loaded magnetite/PLLA composite nanoparticles. *Biomaterials*, **27** (33), 5725–33.

86 Kim, D.K., Mikhaylova, M., Wang, F.H., Kehr, J., Bjelke, B., Zhang, Y., Tsakalakos, T. and Muhammed, M. (2003) Starch-coated superparamagnetic nanoparticles as MR contrast agents. *Chemistry of Materials*, **15** (23), 4343–51.

87 Bulte, J.W.M., de Cuyper, M., Despres, D. and Frank, J.A. (1999) Preparation, relaxometry, and biokinetics of PEGylated magnetoliposomes as MR contrast agent. *Journal of Magnetism and Magnetic Materials*, **194**, 204–9.

88 Shultz, M.D., Calvin, S., Fatouros, P.P., Morrison, S.A. and Carpenter, E.E. (2007) Enhanced ferrite nanoparticles as MRI contrast agents. *Journal of Magnetism and Magnetic Materials*, **311** (1), 464–8.

89 Martina, M.-S., Fortin, J.-P., Ménager, C., Clément, O., Barratt, G., Grabielle-Madelmont, C., Gazeau, F., Cabuil, V. and Lesieur, S. (2005) Generation of superparamagnetic liposomes revealed as highly efficient MRI contrast agents for in vivo imaging. *Journal of the American Chemical Society*, **127**, 10676–85.

90 Nitin, N., LaConte, L.E.W., Zurkiya, O., Hu, X. and Bao, G. (2004) Functionalization and peptide-based delivery of magnetic nanoparticles as an intracellular MRI contrast agent. *Journal of Biological Inorganic Chemistry*, **9** (6), 706–12.

91 Kohler, N., Fryxell, G.E. and Zhang, M.Q. (2004) A bifunctional poly(ethylene glycol) silane immobilized on metallic oxide-based nanoparticles for conjugation with cell targeting agents. *Journal of the American Chemical Society*, **126** (23), 7206–11.

92 Ai, H., Flask, C., Weinberg, B., Shuai, X., Pagel, M.D., Farrell, D., Duerk, J.

and Gao, J.M. (2005) Magnetite-loaded polymeric micelles as ultrasensitive magnetic-resonance probes. *Advanced Materials*, **17** (16), 1949–52.

93 Li, Z., Wei, L., Gao, M.Y. and Lei, H. (2005) One-pot reaction to synthesize biocompatible magnetite nanoparticles. *Advanced Materials*, **17** (8), 1001–5.

94 Sun, C., Sze, R. and Zhang, M.Q. (2006) Folic acid-PEG conjugated superparamagnetic nanoparticles for targeted cellular uptake and detection by MRI. *Journal of Biomedical Materials Research. Part A*, **78A** (3), 550–7.

95 Xie, J., Xu, C., Kohler, N., Hou, Y. and Sun, S. (2007) Controlled PEGylation of monodisperse Fe_3O_4 nanoparticles for reduced non-specific uptake by macrophage cells. *Advanced Materials*, **19** (20), 3163–6.

96 Fan, Q.L., Neoh, K.G., Kang, E.T., Shuter, B. and Wang, S.C. (2007) Solvent-free atom transfer radical polymerization for the preparation of poly(poly(ethyleneglycol) monomethacrylate)-grafted Fe_3O_4 nanoparticles: synthesis, characterization and cellular uptake. *Biomaterials*, **28** (36), 5426–36.

97 Wang, Y., Ng, Y.W., Chen, Y., Shuter, B., Yi, J., Ding, J., Wang, S.C. and Feng, S.S. (2008) Formulation of superparamagnetic iron oxides by nanoparticles of biodegradable polymers for magnetic resonance imaging. *Advanced Functional Materials*, **18** (2), 308–18.

98 Lee, H., Lee, E., Kim, D.K., Jang, N.K., Jeong, Y.Y. and Jon, S. (2006) Antibiofouling polymer-coated superparamagnetic iron oxide nanoparticles as potential magnetic resonance contrast agents for in vivo cancer imaging. *Journal of the American Chemical Society*, **128** (22), 7383–9.

99 Kaufner, L., Cartier, R., Wustneck, R., Fichtner, I., Pietschmann, S., Bruhn, H., Schutt, D., Thunemann, A.F. and Pison, U. (2007) Poly(ethylene oxide)-block-poly(glutamic acid) coated maghemite nanoparticles: in vitro characterization and in vivo behaviour. *Nanotechnology*, **18** (11), article 115710.

100 Hu, F.Q., Wei, L., Zhou, Z., Ran, Y.L., Li, Z. and Gao, M.Y. (2006) Preparation of biocompatible magnetite nanocrystals for in vivo magnetic resonance detection of cancer. *Advanced Materials*, **18** (19), 2553–5.

101 Sun, C., Veiseh, O., Gunn, J., Fang, C., Hansen, S., Lee, D., Sze, R., Ellenbogen, R.G., Olson, J. and Zhang, M. (2008) In vivo MRI detection of gliomas by chlorotoxin-conjugated superparamagnetic nanoprobes. *Small*, **4** (3), 372–9.

102 Dodd, C.H., Hsu, H.C., Chu, W.J., Yang, P.G., Zhang, H.G., Mountz, J.D., Zinn, K., Forder, J., Josephson, L., Weissleder, R., Mountz, J.M. and Mountz, J.D. (2001) Normal T-cell response and in vivo magnetic resonance imaging of T cells loaded with HIV transactivator-peptide-derived superparamagnetic nanoparticles. *Journal of Immunological Methods*, **256** (1–2), 89–105.

103 Dodd, C., Mountz, J., Chu, W.J., Josephson, L., Zhang, H.G., Weissleder, R., Mountz, J.M., Zinn, K., Mountz, J.D. and Hsu, H.C. (2001) In vivo magnetic resonance imaging (MRI) of T cells loaded with HIV transactivator (tat) peptide-derived super-paramagnetic nanoparticles. *The FASEB Journal*, **15** (5), A744.

104 Hsu, H.C., Dodd, C., Chu, W.J., Yang, P.A., Josephson, L., Sun, S.H., Zhang, H.G., Weissleder, R. and Mountz, J.D. (2001) Normal response of T cells loaded with HIV transactivator (tat) peptide-derived super-paramagnetic nanoparticles for magnetic resonance imaging (MRI). *The FASEB Journal*, **15** (4), A330.

105 Nasongkla, N., Bey, E., Ren, J.M., Ai, H., Khemtong, C., Guthi, J.S., Chin, S.F., Sherry, A.D., Boothman, D.A. and Gao, J.M. (2006) Multifunctional polymeric micelles as cancer-targeted, MRI-ultrasensitive drug delivery systems. *Nano Letters*, **6** (11), 2427–30.

106 von zur Muhlen, C., von Elverfeldt, D., Bassler, N., Neudorfer, I., Steitz, B., Petri-Fink, A., Hofmann, H., Bode, C. and Peter, K. (2007) Superparamagnetic iron oxide binding and uptake as imaged

by magnetic resonance is mediated by the integrin receptor Mac-1 (CD11b/CD18): implications on imaging of atherosclerotic plaques. *Atherosclerosis*, **193** (1), 102–11.

107 Martina, M.S., Fortin, J.P., Menager, C., Clement, O., Barratt, G., Grabielle-Madelmont, C., Gazeau, F., Cabuil, V. and Lesieur, S. (2005) Generation of superparamagnetic liposomes revealed as highly efficient MRI contrast agents for in vivo imaging. *Journal of the American Chemical Society*, **127** (30), 10676–85.

108 Larsen, B.A., Haag, M.A., Serkova, N.J., Shroyer, K.R. and Stoldt, C.R. (2008) Controlled aggregation of superparamagnetic iron oxide nanoparticles for the development of molecular magnetic resonance imaging probes. *Nanotechnology*, **19** (26), article 265102.

109 Meincke, M., Schlorf, T., Kossel, E., Jansen, O., Glueer, C.C. and Mentlein, R. (2008) Iron oxide-loaded liposomes for MR imaging. *Frontiers in Bioscience*, **13**, 4002–8.

110 Hultman, K.L., Raffo, A.J., Grzenda, A.L., Harris, P.E., Brown, T.R. and O'Brien, S. (2008) Magnetic resonance imaging of major histocompatibility class II expression in the renal medulla using immunotargeted superparamagnetic iron oxide nanoparticles. *ACS Nano*, **2** (3), 477–84.

111 Lee, H.Y., Lim, N.H., Seo, J.A., Yuk, S.H., Kwak, B.K., Khang, G., Lee, H.B. and Cho, S.H. (2006) Preparation and magnetic resonance imaging effect of polyvinylpyrrolidone-coated iron oxide nanoparticles. *Journal of Biomedical Materials Research B: Applied Biomaterials*, **79B** (1), 142–50.

112 Liu, H.L., Ko, S.P., Wu, J.H., Jung, M.H., Min, J.H., Lee, J.H., An, B.H. and Kim, Y.K. (2007) One-pot polyol synthesis of monosize PVP-coated sub-5 nm Fe_3O_4 nanoparticles for biomedical applications. *Journal of Magnetism and Magnetic Materials*, **310** (2), E815–17.

113 Lee, H.Y., Lee, S.H., Xu, C.J., Xie, J., Lee, J.H., Wu, B., Koh, A.L., Wang, X.Y., Sinclair, R., Xwang, S., Nishimura, D.G., Biswal, S., Sun, S.H., Cho, S.H. and Chen, X.Y. (2008) Synthesis and characterization of PVP-coated large core iron oxide nanoparticles as an MRI contrast agent. *Nanotechnology*, **19** (16), article 165101.

114 Park, I.K., Ng, C.P., Wang, J., Chu, B., Yuan, C., Zhang, S. and Pun, S.H. (2008) Determination of nanoparticle vehicle unpackaging by MR imaging of a T-2 magnetic relaxation switch. *Biomaterials*, **29** (6), 724–32.

115 Albornoz, C. and Jacobo, S.E. (2006) Preparation of a biocompatible magnetic film from an aqueous ferrofluid. *Journal of Magnetism and Magnetic Materials*, **305** (1), 12–15.

116 Schopf, B., Neuberger, T., Schulze, K., Petri, A., Chastellain, M., Hofmann, M., Hofmann, H. and von Rechenberg, B. (2005) Methodology description for detection of cellular uptake of PVA coated superparamagnetic iron oxide nanoparticles (SPION) in synovial cells of sheep. *Journal of Magnetism and Magnetic Materials*, **293** (1), 411–18.

117 Chastellain, A., Petri, A. and Hofmann, H. (2004) Particle size investigations of a multistep synthesis of PVA coated superparamagnetic nanoparticles. *Journal of Colloid and Interface Science*, **278** (2), 353–60.

118 Corr, S.A., Byrne, S.J., Tekoriute, R., Meledandri, C.J., Brougham, D.F., Lynch, M., Kerskens, C., O'Dwyer, L. and Gun'ko, Y.K. (2008) Linear assemblies of magnetic nanoparticles as MRI contrast agents. *Journal of the American Chemical Society*, **130** (13), 4214–15.

119 Berret, J.F., Schonbeck, N., Gazeau, F., El Kharrat, D., Sandre, O., Vacher, A. and Airiau, M. (2006) Controlled clustering of superparamagnetic nanoparticles using block copolymers: design of new contrast agents for magnetic resonance imaging. *Journal of the American Chemical Society*, **128** (5), 1755–61.

120 Groman, E.V., Bouchard, J.C., Reinhardt, C.P. and Vaccaro, D.E. (2007) Ultrasmall mixed ferrite colloids as

multidimensional magnetic resonance imaging, cell labeling, and cell sorting agents. *Bioconjugate Chemistry*, **18** (6), 1763–71.

121 Park, J.A., Lee, J.J., Kim, I.S., Park, B.H., Lee, G.H., Kim, T.J., Ri, H.C., Kim, H.J. and Chang, Y.M. (2008) Magnetic and MR relaxation properties of avidin-biotin conjugated superparamagnetic nanoparticles. *Colloids and Surfaces A: Physicochemical and Engineering Aspects*, **313**, 288–91.

122 Rabias, I., Pratsinis, H., Drossopoulou, G., Fardis, M., Maris, T., Boukos, N., Tsotakos, N., Kletsas, D., Tsilibary, E. and Papavassiliou, G. (2007) In vitro studies on ultrasmall superparamagnetic iron oxide nanoparticles coated with gummic acid for T2 MRI contrast agent. *Biomicrofluidics*, **1** (4), article 144104.

123 He, H.W., Liu, H.J., Zhou, K.C., Wang, W. and Rong, P.F. (2006) Characteristics of magnetic Fe_3O_4 nanoparticles encapsulated with human serum albumin. *Journal of Central South University of Technology*, **13** (1), 6–11.

124 Raty, J.K., Liimatainen, T., Wirth, T., Airenne, K.J., Ihalainen, T.O., Huhtala, T., Hamerlynck, E., Vihinen-Ranta, M., Narvanen, A., Yla-Herttuala, S. and Hakumaki, J.M. (2006) Magnetic resonance imaging of viral particle biodistribution in vivo. *Gene Therapy*, **13** (20), 1440–6.

125 Schellenberger, E., Schnorr, J., Reutelingsperger, C., Ungethum, L., Meyer, W., Taupitz, M. and Hamm, B. (2008) Linking proteins with anionic nanoparticles via protamine: ultrasmall protein-coupled probes for magnetic resonance imaging of apoptosis. *Small*, **4** (2), 225–30.

126 Byrne, S.J., Corr, S.A., Gun'ko, Y.K., Kelly, J.M., Brougham, D.F. and Ghosh, S. (2004) Magnetic nanoparticle assemblies on denatured DNA show unusual magnetic relaxivity and potential applications for MRI. *Chemical Communications*, **22**, 2560–1.

127 Tartaj, P., Morales, M.D., Veintemillas-Verdaguer, S., Gonzalez-Carreno, T. and Serna, C.J. (2003) The preparation of magnetic nanoparticles for applications in biomedicine. *Journal of Physics D*, **36** (13), R182–97.

128 Philipse, A.P., Vanbruggen, M.P.B. and Pathmamanoharan, C. (1994) Magnetic silica dispersions – preparation and stability of surface-modified silica particles with a magnetic core. *Langmuir*, **10** (1), 92–9.

129 Yan, F., Xu, H., Anker, J., Kopelman, R., Ross, B., Rehemtulla, A. and Reddy, R. (2004) Synthesis and characterization of silica-embedded iron oxide nanoparticles for magnetic resonance imaging. *Journal of Nanoscience and Nanotechnology*, **4** (1–2), 72–6.

130 Liang, S., Wang, Y.X., Zhang, C.F., Liu, X.Q., Liu, Z.F., Xu, R.H. and Yin, D.Z. (2006) Synthesis of amino-modified magnetite nanoparticles coated with Hepama-1 and radiolabeled with Re-188 for bio-magnetically targeted radiotherapy. *Journal of Radioanalytical and Nuclear Chemistry*, **269** (1), 3–7.

131 Stober, W., Fink, A. and Bohn, E. (1968) Controlled growth of monodisperse silica spheres in micron size range. *Journal of Colloid and Interface Science*, **26** (1), 62–9.

132 Lu, Y., Yin, Y.D., Mayers, B.T. and Xia, Y.N. (2002) Modifying the surface properties of superparamagnetic iron oxide nanoparticles through a sol-gel approach. *Nano Letters*, **2** (3), 183–6.

133 Barnakov, Y.A., Yu, M.H. and Rosenzweig, Z. (2005) Manipulation of the magnetic properties of magnetite-silica nanocomposite materials by controlled Stober synthesis. *Langmuir*, **21** (16), 7524–7.

134 Im, S.H., Herricks, T., Lee, Y.T. and Xia, Y.N. (2005) Synthesis and characterization of monodisperse silica colloids loaded with superparamagnetic iron oxide nanoparticles. *Chemical Physics Letters*, **401** (1–3), 19–23.

135 Santra, S., Tapec, R., Theodoropoulou, N., Dobson, J., Hebard, A. and Tan, W.H. (2001) Synthesis and characterization of silica-coated iron oxide nanoparticles in microemulsion: the effect of nonionic surfactants. *Langmuir*, **17** (10), 2900–6.

136 Tartaj, P. and Serna, C.J. (2002) Microemulsion-assisted synthesis of tunable superparamagnetic composites. *Chemistry of Materials*, **14** (10), 4396–402.
137 Tartaj, P. and Serna, C.J. (2003) Synthesis of monodisperse superparamagnetic Fe/silica nanospherical composites. *Journal of the American Chemical Society*, **125** (51), 15754–5.
138 Yang, H.H., Zhang, S.Q., Chen, X.L., Zhuang, Z.X., Xu, J.G. and Wang, X.R. (2004) Magnetite-containing spherical silica nanoparticles for biocatalysis and bioseparations. *Analytical Chemistry*, **76** (5), 1316–21.
139 Tartaj, P., Gonzalez-Carreno, T. and Serna, C.J. (2001) Single-step nanoengineering of silica coated maghemite hollow spheres with tunable magnetic properties. *Advanced Materials*, **13** (21), 1620–4.
140 Tartaj, P., Gonzalez-Carreno, T. and Serna, C.J. (2002) Synthesis of nanomagnets dispersed in colloidal silica cages with applications in chemical separation. *Langmuir*, **18** (12), 4556–8.
141 Hahn, P.F., Stark, D.D., Lewis, J.M., Saini, S., Elizondo, G., Weissleder, R., Fretz, C.J. and Ferrucci, J.T. (1990) 1st Clinical-trial of a new superparamagnetic iron-oxide for use as an oral gastrointestinal contrast agent in MR imaging. *Radiology*, **175** (3), 695–700.
142 Heusler, R.C.H., Wight, E. and Marincek, B. (1995) Oral superparamagnetic contrast agent (Ferumoxsil)–tolerance and efficacy in MR-imaging of gynecologic diseases. *Journal of Magnetic Resonance Imaging*, **5** (4), 385–91.
143 Carpenter, E.E., Sangregorio, C. and O'Connor, C.J. (1999) Effects of shell thickness on blocking temperature of nanocomposites of metal particles with gold shells. *IEEE Transactions on Magnetics*, **35** (5), 3496–8.
144 Lin, J., Zhou, W.L., Kumbhar, A., Wiemann, J., Fang, J.Y., Carpenter, E.E. and O'Connor, C.J. (2001) Gold-coated iron (Fe@Au) nanoparticles: synthesis, characterization, and magnetic field-induced self-assembly. *Journal of Solid State Chemistry*, **159** (1), 26–31.
145 Cho, S.J., Idrobo, J.C., Olamit, J., Liu, K., Browning, N.D. and Kauzlarich, S.M. (2005) Growth mechanisms and oxidation resistance of gold-coated iron nanoparticles. *Chemistry of Materials*, **17** (12), 3181–6.
146 Park, J.I. and Cheon, J. (2001) Synthesis of "solid solution" and "core-shell" type cobalt-platinum magnetic nanoparticles via transmetalation reactions. *Journal of the American Chemical Society*, **123** (24), 5743–6.
147 Ban, Z.H., Barnakov, Y.A., Golub, V.O. and O'Connor, C.J. (2005) The synthesis of core-shell iron@gold nanoparticles and their characterization. *Journal of Materials Chemistry*, **15** (43), 4660–2.
148 Lyon, J.L., Fleming, D.A., Stone, M.B., Schiffer, P. and Williams, M.E. (2004) Synthesis of Fe oxide core/Au shell nanoparticles by iterative hydroxylamine seeding. *Nano Letters*, **4** (4), 719–23.
149 Kim, J., Park, S., Lee, J.E., Jin, S.M., Lee, J.H., Lee, I.S., Yang, I., Kim, J.S., Kim, S.K., Cho, M.H. and Hyeon, T. (2006) Designed fabrication of multifunctional magnetic gold nanoshells and their application to magnetic resonance imaging and photothermal therapy. *Angewandte Chemie, International Edition in English*, **45** (46), 7754–8.
150 Hayashi, T., Hirono, S., Tomita, M. and Umemura, S. (1996) Magnetic thin films of cobalt nanocrystals encapsulated in graphite-like carbon. *Nature*, **381** (6585), 772–4.
151 Nikitenko, S.I., Koltypin, Y., Palchik, O., Felner, I., Xu, X.N. and Gedanken, A. (2001) Synthesis of highly magnetic, air-stable iron carbide nanocrystalline particles by using power ultrasound. *Angewandte Chemie, International Edition in English*, **40** (23), 4447–9.
152 Jung, H.I., Kettunen, M.I., Davletov, B. and Brindle, K.M. (2004) Detection of apoptosis using the C2A domain of synaptotagmin I. *Bioconjugate Chemistry*, **15** (5), 983–7.
153 Artemov, D., Mori, N., Okollie, B. and Bhujwalla, Z.M. (2003) MR molecular imaging of the Her-2/neu receptor in

breast cancer cells using targeted iron oxide nanoparticles. *Magnetic Resonance in Medicine*, **49** (3), 403–8.

154 Go, K.G., Bulte, J.W.M., Deley, L., The, T.H., Kamman, R.L., Hulstaert, C.E., Blaauw, E.H. and Ma, L.D. (1993) Our approach towards developing a specific tumor-targeted MRI contrast agent for the brain. *European Journal of Radiology*, **16** (3), 171–5.

155 Johansson, L.O., Bjornerud, A., Ahlstrom, H.K., Ladd, D.L. and Fujii, D.K. (2001) A targeted contrast agent for magnetic resonance imaging of thrombus: implications of spatial resolution. *Journal of Magnetic Resonance Imaging*, **13** (4), 615–18.

156 Kresse, M., Wagner, S., Pfefferer, D., Lawaczeck, R., Elste, V. and Semmler, W. (1998) Targeting of ultrasmall superparamagnetic iron oxide (USPIO) particles to tumor cells in vivo by using transferrin receptor pathways. *Magnetic Resonance in Medicine*, **40** (2), 236–42.

157 Zhao, M., Beauregard, D.A., Loizou, L., Davletov, B. and Brindle, K.M. (2001) Non-invasive detection of apoptosis using magnetic resonance imaging and a targeted contrast agent. *Nature Medicine*, **7** (11), 1241–4.

158 Weissleder, R., Lee, A.S., Fischman, A.J., Reimer, P., Shen, T., Wilkinson, R., Callahan, R.J. and Brady, T.J. (1991) Polyclonal human immunoglobulin-G labeled with polymeric iron-oxide–antibody MR imaging. *Radiology*, **181** (1), 245–9.

159 Toma, A., Otsuji, E., Kuriu, Y., Okamoto, K., Ichikawa, D., Hagiwara, A., Ito, H., Nishimura, T. and Yamagishi, H. (2005) Monoclonal antibody A7-superparamagnetic iron oxide as contrast agent of MR imaging of rectal carcinoma. *British Journal of Cancer*, **93** (1), 131–6.

160 Remsen, L.G., McCormick, C.I., RomanGoldstein, S., Nilaver, G., Weissleder, R., Bogdanov, A., Hellstrom, K.E., Hellstrom, I., Kroll, R.A. and Neuwelt, E.A. (1996) MR of carcinoma-specific monoclonal antibody conjugated to monocrystalline iron oxide nanoparticles: the potential for noninvasive diagnosis. *American Journal of Neuroradiology*, **17** (3), 411–18.

161 Funovics, M.A., Kapeller, B., Hoeller, C., Su, H.S., Kunstfeld, R., Puig, S. and Macfelda, K. (2004) MR imaging of the her2/neu and 9.2.27 tumor antigens using immunospecific contrast agents. *Magnetic Resonance Imaging*, **22** (6), 843–50.

162 Vaneverdingen, K.J., Enochs, W.S., Bhide, P.G., Nossiff, N., Papisov, M., Bogdanov, A., Brady, T.J. and Weissleder, R. (1994) Determinants of in-vivo MR-imaging of slow axonal-transport. *Radiology*, **193** (2), 485–91.

163 Brandriss, S. and Margel, S. (1993) Synthesis and characterization of self-assembled hydrophobic monolayer coatings on silica colloids. *Langmuir*, **9** (5), 1232–40.

164 Fauconnier, N., Pons, J.N., Roger, J. and Bee, A. (1997) Thiolation of maghemite nanoparticles by dimercaptosuccinic acid. *Journal of Colloid and Interface Science*, **194** (2), 427–33.

165 Halbreich, A., Roger, J., Pons, J.N., Geldwerth, D., Da Silva, M.F., Roudier, M. and Bacri, J.C. (1998) Biomedical applications of maghemite ferrofluid. *Biochimie*, **80** (5-6), 379–90.

166 Roger, J., Pons, J.N., Massart, R., Halbreich, A. and Bacri, J.C. (1999) Some biomedical applications of ferrofluids. *The European Physical Journal Applied Physics*, **5** (3), 321–5.

167 Huh, Y.M., Jun, Y.W., Song, H.T., Kim, S., Choi, J.S., Lee, J.H., Yoon, S., Kim, K.S., Shin, J.S., Suh, J.S. and Cheon, J. (2005) In vivo magnetic resonance detection of cancer by using multifunctional magnetic nanocrystals. *Journal of the American Chemical Society*, **127** (35), 12387–91.

168 Sun, E.Y., Josephson, L. and Weissleder, R. (2006) "Clickable" nanoparticles for targeted imaging. *Molecular Imaging*, **5** (2), 122–8.

169 Lu, H.M., Zheng, W.T. and Jiang, Q. (2007) Saturation magnetism of ferromagnetic and ferrimagnetic nanocrystals at room temperature. *Journal of Physics D*, **40**, 320–5.

170 Roch, A., Muller, R.N. and Gillis, P. (1999) Theory of proton relaxation

induced by superparamagnetic particles. *Journal of Chemical Physics*, **110** (11), 5403–11.

171 Chantrell, R.W., Popplewell, J. and Charles, S.W. (1977) Effect of a particle-size distribution on coercivity and remanence of a fine particle system. *Physica B & C*, **86**, 1421–2.

172 Moore, A., Sun, P.Z., Cory, D., Hogemann, D., Weissleder, R. and Lipes, M.A. (2002) MRI of insulitis in autoimmune diabetes. *Magnetic Resonance in Medicine*, **47** (4), 751–8.

173 Pecora, R. (2000) Dynamic light scattering measurements of nanometer particles in liquids. *Journal of Nanoparticle Research*, **2**, 123–31.

174 Berne, B.J. and Pecora, R. (2003) *Dynamic Light Scattering*, Dover Publications, Inc.

175 Ouakssim, A., Roch, A., Pierart, C. and Muller, R.N. (2002) Characterization of polydisperse superparamagnetic particles by nuclear magnetic resonance dispersion (NMRD) profiles. *Journal of Magnetism and Magnetic Materials*, **252**, 49–52.

176 Anoardo, E., Galli, G. and Ferrante, G. (2001) Fast-field-cycling NMR: applications and instrumentation. *Applied Magnetic Resonance*, **20** (3), 365–404.

177 Berret, J.F., Schonbeck, N., Gazeau, F., El Kharrat, D., Sandre, O., Vacher, A. and Airiau, M. (2006) Controlled clustering of superparamagnetic nanoparticles using block copolymers: design of new contrast agents for magnetic resonance imaging. *Journal of the American Chemical Society*, **128** (5), 1755–61.

178 Roch, A., Gossuin, Y., Muller, R.N. and Gillis, P. (2005) Superparamagnetic colloid suspensions: water magnetic relaxation and clustering. *Journal of Magnetism and Magnetic Materials*, **293** (1), 532–9.

179 McDermott, R., Lee, S.K., ten Haken, B., Trabesinger, A.H., Pines, A. and Clarke, J. (2004) Microtesla MRI with a superconducting quantum interference device. *Proceedings of the National Academy of Sciences of the United States of America*, **101**, 7857–61.

180 Corti, M., Lascialfari, A., Micotti, E., Castellano, A., Donativi, M., Quarta, A., Cozzoli, P.D., Manna, L., Pellegrino, T. and Sangregorio, C. (2008) Magnetic properties of novel superparamagnetic MRI contrast agents based on colloidal nanocrystals. *Journal of Magnetism and Magnetic Materials*, **320** (14), E320–3.

181 Corti, M., Lascialfari, A., Marinone, M., Masotti, A., Micotti, E., Orsini, F., Ortaggi, G., Poletti, G., Innocenti, C. and Sangregorio, C. (2008) Magnetic and relaxometric properties of polyethylenimine-superparamagnetic MRI contrast agents. *Journal of Magnetism and Magnetic Materials*, **320**, E316–19.

182 Wan, J., Cai, W., Meng, X. and Liu, E. (2007) Monodisperse water-soluble magnetite nanoparticles prepared by polyol process for high-performance magnetic resonance imaging. *Chemical Communications*, **47**, 5004–6.

183 Qin, J., Laurent, S., Jo, Y.S., Roch, A., Mikhaylova, M., Bhujwalla, Z.M., Muller, R.N. and Muhammed, M. (2007) A high-performance magnetic resonance imaging T-2 contrast agent. *Advanced Materials*, **19** (14), 1874–8.

184 Atanasijevic, T., Shusteff, M., Fam, P. and Jasanoff, A. (2006) Calcium-sensitive MRI contrast agents based on superparamagnetic iron oxide nanoparticles and calmodulin. *Proceedings of the National Academy of Sciences of the United States of America*, **103** (40), 14707–12.

185 Perez, J.M., Josephson, L. and Weissleder, R. (2004) Use of magnetic nanoparticles as nanosensors to probe for molecular interactions. *Chembiochem*, **5** (3), 261–4.

186 Yigit, M.V., Mazumdar, D. and Lu, Y. (2008) MRI detection of thrombin with aptamer functionalized superparamagnetic iron oxide nanoparticles. *Bioconjugate Chemistry*, **19** (2), 412–17.

187 Kim, G.Y., Josephson, L., Langer, R. and Cima, M.J. (2007) Magnetic relaxation switch detection of human chorionic

gonadotrophin. *Bioconjugate Chemistry*, **18** (6), 2024–8.

188 Laghi, A., Paolantonio, P., Iafrate, F., Altomari, F., Miglio, C. and Passariello, R. (2002) Oral contrast agents for magnetic resonance imaging of the bowel. *Topics in Magnetic Resonance Imaging*, **13**, 389–96.

189 Debatin, J.F. and Patak, M.A. (1999) MRI of the small and large bowel. *European Radiology*, **9** (8), 1523–34.

190 Johnson, W.K., Stoupis, C., Torres, G.M., Rosenberg, E.B. and Ros, P.R. (1996) Superparamagnetic iron oxide (SPIO) as an oral contrast agent in gastrointestinal (GI) magnetic resonance imaging (MRI): comparison with state-of-the-art computed tomography (CT). *Magnetic Resonance Imaging*, **14** (1), 43–9.

191 Grubnic, S., Padhani, A.R., Revell, P.B. and Husband, J.E. (1999) Comparative efficacy of and sequence choice for two oral contrast agents used during MR imaging. *American Journal of Roentgenology*, **173** (1), 173–8.

192 Jacobsen, T.F., Laniado, M., Van Beers, B.E., Dupas, B., Boudghene, F.P., Rummeny, E., Falke, T.H.M., Rinck, P.A., MacVicar, D. and Lundby, B. (1996) Oral magnetic particles (ferristene) as a contrast medium in abdominal magnetic resonance imaging. *Academic Radiology*, **3** (7), 571–80.

193 Li, W., Tutton, S., Vu, A.T., Pierchala, L., Li, B.S.Y., Lewis, J.M., Prasad, P.V. and Edelman, R.R. (2005) First-pass contrast-enhanced magnetic resonance angiography in humans using ferumoxytol, a novel ultrasmall superparamagnetic iron oxide (USPIO)-based blood pool agent. *Journal of Magnetic Resonance Imaging*, **21** (1), 46–52.

194 Simon, G.H., von Vopelius-Feldt, J., Fu, Y.J., Schlegel, J., Pinotek, G., Wendland, M.F., Chen, M.H. and Daldrup-Link, H.E. (2006) Ultrasmall supraparamagnetic iron oxide-enhanced magnetic resonance imaging of antigen-induced arthritis–a comparative study between SHUSSSC, ferumoxtran-10, and ferumoxytol. *Investigative Radiology*, **41** (1), 45–51.

195 Stark, D.D., Weissleder, R., Elizondo, G., Hahn, P.F., Saini, S., Todd, L.E., Wittenberg, J. and Ferrucci, J.T. (1988) Superparamagnetic iron oxide: clinical applications as contrast agent for MR imaging of the liver. *Radiology*, **168**, 297–301.

196 Semelka, R.C. and Helmberger, T.K.G. (2001) Contrast agents for MR imaging of the liver. *Radiology*, **218** (1), 27–38.

197 Reimer, P. and Tombach, B. (1998) Hepatic MRI with SPIO: detection and characterization of focal liver lesions. *European Radiology*, **8** (7), 1198–204.

198 Grangier, C., Tourniaire, J., Mentha, G., Schiau, R., Howarth, N., Chachuat, A., Grossholz, M. and Terrier, F. (1994) Enhancement of liver hemangiomas on T1-weighted MR Se images by superparamagnetic iron-oxide particles. *Journal of Computer Assisted Tomography*, **18** (6), 888–96.

199 Reimer, P., Allkemper, T., Matuszewski, L. and Balzer, T. (1999) Contrast-enhanced 3D-MRA of the upper abdomen with a bolus-injectable SPIO (SH U 555 A). *Journal of Magnetic Resonance Imaging*, **10** (1), 65–71.

200 Harisinghani, M.G., Saini, S., Weissleder, R., Halpern, E.F., Schima, W., Rubin, D.L., Stillman, A.E., Sica, G.T., Small, W.C. and Hahn, P.F. (1997) Differentiation of liver hemangiomas from metastases and hepatocellular carcinoma at MR imaging enhanced with blood-pool contrast agent Code-7227. *Radiology*, **202** (3), 687–91.

201 Saini, S., Edelman, R.R., Sharma, P., Li, W., Mayosmith, W., Slater, G.J., Eisenberg, P.J. and Hahn, P.F. (1995) Blood-pool MR contrast material for detection and characterization of focal hepatic lesions–initial clinical experience with ultrasmall superparamagnetic iron-oxide (Ami-227). *American Journal of Roentgenology*, **164** (5), 1147–52.

202 Deserno, W., Harisinghani, M.G., Taupitz, M., Jager, G.J., Witjes, J.A., Mulders, P.F., van de Kaa, C.A.H., Kaufmann, D. and Barentsz, J.O. (2004) Urinary bladder cancer: preoperative nodal staging with ferumoxtran-10-

enhanced MR imaging. *Radiology*, **233** (2), 449–56.

203 Koh, D.M., Brown, G., Temple, L., Blake, H., Raja, A., Toomey, P., Bett, N., Farhat, S., Norman, A.R., Daniels, I. and Husband, J.E. (2005) Distribution of mesorectal lymph nodes in rectal cancer: in vivo MR imaging compared with histopathological examination. Initial observations. *European Radiology*, **15** (8), 1650–7.

204 Anzai, Y., Brunberg, J.A. and Lufkin, R.B. (1997) Imaging of nodal metastases in the head and neck. *Journal of Magnetic Resonance Imaging*, **7** (5), 774–83.

205 Bellin, M.F., Beigelman, C. and Precetti-Morel, S. (2000) Iron oxide-enhanced MR lymphography: initial experience. *European Journal of Radiology*, **34** (3), 257–64.

206 Rogers, J.M., Lewis, J. and Josephson, L. (1994) Visualization of superior mesenteric lymph-nodes by the combined oral and intravenous administration of the ultrasmall superparamagnetic iron-oxide, Ami-227. *Magnetic Resonance Imaging*, **12** (8), 1161–5.

207 Anzai, Y., McLachlan, S., Morris, M., Saxton, R. and Lufkin, R.B. (1994) Dextran-coated superparamagnetic iron-oxide, an MR contrast agent for assessing lymph-nodes in the head and neck. *American Journal of Neuroradiology*, **15** (1), 87–94.

208 Anzai, Y., Blackwell, K.E., Hirschowitz, S.L., Rogers, J.W., Sato, Y., Yuh, W.T.C., Runge, V.M., Morris, M.R., McLachlan, S.J. and Lufkin, R.B. (1994) Initial clinical-experience with dextran-coated superparamagnetic iron-oxide for detection of lymph-node metastases in patients with head and neck-cancer. *Radiology*, **192** (3), 709–15.

209 Hudgins, P.A., Anzai, Y., Morris, M.R. and Lucas, M.A. (2002) Ferumoxtran-10, a superparamagnetic iron oxide as a magnetic resonance enhancement agent for imaging lymph nodes: a phase 2 dose study. *American Journal of Neuroradiology*, **23** (4), 649–56.

210 Will, O., Purkayastha, S., Chan, C., Athanasiou, T., Darzi, A.W., Gedroyc, W. and Tekkis, P.P. (2006) Diagnostic precision of nanoparticle-enhanced MRI for lymph-node metastases: a meta-analysis. *The Lancet Oncology*, **7** (1), 52–60.

211 Nishimura, H., Tanigawa, N., Hiramatsu, M., Tatsumi, Y., Matsuki, M. and Narabayashi, I. (2006) Preoperative esophageal cancer staging: magnetic resonance imaging of lymph node with ferumoxtran-10, an ultrasmall superparamagnetic iron oxide. *Journal of the American College of Surgeons*, **202** (4), 604–11.

212 Bellin, M.F., Roy, C., Kinkel, K., Thoumas, D., Zaim, S., Vanel, D., Tuchmann, C., Richard, F., Jacqmin, D., Delcourt, A., Challier, E., Lebret, T. and Cluzel, P. (1998) Lymph node metastases: safety and effectiveness of MR imaging with ultrasmall superparamagnetic iron oxide particles – initial clinical experience. *Radiology*, **207** (3), 799–808.

213 Harisinghani, M.G., Saini, S., Slater, G.J., Schnall, M.D. and Rifkin, M.D. (1997) MR imaging of pelvic lymph nodes in primary pelvic carcinoma with ultrasmall superparamagnetic iron oxide (Combidex): preliminary observations. *Journal of Magnetic Resonance Imaging*, **7** (1), 161–3.

214 Stadnik, T.W., Everaert, H., Makkat, S., Sacre, R., Lamote, J. and Bourgain, C. (2006) Breast imaging. Preoperative breast cancer staging: comparison of USPIO-enhanced MR imaging and 18F-fluorodeoxyglucose (FDC) positron emission tomography (PET) imaging for axillary lymph node staging – initial findings. *European Radiology*, **16** (10), 2153–60.

215 Koh, D.M., Brown, G., Temple, L., Raja, A., Toomey, P., Bett, N., Norman, A.R. and Husband, J.E. (2004) Rectal cancer: mesorectal lymph nodes at MR imaging with USPIO versus histopathologic findings – initial observations. *Radiology*, **231** (1), 91–9.

216 Harisinghani, M.G. and Weissleder, R. (2004) Sensitive, noninvasive detection of lymph node metastases. *PLoS Medicine*, **1** (3), 202–9.

217 Daldrup-Link, H.E., Henning, T. and Link, T.M. (2007) MR imaging of therapy-induced changes of bone marrow. *European Radiology*, **17** (3), 743–61.

218 Daldrup-Link, H.E., Rummeny, E.J., Ihssen, B., Kienast, J. and Link, T.M. (2002) Iron-oxide-enhanced MR imaging of bone marrow in patients with non-Hodgkin's lymphoma: differentiation between tumor infiltration and hypercellular bone marrow. *European Radiology*, **12** (6), 1557–66.

219 Daldrup-Link, H.E., Franzius, C., Laukamp, D., Rummeny, E.J., Juergens, H. and Link, T.M. (1999) Whole body MR imaging for detection of bone marrow metastases in pediatric patients: comparison with skeletal scintigraphy and FDG-PET. *Radiology*, **213P**, 293.

220 Daldrup-Link, H.E., Rummeny, E.J., Ihssen, B., Silling-Engelhardt, H. and Link, T.M. (2000) Comparison of SPIO and USPIO for MRI of the bone marrow in patients with non-Hodgkins lymphomas. *Radiology*, **217**, 356.

221 Daldrup-Link, H.E., Decker, T., Rummeny, E.J., Metz, S. and Link, T.M. (2001) Ferumoxtran-enhanced MRI quantification of microvascular permeability in patients with diffuse bone marrow neoplasias before and after total body irradiation. *Radiology*, **221**, 234.

222 Metz, S., Lohr, S., Settles, M., Beer, A., Woertler, K., Rummeny, E. and Daldrup-Link, H.E. (2006) Ferumoxtran-10-enhanced MR imaging of the bone marrow before and after conditioning therapy in patients with non-Hodgkin lymphomas. *European Radiology*, **16** (3), 598–607.

223 Banati, R.B., Gehrmann, J., Schubert, P. and Kreutzberg, G.W. (1993) Cytotoxicity of microglia. *Glia*, **7** (1), 111–18.

224 Saleh, A., Schroeter, M., Jonkmanns, C., Hartung, H.P., Modder, U. and Jander, S. (2004) In vivo MRI of brain inflammation in human ischaemic stroke. *Brain*, **127**, 1670–7.

225 Dousset, V., Brochet, B., Deloire, M.S.A., Lagoarde, L., Barroso, B., Caille, J.M. and Petry, K.G. (2006) MR Imaging of relapsing multiple sclerosis patients using ultra-small-particle iron oxide and compared with gadolinium. *American Journal of Neuroradiology*, **27** (5), 1000–5.

226 Manninger, S.P., Muldoon, L.L., Nesbit, G., Murillo, T., Jacobs, P.M. and Neuwelt, E.A. (2005) An exploratory study of ferumoxtran-10 nanoparticles as a blood-brain barrier imaging agent targeting phagocytic cells in CNS inflammatory lesions. *American Journal of Neuroradiology*, **26** (9), 2290–300.

227 Varallyay, P., Nesbit, G., Muldoon, L.L., Nixon, R.R., Delashaw, J., Cohen, J.I., Petrillo, A., Rink, D. and Neuwelt, E.A. (2002) Comparison of two superparamagnetic viral-sized iron oxide particles ferumoxides and ferumoxtran-10 with a gadolinium chelate in imaging intracranial tumors. *American Journal of Neuroradiology*, **23** (4), 510–19.

228 Taschner, C.A., Wetzel, S.G., Tolnay, M., Froehlich, J., Merlo, A. and Radue, E.W. (2005) Characteristics of ultrasmall superparamagnetic iron oxides in patients with brain tumors. *American Journal of Roentgenology*, **185** (6), 1477–86.

229 Maier-Hauff, K., Rothe, R., Scholz, R., Gneveckow, U., Wust, P., Thiesen, B., Feussner, A., von Deimling, A., Waldoefner, N., Felix, R. and Jordan, A. (2007) Intracranial thermotherapy using magnetic nanoparticles combined with external beam radiotherapy: results of a feasibility study on patients with glioblastoma multiforme. *Journal of Neuro-Oncology*, **81** (1), 53–60.

230 Saeed, M., Wendland, M.F. and Higgins, C.B. (2000) Blood pool MR contrast agents for cardiovascular imaging. *Journal of Magnetic Resonance Imaging*, **12** (6), 890–8.

231 Hamoudeh, M., Al Faraj, A., Canet-Soulas, E., Bessueille, F., Leonard, D. and Fessi, H. (2007) Elaboration of PLLA-based superparamagnetic nanoparticles: characterization, magnetic behaviour study and in vitro relaxivity evaluation. *International Journal of Pharmaceutics*, **338** (1–2), 248–57.

232 Bjornerud, A. and Johansson, L. (2004) The utility of superparamagnetic contrast agents in MRI: theoretical consideration and applications in the cardiovascular system. *NMR in Biomedicine*, **17** (7), 465–77.

233 Simonsen, C.Z., Ostergaard, L., Vestergaard-Poulsen, P., Rohl, L., Bjornerud, A. and Gyldensted, C. (1999) CBF and CBV measurements by USPIO bolus tracking: reproducibility and comparison with Gd-based values. *Journal of Magnetic Resonance Imaging*, **9** (2), 342–7.

234 Stillman, A.E., Wilke, N. and Jerosch-Herold, M. (1997) Use of an intravascular T1 contrast agent to improve MR cine myocardial-blood pool definition in men. *Journal of Magnetic Resonance Imaging*, **7** (4), 765–7.

235 Stillman, A.E., Wilke, N., Li, D.B., Haacke, E.M. and McLachlan, S. (1996) Ultrasmall superparamagnetic iron oxide to enhance MRA of the renal and coronary arteries: studies in human patients. *Journal of Computer-Assisted Tomography*, **20** (1), 51–5.

236 Mayo-Smith, W.W., Saini, S., Slater, G., Kaufman, J.A., Sharma, P. and Hahn, P.F. (1996) NIR contrast material for vascular enhancement: value of superparamagnetic iron oxide. *American Journal of Roentgenology*, **166** (1), 73–7.

237 Reimer, P., Bremer, C., Allkemper, T., Engelhardt, M., Mahler, M., Ebert, W. and Tombach, B. (2004) Myocardial perfusion and MR angiography of chest with SHU555C: results of placebo controlled clinical phase I study. *Radiology*, **231** (2), 474–81.

238 Smith, B.R., Heverhagen, J., Knopp, M., Schmalbrock, P., Shapiro, J., Shiomi, M., Moldovan, N.I., Ferrari, M. and Lee, S.C. (2007) Localization to atherosclerotic plaque and biodistribution of biochemically derivatized superparamagnetic iron oxide nanoparticles (SPIONs) contrast particles for magnetic resonance imaging (MRI). *Biomedical Microdevices*, **9** (5), 719–27.

239 Kooi, M.E., Cappendijk, V.C., Cleutjens, K., Kessels, A.G.H., Kitslaar, P., Borgers, M., Frederik, P.M., Daemen, M. and van Engelshoven, J.M.A. (2003) Accumulation of ultrasmall superparamagnetic particles of iron oxide in human atherosclerotic plaques can be detected by in vivo magnetic resonance imaging. *Circulation*, **107** (19), 2453–8.

240 Howarth, S., Im, J.U.K., Trivedi, R., Graves, M.J., Brown, A., Kirkpatrick, P.J. and Gillard, J.H. (2006) Noninvasive determination of macrophage burden in asymptomatic carotid atheroma: a USPIO enhanced MR imaging study. *Stroke*, **37** (2), 650.

241 Trivedi, R.A., U-King-Im, J.M., Graves, M.J., Cross, J.J., Horsley, J., Goddard, M.J., Skepper, J.N., Quartey, G., Warburton, E., Joubert, I., Wang, L.Q., Kirkpatrick, P.J., Brown, J. and Gillard, J.H. (2004) In vivo detection of macrophages in human carotid atheroma–temporal dependence of ultrasmall superparamagnetic particles of iron oxide-enhanced MRI. *Stroke*, **35** (7), 1631–5.

242 Rogers, W.J., Meyer, C.H. and Kramer, C.M. (2006) Technology insight: in vivo cell tracking by use of MRI. *Nature Clinical Practice. Cardiovascular Medicine*, **3** (10), 554–62.

243 Frank, J.A., Anderson, S.A., Kalsih, H., Jordan, E.K., Lewis, B.K., Yocum, G.T. and Arbab, A.S. (2004) Methods for magnetically labeling stem and other cells for detection by in vivo magnetic resonance imaging. *Cytotherapy*, **6** (6), 621–5.

244 Bulte, J.W.M. and Kraitchman, D.L. (2004) Monitoring cell therapy using iron oxide MR contrast agents. *Current Pharmaceutical Biotechnology*, **5** (6), 567–84.

245 Heyn, C., Ronald, J.A., Mackenzie, L.T., MacDonald, I.C., Chambers, A.F., Rutt, B.K. and Foster, P.J. (2006) In vivo magnetic resonance imaging of single cells in mouse brain with optical validation. *Magnetic Resonance in Medicine*, **55** (1), 23–9.

246 Rogers, W.J. and Basu, P. (2005) Factors regulating macrophage endocytosis of nanoparticles: implications for targeted magnetic

resonance plaque imaging. *Atherosclerosis*, **178** (1), 67–73.

247 Billotey, C., Wilhelm, C., Devaud, M., Bacri, J.C., Bittoun, J. and Gazeau, F. (2003) Cell internalization of anionic maghemite nanoparticles: quantitative effect on magnetic resonance imaging. *Magnetic Resonance in Medicine*, **49** (4), 646–54.

248 Wiart, M., Davoust, N., Pialat, J.B., Desestret, V., Moucharaffie, S., Cho, T.H., Mutin, M., Langlois, J.B., Beuf, O., Honnorat, J., Nighoghossian, N. and Berthezene, Y. (2007) MRI monitoring of neuroinflammation in mouse focal ischemia. *Stroke*, **38** (1), 131–7.

249 Korosoglou, G., Weiss, R.G., Kedziorek, D.A., Walczak, P., Gilson, W.D., Schar, M., Sosnovik, D.E., Kraitchman, D.L., Boston, R.C., Bulte, J.W.M., Weissleder, R. and Stuber, M. (2008) Noninvasive detection of macrophage-rich atherosclerotic plaque in hyperlipidemic rabbits using "positive contrast" magnetic resonance imaging. *Journal of the American College of Cardiology*, **52** (6), 483–91.

250 Kalambur, V.S., Longmire, E.K. and Bischof, J.C. (2007) Cellular level loading and heating of superparamagnetic iron oxide nanoparticles. *Langmuir*, **23** (24), 12329–36.

251 Ko, I.K., Song, H.T., Cho, E.J., Lee, E.S., Huh, Y.M. and Suh, J.S. (2007) In vivo MR imaging of tissue-engineered human mesenchymal stem cells transplanted to mouse: a preliminary study. *Annals of Biomedical Engineering*, **35** (1), 101–8.

252 Terrovitis, J.V., Bulte, J.W.M., Sarvananthan, S., Crowe, L.A., Sarathchandra, P., Batten, P., Sachlos, E., Chester, A.H., Czernuszka, J.T., Firmin, D.N., Taylor, P.M. and Yacoub, M.H. (2006) Magnetic resonance imaging of ferumoxide-labeled mesenchymal stem cells seeded on collagen scaffolds – relevance to tissue engineering. *Tissue Engineering*, **12** (10), 2765–75.

253 Ju, S.H., Teng, G.J., Zhang, Y., Ma, M., Chen, F. and Ni, Y.C. (2006) In vitro labeling and MRI of mesenchymal stem cells from human umbilical cord blood. *Magnetic Resonance Imaging*, **24** (5), 611–17.

254 Ittrich, H., Lange, C., Togel, F., Zander, A.R., Dahnke, H., Westenfelder, C., Adam, G. and Nolte-Ernsting, C. (2007) In vivo magnetic resonance imaging of iron oxide-labeled, arterially-injected mesenchymal stem cells in kidneys of rats with acute ischemic kidney injury: detection and monitoring at 3T. *Journal of Magnetic Resonance Imaging*, **25** (6), 1179–91.

255 Omidkhoda, A., Mozdarani, H., Movasaghpoor, A. and Fatholah, A.A.P. (2007) Study of apoptosis in labeled mesenchymal stem cells with superparamagnetic iron oxide using neutral comet assay. *Toxicology In Vitro*, **21** (6), 1191–6.

256 Jing, X.H., Yang, L., Duan, X.J., Xie, B., Chen, W., Li, Z. and Tan, H.B. (2008) In vivo MR imaging tracking of magnetic iron oxide nanoparticle labeled, engineered, autologous bone marrow mesenchymal stem cells following intra-articular injection. *Joint, Bone, Spine*, **75** (4), 432–8.

257 Sun, J.H., Teng, G.J., Ju, S.H., Ma, Z.L., Mai, X.L. and Ma, M. (2008) MR tracking of magnetically labeled mesenchymal stem cells in rat kidneys with acute renal failure. *Cell Transplantation*, **17** (3), 279–90.

258 Heymer, A., Haddad, D., Weber, M., Gbureck, U., Jakob, P.M., Eulert, J. and Noth, U. (2008) Iron oxide labelling of human mesenchymal stem cells in collagen hydrogels for articular cartilage repair. *Biomaterials*, **29** (10), 1473–83.

259 Wang, F.H., Lee, I.H., Holmstrom, N., Yoshitake, T., Kim, D.K., Muhammed, M., Frisen, J., Olson, L., Spenger, C. and Kehr, J. (2006) Magnetic resonance tracking of nanoparticle labelled neural stem cells in a rat's spinal cord. *Nanotechnology*, **17** (8), 1911–15.

260 Amsalem, Y., Mardor, Y., Feinberg, M.S., Landa, N., Miller, L., Daniels, D., Ocherashvilli, A., Holbova, R., Yosef, O., Barbash, I.M. and Leor, J. (2007) Iron-oxide labeling and outcome of transplanted mesenchymal stem cells in

the infarcted myocardium. *Circulation*, **116** (11), I38–45.

261 Guzman, R., Uchida, N., Bliss, T.M., He, D.P., Christopherson, K.K., Stellwagen, D., Capela, A., Greve, J., Malenka, R.C., Moseley, M.E., Palmer, T.D. and Steinberg, G.K. (2007) Long-term monitoring of transplanted human neural stem cells in developmental and pathological contexts with MRI. *Proceedings of the National Academy of Sciences of the United States of America*, **104** (24), 10211–16.

262 Hoehn, M., Kustermann, E., Blunk, J., Wiedermann, D., Trapp, T., Wecker, S., Focking, M., Arnold, H., Hescheler, J., Fleischmann, B.K., Schwindt, W. and Buhrle, C. (2002) Monitoring of implanted stem cell migration in vivo: a highly resolved in vivo magnetic resonance imaging investigation of experimental stroke in rat. *Proceedings of the National Academy of Sciences of the United States of America*, **99** (25), 16267–72.

263 Berry, C.C., Wells, S., Charles, S. and Curtis, A.S.G. (2003) Dextran and albumin derivatised iron oxide nanoparticles: influence on fibroblasts in vitro. *Biomaterials*, **24** (25), 4551–7.

264 Sun, R., Dittrich, J., Le-Huu, M., Mueller, M.M., Bedke, J., Kartenbeck, J., Lehmann, W.D., Krueger, R., Bock, M., Huss, R., Seliger, C., Grone, H.J., Misselwitz, B., Semmler, W. and Kiessling, F. (2005) Physical and biological characterization of superparamagnetic iron oxide- and ultrasmall superparamagnetic iron oxide-labeled cells–a comparison. *Investigative Radiology*, **40** (8), 504–13.

265 Pawelczyk, E., Arbab, A.S., Chaudhry, A., Balakumaran, A., Robey, P.G. and Frank, J.A. (2008) In vitro model of bromodeoxyuridine or iron oxide nanoparticle uptake by activated macrophages from labeled stem cells: implications for cellular therapy. *Stem Cells*, **26** (5), 1366–75.

266 Baumjohann, D., Hess, A., Budinsky, L., Brune, K., Schuler, G. and Lutz, M.B. (2006) In vivo magnetic resonance imaging of dendritic cell migration into the draining lymph nodes of mice. *European Journal of Immunology*, **36** (9), 2544–55.

267 Ahrens, E.T., Feili-Hariri, M., Xu, H., Genove, G. and Morel, P.A. (2003) Receptor-mediated endocytosis of iron-oxide particles provides efficient labeling of dendritic cells for in vivo MR imaging. *Magnetic Resonance in Medicine*, **49** (6), 1006–13.

268 Perea, H., Aigner, J., Heverhagen, J.T., Hopfner, U. and Wintermantel, E. (2007) Vascular tissue engineering with magnetic nanoparticles: seeing deeper. *Journal of Tissue Engineering and Regenerative*, **1** (4), 318–21.

269 Bulte, J.W.M., Zhang, S.C., van Gelderen, P., Herynek, V., Jordan, E.K., Duncan, I.D. and Frank, J.A. (1999) Neurotransplantation of magnetically labeled oligodendrocyte progenitors: magnetic resonance tracking of cell migration and myelination. *Proceedings of the National Academy of Sciences of the United States of America*, **96** (26), 15256–61.

270 Koch, A.M., Reynolds, F., Kircher, M.F., Merkle, H.P., Weissleder, R. and Josephson, L. (2003) Uptake and metabolism of a dual fluorochrome tat-nanoparticle in HeLa cells. *Bioconjugate Chemistry*, **14** (6), 1115–21.

271 Zhao, M., Kircher, M.F., Josephson, L. and Weissleder, R. (2002) Differential conjugation of tat peptide to superparamagnetic nanoparticles and its effect on cellular uptake. *Bioconjugate Chemistry*, **13** (4), 840–4.

272 Josephson, L., Tung, C.H., Moore, A. and Weissleder, R. (1999) High-efficiency intracellular magnetic labeling with novel superparamagnetic-tat peptide conjugates. *Bioconjugate Chemistry*, **10** (2), 186–91.

273 Hilger, I., Trost, R., Reichenbach, J.R., Linss, W., Lisy, M.R., Berndt, A. and Kaiser, W.A. (2007) MR imaging of Her-2/neu protein using magnetic nanoparticles. *Nanotechnology*, **18** (13), article 135103.

274 Zhang, Y., Kohler, N. and Zhang, M.Q. (2002) Surface modification of superparamagnetic magnetite

nanoparticles and their intracellular uptake. *Biomaterials*, **23** (7), 1553–61.

275 Stella, B., Arpicco, S., Peracchia, M.T., Desmaele, D., Hoebeke, J., Renoir, M., D'Angelo, J., Cattel, L. and Couvreur, P. (2000) Design of folic acid-conjugated nanoparticles for drug targeting. *Journal of Pharmaceutical Sciences*, **89** (11), 1452–64.

276 Kohler, N., Sun, C., Wang, J. and Zhang, M.Q. (2005) Methotrexate-modified superparamagnetic nanoparticles and their intracellular uptake into human cancer cells. *Langmuir*, **21** (19), 8858–64.

277 Smirnov, P., Lavergne, E., Gazeau, F., Lewin, M., Boissonnas, A., Doan, B.T., Gillet, B., Combadiere, C., Combadiere, B. and Clement, O. (2006) In vivo cellular imaging of lymphocyte tracking by MRI: a tumor model approach to cell-based anticancer therapy. *Magnetic Resonance in Medicine*, **56** (3), 498–508.

278 Rad, A.M., Arbab, A.S., Iskander, A.S.M., Jiang, Q. and Soltanian-Zadeh, H. (2007) Quantification of superparamagnetic iron oxide (SPIO)-labeled cells using MRI. *Journal of Magnetic Resonance Imaging*, **26** (2), 366–74.

279 Lanza, G.M., Winter, P.M., Caruthers, S.D., Morawski, A.M., Schmieder, A.H., Crowder, K.C. and Wickline, S.A. (2004) Magnetic resonance molecular imaging with nanoparticles. *Journal of Nuclear Cardiology*, **11** (6), 733–43.

280 Bulte, J.W.M. and Kraitchman, D.L. (2004) Iron oxide MR contrast agents for molecular and cellular imaging. *NMR in Biomedicine*, **17** (7), 484–99.

281 Schmieder, A.H., Winter, P.M., Caruthers, S.D., Harris, T.D., Williams, T.A., Allen, J.S., Lacy, E.K., Zhang, H.Y., Scott, M.J., Hu, G., Robertson, J.D., Wickline, S.A. and Lanza, G.M. (2005) Molecular MR imaging of melanoma angiogenesis with alpha(nu)beta(3)-targeted paramagnetic nanoparticles. *Magnetic Resonance in Medicine*, **53** (3), 621–7.

282 Winter, P.M., Caruthers, S.D., Kassner, A., Harris, T.D., Chinen, L.K., Allen, J.S., Lacy, E.K., Zhang, H.Y., Robertson, J.D., Wickline, S.A. and Lanza, G.M. (2003) Molecular imaging of angiogenesis in nascent vx-2 rabbit tumors using a novel alpha(v)beta(3)-targeted nanoparticle and 1.5 tesla magnetic resonance imaging. *Cancer Research*, **63** (18), 5838–43.

283 Xie, J., Chen, K., Lee, H.Y., Xu, C.J., Hsu, A.R., Peng, S., Chen, X.Y. and Sun, S.H. (2008) Ultrasmall c(RGDyK)-coated Fe_3O_4 nanoparticles and their specific targeting to integrin alpha(v) beta(3)-rich tumor cells. *Journal of the American Chemical Society*, **130** (24), 7542–3.

284 Lee, J.H., Huh, Y.M., Jun, Y., Seo, J., Jang, J., Song, H.T., Kim, S., Cho, E.J., Yoon, H.G., Suh, J.S. and Cheon, J. (2007) Artificially engineered magnetic nanoparticles for ultra-sensitive molecular imaging. *Nature Medicine*, **13** (1), 95–9.

285 Suwa, T., Ozawa, S., Ueda, M., Ando, N. and Kitajima, M. (1998) Magnetic resonance imaging of esophageal squamous cell carcinoma using magnetite particles coated with anti-epidermal growth factor receptor antibody. *International Journal of Cancer*, **75** (4), 626–34.

286 Lee, J., Yang, J., Ko, H., Oh, S.J., Kang, J., Son, J.H., Lee, K., Lee, S.W., Yoon, H.G., Suh, J.S., Huh, Y.M. and Haam, S. (2008) Multifunctional magnetic gold nanocomposites: human epithelial cancer detection via magnetic resonance imaging and localized synchronous therapy. *Advanced Functional Materials*, **18** (2), 258–64.

287 Tiefenauer, L.X., Kuhne, G. and Andres, R.Y. (1993) Antibody magnetite nanoparticles – in-vitro characterization of a potential tumor-specific contrast agent for magnetic-resonance-imaging. *Bioconjugate Chemistry*, **4** (5), 347–52.

288 Kumagai, M., Imai, Y., Nakamura, T., Yamasaki, Y., Sekino, M., Ueno, S., Hanaoka, K., Kikuchi, K., Nagano, T., Kaneko, E., Shimokado, K. and Kataoka, K. (2007) Iron hydroxide nanoparticles coated with poly(ethylene glycol)-poly(aspartic acid) block copolymer as novel magnetic resonance contrast agents for in vivo cancer imaging.

Colloids and Surfaces. B, Biointerfaces, **56** (1–2), 174–81.

289 Swanson, S.D., Kukowska-Latallo, J.F., Patri, A.K., Chen, C.Y., Ge, S., Cao, Z.Y., Kotlyar, A., East, A.T. and Baker, J.R. (2008) Targeted gadolinium-loaded dendrimer nanoparticles for tumor-specific magnetic resonance contrast enhancement. *International Journal of Nanomedicine*, **3** (2), 201–10.

290 Fortina, P., Kricka, L.J., Graves, D.J., Park, J., Hyslop, T., Tam, F., Halas, N., Surrey, S. and Waldman, S.A. (2007) Applications of nanoparticles to diagnostics and therapeutics in colorectal cancer. *Trends in Biotechnology*, **25** (4), 145–52.

291 Sunderland, C.J., Steiert, M., Talmadge, J.E., Derfus, A.M. and Barry, S.E. (2006) Targeted nanoparticles for detecting and treating cancer. *Drug Development Research*, **67** (1), 70–93.

292 Buxton, D.B. (2007) Nanotechnology in the diagnosis and management of heart, lung and blood diseases. *Expert Review of Molecular Diagnostics*, **7** (2), 149–60.

293 Weissleder, R., Lee, A.S., Khaw, B.A., Shen, T. and Brady, T.J. (1992) Antimyosin-labeled monocrystalline iron-oxide allows detection of myocardial infarct–MR antibody imaging. *Radiology*, **182** (2), 381–5.

294 Wu, E.X., Tang, H.Y., Wong, K.K. and Wang, J. (2004) Mapping cyclic change of regional myocardial blood volume using steady-state susceptibility effect of iron oxide nanoparticles. *Journal of Magnetic Resonance Imaging*, **19** (1), 50–8.

295 Sosnovik, D.E., Nahrendorf, M. and Weissleder, R. (2008) Magnetic nanoparticles for MR imaging: agents, techniques and cardiovascular applications. *Basic Research in Cardiology*, **103** (2), 122–30.

296 Winter, P.M., Morawski, A.M., Caruthers, S.D., Fuhrhop, R.W., Zhang, H.Y., Williams, T.A., Allen, J.S., Lacy, E.K., Robertson, J.D., Lanza, G.M. and Wickline, S.A. (2003) Molecular imaging of angiogenesis in early-stage atherosclerosis with alpha(v)beta(3)-integrin-targeted nanoparticles. *Circulation*, **108** (18), 2270–4.

297 Flacke, S., Fischer, S., Scott, M.J., Fuhrhop, R.J., Allen, J.S., McLean, M., Winter, P., Sicard, G.A., Gaffney, P.J., Wickline, S.A. and Lanza, G.M. (2001) Novel MRI contrast agent for molecular imaging of fibrin implications for detecting vulnerable plaques. *Circulation*, **104** (11), 1280–5.

298 Wickline, S.A., Neubauer, A.M., Winter, P.M., Caruthers, S.D. and Lanza, G.M. (2007) Molecular imaging and therapy of atherosclerosis with targeted nanoparticles. *Journal of Magnetic Resonance Imaging*, **25** (4), 667–80.

299 Morgul, M.H., Raschzok, N., Schwartlander, R., Vondran, F.W., Michel, R., Stelter, L., Pinkernelle, J., Jordan, A., Teichgraber, U. and Sauer, I.M. (2008) Tracking of primary human hepatocytes with clinical MRI: initial results with Tat-peptide modified superparamagnetic iron oxide particles. *The International Journal of Artificial Organs*, **31** (3), 252–7.

300 Park, B.H., Chang, Y.M., Lee, Y.J., Park, J.A., Kim, I.S., Bae, S.J., Lee, G.H., Kim, T.J., Kim, J.Y., Kim, H.J. and Jung, J.C. (2008) Targeting of membrane type 1-matrix metalloproteinase (MT1-MMP) using superparamagnetic nanoparticles in human liver cancer cells. *Colloids and Surfaces A: Physicochemical and Engineering Aspects*, **313**, 647–50.

301 Shieh, D.B., Cheng, F.Y., Su, C.H., Yeh, C.S., Wu, M.T., Wu, Y.N., Tsai, C.Y., Wu, C.L., Chen, D.H. and Chou, C.H. (2005) Aqueous dispersions of magnetite nanoparticles with NH3+ surfaces for magnetic manipulations of biomolecules and MRI contrast agents. *Biomaterials*, **26** (34), 7183–91.

302 Sundstrom, J.B., Mao, H., Santoianni, R., Villinger, F., Little, D.M., Huynh, T.T., Mayne, A.E., Hao, E. and Ansari, A.A. (2004) Magnetic resonance imaging of activated proliferating rhesus macaque T cells labeled with superparamagnetic monocrystalline iron oxide nanoparticles. *Journal of Acquired Immune Deficiency Syndromes*, **35** (1), 9–21.

303 Muldoon, L.L., Sandor, M., Pinkston, K.E. and Neuwelt, E.A. (2005) Imaging, distribution, and toxicity of superparamagnetic iron oxide magnetic resonance nanoparticles in the rat brain and intracerebral tumor. *Neurosurgery*, **57** (4), 785–96.

304 Wei, L., Zhou, G., Li, Z., He, L., Gao, M.Y., Tan, J.Q. and Lei, H. (2007) Detection of toxoplasmic lesions in mouse brain by USPIO-enhanced magnetic resonance imaging. *Magnetic Resonance Imaging*, **25** (10), 1442–8.

305 Peira, E., Marzola, P., Podio, V., Aime, S., Sbarbati, A. and Gasco, M.R. (2003) In vitro and in vivo study of solid lipid nanoparticles loaded with superparamagnetic iron oxide. *Journal of Drug Targeting*, **11** (1), 19–24.

306 Rousseau, V., Denizot, B., Pouliquen, D., Jallet, P. and LeJeune, J.J. (1997) Investigation of blood-brain barrier permeability to magnetite-dextran nanoparticles (MD3) after osmotic disruption in rats. *Magnetic Resonance Materials in Physics, Biology and Medicine*, **5** (3), 213–22.

307 Mykhaylyk, O., Cherchenko, A., Ilkin, A., Dudchenko, N., Ruditsa, V., Novoseletz, M. and Zozulya, Y. (2001) Glial brain tumor targeting of magnetite nanoparticles in rats. *Journal of Magnetism and Magnetic Materials*, **225** (1–2), 241–7.

308 Montet, X., Weissleder, R. and Josephson, L. (2006) Imaging pancreatic cancer with a peptide-nanoparticle conjugate targeted to normal pancreas. *Bioconjugate Chemistry*, **17** (4), 905–11.

309 Hogemann, D., Josephson, L., Weissleder, R. and Basilion, J.P. (2000) Improvement of MRI probes to allow efficient detection of gene expression. *Bioconjugate Chemistry*, **11** (6), 941–6.

310 Reynolds, P.R., Larkman, D.J., Haskard, D.O., Hajnal, J.V., Kennea, N.L., George, A.J.T. and Edwards, A.D. (2006) Detection of vascular expression of e-selectin in vivo with MR imaging. *Radiology*, **241** (2), 469–76.

311 Montet, X., Funovics, M., Montet-Abou, K., Weissleder, R. and Josephson, L. (2006) Multivalent effects of RGD peptides obtained by nanoparticle display. *Journal of Medicinal Chemistry*, **49** (20), 6087–93.

312 Montet, X., Montet-Abou, K., Reynolds, F., Weissleder, R. and Josephson, L. (2006) Nanoparticle imaging of integrins on tumor cells. *Neoplasia*, **8** (3), 214–22.

313 Josephson, L., Kircher, M.F., Mahmood, U., Tang, Y. and Weissleder, R. (2002) Near-infrared fluorescent nanoparticles as combined MR/optical imaging probes. *Bioconjugate Chemistry*, **13** (3), 554–60.

314 Aime, S., Barge, A., Castelli, D.D., Fedeli, F., Mortillaro, A., Nielsen, F.U. and Terreno, E. (2002) Paramagnetic lanthanide(III) complexes as pH-sensitive chemical exchange saturation transfer (CEST) contrast agents for MRI applications. *Magnetic Resonance in Medicine*, **47** (4), 639–48.

315 Shapiro, M.G., Atanasijevic, T., Faas, H., Westmeyer, G.G. and Jasanoff, A. (2006) Dynamic imaging with MRI contrast agents: quantitative considerations. *Magnetic Resonance Imaging*, **24** (4), 449–62.

316 Ittrich, H., Lange, C., Dahnke, H., Zander, A.R., Adam, G. and Nolte-Ernsting, C. (2005) Labeling of mesenchymal stem cells with different superparamagnetic particles of iron oxide and detectability with MRI at 3T. *Rofo-Fortschritte Gebiet Rontgenstrahlen Bildgebenden Verfah*, **177** (8), 1151–63.

317 Farrar, C.T., Dai, G.P., Novikov, M., Rosenzweig, A., Weissleder, R., Rosen, B.R. and Sosnovik, D.E. (2008) Impact of field strength and iron oxide nanoparticle concentration on the linearity and diagnostic accuracy of off-resonance imaging. *NMR in Biomedicine*, **21** (5), 453–63.

318 McDermott, R., Lee, S.K., ten Haken, B., Trabesinger, A.H., Pines, A. and Clarke, J. (2004) Microtesla MRI with a superconducting quantum interference device. *Proceedings of the National Academy of Sciences of the United States of America*, **101** (21), 7857–61.

319 Zotev, V.S., Matlachov, A.N., Volegov, P.L., Sandin, H.J., Espy, M.A., Mosher, J.C., Urbaitis, A.V., Newman, S.G. and

Kraus, R.H. (2008) Multi-sensor system for simultaneous ultra-low-field MRI and MEG. *Journal of Magnetic Resonance*, **194** (1), 115–20.

320 Kraus, R.H. Jr, Volegov, P., Matlachov, A. and Espy, M. (2008) Toward direct neural current imaging by resonant mechanisms at ultra-low field. *Neuroimage*, **39** (1), 310–17.

321 Kleinschnitz, C., Bendszus, T., Frank, M., Solymosi, T., Toyka, K.V. and Stoll, G. (2003) In vivo monitoring of macrophage infiltration in experimental ischemic brain lesions by magnetic resonance imaging. *Journal of Cerebral Blood Flow and Metabolism*, **23** (11), 1356–61.

322 Lewin, M., Carlesso, N., Tung, C.H., Tang, X.W., Cory, D., Scadden, D.T. and Weissleder, R. (2000) Tat peptide-derivatized magnetic nanoparticles allow in vivo tracking and recovery of progenitor cells. *Nature Biotechnology*, **18** (4), 410–14.

323 Taktak, S., Sosnovik, D., Cima, M.J., Weissfeder, R. and Josephson, L. (2007) Multiparameter magnetic relaxation switch assays. *Analytical Chemistry*, **79** (23), 8863–9.

324 Sosnovik, D.E., Schellenberger, E.A., Nahrendorf, M., Novikov, M.S., Matsui, T., Dai, G., Reynolds, F., Grazette, L., Rosenzweig, A., Weissleder, R. and Josephson, L. (2005) Magnetic resonance imaging of cardiomyocyte apoptosis with a novel magneto-optical nanoparticle. *Magnetic Resonance in Medicine*, **54** (3), 718–24.

325 Zabow, G., Dodd, S., Moreland, J. and Koretsky, A. (2008) Micro-engineered local field control for high-sensitivity multispectral MRI. *Nature*, **453** (7198), 1058-U2.

326 Jordan, A., Scholz, R., Wust, P., Fahling, H. and Felix, R. (1998) Magnetic fluid hyperthermia (MFH): Cancer treatment with AC magnetic field induced excitation of biocompatible superparamagnetic nanoparticles. 8th International Conference on Magnetic Fluids (ICMF), Timisoara, Romania, June 29–July 3, 1998. Timisoara, Romania, pp. 413–19.

327 Viroonchatapan, E., Sato, H., Ueno, M., Adachi, I., Tazawa, K. and Horikoshi, I. (1997) Release of 5-fluorouracil from thermosensitive magnetoliposomes induced by an electromagnetic field. *Journal of Controlled Release*, **46** (3), 263–71.

328 Brusentsov, N.A., Brusentsova, T.N., Filinova, E.Y., Jurchenko, N.Y., Kupriyanov, D.A., Pirogov, Y.A., Dubina, A.I., Shumskikh, M.N., Shumakov, L.I., Anashkina, E.N., Shevelev, A.A. and Uchevatkin, A.A. (2007) Magnetohydrodynamic thermochemotherapy and MRI of mouse tumors. *Journal of Magnetism and Magnetic Materials*, **311** (1), 176–80.

329 Klostergaard, J., Bankson, J., Auzenne, E., Gibson, D., Yuill, W. and Seeney, C.E. (2007) Magnetic vectoring of magnetically responsive nanoparticles within the murine peritoneum. *Journal of Magnetism and Magnetic Materials*, **311** (1), 330–5.

330 Kim, J., Lee, J.E., Lee, S.H., Yu, J.H., Lee, J.H., Park, T.G. and Hyeon, T. (2008) Designed fabrication of a multifunctional polymer nanomedical platform for simultaneous cancer-targeted imaging and magnetically guided drug delivery. *Advanced Materials*, **20** (3), 478–83.

331 Jurgons, R., Seliger, C., Hilpert, A., Trahms, L., Odenbach, S. and Alexiou, C. (2006) Drug loaded magnetic nanoparticles for cancer therapy. *Journal of Physics – Condensed Matter*, **18** (38), S2893–902.

332 Hanessian, S., Grzyb, J.A., Cengelli, F. and Juillerat-Jeanneret, L. (2008) Synthesis of chemically functionalized superparamagnetic nanoparticles as delivery vectors for chemotherapeutic drugs. *Bioorganic and Medicinal Chemistry*, **16** (6), 2921–31.

333 Medarova, Z., Pham, W., Farrar, C., Petkova, V. and Moore, A. (2007) In vivo imaging of siRNA delivery and silencing in tumors. *Nature Medicine*, **13** (3), 372–7.

Keywords

magnetic nanoparticles; magnetic resonance imaging; iron oxide nanoparticles; USPIO; clinical applications; molecular imaging; cellular labeling

5
Magnetic Nanomaterials for *In Vivo* and *In Vitro* Cancer Diagnostics

Kelly Y. Kim

5.1
Introduction

Magnetic nanoparticles were first introduced as magnetic resonance imaging (MRI) contrast agents during the late 1980s. Since that time, contrast agents such as GastroMARK® (ferumoxsil), an oral MRI agent used for gastrointestinal tract imaging, and Feridex® (ferumoxide), which is also known as ferumoxide, an MRI agent for the detection of liver lesions, have become commercially available, while superparamagnetic iron oxides (SPIOs) as MRI contrast agents have also paved the way for the application of magnetic nanoparticles in current clinical practice. The surge of interest in nanotechnology during the recent years has significantly expanded the breadth of research on magnetic nanoparticles. This has led not only to their utility being optimized for *in vivo* cancer diagnostics, but also to explorations of their application as multifunctional agents, where they serve simultaneously as carriers for targeted chemotherapy delivery and as MRI contrast agents for real-time monitoring of drug distribution to target sites. In addition, they may be used to follow the effects of therapy on the progression of a disease.

The use of magnetic nanoparticles for *in vivo* diagnostics – that is, for imaging – has been well established (as noted in Chapter 4); consequently, in this chapter we will describe the advantages imparted by nanoparticles as compared to gadolinium (Gd) chelates, which currently are the most widely used MRI contrast agents. More importantly, multifunctional magnetic nanoparticles are actively being developed for the monitoring of treatment responses via *in vivo* imaging, and some of these state-of-the-art advances are described in this chapter.

Today, tremendous progress is also being made on new strategies for incorporating magnetic nanoparticles into *in vitro* molecular diagnostics. The major goals for *in vitro* diagnostics are to exploit the unique properties of magnetic nanoparticles to develop assays that are rapid, simple to perform, and cost-effective; and then to fabricate these assay platforms into devices with nanoscale components that are portable. From the perspective of point-of-care diagnostics, there is great interest in developing miniaturized "lab-on-a-chip" devices that combine

Nanomaterials for the Life Sciences Vol. 4: Magnetic Nanomaterials. Edited by Challa S. S. R. Kumar

ISBN: 978-3-527-32154-4

microfluidics with magnetic nanosensors. There are myriad challenges to the successful development of diagnostic assays with high sensitivity and specificity, and robust performance characteristics. The fundamental challenges include an ability to detect low-expression cancer biomarkers in complex biological samples, and to accurately and precisely quantitate the levels of these analytes.

Advances are continually being made in nanotechnology that will enable us to engineer precisely the critical features of magnetic nanoparticles, such as their composition, size, and surface chemistry. In this chapter, we review some of the most recent research and development efforts to optimize the biomedical application of magnetic nanoparticles. The text does not delve into the specific chemical reactions involved in the synthesis protocols, but rather focuses on the design schemes for the magnetic nanoparticle platforms to improve their functionality.

In order to facilitate an understanding of the unique opportunities afforded by magnetic nanoparticles for biomedical application, the chapter begins with a brief overview of the fundamental concepts of magnetism and the physicochemical properties of magnetic nanoparticles, as well as the principles behind magnetic resonance. Subsequently, the challenges of magnetic nanoparticle design for systemic administration and the progress that is being made to overcome those challenges are discussed. Finally, several technological developments in magnetic nanoparticle-based platforms for *in vitro* molecular diagnostics are highlighted.

5.2
Physico-Chemical Properties of Magnetic Nanoparticles

When placed in an applied magnetic field with strength H, materials exhibit an induced magnetization M characterized by $M = \chi H$, where χ is the magnetic susceptibility. Materials with magnetic moments aligned parallel to H and susceptibilities on the order of 10^{-6} to 10^{-1} are described as paramagnetic. At very small sizes (usually <50 nm), iron oxide nanoparticles [typically magnetite (Fe_3O_4) or maghemite (γ-Fe_2O_3) nanocrystals with the oxygen ions forming a cubic lattice with iron cations located at the interstices] exhibit unique magnetic properties through quantum tunneling of magnetization, which gives rise to a single magnetic domain behavior and one large magnetic moment. As a result of the alignment of electron spins in the single domain, the individual magnetic dipole moments of ferromagnetic nanoparticles are several orders of magnitude larger than those of paramagnetic materials and, hence, exhibit superparamagnetism. That is, the coupling interactions between the electrons within these single magnetic domains result in much higher magnetic susceptibilities than those of paramagnetic materials. Thus, a relatively weak magnetic field – for example, 35 Gauss – would be sufficient to align the dipole moments of superparamagnetic nanoparticles to form essentially a large dipole magnet while the field is turned on.

When the external magnetic field is turned off, however, superparamagnetic nanoparticles revert to their normally random orientations due to the thermal activity involving free rotation of the particles. This results in a loss of net magnetization when the external field is removed, and the superparamagnetic property is marked by this lack of remnant magnetization. When superparamagnetic nanoparticles are bound, for example to cells, they become hindered in their ability to rotate and are unable to disorient very rapidly via the Brownian mechanism. Hence, there is a strong difference in the persistence of the induced magnetic field (i.e., remnant magnetization) between the bound and unbound superparamagnetic nanoparticles, and this property is exploited in molecular imaging applications to produce a better contrast between nanoparticles that have attached to cancer cells compared to those that are circulating freely in the body. The magnetic characteristics of a particle can alternate between ferromagnetic and superparamagnetic behavior for a given field and, as already noted, would be dependent on the particle size. This means that it would be necessary to limit the size distribution of the particles in nanoparticle production to ensure a homogeneous magnetic response to a given field.

Although superparamagnetism is a desirable property of nanoparticles, the reduction in particle size is not without some challenges. As the particle size decreases, the surface-to-volume ratio will increases, and this results in pronounced surface effects, such as noncollinear spins, spin canting, and spin-glass-like behavior, which can significantly impact upon the magnetic property of the material [1]. Furthermore, significant differences in magnetic property can be observed with magnetic nanoparticles generated through different chemical synthesis processes, due to the incorporation of impurities that may disrupt the crystal structure, as well as different degrees of order in the crystal structure resulting from different surface curvature (e.g., a higher surface curvature causes a more disordered crystal structure).

5.3
Surface Coating for Improved Biocompatibility and Bioavailability

Surface coating is an integral component of all magnetic nanoparticles for biomedical applications. Since magnetic nanoparticles have a tendency to aggregate as a result of their high surface energy, surface coating becomes necessary to inhibit nanoparticle aggregation. Surface coating is also needed to render the nanoparticles water-soluble, as well as enable their functionalization – that is, their conjugation with biomolecules, ligands, or probes. Finally, most nanoparticles, including magnetic nanoparticles, are subject to opsonization (the adsorption of plasma proteins onto the nanoparticle surface) as the first step in their clearance by the reticuloendothelial system (RES); this not only compromises their efficacy but also raises a major challenge for their intravenous administration.

In order to help nanoparticles evade uptake by the RES, and thus maintain a long plasma half-life so as to increase their likelihood of reaching the target tissues,

several techniques such as coating with nonfouling polymers have been employed. ("nonfouling" or "antifouling" means resistant to protein adsorption.) Polymeric coatings also provide a steric barrier to prevent nanoparticle aggregation, and a means to tailor the surface properties of magnetic nanoparticles for functionalization. Moreover, the nature of the chemical properties of the polymer (e.g., hydrophilicity/hydrophobicity), its length or molecular weight, its conformation, the manner in which the polymer was attached (e.g., electrostatic, covalent bonding), and the degree of particle surface coverage are all factors that can affect the performance of the magnetic nanoparticle.

Two of the most widely utilized polymer coatings for *in vivo* applications have been the polysaccharide dextran and poly(ethylene glycol) (PEG). The antifouling nature of PEG has been shown to reduce nanoparticle uptake by macrophages and extend its blood circulation time [2, 3]. In order to control polymer conformation and enable stable covalent linkages to the surface of iron oxide nanoparticles, Kohler *et al*. recently developed bifunctional PEG silanes capable of forming self-assembled monolayers that increase the packing density of the polymer chains onto the nanoparticles surface [4].

Various monomeric species, such as bisphosphonates [5], dimercaptosuccinic acid (DMSA) [6] and alkoxysilanes [7], have also been evaluated for their ability to facilitate the attachment of polymer coatings onto magnetic nanoparticles, as well as their ability to ensure biosafety. For example, the use of cobalt ferrites and nickel ferrites has been explored recently for *in vivo* biomedical applications, despite the known toxicities of these elements. In assessing the effectiveness of polymer coating over the $CoFe_2O_4$ to prevent leakage of the toxic cobalt component, Baldi *et al*. tested 5 nm particles coated with mono- and difunctional phosphonic and hydroxamic acids for cobalt leakage, and found the level of leakage to correspond with the quality of surface coverage by the attached ligand [8].

Very recently, Jain *et al*. developed and evaluated a novel formulation of magnetic nanoparticles in which the iron oxide core was first coated with oleic acid and then stabilized with pluronic F-127 to form a water-dispersible system [9]. The hydrodynamic diameter of these nanoparticles ranged from 210–250 nm. When the authors investigated the ability of their formulation for simultaneous MRI and delivery of chemotherapeutic drugs, they showed that it was feasible to incorporate either a single drug (doxorubicin or paclitaxel) or a combination of drugs (doxorubicin and paclitaxel) into their magnetic nanoparticles with high efficiency (74–95%). It was also found that the combination of drugs in magnetic nanoparticles produced synergistic antiproliferative effects in breast cancer cell culture studies and, most importantly, that the incorporated drugs did not adversely influence the magnetic and imaging properties of the magnetic nanoparticles *in vivo*. Consequently, it was possible to measure the circulation half-life of the magnetic nanoparticles by following changes in MRI signal intensity in the carotid arteries in a mouse model. In fact, when these authors compared the imaging properties of their nanoparticles to those of Feridex (100 nm), they showed the T_2 relaxivity to be higher for the oleic acid-coated, pluronic-stabilized magnetic nanoparticles

than for Feridex, while the T_1 relaxivity was better for Feridex, suggesting a greater sensitivity of their magnetic nanoparticle in T_2-weighted imaging.

A variety of processes are available for coating nanoparticles, including *in situ* coating (i.e., coated during the synthesis process) and post-synthesis coating. The coating can further be crosslinked chemically to increase its stability, and this crosslinking approach is frequently used to produce dextran-coated SPIO nanoparticles that are both biocompatible and water-miscible. Polymer coating usually involves post-synthesis coating methods, although recent studies have explored ways of coating with polymers or copolymers *in situ* [10, 11]. This type of process, which is sometimes referred to as the "one-pot synthesis" method, has several advantages over other methods, including a reduced aggregation because the particles are coated immediately and there are fewer processing procedures. However, the presence of polymers during nanocrystal nucleation and growth can cause imperfections on the crystal structure and morphology of the magnetic nanoparticles obtained through these processes, which could in turn significantly compromise their magnetic properties.

One of the challenges with polymer chemistry is that it needs to be compatible with the material that it encapsulates, particularly if the nanoparticles are biodrug- or protein-loaded, and also with the types of ligand that are to be attached to the surface. This is not simple or straightforward, however. Encapsulation efficiency is not great or consistent for all methods, and the ability to control the thickness of the coating and limit the size of the nanoparticles to just tens of nanometers may not always be feasible.

One state-of-the-art technology for the synthesis of nanocapsules involves electrohydrodynamic (EHD) technology [12, 13]. The EHD encapsulation process involves pumping nanoparticle components as fluids via coaxially arranged capillaries/needles across a high-voltage region onto a collector surface. The action of the electric field and rapid solvent evaporation between the fluid ejection nozzle and the collector electrode cause the electrosprayed liquids to form polymeric nanocapsules. The advantage of EHD technology over conventional encapsulation strategies is that it is possible to control shell thickness and shell porosity.

The use of biocompatible silica or gold is also widespread in the encapsulation of magnetic nanoparticles for developing MRI contrast agents. These inert shells serve to both protect against chemical degradation of the magnetic cores and prevent the release of potentially toxic components from the core. In addition, the use of alkoxysilanes such as 3-aminopropyltriethyoxysilane (APS) allows surface-reactive groups to be easily added to these shell structures for functionalization with specific targeting agents and other ligands. Recently, Ma *et al.* described a multifunctional magnetic nanoparticle composed of iron oxide cores of approximately 10 nm, surrounded by a shell of SiO_2 which was 10–15 nm thick [14]. In these studies, an organic dye was doped inside a second silica shell to create a superparamagnetic nanoparticle with luminescent properties for application in biomedical imaging.

5.4 MRI for *In Vivo* Diagnostics

5.4.1 Principles of MRI

MRI is a powerful *in vivo* imaging modality for cancer detection and diagnosis. The technique is based on the property that hydrogen protons will align themselves according to an applied magnetic field, B_0. A radiofrequency (RF) pulse sequence is applied perpendicular to the applied magnetic field, and the net magnetic moment of the protons that are perturbed from B_0 is measured when the pulse sequence ends. The process through which these protons return to their original state after the pulse sequence is referred to as relaxation. The relaxation of the proton is measured by coils in the MR scanner, whereupon longitudinal relaxation (T_1-recovery) and transverse relaxation (T_2-decay) times are acquired to generate an MR image. Local variation in relaxation due to variations in the chemical and physical nature of the tissues within the body corresponds to image contrast. The ability of MRI techniques to generate excellent contrast based on the intrinsic properties of the tissue means that the use of an exogenous contrast agent is not always necessary. However, there are many instances where better lesion visualization and vascular characterization are desirable, particularly for evaluating tumors.

SPIO nanoparticles provide MR contrast enhancement by shortening both the longitudinal and transverse relaxation times of surrounding proton nuclear spins. Compared to micrometer-sized magnetic particles or chelates of paramagnetic ions, such as gadolinium diethylenetriaminopenta-acetic acid (Gd-DTPA), magnetic nanoparticles are much more efficient at promoting relaxation. The effect of magnetic nanoparticles on T_2 shortening is caused by the large magnetic susceptibility difference between the particles and the surrounding medium, which results in magnetic field gradients. SPIOs affect the T_2 relaxation time more significantly than T_1, whereas Gd chelates predominantly affect T_1. This more pronounced shortening of T_2 results in a darkening of the image (negative contrast) where the SPIOs are located.

Relaxivity refers to the property of metal ions to increase the proton relaxation time. The relaxivity of a sample varies with not only the experimental variables such as the magnetic field strength, temperature, and the medium in which the measurements are made, but also the magnetic properties of the contrast agent, which can be affected by the characteristics of the coating on the surface of the nanoparticle and by the composition of the iron oxide core. Novel formulations of magnetic nanoparticle cores, such as metal-doped iron oxide nanocrystals and metallic/alloy nanocomposites, produce high magnetic moments that increase their signal-to-background ratios under MRI and generate better imaging results. These metal ferrites with a composition of MFe_2O_4 (where M is a +2 cation of Mn, Fe, Co or Ni) have been fabricated by various methods to tune specific magnetic properties [15]. Through a comparison of various metal-doped ferrite nanoparti-

cles, Lee *et al*. have shown that $MnFe_2O_4$ nanoparticles appear to possess a higher magnetic susceptibility than magnetite nanoparticles, and hence would make better MRI probes [16].

5.4.2
SPIOs as MRI Contrast Agents

Currently, Gd-based contrast agents for MRI are used routinely in clinical practice. While the gadolinium(III) ion has an excellent ability to catalyze the relaxation of the MRI water signal due to its seven unpaired electrons [17], it must be chelated to a low-molecular-weight organic molecule (usually DTPA) to make it biosafe. In addition to the differences mentioned in Section 5.4.1, Gd chelates and SPIOs differ in their biodistribution: Gd chelates distribute in the extracellular, interstitial space, whereas SPIOs are taken up by phagocytic cells [18].

SPIO nanoparticles have been explored for several years as improved MRI contrast agents for the detection and diagnosis of solid tumors. MRI of liver tumors and metastases via the RES-mediated uptake of SPIOs has been shown capable of distinguishing lesions as small as 2–3 mm [19]. SPIOs, when used as MRI agents, have also been shown to be effective in the identification of clinically occult lymph node metastases in prostate cancer [20]. Such capabilities have significant clinical value, as the identification of lymph node metastases is an essential component of tumor staging, and is critical for making therapeutic decisions when treating diseases such as cancer of the prostate gland, breast, and colon.

It has been known for many years that SPIOs have the potential for an improved delineation of brain tumor margins and for quantifying tumor volumes in MR images [21]. Gd chelate-based contrast agents are typically limited by the edema that typically surrounds the tumor and the diffusion of these small molecules from the tumor vasculature. Varallyay *et al*. conducted a comparison of SPIO nanoparticles – ferumoxide (100 nm) and ferumoxtran-10 (30 nm iron oxide coated with dextran) – with Gd chelate for imaging intracranial tumors, and showed that the SPIO-based contrast agents allowed a prolonged delineation of the tumor margins due to an enhanced cellular internalization and a slower clearance from the tumor site [22]. Neuwelt *et al*. have utilized ferumoxytol nanoparticles (30 nm iron oxide coated with semi-synthetic carbohydrate) for MRI and magnetic resonance angiography (MRA) in brain malignancy, where ferumoxytol served as a blood pool agent [23].

5.4.3
Specific Targeting of Tumors for Imaging

In vivo imaging modalities have traditionally been employed for assessing the location, size, and other anatomical features of tumors for diagnosis, as well as changes in those features for determining any response to treatment and prognosis. However, as molecular abnormalities might correlate with an abnormal

behavior of cancer cells, the detection of such biomarkers may help diagnose and predict the aggressive and invasive natures of malignant lesions, and thus provide additional clinical insight into the management of cancers. Targeting ligands (e.g., proteins, peptides, aptamers, small molecules) possess a high affinity for the unique molecules found on cancer cells, and hence can facilitate their detection. Monoclonal antibodies (mAbs) are the most prevalent targeting agents used in myriad techniques and methods, including the targeting of magnetic nanoparticles to tumors. For example, trastuzumab (Herceptin®)–an FDA-approved therapeutic mAb against the HER2/neu (erbB2) receptor–was recently used as a targeting agent by Huh *et al.* to demonstrate Herceptin-mediated specific targeting of DMSA-coated magnetite nanoparticles to cells expressing the HER2/neu cancer marker for the *in vivo* magnetic resonance detection of cancer [24].

Chlorotoxin (CTX), a scorpion-derived peptide that can specifically bind to gliomas and tumors of neuroectodermal origin, has recently been shown to serve as an effective targeting agent for tumors of neuroectodermal origin [25, 26]. According to Deshane *et al.*, CTX might target the matrix metalloproteinase-2 protein complex, which is upregulated in gliomas [27]. Magnetic nanoparticles functionalized with CTX have been shown to accumulate in gliomas and to provide a more thorough contrast enhancement of these tumors [28].

An area of extensive investigation has been the targeting of magnetic nanoparticles to receptors overexpressed on the tumor neovasculature. The formation of new blood vessels–termed angiogenesis–is an essential component of tumor growth, and has been shown to be highly specific for neoplasia [29]. A large number of angiogenesis markers, including the $\alpha_v\beta_3$ integrin, vascular endothelial growth factor (VEGF), and cell surface nucleolin, have been identified as potential targets for the tumor vasculature [30]. Targeting agents, such as the Arg-Gly-Asp (RGD) peptide that has a high affinity for the $\alpha_v\beta_3$ integrin, have been evaluated for the specific targeting of magnetic nanoparticles for imaging of a variety of tumors, as well as tumor angiogenesis [31, 32].

5.5 MRI for the Monitoring of Treatment

While liposomal nanoparticles have already been shown capable of targeting brain tumors after their intravenous administration [33], an assessment of nanoparticle accumulation and retention has been hindered by a lack of noninvasive methods to monitor the time course of nanoparticle distribution within the brain. Chertok *et al.* explored the opportunity provided by magnetic nanoparticles for both magnetically targeted accumulation of drug in the brain tumor and noninvasive MRI monitoring [34]. These authors were able to actively retain (via an externally applied magnetic field) the fraction of magnetic nanoparticles that passively reached the brain tumor site after intravenous administration, and to

successfully monitor the nanoparticle accumulation and time course of distribution and elimination of magnetic nanoparticles in brain tumors. For this, the magnetic targeting was tested in rats harboring orthotopic gliosarcomas, after which image analysis revealed that the magnetic targeting had induced a five-fold increase in total glioma exposure to magnetic nanoparticles compared to nontargeted tumors.

In another recent study conducted in a rat model, Reddy *et al*. showed that magnetic nanoparticles linked to the F3 peptide, which binds to nucleolin expressed on cancer cells, could be used to target brain tumors, to treat the gliomas by photodynamic therapy, and to monitor the treatment efficacy by using the magnetic nanoparticles as a contrast agent for MRI [35]. This research group was thus able to show that magnetic nanoparticles could be used to combine photodynamic therapy and treatment monitoring.

Convection-enhanced delivery (CED) represents a creative approach for bypassing the blood–brain barrier (BBB) when delivering magnetic nanoparticles to the brain. CED is a direct intracranial delivery method that involves distributing drugs through the brain tissue via surgically implanted catheters. The technique uses hydrostatic pressure gradient to convect agents by bulk flow to an area that is larger than could be achieved via diffusion alone [36]. The drugs can be delivered continuously through the catheter, thus enabling a large-volume distribution of high drug concentrations, and with minimal systemic toxicity. However, successful delivery of magnetic nanoparticles using the CED method was not demonstrated until very recently, when Perlstein *et al*. reported the successful delivery of maghemite nanoparticles [37]. By using a rat brain model, these authors showed that the addition of sucrose or PEG to saline, which contained magnetic nanoparticles, to increase the viscosity of the infusate could lead to an increase in CED efficacy. The same group also established the use of MRI for the reliable depiction of magnetic nanoparticle distribution. Hence, a combination of CED and the advantages of magnetic nanoparticles could represent a powerful means of monitoring not only the delivery of therapeutic agents but also the spatial distribution of the delivery system.

5.6
Application of Magnetic Nanoparticles in *In Vitro* Diagnostics

One of the most common uses of magnetic nanoparticles for *in vitro* diagnostics has involved the ability to manipulate their movement by applying an external magnetic field, and thus to simplify the isolation, extraction, and purification of macromolecules (i.e., proteins or nucleic acids) and cells. In this way, magnetic nanoparticles can be used to separate out and enrich rare cells and molecules from complex biological samples. Moreover, such an ability to detect rare cancer cells could provide a means of not only detecting the development of cancer but also of monitoring residual disease for determining a patient's susceptibility to recurrence/relapse. By coating iron oxide nanoparticles with a shell of quantum dots

(QDs) [38] or dye-doped silica [39], or by constructing nanocomposites comprised of magnetic nanoparticles and QDs [40, 41], fluorescent magnetic nanoparticles have been cleverly synthesized for simultaneous cell separation and *in vitro* fluorescent imaging.

Another clear way in which magnetic nanoparticles have contributed to state-of-the-art advances in diagnostics has been by eliminating the dependence of immunoassays and DNA detection systems on fluorescent and/or radiolabeled antibodies (specific design schemes and technologies are described in greater detail below). Overall, the impact of magnetic nanoparticles on *in vitro* diagnostics has not been via the creation of entirely novel technologies *per se*, but rather by their ingenious incorporation into improved designs for detection platforms that enhance the usability, efficiency, and performance of the assays.

5.6.1
Magnetic Nanoparticle-Based Improvements on Immunoassays

5.6.1.1 Electrochemical Immunoassays

Electrochemical detection, which is also referred to as the potentiometric technique, involves a field effect transistor device in which the current flowing between the source and the drain is affected by the presence of analytes. By measuring the voltage as the current is affected, it is possible to determine the analyte concentrations. Tang *et al.* built an immunoassay system that utilized magnetic nanoparticles as an integral component of an electrochemical measurement device that could be regenerated, and this microfluidic immunosensor has the potential to be developed into a lab-on-a-chip device [42]. The assay system consisted of four gold electrodes for measuring four different analytes, plus an Ag/AgCl reference electrode. Antibodies to four cancer biomarkers – carcinoembryonic antigen (CEA), α-fetoprotein (AFP), and cancer antigens CA125 and CA15-3 were adsorbed onto $NiFe_2O_4$ (core)/SiO_2 (shell) nanoparticles (25 nm). The functionalized nickel ferrite nanoparticles were then attached to the surface of the gold electrodes via an external magnet close to each electrode. Each electrode contained a *different* set of antibodies immobilized on the magnetic nanoparticle.

When antibodies are immobilized on the electrode, the surface charge of the electrode reflects the net charge of the immobilized antibody. (Proteins in aqueous solution have a net electrical charge polarity, which is dependent on the isoelectric points of the protein and the ionic composition of the solution.) When antigen molecules are present in the solution and bind to antibodies on the electrode surface, this immunochemical reaction causes a change in the surface charge, which can be measured potentiometrically against the reference electrode as a shift in electric potential (in mV). After each immunoassay, the electrodes can be regenerated by pulling away the magnetic nanoparticles via an external magnetic field, and subsequently washing the electrodes.

Immunoassays represent the predominant analytical methods for the quantitative detection of protein or peptide biomarkers of cancer. While the majority of immunosensor strategies require the labeling of antibodies, the technology

developed by Tang *et al.* is based on the measurement of electrochemical signals and does not require antibody labeling, which could make signal quantification easier. Electrochemical detection strategies have been employed not only for protein detection and analysis [43, 44] but also for monitoring hybridization reactions [45].

5.6.1.2 Immunoassays Using Magnetic Luminescent Nanoparticles (MLNPs)

Nichkova *et al.* developed magnetic nanoparticles (200–400 nm) with an iron oxide core doped with cobalt and neodymium (Co:Nd:Fe_2O_3) and a luminescent shell of gadolinium oxide and europium (Eu:Gd_2O_3), and have shown that the application of these MLNPs as an internal luminescent standard in quantitative immunoassays can eliminate the experimental error that could be introduced in particle handling [46]. The multiplexed sandwich immunoassay involved dual binding events on the surface of the MLNPs that had been functionalized with capture antibodies – the target proteins were first captured by the antibodies immobilized on the surface of the MLNPs, after which the secondary (reporter) antibodies labeled with conventional organic dyes were allowed to bind to the captured proteins.

The magnetic property of the MLNPs allowed the manipulation of this MLNP-immunocomplex by an external magnetic field in the separation and washing steps, and eliminated the need for centrifugation and filtration. The identity and concentration of each analyte were determined by the position and intensity of its distinct peak in the fluorescence spectrum. The intrinsic luminescence property of MLNPs served as an internal standard and enabled calibration, as well as quality control of extraction, detection system, and assay performance. The ratio of the intensity of the fluorescent peak and the intensity of the MLNP emission ($I_{reporter}/I_{Eu}$) was directly proportional to the analyte concentration. The authors noted that MLNPs with different emission wavelengths could be easily obtained by the incorporation of different lanthanide ions (e.g., Eu and Tb).

Through this study, the authors have demonstrated proof of concept by functionalizing MLNPs with goat anti-mouse, anti-rabbit, and anti-human IgG antibodies for the quantitation of rabbit, mouse, and human IgG as analytes. However, further studies are required to test the functionality of these nanoparticles in quantitating cancer biomarkers in clinical samples.

5.6.2 Magnetic Relaxation Switch (MRSw) Biosensors for Multi-Sample Analysis

To date, MR-based diagnostics have been associated primarily with *in vivo* MRI, the application of MR for *in vitro* diagnostics having been precluded because MRI technology was not designed for the analysis of small volumes (<1 ml) of body fluids. During the past few years, however, there has been a surge in research on superparamagnetic nanoparticles known as magnetic relaxation switches (MRSws), which have enabled these limitations to be overcome [47]. Today, MRSws have enabled the detection of many different types of analyte, including

nucleic acids, proteins, and cells [48–51]. In fact, one of the most promising attributes of an MRSw assay is that it allows the analysis of complex samples (e.g., blood) without having to undertake time-consuming purification and processing steps [51, 52].

The general principle behind the MRSw is based on the phenomenon where, in the presence of a magnetic field, the formation of induced magnetic dipoles in the superparamagnetic nanoparticles creates field nonuniformities. These nonuniformities cause a spin dephasing of the hydrogen protons (^{1}H) of water, which in turn leads to a time-dependent exponential decrease in the proton signal that is detected by applying a RF pulse sequence [50]. The resulting exponential relaxation curve decays according to a time constant, T_2, and change in T_2 is linearly correlated with the analyte concentration. The key event in MRSw assays is the *clustering of functionalized nanoparticles in the presence of target analytes*. This transition (or "switch") from a dispersed to a clustered state leads to a decrease in T_2 of the aqueous medium surrounding the particles. In order to measure T_2 variations between samples, measurements from the test sample and at least one reference sample must be taken to produce calibrated results. To date, this has been achieved by making sequential measurements.

Recently, Lowery *et al*. developed a simpler MRSw diagnostics system which involved a single-step signal acquisition method for measuring the T_2 values for two samples (test and reference) simultaneously, inside a single RF coil [53]. The nanoparticles (25–30 nm) consisted of monocrystalline iron oxide cores with crosslinked dextran coatings and were functionalized to selectively bind the desired analyte. The analysis of signals from multiple samples meant having to overcome problems associated with a multiexponential analysis, one major limitation of which is the poor resolution of closely spaced T_2 constants. Relatedly, when the difference in decay constants is below the limit of resolution, the output results become unreliable and could lead to false positive or false negative results if used for medical diagnostics [54]. Lowery *et al*. showed that it was possible to reliably discriminate T_2 values from biexponential relaxation curves, and demonstrated the resolution of T_2 values at ratio of ~2.5 [53]. However, this technology is still at an early proof-of-concept stage, as the experiments have been performed on biotinylated nanoparticles to measure avidin concentrations in samples.

Kim *et al*. employed MRSws to successfully detect the presence of the β subunit of human chorionic gonadotrophin-β (hCG-β), the elevated serum levels of which are associated with malignancies that include testicular and ovarian cancers [55]. Ordinarily, the analyte should be multivalent (i.e., able to bind to multiple antibodies) in order for the MRSw assay to work, but because hCG-β is not multivalent, Kim *et al*. designed a two-particle system in which a pair of mAbs that could recognize two nonoverlapping epitopes on hCG-β were conjugated to the crosslinked iron oxide nanoparticles. Again, the goal of the study was to demonstrate proof-of-concept, and the authors noted that the control of aggregate size would be important in enhancing the dynamic range and stability of this type of assay.

5.6.3
DNA Sequence Detection by Brownian Relaxation Frequency Measurement

While previous sections have dealt with assays primarily for protein detection, this section highlights an advance that employs magnetic nanoparticles in the label-free detection and quantitation of specific DNA sequences. Having information regarding the presence and abundance of specific DNA sequences would be vitally important in clinical diagnostics. Previously, DNA sequence detection strategies have generally relied on a hybridization reaction between a target DNA molecule and a probe molecule that is complementary to the target. One approach towards improving the existing technology has been to develop an assay system in which these hybridizations could be monitored without having to use fluorescence-based detection methods.

Stromberg *et al*. developed a DNA sequence detection assay that uses magnetic nanobeads functionalized with single-stranded oligonucleotides (~150 nm) to serve as signal generators in a system where the target DNA is recognized and amplified by rolling circle amplification (RCA) [56]. In order to achieve a high detection sensitivity, it is often necessary to amplify the number of target molecules or the signal from the target. RCA could be considered an alternative approach to the polymerase chain reaction (PCR) for the amplification of gene sequences to be detected. RCA involves the use of oligonucleotide probes that are able to circularize upon binding to the target DNA (padlock probes) [57]. The padlock probes are designed in such a way that when they are properly hybridized to the target strand, the 5′ and 3′ ends of the linear form of the probe line up next to each other, and are then joined by DNA ligase to form a closed, circular probe. Once circularized, they can serve as a template for enzymatic amplification by DNA polymerase via the RCA mechanism [58]. What is then generated is a long coil of single-stranded DNA consisting of many tandem copies of the padlock probe.

Stromberg *et al*. adopted an approach originally developed by Connolly and St. Pierre [59], which involves measurement of the change in Brownian relaxation frequency of magnetic nanobeads in aqueous solution. When the oligonucleotide-tagged magnetic nanobeads hybridize by base-pairing to a specific repeating sequence motif in the RCA coils, the result is an increased hydrodynamic diameter of the nanobeads (essentially corresponding to the diameter of the RCA coil) and a decreased Brownian relaxation frequency. This can be visualized in a magnetization spectrum. In other words, the change in magnetic response of the nanobeads due to the hydrodynamic volume increase would occur only if there were RCA coils to which the magnetic nanobeads could attach, and the RCA coils would have been produced only if the target DNA sequence were initially present to enable the circularization of the padlock probe. Stromberg *et al*. referred to this as "volume-amplified" detection [56].

The magnetization spectrum (magnetic response plotted as a function of Brownian relaxation frequency, $m''(f)$) exhibits two peaks for positive samples. The smaller peak at low frequency corresponds to RCA coils with incorporated

nanobeads, and the taller peak at high frequency arises from, and gives a measure of, the number of free beads. According to Stromberg *et al.*, the samples can be discriminated as being positive or negative for target DNA sequence by measuring the level of m″ (emu g^{-1}) at the high-frequency peak (i.e., at the Brownian relaxation frequency for the free beads), while the concentration of RCA coils can be determined down to the p*M* range from the magnetization spectrum [56]. Sample preparation, RCA times, nanobead surface coverage with oligonucleotides, and other aspects of the experimental protocol still require optimization. Nonetheless, with a view towards developing this into a point-of-care diagnostic device, the authors have proposed that if sufficiently small beads were used it would be possible to detect the magnetic signal at a sufficiently high frequency where the intrinsic voltage noise of the sensor (white noise) would be minimal. This detection principle, based on Brownian relaxation frequency, has also been demonstrated in the case of antigen–antibody binding [60].

5.7
Detection of Circulating Tumor Cells

The most notable success of the application of magnetic nanoparticles in *in vitro* diagnostics has been in the commercialization of the CellSearch System by Veridex, LLC, for monitoring disease progression in patients with metastatic breast, colorectal, or prostate cancer [61]. The CellSearch System is being promoted as a powerful tool for measuring the number of circulating tumor cells (CTCs) in the blood to derive prognostic information. The system involves enriching for CTCs using ferrofluid (colloidal fluid of magnetic nanoparticles coated with antibodies targeting the epithelial cell adhesion molecule); in this way, tumor cells of epithelial origin can be magnetically separated from the bulk of the cellular material within the blood sample. The CTCs are then stained with mAbs against cytokeratin, the intermediate filaments of epithelial cells. In order to distinguish contaminating leukocytes from CTCs, a pan-leukocyte mAb against CD45 is also used to stain the cells. An external magnetic force is applied to pull the cells to the surface of the cartridge that contains the sample, and to hold the cells in place at a single focal depth. These cells are then scanned by the fluorescence optical system, and the images of fluorescence events presented to the user for classification of the cells: CTCs are positive for cytokeratin, but negative for CD45. When using this CellSearch System, it is possible to detect just a few CTCs per 7.5 ml of blood. Moreover, the results of clinical studies have shown that, in patients with metastatic breast cancer, the presence of more than five CTCs per 7.5 ml of blood is prognostic of a short progression-free survival and short overall survival [62].

Magnetic nanoparticles have tremendous potential to be developed into various platforms for the enrichment and detection of CTCs in the peripheral blood of patients with cancer, and this has enormous clinical implications for the monitoring and treatment of cancer patients. Recent studies have shown that CTCs are present in 30% of patients with early-stage breast cancer, and in over 50% of those

with metastatic breast cancer [63]. Some new approaches that can be adapted for CTC detection are described in the following section.

5.8
Aptamers as an Alternative to Antibodies

Although many of the above-described platforms and methods require the use of antibodies for specific targeting, several challenges and limitations exist with regards to the use of antibodies. First, the production of antibodies involves raising them in animals (as opposed to chemical synthesis), and a newly produced batch may behave quite differently from an older batch (e.g., they may not have the same level of specificity or binding characteristics). This is a concern particularly for *in vitro* diagnostics, where the reproducibility of quantitative measurements is heavily dependent on the consistent quality of reagents. While it is important to conjugate antibodies to nanoparticles in a reproducible manner to consistently generate a certain level of specificity, the controlled conjugation of antibodies to nanoparticle surfaces is not always possible. Most importantly, specific antibodies against many of the protein analytes or cell-surface molecules of interest are simply unavailable. Consequently, one very active area of research is the development of aptamers as a promising antibody alternative for conjugation to nanoparticles when targeting cancer cells.

Aptamers may be peptide, DNA, or RNA segments that fold into complex three-dimensional structures with distinct molecular binding motifs. The aptamers in all of the following studies were selected using a process known as cell-based SELEX (systematic evolution of ligands by exponential enrichment), which identifies sequences with strong binding affinities for live cancer cells that express a variety of unique surface markers. The process starts out with a DNA library and generally involves multiple binding and washing/elution steps (upwards of 25 rounds of selection) with increasing stringency of washes (e.g., longer wash times, greater wash volumes, increasing numbers of wash cycles), where the unbound DNA is washed away and the bound DNA is eluted. The eluate containing aptamers with an affinity for the target cells can be counterselected against control cells, so as to increase the specificity of the aptamers.

It has been shown that acute leukemia cells could be detected successfully by using high-affinity DNA aptamer-conjugated magnetic nanoparticles [64]. Here, the aptamer was an 88-base oligonucleotide with binding specificity for acute leukemia cells, and the aptamer was attached to iron oxide nanoparticles (65 nm) and fluorescent nanoparticles to develop a platform for the collection and imaging, respectively, of intact leukemia cells from whole blood samples. Smith *et al.* used this platform to demonstrate that multiple cancer cell types can be extracted from a complex mixture (i.e., fetal bovine serum spiked with CCRF-CEM, Ramos, and Toledo cancer cells) by a multiple cell extraction procedure using three different sets of aptamers with specificity for acute leukemia cells (CCRF-CEM), Burkitt's lymphoma cells (Ramos), and non-Hodgkin B-cell lymphoma cells

(Toledo) [65]. For imaging, these aptamers were bound to three spectrally different fluorophore-doped silica nanoparticles (cy5-doped, Rubpy-doped, and TMR-doped nanoparticles).

Chen *et al.* showed that aptamers conjugated to magnetic and fluorescent nanoparticles could be effectively employed to extract and enrich small cell lung cancer (SCLC) cells from whole blood (spiked with SCLC cells), and to detect SCLC cells in sections of formalin-fixed paraffin-embedded SCLC and non-small cell lung cancer (NSCLC) cells [66]. This cell-based SELEX strategy involved generating DNA aptamers (71-base single-stranded DNA) that were specific for molecular markers on SCLC cells but did not cross-react with normal epithelial cells nor NSCLC cells; the result was fewer false positives and a greater selectivity. This approach could represent a tremendous advantage over the use of antibodies, which may cross-react with atypical epithelial cells and not have sufficient specificity. As noted above, this method also has the potential for enriching rare CTCs from peripheral blood for analysis.

5.9 Conclusions

Today, magnetic nanoparticles of novel and various formulations are being developed for the improved *in vivo* and *in vitro* diagnosis of cancer. Areas of focus for magnetic nanoparticle research and development have included improved biocompatibility, optimization of specific targeting, enhanced *in vivo* imaging, and novel signal detection and measurement platforms for molecular diagnostics. In particular, the use of magnetic nanoparticles as both MRI contrast agents and nanocarriers has attracted enormous attention, as they hold tremendous promise as multifunctional agents that can perform imaging, drug delivery, and real-time monitoring simultaneously. Bioengineers and chemists are making great advances in the synthesis of new metal/alloy composite nanoparticle cores to enhance their magnetic properties. They are also exploring novel nanomaterials for surface coating to improve the biocompatibility and biosafety of magnetic nanoparticles. One critical component of the bench-to-bedside translation of these advances for magnetic nanoparticle-based therapy is the continued investigation into relationships between the physico-chemical properties of the nanostructures and their behavior *in vivo*, which is currently poorly understood. Hence, a greater insight into the mechanisms that dictate the fate of nanoparticles *in vivo* is required.

In the case of magnetic nanoparticle-based *in vitro* diagnostics, one major challenge in the translation of these platforms – for which proof-of-concept has been demonstrated in simple test solutions of analytes, or by using common biomarkers found in great abundance – is to determine whether their performance holds up in clinical samples and for low-expression cancer biomarkers that are meaningful for diagnosis, prognosis, and a prediction of response to therapy. As research groups begin to consider moving their assay systems forward, beyond the proof-of-concept stage, a variety of factors related to assay performance must be consid-

ered. What types of controls are used? What will be used as calibrators and reference standards? How robust and reproducible are the readouts, and what are the error rates? Ultimately, the assay's fitness for purpose must be established by assessing its performance on specimens or models that parallel clinical practice. However, because the specimens obtained for laboratory diagnostics are frequently contaminated with stabilizers and fixatives, any detection platforms developed using simple solutions of analytes may fail completely in the presence of these contaminants. Hence, it would be critical for the bioengineers and chemists to collaborate with molecular biologists, laboratory pathologists, and clinicians as soon as possible in the timeline of development for these assays.

References

1 Lu, A.H., Salabas, E.L. and Schuth, F. (2007) Magnetic nanoparticles: synthesis, protection, functionalization, and application. *Angewandte Chemie, International Edition in English*, **46**, 1222–44.

2 Gref, R., Minamitake, Y., Peracchia, M.T., Trubetskoy, V., Torchilin, V. and Langer, R. (1994) Biodegradable long-circulating polymeric nanospheres. *Science*, **263**, 1600–3.

3 Zhang, Y., Kohler, N. and Zhang, M.Q. (2002) Surface modification of superparamagnetic magnetite nanoparticles and their intracellular uptake. *Biomaterials*, **23**, 1553–61.

4 Kohler, N., Fryxell, G.E. and Zhang, M.Q. (2004) A bifunctional poly(ethylene glycol) silane immobilized on metallic oxide-based nanoparticles for conjugation with cell targeting agents. *Journal of the American Chemical Society*, **126**, 7206–11.

5 Portet, D., Denizot, B., Rump, E., Lejeune, J.J. and Jallet, P. (2001) Nonpolymeric coatings of iron oxide colloids for biological use as magnetic resonance imaging contrast agents. *Journal of Colloid and Interface Science*, **238**, 37–42.

6 Fauconnier, N., Pons, J.N., Roger, J. and Bee, A. (1997) Thiolation of maghemite nanoparticles by dimercaptosuccinic acid. *Journal of Colloid and Interface Science*, **194**, 427–33.

7 Zhang, C., Wangler, B., Morgenstern, B. *et al.* (2007) Silica- and alkoxysilane-coated ultrasmall superparamagnetic iron oxide particles: a promising tool to label cells for magnetic resonance imaging. *Langmuir*, **23**, 1427–34.

8 Baldi, G., Bonacchi, D., Franchini, M.C. *et al.* (2007) Synthesis and coating of cobalt ferrite nanoparticles: a first step toward the obtainment of new magnetic nanocarriers. *Langmuir*, **23**, 4026–8.

9 Jain, T.K., Richey, J., Strand, M., Leslie-Pelecky, D.L., Flask, C.A. and Labhasetwar, V. (2008) Magnetic nanoparticles with dual functional properties: drug delivery and magnetic resonance imaging. *Biomaterials*, **29**, 4012–21.

10 Lutz, J.F., Stiller, S., Hoth, A., Kaufner, L., Pison, U. and Cartier, R. (2006) One-pot synthesis of PEGylated ultrasmall iron-oxide nanoparticles and their *in vivo* evaluation as magnetic resonance imaging contrast agents. *Biomacromolecules*, **7**, 3132–8.

11 Wang, L.Y., Bao, J., Wang, L., Zhang, F. and Li, Y.D. (2006) One-pot synthesis and bioapplication of amine-functionalized magnetite nanoparticles and hollow nanospheres. *Chemistry – A European Journal*, **12**, 6341–7.

12 Ahmad, Z., Zhang, H.B., Farook, U., Edirisinghe, M., Stride, E. and Colombo, P. (2008) Generation of multilayered structures for biomedical applications using a novel tri-needle coaxial device and electrohydrodynamic flow. *Journal of the Royal Society Interface*, **5**, 1255–61.

13 Loscertales, I.G., Barrero, A., Marquez, M., Spretz, R., Velarde-Ortiz, R. and

Larsen, G. (2004) Electrically forced coaxial nanojets for one-step hollow nanofiber design. *Journal of the American Chemical Society*, **126**, 5376–7.

14 Ma, D.L., Guan, J.W., Normandin, F. *et al.* (2006) Multifunctional nano-architecture for biomedical applications. *Chemistry of Materials*, **18**, 1920–7.

15 Willard, M.A., Kurihara, L.K., Carpenter, E.E., Calvin, S. and Harris, V.G. (2004) Chemically prepared magnetic nanoparticles. *International Materials Reviews*, **49**, 125–70.

16 Lee, J.H., Huh, Y.M., Jun, Y.W. *et al.* (2007) Artificially engineered magnetic nanoparticles for ultra-sensitive molecular imaging. *Nature Medicine*, **13**, 95–9.

17 Caravan, P., Ellison, J.J., McMurry, T.J. and Lauffer, R.B. (1999) Gadolinium(III) chelates as MRI contrast agents: structure, dynamics, and applications. *Chemical Reviews*, **99**, 2293–352.

18 Wu, Y.J., Muldoon, L.L., Varallyay, C., Markwardt, S., Jones, R.E. and Neuwelt, E.A. (2007) In vivo leukocyte labeling with intravenous ferumoxides/protamine sulfate complex and *in vitro* characterization for cellular magnetic resonance imaging. *American Journal of Physiology–Cell Physiology*, **293**, C1698–708.

19 Semelka, R.C. and Helmberger, T.K. (2001) Contrast agents for MR imaging of the liver. *Radiology*, **218**, 27–38.

20 Harisinghani, M.G., Barentsz, J., Hahn, P.F. *et al.* (2003) Noninvasive detection of clinically occult lymph-node metastases in prostate cancer. *New England Journal of Medicine*, **348**, U2491–5.

21 Enochs, W.S., Harsh, G., Hochberg, F. and Weissleder, R. (1999) Improved delineation of human brain tumors on MR images using a long-circulating, superparamagnetic iron oxide agent. *Journal of Magnetic Resonance Imaging*, **9**, 228–32.

22 Varallyay, P., Nesbit, G., Muldoon, L.L. *et al.* (2002) Comparison of two superparamagnetic viral-sized iron oxide particles ferumoxides and ferumoxtran-10 with a gadolinium chelate in imaging intracranial tumors. *American Journal of Neuroradiology*, **23**, 510–19.

23 Neuwelt, E.A., Varallyay, C.G., Manninger, S. *et al.* (2007) The potential of ferumoxytol nanoparticle magnetic resonance imaging, perfusion, and angiography in central nervous system malignancy: a pilot study. *Neurosurgery*, **60**, 601–11.

24 Huh, Y.M., Jun, Y.W., Song, H.T. *et al.* (2005) In vivo magnetic resonance detection of cancer by using multifunctional magnetic nanocrystals. *Journal of the American Chemical Society*, **127**, 12387–91.

25 Lyons, S.A., O'Neal, J. and Sontheimer, H. (2002) Chlorotoxin, a scorpion-derived peptide, specifically binds to gliomas and tumors of neuroectodermal origin. *Glia*, **39**, 162–73.

26 Veiseh, M., Gabikian, P., Bahrami, S.B. *et al.* (2007) Tumor paint: a Chlorotoxin : Cy5.5 bioconjugate for intraoperative visualization of cancer foci. *Cancer Research*, **67**, 6882–8.

27 Deshane, J., Garner, C.C. and Sontheimer, H. (2003) Chlorotoxin inhibits glioma cell invasion via matrix metalloproteinase-2. *The Journal of Biological Chemistry*, **278**, 4135–44.

28 Veiseh, O., Sun, C., Gunn, J. *et al.* (2005) Optical and MRI multifunctional nanoprobe for targeting gliomas. *Nano Letters*, **5**, 1003–8.

29 Folkman, J. (1971) Tumor angiogenesis: therapeutic implications. *The New England Journal of Medicine*, **285**, 1182–6.

30 Neri, D. and Bicknell, R. (2005) Tumour vascular targeting. *Nature Reviews Cancer*, **5**, 436–46.

31 Montet, X., Montet-Abou, K., Reynolds, F., Weissleder, R. and Josephson, L. (2006) Nanoparticle imaging of integrins on tumor cells. *Neoplasia*, **8**, 214–22.

32 Zhang, C.F., Jugold, M., Woenne, E.C. *et al.* (2007) Specific targeting of tumor angiogenesis by RGD-conjugated ultrasmall superparamagnetic iron oxide particles using a clinical 1.5-T magnetic resonance scanner. *Cancer Research*, **67**, 1555–62.

33 Siegal, T., Horowitz, A. and Gabizon, A. (1995) Doxorubicin encapsulated in sterically stabilized liposomes for the treatment of a brain-tumor

model–biodistribution and therapeutic efficacy. *Journal of Neurosurgery*, **83**, 1029–37.

34 Chertok, B., Moffat, B.A., David, A.E. *et al.* (2008) Iron oxide nanoparticles as a drug delivery vehicle for MRI monitored magnetic targeting of brain tumors. *Biomaterials*, **29**, 487–96.

35 Reddy, G.R., Bhojani, M.S., McConville, P. *et al.* (2006) Vascular targeted nanoparticles for imaging and treatment of brain tumors. *Clinical Cancer Research*, **12**, 6677–86.

36 Bobo, R.H., Laske, D.W., Akbasak, A., Morrison, P.F., Dedrick, R.L. and Oldfield, E.H. (1994) Convection-enhanced delivery of macromolecules in the brain. *Proceedings of the National Academy of Sciences of the United States of America*, **91**, 2076–80.

37 Perlstein, B., Ram, Z., Daniels, D. *et al.* (2008) Convection-enhanced delivery of maghemite nanoparticles: increased efficacy and MRI monitoring. *Neuro-Oncology*, **10**, 153–61.

38 Wang, D.S., He, J.B., Rosenzweig, N. and Rosenzweig, Z. (2004) Superparamagnetic Fe_2O_3 beads-CdSe/ZnS quantum dots core-shell nanocomposite particles for cell separation. *Nano Letters*, **4**, 409–13.

39 Levy, L., Sahoo, Y., Kim, K.S., Bergey, E.J. and Prasad, P.N. (2002) Nanochemistry: synthesis and characterization of multifunctional nanoclinics for biological applications. *Chemistry of Materials*, **14**, 3715–21.

40 Sathe, T.R., Agrawal, A. and Nie, S.M. (2006) Mesoporous silica beads embedded with semiconductor quantum dots and iron oxide nanocrystals: dual-function microcarriers for optical encoding and magnetic separation. *Analytical Chemistry*, **78**, 5627–32.

41 Yi, D.K., Selvan, S.T., Lee, S.S., Papaefthymiou, G.C., Kundaliya, D. and Ying, J.Y. (2005) Silica-coated nanocomposites of magnetic nanoparticles and quantum dots. *Journal of the American Chemical Society*, **127**, 4990–1.

42 Tang, D., Yuan, R. and Chai, Y. (2007) Magnetic control of an electrochemical microfluidic device with an arrayed immunosensor for simultaneous multiple immunoassays. *Clinical Chemistry*, **53**, 1323–9.

43 Hirakawa, K., Katayama, M., Soh, N., Nakano, K. and Imato, T. (2006) Electrochemical immunoassay for vitellogenin based on sequential injection using antigen-immobilized magnetic microbeads. *Analytical Sciences*, **22**, 81–6.

44 Wilson, M.S. and Nie, W.Y. (2006) Multiplex measurement of seven tumor markers using an electrochemical protein chip. *Analytical Chemistry*, **78**, 6476–83.

45 Kerman, K., Kobayashi, M. and Tamiya, E. (2004) Recent trends in electrochemical DNA biosensor technology. *Measurement Science and Technology*, **15**, R1–11.

46 Nichkova, M., Dosev, D., Gee, S.J., Hammock, B.D. and Kennedy, I.M. (2007) Multiplexed immunoassays for proteins using magnetic luminescent nanoparticles for internal calibration. *Analytical Biochemistry*, **369**, 34–40.

47 Josephson, L., Perez, J.M. and Weissleder, R. (2001) Magnetic nanosensors for the detection of oligonucleotide sequences. *Angewandte Chemie, International Edition in English*, **40**, 3204–6.

48 Perez, J.M., Josephson, L., O'Loughlin, T., Hogemann, D. and Weissleder, R. (2002) Magnetic relaxation switches capable of sensing molecular interactions. *Nature Biotechnology*, **20**, 816–20.

49 Tsourkas, A., Hofstetter, O., Hofstetter, H., Weissleder, R. and Josephson, L. (2004) Magnetic relaxation switch immunosensors detect enantiomeric impurities. *Angewandte Chemie, International Edition in English*, **43**, 2395–9.

50 Perez, J.M., Josephson, L. and Weissleder, R. (2004) Use of magnetic nanoparticles as nanosensors to probe for molecular interactions. *Chembiochem*, **5**, 261–4.

51 Kaittanis, C., Naser, S.A. and Perez, J.M. (2007) One-step, nanoparticle-mediated bacterial detection with magnetic relaxation. *Nano Letters*, **7**, 380–3.

52 Zhao, M., Josephson, L., Tang, Y. and Weissleder, R. (2003) Magnetic sensors for protease assays. *Angewandte Chemie, International Edition in English*, **42**, 1375–8.

53 Lowery, T.J., Palazzolo, R., Wong, S.M., Prado, P.J. and Taktak, S. (2008) Single-coil, multisample, proton relaxation method for magnetic relaxation switch assays. *Analytical Chemistry*, **80**, 1118–23.

54 Istratov, A.A. and Vyvenko, O.F. (1999) Exponential analysis in physical phenomena. *Review of Scientific Instruments*, **70**, 1233–57.

55 Kim, G.Y., Josephson, L., Langer, R. and Cima, M.J. (2007) Magnetic relaxation switch detection of human chorionic gonadotrophin. *Bioconjugate Chemistry*, **18**, 2024–8.

56 Stromberg, M., Goransson, J., Gunnarsson, K., Nilsson, M., Svedlindh, P. and Stromme, M. (2008) Sensitive molecular diagnostics using volume-amplified magnetic nanobeads. *Nano Letters*, **8**, 816–21.

57 Nilsson, M., Malmgren, H., Samiotaki, M., Kwiatkowski, M., Chowdhary, B.P. and Landegren, U. (1994) Padlock probes–circularizing oligonucleotides for localized DNA detection. *Science*, **265**, 2085–88.

58 Fire, A. and Xu, S.Q. (1995) Rolling replication of short DNA circles. *Proceedings of the National Academy of Sciences of the United States of America*, **92**, 4641–5.

59 Connolly, J. and St Pierre, T.G. (2001) Proposed biosensors based on time-dependent properties of magnetic fluids. *Journal of Magnetism and Magnetic Materials*, **225**, 156–60.

60 Astalan, A.P., Ahrentorp, F., Johansson, C., Larsson, K. and Krozer, A. (2004) Biomolecular reactions studied using changes in Brownian rotation dynamics of magnetic particles. *Biosensors and Bioelectronics*, **19**, 945–51.

61 Veridex, LLC website; CellSearch System link, http://www.immunicon.com/CellSearch/CellSearchHCP.aspx (accessed 11 March 2008).

62 Cristofanilli, M., Budd, G.T., Ellis, M.J. *et al.* (2004) Circulating tumor cells, disease progression, and survival in metastatic breast cancer. *New England Journal of Medicine*, **351**, 781–91.

63 Hayes, D.F. and Smerage, J. (2008) Is there a role for circulating tumor cells in the management of breast cancer? *Clinical Cancer Research*, **14**, 3646–50.

64 Herr, J.K., Smith, J.E., Medley, C.D., Shangguan, D.H. and Tan, W.H. (2006) Aptamer-conjugated nanoparticles for selective collection and detection of cancer cells. *Analytical Chemistry*, **78**, 2918–24.

65 Smith, J.E., Medley, C.D., Tang, Z.W., Shangguan, D., Lofton, C. and Tan, W.H. (2007) Aptamer-conjugated nanoparticles for the collection and detection of multiple cancer cells. *Analytical Chemistry*, **79**, 3075–82.

66 Chen, H.W., Medley, C.D., Sefah, K. *et al.* (2008) Molecular recognition of small-cell lung cancer cells using aptamers. *ChemMedChem*, **3**, 991–1001.

Keywords

cancer diagnosis; magnetic nanoparticles; immunoassays; circulating tumor cells

6
Magnetic Nanoparticles for Cancer Imaging and Therapy

Arutselvan Natarajan, Rajeswari Sundrarajan, and Sally J. DeNardo

6.1
Introduction

Magnetic iron oxide nanoparticles (MNPs) have been widely studied for applications in biology and medicine, such as drug delivery and targeting (drugs, antibodies, antibody fragments, streptavidin, genes, and radiopharmaceuticals), magnetic resonance imaging (MRI), diagnostics, immunoassays, RNA and DNA purification, cell separation and purification, as well as hyperthermia. For biomedical applications, most MNPs are prepared from either magnetite (Fe_3O_4) or maghemite (γ-Fe_2O_3), with the iron particle size being a determining factor in most biological applications. For example, a particle size of <100 nm is more effective for providing a uniform dispersion, an optimal surface area, and improved tissue penetration. Therefore, MNPs in the nanometer range are advantageous *in vivo* applications, not only for their favorable circulation time but also for their ability to pass through the capillary systems of the tissues, thus avoiding vessel embolism.

Today, MNPs continue to gain importance in the biomedical field due to their properties such as nontoxicity, nonimmunogenicity, biocompatiblility, and an ability to accumulate in target tissues or organ. Another attraction of MNPs is their high magnetic flux density, a feature which is used for applications such as drug targeting and bioseparation, including cell sorting. Currently, MNPs continue to attract attention due to their potential use as contrast agents for MRI, and also as heating mediators for cancer thermotherapy (hyperthermia). Originally, small iron oxide (SIO) particles, which were designed as liver contrast agents, had diameters in the range of 200–300 nm. Subsequently, ultra-small paramagnetic iron oxide (USPIO) particles were developed to address the need for a macromolecular agent to be used in MR angiography, and which was based on iron. In the formulation known commercially as Combidex® and chemically as ferumoxtran-10, the USPIO are dextran-coated; with diameters of 20–30 nm they can serve as blood pool agents.

When injected intravenously, MNPs circulate intravascularly and can be used to evaluate both renal blood volume and renal blood flow [1]. Unlike SIO particles,

Nanomaterials for the Life Sciences Vol. 4: Magnetic Nanomaterials. Edited by Challa S. S. R. Kumar

ISBN: 978-3-527-32154-4

which must be administered slowly, the newer versions of USPIO particles (e.g., ferumoxytol) appear to be safe even when injected rapidly [2, 3], and consequently dynamic intravascular blood flow measurements are possible when using these agents. Hence, MNPs with a diameter <100 nm are currently and effectively utilized in a variety of biomedical applications, and are becoming established products in many patients. In this chapter, attention is focused on the use of various forms of MNPs, modified for applications in cancer imaging and therapy.

During recent years, a considerable improvement has been achieved in the development of MNPs, notably for biomedical applications. Indeed, they have become important tools for diagnosis, imaging and therapy to prevent various diseases, such as cancer, atherosclerosis, and diabetes, with almost 250 reports having been made during the past two years. In this chapter, the aim is to update recent developments in MNPs, particularly in their use for cancer imaging and therapy. For this purpose, the development scheme has been segregated into five areas: (i) MNP fabrication and surface modification for cancer treatment; (ii) conjugation of various cancer targeting agents on MNPs; (iii) *in vitro* and *in vivo* characterization of cancer-targeting nanoparticles; (iv) the application of ligand-directed MNPs for imaging and therapy; and (v) ligand-directed MNPs for focused hyperthermia.

Over the past two decades, iron oxide nanoparticles have been used in cellular therapy, tissue repair, drug delivery, hyperthermia [4, 5], MRI [6–8] for magnetic resonance spectroscopy [9], for magnetic separation [10] and, more recently, as sensors for metabolites and other biomolecules [11–13]. Recent research has focused on the targeted delivery of iron oxide nanoparticles to sites of interest, and this has been accomplished with peptides, antibodies, and small molecules. These ligands have emerged from phage or small-molecule screens, or are based on antibodies or aptamers. Secondary reporters and combined therapeutic molecules have further opened potential clinical applications of these materials. The newer generation of MNPs has been developed to target specific cell types and molecular targets via such affinity ligands when compared to the first-generation nanoparticles that were mostly nonspecific.

As noted above, several studies have demonstrated the successful biological application of MNPs for drug delivery, molecular imaging, and targeted therapy. Although many articles [14–17] relating to MNPs and their biological applications have been produced, they provide very limited information with regards to applications in cancer. Hence, the aim of this chapter is to provide a comprehensive update of the cancer-related applications of MNPs, including drug delivery, imaging [including MRI, optical, nuclear, positron emission tomography (PET), computed tomography (CT), and single photon emission computed tomography (SPECT)], multimodal imaging, and therapy. The chapter is organized in three sections. Initially, the synthesis and surface modifications of MNPs for biological applications is outlined, including methods of fabrication, surface chemistry, and physico-chemical characterization. Further, following details of the development of MNPs as cancer diagnosis and imaging agents, after which an update is provided of the application of MNPs in cancer therapy, including cancer therapy, hyperthermia and thermal ablation, and MNP-directed toxicity studies.

6.2
Synthesis and Surface Modifications of MNPs for Biological Applications

6.2.1
Fabrication of the Magnetic Nanoparticle Core

Iron oxide particle cores can be prepared using a variety of methods, the most commonly used are listed in Table 6.1. The most-often used techniques for preparing nanoparticles are colloidal chemistry, milling, chemical vapor deposition (CVD) and sol–gel methodology. Iron oxides magnetic nanoparticles have been prepared from either aqueous or organic media using colloidal chemistry methods, with the overall, final specifications meeting requirements for the biological applications, such as control of particle size and shape, their stability in physiological media, and their nontoxicity. A number of reviews have been prepared on the various methods of nanomaterials fabrication for biomedical applications [18–20].

6.2.2
Surface Coatings and Chemistry

In order to impart stability and ensure nontoxicity under physiological conditions, and also to allow for functionalization and targeting, these nanoparticulate materials require sophisticated coatings. Ideally, the coating materials will have a high affinity for the iron oxide core, be nonimmunogenic, and also prevent opsonization by plasma proteins. While the synthesis of particles at high temperatures in organic solvents allows for a better control of particle size and morphology [18, 19], the particles must be transferred to aqueous solutions for biological applications. The aqueous synthesis of iron oxide nanoparticles usually involves the neutralization of acidic iron salts in the presence of a coating material [20]. The coatings used have included lipids [21, 22], liposomes [23–25], proteins [24, 26], dendrimers [27], polyethylene glycol (PEG) [28], polyacrylamide [29], polysaccharides [30, 31], and bisphosphonates [32]. Many iron oxide particles have been

Table 6.1 General classification of nanoparticles synthesis/processing methods.[a]

Vapor phase	Chemical vapor condensation; hydrogen plasma; laser ablation; flame pyrolysis, chemical vapor deposition
Liquid phase	Sol–gel; microemulsion; hydrothermal; sonochemical; supercritical fluid precipitation process; biological/biomimetic techniques; colloidal chemistry approach; microbial
Solid phase	Mechanical grinding/milling; mechanical alloying techniques

a Courtesy of W & W Services, Spain.

commercially prepared and utilized for clinical use (e.g., Ferridex®, Combidex®, Resovist®, and AMI-228/ferumoxytrol); all of these particles differ in terms of their surface coatings, which include dextran, carbohydrate, and citrate [6–8, 22, 33–38].

Dextran-coated iron oxide nanoparticles have become an important part of clinical cancer imaging, and have been shown to increase the accuracy of cancer nodal staging [39–41]. These particles have also been utilized to better delineate primary tumors [42], to image angiogenesis [43], and in the detection of metastases [44, 45]. The particles have also been used to image the inflammatory components of atherosclerosis [46]. A modification of dextranated iron oxide with targeting ligands, such as antibodies [47], has also been achieved to increase the affinity of the nanoparticles for their target tissues. One of the main drawbacks, however, is that the dextran coating is in equilibrium with the surrounding medium, as it is not strongly associated with the iron oxide core.

In one report, it was noted that dextran-coated iron oxide nanoparticles had the crosslinking (caging) of dextran and its amination [48]. The resultant particle, crosslinked iron oxide (CLIO), allows for a simple functionalization via amide bond formation, and also offers superb stability under harsh conditions (e.g., a change in size of the dextran coat to increase circulation time). Although CLIO has served as an ideal model compound for many experimental applications, is unlikely to be developed for clinical use, given the epichlorohydrin-induced crosslinking involved (this is similar to Sephadex particles). In order to circumvent this situation, magnetic nanoparticle preparations with biodegradable, high-affinity coatings are currently being developed by the present authors' group, and by others.

6.2.3
Physico-Chemical Characterization of MNPs

Previously, MNPs have been characterized using X-ray diffraction (XRD), vibrating sample magnetometry (VSM), scanning electron microscopy (SEM), transmission electron microscopy (TEM), and atomic force microscopy (AFM) [49]. The molecular weight and number of functional groups on the MNP's surface have been determined using analytical methods such as gel permeation chromatography (GPC), nuclear magnetic resonance spectroscopy (NMR), potentiometric titration, high-performance liquid chromatography (HPLC), and ultraviolet (UV) spectroscopy.

6.2.4
Plasma Stability and Pharmacokinetic Profile of the MNPs

The biological properties, interaction with plasma proteins, and biodistribution (monitored as the pharmacokinetic profile) of the MNPs throughout the body depends on physico-chemical factors such as particle size, surface charge, protein adsorption ability, surface hydrophobicity or hydophilicity, drug loading and

release kinetics, stability, degeneration of carrier systems, hydration behavior, electrophoretic mobility, porosity, specific surface characteristics, density, crystallinity, contact angle, and molecular weight [50]. Yet, the *in vivo* behavior of MNPs also depends on the dose and administration route (oral or parenteral, including delivery routes such as intravenous, pulmonary, transdermal, and ocular), in addition to less conventional routes, for example when used as scaffold coatings [51].

For biomedical applications, MNPs should be stable at room temperature in water or at neutral pH, they should not aggregate, and they should be biocompatible. Whilst the colloidal stability will depend on the particle size (i.e., it must be sufficiently small so as to avoid sedimentation due to gravity), it will also depend on the charge and surface chemistry, which in turn give rise to steric and coulombic repulsions [52, 53].

Another important criterion for the surface-coating is that it should be physiologically well tolerated; for example, dextran–magnetite has been reported to have a low toxicity index (LD_{50}) [54], though this has been the subject of much debate. In general, when the MNPs are injected into the bloodstream they are rapidly coated by plasma proteins; this process, known as opsonization, is critical in dictating the fate of the injected particles [55]. Normally, opsonization will render the MNPs recognizable by the reticuloendothelial system (RES), which serves as the body's major defense system. The RES is a diffuse system of specialized cells that are phagocytic (i.e., they engulf inert material) and are in association with the connective tissue framework of the liver, spleen, and lymph nodes [56, 57]. The macrophage (Kupffer) cells of the liver, and to a lesser extent the macrophages of the spleen and circulation, therefore play a critical role in the removal of opsonized particles. As a result, the application of nanoparticles, either *in vivo* or *in vitro*, requires a surface modification that will ensure the particles are biocompatible, and are also less prone to opsonization and thus phagocytosed to a lesser degree by the RES.

The MNPs' surface coatings play an essential role in retarding clearance by the RES. Uncoated MNPs were shown to be absorbed by the mononuclear phagocyte system after systemic administration, followed by clearance by the liver, spleen, and bone marrow. Different proteins (antibodies) of the blood serum (opsonins) bind to the surface of foreign bodies, accelerating phagocytosis of the particles. In order to avoid detection by the RES, biodegradable (e.g., dextran) and nonbiodegradable organic and inorganic coatings can be used. However, PEGylated surfaces in particular have demonstrated the desired protein-resistant characteristic, this having been attributed to the combination of a low interfacial energy in water and a steric stabilization effect [58].

Whereas, MNPs with hydrophobic surfaces are efficiently coated by plasma components and thus rapidly removed from the circulation, those particles which are more hydrophilic can resist this coating process and are cleared more slowly [59]. This effect has been used to advantage when attempting to synthesize RES-evading particles by sterically stabilizing the particles with a layer of hydrophilic polymer chains [60]. For example, the most common coating materials are derivatives of dextran, PEG, polyethylene oxide (PEO), poloxamers and polyoxamines

[61]. The role of these dense polymer coating brushes is to inhibit opsonization, thereby permitting a longer circulation time [32, 62]. Another strategy to avoid RES is to reduce the particle size [63, 64] yet, despite all of these efforts, a complete evasion of the RES by these coated nanoparticles has not yet been possible [59].

6.3 Development of MNPs as Cancer Diagnosis and Imaging Agents

The ability of nanoparticles to diagnose, image, and treat cancer is an upcoming area in the field of biomedical nanotechnology. Today, MNPs are used as MRI reagents for numerous diseases, and have recently emerged as the leading imaging agents (in both MRI and optical methods) for increasing the accuracy and specificity of cancer cell imaging, thereby providing new imaging opportunities in preclinical and translational research. The labeling of cells with MNPs has also emerged as a powerful tool to monitor the trafficking of a large number of cells in cell therapy, although the addition of cancer-targeting ligands such as antibodies, peptides, and small ligands has yet to develop in full. The emergence of multifunctional nanoparticles as tools to investigate various diseases via imaging modalities should provide essential information for patient care. Hence, recent advances in the use of MNPs in diagnostic cancer imaging are outlined in the next section.

6.3.1 MNPs Used in MR Imaging for Cancer Diagnosis

SPIO nanoparticles are well known as MRI agents that provide a noninvasive method for detecting and labeling tumor cells. As these nanoparticles exhibit the unique properties of superparamagnetism, they can be used as excellent probes for MRI studies. The majority of investigations have been conducted using a magnetic resonance scanner with a high field strength of up to 7 T. SPIO nanoparticles have also emerged as a suitable tool for labeling molecular probes that target specific tumor-associated markers for *in vitro* and *in vivo* detection by MRI. Recently, a number of studies have shown that MRI does indeed allow the very sensitive detection of tumor cells, both *in vitro* and *in vivo*, by using ligand-directed SPIO nanoparticles. As an example, Daga *et al.* [65] showed that the magnetic resonance signal intensity correlated with the concentration of USPIO nanoparticle-linked antibody and antigen density at the cell surface. The same group also studied the labeling of natural killer cells with iron nanoparticles, to a level that would allow the detection of their signal intensity with a clinical magnetic resonance scanner at 1.5 T.

Harisinghani *et al.* [40, 66–69] have performed extensive studies with lymphotropic superparamagnetic particles for MRI. Here, the superparamagnetic particles were absorbed by the macrophages in the lymph nodes, and caused changes in the magnetic properties detectable by MRI. After being injected, the particles

accumulate in normal lymph nodes and produce a decrease in signal intensity, whereas in a lymph node with metastatic disease the signal intensity tends to remain high [66]. Lymphotropic nanoparticle-enhanced MRI, when compared to conventional MRI, has been shown to have a higher sensitivity (90.5% versus 35.4%, $P < 0.001$) and specificity (97.8% versus 90.4%) [40, 70]. The main potential of the technique lies in the fact that it can be used to identify micrometastases, even if they do not grossly alter size or shape of lymph nodes with metastatic disease. Indeed, the original report identified metastases of only 2 mm diameter. Shih *et al*. [71] have shown, by using lymphotropic nanoparticle-enhanced magnetic resonance imaging (LNMRI), that the "at-risk" pelvic nodes confirm more to the vascular than to the skeletal anatomy of an individual. A total of 18 patients with nodal disease had their malignant lymph nodes mapped by LNMRI. A nodal clinical target volume that included a 2 cm radial margin was found to encompass almost 95% of the nodes at risk. Among 20 patients with gynecologic malignancies [72], LNMRI was used to assess the pelvic nodes and their relationship to the blood vessels. Guidelines for outlining the pelvic lymph nodes were also proposed. Clearly, LNMRI is a technique that will most likely be used to guide regional radiotherapy for many disease sites.

Zhang *et al*. developed $\alpha_v\beta_3$ integrin-targeting USPIOs and used these to monitor specific uptake by endothelial cells, the aim being to assess the angiogenic profile of tumors, both *in vitro* and *in vivo* [73]. Angiogenesis is an important step for the growth and spread of malignant tumors [74, 75] and is implicated in several cancers, including breast cancer, malignant melanoma, and skin squamous cell carcinoma [76–78]. Monitoring of expression of the cell adhesion molecule $\alpha_v\beta_3$ in living subjects would allow a better characterization of tumors, and also help to identify tumor regions and provide important targets for tumor diagnosis and therapy.

Many studies have reported using $\alpha_v\beta_3$ expression-targeting vectors with PET [79–81], SPECT [82, 83], optical imaging [84, 85], and ultrasound [84–87]. In order to target angiogenic vessels, $\alpha_v\beta_3$ integrin antibodies have been created and are currently undergoing evaluation in clinical trials as anti-angiogenic therapeutics [88, 89]. Short polypeptides, containing Arg-Gly-Asp (RGD), in both linear [90] and cyclic [91] formats, have been tested to target $\alpha_v\beta_3$ integrins for different purposes. Thus, the development of $\alpha_v\beta_3$ integrin-targeting nanoparticle platforms may be of great value for improving radiotherapy planning and also for monitoring anti-angiogenic and other noninvasive antitumor therapies [92].

In this study, the USPIOs were coated with 3-aminopropyltrimethoxysilane and conjugated to RGD peptides, so as to enhance the diagnostic capabilities of MRI. Prussian blue staining, TEM, MRI, and inductively coupled plasma mass spectrometry were all used to show that the molecular imaging agents had accumulated in the human umbilical vein endothelial cells (HUVECs). The $\alpha_v\beta_3$ integrin-positive vessels were evaluated using a 1.5 T MR scanner.

The study results showed that the RGD-USPIO particles were visualized by targeting $\alpha_v\beta_3$ integrins expressed in nude mice bearing HaCaT-ras-A-5RT3 and A431 tumor xenografts (Figure 6.1). Tumors with different angiogenic profiles

were assessed *in vivo*. The T_2*-weighted images clearly identified the heterogeneous arrangement of vessels with $\alpha_v\beta_3$ integrins expressed on endothelial cells (Figure 6.1). The uptake of RGD-USPIO by HUVECs was significantly increased when compared with unlabeled USPIOs, and could be competitively inhibited by the addition of unbound RGD. The RGD-USPIO noninvasively distinguish tumors with higher (HaCaT-ras-A-5RT3) and lower (A431) area fractions of $\alpha_v\beta_3$ integrins in HaCaT-ras-A-5RT3 tumors. A visual inspection of the T_2- and T_2^*-weighted images of HaCaT-ras-A-5RT3 and A431 tumors elucidated differences in the distribution pattern of RGD-USPIO. In HaCaT-ras-A-5RT3 tumors, a branched network of strong signal intensity (SI) decrease was found at the border and in certain central parts of the tumor, which was consistent with the heterogeneous pattern of angiogenesis described in these tumors [93]. In contrast, SI changes in A431 tumors were less pronounced and more homogeneous, with only a few spots with a strong SI decrease being observed at the tumor periphery (Figure 6.1a). Both, in HaCaT-ras-A-5RT3 and in A431 tumors, the T_2 relaxation times were decreased significantly more ($P < 0.05$) after the injection of RGD-USPIO than after the injection of plain particles (Figure 6.1b). In addition, the decrease in T_2 relaxation time in HaCaT-ras-A-5RT3 tumors (28 ± 41 ms) was more pronounced than in A431 tumors (14 ± 8 ms).

On fluorescence images, HaCaT-ras-A-5RT3 tumors showed a highly heterogeneous vascularization with not only large, intensively branched vascular networks but also low-vascularized areas with only [a] few small vessels. As described elsewhere [94], both discontinuous and heterogeneous $\alpha_v\beta_3$ integrin expression was found on endothelial cells and in perivascular stromal cells. In contrast, A431 tumors showed a homogeneous vascularization with predominantly small vessels of <20 μm diameter. These differences in vascular phenotypes with focal intense vascularized areas showing high levels of $\alpha_v\beta_3$ integrins in HaCaT-ras-A5RT3 tumors, and with the more homogeneous vascularization in A431 tumors, provide a plausible explanation of the different SI change pattern seen on the T_2^*-weighted MR images. In summary, RGD-coupled, APTMS-coated USPIOs efficiently targeted $\alpha_v\beta_3$ integrin expressions and provided an angiogenesis imaging profile [73].

Sun *et al*. demonstrated an MRI nanoprobe that targets gliomas, expressing membrane-bound matrix metalloproteinase-2 (MMP-2) with high-level specificity, both *in vitro* and *in vivo* [95]. The nanoprobe is composed of an iron oxide core coated with PEG and conjugated with the targeting agent, chlorotoxin (CTX), a 36-amino acid peptide, and demonstrated a high selectivity and binding affinity towards gliomas as well as towards other tumors of neuroectodermal origin [96, 97]. Reports have been made which show that CTX specifically binds to glioma, medulloblastoma, prostate cancer, sarcoma, and intestinal cancer [98]. Furthermore, an ^{131}I-linked version of CTX is currently undergoing Phase II clinical trials for the targeted radiation of tumor cells [99]. Previously, the same research group tested the glioma-targeting ability of the CTX-conjugated nanoparticles [100], but the current improved version of CTX-conjugated nanoprobes has an ability to target gliomas specifically. The tumor specificity of the nanoprobe was evaluated *in vitro* using a 9L gliosarcoma cell line through cellular uptake assays, and also

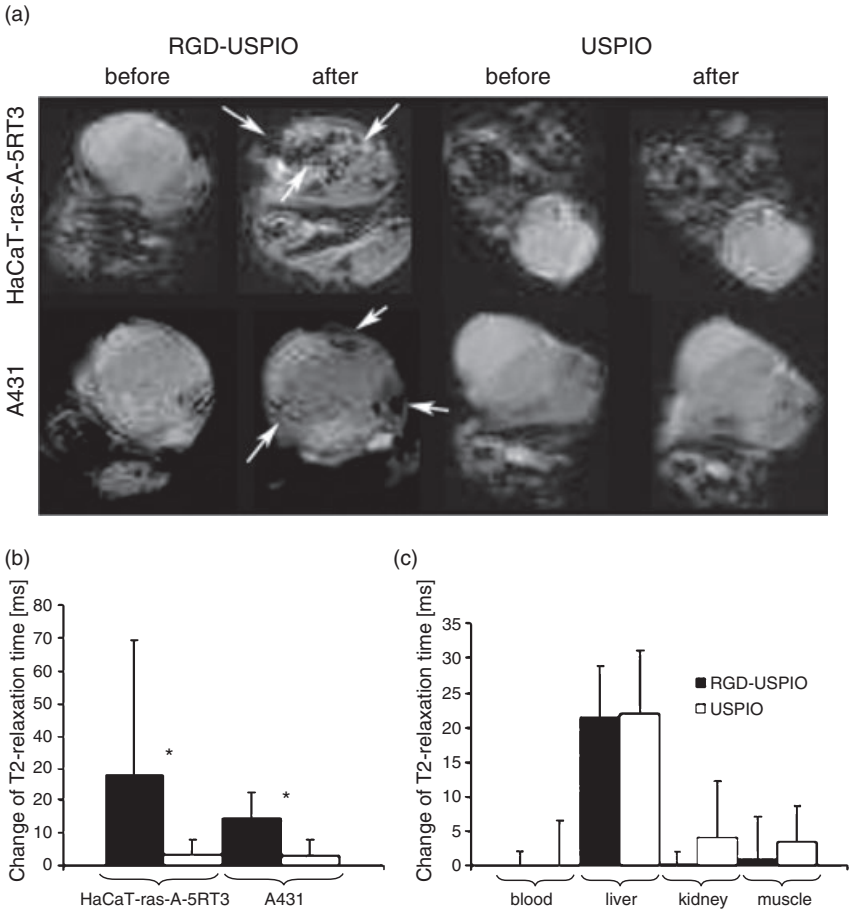

Figure 6.1 (a) T_2^*-weighted MR images of nude mice bearing subcutaneous HaCaT-ras-A-5RT3 (top row) and A431 (bottom row) tumors, before and at 6 h after intravenous injection of RGD-USPIO and USPIO, respectively. Focal areas with strong and heterogeneous SI decrease were observed in the tumor center and periphery after injection of RGD-USPIO in HaCaT-ras-A-5RT3 tumors (arrows). Only a few spots with high susceptibility were found at the margin of the control tumor after injection of USPIO. SI changes in the A431 tumor were much less pronounced and more homogeneous, while focal areas with a strong SI decrease were only found at the tumor margins (arrows). Visual inspection showed no signal changes in control tumors; (b) Change of T_2 relaxation times in HaCaT-ras-A-5RT3 ($n = 8$) and A431 ($n = 6$) tumors after injection of RGD-USPIO and USPIO, respectively; (c) Change of T_2 relaxation times in blood, liver, kidney, and muscle of A431 tumor-bearing mice after injection of RGD-USPIO ($n = 6$) and USPIO ($n = 6$), respectively. Reprinted with permission from Ref. [73].

in vivo by MRI of athymic (nu/nu) mice bearing xenografts (this is a widely used and well-established animal model which mimics natural gliomas) [101, 102]. Nanoparticle internalization by glioma cells was visualized using TEM, and quantified by measuring the intracellular iron content using colorimetry. *In vitro* MR phantom imaging and *in vivo* small-animal MRI demonstrated the targeting ability of the nanoprobes in tumor cells. In addition, the R_2 relaxation rates were measured to quantify the degree of contrast enhancement.

The specificity of the nanoprobes was evaluated by comparing the contrast enhancement between the tumor and normal tissue regions of mice. NP-PEG-CTX and NP-PEG-succinimidyl iodoacetate (SIA) were administered at the same concentration, after which each of the mice were imaged prior to, and at various time points after, an intravenous injection of the nanoprobes (at a dosage of 6 mg Fe kg^{-1}). Figures 6.2a and b show the anatomical images of coronal and sagittal planes used to determine the tumor position along the flank of the animal. Multi-spin-echo pulse sequences were utilized to obtain a series of images over a range of echo times (TEs) for the tumor regions of axial cross-sectional. The targeting ability of the NP-PEG-CTX (Figure 6.2d), in comparison to NP-PEG-SIA (Figure 6.2c), was evident in MR images acquired in the tumor at 3 h post-injection in mice.

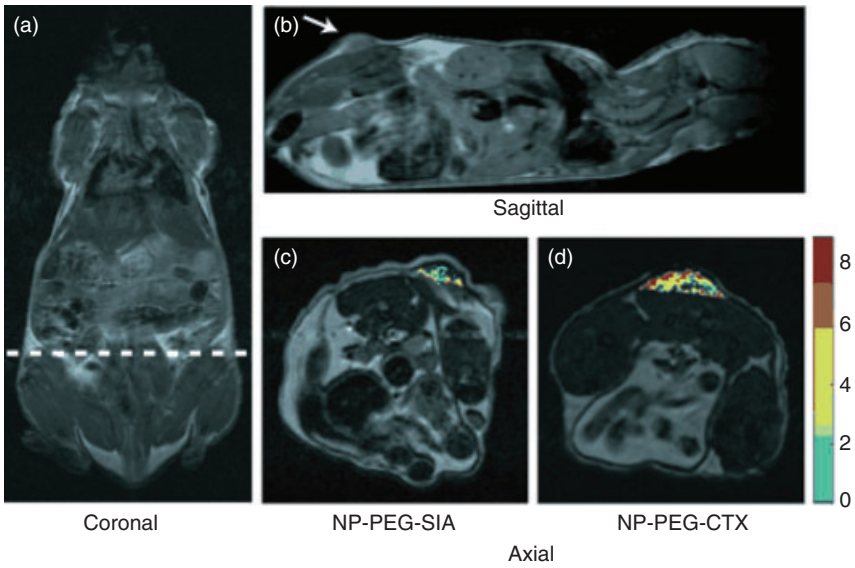

Figure 6.2 MRI anatomical image of a mouse in (a) the coronal plane. The dotted line shows the approximate location of the axial cross-sections displayed in panels (c) and (d); (b) Anatomical image in the sagittal plane. This displays the location of the 9L xenograft tumor; (c, d) Changes in R2 relaxivity values for the tumor regions (superimposed over anatomical MR images) for mice receiving (c) nontargeting NP-PEG-SIA and (d) NP-PEG-CTX at 3 h post injection. The arrow in (b) marks the tumor location. These are representative images from three independent experiments with similar results. Reprinted with permission from Ref. [95].

Histological analyses were performed on tissues obtained from the clearance organs (kidney, spleen, and liver), in order to investigate the toxicity (if any) of the nanoparticles. No apparent toxicity was reported in the tissues of animals receiving the nanoprobes, when compared to normal mice receiving no injection. The mice injected with nanoprobes were also tested for any physical and/or neurological acute toxicity associated with nanoprobe administration. For this, the accumulation and retention of the targeting nanoprobe in the tumor and surrounding normal tissues were evaluated at intervals of 0, 0.3, 2, 12, and 24 h post-injection, the aim being to quantify nanoprobe accumulation and to define the time window when animals could be imaged so as to achieve maximum MRI contrast, as well as to gain an understanding of the pharmacokinetics of the nanoprobe. A high targeting specificity and a benign biological response, as were established by this nanoprobe, might represent a potential platform to aid in the diagnosis and treatment of gliomas and other tumors of neuroectodermal origin.

Veiseh *et al.* [100] prepared magnetite nanoparticles with a PEG coating, and subsequently functionalized these with CTX and the fluorescent molecule, Cy5.5. The nanoparticle–CTX conjugates were seen to target glioma tumor cells, with internalization into the cells being visualized by confocal imaging. The reported T_2 relaxation times (5 ms for CTX-coated particles, 95 ms for non-coated) showed much promise for glioma detection, and also demonstrated an affinity of these nanocomposites for glioma cells over healthy tissues.

6.3.2
MNPs Used in Optical Imaging for Cancer Diagnosis

A number of magnetic nanoparticle preparations have been developed over the past decade for cancer staging, angiogenesis imaging, and the tracking of immune cells (monocyte/macrophage, T cells), and also for molecular and cellular targeting [103], by utilizing MRI. However, increasing reports during the past few years have shown that MNPs conjugated to optically active fluorescent molecules (magneto-fluorescent) have become important tools for *in vitro* and *in vivo* imaging, using magnetic resonance and fluorescent optical methods. A combination of magnetic and optical imaging into a nanostructured system would greatly benefit the *in vivo* disease diagnosis, as well as the *in situ* monitoring of responses of living cells [104–107].

One of the major attractions of magnetic nanoparticles is they can be easily functionalized to provide additional properties so as to form a multifunctional platform or scaffold. These include drug molecules, fluorescent compounds, and various hydrophobic and hydrophilic coatings. Fluorescent organic dyes have been used extensively in biology for labeling and staining various markers; examples are DAPI, Mitotracker and Hoescht dyes, all of which have been used to label cellular features. Although, the association of magnetic and fluorescent fluorophore-linked MNPs has provided an attractive dual-imaging scaffold, the synthetic procedure has required multistep chemical treatments in order to conjugate

fluorescent dyes onto the MNP surface, and to improve the colloidal stability in an aqueous medium.

Another family of fluorescent nanomaterials is that of semiconductor-based quantum dots (QDs). These have a strong, characteristic spectral emission that is tunable to a desired energy by selecting variable particle size, size distribution, and composition of the nanocrystals. Recently, QDs have attracted much interest due to their unique photophysical properties and range of potential applications in photonics and biochemistry [108, 109]. With advances in current organic and bioorganic synthetic chemistry, capping group formation and bioconjugation strategies, QDs are becoming increasingly used as biological imaging agents [108, 110–112]. QDs can be treated with drug moieties (e.g., nonsteroidal anti-inflammatories) in order to specifically target certain organs or cell organelles [113]. One of the most attractive properties of QDs is the fact that their emission spectra may be tuned by varying the primary particle size or composition. Those QDs which emit at several different wavelengths can be excited with a single wavelength, and are suitable for the multiplex detection of a number of different targets in a single experiment [114]. QDs also have advantages over commercially available dyes due to their high photochemical stability [108].

Thus, a combination of MNPs and QDs can provide both the magnetic and fluorescent properties that have been shown to play significant roles in nanotechnology. Moreover, the combination of magnetic and fluorescent properties in one nanocomposite provides excellent prospects for both nanotechnology and biotechnology, and enables the creation of unique targeted, nanoscale photonic devices that can be manipulated by using an external magnetic field to provide dual-imaging agents for cancer diagnosis [115].

Bertorelle *et al*. later developed fluorescent modified anionic superparamagnetic nanoparticles and demonstrated the potential use of magnetofluorescent nanoagents (for MRI and optical imaging at the cellular level) for adsorption and internalization into the cells [105]. Fluorescent microscopy showed the cells to be loaded with millions of fluorescent magnetic particles. Yang *et al*., by using a nanoemulsion method, synthesized simple and stable fluorescent magnetic nanohybrids for multimodal imaging agents in the detection of cancer cells [115].

Targeted cancer imaging has also been investigated by Choi *et al*. [107], using folate-treated magnetic nanoparticles. The folate receptor is a protein that is overexpressed in various types of human cancer, where it acts to capture the folate required to feed rapidly dividing cells. The suggestion here was to use dextran-coated magnetic nanoparticles that had been tethered to folic acid and a fluorescent imaging agent (fluorescein isothiocyanate; FITC). In this way, when the particles had been internalized into the cancer cells, it would be possible to obtain and analyze a tumor image *in vivo*. The FITC-conjugated iron oxide nanoparticles were developed to allow the direct visualization of nanoparticle uptake into the cancer cells [107]. The fluorescence image demonstrated the presence of folate–FITC–iron oxide nanoparticles in KB cells after 1 h of culture in solution; the internalization of folate–FITC–iron oxide nanoparticles into KB cells was also

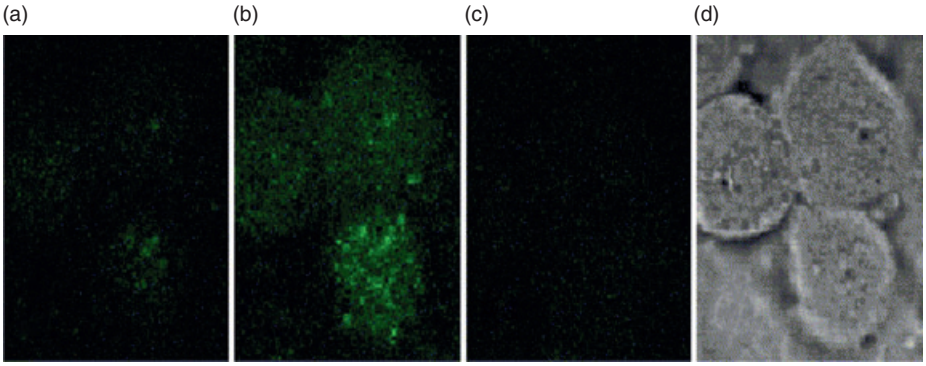

Figure 6.3 Confocal micrographs of KB cells after a 1 h incubation with folate-FITC-IO nanoparticles at different focal positions: (a), (b), (c), and (d) of the cells. The strong signal of (b) and the corresponding phase-contrast image of the cell (d) confirm that the cell interior is the origin of the fluorescence signal. Reprinted with permission from Ref. [107].

confirmed with confocal microscopy (Figure 6.3a–d) performed at various depths from the cell surface [107]. The T_2-weighted MR images revealed a 38% decrease in the intensity of the cancer tissue owing to the presence of the folate-coated nanoparticles.

In another study by Tsourkas *et al.* [116], crosslinked dextran-coated iron oxide nanoparticles labeled with the near-infrared fluorochrome Cy5.5 and conjugated to an anti-VCAM-1 antibody were investigated for imaging of the tumor necrosis factor-α (TNF-α) -activated endothelium in an inflammatory murine ear model. Both, magnetic resonance and optical imaging demonstrated the presence of magnetofluorescent nanoparticles that were capable of detecting VCAM-1 expression. Thus, disease screening by MRI and the surgical identification of diseased areas by intraoperative fluorescence imaging could be conducted within the same investigation.

In a similar approach, thermally crosslinked superparamagnetic iron oxide nanoparticles (TCL-SPION) modified with Cy5.5 dye were used in dual mode (magnetic resonance/optical) for *in vivo* cancer imaging [117]. The TCL-SPION-Cys5.5, when injected intravenously into a Lewis lung carcinoma, was detected by using MRI, while the optical fluorescence images showed, within 4 h of injection, a high accumulation of TCL-SPION-Cys5.5 at the tumor site *in vivo* (Figure 6.4). Most importantly, however, although the TCL-SPION-Cys5.5 did not include any tumor-targeting ligands, the tumor was detected effectively by dual imaging [117].

In a novel approach, a biotinylated magnetic dendrimer-based MRI agent was prepared, in which a unique disulfide bond in the core of the Gd(III)-1B4M-DTPA-

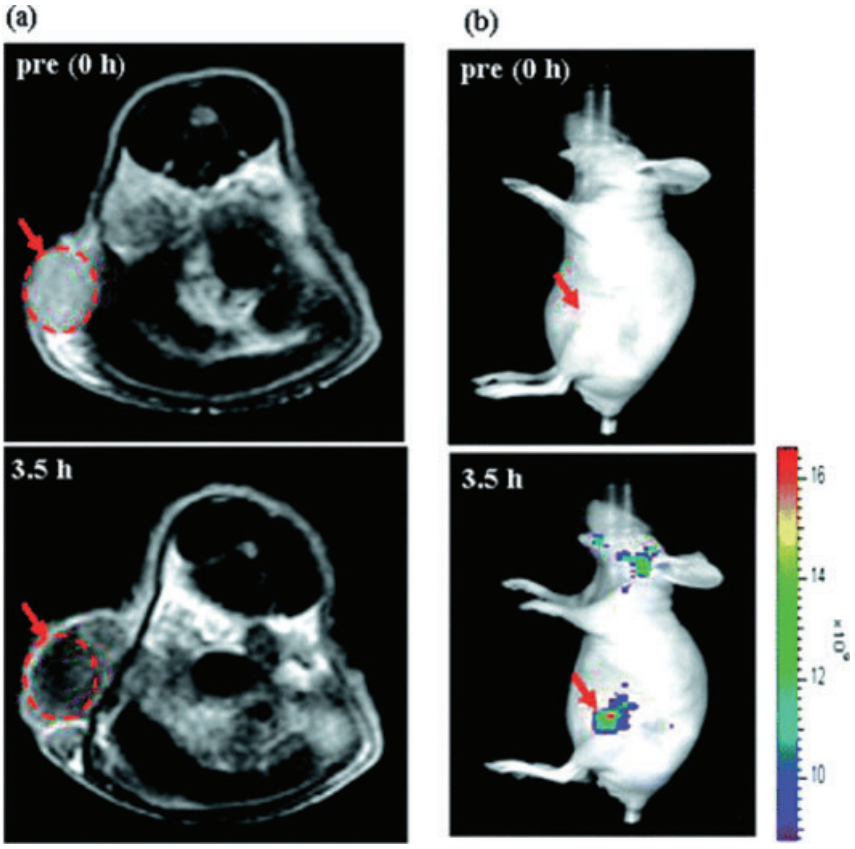

Figure 6.4 (a) T_2-weighted fast spin-echo images (TR/TE of 4200 ms/102 ms) at 0 and 3.5 h post injection of 14.7 mg Fe kg^{-1} of Cy5.5 TCL-SPION at the level of tumor (320 mm^3) on the flank above the upper left thigh of a nude mouse. The allograft tumor region is shown by the dashed circle with the red arrow; (b) Optical fluorescence images (exposure time 1 s with a Cy5.5 filter channel) of the same mouse at 0 and 3.5 h post injection. The position of the allograft tumor is marked by the red arrows. The color scale indicates relative fluorescence intensity. (Reprinted with permission from Ref. [117].

chelated G2 PAMAM dendrimer was reduced and then attached to a maleimide-functionalized biotin. The new MRI agent had a well-defined dendron structure and a unique biotin functionality. The immobilization of up to four copies of biotinylated dendrimer to fluorescently labeled avidin yielded a supramolecular avidin–biotin–dendrimer–Gd(III) complex. The avidin–biotin–dendrimer targeting system efficiently targeted ovarian cancer in mice, and delivered sufficient amounts of chelated Gd(III) and rhodamine green fluorophores. This dual-imaging probe produced visible changes in the tumors by both MRI and optical imaging, respectively [118].

MNPs coated with poly-(amidoamine) dendrimer-based multifunctional cancer therapeutic conjugates have been designed and synthesized to provide enhanced solubility. The functional molecules of FITC, folic acid and paclitaxel (taxol, a chemotherapeutic drug) were conjugated to the nonacetylated primary amino groups; the appropriate control dendrimer conjugates were also synthesized. The conjugation of FITC and folic acid prevented any nonspecific targeting of the MNP interactions (both *in vitro* and *in vivo*) during delivery [119]. In another interesting experiment, the potential use of multimodal fluorescent-magnetic polymer capsules loaded with cancer agents for targeted drug delivery and cancer therapy [120] was demonstrated.

Gu *et al.* [121] have shown that iron oxide nanoparticles, when conjugated to porphyrin, can be utilized as bimodal anticancer agents for combined photodynamic and hyperthermic therapies. These conjugates can be effectively taken up by HeLa cancer cells; subsequent exposure of the cells containing nanocomposites to yellow light resulted in a significant change in their morphology, due to cell apoptosis. The authors suggested that these findings might represent another potential use for MNPs in cancer imaging and therapy.

Kircher *et al.* employed dual-modality imaging nanoparticles for preoperative MRI and intraoperative optical imaging in an experimental brain tumor model [122, 123]. Long-term-circulating iron oxide nanoparticles, with a near-infrared fluorescence (NIRF) dye attached to a coating of crosslinked dextran (Cy5.5-CLIO), were synthesized and investigated as a combined preoperative magnetic resonance contrast agent and intraoperative optical probe. A series of studies was carried out to determine the cellular distribution of Cy5.5-CLIO, using triple-channel laser scanning confocal microscopy. Figure 6.5 compares the distribution of Cy5.5-CLIO (Cy5.5 channel; Figure 6.5a) with the distribution of tumor cells [green fluorescent protein (GFP) channel; Figure 6.5b] and microglia and macrophages (CD11b immunohistochemistry using the rhodamine channel; Figure 6.5c). Cy5.5-CLIO was strongly associated with CD11b-positive cells (Figure 6.5d), and much less with GFP-positive cells (Figure 6.5e).

These multimodal magneto/optical nanoparticles were also used with great effect to compare the visual presentation of a brain tumor during surgery with the multislice topographical capability of preoperative MRI. The results indicated the feasibility of this approach using nanoparticles similar to those used in clinical studies, to provide a strong NIRF signal and thus enable real-time imaging. This method was an extension of the existing MRI and simple NIRF/optical instrumentation. The study results indicated that the key features of the nanoparticles, such as intracellular sequestration and slow degradation, together with the combined optical and magnetic properties of Cy5.5-CLIO, would allow visualization of the same probes in the same cells by both radiologists and neurosurgeons. This may increase the precision of surgical resection and improve the outlook for many brain cancer patients.

In another key publication, Lv *et al.* showed that the nanocomposites could effectively facilitate an interaction of the anticancer drug daunorubicin with leukemia cells, and remarkably enhance the permeation and drug uptake of anticancer

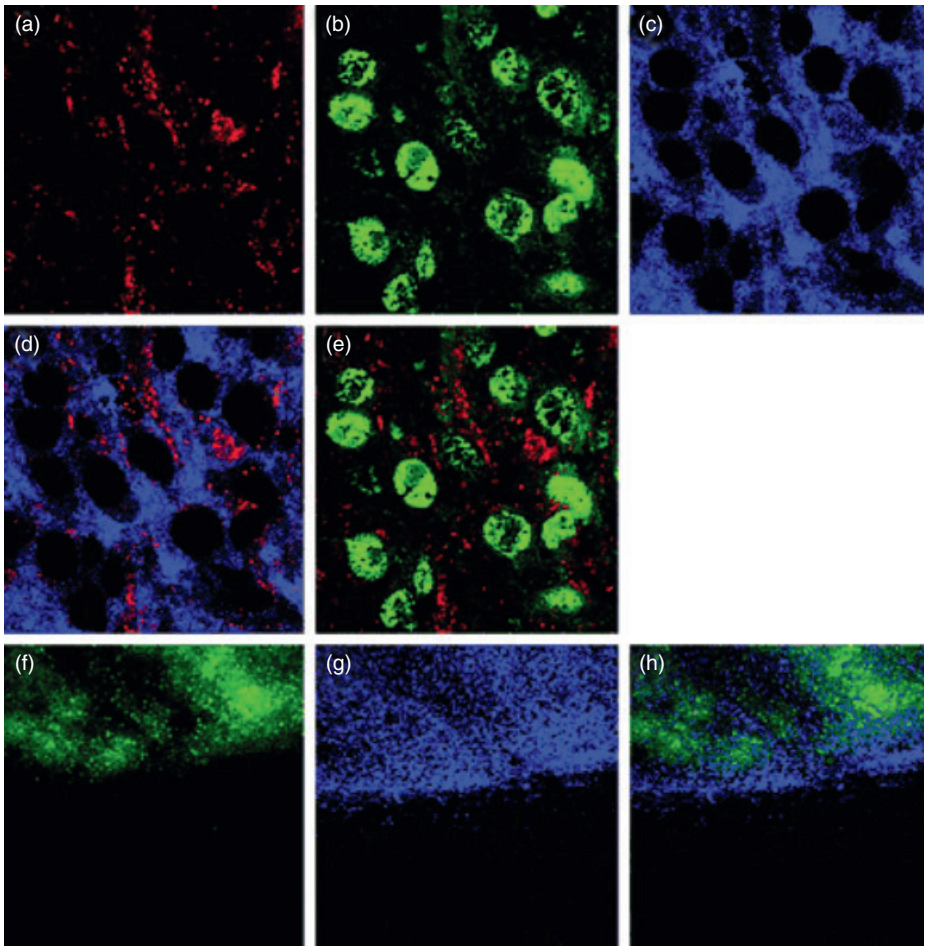

Figure 6.5 Laser scanning confocal microscopy images of cell type internalizing Cy5.5-CLIO as determined by: (a–e) area from tumor center (original magnification, ×200); and (f–h) area from tumor–brain interface (original magnification, ×10). (a) Distribution of Cy5.5-CLIO in Cy5.5 channel; (b) GFP channel; (c) Anti-CD11b staining for microglia and macrophages in rhodamine channel; (d) Overlay of (a) and (c); (e) Overlay of (a) and (b). Cy5.5-CLIO is internalized predominantly by microglial cells and infiltrating macrophages; (f) Tumor border in the GFP channel; (g) Tumor border in the rhodamine channel (CD11b); (h) Overlay of (f) and (g). Cells positive for CD11b extend slightly beyond the border of the GFP fluorescence. Reprinted with permission from Ref. [122].

agents in cancer cells [124]. These novel nanocomposites were prepared by utilizing polylactide (PLA) nanofibers and tetraheptylammonium-capped Fe_3O_4 magnetic nanoparticles. Both, optical microscopy and confocal fluorescence microscopy observations indicated that the PLA nanofibers and Fe_3O_4 nanoparticles enhanced the accumulation of daunorubicin on the membrane of leukemia K562 cell lines.

6.3.3 Ligand-Directed MNPs for Cancer Imaging

Antibody-conjugated magnetic nanoparticles represent a specific and sensitive tool to enhance the MRI of both local and metastatic cancers. MNPs, when linked to immunomolecules, may provide multimodality imaging options when tagged with radioisotopes or fluorescent molecules that thus provide the capability of being tracked and imaged in humans. This approach could be extended to a new model for targeted or pre-targeted therapy. Many study reports (the majority of which were published after 2006) indicated that ligand-directed nanoparticles were utilized very effectively for cancer targeting.

6.3.3.1 Antibody-Directed MNPs

Guo *et al.* recently reported the use of ultrasmall superparamagnetic iron oxide particles linked to humanized SM5-1 antibodies (SM-USPIO) for the specific targeting of human hepatocellular carcinoma (HCC) cells [125]. When the binding and internalization of SM-USPIO to the HCC cell line of ch-hep-3 was demonstrated using flow cytometry and confocal microscopy, the study results showed that SM-USPIO was able to accumulate selectively in the tumor cells, producing a marked decrease in the MRI T_2-weighted signal intensity. The results of biodistribution studies demonstrated an efficient accumulation of SM-USPIO in the ch-hep-3 tumor in nude mice. In an *in vivo* study in ch-hep-3 tumor-bearing nude mice, the results indicated that MRI using SM-USPIOs as a contrast agent provided a good diagnostic ability, which in turn suggested that SM-USPIOs were potentially a promising targeted contrast agent for the diagnosis of HCC.

The tyrosine kinase Her-2/neu receptor is a clinically relevant target in breast cancer, and plays a significant role in the staging and treatment of cancer. Artemove *et al.* [126] used streptavidin-conjugated superparamagnetic nanoparticles as a targeted MR contrast agent. In their study, Her-2/neu receptors were imaged in a panel of breast cancer cells expressing different numbers of receptors on the cell membrane. The nanoparticles were directed to receptors by being preconjugated with biotinylated monoclonal antibodies, and generated strong T(2) MR contrast in Her-2/neu-expressing cells. The contrast observed in MR images was proportional to the expression level of the Her-2/neu receptors determined independently with fluorescence-activated cell sorting (FACS) analysis. In these experiments, the iron oxide nanoparticles were attached to the cell surface rather than being internalized into the cells, which might represent a major advantage for *in vivo* applications such as pretargeting radioimmunotherapy.

Streptavidin-labeled iron oxide nanoparticles conjugated to biotinylated anti-prostate-specific membrane antigen (PSMA) antibody was used in MRI and confocal laser scanning microscopy imaging studies using LNCaP prostate cancer cells. PSMA is predominantly expressed on the neovasculature of solid tumors and on the surface of prostate cells, with an enhanced expression following androgen-deprivation therapy. Labeled iron oxide nanoparticles were internalized by receptor-mediated endocytosis, which involves the formation of clathrin-coated vesicles

[127]. The endocytosed particles were not targeted to the Golgi apparatus for recycling, but rather accumulated within the lysosomes. In T_1-weighted MR images, signal enhancement owing to the magnetic particles was greater for cells with magnetic particles bound to the cell surface than for cells that internalized the particles. These findings indicated that the targeting of prostate cancer cells using PSMA offered a specific and sensitive technique for the enhancement of MR images [127].

6.3.3.2 Antibody Fragment-Directed MNPs

A single-chain Fv (scFv) gene which was specific to γ-seminoprotein was developed for the treatment of prostate cancer; the ScFv antibody fragments were subsequently linked with MNPs for molecular-targeting in prostate cancer therapy or diagnosis, as reported by Han *et al.* [128]. In this case, the human seminoprotein secreted by the prostate tumor provides a specific antigen [129]. In this study, the ScFv were used to deliver MNPs into prostate cancer cells for imaging the tumors. The results also showed that ScFv specific for seminoprotein were able to bind prostate cells specifically, and to transport the magnetic beads rapidly (within 15 min) into the tumor cells. The quantity of magnetic beads located inside the tumor was increased as the culture time was prolonged. ScFv-conjugated magnetic beads did not enter non-specific control cells [128]. Antibody scFv fragments were also used by Natarajan *et al.* [130], who linked the MNPs to anti MUC-1 di-scFv by site-specific coupling methods to target breast cancer cells for the focused hyperthermia created within them by an alternating magnetic field (AMF). In this preparation, MNPs were attached to di-scFv-cysteine at a well-defined site. Studies with whole-body auto radiography (Figure 6.6a) and pharmacokinetic investigations (Figure 6.6b) showed the di-scFv-directed MNPs to be effectively targeted in breast cancer cells in mice [130].

Lee *et al.* [131] developed engineered iron oxide nanoparticles (MEIO) and MnMEIO to target cancer and to provide ultra-sensitive MRI. In particular, molecular probes based on MnMEIO have strong magnetic properties, demonstrated a considerably enhanced sensitivity for cancer cell detection, and also permitted imaging of the smallest possible tumors *in vivo*. MnMEIO nanoparticles were also conjugated to the cancer-targeting Herceptin antibody [132, 133], which binds specifically to the HER2/neu marker that is overexpressed in breast and ovarian cancers [134]. Both, MnMEIO – and MnMEIO–Herceptin proved to be biologically nontoxic. When these particles were compared to the CLIO–Herceptin conjugates [135] for their cancer cell-detecting ability, FACS analyses indicated that almost identical numbers of MnMEIO and CLIO nanoparticles were bound to cancer cells.

In these studies, MnMEIO–Herceptin conjugates (200 ml) were administered ($n = 8$, dose 20 mg kg^{-1}) to nude mice implanted with NIH3T6.7 cells in the proximal femur region, and MR images subsequently obtained before and at 1 and 2 h after injection. The color-coded MR images shown in Figure 6.7a–c indicated that the tumor site had been targeted and well detected. When the same experiment was performed with CLIO–Herceptin conjugates at the same dose level, no

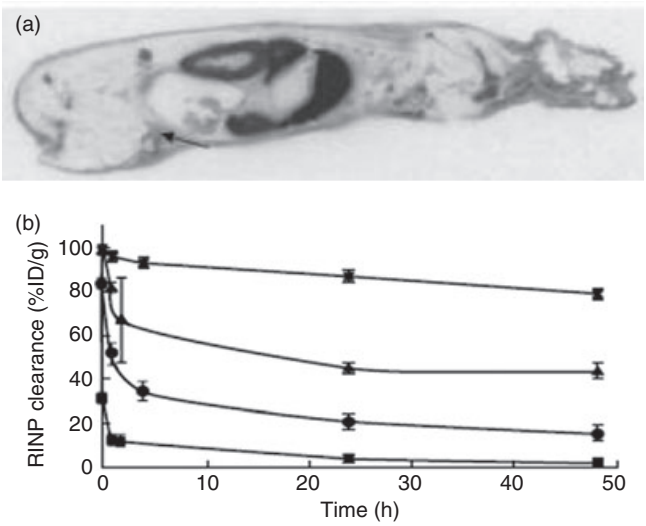

Figure 6.6 Autoradiography of whole body of mice euthanized at 24 h after an intravenous injection of 40 mCi (50 μg) of di-scFv/4 mg of ^{111}In-DOTA-di-scFv-NP. Radioimmunonanoparticles were mostly accumulated in the kidney and liver. The tumor localization was ~5% (black arrow). (b) Pharmacokinetic study of radioimmunonanoparticles (RINP) in mice with HBT3477 human breast cancer xenografts. Clearances of the blood (■) and body (▲) of RINP was compared to the blood (●) and body (×) of bioprobes at various time points of 2, 4, 24, and 48 h. The bioprobe data were plotted from previously published data in Ref. [5]. Reprinted with permission from Ref. [130].

apparent change was observed in the color-coded MR images (Figure 6.7d–f). The percentage change in R2 at the tumor tissue was –25% at 1 h, and –34% at 2 h for MnMEIO–Herceptin, and in the case of CLIO–Herceptin was almost zero or <5%, respectively, at the tumor site (Figure 6.7g). The color-coded MR images (Figure 6.7h) of tumor tissue explanted from a mouse treated with the MnMEIO–Herceptin conjugate showed darkened MR images, with R2 signal enhancement ($\Delta R2/R2_{control} = -31\%$; Figure 6.7g, h), whereas very little MR contrast ($\Delta R2/R2_{control}$ <5%) was seen at the tumor site of a mouse treated with CLIO–Herceptin conjugate (Figure 6.7g, h). These *in vivo* results indicated that the high MR sensitivity of MnMEIO–Herceptin conjugates enables the MR detection of tumors as small as 50 mg [136].

Biodistribution studies of MnMEIO–Herceptin conjugates labeled with radioactive ^{111}In using gamma-counter analyses showed that the uptake of injected particles by various organs (expressed as % of the dose per g tissue) was 3.4% in tumor tissue, 12.8% in the liver, 8.7% in the spleen, and 1.0% in muscle. These results provided further support for the use of MNPs, when linked with appropriate cancer-targeting molecules, for the diagnosis of various cancers by ultrasensitive MRI and radioimmunodetection systems. Ultimately, high-performance

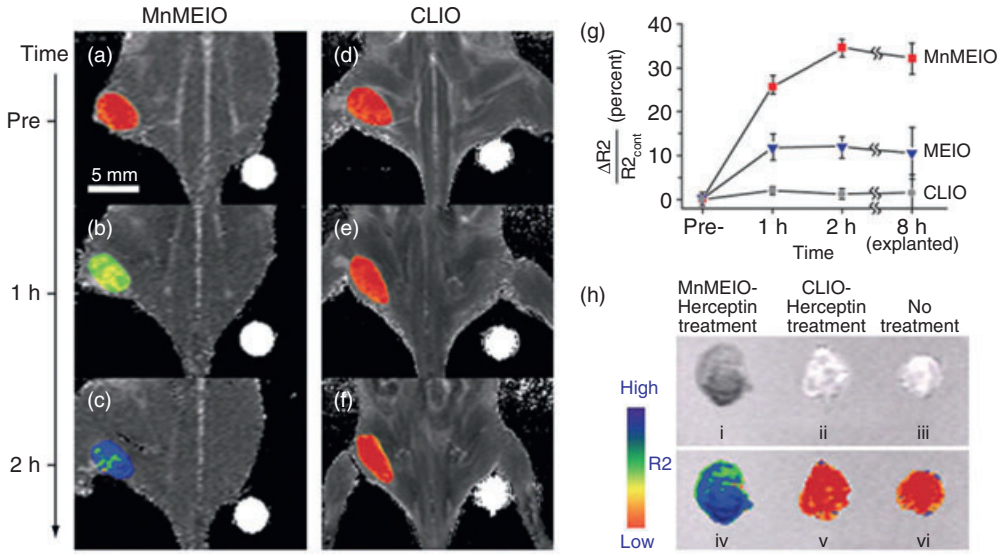

Figure 6.7 (a–f) Color maps of T_2-weighted MR images of a mouse implanted with the cancer cell line NIH3T6.7, at different time points after injection of MnMEIO–Herceptin conjugates or CLIO–Herceptin conjugates (preinjection (a, d); and 1 h (b, e) or 2 h (c, f) after injection). In (a–c), the gradual color changes at the tumor site, from red (i.e., low R2) to blue (i.e., high R2), indicates progressive targeting by the MnMEIO–Herceptin conjugates. In contrast, almost no change was seen in mice treated with CLIO–Herceptin conjugate (d–f); (g) Plot of R2 change versus time. In mice treated with MnMEIO–Herceptin conjugate (■), significant R2 changes (up to 34%) were observed with time after treatment. In contrast, R2 changed by <5% after treatment with CLIO–Herceptin conjugate (●) and by <13% after treatment with 12-nm-MEIO–Herceptin conjugate (▼); (h) *Ex vivo* MR images (i–iii) of explanted tumors (8 h) and their color maps (iv–vi). The tumor explanted after treatment with MnMEIO–Herceptin conjugate (i) was dark; that explanted following CLIO–Herceptin conjugate treatment (ii) or no treatment (iii) showed no contrast. Consistently, in the image color-coded according to R2, the tumor explanted after MnMEIO–Herceptin conjugate treatment was blue (iv), whereas that after CLIO–Herceptin conjugate treatment (v) or no treatment (vi) was red. Reprinted with permission from Ref. [131].

magnetic nanoprobing systems may play a pivotal role in the real-time visualization of other biological events, such as cell trafficking, cancer metastasis, cellular signaling, and interactions at the molecular and cellular levels.

6.3.4
Radioimmunonanoparticles

Biologically active radioimmunoconjugates (RICs) were ligated to MNPs to form radioimmunonanoparticles (RINPs). Both, Natarajan *et al.* [137, 138] and DeNardo *et al.* [139–141] applied this technique for hyperthermia in a human breast cancer mouse model. An overview of reports related to immunonanoparticle (INP) and

RINP applications in various cancer models for imaging is provided in the following subsection.

In these studies, SPIONs were conjugated to prepare Hepama-1, a humanized monoclonal antibody linked to MNPs for the treatment of human liver cancer. A direct method was used to radiolabel INPs with ^{188}Re, with the radiolabeled INPs subsequently demonstrating an effective killing of SMMC-7721 liver cancer cells. It was suggested that such SPIONs might also be very useful for biomagnetically targeted radiotherapy in liver cancer treatment [49].

Alpha(nu)beta(3)-targeted ^{111}In-nanoparticles were developed and studied for the detection of tumor angiogenesis [142]. Studies were conducted in New Zealand White rabbits which had been implanted 12 days earlier with the Vx-2 tumor. Alpha(nu)beta(3)-targeted ^{111}In-NPs bearing approximately 10 ^{111}In per NP versus ^{111}In per NP nuclide payloads were compared to nontargeted, radiolabeled control particles. *In vivo* competitive binding studies were used to assess the ligand-targeting specificity. Alpha(nu)beta(3)-integrin-targeted NP with approximately 10 ^{111}In per NP provided a better tumor-to-muscle ratio contrast (6.3 ± 0.2) than approximately 1 ^{111}In per NP (5.1 ± 0.1), or nontargeted particles with approximately 10 ^{111}In per NP (3.7 ± 0.1), over the initial 2 h period after injection. After 18 h, the mean tumor activity in rabbits receiving alpha(nu)beta(3)-integrin-targeted NP was fourfold higher than that in nontargeted controls (Figure 6.8). Specificity of the NP for the tumor neovasculature was supported by *in vivo* competition studies and by fluorescence microscopy of alpha(nu)beta(3)-targeted fluorescence-labeled NP. Biodistribution studies revealed that, in rabbits, the primary organ of clearance was the spleen. It would appear that alpha(nu)beta(3)-targeted ^{111}In-NP may provide a clinically useful tool for the sensitive detection of angiogenesis in tumors, particularly in combination with secondary high-resolution imaging modalities, such as MRI [142].

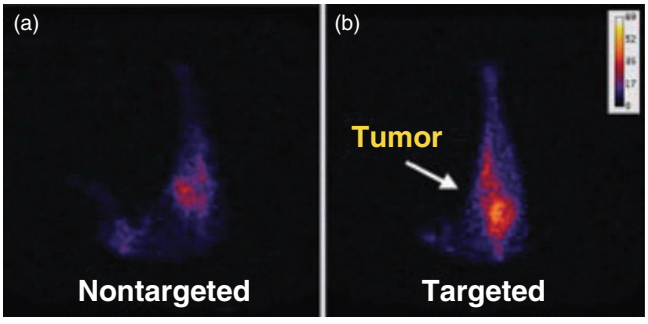

Figure 6.8 The 18-h ^{111}In planar image (15 min scan, 128 × 128 matrix) of rabbits implanted 12 days previously with Vx-2 tumor following 22 MBq kg^{-1} (i.v.) of nontargeted (a) or $\alpha_v\beta_3$-targeted (b) ^{111}In nanoparticles (NP) bearing –10 ^{111}In per NP. Both images were windowed to have identical dynamic ranges, as shown in (b). Reprinted with permission from Ref. [142].

6.3.5
Annexin 5-Directed MNPs

Bimodal contrast agents were developed to permit the detection of apoptotic cells with both MRI and optical techniques [143]. MR contrast was provided either by the entrapment of iron oxide particles within PEGylated micelles, or by the incorporation of Gd-DTPA-bis(stearylamide) (Gd-DTPA-BSA) lipids within the lipid bilayer of PEGylated liposomes. Apoptosis (programmed cell death) plays an important role in the etiology of a variety of diseases, including cancer and myocardial infarction. The visualization of apoptosis would allow both the early detection of therapy efficiency and an evaluation of disease progression. These contrast agents were approximately 10 and 100 nm in diameter, respectively. Additional fluorescent lipids were incorporated into the lipid (bi)layer of the contrast agents so as to allow parallel detection with optical methods. Multiple human recombinant annexin A5 molecules were covalently coupled to direct the NPs specifically towards apoptotic cells. Both annexin A5-conjugated contrast agents were shown to significantly increase the relaxation rates of apoptotic cell pellets compared to untreated control cells and apoptotic cells treated with nonfunctionalized nanoparticles. Increased relaxation rates were confirmed, by using confocal microscopy, to originate from an association of the contrast agents with apoptotic cells. The targeted nanoparticles presented in this study, which differed both in their size and in their magnetic properties, may have applications for the *in vivo* detection of apoptosis [143].

6.3.6
Chemotherapeutic Drugs Loaded with MNPs for Cancer Therapy

Bacterial magnetosomes (BMs) as magnetic-targeted drug carriers were used to load antitumor doxorubicin (DOX-loaded BMs; DBMs), and the latter evaluated in EMT-6 and HL60 cell lines [144]. The antineoplastic effects of DBMs on hepatic cancer were evaluated both *in vitro* and *in vivo*. The administration of DBMs, DOX and BMs led to tumor suppression rates of 86.8%, 78.6% and 4.3%, respectively, in H22 cell-bearing mice, while mortality rates were 20%, 80% and 0%, respectively. A pathological examination of the hearts and tumors revealed that both DBMs and DOX effectively inhibited tumor growth, although DBMs displayed a much lower cardiac toxicity compared to DOX. The DBMs were cytotoxic to H22 cells; this manifested as an inhibition of cell proliferation and c-myc expression, and was consistent with DOX. The antitumor properties of DBMs were similar to those of DOX, while cardiac toxicity was significantly reduced in DBMs compared to DOX. Overall, these studies provided an evaluation of the therapeutic potential of DBMs for targeted therapy against liver cancer.

Magnetic poly(ethyl-2-cyanoacrylate) (PECA) nanoparticles containing anticancer drugs (cisplatin and gemcitabine) were prepared by interfacial polymerization [145]. The amount of magnetite encapsulated inside the polymer matrix was increased to 14.26% (w/w) by controlling the initial weight ratio of monomer/magnetite. The amount of cisplatin encapsulated in the magnetic nanoparticle was

much higher than that of gemcitabine, mainly because cisplatin (hydrophobic) is highly soluble in the oil phase and is encapsulated more easily inside nanoparticles than is gemcitabine (hydrophilic). *In vitro* experiments of drug release and magnetic mobility under an external magnetic field showed that these magnetic poly(ethyl-2-cyanoacrylate) (PECA) nanoparticles could serve as a highly versatile magnetic drug carrier, with sustained release behavior and sufficient magnetic susceptibility.

Magnetic nanoparticles containing 5-fluorouracil (5-FU) were tested against HCC induced in nude mice [146]. Following treatment of the mice with the 5-FU-linked MNPs, the tumor volume was seen to be markedly reduced and the expression of protein and mRNA of bcl-2 markedly lowered, while the expression of bax and caspase 3 was significantly increased. Overall, the study results showed that targeted magnetic nanoparticles containing 5-FU could improve the chemotherapeutic effect of 5-FU against hepatocellular carcinoma by decreasing expression of the *bcl-2* gene, and increasing the expression of *bax* and *caspase 3* genes.

MNPs with poly(ε-caprolactone) (PCL) nanoparticles linked to an anticancer drug (gemcitabine) were developed using an emulsion–diffusion method to increase the efficiency of drug delivery for cancer treatment [147]. These particles were injected into nude mice bearing subcutaneous human pancreatic adenocarcinoma cells (HPAC) *in vivo*. The antitumor effect was demonstrated 15-fold higher dose when compared to free gemcitabine. The study results indicated that the magnetic PCL nanoparticles could provide a therapeutic benefit by delivering drugs efficiently to magnetically targeted tumor tissues, thus providing safe and successful antitumor effects, with low toxicity.

6.3.7
Lymph Node-Targeting MNPs

Sentinel node imaging is commonly performed prior to surgery for breast cancer and melanoma. While current methods are based on radionuclide lymphoscintigraphy, MR lymphangiography (MRL) offers the benefits of a better spatial resolution, without the use of ionizing radiation, if specificity can be developed. For this, Kobayashi *et al.* studied a series of dendrimer-based MNPs; the G6 Gd dendrimer provided the lymphatic system and lymph nodes with peak concentrations, at 24–36 min after injection [148]. Based on *ex vivo* concentration phantoms, high levels of Gd(III) ions were seen to accumulate within lymph nodes (1.7–4.4 m*M* Gd; 270–680 ppm Gd), with high target-to-background ratios (>100). The authors concluded that the PAMAM-G6 Gd dendrimer might represent a potential agent for the imaging and targeted therapy of sentinel lymph nodes.

6.3.8
Other Novel MNPs for Cancer Targeting

Arsenic trioxide (ATO) is a potent drug in the treatment of acute promyelocytic leukemia (APL), and has been shown to induce differentiation and apoptosis of

APL cells. Magnetic ATO nanoparticles have been developed against osteosarcoma, and have been investigated for their therapeutic efficacy *in vivo* in a tumor model [149]. For this, ATO was incorporated into the MNPs and encapsulated by poly(lactic acid). Following the subcutaneous injection of human MG-63 osteosarcoma cells into nude mice, ATO was shown to be released rapidly from the nanoparticles *in vitro* and delivered to the target tissues. The magnetic ATO evaluation indicated that the MNPs might localize beneath the magnet *in vivo*. An examination of the tumor volume showed that treatment with magnetic ATO nanoparticles achieved a similar degree of inhibition on osteosarcoma as did cisplatin or ATO alone. Electron microscopic features typical of apoptosis were identified in the tumor tissue following magnetic ATO treatment. Thus, "magnetic ATO targeting" may offer the opportunity to treat osteosarcoma with a lower dose compared to cisplatin.

6.4 MNPs Applied to Cancer Therapy

6.4.1 MNPs Utilized in Targeted Therapy for Cancer

6.4.1.1 Brain Tumor Therapy

Chertok *et al.* [150] utilized magnetic targeting nanoparticles for localized drug delivery to treat brain tumors. The treatment of brain tumors is complicated by their deep intracranial location, as magnetic field density cannot be focused very far from an externally applied magnet. These studies were aimed at examining whether, with magnetic targeting, a pathological alteration in brain tumor flow dynamics might be of value for discriminating a diseased site from the healthy brain. To address this question, the capture of MNPs was first assessed *in vitro* using a simple flow system under theoretically estimated glioma and normal brain flow conditions. Second, the accumulation of nanoparticles via magnetic targeting was evaluated *in vivo* using 9L-glioma-bearing rats. The *in vitro* results showed that a 7.6-fold increase in nanoparticle capture at glioma-relevant versus contralateral brain-relevant flow rates was relatively consistent with the 9.6-fold glioma selectivity of nanoparticle accumulation over the contralateral brain observed *in vivo*. Based on these findings, the *in vitro* ratio of nanoparticle capture can be viewed as a plausible indicator of *in vivo* glioma selectivity.

Magnetic nanoparticles were administered intravenously and passively distributed throughout the animal body by the systemic circulation. The study results of MRI images of control and experimental animals showed a region of pronounced hypointensity in the brain of the targeted animals, which reflected the presence of MNPs. This region corresponded to the tumor location, and was clearly visualized on T_2-weighted MRI scans due to positive contrast. Interestingly, no detectable hypointensity was observed in the contralateral brain of the targeted animal. This finding implicated tumor selectivity in nanoparticle accumulation, which was

in good agreement with the *in vitro* results [150]. The presence of nanoparticles within the glioma lesion of targeted animals was demonstrated by electron microscopy. In the contralateral brain sections of targeted animals, or in control animals, nanoparticles were not detected by TEM. Overall, this study provided the conclusion that the decreased blood flow rate in glioma, which reflected tumor vascular abnormalities, is an important contributor to glioma-selective nanoparticle accumulation with magnetic targeting.

Reddy *et al.* [151] prepared an F3-targeted polymeric nanoparticle which consisted of an encapsulated imaging agent (iron oxide or fluorescent) and a photosensitizer (Photofrin) to target brain tumors. F3 is a 31-amino acid sequence of the NH_2-terminal fragment of human high-mobility group protein 2, which was discovered using phage-displayed cDNA libraries [152]. F3, vascular homing peptide, has been reported to have cell-penetrating properties [152–156], and binds nucleolin on the surface of tumor cells and angiogenic endothelial cells, which subsequently traffics into the nucleus. For *in vitro* cellular studies, the nanoparticles were labeled with Alexa Fluor 594; the final particle size was approximately 40 nm and the average numbers of F3 peptides and fluorochromes per nanoparticle were 30 and 10, respectively. This nanoparticle was evaluated in a series of *in vitro* experiments for its ability to produce singlet oxygen, to target the nucleolin cell-surface receptor, and to confer photosensitivity.

The cellular uptake and phototoxicity of the particles were determined after a 4 h incubation with F3-tagged nanoparticles, followed by laser light illumination. The study resulted in 90% of breast cancer cells (MDA-435) being killed as a result of the cytotoxicity delivered by photoactivation of the nanoparticles (as monitored by the presence of propidium iodide-stained red nuclei). The *in vitro* study report demonstrated F3-targeted nanoparticles to be effectively internalized, transported, and concentrated within the tumor cell nuclei.

In vivo studies showed that iron oxide/Photofrin-encapsulated F3-targeted nanoparticles were targeted to 9L gliomas using MRI. The application of laser light via a fiber-optic applicator into the tumor sites activates the photosensitizer that is linked to nanoparticles. Subsequently, the therapeutic effect of the nanoparticles was evaluated, and a significant benefit of F3-targeted nanoparticles in comparison with nanoparticles without photosensitizer was demonstrated. These particles provided a significantly increased survival time over that of nontargeted Photofrin-encapsulated nanoparticles or Photofrin alone. The ability of the various nanoparticle formulations to be used for tumor treatment was evaluated using diffusion MRI as well as survival as the quantitative end points (Figure 6.9).

The F3-targeted Photofrin-encapsulated nanoparticles resulted in the most significant apparent diffusion. The tumor images were compared to pre- and post-treatment of the same animal after 40 days, and demonstrated a high diffusion value indicative of a cystic cavity that was confirmed at the end of the experimental period. An evaluation of the effects of each of the treatment groups on animal median survival was as follows: untreated controls (7.0 days), the laser-only group (8.5 days), the Photofrin group (13.0 days), and the F3-targeted nanoparticle with Photofrin group (33 days), with three animals surviving for up to 60 days. Two of

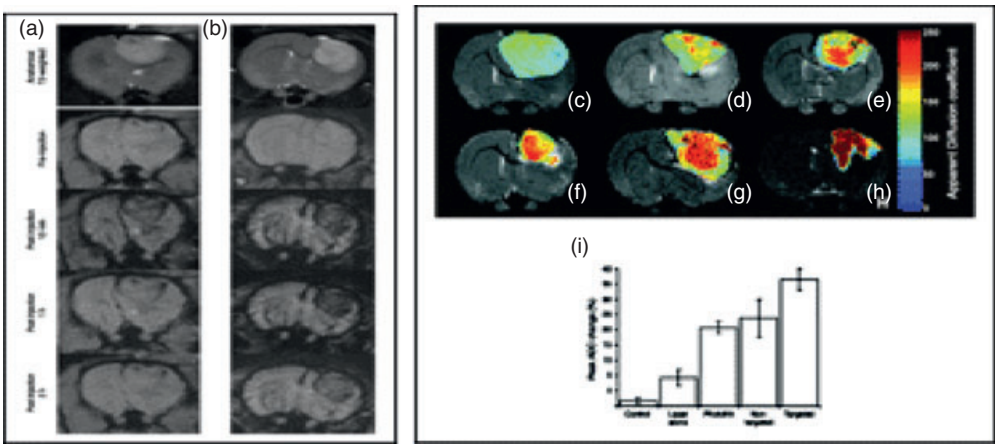

Figure 6.9 Imaging and monitoring of therapeutic efficacy using multifunctional nanoparticles in 9L brain tumors. (a, b) Top, T_2-weighted coronal images through the tumor of two different rats, revealing the anatomic extent of the tumor mass. Fast spin-echo images of the tumor following administration of (a) nontargeted nanoparticles and (b) F3-targeted nanoparticles obtained at the time points indicated. T_2-weighted magnetic resonance images at day 8 after treatment from (c) a representative control intracerebral 9L tumor and tumors treated with (d) laser light only; (e) Intravenous administration of Photofrin plus laser light, (f) nontargeted nanoparticles containing Photofrin plus laser light, and (g) targeted nanoparticles containing Photofrin plus laser light. The image shown in panel (h) is from the same tumor shown in panel (g), which was treated with the F3-targeted nanoparticle preparation but at day 40 after treatment. The color diffusion maps overlaid on top of T_2-weighted images represent the apparent diffusion coefficient (ADC) distribution in each tumor slice shown; (i) The columns indicate the mean peak percentage change in tumor apparent diffusion coefficient values for each of the experimental groups; the bars indicate the standard errors. Reprinted with permission from Ref. [151].

these three animals were found to be disease-free at up to 6 months following treatment. Overall, the polymeric multifunctional nanoparticle formulation reported in this study was found to represent a versatile application for the delivery of imaging and therapeutic applications for cancer.

6.4.1.2 **Breast Cancer Therapy**

In another study, multifunctional magneto-polymeric nanohybrids (MMPNs) composed of magnetic nanocrystals and an anticancer drug (doxorubicin, DOX) encapsulated by an amphiphilic block copolymer was prepared by Yang *et al.* for a targeted drug delivery to breast cancer [157]. MMPNs with $MnFe_2O_4$ nanoparticles were conjugated to human epidermal growth factor receptor 2 (HER2) targeting anti-HER antibody (HER, Herceptin) by utilizing the carboxyl group on the surface of the MMPNs. The antibody-modified MMPNs (HER-MMPNs) were utilized for ultra-sensitive targeted detection by MRI both *in vitro* (cellular) and *in vivo* (mouse) models. Fibroblast NIH3T6.7 cells, which highly express the HER2/

neu cancer markers [134], were compared with MDA-MB-231 cells, which express low levels of the cancer markers [131]. Both, HER-MMPNs and IRR-MMPNs (nonspecific) particles were studied for the MRI and therapeutic efficacy, using an animal model xenografted with NIH3T6.7 breast cancer cells, and the tumor growth inhibitory effect was evaluated.

MRI of the mice was performed at different temporal points (pre-injection, immediately post-injection and at 4 and 12 h) after the intravenous tail injection of the HER-MMPNs (120 g Fe + Mn). After injection of the HER-MMPNs, the value of R_2/R_2^{pre} increased to 50.5% and 23.2% at 12 h. The T_2-weighted MR images for IRR-MMPNs were used as a control (R_2/R_2^{pre} value increase of approximately 14.4% after injection and 6.2% at 12 h), and were consistent with previous *in vitro* studies and showed a mild enhanced permeability and retention (EPR) effect at the tumor site.

HER-MMPNs (79.3 ± 7.9 nm) demonstrated a more effective tumor growth inhibition than IRR-MMPNs. The results suggested that injected HER-MMPNs were targeted specifically to overexpressed HER2/neu receptors on NIH3T6.7 cells in the mouse model, and taken up by a receptor-mediated endocytosis process. The release of DOX from the HER-MMPNs demonstrated an exceptional therapeutic efficacy. In addition, the HER-MMPNs showed excellent synergistic effects for the inhibition of tumor growth.

Simberg *et al.* [158] studied a biomimetic iron oxide nanoparticle coated with liposomes and tumor-homing CREKA (Cys-Arg-Glu-Lys-Ala) peptides in MMTV-PyMT transgenic breast cancer tumor-bearing mice [159, 160]. The CREKA peptide was used as the targeting agent for nanoparticles, based on its specific affinity towards clotted plasma proteins. The interstitial spaces of tumors contain fibrin and proteins that become crosslinked to fibrin in blood clotting, such as fibronectin [161, 162]. The presence of these products in tumors, but not in normal tissues, is thought to be a result of the leakiness of tumor vessels, and allows the plasma proteins to enter from the blood into tumor tissue, where the leaked fibrinogen is converted to fibrin by tissue procoagulant factors [161, 163]; this creates additional clotting that can be targeted by the synthetic peptides [162]. Thus, the novel self-amplifying nanoparticles accumulated in tumor vessels, where they induce additional local clotting and thereby produce new binding sites for more particles (i.e., nanoparticles), not only home to the tumors but also amplify their own homing. This self-amplifying homing is a novel function of nanoparticles. The function of the nanoparticles system is based on a peptide that recognizes clotted plasma proteins and selectively homes to tumors, where it binds to vessel walls and tumor stroma.

The system mimics platelets, which also circulate freely but accumulate selectively in tumor sites. The clotting-based amplification greatly enhances tumor imaging, and the addition of a drug carrier function to the particles is envisioned. The CREAK-Alexa Fluor 647 alone effectively targeted the breast cancer xenografts. These peptides were linked to SPIO nanoparticles (Alexa fluor-CREAK-SPIO) studied *in vitro* in mouse or human plasma. For *in vivo* experiments, however, the particles did not accumulate effectively in MDA-MB-435 breast cancer xenografts.

Overall, the results of the study showed that the new nanoparticles system created has the following features: specific tumor homing; an avoidance of the RES; and the provision of effective tumor imaging. Although the binding of CREKA-SPIO to tumor vessels does not require clotting activity, the clotting does improve the efficiency of the tumor homing and enhances the tumor signal in whole-body scans.

Leuschner *et al.* [164] utilized SPIONs for targeted delivery to metastatic cancer cells in peripheral tissues, lymph nodes and bones to enhance the sensitivity of MRI. Up to 60% of human breast cancers express receptors for luteinizing hormone/chorionic gonadotropin (LH/CG) and luteinizing hormone-releasing hormone (LHRH) [165–168]. In this study, SPIONs were linked to LHRH, with LH/CG-bound SPIONs being developed to test their ability to accumulate in LHRH-expressing human breast cancer cells, both *in vitro* and *in vivo*. When particles were incubated with MDA-MB-435S luc cells, the highest iron accumulation was 452.6 pg Fe per cell for LHRH-SPIONs, 203.6 pg Fe per cell for beta-CG-SPIONs, and 51.3 pg Fe per cell for SPIONs. Similarly, *in vivo* in a nude mouse model, LHRH-SPIONs were specifically targeted and accumulated into tumors and metastatic cells of human breast cancer xenografts. The amount of LHRH-SPIONs in the lungs was directly dependent on the number of metastatic cells, and amounted to 77.8 pg Fe per metastatic cell. In contrast, unconjugated SPIONs accumulated in the liver, showed a poor affinity to the tumor, and were not detectable in metastatic lesions in the lungs. LHRH-SPIONs accumulated in the cytosolic compartment of the target cells and formed clusters, but did not accumulate in the livers of normal mice. Thus, the study results provided another contrast agent for MRI *in vivo* and demonstrated an increased sensitivity for the detection of metastases and disseminated cells in lymph nodes, bones, and peripheral organs.

During recent years, many reports have been made of *in vivo* gene silencing by short interfering RNAs (siRNAs) [169–172]. In this connection, RNA interference (RNAi) has emerged as one of the promising strategies in the development of therapeutics, and dual-purpose probes have been developed for the detection of siRNA delivery and silencing of genes by novel noninvasive methods [173]. In order to develop these probes, MNPs were effectively used as nanoplatforms for the dual imaging and delivery of siRNA therapeutics. The probes were capable of the *in vivo* transfer of siRNA and the simultaneous imaging of its accumulation in tumors, both by MRI and near-infrared *in vivo* optical imaging (NIRF).The reported multifunctional MNPs were tagged with a near-infrared dye and covalently linked to siRNA molecules that were specific for model or therapeutic targets. Additionally, these nanoparticles were modified with a membrane translocation peptide for intracellular delivery. An *in vivo* tracking of tumor uptake of these probes by MRI and optical imaging in two separate tumor models was established. This study represented the first step towards an advancement of the siRNA delivery and imaging strategies that are essential for cancer therapeutic product development and optimization, utilizing MNPs as a multifunctional platform [173].

6.4.1.3 MNPs in Hyperthermia and Thermal Ablation

The application of sufficient heat to kill cells in the treatment of cancer is referred to as hyperthermia [174, 175], and can be used in combination with conventional treatment modalities. Although clinical trials have demonstrated the efficacy of such combinations [176, 177], the major limitations of hyperthermia have been the selective targeting and homogeneous distribution of heat within the tumor. Hyperthermia procedures use different sources of heat within the tissue, including externally applied electromagnetic waves (e.g., RF or microwaves), ultrasound (external or interstitial), a current flow between two or more electrodes, electric or magnetic fields between antennas, or electrically or magnetically induced thermo seeds [176]. The use of biocompatible SPIONs coupled with a magnetic field by an alternating magnetic field to produce heat due to Brownian and Neel relaxation processes, is a well-known procedure [139, 178].

Magnetic particles in a range of sizes have been utilized for hyperthermia and tested on a variety of cancers (mammary, prostate, melanoma, breast, prostate, glioma) in animal models [179–185] and in a clinical trial [186]. Hyperthermia treatment depends on the applied temperature, with the duration of heating resulting either in direct tumor cell killing or rendering the cells more susceptible to concomitant radiotherapy or chemotherapy. In recent years, numerous groups have been developing this area worldwide, with the result that two efficacy trials are currently being conducted for glioblastoma multiforme (in combination with radiotherapy) and prostate cancer (intermediate risk patients, in combination with low-dose rate brachytherapy). Jordan *et al*. have conducted extensive studies with MNPs, both in animals and in clinical trials, by using magnetic fluid-induced hyperthermia (MFH) [174, 175]. Their study results (Figure 6.10; Table 6.2) have shown that MFH could be applied to humans (Figure 6.11), the group having achieved a mean cumulative equivalent minutes (CEM) thermal dose at 43 °C at the index temperature (T90), in comparison with results reported by other groups [187–189]. Currently, Phase II clinical trials using MFH are still ongoing [174].

Many new developments are currently under way to improve hyperthermia. One example is that of tumor-targeting ligands on the surface of iron oxide nanoparticles, which should bind specifically to certain tumor cell epitopes or vascular targeting molecules, or perhaps accumulate in the lymph nodes after systemic administration. Focused hyperthermia represents another approach, an example being the ^{111}In-ChL6-MAb-conjugated SPIONs (bioprobes) developed by DeNardo *et al*. to target breast cancer cell membrane antigens in mice. Such therapy would be carried out with an externally applied alternating magnetic field (AMF) so as to deliver thermoablative cancer therapy [139, 178]. AMF-responsive bioprobes have enabled specific cancer cell thermal ablation by the selective targeting of extravascular cancer cells.

Electron microscopy images have confirmed the presence of bioprobes on the surfaces of HBT 3477 cells from *ex vivo* tumors; tumor necrosis was observed in these samples at 24 and 48 h after treatment with AMF/bioprobe therapy (Figure 6.12). Significant therapeutic responses were reported, with an up to eightfold longer mean time to quintuple the tumor volume with therapy compared to no

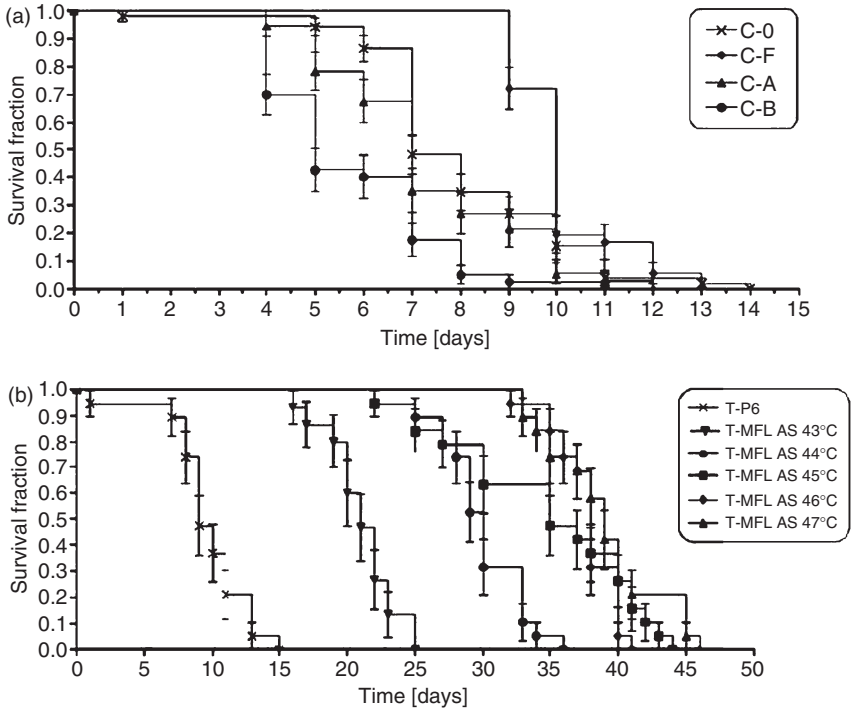

Figure 6.10 Survival rate after thermotherapy using magnetic nanoparticles (Kaplan–Meier method). (a) C-0 = tumor growth control, C-A = application of magnetic fluid DDM128 P6, no magnetic field, C-B = application of magnetic fluid MFL AS, no magnetic field, C-F = application of normal saline and magnetic field treatment; (b) T-DDM128 P6 (P6) = application of dextran-coated nanoparticles, treatment temperature 39 °C, T-MFL AS = application of aminosilane-coated nanoparticles, treatment temperatures 43–47 °C. Reprinted with permission from Ref. [174].

treatment ($P = 0.0013$) (Table 6.3). In another thermal dosimetry predictive and efficacy study of ^{111}In-ChL6 nanoparticles, an AMF was delivered at 72 h after bioprobe injection at amplitudes of 1410 (113 kA m^{-1}), 1300 (104 kA m^{-1}), and 700 (56 kA m^{-1}) Oersted (Oe) at 30%, 60%, and 90% "on" time (duty), respectively, and at 1050 Oe (84 kA m^{-1}) at 50% and 70% duty over the 20-min treatment period (Figure 6.13; Table 6.4). Both, treated and control mice were monitored for 90 days, with the tumor total heat dose (THD) from activated tumor bioprobes being calculated for each treatment group, using the ^{111}In-bioprobe tumor concentration and premeasured particle heat response to AMF amplitudes. Toxicity was seen only in the 1300 Oe AMF cohorts, with four of 12 immediate deaths and skin erythema [139, 178]. The tumor responses of these study groups showed evidence of a heat dose dependence and thermal dosimetry relevant to the THD, which represents a conceptual parallel to radiation dosimetry. The reported thermal treatment study outcome could be combined with radioisotope therapy, or in series

Table 6.2 Survival rate after thermography using magnetic nanoparticles.

Treatment group	Mean survival (days)	Significance	Factor[a]
C-0	8.9 ± 3.1		–
C-A	8.0 ± 1.6		0.9
C-B	7.6 ± 0.7		0.9
C-F	10.1 ± 1.1		1.1
T-DDM128 P6, 39 °C	10.3 ± 2.1		1.2
T-MFL AS, 43 °C	15.4 ± 6.3	$P < 0.01$	1.7
T-MFL AS, 44 °C	28.3 ± 7.4	$P < 0.01$	3.2
T-MFL AS, 45 °C	34.7 ± 6.8	$P < 0.01$	3.6
T-MFL AS, 46 °C	37.8 ± 2.2	$P < 0.01$	4.3
T-MFL AS, 47 °C	39.7 ± 3.5	$P < 0.01$	4.5

a Factor describes the prolongation of survival in correlation to group C-0: tumor growth control, C-A: applications of magnetic fluid DDM128 P6, no magnetic treatment; C-B: application of magnetic fluid MFL AS, no magnetic field treatment; C-F: application of normal saline and magnetic field treatment; T-DDM128 P6: application of dextran-coated nanoparticles, treatment temperature 39 °C; T-MFL AS: application of aminosilane-coated nanoparticles, treatment temperature 43–47 °C. Reprinted with permission from Ref. [175].

Figure 6.11 Thermotherapy treatment of the pelvic region after intratumoral injection of magnetic nanoparticles using the alternating magnetic field applicator MFH 300F® (MagForce Nanotechnologies AG, Berlin, Germany). Reprinted with permission from Ref. [175].

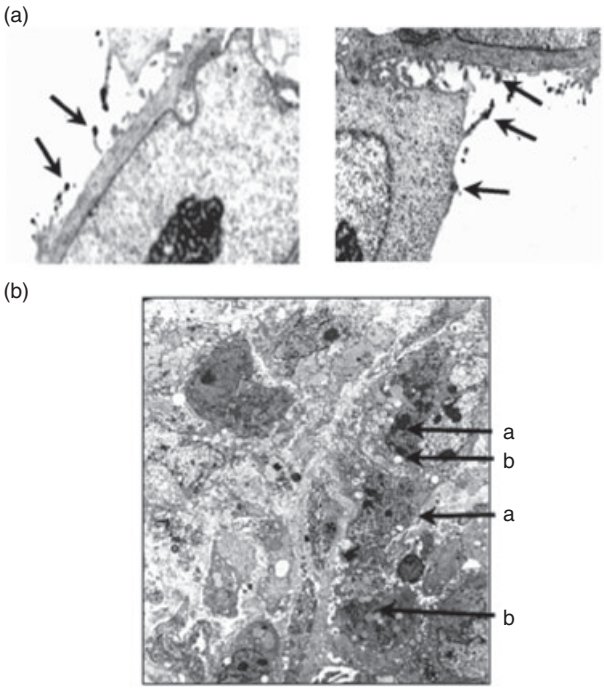

Figure 6.12 Electron microscopy images (original magnification factor: 2.7 (6500) = 17550) of HBT 3477 xenograft tumors which had been excised from the mice, at the time of sacrifice for biodistribution study, 48 h post injection. (a) Intact bioprobes can be seen on the cancer cell surfaces (arrows), inferring cell binding and retention; the nuclear membrane and nucleolus are clearly seen in these untreated cells; (b) Electron microscopy image at 120 h after bioprobe injection, 48 h after AMF treatment at 1300 Oe, demonstrating substantial necrosis of the cancer cells (a = nuclei of cells seen as fragments; b = abundant cytoplasmic vacuoles; c = disintegration of cell and nuclear membranes). Reprinted with permission from Ref. [139].

with external beam radiation treatment [190]. Therefore, tumor-specific magnetic iron oxide nanoparticles may lead to advances in thermotherapy, thermochemotherapy and diagnostic imaging, or they may be combined as a so-called "theranostic" approach [191]. The controlled release of drugs from heat-sensitive particle–drug conjugates may also have the potential to reduce the adverse side effects of conventional chemotherapeutic regimens.

6.4.1.4 **MNPs-Directed Toxicity**

The degradation of iron oxide nanoparticles *in vivo* is carried out via normal metabolism, the natural pathways leading to an increased iron storage in the body. Human tissues contain iron, iron oxides, ferritin, transferrin and hemosiderin for

Table 6.3 Reduction in tumor growth rate related to Oersted treatment level.

Treatment level (Oe)	*n*	Mean ± SD	Two-sided *P*
A			
1300	12	35 ± 28	0.0277
1000	8	32 ± 19	0.0300
700	12	29 ± 23	0.1194
All treated	32	35 ± 28	0.0114
Control	14	13 ± 7	–
B			
1300	12	49 ± 27	0.0335
1000	8	50 ± 25	0.0206
700	12	45 ± 19	0.0029
All treated	32	48 ± 24	0.0013
Control	14	24 ± 9	–

Note: Mean time for the HBT3477 human breast xenografts to triple (A) and quadruple (B) in volume segregated by Oersted treatment group. Two-sided *P* values when compared to control group (Willcoxon–Mann–Whitney test). The decrease in tumor growth rate was related to the Oersted level received by that cohort, and was significant ($P \leq 0.05$) for most groups. Reprinted with permission from Ref. [139].

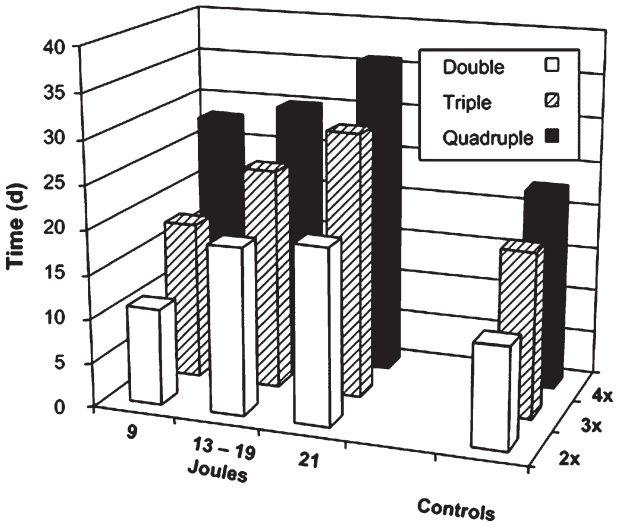

Figure 6.13 Tumor response relationship to bioprobe AMF Rx. The increased time to double, triple, and quadruple the tumor volume reflects the therapeutic response in mice receiving a higher total heat dose (THD) (J). A statistical relationship between response and THD was shown for tumors receiving 13–19 and 21 $J\,g^{-1}$ compared to that of controls (data not shown). The control includes tumor growth of AMF alone, bioprobes alone, and untreated. Reprinted with permission from Ref. [178].

Table 6.4 Wilcoxon rank sum comparisons of tumor doubling, tripling, and quadrupling times for treatment versus control groups of mice.

Joules	*n*	Mean ± SD	Two-sided *P*
Doubling times			
9	10	10.5 ± 3.3	0.12
13–19	19	19.0 ± 22.7	0.01
21	9	20.0 ± 23.0	0.03
All treated	38	17.0 ± 20.0	0.004
Controls	34	11.5 ± 16.2	NA
Tripling times			
9	10	17.6 ± 5.4	0.12
13–19	19	24.6 ± 21.1	0.02
21	9	30.2 ± 20.2	0.007
All treated	38	24.1 ± 18.6	0.004
Controls	34	18.7 ± 21.2	NA
Quadrupling times			
9	10	28.3 ± 19.3	0.11
13–19	19	29.9 ± 20.0	0.03
21	9	36.2 ± 18.8	0.005
All treated	38	31.0 ± 19.7	0.004
Controls	34	22.7 ± 20.3	NA

NA = not applicable.
Reprinted with permission from Ref. [178].

iron metabolism. A study of animal models indicated that a dose level of 600 mg kg^{-1} Fe was not fatal; indeed, many data were available that show MNPs to be relatively benign. For example, Feridex was visible under MRI at more than 4 weeks after administration, but demonstrated no pathological damage. However, one type of iron oxide nanoparticle (MION-46) was shown to induce seizures in rats, and was not readily broken down in the brain due to a lack of response from local macrophages and reactive astrocytes. Although the major constituents of MNPs are biocompatible and nontoxic, their size and surface modifications might determine their physiological function and host responses.

6.5 Summary

In this chapter, details have been provided of some of the latest developments in MNPs for cancer diagnosis and therapy (Table 6.5). The chapter has focused on MNP applications in areas relevant to cancer, including MRI, multimodal imaging (e.g., MRI, optical, and radioactive), chemical drug delivery, targeted delivery, and

Table 6.5 Magnetic nanoparticles utilized in cancer diagnosis, imaging and therapy.

Serial no.	Imaging modality[a]	Treatment[b]	Study model	Cancer type/target	Reference(s)
1	MR	PK	Patient	Brain	[192]
2	CT/MR		Animal	Brain	[193]
3	MR	IMA	Animal	Brain	[194]
4	MR	DD	Animal	Brain	[151]
5	MR	DD	*In vitro*/*In vivo*	Brain	[150]
6	MR	IMA	*In vitro*	Breast	[164]
7	MR/Optical		*In vitro*	Breast	[157]
8	MR/Optical		*In vitro*	Epithelial	[115]
9	Nuclear	HT	Animal	Breast	[178]
10	MR/PET/Optical		Animal	Colorectal	[195]
11	MR	DIA	Animal	Glioma	[95]
12	MR/PET	HT	Animal	Glioblastoma	[196]
13	MR	DD	*In Vitro*	Glioma	[197]
14	MR		Animal	Glioma	[198]
15	FM/MTT	DD	*In vitro*	Leukemia	[124]
16	MR	IMA	Animal	Liver	[199]
17	RT-PCR	DD	Animal	Liver	[146]
18	RT-PCR/EM	DD	*In vitro*/*In vivo*	Liver	[144]
19	MR	IMA	*In vitro*/*In vivo*	Liver	[125]
20	MR	HT	Animal	Liver	[174]
21	MR		Animal	Lung carcinoma	[200]
22	MR/Optical		Animal	Lung carcinoma	[117]
23	MR	IMA	Animal	Lung	[131]
24	MR/Optical		Animal	Lymph node	[201]
25	MR	IMA	Animal	Lymph node	[148]
26	MR/Optical	IMA	Animal	Lymph node	[66]
27	MR	IMA	*In vitro*/*In vivo*	Lymph	[65]
28	MR/Optical	IMA	Animal	Muc-1	[202]
29	MR/EM		Animal	Osteosarcoma	[149]
30	MR	DD	Animal	Ovalbumin	[203]
31	MR/Optical		Animal	Ovarian	[118]
32	MR	DD	Animal	Pancreatic	[147]
33	Western blot	IMA	*In vitro*	Prostate	[128]
34	MR	IMA	*In vitro*	Prostate	[127]
35	CT	HT	Animal	Prostate	[204]
36	MR/Optical	IMA	Animal	RNA delivery	[173]
37	MR/Optical	IMA	Animal	Solid	[205]
38	FM/MR	IMA	Animal	Spleen	[142]
39	MR, Optical	IMA, DD	*In vitro*/*In vivo*	Apoptosis	[143, 158]
40	TEM		*In vitro*/*In vivo*		[73]

a CT = computed tomography; EM = electron microscopy; MTT = microculture tetrazolium test; PET = positron emission tomography; RT-PCR = reverse-transcribed polymerase chain reaction; TEM = transmission electron microscopy.

b DD = Drug Delivery; IMA = Imaging; DIA = Diagnosis.

hyperthermia. The chapter has also highlighted the significant developments of MNPs as multimodality imaging agents, both *in vitro* and *in vivo* in animal models. Although the combination of magnetic, optical, and nuclear imaging properties, along with target-directed multifunctional MNPs progress, has been briefly described, studies relating to the toxicity of MNPs have been few in number. Likewise, details were provided of pharmacokinetic, dosimetry, efficacy and therapy studies of MNPs in animal models.

Despite much progress having been achieved in the use of MNPs as a multifunctional platform for cancer diagnosis, the area is still in its infancy and much effort is required before these materials acquire clinical use. Many challenges remain if MNPs are to become a multifunctional platform for clinical diagnosis and therapy. Ideally, MNPs should be simple with a defined conjugation chemistry, have a small size (for favorable pharmacokinetics), show a high affinity towards specific cell-surface receptor(s), or provide specific cell endocytotic ability. In the treatment of human disease, MNPs should have the following requisites: a well-defined and characterized particle size; a nontoxic nature; a specific target; and a multifunctional profile. It follows, therefore, that the success of particle development and its subsequent application in biomedicine will depend heavily on an interdisciplinary approach to research.

Ligand-directed multifunctional MNP platforms show great promise for the future development of clinical diagnostic and therapeutic applications. However, this will be possible only by maintaining an effective collaboration between the broad fields of materials chemistry, chemistry, cell biology, molecular biology, biophysics and immunology, in association with clinicians.

References

1 Kobayashi, H., Jo, S.K., Kawamoto, S., Yasuda, H., Hu, X., Knopp, M.V., Brechbiel, M.W., Choyke, P.L. and Star, R.A. (2004) Polyamine dendrimer-based MRI contrast agents for functional kidney imaging to diagnose acute renal failure. *Journal of Magnetic Resonance Imaging*, **20** (3), 512–18.

2 Kobayashi, H., Kawamoto, S., Jo, S.K., Sato, N., Saga, T., Hiraga, A., Konishi, J., Hu, S., Togashi, K., Brechbiel, M.W. and Star, R.A. (2002) Renal tubular damage detected by dynamic micro-MRI with a dendrimer-based magnetic resonance contrast agent. *Kidney International*, **61** (6), 1980–5.

3 Ersoy, H., Jacobs, P., Kent, C.K. and Prince, M.R. (2004) Blood pool MR angiography of aortic stent-graft endoleak. *American Journal of Roentgenology*, **182** (5), 1181–6.

4 Halbreich, A., Roger, J., Pons, J.N., Geldwerth, D., Da Silva, M.F., Roudier, M. and Bacri, J.C. (1998) Biomedical applications of maghemite ferrofluid. *Biochimie*, **80** (5–6), 379–90.

5 Pankhurst, Q.A., Connolly, J., Jones, S.K. and Dobson, J. (2003) Applications of magnetic nanoparticles in biomedicine. *Journal of Physics D: Applied Physics*, **36**, R167–81.

6 Weissleder, R., Stark, D.D., Compton, C.C., Wittenberg, J. and Ferrucci, J.T. (1987) Ferrite-enhanced MR imaging of hepatic lymphoma: an experimental study in rats. *American Journal of Roentgenology*, **149** (6), 1161–5.

7 Weissleder, R., Elizondo, G., Wittenberg, J., Lee, A.S., Josephson, L. and Brady,

T.J. (1990) Ultrasmall superparamagnetic iron oxide: an intravenous contrast agent for assessing lymph nodes with MR imaging. *Radiology*, **175** (2), 494–8.

8 Weissleder, R., Hahn, P.F., Stark, D.D., Rummeny, E., Saini, S., Wittenberg, J. and Ferrucci, J.T. (1987) MR imaging of splenic metastases: ferrite-enhanced detection in rats. *American Journal of Roentgenology*, **149** (4), 723–6.

9 Le Duc, G., Vander Elst, L., Colet, J.M., Roch, A., Gillis, P., Le Bas, J.F. and Muller, R.N. (2001) Ultrasmall particulate iron oxides as contrast agents for magnetic resonance spectroscopy: a dose-effect study. *Journal of Magnetic Resonance Imaging*, **13** (4), 619–26.

10 Whitesides, G.M., Kazlaukas, R.J. and Josephson, L. (1983) Magnetic separations in biotechnology. *Trends in Biotechnology*, **1**, 144–8.

11 Grimm, J., Perez, J.M., Josephson, L. and Weissleder, R. (2004) Novel nanosensors for rapid analysis of telomerase activity. *Cancer Research*, **64** (2), 639–43.

12 Kim, G.Y., Josephson, L., Langer, R. and Cima, M.J. (2007) Magnetic relaxation switch detection of human chorionic gonadotrophin. *Bioconjugate Chemistry*, **18** (6), 2024–8.

13 Perez, J.M., Josephson, L., O'Loughlin, T., Hogemann, D. and Weissleder, R. (2002) Magnetic relaxation switches capable of sensing molecular interactions. *Nature Biotechnology*, **20** (8), 816–20.

14 Cheon, J. and Lee, J.-H. (2008) Synergistically integrated nanoparticles as multimodal probes for nanobiotechnology. *Accounts of Chemical Research*, **41**, (12), 1630–40.

15 McCarthy, J.R. and Weissleder, R. (2008) Multifunctional magnetic nanoparticles for targeted imaging and therapy. *Advanced Drug Delivery Reviews*, **60** (11), 1241–51.

16 Häfeli, U., Schutt, W., Teller, J. and Zborowski, M. (1997) *Scientific and Clinical Applications of Magnetic Carriers*, Springer, Rostock, Germany.

17 Yu, M.K., Jeong, Y.Y., Park, J., Park, S., Kim, J.W., Min, J.J., Kim, K. and Jon, S. (2008) Drug-loaded superparamagnetic iron oxide nanoparticles for combined cancer imaging and therapy in vivo. *Angewandte Chemie, International Edition in English*, **47** (29), 5362–5.

18 Hou, Y., Xu, Z. and Sun, S. (2007) Controlled synthesis and chemical conversions of FeO nanoparticles. *Angewandte Chemie, International Edition in English*, **46** (33), 6329–32.

19 Rockenberger, J., Scher, E.C. and Alivisators, A.P. (1999) A new nonhydrolytic single-precursor approach to surfactant-capped nanocrystals of transition metal oxides. *Journal of the American Chemical Society*, **121**, 11595–6.

20 Josephson, L., Tung, C.H., Moore, A. and Weissleder, R. (1999) High-efficiency intracellular magnetic labeling with novel superparamagnetic-Tat peptide conjugates. *Bioconjugate Chemistry*, **10** (2), 186–91.

21 De Cuyper, M.J. (1991) M, Mechanistic aspects of the adsorption of phospholipids onto lauric acid stabilized magnetite nanocolloids. *Langmuir*, **7**, 647–52.

22 Nitin, N., LaConte, L.E., Zurkiya, O., Hu, X. and Bao, G. (2004) Functionalization and peptide-based delivery of magnetic nanoparticles as an intracellular MRI contrast agent. *Journal of Biological Inorganic Chemistry*, **9** (6), 706–12.

23 Bogdanov, A.A., Jr, Martin, C., Weissleder, R. and Brady, T.J. (1994) Trapping of dextran-coated colloids in liposomes by transient binding to aminophospholipid: preparation of ferrosomes. *Biochimica et Biophysica Acta*, **1193** (1), 212–18.

24 Bulte, J.W., Douglas, T., Mann, S., Frankel, R.B., Moskowitz, B.M., Brooks, R.A., Baumgarner, C.D., Vymazal, J., Strub, M.P. and Frank, J.A. (1994) Magnetoferritin: characterization of a novel superparamagnetic MR contrast agent. *Journal of Magnetic Resonance Imaging*, **4** (3), 497–505.

25 Bulte, J.W. and De Cuyper, M. (2003) Magnetoliposomes as contrast agents. *Methods in Enzymology*, **373**, 175–98.

26 Wilhelm, C., Billotey, C., Roger, J., Pons, J.N., Bacri, J.C. and Gazeau, F. (2003) Intracellular uptake of anionic superparamagnetic nanoparticles as a function of their surface coating. *Biomaterials*, **24** (6), 1001–11.

27 Bulte, J.W., Douglas, T., Witwer, B., Zhang, S.C., Strable, E., Lewis, B.K., Zywicke, H., Miller, B., van Gelderen, P., Moskowitz, B.M., Duncan, I.D. and Frank, J.A. (2001) Magnetodendrimers allow endosomal magnetic labeling and in vivo tracking of stem cells. *Nature Biotechnology*, **19** (12), 1141–7.

28 Illum, L., Church, A.E., Butterworth, M.D., Arien, A., Whetstone, J. and Davis, S.S. (2001) Development of systems for targeting the regional lymph nodes for diagnostic imaging: in vivo behaviour of colloidal PEG-coated magnetite nanospheres in the rat following interstitial administration. *Pharmaceutical Research*, **18** (5), 640–5.

29 Moffat, B.A., Reddy, G.R., McConville, P., Hall, D.E., Chenevert, T.L., Kopelman, R.R., Philbert, M., Weissleder, R., Rehemtulla, A. and Ross, B.D. (2003) A novel polyacrylamide magnetic nanoparticle contrast agent for molecular imaging using MRI. *Molecular Imaging*, **2** (4), 324–32.

30 Kellar, K.E., Fujii, D.K., Gunther, W.H., Briley-Saebo, K., Bjornerud, A., Spiller, M. and Koenig, S.H. (2000) NC100150 injection, a preparation of optimized iron oxide nanoparticles for positive-contrast MR angiography. *Journal of Magnetic Resonance Imaging*, **11** (5), 488–94.

31 Kellar, K.E., Fujii, D.K., Gunther, W.H., Briley-Saebo, K., Spiller, M. and Koenig, S.H. (1999) 'NC100150', a preparation of iron oxide nanoparticles ideal for positive-contrast MR angiography. *Magma*, **8** (3), 207–13.

32 Portet, D., Denizot, B., Rump, E., Lejeune, J.J. and Jallet, P. (2001) Nonpolymeric coatings of iron oxide colloids for biological use as magnetic resonance imaging contrast agents. *Journal of Colloid and Interface Science*, **238** (1), 37–42.

33 Stark, D.D., Weissleder, R., Elizondo, G., Hahn, P.F., Saini, S., Todd, L.E., Wittenberg, J. and Ferrucci, J.T. (1988) Superparamagnetic iron oxide: clinical application as a contrast agent for MR imaging of the liver. *Radiology*, **168** (2), 297–301.

34 Weissleder, R. and Stark, D.D. (1989) Magnetic resonance imaging of the liver. *Magnetic Resonance Quarterly*, **5** (2), 97–121.

35 Weissleder, R. and Stark, D.D. (1989) Magnetic resonance imaging of liver tumors. *Seminars in Ultrasound, CT, and MR*, **10** (1), 63–77.

36 Weissleder, R., Stark, D.D., Engelstad, B.L., Bacon, B.R., Compton, C.C., White, D.L., Jacobs, P. and Lewis, J. (1989) Superparamagnetic iron oxide: pharmacokinetics and toxicity. *American Journal of Roentgenology*, **152** (1), 167–73.

37 Jung, C.W. (1995) Surface properties of superparamagnetic iron oxide MR contrast agents: ferumoxides, ferumoxtran, ferumoxsil. *Magnetic Resonance Imaging*, **13** (5), 675–91.

38 Taupitz, M., Wagner, S., Schnorr, J., Kravec, I., Pilgrimm, H., Bergmann-Fritsch, H. and Hamm, B. (2004) Phase I clinical evaluation of citrate-coated monocrystalline very small superparamagnetic iron oxide particles as a new contrast medium for magnetic resonance imaging. *Investigative Radiology*, **39** (7), 394–405.

39 Ferrari, M. (2005) Cancer nanotechnology: opportunities and challenges. *Nature Reviews. Cancer*, **5** (3), 161–71.

40 Harisinghani, M.G., Barentsz, J., Hahn, P.F., Deserno, W.M., Tabatabaei, S., van de Kaa, C.H., de la Rosette, J. and Weissleder, R. (2003) Noninvasive detection of clinically occult lymph-node metastases in prostate cancer. *The New England Journal of Medicine*, **348** (25), 2491–9.

41 Harisinghani, M.G. and Weissleder, R. (2004) Sensitive, noninvasive detection of lymph node metastases. *PLoS Medicine*, **1** (3), e66.

42 Enochs, W.S., Harsh, G., Hochberg, F. and Weissleder, R. (1999) Improved

delineation of human brain tumors on MR images using a long-circulating, superparamagnetic iron oxide agent. *Journal of Magnetic Resonance Imaging*, **9** (2), 228–32.

43 Tang, Y., Kim, M., Carrasco, D., Kung, A.L., Chin, L. and Weissleder, R. (2005) In vivo assessment of RAS-dependent maintenance of tumor angiogenesis by real-time magnetic resonance imaging. *Cancer Research*, **65** (18), 8324–30.

44 Harisinghani, M.G., Saini, S., Weissleder, R., Rubin, D., de Lange, E., Harms, S., Weinreb, J., Small, W., Sukerkar, A., Brown, J.J., Zelch, J., Lucas, M., Morris, M. and Hahn, P.F. (2001) Splenic imaging with ultrasmall superparamagnetic iron oxide ferumoxtran-10 (AMI-7227): preliminary observations. *Journal of Computer Assisted Tomography*, **25** (5), 770–6.

45 Saini, S., Sharma, R., Baron, R.L., Turner, D.A., Ros, P.R., Hahn, P.F., Small, W.C., de Lange, E.E., Stillman, A.E., Edelman, R.R., Runge, V.M. and Outwater, E.K. (2000) Multicentre dose-ranging study on the efficacy of USPIO ferumoxtran-10 for liver MR imaging. *Clinical Radiology*, **55** (9), 690–5.

46 Trivedi, R.A., U-King-Im, J.M., Graves, M.J., Kirkpatrick, P.J. and Gillard, J.H. (2004) Noninvasive imaging of carotid plaque inflammation. *Neurology*, **63** (1), 187–8.

47 Weissleder, R., Lee, A.S., Khaw, B.A., Shen, T. and Brady, T.J. (1992) Antimyosin-labeled monocrystalline iron oxide allows detection of myocardial infarct: MR antibody imaging. *Radiology*, **182** (2), 381–5.

48 Josephson, L., Tung, C.H., Moore, A. and Weissleder, R. (1999) High-efficiency intracellular magnetic labeling with novel superparamagnetic-tat peptide conjugates. *Bioconjugate Chemistry*, **10** (2), 186–91.

49 Liang, S., Wang, Y., Yu, J., Zhang, C., Xia, J. and Yin, D. (2007) Surface modified superparamagnetic iron oxide nanoparticles: as a new carrier for bio-magnetically targeted therapy. *Journal of Materials Science: Materials in Medicine*, **18** (12), 2297–302.

50 Neuberger, T., Schöpf, B., Hofmann, H., Hofmann, M. and von Rechenberg, B. (2005) Superparamagnetic nanoparticles for biomedical applications: possibilities and limitations of a new drug delivery system. *Journal of Magnetism and Magnetic Materials*, **293** (1), 483–96.

51 Arruebo, M., Fernández-Pacheco, R., Ibarra, M.R. and Santamaría, J. (2007) Magnetic nanoparticles for drug delivery. *Nano Today*, **2** (3), 22–32.

52 Tartaj, P., Morales, M. d. Veintemillas-Verdaguer, P., Gonzalez-Carreno, S., Serna, T. and C.J. (2003) The preparation of magnetic nanoparticles for applications in biomedicine. *Journal of Physics D: Applied Physics*, **36** (13), R182–97.

53 Berry, C.C. (2005) Possible exploitation of magnetic nanoparticle-cell interaction for biomedical applications. *Journal of Materials Chemistry*, **15**, 543–7.

54 Babincová, M., Leszczynska, D., Sourivong, P. and Babinec, P. (2000) Selective treatment of neoplastic cells using ferritin-mediated electromagnetic hyperthermia. *Medical Hypotheses*, **54** (2), 177–9.

55 Davis, S.S. (1997) Biomedical applications of nanotechnology–implications for drug targeting and gene therapy. *Trends in Biotechnology*, **15** (6), 217–24.

56 Araujo, L., Lobenberg, R. and Kreuter, J. (1999) Influence of the surfactant concentration on the body distribution of nanoparticles. *Journal of Drug Targeting*, **6** (5), 373–85.

57 Kreuter, J. (1994) Drug targeting with nanoparticles. *European Journal of Drug Metabolism and Pharmacokinetics*, **19** (3), 253–6.

58 Meng, F., Engbers, G.H.M. and Feijen, J. (2004) Polyethylene glycol-grafted polystyrene particles. *Journal of Biomedical Materials Research Part A*, **70A** (1), 49–58.

59 Gaur, U., Sahoo, S.K., De, T.K., Ghosh, P.C., Maitra, A. and Ghosh, P.K. (2000) Biodistribution of fluoresceinated dextran using novel nanoparticles

evading reticuloendothelial system. *International Journal of Pharmaceutics*, **202** (1–2), 1–10.

60 Allemann, E., Leroux, J.C., Gurny, R. and Doelker, E. (1993) In vitro extended-release properties of drug-loaded poly(DL-lactic acid) nanoparticles produced by a salting-out procedure. *Pharmaceutical Research*, **10** (12), 1732–7.

61 Lacava, L.M., Lacava, Z.G., Da Silva, M.F., Silva, O., Chaves, S.B., Azevedo, R.B., Pelegrini, F., Gansau, C., Buske, N., Sabolovic, D. and Morais, P.C. (2001) Magnetic resonance of a dextran-coated magnetic fluid intravenously administered in mice. *Biophysical Journal*, **80** (5), 2483–6.

62 Shen, T.T., Bogdanov, A., Jr, Bogdanova, A., Poss, K., Brady, T.J. and Weissleder, R. (1996) Magnetically labeled secretin retains receptor affinity to pancreas acinar cells. *Bioconjugate Chemistry*, **7** (3), 311–16.

63 Gref, R., Minamitake, Y., Peracchia, M.T., Trubetskoy, V., Torchilin, V. and Langer, R. (1994) Biodegradable long-circulating polymeric nanospheres. *Science*, **263** (5153), 1600–3.

64 Moghimi, S.M., Hunter, A.C. and Murray, J.C. (2001) Long-circulating and target-specific nanoparticles: theory to practice. *Pharmacological Reviews*, **53** (2), 283–318.

65 Neumaier, C.E., Baio, G., Ferrini, S., Corte, G. and Daga, A. (2008) MR and iron magnetic nanoparticles. Imaging opportunities in preclinical and translational research. *Tumori*, **94** (2), 226–33.

66 John, S.S., Zietman, A.L., Shipley, W.U. and Harisinghani, M.G. (2008) Newer imaging modalities to assist with target localization in the radiation treatment of prostate cancer and possible lymph node metastases. *International Journal of Radiation Oncology, Biology, Physics*, **71** (Suppl. 1), S43–7.

67 Saksena, M., Harisinghani, M., Hahn, P., Kim, J., Saokar, A., King, B. and Weissleder, R. (2006) Comparison of lymphotropic nanoparticle-enhanced MRI sequences in patients with various primary cancers. *American Journal of Roentgenology*, **187** (6), W582–8.

68 Saokar, A., Braschi, M. and Harisinghani, M. (2006) Lymphotrophic nanoparticle enhanced MR imaging (LNMRI) for lymph node imaging. *Abdominal Imaging*, **31** (6), 660–7.

69 Saksena, M.A., Saokar, A. and Harisinghani, M.G. (2006) Lymphotropic nanoparticle enhanced MR imaging (LNMRI) technique for lymph node imaging. *European Journal of Radiology*, **58** (3), 367–74.

70 Ross, R. and Harisinghani, M. (2006) New clinical imaging modalities in prostate cancer. *Hematology/Oncology Clinics of North America*, **20** (4), 811–30.

71 Shih, H.A., Harisinghani, M., Zietman, A.L., Wolfgang, J.A., Saksena, M. and Weissleder, R. (2005) Mapping of nodal disease in locally advanced prostate cancer: rethinking the clinical target volume for pelvic nodal irradiation based on vascular rather than bony anatomy. *International Journal of Radiation Oncology, Biology, Physics*, **63** (4), 1262–9.

72 Taylor, A., Rockall, A.G., Reznek, R.H. and Powell, M.E. (2005) Mapping pelvic lymph nodes: guidelines for delineation in intensity-modulated radiotherapy. *International Journal of Radiation Oncology, Biology, Physics*, **63** (5), 1604–12.

73 Zhang, C., Jugold, M., Woenne, E.C., Lammers, T., Morgenstern, B., Mueller, M.M., Zentgraf, H., Bock, M., Eisenhut, M., Semmler, W. and Kiessling, F. (2007) Specific targeting of tumor angiogenesis by RGD-conjugated ultrasmall superparamagnetic iron oxide particles using a clinical 1.5-T magnetic resonance scanner. *Cancer Research*, **67** (4), 1555–62.

74 Carmeliet, P. and Jain, R.K. (2000) Angiogenesis in cancer and other diseases. *Nature*, **407** (6801), 249–57.

75 Folkman, J. (1995) Angiogenesis in cancer, vascular, rheumatoid and other disease. *Nature Medicine*, **1** (1), 27–31.

76 Horak, E.R., Leek, R., Klenk, N., LeJeune, S., Smith, K., Stuart, N., Greenall, M., Stepniewska, K. and Harris, A.L. (1992) Angiogenesis,

assessed by platelet/endothelial cell adhesion molecule antibodies, as indicator of node metastases and survival in breast cancer. *Lancet*, **340** (8828), 1120–4.

77 Meitar, D., Crawford, S.E., Rademaker, A.W. and Cohn, S.L. (1996) Tumor angiogenesis correlates with metastatic disease, N-myc amplification, and poor outcome in human neuroblastoma. *Journal of Clinical Oncology*, **14** (2), 405–14.

78 Vosseler, S., Mirancea, N., Bohlen, P., Mueller, M.M. and Fusenig, N.E. (2005) Angiogenesis inhibition by vascular endothelial growth factor receptor-2 blockade reduces stromal matrix metalloproteinase expression, normalizes stromal tissue, and reverts epithelial tumor phenotype in surface heterotransplants. *Cancer Research*, **65** (4), 1294–305.

79 Chen, X., Hou, Y., Tohme, M., Park, R., Khankaldyyan, V., Gonzales-Gomez, I., Bading, J.R., Laug, W.E. and Conti, P.S. (2004) Pegylated Arg-Gly-Asp peptide: ^{64}Cu labeling and PET imaging of brain tumor alphavbeta3-integrin expression. *Journal of Nuclear Medicine*, **45** (10), 1776–83.

80 Chen, X., Park, R., Tohme, M., Shahinian, A.H., Bading, J.R. and Conti, P.S. (2004) MicroPET and autoradiographic imaging of breast cancer alpha v-integrin expression using 18F- and 64Cu-labeled RGD peptide. *Bioconjugate Chemistry*, **15** (1), 41–9.

81 Haubner, R., Wester, H.J., Weber, W.A., Mang, C., Ziegler, S.I., Goodman, S.L., Senekowitsch-Schmidtke, R., Kessler, H. and Schwaiger, M. (2001) Noninvasive imaging of alpha(v)beta3 integrin expression using 18F-labeled RGD-containing glycopeptide and positron emission tomography. *Cancer Research*, **61** (5), 1781–5.

82 Janssen, M.L., Oyen, W.J., Dijkgraaf, I., Massuger, L.F., Frielink, C., Edwards, D.S., Rajopadhye, M., Boonstra, H., Corstens, F.H. and Boerman, O.C. (2002) Tumor targeting with radiolabeled alpha(v)beta(3) integrin binding peptides in a nude mouse model. *Cancer Research*, **62** (21), 6146–51.

83 Sadeghi, M.M., Krassilnikova, S., Zhang, J., Gharaei, A.A., Fassaei, H.R., Esmailzadeh, L., Kooshkabadi, A., Edwards, S., Yalamanchili, P., Harris, T.D., Sinusas, A.J., Zaret, B.L. and Bender, J.R. (2004) Detection of injury-induced vascular remodeling by targeting activated alphavbeta3 integrin in vivo. *Circulation*, **110** (1), 84–90.

84 Achilefu, S., Bloch, S., Markiewicz, M.A., Zhong, T., Ye, Y., Dorshow, R.B., Chance, B. and Liang, K. (2005) Synergistic effects of light-emitting probes and peptides for targeting and monitoring integrin expression. *Proceedings of the National Academy of Sciences of the United States of America*, **102** (22), 7976–81.

85 Chen, X., Conti, P.S. and Moats, R.A. (2004) In vivo near-infrared fluorescence imaging of integrin alphavbeta3 in brain tumor xenografts. *Cancer Research*, **64** (21), 8009–14.

86 Dayton, P.A., Pearson, D., Clark, J., Simon, S., Schumann, P.A., Zutshi, R., Matsunaga, T.O. and Ferrara, K.W. (2004) Ultrasonic analysis of peptide- and antibody-targeted microbubble contrast agents for molecular imaging of alphavbeta3-expressing cells. *Molecular Imaging*, **3** (2), 125–34.

87 Leong-Poi, H., Christiansen, J., Klibanov, A.L., Kaul, S. and Lindner, J.R. (2003) Noninvasive assessment of angiogenesis by ultrasound and microbubbles targeted to alpha(v)-integrins. *Circulation*, **107** (3), 455–60.

88 Lainer, D.T. and Brahn, E. (2005) New antiangiogenic strategies for the treatment of proliferative synovitis. *Expert Opinion on Investigational Drugs*, **14** (1), 1–17.

89 Mikecz, K. (2000) Vitaxin applied molecular evolution. *Current Opinion in Investigational Drugs*, **1** (2), 199–203.

90 Hirano, Y., Kando, Y., Hayashi, T., Goto, K. and Nakajima, A. (1991) Synthesis and cell attachment activity of bioactive oligopeptides: RGD, RGDS, RGDV, and RGDT. *Journal of Biomedical Materials Research*, **25** (12), 1523–34.

91 Dechantsreiter, M.A., Planker, E., Matha, B., Lohof, E., Holzemann, G., Jonczyk, A., Goodman, S.L. and Kessler, H. (1999) N-Methylated cyclic RGD peptides as highly active and selective alpha(V) beta(3) integrin antagonists. *Journal of Medicinal Chemistry*, **42** (16), 3033–40.

92 Apisarnthanarax, S. and Clifford Chao, K.S. (2005) Current imaging paradigms in radiation oncology. *Radiation Research*, **163** (1), 1–25.

93 Kiessling, F., Heilmann, M., Vosseler, S., Lichy, M., Krix, M., Fink, C., Kiessling, I., Steinbauer, H., Schad, L., Fusenig, N.E. and Delorme, S. (2003) Dynamic T1-weighted monitoring of vascularization in human carcinoma heterotransplants by magnetic resonance imaging. *International Journal of Cancer*, **104** (1), 113–20.

94 Gold, L.I., Jussila, T., Fusenig, N.E. and Stenback, F. (2000) TGF-beta isoforms are differentially expressed in increasing malignant grades of HaCaT keratinocytes, suggesting separate roles in skin carcinogenesis. *The Journal of Pathology*, **190** (5), 579–88.

95 Sun, C., Veiseh, O., Gunn, J., Fang, C., Hansen, S., Lee, D., Sze, R., Ellenbogen, R.G., Olson, J. and Zhang, M. (2008) In vivo MRI detection of gliomas by chlorotoxin-conjugated superparamagnetic nanoprobes. *Small*, **4** (3), 372–9.

96 Kachra, Z., Beaulieu, E., Delbecchi, L., Mousseau, N., Berthelet, F., Moumdjian, R., Del Maestro, R. and Beliveau, R. (1999) Expression of matrix metalloproteinases and their inhibitors in human brain tumors. *Clinical and Experimental Metastasis*, **17** (7), 555–66.

97 Lyons, S.A., O'Neal, J. and Sontheimer, H. (2002) Chlorotoxin, a scorpion-derived peptide, specifically binds to gliomas and tumors of neuroectodermal origin. *Glia*, **39** (2), 162–73.

98 Veiseh, M., Gabikian, P., Bahrami, S.B., Veiseh, O., Zhang, M., Hackman, R.C., Ravanpay, A.C., Stroud, M.R., Kusuma, Y., Hansen, S.J., Kwok, D., Munoz, N.M., Sze, R.W., Grady, W.M., Greenberg, N.M., Ellenbogen, R.G. and Olson, J.M. (2007) Tumor paint: a chlorotoxin:Cy5.5 bioconjugate for intraoperative visualization of cancer foci. *Cancer Research*, **67** (14), 6882–8.

99 Mamelak, A.N. and Jacoby, D.B. (2007) Targeted delivery of antitumoral therapy to glioma and other malignancies with synthetic chlorotoxin (TM-601). *Expert Opinion on Drug Delivery*, **4** (2), 175–86.

100 Veiseh, O., Sun, C., Gunn, J., Kohler, N., Gabikian, P., Lee, D., Bhattarai, N., Ellenbogen, R., Sze, R., Hallahan, A., Olson, J. and Zhang, M. (2005) Optical and MRI multifunctional nanoprobe for targeting gliomas. *Nano Letters*, **5** (6), 1003–8.

101 Barth, R.F. (1998) Rat brain tumor models in experimental neuro-oncology: the 9L, C6, T9, F98, RG2 (D74), RT-2 and CNS-1 gliomas. *Journal of Neuro-Oncology*, **36** (1), 91–102.

102 Weizsaecker, M., Deen, D.F., Rosenblum, M.L., Hoshino, T., Gutin, P.H. and Barker, M. (1981) The 9L rat brain tumor: description and application of an animal model. *Journal of Neurology*, **224** (3), 183–92.

103 McCarthy, J.R., Kelly, K.A., Sun, E.Y. and Weissleder, R. (2007) Targeted delivery of multifunctional magnetic nanoparticles. *Nanomedicine*, **2** (2), 153–67.

104 Albrecht, K., Greindl, M., Kremser, C., Wolf, C., Debbage, P. and Bernkop-Schnurch, A. (2006) Comparative in vivo mucoadhesion studies of thiomer formulations using magnetic resonance imaging and fluorescence detection. *Journal of Controlled Release*, **115** (1), 78–84.

105 Bertorelle, F., Wilhelm, C., Roger, J., Gazeau, F., Menager, C. and Cabuil, V. (2006) Fluorescence-modified superparamagnetic nanoparticles: intracellular uptake and use in cellular imaging. *Langmuir*, **22** (12), 5385–91.

106 Mulder, W.J., Koole, R., Brandwijk, R.J., Storm, G., Chin, P.T., Strijkers, G.J., de Mello Donega, C., Nicolay, K. and Griffioen, A.W. (2006) Quantum dots with a paramagnetic coating as a bimodal molecular imaging probe. *Nano Letters*, **6** (1), 1–6.

107 Choi, H., Choi, S.R., Zhou, R., Kung, H.F. and Chen, I.W. (2004) Iron oxide nanoparticles as magnetic resonance contrast agent for tumor imaging via folate receptor-targeted delivery. *Academic Radiology*, **11** (9), 996–1004.

108 Bruchez, M., Jr, Moronne, M., Gin, P., Weiss, S. and Alivisatos, A.P. (1998) Semiconductor nanocrystals as fluorescent biological labels. *Science*, **281** (5385), 2013–16.

109 Alivisatos, P. (2004) The use of nanocrystals in biological detection. *Nature Biotechnology*, **22** (1), 47–52.

110 Mattoussi, H., Mauro, J.M., Goldman, E.R., Anderson, G.P., Sundar, V.C., Mikulec, F.V. and Bawendi, M.G. (2000) Self-Assembly of CdSe-ZnS quantum dot bioconjugates using an engineered recombinant protein. *Journal of the American Chemical Society*, **122** (49), 12142–50.

111 Ballou, B., Lagerholm, B.C., Ernst, L.A., Bruchez, M.P. and Waggoner, A.S. (2004) Noninvasive imaging of quantum dots in mice. *Bioconjugate Chemistry*, **15** (1), 79–86.

112 Goldman, E.R., Balighian, E.D., Mattoussi, H., Kuno, M.K., Mauro, J.M., Tran, P.T. and Anderson, G.P. (2002) Avidin: a natural bridge for quantum dot-antibody conjugates. *Journal of the American Chemical Society*, **124** (22), 6378–82.

113 Byrne, S.J., le Bon, B., Corr, S.A., Stefanko, M., O'Connor, C., Gun'ko, Y.K., Rakovich, Y.P., Donegan, J.F., Williams, Y., Volkov, Y. and Evans, P. (2007) Synthesis, characterisation, and biological studies of CdTe quantum dot-naproxen conjugates. *ChemMedChem*, **2** (2), 183–6.

114 Rao, J., Dragulescu-Andrasi, A. and Yao, H. (2007) Fluorescence imaging in vivo: recent advances. *Current Opinion in Biotechnology*, **18** (1), 17–25.

115 Yang, J., Lim, E.K., Lee, H.J., Park, J., Lee, S.C., Lee, K., Yoon, H.G., Suh, J.S., Huh, Y.M. and Haam, S. (2008) Fluorescent magnetic nanohybrids as multimodal imaging agents for human epithelial cancer detection. *Biomaterials*, **29** (16), 2548–55.

116 Tsourkas, A., Shinde-Patil, V.R., Kelly, K.A., Patel, P., Wolley, A., Allport, J.R. and Weissleder, R. (2005) In vivo imaging of activated endothelium using an anti-VCAM-1 magneto-optical probe. *Bioconjugate Chemistry*, **16** (3), 576–81.

117 Lee, H., Yu, M.K., Park, S., Moon, S., Min, J.J., Jeong, Y.Y., Kang, H.W. and Jon, S. (2007) Thermally cross-linked superparamagnetic iron oxide nanoparticles: synthesis and application as a dual imaging probe for cancer in vivo. *Journal of the American Chemical Society*, **129** (42), 12739–45.

118 Xu, H., Regino, C.A., Koyama, Y., Hama, Y., Gunn, A.J., Bernardo, M., Kobayashi, H., Choyke, P.L. and Brechbiel, M.W. (2007) Preparation and preliminary evaluation of a biotin-targeted, lectin-targeted dendrimer-based probe for dual-modality magnetic resonance and fluorescence imaging. *Bioconjugate Chemistry*, **18** (5), 1474–82.

119 Majoros, I.J., Myc, A., Thomas, T., Mehta, C.B. and Baker, J.R., Jr (2006) PAMAM dendrimer-based multifunctional conjugate for cancer therapy: synthesis, characterization, and functionality. *Biomacromolecules*, **7** (2), 572–9.

120 Zebli, B., Susha, A.S., Sukhorukov, G.B., Rogach, A.L. and Parak, W.J. (2005) Magnetic targeting and cellular uptake of polymer microcapsules simultaneously functionalized with magnetic and luminescent nanocrystals. *Langmuir*, **21** (10), 4262–5.

121 Gu, H., Xu, K., Yang, Z., Chang, C.K. and Xu, B. (2005) Synthesis and cellular uptake of porphyrin decorated iron oxide nanoparticles-a potential candidate for bimodal anticancer therapy. *Chemical Communications (Cambridge, England)*, (34), 4270–2.

122 Kircher, M.F., Mahmood, U., King, R.S., Weissleder, R. and Josephson, L. (2003) A multimodal nanoparticle for preoperative magnetic resonance imaging and intraoperative optical brain tumor delineation. *Cancer Research*, **63** (23), 8122–5.

123 Corr, S., Rakovich, Y. and Gun'ko, Y. (2008) Multifunctional magnetic-

fluorescent nanocomposites for biomedical applications. *Nanoscale Research Letters*, **3** (3), 87–104.

124 Lv, G., He, F., Wang, X., Gao, F., Zhang, G., Wang, T., Jiang, H., Wu, C., Guo, D., Li, X., Chen, B. and Gu, Z. (2008) Novel nanocomposite of nano fe(3)o(4) and polylactide nanofibers for application in drug uptake and induction of cell death of leukemia cancer cells. *Langmuir*, **24** (5), 2151–6.

125 Kou, G., Wang, S., Cheng, C., Gao, J., Li, B., Wang, H., Qian, W., Hou, S., Zhang, D., Dai, J., Gu, H. and Guo, Y. (2008) Development of SM5-1-conjugated ultrasmall superparamagnetic iron oxide nanoparticles for hepatoma detection. *Biochemical and Biophysical Research Communications*, **374**, 192–7.

126 Artemov, D., Mori, N., Okollie, B. and Bhujwalla, Z.M. (2003) MR molecular imaging of the Her-2/neu receptor in breast cancer cells using targeted iron oxide nanoparticles. *Magnetic Resonance in Medicine*, **49** (3), 403–8.

127 Serda, R.E., Adolphi, N.L., Bisoffi, M. and Sillerud, L.O. (2007) Targeting and cellular trafficking of magnetic nanoparticles for prostate cancer imaging. *Molecular Imaging*, **6** (4), 277–88.

128 Han, Y., Haun, Y., Deng, J., Gao, F., Pan, B. and Cui, D. (2006) Expression of single-chain Fv gene specific for gamma-seminoprotein by RTS and its biological activity identification. *Biotechnology Progress*, **22** (4), 1084–9.

129 Listgarten, J. and Emili, A. (2005) Practical proteomic biomarker discovery: taking a step back to leap forward. *Drug Discovery Today*, **10** (23–24), 1697–702.

130 Natarajan, A., Xiong, C.Y., Gruettner, C., DeNardo, G.L. and DeNardo, S.J. (2008) Development of multivalent radioimmunonanoparticles for cancer imaging and therapy. *Cancer Biotherapy and Radiopharmaceuticals*, **23** (1), 82–91.

131 Lee, J.H., Huh, Y.M., Jun, Y.W., Seo, J.W., Jang, J.T., Song, H.T., Kim, S., Cho, E.J., Yoon, H.G., Suh, J.S. and Cheon, J. (2007) Artificially engineered magnetic nanoparticles for ultra-sensitive molecular imaging. *Nature Medicine*, **13** (1), 95–9.

132 Jun, Y.W., Huh, Y.M., Choi, J.S., Lee, J.H., Song, H.T., Kim, S., Yoon, S., Kim, K.S., Shin, J.S., Suh, J.S. and Cheon, J. (2005) Nanoscale size effect of magnetic nanocrystals and their utilization for cancer diagnosis via magnetic resonance imaging. *Journal of the American Chemical Society*, **127** (16), 5732–3.

133 Hermanson, G.T. (1996) *Heterobifunctional Cross-Linkers*, Vol. **5**, 1st edn, Academic Press, New York, pp. 235–7.

134 Hudziak, R.M., Lewis, G.D., Winget, M., Fendly, B.M., Shepard, H.M. and Ullrich, A. (1989) p185HER2 monoclonal antibody has antiproliferative effects in vitro and sensitizes human breast tumor cells to tumor necrosis factor. *Molecular and Cellular Biology*, **9** (3), 1165–72.

135 Kang, H.W., Josephson, L., Petrovsky, A., Weissleder, R. and Bogdanov, A., Jr (2002) Magnetic resonance imaging of inducible E-selectin expression in human endothelial cell culture. *Bioconjugate Chemistry*, **13** (1), 122–7.

136 Sharkey, R.M., Cardillo, T.M., Rossi, E.A., Chang, C.H., Karacay, H., McBride, W.J., Hansen, H.J., Horak, I.D. and Goldenberg, D.M. (2005) Signal amplification in molecular imaging by pretargeting a multivalent, bispecific antibody. *Nature Medicine*, **11** (11), 1250–5.

137 Natarajan, A., Gruettner, C., Ivkov, R., DeNardo, G.L., Mirick, G., Yuan, A., Foreman, A. and DeNardo, S.J. (2008) NanoFerrite particle based radioimmunonanoparticles: binding affinity and in vivo pharmacokinetics. *Bioconjugate Chemistry*, **19** (6), 1211–18.

138 Natarajan, A., Xiong, C.Y., Albrecht, H., DeNardo, G.L. and DeNardo, S.J. (2005) Characterization of site-specific ScFv PEGylation for tumor-targeting pharmaceuticals. *Bioconjugate Chemistry*, **16** (1), 113–21.

139 DeNardo, S.J., DeNardo, G.L., Miers, L.A., Natarajan, A., Foreman, A.R., Gruettner, C., Adamson, G.N. and Ivkov, R. (2005) Development of tumor

targeting bioprobes ((111)In-chimeric L6 monoclonal antibody nanoparticles) for alternating magnetic field cancer therapy. *Clinical Cancer Research*, **11** (19 Pt 2), S7087–92.

140 DeNardo, S.J., DeNardo, G.L., Natarajan, A., Miers, L.A., Foreman, A.R., Gruettner, C., Adamson, G.N. and Ivkov, R. (2007) Thermal dosimetry predictive of efficacy of 111In-ChL6 nanoparticle AMF–induced thermoablative therapy for human breast cancer in mice. *Journal of Nuclear Medicine*, **48** (3), 437–44.

141 Nie, S., Xing, Y., Kim, G.J. and Simons, J.W. (2007) Nanotechnology applications in cancer. *Annual Review of Biomedical Engineering*, **9**, 257–88.

142 Hu, G., Lijowski, M., Zhang, H., Partlow, K.C., Caruthers, S.D., Kiefer, G., Gulyas, G., Athey, P., Scott, M.J., Wickline, S.A. and Lanza, G.M. (2007) Imaging of Vx-2 rabbit tumors with alpha(nu)beta3-integrin-targeted 111In nanoparticles. *International Journal of Cancer*, **120** (9), 1951–7.

143 van Tilborg, G.A., Mulder, W.J., Deckers, N., Storm, G., Reutelingsperger, C.P., Strijkers, G.J. and Nicolay, K. (2006) Annexin A5-functionalized bimodal lipid-based contrast agents for the detection of apoptosis. *Bioconjugate Chemistry*, **17** (3), 741–9.

144 Sun, J.B., Duan, J.H., Dai, S.L., Ren, J., Zhang, Y.D., Tian, J.S. and Li, Y. (2007) In vitro and in vivo antitumor effects of doxorubicin loaded with bacterial magnetosomes (DBMs) on H22 cells: the magnetic bio-nanoparticles as drug carriers. *Cancer Letters*, **258** (1), 109–17.

145 Yang, J., Lee, H., Hyung, W., Park, S.B. and Haam, S. (2006) Magnetic PECA nanoparticles as drug carriers for targeted delivery: synthesis and release characteristics. *Journal of Microencapsulation*, **23** (2), 203–12.

146 Wang, J.M., Xiao, B.L., Zheng, J.W., Chen, H.B. and Zou, S.Q. (2007) Effect of targeted magnetic nanoparticles containing 5-FU on expression of bcl-2, bax and caspase 3 in nude mice with transplanted human liver cancer. *World Journal of Gastroenterology*, **13** (23), 3171–5.

147 Gang, J., Park, S.B., Hyung, W., Choi, E.H., Wen, J., Kim, H.S., Shul, Y.G., Haam, S. and Song, S.Y. (2007) Magnetic poly epsilon-caprolactone nanoparticles containing Fe3O4 and gemcitabine enhance anti-tumor effect in pancreatic cancer xenograft mouse model. *Journal of Drug Targeting*, **15** (6), 445–53.

148 Kobayashi, H., Kawamoto, S., Bernardo, M., Brechbiel, M.W., Knopp, M.V. and Choyke, P.L. (2006) Delivery of gadolinium-labeled nanoparticles to the sentinel lymph node: comparison of the sentinel node visualization and estimations of intra-nodal gadolinium concentration by the magnetic resonance imaging. *Journal of Controlled Release*, **111** (3), 343–51.

149 Li, X.S., Li, W.Q. and Wang, W.B. (2007) Using targeted magnetic arsenic trioxide nanoparticles for osteosarcoma treatment. *Cancer Biotherapy and Radiopharmaceuticals*, **22** (6), 772–8.

150 Chertok, B., David, A.E., Huang, Y. and Yang, V.C. (2007) Glioma selectivity of magnetically targeted nanoparticles: a role of abnormal tumor hydrodynamics. *Journal of Controlled Release*, **122** (3), 315–23.

151 Reddy, G.R., Bhojani, M.S., McConville, P., Moody, J., Moffat, B.A., Hall, D.E., Kim, G., Koo, Y.E., Woolliscroft, M.J., Sugai, J.V., Johnson, T.D., Philbert, M.A., Kopelman, R., Rehemtulla, A. and Ross, B.D. (2006) Vascular targeted nanoparticles for imaging and treatment of brain tumors. *Clinical Cancer Research*, **12** (22), 6677–86.

152 Porkka, K., Laakkonen, P., Hoffman, J.A., Bernasconi, M. and Ruoslahti, E. (2002) A fragment of the HMGN2 protein homes to the nuclei of tumor cells and tumor endothelial cells in vivo. *Proceedings of the National Academy of Sciences of the United States of America*, **99** (11), 7444–9.

153 Akerman, M.E., Chan, W.C., Laakkonen, P., Bhatia, S.N. and Ruoslahti, E. (2002) Nanocrystal targeting in vivo. *Proceedings of the National Academy of Sciences of the United States of America*, **99** (20), 12617–21.

154 Christian, S., Pilch, J., Akerman, M.E., Porkka, K., Laakkonen, P. and Ruoslahti, E. (2003) Nucleolin expressed at the cell surface is a marker of endothelial cells in angiogenic blood vessels. *The Journal of Cell Biology*, **163** (4), 871–8.

155 Ruoslahti, E. (2004) Vascular zip codes in angiogenesis and metastasis. *Biochemical Society Transactions*, **32** (Pt 3), 397–402.

156 Ruoslahti, E., Duza, T. and Zhang, L. (2005) Vascular homing peptides with cell-penetrating properties. *Current Pharmaceutical Design*, **11** (28), 3655–60.

157 Yang, J., Lee, C.H., Ko, H.J., Suh, J.S., Yoon, H.G., Lee, K., Huh, Y.M. and Haam, S. (2007) Multifunctional magneto-polymeric nanohybrids for targeted detection and synergistic therapeutic effects on breast cancer. *Angewandte Chemie, International Edition in English*, **46** (46), 8836–9.

158 Simberg, D., Duza, T., Park, J.H., Essler, M., Pilch, J., Zhang, L., Derfus, A.M., Yang, M., Hoffman, R.M., Bhatia, S., Sailor, M.J. and Ruoslahti, E. (2007) Biomimetic amplification of nanoparticle homing to tumors. *Proceedings of the National Academy of Sciences of the United States of America*, **104** (3), 932–6.

159 Hutchinson, J.N. and Muller, W.J. (2000) Transgenic mouse models of human breast cancer. *Oncogene*, **19** (53), 6130–7.

160 Pasqualini, R. and Ruoslahti, E. (1996) Organ targeting in vivo using phage display peptide libraries. *Nature*, **380** (6572), 364–6.

161 Dvorak, H.F., Senger, D.R., Dvorak, A.M., Harvey, V.S. and McDonagh, J. (1985) Regulation of extravascular coagulation by microvascular permeability. *Science*, **227** (4690), 1059–61.

162 Pilch, J., Brown, D.M., Komatsu, M., Jarvinen, T.A., Yang, M., Peters, D., Hoffman, R.M. and Ruoslahti, E. (2006) Peptides selected for binding to clotted plasma accumulate in tumor stroma and wounds. *Proceedings of the National Academy of Sciences of the United States of America*, **103** (8), 2800–4.

163 Abe, K., Shoji, M., Chen, J., Bierhaus, A., Danave, I., Micko, C., Casper, K., Dillehay, D.L., Nawroth, P.P. and Rickles, F.R. (1999) Regulation of vascular endothelial growth factor production and angiogenesis by the cytoplasmic tail of tissue factor. *Proceedings of the National Academy of Sciences of the United States of America*, **96** (15), 8663–8.

164 Leuschner, C., Kumar, C.S., Hansel, W., Soboyejo, W., Zhou, J. and Hormes, J. (2006) LHRH-conjugated magnetic iron oxide nanoparticles for detection of breast cancer metastases. *Breast Cancer Research and Treatment*, **99** (2), 163–76.

165 Leuschner, C. and Hansel, W. (2005) Targeting breast and prostate cancers through their hormone receptors. *Biology of Reproduction*, **73** (5), 860–5.

166 Leuschner, C., Enright, F.M., Gawronska, B. and Hansel, W. (2003) Membrane disrupting lytic peptide conjugates destroy hormone dependent and independent breast cancer cells in vitro and in vivo. *Breast Cancer Research and Treatment*, **78** (1), 17–27.

167 Chatzistamou, L., Schally, A.V., Nagy, A., Armatis, P., Szepeshazi, K. and Halmos, G. (2000) Effective treatment of metastatic MDA-MB-435 human estrogen-independent breast carcinomas with a targeted cytotoxic analogue of luteinizing hormone-releasing hormone AN-207. *Clinical Cancer Research*, **6** (10), 4158–65.

168 Lojun, S., Bao, S., Lei, Z.M. and Rao, C.V. (1997) Presence of functional luteinizing hormone/chorionic gonadotropin (hCG) receptors in human breast cell lines: implications supporting the premise that hCG protects women against breast cancer. *Biology of Reproduction*, **57** (5), 1202–10.

169 Aigner, A. (2006) Gene silencing through RNA interference (RNAi) in vivo: strategies based on the direct application of siRNAs. *Journal of Biotechnology*, **124** (1), 12–25.

170 Golzio, M., Mazzolini, L., Ledoux, A., Paganin, A., Izard, M., Hellaudais, L., Bieth, A., Pillaire, M.J., Cazaux, C., Hoffmann, J.S., Couderc, B. and Teissie, J. (2007) In vivo gene silencing in solid tumors by targeted electrically mediated

siRNA delivery. *Gene Therapy*, **14** (9), 752–9.

171 Shen, Y. (2008) Advances in the development of siRNA-based therapeutics for cancer. *IDrugs*, **11** (8), 572–8.

172 Stevenson, M. (2004) Therapeutic potential of RNA interference. *The New England Journal of Medicine*, **351** (17), 1772–7.

173 Medarova, Z., Pham, W., Farrar, C., Petkova, V. and Moore, A. (2007) In vivo imaging of siRNA delivery and silencing in tumors. *Nature Medicine*, **13** (3), 372–7.

174 Thiesen, B. and Jordan, A. (2008) Clinical applications of magnetic nanoparticles for hyperthermia. *International Journal of Hyperthermia*, **24**, 464–77.

175 Jordan, A., Scholz, R., Maier-Hauff, K., van Landeghem, F.K., Waldoefner, N., Teichgraeber, U., Pinkernelle, J., Bruhn, H., Neumann, F., Thiesen, B., von Deimling, A. and Felix, R. (2006) The effect of thermotherapy using magnetic nanoparticles on rat malignant glioma. *Journal of Neuro-Oncology*, **78** (1), 7–14.

176 Wust, P., Hildebrandt, B., Sreenivasa, G., Rau, B., Gellermann, J., Riess, H., Felix, R. and Schlag, P.M. (2002) Hyperthermia in combined treatment of cancer. *The Lancet Oncology*, **3** (8), 487–97.

177 Sneed, P.K., Stauffer, P.R., McDermott, M.W., Diederich, C.J., Lamborn, K.R., Prados, M.D., Chang, S., Weaver, K.A., Spry, L., Malec, M.K., Lamb, S.A., Voss, B., Davis, R.L., Wara, W.M., Larson, D.A., Phillips, T.L. and Gutin, P.H. (1998) Survival benefit of hyperthermia in a prospective randomized trial of brachytherapy boost +/– hyperthermia for glioblastoma multiforme. *International Journal of Radiation Oncology, Biology, Physics*, **40** (2), 287–95.

178 DeNardo, S.J., DeNardo, G.L., Natarajan, A., Miers, L.A., Foreman, A.R., Gruettner, C., Adamson, G.N. and Ivkov, R. (2007) Thermal dosimetry predictive of efficacy of 111In-ChL6 nanoparticle AMF-Induced thermoablative therapy for human breast cancer in mice. *Journal of Nuclear Medicine*, **48** (3), 437–44.

179 Johannsen, M., Gneveckow, U., Eckelt, L., Feussner, A., Waldofner, N., Scholz, R., Deger, S., Wust, P., Loening, S.A. and Jordan, A. (2005) Clinical hyperthermia of prostate cancer using magnetic nanoparticles: presentation of a new interstitial technique. *International Journal of Hyperthermia*, **21** (7), 637–47.

180 Tanaka, K., Ito, A., Kobayashi, T., Kawamura, T., Shimada, S., Matsumoto, K., Saida, T. and Honda, H. (2005) Intratumoral injection of immature dendritic cells enhances antitumor effect of hyperthermia using magnetic nanoparticles. *International Journal of Cancer*, **116** (4), 624–33.

181 Kawai, N., Ito, A., Nakahara, Y., Futakuchi, M., Shirai, T., Honda, H., Kobayashi, T. and Kohri, K. (2005) Anticancer effect of hyperthermia on prostate cancer mediated by magnetite cationic liposomes and immune-response induction in transplanted syngeneic rats. *The Prostate*, **64** (4), 373–81.

182 Johannsen, M., Thiesen, B., Jordan, A., Taymoorian, K., Gneveckow, U., Waldofner, N., Scholz, R., Koch, M., Lein, M., Jung, K. and Loening, S.A. (2005) Magnetic fluid hyperthermia (MFH) reduces prostate cancer growth in the orthotopic Dunning R3327 rat model. *The Prostate*, **64** (3), 283–92.

183 Ito, A., Tanaka, K., Kondo, K., Shinkai, M., Honda, H., Matsumoto, K., Saida, T. and Kobayashi, T. (2003) Tumor regression by combined immunotherapy and hyperthermia using magnetic nanoparticles in an experimental subcutaneous murine melanoma. *Cancer Science*, **94** (3), 308–13.

184 Hilger, I., Hiergeist, R., Hergt, R., Winnefeld, K., Schubert, H. and Kaiser, W.A. (2002) Thermal ablation of tumors using magnetic nanoparticles: an in vivo feasibility study. *Investigative Radiology*, **37** (10), 580–6.

185 Johannsen, M., Jordan, A., Scholz, R., Koch, M., Lein, M., Deger, S., Roigas, J., Jung, K. and Loening, S. (2004) Evaluation of magnetic fluid

hyperthermia in a standard rat model of prostate cancer. *Journal of Endourology/ Endourological Society*, **18** (5), 495–500.

186 Aas, A.T., Brun, A., Blennow, C., Stromblad, S. and Salford, L.G. (1995) The RG2 rat glioma model. *Journal of Neuro-Oncology*, **23** (3), 175–83.

187 Van Vulpen, M., De Leeuw, A.A., Raaymakers, B.W., Van Moorselaar, R.J., Hofman, P., Lagendijk, J.J. and Battermann, J.J. (2004) Radiotherapy and hyperthermia in the treatment of patients with locally advanced prostate cancer: preliminary results. *British Journal of Urology International*, **93** (1), 36–41.

188 Hurwitz, M.D., Kaplan, I.D., Hansen, J.L., Prokopios-Davos, S., Topulos, G.P., Wishnow, K., Manola, J., Bornstein, B.A. and Hynynen, K. (2002) Association of rectal toxicity with thermal dose parameters in treatment of locally advanced prostate cancer with radiation and hyperthermia. *International Journal of Radiation Oncology, Biology, Physics*, **53** (4), 913–18.

189 Anscher, M.S., Samulski, T.V., Dodge, R., Prosnitz, L.R. and Dewhirst, M.W. (1997) Combined external beam irradiation and external regional hyperthermia for locally advanced adenocarcinoma of the prostate. *International Journal of Radiation Oncology, Biology, Physics*, **37** (5), 1059–65.

190 Lehmann, J., Natarajan, A., Denardo, G.L., Ivkov, R., Foreman, A.R., Catapano, C., Mirick, G., Quang, T., Gruettner, C. and Denardo, S.J. (2008) Short communication: nanoparticle thermotherapy and external beam radiation therapy for human prostate cancer cells. *Cancer Biotherapy and Radiopharmaceuticals*, **23** (2), 265–71.

191 Hartman, K.B., Wilson, L.J. and Rosenblum, M.G. (2008) Detecting and treating cancer with nanotechnology. *Molecular Diagnosis and Therapy*, **12** (1), 1–14.

192 Neuwelt, E.A., Varallyay, P., Bago, A.G., Muldoon, L.L., Nesbit, G. and Nixon, R. (2004) Imaging of iron oxide nanoparticles by MR and light microscopy in patients with malignant brain tumours. *Neuropathology and Applied Neurobiology*, **30** (5), 456–71.

193 Regino, C.A., Walbridge, S., Bernardo, M., Wong, K.J., Johnson, D., Lonser, R., Oldfield, E.H., Choyke, P.L. and Brechbiel, M.W. (2008) A dual CT-MR dendrimer contrast agent as a surrogate marker for convection-enhanced delivery of intracerebral macromolecular therapeutic agents. *Contrast Media and Molecular Imaging*, **3** (1), 2–8.

194 Heyn, C., Ronald, J.A., Mackenzie, L.T., MacDonald, I.C., Chambers, A.F., Rutt, B.K. and Foster, P.J. (2006) In vivo magnetic resonance imaging of single cells in mouse brain with optical validation. *Magnetic Resonance in Medicine*, **55** (1), 23–9.

195 Cai, W., Chen, K., Li, Z.B., Gambhir, S.S. and Chen, X. (2007) Dual-function probe for PET and near-infrared fluorescence imaging of tumor vasculature. *Journal of Nuclear Medicine*, **48** (11), 1862–70.

196 Plotkin, M., Gneveckow, U., Meier-Hauff, K., Amthauer, H., Feussner, A., Denecke, T., Gutberlet, M., Jordan, A., Felix, R. and Wust, P. (2006) 18F-FET PET for planning of thermotherapy using magnetic nanoparticles in recurrent glioblastoma. *International Journal of Hyperthermia*, **22** (4), 319–25.

197 Kohler, N., Sun, C., Fichtenholtz, A., Gunn, J., Fang, C. and Zhang, M. (2006) Methotrexate-immobilized poly(ethylene glycol) magnetic nanoparticles for MR imaging and drug delivery. *Small*, **2** (6), 785–92.

198 Liu, W., Dahnke, H., Jordan, E.K., Schaeffter, T. and Frank, J.A. (2008) In vivo MRI using positive-contrast techniques in detection of cells labeled with superparamagnetic iron oxide nanoparticles. *NMR in Biomedicine*, **21** (3), 242–50.

199 Du, L., Chen, J., Qi, Y., Li, D., Yuan, C., Lin, M.C., Yew, D.T., Kung, H.F., Yu, J.C. and Lai, L. (2007) Preparation and biomedical application of a non-polymer coated superparamagnetic nanoparticle. *International Journal of Nanomedicine*, **2** (4), 805–12.

200 Kuhlpeter, R., Dahnke, H., Matuszewski, L., Persigehl, T., von Wallbrunn, A., Allkemper, T., Heindel, W.L., Schaeffter, T. and Bremer, C. (2007) R2 and R2* mapping for sensing cell-bound superparamagnetic nanoparticles: in vitro and murine in vivo testing. *Radiology*, **245** (2), 449–57.

201 Koyama, Y., Talanov, V.S., Bernardo, M., Hama, Y., Regino, C.A., Brechbiel, M.W., Choyke, P.L. and Kobayashi, H. (2007) A dendrimer-based nanosized contrast agent dual-labeled for magnetic resonance and optical fluorescence imaging to localize the sentinel lymph node in mice. *Journal of Magnetic Resonance Imaging*, **25** (4), 866–71.

202 Medarova, Z., Pham, W., Kim, Y., Dai, G. and Moore, A. (2006) In vivo imaging of tumor response to therapy using a dual-modality imaging strategy. *International Journal of Cancer*, **118** (11), 2796–802.

203 Smirnov, P., Lavergne, E., Gazeau, F., Lewin, M., Boissonnas, A., Doan, B.T., Gillet, B., Combadiere, C., Combadiere, B. and Clement, O. (2006) In vivo cellular imaging of lymphocyte trafficking by MRI: a tumor model approach to cell-based anticancer therapy. *Magnetic Resonance in Medicine*, **56** (3), 498–508.

204 Johannsen, M., Gneveckow, U., Thiesen, B., Taymoorian, K., Cho, C.H., Waldofner, N., Scholz, R., Jordan, A., Loening, S.A. and Wust, P. (2007) Thermotherapy of prostate cancer using magnetic nanoparticles: feasibility, imaging, and three-dimensional temperature distribution. *European Urology*, **52** (6), 1653–61.

205 Martina, M.S., Fortin, J.P., Fournier, L., Menager, C., Gazeau, F., Clement, O. and Lesieur, S. (2007) Magnetic targeting of rhodamine-labeled superparamagnetic liposomes to solid tumors: in vivo tracking by fibered confocal fluorescence microscopy. *Molecular Imaging*, **6** (2), 140–6.

Keywords

magnetic nanoparticles; cancer imaging; cancer therapy; small magnetic nanoparticles; ultra-small magnetic nanoparticles; drug delivery; hyperthermia

7
Core–Shell Magnetic Nanomaterials in Medical Diagnosis and Therapy

Marites P. Melancon and Chun Li

7.1
Introduction

Core–shell magnetic nanomaterials generally fall into two categories, both of which consist of a metallic or metallic oxide core with an inorganic or organic shell. The core consists usually of magnetite or maghemite that is magnetic, while the shell makes the nanomaterial biocompatible, stable, and also serves as a platform for attaching target units. Core–shell magnetic nanomaterials offer attractive possibilities in biomedicine. First, their sizes can be tailored to match the dimensions of cells (10–100 μm), viruses (20–450 nm), proteins (5–50 nm), or genes (2 nm wide and 10–100 nm long). Because of the similarity in size between the nanoparticle and the biological entity of interest, these nanoparticles can move within closer proximity with the target, and thus are more likely to interact. Second, the magnetic nanoparticles can be manipulated with an external magnetic field gradient, and therefore can be made to concentrate in target areas. In addition, these particles can be coupled with drugs for selective drug delivery, and/or with reporter molecules for noninvasive imaging, such as dyes for optical imaging and radionuclide atoms for nuclear imaging. Third, the magnetic nanoparticles can be made to resonantly respond to an alternating magnetic field, which results in a heating effect; when this heating reaches a certain temperature (>54 °C) the nanoparticles can be used as an ablation agent. At a certain temperature, these agents can also be used to enhance chemotherapy and radiotherapy. Finally, both magnetite and maghemite possess superparamagnetic properties that enable nanoparticles to be used as agents for magnetic resonance imaging (MRI).

In this chapter, we will discuss the synthesis of magnetic nanomaterials and their potential applications in MRI, hyperthermia-based treatment, and drug delivery.

Nanomaterials for the Life Sciences Vol. 4: Magnetic Nanomaterials. Edited by Challa S. S. R. Kumar

ISBN: 978-3-527-32154-4

7.2 Synthesis

Molecular diagnostics have provided new strategies for tailoring therapies to fit the needs of each cancer patient's unique biology (i.e., individualized cancer therapy). Today, both diagnostic and therapeutic agents are increasingly prepared with controlled properties for specialized uses, although for these agents to perform properly it is important that the synthesized particles have an almost uniform size and shape. The synthesis of core–shell magnetic nanoparticles includes: (i) synthesizing the magnetic core; (ii) forming the core–shell magnetic nanoparticles with an organic or inorganic coating; and (iii) functionalizing the core–shell magnetic nanoparticles for biological applications.

7.2.1 Formation of the Magnetic Core

Several reviews have discussed the synthesis and characterization of the core of magnetic nanoparticles [1, 2]. In this chapter, the discussion will be limited to synthesis of the superparamagnetic iron oxide nanoparticles (SPIONs) most commonly used for biological applications. Magnetite (Fe_3O_4) and maghemite (γ-Fe_2O_3) are the two most common materials; magnetite is oxidized very easily to maghemite so, for the sake of simplicity, we will here discuss maghemite as the iron oxide nanoparticles, unless otherwise noted. In later sections, we will briefly outline the most common synthesis methods, the general synthetic mechanism, the parameters that affect the properties of the nanoparticles, and their advantages and disadvantages over the other methods. Some examples of each method will also be provided.

7.2.1.1 Coprecipitation from Solution

The easiest and most convenient way to synthesize iron oxides (Fe_3O_4 or γ- Fe_2O_3) in the nanometer range is via coprecipitation. In this process, Fe^{2+} or Fe^{3+} is added with a base under inert atmosphere or at elevated temperatures, and the magnetic particle is then precipitated. Two main methods are available for synthesizing maghemite via coprecipitation:

- The first method is based on the partial oxidation of ferrous hydroxide via the addition of Fe^{2+}, a base, and a mild oxidizing agent. For example, Sugimoto *et al.* [3] reacted $FeSO_4$ with KOH in the presence of nitrate ion (the mild oxidizing agent). The resultant gelatinous suspension was maintained at 90 °C in the presence of air for several hours, in order to oxidize the magnetite to maghemite. In this way, spherical magnetite particles with average diameters ranging from 0.03 to 1.1 μm, were obtained [3].
- The second method involves ageing stoichiometric mixtures of ferrous and ferric ions in aqueous solution. For example, Massart *et al.* [4] reacted alkaline Fe^{2+}-Fe^{3+} solutions to produce maghemite particles with good yield.

Because, in addition to the usual flocculation, nanoparticles are also attracted magnetically, the synthesized nanoparticles must be protected through surface modification. The use of organic additives or stabilizers such as, 1% polyvinyl alcohol (PVA) [5] and dextran [6, 7], has been shown to be an important factor in preparing monodisperse magnetite particles of varying sizes.

In coprecipitation, the adjustment of the reaction parameters such as pH, the ionic strength of the precipitation medium, the Fe^{2+} to Fe^{3+} ratio, salt type and reaction temperature, allows one to control the mean size, shape, and composition of the resultant magnetic nanoparticle [1]. Other factors which affect the size and monodispersity of the iron oxide nanoparticles include the amount of stabilizing ions, the presence of other ions, chelation, and the adsorption of additives on the nuclei and growing crystals [1].

Although coprecipitation is probably the most widely used method used to obtain commercial magnetic nanoparticle-based MRI contrast agents, particles prepared by coprecipitation tend to be rather polydisperse, and their shapes are difficult to control. Other methods have been developed to provide a better control over the size and size distribution of magnetic nanoparticles; these will be discussed in the following sections.

7.2.1.2 **Thermal Decomposition**

Thermal decomposition is the decomposition of organometallic precursors in the presence of hot organic surfactants. The organometallic precursors for iron oxide preparation include cupferronates [$Fe^{x}Cup_{x}$] (Cup = *N*-nitrosophenylhydroxylamine, $C_6H_5N(NO)O^-$) [8], carbonyls [9], and acetylacetonates, [$Fe(acac)_n$], where $n = 2$ or 3 [10, 11]. Oleates [12], fatty acids [13], and hexadecylamine [14] are often used as surfactants.

Alivisatos [8] and coworkers were the first to synthesize maghemite nanocrystals in a nonhydrolytic fashion. In this method, solutions of $FeCup_3$ in octylamine were injected into trioctylamine at 250–300 °C in an argon atmosphere. The resultant iron oxide nanocrystals had a size range of 4 to 10 nm in diameter, were crystalline, and could be repeatedly dispersed and reprecipitated in organic solvents [8]. Hyeon *et al*. [9] also prepared monodisperse maghemite nanoparticles using the thermal decomposition method. In their approach, iron pentacarbonyl ($Fe(CO)_5$) was injected into a solution containing surfactants and trimethylamine oxide, a mild oxidant [9]. Later, Hyeon and coworkers [15] modified their procedure and used inexpensive and environmentally friendly $FeCl_3$ and sodium oleate, slowly heating the mixture to 320 °C. Similarly, these nanoparticles have a uniform size of 8–11 nm and were prepared on an ultra-large scale [15]. The research group of Sun and Zeng [10] used acetylacetonates as a precursor in the presence of 1,2-hexadecanediol, oleic acid, and oleylamine in phenol ether to prepare nearly monodispersed Fe_2O_3 nanoparticles which were 3–20 nm in diameter [10].

Factors that affect the size and morphology of magnetic nanomaterials prepared by thermal decomposition include the ratios of the starting reagents, such as organometallic compounds, surfactant, and solvent. The reaction temperature, reaction time, and aging period are also important. Thermal decomposition yields

nanoparticles with a narrow size distribution and good crystallinity of individual and dispersible magnetic iron oxide nanoparticles; however, because the process is complicated and requires an inert atmosphere, it often takes from a few hours to several days to synthesize the nanoparticles. In some of these preparations, it is also unknown whether the synthesized nanoparticles can be suspended in aqueous media, which is important in biological applications [1].

7.2.1.3 **Microemulsions**

Microemulsions are clear, isotropic, thermodynamically stable liquid media. These systems are composed of at least three components – two immiscible phases (generally water and oil) and a surfactant. It was proposed that, when water and oil collided, they would form a microemulsion. Then, when two microemulsions carrying appropriate reactants were put together they would form a surfactant-stabilized microcavity (with diameters typically ranging from 1 to 50 nm), which provide a confinement effect that limits particle nucleation, growth, and agglomeration. The reaction would then take place inside the microcavity containing the reactants, wherein these microdroplets would continuously collide, coalesce, and break again, with a precipitate finally forming in the micelles [16, 17]. By adding a solvent, such as acetone or ethanol, to the microemulsions, the precipitate can be extracted by either filtering or centrifuging the mixture. The size of the reverse micelle is determined by the molar ratio of water to surfactant [17].

An example of the microemulsion method was demonstrated by Pileni [18] and coworkers. In their method, ferrous dodecyl sulfate, $Fe(DS)_2$ micellar solution was used to produce nanosized magnetic nanoparticles with average sizes from 4 to 12 nm, and standard deviation ranging from 0.2 to 0.3. The size of the synthesized magnetic nanoparticle can be controlled by the micellar concentration and the temperature [18].

Although many types of magnetic nanoparticle have been synthesized in a controlled manner using the microemulsion method, the particle size and shapes usually vary widely. The working window for synthesis in microemulsions is usually quite narrow, and the yield of nanoparticles is low compared to other methods, such as thermal decomposition and coprecipitation. Furthermore, because large amounts of solvent are necessary to synthesize appreciable amounts of material, microemulsion is not a very efficient process and is rather difficult to scale-up.

7.2.1.4 **Pyrolysis**

Pyrolysis is the decomposition of a material by heating it in the absence of oxygen. Maghemite nanoparticles are usually prepared via a pyrolytic method by reacting Fe^{3+} salt and a reducing agent. In nanoparticle preparation, pyrolysis can be performed in two ways:

- Spray pyrolysis: This produces ultrafine particles that are usually aggregated. In this process, a solution of precursors serves as the starting materials; these are

misted into droplets that are carried by gas into a hot zone, where they are rapidly heated and decomposed to form a powder [19].

- Laser pyrolysis: This has a shorter reaction time, and produces ultrafine particles that are less aggregated. The process involves heating a flowing mixture of gases with a continuous-wave carbon dioxide laser, which initiates and sustains a chemical reaction. Above a certain pressure and laser power, a critical concentration of nuclei is reached in the reaction zone, leading to the homogeneous nucleation of particles that are further transported by an inert gas to a filter [20].

Both, spray and laser pyrolysis have been shown to be excellent techniques for the direct and continuous production of well-defined magnetic nanoparticles under exhaustive control of the experimental conditions. Indeed, their high production rates indicate a promising future for the preparation of magnetic nanoparticles that can be utilized for both *in vivo* and *in vitro* applications.

7.2.2 Formation of the Core–Shell Structure

Over time, core–shell magnetic particles have evolved to stabilize and protect the naked magnetic nanoparticle against its environment – that is, against oxidation by oxygen, or erosion by an acid or base. In addition, the encapsulation of nanoparticles also reduces their toxicity and improves their dispersibility, chemical stability, and biocompatibility [21]. Magnetic nanoparticles can be coated with either: (i) organic materials, including surfactants and polymers; or (ii) inorganic components, such as carbon, silica, precious metals such as silver and gold, or oxides. In this section, the different methods of coating magnetic nanoparticles with organic or inorganic shells will be discussed, with attention focused on the synthesis of core–shell magnetic nanoparticles with an iron oxide core and gold shell.

7.2.2.1 Inorganic Core with Organic Shell

Surfactants or polymers are normally introduced into the nanoparticle surface during the synthesis (*in situ*) or after synthesis, so as to avoid agglomeration. In general, electrostatic or steric repulsion can be used to disperse the nanoparticles and to maintain them in a stable, colloidal state. In general, surfactants or polymers can be chemically anchored or physically adsorbed onto the magnetic nanoparticles to form a single or double layer [22], that creates repulsive forces (mainly as steric repulsion) to balance the magnetic and van der Waals attractive forces acting on the nanoparticles, thus stabilizing the magnetic particles in suspension. Polymers containing functional groups, such as carboxylic acids, phosphates, and sulfates, can bind to the surface of magnetite [1]. The most common organic coatings include: dextran, carboxymethylated dextran, carboxydextran, starch, arabinogalactan, glycosaminoglycan, sulfonated styrene-divinylbenzene, polyethylene glycol (PEG), polyvinyl alcohol (PVA), poloxamers, and polyoxamines [23]. Most of these polymers have been attached onto the surface of iron oxide

nanoparticles via coprecipitation methods [5, 6, 24], although in order to achieve a better dispersion the magnetite particles are often modified after their precipitation [25].

7.2.2.2 Inorganic Core with Inorganic Shell

The coating of iron oxide magnetic nanoparticles with polymers and surfactants does not always provide a suitable protection, mainly because the organic-coated iron oxides are not stable in air, and are easily leached by acidic solution, resulting in their demagnetization. Another drawback of polymer-coated magnetic nanoparticles is the relatively low intrinsic stability of the coating at higher temperatures, a problem which is enhanced by the possible catalytic action of the metallic cores [1]. Therefore, the development of other methods for protecting magnetic nanoparticles against deterioration is warranted. Precious metals can be coated onto magnetic nanoparticles through reactions in microemulsion, redox transmetalation, iterative hydroxylamine seeding, or other methods, so as to protect the cores against oxidation. Although the use of several inorganic coating materials has been investigated, the use of silica and gold protective coatings is most effective, and this will be discussed in the following sections.

7.2.2.2.1 **Coating with Gold** The preparation of iron oxide nanoparticles coated with gold is of special interest, not only because gold stabilizes the iron core, but also because of the potential applications of these nanoparticles in sensors, drug delivery, and biodetection technologies. Gold is an excellent candidate because of its easily reductive preparation, high chemical stability, biocompatibility, and its affinity for binding to amine and thiol terminal groups in organic molecules. Ideally, gold nanoshells should be thin enough so as to barely alter the magnetic properties of the magnetite core. Detailed below is a variety of synthetic methods for the direct attachment of gold shell with the iron core. These different examples were chosen because of the very interesting structures and morphology of the gold–iron nanoparticle produced. Currently, however, the method of accomplishing a controlled coating of individual magnetite nanoparticles, and the tunability of their shell thickness, remain largely unresolved.

Yu *et al.* [26] prepared dumbbell-like Fe_3O_4@Au nanoparticles, by decomposing iron pentacarbonyl, $Fe(CO)_5$, over the surface of gold nanoparticles in the presence of oleic acid and oleylamine (Figure 7.1). The mixture was heated under reflux (~300 °C), followed by room-temperature oxidation under air. The size of the Au particles, which was tuned at 2–8 nm for Au and 4–20 nm for Fe_3O_4, was controlled by adjusting the temperature at which the $HAuCl_4$ was injected, or the $HAuCl_4$/

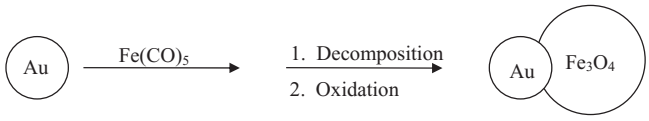

Figure 7.1 The formation of dumbbell-like Fe_3O_4@Au nanoparticles [26].

oleylamine ratio. The particles exhibited surface plasmon absorption characteristic of Au and magnetic properties characteristic of Fe_3O_4, which are affected by interactions between Au and Fe_3O_4. The dumbbell shape was formed through the epitaxial growth of iron oxide on the Au seeds. The polarity of the solvent affected this growth; for example, the use of diphenyl ether resulted in flower-like Au–Fe_3O_4 nanoparticles [26].

Cho *et al.* [27] reported another method for directly attaching Au shells into the iron oxide cores. In their study, Fe-core, Au-shell nanoparticles, of approximately 20 nm diameter, were synthesized using the reverse micelle method. Cho *et al.* [27] proposed that the Au shell appeared to grow by nucleating at selected sites on the Fe core before coalescing. An examination of the nanoparticles, using transmission electron microscopy (TEM), revealed rough shell surfaces that resulted from the gold's less-than-ideal oxidation resistance. However, electrical transport measurements in its pressed pellet form revealed the particles to be fairly stable, as the resistance of the pellet did not change appreciably over time [27].

Caruntu *et al.* [28] successfully coated ~10 nm Fe_3O_4 nanocrystals with 2–3 nm gold particles by using a chemically controlled, two-step procedure The first step in the process involved the formation of a stable methanolic solution of Fe_3O_4 nanospheres coated with an amino-terminated silane, and peptized to induce positive charges on the particles' surfaces. The second step involved treating the particles with a colloidal solution of negatively charged Au nanoparticles to enable the attachment of Au nanograins on the surface of the Fe_3O_4 nanocrystals (Figure 7.2). These novel nanostructures opened up new opportunities for the use of magnetite nanoparticles for *in vivo* biomedical applications through the chemical bonding of bioactive molecules to the attached Au nanoparticles [28].

Lyon *et al.* [29] synthesized water-soluble, Au-coated magnetic Fe oxide nanoparticles with diameters ~60 nm. This was achieved by the reduction of Au^{3+} onto the surfaces of ~9 nm-diameter particles consisting of either γ-Fe_2O_3 or partially oxidized Fe_3O_4 via iterative hydroxylamine seeding. The morphology and optical properties of the core/shell particles were seen to depend on the quantity of deposited Au, while the magnetic properties remained largely independent of the Au addition. The Au-coated particles exhibited a surface plasmon resonance (SPR)

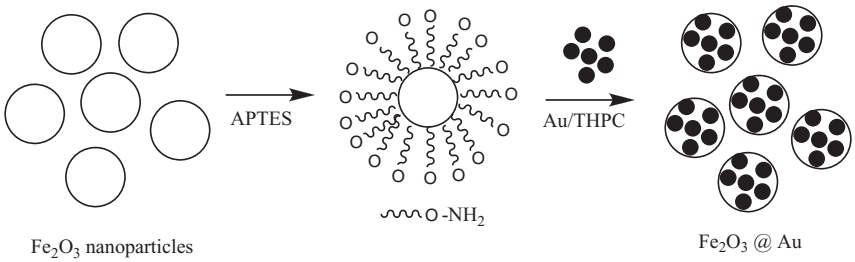

Figure 7.2 The formation of nanograin Fe_2O_3@Au nanoparticles [28]. APTES, 3-aminopropyltriethoxysilane; THPC, tetrakis(hydroxymethyl) phosphonium chloride.

peak that blue-shifted from 570 to 525 nm with increasing Au deposition. Superconducting quantum-interference device (SQUID) magnetometry revealed that the particle magnetic properties were not affected by the overlayer of a moderately thick Au shell.

The final example to be discussed here is the synthesis of a monolayer-capped iron oxide and core (iron oxide)-shell (gold) nanocomposite, and their assembly towards thin film materials. This was the first example of interparticle ligand exchange–precipitation chemistry at the gold shell that has demonstrated the intershell reactivity for constructing thin films of Fe_2O_3@ Au particles (Figure 7.3) [30]. In this method, presynthesized and size-defined iron oxide nanoparticles were used as seeding materials for the reduction of gold precursors, which was shown to be effective for coating the iron oxide cores with gold shells (Fe_2O_3@ Au). The novelty of their assembly strategy is the exploitation of the ligand-exchange reactivity at the gold shells for the thin film assembly of the core–shell nanoparticles. The change in particle size, as detected using TEM, the change in the SPR band as detected by UV-visible observations, and the disappearance of the magnetite diffraction peaks after coating the gold shell, as detected by X-ray diffraction (XRD), support the formation of a core–shell morphology. Moreover, the study's findings provided an important insight into the design of interfacial reactivities via core–shell nanocomposites for magnetic, catalytic, and biological applications [30].

7.2.2.2.2 **Coating with Silica** Magnetic nanoparticles coated with silica is becoming a promising and important approach because of its potential for biolabeling, drug targeting, and drug delivery. First, silica shells not only protect the magnetic cores but also prevent the magnetic cores from coming in direct contact with additional agents linked to the silica surface, thus avoiding unwanted interactions.

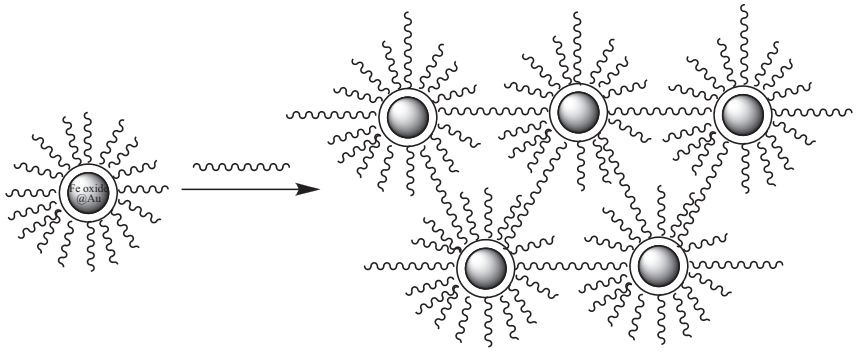

Figure 7.3 The formation of interparticle Fe_3O_4@Au nanoparticles [30]. Monodisperse core–shell-structured Fe_3O_4@Au nanoparticles coated with oleic acid or oleylamine were linked together by the difunctional linker 1,9-nonanedithiol or mercaptoundecanoic acid.

Second, silica contains surface silanol groups that can easily react with alcohols and silane coupling agents that produce dispersions that are not only stable in aqueous solution but also provide the ideal anchorage for the covalent bonding of specific ligands. Third, silica-coated iron oxides are stable in aqueous conditions, particularly in solutions with low pH values. The interparticle interactions, both in solution and within structures, can be easily controlled by varying of the shell thickness. In general, four methods are used to prepare silica-coated magnetic nanoparticles: (i) sol-gel process, (ii) silicic acid method, (iii) aerosol pyrolysis, and (iv) microemulsion method.

The first method, known as the Stober [31] method, is an *in situ* sol–gel process, that uses silicon alkoxides as the source of silica matrix. In this method, silica phase are formed on colloidal magnetic nanoparticles in a basic alcohol and water mixture. Xia [32] and co-workers have shown that commercially available ferrofluids can be directly coated with silica shells by the hydrolysis of tetraethyl orthosilicate. In their study, commercially available ferrofluid (EMG 304) was diluted with deionized water and 2-propanol. Ammonia solution and various amounts of tetraethyl orthosilicate were added stepwise to the reaction mixture under stirring. Coating the magnetic nanoparticles with silica proceeded at room temperature for about 3 h under continuous stirring. The coating thickness could be adjusted by varying the amount of tetraethyl orthosilicate. Because iron oxide surface has a strong affinity towards silica, no primer was required to promote the deposition and adhesion of silica. The silica shells' negative charge enables these magnetic nanoparticles to be redispersed in water without the need for adding other surfactants. Also, because of its relatively mild reaction condition, surfactant-free, and low cost, the sol-gel method has been adopted more widely than the other methods for the preparation of silica-coated magnetic nanoparticles [32].

The second approach is based on silicic acid formed during the addition of hydrochloric acid to sodium silicate solution containing iron oxide nanoparticles [33]. The silicic acid undergoes a polymerization reaction, transforming silanol groups (Si–OH) to siloxane bonds (Si–O–Si) and the silica coating forms around iron oxide nanoparticles. Butterworth *et al.* [34] synthesized a magnetite-silica nanocomposites by the aqueous deposition of silica onto ultrafine magnetite particles 5–20 nm in diameter via the controlled hydrolysis of sodium silicate. This method appeared to be able to provide highly functionalized, well-dispersed iron oxide nanoparticles at low cost [33].

The third method is called aerosol pyrolysis, in which silica-coated magnetic nanoparticles were prepared by aerosol pyrolysis of a precursor mixture composed of a silica precursor and an iron complex in gaseous phase [35–37].

In the fourth method, which is the microemulsion method, uses micelles and inverse micelles to confine and control silica coating. Previous studies have examined different non-ionic surfactants, including Triton X-100, Igepal CO-520, and Brij-97 for preparing microemulsions, and evaluating their effects on the particle size, crystallinity, and the magnetic properties [38]. Yang *et al.* [39] synthesized nanostructured silica-coated magnetite in sol-gel materials using a reverse-micelle technique. Using this method, they were able to synthesize spherical particles that

have a typical diameter of 53 ± 4 nm. They were also able to simultaneously trap biological molecules, such as catalysts within the pores [39].

Recently, Hyeon [40] and co-workers synthesized hollow iron oxide magnetic nanoparticles using a process termed wrap, bake and peel method. Many hollow-structured nanomaterials of metals, metal oxides and other materials have been synthesized using various procedures, including the most popular template approach. However, most of them are unsuitable for biomedical applications because of their poor water-dispersibility, which is derived from their large particle size or hydrophobic nature. In the work of Hyeon and coworkers, the overall process starts with covering (wrap) of β-FeOOH nanoparticles with a silica coating, heating (bake) and then etching (peel) silica layer to produce hollow iron oxide nanocapsules. Depending on the heat treatment conditions, hollow nanocapsules of either hematite or magnetite were produced. The synthesized water-dispersible magnetite nanocapsules were successfully used not only as a drug-delivery vehicle, but also as a T_2 magnetic resonance imaging contrast agent [40].

Coating magnetic iron oxide with silica is a fairly controllable process, as shown in the examples presented above. However, silica is unstable under basic conditions, and may contain pores through which oxygen or other species can diffuse. Coating magnetic nanoparticles with other oxides is a much less developed field; therefore alternative methods, especially those that would enable stabilization under alkaline conditions, are needed.

7.2.2.2.3 **Coating with Silica and Gold** The near infrared (NIR) region is a region of the electromagnetic radiation in which absorption of water and naturally occurring fluorochromes is lowest. Directly coating of gold onto the surface of the magnetic iron oxide core produces a core–shell nanoparticle of plasmon resonance ranging from 500–600 nm. In order for these nanoparticles to absorb light at the near-infrared (NIR) region, the iron oxide cores must be coated with dielectric silica and thin gold shells. Depending on the relative size of the core and the thickness of the shell, this iron oxide coated with silica and gold can be tuned to resonate from the visible to NIR regions. Previously, we have discussed the different ways of coating the iron oxide with gold having different structures, and methods of synthesizing the core–shell particles. Next, we will discuss the different ways of protecting the magnetic core using silica and gold that absorbs at the NIR region.

Hyeon [41] and coworkers synthesized an Au-coated SPION with silica as the dielectric interface. The synthetic approach for the preparation of this Au-coated SPION, with TEM images of the products obtained after each synthetic step, are shown in Figure 7.4. In this synthesis, 100 nm-diameter silica spheres were synthesized using the Stöber [31] method, and the surfaces of the particles then modified with 3-aminopropyltrimethoxysilane. Monodisperse 7-nm Fe_3O_4 nanoparticles stabilized with oleic acid were synthesized and subsequently ligand-exchanged with 2-bromo-2-methylpropionic acid (BMPA). The BMPA-stabilized Fe_3O_4 nanoparticles were then covalently attached to the amino-modified silica spheres through a direct nucleophilic substitution reaction between the bromo

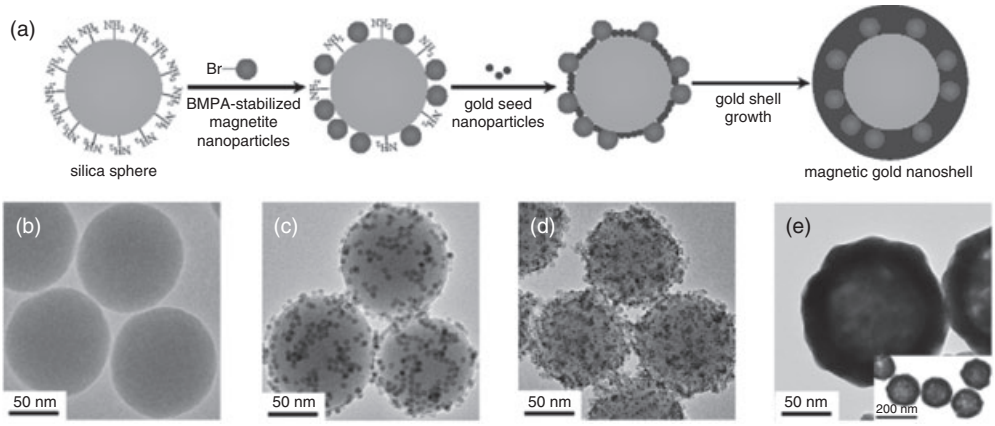

Figure 7.4 The formation of silica-Fe_3O_4@Au nanoparticles [41]. (a) 2-Bromo-2-methylpropionic acid (BMPA)-stabilized Fe_3O_4 nanoparticles were covalently attached to the amino-modified silica spheres, which were in turn coated with a Au layer; (b–e) TEM images showing the different stages in the preparation of silica-Fe_3O_4@Au nanoparticles: (b) silica spheres; (c) silica spheres with Fe_3O_4 nanoparticles on the surface; (d) silica spheres with Fe_3O_4 and a gold seeds on the outer layer; (e) the final product.

groups and the amino groups. Gold seed nanoparticles of 1–3 nm were attached to the residual amino groups of the silica spheres. Finally, a complete 15 nm-thick gold shell with embedded Fe_3O_4 nanoparticles was formed around the silica spheres, resulting in what the authors referred to as a "magnetic gold nanoshell". Similarly structured gold nanoshells embedded with silica-stabilized magnetite nanoparticles were fabricated by the groups of Stoeva *et al.* [42] and Salgauerino-Maceira *et al.* [43]. More recently, Chen [44] and coworkers developed a multifunctional silver nanoshell with a sandwich-like nanostructure which was composed of a yolk-egg magnetic silica core, coated with a layer of silver, and with a thin layer of gold sited between the core and shell. This had very high absorbance in the NIR region, suggesting its possible application in the biomedical field. However, these syntheses yielded Au-coated nanoparticles that had an average diameter of ~200 nm with a shell thickness of ~30 nm [42–44].

It has been shown previously that the cell uptake of nanoparticles is dependent on the nanoparticle size, with a 50 nm diameter being optimal. Recently, the size, charge, and concentration-dependent uptake of iron oxide particles by nonphagocytic cells was evaluated by Thorek and Tsourkas [45], who showed that a 107-nm superparamagnetic iron oxide (SPIO) manifestation led to the largest T_2 signal decrease. Thus, it is desirable to have particles with a mean size <100 nm. In order to meet these needs, a bifunctional gold-coated SPIO-silica nanoparticle was developed which had an average diameter of ~100 nm, a strong absorption at the NIR region, a high T_2 relaxivity value, and could be controlled by an external magnetic field [46]. The multistep synthesis of the Fe@Au nanoparticle is shown in Figure 7.5.

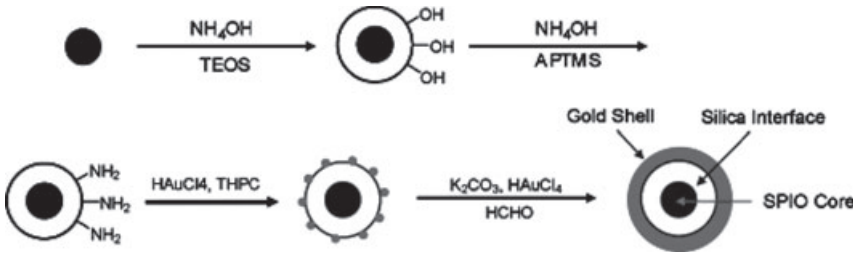

Figure 7.5 The formation of SPIO@Si–Au nanoparticles [46]. SPIO, superparamagnetic iron oxide; TEOS, tetraethylorthosilicate; APTMS, 3-aminopropyltrimethoxysilane; THPC, tetrakis(hydroxymethyl) phosphonium chloride.

In the first step, silica-coated SPIO (Fe_2O_3) nanoparticles were synthesized using the Stöber process. For this, commercially available SPIO (average diameter 10 nm, EMG 304) nanoparticles were stabilized with oleic acid in water. The magnetic nanoparticles were easily coated with amorphous silica via the sol–gel process, because the iron oxide surface has a strong affinity for silica, and no primer was required to promote the deposition and adhesion of silica. The thickness of the silica sphere could be tuned from 2 to 100 nm simply by changing the concentration of the sol–gel precursor, tetraethyl orthosilicate. Next, the surface of the silica shell was functionalized with amine groups by treatment with NH4OH and 3-aminopropyltrimethoxysilane. The 2–3 nm gold nanocrystal seeds were then attached to the amino groups on the silica sphere by reducing chloroauric acid ($HAuCl_4$) with tetrakis(hydroxymethyl) phosphonium chloride (THPC). Because the gold nanoseeds had net negative surface charges, they became firmly attached to the amino groups on the silica sphere, which were positively charged at acidic pH. Finally, the attached gold nanoseeds were used to nucleate the growth of a gold overlayer on the silica surface to form a gold nanoshell. The nanoshells were isolated by centrifugation, washed with deionized water, and then resuspended in sodium citrate buffer (33 m*M*) to stabilize the particle solution. To control the thickness of the gold shells, the concentration of gold-seeded, SPIO-containing silica particles was varied while the concentration of gold precursor ($HAuCl_4$ in 2.5% K_2CO_3 solution) was kept constant. Subsequent TEM images revealed an average diameter of the Au-coated SPIO of 82.2 ± 9.7 nm, with a shell thickness of ~8 nm [46].

7.3
Applications: Magnetic Resonance Imaging

Magnetic resonance imaging is a noninvasive technique used to obtain anatomic and metabolic or functional information with high spatial and temporal resolution. MRI measures changes in the magnetization of hydrogen protons in water

molecules placed in a magnetic field after a pulse of radiofrequency has hit them. Protons from different tissues relax at different rates, and this results in clearly defined anatomical images. However, within a clinical setting, it is very difficult to use MRI alone to differentiate healthy from diseased tissues, and the use of a contrast agent is often necessary to make such a differentiation. Contrast agents alter the relaxation time of the protons in their proximity, thus providing a better contrast. In standard clinical MRI scans, the contrast agents are injected intravenously, thus increasing the contrast systemically. Although the most commonly used MRI contrast media are gadolinium chelates, these small-molecular-weight contrast agents are rapidly cleared from the body, such that only a short time is allowed for the imaging process [48]. Colloidal iron oxides may offer certain advantages over gadolinium chelates as MRI contrast agents, including a long blood circulating time, biocompatibility, and high relaxivity values [49]. Iron oxides are generally imaged through T_2- and T_2-*weighted MRI. To date, a wide variety of particles have been produced, which differ in their size (hydrodynamic particle sizes varying from 10 to 500 nm) and type of coating material used (e.g., dextran, starch, albumin, silicones, PEG) [50]. These particles are classified according to their size, as this influences both their physico-chemical and pharmacokinetic properties. The first particle type – the superparamagnetic iron oxides (SPIOs) – are larger than 50 nm (coating included) in diameter, while the second type – the ultrasmall superparamagnetic iron oxides (USPIOs) are smaller than 50 nm [51]. An extensive review on the imaging applications of magnetic iron oxide nanoparticles has recently been published [23, 47].

Several generations of iron oxide-based magnetic nanoparticles have been developed:

- First-generation MRI contrast agents tend to have a larger size (diameters >200 nm) and are polydisperse. When these agents are introduced into the body, they are rapidly recognized as being "foreign" to the body, and are taken up by the reticuloendothelial system (RES). Because they accumulate passively in the liver and spleen, these agents are used to image liver diseases, especially liver cancer.
- Second-generation agents are mostly nanosized (diameters <200 nm), and their coatings are more extensive. These surface-modified agents are designed to prevent aggregation and avoid sequestration by the RES; consequently, they have a narrow size distribution in solution and a long half-life in the blood circulation. Materials such as dextran, PEG, and PVA have been used to coat these nanoparticles.
- Third-generation agents consist of magnetic cores coated with targeting ligands such as antibodies, and are used for active targeting. These tend to be smaller in size and have targeting units on their surface. These agents are designed to actively target magnetic nanoparticles to the sites of disease.

Examples of the different generations of contrast agent are presented in the following subsections.

Ferumoxide [52] (AMA-25; trade name Feridex® or Endorem®) represents a first-generation MRI contrast agent. This agent is based on SPIONs that have an average diameter of 120–180 nm and are coated with dextran [52, 53]. Ferumoxide was the first organ-specific MRI contrast agent to be approved for clinical applications in detecting and evaluating liver lesions [54]. Second-generation agents of this type are represented by ferumoxytol (Code 7228) [55]. This is an iron oxide nanoparticle of approximately 30 nm diameter, and is coated with carboxymethyl dextran instead of dextran. This second-generation magnetic nanoparticle is used for macrophage and blood pool imaging, and is currently undergoing Phase II clinical trials.

Ferumoxtran [56] (trade names Sinerem®, Combidex®) is also a dextran-coated iron oxide nanoparticle with an average diameter of 15–30 nm that has been clinically approved for use in the US and in EU countries. It is currently being used to detect metastatic disease in lymph nodes. An alternative dextran-derivative coating is carboxydextran. Ferumoxsil [57] (trade names Lumirem® or Gastromark®) and ferucarbotran [58] (trade names Resovist®, Cliavist®) are 300 nm-diameter SPIONs designed for gastrointestinal imaging after oral administration. Resovist® or Cliavist® is also used as an organ-specific MRI contrast agent after bolus intravenous injection to detect and characterize small focal liver lesions.

Several studies have shown that coating the magnetic nanoparticle with PEG, a highly hydrophilic synthetic polymer, renders the nanomaterials biocompatible and prolongs their blood circulation time. Feruglose (Clariscan®) [59] consists of USPIO particles of 4–7 nm diameter, coated with PEG. The blood pool half-life of feruglose is more than 2 h in humans; the particles are taken up by the mononuclear phagocyte system and distributed mainly to the liver and spleen. Recently, the development of feruglose has been discontinued.

Third-generation MRI contrast agents with targeting ligands such as antibodies are important in imaging diseases, especially at the earlier stages. Immunoglobulins can be covalently linked to the dextran coat of the iron oxide nanoparticle, using standard methods [60], by glutaraldehyde crosslinking [61], by complexation through ultrasonication [62, 63], by using the biotin–streptavidin system [64, 65], and by amine sulfhydryl group linkage [66, 67]. These antibodies have been shown to improve the sensitivity of cancer detection because the antibody-coated magnetic nanoparticles can interact with the cancer cells. For example, iron oxide nanoparticles conjugated with trastuzumab have been shown to attach and detect SKBR-3 breast cancer cells [68]. Peptides and other small molecules have also been attached to magnetic nanoparticles; notably, a cyclic peptide with the sequence arginine-glycine-aspartic acid (RGD) has been conjugated to crosslinked iron oxide nanoparticles to target integrins expressed in BT-20 tumor cells [69].

Magnetic nanoparticles can also be used with MRI to track cells, as some units have resolutions (20–25 μm) which approach the size of single cells [65]. This technique can be used very effectively to monitor the fate of certain cells and to evaluate cell-based therapies [70]. The tracking of cells with an MRI-detectable tracer was first attempted about a decade ago, when various research groups

labeled leukocytes, lymphocytes, and monocytes with SPIOs in an attempt to study immune tracking. However, because these nanoparticles were internalized very slowly, it became necessary to attach targeting vectors. For example, HIV-1 Tat peptide carries a transmembrane and a nuclear localization signal within its sequence [71], and is therefore capable of translocating exogenous molecules into cells. The conjugation of HIV-1 Tat peptide into dextran-crosslinked iron oxide nanoparticles has been shown to increase their uptake over 100-fold into lymphocytes when compared to bare nanoparticles [72, 73]. In addition, anionic maghemite nanoparticles (AMNPs) have been shown to have a cell internalization rate comparable to that of dextran-coated iron oxide nanoparticles [74]. This is because the particles' negative surface charge interacts strongly and nonspecifically with the cell's plasma membrane (even if the net surface charge of the membrane is negative, there are also positive sites within it that attract the agent). This increase in internalization substantially increases the detectability of labeled cells by MRI, and consequently increased its ability to isolate and sort cells from tissues following *in vivo* experiments such as transplantations.

Magnetic nanoparticles have also been used for transgene expression with MRI. Other imaging modalities, such as optical and nuclear imaging, have been used to image transgene expression, although the relatively low resolutions or limited depths of penetration of these modalities limits their effectiveness. Although the use of magnetic nanoparticles to image transgene expression is still in its early stages, the results of preliminary studies have demonstrated the feasibility of using MRI to depict the activity of endocytotic receptors, such as the asialoglycoprotein receptor [75, 76]. Human transferrin, which serves as a ligand for the endocytotic transferrin receptor, has been conjugated to monocrystalline iron oxide to image transgene expression using MRI [77, 78]. A universal MRI marker gene to image gene expression may enable research groups to monitor gene therapy in which exogenous genes are introduced into the body so as to eliminate a genetic defect, or to add an additional gene function to the tumor cells. Currently, investigations in this area are leading to the development of techniques that can be used to visualize noninvasively where, when, and in some cases at what level, a gene is being expressed.

7.4
Applications: Hyperthermia and Thermal Ablation

The use of heat for the preferential killing of cancer cells, whether through hyperthermia or thermal ablation, represents a very promising approach to cancer therapy. This method is especially appealing because it is a physical treatment, and therefore there are fewer side effects compared to conventional cancer treatment strategies such as radiotherapy and chemotherapy. Both, hyperthermia and thermal ablation can also be performed repeatedly without any accumulation of toxic side effects. Hyperthermia is defined as the heating of tissues at 42–46 °C [79], while thermal ablation is the heating of tissues at

temperatures in excess of 46 °C [80]. Hyperthermia causes cellular inactivation by inducing and regulating apoptosis, signal transduction and multi-drug resistance. Additionally, repeatedly heating tissues to hyperthermic temperatures signals the release of heat shock proteins [81]. Hyperthermia can also boost the efficacy of radiotherapy [82, 83] and chemotherapy [84]. Thermal ablation kills cells directly, by inducing necrosis [85].

There are several different modalities by which hyperthermia is currently being investigated in the clinics. These include radiofrequency (RF) capacitance, RF probes, microwave radiation, interstitial laser photocoagulation, direct tumor injection of hot water, and direct hyperthermia [86]. In general, these methods have not been successful for treating liver cancer because they are nonspecific and have poor targeting abilities as a result of the uncontrollable homogeneous heat distribution within the tumor, without harming the healthy tissues [86].

The concept of magnetically mediated hyperthermia was first proposed by Gilchrist [87] in 1957. In that study, γ-Fe_3O_4 nanoparticles of 20–100 nm diameter were injected into the submucosa of the instestinal walls of dogs with bowel cancer. The lymph nodes, where γ-Fe_3O_4 would be expected to accumulate, were then surgically removed. When an alternating magnetic field at a power of 200–240 Oersted (Oe) was applied to the resected lymph nodes, they were seen to have a magnetite uptake of 5 mg g^{-1}, and an increase in temperature of 14 °C after a 3 min period of treatment [87]. In theory, all metallic objects placed in an alternating magnetic field should be heated up because of hysteresis loss, Neel relaxation, or induced eddy currents [88]. The presence of magnetic iron should enhance this temperature increase – hence the remarkable increase in the temperature of the lymph nodes with metastasis. This is an important finding because a temperature of 43 °C sustained for at least 240 min (hyperthermia), and a temperature attaining 54 °C, are both cytotoxic to cancer cells.

Some two years after their initial studies on *ex vivo* magnetic fluid hyperthermia, Gilchrist and coworkers performed a series of successful hyperthermia experiments on the lymph nodes of rats and dogs [89, 90]. Since then, several groups have attempted to identify the most effective hyperthermia-based treatment. During the 1960s, the magnetic particles used in such treatments were mostly liquid silicones [91, 92], ferropolysaccharides [93], and metal flakes of iron [94], although the distribution, clearance, and toxicity of these particles were unknown at that time. In addition, because of the nature of these materials, tumors and other sites of interest were often heated unevenly. In 1979, Gordon *et al.* [95] proposed the concept of intracellular hyperthermia, which involves the introduction of submicron magnetic particles capable of penetrating the cell membrane, thus enabling magnetic excitation. Such excitation, which resulted from the application of an external high-frequency or pulsed electromagnetic field, raised the temperature of the particles and thereby generated intracellular heat in precise increments [95]. The technique resulted in the selective thermal destruction of cancer cells, which were known to be more sensitive to temperatures in excess of 43 °C, but had very little effect on normal cells. Although most particles used in

intracellular hyperthermia are typically less than 100 nm in diameter, they must be coated with a material that will allow their selective uptake into tumor cells. Magnetic nanoparticles for intracellular hyperthermia may, or may not, have targeting agents attached to them..

7.4.1 Passive Targeting

Passive targeting is the extravasation of particles within the leaky and disordered neovasculature of tumors. These particles do not have any targeting units, and therefore depend on the particle size and nature of the coating material that interacts with the innate property of the tumors in order to accumulate preferentially via an enhanced permeability and retention (EPR) effect. Details of the magnetic nanomaterials developed for intracellular hyperthermia and capable of accumulating in tumors via an EPR effect are provided in the following sections.

7.4.1.1 Dextran-Coated Magnetite

Dextran-coated magnetite nanoparticles were the first to be investigated with regards to whether nanoparticles would be taken up by cancer cells during hyperthermia-based treatments. Gordon *et al.* [95] administered dextran-coated magnetite intravenously to 26 Sprague-Dawley rats bearing mammary carcinomas, and detected cellular particle uptake in the tumor by electron microscopy and iron staining of the cancerous tissue. The rats were also exposed to a magnetic field alternating at 450 kHz for 12 min. As a result, the tumor temperature was increased by 8 °C, but no adverse side effects or toxicities were observed. However, because the particles were also present outside the tumor cells, they were distributed into the extravascular and extracellular spaces, and so may have contributed to the heating effect [95].

Jordan *et al.* [96] performed additional experiments on intracellular hyperthermia using dextran-coated magnetite, which they showed was taken up by the cells (up to 1.1 pg iron per cell, equivalent to 1.4×10^7 particles per cell), and corresponded to an intracellular specific power absorption value of approximately 44 mW ml^{-1}. Although such specific power absorption should have caused substantial cell death, no adverse biological effects due to intracellular hyperthermia were identified over simply water-bath heating. Jordan *et al.* [96] attributed this inactivity of the intracellular nanoparticles to a loss in the dextran coating and the subsequent formation of large-particle aggregates within the cells; these caused a reduction in the specific power absorption and, in turn, a higher than expected cell survival [96].

7.4.1.2 Aminosilan-Coated Magnetic Particles

The unsuitability of dextran-coated magnetite nanoparticles for intracellular hyperthermia led Jordan *et al.* [97] to develop aminosilan-coated magnetic particles, which demonstrated differential cellular uptake with both malignant and normal cells. Silan has a biocompatibility and a high specific absorption rate similar to

those of dextran [96], and silan coatings are also resistant to enzymatic attacks in lysosomes. In an *in vitro* study [98], Jordan and colleagues inoculated carcinomas (colonic, adenocarcinoma and glioma) and normal human cell controls (fibroblasts and neurons) with dextran- and aminosilan-coated magnetites. The results showed a greater cell kill with aminosilan-coated magnetites with an alternating magnetic field compared to a water bath treatment *in vitro*. The same authors also used these particles to create hyperthermia after directly injecting them into human prostate cancer xenografts [99, 100] and brain tumor xenografts [101] *in vivo*. Both trials involved direct injection inside the tumor mass of an orthotopic Dunning rat model. Following particle administration, prostate cancer growth was significantly inhibited, with the prostate glands retaining 82.5% of the injected iron at 10 days after intratumoral application, and enabling sequential thermal therapies to be performed without the repeated injection of nanoparticles.

The findings of Jordan and coworkers prompted a series of clinical studies with aminosilan-coated particles, these being the first reported clinical applications of interstitial hyperthermia using magnetic nanoparticles in locally recurrent prostate cancer. The study results showed that a single intratumoral application of aminosilan-coated particles was retained in the prostate gland during the 6-week treatment. A recent Phase I clinical trial showed that intracranial thermotherapy using magnetic nanoparticles could be safely applied at therapeutic temperatures, with local efficacy and no adverse side effects [102]. Other clinical trials investigating the use of magnetic nanoparticles to deliver interstitial hyperthermia have included a Phase I study with hepatocellular carcinoma (HCC), esophageal cancer, and local residual tumors of different entities (cervical, uterine and ovarian carcinomas, as well as sarcomas), and also Phase II trials of prostate cancer and glioblastoma.

7.4.1.3 **Magnetic Cationic Liposomes**

In 1999, Kobayashi and coworkers [103] developed magnetic cationic liposomes to facilitate uptake by tumor tissue. These liposomes showed a 10-fold greater affinity towards glioma cells than did neutral, unsubstituted magnetite liposomes, due to the positive charge of the magnetic cationic liposome interacting electrostatically with the negatively charged glioma cells [104]. In an *in vitro* study of rat glioma and agar phantoms subjected to a high-frequency magnetic field (118 kHz), the temperature rose to more than 43 °C, and all cells died after 40 min period of irradiation due to the nanoparticles' hypothermic effect [104].

Other experiments have been conducted to investigate the efficacy of magnetic cationic liposome-mediated hyperthermia in animals with several types of tumor, including B16 mouse melanoma [105], T-9 rat glioma [106], osteosarcoma in hamsters [107], MM46 mouse mammary carcinoma [108], PLS 10 rat prostate cancer [109], and VX-7 squamous cell carcinoma in rabbit tongue [110]. Although several *in vivo* studies have been conducted – including one in which frequent, repeated hyperthermia caused a complete regression of mouse mammary carcinoma which was initially >15 mm in size [110] – no clinical studies have yet been conducted.

7.4.2 Active Targeting

Active targeting is a ligand-directed, site-specific accumulation of nanoparticles. Whereas, in passive targeting it is not possible to kill micrometastases, active targeting can be used to eliminate micrometastases by the intravenous administration of magnetic nanoparticles designed for selective uptake by tumor cells. Currently, attempts are being made to attach tumor cell-specific "address tags" such as antibodies [56–65], peptides [66–67], or folic acid [111] to magnetic complexes (e.g., liposomes, nanoparticles).

7.4.2.1 Antibodies

In a study conducted by Ito *et al.* [112], anti-human epidermal growth factor receptor 2 (HER2) immunoliposomes containing magnetite nanoparticles were constructed to mediate tumor targeting, antibody therapy and hyperthermia [112]. The anti-HER2 monoclonal antibody (mAb) can induce antitumor responses, and be used for delivering drugs to tumors that overexpress HER2. The magnetite nanoparticles would also generate heat in an alternating magnetic field. Ito *et al.* [112] found that 60% of the HER2-targeted magnetic immunoliposomes were incorporated into HER-2-expressing SKBr3 cells, after which heating the cells at 42.5 °C in an alternating magnetic field resulted in strong cytotoxic effects.

Iron oxide nanoparticles have also been conjugated with a ^{111}In-chimeric L6 mAb [113]. The pharmacokinetics, tumor uptake, and therapeutic effect of inductively heating these bioprobes with an external alternating magnetic field were studied in athymic mice bearing hamster blood transfusion (HBT) 3477 human breast cancer xenografts. The results indicated that when these mAb-conjugated magnetic nanoparticles were given intravenously, they escaped into the extravascular space and became bound to the cancer cell membrane antigen. These bioprobes could then be used in concert with an externally applied alternating magnetic field to deliver thermal ablative cancer therapy [113].

An antibody fragment, Fab, was crosslinked to *N*-(6-maleimidocaproyloxy)-dipalmitoyl phosphatidylethanolamine (EMC-DPPE) in magnetic liposomes [114]. The resultant Fab fragment-conjugated magnetic liposomes had a 2.4-fold higher molar immobilization density compared to the whole-antibody-conjugated magnetic liposomes. In *in vitro* studies using U251-SP glioma cells, the Fab-conjugated magnetic liposomes were shown to be taken up sevenfold more frequently than control magnetoliposomes. Similarly, in *in vivo* studies, mice injected with Fab-conjugated magnetic liposomes showed an increase in tumor temperature to 43 °C, and tumor growth was arrested for more than 2 weeks [114].

7.4.2.2 Peptides

Weissleder and colleagues conjugated the cyclic arginine-glycine-aspartic acid (RGD) in iron oxide nanoparticles [115]. The RGD-conjugated magnetic nanoparticle targets integrins on BT-20 tumor as a model system. Other peptides, such as nuclear localization sequence and bombesin receptor peptides, have been

conjugated to Fe_3O_4 nanoparticles [69]. These nuclear localization peptide-coated nanoparticles were introduced into the cell cytoplasm and nuclei, where they remained monodispersed and nonaggregated.

7.4.2.3 Folic Acid

Folate-conjugated superparamagnetic maghemite nanoparticles have been synthesized for treating solid tumors with intracellular hyperthermia [111]. These ultradispersed nanosystems have been characterized for their physico-chemical properties and tumor cell-targeting ability, which is facilitated by their surface modification with folic acid. Preliminary experiments which involved heating these nanoparticles using an alternating magnetic field at 108 kHz have also been performed. The nanoparticles' size, surface charge, and colloidal stability have been assessed for different ionic strengths and varying pH. The ability of the folate-conjugated maghemite nanoparticles to recognize the folate receptor has been investigated, both by SPR and in folate receptor-expressing cell lines using radiolabeled folic acid in competitive binding experiments. The specificity of nanoparticle cellular uptake has been further investigated using TEM, after incubation of these nanoparticles in the presence of three cell lines with different folate receptor expression levels. Both, qualitative and quantitative determinations of folate nanoparticles and nontargeted control nanoparticles have demonstrated a specific cell internalization of the folate superparamagnetic nanoparticles [111].

7.4.3 Laser-Induced Hyperthermia/Thermal Ablation Therapy

Another method of site-specific cancer cell destruction is that of laser-induced hyperthermia or "ablation therapy", which utilizes the absorption of nanoparticles in the NIR region. When light is absorbed, it is converted by the nanoparticles into heat, which in turn destroys the cancer cells. Because of its weak absorption by tissues, NIR light can penetrate more deeply into the skin, but without causing much damage to normal tissues; thus, it can be used in conjunction with nanomaterials to target specific cell types.

Recently, details of the synthesis and characterization of an SPIO@Au nanoshell for NIR laser-induced photothermal ablation therapy were published [46, 116] (details of this synthesis are provided in Section 7.2.2.2.3). The SPIO@Au nanoshells have a strong absorption at 700–800 nm, and laser-induced hyperthermia experiments in solution have resulted in an increase in temperature of 16 °C at a particle concentration of $7.5 \times 10^{12}\,ml^{-1}$ when irradiated with an 810 nm continuous-wave diode laser at 1 W for 15 min. This increase in temperature was also seen to be concentration-dependent [46]. Moreover, because the SPIO@Au nanoshells exhibited a high transverse relaxivity, r_2, and a large r_2/r_1 ratio, they could be imaged using MRI to obtain T_2-weighted images. Experiments on the heat-generating capacity of SPIO@Au nanoshells under an alternating magnetic field could be used with these nanoparticles to mediate thermal ablation, which makes it possible to treat both deep and superficial cancer lesions. Given their

unique magnetic and optical properties, multifunctional SPIO@Au nanoshells could be used to enhance the efficacy of nanoshell-mediated photothermal therapy by making it possible to direct more nanoparticles to tumors through the application of an external magnetic field, and by permitting the real-time *in vivo* MRI imaging of nanoparticle distribution before, during, and after photothermal therapy.

7.5 Application: Drug Delivery

The main problems associated with systemic drug administration include the uneven biodistribution of pharmaceuticals throughout the body, the lack of drug specificity towards a pathological site, the need for a large dose to achieve high local drug concentrations, nonspecific toxicity, and other adverse side effects due to high drug dose levels [2]. Drug targeting based on the use of nanoparticles would aim to resolve many of these problems.

In 1960, Freeman *et al*. [117] proposed that a magnetic field could be used to help transport magnetic particles through the vascular system, and concentrate the particles in a specific part of the body. The main advantages of magnetic particles are that they can be: (i) visualized (superparamagnetic nanoparticles are used in MRI); (ii) guided or held in place using a magnetic field; and (iii) heated in a magnetic field to trigger drug release or hyperthermia, or the thermal ablation of tissue. Based on these advantages, the use of magnetic nanoparticles for delivering chemotherapeutics has evolved since the 1970s. In these drug delivery systems, the drug–carrier complex is injected either intravenously or intra-arterially into the subject, after which the magnetic particle containing the drug is concentrated into the target site with the aid of a high-gradient external magnetic field generated by permanent magnets [117]. When the magnetic carrier is concentrated at the tumor or other targets *in vivo*, the therapeutic agent is released either via enzymatic activity or through changes in physiological conditions such as pH, osmolality, or temperature; the net result is an increased uptake of the drug by tumor cells at the target sites [118].

The above-described method has achieved success in several animal studies. For example, Widder *et al*. [119] conjugated doxorubicin to magnetically responsive albumin microspheres and injected the resultant nanoparticles into the ventral caudal arteries of rats bearing Yoshida sarcoma tumors. A bipolar permanent magnet was placed adjacent to the tumor during the infusion to help localize the agent. Of the 22 animals receiving magnetically localized doxorubicin microspheres, 17 had a total histological remission of their tumors, while the other five demonstrated a marked tumor regression which represented a reduction in tumor size of 500–600 mm^2. While no deaths or metastases occurred in the groups receiving localized drug, those animals treated with free doxorubicin, placebo microspheres, or nonlocalized doxorubicin microspheres exhibited a significant increase in tumor size with metastases; subsequently, 90–100% of these animals died.

Tumor remission has been achieved not only in small animals such as rabbits and rats [118, 120, 121], but also in much larger animals such as swine [122, 123]. For example, in a study conducted by Alexiou *et al.* [118], ferrofluids bound to mitoxantrone were concentrated in VX-2 carcinomas in New Zealand White rabbits by using an external magnetic field. The application of an external alternating magnetic field resulted in a significant, complete, and permanent remission of squamous cell carcinoma, with no signs of toxicity compared to the control group (no treatment). Alexiou *et al.* [124] then conducted a follow-up study to investigate the *in vitro* and *in vivo* capabilities of ferrofluids bound to mitoxantrone, and found the concentration of the chemotherapeutic agent in the tumor region to be much higher than with regular, systemic chemotherapy.

Pulfer *et al.* [121] evaluated the ability of uncharged magnetic nanoparticles (10–20 nm) to target intracerebral rat glioma-2 tumors *in vivo*. In order to determine the ways in which particle size influenced the blood–tumor barrier uptake, these authors injected nanoparticles ($4\,mg\,kg^{-1}$) intra-arterially into male Fisher 344 rats bearing rat glioma-2 tumors, and then applied magnetic fields of between 0 and 6000 G to the rat brains for 30 min. The animals were killed at either 30 min or 6 h after injection, and the tissues collected and analyzed for their magnetite content. It was found that, in the presence of a magnetic field, the nanoparticles localized in brain tumor tissue at levels of 41% and 48% of the dose per gram of tissue after 30 min and 6 h respectively, which was significantly greater than their uptake in nontarget tissues. In the absence of a magnetic field, levels of only 31% and 23% dose per gram were achieved at the same time points. A TEM analysis of the brain tissue revealed magnetic nanoparticles in the interstitial space of the tumors, but only in the vasculature of normal brain tissue. These results suggested that changes in the vascular endothelium of tumor tissue had promoted a selective uptake of the uncharged magnetic nanoparticles, and thus provided a basis for the development of novel drug-loaded nanoparticles as targeted drug delivery systems for brain tumors.

Goodwin [122, 123] and coworkers used a swine model to investigate drug targeting and retention abilities in regions of interest after an intra-arterial infusion of doxorubicin, coupled to magnetically targeted particles composed of elemental iron and activated carbon. The placement of an external magnet over the tumor region enabled an efficient targeting of the doxorubicin-coupled magnetic particles [105].

Recently, Alexiou *et al.* [124] achieved a degree of success in quantifying the distribution of magnetically targeted carriers in a rabbit model using a high-performance liquid chromatography analysis of mitoxantrone bound to ferrofluids, having demonstrated the uptake of magnetically targeted carriers in HeLa cells *in vitro*. In order to overcome problems associated with the spatial configuration of these delivery systems, Kubo *et al.* [125] implanted permanent magnets at solid osteosarcoma sites in hamsters, and then used magnetoliposomes to deliver cytotoxic compounds. These authors discovered a fourfold increase in drug delivery to the tumor site compared to normal intravenous (nonmagnetic) delivery. Kubo *et al.* also reported a significant increase in antitumor activity and a reduction in weight-loss-inducing side effects. The use of implanted magnetic grids to target

the heart muscle may represent another possible solution to the problems of delivery system geometry [126].

Although magnetic targeting has been accomplished in a number of animal models, magnetic targeting in humans has not yet been approved for clinical use. However, two Phase I/II clinical trials have been conducted to investigate the role of magnetic targeting in humans. In the first Phase I clinical trial, which was conducted by Lubbe *et al.* [127] in 1996, a 100-nm ferrofluid was used to which epirubicin (an anthracycline antibiotic) was chemically bound. Briefly, the magnetic particles were coated with special starch polymers and anionic phosphate groups to enable binding of the positively charged amino sugars of epirubicin to the nanoparticles. A total of 14 patients received intravenous infusions of epirubicin-coated nanoparticles and one course of conventional chemotherapy. During, and at 45 min after, the infusion a magnetic field was introduced as close to the tumor as possible (<0.5 cm). In this way, it was found that the ferrofluid could be successfully directed to the tumors in about half of the patients. Although the particles accumulated in the liver, the study results showed that, in general the magnetic carriers were well tolerated.

In a second clinical trial, Koda *et al.* [128] used subselective hepatic artery catheterization to deliver doxorubicin hydrochloride coupled with magnetic nanoparticles to 32 HCC patients. An external magnetic field (500 mT) was used to target the particle–drug complex to the tumor site, and MRI used to examine particle localization. The tumors were targeted effectively in 30 patients. A further analysis of 20 tumors from 17 HCC patients in whom targeting was successful revealed that 15 of the lesions had remained stable or had shrunk, while only five had progressed [129].

More recently, a Phase I/II trial was conducted to evaluate magnetic nanoparticle-based targeting in four HCC patients [130]. The magnetic carrier was bound to doxorubicin and targeted to the liver via a transcatheter delivery through the hepatic artery under concurrent MRI. The final fraction of treated tumor volume ranged from 0.64 to 0.91 cm^3, while the fraction of affected normal liver volume ranged from 0.07 to 0.30 cm^3, indicating that the combination of MRI and angiography could be used to optimize magnetic targeting in some patients.

In addition to cancer treatments, magnetic nanoparticles can also be used to treat anemia caused by chronic kidney disease, as well as disorders associated with the musculoskeletal system. For these disorders, SPIO nanoparticles in conjunction with external magnetic fields appear to offer a suitable alternative for delivering drugs to inflammatory sites by maintaining appropriate local concentrations while reducing the overall dosage and adverse side effects.

7.6 Summary and Perspectives

Magnetic nanoparticles have great potential for MRI, hyperthermia and thermal ablation therapy, and drug delivery. For *in vivo* applications, magnetic

nanoparticles must be coated with biocompatible and diamagnetic materials such as organic polymers or silica matrices, so as to prevent the formation of large aggregates, to provide biocompatible surfaces, and to facilitate drug attachment. During recent years, a major effort has been made to synthesize and characterize magnetic iron/iron oxide nanoparticles coated with a variety of materials ranging from polymers to silica and gold.

As with other nanoparticle platforms, significant efforts have also been made to produce multifunctional magnetic nanoparticles. For example, magnetic nanostructures with highly controlled optical properties have attracted great interest because of their potential diagnostic and therapeutic applications in biological and biomedical systems. Such materials are capable not only of mediating a cell killing effect via both alternating magnetic field and laser light, but also of potentially enhancing the efficacy of treatment with a dual-modality approach. Such an approach also offers opportunities for selective drug delivery through external magnet guided deposition, as well as receptor-mediated active targeting. Among such nanostructures, gold-derived nanoparticles are especially attractive because of their ease of preparation, good biocompatibility, ready bioconjugation, and unique optical properties. One especially attractive advantage of superparamagnetic nanoparticles is their visibility on MRI, which allows the noninvasive monitoring not only of a nanoparticles' *in vivo* distribution but also its delivery efficiency to the disease sites.

In order to realize the potential applications of magnetic nanoparticles in both diagnosis and therapy, it is important that they are efficiently delivered to the target sites. Future studies will, inevitably, be devoted to elucidating those factors that influence the pharmacokinetics and biodistribution of surface-modified magnetic nanoparticles, and developing magnetic nanoparticles targeted to various biomarkers associated with various diseases.

Acknowledgments

These studies were supported by the National Cancer Institute (grant R01 CA119387) and by the John S. Dunn Foundation. The authors thank Joe Munch from M.D. Anderson's Department of Scientific Publications for editorial assistance.

References

1 Lu, A.H., Salabas, E.L. and Schuth, F. (2007) Magnetic nanoparticles: synthesis, protection, functionalization, and application. *Angewandte Chemie, International Edition in English*, **46** (8), 1222–44.

2 Tartaj, P., Morales, M.D.P., Veintemillas-Verdaguer, S., Gonzalez-Carreno, T. and Serna, C.J. (2003) The preparation of magnetic nanoparticles for applications in biomedicine. *Journal of Physics D: Applied Physics*, **36** (13), R182–97.

3 Sugimoto, T. and Matijevic, E. (1980) Formation of uniform spherical magnetite particles by crystallization from ferrous hydroxide gels. *Journal of Colloid and Interface Science*, **74** (1), 227–43.

4 Massart, R.C. and Cabuil, V. (1987) Effect of some parameters on the formation of colloidal magnetite in alkaline medium: yield and particle size control. *The Journal of Chemical Physics*, **84**, 967.

5 Lee, J., Isobe, T. and Senna, M. (1996) Preparation of ultrafine Fe_3O_4 particles by precipitation in the presence of PVA at high pH. *Journal of Colloid and Interface Science*, **177** (2), 490–4.

6 Molday, R.S. and MacKenzie, D. (1982) Immunospecific ferromagnetic iron-dextran reagents for the labeling and magnetic separation of cells. *Journal of Immunological Methods*, **52** (3), 353–67.

7 Palmacci, W.S. and Josephson, L. (1993) US Patent No. 5,262,176.

8 Rockenberger, J., Scher, E.C. and Alivisatos, A.P. (1999) A new nonhydrolytic single-precursor approach to surfactant-Capped nanocrystals of transition metal oxides. *Journal of the American Chemical Society*, **121** (49), 11595–6.

9 Hyeon, T., Lee, S.S., Park, J., Chung, Y. and Na, H.B. (2001) Synthesis of highly crystalline and monodisperse maghemite nanocrystallites without a size-selection process. *Journal of the American Chemical Society*, **123** (51), 12798–801.

10 Sun, S. and Zeng, H. (2002) Size-controlled synthesis of magnetite nanoparticles. *Journal of the American Chemical Society*, **124** (28), 8204–5.

11 Sun, S., Zeng, H., Robinson, D.B., Raoux, S., Rice, P.M., Wang, S.X. and Li, G. (2004) Monodisperse MFe_2O_4 (M = Fe, Co, Mn) Nanoparticles. *Journal of the American Chemical Society*, **126** (1), 273–9.

12 Samia, A.C.S., Hyzer, K., Schlueter, J.A., Qin, C.J., Jiang, J.S., Bader, S.D. and Lin, X.M. (2005) Ligand effect on the growth and the digestion of Co nanocrystals. *Journal of the American Chemical Society*, **127** (12), 4126–7.

13 Jana, N.R., Chen, Y. and Peng, X. (2004) Size- and shape-controlled magnetic (Cr, Mn, Fe, Co, Ni) oxide nanocrystals via a simple and general approach. *Chemistry of Materials*, **16** (20), 3931–5.

14 Li, Y., Afzaal, M. and O'Brien, P. (2006) The synthesis of amine-capped magnetic (Fe, Mn, Co, Ni) oxide nanocrystals and their surface modification for aqueous dispersibility. *Journal of Materials Chemistry*, **16** (22), 2175.

15 Park, J., An, K., Hwang, Y., Park, J.-G., Noh, H.-J., Kim, J.-Y., Park, J.-H., Hwang, N.-M. and Hyeon, T. (2004) Ultra-large-scale syntheses of monodisperse nanocrystals. *Nature Materials*, **3** (12), 891–5.

16 Pileni, M.P. (1993) Reverse micelles as microreactors. *The Journal of Physical Chemistry*, **97** (27), 6961–73.

17 Pileni, M.P. (2003) The role of soft colloidal templates in controlling the size and shape of inorganic nanocrystals. *Nature Materials*, **2** (3), 145–50.

18 Feltin, N. and Pileni, M.P. (1997) New technique for synthesizing iron ferrite magnetic nanosized particles. *Langmuir*, **13** (15), 3927–33.

19 Messing, G.L., Zhang, S.C. and Jayanthi, G.V. (1993) Ceramic powder synthesis by spray pyrolysis. *Journal of The American Ceramic Society*, **76** (11), 2707–26.

20 Veintemillas-Verdaguer, S., Morales, M.P. and Serna, C.J. (1998) Continuous production of [gamma]-Fe_2O_3 ultrafine powders by laser pyrolysis. *Materials Letters*, **35** (3–4), 227–31.

21 Bourgeat-Lami, E. and Lang, J. (1998) Encapsulation of inorganic particles by dispersion polymerization in polar media: 1. Silica nanoparticles encapsulated by polystyrene. *Journal of Colloid and Interface Science*, **197** (2), 293–308.

22 Shen, L., Laibinis, P.E. and Hatton, T.A. (1999) Bilayer surfactant stabilized magnetic fluids: synthesis and interactions at interfaces. *Langmuir*, **15** (2), 447–53.

23 Laurent, S., Forge, D., Port, M., Roch, A., Robic, C., Vander Elst, L. and Muller, R.N. (2008) Magnetic iron oxide

nanoparticles: synthesis, stabilization, vectorization, physicochemical characterizations, and biological applications. *Chemical Reviews*, **108** (6), 2064–110.

24 Kumagai, M., Imai, Y., Nakamura, T., Yamasaki, Y., Sekino, M., Ueno, S., Hanaoka, K., Kikuchi, K., Nagano, T., Kaneko, E., Shimokado, K. and Kataoka, K. (2007) Iron hydroxide nanoparticles coated with poly(ethylene glycol)-poly(aspartic acid) block copolymer as novel magnetic resonance contrast agents for *in vivo* cancer imaging. *Colloids and Surfaces B: Biointerfaces*, **56** (1–2), 174–81.

25 Kataby, G., Ulman, A., Prozorov, R. and Gedanken, A. (1998) Coating of amorphous iron nanoparticles by long-chain alcohols. *Langmuir*, **14** (7), 1512–15.

26 Yu, H., Chen, M., Rice, P.M., Wang, S.X., White, R.L. and Sun, S. (2005) Dumbbell-like bifunctional Au-Fe_3O_4 nanoparticles. *Nano Letters*, **5** (2), 379–82.

27 Cho, S.J., Idrobo, J.C., Olamit, J., Liu, K., Browning, N.D. and Kauzlarich, S.M. (2005) Growth mechanisms and oxidation resistance of gold-coated iron nanoparticles. *Chemistry of Materials*, **17** (12), 3181–6.

28 Caruntu, D., Cushing, B.L., Caruntu, G. and O'Connor, C.J. (2005) Attachment of gold nanograins onto colloidal magnetite nanocrystals. *Chemistry of Materials*, **17** (13), 3398–402.

29 Lyon, J.L., Fleming, D.A., Stone, M.B., Schiffer, P. and Williams, M.E. (2004) Synthesis of Fe oxide core/Au shell nanoparticles by iterative hydroxylamine seeding. *Nano Letters*, **4** (4), 719–23.

30 Wang, L., Luo, J., Fan, Q., Suzuki, M., Suzuki, I.S., Engelhard, M.H., Lin, Y., Kim, N., Wang, J.Q. and Zhong, C.J. (2005) Monodispersed core-shell Fe_3O_4@Au nanoparticles. *The Journal of Physical Chemistry B*, **109** (46), 21593–601.

31 Stöber, W., Fink, A. and Bohn, E. (1968) Controlled growth of monodisperse silica spheres in the micron size range. *Journal of Colloid and Interface Science*, **26** (1), 62–9.

32 Lu, Y., Yin, Y., Mayers, B.T. and Xia, Y. (2002) Modifying the surface properties of superparamagnetic iron oxide nanoparticles through a sol-gel approach. *Nano Letters*, **2** (3), 183–6.

33 Liu, X., Xing, J., Guan, Y., Shan, G. and Liu, H. (2004) Synthesis of amino-silane modified superparamagnetic silica supports and their use for protein immobilization. *Colloids and Surfaces A: Physicochemical and Engineering Aspects*, **238** (1–3), 127–31.

34 Butterworth, M.D., Bell, S.A., Armes, S.P. and Simpson, A.W. (1996) Synthesis and characterization of polypyrrole-magnetite-silica particles. *Journal of Colloid and Interface Science*, **183** (1), 91–9.

35 Bomatí-Miguel, O., Leconte, Y., Morales, M.P., Herlin-Boime, N. and Veintemillas-Verdaguer, S. (2005) Laser pyrolysis preparation of SiO2-coated magnetic nanoparticles for biomedical applications. *Journal of Magnetism and Magnetic Materials*, **290**–291 (Pt 1), 272–5.

36 Pola, J., Bastl, Z., Vorlicek, V., Dumitrache, F., Alexandrescu, R., Morjan, I., Sandu, I. and Ciupina, V. (2004) Laser-induced synthesis of iron-iron oxide/methylmethoxysilicone nanocomposite. *Applied Organometallic Chemistry*, **18** (7), 337–42.

37 Fernández-Pacheco, R., Arruebo, M., Marquina, C., Ibarra, R., Arbiol, J. and Santamaría, J. (2006) Highly magnetic silica-coated iron nanoparticles prepared by the arc-discharge method. *Nanotechnology*, **17**, 1188–92.

38 Philipse, A.P., van Bruggen, M.P.B. and Pathmamanoharan, C. (1994) Magnetic silica dispersions: preparation and stability of surface-modified silica particles with a magnetic core. *Langmuir*, **10** (1), 92–9.

39 Pichyangkul, S., Gettayacamin, M., Miller, R.S., Lyon, J.A., Angov, E., Tongtawe, P., Ruble, D.L., Heppner, D.G., Jr, Kester, K.E., Ballou, W.R., Diggs, C.L., Voss, G., Cohen, J.D. and Walsh, D.S. (2004) Pre-clinical evaluation of the malaria vaccine candidate *P. falciparum* MSP1(42)

formulated with novel adjuvants or with alum. *Vaccine*, **22** (29–30), 3831–40.
40 Piao, Y., Kim, J., Na, H.B., Kim, D., Baek, J.S., Ko, M.K., Lee, J.H., Shokouhimehr, M. and Hyeon, T. (2008) Wrap-bake-peel process for nanostructural transformation from [beta]-FeOOH nanorods to biocompatible iron oxide nanocapsules. *Nature Materials*, **7** (3), 242–7.
41 Kim, J., Park, S., Lee, J., Jin, S.M., Lee, J.H., Lee, I.S., Yang, I., Kim, J.-S., Kim, S.K., Cho, M.-H. and Hyeon, T. (2006) Designed fabrication of multifunctional magnetic gold nanoshells and their application to magnetic resonance imaging and photothermal therapy 13. *Angewandte Chemie, International Edition in English*, **45** (46), 7754–8.
42 Stoeva, S.I., Huo, F., Lee, J.S. and Mirkin, C.A. (2005) Three-layer composite magnetic nanoparticle probes for DNA. *Journal of the American Chemical Society*, **127** (44), 15362–3.
43 Salgueirino-Maceira, V., Correa-Duarte, M.A., Farle, M., Lopez-Quintela, A., Sieradzki, K. and Diaz, R. (2006) Bifunctional gold-coated magnetic silica spheres. *Chemistry of Materials*, **18** (11), 2701–6.
44 Chen, M., Kim, Y.N., Lee, H.M., Li, C. and Cho, S.O. (2008) Multifunctional magnetic silver nanoshells with sandwichlike nanostructures. *The Journal of Physical Chemistry C*, **112** (24), 8870–4.
45 Thorek, D.L. and Tsourkas, A. (2008) Size, charge and concentration dependent uptake of iron oxide particles by non-phagocytic cells. *Biomaterials*, **29** (26), 3583–90.
46 Street, C.N., Lakey, J.R., Shapiro, A.M., Imes, S., Rajotte, R.V., Ryan, E.A., Lyon, J.G., Kin, T., Avila, J., Tsujimura, T. and Korbutt, G.S. (2004) Islet graft assessment in the Edmonton Protocol: implications for predicting long-term clinical outcome. *Diabetes*, **53** (12), 3107–14.
47 Ji, X., Shao, R., Elliott, A.M., Stafford, R.J., Esparza-Coss, E., Bankson, J.A., Liang, G., Luo, Z.P., Park, K., Markert, J.T. and Li, C. (2007) Bifunctional gold nanoshells with a superparamagnetic iron oxide-silica core suitable for both MR imaging and photothermal therapy. *Journal of Physical Chemistry C*, **111** (17), 6245–51.
48 Kubaska, S., Sahani, D.V., Saini, S., Hahn, P.F. and Halpern, E. (2001) Dual contrast enhanced magnetic resonance imaging of the liver with superparamagnetic iron oxide followed by gadolinium for lesion detection and characterization. *Clinical Radiology*, **56** (5), 410–15.
49 Halavaara, J., Tervahartiala, P., Isoniemi, H. and Hockerstedt, K. (2002) Efficacy of sequential use of superparamagnetic iron oxide and gadolinium in liver MR imaging. *Acta Radiologica*, **43** (2), 180–5.
50 Babes, L., Denizot, B., Tanguy, G., Le Jeune, J.J. and Jallet, P. (1999) Synthesis of iron oxide nanoparticles used as MRI contrast agents: a parametric study. *Journal of Colloid and Interface Science*, **212** (2), 474–82.
51 Brigger, I., Dubernet, C. and Couvreur, P. (2002) Nanoparticles in cancer therapy and diagnosis. *Advanced Drug Delivery Reviews*, **54** (5), 631–51.
52 Stark, D.D., Weissleder, R., Elizondo, G., Hahn, P.F., Saini, S., Todd, L.E., Wittenberg, J. and Ferrucci, J.T. (1988) Superparamagnetic iron oxide: clinical application as a contrast agent for MR imaging of the liver. *Radiology*, **168** (2), 297–301.
53 Saini, S., Stark, D.D., Hahn, P.F., Bousquet, J.C., Introcasso, J., Wittenberg, J., Brady, T.J. and Ferrucci, J.T., Jr (1987) Ferrite particles: a superparamagnetic MR contrast agent for enhanced detection of liver carcinoma. *Radiology*, **162** (1 Pt 1), 217–22.
54 Marchal, G., Van Hecke, P., Demaerel, P., Decrop, E., Kennis, C., Baert, A.L. and van der Schueren, E. (1989) Detection of liver metastases with superparamagnetic iron oxide in 15 patients: results of MR imaging at 1.5 T. *American Journal of Roentgenology*, **152** (4), 771–5.
55 Li, W., Tutton, S., Vu, A.T., Pierchala, L., Li, B.S., Lewis, J.M., Prasad, P.V. and Edelman, R.R. (2005) First-pass

contrast-enhanced magnetic resonance angiography in humans using ferumoxytol, a novel ultrasmall superparamagnetic iron oxide (USPIO)-based blood pool agent. *Journal of Magnetic Resonance Imaging*, **21** (1), 46–52.

56 McLachlan, S.J., Morris, M.R., Lucas, M.A., Fisco, R.A., Eakins, M.N., Fowler, D.R., Scheetz, R.B. and Olukotun, A.Y. (1994) Phase I clinical evaluation of a new iron oxide MR contrast agent. *Journal of Magnetic Resonance Imaging*, **4** (3), 301–7.

57 Jung, C.W. (1995) Surface properties of superparamagnetic iron oxide MR contrast agents: ferumoxides, ferumoxtran, ferumoxsil. *Magnetic Resonance Imaging*, **13** (5), 675–91.

58 Reimer, P., Marx, C., Rummeny, E.J., Muller, M., Lentschig, M., Balzer, T., Dietl, K.H., Sulkowski, U., Berns, T., Shamsi, K. and Peters, P.E. (1997) SPIO-enhanced 2D-TOF MR angiography of the portal venous system: results of an intraindividual comparison. *Journal of Magnetic Resonance Imaging*, **7** (6), 945–9.

59 Kellar, K.E., Fujii, D.K., Gunther, W.H., Briley-Saebo, K., Bjornerud, A., Spiller, M. and Koenig, S.H. (2000) NC100150 Injection, a preparation of optimized iron oxide nanoparticles for positive-contrast MR angiography. *Journal of Magnetic Resonance Imaging*, **11** (5), 488–94.

60 Dutton, A.H., Tokuyasu, K.T. and Singer, S.J. (1979) Iron-dextran antibody conjugates: general method for simultaneous staining of two components in high-resolution immunoelectron microscopy. *Proceedings of the National Academy of Sciences of the United States of America*, **76** (7), 3392–6.

61 Renshaw, P.F., Owen, C.S., McLaughlin, A.C., Frey, T.G. and Leigh, J.S., Jr (1986) Ferromagnetic contrast agents: a new approach. *Magnetic Resonance in Medicine*, **3** (2), 217–25.

62 Cerdan, S., Lotscher, H.R., Kunnecke, B. and Seelig, J. (1989) Monoclonal antibody-coated magnetite particles as contrast agents in magnetic resonance imaging of tumors. *Magnetic Resonance in Medicine*, **12** (2), 151–63.

63 Suwa, T., Ozawa, S., Ueda, M., Ando, N. and Kitajima, M. (1998) Magnetic resonance imaging of esophageal squamous cell carcinoma using magnetite particles coated with anti-epidermal growth factor receptor antibody. *International Journal of Cancer*, **75** (4), 626–34.

64 Artemov, D., Mori, N., Ravi, R. and Bhujwalla, Z.M. (2003) Magnetic resonance molecular imaging of the HER-2/neu receptor. *Cancer Research*, **63** (11), 2723–7.

65 Bulte, J.W., Hoekstra, Y., Kamman, R.L., Magin, R.L., Webb, A.G., Briggs, R.W., Go, K.G., Hulstaert, C.E., Miltenyi, S., The, T.H. *et al.* (1992) Specific MR imaging of human lymphocytes by monoclonal antibody-guided dextran-magnetite particles. *Magnetic Resonance in Medicine*, **25** (1), 148–57.

66 Tiefenauer, L.X., Kuhne, G. and Andres, R.Y. (1993) Antibody-magnetite nanoparticles: *in vitro* characterization of a potential tumor-specific contrast agent for magnetic resonance imaging. *Bioconjugate Chemistry*, **4** (5), 347–52.

67 Tiefenauer, L.X., Tschirky, A., Kuhne, G. and Andres, R.Y. (1996) In vivo evaluation of magnetite nanoparticles for use as a tumor contrast agent in MRI. *Magnetic Resonance Imaging*, **14** (4), 391–402.

68 Jun, Y.W., Huh, Y.M., Choi, J.S., Lee, J.H., Song, H.T., Kim, S.J., Yoon, S., Kim, K.S., Shin, J.S., Suh, J.S. and Cheon, J. (2005) Nanoscale size effect of magnetic nanocrystals and their utilization for cancer diagnosis via magnetic resonance imaging. *Journal of the American Chemical Society*, **127** (16), 5732–3.

69 Montet, X., Weissleder, R. and Josephson, L. (2006) Imaging pancreatic cancer with a peptide-nanoparticle conjugate targeted to normal pancreas. *Bioconjugate Chemistry*, **17** (4), 905–11.

70 Jun, Y.W., Lee, J.H. and Cheon, J. (2008) Chemical design of nanoparticle probes for high-performance magnetic resonance imaging. *Angewandte Chemie,*

International Edition in English, **47** (28), 5122–35.

71 Vives, E., Brodin, P. and Lebleu, B. (1997) A truncated HIV-1 Tat protein basic domain rapidly translocates through the plasma membrane and accumulates in the cell nucleus. *The Journal of Biological Chemistry*, **272** (25), 16010–17.

72 Josephson, L., Tung, C.H., Moore, A. and Weissleder, R. (1999) High-efficiency intracellular magnetic labeling with novel superparamagnetic-Tat peptide conjugates. *Bioconjugate Chemistry*, **10** (2), 186–91.

73 Allport, J.R. and Weissleder, R. (2001) In vivo imaging of gene and cell therapies. *Experimental Hematology*, **29** (11), 1237–46.

74 Wilhelm, C., Gazeau, F., Roger, J., Pons, J.N. and Bacri, J.C. (2002) Interaction of anionic superparamagnetic nanoparticles with cells: kinetic analyses of membrane adsorption and subsequent internalization. *Langmuir*, **18** (21), 8148–55.

75 Josephson, L., Groman, E.V., Menz, E., Lewis, J.M. and Bengele, H. (1990) A functionalized superparamagnetic iron oxide colloid as a receptor directed MR contrast agent. *Magnetic Resonance Imaging*, **8** (5), 637–46.

76 Weissleder, R., Elizondo, G., Wittenberg, J., Rabito, C.A., Bengele, H.H. and Josephson, L. (1990) Ultrasmall superparamagnetic iron oxide: characterization of a new class of contrast agents for MR imaging. *Radiology*, **175** (2), 489–93.

77 Hogemann, D., Josephson, L., Weissleder, R. and Basilion, J.P. (2000) Improvement of MRI probes to allow efficient detection of gene expression. *Bioconjugate Chemistry*, **11** (6), 941–6.

78 Moore, A., Josephson, L., Bhorade, R.M., Basilion, J.P. and Weissleder, R. (2001) Human transferrin receptor gene as a marker gene for MR imaging. *Radiology*, **221** (1), 244–50.

79 Hilger, I., Fruhauf, K., Andra, W., Hiergeist, R., Hergt, R. and Kaiser, W.A. (2002) Heating potential of iron oxides for therapeutic purposes in interventional radiology. *Academic Radiology*, **9** (2), 198–202.

80 Hilger, I., Andra, W., Hergt, R., Hiergeist, R., Schubert, H. and Kaiser, W.A. (2001) Electromagnetic heating of breast tumors in interventional radiology: *in vitro* and *in vivo* studies in human cadavers and mice. *Radiology*, **218** (2), 570–5.

81 Milani, V., Endres, M., Kuppner, M.C., Issels, R.D. and Noessner, E. (2004) [Heat shock proteins, immune competence and vaccination]. *Deutsche Medizinische Wochenschrift*, **129** (1-2), 31–5.

82 Overgaard, J. (1989) The current and potential role of hyperthermia in radiotherapy. *International Journal of Radiation Oncology, Biology, Physics*, **16** (3), 535–49.

83 Overgaard, J., Gonzalez Gonzalez, D., Hulshof, M.C., Arcangeli, G., Dahl, O., Mella, O. and Bentzen, S.M. (1995) Randomised trial of hyperthermia as adjuvant to radiotherapy for recurrent or metastatic malignant melanoma. European Society for Hyperthermic Oncology. *Lancet*, **345** (8949), 540–3.

84 Engelhardt, R. (1987) Hyperthermia and drugs. *Recent Results in Cancer Research*, **104**, 136–203.

85 Dewey, W.C. (1994) Arrhenius relationships from the molecule and cell to the clinic. *International Journal of Hyperthermia*, **10** (4), 457–83.

86 Moroz, P., Jones, S.K. and Gray, B.N. (2002) Magnetically mediated hyperthermia: current status and future directions. *International Journal of Hyperthermia*, **18** (4), 267–84.

87 Gilchrist, R.K., Medal, R., Shorey, W.D., Hanselman, R.C., Parrott, J.C. and Taylor, C.B. (1957) Selective inductive heating of lymph nodes. *Annals of Surgery*, **146** (4), 596–606.

88 Hiergeist, R., Andrä, W., Buske, N., Hergt, R., Hilger, I., Richter, U. and Kaiser, W. (1999) Application of magnetite ferrofluids for hyperthermia. *Journal of Magnetism and Magnetic Materials*, **201** (1–3), 420–2.

89 Gilchrist, R.K., Shorey, W.D., Hanselman, R.C., Depeyster, F.A., Yang,

J. and Medal, R. (1965) Effects of electromagnetic heating on internal viscera: a preliminary to the treatment of human tumors. *Annals of Surgery*, **161**, 890–6.

90 Medal, R., Shoney, W.D., Gilchrist, R.K., Barker, W. and Hanselman, R. (1959) Controlled radiofrequency generator for production of localized heat in intact animal. *Archives of Surgery*, **79**, 427–31.

91 Rand, R.W., Snyder, M., Elliott, D. and Snow, H. (1976) Selective radiofrequency heating of ferrosilicone occluded tissue: a preliminary report. *Bulletin of the Los Angeles Neurological Societies*, **41** (4), 154–9.

92 Rand, R.W. and Mosso, J.A. (1972) Ferromagnetic silicone vascular occlusion in a superconducting magnetic field. Preliminary report. *Bulletin of the Los Angeles Neurological Societies*, **37** (2), 67–74.

93 Brilis, G.M., Lyon, J.G., Worthington, J.C. and Lysakowski, R. (2004) Implementing and auditing electronic recordkeeping systems used in scientific research and development. *Quality Assurance*, **11** (1), 5–24.

94 Matsuki, H., Yanada, T., Sato, T., Murakami, K. and Minakawa, S. (1994) Temperature-sensitive amorphous magnetic flakes for intratissue hyperthermia. *Materials Science and Engineering: A*, **181-182**, 1366–8.

95 Gordon, R.T., Hines, J.R. and Gordon, D. (1979) Intracellular hyperthermia. A biophysical approach to cancer treatment via intracellular temperature and biophysical alterations. *Medical Hypotheses*, **5** (1), 83–102.

96 Jordan, A., Wust, P., Scholz, R., Tesche, B., Fahling, H., Mitrovics, T., Vogl, T., Cervos-Navarro, J. and Felix, R. (1996) Cellular uptake of magnetic fluid particles and their effects on human adenocarcinoma cells exposed to AC magnetic fields *in vitro*. *International Journal of Hyperthermia*, **12** (6), 705–22.

97 Jordan, A., Wust, P., Fahling, H., John, W., Hinz, A. and Felix, R. (1993) Inductive heating of ferrimagnetic particles and magnetic fluids: physical evaluation of their potential for hyperthermia. *International Journal of Hyperthermia*, **9** (1), 51–68.

98 Jordan, A., Scholz, R., Wust, P., Fahling, H., Krause, J., Wlodarczyk, W., Sander, B., Vogl, T. and Felix, R. (1997) Effects of magnetic fluid hyperthermia (MFH) on C3H mammary carcinoma *in vivo*. *International Journal of Hyperthermia*, **13** (6), 587–605.

99 Johannsen, M., Jordan, A., Scholz, R., Koch, M., Lein, M., Deger, S., Roigas, J., Jung, K. and Loening, S. (2004) Evaluation of magnetic fluid hyperthermia in a standard rat model of prostate cancer. *Journal of Endourology/ Endourological Society*, **18** (5), 495–500.

100 Johannsen, M., Thiesen, B., Gneveckow, U., Taymoorian, K., Waldofner, N., Scholz, R., Deger, S., Jung, K., Loening, S.A. and Jordan, A. (2006) Thermotherapy using magnetic nanoparticles combined with external radiation in an orthotopic rat model of prostate cancer. *The Prostate*, **66** (1), 97–104.

101 Jordan, A. and Maier-Hauff, K. (2007) Magnetic nanoparticles for intracranial thermotherapy. *Journal of Nanoscience and Nanotechnology*, **7** (12), 4604–6.

102 Wust, P., Gneveckow, U., Johannsen, M., Bohmer, D., Henkel, T., Kahmann, F., Sehouli, J., Felix, R., Ricke, J. and Jordan, A. (2006) Magnetic nanoparticles for interstitial thermotherapy–feasibility, tolerance and achieved temperatures. *International Journal of Hyperthermia*, **22** (8), 673–85.

103 Shinkai, M., Yanase, M., Suzuki, M., Hiroyuki, H., Wakabayashi, T., Yoshida, J. and Kobayashi, T. (1999) Intracellular hyperthermia for cancer using magnetite cationic liposomes. *Journal of Magnetism and Magnetic Materials*, **194** (1–3), 176–84.

104 Shinkai, M., Yanase, M., Honda, H., Wakabayashi, T., Yoshida, J. and Kobayashi, T. (1996) Intracellular hyperthermia for cancer using magnetite cationic liposomes: *in vitro* study. *Cancer Science*, **87** (11), 1179–83.

105 Suzuki, M., Shinkai, M., Honda, H. and Kobayashi, T. (2003) Anticancer effect and immune induction by hyperthermia

of malignant melanoma using magnetite cationic liposomes. *Melanoma Research*, **13** (2), 129–35.

106 Yanase, M., Shinkai, M., Honda, H., Wakabayashi, T., Yoshida, J. and Kobayashi, T. (1998) Intracellular hyperthermia for cancer using magnetite cationic liposomes: an *in vivo* study. *Japanese Journal of Cancer Research*, **89** (4), 463–9.

107 Matsuoka, F., Shinkai, M., Honda, H., Kubo, T., Sugita, T. and Kobayashi, T. (2004) Hyperthermia using magnetite cationic liposomes for hamster osteosarcoma. *Biomagnetic Research and Technology*, **2** (1), 3.

108 Ito, A., Tanaka, K., Kondo, K., Shinkai, M., Honda, H., Matsumoto, K., Saida, T. and Kobayashi, T. (2003) Tumor regression by combined immunotherapy and hyperthermia using magnetic nanoparticles in an experimental subcutaneous murine melanoma. *Cancer Science*, **94** (3), 308–13.

109 Kawai, N., Ito, A., Nakahara, Y., Futakuchi, M., Shirai, T., Honda, H., Kobayashi, T. and Kohri, K. (2005) Anticancer effect of hyperthermia on prostate cancer mediated by magnetite cationic liposomes and immune-response induction in transplanted syngeneic rats. *The Prostate*, **64** (4), 373–81.

110 Ito, A., Tanaka, K., Honda, H., Abe, S., Yamaguchi, H. and Kobayashi, T. (2003) Complete regression of mouse mammary carcinoma with a size greater than 15 mm by frequent repeated hyperthermia using magnetite nanoparticles. *Journal of Bioscience and Bioengineering*, **96** (4), 364–9.

111 Sonvico, F., Mornet, S., Vasseur, S., Dubernet, C., Jaillard, D., Degrouard, J., Hoebeke, J., Duguet, E., Colombo, P. and Couvreur, P. (2005) Folate-conjugated iron oxide nanoparticles for solid tumor targeting as potential specific magnetic hyperthermia mediators: synthesis, physicochemical characterization, and *in vitro* experiments. *Bioconjugate Chemistry*, **16** (5), 1181–8.

112 Ito, A., Kuga, Y., Honda, H., Kikkawa, H., Horiuchi, A., Watanabe, Y. and Kobayashi, T. (2004) Magnetite nanoparticle-loaded anti-HER2 immunoliposomes for combination of antibody therapy with hyperthermia. *Cancer Letters*, **212** (2), 167–75.

113 DeNardo, S.J., DeNardo, G.L., Miers, L.A., Natarajan, A., Foreman, A.R., Gruettner, C., Adamson, G.N. and Ivkov, R. (2005) Development of tumor targeting bioprobes (^{111}In-chimeric L6 monoclonal antibody nanoparticles) for alternating magnetic field cancer therapy. *Clinical Cancer Research*, **11** (19), S7087–92.

114 Shinkai, M., Le, B., Honda, H., Yoshikawa, K., Shimizu, K., Saga, S., Wakabayashi, T., Yoshida, J. and Kobayashi, T. (2001) Targeting hyperthermia for renal cell carcinoma using human MN antigen-specific magnetoliposomes. *Japanese Journal of Cancer Research*, **92** (10), 1138–45.

115 Montet, X., Montet-Abou, K., Reynolds, F., Weissleder, R. and Josephson, L. (2006) Nanoparticle imaging of integrins on tumor cells. *Neoplasia*, **8** (3), 214–22.

116 Park, K., Liang, G., Ji, X., Luo, Z.P., Li, C., Croft, M.C. and Markert, J.T. (2007) Structural and magnetic properties of gold and silica doubly coated γ-Fe_2O_3 nanoparticles. *The Journal of Physical Chemistry C*, **111** (50), 18512–19.

117 Freeman, M.W., Arrott, A. and Watson, J.H.L. (1960) Magnetism in medicine. *Journal of Applied Physics*, **31** (5), S404–5.

118 Alexiou, C., Arnold, W., Klein, R.J., Parak, F.G., Hulin, P., Bergemann, C., Erhardt, W., Wagenpfeil, S. and Lubbe, A.S. (2000) Locoregional cancer treatment with magnetic drug targeting. *Cancer Research*, **60** (23), 6641–8.

119 Widder, K.J., Senyel, A.E. and Scarpelli, G.D. (1978) Magnetic microspheres: a model system of site specific drug delivery *in vivo*. *Proceedings of the Society for Experimental Biology and Medicine*, **158** (2), 141–6.

120 Lübbe, A.S., Alexiou, C. and Bergemann, C. (2001) Clinical applications of magnetic drug targeting. *Journal of Surgical Research*, **95** (2), 200–6.

121 Pulfer, S.K., Ciccotto, S.L. and Gallo, J.M. (1999) Distribution of small magnetic particles in brain tumor-bearing rats. *Journal of Neuro-Oncology*, **41** (2), 99–105.

122 Goodwin, S., Peterson, C., Hoh, C. and Bittner, C. (1999) Targeting and retention of magnetic targeted carriers (MTCs) enhancing intra-arterial chemotherapy. *Journal of Magnetism and Magnetic Materials*, **194** (1-3), 132–9.

123 Goodwin, S.C., Bittner, C.A., Peterson, C.L. and Wong, G. (2001) Single-dose toxicity study of hepatic intra-arterial infusion of doxorubicin coupled to a novel magnetically targeted drug carrier. *Toxicological Sciences*, **60** (1), 177–83.

124 Alexiou, C., Jurgons, R., Schmid, R., Hilpert, A., Bergemann, C., Parak, F. and Iro, H. (2005) In vitro and *in vivo* investigations of targeted chemotherapy with magnetic nanoparticles. *Journal of Magnetism and Magnetic Materials*, **293** (1), 389–93.

125 Kubo, T., Sugita, T., Shimose, S., Nitta, Y., Ikuta, Y. and Murakami, T. (2000) Targeted delivery of anticancer drugs with intravenously administered magnetic liposomes in osteosarcoma-bearing hamsters. *International Journal of Oncology*, **17** (2), 309–15.

126 Yellen, B.B., Forbes, Z.G., Halverson, D.S., Fridman, G., Barbee, K.A., Chorny, M., Levy, R. and Friedman, G. (2005) Targeted drug delivery to magnetic implants for therapeutic applications. *Journal of Magnetism and Magnetic Materials*, **293** (1), 647–54.

127 Lubbe, A.S., Bergemann, C., Huhnt, W., Fricke, T., Riess, H., Brock, J.W. and Huhn, D. (1996) Preclinical experiences with magnetic drug targeting: tolerance and efficacy. *Cancer Research*, **56** (20), 4694–701.

128 Koda, J., Venook, A., Walser, E. and Goodwin, S. (2002) A multicenter, phase I/II trial of hepatic intra-arterial delivery of doxorubicin hydrochloride adsorbed to magnetic targeted carriers in patients with hepatocellular carcinoma. *European Journal of Cancer*, **38** (Suppl. 7), S18.

129 McBain, S.C., Yiu, H.H. and Dobson, J. (2008) Magnetic nanoparticles for gene and drug delivery. *International Journal of Nanomedicine*, **3** (2), 169–80.

130 Wilson, M.W., Kerlan, R.K., Jr, Fidelman, N.A., Venook, A.P., LaBerge, J.M., Koda, J. and Gordon, R.L. (2004) Hepatocellular carcinoma: regional therapy with a magnetic targeted carrier bound to doxorubicin in a dual MR imaging/conventional angiography suite–initial experience with four patients. *Radiology*, **230** (1), 287–93.

Keywords

nanomaterials; core–shell structure; magnetic resonance imaging; thermal ablation; targeting; drug delivery

8
The Use of Magnetic Particles in Tissue Engineering

Sarah H. Cartmell and Jon Dobson

8.1
Introduction

Magnetic microparticles and nanoparticles, primarily iron oxides, have been used in biomedical applications such as tissue engineering [1], cell separation/immunoassay, drug targeting and delivery, gene delivery and transfection, and as magnetic resonance imaging (MRI) contrast agents [2–4]. These particles often consist of a magnetic iron oxide core coated with a biocompatible polymer that can be functionalized in order to attach binding molecules such as antibodies, peptides, and other functional groups [5, 6].

More recently, magnetic nanoparticles have been used increasingly for tissue engineering applications. Tissue engineering has been described as "... an interdisciplinary field that applies the principles of engineering and life sciences toward the development of biological substitutes that restore, maintain, or improve tissue function or a whole organ" [7]. In many cases, the objective is to seed a patient's own cells onto a porous, biodegradable scaffold, and then to coax the cells to produce the required tissue matrix as the scaffold decays. Ultimately, all that remains is the new tissue construct ready for implantation into the site of the defect. By using the patient's own cells, the problem of immunorejection is overcome, although in practice this is proving difficult to achieve. By utilizing the benefits of magnetic particles as "mechanotransducers", it is possible to control cellular behavior in a remote fashion, to influence the three-dimensional (3-D) structure, and aid in the formation of functional tissue constructs [8]. In this chapter, we will review the progress of these approaches in tissue engineering as applied to various tissue types.

8.1.1
Mechanotransduction

By attaching magnetic nanoparticles to functional sites, both on the cell membrane and on internal cellular components, the particles can act as transducers of applied

Nanomaterials for the Life Sciences Vol. 4: Magnetic Nanomaterials. Edited by Challa S. S. R. Kumar

ISBN: 978-3-527-32154-4

magnetic fields and enable the noninvasive control of various cellular functions. Although this method was first described during the 1950s by Francis Crick [9], it was not studied further until the 1980s by Valberg and others [10–15]. Based on these earlier findings, Ning Wang and Donald Ingber developed the technique of "magnetic twisting cytometry" (MTC). By coating magnetic microparticles with ligands targeted at different receptors on the cell surface, and then applying and measuring the magnetic fields required to "twist" the magnetically blocked particles, it was possible to study the mechanical linkage between the cell membrane receptor and the cytoskeletal network [16]. Since then, basic scientific experiments have been performed on a variety of cell types using different particles and coatings to investigate mechanotransduction [17–25].

In addition to twisting magnetically blocked microparticles and nanoparticles, it is also possible to "pull" the particles towards a magnetic field source, provided that there is a gradient to the field [2]. Magnetic nanoparticles will be attracted to such a field according to the equation:

$$F_{mag} = (\chi_2 - \chi_1) V \frac{1}{\mu_0} B(\nabla B) \tag{8.1}$$

where F_{mag} is the force on the magnetic particle, χ_2 is the volume magnetic susceptibility of the magnetic particle, χ_1 is the volume magnetic susceptibility of the surrounding medium, μ_o is the magnetic permeability of free space, V is the particle volume, B is the magnetic flux density in Tesla (T), ∇B is field gradient, which can be reduced to $\partial B/\partial x$, $\partial B/\partial y$, $\partial B/\partial z$.

This attractive force (sometimes in combination with torque), when applied to magnetic nanoparticles which are attached in some way to cell membrane receptors or cellular components, presents opportunities to employ magnetic actuation in a way that may be used to control specific cellular processes (Figure 8.1).

It is well established that mechanical forces influence cellular function, most likely through their effects on mechanosensitive ion channels. The differentiation

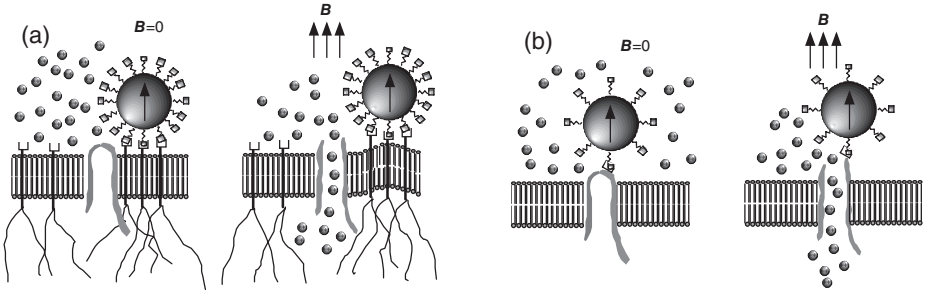

Figure 8.1 Schematic representation of magnetic nanoparticle-based ion channel activation. (a) By general membrane stretch/deformation; (b) By targeted ion channel attachment and actuation. Figure adapted from Ref. [8].

of stem cells can be controlled by mechanical forces [26, 27]. Extracellular matrix-associated gene expression of more mature cells such as osteoblasts can be upregulated using mechanical forces [28]. It is this concept of remote control of mechanotransduction that has led to developments in the application of magnetic microparticles and nanoparticles to tissue engineering.

Mechanical forces can be applied to cells that are seeded onto a 3-D scaffold in a variety of ways. Such methods include shear forces induced from fluid flow and compressive/tensile forces applied directly to the cell-seeded scaffold (and thus transmitted indirectly to the cells seeded onto the scaffold). There are various limitations using these techniques, but these may be overcome by using magnetic microparticles and nanoparticles as mechanotransducers.

By using magnetic particles to transmit force directly to the cells, the scaffold geometry can be complex, whereas in compressive/tensile regimes the scaffold must be of uniform dimensions in order to allow cell loading throughout the scaffold. In addition, shear forces applied using fluid flow through complex scaffold structures vary greatly with little control. The technique also allows a controllable level of force to be varied in different regions of the tissue-engineered construct, simply by changing the magnetic field geometry, the type of particle attached to the cells in each region, or the number of particles attached to each cell in each region.

In order to exploit this, a magnetic ion channel activation (MICA) bioreactor has been designed specifically for tissue engineering purposes [29]. This system uses permanent NdFeB magnet arrays to apply cyclical magnetic fields to cells (in either 2-D or 3-D configuration) that have magnetic particles attached to the cell membranes (Figure 8.2). In this way, forces in the order of a few piconewtons per particle can be applied to each cell. These forces are sufficient to activate the mechanosensitive ion channels and, by targeting specific receptors on the cell surface, it is possible to control the production of tissue matrix components. Short-term experiments have demonstrated an upregulation of extracellular matrix (ECM)-related gene expression for both cartilage and bone, while longer-term

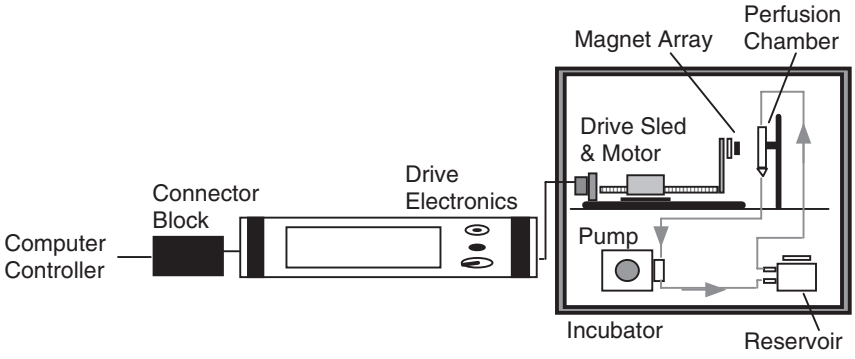

Figure 8.2 Schematic of the 3-D magnetic ion channel activation system housed inside an incubator.

experiments have demonstrated the early deposition of ECM from primary human cells [29].

8.1.2 Cell Seeding: Scaffolds and 3-D Structures

The applications of magnetic nanoparticles in tissue engineering are not only limited to applying forces to cells that are already attached to a substrate. These particles can also be used to guide cell adherence location; that is, cell seeding onto a scaffold or into a predetermined shape. Continuous cell sheets have been created by using magnetic nanoparticles (Figure 8.3) [30], the technique comprising the coating of magnetic particles with a protein and holding the magnetic particle "layer" in place using a magnetic field. Cells are then seeded on top of the magnetic particle "layer" (to which they attach via the proteins with which the particles are coated), and then cultured. The cell layer can be easily detached by removing the magnetic field (the cells will then adhere to the free-floating particle layer rather than to the bottom of the tissue culture dish). Tubes can be easily created from these cultured cell layers by using a rotating cylindrical magnet to attract the 2-D cell layer, and then rolling it into the desired configuration [31].

Cell seeding onto porous 3-D scaffolds such as collagen and poly L-lactic acid (PLLA) has also been improved using magnetic particles [32]. Fibroblasts attached to magnetic particles have been placed onto the porous scaffolds; a permanent magnet is then placed underneath the scaffolds to improve the penetration depth of the magnetically tagged cell suspension. Sasaki *et al.* have also described a dynamic seeding regime where cells with attached magnetic nanoparticles were "pulled" through a porous chitosan scaffold using a magnetic field [33]. An improved cell density in the center of this porous 3-D chitosan sponge was demonstrated, as well as an upregulation of matrix metalloproteinases and adhesion molecules. Notably, the higher the magnetic force applied, the greater invasion of cells into the scaffold was seen.

While working at the Massachusetts Institute of Technology and Harvard, Ingber's group have used applied magnetic fields and thrombin-coated magnetic microparticles (4.5 μm diameter) to create 2-D hexagonal arrays [34]. These particles nucleate the growth of fibrin fibrils, which then grow into an ordered fibrin

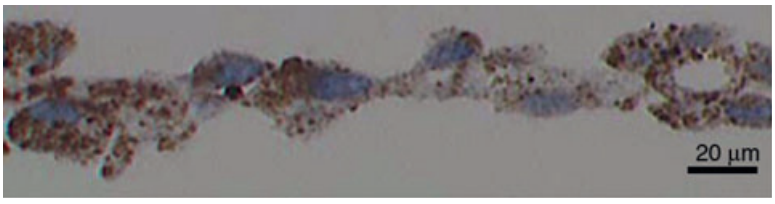

Figure 8.3 Cell sheets fabricated by Magnetic-Tissue Engineering using RGD-coated magnetic cationic liposomes. Reproduced with permission from Ref. [30].

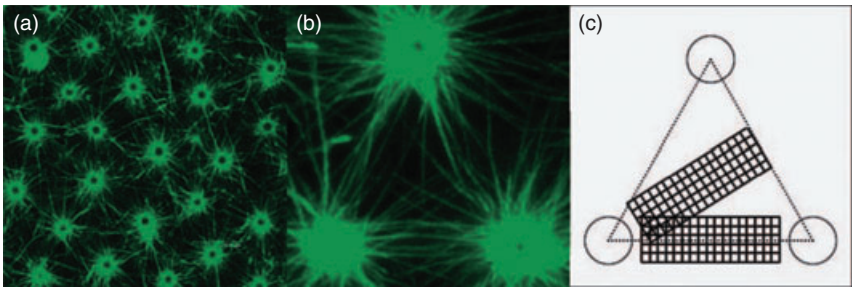

Figure 8.4 (a) Low- and (b) high-magnification confocal microscopic images showing fibrin scaffolds produced using a magnetic microbead array; (c) Diagrammatic view of the grid overlay. Panel (a) was composed by overlaying seven confocal Z-slices, each 1 mm apart. Reproduced with permission from Ref. [34].

gel scaffold that can be used to support the growth and propagation of endothelial cells (Figure 8.4). By staining actin filaments within the endothelial cells, the group was able to observe preferential alignment within the scaffold structure. By using constructing larger scaffolds using this method, the technique may prove useful for *in vivo* applications in regenerative medicine.

The following section relates to the techniques described above using magnetic microparticles and nanoparticles for tissue engineering. Whilst an overview of the technical details of the techniques involved can be found in Ref. [8], only specific tissue types will be addressed at this point.

8.2
Magnetic Particle Technology Used in Various Tissue Types

8.2.1
Bone and Cartilage

In 2002, the present authors' group described an experiment using the MICA system whereby primary human osteoblasts were attached to RGD-coated 4.5 µm chromium dioxide particles and exposed to a 1 h per day, 1 Hz, time-varying magnetic field (~60 mT) [35]. After a three-weeks period of *in vitro* culture, the mechanically stimulated samples exhibited an elevated bone-related gene expression and an early deposition of mineralized matrix (Figure 8.5), thus demonstrating the potential of the technique for *ex vivo* bone tissue engineering.

Yuge *et al.* have also shown that the differentiation of human osteoblasts can be influenced using magnetic particle force application [36]. In these experiments, magnetic nanoparticles (50 nm) were driven into electroporated NHOst cells (cell line) at a concentration of 20 000 particles ml^{-1}. A permanent magnet applied a

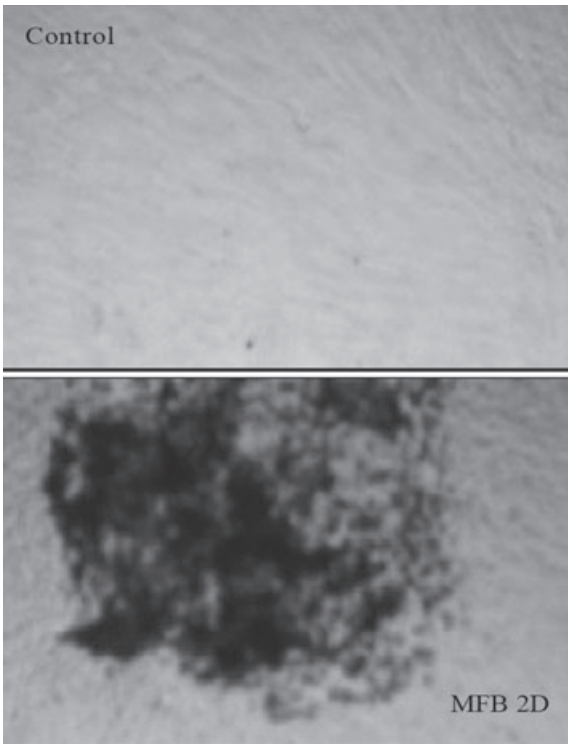

Figure 8.5 von Kossa staining showing bone matrix mineralization in MG63 osteoblast cultures mechanically conditioned using the 2-D MICA system at 1 Hz with 4.5 µm magnetic particles (bottom) versus control cells (top) which were not exposed to mechanical conditioning. Reproduced with permission from Ref. [35].

field which ranged from 1 to 50 mT over a 21-day period. An upregulation of bone-related gene expression was observed which was shown to be linked to early activation of the p38 mechanotransduction pathway.

Shimizu *et al.* have shown that sheets of human mesenchymal stem cells can be created for bone tissue engineering purposes [37]. A 400 mT magnet was applied to the underside of a tissue culture dish containing the magnetic particle layer (as described above) for a 24-h period. An electromagnet was then used to harvest and transplant the sheets into a rat cranial defect model. After 14 days *in vivo*, new bone was seen at the site of the mesenchymal stem cell/magnetic particle sheet, whereas no new bone was seen at the control site (no implant).

The same group have also described the effective cell seeding of bone marrow stromal cell through a porous 3-D scaffold using magnetic particle-tagged cells and a 1 T magnetic field placed underneath the scaffold to "draw" the cells through the scaffold [38]. The particles were positively charged in order to improve cell

attachment to their surface, and the cell seeding efficiency of the technique was improved threefold in comparison to traditional static culture seeding regimes. At 14 days, the "mag-seeded" groups showed significantly more levels of osteogenic markers (alkaline phosphatase and osteocalcin) than the static-seeded constructs.

8.2.2 Blood Vessels and Cardiac Structure

Damage to the small blood vessels of the body is difficult to repair due to the threat of thrombosis and neointima formation. Pislaru *et al.* recently described a technique using superparamagnetic iron oxide magnetic particles engulfed by endothelial cells, which were then seeded onto a magnetic Dacron graft [39]. A flexible magnetic sheet was annealed to the external surface of a knitted Dacron graft, and the labeled cells were placed within the graft for 5 min. Cell viability was assessed using trypan blue exclusion, and a dose-dependent survival rate of 75–95% was demonstrated. Both, confocal and electron microscopy showed a uniform cell capture on the magnetic surface of the magnetically treated Dacron graft. The group hypothesized that rapid endothelialization may overcome the incidence of thrombosis and neointima during vessel healing. The endocytosed superparamagnetic iron oxide particles assisted cell adherence up to 400 ml min^{-1} under *in vitro* conditions. *In vivo* studies demonstrated a good cell adherence at one day after implantation into a porcine circulatory system [39].

Shimizu *et al.* have described the construction of blood vessels using magnetic particle/cell-guided adherence [40]. NIH-3T3 fibroblasts were labeled with magnetite cationic liposomes, after which a cylindrical magnet was placed into the lumen of a decellularized porcine carotid artery and the cell/particles were placed onto the scaffold. The cell/particle-seeded sample retained a far greater number of cells in comparison to the cell-only (no magnetic particles) control. Higher numbers of particles per cell increased the seeding efficiency. The porcine graft was also successfully seeded with a coculture of smooth muscle cells and dermal fibroblasts using this technique.

The reconstruction of 3-D capillaries was attempted by Ino *et al.*, using a coculture rolled sheet approach with magnetic particles [41]. For this, 10 nm magnetic cationic particles were attached to normal human dermal fibroblasts, and the cell/particle suspension was then seeded onto a plate, below which was placed a magnet that attracted the cells to the plate bottom. After 24 h, the cells had formed a sheet, onto which human umbilical vein endothelial cells were seeded, using the same magnetic particle technique. These methods gave rise to tube-like formations that resembled early-stage capillaries.

Small blood vessels have also been tissue-engineered using a cell patterning device [42]. Here, the technique is similar to the sheet creation technique, using cells with adhered magnetic particles as the bottom layer. In this method, stainless steel plates were positioned on a magnet under the cell culture surface, and the magnetic particle-tagged cells lined up with the surface of the steel. Subsequently,

patterned lines of single cells (curves, parallel lines, and crossing patterns) were achieved using this technique.

Amsalem *et al*. have investigated the effect of injecting mesenchymal stem cells (MSCs) into the circulation, using a rat myocardial infarction model. The MSCs were labeled with superparamagnetic iron oxide nanoparticles in order to track them during the repair process [43]. The inclusion of nanoparticles was found not to alter the MSC activity (attenuation of left ventricular dilatation and dysfunction after myocardial infarction, but not in the scar tissue) in comparison to nontagged MSCs.

Shimizu *et al*. have created 3-D tissues of tightly connected cardiomyocytes using magnetic particle technology [44]. For this, positively charged magnetic particles were attached to primary rat cardiomyocytes at varying concentrations (25, 50, and 100 pg per cell), with no toxicity being observed after 24 h. When using a 100 pg per cell concentration, multilayered sheets were constructed by seeding the particle/cell suspension into a tissue culture plate and applying a magnetic field to draw all cells to the bottom of the dish. Fluorescence staining was positive for connexin43, indicating a presence of the gap junctions necessary for effective cardiac function.

Endothelial progenitor cells, which have a therapeutic potential for revascularization, have also been tagged with magnetic nanoparticles, [45]. Negatively charged magnetic particles were shown to attach nonspecifically to the cell membrane of endothelial progenitor cells. The label was shown to be nontoxic, and to have no adverse effect on the cells' proliferative capacity. When Matrigel was used to support the cell attachment into a tubular form, magnetic fields applied to the Matrigel/cell/particle suspension allowed manipulation of the positions of cells within the Matrigel.

8.2.3 Skin

Fibroblasts have been investigated with regards to magnetic nanoparticles due to their well-established relevance for cytotoxicity characterization and ease of use. Since this cell type is also relevant to the dermis (and other connective tissue), information has also been acquired with regards to the influence of magnetic particles on the skin.

Berry *et al*. have shown, *in vitro*, that elastin-coated iron oxide particles affect human fibroblast behavior and morphology differently in comparison to uncoated particles, but that the particle size (520 nm versus 20 nm) had only a minimal influence [46]. More specifically, after 24 h, elastin-coated 20 nm particles significantly increased cell proliferation in comparison to the control. At 12 h, the morphology of cells exposed to 20 nm elastin-coated particles was similar to that of the cells-only control, whereas cells exposed to 520 nm elastin-coated particles exhibited a disrupted cell shape with no clear cytoskeletal organization. The same group has also shown that, when iron oxide particles are coated with transferrin and attached via this receptor to human dermal fibroblasts, endocytosis was inhibited, whereas uncoated particles were endocytosed [47]. It was also shown that altering

the surface chemistry of the particles to present either dextran or albumin had an effect on cell behavior and morphology [48, 49]. Berry *et al*. demonstrated that the exposure of cells to 7–15 nm dextran-coated particles significantly delayed cell spreading in comparison to the cells-only control. Dextran-coated particles stimulated a far greater cell membrane disruption (associated with endocytosis) than plain, non-coated particles, even though the level of uptake was similar. Further cytoskeletal staining demonstrated that F-actin and beta-tubulin were structurally responsible for these membrane disruptions. Gupta and Curtis have shown that the surface modification of poly(ethylene glycol) (PEG)-coated magnetic nanoparticles affects fibroblast adhesion/viability, morphology, particle uptake and cytoskeletal organization differently to uncoated particles [50]. The PEG-coated particles demonstrated a significantly higher cell adhesion and cellular uptake in comparison to the uncoated particle controls. The use of insulin, lactoferrin, cerruloplasmin and pullulan as surface coatings for magnetic particles in order to prevent endocytosis have also been investigated [51–53].

Ito *et al*. have shown that human keratinocytes (HaCaT cell line) attach to positively charged and Arg-Gly-Asp (RGD) -coated magnetic particles, and can be influenced to form layers *in vitro* when a magnetic field is placed under the dish (the culture surface of which was coated with a negatively charged hydrogel) in order to attract the cell/particle suspension [54]. Cell patterning was created by using a magnetic field and a 200 μm-wide stainless steel plate beneath the culture surface, while cell adhesion, spreading and fibronectin production was observed with the RGD-coated particles.

8.2.4 Lung

Maruyama *et al*. have used nanoscale biogenic magnetite to detect mutations in the epidermal growth factor receptor (EGFR) gene in non-small lung cancer cells [55]. The magnetic particles were isolated from magnetotactic bacteria and conjugated to streptavidin. Biotin-labeled PCR products then were bound to the magnetic material and fluorescently labeled. An early detection (3.5 h) was reported for *EGFR* gene mutations.

Lung cancer cells have been transfected with the gene *Lac Z*, and tagged using green fluorescent protein (GFP), by using Fe_3O_4 nanoparticles [56]. The particle size, including the gene/virus, was less than 100 nm, and no particle-related toxicity was observed. The particles plus viral delivery of the *Lac Z* gene, when exposed to magnetic fields, demonstrated a much higher transfection efficiency when compared to traditional transfection with liposomes or lipofectamine.

8.2.5 Eye

Formanek *et al*. have described an efficient method for isolating human oral keratinocytes using magnetic cell separation techniques [57]. In order to study human

keratinocytes, a pure population of cells was required, and Formanek *et al.* described an immunomagnetic separation technique for this purpose. Initially, a two-step enzymatic digestion phase was applied to human eye tissue, after which the mononuclear cells in the cell suspension were tagged using a mouse anti-CD45 antibody. A rat anti-mouse antibody conjugated to colloidal superparamagnetic particles was then incubated with the cell suspension. A permanent magnet was used to collect the magnetically tagged mononuclear cells from the heterogeneous population; in this way, a >98% pure population of keratinocytes was collected, as determined by subsequent fluorescence-activated cell sorting (FACS) analysis.

Chorodial neovascularization is a severe form of age-related macular degeneration for which the transplantation of a tissue-engineered retinal pigment epithelium may represent a possible treatment. Ito *et al.* used a magnetic particle sheet-layering technique to construct sheets of human retinal pigment epithelium cells in which approximately 50% of the cell population contained 25–50 μg magnetite per cell [58]. After 24 h, a layered sheet (approximately 15 cells thick) was created and easily detached from the tissue culture dish when the magnetic field was removed. Layer with thicknesses of five cells have also been created in this manner, using keratinocytes [59].

8.2.6
Liver

A coculture of hepatocytes and endothelial cells has been created using the magnetic particle sheet layering method described above [60]. This cocultured model significantly enhanced albumin secretion by hepatocytes compared to that of single-cell cultures of hepatocytes, or of cocultures of hepatocytes and endothelial cells without magnets.

Ito *et al.* have described a system where a 3-D coculture of hepatocytes and MSCs was created by using magnetic particle technology [61]. In this study, magnetite cationic liposomes were used to tag NIH-3T3 cells, which were then subsequently collected onto the surface of a hydrophilic hydrogel by using a magnetic field to retain the particle-tagged cells. After a 24 h period, the cells had formed a sheet, onto which hepatocytes (HepG2) were tagged and seeded onto the MSC sheet, again using a magnetic field. The successful construction of these multicellular layered sheets led to an enhanced albumin secretion by the HepG2 cells.

8.2.7
Nervous Tissue

Superparamagnetic iron oxide particles have been attached to human neural precursor cells and transplanted into an adult murine brain [62]. The initial experiments were performed *in vitro*, in order to minimize any superparamagnetic particle effects on expanded human neural precursor cells with regards to their viability, proliferation, and multipotency. A small number of magnetic particle-labeled cells ($5\times10^3 - 1\times10^4$) were implanted into the murine brain model and

tracked for at least one month following implantation by using magnetic resonance. This approach also enabled a clarification of the impact of donor cell death on the magnetic resonance signal. Although this technique may lend itself to noninvasive imaging of donor cell implantation to the brain, it has potential limitations with regards to neural-based clinical applications.

8.2.8
Stem Cell Targeting

Adult MSCs and human embryonic stem cells have been labeled with superparamagnetic iron oxide particles and tracked using MRI after implantation into rats [63, 64]. The same particles have been visualized using MRI in a tissue-engineered collagen hydrogel construct of human MSCs for articular cartilage treatment [65]. A magnetic particle technique has also been developed for the separation of stem cells from a heterogeneous population [66].

Dobson *et al*. have shown that primary human MSCs can be stimulated towards osteogenesis by using magnetic particles (4.5 μm chromium dioxide, RGD-coated) [29]. It has also recently been shown that the MICA technique can be used for the activation of internalized magnetic particles targeted towards specific ion channels (in this case, the TREK-1 potassium channel) [67]. The genes activated (e.g., Sox-9) using this technique indicate that TREK-1 is likely implicated in the formation of cartilage.

8.2.9
Use of Magnetic Particles to Create Acellular Scaffolds

Hu *et al*. have used magnetic nanoparticles to create a tissue engineering scaffold [68]. For this, the iron oxide particles were created *in situ* in a bioresorbable gelatin hydrogel; subsequent variation of the gelatin concentration led to changes in the yield of magnetic particles, with the yield of iron oxide particles decreasing as the gelatin content increased. The highest yield of magnetic particles was 9.41%, with the creation of pore sizes ranging from 50 to 200 μm. When a magnetic field was applied, the magnetic interparticle forces formed reduced the drug release rates in the ferrous scaffolds; this reduction was caused by the increased stability of the iron oxide/gelatin scaffold lowering the degradation rate of the gelatin.

8.3
Summary and Concluding Remarks

It is clear from this brief overview that the use of magnetic nanoparticles in tissue engineering is currently undergoing a rapid expansion. By loading cells with magnetic nanoparticles, it is possible to monitor and track their movements *in vivo* using MRI. Yet, in the future, it should be possible to combine both tracking and nanomagnetic actuation in order to control and monitor cell behavior in the

body, and this will undoubtedly contribute significantly to the field of regenerative medicine.

The ability to manipulate cellular processes remotely via nanomagnetic actuation opens up myriad opportunities not only for the mechanical conditioning of cells and tissue constructs within bioreactors and *in vivo*, but also for stem cell targeting and differentiation. Although many investigations must still be conducted in order to realize the potential of these techniques and, in many ways, this field is still in its infancy, rapid progress is already leading us in directions considered impossible just a decade ago.

References

1 Ito, A. and Honda, H. (2006) Magnetic nanoparticles for tissue engineering, in: *Nanotechnologies for the Life Sciences*, (ed. C. Kumar), Vol. 9, pp. 308–37.

2 Pankhurst, Q.A., Connoly, J., Jones, S.K. and Dobson, J. (2003) Applications of magnetic nanoparticles in biomedicine. *Journal of Physics*, **36**, R167–181.

3 Dobson, J. (2006) Gene therapy progress and prospects: magnetic nanoparticle-based gene delivery. *Gene Therapy*, **13**, 283–7.

4 Weissleder, R., Elizondo, G., Wittenberg, J., Rabito, C.A., Bengele, H.H. and Josephson, L. (1990) Ultrasmall superparamagnetic iron oxide: characterization of a new class of contrast agents for MR imaging. *Radiology*, **175**, 489–93.

5 McBain, S.C., Yiu, H.H. and Dobson, J. (2008) Magnetic nanoparticles for gene and drug delivery. *International Journal of Nanomedicine*, **3**, 169–80.

6 Neuberger, T., Schopf, B., Hofmann, H., Hofmann, M. and von Rechenberg, B. (2005) Superparamagnetic nanoparticles for biomedical applications: possibilities and limitations of a new drug delivery system. *Journal of Magnetic Materials*, **293**, 483–96.

7 Langer, R. and Vacanti, J.P. (1993) Tissue engineering. *Science*, **260**, 920–6.

8 Dobson, J. (2008) Remote control of cellular behavior with magnetic nanoparticles. *Nature Nanotechnology*, **3**, 139–43.

9 Crick, F. (1950) The physical properties of cytoplasm. A study by means of the magnetic particle method part II. *Experimental Cell Research*, **1**, 505–33.

10 Gehr, P., Brain, J.D., Bloom, S.B. and Valberg, P.A. (1983) Magnetic particles in the liver: a probe for intracellular movement. *Nature*, **302**, 336–8.

11 Gehr, P., Brain, J.D. and Bloom, S.B. (1984) Noninvasive studies of Kupffer cells in situ by magnetometry. *Journal of Leukocyte Biology*, **35**, 19–30.

12 Valberg, P.A. and Feldman, H.A. (1987) Magnetic particle motions within living cells. Measurement of cytoplasmic viscosity and motile activity. *Biophysical Journal*, **52**, 551–61.

13 Valberg, P.A. and Butler, J.P. (1987) Magnetic particle motions within living cells. Physical theory and techniques. *Biophysical Journal*, **52**, 537–50.

14 Valberg, P.A. and Albertini, D.F. (1985) Cytoplasmic motions, rheology, and structure probed by a novel magnetic particle method. *The Journal of Cell Biology*, **101**, 130–40.

15 Valberg, P.A., Meyrick, B., Brain, J.D. and Brigham, K.L. (1988) Phagocytic and motile properties of endothelial cells measured magnetometrically: effects of endotoxin. *Tissue Cell*, **20**, 345–54.

16 Wang, N., Butler, J.P. and Ingber, D.E. (1993) Mechanotransduction across the cell surface and through the cytoskeleton. *Science*, **260**, 1124–7.

17 Bausch, A.R., Ziemann, F., Boulbitch, A.A., Jacobson, K. and Sackmann, E. (1998) Local measurements of viscoelastic parameters of adherent cell surfaces by magnetic bead

microrheometry. *Biophysical Journal*, **75**, 2038–49.
18 Bausch, A.R., Moller, W. and Sackmann, E. (1999) Measurement of local viscoelasticity and forces in living cells by magnetic tweezers. *Biophysical Journal*, **76**, 573–9.
19 D'Addario, M., Arora, P.D., Ellen, R.P. and McCulloch, C.A. (2003) Regulation of tension-induced mechanotranscriptional signals by the microtubule network in fibroblasts. *The Journal of Biological Chemistry*, **278**, 53090–7.
20 Glogauer, M., Ferrier, J. and McCulloch, C.A. (1995) Magnetic fields applied to collagen-coated ferric oxide beads induce stretch-activated Ca^{2+} flux in fibroblasts. *The American Journal of Physiology*, **269**, C1093–104.
21 Glogauer, M., Arora, P., Yao, G., Sokholov, I., Ferrier, J. and McCulloch, C.A. (1997) Calcium ions and tyrosine phosphorylation interact coordinately with actin to regulate cytoprotective responses to stretching. *Journal of Cell Science*, **110** (Pt 1), 11–21.
22 Glogauer, M. and Ferrier, J. (1998) A new method for application of force to cells via ferric oxide beads. *Pflügers Archiv : European Journal of Physiology*, **435**, 320–7.
23 Glogauer, M., Arora, P., Chou, D., Janmey, P.A., Downey, G.P. and McCulloch, C.A. (1998) The role of actin-binding protein 280 in integrin-dependent mechanoprotection. *The Journal of Biological Chemistry*, **273**, 1689–98.
24 Pommerenke, H., Schreiber, E., Durr, F., Nebe, B., Hahnel, C., Moller, W. and Rychly, J. (1996) Stimulation of integrin receptors using a magnetic drag force device induces an intracellular free calcium response. *European Journal of Cell Biology*, **70**, 157–64.
25 Pommerenke, H., Schmidt, C., Durr, F., Nebe, B., Luthen, F., Muller, P. and Rychly, J. (2002) The mode of mechanical integrin stressing controls intracellular signaling in osteoblasts. *Journal of Bone and Mineral Research*, **17**, 603–11.
26 Titushkin, I. and Cho, M. (2007) Modulation of cellular mechanics during osteogenic differentiation of human mesenchymal stem cells. *Biophysical Journal*, **93**, 3693–702.
27 Yanagisawa, M., Suzuki, N., Mitsui, N., Koyama, Y., Otsuka, K. and Shimizu, N. (2007) Effects of compressive force on the differentiation of pluripotent mesenchymal cells. *Life Sciences*, **81**, 405–12.
28 Cartmell, S.H., Porter, B.D., Garcia, A.J. and Guldberg, R.E. (2003) Effects of medium perfusion rate on cell-seeded three-dimensional bone constructs in vitro. *Tissue Engineering*, **9**, 1197–203.
29 Dobson, J., Cartmell, S.H., Keramane, A. and El Haj, A.J. (2006) Principles and design of a novel magnetic force mechanical conditioning bioreactor for tissue engineering, stem cell conditioning, and dynamic in vitro screening. *IEEE Transactions on Nanobioscience*, **5**, 173–7.
30 Ito, A., Ino, K., Kobayashi, T. and Honda, H. (2005) The effect of RGD peptide-conjugated magnetite cationic liposomes on cell growth and cell sheet harvesting. *Biomaterials*, **26**, 6185–93.
31 Ito, A., Ino, K., Hayashida, M., Kobayashi, T., Matsunuma, H., Kagami, H., Ueda, M. and Honda, H. (2005) Novel methodology for fabrication of tissue-engineered tubular constructs using magnetite nanoparticles and magnetic force. *Tissue Engineering*, **11**, 1553–61.
32 Shimizu, K., Ito, A. and Honda, H. (2006) Enhanced cell-seeding into 3D porous scaffolds by use of magnetite nanoparticles. *Journal of Biomedical Materials Research. Part B, Applied Biomaterials*, **77**, 265–72.
33 Sasaki, T., Iwasaki, N., Kohno, K., Kishimoto, M., Majima, T., Nishimura, S. and Minami, A. (2008) Magnetic nanoparticles for improving cell invasion in tissue engineering. *Journal of Biomedical Materials Research. Part A*, **86**, 969–78.
34 Alsberg, E., Feinstein, E., Joy, M.P., Prentiss, M. and Ingber, D.E. (2006) Magnetically-guided self-assembly of fibrin matrices with ordered nano-scale structure for tissue engineering. *Tissue Engineering*, **12**, 3247–56.

35 Cartmell, S.H., Dobson, J., Verschueren, S.B. and El Haj, A.J. (2002) Development of magnetic particle techniques for long-term culture of bone cells with intermittent mechanical activation. *IEEE Transactions on Nanobioscience*, **1**, 92–7.

36 Yuge, L., Okubo, A., Miyashita, T., Kumagai, T., Nikawa, T., Takeda, S., Kanno, M., Urabe, Y., Sugiyama, M. and Kataoka, K. (2003) Physical stress by magnetic force accelerates differentiation of human osteoblasts. *Biochemical and Biophysical Research Communications*, **311**, 32–8.

37 Shimizu, K., Ito, A., Yoshida, T., Yamada, Y., Ueda, M. and Honda, H. (2007) Bone tissue engineering with human mesenchymal stem cell sheets constructed using magnetite nanoparticles and magnetic force. *Journal of Biomedical Materials Research. Part B, Applied Biomaterials*, **82**, 471–80.

38 Shimizu, K., Ito, A. and Honda, H. (2007) Mag-seeding of rat bone marrow stromal cells into porous hydroxyapatite scaffolds for bone tissue engineering. *Journal of Bioscience and Bioengineering*, **104**, 171–7.

39 Pislaru, S.V., Harbuzariu, A., Agarwal, G., Witt, T., Gulati, R., Sandhu, N.P., Mueske, C., Kalra, M., Simari, R.D. and Sandhu, G.S. (2006) Magnetic forces enable rapid endothelialization of synthetic vascular grafts. *Circulation*, **114**, I314–18.

40 Shimizu, K., Ito, A., Arinobe, M., Murase, Y., Iwata, Y., Narita, Y., Kagami, H., Ueda, M. and Honda, H. (2007) Effective cell-seeding technique using magnetite nanoparticles and magnetic force onto decellularized blood vessels for vascular tissue engineering. *Journal of Bioscience and Bioengineering*, **103**, 472–8.

41 Ino, K., Ito, A., Kumazawa, H., Kagami, H., Ueda, M. and Honda, H. (2007) Incorporation of capillary-like structures into dermal sheets constructed by magnetic force-based tissue engineering. *Journal of Chemical Engineering of Japan*, **40**, 51–8.

42 Ino, K., Ito, A. and Honda, H. (2007) Cell patterning using magnetite nanoparticles and magnetic force. *Biotechnology and Bioengineering*, **97**, 1309–17.

43 Amsalem, Y., Mardor, Y., Feinberg, M.S., Landa, N., Miller, L., Daniels, D., Ocherashvilli, A., Holbova, R., Yosef, O., Barbash, I.M. and Leor, J. (2007) Iron-oxide labeling and outcome of transplanted mesenchymal stem cells in the infarcted myocardium. *Circulation*, **116**, I38–45.

44 Shimizu, K., Ito, A., Lee, J.K., Yoshida, T., Miwa, K., Ishiguro, H., Numaguchi, Y., Murohara, T., Kodama, I. and Honda, H.(2007) Construction of multi-layered cardiomyocyte sheets using magnetite nanoparticles and magnetic force. *Biotechnology and Bioengineering*, **96**, 803–9.

45 Wilhelm, C., Bal, L., Smirnov, P., Galy-Fauroux, I., Clement, O., Gazeau, F. and Emmerich, J. (2007) Magnetic control of vascular network formation with magnetically labeled endothelial progenitor cells. *Biomaterials*, **28**, 3797–806.

46 Berry, C.C., Rudershausen, S., Teller, J. and Curtis, A.S. (2002) The influence of elastin-coated 520-nm- and 20-nm-diameter nanoparticles on human fibroblasts in vitro. *IEEE Transactions on Nanobioscience*, **1**, 105–9.

47 Berry, C.C., Charles, S., Wells, S., Dalby, M.J. and Curtis, A.S. (2004) The influence of transferrin stabilised magnetic nanoparticles on human dermal fibroblasts in culture. *International Journal of Pharmaceutics*, **269**, 211–25.

48 Berry, C.C., Wells, S., Charles, S. and Curtis, A.S. (2003) Dextran and albumin derivatised iron oxide nanoparticles: influence on fibroblasts in vitro. *Biomaterials*, **24**, 4551–7.

49 Berry, C.C., Wells, S., Charles, S., Aitchison, G. and Curtis, A.S. (2004) Cell response to dextran-derivatised iron oxide nanoparticles post internalisation. *Biomaterials*, **25**, 5405–13.

50 Gupta, A.K. and Curtis, A.S. (2004) Surface modified superparamagnetic nanoparticles for drug delivery: interaction studies with human fibroblasts in culture. *Journal of Materials Science. Materials in Medicine*, **15**, 493–6.

51 Gupta, A.K., Berry, C., Gupta, M. and Curtis, A. (2003) Receptor-mediated

targeting of magnetic nanoparticles using insulin as a surface ligand to prevent endocytosis. *IEEE Transactions on Nanobioscience*, **2**, 255–61.

52 Gupta, A.K. and Gupta, M. (2005) Cytotoxicity suppression and cellular uptake enhancement of surface modified magnetic nanoparticles. *Biomaterials*, **26**, 1565–73.

53 Gupta, A.K. and Curtis, A.S. (2004) Lactoferrin and ceruloplasmin derivatized superparamagnetic iron oxide nanoparticles for targeting cell surface receptors. *Biomaterials*, **25**, 3029–40.

54 Ito, A., Akiyama, H., Kawabe, Y. and Kamihira, M. (2007) Magnetic force-based cell patterning using Arg-Gly-Asp (RGD) peptide-conjugated magnetite cationic liposomes. *Journal of Bioscience and Bioengineering*, **104**, 288–93.

55 Maruyama, K., Takeyama, H., Mori, T., Ohshima, K., Ogura, S., Mochizuki, T. and Matsunaga, T. (2007) Detection of epidermal growth factor receptor (EGFR) mutations in non-small cell lung cancer (NSCLC) using a fully automated system with a nano-scale engineered biomagnetite. *Biosensors & Bioelectronics*, **22**, 2282–8.

56 Yang, S.Y., Sun, J.S., Liu, C.H., Tsuang, Y.H., Chen, L.T., Hong, C.Y., Yang, H.C. and Horng, H.E. (2008) Ex vivo magnetofection with magnetic nanoparticles: a novel platform for nonviral tissue engineering. *Artificial Organs*, **32**, 195–204.

57 Formanek, M., Temmel, A., Knerer, B., Willheim, M., Millesi, W. and Kornfehl, J. (1998) Magnetic cell separation for purification of human oral keratinocytes: an effective method for functional studies without prior cell subcultivation. *European Archives of Oto-Rhino-Laryngology*, **255**, 211–15.

58 Ito, A., Hibino, E., Kobayashi, C., Terasaki, H., Kagami, H., Ueda, M., Kobayashi, T. and Honda, H. (2005) Construction and delivery of tissue-engineered human retinal pigment epithelial cell sheets, using magnetite nanoparticles and magnetic force. *Tissue Engineering*, **11**, 489–96.

59 Ito, A., Hayashida, M., Honda, H., Hata, K., Kagami, H., Ueda, M. and Kobayashi, T. (2004) Construction and harvest of multilayered keratinocyte sheets using magnetite nanoparticles and magnetic force. *Tissue Engineering*, **10**, 873–80.

60 Ito, A., Takizawa, Y., Honda, H., Hata, K., Kagami, H., Ueda, M. and Kobayashi, T. (2004) Tissue engineering using magnetite nanoparticles and magnetic force: heterotypic layers of cocultured hepatocytes and endothelial cells. *Tissue Engineering*, **10**, 833–40.

61 Ito, A., Jitsunobu, H., Kawabe, Y. and Kamihira, M. (2007) Construction of heterotypic cell sheets by magnetic force-based 3-D coculture of HepG2 and NIH3T3 cells. *Journal of Bioscience and Bioengineering*, **104**, 371–8.

62 Neri, M., Maderna, C., Cavazzin, C., Deidda-Vigoriti, V., Politi, L.S., Scotti, G., Marzola, P., Sbarbati, A., Vescovi, A.L. and Gritti, A. (2007) Efficient in vitro labeling of human neural precursor cells with superparamagnetic iron oxide particles: relevance for in vivo cell tracking. *Stem Cells*, **26** (2), 505–16.

63 Schafer, R., Kehlbach, R., Wiskirchen, J., Bantleon, R., Pintaske, J., Brehm, B.R., Gerber, A., Wolburg, H., Claussen, C.D. and Northoff, H. (2007) Transferrin receptor upregulation: in vitro labeling of rat mesenchymal stem cells with superparamagnetic iron oxide. *Radiology*, **244**, 514–23.

64 Tallheden, T., Nannmark, U., Lorentzon, M., Rakotonirainy, O., Soussi, B., Waagstein, F., Jeppsson, A., Sjogren-Jansson, E., Lindahl, A. and Omerovic, E. (2006) In vivo MR imaging of magnetically labeled human embryonic stem cells. *Life Sciences*, **79**, 999–1006.

65 Heymer, A., Haddad, D., Weber, M., Gbureck, U., Jakob, P.M., Eulert, J. and Noth, U. (2008) Iron oxide labelling of human mesenchymal stem cells in collagen hydrogels for articular cartilage repair. *Biomaterials*, **29**, 1473–83.

66 Kamihira, M. and Kumar, A. (2008) Development of separation technique for stem cells. *Advances in Biochemical Engineering/Biotechnology*, **106**, 173–93.

67 Hughes, S., McBain, S., Dobson, J. and El Haj, A.J. (2008) Selective activation of mechanosensitive ion channels using magnetic particles. *Journal of the Royal Society, Interface*, **5**, 855–63.

68 Hu, S.H., Liu, T.Y., Tsai, C.H. and Chen, S.Y. (2007) Preparation and characterization of magnetic ferroscaffolds for tissue engineering. *Journal of Magnetism and Magnetic Materials*, **310**, 2871–3.

Keywords

magnetic nanoparticles; microparticles; tissue engineering; actuation; nanomagnetic; cartilage; bone; regenerative medicine

Abstract

Magnetic microparticles and nanoparticles have been utilized in a variety of tissues to influence cell seeding, cell growth and mechanotransduction for regenerative medicine strategies. These particles vary in size, surface chemistry, magnetic properties and bulk chemistry. This chapter describes the latest research and findings regarding magnetic particles and their applications in tissue engineering. Tissues have been grown in sheet form, tubular form, and in three-dimensional (3-D) porous network dimensions. The construction of multilayered tissues such as cardiomyocyte/vascular networks is described, as well as magnetic force mechanical conditioning bioreactors designed for use with stem cell targeting and bone tissue engineering strategies. The use of magnetic particles for epithelial tissue manipulation, keratinocyte growth, hepatocyte and endothelial cells is also discussed, as are future directions for magnetic particles in tissue engineering and regenerative medicine. In 2006, Ito and Honda [1] described the potential of their research using magnetic particles to create 3-D sheets for tissue engineering purposes, based primarily on the group's own findings. In 2008, Dobson briefly reviewed nanomagnetic actuation, outlining the mechanisms of nanomagnetic actuation and highlighting tissue engineering applications, although the main focus of the review was on the techniques and various applications other than tissue engineering. In this chapter, we will update the results obtained since Ito and Honda's first report, and discuss other tissue engineering applications such as mechanotransduction and gene therapy approaches to tissue engineering using magnetic particles.

9
Magnetic Nanomaterials for Environmental Applications

Marvin G. Warner, Cynthia L. Warner, R. Shane Addleman, and Wassana Yantasee

9.1
Introduction

9.1.1
The Aim of the Chapter

The aim of this chapter is to provide details of the current state of the art and trends in the development of magnetic nanoparticles for environmental sensing applications, notably for the detection and removal of heavy metals and biological contaminants from complex samples. Recent advances in the use of nanoscale materials for environmental applications have been possible due to tremendous development efforts in the design and synthesis of engineered nanomaterials – that is, materials consisting of nanosized chemical domains and/or materials having extremely high surface areas arising from their nanoscale dimensions [1]. In particular, attention will be focused on the synthesis, functionalization, and application of engineered magnetic nanoparticles (diameter <100 nm in most cases) for the purpose of separating and detecting a wide variety of analytes from complex environmental and biological matrices. Recently, the use of functionalized magnetic nanoparticles in environmentally relevant applications, such as the selective capture and preconcentration of specific analytes from complex samples for sensitive detection, has been described in an increasingly large number of reports [2–18]. In addition, methods to synthesize magnetic nanoparticles with the appropriate attributes for environmental sensing have been exhaustively reviewed in the recent past, and are summarized in Section 9.2 [4, 14, 17].

9.1.2
The Role of Nanomaterials in Environmental Detection

The world's supply of drinking water is contained predominantly in manmade and natural lakes, rivers, and underground aquifers. Unfortunately, these sources often become polluted by a wide range of substances that are deleterious to human

Nanomaterials for the Life Sciences Vol. 4: Magnetic Nanomaterials. Edited by Challa S. S. R. Kumar

ISBN: 978-3-527-32154-4

health, and that may have a substantial impact on the quality of life of those who depend on the polluted aquatic systems. Drinking water has two major classes of contamination, namely biological and chemical [19, 20]. Biological contamination, such as coliform bacteria (e.g., *Escherichia coli*) and viruses, if detected before exposure to human populations, can be remedied by a number of well-established technologies. However, the detection of these analytes in natural environments is a daunting challenge, and much ongoing research is being carried out to improve the current state of the art.

The detection, remediation, and removal of chemical and heavy-metal contamination (e.g., pesticides, radionuclides, and heavy metals such Hg and Pb) are, likewise, difficult challenges [19] (http://www.epa.gov/ogwdw/hfacts.html). The remediation of common organic contaminants such as pesticides, agricultural chemicals, industrial solvents, and fuels can be accomplished using treatments such as UV/ozone, activated-carbon, or plasma technologies [19]. The remediation and/or removal of toxic heavy-metal contaminants (e.g., Hg, Pb, Cd) can be partially addressed by using traditional sorbent materials such as ceramic oxides, although these materials will bind metal ions nonspecifically and can easily be saturated with ubiquitous species (e.g., Ca, Mg, Zn) [19]. Another weakness of traditional ceramic oxide sorbent materials is that metal ion sorption to the surface is a reversible process. Therefore, a functionalized sorbent material with a high chemical specificity that is capable of permanently sequestering the target analytes from the contaminated water system is needed [19, 20]. An ideal sorbent material candidate should have rapid kinetics for sorption of the analyte, while the interaction between the sorbent and analyte should be effectively irreversible in all but specific applications where analyte release is desirable. In addition, sorbent materials that enable a more sensitive detection for a wide variety of analytical methods through separation and preconcentration prior to analysis are needed [6]. These types of materials would allow the analysis of complex samples containing small amounts of analyte, without the high background signals typically associated with environmental samples.

Magnetic nanoparticles have the potential to meet many of the above-mentioned needs for the preconcentration, removal, and detection of both environmental and biological contaminants. These materials have a unique property – namely, superparamagnetism – that arises from their nanoscale single magnetic domain structures [17]. Superparamagnetic behavior manifests itself in nanoparticles that are smaller than the critical diameter, which is both material- and temperature-dependent. Throughout this chapter, the predominant topic of discussion will be iron oxide nanoparticles with diameters ranging from ~5 to 20 nm, which falls within the established critical diameter for this material (~15–20 nm) [17]. From a practical standpoint, a superparamagnetic nanoparticle has little to no remnant magnetization after exposure to a magnetic field, and low to no coercivity (the field required to bring the magnetization to zero); this means that such nanoparticles will not agglomerate magnetically at room temperature [17]. This is a significant factor for sensing applications, where it is desirable for the nanoparticles to be well dispersed in the sample matrix and easily manipulable by an applied external

magnetic field. By exploiting not only the ability to remove magnetic nanoparticles from solution with an external field, but also the ability to tailor the surface functionality of the nanoparticles through synthetic means, it is possible to both separate and detect – with great sensitivity – a wide range of analytes. In this chapter, attention will be focused on the attachment of small molecules, polymers, and biomolecules (e.g., nucleic acids and proteins) for the purposes not only of separating the target analyte from complex samples containing interferents, but also of detecting them when the separation is complete. Some selected examples will also be presented of the application of functionalized magnetic nanoparticles for sensing and detection. Thus, the aim is to demonstrate the efficacy and future potential of magnetic nanomaterials for the effective preconcentration and sensing of environmentally relevant analytes from complex matrices such as river, ground, and ocean water.

9.2
Synthesis and Functionalization of Magnetic Nanoparticles

9.2.1
Synthetic Strategies for Magnetic Metal Oxide Nanoparticles

For the majority of sensing applications described in this chapter, the selection of a magnetic nanomaterial containing specific attributes to enable the best sensing performance is vital. Variations in nanoparticle core size, shape, and surface functionality may often have dramatic effects on the performance of the material in sensing applications. A wide range of synthetic methods is available to produce nanoparticles with properties desirable for use in separation and preconcentration applications [4, 5, 14, 16, 17, 21–24]. Such properties include:

- An ability to specifically functionalize the nanoparticle with small molecules or biological molecules so that they have a chemical affinity toward the analyte of interest.
- A high magnetic susceptibility, so that they might be easily captured or manipulated after being placed in contact with the sample of interest.
- A high dispersibility in the sample of interest (typically aqueous systems).
- Paramagnetic or superparamagnetic characteristics to prevent any irreversible magnetic agglomeration of the nanoparticles in solution, while still enabling magnetic recovery and manipulation.

Iron oxide nanoparticles (Fe_3O_4 and γ-Fe_2O_3) have shown the most promise as potential environmental magnetic sensing materials, as the synthesis, tuning of physical properties, and surface functionalization of these materials have been so well established. With this in mind, details of the more common methods of iron oxide nanomaterials synthesis have been summarized here, with a special

emphasis placed on those methods that allow for the most versatility in tuning the characteristics of the prepared nanomaterials, particularly for sensing applications. The most frequently described methods are summarized in Table 9.1.

9.2.1.1 **Coprecipitation**

The synthesis of iron oxide nanoparticles using the coprecipitation method first described by Massart [25], is the simplest and most readily scaled synthetic approach. The precipitation of Fe_3O_4 (magnetite) nanoparticles is achieved by the addition of NaOH or NH_4OH to an aqueous solution of Fe^{3+} and Fe^{2+}, typically in a 2 : 1 ratio of the iron salts, to form Fe_3O_4 nanoparticles as described in Equation 9.1:

Table 9.1 Some common methods for preparing iron oxide nanoparticles.

Synthesis method	Chemical precursors	Benefits/Drawbacks	Reference(s)
Coprecipitation	Iron salts, base	↑ Rapid synthesis with high yield	[14, 25, 26]
		↓ Unprotected magnetite vulnerable to oxidation/ aggregation	
Hydrothermal	Iron salt, surfactant, high-b.p. reducing agent	↑ Narrow size distribution and good shape control	[27, 28]
		↑ Scalable	
		↓ Long reaction times	
High-temperature decomposition	Iron–organic complex, surfactant, 1,2-diol	↑ Good control of size and shape with high yields	[29–31]
		↑ Ability to easily make different mixed metal oxide nanoparticles	
		↓ Further steps required to make water-soluble	
Microemulsion	Oil/water/surfactant	↑ Control over particle size	[32–34]
		↑ *In situ* stabilization possible	
		↓ Poor yield and large amounts of solvent required	

$$2Fe^{3+} + Fe^{2+} \xrightarrow{8\,OH^-} Fe_3O_4 + 4H_2O \quad (9.1)$$

Adjustment of the ratios of Fe^{3+} to Fe^{2+}, the iron salt source (chlorides, sulfates, nitrates), the solution pH, and the presence of an organic stabilizing ligand will all have an effect on the final size, shape, dispersion, and stability of the Fe_3O_4 nanoparticles formed [14]. As unprotected Fe_3O_4 nanoparticles are vulnerable to oxidation, a controlled oxidation can be purposely carried out to form γ-Fe_2O_3 (maghemite) nanoparticles by dispersion in an acidic medium and heating in the presence of iron(III) nitrate. The γ-Fe_2O_3 nanoparticles obtained in this manner are more stable over a broader pH range and are more resistant to aggregation, although with a lower saturation magnetization than the Fe_3O_4 nanoparticles.

Preparations of iron oxide nanoparticles using this technique can generate superparamagnetic nanoparticles which range from 2 to 17 nm in diameter, simply by adjusting the various synthetic conditions [14]. The typical measured saturation magnetization of unfunctionalized Fe_3O_4 nanoparticles depends strongly on the overall size, and also appears to depend on the preparation temperature [26], although reported values are typically between 30 and 70 emu g^{-1}, slightly lower than the experimental value of 82 emu g^{-1} obtained for bulk Fe_3O_4. The specific surface area of nanoparticles of ~ 7 nm diameter is up to 124 $m^2 g^{-1}$, with higher values being obtained from smaller nanoparticles, albeit with the trade-off of lowered saturation magnetization values. Nanoparticles prepared using this method can be functionalized with a sensing moiety of interest either *in situ* or immediately following synthesis, and are described in more detail in Section 9.2.2.

9.2.1.2 **Thermal Decomposition**

The synthesis of magnetic nanoparticles using a thermal decomposition method offers the most versatility, as the technique allows for the greatest degree of control over the particle size, shape, size distribution, and crystallinity. An enhanced control over particle saturation magnetization and susceptibility is also possible, and has great importance for many sensing applications. The preparation of monodisperse Fe_3O_4 and γ-Fe_2O_3 by the high-temperature decomposition of an organic iron complex has been reported [29–31], where an iron precursor [e.g., Fe(III) acetylacetonate, Fe(II) oleate, $Fe(CO)_5$] is dispersed in a high-boiling solvent (e.g., benzyl, octyl, or phenyl ether) in the presence of a stabilizing surfactant (e.g., oleic or lauric acid) in an inert atmosphere. Sun *et al.* described the decomposition of Fe(III) acetylacetonate in the presence of oleic acid, oleylamine, and 1,2-hexadecandiol in either phenyl or benzyl ether. Under varying conditions of heating ramp rate and reflux times, nanoparticles of various sizes with a very narrow size dispersity were produced. This method of preparing nanoparticles can also be scaled up, with no effect on the quality of material produced. If larger particle sizes are desired, the smaller (4–6 nm-diameter) nanoparticles may be used as seeds in the synthesis of nanoparticles of up to 20 nm diameter.

Methods using an iron-oleate precursor have provided the ability to tune the particle size and shape by adjusting the ratios and chain length of the stabilizing surfactant to a synthesized iron-oleate complex [30, 35]. Particles obtained in this manner can range from 5 to 50 nm and may be spherical, cubic, or prismatic, depending on the conditions used, and with very narrow size dispersity, as shown in Figure 9.1. Typical reaction conditions yield ~40 g of material, and can be scaled up to produce even larger quantities.

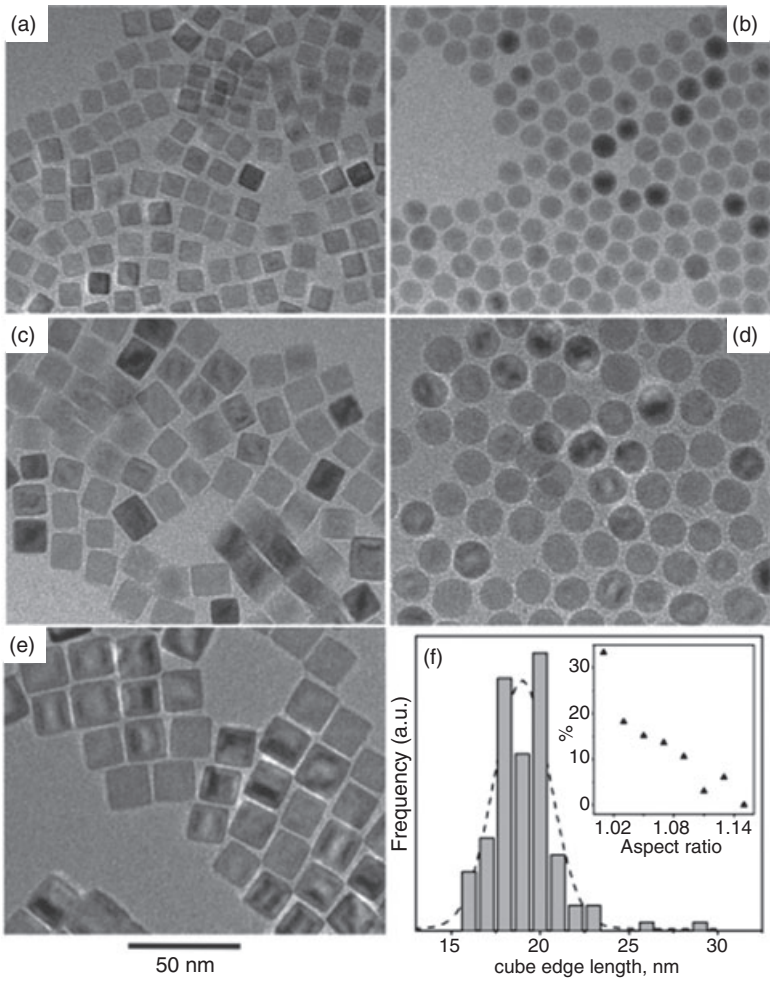

Figure 9.1 Transmission electron microscopy (TEM) images of monodisperse cubic (a,c,e) and spherical (b,d) iron oxide nanoparticles, and size histogram of cubic nanoparticles (f) using the iron-oleate precursor method. Reprinted with permission from Ref. [35]; © The American Chemical Society.

The stabilizing surfactants typically used for each of the described methods are fatty acids of at least six carbon atoms. Oleic acid is the most widely reported, as it is believed that the unsaturated bonds in the chain contribute to the particle's stabilization. Although other surfactants have often been reported, all of the nanoparticles generated using a high-temperature decomposition method typically yield nanoparticles with hydrophobic ligand shells. Regardless of the stabilizing ligand used, a water-soluble moiety is frequently desired, and modification of the as-prepared nanoparticles by thermal decomposition can be carried out in a number of ways (for more detail, see Section 9.2.2).

9.2.1.3 Other Synthetic Methods

As noted in Table 9.1, several other methods are available that generate superparamagnetic iron oxide nanoparticles. Although some of their drawbacks make them less desirable techniques, these routes are often preferred for *in situ* modifications over the multistepped, post-synthetic modification approach.

The *microemulsion technique* utilizes a ternary system of water, oil, and surfactant that allows for the formation of uniform-sized droplets in which the surfactant-stabilized nanoparticles are formed. The most commonly used method for synthesizing nanoparticles in this manner is that of *reverse microemulsion* (water in oil, w/o), where the hydrophilic acid head group is solubilized in the water droplet with the long-chain fatty acids dispersed in the oil phase. The size of the nanoparticles can be tuned by varying the water/oil/surfactant ratios. Under optimal conditions, the dispersity of these nanoparticles is narrow. Whilst the preparation of bare particles using this technique is less practical, either polymer or inorganic shells can be incorporated *in situ* using this technique (see Section 9.2.2). Again, the most significant drawbacks are the low material yield and the large volume of solvents required.

The *hydrothermal method* also has some benefits, particularly when tailoring the surface coatings of the nanoparticles. Here, nanoparticles are formed by placing all of the reactants (e.g., iron salt, 1,2-diol, stabilizing surfactant) into an autoclave and heating for a defined period of time, depending on the desired final nanoparticle size. Although this method is still fairly new, and very few reports of synthetic modifications have been made, it shows much promise for the formation of carbon-encased iron oxide (as described in more detail in Section 9.2.2).

9.2.2 Functionalization of Magnetic Nanoparticles

For most sensing applications, the nanoparticle's utility lies in both its magnetic character and its surface functionality. Although the preparation of iron oxide cores of various sizes, shapes, and magnetic susceptibility is relatively straightforward (see Section 9.2.1), further modifications are generally necessary to add the required affinity ligand to the particle surface for sensing applications. Surface modification can have a mild to dramatic effect on the core magnetic character; consequently, the selection of an appropriate surface coating must take these

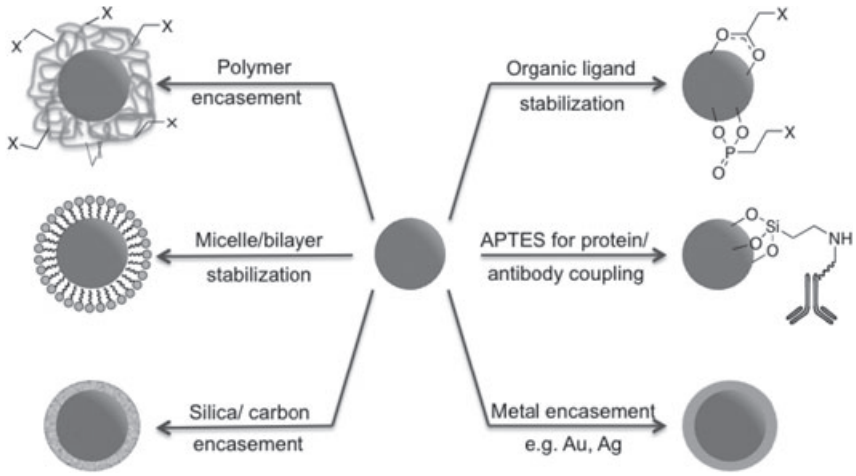

Figure 9.2 Some of the more commonly used methods for coating iron oxide nanoparticles for sensing applications.

requirements into account. Some of the more common methods of surface passivation are described in the following subsections and shown schematically in Figure 9.2.

9.2.2.1 **Organic Ligand Modification**

The use of organic ligands represents a straightforward method of imparting a specific functionality to the iron oxide surface. In this manner, the nanoparticle's solubility and functionality can be tuned to the application of interest. Ligands can be designed to take advantage of the iron oxide affinity toward carboxylates [6, 7, 36, 37], phosphonates [38–40], sulfonates [36, 41], silanes [42–44], hydroxamic acids [45], and 1,2-diols [46, 47]. The chosen ligand would contain one of these headgroups, as well as an ω-functionality at the periphery of the resulting ligand shell for binding to the analyte of interest. For example, in the sensing of biological materials this ω-functionality would contain an amine, thiol, or carboxylate to facilitate the coupling of antibodies or nucleic acids to the nanoparticle surface. In addition, some of these same functional groups (e.g., thiol) can be used to directly bind and detect environmental contaminants such as heavy metals.

Iron oxide nanoparticles (Fe_3O_4 or γ-Fe_2O_3) prepared using the coprecipitation method can be functionalized either *in situ* or immediately following synthesis. If a water-soluble moiety is desired, the *in situ* modification will require a simple addition of the ligand to the reaction flask (e.g., sodium citrate), followed by heating and subsequent purification of the product. Post-synthetic functionalization will require suspension of the iron oxide nanoparticles in an appropriate solvent and stirring, heating, or sonication [39, 43] in order to achieve attachment of the desired ligand.

If the nanoparticles are prepared by the high-temperature decomposition of an organic iron precursor complex, the as-synthesized nanoparticles can undergo simple ligand-exchange reactions, such that the surface ligand is replaced with the functional molecule of choice. This and similar methods are described elsewhere for an exhaustive number of specific functionalities [4, 14, 15, 17, 42]. More general methods can be selected based on the type of ligand desired. For example, a carboxylate for carboxylate exchange represents one of the more common methods, and allows for an exchange of the surface ligand using either monophasic or biphasic exchange conditions. Ligand-exchange reactions are typically carried out under stirring and/or mild heat, or sonication. Depending on the replacement ligand selected, the ligand exchange will usually occur when using a combination of solvents to promote miscibility of both the starting nanoparticle and the desired incoming ligand. If a solubility change is expected, a successful exchange is evident following purification based solely on the solubility of the resultant nanoparticles. An analysis of the final product, using Fourier-transform infrared (FT-IR) spectroscopy, will confirm successful ligand exchange.

9.2.2.2 Stabilization with Polymers

The polymer encasement of iron oxide nanoparticles is sometimes employed in the preparation of nanoparticles for sensing applications, as an appropriate polymer can greatly enhance dispersibility and biological compatibility, as well as prevent agglomeration of the iron oxide [48–50]. In most cases, polymer encasement leads to the formation of larger particles (often >100 nm in diameter) or very large aggregates, but the superparamagnetic character of the starting nanoparticles is retained. Some of the more commonly used polymers include polystyrene [51], poly(*N*-isopropylacrylamide) [51], poly(vinyl alcohol) [52, 53], poly(acrylic acid) [54], dextran [55], and starch [44], to name but a few.

The polymer encasement is carried out either post-synthetically in the case of thermal decomposition and some coprecipitation methods [53, 56], or *in situ* for other coprecipitation [57] and microemulsion [32] methods. Functional groups can be introduced into the polymer backbone itself, or onto the encasing polymer with further modification. This allows the desired functionality to be added, so as to render the particles useful for organic or environmental extraction. It is also possible to encase dyes into the polymer coating for added optical detection capabilities [8]. This typically involves attachment of the dye to the polymer backbone, or inclusion of the dye into the polymer matrix. By constructing these magnetic/optical polymer composite materials, it will be possible to provide sensitive optical detection platforms that seek to utilize the magnetic properties of the core nanoparticle for sample separation and preconcentration.

9.2.2.3 Inorganic Stabilization with Silica or Carbon

Stabilization of the magnetic core using an inorganic shell incorporates a variety of benefits not realized with organic stabilization. As organic ligands are only chemisorbed to the iron oxide surface, desorption of the passivating ligand is possible under certain conditions. Thus, it is often beneficial to coat the magnetic

sensing material with a chemically inert shell; some of the more commonly described inorganic coatings are listed in Table 9.2 and discussed in more detail in the following subsections.

The coating of magnetic nanoparticles with silica has many advantages, and is by far the most common inorganic coating method, in part due to its synthetic simplicity. Particles formed in this manner contain a high number of surface silanol groups, which allows advantage to be taken of the abundance of functional ligands which contain a siloxane headgroup. As the silica shell is chemically inert, nanoparticles coated and further functionalized in this manner are easily dispersed in solution, and serve as excellent candidates for sensing in low-pH media. Many methods have been reported for producing these core–shell materials [58–75], with the most common – the sol–gel process – typically being a modification of the Stöber method [59], which relies on a silicon alkoxide [e.g., tetraethoxysilane (TEOS)] as the silica source. Varying the concentrations of TEOS, ethanol, and ammonium hydroxide allows the silica shell thickness to be tuned. Many studies have described the effects of varying the concentration of each of these precursors on shell thickness, the degree of aggregation, and the subsequent effect on measured saturation magnetization associated with increased shell thickness. Deng *et al.* demonstrated the dramatic effect of shell thickness on the final saturation magnetization. Here, the size [monitored using transmission electron microscopy (TEM) and vibrating sample magnetometry (VSM)] showed a drop in saturation magnetization, from 55 emu g^{-1} for the uncoated Fe_3O_4, alongside the $Fe_3O_4@SiO_2$ values which decreased from 7.5 to ~1 emu g^{-1} as the shell thickness increased with the greater volumes of TEOS used [60]. Thus, it is the prerogative of the research group to tune the shell thickness to a level which is appropriate for the application, without losing the magnetic characteristic that renders nanoparticles useful in their desired sensing platform.

Despite the loss in magnetic character, one benefit of using an optically transparent material such as silica (as opposed to another inorganic material) is the ability to incorporate dye molecules [58, 76, 77], luminescent inorganic complexes [78, 79], or quantum dots (QDs) [80–82] into the silica matrix, thus adding another dimension to the material for broader detection applications. For example, Yu *et al.* described the encasement of iron oxide nanoparticles in silica, the attachment of a terbium ion, and then further encasement with silica. Although the resultant nanoparticles retained some magnetic character, they also contained a luminescent lanthanide center [78]. The dispersion of these nanoparticles, while retaining magnetic characteristics when exposed to UV and broad-spectrum light, is shown in Figure 9.3; in addition, both scanning electron microscopy (SEM) and TEM images of the materials clearly show the iron oxide core to be surrounded by a uniform silica shell and a luminescent border.

Chih-Wei Lai *et al.* have also reported a microemulsion method for the generation of an iridium complex which was incorporated into the silica shell [79]. The resultant materials were both magnetic and luminescent, with a final core–shell composite diameter of ~80–100 nm.

The carbon-coating of magnetic nanoparticles may have potential in a number of environmental and biological sensing applications, as the carbon shell affords

Table 9.2 Common inorganic coatings for magnetic nanoparticles.

Inorganic coating material	Conditions	Benefits/Drawbacks	Reference(s)
Silica	Sol–gel/ Stöber method, reverse micelle	↑ Good dispersion in aqueous solutions	[17, 58–61]
		↑ Surface silanols for easy siloxane modification	
		↑ Ability to incorporate dyes and QDs	
		↓ Drastic loss of core magnetic character	
Carbon	Hydrothermal, pyrolysis	↑ Biocompatible	[62–64]
		↑ High chemical and thermal stability	
		↓ Few synthetic methods/lack of understanding of formation mechanism	
Gold	Microemulsion, solution based reduction	↑ Chemical inertness	[65–68]
		↑ Thiol surface ligand modification	
		↑ Minor loss of core magnetic susceptibility	
		↑ Surface plasmon peaks for optical detection	
Silver	Solution-based reduction	↑ Surface plasmon peaks for optical detection	[67, 69, 70]
		↓ Difficulty functionalizing the Ag surface	
CdSe or CdS	Solution-based shell growth	↑ Tunable fluorescent shell	[71–73]
		↓ Synthetically challenging	
		↓ Subject to photobleaching	
		↓ Loss of core magnetic susceptibility	

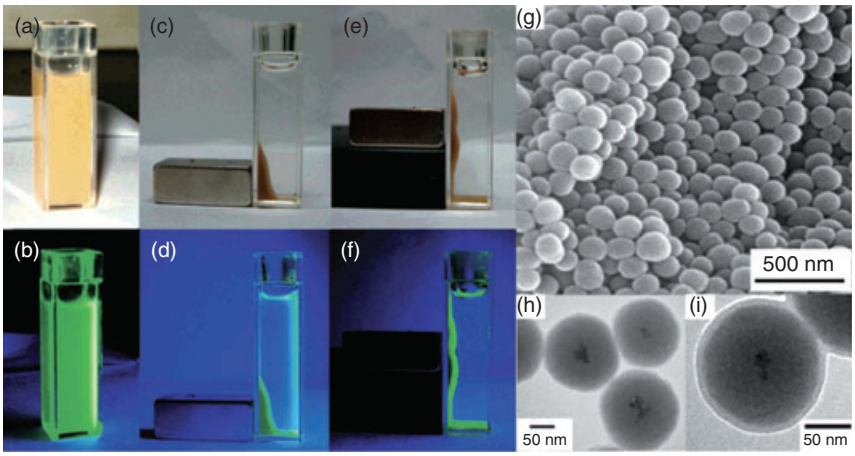

Figure 9.3 Magnetic/luminescent nanoparticles in white light (a,c,e) and ultraviolet (b,d,f) illumination, either dispersed (a,b) or close to a magnetic field (c,e,d,f). Scanning electron microscopy (g) and TEM (h,i) of the Fe_3O_4@SiO_2 core–shell materials with the visible luminescent band in (i). Reprinted with permission from Ref. [78]; © The American Chemical Society.

the magnetic material a greater stability in harsh chemical and physical environments (e.g., low- or high-pH waste streams). Although, until recently, the synthesis of these materials has been expensive and required specialized equipment, more recent reports have described the development of synthetic techniques to produce core–shell material, using much less specialized equipment [62, 83]. As an example, Wang *et al.* [63] described a solution-based method that involved the preparation of oleic acid-stabilized iron oxide nanoparticles for incorporation into carbon spheres; this method employed hydrothermal techniques with a carbon source derived from glucose. By carefully controlling the ratio of nanoparticles to glucose, it was possible to create carbon spheres of approximately 100–200 nm diameter, into which iron nanoparticles were embedded. Likewise, Xuan *et al.* [64] described a one-step method using an iron salt, urea, and glucose in an autoclave to generate a 100 nm ferromagnetic magnetite core with a ~30 nm carbon shell, as shown in Figure 9.4. Although the particles exhibited a ferromagnetic behavior, with a saturation magnetization value of ~42 emu g^{-1} (this was less than the bulk material, but a less dramatic loss than seen with silica encasement), their increased stability and ease of functionalization compared to the non-core–shell materials suggested that they might be potentially useful materials for environmental sensing applications.

9.2.2.3.1 **Precious Metal Encapsulation** Encapsulation of the magnetic nanoparticle core with a metal coating can have a variety of benefits, as the loss of magnetic behavior seen with silica coating (and, to a lesser extent, with carbon coating) does

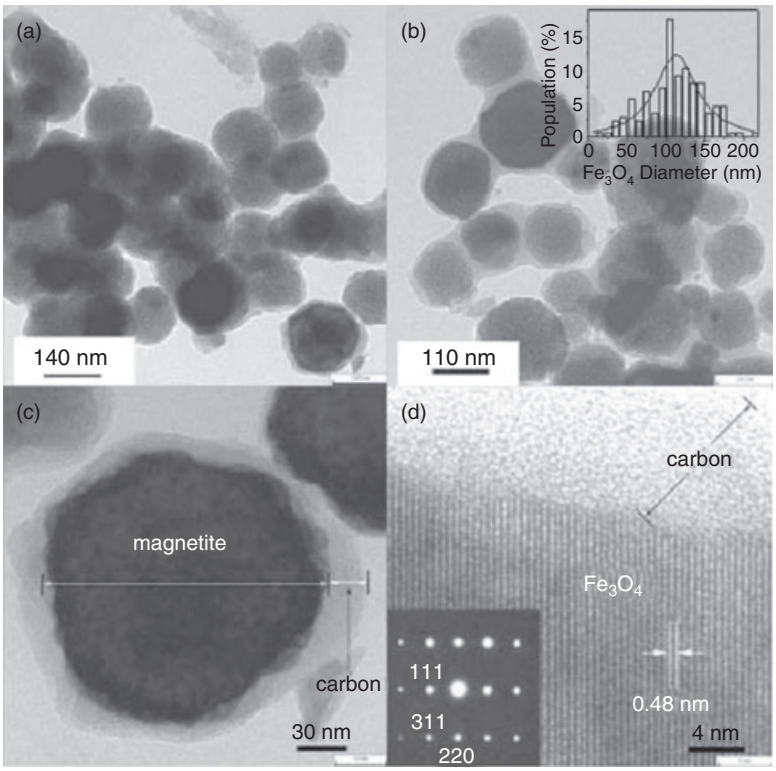

Figure 9.4 Transmission electron microscopy (TEM) images of carbon-coated Fe_3O_4. (a,b) Low magnification; (c) High magnification; (d) High-resolution TEM image of a typical Fe_3O_4@C particle. Reprinted with permission from Ref. [64]; © IOP Publishing.

not always occur when select metals are used. Additionally, the metal itself can aid in the sensing application. For example, when gold or silver is used to coat the Fe_3O_4, small changes in the dielectric environment close to the particle surface can result in wavelength shifts in the surface plasmon peaks, making such particles excellent sensing materials for biological applications.

The coating of iron oxide nanoparticles with gold has the advantage of an increased choice of functional ligands by exploiting the strong gold–thiol interaction, the plasmonic peak at 520 nm, and also the reduced drop in overall saturation magnetization of the core–shell magnetic nanoparticles. Numerous methods have been developed for the preparation of Fe_3O_4@Au core–shell materials using microemulsion techniques [84, 85], citrate reduction [86, 87], the deposition of the noble metal to the Fe_3O_4 surface by heat and/or sonication [69], and the deposition of Au nanoparticle seeds onto the iron oxide nanoparticle surface [65, 66]. Most of these methods allow the gold shell thickness to be tuned simply by adjusting

the ratio of the iron precursor and the gold source. For example, Xu *et al*. described the use of $HAuCl_4 \cdot 3H_2O$ [67] to coat oleic acid-stabilized Fe_3O_4 nanoparticles by stirring the gold salt in the presence of the nanoparticles and oleylamine for 20 h at room temperature. The gold shell thickness prepared using this method was ~1 nm, with subsequent gold layers being grown up to 3.5 nm. The resultant nanoparticles could be further functionalized with an organic ligand, or the Ag could be nucleated and grown over the gold. An alternative method describing the growth of a gold shell on an iron oxide core utilizes $Au(OOCCH_3)_3$ [68] as the gold source, with the coating being achieved by heating the reactants at a high temperature for 1.5 h. In this case, the resultant gold shell thickness was ~0.7 nm.

Although less ubiquitous than silica or gold coating, a silver shell on the Fe_3O_4 core also offers the combination of a magnetic core with a surface plasmon resonance at ~400 nm. Several methods have involved silver encasement, including microemulsion [88], sintering [89], and various solution-based growths on iron oxide surfaces [69, 70, 90]. Tang *et al*. proposed the use of core–shell materials for a biosensing application, where the Fe_3O_4@Ag were prepared using the heating and sonication method originally described by Mandal *et al*. to generate core–shell materials with varying shell thicknesses. The nanoparticles prepared in this manner were further functionalized with carcinoembryonic antigen (CEA), a common cancer protein marker, by agitation in the presence of the nanoparticles at 4 °C. The nanoparticles produced showed absorption shifts at different stages of their modification, which simplified their characterization; electrochemical sensing could then be used to detect the specific presence of cancer cells.

9.2.2.4 Less Common Methods of Passivation

More recently, several groups have described the formation of a QD shell grown over a magnetic core seed. Core–shell structures of Co/CdS [71], FePt/CdS [72] and/or FePt/CdSe [91] have each shown potential for generating bifunctional materials for sensing applications. When a Co core was used, there was a complete loss in saturation magnetization, yet the FePt core appeared to retain its magnetic character following coating with CdS or CdSe [72, 91]. Since this method is still in its infancy, there remain many synthetic challenges to creating functional materials of this core–shell composition; however, the promise of a magnetic/fluorescent hybrid material with tunable magnetic and optical properties represents an intriguing topic for many sensing applications.

9.3 Magnetic Nanoparticles for the Separation and Detection of Analytes

9.3.1 Chemical Separations with Functionalized Magnetic Nanoparticles

The subject here is the use of functionalized magnetic nanoparticles as sorbent materials for chemical, biological, and heavy-metal contaminants, that enable

sensitive detection among relevant environmental and clinical samples. Whilst the predominant use for these types of functionalized nanomaterials relates to biosensors in the clinical setting, much attention has also been paid to the benefits of using nanomaterial-enhanced biosensor-type systems (i.e., those which use biomolecules as affinity reagents or recognition elements) for the detection of environmentally relevant analytes such as bacteria, pesticides, and viruses [12]. These types of material provide the means to separate analytes from a complex sample and, in cases where a trace sensing of the contaminants is desired, they may also serve as a preconcentration material for sensor enhancement.

A fundamental approach for improving any analytical method is to selectively separate the analyte(s) from the sample matrix and to concentrate them into a smaller volume prior to measurement. The preconcentration of analytes before assay allows improvements to be made to the sensitivity, selectivity, and speed of the analytical process. One approach to improving any analytical method is to separate the analyte(s) from the sample matrix and to concentrate them into a smaller volume prior to measurement. Figure 9.5 illustrates the general analytical process of sample preconcentration (steps 1–3) and detection (step 4) using sorbent materials in a generic sense.

Preconcentration represents an ideal application for functionalized magnetic nanoparticles. Once dispersed in solution, the nanoparticles can rapidly contact high volumes of solution (Stage 1), selectively capture target analytes (Stage 2), and then be magnetically recovered and manipulated by the application of a relatively strong (often >1 T), but easy to generate, magnetic field (Stage 3). The functionalized magnetic nanoparticles may also provide a magnetically controllable sorbent material for solid-phase extraction (SPE). Previously, it has been shown that the

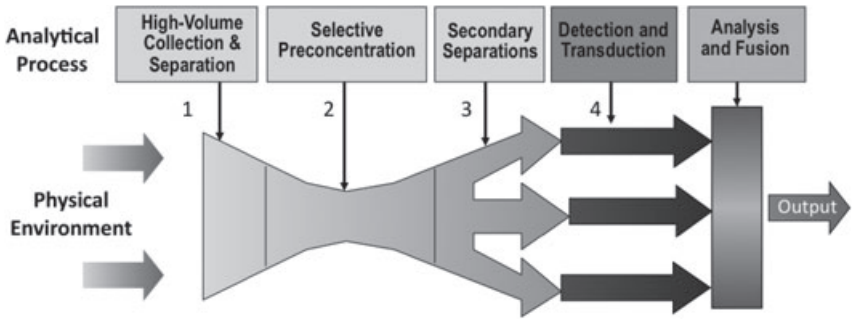

Figure 9.5 Schematic showing the general analytical process used to preconcentrate and detect low levels of analytes in environmental samples. In steps 1–3, the sorbent material (i.e., functionalized magnetic nanoparticles) are used to first bind a target analyte and then, through the application of an external magnetic field, separate it from other constituents of complex samples. In step 4 and beyond, the analyte is measured using the desired analytical method, prior to sending data output that signifies the presence of the intended target in the sample. As can be seen from this schematic, magnetic nanoparticles can play a variety of roles in going from sample to answer using solid-phase extraction and/or preconcentration.

intrinsic high surface area arising from the nanoscale dimensions of these materials, coupled with the ability to impart specific surface functionalization, renders magnetic nanoparticles very effective for SPE [92]. In addition, the magnetic nanoparticles have the advantage that very small quantities of material are required to accomplish an effective preconcentration (Stages 1–3) and detection. Once the preconcentration is complete, the analyte can be stripped from the SPE material for assay as appropriate (e.g., via acid, organic solvent, thermalization, etc). Alternatively, for some applications the SPE material can be assayed directly [92].

The amount of analyte extracted by the SPE material is limited by the magnitude of the partition or distribution coefficient (K_d) of the analyte between the sorbent material and the sample matrix, since at trace levels saturation does not become an issue. The K_d of a sorbent material is simply the mass-weighted partition coefficient between the solid sorbent phase and the liquid supernatant phase, as described in Equation 9.2:

$$K_d = \frac{(C_0 - C_f)}{C_f}\frac{V}{M} \tag{9.2}$$

where C_O and C_f are the initial and final concentrations in the solution of the target analyte, V is the solution volume (in ml), and M is the mass of the sorbent (in g) [7]. By employing high-surface-area (typically $>100\,m^2\,g^{-1}$), dispersible, and specifically functionalized magnetic nanoparticles, it is possible to drive the interaction of the nanoparticle sorbents with the analytes in the sample, thus effectively facilitating both separation and preconcentration. The higher the K_d value, the better the SPE material will function for trace-level assays. Large surface areas (usually $>100\,m^2\,g^{-1}$) and high-affinity surface chemistries provide the large K_d values required for effective SPE. The surface chemistry of the SPE material will determine which analytes it will be selective for. An adjustment of the surface chemistry of the SPE material then allows its application to a different class of analytes or functions in different matrices. A summary of the K_d values for a variety of different SPE materials, including functionalized superparamagnetic nanoparticles, in filtered ground water is shown in Table 9.3 [7].

The K_d values of metal ions measured on different sorbent materials containing thiol ligands and capable of binding heavy metals are summarized in Table 9.3. In terms of K_d value, the functionalized magnetic nanoparticles (referred to as DMSA-Fe_3O_4) are significantly superior to commercial GT-73 and activated carbon (Darco KB-B) for capturing Hg, Cd, Ag, Pb, and Tl [7]. The affinity of the functionalized magnetic nanoparticle for As was more modest than for other metals, and similar to that of unfunctionalized magnetic nanoparticles (referred to as Fe_3O_4); this indicates that the thiol ligand shell has very little impact on As capture, which in turn supports the irreversible adsorption of As onto the iron oxide core material previously reported by Yavuz *et al.* [93]. Nevertheless, the massive improvement in K_d values clearly shows the excellent utilization of the ligand shell for improved SPE of the target analytes. When compared to the commercial sorbents tested, the functionalized magnetic nanoparticles proved to be outstanding sor-

Table 9.3 K_d (ml g^{-1}) of metal ions on selected sorbents.

Sorbent[a]	Final pH	Cobalt	Copper	Arsenic	Silver	Cadmium	Mercury	Thallium[b]	Lead
Fe_3O_4-DMSA	6.91	3000	270000	5400	3600000	10000	92000	14000	2300000
Bare Fe_3O_4	6.93	1600	7400	5800	13000	2400	16000	4000	78000
SH-SAMMS	6.80	430	1700000	950	67000000	66000	1100000	15000	350000
GT-73	6.76	890	6300	1200	16000	1500	10000	2200	41000
Darco KB-B	6.90	790	26000	750	27000	1300	31000	21	190000

a The liquid-to-solid ratio (L/S) equals 10000 ml g^{-1} in 0.45μm filtered groundwater.

b Thallium added as Tl^{+1}.

bents for Pb, Hg, Cd, Cu, and Ag [7]. In the remainder of this section, we will discuss examples illustrating the use of functionalized magnetic nanoparticles in environmentally relevant detection applications.

9.3.2
High Magnetic Field Gradient Separation and Preconcentration

The concepts of selective capture of a target analyte by a magnetic nanoparticle and subsequent rapid manipulation of the analyte/nanoparticle complex using an applied magnetic field, have been well developed over the past two-plus decades [20]. Most notably, for biological applications magnetic nanoparticles and microparticles (formed primarily from composites of micron-sized polymer beads and nanoparticles) have been used for the better part of the past 20 years for high-gradient magnetic cell-sorting applications, as first reported by Miltenyi *et al.* [94]. Since this seminal report was made, numerous groups have continued development of the use of magnetic nanoparticles for cell sorting within a wide range of molecular biology applications [95–107]. In addition to the more fundamental studies in this field, a commercial line of products that employ biodegradable functionalized superparamagnetic nanoparticles for the separation of cells of all types is marketed under the trade name MACS (http://www.miltenyibiotec.com/en/default.aspx). The concept of high-gradient magnetic cell separation and sorting is shown schematically in Figure 9.6.

As can be seen from Figure 9.6, the magnetic nanoparticle typically plays the role of a tool designed to overcome the mass transport limitations that plague

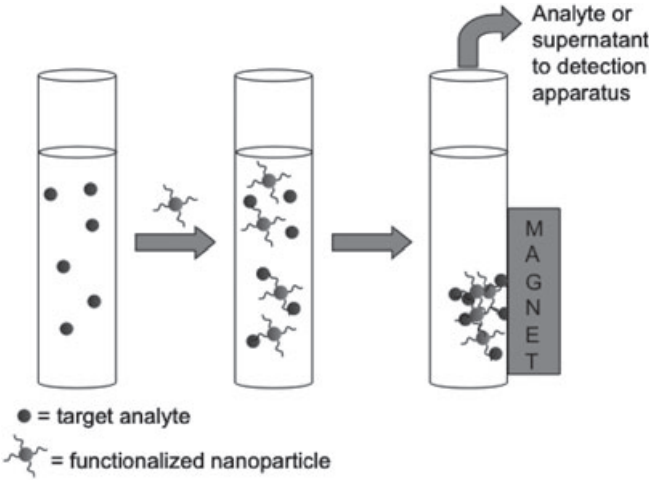

Figure 9.6 Schematic diagram representing the concept of high-field magnetic separation and sorting of analytes. The sample containing the target analyte (left) is exposed to the specifically functionalized magnetic nanoparticle containing an affinity ligand such as a protein, small molecule, or nucleic acid (middle). Then, after a period of incubation, an external magnetic field is applied to separate the nanoparticle/analyte complexes from the sample (right). This effectively enables the selective removal of a target analyte from the sample background, allowing for sensitive detection.

surface-bound sensor systems by attaching to an analyte; this makes the resultant analyte–nanoparticle complex responsive to an applied magnetic field. By using functionalized magnetic nanoparticles and a relatively high-strength magnetic field, it is possible to rapidly pull the bound analytes from solution, independent of any of the other background constituents that might potentially interfere with their processing (e.g., induction and growth of cells) or detection, using a range of techniques.

Studies based on the high-gradient preconcentration and separation methods discussed above have been conducted to target a wide range of analytes that have relevance in both environmental and clinical settings. These include: the separation and sorting of bacteria [102, 105, 107], viruses [104, 108], single cells [96, 97, 99–101, 103, 106], proteins [106, 109, 110], and nucleic acids [111–113]. In most of these cases, the target analytes are bound to the nanoparticles solely for removal from solution, and in order to separate them from background interferents (e.g., proteins, cells, and nucleic acids) common in biological samples. In addition to these examples, a number of studies have shown that magnetic nanoparticles also have potential as analyte preconcentrators for environmental remediation and trace detection sensor systems [20].

In their ongoing studies, the present authors have shown that functionalized superparamagnetic nanoparticles can be effectively dispersed in aqueous environmental samples and sequester a wide variety of analytes, including heavy metals

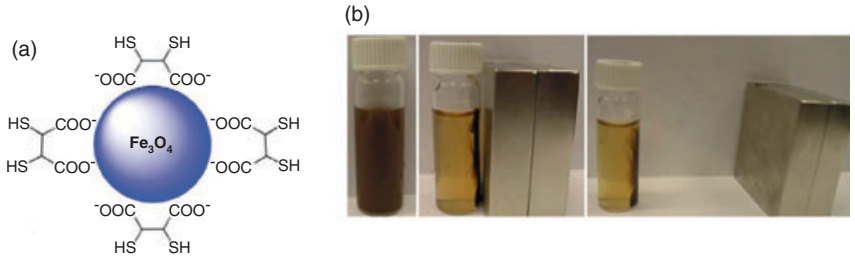

Figure 9.7 (a) Schematic of a DMSA-modified Fe_3O_4 nanoparticle; (b) Removal of the nanoparticles from the liquid phase using NdFeB magnets; initial solution (left panel), after 10 s with the magnet (middle panel), and when the magnet was moved to a distant position (right panel). Reprinted with permission from Ref. [7]; © The American Chemical Society.

[7, 114]. Specifically, thiol-modified Fe_3O_4 nanoparticles that are approximately 6 nm in diameter have been employed to remove Hg, Ag, Pb, Cd, and Tl from natural waters (i.e., river, ground, and ocean water). The scheme is illustrated in Figure 9.7.

The magnetic nanoparticles used in this study had the distinct advantage that they were highly dispersible in aqueous media, but could be removed with relative ease by exposing the sample to a magnetic field. In this case, the field strength used (~1.2 T) was generated by a NdFeB rare earth magnet [7]. By using this set-up, it was shown that the nanoparticles could remove over 99 wt% of 1 mg l^{-1} Pb within 1 min of contact time, and that they have a Hg capacity of over 227 mg g^{-1} (a 30-fold larger capacity than conventional, resin-based sorbents) [7]. In order to determine the efficacy of extraction of heavy metals by the magnetic nanoparticles, a variety of measurements to determine the distribution coefficient (K_d) were made, as summarized in Table 9.3. The data in Figure 9.8 illustrate that, at near-neutral pH in river water, the thiol-modified magnetic nanoparticles proved to be outstanding sorbent materials for soft metals such as Hg, Ag, Pb, Cu, and As ($K_d > 50\,000$), and also a good sorbent for harder metals such as Cd, Co, and Tl [7]. When the metals were extracted, the trace detection of heavy metal analytes was carried out using inductively coupled plasma-mass spectrometry (ICP-MS) after contact with the magnetic nanoparticles [7].

Studies conducted by other groups have shown similar characteristics of functionalized magnetic nanoparticles and microparticles modified with a wide variety of affinity ligands for the extraction of heavy metals from environmental samples [20, 53]. However, due to the need to fully understand the behavior of the materials when dispersed in the environment (e.g., a tendency towards aggregation and/or decomposition, as well as mobility), this field remains relatively undeveloped with regards to the use of superparamagnetic nanoparticles between 5 and 20 nm in diameter. Although more references are available relating to the use of microparticles (mostly constructed from nanoparticle/polymer composites), these

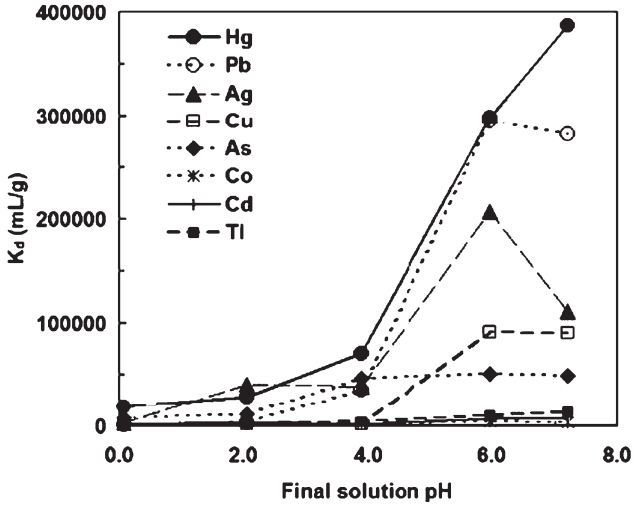

Figure 9.8 Effect of pH on K_d values, measured in HNO_3-spiked unfiltered river water [liquid/solid ratio (L/S) = 10^5]. Reprinted with permission from Ref. [7]; © The American Chemical Society.

materials fall well outside the size range that is traditionally considered a nanomaterial (i.e., their sizes are >100 nm) [20]. In addition to magnetic nanoparticles, a great deal of attention has been paid to nanoporous materials such as silica ceramics (pore sizes ~3–6 nm, but particle size on the order of microns) for the removal and remediation of contaminants from natural waters due to their high surface area and relative ease of functionalization [7, 19, 115–117]. However, although these materials serve as outstanding sorbents for contaminants, they suffer from intrinsic mass transport limitations of moving large volumes of water to the sorbent material. Alternatively, other high-surface-area sorbents that can be surface functionalized and are more readily dispersible in aqueous systems, yet can be easily recovered once bound to the target analyte, offer significant advantages for many applications. Materials such as magnetic nanoparticles [7] and polymer/nanoparticle composites [118–121] offer unique capabilities for magnetically directed separation and sensing processes.

9.3.3 Electrochemical Detection Enhanced by Magnetic Nanomaterials for Preconcentration

Sorbent materials of all types play a role in the binding, separation, and removal of target analytes from complex samples, and may also enable enhancements in the limits of detection for a wide range of sensor systems. Primarily, magnetic nanoparticles have been used in a preconcentration capacity in electrochemical

and optical (i.e., fluorescent) detection schemes. Their role is to bind the target analyte in solution and rapidly bring it to the sensor surface, or to separate it from the background interferents upon the application of an external magnetic field. In most cases, an applied magnetic field from either an electromagnet or permanent magnet is typically employed to capture the nanoparticle/analyte complex from solution prior to analysis [6, 13, 122, 123].

The present authors' group has demonstrated the use of both magnetic [6] and nonmagnetic [114] high-surface-area sorbent materials to enhance the electrochemical detection of toxic heavy metals from natural waters. The sorbent materials, which were either functionalized magnetic nanoparticles or mesoporous silica, were modified with a wide range of thiol-containing organic molecules that possesses a high affinity towards heavy metals (e.g., Hg, Pb, Cd), and were placed or collected at an electrode surface (Figure 9.9) [6, 114]. By using these high-surface-area sorbent materials, it has been possible to demonstrate the sensitive electrochemical detection of environmentally relevant heavy metals (e.g., Pb, Hg, Cd) in complex environmental (e.g., river water) and clinical (e.g., urine) samples [6, 114]. Superparamagnetic Fe_3O_4 nanoparticles functionalized with dimercaptosuccinic acid (DMSA) (similar to those discussed above) were used to first bind the heavy-metal contaminants from complex samples, and then subsequently to carry them to the surface of a magnetic electrode (see Figure 9.9) [6].

By using an applied magnetic field to remove the target analytes from solution prior to electrochemical analysis, the analytes are effectively isolated from the huge number of potential interferents present in complex sample matrices. In using this system, two of the biggest problems that have prevented the widespread

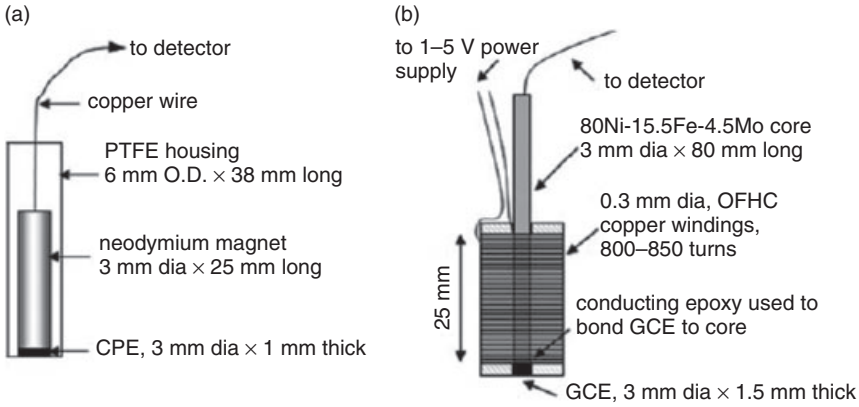

Figure 9.9 Schematics of (a) the magnetic electrode and (b) the electromagnetic electrode which preconcentrate metal ions using superparamagnetic nanoparticles. Reprinted with permission from Ref. [6]; © The Royal Society of Chemistry (RSC).

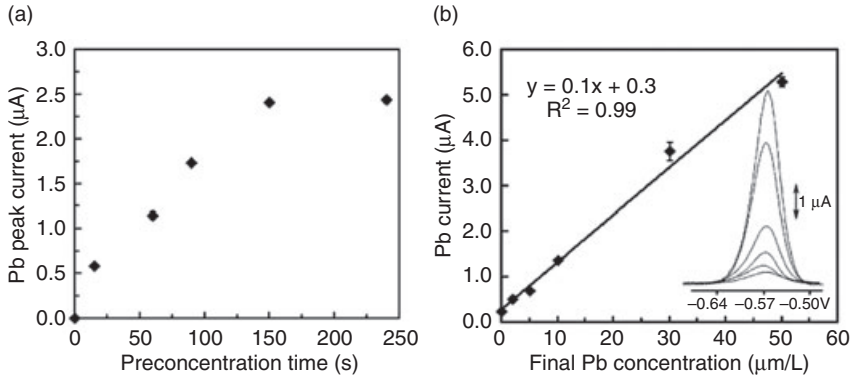

Figure 9.10 (a) Signals of 10 ppb Pb measured at DMSA–Fe_3O_4-magnetic sensors in samples containing 25 vol.% rat urine with varied preconcentration time; (b) Linear Pb calibration curve measured at DMSA–Fe_3O_4-magnetic sensors in Pb-spiked samples containing 25 vol.% rat urine. Reprinted with permission from Ref. [6]; © The Royal Society of Chemistry (RSC).

adoption of electrochemical sensors for the analysis of metal ions in biological samples have been successfully overcome, at least to some extent: (i) binding of the target metals to proteins present in the sample matrix, leading to a lowered signal response; and (ii) electrode fouling caused by proteins. As shown in Figure 9.10, this approach has permitted the successful measurement of Pb concentrations in rat urine samples (25%, v/v) as low as 10 ppb, with as little as 20 s preconcentration (after an optimal 90 s preconcentration period, the detection limit was 2.5 ppb Pb).

Further, the data in Figure 9.11 show that the magnetic nanoparticles are also capable of enabling the detection of multiple heavy metals (i.e., Cd, Pb, Cu, Ag) from a variety of natural waters (river and ocean) with a preconcentration time of only ~2.5 min.

In addition to these studies, several other groups have reported the use of magnetic nanoparticles in the electrochemical analysis of other environmentally relevant targets other than heavy metals, such as proteins and nucleic acids [13, 15, 124]. At this point, the reader is directed to a number of recent reviews on the application of high-surface-area magnetic nanomaterials for the detection of biological analytes [13, 123]. It is important to note here that, even though the bulk of the studies conducted in this area was aimed at clinical applications, the detection of biological species is of paramount importance for environmental sensing, due to the fact that many common environmental contaminants are of biological origin. A recent example in which magnetic nanomaterials were used to detect a protein biomarker to pesticide exposure utilizes a similar magnetic electrode as described above (see also Figure 9.9) [125]. In these studies, the magnetic particles

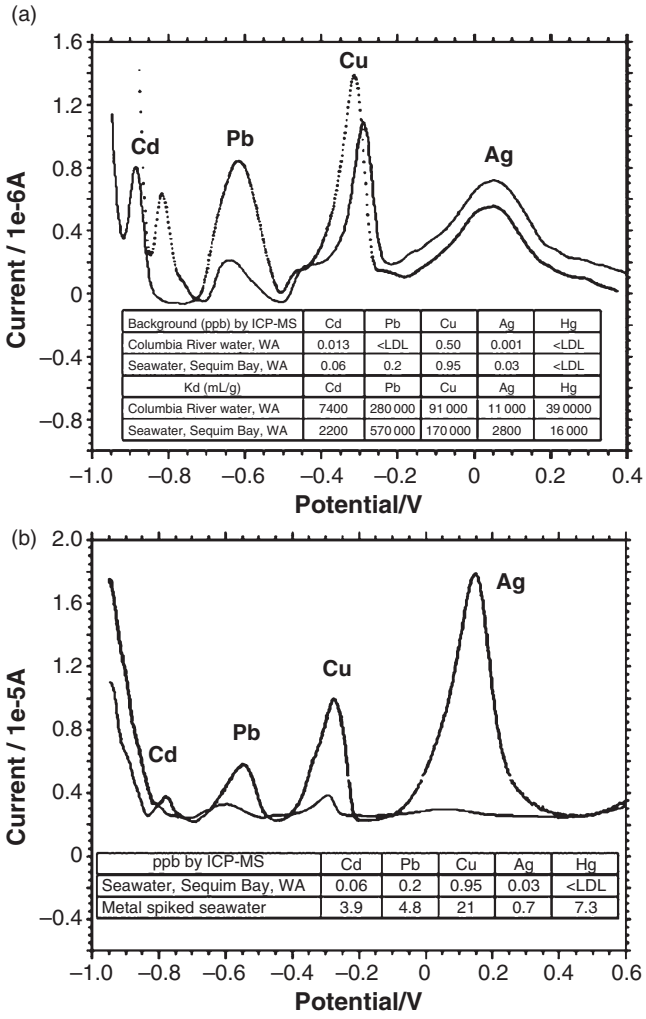

Background (ppb) by ICP-MS	Cd	Pb	Cu	Ag	Hg
Columbia River water, WA	0.013	<LDL	0.50	0.001	<LDL
Seawater, Sequim Bay, WA	0.06	0.2	0.95	0.03	<LDL
Kd (mL/g)	Cd	Pb	Cu	Ag	Hg
Columbia River water, WA	7400	280 000	91 000	11 000	39 0000
Seawater, Sequim Bay, WA	2200	570 000	170 000	2800	16 000

ppb by ICP-MS	Cd	Pb	Cu	Ag	Hg
Seawater, Sequim Bay, WA	0.06	0.2	0.95	0.03	<LDL
Metal spiked seawater	3.9	4.8	21	0.7	7.3

Figure 9.11 Sensor measurements of (a) background metal ions in seawater (dashed line) and river water (solid line) and (b) background metal ions (thin line) and metals spiked (thick line) in seawater, after 150 s of preconcentration time. The inset tables show metal concentrations, measured with ICP-MS, and distribution coefficients of multiple metal ions (L/S of 0.01 g l^{-1} DMSA–Fe_3O_4, initial metal concentration 500 ppb each, pH of 7.2 for river water and 7.64 for seawater). Reprinted with permission from Ref. [6];

were bound with gold nanoparticles to provide an extremely responsive material for the electrochemical analysis [122, 125]. These composite nanomaterials were then used to bind and separate protein biomarker targets from solution, followed by their detection, without the need for any amplification that is typically important in many protein-detection systems [122, 125].

9.3.4
Analyte Detection Using Magnetic Nanoparticles through Nonelectrochemical Methods

The use of magnetic nanoparticles in optical detection scenarios has also received much recent attention, with the reviews of Corr *et al.* and Katz *et al.* examining at great depth the formation of nanomaterial composites for biological detection and biomedical applications [8, 15]. However, it is important to note that the bulk of reported detection schemes center on the use of magnetic nanoparticles in electrochemical assays. This is because, even when all of the potential benefits associated with using a fluorescent nanomaterial that also is magnetic (e.g., ability to separate bound analyte from a sample and monitor the process optically) are considered, it is possible still for many complications to arise. Primarily, the use of materials such as magnetic nanoparticles in an optical detection platform can scatter, absorb, or even quench, the optical signal from the fluorescent reporter, which in turn will lead to a decrease in signal output [8]. To that end, many different types of magnetic/fluorescent nanomaterial composite have been constructed, as shown in Figure 9.12.

Each of these nanomaterial composites has unique features that overcome some of the potential limitations, and perhaps make them useful for select environmen-

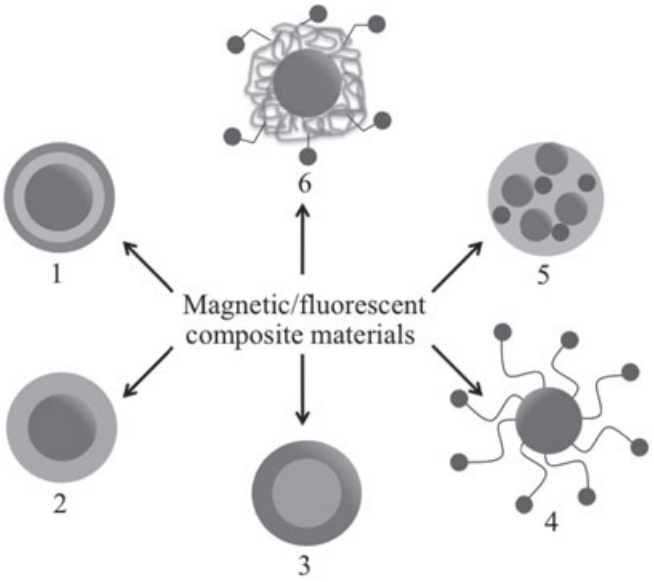

Figure 9.12 Examples of some composite magnetic/fluorescent nanoparticles for optical sensing applications. 1, Fe_3O_4@SiO_2 coated with a silica or polymer shell containing fluorescent molecules; 2, Fe_3O_4@CdS; 3, CdS@Fe_3O_4 core–shell nanoparticles; 4, fluorescent molecules attached to the Fe_3O_4 core using organic ligands; 5, Fe_3O_4 and fluorescent molecules or quantum dots encased in a silica or polymer matrix; 6, fluorescent molecules attached to polymer-encased Fe_3O_4.

tal sensing applications. In addition, Figure 9.12 demonstrates that, by using the synthetic methods discussed in Section 9.2, and which are typical for the production of magnetic nanomaterials (e.g., polymer and silica encasement and core–shell structure formation), it is possible to construct a wide range of useful nanomaterial composites that should enable a variety of applications [8]. These types of material have shown great promise in environmental sensing, mainly because they allow a target analyte to be separated/preconcentrated from a complex sample prior to analysis, thus preventing unwanted optical noise from background interferents. Yet, at the same time, they allow the optical labeling of a target analyte upon binding, such that a rapid sample analysis using traditional optical methods with exquisite sensitivity can be conducted when the separation is complete. It is believed that, as materials production methods continue to mature and more magnetic/fluorescent composite nanomaterials become available, there will be an explosion in the use of these types of material in environmental sensing applications.

The use of magnetic nanoparticles in sensor systems designed to take advantage of the intrinsic properties (e.g., magnetoresistance) of individual nanoparticles has grown tremendously during recent years, especially in the field of biosensors. While this type of sensor has not found great favor among the environmental sensing community, it is nonetheless an important sensing application of magnetic nanoparticles of all types, as biological targets are of major interest in this area. At this point, we will review some of the most common sensing scenarios that utilize the intrinsic properties of magnetic nanoparticles, and also provide some insight into the future of this type of sensor for the detection of environmentally relevant analytes. Most of the examples here focus on the detection of target analytes that are predominantly relevant in a biological laboratory or clinical setting, but they also provide context and performance metrics for a wide range of promising sensors. In addition, the examples provide a proof-of-concept and lay the foundations for the eventual widespread adoption of these types of sensors in the environmental sensing community.

The intrinsic properties of nanoparticles, which are typically exploited for the types of sensors discussed here, include magnetoresistance, giant magnetoresistance (GMR), and spin-valve GMR [3, 126–128]. While these properties have been exploited at length in the production of magnetic storage media (e.g., hard-disk drives) since their discovery in 1988 (which led to the Nobel Prize in Physics in 2007 for its discoverers, Fert and Grunberg), they are only now (within the past five to seven years) beginning to gain wide acceptance as viable methods of signal transduction in sensor systems [128]. First, a broad definition of these properties is provided, within the context of how they can be used for sensitive biodetection assays.

In their most basic implementations, sensors that seek to utilize the intrinsic GMR properties of the magnetic nanoparticles measure a change in sensor resistance in response to the concentration or binding of nanoparticles onto a functionalized magnetic transducer surface, after binding a target analyte [126]. The magnetoresistive effect arises from the change in resistance of the magnetic

materials as the overall magnetization of the sample changes from parallel with respect to current flow to perpendicular or transverse [3, 126]. (For a detailed explanation of the construction and driving principles behind GMR sensors, the reader should refer to recent reviews, as the explanation falls beyond the scope of this chapter [126, 128–131].) By using this configuration, it is possible to sensitively detect the fringe magnetic field of nanoscale magnetic particles once they have been brought, through specific interactions, to the engineered surface. Typically, the nanoparticles are on the order of 10–20 nm in diameter, and display either paramagnetic or superparamagnetic character with little to no remnant magnetization in order to prevent magnetic agglomeration in solution prior to binding the target analyte [128].

A typical biodetection reaction is carried out by either labeling the target analyte in solution with a magnetic nanoparticle prior to binding the nanoparticle–analyte complex to a substrate with a complementary probe molecule bound to the engineered surface, or by capturing the analyte on the surface and labeling with a magnetic particle in a second step [126]. A change in the sensor resistance at a fixed sense current signifies the presence of the magnetic nanoparticle, and subsequently the analyte. Any analyte that is not specifically bound to the sensor surface through the complementary probes or the nanoparticle can then be washed away to reveal a signal that is derived only from the desired target analyte [126, 128]. One type of sensor that utilizes magnetic nanoparticles as intrinsic labels exploits the magnetoresistance of the nanoparticle to signal molecular affinity interactions in bioassays [3]. In order to measure changes in magnetoresistance, arrays of specialized magnetic transducers are employed to measure the binding events between an affinity ligand (e.g., antibody or nucleic acid) and an analyte of interest (e.g., cell, organism, or protein). One manifestation of this type of assay comes in the form of a magnetoimmunoassay, in which primary and secondary antibodies are used to first capture an analyte from a sample, and second to label the captured analyte with an antibody that has been coupled to a magnetic nanoparticle [3]. Based on the current state of the art, magnetoresistive sensors have the potential to play a large role in the detection of biological analytes that have environmental relevance such as protein toxins, bacteria, and viruses [20, 126].

9.4 Summary and Future Perspective

Functionalized magnetic nanoparticles synthesized using the methods described in the chapter provide a number of unique and interesting opportunities for the improvement of environmentally relevant sensing applications. We have highlighted the myriad possibilities that exist for the synthesis and functionalization of magnetic nanoparticles that display the attributes that are most desirable for sensing applications, namely dispersbility, high surface area ($>100\,m^2\,g^{-1}$), flexible surface chemistry, and superparamagnetism. These characteristics make the magnetic nanoparticles ideal for applications where it is necessary to first bind and

separate an analyte from a complex sample matrix prior to analysis, by using a variety of methods which range from electrochemical detection to optical and magnetoresistive sensing platforms. In addition, the functionalized nanoparticles continue to show enormous promise as renewable surface sensors, since it is possible simply to bring new materials into contact with the sample of interest to regenerate both the sorbent material and the sensor surface. Ultimately, this will allow their use in samples that would cause other types of sorbent material to be fouled irreversibly. Further, functionalized magnetic nanoparticles have promise in the separation and sensing of analytes, ranging from heavy metals and biological species to chemical and radiological contaminants. This flexibility is limited only by the availability of the appropriate affinity ligand or surface coating. For bench-scale applications where cost is a greater consideration, the functionalized magnetic nanoparticles have the potential to be inexpensive and, as only small amounts are required for preconcentration and detection, the materials costs will remain very low. In situations requiring the large-scale environmental release of these materials, additional investigations must be completed before the systems can be claimed as cost effective. Nonetheless, the current state of the art shows great promise for these nanomaterials in the above-described applications, as evidenced by the many reports which have been made recently in the biological realm. In addition, a large rise should also be expected in the number of occasions where these materials are applied within the environmental sensing arena.

Acknowledgments

The authors gratefully acknowledge support through grants from NIOSH (R21 OH008900), NIEHS (R21 ES015620), NIAD (R01 AI080502), and the Safer Nanomaterials Nanomanufacturing Initiative (SNNI) of the Oregon Nanoscience and Microtechnologies Institute (ONAMI) and Pacific Northwest National Laboratory (PNNL). PNNL is operated for the U.S. Department of Energy by Battelle under contract DE-AC06-67RLO 1830. A portion of this research was performed using EMSL, a national scientific user facility sponsored by the Department of Energy's Office of Biological and Environmental Research located at Pacific Northwest National Laboratory.

References

1 Olkhovyk, O. and Jaroniec, M. (2007) In *Environmental Applications of Nanomaterials*, (eds G.E. Fryxell and G. Cao), Imperial College Press, London, pp. 179–212.

2 Tartaj, P., Morales, M.D., Veintemillas-Verdaguer, S., Gonzalez-Carreno, T. and Serna, C.J. (2003) The preparation of magnetic nanoparticles for applications in biomedicine. *Journal of Physics D: Applied Physics*, **36**, R182–97.

3 Hsing, I.M., Xu, Y. and Zhao, W. (2007) Micro- and nano-magnetic particles for applications in biosensing. *Electroanalysis*, **19**, 755–68.

4 Latham, A.H. and Williams, M.E. (2008) Controlling transport and chemical functionality of magnetic nanoparticles. *Accounts of Chemical Research*, **41**, 411–20.

5 Huber, D.L. (2005) Synthesis, properties, and applications of iron nanoparticles. *Small*, **1**, 482–501.

6 Yantasee, W., Hongsirikarn, K., Warner, C.L., Choi, D., Sangvanich, T., Toloczko, M.B., Warner, M.G., Fryxell, G.E., Addleman, R.S. and Timchalk, C. (2008) Direct detection of Pb in urine and Cd, Pb, Cu, and Ag in natural waters using electrochemical sensors immobilized with DMSA functionalized magnetic nanoparticles. *Analyst*, **133**, 348.

7 Yantasee, W., Warner, C.L., Sangvanich, T., Addleman, R.S., Carter, T.G., Wiacek, R.J., Fryxell, G.E., Timchalk, C. and Warner, M.G. (2007) Removal of heavy metals from aqueous systems with thiol functionalized superparamagnetic nanoparticles. *Environmental Science & Technology*, **41**, 5114–19.

8 Corr, S.A., Rakovich, Y.P. and Gun'ko, Y.K. (2008) Multifunctional magnetic-fluorescent nanocomposites for biomedical applications. *Nanoscale Research Letters*, **3**, 87–104.

9 Seydack, M. (2005) Nanoparticle labels in immunosensing using optical detection methods. *Biosensors & Bioelectronics*, **20**, 2454–69.

10 Pankhurst, Q.A. (2006) Nanomagnetic medical sensors and treatment methodologies. *BT Technology Journal*, **24**, 33–8.

11 Pankhurst, Q.A., Connolly, J., Jones, S.K. and Dobson, J. (2003) Applications of magnetic nanoparticles in biomedicine. *Journal of Physics D: Applied Physics*, **36**, R167–81.

12 Rodriguez-Mozaz, S., de Alda, M.J.L. and Barcelo, D. (2006) Biosensors as useful tools for environmental analysis and monitoring. *Analytical and Bioanalytical Chemistry*, **386**, 1025–41.

13 Katz, E., Willner, I. and Wang, J. (2004) Electroanalytical and bioelectroanalytical systems based on metal and semiconductor nanoparticles. *Electroanalysis*, **16**, 19–44.

14 Laurent, S., Forge, D., Port, M., Roch, A., Robic, C., Van der Elst, L., Muller, R.N. and Iron, M. (2008) Oxide nanoparticles: synthesis, stabilization, vectorization, physicochemical characterizations, and biological applications. *Chemical Reviews*, **108**, 2064–110.

15 Katz, E. and Willner, I. (2004) Integrated nanoparticle-biomolecule hybrid systems: synthesis, properties, and applications. *Angewandte Chemie, International Edition in English*, **43**, 6042–108.

16 Salgueirino-Maceira, V. and Correa-Duarte, M.A. (2007) Increasing the complexity of magnetic core/shell structured nanocomposites for biological applications. *Advanced Materials*, **19**, 4131–44.

17 Lu, A.H., Salabas, E.L. and Schueth, F. (2007) Magnetic nanoparticles: synthesis, protection, functionalization, and application. *Angewandte Chemie, International Edition in English*, **46**, 1222–44.

18 Magnani, M., Galluzzi, L. and Bruce, I.J. (2006) The use of magnetic nanoparticles in the development of new molecular detection systems. *Journal of Nanoscience and Nanotechnology*, **6**, 2302–11.

19 Fryxell, G.E. (2007) In *Environmental Applications of Nanomaterials* (eds. G.E. Fryxell and G. Cao), Imperial College Press, London, pp. 159–78.

20 Ngomsik, A., Bee, A., Draye, M., Cote, G. and Cabuil, V. (2005) Magnetic nano- and microparticles for metal removal and environmental applications: a review. *Comptes Rendus Chimie*, **8**, 963–70.

21 Jun, Y., Choi, J. and Cheon, J. (2006) Shape control of semiconductor and metal oxide nanocrystals through nonhydrolytic colloidal routes. *Angewandte Chemie, International Edition in English*, **45**, 3414–39.

22 Park, J., Joo, J., Kwon, S., Jang, Y. and Hyeon, T. (2007) Synthesis of monodisperse spherical nanocrystals. *Angewandte Chemie, International Edition in English*, **46**, 4630–60.

23 Cushing, B.L., Kolesnichenko, V.L. and O'Connor, C.J. (2004) Recent advances in the liquid-phase syntheses of inorganic nanoparticles. *Chemical Reviews*, **104**, 3893–946.

24 Neouze, M.A. and Schubert, U. (2008) Surface modification and functionalization of metal and metal oxide nanoparticles by organic ligands. *Monatshefte Chemistry*, **139**, 183–95.

25 Massart, R. (1981) Preparation of aqueous magnetic liquids in alkaline and acidic media. *IEEE Transactions on Magnetics*, **17**, 1247–8.

26 Tao, K., Dou, H. and Sun, K. (2006) Facile interfacial coprecipitation to fabricate hydrophilic amine-capped magnetite nanoparticles. *Chemistry of Materials*, **18**, 5273–8.

27 Wang, X., Zhuang, J., Peng, Q. and Li, Y. (2005) A general strategy for nanocrystal synthesis. *Nature*, **437**, 121–4.

28 Takami, S., Sato, T., Mousavand, T., Ohara, S., Umetsu, M. and Adschiri, T. (2007) Hydrothermal synthesis of surface-modified iron oxide nanoparticles. *Material Letters*, **61**, 4769–72.

29 Sun, S.H., Zeng, H., Robinson, D.B., Raoux, S., Rice, P.M., Wang, S. and Li, G. (2004) Monodisperse MFe_2O_4 (M = Fe, Co, Mn) nanoparticles. *Journal of the American Chemical Society*, **126**, 273–9.

30 Park, J., An, K., Hwang, Y., Park, J.-G., Noh, H.-J., Kim, J.-Y., Park, J.-H., Hwang, N.-M. and Hyeon, T. (2004) Ultra-large-scale syntheses of monodisperse nanocrystals. *Nature Materials*, **3**, 891–5.

31 Hyeon, T., Lee, S.S., Park, J., Chung, Y. and Na, H.B. (2001) Synthesis of highly crystalline and monodisperse maghemite nanocrystallites without a size-selection process. *Journal of the American Chemical Society*, **123**, 12798–801.

32 Dresco, P.A., Zaitsev, V.S., Gambino, R.J. and Chu, B. (1999) Preparation and properties of magnetite and polymer magnetite nanoparticles. *Langmuir*, **15**, 1945–51.

33 Liu, C., Zou, B., Rondinone, A.J., Zhang, Z.J. and Micelle, R. (2000) Synthesis and characterization of superparamagnetic $MnFe_2O_4$ spinel ferrite nanocrystallites. *The Journal of Physical Chemistry B*, **104**, 1141–5.

34 Woo, K., Lee, H.J., Ahn, J.P. and Park, Y.S. (2003) Sol-gel mediated synthesis of Fe_2O_3 nanorods. *Advanced Materials*, **15**, 1761–4.

35 Kovalenko, M.V., Bodnarchuk, M.I., Lechner, R.T., Hesser, G., Schaffler, F. and Heiss, W. (2007) Fatty acid salts as stabilizers in size- and shape-controlled nanocrystal synthesis: the case of inverse spinel iron oxide. *Journal of the American Chemical Society*, **129**, 6352–3.

36 Portet, D., Denizot, B., Rump, E., Lejeune, J.-J. and Jallet. P. (2001) Nonpolymeric coatings of iron oxide colloids for biological use as magnetic resonance imaging contrast agents. *Journal of Colloid and Interface Science*, **238**, 37–42.

37 Fauconnier, N., Pons, J.N., Roger, J. and Bee, A. (1997) Thiolation of maghemite nanoparticles by dimercaptosuccinic acid. *Journal of Colloid and Interface Science*, **194**, 427–33.

38 Sahoo, Y., Pizem, H., Fried, T., Golodnitsky, D., Burstein, L., Sukenik, C.N. and Markovich, G. (2001) Alkyl phosphonate/phosphate coating on magnetite nanoparticles: a comparison with fatty acids. *Langmuir*, **17**, 7907–11.

39 Das, M., Mishra, D., Maiti, T.K., Basak, A. and Pramanik, P. (2008) Bio-functionalization of magnetite nanoparticles using an aminophosphonic acid coupling agent: new, ultradispersed, iron-oxide folate nanoconjugates for cancer-specific targeting. *Nanotechnology*, **19**, 415101.

40 Daou, T.J., Buathong, S., Ung, D., Donnio, B., Pourroy, G., Guillon, D. and Begin, S. (2007) Investigation of the grafting rate of organic molecules on the surface of magnetite nanoparticles as a function of the coupling agent. *Sensors and Actuators B, Chemical*, **126**, 159–62.

41 Yee, C., Kataby, G., Ulman, A., Prozorov, T., White, H., King, A., Rafailovich, M., Sokolov, J. and Gedanken, A. (1999)

Self-assembled monolayers of alkanesulfonic and -phosphonic acids on amorphous iron oxide nanoparticles. *Langmuir*, **15**, 7111–15.

42 DePalma, R., Peeters, S., Van Bael, M.J., Van den Rul, H., Bonroy, K., Laureyn, W., Mullens, J., Borghs, G. and Maes, G. (2007) Silane ligand exchange to make hydrophobic superparamagnetic nanoparticles water-dispersible. *Chemistry of Materials*, **19**, 1821–31.

43 Kohler, N., Fryxell, G.E., Zhang, M. and Bifunctional, A. (2004) Poly(ethylene glycol) silane immobilized on metallic oxide-based nanoparticles for conjugation with cell targeting agents. *Journal of the American Chemical Society*, **126**, 7206–11.

44 Kim, D.K., Mikhaylova, M., Zhang, Y. and Muhammed, M. (2003) Protective coating of superparamagnetic iron oxide nanoparticles. *Chemistry of Materials*, **15**, 1617–27.

45 Kim, M., Chen, Y., Liu, Y. and Peng, X. (2005) Super-stable, high-quality Fe_3O_4 dendron-nanocrystals dispersible in both organic and aqueous solutions. *Advanced Materials*, **17**, 1429–32.

46 Binder, W.H. and Weinstabl, H.C. (2007) Surface-modified superparamagnetic iron-oxide nanoparticles. *Monatshefte Chemistry*, **138**, 315–20.

47 Binder, W.H., Weinstabl, H. and Sachsenhofer, R. (2008) Superparamagnetic iron oxide nanoparticles via ligand exchange reactions: organic 1,2-diols as versatile building blocks for surface engineering. *Journal of Nanomaterials*, Article 383020.

48 Kryszewski, M. and Jeszka, J.K. (1998) Nanostructured conducting polymer composites – superparamagnetic particles in conducting polymers. *Synthetic Metals*, **94**, 99–104.

49 Harris, L.A., Goff, J.D., Carmichael, A.Y., Riffle, J.S., Harburn, J.J., St Pierre, T.G. and Saunders, M. (2003) Magnetite nanoparticle dispersions stabilized with triblock copolymers. *Chemistry of Materials*, **15**, 1367–77.

50 Lattuada, M. and Hatton, T.A. (2007) Functionalization of monodisperse magnetic nanoparticles. *Langmuir*, **23**, 2158–68.

51 Sauzedde, F., Elaïssari, A. and Pichot, C. (1999) Hydrophilic magnetic polymer latexes. 1. Adsorption of magnetic iron oxide nanoparticles onto various cationic latexes. *Colloid and Polymer Science*, **277**, 846–55.

52 Lin, H., Watanabe, Y., Kimura, M., Hanabusa, K. and Shirai, H. (2003) Preparation of magnetic poly(vinyl alcohol) (PVA) materials by in situ synthesis of magnetite in a PVA matrix. *Journal of Applied Polymer Science*, **87**, 1239–47.

53 Shin, S. and Jang, J. (2007) Thiol containing polymer encapsulated magnetic nanoparticles as reusable and efficiently separable adsorbent for heavy metal ions. *Chemical Communications*, 4230–2.

54 Liao, M.-H. and Chen, D.-H. (2002) Preparation and characterization of a novel magnetic nano-adsorbent. *Journal of Material Chemistry*, **12**, 3654–9.

55 Pardoe, H., Chua-anusorn, W., St Pierre, T.G. and Dobson, J. (2001) Structural and magnetic properties of nanoscale iron oxide particles synthesized in the presence of dextran or polyvinyl alcohol. *Journal of Magnetism and Magnetic Materials*, **225**, 41–6.

56 Lee, J., Isobe, T. and Senna, M. (1996) Preparation of ultrafine Fe_3O_4 particles by precipitation in the presence of PVA at high pH. *Journal of Colloid and Interface Science*, **177**, 490–4.

57 Li, Z., Tan, B., Allix, M., Cooper, A.I. and Rosseinsky, M.J. (2008) Direct coprecipitation route to monodisperse dual-functionalized magnetic iron oxide nanocrystals without size selection. *Small*, **4**, 231–9.

58 Lu, Y., Yin, Y., Mayers, B.T. and Xia, Y. (2002) Modifying the surface properties of superparamagnetic iron oxide nanoparticles through a sol-gel approach. *Nano Letters*, **2**, 183–6.

59 Stober, W., Fink, A. and Bohn, E. (1968) Controlled growth of monodisperse silica spheres in the micron size range. *Journal of Colloid and Interface Science*, **26**, 62–9.

60 Deng, Y.-H., Wang, C.-C., Hu, J.-H., Yang, W.-L. and Fu, S.-K. (2005) Investigation of formation of silica-coated magnetite nanoparticles via sol-gel approach. *Colloid Surface A*, **262**, 87–93.

61 Philipse, A.P., van Bruggen, M.P.B. and Pathmamanoharan, C. (1994) Magnetic silica dispersions: preparation and stability of surface-modified silica particles with a magnetic core. *Langmuir*, **10**, 92–9.

62 Grass, R., Athanassiou, E. and Stark, W. (2007) Covalently functionalized cobalt nanoparticles as a platform for magnetic separations in organic synthesis. *Angewandte Chemie, International Edition in English*, **46**, 4909–12.

63 Wang, Z., Guo, H., Yu, Y. and He, N. (2006) Synthesis and characterization of a novel magnetic carrier with its composition of Fe_3O_4/carbon using hydrothermal reaction. *Journal of Magnetism and Magnetic Materials*, **302**, 397–404.

64 Xuan, S., Hao, L., Jiang, W., Gong, X., Hu, Y. and Chen, Z. (2007) A facile method to fabricate carbon-encapsulated Fe_3O_4 core/shell composites. *Nanotechnology*, **18**, 035602.

65 Park, H.Y., Schadt, M.J., Wang, L.Y., Lim, I.I.S., Njoki, P.N., Kim, S.H., Jang, M.Y., Luo, J. and Zhong, C.J. (2007) Fabrication of magnetic core@shell Fe oxide@Au nanoparticles for interfacial bioactivity and bio-separation. *Langmuir*, **23**, 9050–6.

66 Lim, J., Eggeman, A., Lanni, F., Tilton, R.D. and Majetich, S.A. (2008) Synthesis and single-particle optical detection of low-polydispersity plasmonic-superparamagnetic nanoparticles. *Advanced Materials*, **20**, 1721–6.

67 Xu, Z., Hou, Y. and Sun, S. (2007) Magnetic core/shell Fe_3O_4/Au and Fe_3O_4/Au/Ag nanoparticles with tunable plasmonic properties. *Journal of the American Chemical Society*, **129**, 8698–9.

68 Wang, L., Luo, J., Maye, M.M., Fan, Q., Rendeng, Q., Engelhard, M.H., Wang, C., Lin, Y. and Zhong, C.-J. (2005) Iron oxide-gold core-shell nanoparticles and thin film assembly. *Journal of Materials Chemistry*, **15**, 1821–32.

69 Mandal, M., Kundu, S., Ghosh, S.K., Panigrahi, S., Sau, T.K., Yusuf, S.M. and Pal, T. (2005) Magnetite nanoparticles with tunable gold or silver shell. *Journal of Colloid and Interface Science*, **286**, 187–94.

70 Tang, D.P., Yuan, R. and Chai, Y.Q. (2006) Magnetic core-shell Fe_3O_4@Ag nanoparticles coated carbon paste interface for studies of carcinoembryonic antigen in clinical immunoassay. *Journal of Physical Chemistry B*, **110**, 11640–6.

71 Kim, H., Achermann, M., Balet, L.P., Hollingsworth, J.A. and Klimov, V.I. (2005) Synthesis and characterization of Co/CdSe core/shell nanocomposites: bifunctional magnetic-optical nanocrystals. *Journal of the American Chemical Society*, **127**, 544–6.

72 Gu, H., Zheng, R., Zhang, X. and Xu, B. (2004) Facile one-pot synthesis of bifunctional heterodimers of nanoparticles: a conjugate of quantum dot and magnetic nanoparticles. *Journal of the American Chemical Society*, **126**, 5664–5.

73 Gao, L., Zhuang, J., Nie, L., Zhang, J., Zhang, Y., Gu, N., Wang, T., Feng, J., Yang, D., Perrett, S. and Yan, X. (2007) Intrinsic peroxidase-like activity of ferromagnetic nanoparticles. *Nature Nanotechnology*, **2**, 577–83.

74 Santra, S., Tapec, R., Theodoropoulou, N., Dobson, J., Hebard, A. and Tan, W. (2001) Synthesis and characterization of silica-coated iron oxide nanoparticles in microemulsion: the effect of nonionic surfactants. *Langmuir*, **17**, 2900–6.

75 Ennas, G., Musinu, A., Piccaluga, G., Zedda, D., Gatteschi, D., Sangregorio, C., Stanger, J.L., Concas, G. and Spano, G. (1998) Characterization of iron oxide nanoparticles in an Fe_2O_3-SiO_2 composite prepared by a sol-gel method. *Chemistry of Materials*, **10**, 495–502.

76 Ma, D.L., Jakubek, Z.J. and Simard, B. (2006) A new approach towards controlled synthesis of multifunctional core-shell nano-architectures: luminescent and superparamagnetic.

Journal of Nanoscience and Nanotechnology, **6**, 3677–84.

77 Ma, D.L., Guan, J.W., Normandin, F., Denommee, S., Enright, G., Veres, T. and Simard, B. (2006) Multifunctional nano-architecture for biomedical applications. *Chemistry of Materials*, **18**, 1920–7.

78 Yu, S.Y., Zhang, H.J., Yu, J.B., Wang, C., Sun, L.N. and Shi, W.D. (2007) Bifunctional magnetic-optical nanocomposites: grafting lanthanide complex onto core-shell magnetic silica nanoarchitecture. *Langmuir*, **23**, 7836–40.

79 Lai, C.-W., Wang, Y.-H., Lai, C.-H., Yang, M.-J., Chen, C.-Y., Chou, P.-T., Chan, C.-S., Chi, Y., Chen, Y.-C. and Hsiao, J.-K. (2008) Iridium-complex-functionalized Fe_3O_4/SiO_2 core/shell nanoparticles: a facile three-in-one system in magnetic resonance imaging, luminescence imaging, and photodynamic therapy. *Small*, **4**, 218–24.

80 Sathe, T.R., Agrawal, A. and Nie, S. (2006) Mesoporous silica beads embedded with semiconductor quantum dots and iron oxide nanocrystals: dual-function microcarriers for optical encoding and magnetic separation. *Analytical Chemistry*, **78**, 5627–32.

81 Guo, J., Yang, W., Wang, C., He, J. and Chen, J. (2006) Poly(*N*-isopropylacrylamide)-coated luminescent/magnetic silica microspheres: preparation, characterization, and biomedical applications. *Chemistry of Materials*, **18**, 5554–62.

82 Zhang, Y., Wang, S.-N., Ma, S., Guan, J.-J., Li, D., Zhang, X.-D. and Zhang, Z.-D. (2008) Self-assembly multifunctional nanocomposites with Fe_3O_4 magnetic core and CdSe/ZnS quantum dots shell. *Journal of Biomedical Materials Research. Part A*, **85A**, 840–6.

83 Athanassiou, E.K., Grass, R.N. and Stark, W.J. (2006) Large-scale production of carbon-coated copper nanoparticles for sensor applications. *Nanotechnology*, **17**, 1668–73.

84 Carpenter, E.E. (2001) Iron nanoparticles as potential magnetic carriers. *Journal of Magnetism and Magnetic Materials*, **225**, 17–20.

85 Mikhaylova, M., Kim, D.K., Bobrysheva, N., Osmolowsky, M., Semenov, V., Tsakalakos, T. and Muhammed, M. (2004) Superparamagnetism of magnetite nanoparticles: dependence on surface modification. *Langmuir*, **20**, 2472–7.

86 Lo, C.K., Xiao, D. and Choi, M.M.F. (2007) Homocysteine-protected gold-coated magnetic nanoparticles: synthesis and characterisation. *Journal of Material Chemistry*, **17**, 2418–27.

87 Lu, Q.H., Yao, K.L., Xi, D., Liu, Z.L., Luo, X.P. and Ning, Q. (2006) Synthesis and characterization of composite nanoparticles comprised of gold shell and magnetic core/cores. *Journal of Magnetism and Magnetic Materials*, **301**, 44–9.

88 Gong, P., Li, H., He, X., Wang, K., Hu, J., Tan, W., Zhang, S. and Yang, X. (2007) Preparation and antibacterial activity of Fe_3O_4@Ag nanoparticles. *Nanotechnology*, **18**, 285604.

89 Kimishima, Y., Yamada, W., Uehara, M., Asaka, T., Kimoto, K. and Matsui, Y. (2007) Study on anomalous magnetoresistance in nano-Fe_3O_4/Ag granular system. *Materials Science and Engineering B*, **138**, 69–73.

90 Liu, C., Zhou, Z., Yu, X., Lv, B., Mao, J. and Xiao, D. (2008) Preparation and characterization of Fe_3O_4/Ag composite magnetic nanoparticles. *Inorganic Materials*, **44**, 291–5.

91 Gao, J., Zhang, B., Gao, Y., Pan, Y., Zhang, X., Xu, B. and Magnetic, F. (2007) Nanocrystals by sequential addition of reagents in a one-pot reaction: a simple preparation for multifunctional nanostructures. *Journal of the American Chemical Society*, **129**, 11928–35.

92 Poole, C.F. (2003) New trends in solid-phase extraction. *Trends in Analytical Chemistry*, **22**, 362–73.

93 Yavuz, C., Mayo, J.T., Yu, W., Prakash, A. and Falkner, J. (2006) Low-field magnetic separation of monodisperse Fe_3O_4 nanocrystals. *Science*, **314**, 964–7.

94 Miltenyi, S., Muller, W., Weichel, W. and Radbruch, A. (1990) High-gradient separation with MACS. *Cytometry*, **11**, 231–8.

95 Huang, Y., Mather, E.L., Bell, J.L. and Madou, M. (2002) MEMS-based sample preparation for molecular diagnostics. *Analytical and Bioanalytical Chemistry*, **372**, 49–65.

96 Karumanchi, R., Doddamane, S.N., Sampangi, C. and Todd, P.W. (2002) Field-assisted extraction of cells, particles and macromolecules. *Trends in Biotechnology*, **20**, 72–8.

97 Inglis, D.W., Riehn, R., Austin, R.H. and Sturm, J.C. (2004) Continuous microfluidic immunomagnetic cell separation. *Applied Physics Letters*, **85**, 5093–5.

98 Sonvico, F., Dubernet, C., Colombo, P. and Couvreur, P. (2005) Metallic colloid nanotechnology, applications in diagnosis and therapeutics. *Current Pharmaceutical Design*, **11**, 2091–105.

99 Inglis, D.W., Riehn, R., Sturm, J.C. and Austin, R.H. (2006) Microfluidic high gradient magnetic cell separation. *Journal of Applied Physics*, **99**, 08K101.

100 Mattanovich, D. and Borth, N. (2006) Applications of cell sorting in biotechnology. *Microbial Cell Factories*, 5.

101 Pamme, N. and Wilhelm, C. (2006) Continuous sorting of magnetic cells via on-chip free-flow magnetophoresis. *Lab on a Chip*, **6**, 974–80.

102 Chang, S.C. and Adriaens, P. (2007) Nano-immunodetection and quantification of mycobacteria in metalworking fluids. *Environmental Engineering Science*, **24**, 58–72.

103 Koschwanez, J.H., Carlson, R.H. and Meldrum, D.R. (2007) Easily fabricated magnetic traps for single-cell applications. *Review of Scientific Instruments*, **78**, 044301.

104 Lien, K.Y., Lin, J.L., Liu, C.Y., Lei, H.Y. and Lee, G.B. (2007) Purification and enrichment of virus samples utilizing magnetic beads on a microfluidic system. *Lab on a Chip*, **7**, 868–75.

105 Arakaki, A., Nakazawa, H., Nemoto, M., Mori, T. and Matsunaga, T. (2008) Formation of magnetite by bacteria and its application. *Journal of the Royal Society, Interface*, **5**, 977–99.

106 Kersaudy-Kerhoas, M., Dhariwal, R. and Desmulliez, M.P.Y. (2008) Recent advances in microparticle continuous separation. *IET Nanobiotechnology*, **2**, 1–13.

107 Shih, P.H., Shiu, J.Y., Lin, P.C., Lin, C.C., Veres, T. and Chen, P. (2008) On chip sorting of bacterial cells using sugar-encapsulated magnetic nanoparticles. *Journal of Applied Physics*, **103**, 07A316.

108 Lee, W.C., Lien, K.Y., Lee, G.B. and Lei, H.Y. (2008) An integrated microfluidic system using magnetic beads for virus detection. *Diagnostic Microbiology and Infectious Disease*, **60**, 51–8.

109 Chen, W., Shen, H.B., Li, X.Y., Jia, N.Q. and Xu, J.M. (2006) Synthesis of immunomagnetic nanoparticles and their application in the separation and purification of CD34(+) hematopoietic stem cells. *Applied Surface Science*, **253**, 1762–9.

110 Bao, J., Chen, W., Liu, T.T., Zhu, Y.L., Jin, P.Y., Wang, L.Y., Liu, J.F., Wei, Y.G. and Li, Y.D. (2007) Bifunctional Au-Fe_3O_4 nanoparticles for protein separation. *ACS Nano*, **1**, 293–8.

111 Wang, F., Shen, H.B., Feng, J. and Yang, H.F. (2006) PNA-modified magnetic nanoparticles and their hybridization with single-stranded DNA target: surface enhanced Raman scatterings study. *Microchimica Acta*, **153**, 15–20.

112 Zhu, L.Z., Yu, P.G., Shen, H.B., Jia, N.Q., Long, D.H. and Zhou, H.Q. (2008) Extraction and detection of mRNA from a single K562 cell based on the functionalized superparamagnetic nanoparticles. *Chinese Journal of Chemistry*, **26**, 1041–4.

113 Willner, I., Cheglakov, Z., Weizmann, Y. and Sharon, E. (2008) Analysis of DNA and single-base mutations using magnetic particles for purification, amplification and DNAzyme detection. *Analyst*, **133**, 923–7.

114 Yantasee, W., Lin, Y., Hongsirikarn, K., Fryxell, G.E., Addleman, R. and Timchalk, C. (2007) Electrochemical sensors for the detection of lead and

other toxic heavy metals: the next generation of personal exposure biomonitors. *Environmental Health Perspectives*, **115**, 1683–90.

115 Fryxell, G.E., Mattigod, S.V., Lin, Y., Wu, H., Fiskum, S., Parker, K., Zheng, F., Yantasee, W., Zemanian, T.S., Addleman, R.S., Liu, J., Kemner, K., Kelly, S. and Feng, X. (2007) Design and synthesis of self-assembled monolayers on mesoporous supports (SAMMS): the importance of ligand posture in functional nanomaterials. *Journal of Materials Chemistry*, **17**, 2863–74.

116 Mattigod, S.V., Fryxell, G.E., Alford, K., Gilmore, T., Parker, K., Serne, J. and Engelhard, M. (2005) Functionalized TiO_2 nanoparticles for use for in situ anion immobilization. *Environmental Science and Technology*, **39**, 7306–10.

117 Mattigod, S.V., Fryxell, G.E. and Parker, K.E. (2007) Anion binding in self-assembled monolayers in mesoporous supports (SAMMS). *Inorganic Chemical Communications*, **10**, 646–8.

118 Santandreu, M., Sole, S., Fabregas, E. and Alegret, S. (1998) Development of electrochemical immunosensing systems with renewable surfaces. *Biosensors and Bioelectronics*, **13**, 7–17.

119 Riskin, M., Basnar, B., Huang, Y. and Willner, I. (2007) Magnetoswitchable charge transport and bioelectrocatalysis using maghemite-Au core-shell nanoparticle/polyaniline composites. *Advanced Materials*, **19**, 2691–3.

120 Liu, H.B., Guo, J., Jin, L., Yang, W.L. and Wang, C.C. (2008) Fabrication and functionalization of dendritic poly(amidoamine)-immobilized magnetic polymer composite microspheres. *The Journal of Physical Chemistry B*, **112**, 3315–21.

121 Cai, J., Guo, J., Ji, M.L., Yang, W.L., Wang, C.C. and Fu, S.K. (2007) Preparation and characterization of multiresponsive polymer composite microspheres with core-shell structure. *Colloid and Polymer Science*, **285**, 1607–15.

122 Liu, G. and Lin, Y. (2005) A renewable electrochemical magnetic immunosensor based on gold nanoparticle labels. *Journal of Nanoscience and Nanotechnology*, **5**, 1060–5.

123 de la Escosura-Muniz, A., Ambrosi, A. and Merkoci, A. (2008) Electrochemical analysis with nanoparticle-based biosystems. *Trends in Analytical Chemistry*, **27**, 568–84.

124 Palecek, E. and Fojta, M. (2007) Magnetic beads as versatile tools for electrochemical DNA and protein biosensing. *Talanta*, **74**, 276–90.

125 Liu, G.D., Timchalk, C. and Lin, Y.H. (2006) Bioelectrochemical magnetic immunosensing of trichloropyridinol: a potential insecticide biomarker. *Electroanalysis*, **18**, 1605–13.

126 Graham, D.L., Ferreira, H.A. and Freitas, P.P. (2004) Magnetoresistive-based biosensors and biochips. *Trends in Biotechnology*, **22**, 455–62.

127 Tansil, N.C. and Gao, Z.Q. (2006) Nanoparticles in biomolecular detection. *Nano Today*, **1**, 28–37.

128 Wang, S.X. and Li, G. (2008) Advances in giant magnetoresistance biosensors with magnetic nanoparticle tags: review and outlook. *IEEE Transactions on Magnetics*, **44**, 1687–702.

129 Zhang, X.Y., Chen, Y.J. and Li, Z.Y. (2006) Enhanced magnetoresistance and surface state of CrO_2 particles improved by chemical process. *Journal of Magnetism and Magnetic Materials*, **307**, 134–8.

130 Reiss, G., Brueckl, H., Huetten, A., Schotter, J., Brzeska, M., Panhorst, M., Sudfeld, D., Becker, A., Kamp, P., Puehler, A., Wojczykowski, K. and Jutzi, P. (2005) Magnetoresistive sensors and magnetic nanoparticles for biotechnology. *Journal of Materials Research*, **20**, 3294–302.

131 Millen, R.L., Kawaguchi, T., Granger, M.C. and Porter, M.D. (2005) Giant magnetoresistive sensors and superparamagnetic nanoparticles: a chip-scale detection strategy for immunosorbent assays. *Analytical Chemistry*, **77**, 6581–7.

Keywords

magnetic nanoparticles; synthesis; heavy metals; remediation; separation

10
Magnetic Core–Polymer Shell Nanoparticles: Synthesis and Biomedical Applications

Koon Gee Neoh, Lihan Tan, and En-Tang Kang

10.1
Introduction

There has been increasing interest in the use of superparamagnetic iron oxide nanoparticles for biomedical applications. Progress in this field has been rapid, and in recent years a number of reviews have been published [1–6] on the applications of magnetic nanoparticles (MNPs) in biomedicine. These reviews have provided details on the physical principles underlying the biomedical applications of MNPs, their synthesis methods, the properties required of MNPs, and the challenges and solutions envisaged for this emerging technology. The iron oxide nanoparticles have low toxicity and are suitable for *in vivo* applications as they are biodegradable, with the Fe product being recycled by cells. The dimensions of the MNPs also allow a close interaction with cells and, with their magnetic properties, manipulation *in vivo* using an external magnetic field is possible. The potential of these nanoparticles can be greatly enhanced by tailoring them for specific applications through proper functionalization. This frequently entails the use of polymers to provide either a coating with the desired properties, or to serve as a platform for the attachment of other functional groups.

In this chapter, attention is focused on the synthesis of magnetic core–polymer shell nanoparticles, with emphasis on the role played by the polymer in tailoring the MNPs to meet the promises and challenges for biomedical applications. Two classes of magnetic core–polymer shell nanoparticle will be described, namely the single magnetic nanoparticle with a polymeric shell, and multiple magnetic nanoparticles encapsulated in a polymeric matrix. The term "nanospheres" will be used in this chapter to denote the latter type of nanoparticle, in order to differentiate them from the single nanoparticles with a polymeric coating. There are a number of synthetic routes for the seed MNPs, and the characteristics of these MNPs, will be determined by the chosen route. While the synthesis of MNPs is an important topic, it will not be discussed in detail here. Rather, a short review of the more commonly used synthesis techniques will be provided, after which attention will be focused on the various methodologies for integrating a polymer shell with the MNPs, and their subsequent functionalization. The biomedical applications

Nanomaterials for the Life Sciences Vol. 4: Magnetic Nanomaterials. Edited by Challa S. S. R. Kumar

ISBN: 978-3-527-32154-4

described herein relate primarily to bioimaging/cell labeling and drug/gene delivery. Those reports made more recently (within the past three years) will be highlighted in greater detail.

10.2
Synthesis of Magnetic Nanoparticles

10.2.1
Primary Synthesis Methods

For biomedical applications, superparamagnetic particles which do not retain any magnetism when removed from a magnetic field are preferred. Among these, ferrous or ferric oxides with low toxicity constitute the most commonly employed MNPs, as other highly magnetic materials (e.g., cobalt or nickel) may pose toxicity issues. Several techniques have been developed to prepare MNPs of uniform size and shape. The two primary techniques are coprecipitation and the thermal decomposition of organic precursors.

In *coprecipitation*, Fe_3O_4 is precipitated from an aqueous solution of ferric and ferrous salts upon the addition of a base [7]. A stabilizing agent may be added at the point of, or after, precipitation. For instance, the precipitation of stable magnetite colloidal dispersions with an average diameter of 4–7 nm was achieved in the presence of poly(vinyl alcohol) (PVA) [8]. Other stabilizing agents include dextran [9, 10], albumin [11], oleic acid [12], methoxypoly(ethylene glycol) (methoxyPEG), and starch [13]. The wide choice of stabilizing agents lends flexibility to this method in terms of providing a variety of platforms for further functionalization, and the stability in different media also depends on the agent employed. However, the control of particle size and monodispersity is difficult to achieve due to the uncontrolled rate of nucleation that occurs in aqueous solutions [14]. A modification of the coprecipitation method is the sonochemical method, whereby a mixed solution of $FeCl_2$ and $FeCl_3$ was irradiated with ultrasonic waves, followed by the immediate and rapid addition of NH_4OH solution to precipitate black nanoparticles at room temperature [15]. The resultant spherical magnetite nanoparticles (average diameter ~15 nm) had a higher crystallinity than those prepared by the coprecipitation method.

The *high-temperature decomposition* process for the synthesis of monodisperse Fe_3O_4 nanoparticles of <20 nm is a more recent development. Sun and Zeng [16] reported a high-temperature reaction (at 265 °C) of iron (III) acetylacetonate ($Fe(acac)_3$) in phenyl ether, alcohol, oleic acid, and oleylamine. This process resulted in particles of ~4 nm diameter. By using these smaller nanoparticles as seeds, larger monodisperse magnetite nanoparticles of up to 20 nm in diameter could be synthesized by seed-mediated growth. In this process, the smaller particles were mixed with additional precursor materials and the mixture was heated as for the synthesis of the 4 nm nanoparticles [17]. By controlling the diameter and quantity of the nanoparticle seeds used, Fe_3O_4 nanoparticles of various sizes can

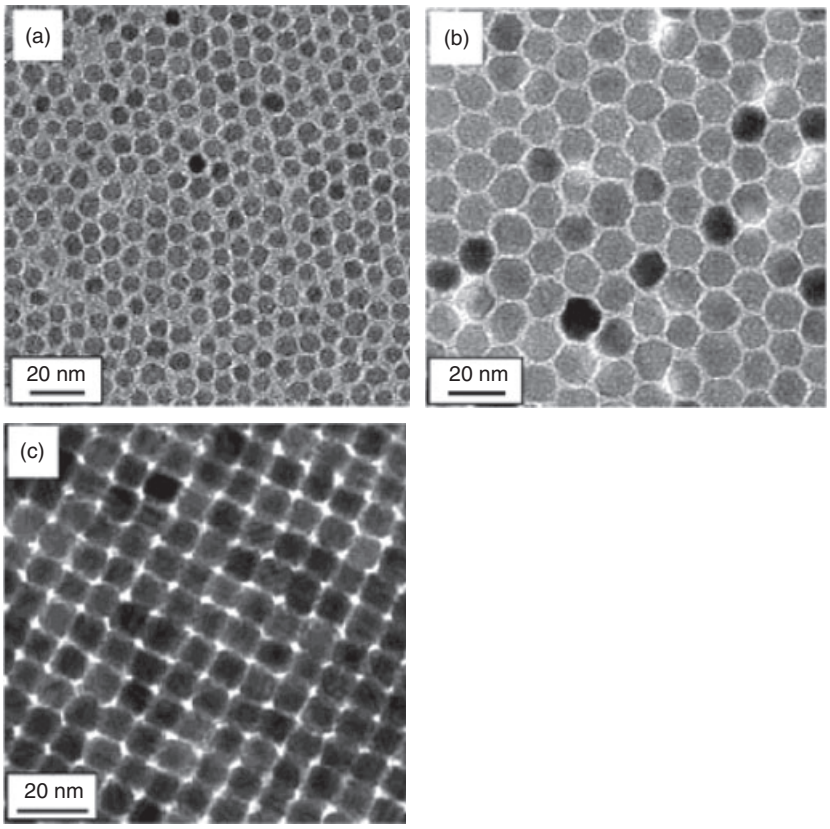

Figure 10.1 Transmission electron microscopy bright-field images of (a) 6 nm and (b) 12 nm Fe_3O_4 nanoparticles deposited from their hexane dispersion on an amorphous carbon-coated copper grid and dried at room temperature; (c) A 3-D superlattice of 10 nm Fe_3O_4 nanoparticles deposited from their octane dispersion on an amorphous carbon surface and dried at room temperature. Reprinted with permission from Ref. [17]; © 2004, American Chemical Society.

be formed. Figure 10.1 shows the typical transmission electron microscopy (TEM) images of representative 6, 10, and 12 nm Fe_3O_4 nanoparticles deposited from their hexane (or octane) dispersions. The thermal decomposition of $Fe(acac)_3$ has also been conducted in 2-pyrrolidinone in the presence of monocarboxyl-terminated PEG (MPEG-COOH); this results in MPEG being covalently bound to the nanoparticle surface via the COOH group [18].

10.2.2
Effect of Synthesis Conditions on Particle Size and Surface Properties

The synthesis conditions play important roles in determining not only the particle size but also its bulk and surface properties. Fe_3O_4 nanoparticles prepared using

the thermal decomposition method of Sun *et al.* [16, 17] disperse well in organic solvents such as hexane and toluene. The addition of MPEG-COOH to the reaction mixture during the thermal decomposition of $Fe(acac)_3$ resulted in nanoparticles which were water-soluble due to the presence of surface-bound MPEG [18]. The solubility and surface properties of the nanoparticles are critical factors in determining the biomedical applicability. For example, a comparison of the effect of uncoated, dextran-, and albumin-coated MNPs prepared using the coprecipitation method on fibroblasts *in vitro* showed distinct differences in particle uptake and cellular response [11]. The uncoated MNPs were largely internalized by the fibroblasts, resulting in eventual cell death. A similar result was obtained with the dextran-coated particles, while the albumin-coated particles resulted in cell proliferation. The modification of the surfaces of MNPs to mediate their interactions with cells will be discussed in greater detail later in the chapter.

10.3
Magnetic Nanoparticles with Polymeric Shell

One of the major challenges faced when using MNPs *in vivo* is their rapid elimination from the bloodstream by the mononuclear phagocyte system (MPS), which comprises the bone marrow progenitors, blood monocytes and tissue macrophages. Unfortunately, this rapid clearance of MNPs by the MPS prevents them from reaching the target cells. Hence, in order to increase the MNPs' circulation time in the bloodstream they can be modified with a polymeric coating so as to minimize plasma protein adsorption and render them less susceptible to clearance by the macrophages [4]. The polymer can also provide a platform for the attachment of targeting ligands which are crucial for site-specific targeting required for imaging, drug delivery, and hyperthermia applications.

The discussion of magnetic core–polymer shell nanoparticles synthesis will be divided into subsections focusing on the different methods of preparation. The techniques described here apply to the synthesis of single magnetic nanoparticles with polymeric shells. It should be noted that polymer-coated MNPs are commercially available as magnetic resonance contrast agents (e.g., Feridex, Endorem, Resovist); these products are primarily coated with dextran or dextran derivatives, and their specific preparation methods will not be described here.

10.3.1
Coating with Polymer During MNP Synthesis

10.3.1.1 Dextran-Coated MNPs via the Coprecipitation Method

As noted in Section 10.2, MNPs with polymer coatings may be prepared *in situ* during the nucleation and growth of the Fe_3O_4. This simultaneous process is often referred to as the "one-pot" method. One of the earliest studies using such a technique was that conducted by Molday and MacKenzie [9] who, reacted ferrous chloride with ferric chloride under alkaline condition in the presence of dextran

polymers [molecular weight (M_w) ~40 000 Da] to yield a suspension of dextran-coated ferromagnetic (Fe_3O_4) colloidal particles. Dextran, which is deemed to be noncytotoxic, is one of the most common coatings used for MNPs. By using TEM, the iron core was seen to range in size from 10–20 nm, while the dextran-coated particles were roughly spherical in shape, with a diameter of 40 nm. The dextran-coated particles contained 50% by weight Fe, were stable in physiological buffers, and did not aggregate over a pH range of 3–10. The use of dextran polymers with M_w ranging from 10 000 to 70 000 Da in the reaction resulted in particles which exhibited similar properties. On the other hand, the blood half-life and biodistribution of the MNPs were shown to be influenced by the various synthesis conditions [19]. Iron oxide nanoparticles prepared by precipitation, with subsequent dextran adsorption onto the particle surface, generally demonstrated shorter half-lives than those prepared by particle formation in the presence of dextran. Furthermore, synthesis conditions such as pH and temperature affected the structure of the surface-bound dextran. The longest circulation times were achieved by MNPs covered by a relatively dense brush of dextran molecules that protected the iron oxide core against contact with blood proteins and phagocytosis-associated receptors.

Experiments conducted with human fibroblasts indicated that the dextran-coated particles were taken into the cells probably through fluid phase endocytosis, and the cell behavior was adversely affected by this internalization; this resulted in possible apoptosis, aberrations in cell morphology, and resultant decreases in cell motility [20]. A recent report included investigations into the possible acute toxicity and irritation of dextran-coated MNPs injected subcutaneously into the tissues of mice [21]. The LD_{50} dosage (single treatment) for death to occur within 2 weeks was found to be ~4410 mg kg^{-1}, whereas the injection of 0.3 ml of 10% dextran-coated MNPs fluid [containing 30 mg particles in 50% (w/v) aqueous dextran solution] induced reversible effects that were well tolerated by mice. Furthermore, a crosslinked dextran coating on the MNPs was reported to be nonbiodegradable [4].

Among the various types of dextran-coated MNP, differences in the functional group of the shell polymer can have a significant effect on the efficacy of cell labeling. This was illustrated by a recent study which compared the feasibility and efficiency of labeling human mesenchymal stem cells (MSCs) and human cervix carcinoma (HeLa) cancer cells with two commercially available MNPs, Feridex and Resovist [22]. Both nanoparticle preparations have superparamagnetic cores of 10–12 nm embedded in a biocompatible polymer, yielding particles of a hydrodynamic diameter of 70–150 nm. However, Resovist comprises magnetite nanoparticles stabilized by carboxydextran, while Feridex is coated with nonfunctionalized dextran. For MSC labeling, Resovist was found to be a suitable agent, without the need for a transfection agent, and was more efficient than Feridex. In the case of the HeLa cells, Resovist was still effective, but the uptake of Feridex was very low. This difference in uptake behavior was attributed to the presence of carboxyl groups in Resovist. Under physiological conditions (pH 7.4), the carboxydextran is expected to be mainly in the deprotonated form, that is, negatively charged. The

uptake of anionic nanoparticles possibly consists of two processes which occur concomitantly: (i) the binding of anionic nanoparticles onto reactive cationic sites on the cell membrane; and (ii) an internalization of the reactive sites via the endocytosis pathway [23].

Dextran-coated MNPs with surface functionalities can provide sites for further tailoring of these nanoparticles. For example, 50 nm aminated dextran-coated MNPs from Micromod were conjugated with 30 bp DNA, and a complement of 12, 18, or 24 bp linked to a model drug, a fluorophore, was added [24]. The nucleic acid duplex served as a heat-labile linker and the heat produced by the MNPs in a radiofrequency electromagnetic field (EMF) was used to trigger the release of the fluorophore *in vitro*. The functionalized MNPs were also mixed with Matrigel and injected subcutaneously near the posterior mammary fat pad of mice, forming model tumors. The MNPs allowed noninvasive visualization by magnetic resonance imaging (MRI), and the application of an EMF to the implant resulted in the release of the model drug and penetration into the tissue. The average distance of fluorescence signal from the tissue/implant boundary in animals treated with an EMF was approximately sixfold that of unexposed controls (250 versus 42 μm).

10.3.1.2 Starch-Coated MNPs via the Coprecipitation Method

The synthesis of Fe_3O_4 via the coprecipitation method in the presence of starch resulted in biocompatible MNPs [25]. Starch is one of the most abundant naturally occurring polysaccharides. Swollen starch granules form a three-dimensional (3-D) polymeric matrix which prevents agglomeration of the iron oxide particles when they begin to nucleate from the precipitation of Fe^{2+} and Fe^{3+}. This method resulted in a homogeneous distribution of colloidal particles (~7.2 nm) in the polymeric starch matrix. The particles in the starch matrix were stable for one year in aqueous media at room temperature. The particle size, determined using a dynamic light scattering (DLS) method, was ~87 nm. When H_2O_2 was used as an oxidizing agent to cleave the polymeric starch chains, the particle size was reduced to ~42 nm, which suggested that the MNPs existed as agglomerated clusters rather than as individual particles. When starch-coated MNPs were injected into the brain parenchyma of rats for *in vivo* monitoring, the results indicated that they might be transported into the extracellular space, and also internalized in nerve cells.

Starch-coated MNPs (hydrodynamic diameter 110 nm, 94 emu g^{-1} Fe and T_2 relaxivity of 43 s^{-1} mM^{-1}) have also been investigated for MRI-monitored magnetic targeting of brain tumors in rats [26]. These MNPs were reported earlier to be nontoxic and well tolerated in both preclinical and clinical trials after systemic administration [27, 28]. The nanoparticles were injected intravenously into rats (12 mg Fe kg^{-1}) under a magnetic field density of 0 T (control) or 0.4 T (experimental) for 30 min. The MR images were acquired prior to administration of nanoparticles, and immediately after magnetic targeting at 1 h intervals over a period of 4 h. An analysis of the images revealed that magnetic targeting had induced a fivefold increase in the total glioma exposure to MNPs over nontargeted tumors

($p = 0.005$), and a 3.6-fold enhancement in the target selectivity index of nanoparticle accumulation in glioma over the normal brain ($p = 0.025$). In the magnetically targeted animals, the glioma retention of MNPs persisted for ~100 min following removal of the external magnetic field.

10.3.1.3 PEG-Coated MNPs via the Coprecipitation Method

A one-pot synthesis of MNPs coated with copolymers of PEG has also been reported [29, 30]. The iron oxide nanoparticle dispersions were prepared by coprecipitation of Fe^{2+} and Fe^{3+} from an aqueous solution by a base in the presence of the graft copolymer. One of the copolymers of PEG used was poly(glycerol monoacrylate)-*g*-poly(PEG methyl ether acrylate) (PGA-*g*-PEG) [29]. PGA-*g*-PEG was prepared by the acid hydrolysis of poly(solktal acrylate)-*g*-poly(PEG methyl ether acrylate), which was synthesized via the copolymerization of solktal acrylate and PEG methyl ether acrylate by atom transfer radical polymerization (ATRP). The size of the superparamagnetic magnetite nanoparticles could be controlled from 4 to 18 nm by varying the graft density of the copolymers.

In another method, the poly(oligo(ethylene glycol) methacrylate-*co*-methacrylic acid) (P(OEGMA-*co*-MAA)) copolymer was used [30]. This copolymer was prepared via a two-step procedure: a well-defined precursor poly(oligo(ethylene glycol) methacrylate-*co*-*tert*-butyl methacrylate), P(OEGMA-*co*-*t*BMA) ($M_n = 17\,300\,g\,mol^{-1}$; $M_w/M_n = 1.22$), was first synthesized by ATRP in the presence of the copper (I) chloride/2,2′-bipyridyl catalyst system, and subsequently selectively hydrolyzed in acid conditions. The resultant P(OEGMA-*co*-MAA) was directly utilized as a polymeric stabilizer in the MNP synthesis via the coprecipitation of iron salts method. The diameter of the MNPs could be tuned in the range 10–25 nm by varying the initial copolymer concentration. The PEGylated MNPs exhibited a long-term colloidal stability in physiological buffer. Intravenous injection into rats showed no detectable signal in the liver within the first 2 h, while maximum liver accumulation was found after 6 h, providing indirect proof of a prolonged circulation of the MNPs in the bloodstream.

A third copolymeric system used for the one-pot synthesis of polymer-coated MNPs comprised a "surface anchoring moiety" 3-(trimethoxysilyl)propyl methacrylate (TMSMA) and a protein-resistant PEG methacrylate (PEGMA) moiety [31]. The poly-(TMSMA-*r*-PEGMA) is a random copolymer synthesized from TMSMA and PEGMA by a radical polymerization reaction [32]. The ferrous and ferric chlorides were mixed with poly(TMSMA-*r*-PEGMA) before addition of the base to precipitate the nanoparticles. An external magnetic field was applied to the solution using a rare earth magnet to separate the MNPs from the remaining unreacted polymer in solution. After washing with distilled water, the MNPs were heated at 80 °C for 1 h to achieve crosslinking between the entangled polymer chains on the particle surface. The core sizes of the coated MNPs were in the range of 4–8 nm, with a hydrodynamic diameter of 16 nm. The poly(TMSMA-*r*-PEGMA)-coated MNPs dispersed well in phosphate-buffered saline (PBS) over a range of pH conditions (pH 1–10). In addition, DLS data revealed that their sizes were not altered even after 24 h of incubation in 10% serum containing cell culture medium,

which was indicative of a lack of protein adsorption on their surfaces. The incubation of these MNPs with macrophage cells resulted in an uptake which was significantly lower than that of the commercial contrast agent, Feridex. When the poly(TMSMA-*r*-PEGMA)-coated MNPs were administered to tumor xenograft mice by intravenous injection, the tumor was detected in T_2-weighted MR images within 1 h as a result of the accumulation of these MNPs within the tumor site. The authors also compared the *in vitro* and *in vivo* properties of the poly(TMSMA-*r*-PEGMA)-coated MNPs synthesized via the one-pot method with those synthesized via a two-step process. In the latter, the poly(TMSMA-*r*-PEGMA) was added to the MNPs after their precipitation from a basic solution and washing with water. Although the core diameter of these MNPs was slightly larger than that of particles from the one-pot method, their hydrodynamic diameter (~12 nm) was smaller, which suggested the presence of a thinner polymer coating, which was confirmed using a thermogravimetric analysis (TGA) that showed 15 wt% less polymer. However, the coated MNPs from the two-step process exhibited a higher magnetization (80 emu g^{-1}) than that from the one-pot method (65 emu g^{1}). The lower magnetization of the latter was attributed to interference of the polymer in the crystallization step of iron oxide nanoparticles, and also to an increased proportion of the nonmagnetic polymer component. Both types of nanoparticle exhibited similar anti-fouling and *in vivo* MRI imaging behavior.

10.3.1.4 MPEG-COOH-Coated MNPs via the High-Temperature Decomposition Method

The examples of polymer-coated MNPs obtained via the one-pot method given above were prepared using the coprecipitation method. The high-temperature decomposition process of preparing MNPs provides a better control of particle size and monodispersity, and a one-pot method of preparing biocompatible MNPs from this process was achieved through the decomposition of $Fe(acac)_3$ in 2-pyrrolidinone in the presence of MPEG-COOH [18]. The MPEG-COOH was prepared by oxidizing PEG monomethyl ether with 2,2,6,6-tetramethylpiperidine-1-oxyl (TEMPO) as catalyst at 57 °C and 10 atm of oxygen for 24 h. The particle size was affected by the molar ratio of MPEG-COOH and $Fe(acac)_3$, the M_w of MPEG-COOH, and also the concentration of $Fe(acac)_3$. Gel-permeation chromatography (GPC) experiments on the polymer extracted from the coated MNPs showed that the MPEG had retained its structure when covalently bound to the MNPs via coordination between the polymer's COOH groups and Fe on the surface of the MNPs. The surface-bound MPEG-COOH rendered the MNPs soluble in aqueous medium, almost independent of pH. A higher molar ratio of MPEG-COOH/$Fe(acac)_3$ and a higher M_w of MPEG-COOH led to an increase in water solubility. A higher MPEG-COOH/$Fe(acac)_3$ ratio also decreased the particle size and lowered the saturation magnetization (M_s). Spin-echo MR images of a rat injected with the MPEG-COOH-coated MNPs showed that the signal intensity of the liver continued to decrease after 10 h (Figure 10.2). This suggested that the MNPs have a long circulation time in the bloodstream, which makes them potentially useful as MRI contrast agents.

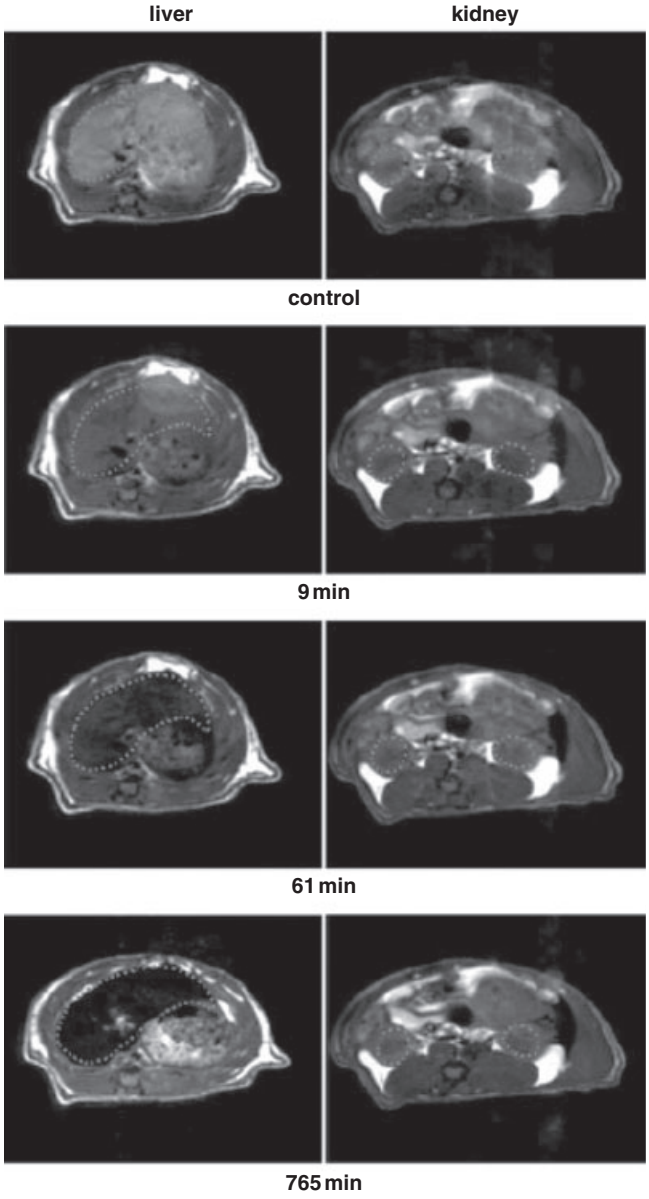

Figure 10.2 Spin-echo abdomen magnetic resonance images of a living rat. The dotted lines indicate the margins of the liver (left image) and kidneys (right image). The images in the first row were acquired before injection of the magnetic nanoparticles; images in the second to fourth rows were captured at the indicated times after injection. Reprinted with permission from Ref. [18]; © 2005, Wiley-VCH Verlag GmbH & Co. KGaA.

10.3.1.5 Triethylene Glycol-Coated MNPs via the High-Temperature Decomposition Method

Another example of the one-pot synthesis of water-soluble MNPs using the high-temperature decomposition of $Fe(acac)_3$ is to use triethylene glycol (TEG) as the reaction medium. Here, TEG played a triple role as a high-boiling point solvent, reducing agent, and stabilizer to efficiently control the particle growth and prevent interparticle aggregation [33, 34]. The size of the MNPs from TEM images was ~8 nm, while the hydrodynamic diameter of the particles in water was 16.5 nm. The cellular uptake of TEG-coated magnetite nanoparticles was investigated with rat C6 glioma cell line and control normal neural cells. Prussian blue-staining experiments indicated that, after a 4 h incubation with 100 μg Fe ml^{-1} of the TEG-coated magnetite nanoparticles, 99.6% of the C6 cells were stained whereas no blue spots were observed in the cytoplasm of control normal neural cells treated under the same conditions. The high uptake of TEG-coated magnetite nanoparticles in the C6 glioma cell line was attributed to a strong interaction between the MNPs and C6 glioma cells that might arise from the unusual metabolic activity of cancer cells, and also from an ultra-small size effect of the MNPs. A subsequent cell viability assay using MTT (3-(4,5-dimethylthiazol-2-yl)-2,5-diphenyltetrazolium bromide) indicated that incubation with these MNPs (up to 200 μg Fe ml^{-1} for 24 h) did not affect the viability of either C6 or normal neural cells.

10.3.1.6 4-Methylcatechol-Coated MNPs via High Temperature Decomposition Method

Finally, an example is given of a combination of the one-pot method to introduce an anchoring group on the MNP surface, and thereafter conjugation with the functional molecule. In this case, the coating was not a polymer but rather a peptide. Fe_3O_4 MNPs of 4.5 nm were synthesized by the thermal decomposition of iron pentacarbonyl (at 220 °C) in benzyl ether in the presence of 4-methylcatechol as surfactant, followed by air oxidation [35]. A coating of 4-methylcatechol was formed on the MNP surface as a result of the strong chelation bond between iron and the catechol unit. The aromatic ring of 4-methylcatechol on the MNPs was utilized to couple with the amine group of a cyclic RGD peptide, via the Mannich reaction in the presence of formaldehyde in dimethylformamide (DMF). The number of RGD peptides per particle was estimated as 100–200, while the overall size of the particles (measured by DLS in water) was ~8.4 nm. The RGD-coated MNPs were stable for several months in aqueous dispersion, without precipitating. Following incubation of the RGD-coated MNPs with U87MG human glioblastoma (high $\alpha_v\beta_3$ integrin level) and MCF-7 human breast cancer (low $\alpha_v\beta_3$ integrin level) cell lines at 37 °C for 30 min, the Fe uptake for U87MG cells was approximately fivefold higher than that of MCF-7 cells. This demonstrated the integrin specificity of the RGD-coated MNPs. The inhibition of RGD-coated MNPs uptake by U87MG cells in the presence of a blocking dose (2 μ*M*) of the cyclic RGD peptide further confirmed the specificity of MNPs. The r_2 relaxivity of these MNPs was measured as 165 mM^{-1} s^{-1}, which was larger than that of the commercial Feridex nanoparticles (104 mM^{-1} s^{-1}) with

a similar core size. This larger r_2 value was attributed to the stronger field perturbation around the MNPs due to the thin RGD coating. The targeting ability of the RGD-coated MNPs *in vivo* was demonstrated by T_2-weighted fast spin-echo MR imaging of mice bearing U87MG tumors. Some deposition of the RGD-coated MNPs was observed in both the liver and spleen, but rarely in kidneys and muscle. The MNPs in the tumor were observed to be mostly localized on the integrin expressing tumor vasculature and tumor cells, and there was insignificant uptake by macrophages.

10.3.2
Modification of Preformed MNPs

Although the one-pot method offers the advantage of convenience in preparing polymer-coated MNPs, a wider range of these materials can be produced by modifying the preformed nanoparticles. The polymer coating can be formed by a number of methods which are grouped under three categories for convenience, namely physical adsorption, "grafting to", and "grafting from". The physical adsorption category will cover those methods in which the interaction between the polymer coating and MNP surface involves weaker forces such as van der Waals forces and hydrogen bonding. In the "grafting to" method, stronger bonds are formed (e.g., covalent bonding or ionic interactions), although there may be situations whereby the boundary between "grafting to" and physical adsorption may not be entirely clear. In the "grafting from" method, the polymer coating results from a build-up of monomer units from the surface rather than from the attachment of polymer chains directly to the surface, as in the "grafting to" method.

10.3.2.1 Physical Adsorption of Polymer onto Preformed MNPs

As an alternative to precipitating MNPs in a PVA aqueous solution [8] to effect a coating (see Section 10.3.1), PVA can also be used to coat MNPs directly after their synthesis [36]. The MNPs were prepared by the coprecipitation of ferric and ferrous chlorides from aqueous solution by concentrated ammonia. The black precipitate, after washing with ultrapure water until neutral pH, was refluxed in a mixture of 0.8 *M* nitric acid and 0.21 *M* aqueous $Fe(NO_3)_3 \cdot 9H_2O$ for 1 h. The brown suspension obtained after dialysis against 0.01 *M* nitric acid for 2 days was mixed at various ratios with different polymer solutions, PVA, or a mixture of PVA and one of the following: vinyl alcohol/vinyl amine copolymer (aminoPVA copolymer) or PVA with randomly distributed carboxylic acid/thiol groups. The adsorption of PVA onto the oxide surfaces was reported to be nonspecific, and to result from hydrogen bonding between polar functional groups of the polymer and hydroxylated and protonated surface of the oxide [37]. These relatively weak interactions were confirmed by preliminary analytical ultracentrifugation experiments which showed polymer desorption under high shear forces. The results demonstrated that, at a low pH, the polymer layer was tightly compressed around the iron oxide core of the MNPs, whereas a strong swelling of the particles was

observed at a higher pH. Hydrogen bonding between the PVA polymer chains resulted in a hydrogel structure which provided steric stabilization to prevent the agglomeration and aggregation of the MNPs. When human melanoma tumor cells were incubated with the functionalized MNPs, it was found that the cells could strongly interact only with MNPs functionalized with the aminoPVA copolymer. The structure of the polymer shell of the iron oxide core determined the efficacy of their interaction with cells, and the physical comportment of the MNPs changed at specific PVA-to-iron oxide ratios. Thus, the cellular uptake of functionalized MNPs by human cancer cells depends both on the presence of amino groups on the coating shell of the nanoparticles and its ratio to the amount of iron oxide.

As a further development to exploit the MNPs functionalized with the aminoPVA copolymer for biomedical applications, therapeutic drugs were linked to the copolymer prior to coating the MNPs [38]. MNPs were prepared by the coprecipitation method and refluxed in a mixture of nitric acid and $Fe(NO_3)_3 \cdot 9H_2O$, as described above [36]. The MNPs were then mixed in ultrapure water with PVA, aminoPVA copolymer, and drug-linker-aminoPVA at various ratios. The MNPs were stabilized at pH 6–7. The drug-linker-aminoPVA synthesis protocol involved first the design and synthesis of bifunctional linkers of varied length and chemical composition. The anti-cancer drugs, 5-fluorouridine or doxorubicin (DOX), were then attached to biologically labile ester or peptide linkers, respectively. These drug-functionalized linkers were in turn coupled to the aminoPVA copolymer by amide linkages. The drug-functionalized-MNPs were evaluated as anticancer agents by using human melanoma cells in culture. The rate of cell uptake of 5-fluorouridine-functionalized MNPs was found to depend on the length of the linker, but not its hydrophobicity. With an optimized ester linker, the 5-fluorouridine-functionalized MNPs proved to be an efficient antitumor agent, resulting in a decreased melanoma cell viability and DNA synthesis ($IC_{50} < 0.5\ \mu M$) after 48 h exposure. However, while the Gly-Phe-Leu-Gly tetrapeptides linking DOX to MNPs were cleaved by lysosomal enzymes, the uptake of DOX-functionalized MNPs by human melanoma cells in culture was poor and hence a low efficacy was observed.

A recent study investigated the influence of the polymer coating composition and nanoparticle surface charge on the colloidal stability of MNPs coated with PVA, aminoPVA copolymer or poly(ethylene imine) (PEI) in different cell media [39]. The MNPs were prepared by the alkaline coprecipitation of ferric and ferrous chlorides in aqueous solution. The PVA used had an average M_n of 14 000 g mol^{-1} and a hydrolysis degree of 83%, while the aminoPVA copolymer had an average M_w of 80 000–140 000 Da. The MNPs were coated with either PVA or a mixture of PVA and aminoPVA copolymer (vinyl alcohol/vinyl alcohol copolymer mass ratio = 45) at various ratios. For the PEI (25 kDa) coating, the MNPs were mixed at a PEI : Fe mass ratio of 2. The colloidal stability of the polymer-coated MNPs was investigated in commonly used cell media such as RPMI and DMEM, in both the presence and absence of 10% fetal calf serum (FCS) and with the iron concentration set at 100 μg ml^{-1}. The polymer-coated MNPs were stable in water and PBS

for several months and over a pH range of 3–11, without showing any agglomeration, whereas the uncoated MNPs agglomerated immediately in PBS and biological fluids. The PVA-coated MNPs showed a high colloidal stability in FCS-supplemented media, and no increase in size was observed within 5 days. However, the agglomeration of particles in DMEM and RPMI without FCS supplementation was rapid, with the particle size increasing from <40 nm to >80 nm after 120 min. When compared to the PVA-coated MNPs, the aminoPVA copolymer-coated MNPs were relatively more stable in DMEM and less stable in RPMI, both with and without FCS supplementation. The agglomeration of these particles was observed in DMEM after 1 h, and the diameter had increased to 110 nm after 2 h, whereas the particles in DMEM supplemented with FCS retained their initial size for up to 9 days. The PEI-coated MNPs agglomerated immediately in the presence of FCS, but remained more stable in the media without FCS.

When an evaluation of cytotoxicity was conducted using HeLa cells, the PVA-coated MNPs were found to be noncytotoxic, while the aminoPVA copolymer-coated MNPs were found to be far less toxic compared to an equal amount of the copolymer in solution. This reduction in cytotoxicity was attributed to the conformational change of the polymer when adsorbed onto the surface of the MNPs. PEI-coated MNPs complexed with DNA also exhibited a lower cytotoxicity towards HeLa cells compared to the PEI-coated MNPs. The density of uncomplexed amino groups of the PEI appeared to play an important role with regards to cytotoxicity. It was postulated that, during the spontaneous PEI–DNA complex formation the PEI would interact with DNA electrostatically, thereby diminishing the high cationic charge and toxicity of PEI. Whilst the results of this study did not establish any clear correlation between the uptake of the MNPs and their cytotoxicity, it did show that the medium had a major influence on the uptake of the MNPs by HeLa cells.

10.3.2.2 **Grafting of Polymer on Preformed MNPs**

Although, as noted in Section 10.3.1, PEG and its derivatives have been used for preparing coated MNPs via the one-pot method, they are also very often used for grafting onto preformed MNPs, as they are biocompatible, hydrophilic and uncharged [40], and the surface-grafted polymer chains provide very high surface mobility leading to a high steric exclusion. Thus, the protein-resistant nature of PEG provides a "stealth" effect to the MNPs for avoiding clearance by the MPS. Unfortunately, the "stealth" effect is frequently concurrent with a loss of biomolecular targeting capabilities [41]. Hence, as will be shown below, molecules with targeting capability must be incorporated into the coatings for efficient cell targeting. The grafting of polymers such as PEG onto the surfaces of MNPs can be achieved by using either the "grafting to" or "grafting from" method. In the former case, preformed polymer chains are grafted to the surfaces of the MNPs via electrostatic interaction or coordination between groups on the polymer chain and the iron oxide. In the latter case, an initiator is first immobilized on the MNP surface, after which the polymerization of selected monomer(s) proceeds from the nanoparticle surface.

10.3.2.2.1 "Grafting to" Method

PEG Coating with Silane as a Linker One of the simplest ways to introduce PEG onto MNPs was illustrated by the reaction of 10 nm MNPs (prepared by precipitation from partially reduced ferric chloride aqueous solution) with methoxy-PEG-silane in toluene [40]. This involved reaction of the silane group of methoxy-PEG-silane with the hydroxyl group on the MNP surface. After 48 h of culture in a medium supplemented with 0.2 mg ml^{-1} PEG-modified nanoparticles, the morphology and viability of both macrophages and breast cancer cells containing the modified nanoparticles were close to those of control cells, which suggested that the nanoparticles were indeed biocompatible. However, the presence of PEG on the nanoparticles affected their internalization by macrophages and cancer cells in different ways. PEGylation was shown to enhance nanoparticle uptake into breast cancer cells (BT20) compared to unmodified nanoparticles, whereas the reverse effect was true with macrophages. In a subsequent report [42], the authors referred to a modification of MNPs with a bifunctional silane-PEG-trifluoroethylester linker, followed by treatment with ethylenediamine and conjugation with folic acid (FA) to the amino-termini of the PEG chains. A schematic of the immobilization procedure is shown in Figure 10.3. The MNP-PEG-FA conjugates were shown to be taken up by target cells at significantly higher levels than were nontargeting nanoparticles coated with PEG or dextran. The specificity of MNP-PEG-FA to target tumor cells was demonstrated by the increased nanoparticle uptake and significant contrast enhancement of HeLa cells (which are known to significantly overexpress the folate receptor) over MG-63 cells (which express very low levels of the folate receptor). In subsequent studies, the same research group applied this method again, but used a bifunctional silane-PEG-trifluoroethylester linker to immobilize the anticancer drug, methotrexate (MTX), onto MNPs [43]. Rat glioma cells (9L) cultured in the presence of 0.1 mg ml^{-1} MNP-PEG-MTX exhibited a marked reduction in viability. The cellular uptake of MNP-PEG-MTX was signifi-

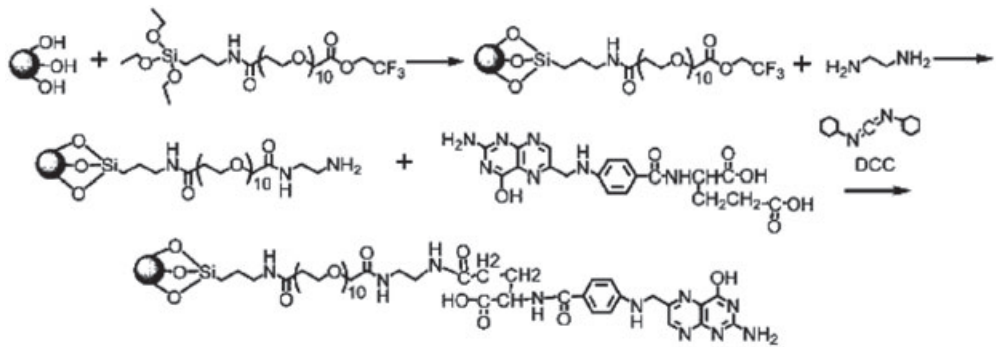

Figure 10.3 The chemical reaction scheme for the synthesis of NP-PEG-FA conjugates. Reprinted with permission from Ref. [42]; © 2006, John Wiley & Sons, Inc.

cantly higher than that of dextran-coated MNPs, and concentration-dependent. The cells incubated with MNP-PEG-MTX at a concentration of 0.1 mg ml^{-1} demonstrated an eight- to ninefold higher uptake than cells incubated with such nanoparticles at a concentration of 0.01 mg ml^{-1}. T_2-weighted MR images of the cells incubated with MNP-PEG-MTX and dextran-coated MNP showed that the former had a much shorter T_2 relaxation time (higher relaxivity) than the dextran-coated MNPs, due to an enhanced magnetism that resulted from a greater uptake of the MNP-PEG-MTX by the 9L glioma cells.

An alternative protocol for preparing MNP-PEG-FA involved first the reaction of FA with *tert*-butyloxycarbonyl (*t*-boc) and *N*-hydroxysuccinimide (NHS), followed by the reaction of (*t*-boc)folate-NHS with amino-PEG-carboxyl [44]. The resultant (*t*-boc)folate-PEG-carboxyl was then reacted with MNPs which had been conferred with NH_2 groups by reaction with (3-aminopropyl)-trimethoxysilane. Finally, the *t*-boc protective group was removed. The PEG-FA-coated MNPs were internalized by BT-20 cancer cells and exhibited a higher efficiency of intracellular uptake than either PEG- or FA-coated MNPs.

PEG Coating with Dopamine as a Linker The "grafting to" techniques described above for imparting MNPs with a PEG coating relied on the use of a silane linker to anchor the polymer coating to the MNP surface. Recently, another anchor, dopamine (DPA), has been proposed due to its high affinity for the iron oxide nanoparticle surface and the possibility of functionalization with other molecules through amide bonds [45]. The PEGylation of hydrophobic MNPs produced from the high-temperature decomposition of $Fe(acac)_3$ via a DPA anchor has been reported [46]. For this, DPA was first linked to a COOH group in PEG diacid (HOOC-PEG-COOH) via *N,N'*-dicyclohexylcarbodiimide (DCC)/NHS chemistry to produce HOOC-PEG-DPA. This was then used to replace the oleate/oleylamine coating on the particles in $CHCl_3$/DMF solution, thereby converting the particle surface from hydrophobic to hydrophilic. After the ligand exchange, the MNPs could be dispersed in water to form a clear solution, and the particles had negative zeta potentials. DLS experiments showed that, before modification, the MNPs in hexane had an overall size of approximately 11 nm, whereas after modification the sizes of the PEG-coated MNPs increased to about 40, 50, 70, and 90 nm for coatings with PEG diacid molecules of M_w 600, 3000, 6000, and 20 000 (PEG600-, PEG3000-, PEG6000-, and PEG20000-coated MNPs), respectively. The uptake of the PEG-coated MNPs by mouse macrophage cells (RAW 264.7) was compared with that of dextran-coated MNPs. At a concentration of 0.01 mg Fe ml^{-1} in the incubation medium, the dextran-coated nanoparticles gave the highest uptake, followed by PEG600-coated MNPs (>5 × 10^{-9} mg Fe per cell). The uptake of the latter was about 30–50% that of the dextran-coated MNPs. The uptakes of the PEG3000-, PEG6000-, and PEG20000-coated MNPs were comparable with the background, indicating a negligible uptake of these nanoparticles by macrophages. However, when the concentration was increased to 0.1 mg Fe ml^{-1}, the uptakes of both dextran- and PEG-coated MNPs increased about 20-fold, indicating that the uptake was concentration-dependent. The comparatively higher uptake of

the PEG600-coated MNPs was attributed to a lower extent of coverage on the MNP surface.

A similar method utilizing DPA coupled to PEG600 to functionalize ferrite nanoparticles, for use as MRI contrast agents, has been reported [47]. These nanoparticles were synthesized using a reverse micelle technique to form iron core and oxide or ferrite shell to prevent further oxidation of the nanoparticles. The relaxivities r_1 and r_2 were determined as 7.19 and 9.96 $s^{-1}\,mM^{-1}$, respectively; these values could be compared with relaxivities of approximately 4–5 $s^{-1}\,mM^{-1}$ corresponding to the commonly used commercial gadolinium chelate contrast agents in human MR examinations. However, the same group also reported that the reaction between Fe^{3+} and DPA facilitated a rapid degradation of the nanoparticles [48]. These authors postulated that the treatment of iron oxide nanoparticles with DPA resulted in an initial structure which was coordinated to the surface of the iron oxide nanoparticle due to an increased orbital overlap of the five-membered ring and a reduced steric environment of the iron complex. However, through the transfer of electrons to the iron cations on the surface and rearrangement of the oxidized DPA, a semiquinone was formed. As a result of free protons in the system, protonation of surface oxygen occurred, which released the Fe^{2+} into the solution as a hydroxide. This released fragment of the nanoparticle would eventually be oxidized in air to form iron (III) oxyhydroxide. The experimental results showed that DPA-treated iron oxide nanoparticles first formed a clear blue/purple aqueous ferrofluid, but after remaining in solution for one day, the particles became a dark-green precipitate. Upon further oxidation, the green precipitate turned red/brown, which was typical of iron (III) oxyhydroxide. A comparison of the TEM images of the DPA-treated iron oxide nanoparticles immediately after drying and after one day in aqueous solution showed the latter to have increased in size dramatically. Further evidence of the surface reaction between Fe^{3+} and DPA was obtained from Fourier-transform infrared (FTIR) and UV-visible spectroscopy. When the authors conducted energetic modeling studies to substantiate their proposed decomposition mechanism, they concluded that the use of DPA as a robust anchor for iron oxide or iron oxide shell particles might not fulfill the need for stable ferrofluids in biomedical applications.

PEG-PAsp Coating Iron hydroxide, β-FeOOH, nanoparticles coated with PEG-poly(aspartic acid) (PEG-PAsp) block copolymer have been shown to possess excellent dispersibility and stability not only in aqueous solution but also in physiological saline [49]. The PEG-PAsp block copolymer was synthesized by the polymerization of the *N*-carboxy anhydride of β-benzyl-L-aspartate, which was initiated from the terminal amino group of α-methoxy-ω-amino-PEG, in a mixed solvent of DMF and dichloromethane (DCM). The PEG-PAsp-coated iron oxide nanoparticles were obtained by the hydrolysis of $FeCl_3 \cdot 6H_2O$ in water and subsequent treatment with the PEG-PAsp block copolymers. The PEG-PAsp molecules were multivalently bound to the surface of the iron oxide nanoparticles via coordination between the carboxylic acid groups in the PAsp segment of the block copolymer and Fe ions on the surface of the iron hydroxide nanoparticles. The prepared nanoparticles

had a needle shape, and were approximately 60 nm long and 10 nm wide. The r_1 and r_2 relaxivities of the β-FeOOH nanoparticles were found to be 4.00 and 4.80 s^{-1} mM^{-1}, and significantly smaller than those for the dextran-coated iron oxide nanoparticles. The authors attributed this to the low magnetic properties of the β-FeOOH nanoparticles. The hydrodynamic diameter (~50–60 nm) of the PEG-PAsp-coated nanoparticles was essentially unchanged after storage in 0.15 *M* sodium chloride solution for one month. *In vivo* MRI experiments conducted in tumor-bearing mice showed that PEG-PAsp-coated nanoparticles, when introduced via an intravenous tail injection, achieved a higher accumulation in the solid tumor than did Feridex.

MethoxyPEG-Asp$_n$ Coating MethoxyPEG-oligo(aspartic acid) hybrid block copolymers, methoxyPEG-Asp$_n$-NH_2 (n = 2–5), have been similarly used to coat Fe_3O_4 nanoparticles [50]. The iron oxide nanoparticles were prepared via the coprecipitation of ferric and ferrous salts. The hybrid block copolymers were synthesized using liquid-phase peptide synthesis strategies, and added to an aqueous suspension of the Fe_3O_4 nanoparticles as stabilizers. The oligo(aspartic acid) portion of the block copolymer coordinated to the iron oxide surface via multiple COO^- groups, while the PEG block extended into the water matrix. The colloidal dispersion of the modified nanoparticles showed high stability when the repeated unit of aspartic acid oligomer was ≥3. The methoxyPEG-Asp$_3$-NH_2-coated iron oxide particles were found to be less toxic to OCTY mouse cells as compared to uncoated, poly(acylic acid)- and methoxyPEG-poly(acrylic acid)-coated iron oxide nanoparticles. After 72 h of culture in medium containing methoxyPEG-Asp$_3$-NH_2-coated nanoparticles, the morphology and viability of the OCTY cells were similar to those of control cells, which suggested that nanoparticles were biocompatible.

PEG Coating via Free Radical Copolymerization As an alternative to the "PEGylation" of MNP surfaces via the "grafting to" processes mentioned above, two methods have been proposed whereby the surface of Fe_2O_3 nanoparticles were coated by the free radical copolymerization of methacrylate-functionalized PEG macromonomers and surface-immobilized methacrylate groups [51]. The nanoparticles were first functionalized with methacrylate groups provided by methacryloxypropyltrimethoxysilane. In the first method, copolymerization between PEGMA macromonomer (M_n 360 g mol^{-1}) and the surface-grafted methacrylate groups was initiated by potassium persulfate and performed on the Fe_2O_3 nanoparticles directly dispersed in water after silylation and washing without any drying step (so as to limit particle aggregation before the reaction). The second method was an inverse emulsion polymerization process where the macromonomer was confined around the Fe_2O_3 nanoparticles and the copolymerization performed within droplets dispersed in heptane, which is a nonsolvent of both the macromonomer and the polymer and a poor dispersant for the silylated Fe_2O_3 nanoparticles. Poly(ethylene oxide)-block-poly(ethylene/butylene), when used as the surfactant, formed inverse micelles in heptane to stabilize the microdroplets containing the macromonomer, the dibenzoyl peroxide initiator, and the silylated

Fe_2O_3 nanoparticles. The first method (direct copolymerization) led to low amounts of grafted polymer due to diffusion limitations. However, in the second method (inverse emulsion polymerization) the local concentration of the macromonomer surrounding the aggregates of silylated Fe_2O_3 nanoparticles was increased and, as a result, the amount of surface-immobilized polymer was greatly increased. In this way, hybrid particles (~100 nm) containing up to 8 g of polymer per gram Fe_2O_3 were achieved.

Poly(L-Lysine) Coating MNPs have recently been deemed to be an attractive agent for the labeling of stem cells. Iron oxide nanoparticles have been modified with poly(L-lysine) for this purpose, and demonstrated a higher efficiency of intracellular uptake by mesenchymal stem cells (MSCs) in comparison with a commercial contrast agent, Endorem (dextran-coated MNPs) [52]. In these studies, magnetite prepared by the coprecipitation method was treated with sodium citrate and oxidized to maghemite by sodium hypochlorite to enhance the redox stability. The addition of poly(L-lysine) solution to the iron oxide resulted in an ionic interaction between the positive charges of the amine groups at the end of the poly(L-lysine) side chains and the citrate complexed on the iron oxide surface. The hydrodynamic diameter of the nanoparticles ranged from ~80 to 240 nm, depending on the poly(L-lysine)/γ-Fe_2O_3 ratio, and showed a significant increase after 5 months of storage due to particle aggregation. The zeta potential of the particles (between −40 and −46 mV) increased with increasing poly(L-lysine)/γ-Fe_2O_3 ratio, indicating that the negatively charged surface was compensated for by the positively charged poly(L-lysine). The latter was strongly associated with the iron oxide nanoparticles, and not released into cell culture medium. The results of both rat and human MSC labeling with the poly(L-lysine)-modified maghemite nanoparticles showed that the degree of iron oxide internalization by the cells increased at higher poly(L-lysine) concentrations, and that the cells took up significantly more poly(L-lysine)-modified nanoparticles than Endorem. The efficiency of cell labeling also increased with the M_w of the poly(L-lysine) up to 388 100 Da, which can be considered an optimum poly(L-lysine) M_w for γ-Fe_2O_3 nanoparticle modification. The *in vitro* MR imaging of labeled cells, and the *in vivo* MR imaging of rat brain with implanted labeled cells, indicated that both the higher r_2 relaxivity of poly(L-lysine)-modified nanoparticles and their better internalization in the cells as compared to Endorem would enable an easier MRI detection and tracking of stem cells in tissues after transplantation. Cellular uptake of the poly(L-lysine)-modified iron oxide was deemed to be facilitated by its interaction with the negatively charged cell surface. However, since anionic nanoparticles can also be effectively taken up by cells (see Section 10.3.1), the nature of the surface charges on the MNPs may be only one factor among many which affect nanoparticle internalization by cells.

Coating with Temperature-Responsive Polymers Temperature-responsive polymers have been designed to encapsulate the MNPs and drug molecules at below body temperature such that, upon exposure to a temperature equivalent to or slightly higher than normal body temperature (37 °C), the polymer would undergo

a phase transition to release the drug molecules [53, 54]. One such thermosensitive polymer is poly(*N*-isopropylacrylamide) (poly(NIPAAm)), which undergoes a coil–globule phase transition in water at its lower critical solution temperature (LCST) of ~32 °C, changing from a hydrophilic state below the LCST to a hydrophobic state above it [55]. The LCST of the polyNIPAAm can be tuned to above normal body temperature by incorporating comonomer units, such as *N,N*-dimethylacrylamide [56]. A major disadvantage of poly(NIPAAm) and its copolymer with *N,N*-dimethylacrylamide, however, is its lack of biodegradability. In order to improve the biodegradability, a water-soluble dextran-*g*-poly(*N*-isopropylacrylamide-*co*-*N,N*-dimethylacrylamide) [dextran-*g*-poly(NIPAAm-*co*-DMAAm)] polymer was synthesized via a four-step process:

- Synthesis of the poly(NIPAAm-*co*-DMAAm) with a methyl ester end group.
- Transformation of the $-COOCH_3$ end group into $-NHNH_2$.
- Reaction of dextran with 4-nitrophenyl chloroformate.
- Synthesis of the dextran-*g*-poly(NIPAAm-*co*-DMAAm) by coupling the 4-nitrophenyl chloroformate-activated dextran to the NH_2 groups of poly(NIPAAm-*co*-DMAAm) [53, 56].

This polymer exhibited a LCST of ~38 °C. The Fe_3O_4 nanoparticles were prepared using a high-temperature decomposition method and were modified with bifunctional methyl-3-mercaptopropionate ($HSCH_2CH_2COOCH_3$), which was chemically bonded to the surface of the magnetite nanoparticles via Fe–S covalent bonds. The $-OCH_3$ group was then converted to the $-NHNH_2$ functional group by a hydrazinolysis reaction to facilitate the subsequent conjugation of the anticancer drug, DOX [53]. The hydrazone linkages formed between DOX and the $-NHNH_2$ end groups are acid-labile, and hence the conjugated drug may be released in the low-acid environment (pH 5–5.5) present in the endosome of cancer cells. The encapsulation of the DOX-conjugated MNPs by the dextran-*g*-poly(NIPAAm-*co*-DMAAm) polymer was carried out by sonicating the DOX-conjugated MNPs, dextran-*g*-poly(NIPAAm-*co*-DMAAm) polymer and 1,6-diaminohexane (in the weight ratio of 2 : 3 : 1) in dimethylsulfoxide (DMSO) for 2 h at 40–50 °C. Since the dextran-*g*-poly(NIPAAm-*co*-DMAAm) polymer contains active 4-nitrophenyl chloroformate groups, it can be crosslinked by 1,6-diaminohexane, thus encapsulating the magnetic nanoparticles. The weight percentage of drug present in the carrier was ~9%. Based on the results of TGA, it was deduced that the drug carrier comprised 60 wt% of Fe_3O_4 nanoparticles and 40 wt% of organic substances, inclusive of the drug and the polymer. After encapsulation by the polymer, the size of the nanoparticles increased from ~5 to ~8 nm. At 20 °C, the drug release was lower as compared to that at 37 or 40 °C, where the release was rapid for the initial 5 h and followed by a sustained release at longer duration, with higher releases in a mildly acidic buffer solution (pH 5.3). The drug release was envisaged to occur by the collapse of the encapsulated thermoresponsive polymer and cleavage of the acid-labile hydrazone linkage.

Another class of temperature-responsive polymers is that of poly(ethylene oxide)-poly(propylene oxide)-poly(ethylene oxide) (PEO-PPO-PEO; Pluronic) block copolymer, which consists of hydrophilic PEO segments and hydrophobic PPO segments [54]. A temperature change at the critical micellization temperature (CMT) would trigger a change in the polymer conformation, and this property was subsequently utilized to control the loading and delivery of drugs. Chen *et al.* modified Pluronic P123 copolymers with PEI to obtain Pluronic-*g*-PEI (2 kDa) [54], where the terminal hydroxyl groups of P123 were covalently grafted to the amino groups of the PEI polymer. The MNPs were synthesized by the coprecipitation method, and hydroxyl groups of their surfaces exchanged with citrate ligands so as to provide excess carboxylate groups and render the surface anionic. The PEI-modified P123 polymers were conjugated to the anionic surface of magnetite nanoparticles through strong ionic interactions. The excess amino groups of PEI provided the functional groups for further interactions with guest molecules such as drugs. As these groups were confined at the layer between the magnetite surface and the P123, the therapeutic molecules would be entrapped and protected by the outer layer of the Pluronic copolymer. The schematic representation of the fabrication strategy of the drug-loaded MNPs is shown in Figure 10.4. The loading and release of drugs utilized the temperature-responsive micellization feature of the Pluronic block. At low temperature, the copolymer chains are fully extended upon interaction with water, and thus the polymer shell is open for the entry of drug molecules. An increase in temperature above the CMT induces copolymer dehydration and contraction of the polymer shell, forming compact barriers that would inhibit the diffusion of the loaded molecules out of the polymer matrix. At 20 °C, the Pluronic-coated nanoparticle has a magnetite core of ~20 nm and a hydrodynamic diameter of ~40 nm. The hydrodynamic diameter decreased to 25 nm when the temperature increased from 20 to 35 °C. The nanoparticles showed good aqueous stability and monodispersity even after 3 months of storage. The M_s was ~51 emu g^{-1} at room temperature, and not significantly different from that of uncoated magnetite. Drug-release experiments were conducted with ibuprofen and eosin Y as hydrophobic and hydrophilic model molecules, respectively. For both ibuprofen and eosin Y, at 0 or 20 °C, almost all adsorbed molecules were dissociated within 6 h. In contrast, at 37 °C, only ~20% of the drug molecules were released in 6 h, and >95% were released in 3 days. When Pluronic-coated nanoparticles loaded with monosialotetrahexosylganglioside (GM-1) were tested for the treatment of spinal cord damage in a mouse model, the particles exhibited good biocompatibility and good recovery of spinal cord injury, despite the amount of GM-1 administered (~6 mg kg^{-1}) being much lower than the traditional dose. As PEI is known to exhibit varying degrees of toxicity, depending on the M_w and degree of branching [57], this issue of toxicity must be further investigated.

10.3.2.2.2 **"Grafting from" Method** Although use of the "grafting to" technique for MNPs has resulted in the successful synthesis of magnetic core–polymer shell nanoparticles for biomedical applications (as discussed above), the technique

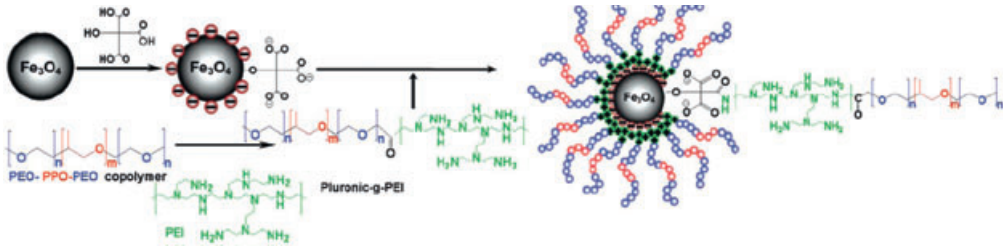

(a)

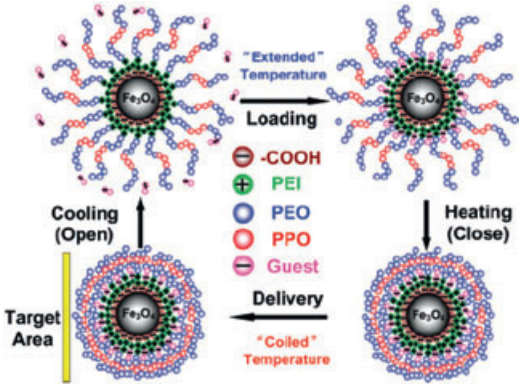

(b)

Figure 10.4 (a) Schematic illustration of the fabrication strategy for MagPluronic nanoparticles; (b) Schematic representation of temperature-responsive MagPluronic nanoparticles working as a targeted drug-delivery system with controlled payload and release. The polymer shell composed of the PEO-PPO-PEO block copolymer acts as temperature-responsive gate. A temperature change around the critical micellization temperature would trigger the opening (extended polymer conformation) and closing (coiled polymer conformation) of the polymeric shell, which favors or prevents the transit of guest substances, respectively. Reprinted with permission from Ref. [54]; © 2007, American Chemical Society.

suffers from certain shortcomings. For example, the grafting density achieved is often low, which in turn results in a polymer layer of limited thickness as the polymer molecules must diffuse through the existing polymer film to reach the reactive sites on the MNP surface. In recent years, surface-initiated graft polymerization using living polymerization techniques such as ATRP- and reversible addition-fragmentation chain transfer (RAFT)-mediated polymerization have gained in popularity. When using such "grafting from" approaches, a dense polymer layer with controlled structures can be achieved as these techniques allow for good control over M_w and monodispersity. Many of the earlier investigations on MNP surface-initiated ATRP focused on the formation of polystyrene or poly(methyl methacrylate) (PMMA) hydrophobic shells on the MNPs [58–62].

Unfortunately, however, these types of functionalized MNP have limited potential for biomedical applications.

PEGMA Coating As noted above, PEG and its derivatives are among the most attractive polymers for bioapplications, and consequently, PEG has been introduced onto the surface of MNPs via the "grafting to" method to enhance their biocompatibility. ATRP has recently been successfully employed to form a PEGMA shell around MNPs, using a "grafting from" approach [63, 64].

In the first approach, a silane initiator, [4-(chloromethyl)phenyl] trichlorosilane, was first immobilized onto the surface of Fe_3O_4 nanoparticles synthesized by the high-temperature decomposition of $Fe(acac)_3$, after which PEGMA was grafted onto the surface of MNPs via a copper-mediated ATRP in water [63]. The grafted poly(PEGMA) chains are stable and enable the modified magnetic nanoparticles to disperse well in aqueous solutions. The morphology and viability of macrophages cultured in a medium containing $0.2\,mg\,ml^{-1}$ of poly(PEGMA)-immobilized magnetic nanoparticles were similar to those of cells in the control experiment, without any nanoparticles. The uptake of nanoparticles by macrophages was greatly reduced, from 158 pg per cell to <2 pg per cell after grafting with the poly(PEGMA) layer.

The second approach is a solvent-free ATRP method where the macroinitiators on the surface of the Fe_3O_4 nanoparticles were introduced through effective ligand exchange of long alkane chain surfactants (oleic acid) by 3-chloropropionic acid [64]. This process rendered the MNPs soluble in the PEGMA monomer. After the solvent-free ATRP, monodispersed poly(PEGMA)-grafted Fe_3O_4 nanoparticles with a hydrodynamic particle size of approximately 36 nm were obtained. These nanoparticles were shown to be superparamagnetic with a M_s of $28\,emu\,g^{-1}$, and to possess good solubility and stability in water. In the solvent-free method, the polymerization rate and resultant M_w are easier to control than by ATRP in aqueous solution. An MTT assay of 3T3 fibroblasts cultured in medium containing $0.2\,mg\,ml^{-1}$ of these nanoparticles confirmed the lack of significant cytotoxicity. Uptake experiments with macrophages yielded similar results as those with the MNPs grafted with poly(PEGMA) in water. The MRI of poly(PEGMA)-grafted MNPs in water confirmed the contrast-enhancement effect in T_2-weighted sequences. Compared to conventional dextran-coated MNPs, the poly(PEGMA)-grafted nanoparticles exhibited a relatively lower r_1, a higher r_2, and higher r_2/r_1 values, indicating that the poly(PEGMA)-grafted nanoparticles may represent a good candidate for a T_2 contrast agent. Furthermore, the preserved chlorine end groups and pendant hydroxyl groups of the poly(PEGMA) can serve as reactive sites for additional functionalization.

Other Polymer Coatings Another method of preparing water-soluble MNPs from MNPs prepared by high-temperature decomposition has also been reported [65]. The oleic groups initially present on the nanoparticle surfaces were replaced via ligand-exchange reactions with various capping agents bearing more reactive moieties. These authors have tested three different compounds for tailoring the par-

ticle surface with a variety of water-soluble polymers and polyelectrolyte brushes (both cationic and anionic). The process is illustrated schematically in Figure 10.5. With ricinoleic acid as the ligand, particles that were soluble in nonpolar and weakly polar solvents were obtained. These particles could either undergo surface-initiated ring-opening polymerization (ROP), through which polylactic acid brushes were grown on the particles, or be further functionalized with 2-bromo-2-methyl propionyl bromide (BMPB) to provide the ATRP macroinitiators. The ATRP of trimethylsilylacrylate (TMSA) or trimethylsilyl methacrylate (TMSMA) resulted in poly(acrylic acid) or poly(methacrylic acid) brushes, respectively, on the particle surfaces. In addition, the ATRP initiators were also used to polymerize hydroxyethylmethacrylate (HEMA) in 1,2-dichlorobenzene, and the poly(HEMA) brushes could be further reacted with succinic anhydride to produce a poly acid on the particle surface. These particles were all water-soluble. With galactaric acid as the ligand, and with it being further acylated with BMPB, particles coated with poly(dimethylaminoethyl methacrylate) could be produced by ATRP in

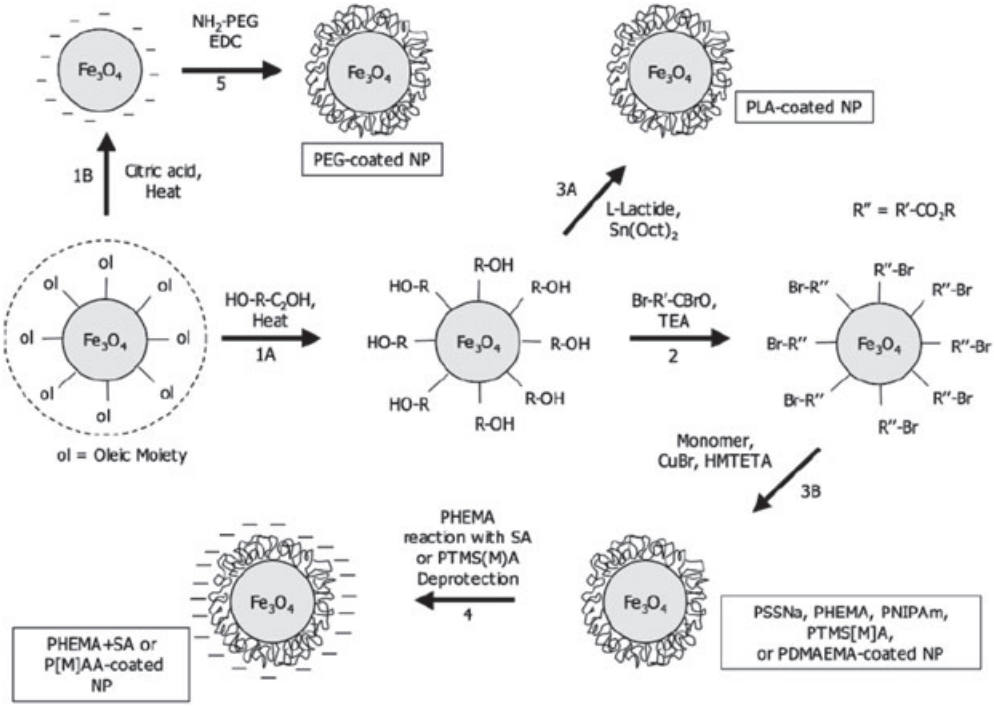

Figure 10.5 Scheme for the magnetic nanoparticles functionalization procedure described in the text. Steps 1A and 1B: ligand-exchange reactions. Step 2: acylation of hydroxyl groups to prepare ATRP surface initiators. Step 3A: surface-initiated ring-opening polymerization of L-lactide. Step 3B: surface-initiated ATRP. Step 4: deprotection or additional reaction after polymerization. Step 5: grafting of end-functionalized PEG chains onto the nanoparticle surface using amidation chemistry. Reprinted with permission from Ref. [65]; © 2007, American Chemical Society.

DMSO at room temperature, to result in positively charged and pH-responsive particles. Finally, when a mixture of citric acid and 2-bromo-2-methyl propionic acid ligands was used, water-soluble (and water-methanol-soluble) particles could be obtained, on which both polystyrene sulfonate and poly(NIPAAm) brushes could be grown through ATRP. Amino-functionalized PEG chains could also be attached to the citric acid-coated nanoparticles using carbodiimide-promoted amidation chemistry.

The surface-initiated ATRP of NIPAAm on MNPs prepared via the high-temperature decomposition of $Fe(acac)_3$ route can also be achieved by utilizing 2-(4-chlorosulfonylphenyl) ethyltrichlorosilane as the initiator and conducting the ATRP in DMSO at 40 °C for 10 h [66]. The preserved active chlorine groups on the MNPs after ATRP of NIPAAm were then used to link up with the heparin molecules in formamide. The heparinized MNPs retained a high level of magnetization (33 emu g^{-1}), and exhibited no significant cytotoxicity towards mouse macrophages (RAW 264.7). As a result of the inhibitory effect of the bound heparin on protein adsorption and cell membrane association processes, the heparinized MNPs were able to delay phagocytosis by the mouse macrophages. The uptake of the heparinized MNPs by macrophages after 8 h was approximately 30% of that for the as-synthesized particles. The activity of the immobilized heparin was also preserved, as illustrated by the effectiveness of the heparinized magnetite nanoparticles in preventing blood clotting *in vitro*. Such MNPs, with an increased plasma circulation time and antithrombotic properties, may be useful in applications where the targeted local delivery of heparin is desired, for example in the prevention or reduction of restenosis.

In another surface-initiated ATRP method, a polymeric shell consisting of NIPAAm crosslinked with PEG 400 dimethacrylate (PEG400DMA) was conferred on MNPs [67]. Either oleic or citric acid was added to the MNPs immediately after coprecipitation from the mixed ferric and ferrous salts by ammonium hydroxide to obtain hydrophobic (oleic acid-coated) or hydrophilic (citric acid-coated) nanoparticles. Subsequent ligand exchange of the oleic acid coating with 2-bromo-2-methyl propionic acid (BMPA), and the citric acid coating with either 2-bromopropionyl bromide (BPB) or bromopropyl trimethoxysilane (BPTS), provided initiating sites for the ATRP of NIPAAm in ethanol at 60 °C. The hydrodynamic diameter of oleic acid-coated particles dispersed in hexane was determined to be approximately 25 nm by DLS measurements, while that of citric acid-coated MNPs dispersed in deionized water was approximately 70 nm. The particle sizes of the poly(NIPAAm)-PEG400DMA-functionalized particles in water were all in the range of 150–300 nm, depending on the ATRP reaction time and the temperature at which the DLS was conducted. A larger particle size was obtained when the reaction time was 24 h compared to 12 h, due to an increase in the polymer shell thickness. At lower temperatures (20–30 °C), the poly(NIPAAm) shell was more hydrated, and this contributed to the increased hydrodynamic size of the composite. As the temperature was increased above the LCST of poly(NIPAAm), the polymer shell took on a collapsed state, and this resulted in the reduced hydrodynamic diameter of the functionalized particles.

The surface-initiated ROP of L-lactide (LLA) on the surface of Fe_3O_4 MNPs has been used to prepare magnetic core–polylactide (PLLA) shell nanoparticles [68]. Fe_3O_4 MNPs synthesized by the coprecipitation method were treated with 0.1 *M* glycolic acid under ultrasonic treatment for 30 min, and then maintained for 12 h at room temperature so as to impart the MNPs with hydroxyl groups. The glycolic acid-modified MNPs were dispersed in dry toluene and the suspension was heated to 130 °C to remove any remnant water by azeotropic dehydration. The residual water was removed in order to prevent the formation of free PLLA. When the suspension had cooled to room temperature, LLA was slowly added and the polymerization carried out with 0.2 wt% $Sn(Oct)_2$ as catalyst, at 130 °C under nitrogen for 20 h. TEM images revealed a shell of ~3 nm thickness around the MNP, while a TGA indicated the amount of grafted PLLA polymer to be approximately 13.3% in weight. The M_s for the glycolic acid-modified MNPs and PLLA-modified MNPs were 53.3 and 52.1 emu g^{-1}, respectively. As the polymer shell was expected to weaken the magnetism of the MNPs, this similarity in values obtained was attributed to an improved crystallinity of the magnetic core resulting from exposure to high temperatures during the coating process. The PLLA-modified MNPs with high magnetization may potentially be useful in the field of biomedicine, since PLLA has already been used in many such applications.

10.4
Encapsulation of Magnetic Nanoparticles in a Polymeric Matrix

In Section 10.3, attention was focused on the modification of single MNPs with a polymeric shell to achieve biocompatibility and possible biomedical applications, especially as MRI contrast agents. Such MNPs can be used for passive tracking or imaging of biological systems via naturally directed physiological processes, and active targeting of specific receptors on cell surfaces via the use of targeting ligands. The most commonly used targeting ligand is FA or its toxic equivalent, MTX. However, whilst other cancer-targeting ligands, such as antibodies, may be as large as 20 nm, conjugation to single MNPs would be difficult and might also result in a loss of activity due to steric hindrance [4]. Similarly, it would be difficult to conjugate both drugs and targeting ligands to single MNPs. Hence, an alternative approach would be to encapsulate multiple MNPs in a polymeric nanosphere. In this section, emphasis will be placed on these larger polymer nanospheres (of a few hundred nm diameter), and their applications.

These larger polymer nanospheres do have some *disadvantages*, at least potentially. In general, the *in vivo* half-life of nanoparticles depends inversely on the particle size [69]; particles with diameters <40 nm would have the longest residence times (of the order of hours), and can accumulate in the lymph nodes and be excreted via the urine and feces. Particles in the range of 40–200 nm can be removed by the liver and spleen in a shorter time, while particles larger than 200 nm would have the shortest half-life as a result of opsonization and clearance by the MPS. Furthermore, receptor-mediated targeting using larger nanoparticles may be less

efficient, as shown by a study of the herceptin (Her)-mediated cellular internalization of Her-gold nanoparticles through ErbB2 receptor overexpressing human breast cancer SK-Br-3 cells [70]. This study showed that 25–50 nm particles were taken up most efficiently within the tested range of 2 to 100 nm. The lower uptake of smaller particles is attributed to their inability to form multivalent binding, as well as to a low binding avidity which causes them to dissociate from the receptors before they can be engulfed by the membrane. On the other hand, the larger particles, despite their enhanced multivalent binding and much higher antibody (Her) density on the particle surface, are unable to effectively pair up the antibody with the receptor within the area of binding (due to a limited availability of receptors on the cellular surface). This might limit the process of membrane wrapping that is necessary for nanoparticle internalization. It appears, therefore, that the influences of immobilized ligand density and particle size of the nanospheres on cellular uptake efficiency are topics which require further investigation.

However, the nanospheres might also have some distinct *advantages*, as the polymer matrix can serve multiple functions, including encapsulating MNPs to utilize their magnetic properties, providing sites for further functionalization with targeting ligands, and serving as a carrier of drugs to be delivered to specific sites *in vivo*. It is envisioned that nanospheres will have different applications in cancer diagnosis and therapy, depending on how the polymer matrix is tailored. Thus, the following sections relate to the application of magnetic nanospheres, namely imaging, active targeting, and drug/gene delivery.

10.4.1 Nanospheres for Imaging

10.4.1.1 PLGA and PLLA Coating

Among the biocompatible polymers used for encapsulating MNPs, poly(D,L-lactide-*co*-glycolic acid) (PLGA) or PLLA can be considered the most popular choices. However, due to the hydrophilic surface properties of magnetite, it is difficult to attain a high magnetite content in hydrophobic biodegradable polymers such as PLGA and PLLA. A method for preparing PLGA nanospheres with a high magnetite content (40–60%) and high magnetization (26–40 emu g^{-1}) via a modified single oil-in-water emulsion-solvent evaporation method has been reported [71]. This method used oleic acid-coated MNPs (which have been washed in acetone to remove excess oleic acid) with a solid magnetite concentration of 84 wt%. The seed MNPs were dispersed into a DCM solution containing PLGA and vortexed to form a stable oily suspension. The oily suspension was then emulsified within an aqueous solution containing PVA. After rapid evaporation of the organic solvent, solid magnetic nanospheres of mean diameter of 360–370 nm with polydispersity indices of 0.12–0.20 were obtained. When the magnetite loading was increased from 16 to 60%, the M_s of the nanospheres was increased from 11 to 40 emu g^{-1}, but there was no significant change in the particle size.

In another study, a solvent evaporation method was used to encapsulate oleic acid-coated magnetite crystals of ~12 nm within nanospheres of PLLA [72]. Simi-

larly, no correlation between the magnetite loading and nanospheres size, polydispersity, or morphology was found. The encapsulation efficiency was approximately 90%, regardless of the magnetite/polymer weight ratio (which ranged from 0.0625 to 0.5). The magnetite crystals were well encapsulated within the polymer matrix, with less than 0.1% of the iron at the nanosphere surface. The factor which influenced the nanosphere size most was the stirring speed and, to a lesser degree, the polymer concentration. A higher stirring speed led to smaller nanospheres and also a narrower size distribution, with the sizes of the nanospheres ranging from 300 to 1300 nm at stirring speeds of 24 000 and 6500 rpm, respectively. An increase in polymer concentration while maintaining other parameters constant, was also found to increase the nanosphere size and polydispersity. The M_s increased with increasing magnetite amount used in formulation, with 14 emu g^{-1} being the highest value obtained. An *in vitro* MRI study showed that these nanospheres had a T_2 relaxivity of 228 s^{-1} mM^{-1}, which made them useful as a negative contrast agent for MRI.

PLGA-methoxyPEG nanospheres loaded with the commercial MRI iron oxide contrast agent, Resovist, were prepared using a modified water-oil-water double-emulsion technique [73]. These nanospheres had a hydrodynamic diameter of 233 nm and contained 1.37% Fe. The M_s of the Resovist-loaded PLGA-methoxyPEG nanospheres was 83.5 emu g^{-1}, compared to 72.9 emu g^{-1} for Resovist. It was postulated that the increased *M*s of the former was due to an agglomeration of the Resovist in the polymeric matrix during the formulation process. Cytotoxicity assays with Caco-2 cells showed that the PLGA-methoxyPEG formulation achieved 36.9 and 35.6% less cytotoxicity in comparison with Resovist after 48 h incubation at the same 20 and 50 μg ml^{-1} Fe concentrations, respectively. Comparisons of *in vitro* MRI of the Resovist and Resovist-loaded PLGA-methoxyPEG nanospheres suspended in water, and *ex vivo* MRI of Sprague-Dawley rat liver at 5 min after the *in vivo* injection of these nanoparticles, showed that the Resovist-loaded PLGA-methoxyPEG nanospheres provided better contrast effects.

10.4.1.2 PEG-PEI, Crosslinked Poly(Maleic Anhydride-*alt*-1-Tetradecene) and Lipid Micelles Coating

A comparative investigation on the effect of various encapsulating matrices in enhancing highly crystalline and monodisperse $MnFe_2O_4$ nanoparticles as negative contrast agents for MRI has been conducted [74]. Superparamagnetic $MnFe_2O_4$ nanocrystals of different sizes were synthesized via the organometallic approach reported by Kang *et al.*, based on the thermal decomposition of $Fe(CO)_5$ and $Mn_2(CO)_{10}$, and resulted in the formation of FeMn alloy nanoparticles, followed by oxidation with trimethylamine-*N*-oxide [75]. The as-synthesized nanoparticles were hydrophobic and not dispersible in aqueous media. Three approaches were used to transfer the nanoparticles into water. First, a ligand exchange of oleic acid against a water-soluble copolymer, obtained by coupling PEG to a small branched PEI, was carried out. This copolymer ligand consisted of a branched PEI moiety with a M_w of 400 g mol^{-1} and two PEG chains attached to it with M_w of 5000 g mol^{-1}.

Three different sizes (3, 9, and 18 nm) of nanoparticle were used to investigate the size-dependent effects on contrast enhancement. The hydrodynamic diameter of the 9 nm nanoparticle increased after ligand exchange, from 15 to 30 nm and 40 nm in water and chloroform, respectively. The difference in hydrodynamic diameter between nanoparticles with core sizes of 9 and 18 nm was approximately 10 nm, demonstrating that the thickness of the polymer shell for particles with different core sizes was similar. Second, the nanoparticles were encapsulated within an amphiphilic polymer shell which consisted of poly(maleic anhydride-*alt*-1-tetradecene), and crosslinked by bis(6-aminohexyl)amine. The particles remained individually dispersed after encapsulation in the amphiphilic copolymer shell. Third, the nanoparticles were embedded into lipid micelles. The nanoparticles were found to be randomly distributed within the micelles, with DLS measurements indicating the micelles to be approximately 250 nm in diameter with a broad size distribution. MRI measurements indicated that the transverse relaxivities (r_2 and r_2*) increased with increasing particle size for the nanoparticles, both after ligand exchange with PEG-PEI and after encapsulation with polymer. For the micellar system, the transverse relaxivity, and in particular r_2^*, was observed to be significantly higher as compared to the polymer-coated particles using nanoparticles of the same size. This behavior was attributed to the relatively high particle density within the micelles resulting in an increased interparticle interaction, a very low influence of diffusion effects of lipid molecules inside the micelles, and to water molecules in their surroundings.

10.4.1.3 **Iodinated Polymer Coating**

An attempt has been made to utilize MNPs for X-ray imaging applications by encapsulating them in an iodinated polymer [76]. This process involved the emulsion polymerization of 2-methacryloyloxyethyl(2,3,5-triiodobenzoate) (MAOETIB) in the presence of γ-Fe_2O_3 magnetic nanoparticles. The Fe_2O_3 magnetic nanoparticles were prepared by nucleation and controlled growth mechanism of magnetic iron oxide thin films onto gelatin nuclei, and were approximately 15 nm in size. The polymerization of MAOETIB was conducted using potassium persulfate in a toluene/water emulsion. The hydrodynamic diameters of the γ-Fe_2O_3 MNPs and γ-Fe_2O_3/polyMAOETIB nanospheres were measured at 63 and 56 nm, respectively. The smaller hydrodynamic diameter of the latter material was attributed to the hydrophobic polyMAOETIB shell, which significantly decreased the water molecule adsorption on the surface of the nanospheres. Based on high-resolution TEM investigations, the polyMAOETIB coating was reported as 9 nm, although it was unclear whether single or multiple MNPs were encapsulated. The MAOETIB concentration had a significant effect on the weight of the polyMAOETIB coating; typically, an increase in MAOETIB concentration from 1 to 2%, and to 3% (w/v H_2O) increased the weight of the polyMAOETIB from 6.9 to 38.4, and 68.9%, respectively. The polyMAOETIB coating on the surface of the MNPs significantly improved the X-ray visibility of the γ-Fe_2O_3 nanoparticles. However, no information is currently available regarding the toxicity of such nanoparticles, or their suitability for *in vivo* applications.

10.1.4.4 Poly(Styrene-*co*-Acrylic Acid) Coating

Fluorescent magnetic nanospheres have been prepared by encapsulating a fluorescent dye and magnetite nanoparticles (10–12 nm) in a hydrophobic poly(styrene-*co*-acrylic acid) shell [77]. This encapsulation was achieved using a three-step miniemulsion process. For this, the magnetite nanoparticles synthesized via the coprecipitation method were first coated with oleic acid and dispersed in octane, and a solution of sodium lauryl sulfate in water then added to form a miniemulsion. A second miniemulsion was formed by mixing styrene, hexadecane, the fluorescent dye, *N*-(2,6-diisopropylphenyl)-perylene-3,4-dicarbonacidimide and an initiator, 2,2'-azobis(2-methylbutyronitrile), with sodium lauryl sulfate in water. The miniemulsions of magnetite and styrene were mixed at a ratio of magnetite powder to monomer of 1 : 1. The polymerization was conducted at 72 °C under mechanical stirring. After 6 h, acrylic acid (0–15 wt% compared to styrene) was added and the polymerization continued overnight. The copolymerization of styrene with the hydrophilic acrylic acid introduced carboxyl groups onto the nanoparticle surface. The amount of magnetite encapsulated by this process was ~30–40% (w/w) and the M_s was 35–40 emu g^{-1} magnetite compared to 80 emu g^{-1} magnetite for uncoated magnetite nanoparticles. An increase in carboxylic surface groups led to a significant increase in the uptake behavior by the four types of cell investigated – HeLa, MSCs, Jurkat cells and KG1a cells – as shown by confocal laser scanning microscopy. However, a quantitative determination of the iron content of the cells was unsuccessful. In order to increase the uptake of the nanospheres, lysine was covalently coupled to the carboxyl groups of the nanospheres using 1-ethyl-3-(3-dimethylaminopropyl)carbodiimide hydrochloride (EDC) and sulfo-NHS. With the lysine-functionalized nanospheres, the amount of iron uptake was 11 pg per cell, a value significantly higher than was obtained with nanospheres where poly-L-lysine was physically adsorbed onto the surface. Subsequent TEM studies showed these nanoparticles to be localized in the cell endosomal compartments.

10.4.2
Nanospheres with Targeting and Recognition Capability

In the previous section, the use of MNPs encapsulated in polymer matrices for passive imaging of biological systems has been described. While passive targeting has a number of potential applications, progress and future developments in the use of MNPs in the imaging of cancers can only be realized through active targeting against specific biomolecules, to enable early and accurate diagnoses to be performed at a time when the disease would be still treatable. There is, however, one major hurdle for active targeting: namely, that of accumulating adequate levels of MNPs at the tumor site so as to allow enhanced contrast and sensitivity for detection. Hence, in the following sections attention is focused on polymer-MNP nanospheres with immobilized cancer-targeting ligands.

10.4.2.1 Polypyrrole Coating with FA as the Targeting Ligand

Recently, a series of experiments has been conducted using polypyrrole (PPY) as the polymer matrix for encapsulating MNPs [78–80]. PPY is a highly conducting polymer which has been studied for the immobilization of enzymes, antibodies, and nucleic acids. It is also suitable as a substrate for cell attachment and proliferation, and possesses excellent biocompatibility *in vivo* [81–83]. Studies with PPY have also shown that it is able to support the *in vitro* growth and differentiation of multiple cell types and the *in vivo* regeneration of damaged peripheral nerves in rats [84, 85]. The preparation of PPY-MNP nanospheres was carried out using a miniemulsion polymerization method, with either PVA or hyaluronic acid (HA) as surfactant. PPY-MNP nanospheres have a distinct spherical shape with a diameter of 80–100 nm. In addition, they are superparamagnetic with high magnetization values (>20 emu g^{-1}) and possess good electrical conductivities (1–2 S cm^{-1}). By varying the starting Fe_3O_4 : pyrrole monomer mass ratio, nanospheres with varying Fe_3O_4 contents (up to ~40 wt%) can be synthesized, although increasing the iron oxide content tends to promote aggregation. These nanospheres are also cytocompatible and, due to the electrically conducting PPY, will demonstrate enhanced specific power absorption rates on a per unit weight Fe basis (26.7 W g^{-1} Fe with an Fe_3O_4 content of 28.0 wt%) when compared to the seed Fe_3O_4 particles. The cancer-targeting ligands immobilized on the PPY-MNPs nanospheres were FA and herceptin, a monoclonal antibody against the HER-2 receptor overexpressed by 25–30% of breast cancers [86]. Both, NHS and EDC were used to facilitate covalent bond formation between the hydroxyl groups of the PVA molecules on the surface of the PPY-MNPs nanospheres and the amino groups in FA. After the immobilization of FA, an increase in hydrodynamic diameter of the nanospheres, from 326 to 400 nm, was observed, though this may be due to the presence of FA and its solvent coordination sphere. A slight increase in aggregation of the nanoparticles in water may also have resulted from the presence of the relatively hydrophobic FA on the nanoparticle surface. The iron uptakes by MCF-7 breast cancer cells when incubated with the as-synthesized and FA-functionalized PPY-MNPs nanospheres for 2 h were determined as 22 and 107 pg per cell, respectively. The corresponding amount of iron taken up by 3T3 fibroblasts cells when incubated with FA-functionalized PPY-MNPs nanospheres was ~20 pg per cell [79]. The lower uptake of FA-coupled particles by 3T3 cells compared to MCF-7 cells occurred because the former do not express folate receptors [87]. Uptake of the as-synthesized PPY-MNPs nanospheres by MCF-7 cells is attributed to nonspecific binding, since similar cell experiments [88–90] have indicated previously that nonspecific binding almost always occurs for nontargeting particles. For the FA-functionalized PPY-MNPs nanospheres, the predominant cell uptake mechanism is likely to be via a receptor-mediated endocytosis, which allows a rapid accumulation of the nanoparticles compared to the slower, nonspecific binding/penetration process [91]. As a result of this rapid receptor-mediated endocytosis, the amount of the FA-functionalized PPY-MNPs nanospheres taken up by MCF-7 cells did not alter significantly between 2 and 24 h (107 versus 101 pg per cell), unlike the case of 3T3 cells where a threefold increase was observed between 2 and 24 h.

10.4.2.2 PPY Coating with Herceptin as the Targeting Ligand

Herceptin can be immobilized on the PPY-MNPs nanospheres prepared with HA as surfactant by utilizing either its carboxyl [80] or amine groups [78]. It was envisioned that a combination of HA (with its cell-adhesive property) and herceptin would result in a high efficacy of internalization of the nanospheres by the cancer cells via a HER-2-mediated endocytosis. Uptake experiments of PPY-MNPs nanospheres, with and without herceptin immobilization, were conducted with three types of human breast cancer cell, namely SK-Br-3, HCC1954, and MDA-MB-231. The first two cell types overexpress the HER-2 receptors, while the third type is a low-HER-2-expressing breast cancer cell. The amounts of iron associated with SK-Br-3 cells after 2, 4, and 24 h of incubation are shown in Figure 10.6; notably, the amount from herceptin-functionalized nanospheres was several-fold greater than from nonfunctionalized nanospheres. This observation was in agreement with results obtained with HCC1954 cells, which showed a sevenfold increase in the internalization of herceptin-functionalized nanospheres over nonfunctionalized nanospheres after 24 h. In contrast, the amount of herceptin-functionalized nanospheres associated with MDA-MB-231 cells after 24 h was sevenfold lower than was observed with SK-Br-3 cells. Overall, these results suggested that the high uptakes of herceptin-functionalized nanospheres by SK-Br-3 and HCC1954 cells

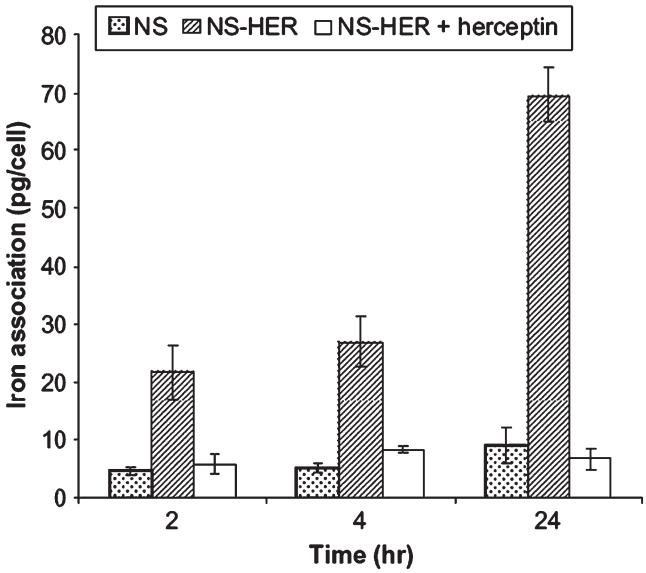

Figure 10.6 Amount of iron associated with SK-Br-3 cells after 2, 4, and 24 h incubation with NS, NS-HER, and NS-HER with free herceptin. Three sets of duplicates were performed for each datum point. The iron association of NS-HER was significantly higher ($P < 0.01$) than that of NS and NS-HER with free herceptin at all time points. Reprinted with permission from Ref. [80]; © 2008, Elsevier.

were, to a large extent, due to endocytosis via a receptor-mediated mechanism, where the immobilized herceptin on the nanospheres targets the HER-2 receptors on the cells. In order to investigate the competitive effects of free herceptin on the endocytosis of herceptin-functionalized nanospheres, the seeded cells were first treated with a medium containing herceptin for 30 min, followed by replacement with a medium containing herceptin-functionalized nanospheres and herceptin. The results shown in Figure 10.6 indicate that, under such circumstances, the uptake of herceptin-functionalized and nonfunctionalized nanospheres became comparable. This in turn indicated that free herceptin in the medium would bind to HER-2 receptors on the SK-Br-3 cells, and effectively prevent herceptin-functionalized nanospheres from interacting with the receptors. TEM images of SK-Br-3 cells cultured with herceptin-functionalized nanospheres, with or without pretreatment and cotreatment with 200 mg ml^{-1} free herceptin, are shown in Figure 10.7. For the former case, the image clearly shows the presence of endocytosed herceptin-functionalized nanospheres (Figure 10.7a), whereas for cells pretreated and cotreated with herceptin (Figure 10.7b) only minimal nanospheres were endocytosed. When cells were incubated with nonfunctionalized nanospheres, few or even no intracellular nanospheres were observed. Cytotoxicity assays indicated an uptake-associated cytotoxic effect on the cancer cells, attributable to a combined effect of bound herceptin and a higher uptake of herceptin-functionalized PPY-MNPs nanospheres, with the consequence of a much higher intracellular concentration of PPY as well as Fe_3O_4 coated with sodium dodecyl sulfate (which is used to aid the dispersion of MNPs in an aqueous medium for the polymerization of pyrrole). While the herceptin-functionalized nanospheres possess magnetic properties sufficient to show promise as an agent for hyperthermia, the magnetization of the nanospheres was seen to be significantly lower in a fluid medium than in the solid state. The diamagnetic nature of the cell environment also resulted in a diminished apparent magnetization.

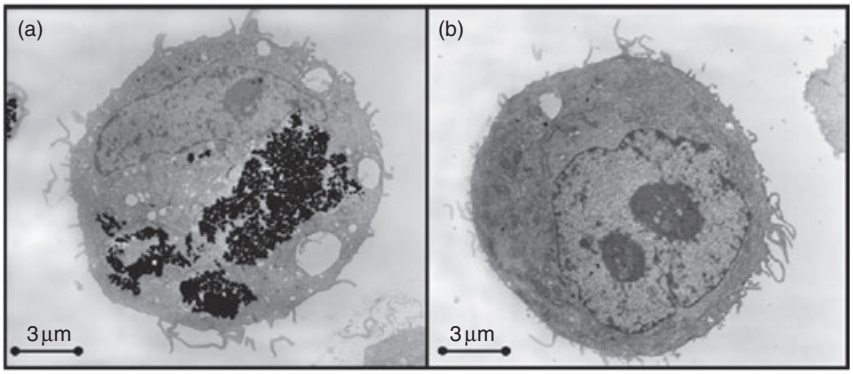

Figure 10.7 Transmission electron microscopy images of cells cultured with (a) NS-HER and (b) NS-HER pretreated and cotreated with 200 µg ml^{-1} free herceptin for 4 h. Reprinted with permission from Ref. [80]; © 2008, Elsevier.

10.4.2.3 PLGA Coating with Arginine Peptide as the Targeting Ligand

Nanospheres of MNPs encapsulated with peptide-conjugated PLGA have been tested as intracellular carriers into human MSCs [92]. Arginine peptide was selected because of its ability to facilitate intracellular translocation across the cellular membrane into the cytoplasm and nucleus. Fluorescein isothiocyanate (FITC)-conjugated arginine was used in this study to visualize the intracellular translocation of magnetic nanospheres. For this, the carboxylic acid end groups of PLGA were first activated using NHS and 1,3-dicyclohexylcarbodiimide, and then converted to primary amine groups using an excess of hexamethylene diamine. The primary amine-terminated PLGA was converted to maleimide-terminated PLGA by reaction with *N*-succinimidyl 4-(4-maleimidophenyl) butyrate. The maleimide groups were then used to conjugate with the thiol-terminated arginine. Maghemite nanoparticles prepared by the coprecipitation method were encapsulated with the arginine-conjugated PLGA via an emulsification–diffusion method. The nanospheres were mainly between 111 and 116 nm in diameter. Cellular internalization of the nanospheres into human MSCs was confirmed using confocal laser scanning microscopy and Prussian blue staining. No significant cytotoxicity was observed after a 2-day incubation of MSCs with the nanospheres.

10.4.2.4 Phospholipid Coating with Antibodies as the Targeting Ligand

Multi-MNP aggregates with surface-bound anti-CA125 monoclonal antibodies have been prepared to demonstrate the targeted *in vitro* molecular MRI of ovarian carcinoma cells [93]. The iron oxide nanoparticles were prepared via the solvothermal process [94] and shown to be almost monodisperse (diameters ranging from 10–14 nm) and with a hydrophobic heptanoic acid surface termination. The encapsulated nanoparticle aggregates were prepared via a three-step process:

- The introduction of acetic acid to partially displace heptanoic acid from the MNP surface; this resulted in the aggregation of MNPs due to a decreased steric hindrance of the MNP surface.
- Drying of the resultant aggregates on a film of dried PEGylated phospholipids.
- Resuspension of the aggregates and phospholipids in aqueous solution, which resulted in the encapsulation of the aggregates to yield micellar multi-MNPs.

The amount of acetic acid used controlled the degree of aggregation, with aggregates of hydrodynamic diameter up to 50 nm and of low polydispersity being achieved. The multi-MNPs possessed an enhanced T_2 relaxivity (368.0 s^{-1} mM^{-1} Fe) as compared to micellar, single-particle MNP (302.0 s^{-1} mM^{-1} Fe). The higher relaxivity of multi-MNPs as compared to MNPs was considered due to the increased proton spin dephasing from the cooperating MNP cores in the aggregates. The increased magnetic moment and radius of multi-MNPs enhanced the T_2 relaxation rate (r_2), without affecting the T_1 relaxation rate (r_1), thus increasing the r_2/r_1 ratio and improving the signal-to-noise ratio (SNR) of multi-MNPs as a T_2 contrast agent. The multi-MNPs were crosslinked to the monoclonal antibodies by forming a thioether bond between the maleimide-functionalized phospholipids on the

multi-MNPs and sulfhydryl groups on the monoclonal antibodies. The cell pellet of OVCAR-3 (CA125-positive) incubated with multi-MNPs conjugated to anti-CA125 monoclonal antibodies showed an enhanced negative T_2 contrast compared to the cell pellet of OVCAR-3 cells incubated with nonspecific multi-MNPs (T_2 change ~66%). Corresponding experiments conducted with the ovarian carcinoma cell line SK-OV-3 (CA125-negative) showed a negligible contrast difference between CA125-specific multi-MNPs and nonspecific multi-MNPs (T_2 change <3%).

10.4.2.5 Poly(MMA-*co*-EGDMA) Coating with BSA Surface-Imprintation

To illustrate the concept of molecular imprinting of magnetic nanospheres for potential biomedical applications, bovine serum albumin (BSA) surface-imprinted magnetic nanospheres of 500–600 nm were prepared via a two-stage core–shell miniemulsion polymerization system using methyl methacrylate (MMA) and ethylene glycol dimethacrylate (EGDMA) as functional and crosslinking monomers, respectively [95]. Fe_3O_4 MNPs of ~18 nm were first prepared using the coprecipitation method, and then encapsulated into poly(MMA-*co*-EGDMA) nanospheres via a miniemulsion polymerization of MMA and EGDMA, initiated by ammonium persulfate. Subsequently, a series of surface functionalization reactions (aminolysis followed by reaction with glutaraldehyde and BSA) were performed to immobilize BSA molecules onto the nanosphere surface. A second-stage core–shell miniemulsion polymerization was carried out to create a poly(MMA-*co*-EGDMA) shell over the BSA-functionalized nanospheres. The template BSA molecules were then removed through base hydrolysis. As a result, complementary binding sites were created for BSA on the particle surface. The magnetite content was determined as 4.44%, and the M_s was 7.6 emu g^{-1}. The imprinted nanospheres exhibited a favorable recognition property toward the template BSA molecules in aqueous medium (BSA adsorption was 6.5-fold higher than that by nonimprinted nanospheres), and also a high affinity for BSA in a mixture of lysozyme and BSA.

10.4.3 Nanospheres as Drug/Gene Delivery System

Polymeric nanospheres encapsulating MNPs and drugs may represent a promising solution to the major drawback of conventional chemotherapy – that is, the nonspecific biodistribution of the drug which can cause the death of normal cells. With this type of nanosphere, targeted delivery direct to cancer cells may be achieved using an external magnetic field. The magnetic drug carriers could be retained near the target site so as to achieve high concentrations of the chemotherapeutic agent for a given period of time, while maintaining the drug concentration in other nontarget organs and tissues at below minimal levels, thereby reducing undesirable toxic side effects. As the magnetic gradient decreases with the distance to the target, the strength of the external magnetic field and magnetization of the nanospheres would be considered important factors in the treatment efficacy. Other parameters that determine the efficacy of these nanospheres include the nanosphere size, the type of drug, and the polymeric matrix.

10.4.3.1 PLGA Loaded with Taxol

PLGA nanospheres loaded with biocompatible MNPs and the anticancer drug taxol (this is used to treat various solid tumors, such as breast and ovarian) is one of many examples of such systems [96]. The MNPs were prepared by the coprecipitation method, and sodium oleate ($C_{17}H_{33}COONa$) was added as the first surfactant to prevent their agglomeration; the result was a stable colloidal suspension. PEG was then added as a second surfactant to the MNP-oleate system, such that the resultant composition was 37.3 wt% magnetite, 50.6 wt% sodium oleate, and 12.1 wt% PEG. A modified nanoprecipitation method was used to entrap the MNPs and taxol into the PLGA nanospheres. An organic phase comprising PLGA (with D,L-lactide to glycolide ratio of 85 : 15; average M_w 50 000–75 000 Da) and taxol in acetone was added dropwise to an aqueous solution of Pluronic F66 (as a stabilizing agent) and the PEG-coated MNPs. The mixture was then stirred vigorously for several hours to allow complete evaporation of the organic solvent at room temperature. The nanospheres formed were near-spherical with a mean diameter of 250 nm, and magnetite and taxol contents of 21.5 wt% and 0.5 wt%, respectively.

10.4.3.2 PLLA and PCL Loaded with Tamoxifen

A similar polymer, PLLA (a biodegradable polyester), has also been used for encapsulating MNPs and tamoxifen, a drug used widely to treat estrogen receptor-positive breast cancer [97]. The composite nanospheres with an average size of 200 nm were synthesized via a solvent evaporation/extraction technique in an oil/water emulsion. The superparamagnetic property (M_s ~7 emu g^{-1}) of the nanospheres was provided by ~6 nm Fe_3O_4 nanoparticles (synthesized via a high-temperature decomposition method) encapsulated in the PLLA matrix. In the preparation process, PLLA, tamoxifen and oleic acid-coated MNPs were dissolved in DCM and vortexed to create the organic phase; this was then poured into a stirred aqueous solution containing 1% PVA as emulsifier. The mixture was sonicated and the formed oil/water emulsion stirred at room temperature overnight to evaporate the organic solvent. The nanospheres were then collected by centrifugation. The encapsulation efficiency for tamoxifen and Fe_3O_4 MNPs was approximately 60% and 80%, respectively, when less than 7.5 mg tamoxifen and 20 mg Fe_3O_4 MNPs were formulated in 100 mg PLLA in DCM. Approximately 57% of the entrapped drug was released into PBS containing sodium lauryl sulfate as surfactant during the first 24 h, and 88% was released in 6 days. Release of the drug from these nanospheres was very much delayed compared to that from poly(ε-caprolactone) (PCL) nanospheres (prepared from an acetone/water system), where 68% of the entrapped tamoxifen was released during the first hour with almost total release within 24 h [98]. The PLLA nanospheres with encapsulated drug and MNPs were readily taken in by MCF-7 cells, with 182 pg of nanospheres (estimated from intracellular iron levels) being internalized into each cell over a 4 h incubation period, with 500 mg nanospheres per ml culture medium. At this nanosphere concentration, the MCF-7 cancer cells exhibited morphological changes within 4 h, such that approximately 80% were no longer viable after 4 days. In contrast, when

an amount of free tamoxifen approximately equal to that encapsulated in 500 mg ml^{-1} of nanospheres was used in the incubation medium, instead of the drug-loaded nanospheres, cell viability was much higher (~67%). The lower cytotoxicity observed when the free drug was used was attributed to the low solubility of free tamoxifen in the medium, and also to its high binding affinity to plasma proteins in the growth medium [99]. On the other hand, uptake of the drug-loaded nanospheres by the MCF-7 cells may lead to tamoxifen being released directly inside the cells, thus increasing the intracellular tamoxifen concentration and hence its anticancer activity.

10.4.3.3 Chitosan Loaded with Cefradine

Magnetic Fe_3O_4 nanoparticles, a model drug and fluorescent CdTe quantum dots (QDs) have been encapsulated into chitosan nanoparticles [100]. Chitosan, a linear polysaccharide comprising glucosamine and *N*-acetyl glucosamine linked in a β(1–4) manner, has been identified to have potentially very useful biomedical applications [101]. The preparation of magnetic and fluorescent chitosan nanoparticles containing a hydrophilic drug, cefradine, was conducted in a water-in-oil microemulsion system containing cyclohexane, Triton X-100, and *n*-hexanol. The Fe_3O_4 nanoparticles, CdTe QDs and cefradine were dispersed in 0.1% chitosan (in 1 vol.% acetic acid) solution, and the mixed solution was added to the microemulsion system. Glutaraldehyde was used as a crosslinking agent, and the degree of crosslinking tailored the size, morphology, surface properties and drug release behaviors of the nanoparticles. With a crosslinking time of 12 h, the hydrodynamic diameter was ~107 nm and the zeta potential 5 mV. With shorter crosslinking times, the nanoparticles were aggregated with a higher zeta potential. The M_s was ~11 emu g^{-1}, and a drug encapsulation efficiency of >99% and loading of ~82 wt% achieved. For nanoparticles prepared with a crosslinking time of 3 h, approximately 42% of the drug was released during the first hour in a pH 7.4 release medium, while the total amount released was 90% in 40 h. When a crosslinking time of 12 h was used, the drug showed a more uniform release rate, with 79% being released in a pH 7.4 release medium within 84 h.

10.4.3.4 PECA or PCL Loaded with Cisplatin or Gemcitabine

Poly(ethyl-2-cyanoacrylate) (PECA), which has the characteristics of a fast degradation rate, low toxicity, and high compatibility with biological systems, has been used to prepare drug- and magnetite-loaded nanospheres [102] by an interfacial polymerization method. The magnetite used was from a commercial source, and two types of anticancer drug were investigated: (i) cisplatin, which is used to treat cancer of the ovary, testis, bladder, head and neck; cisplatin is insoluble in water but soluble in most organic solvents; and (ii) gemcitabine, which is most often used to treat non-small-cell lung cancer, pancreatic and bladder cancer; gemcitabine is soluble in water, slightly soluble in methanol, and practically insoluble in ethanol and polar organic solvents.

A mixture of ethyl-2-cyanoacrylate monomer, magnetite and drug in propylene carbonate constituted the oil phase, while the water phase contained 15% stabilizer

at pH 2.5. The polymerizations were performed by mixing the water and oil phases at a 2:1 weight ratio under stirring (1000 rpm) for 3 h at room temperature. The free magnetite and surfactant were removed by several rounds of centrifugation, after which an external magnetic field was introduced for complete separation of the magnetic PECA nanospheres. Based on results of particle morphology and size, and the amount of drug encapsulated, the optimal monomer/magnetite ratio was determined as 4:3. At this ratio, the magnetite loading capacity was 14.26% (w/w) and the mean particle size approximately 250 nm. The M_s of the PECA nanospheres was 6.5 emu g^{-1}. The drug loadings of cisplatin and gemcitabine were 38.09% (w/w) and 9.37% (w/w), respectively, this difference being attributed to differences in drug solubility. The drug-release behavior was monitored in PBS at 37.5 ± 0.5 °C. Gemcitabine was seen to be released more rapidly, with a plateau being reached before 3 days. In contrast, the release behavior of cisplatin (hydrophobic) was slower (a plateau was reached after 7 days) than that of gemcitabine (hydrophilic), as the affinity of cisplatin to the oil phase was higher than that of gemcitabine.

The same group also tested the use of PCL to prepare drug- and magnetite-loaded nanospheres [102]. PCL (M_w 42 500 Da), magnetite (prepared via coprecipitation and treated with oleic acid at 80 °C), and cisplatin or gemcitabine were dissolved in DCM and added into the aqueous phase containing PVA as stabilizer. After emulsification of the oil-water mixture, solvent evaporation and sample cleaning and separation, nanospheres of approximately 160 nm (as measured by laser scattering) were obtained. The maximum amount of magnetite encapsulated was determined by TGA as 25 wt%, and the M_s of the nanospheres was 17.6 emu g^{-1}. The drug loading of cisplatin and gemcitabine were 24.6 and 7.6 wt%, respectively. Similar to the results obtained with the PECA nanospheres, gemcitabine was released more rapidly and a plateau reached within 5 days, whereas for cisplatin the plateau was reached after 27 days. The mechanism of drug release from the magnetic PCL nanospheres was inferred to be mainly a diffusion process from the oil core through the polymeric network constituting the nanosphere. Magnetic PCL nanospheres containing gemcitabine, and prepared by a slightly different method from above, were tested using nude mice bearing subcutaneous human pancreatic adenocarcinoma cells *in vivo* [103]. The encapsulation efficiency of the nanospheres was rather low, with maximum magnetite and gemcitabine encapsulation efficiencies of ~7.8% and ~18.6%, respectively, of the theoretical loading. The efficacy of the injected gemcitabine-containing magnetic nanospheres in shrinking the tumor was investigated using an external 0.25 T magnet positioned cutaneously over the tumor mass for 2 h. In the absence of a magnetic field, the concentration of gemcitabine was too low for any therapeutic effect to occur. However, in the presence of a magnetic field a significant growth suppression was observed by day 15, and after 19 days the tumor was 36.4% smaller than in the control case. The magnetic field-mediated targeted drug delivery effects were comparable to those observed with systemic drug administration at 10- to 15-fold higher levels. No other significant toxic side effects were reported.

10.4.3.5 Poly(Alkylcyanoacrylate) Loaded with Tegafur or 5-Fluorouracil

Other members of the poly(alkylcyanoacrylate) family besides PECA have also been investigated for forming nanospheres containing magnetite and anticancer drugs [104]. In this investigation, the drug encapsulation and release characteristics of four types of poly(alkylcyanoacrylate) nanosphere with a magnetite core and loaded with tegafur (a broad-spectrum anticancer drug) were compared. The four polymers used were poly(ethyl-2-cyanoacrylate) (PE-2-CA), poly(butylcyanoacrylate) (PBCA), poly(hexylcyanoacrylate) (PHCA) and poly(octylcyanoacrylate) (POCA). Two drug-loading methods were tested: (i) absorption or entrapment of the drug in the polymer matrix by addition of the drug during preparation of the magnetite/poly(alkylcyanoacrylate) core–shell nanospheres (~130–150 nm) via emulsion polymerization of the respective alkylcyanoacrylate monomer; or (ii) surface adsorption onto the preformed magnetite/poly(alkylcyanoacrylate) nanospheres after incubation in the drug solution.

For the first method, the effects of pH of the polymerization medium and drug concentration on the tegafur absorption density (Γm) and encapsulation efficacy (%) for the four types of composite nanosphere tested are listed in Table 10.1. The drug loading was maximum at pH 4 (10^{-4} *M* HCl), since polymerization rate becomes slower and the absorption falls with increasing H^+. The amount of drug loaded was higher with a polymer matrix of shorter alkyl chain length, and this can be explained by the faster polymerization kinetics of shorter-chain monomers. The presence of the magnetite core was found not to affect the amount of drug encapsulated. The release of the encapsulated tegafur from nanospheres followed a biphasic process: first, an early rapid release of approximately 60% within 60 min, while the remaining 40% was released slowly during the next 120 min. The initial rapid release was attributed to the loss of surface-associated and poorly entrapped tegafur, while the slower drug release may have been due to a disintegration of the poly(alkylcyanoacrylate) matrix, to drug diffusion through this polymeric matrix, or both.

For the second method, the drug loading was increased with alkyl chain length and, in each case, the release was almost complete after 60 min. A comparison between all of the polymeric matrices showed drug release to be slightly slower when the alkyl chain was longer, this being due to the slightly stronger interaction of the lipophilic drug with the more hydrophobic poly(alkylcyanoacrylate) surfaces.

The same group also prepared similar types of magnetite core/poly(alkylcyanoacrylate) shell colloidal nanospheres loaded with 5-fluorouracil (a hydrophilic, broad-spectrum anticancer drug) [105]. When the same two drug-loading methods as described above were tested, the overall effects of pH and alkyl chain length of the polymeric matrix on 5-fluorouracil loading were similar to those with tegafur. However, the drug release was slightly slower from polymeric matrices of shorter alkyl chain length; this was most likely due to the slightly stronger interaction of hydrophilic 5-fluorouracil with the less-hydrophobic poly(alkylcyanoacrylate) surfaces.

Table 10.1 Tegafur absorption density (Γm) and encapsulation efficacy (%) for the four types of composite particle tested, as a function of HCl and Tegafur concentration.

Tegafur concentration (*M*)	HCl concentration (*M*)	Γ_m (μmol g^{-1}) / Encapsulation efficacy (%)			
		Fe_3O_4/PE-2-CA	Fe_3O_4/PBCA	Fe_3O_4/PHCA	Fe_3O_4/POCA
10^{-4}	10^{-4}	26.9 ± 1.1/90 ± 4	15.2 ± 0.3/50.5 ± 0.9	11.1 ± 0.4/36.8 ± 1.5	7.6 ± 0.3/25.2 ± 0.9
	10^{-3}	24.1 ± 1.3/80 ± 4	14.2 ± 0.4/47.4 ± 1.3	9.9 ± 0.3/33.2 ± 1.1	6.1 ± 0.3/20.1 ± 1.1
	10^{-2}	22.2 ± 1.2/74 ± 4	13.2 ± 0.6/43.9 ± 2.1	8.1 ± 0.5/27.1 ± 1.7	4.9 ± 0.2/16.3 ± 0.6
5×10^{-3}	10^{-4}	66.9 ± 2.3/95 ± 3	48.1 ± 1.2/68.8 ± 1.7	32.9 ± 0.9/46.9 ± 1.3	23.2 ± 0.7/33.1 ± 0.9
	10^{-3}	62.2 ± 1.9/89 ± 3	45.9 ± 1.4/65.7 ± 2.1	27.2 ± 0.7/38.8 ± 1.1	17.1 ± 0.7/24.4 ± 0.9
	10^{-2}	59.8 ± 1.5/85.4 ± 2.1	41.1 ± 0.7/58.7 ± 0.9	23.5 ± 0.8/33.6 ± 1.2	12.2 ± 0.4/17.4 ± 0.5
10^{-3}	10^{-4}	226 ± 4/98.3 ± 1.8	185 ± 4/80.6 ± 1.7	139.9 ± 2.3/60.8 ± 0.9	104.4 ± 1.9/45.4 ± 0.8
	10^{-3}	210 ± 3/91.2 ± 1.4	173 ± 3/75.4 ± 1.3	112.3 ± 2.3/48.8 ± 0.9	84 ± 3/36.4 ± 1.4
	10^{-2}	193 ± 4/84.1 ± 1.7	159.9 ± 2.3/69.6 ± 0.9	86.9 ± 1.7/37.8 ± 0.7	58 ± 4/25.3 ± 1.6
5×10^{-3}	10^{-4}	400 ± 10/98.5 ± 2.4	336 ± 11/83 ± 3	275 ± 11/67.9 ± 2.7	211 ± 9/52.2 ± 2.1
	10^{-3}	341 ± 12/84 ± 3	269 ± 15/66 ± 4	176 ± 8/43.6 ± 1.9	132 ± 11/33 ± 3
	10^{-2}	249 ± 12/61 ± 3	192 ± 12/47 ± 3	108 ± 10/26.7 ± 2.5	86 ± 6/21.3 ± 1.6
10^{-2}	10^{-4}	461 ± 15/98 ± 3	383 ± 11/81.6 ± 2.3	323 ± 15/69 ± 3	255 ± 8/54.2 ± 1.7
	10^{-3}	412 ± 12/88 ± 3	319 ± 10/67.8 ± 2.2	200 ± 12/42 ± 3	147 ± 6/31.2 ± 1.2
	10^{-2}	375 ± 9/79.8 ± 1.8	237 ± 16/50 ± 3	157 ± 7/33.5 ± 1.5	104 ± 6/22.2 ± 1.3

10.4.3.6 PHDCA-PEI Loaded with Doxorubicin

PEI was used as a coating for poly(hexadecylcyanoacrylate) (PHDCA) nanospheres encapsulating MNPs and the anticancer drug, DOX, in order to improve the cellular uptake of these nanospheres via electrostatic interaction with negatively charged cancer cell membranes, and thus lead to their internalization by charge-mediated endocytosis [106]. Polycationic PEI was deposited via ionic self-assembly onto the anionic PHDCA nanospheres; this led to the zeta potential of the nanospheres being increased from −12.2 mV to 38.0 mV as the weight ratio of PEI/nanospheres in the reaction mixture was increased. MRI of human breast adenocarcinoma MDA-MB-231 cells incubated with the PEI-coated and as-prepared PHDCA nanospheres with encapsulated MNPs showed that the former exhibited a dark/black color (relative T_2 weight, 19.2%), while latter showed only a gray color (relative T_2 weight, 41.0%). The MDA-MB-231 cell viability was >80% when incubated with the PEI-coated and as-prepared PHDCA nanospheres with encapsulated MNPs (but without DOX) in the concentration range of 4.9 to 156 $\mu g\,ml^{-1}$. On the other hand, the PEI-coated nanospheres with encapsulated MNPs and DOX showed a higher tumoricidal efficacy compared to the corresponding nanospheres without a PEI coating. Thus, both MRI findings and cytotoxicity results confirmed that the cationic nanospheres exhibited an increased affinity to cancer cells due to an enhancement of electrostatic interactions with the anionic cell membrane.

10.4.3.7 PLGA Loaded with QDs, DOX, and Functionalized with FA

Recently, a multifunctional polymer-based nanomedical platform for simultaneous cancer-targeted imaging and magnetically guided drug delivery was reported [107]. The platform comprised four components: (i) PLGA to form the polymer matrix for loading and subsequent controlled release of hydrophobic therapeutic agents into cells; (ii) superparamagnetic magnetite and QDs incorporated into the PLGA matrix to provide magnetically guided delivery and act as a MRI contrast agent, and for optical imaging respectively; (iii) DOX was also encapsulated to serve as a therapeutic agent for cancers; and (iv) cancer-targeting folate was conjugated onto the PLGA nanoparticles by PEG groups to target KB cancer cells that overexpressed folate receptors on their cell surface. A schematic of the preparation process is shown in Figure 10.8. A mixture of the hydrophobic magnetite or CdSe/ZnS nanocrystals, DOX and PLGA in DCM was poured into an aqueous solution containing F127 (a nonionic, amphiphilic surfactant used as the emulsifier for the synthesis of polymer nanospheres [108]) with sonication. After evaporation of the organic solvent at room temperature, the PLGA nanospheres incorporating inorganic nanoparticles and DOX were collected. The positively charged, poly(L-lysine) domain of poly(L-lysine)-PEG-folate (PLL-PEG-FOL) was adsorbed on the nanoparticle surfaces through the electrostatic interaction with the negatively charged surface of the PLGA nanoparticles derived from the terminal carboxylate groups of the PLGA chain [108]. The PEG chains conferred biocompatibility and water-dispersity to the polymer nanospheres. TEM images showed the size of polymer nanospheres to range from 100 to 200 nm (Figure 10.9). Both, TGA and UV-visible

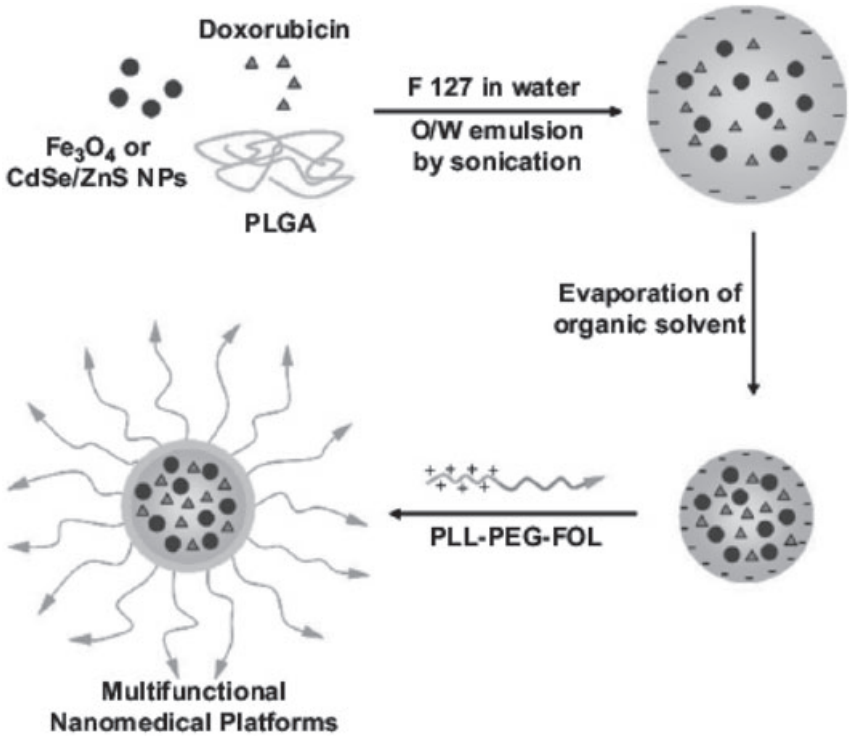

Figure 10.8 Synthetic procedure for the multifunctional polymer nanoparticles. Reprinted with permission from Ref. [107]; © 2008, Wiley-VCH Verlag GmbH & Co. KGaA.

spectroscopy indicated that 30.0 wt% and 0.8 wt% of the Fe_3O_4 nanoparticles and DOX, respectively, were incorporated into the PLGA nanospheres. The size of the polymer nanospheres remained almost unchanged following the PLL-PEG-FOL coating, demonstrating the absence of any marked aggregation. It appeared that aggregation was inhibited due to electrostatic repulsions between the positively charged nanospheres and the steric stabilization between the PEG chains surrounding the nanospheres. The specific relaxivity, r_2, was calculated as $190\,s^{-1}\,mM^{-1}$ for the PLGA nanospheres encapsulating the MNPs and DOXO. The T_2-weighted MR images of KB cancer cells incubated with the folate-functionalized nanospheres, were darker than those of NIH-3T3 fibroblasts treated in the same fashion, indicating that the folate groups on the polymer nanospheres possessed a specific targeting ability for cancer cells that overexpressed the folate receptors, but not for normal cells. The application of an external magnetic field during the incubation period produced an even darker image, indicating that the combination of folate-targeting groups and external magnetic field led to a synergistic enhancement of the cancer-targeting efficiency. Confocal laser scanning microscopy

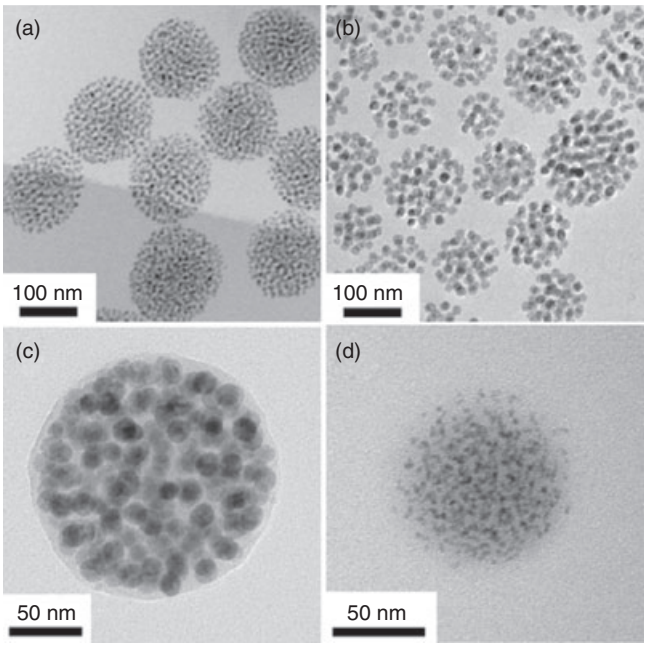

Figure 10.9 Transmission electron microscopy images of PLGA(MNP/DOXO) nanoparticles embedded with (a) 7 nm, and (b), (c) 15 nm Fe_3O_4 nanoparticles, and (d) PLGA(QD/DOXO) nanoparticles embedded with 3 nm CdSe/ZnS nanocrystals. Reprinted with permission from Ref. [107]; © 2008, Wiley-VCH Verlag GmbH & Co. KGaA.

confirmed the effectiveness of the folate-functionalized PLGA nanospheres (containing QDs) in targeting the KB cells. Cytotoxicity studies showed that the PLGA nanospheres with MNPs but without DOX exhibited almost no toxicity in KB cells, whereas the folate-functionalized PLGA nanospheres encapsulating MNPs and DOX were more cytotoxic than free DOX (0.4 μ*M*). In addition, the simultaneous use of folate active targeting and magnetic field on PLGA nanospheres encapsulating MNPs and DOX led to a synergistic increase in the cell growth inhibitory effect on the KB cells.

10.4.3.8 PEI and Transferrin-Mediated Gene Delivery

The use of polymer-coated MNPs for gene delivery has also been reported [109]. Cationic lipid-coated MNPs associated with transferrin were evaluated as gene transfer vectors in the presence of a static magnetic field. MNPs were prepared by the coprecipitation method and surface-coated with cationic lipids, composed of dimethyldioctadecylammonium bromide/soy phosphatidylcholine (DDAB/soy PC) at 60 : 40 (mol/mol). Based on DLS measurements, the size of the cationic lipid-coated MNPs was found to be approximately 78.3 nm, while TEM images

showed that the MNPs consisted of clusters of magnetite cores of <10 nm diameter with a lipid coating. These cationic MNPs were then combined with PEI-condensed plasmid DNA (pDNA), followed by transferrin. PEI and transferrin-coated MNPs exhibited an up to 300-fold higher transfection activity in KB cell line compared to the commonly used cationic liposomes or polymer complexes. The transfection efficiency is dependent on factors such as DDAB/pDNA (+/−) charge ratio, PEI/pDNA ratio, associated transferrin amount, and the magnetic field strength. An optimum transfection for the PEI-transferrin-MNPs was obtained at a DDAB/pDNA (+/−) charge ratio of 4 and a PEI nitrogen to pDNA phosphate (N/P) ratio of 1. The cytotoxicity assay of the optimized MNPs showed a KB cell viability of approximately 92%. PEI acts both as a pDNA condensation agent and a proton sponge in order to facilitate endosomal lysis. The incorporation of transferrin was shown to further enhance gene delivery, most likely due to a transferrin receptor-mediated cellular uptake of the vectors. In the absence of a magnetic field, the transfection efficiency was drastically reduced. Hence, the magnetic field was deemed to facilitate particle sedimentation onto the cell surface, while nonspecific electrostatic or receptor-based mechanisms may be responsible for the cellular uptake of magnetic vectors.

10.4.3.9 Polyamidoamine (PAMAM) Dendrimer-Mediated Gene Delivery

As another example, PAMAM dendrimer was grown on the surface of 8 nm MNPs and used as a vector for the transfection of anti-sense *survivin* oligodeoxynucleotide (asODN) [110]. A schematic of the synthesis of PAMAM dendrimer-modified MNPs, followed by complexation of the modified MNPs with asODN and the internalization process of the thus-formed complex, is presented in Figure 10.10. The dendrimer-modified MNPs formed composites of 20–40 nm. The fifth-generation dendrimer-modified MNPs with asODNs showed the highest growth inhibition (~45%) of cancer cells (MCF-7, MDA-MB-435, and HepG2) at a concentration of 10.0[C] (where [C] is equivalent to 0.025 mg ml^{-1} dendrimer-modified MNPs with 2 μ*M* asODN). The asODNs combine with dendrimer-modified MNPs via an electrostatic interaction, and the resultant asODN-MNPs have a positive charge on their surface which facilitates attachment to the tumor cells; this is followed by endocytosis. The asODNs then escape from the composites, enter the ribosome, bind the start sites of *survivn* mRNA, block translation of *survivin* mRNA into *survivin* protein, eliminate the function of *survivn* protein against apoptosis, and induce cell apoptosis. These results show that PAMAM dendrimer-modified MNPs may represent a good gene delivery system and have potential applications in cancer therapy and molecular imaging diagnosis.

10.5 Future Perspectives

During the past decade, important advances in MNP synthesis and surface modifications have been achieved, such that a number of MNP products are now

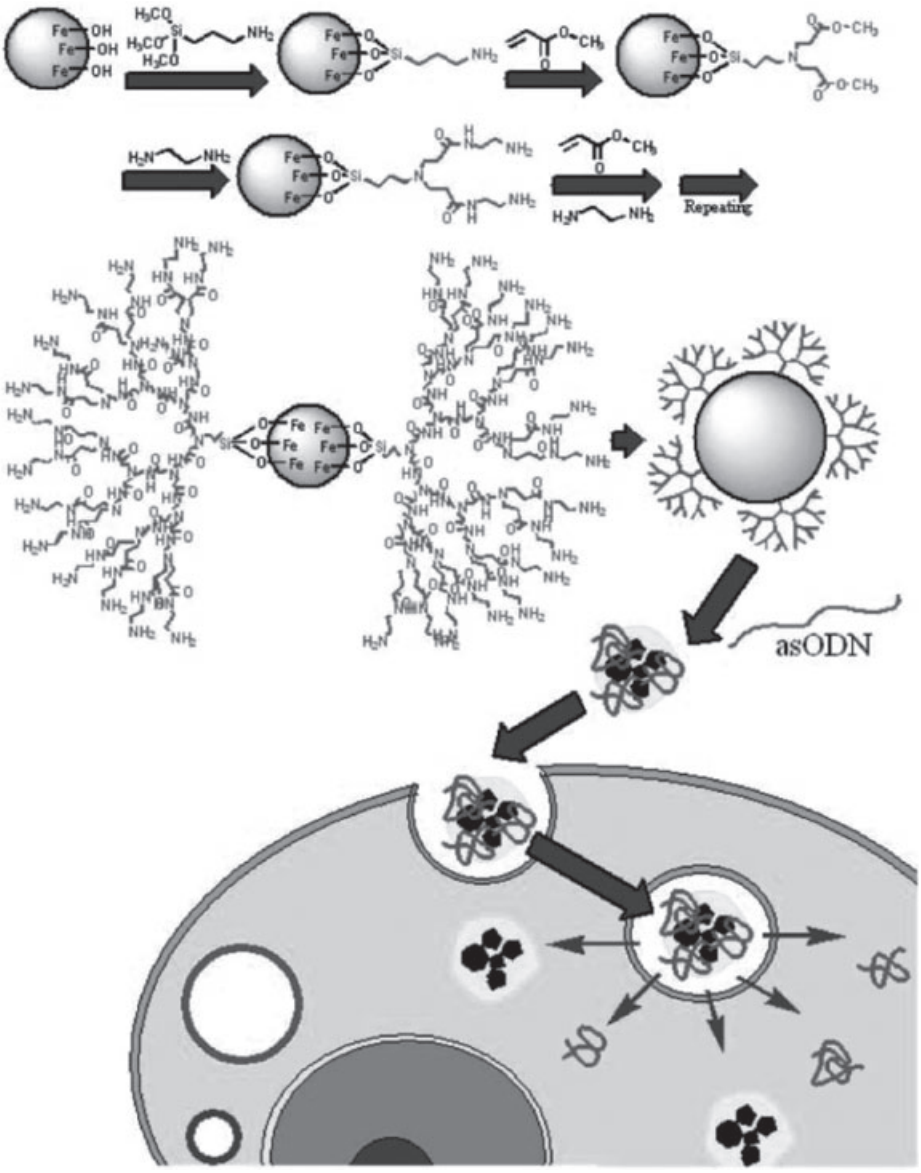

Figure 10.10 Growth of PAMAM dendrimer on the surface of MNPs for nonviral gene transfection based on complexation with an asODN. Nine steps are shown in the process: 3-aminopropyltriethoxysilane (APTS) was added to form amine-terminated MNPs (G_0 dMNP), excessive methacrylate was added to obtain ester-terminated MNPs, ethylenediamine was added to form amine-terminated $G_{1.0}$ dMNP, methacrylate and ethylenediamine were added alternately to obtain dMNP with generations from 1.0 to 5.0, complexation between dMNP and asODN, adsorption of dMNP–asODN complexes onto the cancer cell surfaces, dMNP–asODN complexes were endocytosed by cancer cells, endosome-containing dMNP–asODN complexes were located around the nucleus, and dMNP and asODN escaped from the endosome into the cytoplasm. Reprinted with permission from Ref. [110]; © 2007, American Association for Cancer Research.

available on a commercial basis. Nevertheless, a number of challenges remain to be addressed before the potential of technologies using MNPs can be fully realized for biomedical applications, such as targeted MR imaging, drug/gene delivery, and hyperthermia for cancer diagnosis and treatment. The increase in uniformity and relaxivity of MNPs will improve MRI sensitivity, and $MnFe_2O_4$ nanoparticles with r_2 relaxivities significantly higher than those of conventional crosslinked iron oxide MR contrast agents have been reported [111]. Improvements in contrast agents can be expected to lead to significant enhancements in MRI due to the lower inherent sensitivity of the technique as compared to optical imaging and positron emission tomography [112]. As newer types of MNP with more favorable physicochemical properties continue to be developed, their nonspecific toxicological aspects must also be minimized. The toxicity of nanoparticles may be the result of many factors, including their size, chemical composition, biodegradability and surface chemistry; indeed, the surface modifications of nanoparticles may play a clear role in minimizing their toxicological effects [41].

The active targeting of MNPs against specific biomolecules on tumors will result in a higher accumulation of MNPs at the disease sites, and thus allow an enhanced detection contrast and sensitivity. The ability to target small and early-stage tumors will be highly advantageous, as an early and accurate diagnosis can greatly increase the probability of successful treatment. Furthermore, those MNPs accumulated in tumor cells may also serve as a heating agent in magnetic fluid hyperthermia to allow the localized treatment of tumors. Consequently, the development of target recognition moieties and strategies to couple these moieties to the MNPs, without degrading their functions, represent critical factors for achieving these desired treatment strategies. The functionalized MNPs must also meet further requirements, in that they are not taken up to any significant degree by normal tissue cells and macrophages. Multimodality treatments which combine targeted chemotherapy and magnetically mediated hyperthermia may also bring about synergistic effects; for example, when MNPs are positioned in or close to cancer cells, they may act both as a chemotherapeutic drug carrier and as a heating agent in the presence of a magnetic field. Any drug transported by the MNPs to the cancer cell must retain its biological activity and be released at the target site. For this, the use of heat-labile linkers to conjugate the drug to the MNP will offer another degree of control for the release of drugs through heating of the MNPs using external magnetic fields.

The large volume of research on MNPs which has been carried out during the past few years has produced many encouraging results relating to the application of MNPs as a targeting, imaging, and heating agents in the treatment of cancer. However, it is important also to realize the limitations of these investigations, and in particular the problems associated with scaling up from *in vitro* studies, via animal models, to human applications. There is, nonetheless, a strong impetus for interdisciplinary research into MNPs which will surely bring about improvements in both experimental and materials design in order to meet these challenges. Clearly, new opportunities for the use of these nanoparticles for biomedical applications are to be expected in the near future.

References

1 Pankhurst, Q.A., Connolly, J., Jones, S.K. and Dobson, J. (2003) Applications of magnetic nanoparticles in biomedicine. *Journal of Physics D: Applied Physics*, **36**, R167–81.

2 Ito, A., Shinkai, M., Honda, H. and Kobayashi, T. (2005) Medical application of functionalized magnetic nanoparticles. *Journal of Bioscience and Bioengineering*, **100**, 1–11.

3 Monet, S., Vasseur, S., Grasset, F. and Duguet, E. (2004) Magnetic nanoparticle design for medical diagnosis and therapy. *Journal of Materials Chemistry*, **14**, 2161–75.

4 McCarthy, J.R., Kelly, K.A., Sun, E.Y. and Weissleder, R. (2007) Targeted delivery of multifunctional magnetic nanoparticles. *Nanomedicine*, **2**, 153–7.

5 Xu, S. and Sun, S. (2007) Monodisperse magnetic nanoparticles for biomedical applications. *Polymer International*, **56**, 821–6.

6 Majewski, P. and Thierry, B. (2007) Functionalized magnetite nanoparticles – synthesis, properties, and bioapplications. *Critical Reviews in Solid State and Materials Sciences*, **32**, 203–15.

7 Massart, R. and Cabuil, V. (1987) Effect of some parameters on the formation of colloidal magnetite in alkaline medium – yield and particle-size control. *Journale de Chimie Physique et de Physico-Chimie Biologique*, **84**, 967–73.

8 Lee, J., Isobe, T. and Senna, M. (1996) Preparation of ultrafine Fe_3O_4 particles by precipitation in the presence of PVA at high pH. *Journal of Colloid and Interface Science*, **177**, 490–4.

9 Molday, R.S. and MacKenzie, D. (1982) Immunospecific ferromagnetic iron-dextran reagents for the labeling and magnetic separation of cells. *Journal of Immunological Methods*, **52**, 353–67.

10 Pardoe, H., Chua-anusorn, W. St, Pierre, T.G. and Dobson, J. (2001) Structural and magnetic properties of nanoscale iron oxide particles synthesized in the presence of dextran or polyvinyl alcohol. *Journal of Magnetism and Magnetic Materials*, **225**, 41–6.

11 Berry, C.C., Wells, S., Charles, S. and Curtis, A.S.G. (2003) Dextran and albumin derivatized iron oxide nanoparticles: influence on fibroblasts in vitro. *Biomaterials*, **24**, 4551–7.

12 Liu, X., Guan, Y., Ma, Z. and Liu, H. (2004) Surface modification and characterization of magnetic polymer nanospheres prepared by miniemulsion polymerization. *Langmuir*, **20**, 10278–82.

13 Mikhaylova, M., Kim, D.K., Bobrysheva, N., Osmolowsky, M., Semenov, V., Tsakalakos, T. and Muhammed, M. (2004) Superparamagnetism of magnetite nanoparticles: dependence on surface modification. *Langmuir*, **20**, 2472–7.

14 Moeser, G.D., Green, W.H., Laibinis, P.E., Linse, P. and Hatton, T.A. (2004) Structure of polymer-stabilized magnetic fluids: small-angle neutron scattering and mean-field lattice modeling. *Langmuir*, **20**, 5223–34.

15 Kim, E.H., Lee, H.S., Kwak, B.K. and Kim, B.-K. (2005) Synthesis of ferrofluid with magnetic nanoparticles by sonochemical method for MRI contrast agent. *Journal of Magnetism and Magnetic Materials*, **289**, 328–30.

16 Sun, S. and Zeng, H. (2002) Size-controlled synthesis of magnetite nanoparticles. *Journal of the American Chemical Society*, **124**, 8204.

17 Sun, S., Zeng, H., Robinson, D.B., Raoux, S., Rice, P.M., Wang, S.X. and Li, G. (2004) Monodisperse MFe_2O_4 (M = Fe, Co, Mn) nanoparticles. *Journal of the American Chemical Society*, **126**, 273–9.

18 Li, Z., Wei, L., Gao, M.Y. and Lei, H. (2005) One-pot reaction to synthesize biocompatible magnetite nanoparticles. *Advanced Materials*, **17**, 1001–5.

19 Weissleder, R., Bogdanov, A., Neuwelt, E.A. and Papisov, M. (1995) Long-circulating iron oxides for MR imaging. *Advanced Drug Delivery Reviews*, **16**, 321–34.

20 Berry, C.C., Wells, S., Charles, S., Aitchison, G. and Curtis, A.S.G. (2004) Cell response to dextran-derivatised iron

oxide nanoparticles post internalization. *Biomaterials*, **25**, 5405–13.
21 Zhai, Y., Wang, X., Wang, X., Xie, H. and Gu and H. (2008) Acute toxicity and irritation of water-based dextran-coated magnetic fluid injected in Mice. *Journal of Biomedical Materials Research A*, **85**A, 582–7.
22 Mailänder, V., Lorenz, M.R., Holzapfel, V., Musyanovych, A., Fuchs, K., Wiesneth, M., Walther, P., Landfester, K. and Schrezenmeier, H. (2008) Carboxylated superparamagnetic iron oxide particles label cells intracellularly without transfection agents. *Molecular Imaging and Biology*, **10**, 138–46.
23 Wilhelm, C. and Gazeau, F. (2008) Universal cell labelling with anionic magnetic nanoparticles. *Biomaterials*, **29**, 3161–74.
24 Derfus, A.M., Maltzahn, G., Harris, T.J., Duza, T., Vecchio, K.S., Ruoslahti, E. and Bhatia, S.N. (2007) Remotely triggered release from magnetic nanoparticles. *Advanced Materials*, **19**, 3932–6.
25 Kim, D.K., Mikhaylova, M., Wang, F.H., Kehr, J., Bjelke, B., Zhang, Y., Tsakalakos, T. and Muhammed, M. (2003) Starch-coated superparamagnetic nanoparticles as MR contrast agents. *Chemistry of Materials*, **15**, 4343–51.
26 Chertok, B., Moffat, B.A., David, A.E., Yu, F., Bergemann, C., Ross, B.D. and Yang, V.C. (2008) Iron oxide nanoparticles as a drug delivery vehicle for MRI monitored magnetic targeting of brain tumors. *Biomaterials*, **29**, 487–96.
27 Lubbe, A.S., Bergemann, C., Huhnt, W., Fricke, T., Riess, H., Brock, J.W. and Huhn, D. (1996) Preclinical experiences with magnetic drug targeting: tolerance and efficacy. *Cancer Research*, **56**, 4694–701.
28 Lubbe, A.S., Bergemann, C., Riess, H., Schriever, F., Reichardt, P., Possinger, K., Matthias, M., Dorken, B., Herrmann, F., Gurtler, R., Hohenberger, P., Hass, N., Sohr, R., Sander, B., Lemke, A.-J., Ohlendorf, D., Huhnt, W. and Huhn, D. (1996) Clinical experiences with magnetic drug targeting: a phase I study with 40-epidoxorubicin in 14 patients with advanced solid tumors. *Cancer Research*, **56**, 4686–93.
29 Wan, S.R., Huang, J.S., Yan, H.S. and Liu, K.L. (2006) Size-controlled preparation of magnetite nanoparticles in the presence of graft copolymers. *Journal of Materials Chemistry*, **16**, 298–303.
30 Lutz, J.-F., Stiller, S., Hoth, A., Kaufner, L., Pison, U. and Cartier, R. (2006) One-pot synthesis of PEGylated ultrasmall iron-oxide nanoparticles and their in vivo evaluation as magnetic resonance imaging contrast agents. *Biomacromolecules*, **7**, 3132–8.
31 Lee, H., Lee, E., Kim, D.K., Jang, N.K., Jeong, Y.Y. and Jon, S. (2006) Antibiofouling polymer-coated superparamagnetic iron oxide nanoparticles as potential magnetic resonance contrast agents for in vivo cancer imaging. *Journal of the American Chemical Society*, **128**, 7383–9.
32 Jon, S.Y., Seong, J.H., Khademhosseini, A., Tran, T.N.T., Laibinis, P.E. and Langer, R. (2003) Construction of nonbiofouling surfaces by polymeric self-assembled monolayers. *Langmuir*, **19**, 9989–93.
33 Cai, W. and Wan, J. (2007) Facile synthesis of superparamagnetic magnetite nanoparticles in liquid polyols. *Journal of Colloid and Interface Science*, **305**, 366–70.
34 Wan, J., Cai, W., Meng, X. and Liu, E. (2007) Monodisperse water-soluble magnetite nanoparticles prepared by polyol process for high-performance magnetic resonance imaging. *Chemical Communications (Cambridge, England)*, **47**, 5004–6.
35 Xie, J., Chen, K., Lee, H.-Y., Xu, C., Hsu, A.R., Peng, S., Chen, X. and Sun, S. (2008) Ultrasmall c(RGDyK)-coated Fe_3O_4 nanoparticles and their specific targeting to integrin alpha(v)beta3-rich tumor cells. *Journal of the American Chemical Society*, **130**, 7542–3.
36 Petri-Fink, A., Chastellain, M., Juillerat-Jeanneret, L., Ferraria, A. and Hofmann, H. (2005) Development of functionalized superparamagnetic iron oxide

nanoparticles for interaction with human cancer cells. *Biomaterials*, **26**, 2685–94.

37 Lee, L.T. and Somasundaran, P. (1989) Adsorption of polyacrylamide on oxide minerals. *Langmuir*, **5**, 854–60.

38 Hanessian, S., Grzyb, J.A., Cengelli, F. and Juillerat-Jeanneret, L. (2008) Synthesis of chemically functionalized superparamagnetic nanoparticles as delivery vectors for chemotherapeutic drugs. *Bioorganic and Medicinal Chemistry*, **16**, 2921–31.

39 Petri-Fink, A., Steitz, B., Finka, A., Salaklang, J. and Hofmann, H. (2008) Effect of cell media on polymer coated superparamagnetic iron oxide nanoparticles (SPIONs): colloidal stability, cytotoxicity, and cellular uptake studies. *European Journal of Pharmaceutics and Biopharmaceutics*, **68**, 129–37.

40 Zhang, Y., Kohler, N. and Zhang, M. (2002) Surface modification of superparamagnetic magnetite nanoparticles and their intracellular uptake. *Biomaterials*, **23**, 1553–61.

41 Arruebo, M., Fernandez-Pacheco, R., Ibarra, M.R. and Santamaria, J. (2007) Magnetic nanoparticles for drug delivery. *Nano Today*, **2**, 22–32.

42 Sun, C., Sze, R. and Zhang, M. (2006) Folic acid-PEG conjugated superparamagnetic nanoparticles for targeted cellular uptake and detection by MRI. *Journal of Biomedical Materials Research. A*, **78**A, 550–7.

43 Kohler, N., Sun, C., Fichtenholtz, A., Gunn, J., Fang, C. and Zhang, M. (2006) Methotrexate-immobilized poly(ethylene glycol) magnetic nanoparticles for MR imaging and drug delivery. *Small*, **2**, 785–92.

44 Zhang, Y. and Zhang, J. (2005) Surface modification of monodisperse magnetite nanoparticles for improved intracellular uptake to breast cancer cells. *Journal of Colloid and Interface Science*, **283**, 352–7.

45 Xu, C.J., Xu, K.M., Gu, H.W., Zheng, R.K., Liu, H., Zhang, X.X., Guo, Z.H. and Xu, B. (2004) Dopamine as a robust anchor to immobilize functional molecules on the iron oxide shell of magnetic nanoparticles. *Journal of the American Chemical Society*, **126**, 9938–9.

46 Xie, J., Xu, C., Kohler, N., Hou, Y. and Sun, S. (2007) Controlled PEGylation of monodisperse Fe_3O_4 nanoparticles for reduced non-specific uptake by macrophage cells. *Advanced Materials*, **19**, 3163–6.

47 Shultz, M.D., Calvin, S., Fatouros, P.P., Morrison, S.A. and Carpenter, E.E. (2007) Enhanced ferrite nanoparticles as MRI contrast agents. *Journal of Magnetism and Magnetic Materials*, **311**, 464–8.

48 Shultz, M.D., Reveles, J.U., Khanna, S.N. and Carpenter, E.E. (2007) Reactive nature of dopamine as a surface functionalization agent in iron oxide nanoparticles. *Journal of the American Chemical Society*, **129**, 2482–7.

49 Kumagai, M., Imai, Y., Nakamura, T., Yamasaki, Y., Sekino, M., Ueno, S., Hanaoka, K., Kikuchi, K., Nagano, T., Kaneko, E., Shimokado, K. and Kataoka, K. (2007) Iron hydroxide nanoparticles coated with poly(ethylene glycol)-poly(aspartic acid) block copolymer as novel magnetic resonance contrast agents for in vivo cancer imaging. *Colloids and Surfaces. B, Biointerfaces*, **56**, 174–81.

50 Wan, S.R., Huang, J.S., Guo, M., Zhang, H.K., Cao, Y.J., Yan, H.S. and Liu, K.L. (2007) Biocompatible superparamagnetic iron oxide nanoparticle dispersions stabilized with poly(ethyleneglycol)-oligo(aspartic acid) hybrids. *Journal of Biomedical Materials Research A*, **80**A, 946–54.

51 Flesch, C., Unterfinger, Y., Bourgeat-Lami, E., Duguet, E., Delaite, C. and Dumas, P. (2005) Poly(ethylene glycol) surface coated magnetic particles. *Macromolecules Rapid Communications*, **26**, 1494–8.

52 Babic, M., Horak, D., Trchova, M., Jendelova, P., Glogarova, K., Lesny, P., Herynek, V., Hajek, M. and Sykova, E. (2008) Poly(L-lysine)-modified iron oxide nanoparticles for stem cell labeling. *Bioconjugate Chemistry*, **19**, 740–50.

53 Zhang, J. and Misra, R.D.K. (2007) Magnetic drug-targeting carrier

encapsulated with thermosensitive smart polymer: core-shell nanoparticle carrier and drug release response. *Acta Biomaterialia*, **3**, 838–50.

54 Chen, S., Li, Y., Guo, C., Wang, J., Ma, J.H., Liang, X.F., Yang, L.-R. and Liu, H.-Z. (2007) Temperature-responsive magnetite/PEO-PPO-PEO block copolymer nanoparticles for controlled drug targeting delivery. *Langmuir*, **23**, 12669–76.

55 Alarcon, C.H., Pennadam, S. and Alexander, C. (2005) Stimuli responsive polymers for biomedical applications. *Chemical Society Reviews*, **34**, 276–85.

56 Zhang, J.L., Srivastava, R.S. and Misra, R.D.K. (2007) Core-shell magnetite nanoparticles surface encapsulated with smart stimuli-responsive polymer: synthesis, characterization, and LCST of viable drug-targeting delivery system. *Langmuir*, **23**, 6342–51.

57 Fischer, D., Bieber, T., Li, Y., Elsasser, H.P. and Kissel, T. (1999) A novel non-viral vector for DNA delivery based on low molecular weight, branched polyethyleneimine: effect of molecular weight on transfection efficiency and cytotoxicity. *Pharmaceutical Research*, **16**, 1273–9.

58 Vestal, C.R. and Zhang, Z.J. (2002) Atom transfer radical polymerization synthesis and magnetic characterization of $MnFe_2O_4$/polystyrene core/shell nanoparticles. *Journal of the American Chemical Society*, **124**, 14312–13.

59 Wang, Y., Teng, X.W., Wang, J.S. and Yang, H. (2003) Solvent-free atom transfer radical polymerization in the synthesis of Fe_2O_3 @ polystyrene core-shell nanoparticles. *Nano Letters*, **3**, 789–93.

60 Garcia, I., Tercjak, A., Zafeiropoulos, N.E., Stamm, M. and Mondragon, I. (2007) Generation of core/shell iron oxide magnetic nanoparticles with polystyrene brushes by atom transfer radical polymerization. *Journal of Polymer Science Part A: Polymer Chemistry*, **45**, 4744–50.

61 Marutani, E., Yamamoto, S., Ninjbadgar, T., Tsujii, Y., Fukuda, T. and Takano, M. (2004) Surface-initiated atom transfer radical polymerization of methyl methacrylate on magnetite nanoparticles. *Polymer*, **45**, 2231–5.

62 Garcia, I., Zafeiropoulos, N.E., Janke, A., Tercjak, A., Eceiza, A., Stamm, M. and Mondragon, I. (2007) Functionalization of iron oxide magnetic nanoparticles with poly(methyl methacrylate) brushes via grafting-from atom transfer radical polymerization. *Journal of Polymer Science Part A: Polymer Chemistry*, **45**, 925–32.

63 Hu, F.X., Neoh, K.G., Cen, L. and Kang, E.-T. (2006) Cellular response to magnetic nanoparticles "PEGylated" via surface-initiated atom transfer radical polymerization. *Biomacromolecules*, **7**, 809–16.

64 Fan, Q.L., Neoh, K.G., Kang, E.-T., Shuter, B. and Wang, S.-C. (2007) Solvent-free atom transfer radical polymerization for the preparation of poly(poly(ethyleneglycol) monomethacrylate)-grafted Fe_3O_4 nanoparticles: synthesis, characterization and cellular uptake. *Biomaterials*, **28**, 5426–36.

65 Lattuada, M. and Hatton, T.A. (2007) Functionalization of monodisperse magnetic nanoparticles. *Langmuir*, **23**, 2158–68.

66 Wuang, S.C., Neoh, K.G., Kang, E.-T., Pack, D.W. and Leckband, D.E. (2006) Heparinized magnetic nanoparticles: in-vitro assessment for biomedical applications. *Advanced Functional Materials*, **16**, 1723–30.

67 Frimpong, R.A. and Hilt, J.Z. (2008) Poly(*N*-isopropylacrylamide)-based hydrogel coatings on magnetite nanoparticles via atom transfer radical polymerization. *Nanotechnology*, **19**, 175101–7.

68 Chen, F.H., Gao, Q., Hong, G.Y. and Ni, J.Z. (2008) Synthesis of magnetite core-shell nanoparticles by surface-initiated ring-opening polymerization of L-lactide. *Journal of Magnetism and Magnetic Materials*, **320**, 1921–7.

69 Duran, J.D., Arias, J.L., Gallardo, V. and Delgado, A.V. (2008) Magnetic colloids as drug vehicles. *Journal of Pharmaceutical Sciences*, **97**, 2948–83.

70 Jiang, W., Kim, B.Y.S., Rutka, J.T. and Chan, W.C.W. (2008) Nanoparticle-mediated cellular response is size-dependent., Nature. *Nanotechnology*, **3**, 145–50.

71 Liu, X., Kaminski, M.D., Chen, H., Torno, M., Taylor, L. and Rosengart, A.J. (2007) Synthesis and characterization of highly-magnetic biodegradable poly(D,L-lactide-*co*-glycolide) nanospheres. *Journal of Controlled Release*, **119**, 52–8.

72 Hamoudeh, M., Al Faraj, A., Canet-Soulas, E., Bessueille, F., Leonard, D. and Fessi, H. (2007) Elaboration of PLLA-based superparamagnetic nanoparticles: characterization, magnetic behaviour study and in vitro relaxivity evaluation. *International Journal of Pharmaceutics*, **338**, 248–57.

73 Wang, Y., Ng, Y.W., Chen, Y., Shuter, B., Yi, J., Ding, J., Wang, S.-C. and Feng, S.-S. (2008) Formulation of superparamagnetic iron oxides by nanoparticles of biodegradable polymers for magnetic resonance Imaging. *Advanced Functional Materials*, **18**, 308–18.

74 Tromsdorf, U.I., Bigall, N.C., Kaul, M.G., Bruns, O.T., Nikolic, M.S., Mollwitz, B., Sperling, R.A., Reimer, R., Hohenberg, H., Parak, W.J., Forster, S., Beisiegel, U., Adam, G. and Weller, H. (2007) Size and surface effects on the MRI relaxivity of manganese ferrite nanoparticle contrast agents. *Nano Letters*, **7**, 2422–7.

75 Kang, E., Park, J., Hwang, Y., Kang, M., Park, J. and Hyeon, T. (2004) Direct synthesis of highly crystalline and monodisperse manganese ferrite nanocrystals. *The Journal of Physical Chemistry B*, **108**, 13932–5.

76 Galperin, A. and Margel, S. (2007) Synthesis and characterization of radiopaque magnetic core-shell nanoparticles for x-ray imaging applications. *Journal of Biomedical Materials Research. B - Applied Biomaterials*, **83**B, 490–8.

77 Holzapfel, V., Lorenz, M., Weiss, C.K., Schrezenmeier, H., Landfester, K. and Mailaender, V. (2006) Synthesis and biomedical applications of functionalized fluorescent and magnetic dual reporter nanoparticles as obtained in the miniemulsion process. *Journal of Physics: Condensed Matter*, **18**, S2581–94.

78 Wuang, S.C., Neoh, K.G., Kang, E.-T., Pack, D.W. and Leckband, D.E. (2007) Polypyrrole nanospheres with magnetic and cell-targeting capabilities. *Macromolecular Rapid Communications*, **28**, 816–21.

79 Wuang, S.C., Neoh, K.G., Kang, E.-T., Pack, D.W. and Leckband, D.E. (2007) Synthesis and functionalization of polypyrrole-Fe_3O_4 nanoparticles for applications in biomedicine. *Journal of Materials Chemistry*, **17**, 3354–62.

80 Wuang, S.C., Neoh, K.G., Kang, E.-T., Pack, D.W. and Leckband, D.E. (2008) HER-2-mediated endocytosis of magnetic nanospheres and the implications in cell targeting and particle magnetization. *Biomaterials*, **29**, 2270–9.

81 Zelikin, A.N., Lynn, D.M., Farhadi, J., Martin, I., Shastri, V. and Langer, R. (2002) Erodible conducting polymers for potential biomedical applications, *Angewandte Chemie, International Edition in English*, **41**, 141–4.

82 Kotwal, A. and Schmidt, C.E. (2001) Electrical stimulation alters protein adsorption and nerve cell interactions with electrically conducting biomaterials. *Biomaterials*, **22**, 1055–64.

83 Sanghvi, A.B., Miller, K.P.-H., Belcher, A.M. and Schmidt, C.E. (2005) Biomaterials functionalization using a novel peptide that selectively binds to a conducting polymer. *Nature Materials*, **4**, 496–502.

84 Schmidt, C.E., Shastri, V.R., Vacanti, J.P. and Langer, R. (1997) Stimulation of neurite outgrowth using an electrically conducting polymer. *Proceedings of the National Academy of Sciences of the United States of America*, **94**, 8948–53.

85 Collier, J.H., Camp, J.P., Hudson, T.W. and Schmidt, C.E. (2000) Synthesis and characterization of polypyrrole/hyaluronic acid composite biomaterials for tissue engineering. *Journal of Biomedical Materials Research*, **50**, 574–84.

86 Emens, L.A. and Davidson, N.E. (2004) Trastuzumab in breast cancer. *Oncology*, **18**, 1117–28.

87 Quintana, A., Raczka, E., Piehler, L., Lee, I., Myc, A., Majoros, I., Patri, A.K., Thomas, T., Mule, J. and Baker, J.R. (2002) Design and function of a dendrimer-based therapeutic nanodevice targeted to tumor cells through the folate receptor. *Pharmaceutical Research*, **19**, 1310–16.

88 Zhang, Y., Kohler, N. and Zhang, M. (2002) Surface modification of superparamagnetic magnetite nanoparticles and their intracellular uptake. *Biomaterials*, **23**, 1553–61.

89 Sun, C., Sze, R. and Zhang, M. (2006) Folic acid-PEG conjugated superparamagnetic nanoparticles for targeted cellular uptake and detection by MRI. *Journal of Biomedical Materials Research A*, **78**, 550–7.

90 Porto, C.S., Musto, N.A., Bardin, C.W. and Gunsalus, G.L. (1992) Binding of an extracellular steroid-binding globulin to membranes and soluble receptors from human breast cancer cells (MCF-7 cells). *Endocrinology*, **130**, 2931–6.

91 Chan, W.Y., Huang, H. and Tam, S.C. (2003) Receptor-mediated endocytosis of trichosanthin in choriocarcinoma cells. *Toxicology*, **186**, 191–203.

92 Lee, S.J., Jeong, J.R., Shin, S.C., Huh, Y.M., Song, H.T., Suh, J.S., Chang, Y.H., Jeon, B.S. and Kim, J.D. (2005) Intracellular translocation of superparamagnetic iron oxide nanoparticles encapsulated with peptide-conjugated poly(D,L lactide-*co*-glycolide). *Journal of Applied Physics*, **97**, 10Q913-1–10Q913-3.

93 Larsen, B.A., Haag, M.A., Serkova, N.J., Shroyer, K.R. and Stoldt, C.R. (2008) Controlled aggregation of superparamagnetic iron oxide nanoparticles for the development of molecular magnetic resonance imaging probes. *Nanotechnology*, **19**, 265102.

94 Barker, A.J., Cage, B., Russek, S. and Stoldt, C.R. (2005) Ripening during magnetite nanoparticle synthesis: resulting interfacial defects and magnetic properties. *Journal of Applied Physics*, **98**, 063528-1–063528-7.

95 Tan, C.J., Chua, M.G., Ker, K.H. and Tong, Y.W. (2008) Preparation of bovine serum albumin surface-imprinted submicrometer particles with magnetic susceptibility through core-shell miniemulsion polymerization. *Analytical Chemistry*, **80**, 683–92.

96 Koneracka, M., Muckova, M., Zavisova, V., Tomasovicova, N., Kopcansky, P., Timko, M., Jurikova, A., Csach, K. and Lancz, G. (2008) Encapsulation of anticancer drug and magnetic particles in biodegradable polymer nanospheres. *Journal of Physics: Condensed Matter*, **20**, 204151.

97 Hu, F.X., Neoh, K.G. and Kang, E.T. (2006) Synthesis and in vitro anti-cancer evaluation of tamoxifen-loaded magnetite/PLLA composite nanoparticles. *Biomaterials*, **27**, 5725–33.

98 Chawla, J.S. and Amiji, M.M. (2002) Biodegradable poly(o-caprolactone) nanoparticles for tumor targeted delivery of tamoxifen. *International Journal of Pharmaceutics*, **249**, 127–38.

99 Cavallaro, G., Maniscalco, L., Licciardi, M. and Giammona, G. (2004) Tamoxifen loaded polymeric micelles: preparation, physico-chemical characterization and in vitro evaluation studies. *Macromolecular Bioscience*, **4**, 1028–38.

100 Li, L., Chen, D., Zhang, Y., Deng, Z., Ren, X., Meng, X., Tang, F., Ren, J. and Zhang, L. (2007) Magnetic and fluorescent multifunctional chitosan nanoparticles as a smart drug delivery system. *Nanotechnology*, **18**, 405102.

101 Sashiwa, H. and Aiba, S.-I. (2004) Chemically modified chitin and chitosan as biomaterials. *Progress in Polymer Science*, **29**, 887–908.

102 Yang, J., Park, S.-B., Yoon, H.-G., Huh, Y.-M. and Haam, S. (2006) Preparation of poly epsilon-caprolactone nanoparticles containing magnetite for magnetic drug carrier. *International Journal of Pharmaceutics*, **324**, 185–90.

103 Gang, J., Park, S.-B., Hyung, W., Choi, E.H., Wen, J., Kim, H.-S., Shul, Y.-G., Haam, S. and Song, S.Y. (2007) Magnetic poly epsilon-caprolactone

nanoparticles containing Fe_3O_4 and gemcitabine enhance anti-tumor effect in pancreatic cancer xenograft mouse model. *Journal of Drug Targeting*, **15**, 445–53.

104 Arias, J.L., Ruiz, M.A., Gallardo, V. and Delgado, A.V. (2008) Tegafur loading and release properties of magnetite/poly(alkylcyanoacrylate) (core/shell) nanoparticles. *Journal of Controlled Release*, **125**, 50–8.

105 Arias, J.L., Gallardo, V., Ruiz, M.A. and Delgado, A.V. (2008) Magnetite/poly(alkylcyanoacrylate) (core/shell) nanoparticles as 5-fluorouracil delivery systems for active targeting. *European Journal of Pharmaceutics and Biopharmaceutics*, **69**, 54–63.

106 Seo, S.-B., Yang, J., Hyung, W., Cho, E.-J., Lee, T.-I., Song, Y.J., Yoon, H.-G., Suh, J.-S., Huh, Y.-M. and Haam, S. (2007) Novel multifunctional PHDCA/PEI nano-drug carriers for simultaneous magnetically targeted cancer therapy and diagnosis via magnetic resonance imaging. *Nanotechnology*, **18**, 475105.

107 Kim, J., Lee, J.E., Lee, S.H., Yu, J.H., Lee, J.H., Park, T.G. and Hyeon, T. (2008) Designed fabrication of a multifunctional polymer nanomedical platform for simultaneous cancer-targeted imaging and magnetically guided drug delivery. *Advanced Materials*, **20**, 478–83.

108 Kim, S.H., Jeong, J.H., Chun, K.W. and Park, T.G. (2005) Target-specific cellular uptake of PLGA nanoparticles coated with poly(L-lysine)-poly(ethylene glycol)-folate conjugate. *Langmuir*, **21**, 8852–7.

109 Pan, X., Guan, J., Yoo, J.-W., Epstein, A.J., Lee, L.J. and Lee, R.J. (2008) Cationic lipid-coated magnetic nanoparticles associated with transferrin for gene delivery. *International Journal of Pharmaceutics*, **358**, 263–70.

110 Pan, B., Cui, D., Sheng, Y., Ozkan, C., Gao, F., He, R., Li, Q., Xu, P. and Huang, T. (2007) Dendrimer-modified magnetic nanoparticles enhance efficiency of gene delivery system. *Cancer Research*, **67**, 8156–63.

111 Lee, J.-H., Huh, Y.-M., Jun, Y.-W., Seo, J.-W., Jang, J.-T., Song, H.-T., Kim, S., Cho, E.-J., Yoon, H.-G., Suh, J.-S. and Cheon, J. (2007) Artificially engineered magnetic nanoparticles for ultra-sensitive molecular imaging. *Nature Medicine*, **13**, 95–9.

112 Yang, J., Gunn, J., Dave, S.R., Zhang, M., Wang, A. and Gao, X. (2008) Ultrasensitive detection and molecular imaging with magnetic nanoparticles. *Analyst*, **133**, 154–60.

Keywords

magnetic nanoparticles; MRI contrast agent; cancer targeting; drug delivery; polymer coating; surface functionalization; encapsulation

Abstract

Magnetic core–polymer shell nanoparticles, with the core mainly in the form of magnetite (Fe_3O_4) or maghemite (γ-Fe_2O_3), offer great opportunities for applications in biomedicine. Such a configuration provides a synergistic combination of the intrinsic properties of the magnetic core with special biochemical functions, achieved through proper tailoring of the polymer shell. Active research and development efforts on the applications of such nanoparticles are ongoing in biomedical areas, such as contrast agents for magnetic resonance imaging to achieve increasingly high spatial resolution, down to the cellular and even molecular level; delivery vehicles of drugs to targeted organs or tumors; and as a heating mediator for cancer thermotherapy (hyperthermia). The controllability of these nanoparticles with respect to their physico-chemical properties, biodistribution and site specificity within the physiological environment, are major challenges which need to be addressed. In this chapter we review the synthetic routes of magnetic core–polymer shell nanoparticles, with emphasis on the tailoring of the polymer shell to confer the nanoparticles with desired properties for biomedical applications.

11
Magnetosomes: Bacterial Biosynthesis of Magnetic Nanoparticles and Potential Biomedical Applications

Sarah S. Staniland

11.1
Introduction

Magnetosomes are magnetic nanocrystals of magnetite within a lipid coating that are produced biologically (biomineralization) within magnetic bacteria. Such bacteria biomineralize magnetosomes in a chain motif of 20–30 units, with the magnetic particles produced being responsible for the bacteria aligning and swimming along magnetic field lines. The biomineralization of these magnetite nanoparticles is strictly regulated and controlled by the organism, and this results in highly crystalline, single-domain particles of a highly defined shape and size. The material, shape, and size of magnetosomes vary for different magnetic bacteria, but are strictly adhered to within each strain. The magnetite is deposited within a lipid vesicle that forms the reaction vessel for the biomineralization to occur. This lipid bilayer then provides a biological, fatty-acid and protein coating for the magnetic particles. Magnetic bacteria and magnetosomes have been the subject of intensive research among a range of scientific disciplines, from microbiology to paleomagnetism, and some excellent reviews have been produced [1–3], with more specific literature detailing aspects such as biomolecular magnetosome formation process [2–7], bacterial phylogeny [8], magnetosome characterization [9], crystal habits [10, 11], magnetism [12], paleomagnetism [13], and geological and environmental significance [14].

Interestingly, magnetosomes have been considered for applications in nanotechnology – and particularly for biomedical applications – only relatively recently. In fact, this area of research is very much in its infancy; to date the only development of magnetosomes for biomedical applications has been exclusively for *in vitro* systems developed at the laboratory of Matsunaga [3, 15]. Research in the field of biomedical nanotechnology has, however, accelerated rapidly over the past few years such that today, nanomagnetic particles serve as important biomedical materials in the development of magnetically targeted therapies. Such therapies utilize the particles' magnetic properties to guide treatment to a specific area, which means not only lower doses but also fewer adverse side effects. Again, a number

Nanomaterials for the Life Sciences Vol. 4: Magnetic Nanomaterials. Edited by Challa S. S. R. Kumar

ISBN: 978-3-527-32154-4

of high-quality reviews have been produced on the development of magnetic nanoparticles for targeted drug and gene delivery [16–18] and on the physical principles of magnetic nanoparticles for biomedical applications [19]. However, this chapter is the first to consider the wider potential of magnetosomes in biomedical applications, and the future developments which will place them at the center of advanced healthcare solutions. In the chapter, we will discuss the biomedical applications of magnetic nanoparticles and their required specifications. Magnetosomes represent an ideal material to be modified for magnetically targeted therapies, as they are high-quality in nature, morphologically uniform, and have an inherent lipid coating that increases their dispersion in solution and provides a biocompatible shell that can easily be adapted to several applications. The chapter will contextualize magnetic bacteria, magnetosomes and how they are formed, and also discuss their unique properties and how these properties can be utilized in magnetic biomedical nanotechnology. A review will be provided of the latest developments in these fields – how such developments will affect the biomedical application of magnetosomes, and how we can build on current research strategies in order to exploit magnetosomes for applications such as targeted drug delivery and hyperthermic treatments.

11.2
Magnetic Nanoparticles for Medical Applications

11.2.1
Introduction

The concept of using magnetic nanoparticles for biomedical applications is a simple one: the small size of nanoparticles allows them to travel unhindered throughout the body, where their magnetic properties can then be exploited for a range of biomedical purposes. This includes using the particles to: (i) guide any drugs that are tethered to the particle to a target site by using a magnetic field; (ii) to activate a drug or heat a site by using an alternating magnetic field; (iii) to reduce magnetic relaxation times so as to enhance contrast for magnetic resonance imaging (MRI) scanning; or (iv) simply to separate – magnetically – biomolecules from a biological matrix or solution. Although the idea of using magnetic nanoparticles for biomedical applications, such as targeted drug delivery, was first proposed during the late 1970s [2], its realization has been slow to materialize, with the first demonstration of magnetically targeted transfection recorded only in 2000 [20]. A major problem in the development of this technology has been the challenges of designing and fabricating nanoscale, uniform, functionalized particles, that would produce a consistent and predictable response, but with limited toxicity.

In recent years, however, nanoscience research has expanded rapidly, and this has led to the provision of many more tools and methods for the creation of high-quality nanomaterials for medical purposes. Furthermore, the increased interest

and research into nanoscale medicine has led to new innovations which have themselves expanded the range of possible applications for nanomaterials. For example, nanomagnetic cell actuation has been developed; this is a method which allows cell function/stress to be controlled remotely by a magnetic field, and can be utilized for conditioning cells for regenerative medicine [21]. The realization of these medical applications is crucially dependent on the synthetic quality of the nanomaterials, however. In this chapter, we will explore some novel *biological* routes for the production of superior nanoparticles, specifically the bacterial biomineralization of nanomagnets for new medical applications.

11.2.2
Requirements and Specifications for Biomedical Applications

Before discussing the biological synthesis of medical nanomagnets, it is first necessary to outline the properties and specifications which define and shape their usefulness. For this, we will consider a generic magnetic biomedical nanoparticle (Figure 11.1) and briefly discuss the specifications of size, shape, consistency, magnetic character, toxicity, coating, and bioactivity.

11.2.2.1 Safety Aspects

If a particle is being designed to interact with the body, the primary consideration is *safety*. This means that the choice of magnetic material is limited to nontoxic compounds, such as inert and/or materials that are already present in the body; examples include silicates and iron compounds. Toxicity can be seen as a very delicate balance between curing a disease but not killing the patient, and consequently biomedical particles must have highly consistent properties to ensure that the correct, nontoxic specifications are always adhered to. In order to achieve these specific properties accurately, the particles must be uniform in all respects of their

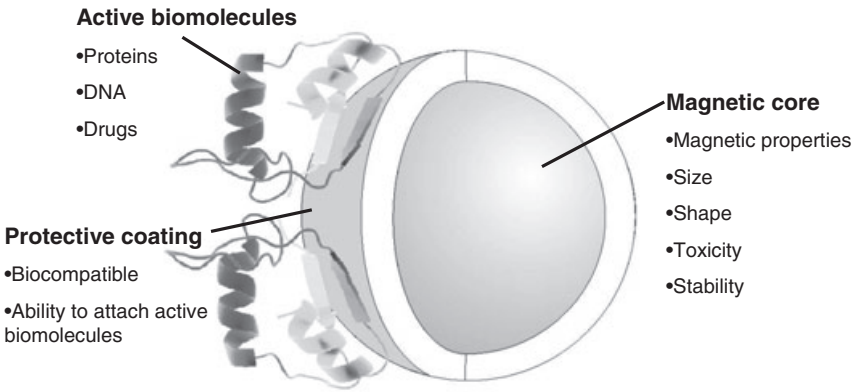

Figure 11.1 Generic design and considerations of a biomedical magnetic nanoparticle.

size, magnetic and coating characteristics. It is therefore crucial that the synthetic method chosen can achieve a uniform formation of the required particles, hopefully at low cost.

11.2.2.2 **Magnetic Properties**

The required magnetic properties of particles depend on the intended application. Some applications require a weak magnetic moment, whereas others need an increased magnetic moment. Many applications will require a material that is magnetically "soft" (i.e., the magnetization is easily reversed, and lost when a field is reversed or removed), while some applications require a hard magnet (i.e., the magnetization is retained when the field is reversed or removed). For example, MRI enhancers typically need to be soft magnets, whereas potential hysteric hyperthermic cancer treatments require hard magnetic properties, and magnetic-fluid hyperthermic treatments utilize smaller super-paramagnetic particles. The magnetic properties are defined by the composition and type of material used. All magnetic materials are super-paramagnetic below a certain size (i.e., depending on the material and shape, typically between 5 and 40 nm), and above this size will obtain a bulk magnetism, becoming either ferro/ferri or antiferromagnetic. Above a critical size, the magnetism of the material will compartmentalize into "multiple domains" in order to stabilize the material. This is again dependent on the material and its shape: elongated, needle-shaped particles will remain single domain over much larger sizes and have a much larger magnetic anisotropy associated with them than will more spherical particles. Typically, the multiple domain transition is approximately 100 nm, and so "single-domain" magnets can usually be found with sizes in range of tens of nanometers.

11.2.2.3 **Particle Size and Shape**

The size and shape of the particles must also be considered; both factors will influence a particle's magnetic characteristics, such as whether they are super-paramagnetic or single domain. But size and shape are significant for their other effects also. For example, micrometer-sized particles are limited to traveling in the blood vessels, while nanosized particles can penetrate the tissues and cells. Particle shape must also be considered, as different-shaped particles interact differently with the various biological components. For example, needle-shaped particles may often be toxic, although a "spearing" effect can occasionally have a positive functionality.

11.2.2.4 **Particle Coatings**

One of the most important design features of magnetic nanoparticles for biomedical applications is the nanomagnet's coating and medical functionalization. This not only provides the active medicine, such as the drug, protein, selection site or genetic material, but can also act as a barrier between the magnet and the body, helping to preventing degradation of the particle and the possible leaching out of any toxic particle components. Essentially, the coating must be nontoxic and biocompatible, as well as having the synthetic means to attach any functional biomol-

ecules such as proteins or drugs to suit the application. When considering these factors, coatings are almost exclusively organic/biological materials; consequently, the synthesis of such "inorganic-nanocrystal within a bio-shell"-type particles can present a variety of challenges.

11.2.3 General Synthetic Methods

The huge number of different magnetic materials available, and the vast array of associated synthetic routes, prevent a full description of the subject at this point, for reasons of limited space. Rather, in this section we will focus on the synthesis of magnetite nanoparticles, mainly because iron oxide nanoparticles are the most common material of choice for many applications. They are also relatively safe when compared to other magnetic materials, such as mixed-metal oxides, which contain large amounts of toxic Ni, Ba, Mn, or Co that may leach out to poison the body. (Although iron oxide is inertly present in the body, excessive amounts have been linked with certain degenerative diseases.) Iron oxides are robust and much more stable to oxidation than other materials, including pure iron, which will corrode and oxidize in water. Iron oxides also have cheap synthetic precursors, while oxides such as maghemite (γ-Fe_2O_3) and magnetite (Fe_3O_4) are strongly ferrimagnetic. These materials are single domain above approximately 10 and 30 nm, respectively, and both can be synthesized in a range of particle sizes and shapes, thus offering different magnetic characteristics. Some of the advantages and disadvantages of the different wet chemical synthetic methods used to produce functionally coated magnetite nanoparticles will be compared in the following section (see Table 11.1).

11.2.3.1 Precipitation

The first – and most simple – method of producing nanoparticulate magnetite is its precipitation from a solution of iron ions by increasing the pH. Although this method is quick, cheap, and produces large yields, a very precise control is required over all of the conditions employed. For example, varying the type and method of base addition, the speciation of the iron ions (ferric/ferrous), the ratio of the ions, the iron salt's anions, the available oxygen in the atmosphere, and the temperature can each result in different sized and shaped particles, as well as iron oxides of varying crystallinity. For example, a coprecipitation of ferric and ferrous ions at room temperature under N_2, with KOH added to raise the pH to 5.4 (at which point magnetite precipitation will occur), will result in tiny nanoparticles with a huge range of shapes and sizes, and poor crystallinity (from <5 nm to micrometer size). In contrast, the partial oxidation of ferrous hydroxide using NaOH under N_2 at 90 °C will cause the precipitation of octahedral magnetite particles which are approximately 20–80 nm in size. Interestingly, changing the base used can result in needle-shaped FeOOH byproducts [22]. Although this method does allow a degree of scope to synthesize a range of materials of various sizes, the overwhelming drawback is that it is almost impossible to synthesize a monodispersed and

Table 11.1 Comparison of different wet synthetic techniques with respect to favorable qualities for biomedical functional magnetic nanoparticles.

	Precipitation	Precipitation + micelles	Improved thermal decomposition	Bacterial biomineralization
Reproducibility	Low. Very difficult to control all parameters	High	High	High
Monodispersed (size and shape)	Low. Various products at low temperatures. Defined shape at high temperatures, various sizes	High. Micelles restricted to a defined size	High	High. Genetic control gives highly defined sizes and shapes
Range of particle variety	Many different particle morphologies. Can be difficult to specify	2–500 nm-diameter spherical particles can be formed using various surfactants	Low. Method can only produce small particles <20 nm	Many different shapes and sizes of magnetosomes known, but very few able to be utilized at present
Organic/ biological coating	Multiple steps needed	Difficult. Inorganic coating only, unless use multiple steps	Multiple steps needed	Integral lipid coating already present
Ambient conditions (biomolecule friendly)	Can be compatible	Can be compatible	Multiple steps needed due to harsh synthetic conditions	Very compatible with lipids and proteins present
Cost	Lowest cost	Quite low cost (demands specialist surfactants)	Higher cost. High temperature, costly starting materials	Higher cost. Fermenter running and media costs
Yield	High	High	High	Low

reproducible product with regards to size and shape distribution. Furthermore, the presence of ferric oxide impurities is commonplace.

The precipitation method can be refined with a greater degree of control over particle size by the addition of a surfactant to the reaction, so as to form micelles. In this improved synthesis, the reaction is carried out in an organic solvent so that the surfactant forms reverse micelles with a central core of a well-defined volume of inorganic reaction solution. The particles are then synthesized and controlled

within these restricted dimensions. The resultant particles are uniform in size, and can be produced in sizes ranging from 2 to 500 nm by varying the surfactant and the conditions [23]. An inorganic coating can also be subsequently added. Unfortunately, an organic coating cannot be added using this method as it will remain in the organic solvent.

11.2.3.2 Thermal Decomposition

Thermal decomposition represents another synthetic route for magnetic nanoparticles. Although, historically, this method has struggled to produce uniform particles with regards to size and shape, recently improved decomposition methods have yielded nanoparticles of γ-Fe_2O_3 from an iron Cupferron precursor with a narrow size distribution [24]. This method has been further improved by addition of the surfactant oleic acid to form an iron-oleide precursor that then oxidizes to ferrite nanoparticles of 13 nm, with good monodispersity [25]. Particles produced in this way are confined to being very small, however; moreover, the method demands high temperatures as well as more expensive (and sometimes toxic) starting materials. The synthesis must also be a multistep process, as the coating/addition of functional medical compounds must be carried out separately because the high temperatures and organic solvents may damage any bioactive molecules.

To summarize, it is clear that the control of particle size and shape can be costly since, even when monodispersity has been achieved, the coating of such particles with organic outer layers and bioactive compounds is not straightforward. However, many of these problems could be resolved by using biological synthesis, as biomineralization offers a strict control over particle size and shape, combined with an inherent lipid coating. Hence, the biomineralization of magnetite nanoparticles in magnetic bacteria will now be considered, together with some suggestions as to how the process might be exploited for biomedical applications.

11.3
What Is Biomineralization? Biogenic Inorganic Materials

Biomineralization is the controlled formation of solid inorganic compounds by biological systems. This involves the uptake of specific elements from the environment by the organism, and their deliberate incorporation into a solid mineral structure under precise biological control. Usually, these inorganic biomaterials also contain biological molecules and are not chemically stoichiometric, but rather are formed with such precise control and composition that they will have specific and often remarkable properties, such as regeneration, mechanical strength, and flexibility. The biomaterials will also perform key structural, mechanical and/or even sensing functions within the organisms. The precision of the materials is also observed in their intricate, exact, and often beautifully ornate structures (Figure 11.2).

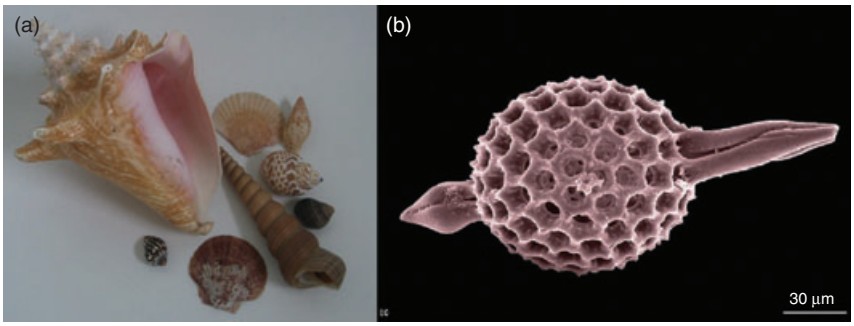

Figure 11.2 Examples of biomineralization. (a) Shells made from calcium carbonates; (b) Silicates in a diatom. (Image reproduced with kind permission from Eric Condliffe, Earth Science, Leeds.)

The process of biomineralization occurs in a variety of organisms, ranging from bacteria to humans. Some such materials are very well known; for example, many calcium-based skeletal–structural biominerals exist where calcium is deposited as a calcium phosphate compound known as hydroxyapatite (or carbonated apatite) in bones and teeth, and as calcium carbonate (mostly calcite and/or aragonite) in many different types of shell (Figure 11.2). Other examples of calcium biominerals include eye lenses (in triobites), defensive weapons (claws for many mammals and birds), and "love darts" (used in the reproduction of gastropods). Another major family of biominerals is that of amorphous silicates which, again, have a mainly structural role. The amorphous nature of these materials may be advantageous since, with no set pattern or planes of crystallization, they can be molded and worked into a range of fluid architectural shapes, without any loss in mechanical strength. Typically intricate lace-like structures are formed by radiolarians and diatoms (Figure 11.2), while algae biomineralize a protective shell from silicate. Silicates are also widely used in plants to form spines and cell walls.

Another major mineral category found in biology is iron oxides. These are generally strong and dense, and may also be magnetic; consequently, they are rarely deposited in organisms for structural purposes, but more often as teeth and magnetic sensors. Iron oxides can also be deposited primarily for the sequestering and storing of large quantities of essential iron, as ferrihydrite. This process is carried out by a protein, ferritin, which assembles into a large hollow, spherical, cage-like protein aggregate with the ferrihydrite accumulated in the center. This is a very common strategy and occurs in a wide range of organisms.

Iron oxide is also biomineralized indirectly (albeit with less control) in another process known as biologically induced mineralization. Several types of bacteria can produce magnetite extracellularly, this being initiated by redox processes on the cell surface that lead to the precipitation of magnetite particles into the environment. Here, the mineralization is a byproduct of respiration processes, and the materials produced serve little function to the cells and so are not precisely defined,

although single-domain particles may be formed under certain conditions [26]. The *in vitro* formation of magnetite may also be catalyzed by bacteria or fungi [27]. Equally, magnetite nanoparticles can be biomineralized intracellularly, and these particles are present in many higher organisms including honeybees, pigeons, pelagic fish, bats, rodents, and humans [28]; typically, the human brain contains approximately 5×10^6 crystals per gram of tissue. Although the purpose of these particles has not yet been assigned in all cases, the majority are proposed to have sensing/navigational roles. They have also been considered to have a destructive role when present in excess, with recent studies having been conducted to investigate possible associations between increased magnetite levels in the human brain and neurodegenerative conditions such as Alzheimer's and Parkinson's diseases [29].

Finally, the occurrence of intracellular magnetite in prokaryotes is limited to few bacteria, all of which are magnetic. These bacteria deliberately biomineralize highly morphologically defined single-domain crystals of magnetite within their cells; it is this nanomaterial that will be considered for nanomagnetic medical applications.

11.4
Magnetosomes: Biomineralization in Magnetic Bacteria

Although magnetotactic bacteria were first observed by Bellini in 1963 [30], they were not widely reported until 1975, following their (independent) rediscovery by Blakemore [31]. Both Bellini and Blakemore observed that some bacteria in environmental samples consistently moved north, and would respond to the movement of a magnet. Magnetic bacteria are ubiquitous and are found in a wide variety of shapes, sizes, and environments; what unites them is their magnetotaxis – the ability to recognize and align with a magnetic field. This property is due to the presence of single-domain, magnetic iron mineral nanoparticles (magnetite, but occasionally greigite, Fe_3S_4) within the bacterial cell. These nanomagnets, which are biomineralized within lipid vesicles, are known as magnetosomes, and are usually arranged in chains of 20–30 magnetosomes in length, lying approximately parallel to the principal axis of the cell (Figure 11.3). The motifs, chain arrangements and number of chains may vary from strain to strain, however.

Magnetic bacteria and magnetosomes have attracted a huge amount of research interest since the late 1970s. While the initial research investigations concentrated on the analysis of the magnetite mineral, most of the subsequent studies focused on the biomineralization processes from a biological perspective.

Magnetic bacteria are the smallest and simplest organisms capable of performing biologically controlled mineralization within their cells and, as such, provide an ideal model to study and help understand the biomineralization process. This is of inherent importance for both practical and academic reasons. In practical terms, a better understanding of biomineralization will help to further medicine and improve biomaterials such as artificial bones, as well as open new possibilities

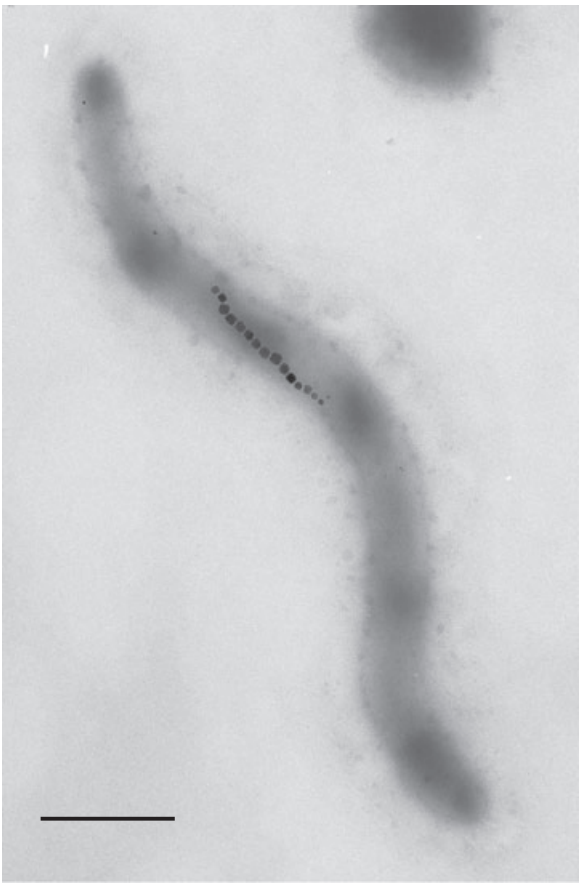

Figure 11.3 Image of *Magnetospirillum magnetotacticum* MS-1. Scale bar = 1 μm.

for creating hybrid artificial biominerals. From an academic perspective, understanding biomineralization at the simplest level has evolutionary significance, as it was the rapid increase in biomineralization and skeletal organisms that was thought to be responsible for the "Cambrian explosion" [32]. Consequently, over the past 35 years, a wide range of prolific and detailed environmental, geobiological, physiological, ecological, cell biological, genetic, proteomic and biotechnological research investigations have been undertaken. (Additional, in-depth knowledge of the subject is available in the many reviews and articles recommended in Section 11.1.)

At this point, we will explore and characterize magnetic bacteria and magnetosomes, and attempt to explain the biological process and formation mechanism as presently understood. First, the ideal role of magnetosomes in biomedical applications and the role of such applications in biomedical science are considered. We will then outline – and suggest solutions for – the problems associated with the

production of functional magnetosome nanomaterials. The future roles of magnetosomes and the biomimetic synthetic routes to biomedical materials will also be discussed.

11.4.1 Bacteria Characterization

All of the magnetic bacteria identified to date are Gram-negative, highly motile, and are located in specific regions of chemically stratified aquatic environments, ranging from marine to fresh-water ponds. Magnetic bacteria are microaerophiles and are located and isolated from the microaerobic and anoxic region of the oxic–anoxic transition zone (OATZ) of these environments. These bacteria all have flagella (long, rotating filaments for propulsion) that they use to travel around these highly chemically defined regions.

The first isolated and cultured magnetic bacterium, *Magnetospirillum magnetotacticum* MS-1 (Figure 11.3; originally known as *Aquaspirillum magnetotacticum*), was first isolated from a freshwater pond in Massachusetts. The organism was found to produce magnetite and to belong to the α-Proteobacteria group. This bacterium is respiratory, utilizes oxygen and nitrates, and grows chemo-organoheterotrophically, using organic acids as carbon and electron sources. Many subsequent magnetic bacteria that have been isolated have shown a large diversity of morphotypes (Table 11.2); examples include spirillia (helical), bacillus (rod-like), vibro (curved rod), and cocci (round), though all were of a similar size (1×1–$6\,\mu m$). The fact that these α-Proteobacteria produced magnetite in a chain motif led to the assumption of a common evolutionary lineage of the magnetotaxis trait. Magnetic bacteria have proved to be notoriously difficult to cultivate, most likely because of their highly defined complex and various chemical environments. To date, although cocci seem to be dominant in environmental samples, the majority of the cultured strains belong to the *Magnetospirillum* subfamily. Most magnetic bacteria which have been isolated belong to the α-Proteobacteria group, although several magnetic bacteria have now been identified as deriving from phylogenetically diverse groups, some of which biomineralize greigite (Fe_3S_4) [33–35] as opposed to magnetite; these include multicellular magnetic prokaryotes (MMPs) [35–37]. Neither greigite-producing bacteria nor MMPs have yet been cultivated, and consequently few ecological or genetic data are available to describe them. However, it has been noted that they are located in sulfide-rich anaerobic salt-water environments, and partial DNA sequencing has suggested that one bacterium belonged to the γ-Proteobacteria group, whereas MMPs are δ-Proteobacteria related to sulfate-reducing bacteria. Originally, it was thought that the composition of the magnetosomes (greigite or magnetite) was determined by their phylogenetic group (α as opposed to γ or δ-Proteobacteria), and this led to a proposed theory of dual evolutionary origins [38]. However, another magnetic sulfate-reducing δ-proteobacterium has recently been isolated, cultivated and characterized – the freshwater *Desulfovibrio magneticus* RS-1 – which, interestingly, biomineralizes magnetite, in contrast to the other δ-Proteobacteria greigite-producers, thus

Table 11.2 Cell and magnetosome dimensions for some selected magnetic bacteria.

Bacterial family	Strain	Cell length (μm)	Magnetosomes			Arrangement in cell		Reference(s)
			Size (nm)	Shape	Mineral[a]	Chain motif	No. of particles/chain	
α-Proteobacteria	*Magnetospirillum magnetotacticum* MS-1	3–5	~40	Cubo-octahedral	M	Linear	~22	[56, 57, 62]
	Magnetospirillum magneticum AMB-1	3–5	~52	Cubo-octahedral	M	Linear	~20	[62, 63]
	Magnetospirillum gryphiswaldense MSR-1	3–6	~45	Cubo-octahedral	M	Linear	25–40	[62, 64]
	Magnetococcus spp. *MC-1*	1–2	70–100	Elongated	M	Linear	5–14	[10, 65]
	Magnetic *Vibrio* MV-1	2	~60	Truncated hexaoctahedral	M	Linear	~15	[57]
δ-Proteobacteria	*Desulfovibrio magneticus* RS-1	3–5	~35	Irregular/bullet	M	Irregular linear	1–18.	[59]
γ- Proteobacteria	Uncultured rods	3–4	~60	Variable	G	Irregular Double chains	57	[66]
Nitrospira phylum	*Magnetobacterium bavaricum*	9	110–150	Irregular	M	3–5 rope-shaped bundles	Up to 200	[42, 67]
Unknown	Uncultured rods	~3	~65	Irregular/bullet	M/G	Irregular double chains	20–40	[40]

a M = magnetite, G = greigite.

dispelling the proposed dual evolution. *D. magneticus* respires on sulfates and thiosulfates, is strictly anaerobic, but is also chemo-organoheterotrophic and utilizes organic acids as carbon and electron sources. In order to further dispel any discrete relationship between mineral and phylogenetics, an uncharacterized magnetic bacterium has been observed to contain both magnetite and greigite particles within the same cell (and even the same chain), with the ratio of magnetite to greigite depending on the available oxygen and sulfide in the environment [39, 40].

The diversity of magnetic bacteria was further illustrated by the discovery of an exotic strain from the *Nitrospira phylum* prokaryotic group. *Magnetobacterium bavaricum* is a very large magnetic bacterium that has a number of chains of several hundred tooth-shaped magnetite magnetosomes [40]. The recent sampling of hot springs and saline lakes has revealed yet more diversity, with magnetic bacteria being observed in extreme environments, and the suggested tentative discovery of magnetotactic archaea [42]. Thus, as more magnetic bacteria are discovered and isolated from more diverse environments, it can be seen that magnetotaxis does not have a simple evolutionary lineage. Rather, with its very wide phylogenetic distribution, magnetotaxis is most likely the result of horizontal gene transfer, or might even be an ancient underlying trait. The details of some of these different bacteria are listed in Table 11.2.

In recent years there has been much debate over the purpose of magnetosomes and magnetotaxis. It appears that magnetotaxis is a deliberate trait [1], as the magnetism of the magnetosomes is optimized by the single-domain crystals in the chain formation providing the maximum magnetic moment. Initially, magnetotaxis was thought to have a simple navigational role, since swimming towards the pole takes the bacteria down the inclination angle of the Earth's magnetic field towards their preferred environment [43]. It was also noted that magnetic bacteria found in the Northern Hemisphere were exclusively north-seeking [31], and *vice-versa* for the Southern Hemisphere [44]. Unfortunately, however, this theory has several flaws: first, many magnetic bacteria orientate axially, swimming in either direction along the field line; and second, magnetic bacteria show an aerotaxial dominance, leading to a modified magneto-aerotaxis model. Here, it is suggested that aerotaxis is aided by magnetic navigation, although in practical terms this is not the case. While magnetic bacteria orientate at the correct oxygen tension faster in a magnetic field than do their nonmagnetic counterparts [45], this difference is not very significant and is negligible under the Earth's magnetic field. Indeed, it appears that this navigational role of the magnetosomes is advantageous, but not beneficial enough to warrant the cells' large biological investment into magnetosome synthesis; this suggests that navigation has an advantageous and coincidental secondary role. The third – and most important – flaw is seen when it is considered that magnetosome synthesis does not occur under aerobic conditions (>2% oxygen) [46]. The question then is that, if the purpose of magnetosomes is to navigate to microaerobic environments, why are they absent when they are needed the most? This again suggests navigation as a secondary feature, and therefore the primary question of why magnetosomes are synthesized remains unclear. It has been proposed that magnetosomes might have a detoxifying

catalytic role, replacing catalase in the processing of hydrogen peroxide [47]. However, the fact that biomineralization is induced at low oxygen tensions (a respiratory feature) seems to suggest that magnetosomes and/or magnetosome synthesis have a role in respiration/energy conservation; moreover, there is evidence for iron-dependence [48] and redox cycling [48, 49], and the formation of magnetite is energetically favorable. This, coupled with the presence of many hemerythrins (which are indicative of complex microaerobic/anaerobic pathways), shows that the present understanding of the respiration of these microbes is far from complete. Indeed, there is no simple answer to this question, as it seems that biomineralization is intrinsically linked to environmental and respiratory considerations for which it is difficult to distinguish between what is cause, what is effect, and what is coincidence.

11.4.2 Magnetosome Characterization

When magnetic bacteria produce magnetosomes, the key differences between these biologically synthesized magnetic nanomaterials and other nanomagnets are the magnetosome's inherent regularity and lipid bilayer coating, both of which confer advantages for biomedical applications. Specifically, the regularity provides consistency and predictable properties, while the coating reduces aggregation and/or increases dispersion, and provides the particles with increased biocompatibility. In addition, the coating can be easily modified by the addition of biomolecules such as drugs and antibodies.

The nature of the magnetic mineral within the magnetosome was first identified as magnetite using Mössbauer spectroscopy [50]. Interestingly, the spectrum of this biogenic magnetite deviated slightly from that of pure stoichiometric magnetite, which indicated that the biogenic magnetite contained either a small percentage of vacancies in the octahedral sublattice, or a different iron oxide phase (such as γ-Fe_2O_3), or both [50]. These results have been confirmed by subsequent analyses, with Mössbauer spectral analyses indicating the presence of a small amount of another iron oxide phase [51]. Additional magnetic [52] and X-ray magnetic circular dichroism (XMCD) studies [53] confirmed that the magnetosome magnetite was of a slightly reduced form when compared to stoichiometric magnetite. The magnetic properties of magnetosomes are quite distinct, with a lower and sharp Verwey transition (T_v) of ~100 K (Figure 11.4a) (as opposed to 120 K), as well as a distinct demagnetization of isothermal remanent magnetization and $\delta_{FC}/\delta_{ZFC} > 2$ for intact chains of magnetosomes [12, 54, 55] (δ is a measure of the amount of remanence lost by warming through the Verwey transition; FC and ZFC denote field-cooled and zero-field-cooled conditions, respectively). These unique magnetic characteristics seem to be based on the fact that the particles have a narrow size distribution (sharp transition), are small and slightly reduced (lower T_n) and show a distinctive pattern, with the particles being arranged in a stabilizing chain formation within the cell. Further evidence for the magnetic stabilizing effect of the chain formation can be seen by mapping the magnetic inductance using off-axial

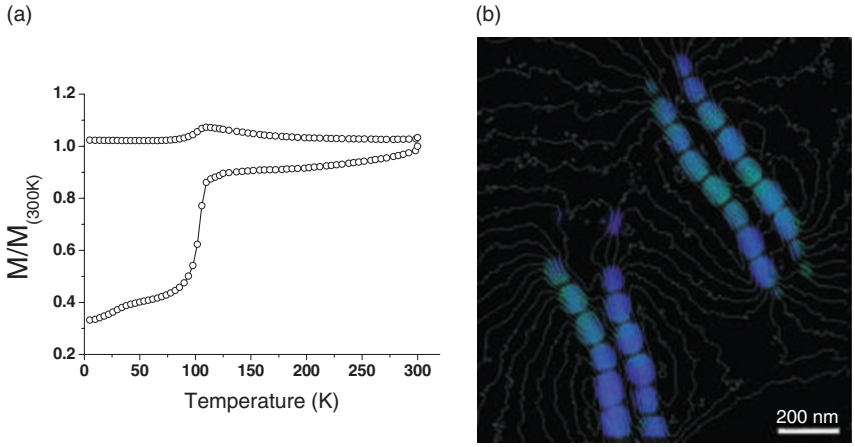

Figure 11.4 Magnetic characteristics of magnetosomes. (a) Field-cooled and zero field-cooled magnetization versus temperature; (b) Off-axial electron holographic transmission electron microscopy image of magnetite magnetosomes. (Image reproduced with kind permission from R. Dunin-Borkowski.)

electron holography; the result is a series of beautiful images of the magnetic nanostructure [56, 57] which reveal the particles to be single domain, and also show that small particles at the end of the chains, which should be superparamagnetic, are aligned with the other particles due to this dominant chain interaction (Figure 11.4b). The measurements and calculations show that the chains are magnetically saturated and, interestingly, that different chains of magnetosomes of different morphologies (i.e., from different strains) have the same magnetic moment. It can be seen that the larger, more anisotropic elongated magnetosomes of *Magnetospirillum vibros* (MV-1) are spaced further apart than the smaller, more isotropic magnetosomes in MS-1, with this closer spacing increasing chain interactions to compensate for the larger anisotropy of MV-1 [56, 57]. Indeed, it should be noted that magnetosomes of different morphologies will have different magnetic properties, with elongated particles having squarer remanence curves with increased coercivity, compared to more isotropic morphologies [58].

The distribution profile of magnetosome sizes also differs from that of synthetic magnetite nanoparticles. While synthetic particles generally have a larger distribution, with a bias to smaller particles, magnetosomes have a narrow distribution with a bias to the larger particles and a dramatic cut-off at the largest size, showing a greater degree of restriction and control over the growth process [10]. Equally, the morphology of magnetosomes is highly defined when compared to synthetic methods [10]. Both, size and shape are remarkably highly conserved within each magnetic bacterial strain, but may vary from strain to strain (Figure 11.5; Table 11.2). The most readily culturable subfamily, *Magnetospirilla*, all produce

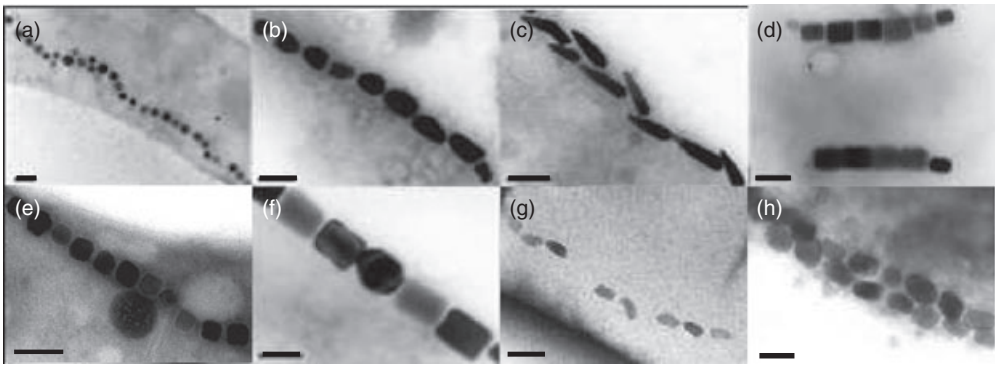

Figure 11.5 Transmission electron microscopy images of different magnetosome morphologies. (a–g) Magnetite particles; (h) Greigite particles. (a, e) Cubo-octahedral magnetosomes: (a) from *M. gryphiswaldense* MSR-1; (e) from *M. magnetotacticum* MS-1; (b) Bullet-shaped magnetosomes; (c) Tooth-shaped magnetosomes; (d, f) Elongated magnetosomes from (d) *M. coccus* MC-1 and (f) *M. vibros* MV-1; (g, h) Irregular bullet-shaped magnetosomes from (g) *D. magneticus* RS-1 and (h) uncharacterized greigite-producing bacterium. Scale bars = 100 nm. Some images reproduced with kind permission from D. Schuler and T. Matsunaga.

cubo-octahedral magnetite crystals which are on average 40–55 nm in length and in single chains (Figure 11.5 a & e). The *Magnetovibrio* strains produce single chains of elongated particles of average length 50–65 nm (Figure 11.5 f). Similarly, *Magnetococcus* sp. have elongated magnetosomes that are hexagonal-prismatic, but are larger with an average size of 100 nm; interestingly, these bacteria form two chains, one down each side of the cell (Figure 11.5 d). It is also interesting to note that this quite different chain motif is present in the *Magnetococcus* subfamily, which is phylogenetically quite distant from the other two α-Proteobacteria. Even more distant is the sulfate-reducing *D. magneticus* RS-1, which produces irregularly bullet-shaped magnetite magnetosomes of average length 30–40 nm, in single chains (Figure 11.5 g). Bulk magnetic measurements show these particles to be only weakly magnetic because of their small size, placing them just inside the superparamagnetic region. Their very low T_v (=86 K) suggests there is some degree of oxidation, and the particles show no chain interactive cooperation because they are spaced too far apart. This means that the cells have little to no real magnetotaxis, and reinforces the point that the magnetosomes in this cell have a different biological purpose [59].

Many more uncultured magnetic bacteria have revealed an assortment of magnetosomes of different morphology, sizes, and motif arrangements. To mention a few, the magnetosomes of *Magnetobacterium bavaricum* are large (average 110–150 nm long) and have an irregular, elongated tooth-like shape, with many hundreds of them being bundled together to form a rope-like chain structure of which there are several within each cell [60]. Organisms that produce greigite magnetosomes seem to exert less control over the magnetosome shape and chain structure

than do magnetite-producing cells. Interestingly, greigite magnetosomes in MMPs have several morphologies within the same organism, including bullet-shaped, cubic, and smaller more irregular particles [1]. Other uncultured greigite-producing bacteria have irregular elongated magnetosomes of approximately 60 nm length, often in more disordered double chains (Figure 11.5 h). Greigite-producing cells analyzed using off-axial electron holography were seen to contain magnetosomes that were elongated along the [111] axis but were irregular with respect to crystallographic orientation, morphology, and chain organization; the result of this was many magnetosomes which had a much reduced magnetic moment [61].

The application of magnetosomes as nanomaterials has been envisaged from a technological standpoint only quite recently, and this has occurred almost exclusively in the field of biomedical applications. The reason for this is because magnetosomes lend themselves perfectly for use as biomedical nanomagnetic particles, in several ways:

- The magnetic particles are obtained directly from the cell with an inherent lipid coating, which is ideal if the particle is to be modified with bioactive compounds.
- The strict control that a biological system offers over particle size, shape and crystal quality allows the provision of a highly uniform geometric and crystallinity.
- Although the particle size and shape is well conserved within each strain of bacteria, a range of magnetosome morphologies and sizes have been observed in various bacteria (Figure 11.5; Table 11.2), with some of these shapes being irreproducible synthetically *in vitro*.
- Magnetosomes have highly defined and distinctive magnetic properties, which results in a very attractive range of nanomagnetic materials that may be used for biomedical applications.

11.4.3
Magnetosome Formation

The biological machinery and mechanism of biomineralization of magnetite within magnetosomes has been the subject of intensive research over the past 20 years, with the quantity and quality of data obtained increasing dramatically recently with the advent of new and improved bioanalytical tools in areas such as gene sequencing and bioinformatics. The study and understanding of this process has derived from two investigative approaches: (i) proteomics studies, analyzing the proteins associated with the magnetosome; and (ii) genomic studies, which have been performed in parallel and have concentrated on gene sequence, mutagenesis and bioinformatic comparative analysis. Both approaches have also been complemented by physical analyses such as high-resolution transmission electron microscopy (TEM). Although the biomineralization of magnetite has not been completely elucidated, the information obtained via these approaches has provided a comprehensive foundation and solid hypothetical models.

11.4.3.1 Proteomics

Initially, microbiological investigations began with the analysis of proteins expressed on the magnetosome membrane [68]. This membrane was found to be very similar to the cytoplasmic (inner) membrane of the cell, containing many of the same proteins, with the addition of some proteins unique to the magnetosome membrane [69, 70]. From these data a model was proposed whereby the magnetosome membrane was invaginated from the cytoplasmic membrane and unique biomineralization proteins were then recruited to the vesicle. Studies using thin-section cryo-TEM showed that the magnetosome membrane vesicle did indeed originate from the cytoplasmic membrane, and that this occurred before magnetite synthesis, revealing empty vesicles prior to formation [71]. Further imaging using electron cryotomography allowed the three-dimensional (3-D) visualization of magnetosomes *in vivo*, and also showed that the magnetosomes were not in fact separate vesicles but remained attached to the cytoplasmic membrane [72].

Protein analyses of the magnetosome membrane conducted in several culturable strains of *Magnetospirillum* led to the identification of several magnetosome membrane-specific (Mms) proteins [69, 70, 73–75], with functional and comparative analysis showing homology of these proteins in several different magnetic bacteria. It is worth noting here that simultaneous investigations on different strains in different laboratories have led to complications of nomenclature. While the Matsunaga laboratory working on AMB-1 labelled new proteins MmsX, the Schüler laboratory, while working with MSR-1, labelled the new proteins magnetosome-associated membrane (MamX) proteins. Recently, it has been found that many of these differently labelled proteins and genes are in fact identical or homologous to each other.

Several homologous Mms proteins have been identified [73] in different magnetic bacteria. For example, Mms24 (MamA in MSR-1 [76], Mam22 in MS-1 [74]) has been identified and found to mediate protein interactions, suggesting a function of initial magnetosome membrane activation [71]. However, it should be noted that a genetic knockout mutant was still capable of forming a small number of magnetosomes, showing Mms24 to be non-essential to the process. Another Mms GTPase protein, Mms16, was also identified which, due to its GTPase activity, has been linked to the magnetosome membrane initial budding [74]. However, it remains unclear as to whether Mms16 is in fact a Mms protein or is a contaminant, as the protein was found in a different site to the magnetosome in MSR-1 and the MSR-1 knockout mutant showed no change in magnetosome formation [77]. Four magnetosome-specific proteins have also been found in tight association with the magnetite mineral; because of their size, these have been named Mms5, 6, 7, and 13 (Mms5 is similar to MamG and D, Mms7 = MamD, Mms13 = MamC in MSR-1). Mms6 has been expressed in *Escherichia coli*, was purified, and found to control the size (restricted to 20–30 nm) and shape (similar to magnetosomes) of chemically precipitated magnetite *in vitro*, under several different reaction conditions [78, 79, 80]. Mms6 has a hydrophobic magnetosome membrane-bound N-terminal end and a hydrophilic iron-binding-specific C-terminal end, describing a membrane-anchored iron interacting protein. Interestingly Mms 5, 6, and 7 have

a common repetitive leucine-glycine (LG) residue motif, which is a common repetitive sequence for many structural scaffold proteins such as fibroin and mollusk shell framework proteins. An analysis of Mms6 indicated that it also forms large aggregates, characteristic of such scaffold proteins [77], and suggests the presence of a structural scaffold function of Mms6 (as well as Mms5 and 7), restricting and controlling the size and shape of the magnetite crystal.

11.4.3.2 **Genetics**

The genetic analysis of magnetic bacteria was initially based on analyzing nonmagnetic mutants, either spontaneously or by deliberate gene disruption (transposon mutagenesis). Nonmagnetic mutants are easily assayed, and the missing or disrupted gene can then be identified. This approach was used to identify the *magA* gene (and MagA protein) that is required for magnetosome biomineralization and is seen to transport iron [81]. Significantly, Grunberg *et al*. found that the genes encoding many magnetosome membrane-specific proteins, when identified by proteomic analysis, could be grouped into two distinct and closely located regions of the genome (*mamA*, *B*, *E* and *mamC* and *D*) [75]. Further to this, a spontaneous and persistent nonmagnetic mutant in MSR-1 was characterized and found to have a large 80 kb fraction of deleted sequence. This fraction contained both the distinct region identified by Grunberg and all the genes encoding the biomineralization proteins found to date [82]. The same was found to be true for a 98 kb region in AMB-1 and, more recently, it was proposed that this region might extend to 130 kb of genome [83]. This region was found to contain a large number of insertion elements and to be highly unstable under several stress conditions. This would explain its spontaneous loss to form nonmagnetic cells, and also provide weight to the hypothesis that magnetotaxis is derived from horizontal gene transfer. It was found that these two regions, and a third region containing the *mms6* gene, were all within a 35 kb region named the "Magnetosome Island." Of the three distinct magnetosome gene clusters, the *mms* cluster was shown to contain five genes, including *mms6*, while *mamGFDC* contained four genes and was recently shown to be nonessential for magnetite formation, as deletion mutants were still able to produce magnetite, albeit of a smaller size and more irregular shape. It also showed that the proteins encoded in this cluster could affect particle morphology [84]. The final region, known as the "mamAB cluster", was shown to contain 17 different genes, from *mamH* to *mamU* [85].

The partial genome sequences for MS-1 and MSR-1 have been available for some time, and the full annotated genomic sequence for AMB-1 was completed a few years ago [86]. However, in recent years the advances in sequencing technology have led to a very rapid increase in the quality and quantity of genetic data. All of these genomes are now completed, as well as the genome for MC-1 [87], and studies to complete MV-1 are currently under way [88]. This will provide highly valuable information to enable comparative analyses [87]. Indeed, all three clusters have been found in all strains sequenced, these being similar over the *Magnetospirillum* strains with a few minor variations [4]. MC-1 has similar clusters, but deviates more from the others.

Systematic deletion mutations of genes within the Magnetosome Island have led to the identification of several protein functions. The *mamK* gene encodes a cytoskeletal fibrous actin-like protein MamK, while another gene unique to magnetic bacteria, *mamJ*, was also found within the Magnetosome Island. The deletion mutants of each of these genes produced cells capable of producing magnetosomes, but not in a chain formation; rather, they were randomly displaced throughout the cell. Thus, it has been shown that MamK is a stabilizing filamentous protein which runs alongside the magnetosomes, while MamJ interacts between the magnetosome and MamK, so as to "stick" magnetosome "beads" to a MamK "string" [72, 89].

11.4.3.3 **Mechanism**

Today, a rich array of microbiological, physical, genetic and proteomic data are available with which to propose a substantial mechanism of magnetosome formation. Initially, budding and invagination of the cytoplasmic membrane occurs, during which vesicle formation the magnetosome membrane-specific proteins are expressed or recruited to specific locations on the vesicle; this activation step is thought to be associated with Mms24. In order to commence magnetite biomineralization, large quantities of iron must be taken up by the cell from the environment. Generally, it is suggested that ferrous ions are transported, based on the kinetics and the abundant ferrous ion transport proteins, although siderophores have been observed in some magnetic bacteria [90] and the complete picture of iron transport remains unknown. However, more recent transcriptome analyses of iron transport protein expression have revealed that high-affinity ferrous ion transport occurs under iron-rich conditions, whereas siderophore ferric ion transport dominates in a more depleted iron environment [91].

It is now known that the magnetosome membrane is not a true vesicle, but remains attached to the cytoplasmic membrane. What is not known, however, is whether the neck of the vesicle is open or plugged with proteins, and also whether the iron ions are transported across the outer and inner membranes and then into the magnetosome membrane, or are simply transported across the outer membrane directly into the periplasm and into the neck of the magnetosome. The accumulated ferrous ions within the magnetosomes are then thought to bind and nucleate on Mms6 (and probably also 5 and 7) and begin magnetite formation with partial oxidation (possibly by MamT) and pH regulation (possibly by Mam N). Initial iron-storage phases and precursors such as ferritin have been proposed [92], although there is no direct evidence of this, and it seems that the magnetite is directly mineralized. Magnetosome formation occurs simultaneously in all of the empty vesicles nucleating from similar locations within the vesicle [53, 71]. The crystal growth, size, and shape is then regulated by Mms6 (and probably also 5 and 7). The magnetosomes are aligned in chains by using MamJ to attach to the fibrous MamK protein. The speed at which magnetite formation occurs has proved to be highly variable, and appears to depend on iron and nutrient uptake. Indeed, several studies in limited media (to inhibit growth) have provided formation times in excess of 5 h [71, 92, 93], while large-scale fermentor growth has shown a slow

magnetite formation time [93] coinciding with a slower iron uptake. Conversely, standard media and available iron show mineralization to occur within 30 min [53, 91], with rapid iron uptake occurring within this time frame [53, 91]. Interestingly, it seems that magnetosome formation is dependent on, and occurs concomitantly with, iron uptake, and that a faster iron uptake occurs when the cells have been starved of iron. However, a full explanation of the factors that affect the speed of iron uptake and magnetite formation has not yet been provided.

11.5
Progress and Applications of Novel Biomedical Magnetosome Materials

When considering the types and specifications of nanomagnets used for biomedical applications, it is clear that magnetosomes represent ideal starting materials for biomedical nanomagnets. These magnetosomes composed of magnetite that is ferrimagnetic up to high temperatures, is nontoxic, and also stable. The particles are ideally sized (30–100 nm) for many applications, with highly regulated size and morphology providing a uniform, consistent, and well-defined magnetic signal. Moreover – and most significantly – magnetosomes have an integral 4 nm-thick lipid coating that makes them ideal for biomedical functionalization and ensures that they will not aggregate. As these materials are synthesized biologically, active biosubstrates can be attached and integrated into the lipid membrane by elegantly using genetic manipulations of the magnetosomes. All of these advantages show huge potential for magnetosomes in biomedical applications, and several significant systems to modify magnetosomes *in vitro* are currently under development, mainly by Matsunaga and coworkers [3]. Magnetosome-based systems are being developed by attaching proteins (e.g., luminescent proteins and antibodies) and DNA, for applications such as immunoassays, cell separation, labelling (e.g., biomarker detection) and drug screening, by utilizing several different functionalization strategies to attach bioactive substrates. One method of attaching proteins to magnetosomes is via a crosslinker reaction, where the lipid's surface amine groups bind aldehydes or esters that in turn link to a range of proteins. This has been successful for the display of antibodies and the immobilization of streptavidin, by using biotin-modified magnetosomes [94].

Another more elegant method of protein attachment uses genetic engineering to express fusion proteins on the magnetosomes *in vivo*; the fusion proteins consist of a native magnetosome membrane protein as an anchor, attached to a functional protein. For this method, the choice of anchor protein is very important for the stability and coverage of the active protein. MagA was the original choice of anchor protein, but was found to be too large and hydrophobic to accommodate other bulky membrane fusion proteins. Thus, the smaller Mms16 protein was used and found to show a greater expression on the magnetosome, especially for large transmembrane receptors. However, the stability and density of attachment was seen to be far more effective when utilizing Mms13 as the anchor protein [95]. Mms13 is not only very small, providing next to no steric hindrance and increased

density, but it is also tightly bound to the magnetite surface, stabilizing large proteins such as luciferase. For comparison, the luminescence of luciferase was 400- to 1000-fold brighter when Mms13 was the anchor protein as opposed to Mms16 and MagA. The density of expression on the magnetosomes can be increased further with the use of strong expression promoters for the fusion proteins [96]. This method has been successfully used to functionalize magnetosomes with constituents such as protein A [97], G protein-coupled receptor [98], acetate kinase, and luciferase [3]. Equally, these fusion proteins can be expressed in *E. coli* and inserted into the magnetosome membrane post-extraction by means of sonication to give increased yields [99].

These functionalized magnetosomes have been utilized in competitive chemiluminescence antibody immunoassays for the quick and convenient detection of hormones and environmental pollutants, with a much lower detection limit. For example, xenoestrogen can be detected by a competitive reaction with monoclonal antibodies displayed on magnetosomes in a process that takes 15 min, compared to 2.5 h for alternative methods. Furthermore, the magnetosome system has increased range and sensitivity [100]. Protein A has been attached to magnetosomes to produce a chemiluminescence sandwich immunoassay that can be utilized for the measurement of insulin in blood in a fully automated, sensitive, fast, and convenient system [97]. The immobilization of protein G-coupled receptors on magnetosomes is also significant, as such transmembrane proteins are notoriously difficult to express and can also be especially difficult to express in their correct conformation, which often renders them inactive. Their expression on magnetosomes was, however, successful and has been used for competitive dopamine-binding assays [98]. Protein-functionalized magnetosomes have also proved ideal for *in vitro* cell separations, as they are of an ideal size and magnetism. The particles must be nanosized in order to avoid any negative effect on the cells, but many commercial nanomagnetic particles are so small that they are superparamagnetic. Magnetosomes are nanosized but single-domain ferrimagnets, and as such can easily be magnetically separated using a simple permanent magnet. Antibodies on magnetosomes have been used to separate mononuclear cells from periplasmic blood with remarkably high purity [101].

However, it is not only proteins that have been used to functionalize magnetosomes; rather, DNA has been adsorbed onto polyamidoamine dendrimer-modified magnetosomes to almost 100% efficiency [102]. Magnetosomes are also being used for a high-throughput, multiple assay systems for the analysis of single-nucleotide polymorphisms (SNPs), which may be used to identify the genes responsible for diseases such as cancer. The fully automated magnetosome system combines polymerase chain reaction (PCR) methods, and has proved to have a superior discrimination between genotypes [3]. Many of the assays mentioned here are currently being developed into fully automated systems, a situation which is assisted by the fact that magnetosomes are easily and simply magnetized.

There is a great potential for the development of functionalized magnetosomes for *in vivo* medical applications, such as drug delivery and hyperthermic treatments. As noted above, magnetosomes are consistently uniform in size shape and

magnetism, and have an inherent lipid coating for biological functionalization. This lipid layer also increases the dispersive properties, reducing the risk of blocked vessels and embolization. Although magnetic nanoparticles have been used in medicine for several years as MRI contrast agents, their application as functional targeted therapeutic agents is in its infancy and has only recently been realized at the clinical level. Many animal studies conducted during the early 1980s yielded very successful results. For example, sarcomas in rats were successfully magnetically targeted with much smaller doses of doxorubicin [103], since then many more detailed magnetic targeted drug studies on animals have been performed, modeled, and analyzed [104]. Although the preliminary investigations of magnetically targeted gene delivery showed promising results in animal models [20], these findings were only very slowly translated and developed into clinical trials for humans, mainly due to problems when targeting sites deep within the body [16]. Attempts to combat these issues have involved the surgical implantation of magnets close to the site of the disease [105], altering the type of magnetic fields applied [17], and also the use of a combination of magnetic and "cancer-seeking" monocytes to target diseased cells [106]. Clearly, advancements have been made in this area, with positive results being obtained from ongoing research investigations and clinical trials [107].

One other major area of magnetically targeted therapeutic treatment is that of hyperthermic cancer treatment. When nanomagnetic particles are placed in an alternating magnetic field, they heat up; the heat produced can then be used at a targeted area either to burn and kill a tumor or to heat-activate a drug. The heating effect occurs due to a high specific power loss which is dependent on the magnetic of the particles; this energy is then dissipated to the surrounding areas in the form of heat. For hyperthermic targeted cancer treatments, magnetosomes have been proved to be particularly superior nanomaterials. Significantly, magnetosomes have by far the greatest specific heating power ($1\,kW\,g^{-1}$ at 410 kHz and $10\,kA\,m^{-1}$) when compared to other nanomagnetite [108]. This is due not only to the single-domain and narrow size-distribution of magnetosomes, but also to the inherent defects/vacancies that are characteristic of biogenic magnetite. Therefore, although the exact reason has not yet been completely ascertained, magnetosomes are the best materials identified to date for hyperthermic treatments [108–110].

Despite their many advantages, magnetosomes do have certain disadvantages for practical applications when compared to other synthetic nanomagnets. The most well-known disadvantage is that magnetic bacteria are notoriously difficult to grow, they tend to grow in low cell densities, and they produce very small yields of magnetosomes at a relatively high cost that is not commercially viable. The second disadvantage relates to their adaptation. Although the magnetosome membrane has proved highly accommodating to functionalization and modification, the nature of the magnetite mineral itself is less flexible (in fact, this level of genetic control of the mineral might be considered an advantage). It was noted earlier that the magnetic properties of magnetosomes can be altered by varying their size, shape, and composition. Although many magnetosomes have been identified with well-defined sizes and shapes, the only strains of magnetic bacteria

that are well characterized and have been investigated for biomedical application are all *Magnetospirillum*, and all of these form cubo-octahedral magnetosomes, with no shape variation. Equally, although the biomineralization process results in a pure and consistent magnetite with rigid magnetic characteristics, it provides no flexibility by which the magnetic properties of the particles can be altered and thus enhanced, for various purposes.

Importantly, both of these disadvantages are being addressed via research investigations. In recent years, the growth and yields of magnetic bacteria and magnetosomes have increased vastly, due to the optimization of large-scale fermenter growth [46, 111], where magnetosome yields of 6.3 $mg\,l^{-1}$ of bacterial medium per day were achieved [46]. Growth has also been increased and optimized for genetically engineered magnetic bacteria harboring fusion genes for magnetosome functionalization [112]. More recent optimizations have shown dramatic increases in cell and magnetosome yields, with cell culture densities reaching $OD_{565} = 7.24$, and cell yields of 2.17 $g\,l^{-1}$ giving impressive magnetosome yields of 16.7 $mg\,l^{-1}$ per day [93]. Although it must be recognized that syntheses using fermenters may be costly, these recent levels of yield make magnetosome considerably more commercially viable.

Recent developments have also been made to combat the lack of flexibility in the magnetic characteristics of magnetosomes. Magnetite is magnetically isotropic and soft, but becomes harder if it becomes anisotropic, which in turn endows the material with a preferential bias so as to increase the coercivity. Whilst this can be achieved by increasing the length/width ratio of the particles, such a change in shape may have wider implications on their behavior and toxicity. An increased coercivity can also be achieved by the addition a small amount of cobalt; this adds atomic anisotropy and increases magnetic hardness, without affecting the particle shape. Recently, the cobalt doping of magnetosomes was achieved *in vivo* for three strains of *Magnetospirillum*, simply by growing the bacterial cells in a medium containing specific concentrations of iron and cobalt [63]. These cobalt-doped magnetosomes showed an increased magnetic coercivity, which in turn should increase the magnetic heating power of the magnetosomes, making them a very attractive proposition as a practical material for hyperthermic cancer treatments.

11.6 The Future for Biomedical Magnetosomes

Over the past few years, investigations into biomedical nanoscience have increased dramatically, such that research activity in the area is now intense and pushing forward towards the development of therapies. This, in time, should result in additional clinical trials and the production of commercial, magnetically targeted therapies. Although magnetosomes show superior characteristics for biomedical applications, they have in the past been overlooked due to their low yields and costly specialized syntheses. Yet, recent advances in growth optimization have led to magnetosome yields being dramatically improved. Increasing magnetosome

yields even further and reducing the cost of biomineralization methods will require imaginative solutions, including both production in different hosts and *in vitro* synthesis. If magnetosomes can be prepared with increased yields and superior modification/functionalization, they will become attractive materials for commercial biomedical nanomagnets, although for this to occur it will be important not only to develop *in vitro* biomedical systems on a commercial basis but also to develop *in vivo*-based systems for targeted therapies.

This may be achieved by utilizing the present knowledge base for immobilizing and displaying proteins and DNA on magnetosomes (see Section 11.5). It should be possible to adapt and modify crosslinking and genetically modified fusion protein expression to accommodate new proteins, drugs, and genes as they are developed. It should be noted here that magnetosomes that express fusion proteins may prove to be particularly advantageous. In addition, if several bioactive compounds can be attached to one particle in specific quantities, by utilizing different anchor-fusion proteins and expression promoters, then biomedical nanomagnetic particles with multiple and complex functions could be developed.

Whilst magnetosomes are perhaps the best heat-loss material for hyperthermic therapies studied to date, cobalt-enhanced magnetosomes may improve this effect further. Future studies in this area should not only test the specific heat-loss of cobalt-enhanced magnetosomes, but also be followed by toxicology studies, further functionalization and animal and clinical trials. In this respect, the cobalt doping of magnetosomes has opened up a range of possibilities to manipulate the composition of biomagnetite. The knowledge that cobalt doping is possible, and that magnetic characteristics could also be varied with other magnetic metal dopants such as nickel or manganese, will surely lead to future investigations.

The ability to alter the magnetic properties of magnetite, and in turn other particle specifications, by varying the particles' sizes is vital. At present, despite magnetic bacteria having been identified with variously shaped and sized magnetosomes, only cubo-octahedral particles may be used, and consequently a vast potential of various magnetosomes is left untapped. To overcome such limits, a concerted effort must be made to isolate and culture magnetic bacteria with magnetosomes of different shapes and sizes. Likewise, studies must be conducted to increase and optimize cell growth, the eventual aim being to provide multiple sizes and shapes of magnetosomes for biomedical specifications. In this regard, recent investigations have been conducted with MV-1, MC-1 and RS-1 strains, all of which produce magnetosomes of various shapes. MV-1 produces larger, elongated particles with an increased coercivity, and may be grown on a large scale, at higher densities; moreover, the cobalt-doping of these elongated particles should increase coercivity even further.

In the long-term approach to using magnetosomes as biomedical nanomagnetic materials, it will be necessary to determine details of not only the biomineralization process but also the biomineralization proteins. Having identified exactly which proteins are required, it may become possible to insert biomineralization genes into other bacteria/cells or hosts, allowing them to produce magnetosomes in higher yields. Alternatively, a magnetic function may be added to an already

functionalized cell, for example a magnetically targeted "cancer-seeking" monocyte [106]. A greater in-depth knowledge of magnetosome formation should facilitate the approach to synthesizing enhanced magnetosomes or magnetosome-inspired biomimetic nanomagnetic materials. For example, the biomineralization/iron-binding/scaffold protein Mms6 can control the size and shape of nanoparticulate magnetite *in vitro* in a chemical precipitation. It follows that, the greater the number of biomineralization proteins that can be identified, overexpressed, purified, and their function ascertained, the more the biomineralization process can be used *in vitro* to impose a precise biological control over particle size and shape. This should lead, eventually, to systems whereby specific combinations of proteins are applied, depending on the particle's tailored specifications, to produce high-yield, high-quality, customized nanomagnetic particles.

References

1 Schüler, D. (ed.) (2007) *Magnetoreception and Magnetosomes in Bacteria. Microbiology Monographs*, Springer-Verlag, Berlin, Heidelberg.

2 Bazylinski, D.A. and Frankel, R.B. (2004) Magnetosome formation in prokaryotes. *Nature Reviews. Microbiology*, **2** (3), 217–30.

3 Arakaki, A., Nakazawa, H., Nemoto, M., Mori, T. and Matsunaga, T. (2008) Formation of magnetite by bacteria and its application. *Journal of the Royal Society, Interface*, **5** (26), 977–99.

4 Jogler, C. and Schueler, D. (2007) Genetic and biochemical analysis of magnetosome formation in *Magnetospirillum gryphiswaldense*, in *Handbook of Biomineralization. Vol. 1. Biological Aspects and Structure Formation*, (ed. E. Bauerlein), VCH, Weinheim, pp. 145–61.

5 Komeili, A. (2007) Molecular mechanisms of magnetosome formation. *Annual Review of Biochemistry*, **76**, 351–66.

6 Matsunaga, T. and Okamura, Y. (2003) Genes and proteins involved in bacterial magnetic particle formation. *Trends in Microbiology*, **11** (11), 536–41.

7 Schueler, D. (2008) Genetics and cell biology of magnetosome formation in magnetotactic bacteria. *FEMS Microbiology Reviews*, **32** (4), 654–72.

8 Amann, R., Rossello-Mora, R. and Schuler, D. (2000) Phylogeny and in situ identification of magnetotactic bacteria. *Biomineralization*, 47–60.

9 Lang, C. and Schuler, D. (2006) Biogenic nanoparticles: production, characterization, and application of bacterial magnetosomes. *Physical Review. B, Condensed Matter*, **18**, S2815–28.

10 Devouard, B., Posfai, M., Hua, X. *et al.* (1998) Magnetic from magnetotactic bacteria: size distributions and twinning. *The American Mineralogist*, **83** (11–12 Pt 2), 1387–98.

11 Arato, B., Szanyi, Z., Flies, C. *et al.* (2005) Crystal-size and shape distributions of magnetite from uncultured magnetotactic bacteria as a potential biomarker. *The American Mineralogist*, **90** (8–9), 1233–40.

12 Pan, Y. Petersen, N., Winklhofer, M. *et al.* (2005) Rock magnetic properties of uncultured magnetotactic bacteria. *Earth and Planetary Science Letters*, **237** (3–4), 311–25.

13 Kopp, R.E., Weiss, B.P., Maloof, A.C. *et al.* (2006) Chains, clumps, and strings: magnetofossil taphonomy with ferromagnetic resonance spectroscopy. *Earth and Planetary Science Letters*, **247** (1–2), 10–25.

14 Bazylinski, D.A. and Moskowitz, B.M. (1997) Microbial biomineralization of magnetic iron minerals. microbiology,

magnetism and environmental significance. *Reviews in Mineralogy*, **35**, 181–223.
15 Matsunaga, T. and Arakaki, A. (2007) Molecular bioengineering of bacterial magnetic particles for biotechnological application, in *Magnetoreception and Magnetosomes in Bacteria. Microbiology Monographs* (ed. D. Schuler), Springer-Verlag, Berlin, Heidelberg, p. 227.
16 Dobson, J. (2006) Magnetic micro- and nano-particle-based targeting for drug and gene delivery. *Nanomedicine*, **1** (1), 31–7.
17 Dobson, J. (2006) Gene therapy progress and prospects: magnetic nanoparticle-based gene delivery. *Gene Therapy*, **13** (4), 283–7.
18 McBain, S.C., Yiu, H.H. and Dobson, J. (2008) Magnetic nanoparticles for gene and drug delivery. *International Journal of Nanomedicine*, **3** (2), 169–80.
19 Pankhurst, Q.A., Connolly, J., Jones, S.K. and Dobson, J. (2003) Applications of magnetic nanoparticles in biomedicine. *Journal of Physics D: Applied Physics*, **36** (13), R167–81.
20 Mah, C., Fraites, T.J., Jr, Zolotukhin, I. *et al.* (2002) Improved method of recombinant AAV2 delivery for systemic targeted gene therapy. *Molecular Therapy: The Journal of the American Society of Gene Therapy*, **6** (1), 106–12.
21 Dobson, J. (2008) Remote control of cellular behaviour with magnetic nanoparticles. *Nature Nanotechnology*, **3** (3), 139–43.
22 Regazzoni, A.E., Urrutia, G.A., Blesa, M.A. and Maroto, A.J.G. (1981) Some observations on the composition and morphology of synthetic magnetites obtained by different routes. *Journal of Inorganic Nuclear Chemistry*, **43** (7), 1489–93.
23 Lee, Y., Lee, J., Bae, J.B., Park, J.-G., Noh, H.-J., Park, J.-H. and Hyeon, T. (2005) Large-scale synthesis of uniform and crystalline magnetite nanoparticles using reverse micelles as nanoreactions under reflux conditions. *Advanced Functional Materials*, **15** (3), 503–9.
24 Rockenberger, J., Scher, E.C. and Alivisatos, A.P. (1999) A new nonhydrolytic single-precursor approach to surfactant-capped nanocrystals of transition metal oxides. *Journal of the American Chemical Society*, **121** (49), 11595–6.
25 Hyeon, T., Lee, S.S., Park, J., Chung, Y. and Na, H.B. (2001) Synthesis of highly crystalline and monodisperse maghemite nanocrystallites without a size-selection process. *Journal of the American Chemical Society*, **123** (51), 12798–801.
26 Vali, H., Weiss, B., Li, Y-L. *et al.* (2004) Formation of tabular single-domain magnetite induced by *Geobacter metallireducens* GS-15. *Proceedings of the National Academy of Sciences of the United States of America*, **101** (46), 16121–6.
27 Bharde, A., Rautaray, D., Bansal, V. *et al.* (2006) Extracellular biosynthesis of magnetite using fungi. *Small*, **2** (1), 135–41.
28 Kirschvink, J.L., Kobayashi-Kirschvink, A. and Woodford, B.J. (1992) Magnetite biomineralization in the human brain. *Proceedings of the National Academy of Sciences of the United States of America*, **89** (16), 7683–7.
29 Collingwood, J.F., Mikhaylova, A., Davidson, M. *et al.* (2005) In situ characterization and mapping of iron compounds in Alzheimer's disease tissue. *Journal of Alzheimer's Disease*, **7** (4), 267–72.
30 Bellini, S. (1963) About a unique behaviour of freshwater bacteria, dell'Universita di Pavia.
31 Blakemore, R. (1975) Magnetotactic bacteria. *Science*, **190** (4212), 377–9.
32 Knoll, A.H. (2003) Biomineralization and evolutionary history. *Reviews in Mineralogy and Geochemistry*, **54**, 329–56.
33 Heywood, B.R., Bazylinski, D.A., Garratt-Reed, A., Mann, S. and Frankel, R.B. (1990) Controlled biosynthesis of greigite (Fe_3S_4) in magnetotactic bacteria. *Naturwissenschaften*, **77** (11), 536–8.
34 Sparks, N.H.C., Mann, S., Bazylinski, D.A. *et al.* (1990) Structure and morphology of magnetite anaerobically-produced by a marine magnetotactic bacterium and a dissimilatory iron-

reducing bacterium. *Earth and Planetary Science Letters*, **98** (1), 14–22.
35 Mann, S., Sparks, N.H.C., Frankel, R.B., Bazylinski, D.A. and Jannasch, H.W. (1990) Biomineralization of ferrimagnetic greigite (Fe_3S_4) and iron pyrite (FeS_2) in a magnetotactic bacterium. *Nature*, **343** (6255), 258–61.
36 Farina, M., Esquivel, D.M.S. and de Barros, H.G.P.L. (1990) Magnetic iron-sulphur crystals from a magnetotactic microorganism. *Nature*, **343** (6255), 256–8.
37 Rodgers, F., Blakemore, R., Blakemore, N. *et al.* (1990) Intercellular structure in a many-celled magnetotactic prokaryote. *Archives of Microbiology*, **154** (1), 18–22.
38 DeLong, E.F., Frankel, R.B. and Bazylinski, D.A. (1993) Multiple evolutionary origins of magnetotaxis in bacteria. *Science*, **259** (5096), 803–6.
39 Bazylizinki, D.A., Heywood, B.R., Mann, S. and Frankel, R.B. (1993) Fe_3O_4 and Fe_3S_4 in a bacterium. *Nature*, **366** (6452), 218.
40 Bazylinski, D.A., Frankel, R.B., Heywood, B.R. *et al.* (1995) Controlled biomineralization of magnetite (Fe_3O_4) and greigite (Fe_3S_4) in a magnetotactic bacterium. *Applied and Environmental Microbiology*, **61** (9), 3232–9.
41 Spring, S., Amann, R., Ludwig, W. *et al.* (1993) Dominating role of an unusual magnetotactic bacterium in the microaerobic zone of a freshwater sediment. *Applied and Environmental Microbiology*, **59** (8), 2397–403.
42 Nash, C.Z. (2008) Mechanism and evolution of magnetotactic bacteria, Ph.D. Thesis, California Institute of Technology, Pasadena.
43 Blakemore, R.P. and Frankel, R.B. (1981) Magnetic navigation in bacteria. *Scientific American*, **245** (6), 58–65.
44 Blakemore, R.P., Frankel, R.B. and Kalmijn, A.J. (1980) South-seeking magnetotactic bacteria in the Southern Hemisphere. *Nature*, **286** (5771), 384–5.
45 Smith, M.J., Sheehan, P.E., Perry, L.L. *et al.* (2006) Quantifying the magnetic advantage in magnetotaxis. *Biophysical Journal*, **91** (3), 1098–107.
46 Heyen, U. and Schuler, D. (2003) Growth and magnetosome formation by microaerophilic *Magnetospirillum* strains in an oxygen-controlled fermentor. *Applied Microbiology and Biotechnology*, **61** (5–6), 536–44.
47 Blakemore, R.P. (1982) Magnetotactic bacteria. *Annual Review of Microbiology*, **36**, 217–38.
48 Guerin, W.F. and Blakemore, R.P. (1992) Redox cycling of iron supports growth and magnetite synthesis by *Aquaspirillum magnetotacticum*. *Applied and Environmental Microbiology*, **58** (4), 1102–9.
49 Short, K.A. and Blakemore, R.P. (1986) Iron respiration-driven proton translocation in aerobic bacteria. *Journal of Bacteriology*, **167** (2), 729–31.
50 Frankel, R.B. and Blakemore, R.P. and Wolfe, R.S. (1979) Magnetite in freshwater magnetotactic bacteria. *Science*, **203** (4387), 1355–6.
51 Frankel, R.B., Papaefthymiou, G.C., Blakemore, R.P. and O'Brien, W. (1983) Fe3O4 precipitation in magnetotactic bacteria. *Biochimica et Biophysica Acta – Molecular Cell Research*, **763** (2), 147–59.
52 Weiss, B.P., Kim, S.S., Kirschvink, J.L. *et al.* (2004) Ferromagnetic resonance and low-temperature magnetic tests for biogenic magnetite. *Earth and Planetary Science Letters*, **224** (1–2), 73–89.
53 Staniland, S.S., Ward, B., Harrison, A., van der Laan, G. and Telling, N. (2007) Rapid magnetosome formation shown by real-time X-ray magnetic circular dichroism. *Proceedings of the National Academy of Sciences of the United States of America*, **104** (49), 19524–8.
54 Moskowitz, B.M., Frankel, R.B., Flanders, P.J., Blakemore, R.P. and Schwartz, B.B. (1988) Magnetic properties of magnetotactic bacteria. *Journal of Magnetism and Magnetic Materials*, **73** (3), 273–88.
55 Moskowitz, B.M., Frankel, R.B. and Bazylinski, D.A. (1993) Rock magnetic criteria for the detection of biogenic magnetite. *Earth and Planetary Science Letters*, **120** (3–4), 283–300.
56 Dunin-Borkowski, R.E., McCartney, M.R., Frankel, R.B. *et al.* (1998)

Magnetic microstructure of magnetotactic bacteria by electron holography. *Science*, **282** (5395), 1868–70.
57 Dunin-Borkowski, R.E., McCartney, M.R., Posfai, M. *et al.* (2001) Off-axis electron holography of magnetotactic bacteria: magnetic microstructure of strains MV-1 and MS-1. *European Journal of Mineral*, **13** (4), 671–84.
58 Hanzlik, M., Winklhofer, M. and Petersen, N. (2002) Pulsed-field-remanence measurements on individual magnetotactic bacteria. *Journal of Magnetism and Magnetic Materials*, **248** (2), 258–67.
59 Posfai, M., Moskowitz, B.M., Arato, B. *et al.* (2006) Properties of intracellular magnetite crystals produced by Desulfovibrio magneticus strain RS-1. *Earth and Planetary Science Letters*, **249** (3–4), 444–55.
60 Hanzlik, M., Winklhofer, M. and Petersen, N. (1996) Spatial arrangement of chains of magnetosomes in magnetotactic bacteria. *Earth and Planetary Science Letters*, **145** (1–4), 125–34.
61 Kasama, T., Posfai, M., Chong, R.K.K. *et al.* (2006) Magnetic microstructure of iron sulfide crystals in magnetotactic bacteria from off-axis electron holography. *Physica B (Amsterdam, Netherlands)*, **384** (1–2), 249–52.
62 Staniland, S., Williams, W., Telling, N. *et al.* (2008) Controlled cobalt doping of magnetosomes in vivo. *Nature Nanotechnology*, **3** (3), 158–62.
63 Matsunaga, T., Sakaguchi, T. and Tadokoro, F. (1991) Magnetite formation by a magnetic bacterium capable of growing aerobically. *Applied Microbiology and Biotechnology*, **35** (5), 651–5.
64 Schleifer, K.H., Schueler, D., Spring, S. *et al.* (1991) The genus *Magnetospirillum* gen. nov. Description of *Magnetospirillum gryphiswaldense* sp. nov. and transfer of *Aquaspirillum magnetotacticum* to *Magnetospirillum magnetotacticum* comb. nov. *Systematic and Applied Microbiology*, **14** (4), 379–85.
65 Meldrum, F.C., Mann, S., Heywood, B.R., Frankel, R.B., Bazylinski, D.A. and Microscopy, E. (1993) Study of magnetosomes in a cultured coccoid magnetotactic bacterium. *Proceedings of the Royal Society of London. B: Biological Sciences*, **251** (1332), 231–6.
66 Kasama, T., Posfai, M., Chong, R.K.K. *et al.* (2006) Magnetic properties, microstructure, composition, and morphology of greigite nanocrystals in magnetotactic bacteria from electron holography and tomography. *The American Mineralogist*, **91** (8–9), 1216–29.
67 Hanzlik, M., Winklhofer, M. and Petersen, N. (1996) Spatial arrangement of chains of magnetosomes in magnetotactic bacteria. *Earth and Planetary Science Letters*, **145** (1–4), 125–34.
68 Gorby, Y.A., Beveridge, T.J. and Blakemore, R. (1988) Characterization of the bacterial magnetosome membrane. *Journal of Bacteriology*, **170** (2), 834–41.
69 Tanaka, M., Okamura, Y., Arakaki, A. *et al.* (2006) Origin of magnetosome membrane: proteomic analysis of magnetosome membrane and comparison with cytoplasmic membrane. *Proteomics*, **6** (19), 5234–47.
70 Gruenberg, K., Mueller, E.-C., Otto, A. *et al.* (2004) Biochemical and proteomic analysis of the magnetosome membrane in *Magnetospirillum gryphiswaldense*. *Applied and Environmental Microbiology*, **70** (2), 1040–50.
71 Komeili, A., Vali, H., Beveridge, T.J. and Newman, D.K. (2004) Magnetosome vesicles are present before magnetite formation, and MamA is required for their activation. *Proceedings of the National Academy of Sciences of the United States of America*, **101** (11), 3839–44.
72 Komeili, A., Li, Z., Newman, D.K. and Jensen, G.J. (2006) Magnetosomes are cell membrane invaginations organized by the actin-like protein mamk. *Science*, **311** (5758), 242–5.
73 Okamura, Y., Takeyama, H. and Matsunaga, T. (2000) Two-dimensional analysis of proteins specific to the bacterial magnetic particle membrane from *Magnetospirillum* sp. AMB-1. *Applied Biochemistry and Biotechnology*, **84–86**, 441–6.

74 Okamura, Y., Takeyama, H. and Matsunaga, T. (2001) A magnetosome-specific GTPase from the magnetic bacterium *Magnetospirillum magneticum* AMB-1. *The Journal of Biological Chemistry*, **276** (51), 48183–8.

75 Okuda, Y., Denda, K. and Fukumori, Y. (1996) Cloning and sequencing of a gene encoding a new member of the tetratricopeptide protein family from magnetosomes of *Magnetospirillum magnetotacticum*. *Gene*, **171** (1), 99–102.

76 Grunberg, K., Wawer, C., Tebo, B.M. and Schuler, D. (2001) A large gene cluster encoding several magnetosome proteins is conserved in different species of magnetotactic bacteria. *Applied and Environmental Microbiology*, **67** (10), 4573–82.

77 Schultheiss, D., Handrick, R., Jendrossek, D., Hanzlik, M. and Schueler, D. (2005) The presumptive magnetosome protein Mms16 is a poly(3-hydroxybutyrate) granule-bound protein (phasin) in *Magnetospirillum gryphiswaldense*. *Journal of Bacteriology*, **187** (7), 2416–25.

78 Amemiya, Y., Arakaki, A., Staniland Sarah, S., Tanaka, T. and Matsunaga, T. (2007) Controlled formation of magnetite crystal by partial oxidation of ferrous hydroxide in the presence of recombinant magnetotactic bacterial protein Mms6. *Biomaterials*, **28** (35), 5381–9.

79 Arakaki, A., Webb, J. and Matsunaga, T. (2003) A novel protein tightly bound to bacterial magnetic particles in *Magnetospirillum magneticum* strain AMB-1. *The Journal of Biological Chemistry*, **278** (10), 8745–50.

80 Prozorov, T., Mallapvoyada, S.K., Narusimhar, B., Wang, L., Palo, P., Nilson-Hamilton, M., Williams, T.J., Bazylinski, D.A., Prozorov, R. and Canfield, P.C. (2007) Protien-mediated synthesis of uniform superparamagnetic magnetite nanocrystals. *Advanced Functional Materials*, **17**, 951–7.

81 Nakamura, C., Burgess, J.G., Sode, K. and Matsunaga, T. (1995) An iron-regulated gene, magA, encoding an iron transport protein of *Magnetospirillum* sp. strain AMB-1. *The Journal of Biological Chemistry*, **270** (47), 28392–6.

82 Schubbe, S., Kube, M., Scheffel, A. *et al.* (2003) Characterization of a spontaneous nonmagnetic mutant of *Magnetospirillum gryphiswaldense* reveals a large deletion comprising a putative magnetosome island. *Journal of Bacteriology*, **185** (19), 5779–90.

83 Ullrich, S., Kube, M., Schubbe, S., Reinhardt, R. and Schuler, D. (2005) A hypervariable 130-kilobase genomic region of *Magnetospirillum gryphiswaldense* comprises a magnetosome island which undergoes frequent rearrangements during stationary growth. *Journal of Bacteriology*, **187** (21), 7176–84.

84 Scheffel, A., Gaerdes, A., Gruenberg, K., Wanner, G. and Schueler, D. (2008) The major magnetosome proteins MamGFDC are not essential for magnetite biomineralization in *Magnetospirillum gryphiswaldense* but regulate the size of magnetosome crystals. *Journal of Bacteriology*, **190** (1), 377–86.

85 Schubbe, S., Wurdemann, C., Peplies, J. *et al.* (2006) Transcriptional organization and regulation of magnetosome operons in *Magnetospirillum gryphiswaldense*. *Applied and Environmental Microbiology*, **72** (9), 5757–65.

86 Matsunaga, T., Okamura, Y., Fukuda, Y., Wahyudi, A., Murase, Y. and Takeyama, H. (2005) Complete genome sequence of the facultative anaerobic magnetotactic bacterium *Magnetospirillum* sp. strain AMB-1. *DNA Research*, **12** (3), 157–66.

87 Richter, M., Kube, M., Bazylinski, D.A. *et al.* (2007) Comparative genome analysis of four magnetotactic bacteria reveals a complex set of group-specific genes implicated in magnetosome biomineralization and function. *Journal of Bacteriology*, **189** (13), 4899–910.

88 Jogler, G., Kube, M., Schübbe, S., Ullrich, S., Teeling, H., Bazylinski, D.A., Reinhardt, R. and Schüler, D. (2009) Comparative analysis of magnetosome gene clusters in magnetostatic bacteria provides further evidence for horizontal

gene transfer. *Environmental Microbiology*, **11** (5), 1267–77.
89 Scheffel, A., Gruska, M., Faivre, D. *et al.* (2006) An acidic protein aligns magnetosomes along a filamentous structure in magnetotactic bacteria. *Nature*, **441** (7090), 248.
90 Calugay, R.J., Miyashita, H., Okamura, Y. and Matsunaga, T. (2003) Siderophore production by the magnetic bacterium *Magnetospirillum magneticum* AMB-1. *FEMS Microbiology Letters*, **218** (2), 371–5.
91 Suzuki, T., Okamura, Y., Calugay, R.J., Takeyama, H. and Matsunaga, T. (2006) Global gene expression analysis of iron-inducible genes in *Magnetospirillum magneticum* AMB-1. *Journal of Bacteriology*, **188** (6), 2275–9.
92 Faivre, D., Boettger, L.H., Matzanie, B.F. and Schueler, D. (2007) Intracellular magnetite biomineralization in bacteria proceeds by a distinct pathway involving membrane-bound ferritin and an iron(II) species. *Angewandte Chemie. International Edition in English*, **46**, 8495–9.
93 Sun, J.-B., Zhao, F., Tang, T. *et al.* (2008) High-yield growth and magnetosome formation by *Magnetospirillum gryphiswaldense* MSR-1 in an oxygen-controlled fermentor supplied solely with air. *Applied Microbiology and Biotechnology*, **79** (3), 389–97.
94 Amemiya, Y., Tanaka, T., Yoza, B. and Matsunaga, T. (2005) Novel detection system for biomolecules using nano-sized bacterial magnetic particles and magnetic force microscopy. *Journal of Biotechnology*, **120** (3), 308–14.
95 Yoshino, T. and Matsunaga, T. (2006) Efficient and stable display of functional proteins on bacterial magnetic particles using Mms13 as a novel anchor molecule. *Applied and Environmental Microbiology*, **72** (1), 465–71.
96 Yoshino, T. and Matsunaga, T. (2005) Development of efficient expression system for protein display on bacterial magnetic particles. *Biochemical and Biophysical Research Communications*, **338** (4), 1678–81.
97 Tanaka, T. and Matsunaga, T. (2000) Fully automated chemiluminescence immunoassay of insulin using antibody-protein A-bacterial magnetic particle complexes. *Analytical Chemistry*, **72**, 3518–22.
98 Yoshino, T., Takahashi, M., Takeyama, H. *et al.* (2004) Assembly of G protein-coupled receptors onto nanosized bacterial magnetic particles using Mms16 as an anchor molecule. *Applied and Environmental Microbiology*, **70** (5), 2880–5.
99 Matsunaga, T., Arakaki, A. and Takahoko, M. (2002) Preparation of luciferase-bacterial magnetic particle complex by artificial integration of MagA-Luciferase fusion protein into the bacterial magnetic particle membrane. *Biotechnology and Bioengineering*, **77** (6), 614–18.
100 Matsunaga, T., Ueki, F., Obata, K. *et al.* (2003) Fully automated immunoassay system of endocrine disrupting chemicals using monoclonal antibodies chemically conjugated to bacterial magnetic particles. *Analytica Chimica Acta*, **475**, 75–83.
101 Kuhara, M., Takeyama, H., Tanaka, T. and Matsunaga, T. (2004) Magnetic cell separation using antibody binding with protein A expressed on bacterial magnetic particles. *Analytical Chemistry*, **76**, 6207–13.
102 Yoza, B., Arakaki, A. and Matsunaga, T. (2003) DNA extraction using bacterial magnetic particles modified with hyperbranched polyamidoamine dendrimer. *Journal of Biotechnology*, **101** (3), 219–28.
103 Widder, K.J., Morris, R.M., Poore, G.A., Howard, D.P. and Senyei, A.E. (1983) Selective targeting of magnetic albumin microspheres containing low-dose doxorubicin-total remission in Yoshida sarcoma-bearing rats. *European Journal of Cancer Research and Clinical Oncology*, **19**, 135–9.
104 Lübbe, A.S., Bergemann, C., Brock, J.W. and McClure, D.G. (1999) Physiological aspects in magnetic drug-targeting. *Journal of Magnetism and Magnetic Materials*, **194**, 149–55.

105 Kubo, T., Sugita, T., Shimose, S. *et al.* (2000) Targeted delivery of anticancer drugs with intravenously administered magnetic liposomes in osteosarcoma-bearing hamsters. *International Journal of Oncology*, **17**, 309–16.

106 Muthana, M., Scott, S.D., Farrow, N. *et al.* (2008) A novel magnetic approach to enhance the efficacy of cell-based gene therapies. *Gene Therapy*, **15**, 902–10.

107 Lubbe, A.S., Bergemann, C., Riess, H. *et al.* (1996) Clinical experiences with magnetic drug targeting: a phase I study with 4′-epidoxorubicin in 14 patients with advanced solid tumors. *Cancer Research*, **56** (20), 4686–93.

108 Hergt, R., Hiergeist, R., Zeisberger, M. *et al.* (2005) Magnetic properties of bacterial magnetosomes as potential diagnostic and therapeutic tools. *Journal of Magnetism and Magnetic Materials*, **293** (1), 80–6.

109 Hergt, R. and Dutz, S. (2007) Magnetic particle hyperthermia-biophysical limitations of a visionary tumour therapy. *Journal of Magnetism and Magnetic Materials*, **311** (1), 187–92.

110 Hergt, R., Dutz, S., Mueller, R. and Zeisberger, M. (2006) Magnetic particle hyperthermia: nanoparticle magnetism and materials development for cancer therapy. *Journal of Physics. Condensed Matter*, **18** (38), S2919–34.

111 Yang, C.D., Takeyama, H., Tanaka, T. and Matsunaga, T. (2001) Effects of growth medium composition, iron sources and atmospheric oxygen concentrations on production of luciferase-bacterial magnetic particle complex by a recombinant *Magnetospirillum magneticum* AMB-1. *Enzyme and Microbial Technology*, **29** (1), 13–19.

112 Matsunaga, T., Togo, H., Kikuchi, T. and Tanaka, T. (2000) Production of luciferase-magnetic particle complex by recombinant *Magnetospirillum* sp. AMB-1. *Biotechnology and Bioengineering*, **70** (6), 704–9.

Keywords

biomineralization; magnetite nanoparticles; magnetosomes; customized uniform particles; biomedical applications; *in vitro* magnetic separation; magnetic targeted therapies

12
Approaches to Synthesis and Characterization of Spherical and Anisometric Metal Oxide Magnetic Nanomaterials

Lorenza Suber and Davide Peddis

12.1
Introduction

The synthesis of magnetic materials structured on the nanoscale (10^{-7}–10^{-9} m) is a topic of high relevance, due to the novel properties shown by particles with dimensions in the transition region between atoms (10^{-10} m) and bulk solids (>10^{-6} m) [1–3].

A physical property depends on the size of an object, if its size is comparable to a dimension relevant to that property. In magnetism, typical sizes – as for example the dimensions of magnetic domains or lengths of exchange coupling interactions affecting the polarization of neighboring ferromagnetic particles – are in the nanometer range. For this reason, starting a few decades ago, great attention has been directed towards nanostructured magnetic materials, where the term *nanostructured* describes materials with constituent phase or grain structures modulated on a length scale from 1 to 100 nm [2, 4].

Nanostructured materials can be prepared with dimensionalities of zero-dimensional (0-D: nanoparticles), one-dimensional (1-D: nanowires, nanorods and nanotubes), two-dimensional (2-D: nanostructured surfaces) and three-dimensional (3-D: three dimensional nanostructures). Intermediate cases can also exist: materials containing multiple phases can range from the case in which a nanoscale phase is embedded in a phase of conventional size (e.g., nanoparticles dispersed in a matrix) to the case in which all the constituent phases are nanoscaled (e.g., core–shell particles) [5].

The materials characterized by a zero dimensionality reveal fascinating physical and chemical properties, due mainly to the reduced size of the components and to very high surface-to-volume ratios [6]. In this class of materials, which has been intensely investigated during the past few decades, we will focus on spherical and anisometric nanoparticles as powders and as dispersions in polar and nonpolar fluids (ferrofluids). Conversely, 1-D magnetic nanostructures, a new class of low-dimensional and anisotropic nanomaterials which has emerged recently [7–9],

Nanomaterials for the Life Sciences Vol. 4: Magnetic Nanomaterials. Edited by Challa S. S. R. Kumar

ISBN: 978-3-527-32154-4

have lateral dimensions in the nanometer scale and longitudinal dimensions which range from hundreds of nanometers to hundreds of microns. Such characteristics give aspect ratios (length to diameter) of up to several thousands. The shape of the particles strongly affects the magnetic anisotropy, opening new perspectives in the control and tuning of magnetic properties [10–12].

In this chapter, we will describe approaches to synthesis and magnetic characterization of 0-D and 1-D nanostructured materials, with some attention to intermediate dimensionality, as magnetic nanocomposite materials and nanoparticles with core–shell morphology.

Many research investigations have been conducted on nanostructured magnetic metals such as Fe, Co, and Ni [6, 13–16]. However, nanostructured *metal oxides* are more stable and allow for a relative tunability of the magnetic properties, thus demonstrating great potential for applications. In particular, iron oxides with spinel structures ($MeFe_2O_4$, Me = Fe, Co, Mg, Mn, Zn, etc.) have been intensively studied, both in terms of the fundamental relationships between their magnetic properties and crystal chemistry [4, 17–21], and for applications in fields as diverse as catalysis, medical diagnostics, drug delivery, and environment protection [22–26].

In the present chapter, we will discuss this very large and promising class of materials, with special regard to the most common spinel iron oxides – that is, magnetite (Fe_3O_4) and maghemite (γ-Fe_2O_3). Although during the past few years many reviews have been published on this class of materials, their expanding field of applications, especially in biomedicine and diagnostics [23, 24, 26], and the explosive progress in the ability to tune and control their magnetic properties, requires continuous updating. Moreover, it is fundamental to investigate in more detail the close link existing between the magnetic properties and the preparation method of the material, a feature which up to now has been undervalued but which can greatly affect the magnetic behavior of the nanomaterials [27].

There are two different approaches to the synthesis of nanostructured materials: the "top-down" approach, which utilizes physical methods; and the "bottom-up" approach, which employs solution-phase colloidal chemistry. The advantage of the physical methods is the production of a large quantity of nanomaterials, but the synthesis of uniform-sized nanoparticles and their size control is very difficult to achieve using the top-down approach. In contrast, colloidal chemical synthetic methods are more suited to the synthesis of uniform nanoparticles with controlled particle size, shape, structure, and composition [28]. Hence, in this chapter we will restrict discussions to solution-phase colloidal chemical methods.

In order to design magnetic materials for specific applications and set up convenient synthesis procedures, a basic knowledge of magnetism in nanostructures is essential. In Section 12.2, the fundamental concepts of magnetism are introduced. The direct correlation between crystalline structure, morphology (size, size distribution, and shape) and magnetic properties relevant to applications is discussed on the basis of magnetic anisotropy. Attention will also be given to the most common approaches used to study the magnetic behavior of nanostructures.

The ability to control size, size distribution, morphology and composition of constituent phases is a key point in the synthesis of nanostructured magnetic materials. Tuning the particle size and preparing nanomaterials with a narrow particle size distribution is fundamental in order to control the magnetic properties and to design materials suitable for new applications. The chemical composition of the constituent phases is also of primary importance. This concerns not only the average composition but also the compositional gradients within the material. It must also be taken into account that a reduction in particle size can lead to changes in the structure and thermodynamic properties of crystalline phases [5]. In Section 12.3, we report on the synthetic methods that have emerged during the past 10 years and have provided a noteworthy control of the parameters determining the magnetic properties of nanomaterials.

Finally, we describe some examples that highlight the strong correlations between the preparation methods and the structural and magnetic properties, and complete the chapter with a brief summary and perspectives.

12.2
Magnetism in Nanostructured Metal Oxides

12.2.1
Magnetism in Condensed Matter

In condensed matter, the atomic magnetic moments can mutually act together (cooperative magnetism) and lead to a different behavior from what would be observed if all the magnetic moments were reciprocally isolated (noncooperative magnetism). This, coupled with the different types of magnetic interaction that can be found, leads to a rich variety of magnetic properties in real systems [4, 29, 30].

The two basic types of noncooperative magnetism are paramagnetism and diamagnetism:

- Paramagnetism arises from identical, uncoupled atomic moments located in isotropic surroundings. Hence, in a paramagnetic material, there is no long-range order and, under an external magnetic field, the magnetic moments partially align.
- Diamagnetism, instead, is just due to the effect of an external magnetic field on the motion of the atomic inner electrons [30]. All substances have then a basic diamagnetism, that is nearly always weak and is very often masked when a much larger paramagnetism is present.

In cooperative magnetism, the interactions between adjacent magnetic moments determine the magnetic order in the material. Two classes of interactions can be distinguished, namely direct exchange interaction and indirect exchange interaction. *Direct exchange* occurs between moments close enough to have significant

overlap of their wave functions, whereas *indirect exchange* arises when the atomic magnetic moments are coupled over relatively large distances. It can also be mediated by a nonmagnetic ion which is placed in between the magnetic ions (e.g., oxygen atoms in oxides), and in this case it is called *super exchange* [29]. Generally speaking, exchange interactions between magnetic centers in a 3-D solid can be quantitatively described by the Heisenberg spin Hamiltonian [29]:

$$H_{exch} = 2\sum_{ij} J_{ij}\vec{S}_i \cdot \vec{S}_j \tag{12.1}$$

where J_{ij} is the exchange integral describing the magnitude of energy coupling between the spins $\vec{S}_i$ and $\vec{S}_j$. If the exchange integral has a positive value, below a critical temperature T_C (the Curie temperature), the magnetic moments are aligned parallel to each other and the substance is said to be ferromagnetic. Above the T_C, the material is no longer ferromagnetic, but reverts to paramagnetic because the thermal energy become higher than the exchange energy, destroying the magnetic order. On the other hand, if J_{ij} is negative, the spins are aligned antiparallel to each other and, below a critical temperature (the Néel temperature, T_N), the material is said to be antiferromagnetic (if all the magnetic moments are equal) or ferrimagnetic (if there is no compensation due to the difference between the individual moments).

In principle, then, the magnetic properties in condensed matter can be understood and controlled through magnetic coupling, which is closely related to the chemical composition and crystalline structure of the material [2, 4].

For the first time, in 1907, Weiss proposed that a ferromagnet might contain a number of small regions, with different size and shape, called domains (i.e., uniformly magnetized regions having atomic magnetic moments, μ_a, oriented in the same direction) [29]. Two adjacent domains are separated by a transition region, called the domains wall, in which the spins gradually rotate, either coherently or incoherently, from one domain to the other. (Note: In the coherent rotation mode, all spins remains parallel to each other, whereas in the incoherent reversal mode a nonuniform magnetization process occurs.) When placed in a sufficiently large external magnetic field, the spins in each domain rotate and align parallel to the direction of the applied field. Typically, magnetization increases sharply at lower field, as the domains with a more favorable alignment expand at the expense of others, and saturate when the maximum domain alignment is reached (see Figure 12.1a; inset). This corresponds macroscopically to a plateau region of the magnetization curve (saturation magnetization, M_s), and when the applied field is decreased the magnetization also decreases. The magnetization remaining at a zero-applied field is called remanent magnetization (M_r). Very often, for the characterization of a magnetic hysteresis, the reduced remanent magnetization, defined as M_r/M_s, is also used. The magnetic field to which corresponds a magnetization equal to 0 is called coercive field, or coercivity (H_c) (Figure 12.1a) [29, 31]. All the magnetic properties are strictly dependent on the particle size, and a new physical world opens up when the materials are nanoscaled. An experimental investigation of the dependence of coercivity on particle size is shown schemati-

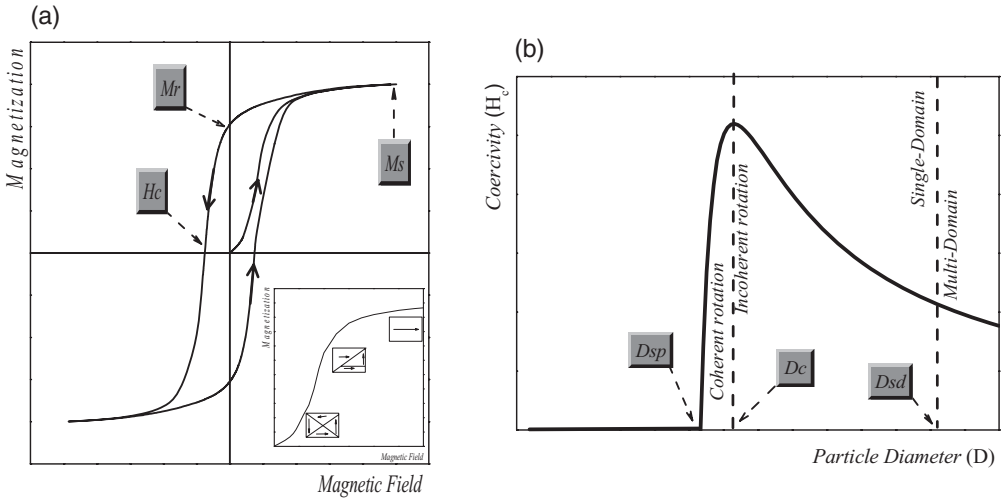

Figure 12.1 (a) Important parameters in a magnetic hysteresis loop: saturation magnetization (M_s), remanent magnetization (M_r) and coercive field (H_c). Inset: Evolution of the magnetic domain structure along the first magnetization curve; (b) Schematic illustration of the dependence of H_c on particle size.

cally in Figure 12.1b. Below a certain critical particle diameter (D_{sd}), a magnetic multidomain structure is not energetically favored and particles with dimension below this size will therefore consist of a single magnetic domain. Typical D_{sd} values for magnetic iron oxides are 166 nm for γ-Fe_2O_3 and 128 nm for Fe_3O_4 [2]. Generally, the rotation of the spins (i.e., the reversal process) occurs at much higher field by incoherent rotation of the spins, and this leads to an increase of coercivity with respect to a multidomain structure. For smaller particles, below a given size (D_c) depending on the material, the rotation is coherent and this induces a decrease in coercivity.

12.2.2 Magnetic Anisotropy Energy

During the magnetization process, the work that is required to bring a ferromagnetic body from the demagnetized to the saturated magnetic state is stored in the body as magnetization potential energy, the magnetic anisotropy energy (E_A). The magnetic anisotropy is extremely relevant in the physics of magnetic materials because it is related, on one hand, to the intrinsic microscopic characteristics of the material and, on the other hand, to its macroscopic characteristics [10]. In a magnetically ordered solid, there are certain preferred orientations of the magnetization, called "easy axes". These easy directions are given by the minima in the magnetic anisotropy energy, which depend on the structure and chemical

composition of the materials. In bulk materials, magnetocrystalline and magnetostatic energies are the main sources of anisotropy. In magnetic nanoparticles, other types of anisotropy (e.g., surface anisotropy) can have the same order of magnitude as those of the bulk materials. A short qualitative discussion of some contributions will be provided at this point, with particular attention being paid to the most important anisotropies of the nanostructured systems. A complete description of magnetic anisotropy energy can be found elsewhere [2, 6, 10].

Magnetocrystalline anisotropy: this property is intrinsic to the material, being related to the crystal symmetry and to the arrangement of atoms in the crystal lattice. Magnetocrystalline anisotropy can show various symmetries, but uniaxial and cubic forms cover the majority of cases.

Magnetostatic anisotropy (shape anisotropy): this contribution is due to the presence of free magnetic poles on the surface of a magnetized body. The poles create a magnetic field inside the system, the demagnetizing field, which is responsible for the magnetostatic energy. For a particle with finite magnetization and nonspherical shape, the magnetostatic energy will be larger for some orientations of the magnetic moments than for others. Thus, the shape determines the magnitude of magnetostatic energy and this type of anisotropy is often known as shape anisotropy [30]. Particle shape has been identified as a major tool for engineering the magnetic properties of nanomaterials, with additional attractive feature of displaying different properties in different directions [11, 32] (see Sections 12.4.1.4 and 12.4.4).

Surface anisotropy: the surface atoms have a lower symmetry compared to that of atoms within the particle. This gives rise to surface anisotropy, which increases with the increase in surface-to-volume ratio (i.e., decrease in particle size) [33]. Surface anisotropy is also strictly related to the chemical and/or physical interactions between surface atoms and other chemical species. The coating and functionalization of the nanoparticle surface can induce important modifications in its magnetic properties (see Section 12.4.1.3) [22, 34].

Finally, it should be taken into account that, in nanoparticle assembly, the magnetic anisotropy energy may differ from one particle to another, due to the presence of physical and/or chemical inhomogeneity, As a consequence, the macroscopic measured anisotropy will be a type of weighted average of the particle anisotropy. Then, in order to design magnetic nanostructured materials suitable for several applications, it will be essential to control the distribution of magnetic anisotropy energy – that is, particle shape, size and size distribution, and chemical homogeneity (see Section 12.4.4.1) [10].

12.2.3
Magnetism in Small Particles: An Experimental Approach

The energy of a magnetic single domain particle is generally dependent on the magnetization direction with respect to the easy axis, resulting in particular equi-

librium directions separated by energy barrier (ΔE_A), depending on particle volume (V_p) and magnetic anisotropy constant (K). In the simplest case, energy barriers have uniaxial form given by $\Delta E_A = KV_p$. Therefore, at any given temperature, there is a critical size (D_{sp}) (Figure 12.1b), below which thermal excitations are sufficient to overcome such a barrier and rotate the particle magnetization, thereby demagnetizing the material [35]. Under such conditions, the behavior of a random assembly of nanoparticles is analogous to paramagnetism (i.e., H_c becomes 0), but with different time and magnetization scales, and for this reason it is referred to as superparamagnetism [6].

The underlying physics of superparamagnetism is based on the law of the relaxation time of the net particle magnetization

$$\tau = \tau_0 \exp\left(\frac{\Delta E_A}{k_B T}\right) \tag{12.2}$$

where $k_B T$ is the thermal energy (k_B is the Boltzmann constant) and τ_0 is a preexponential factor that, for ferromagnetic and ferrimagnetic particles, is of the order of 10^{-10}–10^{-12} s and is weakly dependent on temperature [6, 23].

The observation of magnetic properties of single-domain particles is strongly dependent on time, as expressed by Equation 12.2. Therefore, the observed magnetic properties of an assembly of single-domain particles depend on the experimental measuring time (τ_m) of the technique used to observe the relaxation. In fact, if $\tau << \tau_m$, the relaxation during the experiment is so fast that only a time average of the magnetization is observed and the particles will be in the superparamagnetic state (i.e., zero coercivity and remanent magnetization). On the contrary, if $\tau >> \tau_m$, the relaxation is so slow that only static properties are observed, as in a large ordered magnetic crystal (blocked state). In this condition, the magnetization curves when plotted versus the applied field show hysteresis. The blocking temperature (T_B) is defined as the temperature at which the relaxation time is equal to the experimental measuring time. From the definition of T_B, Equation 12.2 can be rewritten as:

$$\tau_m = \tau_0 \exp\left(\frac{\Delta E_A}{k_B T_B}\right) \tag{12.3}$$

In typical experiments τ_m can range from slow to medium time scales of 10^2 s for direct current (DC) magnetization, and from 10^{-1}–10^{-5} s for alternate current (AC) susceptibility, through to the fast time scales of 10^{-7}–10^{-9} s for ^{57}Fe Mössbauer spectroscopy and 10^{-10}–10^{-12} s for neutron diffraction. It should be pointed out that the parameters K and τ_0 in Equation 12.3 do not depend on τ_m, and are key points in any understanding of the superparamagnetic relaxation.

The magnetic properties of the nanoparticles are usually studied by observing the response of the material to an applied magnetic field and/or to variations of temperature. In addition, it should be noted that the behavior of nanoparticle

systems depends on the magnetothermal history. The most common experimental approach to DC magnetic measurements is described in the following section.

12.2.3.1 Zero Field-Cooled and Field-Cooled Magnetization

The measurements of magnetization versus temperature, performed with the zero field-cooled (ZFC) and field-cooled (FC) protocols, are among the most classical approaches in order to study the behavior of single-domain magnetic particles. The ZFC protocol consists of cooling the sample in a zero magnetic field from high temperature, where all the particles are in superparamagnetic state, to the lowest measuring temperature. A static magnetic field is then applied and magnetization measured during a warming up period (M_{ZFC}, in Figure 12.2a, solid

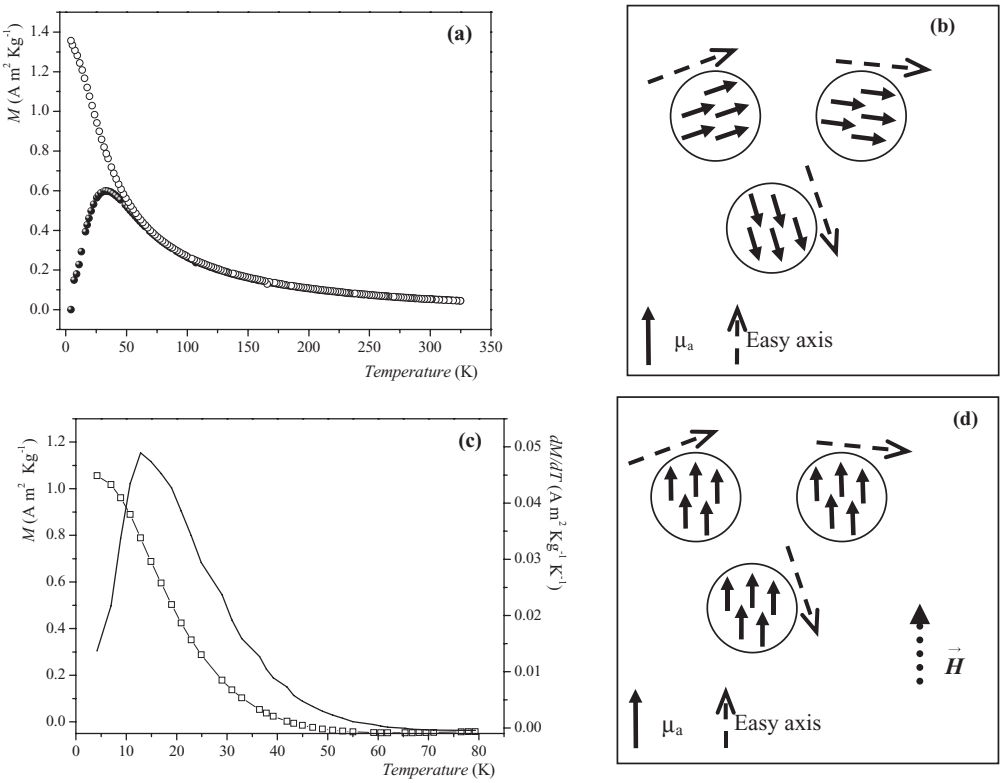

Figure 12.2 (a) Zero field-cooled (ZFC; ●) and field-cooled (FC; ○) 3 nm $CoFe_2O_4$ nanoparticles; (b) Random packing after the ZFC process; (c) Thermoremanent magnetization measurements (□) and distribution of magnetic anisotropy (solid line) of 3 nm $CoFe_2O_4$; (d) Random packing after the FC process.

symbols). The resulting curve is termed ZFC because the sample has been previously cooled in the absence of a magnetic field. All net magnetic moments in each single-domain particle point along the nanoparticle easy axis when the nanoparticles are cooled below the blocking temperature without an applied magnetic field. Magnetic anisotropy acts as an energy barrier to prevent the switching of magnetization from the easy axis. Due to the high number of particles and the random distribution of the easy axis directions, the average magnetization is almost zero (Figure 12.2b) [20]. When the temperature increases, the magnetic anisotropy in some nanoparticles is overcome and the magnetization directions of these thermally activated nanoparticles start to align with the applied field. As a consequence, the total magnetization initially increases with increasing temperature. The ZFC curve then exhibits a maximum, and the corresponding temperature (T_{max}) is, for noninteracting particles, directly proportional to the average blocking temperature:

$$T_{max} = \beta T_B \tag{12.4}$$

where β is a proportionality constant that depends on the type of size distribution. It has been reported that, for a log-normal distribution of nanoparticles, β is typically within 1.5–2.0, while T_{max} can be related to the blocking of particles with a mean particle size [19, 36].

Conversely, the FC protocol consists of cooling the sample in a small DC field and measuring the magnetization during warming up, without removing the field. When a magnetic field is applied during the cooling process, all the net magnetic moments of the nanoparticles are aligned along the field direction, regardless of the easy axis directions of each individual nanoparticle. As the nanoparticles are cooled at low temperature, the magnetization direction of each particle is frozen in the field direction (M_{FC} in Figure 12.2a, open symbols) [19]. By increasing the temperature, an increasing number of particles will be in superparamagnetic state and the magnetization will decrease monotonically, giving rise to a paramagnetic-like behavior. Below a certain temperature, the ZFC and FC curves diverge and an irreversible magnetic behavior is observed. The temperature at which the irreversibility is observed is the irreversibility temperature (T_{irr}), and can be related to the blocking temperature of the biggest particles. The difference between T_{max} and T_{irr} provides a qualitative measure of the width of the blocking distribution (i.e., of the particle size distribution in the absence of any interparticle interactions) [6, 37, 38].

12.2.3.2 Thermoremanent Magnetization

In thermoremanent magnetization (TRM) measurements, the sample is cooled from a high temperature in an external static magnetic field, the field is then turned off, and the remanent magnetization is measured on warming up. In Figure 12.2c (line and symbols), the TRM curve of $CoFe_2O_4$ nanoparticles (mean diameter 3 nm) is shown. After the field-cooling procedure, the nanoparticles are frozen, as shown in Figure 12.2d. Although the magnetic field is turned off at 5 K,

the magnetic anisotropy energy barrier blocks any change in the magnetization direction. As the temperature increases, some of the nanoparticles are able to overcome their energy barrier, on the basis of their thermal activation energy, $k_B T$. Consequently, the magnetization direction of each thermally activated nanoparticle begins to flip randomly faster than the measuring time of the magnetometer [19]. The overall magnetization of the nanoparticles then decreases with increasing temperature.

M_{TRM} is related to the distribution of anisotropy energy barriers:

$$M_{TRM} = M_{nr} \int_{\Delta Ec}^{\infty} f(\Delta E_a) dE \tag{12.5}$$

where M_{nr} is the nonrelaxing component of the magnetization and ΔE_c is a critical value of energy, below which all the particles are blocked [19, 39]. The relationship in Equation 12.5 shows that the derivative of M_{TRM} with respect to temperature provides an estimate of the anisotropy energy barrier distribution. Values of $f(\Delta E_a)$, obtained from the M_{TRM}, are shown in Figure 12.2c (the continuous line).

12.2.4 Magnetic Metal Oxides

Metal oxides represent the most common, and probably the richest, class of materials in terms of chemical, structural, and physical properties. For this reason, they are well known for their interesting optical, electrical, electrochemical, mechanical and magnetic properties. Such diversity originates from the more complex crystal and electronic structure of metal oxides compared to other classes of materials. The combination of such a variety of properties with the peculiar effects of low-dimensionality make the nanostructured magnetic metal oxides suitable for several applications [40].

Among magnetic metal oxides, the compounds with spinel structure ($Me^{II}M_2^{III}O_4$) represent probably the most important class, because the rich crystal chemistry of spinels offers excellent opportunities for fine-tuning the magnetic properties. These have a face-centered cubic (fcc) structure in which the oxygen atoms are cubic close-packed. The structure contains two interstitial sites, occupied by metal cations, with tetrahedral, (A)-site, and octahedral, [B]-site, oxygen coordination, resulting in a different local symmetry. When the (A)-sites are occupied by Me^{II} cations and the [B]-sites by Me^{III} cations, the structure is referred to as normal spinel, (Me^{II}) $[Me^{III}]$. However, if the A sites are completely occupied by Me^{III} and the B-sites are randomly occupied by Me^{II} and Me^{III}, then the structure is referred to as inverse spinel, (Me^{III}) $[Me^{III}$ $Me^{II}]$. In general, the cationic distribution in octahedral and tetrahedral sites is quantified by the "inversion degree" (γ), which is defined as the fraction of divalent ions in octahedral sites [41–43]. In order to simplify the interpretation of some experimental results (Mössbauer spectra in

high-field or neutron diffraction), the cation distribution may occasionally be also quantified by the ratio of Me^{III} ions in the A and B sites (α).

Super exchange interactions between atomic magnetic moments in *A* (J_{AA}) and *B* (J_{BB}) interstices lead to a ferromagnetic ordering between the ions located in the two sites, respectively, giving rise to two magnetic sublattices. On the other hand, interactions between magnetic ions in the *A* and *B* sites (J_{AB}) induce antiferromagnetic order, and are tenfold higher than the J_{AA} and J_{BB} interactions. The dominant intralattice J_{AB} interactions then induce a noncompensated antiferromagnetic order (ferrimagnetism) between the *A* and *B* sublattices. Therefore, the net magnetization can be considered proportional to the difference between the *A* and *B* sublattice magnetizations [41, 44]. From this picture, it is clear that the magnetic properties of spinel oxides can be controlled through magnetic coupling. This coupling is, in turn, closely related to the chemical composition and crystalline structure of the materials. Indeed, by adjusting the chemical identity of Me^{II} and Me^{III}, the magnetic configuration of $Me^{II}M_2^{III}O_4$ can be chemically engineered so as to provide a wide range of magnetic behaviors [17, 42]. Moreover, even small changes in the cationic distribution in compounds with the same chemical composition can result in substantial changes of magnetivzation and/or of the magnetic anisotropy [45].

Oxides with various crystal structures, such as cubic spinel and garnets, have been all classified as ferrites. In this chapter, we limit the discussion to ferrites based on a cubic spinel structure ($Me^{II}Fe_2O_4$; Me = Fe^{2+}, Co^{2+}, Ni^{2+}, Mn^{2+}), which are clearly one of the most interesting classes of materials for application in several fields. In particular, magnetite (Fe_3O_4) and maghemite (γ-Fe_2O_3), due to their biocompatibility, are the most commonly employed magnetic materials in biomedical applications.

Magnetite has a face-centered unit cell based on 32 O^{2-} ions which are regularly cubic close-packed along the [111] face. Fe_3O_4 contains both divalent and trivalent iron ions, occupying 8 of the 64 tetrahedrally coordinating sites and 16 of the 32 octahedrally coordinating sites [46, 47].

Maghemite is a ferrite with a cation-deficient inverse spinel structure, similar to that of magnetite. It differs from magnetite in that all (or most) of the iron atoms are in the trivalent state. Maghemite contains, as in Fe_3O_4, cations in the tetrahedral and octahedral positions, but there are vacancies to compensate for the increased positive charge due to the oxidation of Fe^{II}. The cations are distributed randomly over the tetrahedral and octahedral sites, whereas the vacancies (which are also randomly distributed) are confined to the octahedral sites.

Iron oxides may exhibit not only the maghemite and magnetite phases, but also amorphous and other crystalline forms, among which the most thermodynamically stable phase is hematite (α-Fe_2O_3). For this reason, maghemite and magnetite transform to hematite on heating in the range between 370 and 600 °C [47]. α-Fe_2O_3, which below 923 K is antiferromagnetic, is not particularly interesting for applications in biomedicine [23].

12.3
Synthesis Methods for Spherical and Anisometric Iron Oxide Nanomaterials

Ultradispersed nanoparticle systems are intrinsically thermodynamically metastable due to the high surface areas that represent a positive contribution to the enthalpy of the system. If the activation energies are not too high, spontaneous evolution can occur, causing an increase in nanoparticle size or the formation of nanostructured domains leading to a surface area decrease. It follows that an ultradispersed system with a high surface energy can only be *kinetically* stabilized, and additives and/or synthesis conditions that induce a reduction in surface energy are required to stabilize nanoparticles against sintering, recrystallization, and aggregation processes [48–50].

In order to correlate, for example, size effects with changes in magnetic properties, it is critical to use a synthesis method that allows for control over the nanoparticle size with a narrow size distribution maintaining all other parameters – that is, with particle-shape, -interaction, and -composition unvaried [6]. We then report on the preparation methods that are able to control separately nanomaterial composition, size, morphology, and crystal structure. This ability is fundamental in order to probe, tune and optimize the physical and chemical properties of the nanomaterial, especially of ferrites. For example, particle size variation can be achieved, by some preparation methods, by postsynthesis annealing at various temperatures. In the case of ferrites, however, it has been shown that, although nanoparticle size changes according to the annealing temperature, the cation distribution between the A and B lattice sites is affected by the annealing temperature [18]. Therefore, when the annealing temperature is used to control nanoparticle size, a direct correlation between size effect and magnetic response is not possible due to the variable of cation redistribution [45, 51].

Further on, many applications require stable and concentrated magnetic particle dispersions in fluids. These ultrafine particle dispersions are known commonly as magnetic fluids or ferrofluids. An important issue to be addressed here, in order to obtain ferrofluids that are stable against particle aggregation and precipitation, is the functionalization of the particle surfaces, for example, by adsorbing cationic (positive) or anionic (negative) -charged molecules; in this way, the particles, by having the same positive or negative superficial charge, repel each other and do not aggregate. The preparation of water-stable magnetite dispersions (ferrofluids) is described in Section 12.3.2.

Moreover, especially for biomedical applications, when stable water-soluble dispersions are required, it is often necessary to render hydrophobic particles hydrophilic [23], and the details of hydrophobic–hydrophilic phase transfer are provided in Section 12.3.2.2.

For many applications, multifunctional particles are required – that is, particles which are able to perform different tasks at the same time. To this purpose, a particle must often be composed of different nanostructured materials;

for example, it may be formed by a core of magnetic material covered with a shell of a noble metal to produce an optical response, and covered again by a shell of silica to protect the system from degradation; alternatively, it may contain a hollow into which is incorporated a functional material. Details of the preparation of multifunctional core–shell particles and nanocapsules are provided in Section 12.3.3.

Finally, Section 12.3.4 includes details of preparation of an emerging class of material, namely one-dimensional (1-D) nanostructured magnetic materials, such as magnetic nanotubes.

For each method, following a brief description, the advantages and disadvantages are outlined with respect to the capacity to tailor composition, size, shape, crystal structure and the formation of stable dispersions of the nanomaterial.

12.3.1
Synthesis of Spherical and Anisometric Nanoparticles

During the past few decades, many physical and chemical methods have been tested to prepare monodispersed spherical and anisometric iron oxide particles [41]. Whilst it is beyond the scope of this chapter to review all of these methods, a brief description is provided for some, referring to the bibliography for details. Conversely, some methods which, either alone or in combination with others, have demonstrated an outstanding capacity to control the size, shape, composition and structure of the particles, and may potentially be applied using many different reagents, are described (with specific examples) in greater detail.

In the preparation of magnetic metal oxide nanomaterials, both chemical and physical methods are applied. Physical methods, such as metal evaporation, ball-milling and electrodeposition [52, 53], are advantageous in that they produce nanomaterials of high purity and are applicable to large-scale production. Unfortunately, the size control and synthesis of monodisperse nanoparticles are very difficult with these methods.

In contrast, chemical methods based on solution-phase colloidal chemistry allow uniform-sized iron oxide magnetic particles of different sizes and shapes to be prepared. As examples of this approach, five outstanding methods – namely, metal salts precipitation in water, sol–gel, microemulsions, surfactant-assisted hydrothermal treatment, and surfactant-assisted ultrasound irradiation – are described in the following sections. The autocombustion method is also described, as this is included in one of the examples in Section 12.4.

12.3.1.1 Metal Salt Precipitation in Water

Metal oxide nanoparticles are obtained by precipitation in aqueous solution, using metal salts such as chlorides, nitrates, and sulfates as reagents. The metal cations (in this case, Me = Fe^{2+} and Fe^{3+}) form, in aqueous solution, aquo oxo or hydroxylated complexes, $[Me(OH)_h\ (OH_2)_{N\text{-}h}]^{(z\text{-}h)+}$ or $[MeO_{N\text{-}h}(OH)_h]^{(2N\text{-}z\text{-}h)-}$ respectively. These condense via two basic mechanisms of nucleophilic substitution, depending on

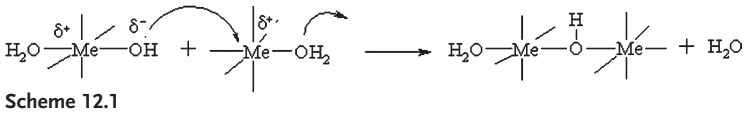

Scheme 12.1

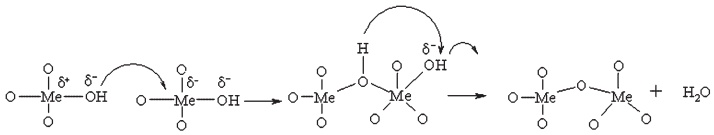

Scheme 12.2

the nature of the coordination sphere of the cations [54, 55]. The condensation of aquohydroxo complexes proceeds by the elimination of water and the formation of hydroxo bridges (olation) (Scheme 12.1).

For oxohydroxo complexes, there is no water molecule in the condensation sphere of the complexes, and therefore no leaving group. Hence, the condensation must proceed in this case via a two-step associative mechanism, leading to the formation of oxo bridges (oxolation) (Scheme 12.2).

The hydroxylation rate *h* of the complexes represents their functionality towards condensation, and also controls the type and structure of the condensed species. The rate is a function of the pH of the medium, and also depends on the characteristics of the cation such as size, charge, and electronegativity. The condensation of hydroxylated and electrically charged complexes ($h < z$) always ends leaving discrete species in solution, either polycations or polyanions. In contrast, the electrically neutral species ($h = z$) condense indefinitely until the precipitation of a solid. These solid phases are made from particles of which the average size may range from a few nanometers to a few micrometers. In order to obtain particles of homogeneous size, it is necessary that the nucleation and growth steps are separated to ensure that a single nucleation stage takes place, followed by a homogeneous nuclei growth [52, 56]. Aging of the suspensions, which may last for hours, days or even months, allows the system to tender towards or even reach stability. This process, which is referred to as Ostwald ripening, is often associated with modifications of some physical or chemical characteristics of the particles. It leads to an increase in the average particle size, and also to a change in the morphology and crystalline structure.

Different techniques exist to form a complex of zero charge and to obtain a solid. The most often-used method involves the addition of a base into an acid solution of the metal salt at room temperature. The mixing of these solutions leads to a rapid formation of a high concentration of hydroxylated complexes, and induces local pH gradients. These in turn cause nonhomogeneity in the hydrolysis prod-

ucts, which condense in random fashion. The Fe^{3+} ions precipitate quasi-instantaneously at pH ≥3 into a poorly defined phase, known as "2-line ferrihydrite" because its X-ray diffraction pattern exhibits only two broad bands [57]. When the suspensions are aged at a pH where the solid is partially soluble, the concentration in solution may be enough to feed the nuclei of a more stable crystalline phase. This type of process is involved in the formation of goethite, α-FeOOH, during the aging of ferrihydrite at pH < 5 > 10. Because of the structural anisotropy of goethite, rod-like particles of mean size 150 × 25 × 15 nm are obtained (Figure 1a in Ref. [48]). These particles form very stable aqueous suspensions that exhibit interesting magnetic properties; notably, the particles orient along the field direction at intensities less than 350 mT, but reorient perpendicularly to the field beyond 350 mT. This behavior may have interesting applications in the field of magnetic biosensors [57].

Precipitation by the addition of a base at room temperature, may also lead to stable crystalline nanoparticles. For instance, magnetite (Fe_3O_4) nanoparticles are easily obtained by coprecipitating aqueous Fe^{3+} and Fe^{2+} ions [58]. Here, the iron ions are distributed into the tetrahedral (A) and octahedral [B] sites of the fcc stacking of oxygen ions according to (Fe^{3+}) $[Fe^{3+}Fe^{2+}]$ O_4) (see Section 12.2.4). Magnetite is characterized by a fast electron hopping between the iron cations in the octahedral sublattice. The crystallization of spinel is quasi-immediate at room temperature, with electron transfer between the Fe^{2+} and Fe $^{3+}$ ions playing a fundamental role in the process [59, 60]. Nanoparticles of magnetite are very sensitive to oxidation, and transform into maghemite, γ-Fe_2O_3, (Fe^{3+}) $[Fe^{3+}_{5/3}\ V_{1/3}]$ O_4, where V represents a cationic vacancy. This high reactivity is clearly due to the high surface-to-volume ratio, and a controlled synthesis of magnetite requires strictly anaerobic conditions. Aerial oxidation is not the only way to proceed to maghemite, however, as different interfacial ionic and/or electron transfers, depending on the pH of the particle dispersion, may also be involved in the transformation.

The main advantages of the precipitation method are the low costs, the good safety aspects, and the high yields. Although the method is simple, many parameters must be controlled, the most important being the chemistry of the aqueous cations, since the major factor in the control of nanoparticle characteristics (e.g., size, shape, crystalline structure) is the acidity of the reaction solution. Other parameters that must also be taken in account include thermolysis temperature, ion concentration, ionic strength, and presence of specific ligands.

12.3.1.2 Sol–Gel

The conventional sol–gel process [61] involves the hydrolysis and condensation of precursors in acidic or basic aqueous-alcohol media. The process uses as precursors metal halides or alkoxides in solution, and these undergo hydrolysis and polycondensation reactions to form a colloid, a system composed of solid particles (size ranging from 1 nm to 1 μm) dispersed in a solvent (the "sol"). The sol then evolves towards the formation of an inorganic continuous network containing a

liquid phase (the gel). The formation of a metal oxide involves connecting the metal centers with oxo (M–O–M) or hydroxo (M–OH–M) bridges, thus generating metal–oxo or metal–hydroxo polymers in solution. The drying process serves to remove the liquid phase from the gel, thus forming a porous material, after which a thermal treatment (firing) is carried out in order to favor further polycondensation and crystallinity. However, the presence of H_2O as an oxygen anion source constitutes a drawback in the preparation of well-crystallized and size-controlled metal oxides; for example, the reaction rate is too fast to control the nanocrystal growth, and the presence of H_2O is not compatible with the high temperature (>200 °C) necessary to obtain crystalline metal oxides. More recently, nonhydrolytic sol–gel reactions have been exploited, these having been classified by Vioux [62] into two classes: *hydroxylation reactions*; and *aprotic condensation reactions*, according to whether or not hydroxy groups are produced.

The hydroxylation reactions include: (i) the thermal decomposition reactions of metal alkoxides or carboxylates, where hydroxy groups are produced on metal cations through thermal decomposition; and (ii) the reactions of metal halides with high-boiling alcohols, where the hydroxylation reaction is favored by the electrodonating coordination of the metal ion on the α-carbon atom of the alcohol.

In the aprotic condensation reactions, the two main reaction routes are alkyl halide elimination and ester elimination. In the case of alkyl halide elimination, the reaction of the metal halide and the metal alkoxide produces a M–O–M linkage, along with an alkyl halide as byproduct (Scheme 12.3). Similarly, in the ester elimination reaction, ester is produced as a byproduct of the reaction of metal carboxylate and metal alkoxide (Scheme 12.4).

Although aprotic condensation reactions proceed at temperatures in the region of 100 °C, vacant sites on the metal cations, which are essential to generate an oxide bridge between the metal ions, cannot be formed owing to the strong

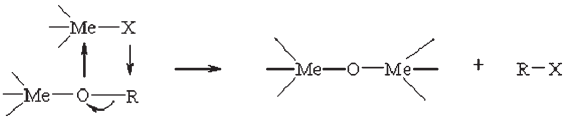

Scheme 12.3

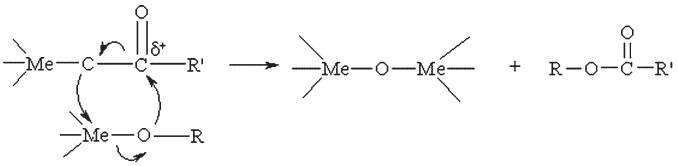

Scheme 12.4

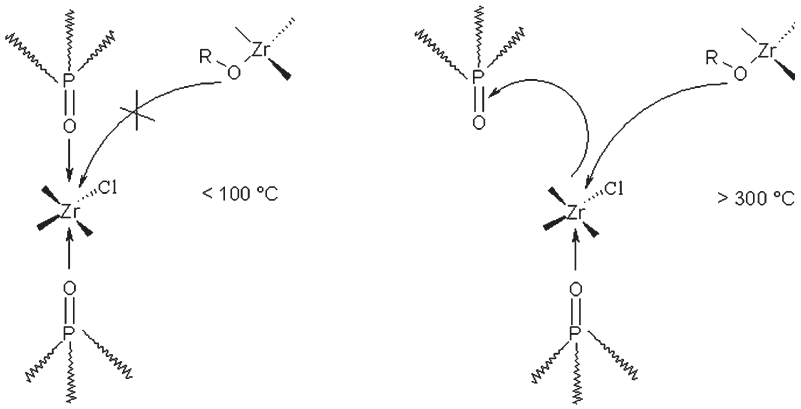

Scheme 12.5

binding affinity of the coordinating surfactant at low temperature. Consequently, nonhydrolytic sol–gel reactions are generally performed at high temperatures (200–300 °C), so that the coordinating surfactant will bind reversibly on the metal cation (Scheme 12.5).

12.3.1.3 **Microemulsions**

Microemulsions are defined as clear, thermodynamically stable dispersions consisting of, at least, a ternary mixture of water, a surfactant or a mixture of surface-active agents, and oil [63]. Depending on the proportion of suitable components and the hydrophile–lypophile balance (HLB) value of the surfactant used, the formation of microdroplets may be either in the form of oil-swollen micelles dispersed in the aqueous phase, or as water-swollen micelles dispersed in oil.

Microemulsion methods can be classified as either "normal micelle" (also known as oil-in-water (o/w) methods, or as "reverse micelle" (also known as water-in-oil (w/o) methods. Surfactants must be used in both cases, with their concentration being maintained above the so-called critical micelle concentration (CMC); this is defined as the concentration of surfactants above which micelles are spontaneously formed.

Pileni and coworkers have exploited the synthesis of many different ferrite nanoparticles in functionalized micelles (i.e., the reactants are the counterions of the surfactants) [64, 65]. In a typical procedure, ferrous dodecylsulfate (previously prepared by the reaction of $FeCl_2$ with sodium dodecyl sulfate, SDS) [66] was solubilized in a methyl amine aqueous solution and stirred for 3 h at 50 °C. The black precipitate of magnetite was separated, purified, and redispersed in water. The resultant particles had a mean diameter of 7.4 nm. Experiments performed at different ferrous dodecyl sulfate concentrations and at different temperatures showed that the particle size can vary between 3.7 and 11.6 nm, with the size being controlled by changing either the precursor concentration (by a factor of 4) or the

temperature. When the syntheses were carried out at 50–80 °C, the particles formed were crystalline, and the size varied between 6 and 11.6 nm. In contrast, at low temperatures, the crystallinity was very low. The formation mechanism of stoichiometric Fe_3O_4 nanoparticles was probably similar to that obtained in aqueous solution, as described in Section 12.3.1.1. However, there was one main difference, namely that the formation of Fe_3O_4 observed in this case at low reactant concentrations was impossible in homogeneous solutions. This effect was attributed to the formation of micelles with a high local concentration of Fe^{2+}.

The main advantages of the microemulsion methods are: (i) the possibility to obtain hydrophobic and hydrophilic particles by using normal or inverse micelles, respectively, as nanoreactors; (ii) to fine-tune the particle size and size distribution; and (iii) to tailor the particle shape, that is, to obtain anisometric particles by varying the concentration ratio of the ternary (or quaternary when a cosurfactant is present) mixture. In contrast, the main disadvantages are: (i) a possibly poor crystallinity because of the mild temperature reaction and thermal instability of the surfactants at high annealing temperatures; and (ii) difficulties in preparing particles larger than 12 nm.

12.3.1.4 **Autocombustion Method**

The method is based on an exothermic rapid and self-sustaining chemical reaction between the metal salts and a suitable organic fuel, usually urea or citric acid. The key feature of this method is that the heat required to sustain the reaction is provided by the reaction itself, and not by an external source. The resultant product is a crystalline, highly fluffy dry powder [67, 68]. The advantages of the method are the high chemical homogeneity and purity, while the main disadvantage is the problem of obtaining a stable particle dispersion. The preparation of ferrite particles dispersed in a silica matrix, using a sol–gel autocombustion method, is described in Section 12.4.3.1.

12.3.1.5 **Surfactant-Assisted Hydrothermal Treatment**

The hydrothermal treatment utilizes water under pressure and at temperatures above its normal boiling point as a means of speeding up the reaction between solids. The process parameters such as solution pH, temperature, and hydrothermal reaction time are important with regards to the final products.

Matsushita and coworkers [69] have recently developed a process for preparing highly dispersed magnetite and maghemite particles by using a surfactant-assisted hydrothermal process. For this, Fe^{2+} and Fe^{3+} (concentration ratio 1 : 2) were dissolved in distilled water; the subsequent addition of sodium oleate turned the suspension from a light yellow color to white, due to the formation of iron/oleate complexes. Aqueous ammonia (25%, v/v) was then added to the solution, at which point the solution turned immediately black. The black suspension was placed in a Teflon vessel, capped with a Teflon cover, and heated in a stainless steal autoclave at 200 °C for 3 h. The product was collected by centrifugation, washed and dried at 60 °C for 12 h. The ferrite powders were then dispersed in hexane and left to rest for 6 h. Following removal of the precipitated ferrite particles, the nonaggre-

gated ferrite particles coated with oleate were obtained by evaporation of the hexane.

The average diameter, calculated from a broadening of the X-ray diffraction (XRD) peak intensity using the Scherrer equation was 10.1 nm for particles prepared before hydrothermal treatment, and 13.8 nm for those prepared after hydrothermal treatment. These results were in agreement with the transmission electron microscopy (TEM) data, which showed that the surfactant-assisted hydrothermal treatment, even if it eventually changed the iron oxide phase from magnetite to maghemite, could be used successfully to increase the size of the as-prepared particles. Moreover, the particles had a narrow size distribution and could be maintained well dispersed in hexane, without forming secondary particles.

12.3.1.6 **Surfactant-Assisted Ultrasound Irradiation**

Sonochemical processing has proven to be a useful technique for preparing materials with unusual properties. The chemical effects of ultrasound irradiation arise from acoustic cavitation phenomena – that is, the formation, growth, and implosive collapse of bubbles in a liquid medium. The high temperature (>5000 K), pressure (>20 MPa), and very high cooling rates (10^{10} K s^{-1}) which are reached during cavitation collapse may lead to many extreme conditions. Gedanken and coworkers have prepared acicular amorphous iron oxide nanoparticles [70], elongated copper nanoparticles [71], and lead hydroxy bromide needles [72]. The group also succeeded in preparing magnetite nanorods by using the sonochemical method [73]. Typically, iron(II) acetate and β-cyclodextrin were dissolved in double-distilled deoxygenated water and irradiated with a high-intensity ultrasonic probe under 1.5 atm Ar, at room temperature, for 3 h. The product was then washed with water and pentane, and dried under vacuum. The magnetite nanorods (see Figure 2 in Ref. [70]) had a mean length of 48 nm and a width of 14 nm. The β-cyclodextrin, a water-soluble sugar with a central hydrophobic cavity, acted as a size-stabilizing agent. The magnetite nanorods were formed in a sonochemical oxidation process due to a radical species generated from the water molecules by the absorption of ultrasound. In this process, hydrogen peroxide (H_2O_2) is generated and initiates the partial oxidation of Fe(II):

$$2\mathrm{Fe(II)} + \mathrm{H_2O_2} \rightarrow \mathrm{Fe(III)} + 2\mathrm{OH^-} \tag{12.6}$$

The basic conditions and the argon atmosphere favor formation of the magnetite phase (see Section 12.3.3.1). This method is outstanding in its ability to produce, very easily, monodispersed anisometric magnetite particles with a high aspect ratio (1 : 3).

12.3.2 **Ferrofluids**

For biomedical applications, magnetic nanoparticles must be dispersable and stable in water in pH range 5–9. In the following, the details are provided, as an

example, of a stable Fe_3O_4 particle dispersion (ferrofluid) prepared by a facile method. As many methods involve the preparation of stable ferrofluids in organic solvents, a general procedure that allows the transform of hydrophobic particles to hydrophilic particles is provided in Section 12.3.2.2.

12.3.2.1 Surfactant-Assisted Dehydration

Water-stable, citrate-capped magnetite (Fe_3O_4) nanoparticle dispersions have been prepared by the reaction at 100 °C of iron sulfate ($FeSO_4$) with sodium citrate in alkaline water [74]. In a typical procedure, 1 mmol $C_6H_5Na_3O_7 \cdot 2H_2O$ (citric acid, trisodium salt dehydrate), 4 mmol NaOH and 0.2 mol $NaNO_3$ were mixed in 19 ml deionized water. The mixture was heated to 100 °C, and formed a transparent solution. A 1 ml aliquot of $FeSO_4 \cdot 4H_2O$ (2 mmol) aqueous solution was added rapidly to the solution and the suspension maintained with stirring at 100 °C for 1 h. The precipitate was separated from the mother liquor by using a magnet, washed several times with water and then redispersed in water. The diameter of the Fe_3O_4 particles could be controlled in the range 20–40 nm by varying the experimental parameters, with 20 nm particles showing the greatest stability in water. The concentration of Fe^{2+} was found to be a key factor for controlling Fe_3O_4 particle size; a reduction from 0.1 to 0.02 *M* allowed an increase in particle size, from approximately 20 to 40 nm. The reason for this is that the ferrous concentration strongly affects the nucleation and growth rate of Fe_3O_4 nanoparticles. A higher initial Fe^{2+} concentration leads to smaller particles due to the formation of a larger number of seeds, providing a higher particle concentration and thus smaller particles.

Fe_3O_4 is formed as a result of the dehydration reaction of ferrous hydroxide and ferric oxohydroxide (as represented by Equation 12.7), in which the latter compound is produced by the partial oxidation of ferrous hydroxide by O_2 dissolved in water:

$$Fe(OH)_2 + 2FeOOH \rightarrow Fe_3O_4 + 2H_2O \tag{12.7}$$

Although a partial superficial oxidation of Fe_3O_4 to γ-Fe_2O_3 cannot exactly be excluded, the remarkable point of this method is that, due to the presence of well-capped citrate molecules on the particle surface, the particles acquire a stability in water which exceeds one month.

12.3.2.2 Hydrophobic–Hydrophilic Phase Transfer

When used in biomedical applications, hydrophobic metal oxide nanoparticles must first be transferred to the aqueous phase. This is not a minor problem, as phase transference often results in multiple nanoparticles being collectively coated within an envelope of the coating [75]. However, a collective coating can negate any benefit of the initial particle uniformity. Many methods have been developed for this, although most are not sufficiently general to be used on any system [76]; alternatively, the result may be low concentrations of nanoparticles being phase-transferred. Krishnan [77] has recently reported a method that allows for high

concentrations of nanoparticles to be phase-transferred; moreover, the technique can be used to phase-transfer surfactant-coated nanoparticles prepared from other materials, and the copolymer used has been shown to be biocompatible. This copolymer, which is known as Pluronic F127, is composed of two A-chains of polyethylene oxide (EO) and one B-chain of polypropylene oxide (PO) in an ABA configuration. Pluronic F127 contains 200.45 EO units and 65.17 PO units, and has a molecular weight of 12 600 Da.

Pluronics have interesting temperature-dependent properties. For example, at temperatures below their critical micellar temperature (CMT), the entire polymer is hydrophilic, whereas above the CMT the PO chain dehydrates to become hydrophobic, thus providing the polymer with an amphiphilic character and allowing it to assemble into micelles. For the phase-transfer procedure, equal volumes of a *n*-hexane dispersion of magnetite nanoparticles (particle diameters 2, 7, and 10 nm) covered with oleic acid and F127 (concentration 100-fold the critical micellar concentration at room temperature) in a phosphate-buffered saline solution were stirred together and left partially covered so as to allow the *n*-hexane slowly to evaporate. After 36 h, the nanoparticles had transferred completely in the water phase. The coating occurred at the interphase between the hexane and aqueous phase. The driving force for Pluronic absorption is the interactions between the hydrophobic PO chain and the particle surface, and the low solubility of the hydrophobic segments of the polymer in the aqueous solute [78].

12.3.3
Core–Shell Spherical and Anisometric Particles

Generally speaking, the encapsulation of nanoparticles in an inert shell inherently modifies their surface properties and prevents any direct contact between the particles [79]. In particular, the silanization of nanoparticles has been especially successful in protecting the surface characteristics [80, 81]. Silica is a good noncytotoxic and biocompatible material, which has been shown to provide certain prime advantages for nanoparticles. First, the silica shell can decrease the polydispersity of the particles, preventing their flocculation and thus offering a greater stability in biological buffers [80, 82]. Second, the shell is optically transparent, chemically inert, and protects the surface of the nanoparticles from oxidation [83, 84]. Third, silica surfaces are easy to functionalize [85]; decoration of the silica shell with functional groups including thiol, amine, and carboxylate, facilitates the solubility of spheres in different solvents.

In the following sections, information is provided on two examples of silica–iron oxide particles where silica has different functions. In the first example, the silica particles embed both iron oxide particles and semiconductor crystals to produce fluorescent magnetic composites. In the second example, a silica shell is used to protect iron oxo-hydroxo particles from sintering during the phase transformation to iron oxide, with the simultaneous formation of magnetic hollow nanocapsules.

12.3.3.1 Core–Shell Fluorescent Magnetic Iron Oxide–Silica Particles

Few reports exist on the use of fluorescent magnetic hybrid particles as biological materials in bioseparation and biolabeling. Furthermore, almost all hybrid particles used organic dyes as fluorophores which, due to the instability of the latter, limits their applications. The main motivation for fabricating magnetic and luminescent silica-coated composite nanoparticles has been to create multifunctional nanocomposites which can be controlled by an external magnetic field and detected on the basis of their luminescence. He and coworkers [86] have prepared both magnetic nanoparticles (MNPs) and semiconductor nanocrystals – commonly known as quantum dots (QDs) – embedded in silica spheres based on a straightforward application of the reverse microemulsion approach at room temperature. By using this simple method, fluorescent magnetic composite nanoparticles (FMCNPs) were obtained that included more MNPs and QDs encapsulated into one silica sphere which exhibited a high luminescence and superparamagnetic properties. The method consisted first of the separate preparation of a stable magnetite dispersion in water by a coprecipitation method (see Section 12.3.1.1) and a dispersion of CdTe nanocrystals (QDs) in water prepared by the reaction of $CdCl_2$ and NaHTe with $NaBH_4$. Finally, the FMCNPs were prepared using a reverse microemulsion approach (see Section 12.3.1.3). Typically, cyclohexane, Triton X-100 [$C_{14}H_{22}O(C_2H_4O)_n$], a nonionic surfactant which has a hydrophilic polyethylene oxide group (on average 9.5 EO units) and a hydrocarbon hydrophobic group, *n*-hexanol, a CdTe stock solution, a Fe_3O_4 stock solution, and tetraethylorthosilicate (TEOS) were mixed together. When the microemulsion had formed, an aqueous solution of ammonia was introduced to initiate the polymerization process. The silica growth was completed after 24 h stirring, after which the dispersion was subjected to magnetic separation; this involved attracting the solid phase to the flask wall by the external application of a magnet, such that the supernatant fluid could be discarded. The resultant composite nanoparticles were washed with ethanol and water to remove any surfactant and unreacted molecules, and dispersed in 5 ml ultra-pure water. In order to functionalize the surface of the composite nanoparticles, ethanol and aminopropylsilane were added to form a mixed solution, and allowed to react at 80 °C for 3 h. The aminosilane-modified nanoparticles were separated by the use of a permanent magnet, and washed several times with water. Ultimately, the FMCNPs were obtained and redispersed in water.

The TEM images of FMCNPs, bare Fe_3O_4 and CdTe nanoparticles are shown in Figure 12.3. It should be noted that the final core–shell particles were rather monodisperse, and most silica shells had trapped several magnetic nanoparticles and CdTe QD cores (see the inset of Figure 12.3a). The FMCNPs had a silica-shell thickness of 20 nm on average, yielding an average total diameter of 50 ± 5 nm. The FMCNPs, because of their functional amino groups, were then ready (through activation with glutaraldeyde) for bioconjugation – that is, to be linked with proteins and to monitor their binding specificities towards different biomolecules by the use of immunofluorescence assays.

The preparation method – considering the multifunctions associated with the material – is straightforward, and provides good control over the FMCNPs' mag-

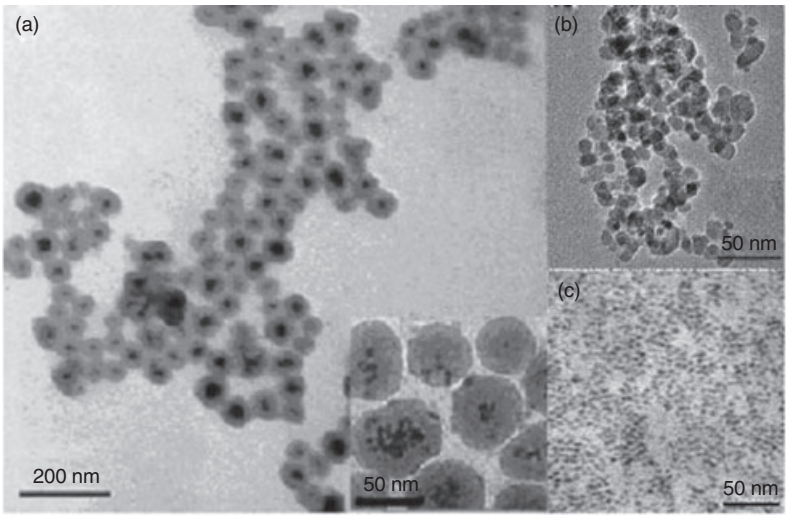

Figure 12.3 Transmission electron microscopy images of: (a) Fluorescent magnetic composite nanoparticles (FMCNPs); (b) Magnetic nanoparticles (Fe_3O_4); (c) Quantum dots (CdTe).

netic and optical properties. This new class of highly fluorescent, photostable magnetic core–shell nanoparticles has the potential for use in many applications such as biolabeling, imaging, drug targeting, bioseparation, and bioassays.

12.3.3.2 Synthesis of Anisometric Iron Oxide Nanocapsules

Piao and coworkers [87] have recently reported the details of a new process termed "wrap-bake-peel", which involves silica coating, heat treatment and subsequent removal of the silica layer, so as to transform the phase and structure of nanostructured materials while preserving their characteristics. By using this method, it has been possible to prepare water-dispersible and biocompatible hollow iron oxide nanocapsules using, as precursors, spindle-shaped akaganeite (β-FeOOH) nanoparticles. Depending on the heat treatment conditions, hollow nanocapsules of either hematite or magnetite have been produced. These synthetized water-dispersible magnetite nanocapsules were used successfully not only as a drug delivery vehicle but also as a magnetic resonance imaging (MRI) contrast agent [23, 88].

Spindle-shaped β-FeOOH nanoparticles were prepared by the hydrolysis of a $FeCl_3$ aqueous solution (see Section 12.3.1.1). In a typical procedure, which is shown schematically in Figure 12.4, $FeCl_3 \cdot 6H_2O$ was dissolved in 2 l of deionized water and the concentration of Fe^{3+} adjusted to 0.02 *M*. The solution was heated at 80 °C, with mechanical stirring, for 12 h to obtain uniform, spindle-shaped β-FeOOH nanoparticles that were then isolated by centrifugation and washed with water. Silica coating of the β-FeOOH nanoparticles was carried out as follows:

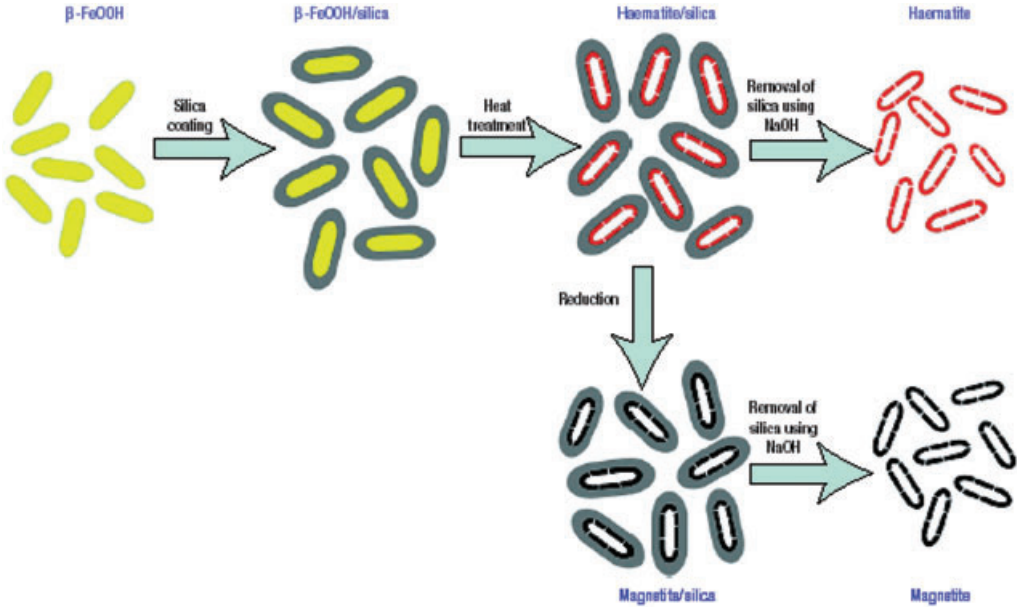

Figure 12.4 Schematic illustration of the procedure for the synthesis of uniform and water-dispersible iron oxide nanocapsules.

300 ml of ammonium hydroxide (30 wt%) was added to a solution containing 5 l ethanol and 500 ml deionized water. After being precoated with polyvinylpyrrolidone (PVP), the as-prepared β-FeOOH nanoparticles were dispersed in the solution. TEOS (7 ml) was then added to the mixture solution at room temperature, with vigorous stirring, and the mixture was held at room temperature for 10 h with constant stirring to yield the uniform silica shell/β-FeOOH core nanocomposite; this was then isolated by centrifugation and washed with water. The composite was heated to 500 °C under an air atmosphere, and the temperature maintained for 5 h to produce the silica shell/hollow hematite nanostructures. The formation of a hollow structure was due to the formation of pores in the β-FeOOH particles at low temperature (≤200 °C) that merge, at higher temperatures, to form single large pores leading to the generation of nanocapsules. This was demonstrated by TEM analyses during the annealing process, and confirmed by thermogravimetric and differential thermal analyses; these showed a weight loss associated with a simultaneous endothermic process between 160 and 330 °C, due to the thermal dehydroxylation of β-FeOOH forming hematite (α-Fe_2O_3).

In order to obtain magnetite nanocapsules, the silica shell/hollow hematite nanostructures were further heated at 500 °C for 10 h under a flow of H_2/Ar (10/90, v/v). The iron oxide/silica nanostructures were immersed in 0.1 *M* of NaOH solution with sonication for 5 h to remove the silica shell (for 1 g of nanocomposite, 250 ml of 0.1 *M* NaOH was added). All ions in the resultant suspensions

were completely removed by several cycles of centrifugation until the pH was neutral.

12.3.4 Maghemite and Magnetite Nanotubes

Nanowires, nanotubes, and nanorods of iron oxides represent a class of one-dimensional (1-D) magnetic materials in which carrier motion is restricted in two directions. The quantum confinement and low-dimensionality inherent to these systems allow the generation of materials with unique properties [7, 74, 87, 89–92]. Magnetic nanotubes, for example, may potentially serve as tunable fluidic channels for tiny magnetic particles, in biomagnetic sensors, and in nanomedicine and catalysis. At present, a variety of methods have been used for the synthesis of 1-D nanostructures, including hydrothermal/solvothermal processes, organometallic precursors, solid-template methods, chemical vapor deposition, vapor–liquid–solid methods, and polymer assembly.

At this point, we report on two different preparation methods used for the synthesis of iron oxide nanotubes; namely, a solid-template method and a soluble-template method (which, in our opinion, have provided good results in terms of high yields of single-crystalline iron oxide nanostructures). For the preparation of iron oxide nanowires (and details of their magnetic properties), the reader is referred to Sections 12.4.4.1 and 12.4.4.2.

12.3.4.1 Solid Nanotube Template

This method was developed by Sun and coworkers [93], and consists of the initial formation of hematite nanotubes which are then reduced by hydrogen and oxidized in air to form single-crystal maghemite nanotubes. In a typical experimental procedure, the nanotubes were obtained by the hydrothermal treatment of a $FeCl_3$ solution in the presence of $NH_4H_2PO_4$ at 220 °C for 48 h. The initial product consisted almost entirely of hematite (α-Fe_2O_3) nanotubes with outer diameters of 90–110 nm, inner diameters of 40–80 nm, and lengths of 250–400 nm. The product obtained after 2 h contained spindle-like particles with diameter 60–70 nm and length 350–400 nm (Figure 12.5a). Prolonging the reaction time to 8 h led to the creation of nanorods with a diameter of approximately 100 nm and a length of 250–400 nm. The tips of these rods were concave (see the inset of Figure 12.5b). A mixture of rod-like, tubular and semitubular (inset of Figure 12.5c) nanostructures was formed after longer reaction times (12 h, Figure 12.5c). Following a reaction time of 48 h (Figure 12.5d), the product consisted predominantly of nanotubes that were completely hollow.

The formation process of the nanotubes can be derived from a "dissolution" of the spindle-like precursors from the tips towards the interior along the long axis, until hollow tubes are formed.

The driving force is the high activity of the sharp spindle tips, which are easily attacked by the protons in acidic solution. As regards the spindle-like precursor, it is well known that the shape is caused by a selective adsorption of phosphate

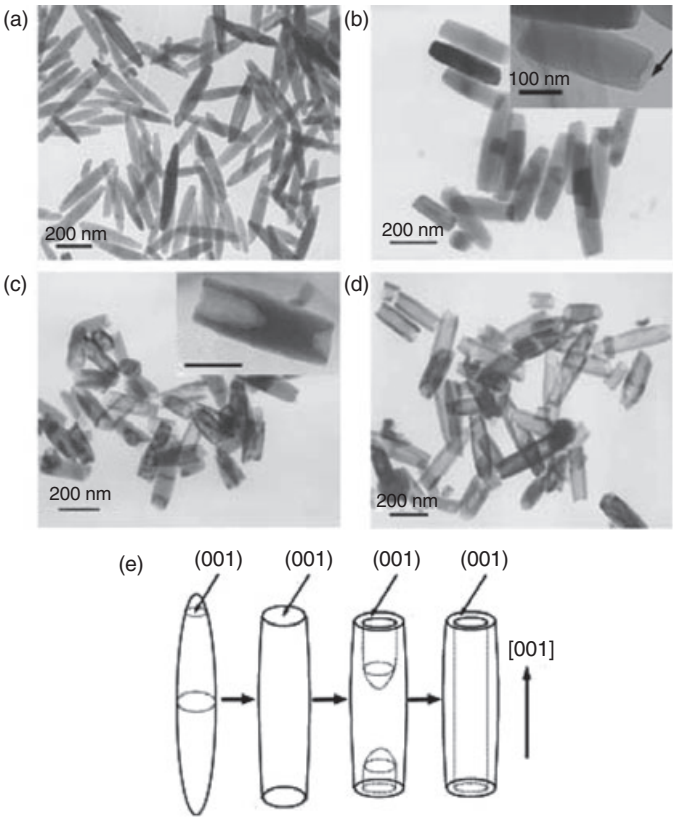

Figure 12.5 Morphology evolution of the hematite nanotubes with reaction time. Transmission electron microscopy images of the products obtained at 220 °C after (a) 2 h, (b) 8 h, (c) 12 h, and (d) 48 h; (e) Schematic illustration of the tube-formation process.

onto the hematite crystalline planes. Moreover, phosphate coordination to Fe^{3+} ions induces a preferential dissolution of the hematite spindle precursors along the long axis. The hematite nanotubes can be reduced by annealing at 360 °C under a continuous hydrogen gas flow for 5 h, and reoxidized in air to form maghemite single-crystalline nanotubes.

12.3.4.2 **Soluble Nanotube Template**

In order to prepare single-crystalline magnetite nanotubes, Zhou and coworkers [8, 84] have used MgO nanowires grown on Si/SiO_2 surfaces as solid templates. The nanowires were first coated epitaxially with a layer of Fe_3O_4, by using a pulsed laser deposition (PLD) technique, to obtain MgO/Fe_3O_4 core–shell nanowires. The

MgO inner core was then selectively etched by using a $(NH_4)_2SO_4$ solution at 80 °C, such that micrometer-long single-crystalline Fe_3O_4 tubes were obtained. The advantages of this method were: (i) the tunability of the nanotube length, inner diameter and wall thickness by controlling the length and diameter of the MgO cores and the deposition rate/time of the shell; and (ii) the versatility of the method, which can be extended to a variety of materials that possess a close lattice match with the template MgO.

12.4 Correlations between Synthesis and Magnetic Behavior in Iron Oxide Nanomaterials

In the following sections, we describe some examples that highlight the strong correlation that exists between preparation method, composition, structure, material shape, and its magnetic properties.

12.4.1 Spherical and Anisometric Iron Oxide Particles

At this point, four examples can be outlined that show a straightforward correlation between the magnetic properties and: (i) particle size and ferrite composition (Sections 12.4.1.1 and 12.4.1.2); (ii) surfactant effects (Section 12.4.1.3); (iii) particle shape (Section 12.4.1.4).

12.4.1.1 Spherical Magnetite (Fe_3O_4) Nanoparticles

Hyeon and coworkers have recently reported on the synthesis of several grams of magnetite nanoparticles using inverse micelles as nanoreactors [94].

The key features of the procedure were: (i) maintenance of the micelle structure during formation of the particles at high reaction temperatures to produce particles of high uniformity and crystallinity; (ii) the yield, which was sensibly increased with respect to conventional methods, due to the lower amount of organic solvent used; (iii) the method, which employed hydrated iron salts rather than the metallo-organic salts generally used (and which were by far more toxic); and (iv) the versatility of the synthesis method, which could be applied for the preparation of different materials (the authors in fact also reported on the preparation of mixed ferrites, $Me^{2+}Fe_2O_4$; $Me^{2+} = Co^{2+}$, Mn^{2+}, Ni^{2+} and Zn^{2+}; see also Section 12.3.1.3).

The microemulsion is formed by water, dimethylbenzene (xylene), the surfactant dodecylbenzenesulfonate (DBS) and an ethanolic solution of $Fe(NO_3)_2$ and $FeCl_3$. After 12 h stirring at room temperature, the microemulsion was heated to 90 °C and an aqueous solution of hydrazine added. The mixture immediately turned black and, after 5 h, the product was separated by centrifugation. The particles were then dispersed in organic solvents such as toluene and alkanes. Depending on the relative amounts of surfactant, solvent and w ratio (where

w = [polar solvents ethanol and water]/[surfactant]), the particle diameter could be tuned to between 3 and 10 nm). TEM images of the 3 nm particles with the histogram of the size distribution showed the high particle uniformity with a size distribution of approximately 11% (Figure 1A in Ref. [94]). Moreover the inset of the figure, which showed the high-resolution (HR) TEM of a single particle, revealed the presence of lattice-fringe patterns, thus demonstrating the highly crystalline nature of the nanoparticles. In order to identify the crystalline phase, XRD analysis in the case of magnetite (although often used as the only proof of phase identification) was insufficient as the peaks of maghemite (the phase formed after oxidation of Fe^{2+} to Fe^{3+}) occurred in almost the same positions. In this case, the authors also carried out X-ray magnetic circular dichroism (XMCD) measurements at the Fe $L_{2,3}$-edges, to confirm that the nanoparticles were indeed dominated by the magnetite phase, and that the presence of a small amount of the oxidized phase, maghemite, could not be excluded.

This effective synthesis method, which allows fine tuning of the particle dimensions and provides excellent particle uniformity and crystallinity – as shown clearly by the chemical and structural characterization – leads to a straightforward correlation between the magnetic behavior of the particles and their size. In particular, the magnetic properties of three samples with particle sizes of approximately 3, 7, and 9 nm are described (Table 12.1). For quantitative comparison, the magnetization is reported in units of emu per gram Fe. The thermal dependence of magnetization, as measured by ZFC protocol and carried out using a SQUID magnetometer, is shown in Figure 4 of Ref [94]. The temperature corresponding to the curve maximum, proportional to T_B, increases as the size of the particles increases (Table 12.1), according to the Néel–Brown model of superparamagnetism (see Section 12.2.3) [6, 95]. A remarkable result, however, is that the magnetic anisotropy, when estimated from experimental values of the blocking temperatures, is above of 10^6 J m^{-3} for each of the three samples, and at least one order of magnitude higher than that of bulk Fe_3O_4 [43]. The reason for such high values can be mainly attributed to surface magnetic state effects, due to the fact that particles larger than 7 nm, where the surface : volume ratio is not high, show a value of magnetic anisotropy close to that of the bulk material. Another

Table 12.1 Average diameter (<*D*>), standard deviation (σ), blocking temperature (T_B), saturation magnetization (M_s) at 300 and 2 K, reduced remanent magnetization (M_r/M_s) and coercive field (H_c) at 2 K.

Particle size label	***<D>*** *(nm)*	***σ*** *(nm)*	***T_B*** *(K)*	***M_s–(300 K)*** *(emu/g)*	***M_s–(2 K)*** *(emu/g)*	***M_r/M_s–2 K***	***H_c–2 K*** *(Oe)*
3	2.92	0.34	45	135	165	0.19	195
5	5.11	0.37	85	152	184	0.23	260
7	7.10	0.53	105	173	228	0.18	170

possible source of such enhancement of magnetic anisotropy could be ascribed to interparticle interactions, which are quite strong in powder samples.

The field dependence of magnetization at 2 K and 300 K was also measured; some magnetic parameters extracted by hysteresis loops are listed in Table 12.1. It is well known that magnetite nanoparticles smaller than 20 nm are superparamagnetic at room temperature [42], and this is confirmed by the magnetization versus field curves at 300 K, as reported in Figure 5 in Ref. [94] ($H_c = 0$, $M_r = 0$). On the other hand, at low temperature, all samples show a hysteretic behavior with coercivity approximately 200 Oe. The authors underlined the fact that H_c values measured in these samples were smaller than those reported elsewhere for Fe_3O_4 nanoparticles [47]. In our opinion, this behavior can be attributed to the fraction of the smallest particles that, at low temperature, are still in the superparamagnetic state. This is confirmed by the low M_r/M_s (Table 12.1) values which reveal the presence at 2 K of a fraction of particles, still in the superparamagnetic state.

The saturation magnetization values at 300 K and 2 K decrease by decreasing the particle size (Table 12.1); this can be ascribed to surface effects that become more important when particle size decreases, as observed earlier in other systems [34, 96–98].

In conclusion, Hyeon and coworkers set up an economical and environmentally friendly synthesis method to obtain magnetite nanoparticles with sizes between 2 and 10 nm, and with a narrow size distribution. The particles were highly crystalline and had magnetic properties suitable for biomedical applications. In particular, the high value of saturation magnetization at room temperature rendered these nanoparticles suitable for drug delivery and magnetic separation applications [94].

12.4.1.2 **Stable Iron Oxide Spherical Nanoparticle Dispersions (Ferrofluids)**

Sun and colleagues [42] have introduced a simple method for the preparation of stable metal and metal oxide nanoparticle dispersions. This consists of the thermal decomposition of metallo-organic compounds in high-boiling solvents, followed by reaction of the metal ions with polyols. In order to avoid particle aggregation, a mixture of oleic acid and oleylamine was used as a surfactant. Both, oleic acid and oleylamine were found necessary for the formation of particles; the sole use of oleic acid resulted in a viscous product which was difficult to purify, while the use of oleylamine produced only iron oxide nanoparticles, at a much lower yield. The two-surfactant mixture was crucial for obtaining stable, highly concentrated particle dispersions. Moreover, it was also possible to transform the as-prepared hydrophobic particles into hydrophilic particles by adding bipolar surfactants. Highly concentrated, stable magnetic particle dispersions in water are very much required for almost all biomedical applications. In this case [42], magnetite (Fe_3O_4) nanoparticles were prepared by the thermal decomposition of iron (III) acetylacetonate ($Fe(acac)_3$) and reduction with 1,2-hexandecandiol, the polyol, in the presence of oleic acid and oleylamine as surfactants.

Similarly, by reaction of $Fe(acac)_3$ and $Co(acac)_2$ or $Mn(acac)_2$ with the same diol, $CoFe_2O_4$ and $MnFe_2O_4$ nanoparticles have been obtained, thereby confirming the versatility of the method. The particle diameter can be tuned from 3 to 20 nm by

varying the reaction conditions or by seed-mediated growth. That is, by using small particles as seeds, mixed with the reagents in solution, to grow approximately 2 nm larger particles; these in turn can be used as seeds, allowing the diameter to be finely tuned.

Typical TEM images of 6, 10, and 12 nm Fe_3O_4 nanoparticles deposited from their hexane or octane dispersions and dried under ambient conditions are shown in Figure 12.6. The particles have a narrow size distribution and can form self-ordered Fe_3O_4 superlattices if the solvent is allowed to evaporate slowly. The structural characterization follows from XRD, electron diffraction and near-edge X-ray absorption fine structure measurements. The resultant particles

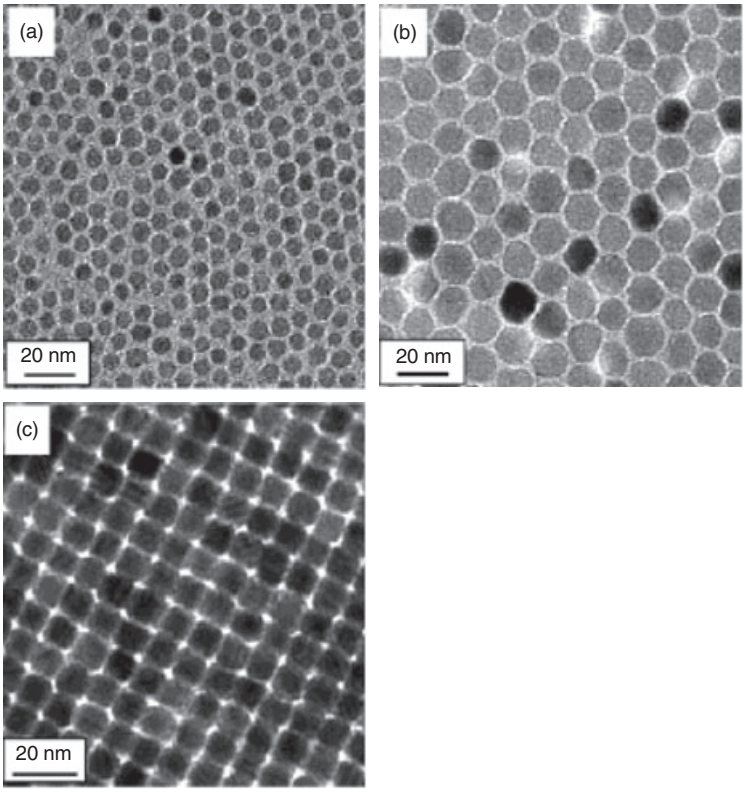

Figure 12.6 Transmission electron microscopy bright-field images of (a) 6 nm and (b) 12 nm Fe_3O_4 nanoparticles deposited from their hexane dispersion on an amorphous carbon-coated copper grid and dried at room temperature; (c) A 3-D superlattice of 10 nm Fe_3O_4 nanoparticles deposited from their octane dispersion on an amorphous carbon surface and dried at room temperature.

were single-crystalline, mostly constituted by the Fe_3O_4 phase, although a small amount of the oxidized phase, γ-Fe_2O_3, cannot be excluded, especially on the particle surface.

Magnetic measurements on all Fe_3O_4 nanoparticles have indicated that the particles are superparamagnetic at room temperature; that is, the thermal energy overcomes the anisotropy energy barrier of a single particle, and consequently the net magnetization in the absence of an external applied magnetic field is zero.

Figure 6 in Ref. [42] shows the hysteresis loop of 16 nm Fe_3O_4 nanoparticles recorded at 10 K and 300 K. At 10 K – that is, at a much lower thermal energy – the material is ferromagnetic with a coercivity of 450 Oe. However, under a large externally applied field the particle magnetization will align with the field direction and reach its saturation value (M_s). For 16 nm Fe_3O_4 particles, the M_s value is 83 emu g^{-1}, very close to the range of values (78–90 emu g^{-1}) expected for the bulk [47, 51]. For particles smaller than 10 nm, the M_s value is lower, most likely due to a spin canting effect which is more relevant for small particles with a high surface-to-volume ratio [45, 97, 99–101].

When Fe is partially substituted by Co, $CoFe_2O_4$ is formed and, due to the higher magnetic anisotropy of Co compared to Fe, the particles are ferromagnetic also at room temperature, and with a coercivity of 400 Oe which at 10 K reaches a value of 20 kOe. In contrast, the incorporation of Mn cations into the Fe–O matrix reduces the magnetic anisotropy of the materials. $MnFe_2O_4$ particles with diameter of 14 nm show, at 10 K, a coercivity of only 140 Oe [17]. This shows clearly that, by varying the chemical composition of metal spinel oxides, it is possible to tune the magnetic anisotropy and then the magnetic properties of the materials.

The magnetic behavior of these particles is well suited to biomedical applications outside the human body or *in vivo*, when they are well protected by a nonbiodegradable shell in order to avoid any risk of toxic cobalt release.

12.4.1.3 **Surfactant Effect**

The functionalization of nanoparticles surface represents a fundamental step for the application of these materials in the biomedical field (drug delivery, tumor targeting), in catalysis, and as sensors. Indeed, the properties of the magnetic nanoparticles may be tailored by adapting their surface molecular coating in order to meet a variety of requirements (i.e., colloidal stability, bioconjugation, etc.) [25].

As described earlier in Section 12.2.2, nanoparticle surface functionalization can induce important modifications on surface magnetic anisotropy, and consequently on the magnetic properties of the material. Consequently, an understanding and an ability to control the effects of surface functionalization on magnetic behavior become important when designing new nanomaterials suitable for new applications.

Recently, Battle *et al.* [34] studied the effects of oleic acid surface particle functionalization on the magnetic properties of Fe_3O_4 particles. Here, the magnetite

nanoparticles were synthesized by thermal decomposition at high temperature, using an iron organic precursor in an organic medium and following the procedure described in Section 12.4.1.2. Oleic acid was used as the surfactant, and in all cases the Fe:oleic acid molecular ratio was maintained at 1:3. The report referred to three samples of different particle size, with XRD patterns showing all three to consist of highly crystalline magnetite particles. A subsequent TEM analysis showed that the particles were poly-disperse below 20% and consisted of a mixture of diamond, cubic, and triangular shapes [102]. Magnetization versus temperature measurements showed the M_s values to be almost size-independent and close to the saturation magnetization of the bulk material ($M_s^{\text{bulk}} = 78 - 90\,\text{emu g}^{-1}$) [30, 47, 51]. The latter result was surprising as M_s^{bulk} in Fe_3O_4 was not achieved up to a particle diameter of 150 nm [103]. This suggested that the crystal field associated with the new O^{2-} surface ligands of oleic acid coordinated to Fe surface cations resembled that of the Fe bulk cations, and this induced a reduction in the surface magnetic disorder. H_c was seen to increase with the increase in particle size, most likely due to shape anisotropy associated with the faceted growth of the particles [102]. These results supported the idea that the oleic acid molecules were bonded covalently to the nanoparticles, and were able to reduce the surface spin disorder.

12.4.1.4 Anisometric Maghemite (γ-Fe_2O_3) Particles

As described in Section 12.2.2, the morphology and shape of magnetic nanocrystals represent potential tools for tuning the magnetic properties of the materials. The formation of monodisperse, spherical magnetite nanoparticles by using spherical micelles as nanoreactors was detailed in Section 12.4.1.1, when low surfactant concentrations were used. Conversely, by increasing the surfactant concentration and/or by adding salts or alcohols, the micelles were seen to grow to a rod-like shape, as predicted by the micellization theory [104]. This anisometric shape could be taken as an ideal template for preparing anisometric structures. Moreover, the surfactant molecules present in the system may selectively interact with preferred crystallographic planes of the forming inorganic nanostructures, thus originating an oriented growth of crystalline nuclei with new morphologies [105, 106].

In this connection, Wang and coworkers [83] reported a systematic variation of the shape of γ-Fe_2O_3 nanostructures by using an anionic surfactant, sodium dodecyl sulfate (SDS), in SDS/*n*-octanol/water microemulsions. By adjusting only two parameters – reaction time and SDS concentration – the group succeeded in controlling the formation of rods and multipod shapes, and in studying the influence of anisometric shape on the magnetic properties.

The samples were prepared by the addition of $FeSO_4$ to a microemulsion formed by mixing (using an ultrasonic oscillator) SDS, deionized water and 1-octanol, and setting the pH value at 10.8 by the dropwise addition of an ammonia solution. The mixture was then held at 40 °C for 3, 4, and 5 h under continuous stirring. The precipitate was then separated and purified.

After a 3 h reaction, mostly spherical γ-Fe_2O_3 nanoparticles were formed, whereas uniform γ-Fe_2O_3 nanorods of 500 nm length and 20 nm width were formed after 4 h, but with an aspect ratio in excess of 25 : 1. The particles formed after a 5 h reaction had undergone a phase transformation from γ-Fe_2O_3 to α-Fe_2O_3. The rod-like shape was derived (as shown by Tulpar and Ducker [107]) by the surfactant molecules being adsorbed onto preferential crystalline planes of the iron oxide nuclei; this prevented them from further grow and consequently induced an anisotropic growth process.

The magnetic hysteresis curves of the 3 h, 4 h, and 5 h samples, when measured at room temperature, showed that the spherical and rod-like γ-Fe_2O_3 particles had comparable saturation magnetization, but differed in their coercivity values, from 0.28 Oe for spherical particles up to 0.7 kOe for the rods. This high coercivity value was ascribed to the contribution of the shape anisotropy to the total magnetic anisotropy. A different magnetic behavior was observed, however, for the sample prepared by a 5 h reaction. In this case, TEM analysis revealed the particles to be almost spherical, whereas the XRD spectrum showed a phase change from maghemite (γ-Fe_2O_3) to the more stable, antiferromagnetic hematite (α-Fe_2O_3). Later, by increasing the SDS surfactant concentration 10-fold, from 1.8 mmol to 18 mmol, and after a 3 h reaction, multipod γ-Fe_2O_3 particles were isolated. In this study the authors ascribed the anisometric morphology to an unbalanced distribution of SDS molecules on the different crystalline faces of the γ-Fe_2O_3 nuclei, which resulted in some facets showing preferential growth compared to others. The hysteresis loops of maghemite aggregated nanoparticles and nonaggregated multipod structures showed the same saturation magnetization value ($M_s \approx 0.02\,\mathrm{emu\,g^{-1}}$), while the coercivity and remanent magnetization values for the aggregated nanoparticle sample ($H_c = 0.28$ kOe; $M_r = 0.0078\,\mathrm{emu\,g^{-1}}$) were higher than those for the sample with multipod morphology ($H_c = 0.09$ kOe; $M_r = 0.0026$ emu $\mathrm{g^{-1}}$). This means that the increased scale of branches grown along uneasy magnetic axes makes the γ-Fe_2O_3 magnetization more difficult.

In this example, it was shown clearly that a control on nanoparticle shape anisometry would lead to a wide alteration of magnetic properties, thus opening perspectives for the design of new magnetic building blocks for different applications [11, 108].

12.4.2
Core–Shell Nanoparticles

Core–shell particles often exhibit improved physical and chemical properties over their single-component counterparts, and hence are potentially useful in a broader range of applications.

Indeed, the shell can alter the charge, functionality, and reactivity of the particle surface; magnetic, optical or catalytic functions may be readily imparted to the dispersed colloidal matter, depending on the properties of the coating. Encasing

colloids in a shell of different composition may also protect the core against chemical and physical changes [79, 109].

In the first example, we describe the preparation and magnetic behavior of high-engineered particles; that is, particles formed by a γ-Fe_2O_3/silica core and a gold shell, all protected by a further polyethylene glycol (PEG) shell.

In the second case, magnetite particles are functionalized with biocompatible polydimethylsiloxane (PDMS) adsorbed onto their surface in order to: (i) provide an experimental tool for particle size tuning by varying the length of the polymer alkyl chains protruding from the magnetite particle surface, together with a theoretical model and (ii) sterically stabilize the particles against flocculation.

12.4.2.1 γ-Fe_2O_3/Silica Core Coated with Gold Nanoshell

Coating magnetic nanoparticles with silica shell represents a promising and important approach in the development of magnetic nanoparticles for technological and biomedical applications. The rich and well-documented biocompatible chemistry of silica colloid may allow the practical implementation of magnetic nanoparticles in magnetically guided drug delivery, tumor targeting and the magnetically assisted chemical separation of cells and/or proteins. Moreover, silica shells greatly improve the hydrophilicity of the magnetic nanoparticles [21, 110]. The coating of nanoparticles with gold is also very interesting for bioconjugation, good biocompatibility and unique optical properties of the Au nanoshells. These systems can be used in biological systems for diagnostic and therapeutic applications, and they are also potential candidates for localized photothermal therapy.

Recently Ji and coworkers [111] described the synthesis, characterization and use of hybrid nanoparticles with a superparamagnetic iron oxide-silica core and a gold nanoshell. The photothermal properties of a gold nanoshell combined with the properties of a magnetic core, open perspectives for the application of this material in target photothermal therapy mediated through an external magnetic field and MRI guidance [111].

A superparamagnetic iron oxide/silica core coated with a bifunctional gold nanoshell was synthesized through a multistep procedure (Figure 12.7). Commercially available superparamagnetic, water-based γ-Fe_2O_3 (Mnp) nanoparticles ($<D>$ = 10 nm) were used as the magnetic core. The silica coating was performed according to the well-known Stöber process, where SiO_2 is formed through the hydrolysis and condensation of a sol–gel precursor (see Section 12.3.1.2) [112, 113]. As the iron oxide surface has a strong affinity for silica, no primes were needed to promote the deposition and adhesion of the SiO_2 coating. In a typical procedure, water-based Mnp nanoparticles were diluted in water and absolute ethanol. An aqueous ammonia solution and TEOS were consecutively added into the Mnp dispersion at room temperature, under continuous mechanical stirring. The clear solution became a turbid suspension in approximately 30 min, indicating the presence of γ-Fe_2O_3 nanoparticles coated with silica shells (Mnp/Si). Although several parameters (e.g., the growth time and concentration

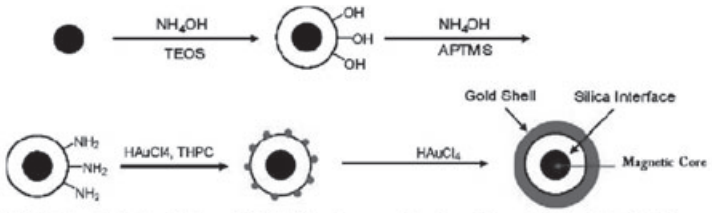

[a] Abbreviations: TEOS, tetraethylorthosilicate; APTMS, 3-aminopropyltrimethoxysilane; THPC, tetrakis(hydroxymethyl)phosphonium chloride.

Figure 12.7 Schematic representation of the synthesis of gold nanoshells with superparamagnetic γ-Fe_2O_3 cores.

of ammonia catalyst and water) could be employed to control the thickness of silica shell, it proved to be more convenient and reproducible to adjust the shell thickness by changing the concentration of the TEOS precursor. With this method, thicknesses ranging from 2 to 100 nm could be obtained [110]. Then, in order to produce amino-terminated silica surfaces, treatment with NH_4OH and 3-aminopropyltrimethoxysilane was carried out. The gold nanocrystals seeds (2–3 nm) were then attached to the amino groups by the reduction of chloroauric acid ($HAuCl_4$) with tetrakis(hydroxymethyl)phosphonium (THPC). The attached gold nanoseeds were used to nucleate a gold overlayer on the silica surface so as to form a gold nanoshell (Mnp/Si/Au). The thickness of the gold shell was tuned by varying the concentration of the Au seeds and Mnp/Si particles, while the concentration of the gold precursor was kept constant. In the last step, the nanoshells were coated with PEG by treating the Mnp/Si/Au nanoparticles with a monofunctional PEG precursor. The PEG coating, as confirmed by Fourier transform infrared (FT-IR) spectroscopy, afforded good temporal particle stability in water (i.e., several weeks at 4 °C).

The TEM images confirmed the presence of γ-Fe_2O_3 nanoparticles encased in silica, although most of the silica shells contained more than one magnetic core. This could be avoided by optimizing the ratio between the concentration of iron oxide nanoparticles and TEOS [110]. The mean diameter of the silica-coated iron oxide nanoparticles was estimated as 66 ± 9.5 nm. After treatment with $HAuCl_4$ and THPC, the gold nanoseeds could be clearly observed on the silica surface. Finally, TEM images of Mnp/Si nanoparticles coated with Au nanoshells showed the gold coating not to be continuous, but to have a topographical roughness at the nanometer scale. The particles had a mean diameter of 82.2 ± 9.7 nm, and the gold shells a thickness of approximately 8 nm.

In order to verify whether the Mnp/Si/Au nanoparticles exhibited any magnetic properties that could be used for magnetic field-guided targeting, a number of investigations were performed. As an example, a nanoparticle dispersion in water was prepared and a Nd–Fe–B magnet (~0.3 T) then used to separate the Mnp/Si/Au. The solution, which initially was dark, became almost transparent after a

15 min period of exposure to a magnetic field; that is, the particles were precipitated at only one side of the vial wall. Magnetization versus field measurements recorded at 300 K on Mnp and Mnp/Si/Au nanoparticles, respectively, showed a lack of hysteretic behavior which indicated that, in both samples, the nanoparticles were in a superparamagnetic state at room temperature. A strong decrease in saturation magnetization was observed in Mnp/Si/Au particles with respect to the saturation magnetization of Mnp particles. Si/Au nanoparticles without Mnp cores exhibited a diamagnetic behavior as expected. This led to the belief that the reduction of Ms in Mnp, in respect to that of Mnp/Si/Au nanoparticles, was the result of the high fraction of silica/Au in the coated nanoparticles, and that the gold and silica layers did not affect the saturation magnetization of Mnp.

When Ji and coworkers [111] conducted magnetic resonance relaxation- and photothermal studies on Mnp/Si/Au nanoparticles, the samples exhibited a strong absorbance in the near-infrared (NIR) region of the electromagnetic spectrum, and an efficient photothermal effect, both of which should open new perspectives in MRI imaging and photothermal therapy.

12.4.2.2 Effect of Particle Size and Particle Size Distribution on the Magnetic Properties of Magnetite/PDMS Nanoparticles

For "*in vivo*" biomedical applications (e.g., drug delivery, dosage and cell uptake), it is important to control not only particle size but also particle size distribution, and it is for this reason that sterically stabilizing polymers on the particle surface are often required. In addition, in order to finely control particle size, magnetic separation is often used as a method of particle size selection, because it offers simplicity and a low-cost throughput.

In a recent report, Riffle and coworkers [114] described the synthesis of magnetite nanoparticles with polydimethyl siloxane (PDMS) chains bound to their surfaces. The size and size distribution of the particles were adjusted by the magnetic removal of any larger particles, via magnetic separation. An accurate characterization was performed in order to evaluate the effect of the magnetic separation on the morphological and magnetic features of the nanoparticles. The report also included some useful elements concerning the general methodology for characterizing metal oxide/polymer nanoparticles.

Magnetite (Fe_3O_4) particles were synthesized by the reaction of a stoichiometric ratio of iron (II) and iron (III) chloride salts (1 : 2) with ammonium hydroxide (NH_4OH). The base was added in the aqueous solution of salts, until it turned black and reached a pH of 9–10 (see Section 12.3.1.1). The surfaces of magnetite nanoparticles were then coated by adsorbing a PDMS oligomer that had three carboxylate groups on one end of the molecule, and a nonfunctional trimethylsilyl group at the other end. To this purpose, a PDMS dispersion, dissolved in dichloromethane (DCM), was added to the basic magnetite dispersion. After stirring the solution for 30 min, aqueous hydrochloric acid was added slowly until the solution became slightly acidic (pH 5–6). Since the isoelectric point of magnetite in water is pH ~6.8, there would be a net positive charge on the metal oxide surface at pH

6. It is then reasonable that the PDMS molecules would adsorb, through an electrostatic binding of the negatively charged carboxylate groups, onto the cationic sites of the nanoparticle surface. On the other hand, the nonfunctional end of the PDMS oligomer would provide a brush layer that extended outwards from the nanoparticle surface to prevent particle aggregation. Finally, the DCM was removed under vacuum and the Fe_3O_4/PDMS particles were decanted, washed with water and methanol, and then dried overnight at 40 °C under reduced pressure. In the following descriptions, this sample will be referred to as *0-pass*.

In order to remove aggregates and large particles, a dispersion of the Fe_3O_4/PDMS nanoparticles in chloroform ($CHCl_3$) was passed through magnetic columns (i.e., ~6 g of soft iron granules firmly packed into 3 ml plastic syringes). A Nd–Fe–B magnet, placed approximately 10 cm apart from the columns, was used to generate a magnetic field of 0.24 T. The basic idea of the magnetic separation was that larger particles and aggregates would be entrapped by the separation column because of their magnetic moments. After sonication, the chloroform dispersion of the particles was passed through a second column at a flow rate of approximately 20 ml min^{-1} (*1-pass* sample). Alternatively, a portion of the chloroform dispersion of nanoparticles was passed through five freshly prepared separation columns (*5-pass* sample). The collected dispersions were dried under vacuum and weighed to determine the amount of material that had been retained in the separation columns. The particles/polymer compositional ratios were determined using thermogravimetric analysis (TGA) under an inert gas (N_2). The materials that had been magnetically separated had lower magnetite concentrations compared to those of the original materials [115]. Since the separations preferentially removed aggregates and larger particles, those complexes that passed through the columns should have higher magnetite specific surface areas, leading to higher mass fractions of polymer in the eluted materials. TEM investigations indicated that magnetically separated samples had a lower fraction of aggregates and larger particles, leading to a decrease in mean particle size. An accurate statistical analysis of the TEM data confirmed that the magnetic separation had resulted in particles of a smaller size and with narrower size distributions. Moreover, multiple passes through the separation columns produced smaller average sizes and a narrower size distribution.

The thermal dependence of magnetization was measured using the ZFC and FC protocols. T_{max} in ZFC measurements was seen to decrease from *0-pass* to *5-pass* samples, due to the decrease in particle size, as showed in the statistical analysis of TEM data. The irreversibility temperature in ZFC-FC curves (see Section 12.2.3.1) for *0-pass* and *1-pass* samples was higher than 300 K, indicating the presence of large particles and aggregates, in agreement with TEM results. T_{irr} for the *5-pass* sample was lower than room temperature, indicating that the magnetic separation technique was an efficient method for removing larger particles and aggregates. The dependence of magnetization on the external magnetic field was also studied. The value of the magnetic moment has been normalized for the magnetite content which, in turn, was extracted from the thermal analysis data. The M_s value decreased with decreasing in particle size,

due to the increased surface contribution [97, 116]. Finally, Riffle and coworkers, in order to predict the distributions of particle size in dispersions, combined a careful TEM characterization (particle size and particle size distribution) with a polymer brush model that originally was developed for star polymers. This approach provided a method for a more precise characterization of the size distribution of polymer–nanoparticle complexes. An ability to fine-tune the nanoparticle size and to predict nanoparticle stability in dispersions is a critical point for many biomedical applications.

12.4.3 Nanocomposites

The term "nanocomposite", which was first coined by R. Komarneni and colleagues during the period 1982–1983, refers to materials with more than a solid phase where at least one dimension is in the nanometer range. The solid phases may be amorphous, semicrystalline, or crystalline; they can also be inorganic, organic, or both, and essentially of any composition [117]. Following the framework used in Section 12.1, the nanocomposites can be classified as multiphase nanomaterials.

Nanoparticles dispersed in a matrix (whether magnetic or nonmagnetic) can be considered as one of the most important classes of nanocomposites. Indeed, embedding nanoparticles in a crystalline or amorphous matrix not only allows a reduction in particle aggregation but also provides a means of controlling the morphological, structural – and consequently magnetic – properties of the material. For this reason, during the past few years nanocomposite materials with matrices such as crystalline alumina [16], polymers [118] and amorphous silica [37, 119, 120] have generated profound interest. The magnetic properties of these nanocomposites are mainly determined by the volume fraction of the magnetic particle, and by the structural and textural properties of the matrix. In addition, a fundamental role is played by the interaction between particle surface and host matrix [2].

Three examples will be presented to detail and explain the interplay between the host matrix and the magnetic ferrite particles, and how these influence the magnetic behavior of the nanocomposite material.

12.4.3.1 Magnetic Properties of Cobalt Ferrite–Silica Nanocomposites Prepared by a Sol–Gel Autocombustion Technique

The use of amorphous silica as a host matrix is widely used because it is easy to prepare and allows improvements in the catalytic, electric, magneto-optic and mechanical properties of the material [121]. The rich and well-documented biocompatible chemistry of silica colloids means that magnetic nanoparticles, when embedded in the SiO_2 host matrix, become suitable for several biomedical applications. For example, composites consisting of superparamagnetic metal oxide nanoparticles (e.g., Fe_3O_4; γ-Fe_2O_3, $CoFe_2O_4$) dispersed in submicron silica diamagnetic particles may be used for biomedical *in vitro* applications, where the size

restrictions are less severe than for *in vivo* applications. The use of a silica host matrix has the added advantage that superparamagnetic composites can be easily functionalized [24].

Recently, Piccaluga and coworkers devised a new sol–gel autocombustion synthesis method [122] that allows the preparation of $CoFe_2O_4$ nanoparticles dispersed in an amorphous silica matrix, with different particle sizes ranging from approximately 3 to 30 nm. The main advantages of this procedure are: (i) the simplicity, inexpensive precursors and short preparation time; (ii) the interesting textural properties of the amorphous silica matrix; (iii) a good control of particle size distribution; and (iv) a very low inversion degree (see below) which is independent of particle size, in the range of 7 to 30 nm. Through a careful choice of precursors and a systematic structural, morphological and magnetic characterization, a good correlation was obtained between the synthesis, structure and physical properties of the materials.

The synthetic procedure combines the traditional sol–gel technique (hydrolysis and condensation of alkoxide precursors; see Section 12.3.1.2) with the sol–gel nitrate–citrate autocombustion method. TEOS was used as a precursor for SiO_2, whereas metal nitrates ($Fe(NO_3)_3 \cdot 9H_2O$ and $Co(NO_3)_2 \cdot 6H_2O$) and citric acid (CA) were used as precursors for the $CoFe_2O_4$ nanoparticles. The iron and cobalt nitrates, in a 2 : 1 molar ratio, were dissolved in water and CA was added to the solution with a 1 : 1 molar ratio of metals (Co^{II} + Fe^{III}) to CA. Liquid ammonia was added dropwise to the aqueous solution so as to adjust the pH value to 2. A suitable amount of TEOS in ethanol was then added to the aqueous solution; the resultant mixture was clear and did not exhibit any phase separation. It should be noted that the addition of ethanol decreases the solubility of the metal–citrate complex, leading to phase separation. In the diluted samples, the amounts of salt and CA were then decreased, and consequently the amounts of TEOS and ethanol were increased. After vigorous stirring for 30 min, the sols were poured into Teflon beakers and allowed to gel in an oven, in static air at 40 °C, for 24 h. TGA of the gels showed that the decomposition of the precursors was complete at temperatures between 200 °C and 230 °C, and on this basis the gels were submitted to thermal treatment at 300 °C in a preheated oven. The gels, following the elimination of large amounts of gases, were burnt through a self-propagating combustion process, leading directly to $CoFe_2O_4/SiO_2$ nanocomposites (samples as-prepared). Elemental analyses confirmed the nominal composition and an iron : cobalt molar ratio of 2, which was within the experimental error (ca. 2%). By combining the autocombustion method with appropriate thermal treatments (between 100 °C and 900 °C), a wide variety of samples have been prepared in which the magnetic properties are finely modulated. In the following subsection, the $(CoFe_2O_4)_x(SiO_2)_{1-x}$ samples as-prepared, with $x = 50$, 30, 15, 10, and 5, are indicated by the acronyms N50, N30, N15, N10, and N5, respectively. In the thermally treated samples, the suffix "*Y*" (Y = 100, 200, ... 900), indicating the treatment temperature, will be added.

In order to show the good correlation obtained between synthesis, structure and magnetic properties, a more detailed description is given for N15, N30 and N50

samples treated at 900 °C, as examples [59]. The XRD patterns showed the presence of the main reflections attributable to the cubic cobalt ferrite phase, superimposed to an amorphous silica halo [45]. No other phase has been detected, thus confirming the stabilizing effect on the $CoFe_2O_4$ phase of the silica matrix, with respect to thermal treatments. TEM investigations allow a highlighting of the effect of the matrix on nanoparticle morphology and particle size distribution. HR-TEM images of the N50_900 and N15_900 samples showed the irregular morphology of the particles for samples with the highest ferrite concentration, and the spherical morphology of the nanocrystals for the diluted samples. The particle size distribution, obtained via TEM images, is well fitted with a log-normal function (Figure 12.8a). The increase in silica content leads to a reduction of $<D>$, and to a sharper particle size distribution.

The magnetic properties have been studied by both static magnetization measurements and Mössbauer spectroscopy. Measurements of magnetization as a function of temperature, carried out using the TRM procedure, showed in all samples that M_{TRM} decreased with increasing temperature, and for N15_T900 and N30_T900 vanished above 108 K and 180 K, respectively. In contrast, N50_T900 showed a nonzero value for the whole temperature range, indicating that the largest particles were blocked, even at room temperature. For an assembly of noninteracting particles, the derivative of M_{TRM} with respect to temperature provides an estimate of the anisotropy energy barrier distribution (Figure 12.8b). The decrease in ferrite contents leads to a more regular distribution of the anisotropy

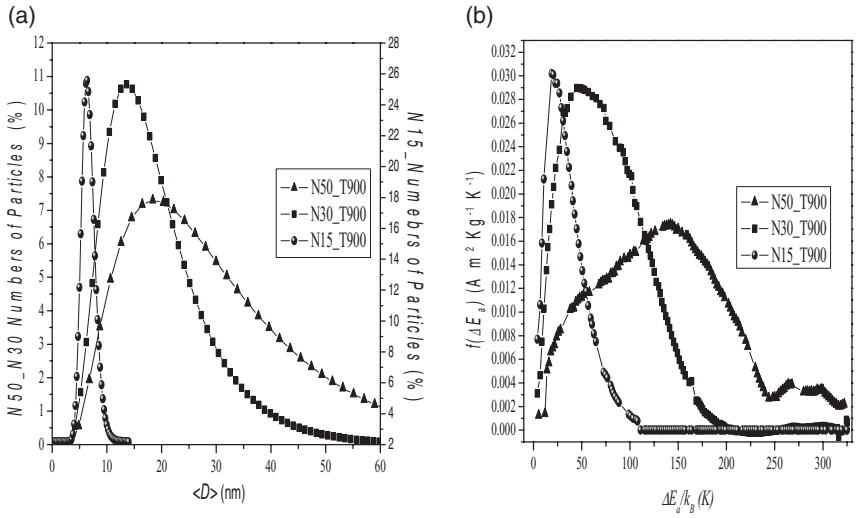

Figure 12.8 (a) Log-normal fits of particles size distribution for the samples N50_T900; N30_T900; N5_T900; (b) Distribution of magnetic anisotropy extracted from thermoremanent magnetization measurements.

energy barriers that increasingly approach a log-normal function. These data are in perfect agreement with the TEM measurements, showing that control of the nanoparticle morphology, size and size distribution is reflected in the control of distribution of magnetic anisotropy and, in turn, of the magnetic behavior.

The magnetic properties of $CoFe_2O_4$ are heavily dependent on the distribution of the iron and cobalt ions in the *A* and *B* sites. As a rule, even small changes in the cationic distribution can result in substantial changes of magnetic moments and of the magnetic anisotropy [123]. The Mössbauer spectra of ferrites in high applied fields may allow a more reliable distinction to be made between the *A*- and *B*-site components than the zero-field spectra, because the applied field usually is added to the *A*-site hyperfine field and subtracted from the *B*-site hyperfine field. Therefore, there is less overlap between the two components in the high-field spectra. Furthermore, such spectra can also provide information about the magnetic structure. The Mössbauer spectra of the samples N15_T900, N30_T900 and N50_T900, all obtained with a magnetic field of 6 T applied parallel to the gamma-ray direction, showed (as expected) that the spectra are clearly resolved into two main six-line components. Lines 2 and 5 have nonzero intensity, which suggests a noncollinear spin structure (spin-canting); that is, some of the spins are not aligned parallel or antiparallel to the external magnetic field. Usually, bulk cobalt ferrite has a partially inverse structure, where the ratio between the iron atoms in *A* and *B* sites (α) has been found to vary from 0.6 to 0.87, depending on the thermal history of the sample [55]. In nanoscaled particles, α value has been found lower, in the range 0.67 [64, 124] to 0.5 [125], depending on the methods of synthesis. All of the samples investigated in this report showed α-values of approximately 0.36.

The near-constant value of α for all samples is a very important result, because a reduction of the dimension usually leads to a modification of the inversion degree, and consequently to a variation in the magnetic properties. Instead, the sol–gel autocombustion synthesis allows $CoFe_2O_4$ nanoparticles to be obtained with a cationic distribution that is independent of the particle size, over a wide range of dimensions (7–28 nm).

In order to evaluate the effect of cationic distribution on magnetic anisotropy energy, a value of anisotropy constant (*K*) was extracted from Mössbauer spectra at low temperatures [45]. The obtained *K*-values were considerably smaller than the bulk values for $CoFe_2O_4$ ($1.8 - 3.0 \times 10^5\,J\,m^{-3}$) [123]. This was rather surprising, because the magnetic anisotropy usually is larger in nanoscaled particles [100, 126, 127]. The lower anisotropy in the present samples could be explained by the lower value of α in the nanoparticles. A reduction in magnetic anisotropy due to a high percentage of Co^{2+} in the tetrahedral sites has been observed earlier [128]. This can be explained by the smaller single ion anisotropy of Co^{2+} located in tetrahedral sites (-79×10^{-24} J per ion) compared to Co^{2+} in octahedral sites ($+850 \times 10^{-24}$ J per ion) [129, 130].

In conclusion, the one-pot, auto-combustion preparation of ferrite–silica nanocomposites allows ferrites to be obtained with a cationic distribution between the *A* and *B* sites of the spinel structure, independent of the particle size and over a

wide range of dimensions (7–28 nm). This is a very important result because normally, a reduction in dimensions leads to a modification of the inversion degree, and consequently to a variation in the magnetic properties.

12.4.3.2 Ordered Mesoporous γ-Fe_2O_3/SiO_2 Nanocomposites

Recently, ordered mesoporous silica (OMS) materials have received much attention due to their superior properties, high surface area, large pore volume, uniform pore size, and tunable surface functional groups. OMS materials are considered to be promising host materials for different doping agents, such as magnetic nanocrystals [131]. The derived composites have shown attractive potential applications in sensor, catalysis and biomedicine. In catalysis, these nanocomposites provide not only large surface areas for the high loading of catalysts, but also an ability to be easily separated from reaction mixtures simply by applying a magnetic field. In biomedicine, iron oxide/OMS nanocomposites may open new opportunities for the generation of multifunctional platforms, possibly applied in complicated situations such as site-selective and controlled drug release [74].

Recently, Wang and coworkers [74] proposed a low-cost, one-step sol–gel approach for preparing ordered magnetic mesoporous nanocomposites. The method allows the preparation, under weakly acidic conditions, of γ-Fe_2O_3/SiO_2 nanocomposites with two-dimensional hexagonal (P6 mm) and three-dimensional cubic (Im3 m) mesostructures. This general synthesis strategy, which is based on an evaporation-induced self-assembly (EISA) process, employs a commercially available nonionic surfactant P123 (the triblock copolymer of poly-ethylene oxide) or F127 (a di-functional block copolymer surfactant terminating with hydroxyl groups; see Section 12.3.2.2) for the synthesis of nanocomposites with P6 mm and Im3 m, respectively. For the synthesis, calculated amounts of surfactant and iron nitrate $Fe(NO_3)_3 \cdot 9H_2O$ were dissolved in ethanol and stirred for 2 h. The pH value of the resultant homogeneous solution was in the range of 0.4–1.8. TEOS was then added to the mixture, which was stirred for 1 h. The resultant homogeneous solution was transferred to Petri dishes and the solvent allowed to evaporate at room temperature for 1–2 days; this resulted in a rigid gel that was dried at 80 °C for 12 h to remove any residual ethanol. Finally, the as-prepared bulk samples were calcined at 550 °C in air for 5 h, at a heating rate of 1 °C min^{-1} to pyrolyze the metal nitrate and remove the surfactant. Samples with different n_{Si}/n_{Fe} molar ratios were prepared. As an example, in the following subsection, the structural, textural and magnetic properties of γ-Fe_2O_3/SiO_2 nanocomposites with 2-D hexagonal mesostructures and n_{Si}/n_{Fe} molar ratios of 9 : 1 (PMM-10), 8 : 2 (PMM-20), and 7 : 3 (PMM-30) in the initial precursor mixture are discussed.

The small-angle XRD patterns showed, for both PMM-10 and PMM-20, one sharp diffraction peak and two weak diffraction peaks at higher angles, which were characteristic of a 2-D hexagonal mesostructure of space group P6mm. The diffraction peak intensity decreased with decreasing n_{Si}/n_{Fe} ratio, which suggested that the higher amount of iron incorporation in the mesoporous materials might reduce the degree of long-range structural order. It is important to note that a broad diffraction peak was still observed in sample PMM-30, indicating that some

regular mesostructure was present also for a high percentage of iron oxide. The wide-angle XRD patterns indicated, for the PMM-10 sample, the presence of ultrasmall iron oxide nanoparticles of poor crystallinity. For the samples PMM-20 and PMM-30, the reflections corresponding to γ-Fe_2O_3 crystallite were more evident due to a larger domain size (ca. 7.5 nm and 11 nm, as estimated from the Debye–Scherrer equation for PMM-20 and PMM-30, respectively,). Although pure γ-Fe_2O_3 usually converts to antiferromagnetic α-Fe_2O_3 above 350 °C, the amorphous silica matrix hinders the transformation, thus stabilizing the γ-phase, even when the samples are heated to 550 °C [119, 132]. Transmission electron microscopy confirmed, for all samples, the presence of a highly ordered mesostructure in which the γ-Fe_2O_3 nanoparticles were homogeneously dispersed, with fewer larger particles aggregated together. When the N_2 sorption isotherms and textural properties of the PMM-10, PMM-20 and PMM-30 samples were reported, all showed a mesoporous structure with a very uniform pore size. The surface area and pore volumes were slightly decreased, while the pore size distribution was broadened by increasing the iron content. These data indicate that the pore uniformity decreases, especially for PMM-30.

Magnetic properties have been investigated on both PMM-10 and PMM-20 samples. For example, the thermal dependence of magnetization were measured with ZFC and FC protocols under an external magnetic field of 100 Oe. The ZFC curve of PMM-10 exhibited a relatively narrow peak, with a mean blocking temperature around 47 K. The continuous increase in the FC curve with decreasing temperature provided the first qualitative suggestion regarding magnetic interparticle interactions, and indicated that these were weak in both samples. For the PMM-20 sample, the ZFC curve showed a broad maximum at approximately 170 K, while the FC curve remained almost constant below T_{max}. The higher value of the blocking temperature, and the relatively broad ZFC cusp in this sample, could be ascribed to a larger nanoparticle size and particle size distribution. Hysteresis loops recorded at 5 K and magnetic parameters extracted from these measurements (coercive field and saturation magnetization) are reported. The increase in coercivity can be ascribed to an increase in anisotropy, which in turn was due to the increase in the surface contribution of smaller particles. In contrast, the decrease in saturation magnetization may be mainly ascribed to the poor crystallinity in the smaller particles. The results can be rationalized on the basis of a direct correlation between the magnetic properties and the morphological features (particle size and particle size distribution) of the nanocomposites.

In the report made by Wang and coworkers, some experimental data were also presented which clearly indicated that γ-Fe_2O_3/OMS nanocomposites are suitable either for loading drugs with larger molecular size, or for magnetic drug targeting.

12.4.3.3 Fe_3O_4/Polymethylmethacrylate

Polymers have traditionally been considered to be excellent host matrices for composite materials. Indeed, the fixing of magnetic particles into a polymer matrix prevents particle agglomeration, increases resistance to chemical reactions,

and also provides control over the interparticle spacing, particle size and particle size distribution. In addition, the magnetic/polymer nanocomposites combine polymer and mechanical functionality with that of the magnetic inclusion [2, 133]. Recently, Kumar and coworkers [134] synthesized Fe_3O_4/polymer nanocomposites and tested these materials as drug delivery systems with multiple controls (magnetically and thermally induced controlled delivery). In particular, these studies focused on the release of fluorescein isothiocyanate (FITC) from poly(methylmethacrylate) (PMMA). PMMA was selected as the polymer for the controlled release, not only because it is biocompatible, but also because several drug delivery systems have already been developed that utilize PMMA for the release of a variety of drugs, in many different applications.

In order to prepare Fe_3O_4/PMMA, magnetic Fe_3O_4 nanoparticles were dispersed in methanol and added step-wise to a PMMA-FITC solution. When all of the magnetic nanoparticles had been added, the polymer mixture was spread onto the flask surface. To increase the thickness of the mixture, some of the methanol was allowed to evaporate by slowly stirring under a flow of nitrogen for 30 min. The composite was finally dried under a nitrogen flow over several hours.

The measured amount of iron in magnetite/PMMA was 23.3%, and the calculated magnetite content in magnetite/PMMA was 32.2%.

The magnetite nanoparticles were roughly spherical in shape, appeared agglomerated in TEM images, and demonstrated a broad particle size distribution and an average diameter of approximately 11 nm. The magnetite/PMMA nanocomposites appeared flat, with a thickness less than 250 nm.

Hysteresis loops recorded at high temperature (300 K) and low temperature (10 K) for Fe_3O_4 and Fe_3O_4/PMMA samples have been reported. A lack of hysteretic behavior at 300 K indicated that both samples were in the superparamagnetic state at this temperature. At low temperature, both samples showed a hysteretic behavior, with the nanoparticles embedded in the polymer showing a higher coercivity compared to unsupported nanoparticles. This difference can be ascribed to a decrease in the magnetic interparticle interactions in the Fe_3O_4/PMMA due to the presence of the polymer host matrix. Indeed, the presence of strong interparticle interactions can induce a decrease in coercivity [135, 136]. Finally, by highlighting the thermally controlled release of FITC from Fe_3O_4/PMMA, the authors have demonstrated the potential of this system for applications in drug delivery.

12.4.4
Iron Oxide Nanowires and Nanotubes

Magnetic 1-D structures continue to attract intense attention, notably because their high anisometric shape contributes to an increase in their magnetic anisotropy, providing them with great appeal in different fields as magnetic storage, gas sensor, and spintronic devices, as well as in biomedical applications. Whereas, a number of different preparation methods, mostly using solid or soluble templates, have been developed to prepare iron oxide nanowires and nanotubes, there remains much to do with regards to the comprehension of their magnetic behav-

ior. Here, the details of two examples are reported: one example relates to item and magnetite particle nanowires, and the other to magnetite nanowires and maghemite nanotubes. Both demonstrate the correlation between anisometric shape and magnetic behavior.

12.4.4.1 Fe_3O_4 Nanowires

Magnetite (Fe_3O_4) wires were prepared by Yang et al. [137] by the controlled oxidation of iron (Fe) nanowires, acting as solid templates. The Fe wires were synthesized by the thermal decomposition at 300–400 °C of iron pentacarbonyl ($Fe(CO)_5$), on glass or silicon substrates placed on a heating plate that was held between permanent magnetic poles. The magnetic field was approximately 1000 Oe, and the system was evacuated to approximately 10 mTorr before the deposition process. The $Fe(CO)_5$ was then decomposed into Fe atoms and CO and, by subsequent nucleation and growth processes, the Fe particles were formed. With aid from the magnetic field, the Fe particles were then assembled as isoaligned wires on the substrate. By using different deposition times and temperatures, Fe wires with diameters ranging from 30 to 1000 nm were formed. The thickest wires comprised bundles of thin wires, and lengths of up to several centimeters were assembled. Magnetite (Fe_3O_4) nanowires were then formed by annealing the as-prepared Fe wires in air at 400 °C for 24 h, followed by treatment in a N_2/alcohol atmosphere for 1 h. The diameter of the thin Fe_3O_4 wire was approximately 90 nm, the wires being composed of fine particles with different crystalline orientations.

The magnetization curves versus temperature and hysteresis loops of the as-prepared Fe and Fe_3O_4 wires were performed using a SQUID magnetometer at 300 and 5 K. The small kink at 125 °C observed in the ZFC curve of Fe wires was ascribed to the Vervey transition temperature of Fe_3O_4 [138], as confirmed by its presence in the ZFC-FC curves of Fe_3O_4 wires. The Vervey transition, which is peculiar to the magnetite phase, originates from a fast electron hopping process between Fe^{3+} and Fe^{2+} ions in the B sites of the ferrite [138]. Its presence suggests that a thin layer of magnetite is formed on the Fe wires, and that a core–shell structure of Fe/Fe_3O_4 may be obtained. Moreover, it is worth noting that the sharpness of the Vervey transition observed for the Fe_3O_4 wires indicates the formation of single-phase magnetite. The Fe_3O_4 wires have coercivities of 261 and 735 Oe along the wire direction at 300 and 5 K, respectively. The remanence ratios, M_r/M_s, were approximately 0.30 and 0.25 in the parallel and perpendicular directions, respectively. The large increase in coercivity at 5 K has also been ascribed to the contribution of the Vervey transition to the magnetic anisotropy.

It should be noted that the ferromagnetic behavior observed at room temperature by the Fe_3O_4 nanowires is mostly ascribed to the increased magnetic anisotropy due to the anisotropy shape contribution of the nanowires.

12.4.4.2 Fe_3O_4 Nanowires and γ-Fe_2O_3 Nanotubes

For the synthesis of magnetite (Fe_3O_4) and maghemite (γ-Fe_2O_3) nanowires and nanotubes, Suber and coworkers [139] have used, as solid templates, nanoporous

polycarbonate and alumina membranes. The method, which was developed by Martin [140], has the major advantage of obtaining a material (the porous membrane) containing in the pores nanowires or nanotubes, all aligned perpendicularly to the membrane plane. In this way, by orienting the membrane plane with respect to the direction of the externally applied field, it is possible to study the effect of their anisometric shape on the magnetic properties. The wires and tubes have a high aspect ratio, as determined by the diameter of the pores and the thickness of the membrane. In this case, the polycarbonate and alumina membranes contained uniformly distributed cylindrical pores with diameters of 20 and 200 nm and thickness of 6 and 60 μm, respectively.

Two different preparation methods have been used – one for the nanowires, and the other for the nanotube structures. Magnetite particle nanowires have been prepared by immersing an alumina nanoporous membrane (pore diameter 20 nm) in a $(CH_3)_4NNO_3$ aqueous solution, adding dropwise a solution of $FeCl_3$ and $FeCl_2$, and then maintaining the pH at 12 by the dropwise addition of a $(CH_3)_4NOH$ solution. A black precipitate of magnetite spherical nanoparticles with a mean diameter of 9 nm was formed inside the membrane pores and due to the hydrolysis and polymerization of the iron ions (see Section 12.3.1.1).

Magnetization versus temperature measurements (Figure 12.9a,b) show the typical features (maximum of ZFC magnetization, low-temperature splitting between FC and ZFC curves) of an assembling of magnetic nanoparticles. By applying the external field either perpendicularly (Figure 12.9a) or parallel (Figure 12.9b) to the wire main axis, a different magnetic behavior is observed,

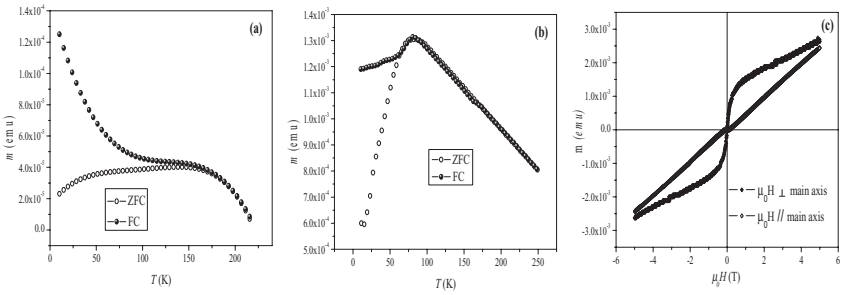

Figure 12.9 Temperature-dependence of ZFC and FC magnetization of magnetite particle nanowires with the applied magnetic field $\mu_0\mathbf{H}$ = 10 mT aligned (a) perpendicularly and (b) parallel to the main axis of the wire; (c) Hysteresis loops for γ-Fe_2O_3 tubes at T = 200 K with the magnetic field aligned both perpendicular and parallel to the main tube axis.

which is attributed entirely to the anisometric wire shape. Interestingly, the main interaction governing the magnetic behavior differs above and below the temperature of the ZFC curve maximum (see Section 12.2.3.1) In fact, T_{max} shifts towards higher values when the external field is applied perpendicular to the wire long axis, most likely due to a stronger interaction between the particles of *neighbor nanowires*, whereas, below T_{max} the magnetic behavior observed in the FC curves is mainly governed by dipolar interactions between nearest particles *in the nanowire*.

In the second case, maghemite nanotubes have been prepared by using the sol–gel method (see Section 12.3.1.2). An alumina membrane (pore diameter 200 nm) was immersed in a degassed ethyl alcohol solution constituted by iron (II) acetyl acetonate and CA. After evaporation of the solvent, the membrane was dried and thermally treated up to 270 °C. The different hysteresis loops were obtained by applying an external magnetic field perpendicular and parallel to the tube long axis (Figure 12.9c) which, in this case, also clearly indicated the existence of a magnetic perpendicular anisotropy. Moreover, the magnetization measurements were capable of distinguishing the contribution due to magnetic interactions between particles in the *same wire* from that due to magnetic interactions between particles in *different wires*. In this regard, the nanoporous membranes can be seen as excellent templates for tuning the second contribution, making it possible to obtain iso-aligned magnetic wires and tubes with controlled interwire or intertube distances.

12.4.4.3 Fe_3O_4 and γ-Fe_2O_3 Tube-in-Tube Nanostructures

The design and preparation of complex tube-in-tube nanostructures appears to be a major challenge, due to the potential for obtaining new or increased magnetic properties that derive both from the anisometric tubular shape and from the very high surface-to-volume aspect ratio. The first of these methods appears to involve the creation of a single-crystalline tube-in-tube nanostructure of magnetic iron oxides by a one-step solution method [93].

Both, magnetite and maghemite tube-in-tube nanostructures were obtained using the hydrothermal coordination-assisted method presented in Section 12.3.3.2. Hematite (α-Fe_2O_3) spindle-like particles are initially formed by the reaction of a $FeCl_3$ solution in the presence of $NH_4H_2PO_4$. The spindle-like form results from a coordination of phosphate ions along preferential hematite crystalline faces. Further hydrothermal reaction under acidic conditions causes the spindle tips, due to the strong interaction with the protons in solution, to promote a controlled dissolution of the iron oxide from the tips towards the particle inside (as illustrated in Figure 12.5e; see also Section 12.3.3.2) forming the tube-like shape. When the reaction is performed also in the presence of Na_2SO_4, the coupled coordination effect of phosphate and sulfate ions induces the formation of two types of precursor, a large amount of spindle-like particles, and a few ellipsoids. In the case of the ellipsoid precursors, their relatively flat tops make it possible for the dissolution to occur not only at the centered tips, but also (simultaneously) at several high-energy sites on the top, and this is confirmed by the presence of

intermediates with multiconcave sites on the tops. With an increase in the reaction time, the neighboring holes merge either partially to create tube-in-tube structures, or completely to form a single nanotube. The magnetite and maghemite tube-in-tube structures are then prepared either by reduction (under a hydrogen/argon gas flow at 300 °C for 5 h) or reduction and reoxidation (by exposing the sample in air at 240 °C for 2 h) using hematite tube-in-tube structures as precursors (Figure 12.10a,b). The transformation to magnetite and maghemite phases is complete, as no peaks of hematite phase precursor are observed in the XRD patterns. Conversely, it is difficult to distinguish between magnetite and maghemite only on the basis of the XRD patterns due to the same spinel structure and similar lattice parameters (Figure 12.10c). Raman spectroscopy represents, for this purpose, a very useful tool. In Figure 12.10d, the Raman spectra show the characteristic bands of magnetite and maghemite, confirming that the nanostructures shown in Figure 12.10a and b can be ascribed to pure magnetite and maghemite, respectively.

The magnetic properties of maghemite and magnetite tube-in-tube structures were also investigated. The temperature-dependence of the magnetization

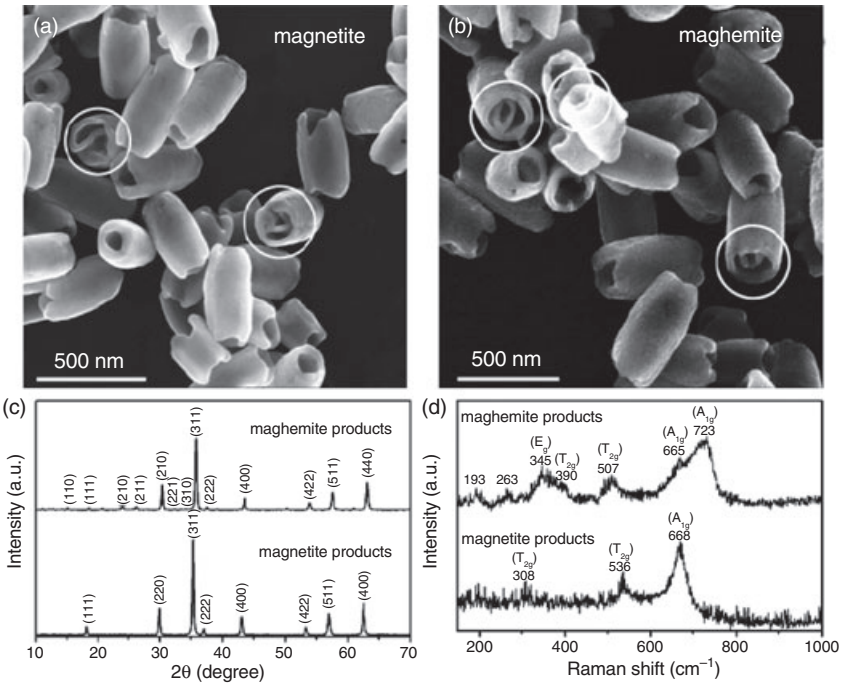

Figure 12.10 Scanning electron microscopy images of (a) magnetite and (b) maghemite products; (c) X-ray diffraction patterns; (d) Raman spectra. The tube-in-tube structures are marked with circles in panels (a) and (b).

measured with ZFC and FC of the two nanostructures measured at an applied field of 10 Oe has been reported. Magnetite shows, in the ZFC curve, a visible magnetic transition at 119 K; this corresponds to the Vervey transition that originates from a fast electron hopping process between Fe^{3+} and Fe^{2+} ions in the B site of the ferrite [138]. The Vervey transition is peculiar to the magnetite phase, and the fact that it is not observed in the ZFC curve of maghemite further confirms the Raman data – that is, that the two tube-in-tube structures are formed by pure maghemite and magnetite phases. The coercivity at 300 K was 210 and 170 Oe, and the saturation magnetization 90 and 70 emu g^{-1} (for the magnetite and maghemite structures, respectively). The measured values of M_s were only a little lower with respect to the bulk values, indicating the absence of any magnetic disorder in these nanostructures. These results show great promise for the application of these tube-in-tube structures in different fields, ranging from catalysis to drug delivery [23].

12.5 Conclusions and Perspectives

In this chapter, based on the experimental results described in Section 12.4, we have attempted to outline the interplay between the magnetic properties and the chemical composition, structure and morphology of magnetic nanostructured iron oxides.

We have endeavored to illustrate that preparation methods have a relevant influence – which is often undervalued – on such parameters. In fact, on the basis of recently devised chemical preparation methods, our understanding of magnetic behavior at the nanoscale has made remarkable progress in the past few years. These improvements in synthetic methods derive mainly from: (i) the ability to combine two or more classical methods (e.g., sol–gel and autocombustion, thermal decomposition and coprecipitation); and (ii) the use of surfactants and complex organic molecules, such as liquid crystals. This has led not only to the control of particle size and size distribution, but also more recently to the use of soluble templates in the fabrication of 1-D nanostructures and microstructures. Such structures are capable of binding reversibly to nanocrystals so as to produce organic–inorganic structures with size and shape specificities that can serve as hybrid building blocks in aggregation-based pathways of crystal growth.

It has been shown how shape anisotropy – by modifying magnetic anisotropy – can alter the magnetic behavior of these materials. Clearly, in the foreseeable future, organic chemistry and biochemistry will take on a fundamental role in the creation of 1-D, 2-D and 3-D ordered magnetic nanostructures. Moreover, as the need for organic and biological molecules in the assembly of such complex structures becomes apparent, biochemists, organic and inorganic chemists will need to share their talents. The result may be a series of well-ordered magnetic nanomaterials which, when assembled into nanodevices, might be used to control and perform highly sophisticated functions.

List of Abbreviations

E_A	Magnetic anisotropy energy
H_c	Coercive field
J_{ij}	Exchange integral
M_s	Saturation magnetization
M_r	Remanent magnetization
M_r/M_s	Reduced remanent magnetization
T_B	Blocking temperature
T_C	Curie temperature
T_N	Néel temperature
V_p	Particle volume
γ	Inversion degree
α	ratio of Me^{III} ions in A and B sites
K	Anisotropy constant
k_B	Boltzmann constant
τ_m	Experimental measuring time
τ	Superparamagnetic relaxation time
τ_0	Relaxation time constant
T_{irr}	Irreversibility temperature in ZFC/FC curves.
μ_a	Atomic magnetic moment

References

1 Gleiter, H. (1992) Materials with ultrafine microstructures: retrospectives and perspectives. *Nanostructured Materials*, **1**, 1.

2 Leslie-Pelecky, D.L. and Rieke, R.D. (1996) Magnetic Properties of nanostructured materials. *Chemistry of Materials*, **8**, 1770–83.

3 Fiorani, D. and Dormann, J.L. (eds) (1992) Magnetic properties of fine particles. Conference Proceedings, Rome, Italy, 1991.

4 Rondinone, A.J. and Zhang, Z.J. (2000) *Magnetic Characterization*, Tsinghua University Press and Springer-Verlag, New York.

5 Siegel, R.W. (1993) Synthesis, structure and properties of nanostructured materials, in Conference Proceedings of Fundamental Properties of Nanostructured Materials, Rimini, Italy (eds G. Sberveglieri and D. Fiorani), World Scientific, Singapore.

6 Dormann, J.L., Fiorani, D. and Tronc, E. (1997) *Advanced in Chemical Physics*, Vol. XCVIII, John Wiley & Sons, Inc.

7 Chang, M.-T., Chou, L.-J., Hsieh, C.-H., Chueh, Y.-L., Wang, Z.L., Murakami, Y. and Shindo, D. (2007) Magnetic and electrical characterizations of half-metallic Fe_3O_4 nanowires. *Advanced Materials*, **19**, 2290–4.

8 Liu, Z., Zhang, D., Han, S., Li, C., Lei, B., Lu, W., Fang, J. and Zhou, C. (2005) Single crystalline magnetite nanotubes. *Journal of the American Chemical Society*, **127**, 6–7.

9 Zhang, D., Liu, Z., Han, S., Li, C., Lei, B., Stewart, M.P., Tour, J.M. and Zhou, C. (2004) Magnetite (Fe_3O_4) core-shell nanowires: synthesis and magnetoresistance. *Nano Letters*, **4**, 2151–5.

10 Solzi, M. (1993) Magnetic anisotropy in nanostructured materials, in Conference Proceedings of Fundamental Properties

of Nanostructured Materials, Rimini, Italy (eds G. Sberveglieri and D. Fiorani), World Scientific, Singapore.
11 Marzan, L.M.L. (2006) (Non Carbon) Anisotropic nanomaterials. *Journal of Materials Chemistry*, **16**, 3891–2.
12 Chen, J.P., Sorensen, C.M., Klabunde, K.J. and Hadjipanayis, G.C. (1994) Magnetic properties of nanophase cobalt particles synthesized in inversed micelles. *Journal of Applied Physics*, **76**, 6316–18.
13 Khanna, S.N. and Linderoth, S. (1991) Magnetic behavior of clusters of ferromagnetic transition metals. *Physical Review Letters*, **67**, 742.
14 Goldfarb, R.B. and Patton, C.E. (1981) Superparamagnetism and spin-glass freezing in nickel-manganese alloys. *Physical Review B*, **24**, 1360.
15 Ennas, G., Falqui, A., Marras, S., Sangregorio, C. and Marongiu, G. (2004) Influence of metal content on size, dispersion, and magnetic properties of iron-cobalt alloy nanoparticles embedded in silica matrix. *Chemistry of Materials*, **16**, 5659–63.
16 Ennas, G., Falqui, A., Paschina, G. and Marongiu, G. (2005) Iron-cobalt alloy nanoparticles embedded in an alumina xerogel matrix. *Chemistry of Materials*, **17**, 6486–91.
17 Liu, C., Zou, B., Rondinone, A.J. and Zhang, Z.J. (2000) Chemical control of superparamagnetic properties of magnesium and cobalt spinel ferrite nanoparticles through atomic level magnetic couplings. *Journal of the American Chemical Society*, **122**, 6263–7.
18 Zhang, Z.J., Wang, Z.L., Chakoumakos, B.C. and Yin, J.S. (1998) Temperature dependence of cation distribution and oxidation state in magnetic Mn-Fe ferrite nanocrystals. *Journal of the American Chemical Society*, **120**, 1800–4.
19 Rondinone, A.J., Samia, A.C.S. and Zhang, Z.J. (1999) Superparamagnetic relaxation and magnetic anisotropy energy distribution in $CoFe_2O_4$ spinel ferrite nanocrystallites. *Journal of Physical Chemistry B*, **103**, 6876–80.
20 Liu, C., Zou, B., Rondinone, A.J. and Zhang, Z.J. (2000) Reverse micelle synthesis and characterization of superparamagnetic $MnFe_2O_4$ spinel ferrite nanocrystallites. *Journal of Physical Chemistry B*, **104**, 1141–5.
21 Vestal, C.R. and Zhang, Z.J. (2003) Synthesis and magnetic characterization of Mn and Co spinel ferrite-silica nanoparticles with tunable magnetic core. *Nano Letters*, **3**, 1739–43.
22 Katz, E. and Willner, I. (2004) Integrated nanoparticle-biomolecule hybrid systems: synthesis, properties, and applications. *Angewandte Chemie, International Edition in English*, **43**, 6042–108.
23 Pankhurst, Q.A., Connelly, J., Jones, S.K. and Dobsonb, J. (2003) Applications of magnetic nanoparticles in biomedicine. *Journal of Physics D: Applied Physics*, **36**, R167–81.
24 Tartaj, P., Del Puerto Morales, M., Veintemillas-Verdaguer, S., Gonzales Carreno, T. and Serna, C.J. (2003) The preparation of magnetic nanoparticles for applications in biomedicine. *Journal of Physics D: Applied Physics*, **36**, R182–97.
25 Vékas, L., Bica, D. and Avdeev, M.V. (2007) Magnetic nanoparticles and concentrated magnetic nanofluids: synthesis, properties and some applications. *China Particuology*, **5**, 43–7.
26 Reiss, G. and Hutten, A. (2005) Applications beyond data storage. *Nature Materials*, **4**, 725–6.
27 Park, J., Joo, J., Kwon, S.G., Jang, Y. and Hyeon, T. (2007) Synthesis of monodisperse spherical nanocrystals. *Angewandte Chemie, International Edition in English*, **46**, 4630–60.
28 Hyeon, T. (2003) Chemical synthesis of magnetic nanoparticles. *Chemical Communications*, **8**, 927–34.
29 Blundell, S. (2003) *Magnetism in Condensed Matter*, Oxford University Press, New York.
30 Crangle, J. (1991) *Solid State Magnetism*, Great Britain Edward Arnold, London.
31 Della Torre, E. (1999) *Magnetic Hysteresis*, IEEE Press, New York.
32 Patzke, G.R., Krumeich, F. and Nesper, R. (2002) Oxidic nanotubes and nanorods – anisotropic modules for a

future nanotechnology. *Angewandte Chemie, International Edition in English*, **41**, 2446–61.

33 Bødker, F., Mørup, S. and Linderoth, S. (1994) Surface effects in metallic iron nanoparticles. *Physical Review Letters*, **72**, 282–5.

34 Guardia, P., Batlle-Brugal, B., Roca, A.G., Iglesias, O., Morales, M.P., Serna, C.J., Labarta, A. and Batlle, X. (2007) Surfactant effects in magnetite nanoparticles of controlled size. *Journal of Magnetism and Magnetic Materials*, **316**, e756–9.

35 Kodama, R.H. (1999) Magnetic nanoparticles. *Journal of Magnetism and Magnetic Materials*, **200**, 359–72.

36 Gittleman, J.I., Abeles, B. and Bozowski, S. (1974) Superparamagnetism and relaxation effects in granular Ni-SiO_2 and Ni-Al_2O_3 films. *Physical Review B*, **9**, 3891–7.

37 Cannas, C., Concas, G., Gatteschi, D., Falqui, A., Musinu, A., Piccaluga, G., Sangregorio, C. and Spano, G. (2001) Superparamagnetic behaviour of γ-Fe_2O_3 nanoparticles dispersed in a silica matrix. *Physical Chemistry Chemical Physics*, **3**, 832–8.

38 Hansen, M.F. and Mørup, S. (1999) Estimation of blocking temperatures from ZFC/FC curves. *Journal of Magnetism and Magnetic Materials*, **203**, 214–16.

39 Chantrell, R.W., El-Hilo, M. and O'Grady, K. (1991) Spin-Glass behaviour in fine particle system. *IEEE Transactions on Magnetics*, **27**, 3570–8.

40 Vayssieres, L. (2004) On the design of advanced metal oxide nanomaterials. *International Journal of Nanotechnology*, **1**, 1–41.

41 Mathew, D.S. and Juang, R.S. (2007) An overview of the structure and magnetism of spinel ferrite nanoparticles and their synthesis in microemulsion. *Chemical Engineering Journal*, **129**, 51–65.

42 Sun, S., Zeng, H., Robinson, D.B., Raoux, S., Rice, P.M., Wang, S.X. and Li, G. (2004) Monodisperse MFe_2O_4 (M = Fe, Co, Mn) Nanoparticles. *Journal of the American Chemical Society*, **126**, 273–9.

43 West, A.R. (1984) *Solid State Chemistry and Its Applications*, John Wiley & Sons, Inc.

44 Anhøj, T.A., Bilenberg, B., Thomsen, B., Damsgaard, C.D., Rasmussen, H.K., Jacobsen, C.S., Mygind, J. and Mørup, S. (2003) Spin canting and magnetic relaxation phenomena in $Mn_{0.25}Zn_{0.75}Fe_2O_4$. *Journal of Magnetism and Magnetic Materials*, **260**, 115–30.

45 Cannas, C., Musinu, A., Piccaluga, G., Fiorani, D., Peddis, D., Rasmussen, H.K. and Mørup, S. (2006) Magnetic properties of cobalt ferrite–silica nanocomposites prepared by a sol-gel autocombustion technique. *Journal of Chemical Physics*, **125**, 164711.

46 Morrison, S.A., Cahill, C.L., Carpenter, E.E., Calvin, S. and Harris, V.G. (2005) Atomic engineering of mixed ferrite and core-shell nanoparticles. *Journal of Nanoscience and Nanotechnology*, **5**, 1323–44.

47 Cornell, R.M. and Schwertmann, U. (1996) *The Iron Oxides–Structure, Properties, Reactions, Occurrence and Uses*, VCH, Weinheim.

48 Jolivet, J.P., Cassaignon, S., Chanéac, C., Chiche, D. and Tronc, E. (2008) Design of oxide nanoparticles by aqueous chemistry. *Journal of Sol-Gel Science and Technology*, **46**, 299–305.

49 Nielsen, A.E. (1964) *Kinetics of Precipitations*, Pergamon Press, Oxford.

50 Sugimoto, T. (1987) Preparation of monodispersed colloidal particles. *Advances in Colloid and Interface Science*, **28**, 65–108.

51 Lima, J.E., Brandl, A.L., Arelaro, A.D. and Goya, G.F. (2006) Spin disorder and magnetic anisotropy in Fe_3O_4 nanoparticles. *Journal of Applied Physics*, **99**, 083908–10.

52 Herzer, G. (1989) Grain structure and magnetism of nanocrystalline ferromagnets. *IEEE Transactions on Magnetics*, **25**, 3327–9.

53 O'Handley, R.C. and Škorvánek, I. (1995) Fine-particle magnetism in nanocrystalline Fe-Cu-Nb-Si-B at elevated temperatures. *Journal of Magnetism and Magnetic Materials*, **140–144**, 467–8.

54 Baes, C.F. and Mesmer, R.E. (1976) *The Hydrolysis of Cations*, John Wiley & Sons, Inc., New York.

55 Tronc, E., Ezzir, A., Cherkaoui, R., Chanéac, C., Noguès, M., Kachkachi, H., Fiorani, D., Testa, A.M., Grenèche, J.M. and Jolivet, J.P. (2000) Surface-related properties of γ-Fe_2O_3 nanoparticles. *Journal of Magnetism and Magnetic Materials*, **221**, 63–79.

56 Haruta, M. and Delmon, B. (1986) Preparation of homodisperse solids. *Journal de Chimie Physique et de Physico-Chimie Biologique*, **83**, 859–68.

57 Jolivet, J.-P., Chaneac, C. and Tronc, E. (2004) Iron oxide chemistry. From molecular clusters to extended solid networks. *Chemical Communications*, 481–7.

58 Jolivet, J.-P., Tronc, É. and Chanéac, C. (2002) Synthesis of iron oxide-based magnetic nanomaterials and composites, *Comptes Rendus Chimie*, **5**, 659–64.

59 Jolivet, J.P., Belleville, P., Tronc, E. and Livage, J. (1992) Influence of iron(II) on the formation of the spinel iron oxide in alkaline medium. *Clays and Clay Minerals*, **40**, 531–9.

60 Tronc, E., Belleville, P., Jolivet, J.P. and Livage, J. (1992) Transformation of ferric hydroxide into spinel by iron(II) adsorption. *Langmuir*, **8**, 313–19.

61 Brinker, C.J. (1990) *Sol-Gel Science*, Academic Press, San Diego.

62 Vioux, A. (1997) Nonhydrolytic sol-gel routes to oxides. *Chemistry of Materials*, **9**, 2292–9.

63 Kumar, P. and Mittal, K.L. (1999) *Handbook of Microemulsion Science and Technology*, Marcel Dekker, New York.

64 Moumen, N., Bonville, P. and Pileni, M.P. (1996) Control of the size of cobalt ferrite magnetic fluids: Mössbauer spectroscopy. *Journal of Physical Chemistry*, **100**, 14410–16.

65 Feltin, N. and Pileni, M.P. (1997) New technique to make ferrite nanosized particles. *Journal de Physique IV*, **7**, C1/609–C601/610.

66 Feltin, N. and Pileni, M.P. (1997) New technique for synthesizing iron ferrite magnetic nanosized particles. *Langmuir*, **13**, 3927–33.

67 Chandrasekaran, G. (2007) Spectroscopic study of autocombustion process in the synthesis of nano particles of Ni-Cu ferrite. *Materials and Manufacturing Processes*, **22**, 366–9.

68 Sui, Y.C., Liu, W., Yue, L.P., Li, X.Z., Zhou, J., Skomski, R. and Sellmyer, D.J. (2005) Template mediated assembly of FePt $L1_0$ clusters under external magnetic field. *Journal of Applied Physics*, **97**, 10J304.

69 Matsushita, N., Nakagawa, K., Taniguchi, T., Handa, H., Tada, M., Abe, M. and Yoshimura, M. (2008) Hundred-nanometer sized biomagnetic beads with large magnetization using ferrite nanoparticles grown by hydrothermal process. *Journal of Applied Physics*, **103**, 07A317.

70 Prozorov, R., Yeshurun, Y., Prozorov, T. and Gedanken, A. (1999) Magnetic irreversibility and relaxation in assembly of ferromagnetic nanoparticles. *Physical Review B*, **59**, 6956–65.

71 Salkar, R.A., Jeevanandam, P., Kataby, G., Aruna, S.T., Koltypin, Y., Palchik, O. and Gedanken, A. (2000) Elongated copper nanoparticles coated with a zwitterionic surfactant. *Journal of Physical Chemistry B*, **104**, 893–7.

72 Jeevanandam, P., Koltypin, Y., Mastai, Y. and Gedanken, A. (2000) Sonochemical synthesis of lead hydroxy bromide needles. *Journal of Materials Chemistry*, **10**, 2143–6.

73 Kumar, R.V., Koltypin, Y., Xu, X.N., Yeshurun, Y., Gedanken, A. and Felner, I. (2001) Fabrication of magnetite nanorods by ultrasound irradiation. *Journal of Applied Physics*, **89**, 6324–8.

74 Wang, Y., Ren, J., Liu, X., Wang, Y., Guo, Y., Guo, Y. and Lu, G. (2008) Facile synthesis of ordered magnetic mesoporous γ-Fe_2O_3/SiO_2 nanocomposites with diverse mesostructures, *Journal of Colloid and Interface Science*, **326**, 158–65.

75 Euliss, L.E., Grancharov, S.G., O'Brien, S., Deming, T.J., Stucky, G.D., Murray, C.B. and Held, G.A. (2003) Cooperative assembly of magnetic nanoparticles and block copolypeptides in aqueous media. *Nano Letters*, **3**, 1489–93.

76 Gittins, D.I. and Caruso, F. (2001) Spontaneous phase transfer of nanoparticulate metals from organic to aqueous media. *Angewandte Chemie, International Edition in English*, **40**, 3001–4.

77 Gonzales, M. and Krishnan, K.M. (2007) Phase transfer of highly monodisperse iron oxide nanocrystals with Pluronic F127 for biomedical applications. *Journal of Magnetism and Magnetic Materials*, **311**, 59–62.

78 Freij-Larsson, C., Nylander, T., Jannasch, P. and Wesslen, B. (1996) Adsorption behaviour of amphiphilic polymers at hydrophobic surfaces: effects on protein adsorption. *Biomaterials*, **17**, 2199–207.

79 Caruso, F. (2001) Nanoengineering of particle surfaces. *Advanced Materials*, **13**, 11–22.

80 Choi, J.S., Jun, Y.w., Yeon, S.I., Kim, H.C., Shin, J.S. and Cheon, J. (2006) Biocompatible heterostructured nanoparticles for multimodal biological detection. *Journal of American Chemical Society*, **128**, 15982–3.

81 Wang, Q., Iancu, N. and Seo, D.-K. (2005) Preparation of large transparent silica monoliths with embedded photoluminescent CdSe@ZnS core/shell quantum dots. *Chemistry of Materials*, **17**, 4762–4.

82 Gerion, D., Pinaud, F., Williams, S.C., Parak, W.J., Zanchet, D., Weiss, S. and Alivisatos, A.P. (2001) Synthesis and properties of biocompatible water-soluble silica-coated CdSe/ZnS semiconductor quantum dots. *Journal of Physical Chemistry B*, **105**, 8861–71.

83 Wang, D., Cao, C., Xue, S. and Zhu, H. (2005) γ-Fe_2O_3 oriented growth by surfactant molecules in microemulsion. *Journal of Crystal Growth*, **277**, 238–45.

84 Zhao, W., Gu, J., Zhang, L., Chen, H. and Shi, J. (2005) Fabrication of uniform magnetic nanocomposite spheres with a magnetic core/mesoporous silica shell structure. *Journal of the American Chemical Society*, **127**, 8916–17.

85 Selvan, S.T., Li, C., Ando, M. and Murase, N. (2004) Formation of luminescent CdTe-silica nanoparticles through an inverse microemulsion technique. *Chemistry Letters*, **33**, 434–5.

86 He, R., You, X., Shao, J., Gao, F., Pan, B. and Cui, D. (2007) Core/shell fluorescent magnetic silica-coated composite nanoparticles for bioconjugation. *Nanotechnology*, **18**, 315601–8.

87 Piao, Y., Kim, J., Na, H.B., Kim, D., Baek, J.S., Ko, M.K., Lee, J.H., Shokouhimehr, M. and Hyeon, T. (2008) Wrap-bake-peel process for nanostructural transformation from β-FeOOH nanorods to biocompatible iron oxide nanocapsules. *Nature Materials*, **7**, 242–7.

88 Sun, C., Lee, J.S.H. and Zhang, M. (2008) Magnetic nanoparticles in MR imaging and drug delivery. *Advanced Drug Delivery Reviews*, **60**, 1252–65.

89 Daly, B., Arnold, D.C., Kulkarni, J.S., Kazakova, O., Shaw, M.T., Nikitenko, S., Erts, D., Morris, M.A. and Holmes, J.D. (2006) Synthesis and characterization of highly ordered cobalt-magnetite nanocable arrays. *Small*, **2**, 1299–307.

90 Ding, Y., Morber, J.R., Snyder, R.L. and Wang, Z.L. (2007) Nanowire structural evolution from Fe_3O_4 to ε-Fe_2O_3. *Advanced Functional Materials*, **17**, 1172–8.

91 Liao, Z.-M., Li, Y.-D., Xu, J., Zhang, J.-M., Xia, K. and Yu, D.-P. (2006) Spin-filter effect in magnetite nanowire. *Nano Letters*, **6**, 1087–91.

92 Terrier, C., Abid, M., Arm, C., Serrano-Guisan, S., Gravier, L. and Ansermet, J.P. (2005) Fe_3O_4 nanowires synthesized by electroprecipitation in templates. *Journal of Applied Physics*, **98**, 086102/086101–086102/086103.

93 Jia, C.J., Sun, L.D., Yan, Z.G., Pang, Y.C., You, L.P. and Yan, C.H. (2007) Iron oxide tube-in-tube nanostructures. *Journal of Physical Chemistry C*, **111**, 13022–7 and references therein.

94 Lee, Y., Lee, J., Bae, C.J., Park, J.G., Noh, H.J., Park, J.H. and Hyeon, T. (2005) Large-scale synthesis of uniform and crystalline magnetite nanoparticles using reverse micelles as nanoreactors under reflux conditions. *Advanced Functional Materials*, **15**, 503–9.

95 Néel, L. (1949) Théorie du trainage magnétique des ferromagnétiques en grains fins avec applications aux terres cuites. *Annales de Gèophysique*, **5**, 99–136.

96 Morales, M.A., Skomski, R., Fritz, S., Shelburne, G., Shield, J.E., Yin, M., O'Brien, S. and Leslie-Pelecky, D.L. (2007) Surface anisotropy and magnetic freezing of MnO nanoparticles. *Physical Review B*, **75**, 134423–5.

97 Peddis, D., Mansilla, M.V., Mørup, S., Cannas, C., Musinu, A., Piccaluga, G., Orazio, F., Lucari, F. and Fiorani, D. (2008) Spin-canting and magnetic anisotropy in ultrasmall $CoFe_2O_4$ nanoparticles. *Journal of Physical Chemistry B*, **112**, 8507–13.

98 Martínez, B., Obradors, X., Balcells, L., Rouanet, A. and Monty, C. (1998) Low-temperature surface spin-glass transition in γ-Fe_2O_3 nanoparticles. *Physical Review Letters*, **80**, 181–4.

99 Morales, M.P., Andres-Verges, M., Veintemillas-Verdaguer, S., Montero, M.I. and Serna, C.J. (1999) Structural effects on the magnetic properties of γ-Fe_2O_3 nanoparticles. *Journal of Magnetism and Magnetic Materials*, **203**, 146–8.

100 Linderoth, S., Hendriksen, P.V., Bødker, F., Wells, S., Davies, K., Charles, S.W. and Mørup, S. (1994) On spin-canting in maghemite particles. *Journal of Applied Physics*, **75**, 6583–5.

101 Morales, M.P., Veintemillas-Verdaguer, S., Montero, M.I., Serna, C.J., Roig, A., Casas, L., Martinez, B. and Sandiumenge, F. (1999) Surface and internal spin canting in γ-Fe_2O_3 nanoparticles. *Chemistry of Materials*, **11**, 3058–64.

102 Roca, A.G., Morales, M.P., O'Grady, K. and Serna, C.J. (2006) Structural and magnetic properties of uniform magnetite nanoparticles prepared by high temperature decomposition of organic precursor. *Nanotechnology*, **17**, 2783–8.

103 Goya, G.F., Berquo, T.S., Fonseca, F.C. and Morales, M.P. (2003) Static and dynamic magnetic properties of spherical magnetite nanoparticles. *Journal of Applied Physics*, **94**, 3520–8.

104 Bauer, A., Woelki, S. and Kohler, H.H. (2004) Rod formation of ionic surfactants: electrostatic and conformational energies. *Journal of Physical Chemistry B*, **108**, 2028–37.

105 Mann, S., Wobb, J. and Williams, R.J.P. (1989) *Biomineralization, Chemical Biomedical and Biochemical Perspectives*, VCH, Weinheim.

106 Rudloff, J. and Colfen, H. (2004) Superstructures of temporarily stabilized nanocrystalline $CaCO_3$ particles: morphological control via water surface tension variation. *Langmuir*, **20**, 991–6.

107 Tulpar, A. and Ducker, W.A. (2004) Surfactant adsorption at solid-aqueous interfaces containing fixed charges: experiments revealing the role of surface charge density and surface charge regulation. *Journal of Physical Chemistry B*, **108**, 1667–76.

108 Roy, V.A.L., Djurisic, A.B., Liu, H., Zhang, X.X., Leung, Y.H., Xie, M.H., Gao, J., Lui, H.F. and Surya, C. (2004) Magnetic properties of Mn-doped ZnO tetrapod structures. *Applied Physics Letters*, **84**, 756–8.

109 Davies, R., Schurr, G.A., Meenan, P., Nelson, R.D., Bergna, H.E., Brevett, C.A.S. and Goldbaum, R.H. (1998) Engineered particle surfaces. *Advanced Materials*, **10**, 1264–70.

110 Lu, Y., Yin, Y., Mayers, B.T. and Xia, Y. (2002) Modifying the surface properties of superparamagnetic iron oxide nanoparticles through a sol-gel approach. *Nano Letters*, **2**, 183–6.

111 Ji, X., Shao, R., Elliott, A.M., Stafford, R.J., Esparza-Coss, E., Bankson, J.A., Liang, G., Luo, Z.P., Park, K., Markert, J.T. and Li, C. (2007) Bifunctional gold nanoshells with a superparamagnetic iron oxide-silica core suitable for both MR imaging and photothermal therapy. *Journal of Physical Chemistry C*, **111**, 6245–51.

112 Andreozzi, P., La Mesa, C., Masci, G. and Suber, L. (2007) Formation and physical-chemical characterisation of silica-based blackberry-like nano-

particles capped by polysaccharides. *Journal of Physical Chemistry C*, **111**, 18004–9.

113 Stöber, W., Fink, A. and Bohn, E. (1968) Controlled growth of monodisperse silica spheres in the micron size range. *Journal of Colloid and Interface Science*, **26**, 62–9.

114 Mefford, O.T., Carroll, M.R.J., Vadala, M.L., Goff, J.D., Mejia-Ariza, R., Saunders, M., Woodward, R.C., St Pierre, T.G., Davis, R.M. and Riffle, J.S. (2008) Size analysis of PDMS-magnetite nanoparticle complexes: experiment and theory. *Chemistry of Materials*, **20**, 2184–91.

115 Zhang, Q., Thompson, M.S., Carmichael-Baranauskas, A.Y., Caba, B.L., Zalich, M.A., Lin, Y.N., Mefford, O.T., Davis, R.M. and Riffle, J.S. (2007) Aqueous dispersions of magnetite nanoparticles complexed with copolyether dispersants: experiments and theory. *Langmuir*, **23**, 6927–36.

116 Morales, M.P., Andres-Vergés, M., Veintemillas-Verdaguer, S., Montero, M.I. and Serna, C.J. (1999) Structural effects on the magnetic properties of γ-Fe_2O_3 nanoparticles. *Journal of Magnetism and Magnetic Materials*, **203**, 146–8.

117 Komarneni, S. (1992) Nanocomposites. *Journal of Materials Chemistry*, **2**, 1219–30.

118 Ahmed, S.R., Ogale, S.B., Papaefthymiou, G.C., Ramesh, R. and Kofinas, P. (2002) Magnetic properties of $CoFe_2O_4$ nanoparticles synthesized through a block copolymer nanoreactor route. *Applied Physics Letters*, **80**, 1616–18.

119 Ennas, G., Musinu, A., Piccaluga, G., Zedda, D., Gatteschi, D., Sangregorio, C., Stanger, J.L., Concas, G. and Spano, G. (1998) Characterization of iron oxide nanoparticles in an Fe_2O_3-SiO_2 composite prepared by a sol-gel method. *Chemistry of Materials*, **10**, 495–502.

120 Caizer, C. (2003) Saturation magnetization of γ-Fe_2O_3 nanoparticles dispersed in a silica matrix. *Physica B: Condensed Matter*, **327**, 27–33.

121 Peddis, D., Cannas, C., Musinu, A. and Piccaluga, G. (2008) Coexistence of superparamagnetism and spin-glass like magnetic ordering phenomena in a $CoFe_2O_4$-SiO_2 nanocomposite. *Journal of Physical Chemistry C*, **112**, 5141–7 and references therein.

122 Cannas, C., Musinu, A., Peddis, D. and Piccaluga, G. (2004) New synthesis of ferrite silica nanocomposites by a sol-gel auto-combustion. *Journal of Nanoparticle Research*, **6**, 223–32.

123 Blaskov, V., Petkov, V., Rusanov, V., Mikhov, M., Martinez, L.M., Muñoz, J.S. and Martinez, B. (1996) Magnetic properties of nanophase $CoFe_2O_4$ particles. *Journal of Magnetism and Magnetic Materials*, **162**, 331–7.

124 Chinnasamy, C.N., Jeyadevan, B., Shinoda, K., Tohji, K., Djayaprawira, D.J., Takahashi, M., Joseyphus, R.J. and Narayanasamy, A. (2003) Unusually high coercivity and critical single-domain size of nearly monodispersed $CoFe_2$ O_4 nanoparticles. *Applied Physics Letters*, **83**, 2862–4.

125 Haneda, K. and Morrish, A.H. (1988) Noncollinear magnetic structure of $CoFe_2O_4$ small particles. *Journal of Applied Physics*, **63**, 4258–60.

126 Bodker, F. and Morup, S. (2000) Size dependence of the properties of hematite nanoparticles. *Europhysics Letters*, **52**, 217–23.

127 Tung, L.D., Kolesnichenko, V., Caruntu, D., Chou, N.H., O'Connor, C.J. and Spinu, L. (2003) Magnetic properties of ultrafine cobalt ferrite particles. *Journal of Applied Physics*, **93**, 7486–8.

128 Hu, G., Choi, J.H., Eom, C.B., Harris, V.G. and Suzuki, Y. (2000) Structural tuning of the magnetic behavior in spinel-structure ferrite thin films. *Physical Review B*, **62**, R779–82.

129 Zhang, H.Y., Gu, B.X., Zhai, H.R., Lu, M., Miao, Y.Z., Zhang, S.Y. and Huang, H.B. (1994) Anisotropy and Faraday effect in Co spinel ferrite films. *Journal of Applied Physics*, **75**, 7099–101.

130 Sturge, M.D., Gyorgy, E.M., LeCraw, R.C. and Remeika, J.P. (1969) Magnetic behavior of cobalt in garnets. II. Magnetocrystalline anisotropy and

ferrimagnetic resonance of cobalt-doped yttrium iron garnet. *Physical Review*, **180**, 413.

131 Yang, H., Lu, Q., Gao, F., Shi, Q., Yan, Y., Zhang, F., Xie, S., Tu, B. and Zhao, D. (2005) One-step synthesis of highly ordered mesoporous silica monoliths with metal oxide nanocrystals in their channels. *Advanced Functional Materials*, **15**, 1377–84.

132 Zayat, M., Del Monte, F., Morales, M.P., Rosa, G., Guerrero, H., Serna, C.J. and Levy, D. (2003) Highly Transparent gamma Fe_2O_3/vycor-glass magnetic nanocomposites exhibiting faraday rotation. *Advanced Materials*, **15**, 1809–12.

133 Wilson, J.L., Poddar, P., Frey, N.A., Srikanth, H., Mohomed, K., Harmon, J.P., Kotha, S. and Wachsmuth, J. (2004) Synthesis and magnetic properties of polymer nanocomposites with embedded iron nanoparticles. *Journal of Applied Physics*, **95**, 1439–43.

134 Urbina, M.C., Zinoveva, S., Miller, T., Sabliov, C.M., Monroe, W.T. and Kumar, C.S.S.R. (2008) Investigation of magnetic nanoparticle-polymer composites for multiple-controlled drug delivery. *Journal of Physical Chemistry C*, **112**, 11102–8.

135 Mørup, S., Bødker, F., Hendriksen, P.V. and Linderoth, S. (1995) Spin-glass-like ordering of the magnetic moments of interacting nanosized maghemite particles. *Physical Review B*, **52**, 287–94.

136 El-Hilo, M., Chantrell, R.W. and O'Grady, K. (1998) A model of interaction effects in granular magnetic solids. *Journal of Applied Physics*, **84**, 5114–22.

137 Yang, J.B., Xu, H., You, S.X., Zhou, X.D., Wang, C.S., Yelon, W.B. and James, W.J. (2006) Large scale growth and magnetic properties of Fe and Fe_3O_4 nanowires. *Journal of Applied Physics*, **99**, 08Q507-503.

138 Verwey, E.J.W. (1939) Electronic conduction of magnetite (Fe_3O_4) and its transition point at low temperatures. *Nature*, **144**, 327.

139 Suber, L., Imperatori, P., Ausanio, G., Fabbri, F. and Hofmeister, H. (2005) Synthesis, morphology, and magnetic characterization of iron oxide nanowires and nanotubes. *Journal of Physical Chemistry B*, **109**, 7103–9.

140 Martin, C.R. (1994) Nanomaterials: a membrane-based synthetic approach. *Science*, **266**, 1961–6.

Keywords

magnetic iron oxides; nanoparticle chemical synthesis methods; iron oxide nanotubes; iron oxide nanowires; ferrite composites; magnetism; core–shell magnetic particles; anisometric magnetic particles

13
Approaches to the Synthesis and Characterization of Spherical and Anisotropic Magnetic Alloy Nanomaterials

Matthew S. Wellons and Charles M. Lukehart

13.1
Introduction

Compared to top-down plasma or sputter-deposition methods, bottom-up chemical synthesis and self-assembly approaches offer more flexibility in creating magnetic alloy nanoparticles of controlled size, shape, composition, and physical properties. This chapter provides a summary of the latest developments in the chemical synthesis of spherical and anisotropic transition metal alloy magnetic nanoparticles, with an emphasis on how synthesis conditions impact nanoparticle shape and composition. The methods used to prepare anisotropic magnetic alloy nanoparticles represent an emerging area of high research interest, and an overview of recent advances in this area over the past two years is included. Recent developments in the synthesis of ferromagnetic and superparamagnetic M–Pt (M = Ni, Fe, Co) noble metal alloy nanoparticles are first reviewed, reflecting the current high interest in the formation of strongly ferromagnetic nanoparticles. A summary of synthesis strategies for preparing magnetically soft binary alloy nanoparticles of the early transition elements Co, Ni, and Fe follows. Other magnetic nanoparticle reviews are available [1–7], focusing on biomedical applications [1, 2], L_10 metal alloys [3, 7], multicomponent heterostructured compositions [5], or broader coverage of magnetic particle synthesis, magnetic properties, and applications to catalysis and biotechnology [4, 6].

The controlled synthesis and assembly of magnetic nanoparticles has attracted much interest for applications in biomedicine [1, 2], in high-density magnetic recording, high-sensitivity magnetic sensors, and advanced nanocomposite permanent magnets [3–5]. Magnetic alloy nanoparticles have been synthesized by several different methods, including:

- Molecular precursor(s) thermal decomposition in organic or aqueous solvents, often coupled with the chemical reduction of metal ions.
- Microemulsion strategies coupled with chemical reduction.
- Pyrolysis of metal–organic polymers, which serve as single-source precursors for desired metal alloys.

Nanomaterials for the Life Sciences Vol. 4: Magnetic Nanomaterials. Edited by Challa S. S. R. Kumar

ISBN: 978-3-527-32154-4

- The reductive decomposition of molecular precursor(s) or thermal treatment of presynthesized nanoparticles on a soluble salt support.

In the first two approaches, surfactants or capping ligands are used to provide kinetic control over the nanoparticle's shape and size. The surface passivation of metal alloy nanoparticles containing at least two different metals on the nanoparticle surface is usually accomplished by using two different passivating agents – one for each metal. For example, for FePt nanoparticles oleic acid passivates the surface Fe atoms while oleylamine passivates the surface Pt atoms. As-prepared metal alloy nanoparticles often have an amorphous atomic structure, and require postsynthesis thermal treatment to form an ordered phase with magnetic properties of interest. Nanoparticle aggregation or sintering during such thermal annealing treatments can become a serious problem for maintaining particle monodispersity. In addition, the metal stoichiometry of metal alloy nanoparticles formed by the reduction of metal ion mixtures is frequently not the same as that of the mixture. The acquisition of high-quality magnetic characteristics of the formed nanoparticles requires careful optimization of the reagent stoichiometries. In the latter two approaches, the use of single-source precursors or preformed metal alloy nanoparticles can be used to minimize such difficulties.

Transition metal alloy nanoparticles are usually characterized for structural and elemental composition determination, and separately for magnetic property measurements. Structural and elemental composition information, usually obtained by transmission electron microscopy (TEM), scanning electron microscopy (SEM), electron or powder X-ray diffraction (XRD), and by various X-ray emission techniques, such as energy dispersive spectroscopy (EDS), will be emphasized. The magnetic property measurements and characterization methods are reviewed in other chapters in this volume.

13.2
Magnetic Noble Metal Alloy Nanoparticles

FePt, FePd, and CoPt binary alloys having a near 1 : 1 metal stoichiometry represent an important class of ferromagnetic materials. These binary alloys exist in two different crystal structures depending on the amount of atomic ordering present. Material synthesized at temperatures <500 °C has a disordered face-centered cubic (fcc) structure, whereas annealing at a higher temperature results in the formation of an ordered face-centered tetragonal (fct) structure. These three binary alloys have a magnetically soft fcc phase with low coercivity, and are described as a fcc unit cell with random atomic placement of the two metal elements (see Figure 13.1). The magnetically hard fct phase (referred to as the Strukturbericht designation, $L1_0$) exhibits high coercivity, and is described as a distorted cubic structure, $c \neq a$, where alternating layers of metal atoms are stacked along the [001] direction (c axis). The magnetic anisotropy (K) for FePt, FePd, and CoPt may be as high as 6.6×10^7, 1.8×10^7, and $4.9 \times 10^7\,\mathrm{J\,m^{-3}}$, respectively, and are

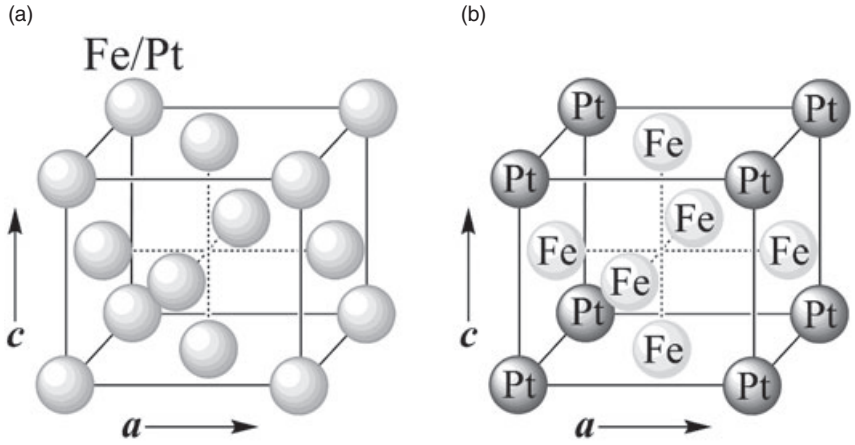

Figure 13.1 Unit cell diagrams. (a) Disordered fcc FePt alloy; (b) Ordered fct FePt alloy.

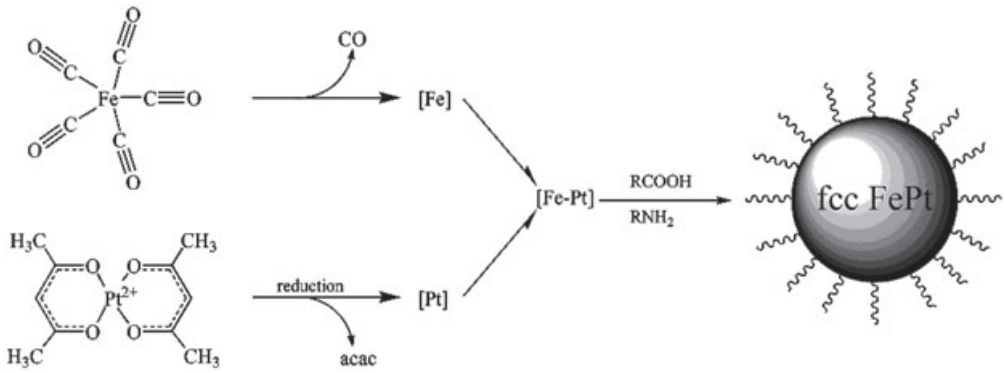

Figure 13.2 Synthesis of fcc FePt nanoparticles by thermal decomposition and reduction of $Fe(CO)_5$ and $Pt(acac)_2$.

some of the highest measured *K*-values for any known substance [6]. The large *K*-values of these materials are due to an interaction of spin-orbit coupling and hybridization between the Pt/Pd 5*d* and the Co/Fe 3*d* states [7].

The synthesis of FePt nanoparticles has been – and continues to be – the most investigated magnetic alloy nanoparticle system to date, due to its attractive materials properties [3]. Typical preparation methods involve thermal and/or reductive decomposition of dual-source precursors containing Fe- and Pt at elevated temperatures (250–300 °C) in a high-boiling point solvent and in the presence of capping agents, such as long monounsaturated carboxylic acids and amines. Sun *et al.* [8] reported the first such synthesis of FePt nanoparticles utilizing coincident thermal decomposition of $Fe(CO)_5$ and reductive decomposition of $Pt(acac)_2$ by the polyol process (see Figure 13.2).

FePt nanoparticle growth is initiated by formation of Pt-rich nuclei that serve as stable seed nuclei for further particle growth. Additional Fe atoms diffuse into the existing Pt-rich nuclei until decomposition of $Fe(CO)_5$ is complete. Refluxing the reaction mixture at elevated temperatures (ca. 290 °C) leads to complete atomic diffusion and the formation of fcc FePt nanoparticles. A stoichiometric concentration of Fe : Pt is controlled by an adjustment of the molar ratio of reactants. When using $Fe(CO)_5$/$Pt(acac)_2$ as reactants, a molar excess of $Fe(CO)_5$ by 2 : 1 is usually required to produce FePt nanoparticles. This reagent stoichiometry is likely required due to differences in the relative rates of precursor decomposition. When alternative Fe-precursors are used (e.g., $FeCl_2$ or $Fe(acac)_3$), the Fe : Pt atomic ratio of the nanoparticle is a equivalent to the molar ratio of the Fe : Pt precursors [9, 10].

The principal challenges in the syntheses of ferromagnetic $L1_0$ FePt nanoparticles are minimizing particle–particle coalescence during thermal annealing, and ensuring the homogeneity of the particle metal–alloy stoichiometry. The fcc to fct phase transition requires temperatures in excess of 500–600 °C. This means that nanoparticles in close proximity to one another, without a diffusion barrier, will coalescence/sinter and result in multidomain agglomerates and positional loss that renders the material unsuitable for magnetic recording media [11, 12]. An elemental stoichiometry very near 1 : 1 is essential for large coercivities and complete formation of the $L1_0$ phase [6]. Traditional synthetic methods, utilizing dual-source precursors, produce nanoparticles with a range of elemental compositions, resulting in particles having variable magnetic properties [13, 14]. Attempts to address these problems have focused on the use of diffusion-limiting inert matrices to inhibit sintering [15–17], of sacrificial tertiary metals to lower the fcc to fct transition temperature, including Au [18], Cu [19], Ag [20], Sb [21], and Zn [22], and the use of a chemically reducing Fe precursor to establish stoichiometric homogeneity [23].

Embedding nanoparticles within a robust carbonaceous or inorganic matrix helps to prevent uncontrolled agglomeration during thermal treatment. Silica nanoparticle shells have been utilized as "nanoreactors" to sequester magnetic alloy nanoparticles (i.e. FePt and CoPt) and eliminate particle–particle coalescence at high temperatures. Tamada *et al.* wrapped 6.5 nm fcc FePt nanoparticles (prepared by the above-mentioned method, reported by Sun *et al.* [8]) with SiO_2 to provide a "nanoreactor" shell encasement for the fcc to fct transformation [24]. The silica nanoparticle shell is formed by the hydrolysis of tetraethylorthosilicate after FePt nanoparticles have first been phase-transferred into aqueous media using water-soluble surfactants [25]. These SiO_2-coated fcc-FePt nanoparticles are annealed at 900 °C for 6 h in flowing H_2 (5%)/Ar (95%) to effect a full fcc-fct phase conversion (Figure 13.3). Silica-coated CoPt nanoparticles have been synthesized in a similar fashion by Kobayashi *et al.* [26]. Here, the CoPt nanoparticles are formed by borohydride reduction of appropriate metal salts in the presence of citric acid, which acts as a surface-stabilizing agent. Displacement of the citric acid surface-passivating layer with 3-aminopropyl-trimethoxylsilane initiates a sol–gel hydrolysis of the added tetraethylorthosilicate to form a silica shell wrap around the metal alloy nanoparticles.

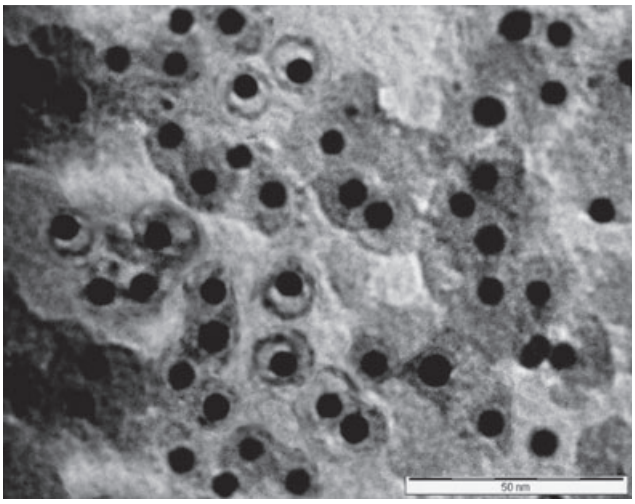

Figure 13.3 Transmission electron microscopy image of SiO_2-coated FePt nanoparticles after 1 h annealing at 600 °C. Reproduced with permission from Ref. [24]; © 2007, American Institute of Physics.

An alternative inorganic matrix useful for preventing particle coalescence is NaCl or other inorganic water-soluble salts. Preformed surface-passivated fcc FePt nanoparticles are dispersed onto balled-milled salt powders by liquid evaporation, and the resultant mixture is annealed at approximately 700 °C to effect a fcc to fct phase transformation. The salt supports are then removed by dissolution in water, leaving behind carbon-coated nanoparticles [17, 27].

Nandwana *et al*. [28] reported a systematic investigation into the size and morphological control of FePt nanoparticles synthesized using the method of Sun *et al*. [8]. A variation of the solution heating rate and the surfactant/precursor molar ratio allowed the final particle size to be tuned between 2 to 9 nm, with an accuracy of ±1 nm. Increasing the surfactant/$Pt(acac)_2$ precursor molar ratio from 0.75 to 10 increased the size of the FePt nanoparticle product from 3 nm to 9 nm. This effect was attributed to the formation of stable surfactant/metal atom complexes which resulted in a suppression of nanoparticle nucleation and a larger particle growth. The relationship between the reaction solution heating rate and FePt particle size was more complicated due to competition between nanoparticle nucleation and growth rates. Increases in the solution heating rate up to approximately 5 °C min^{-1} produce a corresponding increase in FePt particle size, but greater reaction solution heating rates lead to a decrease in the FePt particle size. The smaller particle growth at high heating rates (5–15 °C min^{-1}) can be explained by enhanced nucleation rates; however, at low heating rates the nanoparticle nucleation rate appears to dominate nanoparticle growth. This complexity is attributed to the mechanism of thermal decomposition of the Fe precursor, $Fe(CO)_5$,

since syntheses using $Fe(acac)_3$ or iron (III) ethoxide as precursor show different nanoparticle growth kinetics and dependence on the reaction solution heating rate [13, 29].

The choice of solvent and injection timing for introducing the oleic acid and oleylamine capping agents appears to dramatically alter FePt nanoparticle shape. Two commonly used high-boiling solvents, benzyl and octyl ether, produce FePt nanoparticles having different shapes above the size approximately 7 nm. When benzyl ether is used, monodisperse and near-isotropic FePt nanoparticles with a narrow size distribution are produced, but when octyl ether is used cubic FePt nanoparticles are formed with nanoparticle sizes in excess of 7 nm (Figure 13.4). In addition, when benzyl ether is used as the solvent, the delayed addition of oleylamine (by 5 min) following oleic acid addition produces rod-shaped FePt nanoparticles (see Figure 13.4) [28].

Nandwana *et al.* [28] have also reported that "brick-like" $FePt/CoFe_2O_4$ core–shell nanoparticles can be formed by growing a soft magnetic $CoFe_2O_4$ phase on these cubic FePt nanoparticles [28]. When preformed cubic fcc FePt nanoparticles of 8 nm diameter were mixed with $Co(acac)_2$ and $Fe(acac)_3$ in phenyl ether in the presence of 1,2-hexadecandiol, oleic acid, and oleylamine, and refluxed at 265 °C for 30 min, bimagnetic brick-like particles could be collected by centrifugation. The resultant nanoparticles had an 8 nm FePt inner core and an 8 nm $CoFe_2O_4$ outer shell (Figure 13.5). Upon annealing under a reducing atmosphere at 700 °C, these bimagnetic nanoparticles underwent a FePt fcc to fct phase transformation with an alteration of nanoparticle morphology from a brick-like shape towards a spherical shape, due to metal–atom diffusion [30]. Increasing the soft-phase $CoFe_2O_4$ mass fraction led to a decrease in nanoparticle coercivity and an increase in nanoparticle saturation magnetization, indicating that these magnetic properties were tunable by changing the mass ratio of the two components.

One of the best methods for controlling the elemental composition of metal alloy nanoparticles is to use molecular species that contain all of the requisite components, in the desired atomic ratios. This single-source molecular precursor

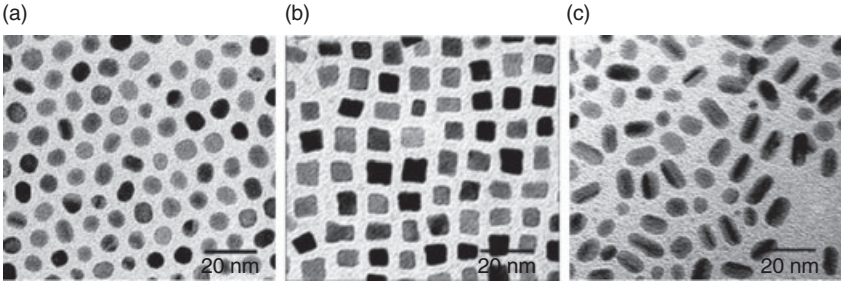

Figure 13.4 Transmission electron microscopy images of (a) spherical, (b) cubic, and (c) rod-like fcc FePt nanoparticles. Reproduced with permission from Ref. [28]; © 2007, American Chemical Society.

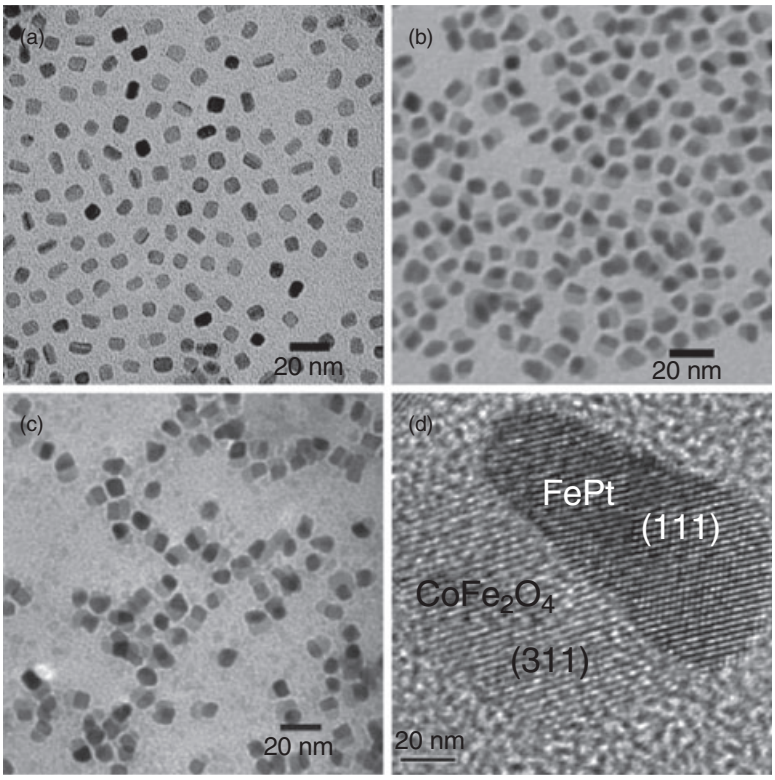

Figure 13.5 Transmission electron microscopy images of as-synthesized nanoparticles. (a) 8 nm FePt; (b) 8 nm/8 nm FePt/$CoFe_2O_4$; (c) 8 nm/10 nm FePt/$CoFe_2O_4$; (d) HRTEM of as-synthesized 8 nm/8 nm FePt/$CoFe_2O_4$. Reproduced with permission from Ref. [30]; © 2008, American Chemical Society.

method facilitates a homogeneous distribution of the relevant elements within the resultant nanoparticles upon molecular decomposition. The synthetic method must be designed such that decomposition of the single-source precursor delivers metal atoms with sufficient energy to form the desired alloy with all undesired precursor atoms readily removed from the system. Undesirable precursor atoms can be displaced typically via a combination of secondary chemical reactions and/or by supplying sufficient thermal energy to remove them as volatile products.

Rutledge *et al.* [31] described the synthesis of FePt nanoparticles which exhibited unexpectedly high room-temperature coercivity by the ultrasonication of toluene solutions of the heteropolynuclear cluster complex, $Pt_3Fe_3(CO)_{15}$, followed by thermal annealing to obtain fct FePt nanoparticles. When the known polyheteronuclear cluster complex, $Pt_3Fe_3(CO)_{15}$ [32], was dissolved in the presence of oleic acid and oleylamine and sonicated under N_2 for 1 h, surface-passivated fcc FePt

nanoparticles formed with the loss of CO gas. Annealing these fcc FePt nanoparticles in a tube furnace at 775 °C for 3 h under getter gas (9 : 1 N_2/H_2) gave highly crystalline fct FePt nanoparticles. Dispersions of these surface-passivated fcc FePt nanoparticles in (1 : 1) hexane/octane solution [33] were shown to form self-assembled particle arrays on SiO_x TEM grids and on oxidized Si wafers when using [3-(2-aminoethylamino)propyl]trimethoxy-silane as a linker molecule [34]. Thermal annealing of these supported nanoparticles gave the corresponding fct nanoparticle arrays. TEM images revealed nanoparticles that exhibited high contrast and single-crystal nanoparticles at high resolution showing lattice-fringe spacings consistent with *d*-spacings known for the (111) and (110) planes of fct FePt (Figure 13.6).

A one-step synthesis method which combines the advantages of both salt-matrix annealing and use of single-source precursors has been demonstrated by Wellons *et al.* [35]. Here, $L1_0$ FePt nanoparticles which were approximately 17 nm in diameter were formed by reductive decomposition of the single-source precursor, $FePt(CO)_4dppmBr_2$ [36], on a water-soluble support (Na_2CO_3). Direct conversion of a $FePt(CO)_4dppmBr_2/Na_2CO_3$ composite to a $L1_0$ $FePt/Na_2CO_3$ nanocomposite occurred at 600 °C under a H_2/N_2 (10%/90%) gas mixture with metal-ion reduction and minimal nanoparticle coalescence. When the post-annealed composite was treated with water, the sodium carbonate solid support dissolved to release the formed fct FePt nanoparticles. These as-prepared FePt nanoparticles proved to be ferromagnetic and exhibited coercivities of 14.5 kOe at 300 K and 21.8 kOe at 5 K. The fct FePt nanoparticles could be size-separated by fractional precipitation after functionalization with methoxypoly(ethylene glycol) surfactant molecules. This synthesis strategy has since been expanded to the synthesis of fct FePd and CoPt nanoparticles with the use of other heteronuclear metal complexes,

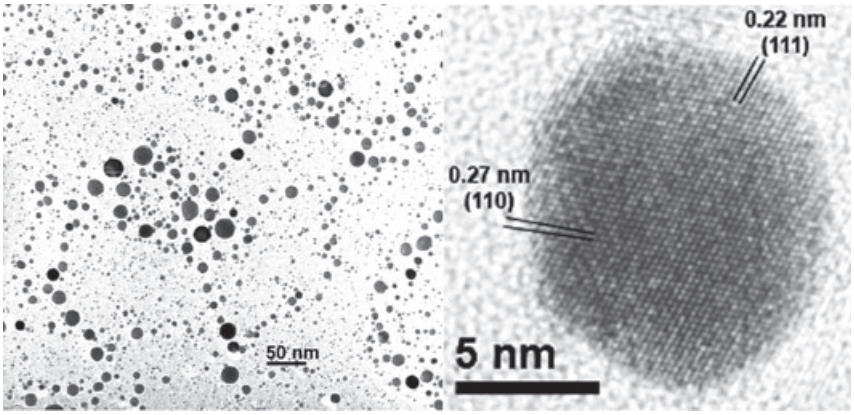

Figure 13.6 Transmission electron microscopy images micrographs at low (left) and high (right) resolution of annealed fct FePt nanoparticles. Adapted with permission from Ref. [31]; © 2006, American Chemical Society.

$[(CO)_4Fe(\mu\text{-}PPh_2)Pd(\mu\text{-}Cl)]_2$ [37] and $CoPt(CO)_4(dppe)Me$ [38], respectively, as single-source precursors.

FePd and CoPt alloys also exist as disordered fcc structures having small coercivity and soft magnetic properties, or as $L1_0$ ordered fct lattices having high coercivity, large magnetic anisotropy, and hard magnetic properties. The production of fct FePd and CoPt nanoparticles exhibiting high room-temperature coercivities is of major interest in the further study of hard ferromagnets, and also possibly of high-density data storage materials [3, 39]. Both alloys undergo a fcc-to-fct transition upon thermal annealing (between 500–700 °C for FePd and between 600–850 °C for CoPt) [40]. A fct-to-fcc phase transition resulting in a material without ferromagnetic properties occurs at high temperatures for both compositions [41, 42].

Recently reported FePd and CoPt nanoparticle syntheses have relied on rapid solution-based synthetic strategies used for the preparation of FePt and other metal alloy nanoparticles [9, 43]. Typical methods utilize a solvo-thermal process where dual-source precursors are dissolved in a high-boiling solvent and reduced to metal atoms by a strong reducing agent (e.g., sodium borohydride) or by a polyol process in the presence of an organic surface-passivating agents to form solubilized fcc nanoparticles. FePd nanoparticles have been prepared using solution-based strategies [44–46], electron-beam evaporation [47], and microwave radiation [48]. CoPt nanoparticles have been prepared using solution-based strategies [45, 49–52], core–shell nanoparticles [53], electrodeposition [54], and ion-implantation [55, 56]. In most preparations, the fcc nanoparticles are formed first and then are annealed, typically on wafer supports, to convert the superparamagnetic fcc material to the ferromagnetic fct phase. Although these annealing steps result in various degrees of interparticle coalescence, they are necessary to alter the magnetic properties.

A unique approach to the formation of supported magnetic binary alloy nanoparticles is the thermal decomposition of metal-atom-containing polymers. For this, Liu *et al.* [57] pyrolyzed a metallized polymer precursor comprised of polyferrocenylsilane with pendant Co clusters under a reducing atmosphere, and this resulted in the formation of magnetic CoFe alloy nanoparticles. Those nanoparticles formed with unprotected surfaces underwent surface oxidation in air; however, a portion of the nanoparticles formed within a silicon carbide matrix that was a reaction byproduct of polymer pyrolysis on a silicon substrate, sufficiently protecting the nanoparticles from air oxidation. The magnetic properties of the substrate-supported CoFe nanoparticles were seen to be wholly dependent on particle size.

More recently, Li, *et al.* [17, 58] described a similar polymer-pyrolysis synthesis of FePt nanoparticles from two different types of polyferroplatinyne polymers (Figure 13.7). The initial metallopolyyne precursor, **P1**, containing *n-tert*-butylphosphino ligands bound to the Pt atom, underwent reductive decomposition to give fct FePt nanoparticles and unwanted metal phosphides (i.e. Fe_2P and PtP_2). In order to overcome the phosphide formation, an alternative poylferroplatinyne precursor was developed, **P2**, where phosphine ligands were replaced with a bipyridine-type ligand.

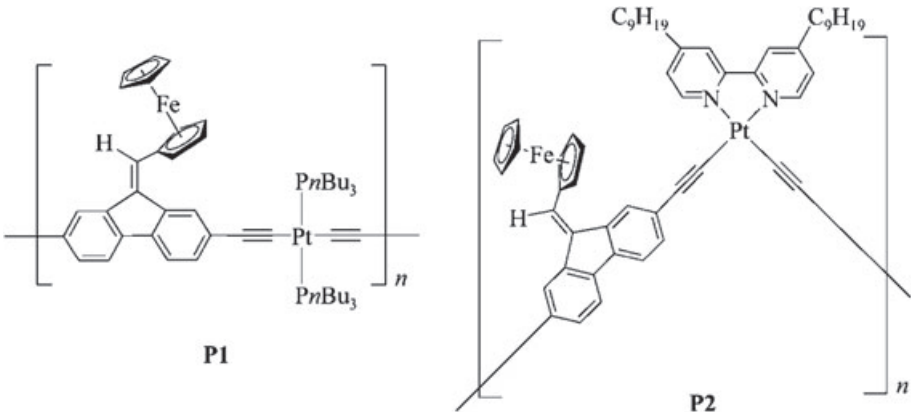

Figure 13.7 Iron- and platinum-containing polymers used for the synthesis of FePt nanoparticle films. Reproduced with permission from Ref. [58]; © Wiley-VCH Verlag GmbH & Co. KGaA.

The thermal decomposition of polymer **P2** at 500 °C resulted in a release of Fe and Pt atoms and the formation of FePt nanoparticles. Aggregation of the nanoparticles was suppressed by the surrounding carbonaceous matrix. An increase in the pyrolysis duration or temperature led to a predictable increase in FePt nanoparticle size and polydispersity. One advantage of the metallopolymer precursor approach to metal alloy nanoparticle synthesis was the potential synthetic control over the location of metal nanoparticle formation using lithographic techniques. Electron-beam lithography has been used to control the deposition of precursor **P2** as a negative resist, affording FePt nanoparticles patterned with strong shape retention (Figure 13.8). The use of metal-containing polymers and various lithographic techniques to form patterned arrays of metal alloy nanoparticles with compositional and particle density control may become important in device and catalyst applications.

Ni–Pt nanoparticles of variable stoichiometry have been synthesized by the polyol reduction of nickel acetate and platinum acetylacetonate in the presence of stabilizing agents, such as oleic acid and oleylamine. Other stabilizing agents, including adamantanecarboxylic acid (ACA), *n*-tetradecylphosphonic acid (TDPA), and trioctylphosphine oxide (TOPO), in combination with other primary amines and carboxylic acids, form colloids having a variety of shapes (Figure 13.9).

Variation of the oleic acid and oleylamine relative concentrations as capping agents affects NiPt nanoparticle growth. For example, increasing the oleic acid concentration with a constant amount of oleylamine leads to a decrease in the alloy nanoparticle size, whereas increasing the oleic acid concentration relative to the oleylamine concentration produces polycrystalline and irregularly shaped particles. The colloid particle size or stability appears to be influenced most by the oleic acid concentration, while nanoparticle shape is determined by the oleylamine

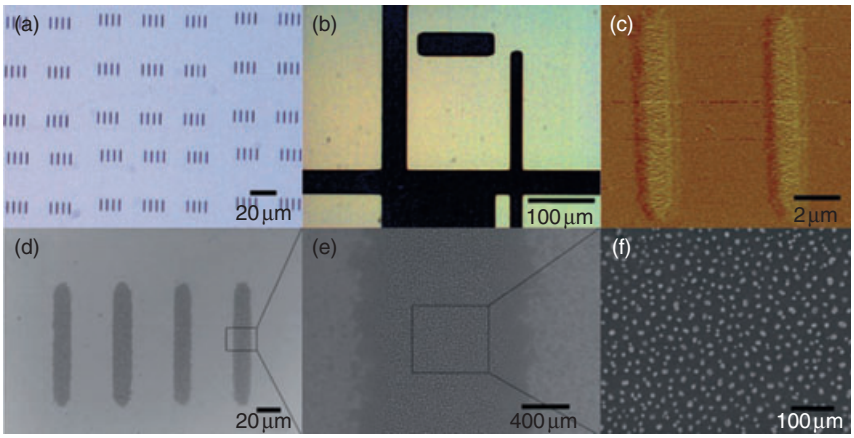

Figure 13.8 Optical micrographs of P2. (a) Microbars formed by electron-beam lithography; (b) Patterns fabricated using UV-photolithography with a chrome contact mask; (c) Magnetic force microscopy and (d–f) SEM images of microbars pyrolyzed at 500 °C under N_2. Reproduced with permission from Ref. [58]; © Wiley-VCH Verlag GmbH & Co. KGaA.

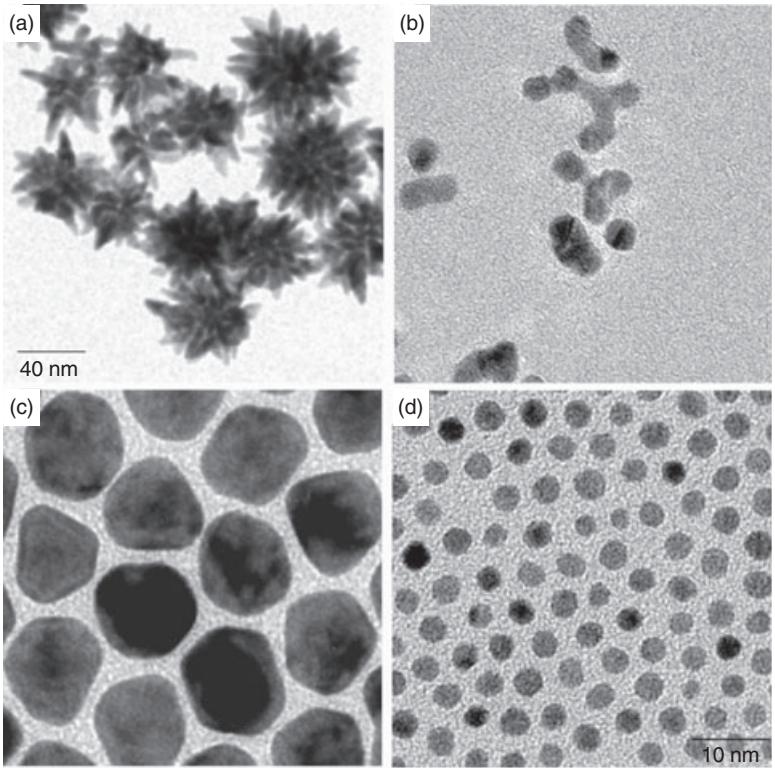

Figure 13.9 Transmission electron microscopy images of Ni_xPt_{1-x}, with (a) HDA/ACA, (b) TDPA/ACA, (c) TOPO/HAD and (d) OA/Oac as stabilizing agents (same magnification for panels b, c, and d). Reproduced with permission from Ref. [59]; © Wiley-VCH Verlag GmbH & Co. KGaA.

relative concentration. Ahrenstorf *et al.* have shown that the nucleation of Ni–Pt nanoparticle growth occurs through Pt-rich species. Oleylamine is presumed to be the surfactant most likely to stabilize the surface Pt atoms. In addition, $Ni_{50}Pt_{50}$ nanoparticles demonstrate superparamagnetic character above a blocking temperature of 7.4 K, below which they are ferromagnetic [59].

13.3
Magnetic Early Transition Metal Alloy Nanoparticles

Iron and cobalt alloys are of major interest as soft magnetic materials, due to their high saturation of magnetization, negligible magnetocrystalline anisotropy, high Curie temperature ($T_c \approx 900\,°C$), and high permeability; taken together, these properties make these alloys desirable materials for magnetic recording, drug delivery, and hyperthermia treatment applications. Wet-chemical synthesis strategies of spherical Co–Fe nanoparticles usually involve the reduction of dual-source precursors by aqueous reductive agents or an alcohol-based polyol process [60, 61]. Amorphous Co–Fe alloys incorporating boron and/or phosphorus dopants [62, 63] and Co–Fe nanoparticles supported on carbonaceous substrates or with dielectric oxide coatings have been prepared using such methods [64, 65].

*n*Co-Fe/multiwall-carbon nanotube (MWCNT) nanocomposites are prepared by first acid-treating the carbon nanotubes with nitric acid to form surface-bound functional groups, such as COOH, –OH, and C O, that act as nucleation sites for metal nanoparticle growth. Surface-oxidized MWCNTs are dispersed into aqueous solutions containing dissolved iron and cobalt nitrate salts, and are then heated to 100 °C until the water has evaporated completely. Subsequent calcination (Ar, 300 °C) and reduction (H_2, 400 °C) results in Co–Fe nanoparticles, the size of which is controlled by varying the loading (as wt%) of metal salts deposited onto the carbonaceous support [65].

Kim *et al.* recently prepared soft magnetic 3 : 7 Co–Fe alloy nanoparticles via a borohydride reduction of aqueous solutions of cobalt chloride and iron chloride; the Co_3Fe_7 nanoparticles formed as atomically disordered naked clusters, without need for a surface-capping agent. These as-prepared nanoparticles could be dispersed by sonication in a solution of oleic acid in isooctane. Upon thermal annealing, amorphous Co_3Fe_7 nanoparticles crystallized to an ordered structure, with only nominal sintering (Figure 13.10) [60].

The reduction of cobalt and nickel acetate precursors at concentrations of 0.1–0.2 *M* by the polyol process in the presence of ruthenium seed material, generates a wide array of shaped Co–Ni nanoparticles. A sodium hydroxide additive appears to be the main directing agent for nanoparticle shape growth, dictating the formation of wires, dumbbells, diabolos, and platelets (see Figure 13.11). These unusual particle shapes are categorized by the relative dimensions of a center column and end-caps. The center column length increases with decreasing NaOH concentration, while end-cap diameter increases with increasing NaOH concentrations. On-particle EDS and electron energy loss spectroscopy (EELS) characterization

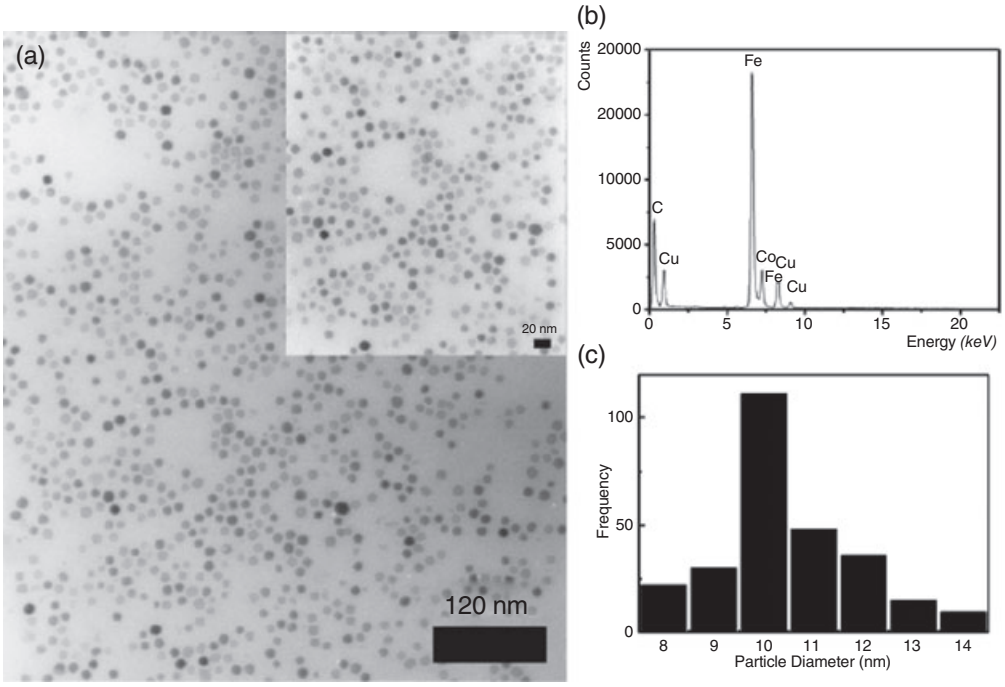

Figure 13.10 (a) Transmission electron microscopy images; (b) Energy-dispersive X-ray spectrum; and (c) Histogram of size distribution of $Co_{30}Fe_{70}$ alloy which was annealed at 400 °C for 1 h. Reproduced with permission from Ref. [60]; © 2006, American Chemical Society.

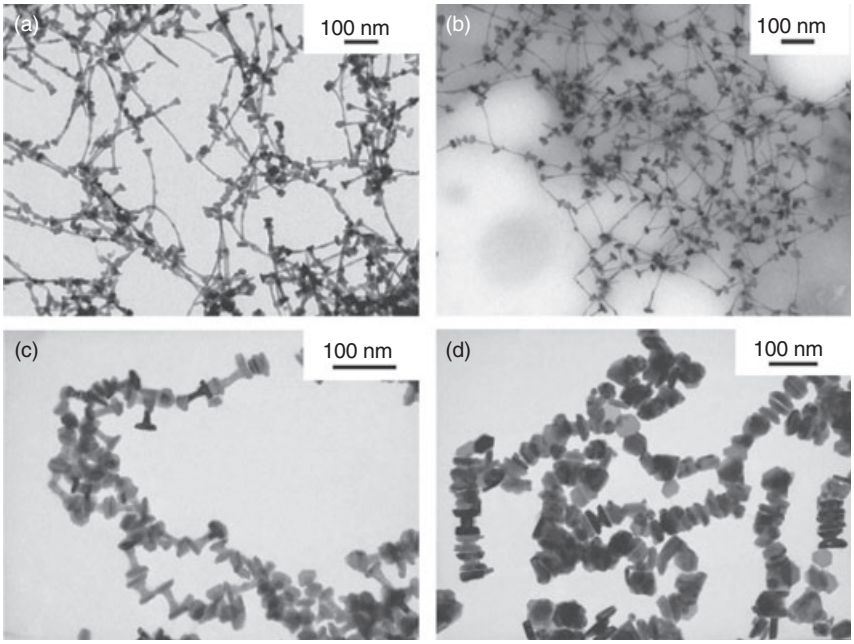

Figure 13.11 Transmission electron microscopy images of CoNi particles prepared by reduction in 1,2-propanediol with various sodium hydroxide concentrations. (a) 0.11 *M*; (b) 0.135 *M*; (c) 0.16 *M*; (d) 0.175 *M*. Reproduced with permission from Ref. [66]; © 2005, Elsevier.

revealed the partial homonuclear segregation of Ni and Co atoms, depending on the region of the shaped nanoparticles, but which was most likely representative of differences in reactivity between the two metals. Subsequent TEM data indicated that the columnar portion of these nanoparticles consisted predominantly of a hcp phase, while the end-caps were comprised of both fcc and hcp phases in similar amounts. These differences in phase composition were consistent with magnetic measurements. NiCo nanoparticles having hcp atomic ordering exhibited a larger coercivity and higher magnetic remanence to saturation ratios compared to those alloy nanoparticles having fcc ordering [66].

13.4 Summary and Future Perspectives

Spherical and anisotropic magnetic alloy nanoparticles continue to be synthesized via predominantly chemical methods, utilizing either the decomposition of single-source precursors or the metal-ion reduction of dual-source precursor mixtures. For the latter syntheses in particular, the choice of capping agent in the reaction solution and the control of reaction parameters, such as the order of addition, rate of reaction, and choice of precursor(s), have major influences on the shape, size, and elemental composition of the resultant nanoparticle product. Metal alloy nanoparticles with highly anisotropic structures and interesting magnetic properties have been synthesized by carefully controlling the reaction conditions. The controlled nanoparticle growth of metal alloy compositions is a relatively new phenomenon, however, and further investigations will be required into the influence of capping agent effects and growth kinetics on nanoparticle structure before synthesis strategies can be developed for the preparation of shape-specific metal alloy nanoparticles.

References

1 Jun, Y.-W., Seo, J.-W. and Cheon, J. (2008) Nanoscaling laws of magnetic nanoparticles and their applicabilities in the biomedical sciences. *Accounts of Chemical Research*, **41**, 179–89.

2 Sounderya, N. and Zhang, Y. (2008) Use of core/shell structured nanoparticles for biomedical applications. *Recent Patents on Biomedical Engineering*, **1**, 34–42.

3 Sun, S. (2006) Recent advances in chemical synthesis, self-assembly, and applications of FePt nanoparticles. *Advanced Materials*, **18**, 393–403.

4 Lu, A.-H., Salabas, E.L. and Schuth, F. (2007) Magnetic nanoparticles: synthesis, protection, functionalization, and applications, *Angewandte Chemie, International Edition in English*, **46**, 1222–44.

5 Jun, Y.-W., Choi, J.-S. and Cheon, J. (2007) Heterostructured magnetic nanoparticles: their versatility and high performance capabilities. *Chemical Communications*, 1203–14.

6 Wirth, S. and von Monlnar, S. (2006) *Handbook of Advanced Magnetic Materials*, Vol. **1**, Springer, New York, NY.

7 Burkert, T., Eriksson, O., Simak, S.I., Ruban, A.V., Sanyal, B., Nordström, L. and Wills, J.M. (2005) Magnetic

anisotropy of L_10 FePt and $Fe_{1-x}Mn_xPt$. *Physical Review B*, **71**, 134411.

8 Sun, S., Murray, C.B., Weller, D., Folks, L. and Moser, A. (2000) Monodisperse FePt nanoparticles and ferromagnetic FePt nanocrystal superlattices. *Science*, **287**, 1989–92.

9 Sun, S., Anders, S., Thomson, T., Baglin, J.E.E., Toney, M.F., Hamann, H.F., Murray, C.B. and Terris, B.D. (2003) Controlled synthesis and assembly of FePt nanoparticles. *Journal of Physical Chemistry B*, **107**, 5419–25.

10 Nakaya, M., Kanehara, M., Yamauchi, M., Kitagawa, H. and Teranishi, T. (2007) Hydrogen-induced crystal structural transformation of FePt nanoparticles at low temperature. *Journal of Physical Chemistry C*, **111**, 7231–4.

11 Terris, B.D. and Thomson, T. (2005) Nanofabrication and self-assembled magnetic structures as data storage media. *Journal of Physics D: Applied Physics*, **38**, R199–222.

12 Zeng, H., Sun, S., Vedantam, T.S., Liu, J.P., Dai, Z.R. and Wang, Z.L. (2002) Exchange-coupled FePt nanoparticle assembly. *Applied Physics Letters*, **80**, 2583–5.

13 Saita, S. and Maenosono, S. (2005) FePt nanoparticles with a narrow composition distribution synthesized via pyrolysis of iron(III) ethoxide and platinum(II) acetylacetonate. *Chemistry of Materials*, **17**, 3705–10.

14 Yu, A.C.C., Mizuno, M., Sasaki, Y. and Kondo, H. (2004) Atomic composition effect on the ordering of solution-phase synthesized FePt nanoparticle films. *Applied Physics Letters*, **85**, 6242–4.

15 Liu, C., Wu, X., Klemmer, T., Shukla, N., Weller, D., Roy, A.G., Tanase, M. and Laughlin, D. (2005) Reduction of sintering during annealing of FePt nanoparticles coated with iron oxide. *Chemistry of Materials*, **17**, 620–5.

16 Lee, D.C., Mikulec, F.V., Pelaez, J.M., Koo, B. and Korgel, B.A. (2006) Synthesis and magnetic properties of silica-coated FePt nanocrystals. *Journal of Physical Chemistry B*, **110**, 11160–6.

17 Li, D., Poudyal, N., Nandwana, V., Jin, Z., Elkins, K. and Liu, J.P. (2006) Hard magnetic FePt nanoparticles by salt-matrix annealing. *Journal of Applied Physics*, **99**, 08E911.

18 Jia, Z., Kang, S.S., Shi, S., Nikles, D.E. and Harrell, J.W. (2005) Size effect on L10 ordering and magnetic properties of chemically synthesized FePt and FePtAu nanoparticles. *Journal of Applied Physics*, **97**, 10J310(1-3).

19 Sun, X., Kang, S., Harrell, J.W., Nikles, D.E., Dai, Z.R., Li, J. and Wang, Z.L. (2003) Synthesis, chemical ordering, and magnetic properties of FePtCu nanoparticle films. *Journal of Applied Physics*, **93**, 7337–9.

20 Kang, S.S., Nikles, D.E. and Harrell, J.W. (2003) Synthesis, chemical ordering, and magnetic properties of self-assembled FePt-Ag nanoparticles. *Journal of Applied Physics*, **93**, 7178–80.

21 Yan, Q.Y., Kim, T., Purkayastha, A., Xu, Y., Shima, M., Gambino, R.J. and Ramanatha, G. (2006) Magnetic properties of Sb-doped FePt nanoparticles. *Journal of Applied Physics*, **99**, 08N709-(1-3).

22 Kim, K.-E., Lee, M.-K., Sunga, Y.-M. and Kim, T.G. (2007) Enhanced L10 chemical ordering and $FePt/Fe_3O_4$ core/shell structure formation in Zn-doped FePt nanoparticles. *Applied Physics Letters*, **90**, 173117-(1-3).

23 Howard, L.E.M., Nguyen, H.L., Giblin, S.R., Tanner, B.K., Terry, I.; Hughes, A.K. and Evans, J.S.O. (2005) A synthetic route to size-controlled fcc and fct FePt nanoparticles. *Journal of the American Chemical Society*, **127**, 10140–1.

24 Tamada, Y., Yamamoto, S., Takano, M., Nasu, S. and Ono, T. (2007) Well-ordered L10-FePt nanoparticles synthesized by improved SiO_2-nanoreactor method. *Applied Physics Letters*, **90**, 162509.

25 Fan, H., Yang, K., Boye, D.M., Sigmon, T., Malloy, K.J., Xu, H., Lopez, G.P. and Brinker, C.J. (2004) Self-assembly of ordered, robust, three-dimensional gold nanocrystal/silica arrays. *Science*, **304**, 567–71.

26 Kobayashi, Y., Horie, M., Nagao, D., Ando, Y., Miyazaki, T. and Konno, M. (2006) Preparation of silica-coated Co-Pt

alloy nanoparticles. *Materials Letters*, **60**, 2046–9.

27 Rong, C.-B., Poudyal, N., Chaubey, G.S., Nandwana, V., Liu, Y., Wu, Y.Q., Kramer, M.J., Kozlov, M.E., Baughman, R.H. and Liu, J.P. (2008) High thermal stability of carbon-coated L10-FePt nanoparticles prepared by salt-matrix annealing. *Journal of Applied Physics*, **103**, 07E131-(1-3).

28 Nandwana, V., Elkins, K.E., Poudyal, N., Chaubey, G.S., Yano, K. and Liu, J.P. (2007) Size and shape control of monodisperse FePt nanoparticles. *Journal of Physical Chemistry C*, **111**, 4185–9.

29 Nandwana, V., Elkins, K.E. and Liu, J.P. (2005) Magnetic hardening in ultrafine FePt nanoparticle assembled films. *Nanotechnology*, **16**, 2823–6.

30 Chaubey, G.S., Nandwana, V., Poudyal, N., Rong, C.-B. and Liu, J.P. (2008) Synthesis and characterization of bimagnetic bricklike nanoparticles. *Chemistry of Materials*, **20**, 475–8.

31 Rutledge, R.D., Morris, W.H., III, Wellons, M.S., Gai, Z., Shen, J., Bentley, J., Wittig, J.E. and Lukehart, C.M. (2006) Formation of FePt nanoparticles having high coercivity. *Journal of the American Chemical Society*, **128**, 14210–11.

32 Adams, R.D., Arafa, I., Chen, G., Li, J. and Wang, J. (1990) New platinum-iron carbonyl clusters and their reactions with alkynes. *Organometallics*, **9**, 2350–7.

33 Chen, M., Nikles, D.E., Yin, H., Wang, S., Harrell, J.W. and Majetich, S.A. (2003) Patterning self-assembled FePt nanoparticles. *Journal of Magnetism and Magnetic Materials*, **266**, 8–11.

34 Yu, A.C.C., Mizuno, M., Sasaki, Y., Inoue, M., Kondo, H., Ohta, I., Djayaprawira, D. and Takahashi, M. (2003) Fabrication of monodispersive FePt nanoparticle films stabilized on rigid substrates. *Applied Physics Letters*, **82**, 4352–4.

35 Wellons, M.S., Morris, W.H., Gai, Z., Shen, J., Bentley, J., Wittig, J. and Lukehart, C.M. (2007) Direct synthesis and size selection of ferromagnetic FePt nanoparticles. *Chemistry of Materials*, **19**, 2483–8.

36 Jacobsen, G.B., Shaw, B.L. and Thornton-Pett, M. (1987) Platinum(II)– and palladium(II)–iron(0) complexes containing one bridging $Ph_2PCH_2PPh_2$ ligand. Crystal structures of $[(OC)_3Fe(\mu\text{-}Ph_2PCH_2PPh_2)(\mu\text{-}CO)PtBr_2]$ and $[(OC)_3Fe(\mu\text{-}Ph_2PCH_2PPh_2)(\mu\text{-}I)PtI]\cdot CH_2Cl_2$. *Journal of the Chemical Society – Dalton Transactions*, **12**, 3079–83.

37 Benson, B.C., Jackson, R., Joshi, K.K. and Thompson, D.T. (1968) A new method for the preparation of mixed metal complexes. *Chemical Communications*, 1506–7.

38 Atsushi Fukuoka, T.S., Sugiura, T., Wu, X., Mizuho, Y. and Komiya, S. (1994) Synthesis and reactivity of platinum-containing heterodinuclear complexes with methyl and 1,2-bis(diphenylphosphino)ethane ligands. X-ray crystal structure of (dpe)MePt-FeCp$(CO)_2$ THF. *Journal of Organometallic Chemistry*, **473**, 139–47.

39 Hyeon, T. (2003) Chemical synthesis of magnetic nanoparticles. *Chemical Communications*, 927–34.

40 Massalski, T.B. and Okamoto, H. (1990) *Binary Alloy Phase Diagrams*, 2nd edn, ASM International, Materials Park, Ohio.

41 Sato, K. and Hirotsu, Y. (2006) Order-disorder transformation in L10-FePd nanoparticles studied by electron diffraction. *Materials Transactions, Japanese Institute of Metals*, **47**, 59–62.

42 Kang, S., Jia, Z., Nikles, D.E. and Harrell, J.W. (2004) Synthesis and phase transition of self-assembled FePd and FePdPt nanoparticles. *Journal of Applied Physics*, **95**, 6744–6.

43 Cushing, B.L., Kolesnichenko, V.L. and O'Connor, C.J. (2004) Recent advances in the liquid-phase syntheses of inorganic nanoparticles. *Chemical Reviews*, **104**, 3893–946.

44 Hou, Y., Kondoh, H., Kogure, T. and Ohta, T. (2004) Preparation and characterization of monodisperse FePd nanoparticles. *Chemistry of Materials*, **16**, 5149–52.

45 Chen, M. and Nikles, D.E. (2002) Synthesis of spherical FePd and CoPt nanoparticles. *Journal of Applied Physics*, **91**, 8477–9.

46 Watanabe, K., Kura, H. and Sato, T. (2006) Transformation to L_10 structure in FePd nanoparticles synthesized by

modified polyol process. *Science and Technology of Advanced Materials*, **7**, 145–9.

47 Sato, K. and Hirotsu, Y. (2003) Structure and magnetic property changes of epitaxially grown $L_1$0-FePd isolated nanoparticles on annealing. *Journal of Applied Physics*, **93**, 6291–9.

48 Nguyen, H.L., Howard, L.E.M., Giblin, S.R., Tanner, B.K., Terry, I., Hughes, A.K., Ross, I.M., Serres, A., Burckstrummer, H. and Evans, J.S.O. (2005) Synthesis of monodisperse fcc and fct FePt/FePd nanoparticles by microwave irradiation. *Journal of Materials Chemistry*, **15**, 5136–43.

49 Mizuno, M., Sasaki, Y., Inoue, M., Chinnasamy, C.N., Jeyadevan, B., Hasegawa, D., Ogawa, T., Takahashi, M., Tohji, K., Sato, K. and Hisano, S. (2005) Structural and magnetic properties of monolayer film of CoPt nanoparticles synthesized by polyol process. *Journal of Applied Physics*, **97**, 10J301-(1-3).

50 Wang, H.L., Zhang, Y., Huang, Y., Zeng, Q. and Hadjipanayis, G.C. (2004) CoPt nanoparticles by chemical reduction. *Journal of Magnetism and Magnetic Materials*, **272–276**, e1279–80.

51 Sun, X., Jia, Z., Huang, Y., Harrell, J.W., Nikles, D.E., Sun, K. and Wang, L.M. (2004) Synthesis and magnetic properties of CoPt nanoparticles. *Journal of Applied Physics*, **95**, 6747–9.

52 Tzitzios, V., Niarchos, D., Maragariti, G., Fidler, J. and Petridis, D. (2005) Synthesis of CoPt nanoparticles by a modified polyol method: characterization and magnetic properties. *Nanotechnology*, **16**, 287–91.

53 Park, J., Kim, M.G., Jun, Y., Lee, J.S., Lee, W. and Cheon, J. (2004) Characterization of superparamagnetic "core-shell" nanoparticles and monitoring their anisotropic phase transition to ferromagnetic "solid-solution" nanoalloys. *Journal of the American Chemical Society*, **126**, 9072–8.

54 Cagnon, L., Dahmane, Y., Voiron, J., Pairis, S., Bacia, M., Ortega, L., Benbrahim, N. and Kadri, A. (2007) Electrodeposited CoPt and FePt alloys nanowires. *Journal of Magnetism and Magnetic Materials*, **310**, 2428–30.

55 White, C.W., Withrow, S.P., Budai, J.D., Thomas, D.K., Williams, J.M., Meldrum, A., Sorge, K.D., Thompson, J.R., Ownby, G.W., Wendelken, J.F. and Boatner, L.A. (2005) Annealing-environment effects on the properties of CoPt nanoparticles formed in single-crystal Al_2O_3 by ion implantation. *Journal of Applied Physics*, **98**, 114311-(1-5).

56 Karanasos, V., Panagiotopoulos, I., Niarchos, D., Okumura, H. and Hadjipanayis, G.C. (2000) Magnetic properties and granular structure of CoPt/B films. *Journal of Applied Physics*, **88**, 2740–4.

57 Liu, K., Clendenning, S.B., Friebe, L., Chan, W.Y., Zhu, X., Freeman, M.R., Yang, G.C., Yip, C.M., Grozea, D., Lu, Z.-H. and Manners, I. (2006) Pyrolysis of highly metallized polymers: Ceramic thin films containing magnetic CoFe alloy nanoparticles from a polyferrocenylsilane with pendant cobalt clusters. *Chemistry of Materials*, **18**, 2591–601.

58 Liu, K., Ho, C.-L., Aouba, S., Zhao, Y.-Q., Lu, Z.-H., Petrov, S., Coombs, N., Dube, P., Ruda, H., Wong, W.-Y. and Manners, A.I. (2008) Synthesis and lithographic patterning of FePt nanoparticles using a bimetallic metallopolyyne precursor. *Angewandte Chemie, International Edition in English*, **47**, 1255–9.

59 Ahrenstorf, K., Albrecht, O., Heller, H., Kornowski, A., Gorlitz, D. and Weller, H. (2007) Colloidal synthesis of Ni_xPt_{1-x} nanoparticles with tuneable composition and size. *Small*, **3**, 271–4.

60 Kim, C.W., Kim, Y.H., Cha, H.G., Kwon, H.W. and Kang, Y.S. (2006) Synthesis and characterization of highly magnetized nanocrystalline $Co_{30}Fe_{70}$ alloy by chemical reduction. *Journal of Physical Chemistry B*, **110**, 24418–23.

61 Kodamaa, D., Shinodab, K., Satoc, K., Satoa, Y., Jeyadevana, B. and Tohjia, K. (2007) Synthesis of size-controlled Fe-Co alloy nanoparticles by modified polyol process. *Journal of Magnetism and Magnetic Materials*, **310**, 2396–8.

62 Wen, M., Zhong, M.E.K., Wu, J., Li, L., Qi, H., Cao, S. and Zhang, T. (2006) Soft

magnetic Co-Fe-B-P and Co-Fe-V-B-P amorphous alloy nano-particles prepared by aqueous chemical reduction. *Journal of Alloys and Compounds*, **417**, 245–9.

63 Concha, B.M., Zyslera, R.D. and Romero, H. (2006) Magnetization enhancement in Fe-Co-B alloy nanoparticles. *Physica B*, **384**, 274–6.

64 Nguyen, Q., Chinnasamy, C.N., Yoon, S.D., Sivasubramanian, S., Sakai, T., Baraskar, A., Mukerjee, S., Vittoria, C. and Harris, V.G. (2008) Functionalization of FeCo alloy nanoparticles with highly dielectric amorphous oxide coatings. *Journal of Applied Physics*, **103**, 07D532-(1-3).

65 Wu, H.-Q., Yuan, P.-S., Xu, H.-Y., Xu, D.-M., Geng, B.-Y. and Wei, X.-W. (2006) Controllable synthesis and magnetic properties of Fe-Co alloy nanoparticles attached on carbon nanotubes. *Journal of Materials Science*, **41**, 6889–9894.

66 Ung, D., Viau, G., Fie'vet-Vincent, F.O., Herbst, F.D.R., Richard, V. and Fie'vet, F. (2005) Magnetic nanoparticles with hybrid shape. *Progress in Solid State Chemistry*, **33**, 137–45.

Keywords

metal alloy; metal nanoparticles; magnetic metal nanoparticles; anisotropic metal nanoparticles

14
Approaches to the Biofunctionalization of Spherical and Anisotropic Iron Oxide Nanomaterials

Christopher J. Thode and Mary Elizabeth Williams

14.1
Introduction

Functional magnetic nanomaterials represent an attractive option for the magnetic-based detection, separation, analysis, and transport of attached materials, ranging from catalysts to cells [1]. Magnetic fields and field gradients can exert force from a distance, and provide a powerful means by which to manipulate nanoscale paramagnetic and superparamagnetic particles. Notably, this approach differs fundamentally from optical methods that use nanoscale noble metal [2, 3] and semiconductor particles [4]. The development of syntheses that define the size and shape of magnetic nanoparticles, and which modify the surface chemical functionality, have been active areas of research in recent years [5–8]. Chemically functional magnetic particles have applications that range from drug delivery and chemotherapeutics in biomedicine [9–11] to magnetic field-induced separations and analyses [12–16]. Polyfunctionality than can be built on the surface of magnetic nanoparticles will, ultimately, provide opportunities to use these materials for complex series of reactions. It is known that the magnetic moments of nanoscale magnetic materials depend on both their size and composition [17], and can be exploited for magnetic-based separation devices, for hyperthermia treatment of malignant cells [18], and in magnetic resonance imaging (MRI) contrast agents [19, 20].

Standard synthetic methods exist with which a wide range of magnetic nanoparticles of desired size and shape, and which are highly crystalline, can be prepared [21–27]. Electrostatic and/or steric stabilization of the particles is necessary to prevent agglomeration and induce solubility in the solvent system of interest [28, 29]. Because aqueous methods for the preparation of magnetic nanoparticles provide an electrostatic stabilization of the particles, slight changes in the pH or ionic strength of the solution can result in particle agglomeration and precipitation. For some applications, a greater control of the shape and size of the particles is required [30, 31]. For these reasons and others, an alternative synthetic approach is high-temperature synthesis [21–27]. A larger and currently very active research

Nanomaterials for the Life Sciences Vol. 4: Magnetic Nanomaterials. Edited by Challa S. S. R. Kumar

ISBN: 978-3-527-32154-4

area is the development of synthetic methods by which the surface chemistry of magnetic particles can be modified, tuned to specific applications, and understood at the molecular level. Some of the chemical methods used to prepare magnetic nanoparticles are briefly described in this chapter, with attention being focused mainly on the approaches developed to render the particles chemically and biologically functional.

14.2 Magnetic Nanoparticle Synthesis

Common high-temperature synthetic methods utilize the thermal decomposition [21, 24, 26, 27] or thermal reductive decomposition [22, 23, 25] of metal precursors in the presence of a stabilizing ligand (or surfactant) to yield metal nanoparticles with diameters ranging from 3 to 15 nm. Typical metal precursors include carbonyl [21] and acetylacetonate (acac) [25] complexes (e.g., $Fe(CO)_5$, $Co(acac)_2$ and $Fe(acac)_3$). The ligands are generally long-chain carboxylic acids and/or amines (e.g., oleic acid and oleylamine). These surfactants are required both to mediate growth during the reaction and to prevent agglomeration of the prepared particles. Shorter-chain lengths are sometimes employed to facilitate surface modification post synthesis [32], but generally chains with at least six carbons are necessary to provide sufficient stabilization [24, 25, 32]. The synthesis and modification of magnetic nanoparticles is a vigorously studied field that continues to expand rapidly, and the key reports outlined in this chapter are representative of a much larger and growing body of work.

Modification of the reaction parameters tunes the nanoparticle size and shape – and therefore the magnetic moment – of a nanoparticle sample. The magnetic moment is intrinsically related to the composition: the incorporation of Co^{2+} into an Fe oxide matrix (i.e., $CoFe_2O_4$) increases the magnetic anisotropy relative to an Fe_3O_4 iron oxide nanoparticle of equivalent size. The insertion of Mn^{2+} (i.e., $MnFe_2O_4$), however, will cause a decrease in the anisotropy [33]. The boiling point (BP) of the solvent (i.e., the temperature of the reaction), the relative molar quantities of metal and ligand, mixing rate, and time each further affect the particle size and morphology. For example, when synthesizing $CoFe_2O_4$ particles, changing the solvent from phenyl ether (BP ~265 °C, 30 min) to benzyl ether (BP ~298 °C, 2 h) causes a 7 nm increase in nanoparticle diameter [25]. It has been shown during the synthesis of $MnFe_2O_4$ nanoparticles that a surfactant to Fe ratio of 3 : 1 yields spherical particles, while a 1 : 3 ratio results in the synthesis of cube-like particles [34]. These examples illustrate that the choice of reaction parameters exerts a clear control over the particles' size, shape, composition, and magnetic properties.

Over the past decade, a wide range of magnetic nanoparticle compositions and structures has been synthesized. The most common of these materials are the Fe oxides (Fe_2O_3 and Fe_3O_4), known for their potential for biological compatibility, and their corresponding ferrites (e.g., $MnFe_2O_4$ and $CoFe_2O_4$). Metals

and alloys such as Mn_3O_4 [35], Fe [24], Co [36], Ni [37], FePt [22], and FePd [38] are less commonly employed, in part because of their rapid oxidation in air and/or potential cytotoxicity in biomedical applications. Unlike well-known monolayer-protected Au clusters [2, 3], the preparation methods for magnetic nanoparticles do not tolerate the presence of reactive termini on the stabilizing ligands (i.e., –Br, –SH, etc.), either because of the thermal instability or the bonding of transition metals to the ligands. Consequently, the synthesis of magnetic nanoparticles in the presence of functional groups has been largely unsuccessful. As a result, the as-prepared particles often must undergo further modifications and post-synthetic reactions to render them chemically functional.

14.3 Nanoparticle Functionalization

The functionalization and characterization of the surfaces of magnetic nanoparticles continue to be important and challenging tasks. Surface functionalization provides the means to add chemical stability, *in situ* and *in vivo* function, and specific molecular recognition to these materials, allowing advantage to be taken of their intrinsic magnetic properties in a wide variety of systems. In this chapter, some recent accomplishments in this area are highlighted to provide a sense of breadth of the field; however, for additional information more detailed information is available, including reviews by Latham and Williams [39], Schüth *et al*. [40], and Sun [41].

14.3.1 Surface Adsorption

Surface adsorption can be considered one of the simplest functionalization strategies. As the field of nanotechnology matures, adsorption continues to be a widely used technique for appending a variety of functional molecules to particle surfaces. Surface adsorption is defined as a process by which ionically stabilized nanoparticles are coated by a functional moiety through either electrostatic interactions or via a covalent attachment to the *naked* particle surface. This must be differentiated from ligand exchange, which is the replacement of one covalently attached surface coating for another, and will be discussed later in the chapter.

Like most nanoparticle functionalization methods, surface adsorption strategies derive from routes developed for monolayer formation on two-dimensional (2-D) surfaces [42], and were followed shortly thereafter by a modification of citrate-stabilized Au colloids [43]. To date, the general method for this approach is to add a surfactant or molecule of interest bearing a charge (i.e., ionic), either a carboxylic acid (CO_2^-) [44], phosphate (PO_3^-) [45], ammonium (NR_3^+, where R is either H or C) [46], or other surface-binding group (e.g., OH [47] or SH [48]), to a solution of ionically stabilized particles. The particles can then be separated by magnetic decantation or centrifugation to remove any unassociated material and to yield

functional particles. The effectiveness of this approach is dictated by the surface charge or zeta potential of the nanoparticles, and the strength of the surface–ligand interaction.

Many of these methods make use of particles that have been produced by coprecipitation, and are most common for metal oxides such as iron oxide. As mentioned above, particles produced by this method are often synthesized in the presence of hydroxide, leaving the native surface terminated with hydroxyl groups and an associated counterion of tetramethylammonium in solution. Lucas *et al.* have reported detailed investigations into the nature of surface charge density under acidic, neutral, and alkaline conditions for iron oxide nanoparticles; from zetometry and potentioconductometric titrations, these authors concluded that the charge density under basic conditions was larger than those under acidic conditions [49].

Recently, surface adsorption has been applied to magnetic nanomaterials in a variety of forms. Stabilization by simple organic compounds such as sodium oleate, citrate with dimercaptosuccinic acid (DMSA) [50], biotin with phosphates [51], have all been used. In the case of citrate and DMSA with citrate, Wilhelm and Gazeau showed that iron oxide particles coated with these anionic "monomers" experienced a more rapid uptake into mammalian cells compared to particles passivated with dextran or albumin [51]. Wan and coworkers showed that the adsorption of block copolymers of methyl-terminated polyetheylene glycol (MPEG; molecular weight ~10^6 g mol^{-1}) and oligo-aspartic acid could stabilize iron oxide nanoparticles over a broad pH range [52]. Furthermore, their investigations revealed that the MPEG copolymer produced a significantly higher relative cell viability compared to that of polyacrylic acid and MPEG–polyacrylic acid.

Surface adsorption is also used as a method of biomolecule immobilization. Rotello and coworkers have used the surface adsorption of bovine serum albumin (BSA) under ultrasonication conditions to effectively heat the surrounding aqueous solution using alternating applied magnetic fields [53]. Particles such as these have potential applications in the localized heating of cells for hypothermia-induced cell death [53]. Ivanisevic *et al.* showed that DNA adsorbed onto cobalt ferrite nanoparticles could still be effectively cleaved using restriction enzymes, even in the presence of excess $CoFe_2O_4$ [54]. Deng and Zhang demonstrated through progressive surface adsorption, imine formation, and then reduction, that trypsin could be attached effectively to iron oxide particle surfaces while still maintaining its ability to digest proteins [55]. The same group also used these magnetically separable enzymatic nanoreactors for rapid mass spectral analysis sample preparation, showing that the particle–protein conjugates maintained statistically equivalent activity for the first eight digestions, with activity rapidly diminishing thereafter [55].

Surface adsorption has also seen use in the biological materials with nanorods. Keating *et al.* have shown that the adsorption of thiolated single-stranded (ss) DNA to segmented nanowires containing magnetic Ni segments provided an effective barcode-based visual assay for fluorescently tagged complementary oligonucleotide strands [56]. The same team also incorporated ssDNA hairpin molecular

beacons for more direct analysis. The surface adsorption of proteins to nanowires has also been of recent interest, when Meyer and coworkers adsorbed palmitic (pentadecanoic) acids onto Ni segments of Au/Ni nanowires to selectively target immunoglobulin G (IgG) to the magnetic segments of the wire by hydrophobic/hydrophobic interactions [57]. Here, adsorption was found to take place following a classical Langmuir isotherm, with an equilibrium constant on the order of $10^6\,M^{-1}$ [57].

14.3.2 Ligand Exchange

Nanoparticles can alternatively be synthesized in the presence of species that covalently bind to their surfaces, acting as ligands that passivate the surface through ionic or van der Waals interactions. The majority of these surface ligands contain little to no chemical functionality for further reactivity or interaction with species other than the particle surface. Thus, to impart chemical and/or biological functionality, these ligands must be "exchanged" for other molecules that contain some chemically or biologically relevant functionality. While the debate of the exact mechanism by which this process occurs is ongoing and beyond the scope of this chapter, ligand exchange is broadly classified as the addition of a surfactant or molecule which has a favorable covalent interaction at the particle surface which, upon addition in excess, eventually reaches an equilibrium state with the existing surface moiety. This approach was originally established as a displacement style functionalization technique of two-dimensional Au monolayers [50b, 58]; the most widely recognized studies have been those of Murray and coworkers on small Au nanoclusters [3, 59]. These fundamental investigations of the mechanism of ligand exchange on Au, and its use in laying the groundwork for further Au monolayer reactivity, are relevant to magnetic particles and should be considered as core materials for any investigator considering this approach, even if the mechanisms and specific chemistries differ.

In this chapter, we will highlight some of the more recent uses of ligand exchange to form functional *magnetic* nanoparticle systems, noting that there are inherent difficulties in characterizing the products of these reactions. Many of the early reports on ligand exchange on Au nanoclusters used nuclear magnetic resonance (NMR) spectroscopy as the primary characterization tool for confirming the identity and number of the molecules on the surface following exchange. Unfortunately, magnetic nanoparticles do not lend themselves to NMR as a method of analysis, because their magnetic core causes inhomogeneities in the magnetic field, leading to broadening, large paramagnetic shifts, and/or a loss of signal. Although several reports have described the use of NMR spectroscopy to analyze magnetic nanoparticles [60], these methods must be supported with additional analytical evidence of surface attachment versus colocation in solution. Confirmation of the molecular composition of nanoparticle surfaces poses a significant challenge, as most analytical methodologies provide an ensemble average of the bulk sample and cannot distinguish between a molecule attached to the

nanoparticle surface and those which are free floating in solution or physisorbed in the solid state. There are, it seems, clear opportunities for future research in the realm of surface characterization of functionalized magnetic nanomaterials.

Ligand exchange has most often been applied to metal oxide and alloy (e.g., MPt) nanoparticles. An early report by Rotello demonstrated that, for iron oxide, the ligand geometry, steric bulk, and denticity were significant factors that determined the stability of the magnetic nanoparticles, both in solution dispersions and in the solid state [61]. The results of these studies revealed that a bidentate binding motif (e.g., using 1,3-propanediol) provided the best solution stabilization of iron oxide, whereas steric bulk was necessary for solid-state stability. The choice of ligand to employ on the particle surface is therefore dictated by the desired application of the material in the solid or solution state. Recent studies conducted by Xu and coworkers have shown that a catechol (i.e., orthohydroxyphenol) -style binding group is extremely effective for both ligand exchange and phase transfer of oxide nanoparticles [62]. Since this finding, a series of reports has followed describing the use of dopamine-based ligands for applications ranging from biological [32, 63], catalytic [64], and fluorescent labeling [65]. Although a recent report has questioned the long-term stability of these materials [66], the effectiveness of dopamine-based ligands for surface stabilization and functionalization of magnetic oxides is undeniable.

The replacement of carboxylic acid-containing surfactants on oxide nanoparticle surfaces with other organic acids, hydroxide and polyols, has also been widely studied. The exchange of surface acids for strongly ionic compounds has been used on several occasions to impart water solubility, for example with citrate [67], tetramethylammonium hydroxide [68], and acetate [69]. Lattuada and Hatton reported the use of retinoic acid as an exchangeable group for further functionalization [70]. The terminal OH group of the acid moiety was used for further synthetic reactions that ultimately led to polymerization with acrylic acid [70]. Whilst polymer-coated particles will be discussed later, it is interesting to note that together with the ligand exchange methods, this chemistry was leveraged to add polymer to only one *side* of particles, forming small Janus-type (i.e., heterogeneity between hemispheres) nanoparticle polymer composites [70]. Baldi and Franchini used glycol-terminated cobalt ferrite nanoparticles and exchanged these with alkylphosphonic acids and alkylhydroxamides by leveraging the preferential binding of these ligands to the native oxides [71], to form both water- and organic-soluble $CoFe_2O_4$ nanoparticles [72].

Thiol-containing ligands have been investigated for the functionalization of FePt nanoparticles: following the exchange of amine-containing ligands for the thiols, Johnson *et al*. concluded that during this process the Pt–N bond is replaced by the Pt–S bond [73], and this was exploited to produce water-soluble FePt nanoparticles bearing terminal amine or pyridine groups [74]. In the case of the amine-functionalized particles, these were titrated with the molecule fluorescamine in a fluorescence assay to determine the amine content per milligram of FePt particles [74]. The pyridine functionality was analogously analyzed using a pH titration [74]. Rotello *et al*. also have used thiol and carboxylic acid ligand

exchange chemistry to functionalize FePt nanoparticles. These particles were reacted to form magnetic superstructures by linking with metal ions [75], ferritin proteins [76], and DNA [77]. This research group has also employed amine–thiol and acid–acid exchanges to form superhydrophobic nanoparticles containing perfluorinated ligands [78].

Several recent reports have described the use of mercaptoalkanoic acids of varying lengths as phase-transfer agents for FePt and ferrite nanoparticles. Cheon and coworkers used 2,3-dimercaptosuccinic acid to cap and link $MnFe_2O_4$ nanoparticles to virus capsids via covalent linkers [79]. Tanaka and Maenosono demonstrated that aminoethane thiol was also an effective aqueous phase-transfer agent for FePt particles [80], while Chiang *et al.* used mercaptoacetic acid [81]. Cobalt and nickel ferrites have also been successfully transferred to aqueous dispersions using 11-mercaptoundecanoic acid [79].

14.3.3
Silanes and Siloxanes

Strong surface bonds can also be achieved via silane or siloxane reaction with hydroxyls on the magnetic oxide nanoparticle surfaces. It should be noted that here that reference is made only to functional silanes bonded *directly* to the metal oxide surface; the related reactions which are used following the introduction of a SiO_2 shell are discussed below. While this could fall under the definition of surface adsorption, it is discussed in this section because of the prevalence with which it has been applied to nanoparticles containing existing monolayers. The silane/siloxane functionalization of magnetic oxide nanoparticles resembles ligand exchange, in that the Si–O–M bond replaces the H–O–M or C–O–M bond at the surface. However, unlike ligand exchange, the Si–O–M bond may not be removed or further exchanged without etching the particle. These reactions also form dense crosslinked networks that are interwoven with the terminal chemical functionality.

There have been several reports of direct siloxane attachment to nanoparticles surfaces [82]; a general reaction scheme for this process (on Fe_2O_3 particles) is shown in Figure 14.1. While the exact reaction conditions vary between reports, the general strategy is to add a functional siloxane (e.g., aminopropyltriethoxy silane; APTES) or the methoxy analogue (APTMS) to nanoparticles that have been

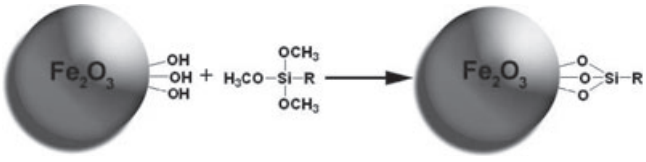

Figure 14.1 Reaction of a trimethoxy-alkyl silane with the surface hydroxyls of iron oxide nanoparticles to modify the surface with alkyl silanes (not to scale).

dispersed by sonication (e.g., in ethanol, toluene, water or a combination of these under slightly acidic or basic conditions). Following heating for several hours (3–24 h), the magnetic particles are isolated by magnetic precipitation and washed to remove excess siloxane. These procedures typically form densely linked network shells with a large number of amine moieties exposed to the solution [83].

Some research groups have sought to avoid reaction in water, and so have explored synthetic alternatives to these reactions. For example, $CoFe_2O_4$ nanoparticles produced by high-temperature reduction in organic solvents were dispersed in hexanes with 0.01% acetic acid by volume, and then reacted with siloxanes that formed covalent bonds to the nanoparticle surfaces [84]. Siloxanes containing NH_2, COOH, and PEG resulted in particles with the highest solubility and good stability. This strategy will likely serve as a starting point for the general use of this functionalization strategy on nanoparticle surfaces. In a similar approach, Shen and coworkers modified the surface chemistry of iron oxide nanoparticles with oleic acid surfactant by reacting these with trichloroalkyl silanes in chloroform to attach octadecyl chains [85]. Whilst HCl is produced during the reaction with the surface, this did not dissolve the nanoparticles, although it is known to do so in water [85].

In almost all cases, silane and siloxane chemistry represents a means by which to covalently attach a simple pendant chemical functionality such as an amine, carboxylic acid, or thiol to the particle surface. This species can ultimately be used for further reaction of the nanoparticle monolayer to create more complex and multifunctional particles. A common goal here is the attachment of biologically relevant species to the particle via imine coupling with aldehydes or amide coupling with carboxylic acids. For example, Katz *et al*. attached microperoxidase-11 via an amide bond using 1-ethyl-3-(3-dimethylaminopropyl) carbodiimide (EDC) [86]. English and coworkers used APTES to coat commercially available 32 ± 18 nm diameter magnetic iron oxide nanoparticles with amine termini, and subsequently used these to imine-link glutaraldehyde [87]. The glutaraldehyde-modified particles were employed to evaluate the on-particle activity of mouse IgG antibodies; the study results showed that approximately 34 antibodies could be bound to each particle, while retaining ~50% of their native activity [92]. Kawamura and Sato used crown ether-functionalized siloxanes to modify iron oxide nanoparticle surfaces, and demonstrated the use of these structures as magnetically separable phase-transfer catalysts [88]. In simple nucleophilic substitutions, the yields of the reactions were comparable or improved when compared to free crown ether [88]. Gao *et al*. have used siloxane chemistry to conjugate Pd crosscoupling catalysts to the surface of magnetic nanoparticles for the synthesis of biaryl products [89]. Figure 14.2 compares the Suzuki reaction on Fe_2O_3 nanoparticle surfaces to the well-known general organic transformation. Using resin-bound starting materials and magnetically recoverable imidazole-ligated Pd Suzuki catalysts, reasonable yields with excellent purity were achieved for several aromatic products [89]. Further investigations of the effect of particle size on the reaction revealed that smaller (~4 nm diameter) particles provided the best synthetic yields, this being attributed to the ability of the resin to incorporate the magnetic particles [89].

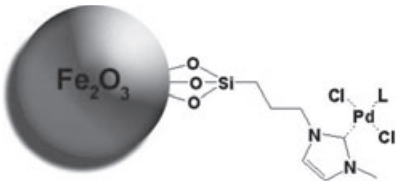

General Suzuki Reaction

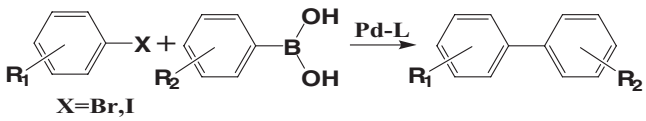

Figure 14.2 (Top) Pd crosscoupling for the Suzuki reaction of Fe_2O_3 particles, compared to (bottom) the general Suzuki reaction (not to scale) [89]. Reproduced with permission from Ref. [91]; © 2006, American Chemical Society.

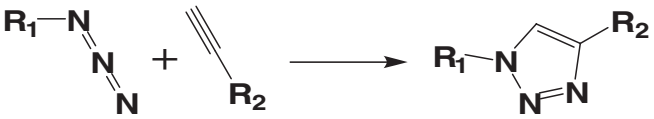

Figure 14.3 General reaction scheme for the 1,3-cycloaddition ("click chemistry") of an azide (N_3) and an alkyne to form a triazole ring.

14.3.4 Monolayer Reactions

The reactions of molecular monolayers to create functional nanomaterials have an enormous variety, yet the available chemistries for magnetic nanoparticles are relatively limited. While the intrinsic magnetic properties of magnetic nanomaterials have been investigated for some time, there has been only limited interest in their chemical functionalization. The chemistries that have been developed are rarely generally applicable methodologies. Several have already been discussed in previous sections (imine and amide coupling, radical polymerization, ester formation), and the reader is again referred to the Au monolayer chemistry of Murray [3, 59b, 90], Fan [91], and Williams [92] for examples of the breadth of monolayer reactions. In this section, we will visit these general methodologies as examples of the chemistries that are still untested, but should ultimately be applied for magnetic nanoparticle functionalization.

Due to its high specificity and mild conditions, the 1,3-dipolar cycloaddition reaction of azides with alkynes shown in Figure 14.3 has been broadly applied in

materials chemistry, including several reports on the surfaces of magnetic nanoparticles. Originally applied as a functionalization strategy to polymeric nanoparticles [93], this reaction was adapted to metallic Au nanoparticles by Williams *et al.* for the attachment of functional moieties to Au nanoparticles [92a]. The uncatalyzed reaction was feasible for the modification of Au particle surfaces using a variety of ligands, although the reaction yields were low, even after stirring for long periods of time (up to 96 h) [92a]. In a later report, infrared spectroscopy was used to show that that similar reaction rates were observed for nanoparticle monolayers and small molecule analogues in solution [92b]. These results showed that the presence of the nanoparticle had little effect on the efficacy of the click reaction, and only small steric effects due to crowding of the azides proximity were observed [92b].

Several reports subsequently used Cu^{+1} catalysts for the click reaction on magnetic nanoparticles: Turro and coworkers demonstrated the use of phosphonic acid-terminated alkyl azides to covalently attach alkyne-containing polymers and small molecules [60a]. Concurrently, Weissleder *et al.* reported that simple carboxylic acid-terminated alkyl azides and alkynes on magnetic particle surfaces could be used to attach biologically active molecules or biomolecular dyes [94]. The *in vivo* function of these materials was examined using optical microscopy. A similar chemistry was used to attach 2,4,6-trinitrophenol to iron oxide nanoparticles bearing alkyl azides to demonstrate the use of 1,2-diols as surface ligands [95]. Similarly, Lin *et al.* have adopted this chemistry for functionalizing iron oxide core/silica shell particles with biologically active agents and proteins.

The pendant groups on as-prepared magnetic nanoparticles have been used to functionalize them by using several chemical transformations other than the above chemistries. Ponti *et al.* first demonstrated tosylation of the pendant alcohols and conversion to thioethers, and then esterification by anhydrides and carbodiimide coupling reagents [96]. In another reaction, *tert*-butyldiphenyl siloxane was shown as an effective protecting group for alcohols during ligand exchange which could be removed with tetra-butylammonium fluoride [97]. By using this synthetic building block, the deprotected alcohol is esterified to the 2-bromo-propionate ester, with both groups capable of being polymerized on the surface of the particles [97]. Instead of the reaction of the pendant hydroxyls, Lin *et al.* took advantage of the double bonds present in oleic acid and reacted these with ozone to form pendant aldehydes [98]. It is hypothesized that the resultant aldehyde-containing particles could be used in standard organic reactions to further modify the particle monolayers.

14.3.5 Encapsulation

Many of the envisioned applications of functional magnetic nanoparticles involve complex environments (e.g., in cells and biological fluids), and consequently the stability of the particle must be considered. The potential for particle decomposition or metal leaching might have a negative impact on the performance of

engineering nanomaterials; for biological systems, the toxicity of nanomaterials represents an ongoing and enormous challenge. Many species present in complex media may be capable of undergoing ligand exchange reactions on the nanoparticle surfaces, displacing the surface molecules and potentially leading to particle insolubility and agglomeration. To address the issue of particle stability, one strategy has been to encapsulate nanoparticles in a complete shell of another material (often denoted as core@shell or core–shell). Nanoparticles have been encased in a wide range of materials from polymers, noble metals, and glass (these are discussed below). The composite materials are designed to protect the magnetism of the core material and, at the same time, to incorporate an outer shell surface that can serve as a robust handle for further chemical modifications. In this section, each of the major types of shell formation, together with some details of recent studies in this area with more exotic materials, will be described.

14.3.5.1 Encapsulation: Silica (SiO_2)

Probably the most well known and widely applied method of nanoparticle encapsulation is the formation of glass or silica shell. Siloxane chemistry (see Section 14.3.4) provides robust surface bonds to many metal oxide nanoparticles; oxide-based materials represent the bulk of the reports describing the encapsulation of magnetic particles by silica shells. These core@SiO_2 materials have the added advantage of well-known silica surface chemistry, and a wide range of chemically functional chlorosilanes and siloxanes are commercially available. However, the silica shell thickness can be difficult to control and many synthetic techniques do not selectively coat individual nanoparticles but instead result in aggregates of many particles conjoined by the silica.

The synthesis of core@SiO_2 materials is straightforward and, although many variations exist, is generally known as the Stöber process (this is shown schematically in Figure 14.4) [99]. Commercially available tetraethylorthosilicate (TEOS) is combined with a sample of metal oxide nanoparticles that have been dispersed in water or water/ethanol. Polymerization is initiated by the addition of aqueous

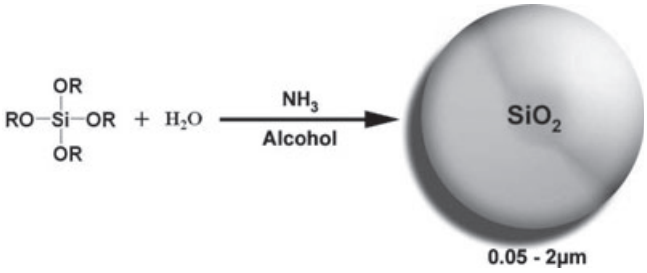

Figure 14.4 General reaction scheme for the Stöber synthesis, during which an alcoholic solution containing water, ammonia and an alkyl silicate are reacted to form silica spheres of relatively uniform size [99].

hydroxide (most commonly ammonium hydroxide), and the material is allowed to polymerize for several hours, after which it is washed and dried. Yang and coworkers carefully investigated the effect of tetramethylammonium hydroxide (TMAOH) on Fe_2O_3@SiO_2 nanoparticles, and showed that the number of particles per silica shell decreased with increasing TMAOH concentration [100].

Often, the addition of an amphiphile that forms reverse micelles can improve the quality of these structures; both encapsulating a single particle in a shell and the shell thickness are reported to be controllable based on the size of the micelle. For example, Korgel and coworkers used Igepal CO-520 in cyclohexane to individually and uniformly coat 6 nm-diameter FePt nanoparticles with a 7 to 23 nm-thick SiO_2 layer, the thickness of which was controlled by variation of the TEOS : FePt ratio [101]. Transmission electron microscopy (TEM) images of the FePt nanoparticles before and after encapsulation in the SiO_2 shell using this approach are shown in Figure 14.5. However, this method was effective only for larger particles; a similar reaction with smaller 2.7 nm-diameter FePt particles resulted in agglomerates [101]. Lee and Lee later demonstrated that Fe_2O_3@SiO_2 nanoparticles of approximately 30 nm diameter and good size uniformity could also be synthesized using this approach. Rossi *et al*. employed polyoxyethylene(5) iso-octylphenyl ether emulsions in cyclohexane to produce Fe_3O_4@SiO_2 particles which were then further functionalized with APTMS and RhCl to produce magnetically recoverable nanoparticle hydrogenation catalysts [102]. Recently, Duran and coworkers investigated the interplay of the relative amounts of surfactant (Triton X-100 in 1-hexanol), water, and cyclohexane to control silica shell formation on Fe_2O_3 nanoparticles [103]. By varying the amount of total water in the system, it was found that the number of particles per core@shell structure could be controlled, and the total diameter was tunable between ~34 and 120 nm [103].

Methods that were initially developed for noble metal particles suffice to encapsulating nonoxide magnetic particles, such as cobalt. These techniques can uniformly and controllably encapsulate the particles in a silica shell by first using

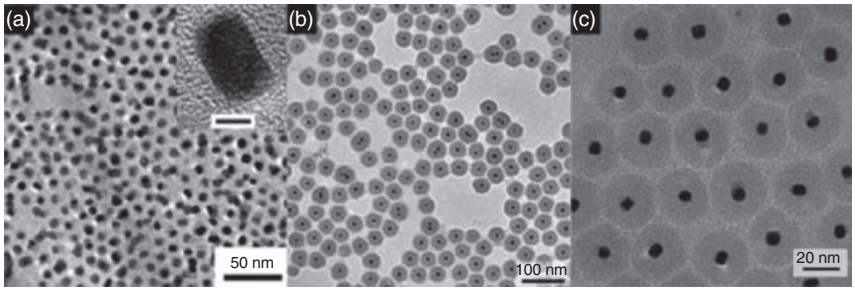

Figure 14.5 Transmission electron microscopy images. (a) FePt particles before reaction; (b) FePt particles following encapsulation in silica; (c) A higher-resolution image of the particles in panel (b). Reproduced with permission from Ref. [101]; © 2006, American Chemical Society.

amino silanes as an initial "sticky" group for the surface from which a shell can grow [104]. Recently, Dravid *et al*. used pure Co nanoparticles prepared by aqueous reduction with $NaBH_4$ and modified their surfaces with APTES as an initial binding layer [105]. This report demonstrated that the Co core size was a function of the initial Co/citrate ratio and, more importantly, that the SiO_2 shell thickness was determined by the subsequent APTES : TEOS ratio [105].

Ultimately, the goal of these encapsulating procedures is to produce nanoparticles capable of simple functionalization via siloxane reagents. Undoubtedly, the majority of these reports involve the use of trialkoxy-aminopropyl silane reagents for the attachment of metals salts [106], biomolecules [82d, 83, 107], or fluorophores [108]. However, there have been many reports of alternative applications of these materials. Chen and Chen attached octadecyl chains to iron oxide@SiO_2 as a method of rapidly desalinating DNA samples [109]. By employing microwave heating, these composite particles trapped DNA at concentrations of up to 625 pmol mg^{-1} nanoparticles [109]. Xue and coworkers employed Fe_3O_4@SiO_2 particles as the substructure for magnetic fluorescent structures [110], where the magnetic nanoparticles were first encapsulated with a SiO_2 shell in a reverse micelle, after which quantum dots (QDs) were added directly to the silanization solution together with additional reactants to form more SiO_2 on the particle surface [110]. The ~80 nm-diameter composite particles retained the strong QD luminescence (blue shift ~20 nm), although the magnetic moment was reduced to 7% of the pure Fe_3O_4 sample [110].

Silica shells have also been used as intermediates for subsequent encapsulation in other materials. Chen and coworkers reported the use of SiO_2 as an intermediary for TiO_2 shells that could then be used to break down biological materials under ultraviolet (UV) irradiation [111]. Sunkara and Misra, on the other hand, used $TiCl_4$ to directly form a titanium oxide shell on the surface of $NiFe_2O_4$ nanoparticles (i.e., $NiFe_2O_4$@TiO_2) [112]. Tungsten doping of the TiO_2 shell further enhanced the effectiveness of the photocatalyst [112]. Qian *et al*. recently prepared Fe_2O_3@SiO_2 particles with an outer shell of lanthanide-doped $NaYF_4$, yielding magnetic particles with luminescent surfaces that could also be functionalized with siloxane chemistry [113]. Finally, Chen and coworkers recently used a thin layer of SiO_2 to coat iron oxide nanoparticles and enable subsequent deposition of a shell of Al_2O_3 using aluminum isopropoxide [114].

14.3.5.2 Encapsulation: Metallic and Semiconductor Shells

Au–thiol monolayer chemistry is arguably the most recognizable method of functionalizing nanoparticles. Significant efforts have therefore been made towards encapsulating magnetic nanoparticles in Au, or analogously in Ag. In addition to their well-defined surface chemistry, noble metal shells are expected to have surface plasmon waves with resonant frequencies in the visible to near-infrared (NIR) region of the spectrum.

Encapsulating magnetic nanomaterials in metallic shells can be synthetically difficult because of the surface energies, lattice matching, and wettability, in addition to the need to selectively deposit metal on the surface of existing particles

rather than the nucleation and growth of new particles in solution. In many instances, the reduction potential of a metal salt at an existing surface is lower than in solution, but careful control over experimental conditions and extensive characterization is required [115]. Many analytical techniques, such as UV-visible absorbance spectroscopy (for plasmon resonance) and powder X-ray diffraction (XRD), provide an ensemble average of the entire sample, and therefore do not conclusively confirm shell formation. Detailed high-resolution TEM and energy-dispersive X-ray (EDX) measurements, with sampling of many particles and statistical analysis, are critical to substantiate formation of the shell on the outer magnetic particle surface.

Despite these challenges, magnetic core@Au or other metallic shells have great potential in the field of functional magnetic nanomaterials. While there is no standard method of producing Au shells for magnetic nanoparticles, methods can be grouped into two categories: (i) those that use Au salts (generally $AuCl_4^-$); and (ii) those that use Au nanoparticles. Here, we will provide a brief discussion of both methods along an extension to other metallic shells and semiconductors.

In 2004, Williams *et al*. reported the use of hydroxylamine seeding to form Au shells on iron oxide magnetic nanoparticles, confirmed by both TEM and EDX analysis [116]. In addition, it was observed that Au preferentially deposited on γ-Fe_2O_3 versus Fe_3O_4, and that the Au shell did not affect the individual particle magnetic moment [116]. Additional methods of producing Au shells have emerged for iron oxide and other magnetic nanoparticles. For example, Tarr and coworkers first deposited amorphous TiO_2 shells on iron oxide nanoparticles, after which the TiO_2 served as a photocatalyst for the surface reduction of $AuCl_4^-$ [117]. The quality of the Au shell was seen to be directly correlated with Au concentration, with roughly shaped aggregates forming at low levels of Au [117]. Inverse micelles prepared from cetyl trimethylammonium bromide (CTAB) were reported to produce Fe_2O_3@Au [118]. Based on a comparison of the properties of these materials with particles coated in MPEG and starch, it was determined that the Au-coated particles had the best long-term stability [118]. Pal *et al*. also used the inverse micelle approach with glucose to prepare Fe_3O_4@Au nanoparticles, which were later used for the bioelectrochemical detection of DNA, antibody capture, and horseradish peroxidase [119].

In contrast, Sun *et al*. used oleylamine- and oleic acid-stabilized iron oxide particles with excess amine in chloroform as a reducing agent for Au^{3+} ions to preferentially deposit Au on the particle surfaces [120]. A continued deposition of Au or Ag while in the CTAB micelle was used to increase and control the thickness of the outer metal shell, effectively controlling the resonant plasmon wave absorbance band over a 60 nm wavelength range [120]. Majectich and coworkers demonstrated the use of a covalent linkage to attach small Au clusters (~2 nm diameter) to iron oxide nanoparticles as surfaces with which to initiate further Au shell growth [121]. The oleic acid and oleylamine surfactants were first stripped from the magnetic particle surface using TMAOH, and the particles stabilized with 11-mercaptoundecanoic acid. The terminal thiol groups were used to capture added Au particles, and these were subsequently used as nucleation points for

further tetrachloroaurate reduction by formaldehyde [121]. Small attached Au particles have also been used as the source of the shell by heating them to cause coalescence, thereby producing a highly uniform Au shell around the iron oxide nanoparticles [122]. Detail of these studies, together with descriptions of other Au shells on iron oxide particles, are provided in a recent review [123].

Several types of magnetic nanoparticle coated with Au shells that have cores made from materials other than iron oxide have been described. Wei *et al*. demonstrated the encapsulation of FePt nanoparticles with Au by the reduction of Au acetate [124], while Wang and coworkers reported the preparation of both FeCo@Au and FeCo@Ag particles by magnetron sputtering, a technique that produced particles that were spherical and cubical, with very thin Au or Ag shells [125]. Co@Au particles have been prepared in solution by using a displacement reaction between the Co nanoparticle core and dissolved $AuCl_4^-$ according to the reaction [126]:

$$Co_n + N[(CH_2)_7CH_3]_4(AuCl_4) \rightarrow Co_{(n-1)}@Au + CoCl_3 + N[(CH_2)_7CH_3]_4Cl \quad (14.1)$$

This method was reported to be capable of carefully controlling the thickness of the Au layer, although due to the removal of Co atoms during the reaction the magnetic particle size (and therefore the magnetic properties) was decreased as additional Au was deposited on the surface [126].

Using this range of methods, several other types of metallic shells on magnetic particles have recently been reported. Ag shells are of particular interest for their plasmonic properties and lower cost relative to Au. Inglesias-Silva *et al*. produced Ag-coated iron oxide nanoparticles by glucose reduction of $AgNO_3$ in a microemulsion [127], while Poddar and Srinath used a displacement reaction analogous to that in Equation 14.1 to produce Co@Ag nanoparticles [126, 128]. Encasing particles in a Pt shell has been of interest for generating magnetically recyclable catalysis: Cheon and coworkers showed that Co@Pt particles could be prepared by using cobalt nanoparticles as "seeds" for the preferential deposition of thermally decomposed Pt(hfac)$_2$ (hexafluoroacetylacetonate) [129]. More recently, Co@Pt particles were used for the catalytic reduction of alkenes under hydrogen, and recovered magnetically from the solution following the reaction [130]. Core@shell Ni@Pt nanoparticles were reported to be produced by the addition of KBH_4 to a solution of 1,2-propane diol containing Ni acetate and oleic acid [131]. The borohydride caused nucleation and growth of small Ni particles, after which H_2PtCl_6 was added to the hot reducing environment to form the reduced Pt on the outer surface of the Ni particles [131].

In addition, several groups have reported the deposition of luminescent semiconductor shells, building on the studies of concentric shell formation and encapsulation in semiconductors and QDs [132], although this discussion is limited to recent reports of magnetic particle cores with semiconductor shells. It is important to distinguish these methods from those that incorporate QDs with magnetic

particles in oxide or polymeric materials [103, 133]. For example, a recent report described a method by which FePt@CdSe or FePt@CdS nanoparticles were formed in a single step, although the products contained both particles with the desired core–shell structure and interconnected agglomerates [134]. The use of CdO as the initial shell surface precursor enabled the controlled formation of the core–shell nanoparticle; the CdO layer was subsequently converted to the semiconductor by the addition of Se or S [134]. Parak and coworkers performed a detailed investigation of a variety of semiconductor shells on FePt nanoparticles [135], and showed that by beginning with a sulfurous layer on the particle surface, CdS, CdSe, ZnS, and PbS could all be layered onto FePt surfaces to produce FePt@ shell structures. Further heating of these structures caused a de-wetting of the surface and the spontaneous formation of discrete heterodimer particles of FePt-semi-conductors [135].

14.3.5.3 Encapsulation: Polymeric and Carbon Shells

By far the largest class of functional magnetic nanomaterials is the core@polymer structures. Although these materials warrant a full review in their own right, for reasons of limited space we will attempt here simply to provide a broad overview of recent data. A summary of core/polymer combinations is provided in Table 14.1, for quick reference. The polymeric shells are generally formed by applying the methods described in Sections 14.3.3 and 14.3.4 (surface adsorption, synthesis in polymeric media, surface-initiated polymerization). Surface adsorption and *in situ* synthesis represent the bulk of reports on this topic. In addition, the types of polymer that have been coated onto magnetic nanoparticle surfaces fall into three categories, namely naturally occurring biopolymers (e.g., polysaccharides), synthetic polymers, and block copolymers.

14.3.5.3.1 Biopolymers Several reports exist of the use of polysaccharides to coat magnetic nanoparticles. For example, dextran (see Figure 14.6a) was reacted in the presence of urea and iron oxide nanoparticles to form dextran-coated magnetic nanoparticles [136]. Fernández-Lafluente *et al.* showed that dextran could be attached to the surface of carboxyl-terminated iron oxide particles using EDC and butylenediamine, and that these nanomaterials could be used as solid supports for the PCR amplification of DNA [137]. The combination of on-particle PCR with ELISA enabled the detection of 10^{-19} g target DNA in the presence of excess non-complementary oligonucleotides [137].

Alternatively, Chen and coworkers used EDC to directly attach carboxymethyl chitosan (an aminated polysaccharide; see Figure 14.6b) to iron oxide nanoparticle surfaces [138]. The chitosan was crosslinked by glutaraldehyde to form a polymeric shell. Crosslinked chitosan shells have been used by Zhang *et al.* to link the enzyme papain to magnetic nanoparticles; an increased hydrolysis rate of casein and longer stability was observed when the enzyme was conjugated to the sugar-coated particles [139]. Imine crosslinking between a chitosan shell and alcohol dehydrogenase was also used to link the enzyme to magnetic particles; this resulted in an improvement of the enzyme's stability but a reduction in its activity [140].

Table 14.1 Compilation of nanoparticle-polymer materials, between 2006 and 2008.

Particle	Polymer	Particle	Polymer
Iron oxide	Maleimide-PEG-*b*-poly(D,L-lactide) [152]	Fe_3O_4	Biotin-PNIPAAm/PNIPAAm
Iron oxide	Gum arabic [162]	Fe_3O_4	PS (COOH, SO_3H, SH, S-) [163]
Iron oxide	PEG-oligo(aspartic acid) [52]	Fe_3O_4	3,4-ECMC [164]
Iron oxide	PVC [165]	Fe_3O_4	Poly(MAPTMS-r-PEGMEMA-r-NAOS) [166]
Iron oxide	PS-*b*-PBD-*b*-PS [168]	Fe_3O_4	PAAm [168]
Iron oxide	Polyaspartate [146]	Fe_3O_4	*N*-vinylcaprolactam-*co*-AAEMA-*co*-Vim [151]
Iron oxide	Gum arabic [169]	Fe_3O_4	PNIPAAm [170]
Iron oxide	PDMS [171]	Fe_3O_4	PMAA [145]
Iron oxide	Poly(maleic acid-alt-1-octadecene) [156]	Fe_3O_4	Poly(MAA-*co*-*N*,*N*′-methylene-bis-(AAm)) [172]
γ-Fe_2O_3/Fe_3O_4	PVP [173]	Fe_3O_4	Poly(1-VIm-*co*-acrolein oxime-*co*-AA) [174]
γ-Fe_2O_3/Fe_3O_4	PS-*b*-PAa [132a]	Fe_3O_4	Dextran-g-PNIPAAm-*co*-*N*,*N*-DMAAm) [175]
γ-Fe_2O_3	PN(2-CC)-*b*-PN [152]	Fe_3O_4	Carboxymethyl chitosan [138]
γ-Fe_2O_3	PS/PPy [176]	Fe_3O_4	Alginate[142]
γ-Fe_2O_3	PNIPAAm [177]	Fe_3O_4	Poly(butyl acrylate-styrene)[178]
γ-Fe_2O_3	PIB/PEO [179]	Fe_3O_4	PS [180]
γ-Fe_2O_3	PA-6 [181]	Fe_3O_4	Poly(ethyl-2-cyanoacrylate) [182]
γ-Fe_2O_3	Poly(*N*-isopropyl-*co*-*tert*-butylacrylamide) [183]	Fe_3O_4	Poly(butylcyanoacrylate) [182]
γ-Fe_2O_3	PS-*b*-PAA [184]	Fe_3O_4	Poly(hexylcyanoacrylate) [182]

Table 14.1 *Continued*

Particle	Polymer	Particle	Polymer
γ-Fe_2O_3	Styrene/Sipomer PAM200 [185]	Fe_3O_4	Poly(octylcyanoacrylate) [182]
γ-Fe_2O_3	Poly(hydroxyethyl methacrylate) [186]	Fe_3O_4	PVP [187]
γ-Fe_2O_3	PTEEMS-*b*-PAAm [188]	Fe_3O_4	PPy [189]
γ-Fe_2O_3	PPy [190]	Fe_3O_4	Pyrene/polyacrylamide [191]
γ-Fe_2O_3	PMMA/Chitosan [192]	Fe_3O_4	PVAL [193]
γ-Fe_2O_3	PEI [194]	Fe_3O_4	PNIPAAm [195]
γ-Fe_2O_3	Poly(divinylbenzene) [196]	Fe_3O_4	PAAm-*co*-PEGDMA [197]
Fe_3O_4	PMMA [198]	Fe_3O_4	PVAL [150b]
Fe_3O_4	Poly(D,L-lactide)-*b*-PEG [199]	Fe_3O_4	Trithiol-terminated PMAA [200]
Fe_3O_4	PS [201]	Fe_3O_4	PEG methyl ether monomethacrylate [202]
Fe_3O_4	PAA [182]	Fe_3O_4	Poly(acrylic acid)-*b*-PNIPAAm [203]
Fe_3O_4	Poly(2-methoxyethyl methacrylate) [146]	Fe_3O_4	PAA-*b*-PNIPAAm-*b*-poly(acrylate methoxy PEO) [203]
Fe_3O_4	PS [202]	Fe_3O_4	PtBA-*b*-PEA-*b*-PMAA [204]
Fe_3O_4	Poly(3-vinylpyridine) [183]	Fe_3O_4	Folate-PEG-*b*-poly(ε-caprolactone) [205]
Fe_3O_4	PAAm [206]	Fe_3O_4	*N*-succinyl-*O*-carboxymethychitosan [141]
Fe_3O_4	PVAL [207]	Fe_3O_4	Chitosan [140]
Fe_3O_4	Poly(2-vinyl-*N*-methylpyridinium iodide) [208]	Co	PS-TOPO [209]
Fe_3O_4	PNIPAAm [210]	Co	PS-NH_2 [209]
Fe_3O_4	Poly(L-lactic acid) [211]	Co	PS [212]
Fe_3O_4	PMMA-*co*-acrylic acid [213]	Co	PAN [212]

Table 14.1 *Continued*

Particle	Polymer	Particle	Polymer
Fe_3O_4	Styrene/Sodium p-styrenesulfonate [214]	Co	PS-DOPO [153]
Fe_3O_4	Poly(3,4-ethylenedioxythiophene) [215]	Co	PS-COOH [153]
Fe_3O_4	PEO-*b*-PUR-*b*-PEO [216]	Co	PS-NH_2 [153]
Fe_3O_4	P(EO/PO)-*b*-PUR-*b*-P(EO/PO) [192]	Co	Poly(*N*-isopropyl-*co*-*tert*-butylacrylamide) [171]
Fe_3O_4	PEO-*b*-PPO-*b*-PUR-*b*-PEO-*b*-PPO [192]	Co	Poly(ε-caprolactone) [149]
Fe_3O_4	PPy [217]	$CoFe_2O_4$	Polyaniline [218]
Fe_3O_4	Poly((PEG) monomethacrylate) [219]	Ni_{wire}	Chitosan/Carboxymethylpullulan [144]
$Zn_{0.6}Cu_{0.4}Cr_{0.5}Fe_{1.5}O_4$	PAA [220]	$Zn_{0.6}Cu_{0.4}Cr_{0.5}Fe_{1.5}O_4$	Polyaniline

PN(2-CC) = Poly(norbornene 2-carboxylic acid 2-cyanoethyl ester).
PN = Poly(norborene).
PBD = Polybutadiene.
PAA = Poly(acrylic acid).
PAAm = Poly(acryl amide).
PTEEMS = Poly(trimethylammonium ethylacrylate methyl sulfate).
PEI = Polyethylenimine.
3,4-ECMC = 3,4-Epoxycyclohexylmethyl-3′,4′-epoxycyclohexanecarboxylate.
MAPTMS = 3-(trimethoxysilyl)propyl methacrylate.
NAOS = *N*-acryloxysuccinimde.
AAEMA = Acetoacetoxy methacrylate.
PMAA = Poly(methacrylic acid).
AAm = Acrylamide.
MAA = Methacrylic acid.
AA = Acrylic acid.
PEG = Polyethylene glycol.
PPO = Polypropylene oxide.
PEO = Poly(ethylene oxide).
EO = Ethylene oxide.
PO = Propylene oxide.
PVP = Polyvinylpyrrolidone.
PVAL = Polyvinyl alcohol.
PVC = Polyvinyl chloride.
PNIPAAm = Poly(*N*-isopropylacrylamide).
PPy = Polypyrrole.
PEGDMA = Poly(ethylene glycol dimethacrylate).
PtBA = Poly(*tert*-butyl acrylate).
PEA = Poly(ethyl acrylate).
PEGMEMA = Poly(ethylene glycol) methyl ether methacrylate.
VIm = Vinylimidizole.
DMAAm = Dimethylacrylamide.
PAN = Polyacrylonitrile.

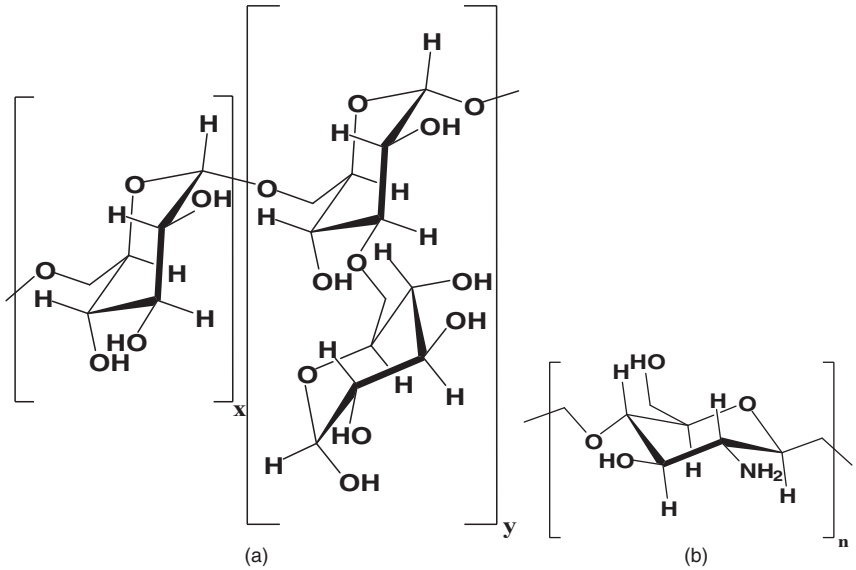

Figure 14.6 Structures of (a) branched polysaccharide dextran and (b) polysaccharide chitosan.

All of these magnetic nanoparticle conjugates have applications in biological systems, and Zhu *et al.* recently investigated their cytotoxicity. Using succinic acid-terminated chitosan shells on iron oxide nanoparticles, no increased toxicity relative to the free polymer was observed over a 72 h period; however, the long-term *in vitro* cell viability was not studied [141].

A number of other biopolymer shells have been attached to magnetic nanoparticles. Iron oxide particles with polyaspartate acid shells were prepared by adsorption of the ionically charged polymer to the particle surface [142]. Compared to polymethyl dextran, the iron oxide@polyaspartate particles were found to have a better uptake in cancer cells and leukocytes, and did not inhibit cell growth [142]. Alginate-protected iron oxide nanoparticles were produced by coprecipitation of the iron salts, immediately followed by the addition of alginate [143]. A layer-by-layer assembly was used for the sequential deposition of carboxymethylpullulan and chitosan on the surface of magnetic Ni nanowires, so as to increase solubility and biocompatibility [144].

14.3.5.3.2 **Synthetic Polymers** As a vast body of literature exists relating to the encapsulation of magnetic nanoparticles with synthetic polymer shells, only recent key examples have been selected here representing this broad area of research.

The *surface adsorption* of polymers to magnetic nanoparticle surfaces represents a major strategy for the formation of polymeric shells. As an example, the trifunctional copolymer shown in Figure 14.7 was used to link to the surfaces of iron oxide nanoparticles [145]. The dopamine groups in the copolymer reacted with the

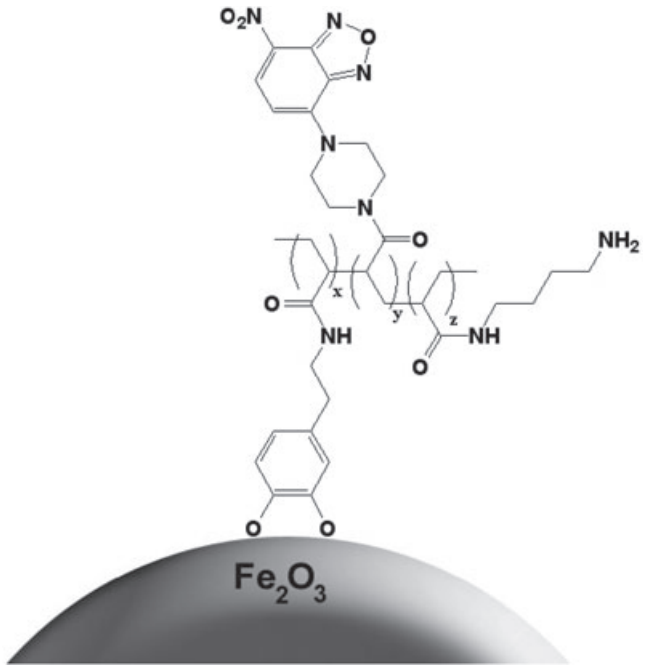

Figure 14.7 Copolymer modification of an iron oxide nanoparticle surface by attachment through dopamine(s). The polymer also contains multiple dopamine substituents (x), a fluorescent monomer piperazinyl-4-chloro-7-nitrobenzofurazane (y), and amine terminated monomer (z) for protein conjugation. Reproduced with permission from Ref. [145]; © 2008, Wiley-VCH Verlag GmbH & Co. KGaA.

hydroxyls on the surface of the iron oxide to form covalent linkages; other species present in the polymer provided fluorescent (for imaging) and amine groups [145]. The free amine groups in the polymeric shell were reacted using amide coupling chemistry (with EDC) to attach double-stranded (ds)RNA-polyinosinic-polycytidyl acid to enable particle localization at the cell wall of Caki-1 cells [145]. Yao *et al.* used methylacrylic acid and *N,N′*-methylene-bis-acrylamide to coat magnetic nanoparticles in a polyacrylate shell for α-chymotrypsin immobilization, which was determined to have 82.7% of its native activity [146].

The *surface-initiated polymerization* of magnetic nanoparticles to form polymer shells is an alternative and effective route. As a representative example, iron oxide nanoparticles were coated in thermally responsive poly(2-methoxyethyl methacrylate) (PMEMA) using surface atom transfer radical polymerization (ATRP) [147]. The Fe_2O_3@PMEMA particles remained soluble in 50 °C methanol, but were completely precipitated when the temperature was lowered to 20 °C [147]. Solubility was impacted upon at a critical temperature that was inversely related to the chain length, this effect being attributed to the steric inhibition of chain coiling [147]. More recently, Schmidt and coworkers used surface-initiated ATRP to coat cobalt

nanoparticles with poly-ε-caprolactone [148] These particles were subsequently used to heat solutions under an AC magnetic field; as the thickness of the polymer coating increased, the AC susceptibility of the nanomaterials decreased due to the weaker interparticle magnetic coupling [148]. Takahara *et al*. investigated both surface-initiated ATRP and nitroxide-mediated radical polymerization (NMRP) on iron oxide nanoparticle surfaces [149]. Here, the surface initiators were bound through siloxane or phosphate groups to the nanoparticle surfaces, and subsequently polymerized with styrene or 3-vinylpyridine [149]. The efficiencies of the surface radical initiation processes varied between 10 and 30%, and the resultant solubilities of the nanoparticle were a direct result of the type of polymer shell [149].

Solution synthesis of nanoparticles in the presence of polymers is the final route for preparing core@polymer materials. Gedanken and coworkers have used sonochemical methods to produce iron oxide nanoparticles in the presence of polyvinyl alcohol [150]. These nanoparticles were then functionalized with APTMS, to produce spherical particles with a final particle diameter of approximately 11 nm and amine termini [150b]. Following the attachment of anti-PKCα, the particles were loaded into sperm cells, after which the antibody was shown to remain active [150b].

Microgels encapsulating magnetic iron oxide nanoparticles were synthesized by iron coprecipitation in the presence of a copolymer containing *N*-vinylcaprolactam, acetoacetoxyethyl methacrylate, and vinylimidizole [151]. The resultant gel-coated magnetic particles were shown to have smaller hydrodynamic radii than the pure polymer, this effect being a function of pH (see Figure 14.8). The critical temperature of these responses was also dependent on the presence of magnetic nanoma-

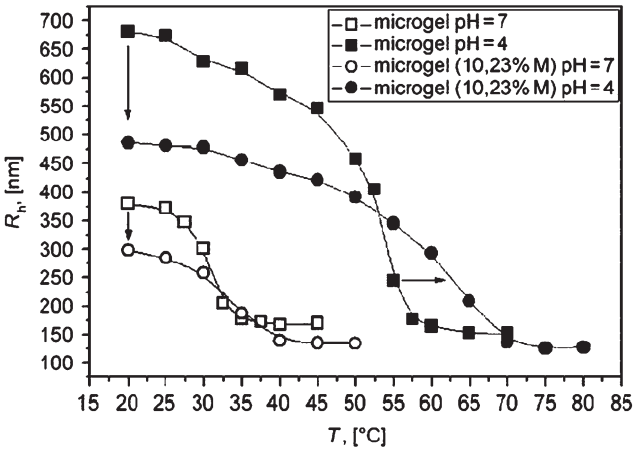

Figure 14.8 The effect of temperature on the hydrodynamic radii (R_h) of iron oxide nanoparticles coated with *N*-vinylcaprolactam-*co*-acetoacetoxyethyl methacrylate-*co*-vinylimidizole copolymer hydrogels under neutral (white) and acidic (black) conditions. Circles and squares indicate gels with and without magnetic particles, respectively. Reproduced with permission from Ref. [151]; © 2007, Wiley-VCH Verlag GmbH & Co. KGaA.

terials [151]. Another interesting nanoparticle composite material was described by Pyun and coworkers, who developed a method to form long chains of Co nanoparticles [153]. Here, the thermal decomposition of $Co_2(CO)_8$ in the presence of a polymer mixture containing amino phosphine oxide, alkyl phosphine oxide, amine, and/or carboxylic acid binding groups, caused the particles to self-assemble into linear structures [153].

In some cases, multifunctional nanoparticles have been used during polymer synthesis (i.e., as monomeric building blocks) to form crosslinked dense networks. As an example, when Park and coworkers used dopamine as the surface binding group and crosslinking agent for polydimethylsiloxane [154], there was a clear impact on the overall mechanical properties of the elastomer, with the particle composite being almost twice as rigid and slightly harder [154].

14.3.5.3.3 **Block Copolymers** Several recent reports have referred to block copolymers being used for the formation of shells and the encapsulation of magnetic nanoparticles. These types of material are advantageous because of the intrinsic and controllable structure of the polymer blocks, this property being especially useful for promoting particle interactions, solubility and – potentially – a uniform shape of the core@shell nanocomposite. Kim and Taton have used block copolymers to encapsulate iron oxide, CdSe@ZnS, and Au nanoparticles into multiparticle composites with polyfunctionality [133]. For this, a polystyrene–polyacrylic acid block copolymer was mixed with hydrophobic nanoparticles to form a microemulsion in water, and a crosslinker then added [152, 133]. The coencapsulation of QDs with iron oxide nanoparticles was found to cause a significant reduction in the quantum yield of the semiconductors [133]. When Gao *et al*. encapsulated iron oxide nanoparticles with doxorubicin (an anti-cancer agent) in block copolymer shells of maleimide-poly(ethylene glycol)-block-poly(D,L lactide) [155], the external surface was functionalized with cyclic Arg-Gly-Asp peptide (cRGD) to specifically target $\alpha_v\beta_3$ endothelial integrins and promote cellular uptake [155]. Subsequent doxorubicin release from the polymer was found to be increased at a higher pH [155].

In another example, Belfield and Zhang used ring-opening metathesis polymerization (ROMP) to form di-block copolymers for the synthesis and stabilization of iron oxide nanoparticles [156]. The block copolymers were synthesized from norbornene and the 2-cyanoethyl ester of norbornene carboxylic acid, with more stable and crystalline iron oxide particles being observed when the cyano ester block was larger than the norbornene [156]. Very recently Svergun, Bronstein and coworkers produced magnetic iron oxide core@block copolymer shell nanoparticles with a good size monodispersity [157]. These iron oxide nanoparticles were produced via a standard high-temperature reduction route with oleic acid to yield highly uniform magnetic nanoparticle sizes [157]. When poly(maleic anhydride-alt-1-octadecene) was added, the hydrophobic chains of the octadecene block were able to interpenetrate the surface-bound oleic acid ligands [157]. An analysis using small-angle X-ray scattering (SAXS) showed that 99.9% of the polymeric shells contained only a single nanoparticle [157].

14.3.5.4 Encapsulation: Carbon Shells

Today, there is growing interest in the use of carbonaceous shells to encapsulate magnetic nanoparticles. These materials are attractive first, because the carbon should be biocompatible, and second because many different chemical approaches can be used to functionalize the carbon surfaces [158]. For example, Ni@C nanoparticles were prepared by laser-induced metal complex heating and then functionalized by oxidizing with sulfuric and nitric acids to produce a carboxylic acid-terminated surface [159]. The carboxylic acids were then used for acid chloride condensation with amines to form amide surface bonds. Alternatively, the carbon shell has been functionalized via radical addition to peroxides to form acid termini [160]. In this study, Hu and coworkers used the base-catalyzed reduction of $KPtCl_4$ to form small Pt nanoparticles on the carbon shell surface; the Pt particles were then used as hydrogenation catalysts on a magnetically recyclable particle [160]. Recently, Wei *et al.* described the use of sugar dehydration to form carbonaceous shells on Ni and FeNi nanoparticles [161]. Here, the resultant carbon shells were shown to be approximately 8 nm thick (total particle diameters 28–65 nm) and to contain both hydroxyl and carboxylic acid functional groups [161].

14.3.6 Lipids and Dendrimers

Nanoparticle surfaces have been modified with both dendrimers and phospholipids, which should be grouped into a separate category for the purposes of organization, as neither can be considered polymeric. The long aliphatic chain of phospholipids will insert into the hydrophobic molecular monolayer on nanoparticle surfaces, forming a micelle-like structure without the formation of any direct bonds or electrostatic attraction to the particle. Dendrimers have also been used to encapsulate nanoparticles and to serve as a template for their synthesis.

14.3.6.1 Lipids

The encapsulation of magnetic nanoparticles by lipids or phospholipids has been explored mainly by the biological community, based on their potential relevance in this area. Phospholipids are commercially available with a large assortment of appended fluorescent dyes, chain termini (e.g., amine, carboxylic acid, biotin, His-tags), PEG chains, and ionic charges [221]. The incorporation of phospholipids on magnetic particles is used so that a host of biocompatible functionalization methods can be applied. The encapsulation by phospholipids is straightforward, and relies on favorable van der Waals interactions between the lipid alkyl chains and the particle monolayer. Using the methodology originally applied to QDs, chloroform solutions of phospholipid are added and stirred with magnetic particles bearing long-chain alkyl ligands [222]. The solutions are then evaporated, suspended in warm water, and purified using standard methods [13]. The general arrangement of phospholipids on the surface of a magnetic particle is shown in Figure 14.9; here, the PEG (molecular weight 3000 Da) termini promote solubility in aqueous solutions. A recent report has provided an in-depth discussion of the

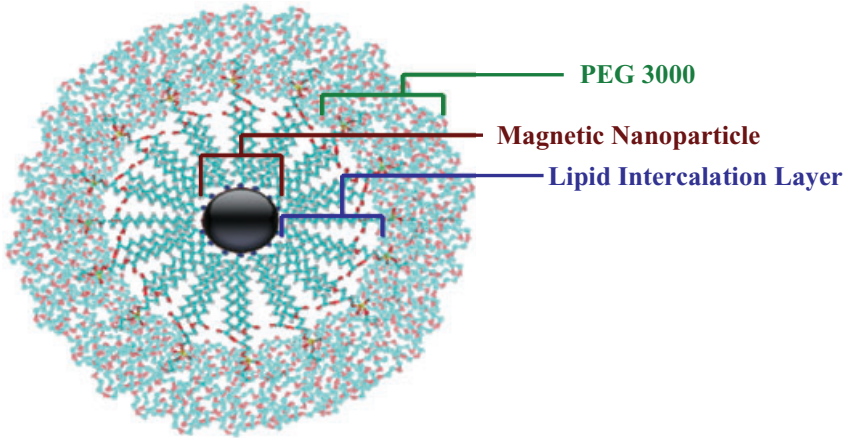

Figure 14.9 Schematic representation of a PEG-phospholipid-encapsulated nanoparticle (not to scale). Reproduced in part with permission from Ref. [39]; © 2008, American Chemical Society.

lipid chemistry of magnetic nanoparticles [223], some details of which will now be discussed.

The use of phospholipids or lipid bilayers has been valuable for functional materials, separations and microfluidics, and the ease with which these highly crystalline, monodisperse nanoparticles may be functionalized and rendered water-soluble has been widely exploited. For example, Held and coworkers used phospholipids which terminated in either single-stranded oligonucleotide DNA or biotin on $MnFe_2O_4$ and Fe_2O_3 particles to pattern these onto surfaces containing complementary DNA or streptavidin [222b]. Chung *et al.* used functional phospholipids containing either PEG or Ni-nitrilotriacetic acid (Ni-NTA) complexes to separate proteins [224], relying on the preferential binding of the Ni for His-tagged proteins [225]. The PEG lipids served to suppress any nonspecific adsorption and thus to improve the selectivity of the nanoparticle capture agent [225]. Due to the increased surface-to-volume ratio, the magnetic nanoparticles were almost two orders of magnitude more effective at capturing His-tagged protein than were commercially available beads [225].

Honda and associates developed a method to form complex lipid bilayers on iron oxide nanoparticle surfaces, the aim being to use these particles in the hypothermic treatment of melanoma [226]. For this, iron oxide nanoparticles of 10 nm diameter were coated in a bilayer containing the chemotherapeutic agent, 4-*S*-cysteaminylphenol, together with three lipid materials, namely (*N*-(α-trimethylammonioacetyl)-didodecyl-D-glutamate chloride, dioleoylphosphatidylethanolamine, and dilauroylphosphatidylcholine [226]. Encapsulation of the nanoparticles in the lipid bilayers allowed a controlled release of the chemotherapeutic drug, while alternating an applied magnetic field caused localized heating

that induced cell death [226]. Williams, Hancock, and coworkers used biotin-terminated PEG-phospholipids on large $CoFe_2O_4$ (15 nm-diameter) nanoparticles for the magnetic labelling of microtubules, the transport of which over kinesin-covered surfaces could be magnetically manipulated [227]. In these studies, either streptavidin or neutravidin was used as a linker unit between the nanoparticle and the biotinylated microtubule [227b].

14.3.6.2 **Dendrimers**

Recently, *dendrimers* have been considered as functional groups for modifying the surface chemistry of magnetic nanoparticles. Dendrimers are highly branched, generational macromolecules with defined three-dimensional (3-D) structures [228, 229] and synthetically controlled terminal reactive groups (i.e., surface chemistry). One major challenge for the functional nanoparticle community is to determine and control the exact number of surface molecules and reactive groups per particle. As nanoparticle samples have a size distribution, so too will there be a distribution in the number of attached molecules. The use of dendrimers to functionalize nanoparticles would circumvent the issue of population dispersity, however, as only a finite number of the macromolecules will stabilize a single nanoparticle. Particles synthesized in the interior of a dendrimer template (i.e., one particle in one dendrimer) have an exactly known number of functional groups that is dictated by the chemical constitution of the macromolecule.

Crooks and coworkers have pioneered the use of dendrimers to encapsulate nanoparticles [230]. In one study, Ni nanoparticles were synthesized in the interior of sixth generation poly(amidoamine) (PAMAM) dendrimers by adding Ni^{2+} and sodium triethylborohydride as the reducing agent [230a]. The size of the resultant nanoparticles was seen to depend on the molar ratio of Ni^{2+} to dendrimer, and they were also protected from oxidation by the dendrimer shell [230a]. Subsequently, Atwater and coworkers demonstrated the use of amine-terminated, fifth-generation PAMAM dendrimers for Co nanoparticle synthesis [231], while Chandler *et al*. synthesized NiAu nanoparticles in hydroxyl-terminated, fifth-generation PAMAM dendrimers [232].

The ligand exchange of dendrimers has also been recently investigated. Carboxyl-terminated, third-generation dendrimers which were adsorbed to stabilize iron oxide nanoparticles were characterized by a variety of techniques, including polyacrylamide gel electrophoresis (PAGE), to measure the binding strength of the ligand and the ionic charge of the particles [233]. Among the several different dendrimers tested, the PAGE results showed those bearing folic acid and succinic acid termini to be the most effective [233]. Banaszak, Holl and Orr used fifth-generation PAMAM dendrimers terminating in folic acid and fluorescent dyes to phase-transfer iron oxide nanoparticles from organic solvents into water, and then characterized their interaction with human KB cells [234]. In these experiments the folic acid acted as both a nanoparticle surface ligand and as a substrate for the cell surfaces. When X-ray fluorescence was used to monitor the iron content of KB cells (which possess folic acid receptors) and UM-SCC-38 cells (which were folic acid knock-outs), a significant nanoparticle uptake was seen only in the KB cells [234].

14.4 Conclusions

In this chapter, we have attempted to describe the most recent and important contributions to the chemical and biological functionalization of magnetic nanomaterials. The wide range of surface chemistries developed will undoubtedly continue to expand, leading ultimately to applications in nanomedicine, in the manipulation and separation of target analytes, in separations, and in sensor devices. A continued expansion of these synthetic tools will be necessary if such materials are to be fully exploited. Coupled to this is the ongoing challenge to quantify and understand the surface chemistry of paramagnetic and superparamagnetic particles. In addition, little is known regarding the bioactivity of nanoscale particles in nature, and extensive characterization will be required of the fate and reactivity of both the surfactant/shell and the nanoparticle core in complex natural environments. Clearly, chemically functional nanomaterials hold great promise for the creation of single nanoparticle vehicles capable of analyte targeting and delivery, while their intrinsic magnetic properties will enable directed transport and diagnostic imaging.

References

1 Odenbach, S. (2003) Magnetic fluids–suspensions of magnetic dipoles and their magnetic control. *Journal of Physics: Condensed Matter*, S1497–508.

2 Daniel, M. and Astruc, C.D. (2004) Gold nanoparticles: assembly, supramolecular chemistry, quantum size-related properties, and applications toward biology, catalysis, and nanotechnology. *Chemical Reviews*, **104**, 293–346.

3 Templeton, A.C., Wuelfing, W.P. and Murray, R.W. (2000) Monolayer-protected cluster molecules. *Accounts of Chemical Research*, **33**, 27–36.

4 Michalet, X., Pinaud, F., Lacoste, T.D., Maxime, D., Bruchez, M.P., Alivisatos, A.P. and Weiss, S. (2001) Properties of fluorescent semiconductor nanocrystals and their application to biological labeling. *Single Molecules*, **4**, 261–76.

5 Hyeon, T. (2003) Chemical synthesis of magnetic nanoparticles. *Chemical Communications (Cambridge, England)*, (8), 927–34.

6 Huber, D.L. and Synthesis (2005) Properties, and Applications or Iron Nanoparticles. *Small*, **1**, 482–501.

7 Cushing, B.L., Kolesnichenko, V.L. and O'Connor, C.J. (2004) Recent advances in the liquid-phase syntheses of inorganic nanoparticles. *Chemical Reviews*, **104**, 3893–946.

8 Murray, C.B., Kagan, C.R. and Bawendi, M.G. (2000) Synthesis and characterization of monodisperse nanocrystals and close-packed nanocrystal assemblies. *Annual Review of Materials Science*, **30**, 545–610.

9 Pankhurst, Q.A., Connolly, J., Jones, S.K. and Dobson, J. (2003) Applications of magnetic nanoparticles in biomedicine. *Journal of Physics D: Applied Physics*, **36**, R167–81.

10 Tartaj, P., Morales, M.P., Veintemillas-Verdaguer, S., González-Carreño, T. and Serna, C.J. (2003) The preparation of magnetic nanoparticles for applications in biomedicine. *Journal of Physics D: Applied Physics*, **36**, R182–97.

11 Berry, C.C. and Curtis, A.S.G. (2003) Functionalisation of magnetic nanoparticles for applications in biomedicine. *Journal of Physics D: Applied Physics*, **36**, R198–206.

12 Latham, A.H., Freitas, R.S., Schiffer, P. and Williams, M.E. (2005) Capillary magnetic field flow fractionation and analysis of magnetic nanoparticles. *Analytical Chemistry*, **77**, 5055–62.

13 Latham, A.H., Tarpara, A.N. and Williams, M.E. (2007) Magnetic field switching of nanoparticles between orthogonal microfluidic channels. *Analytical Chemistry*, **79**, 5746–52.

14 Pamme, N. and Manz, A. (2004) On-chip and free-flow magnetophoresis: continuous flow separation of magnetic particles and agglomerates. *Analytical Chemistry*, **76**, 7250–6.

15 Pamme, N. (2006) Magnetism and microfluidics. *Lab on a Chip*, **6**, 24–38.

16 Gijs, M.A.M. (2004) Magnetic bead handling on-chip: new opportunities for analytical applications. *Microfluid Nanofluid*, **1**, 22–40.

17 Roca, A.G., Morales, M.P., O'Grady, K. and Serna, C.J. (2006) Structural and magnetic properties of uniform magnetite nanoparticles prepared by high temperature decomposition of organic precursors. *Nanotechnology*, **17**, 2783–8.

18 Chan, D.C.F., Kirpotin, D.B. and Bunn, P.A. (1993) Synthesis and evaluation of colloidal magnetic iron oxides for the site-specific radiofrequency-induced hyperthermia of cancer. *Journal of Magnetism and Magnetic Materials*, **122**, 374–8.

19 Veiseh, O., Sun, C., Gunn, J., Kohler, N., Gabikian, P., Lee, D., Bhattarai, N., Ellenbogen, R., Sze, R., Hallahan, A., Olson, J. and Zhang, M. (2005) Optical and MRI multifunctional nanoprobe for targeting gliomas. *Nano Letters*, **5**, 1003–8.

20 Huh, Y.M., Jun, Y.W., Song, H.T., Kim, S., Choi, J.S., Lee, J.H., Yoon, S., Kim, K.S., Shin, J.S., Suh, J.S. and Cheon, J. (2005) In vivo magnetic resonance detection of cancer by using multifunctional magnetic nanocrystals. *Journal of the American Chemical Society*, **127**, 12387–91.

21 Woo, K., Hong, J., Choi, S., Lee, H.W., Ahn, J.P., Kim, C.S. and Lee, S.W. (2004) Easy synthesis and magnetic properties of iron oxide nanoparticles. *Chemistry of Materials*, **16**, 2814–18.

22 Sun, S., Murray, C.B., Weller, D., Folks, L. and Moser, A. (2000) Mondisperse FePt nanoparticles and ferromagnetic FePt nanocrystal superlattices. *Science*, **287**, 1989–92.

23 Sun, S. and Zeng, H. (2002) Size-controlled synthesis of magnetite nanocrystals. *Journal of the American Chemical Society*, **124**, 8204–5.

24 Hyeon, T., Lee, S.S., Park, J., Chung, Y. and Na, H.B. (2001) Synthesis of highly crystalline and monodisperse maghemite nanoparticles without a size-selection process. *Journal of the American Chemical Society*, **123**, 12798–801.

25 Sun, S., Zeng, H., Robinson, D.B., Raoux, S., Rice, P.M., Wang, S.X. and Li, G. (2004) Monodisperse MFe_2O_4 (M = Fe, Co, Mn) nanoparticles. *Journal of the American Chemical Society*, **126**, 273–9.

26 Park, J., An, K., Hwang, Y., Park, J.G., Noh, H.J., Kim, J.Y., Park, J.H., Hwang, N.M. and Hyeon, T. (2004) Ultra-large-scale syntheses of monodisperse nanocrystals. *Nature Materials*, **3**, 891–5.

27 Hyeon, T., Chung, Y., Park, J., Lee, S.S., Kim, Y.W. and Park, B.H. (2002) Synthesis of highly crystalline and monodisperse cobalt ferrite nanocrystals. *The Journal of Physical Chemistry B*, **106**, 6831–3.

28 Frens, G. (1973) Controlled nucleation for the regulation of the particle size in monodisperse gold suspensions. *Nature*, **241**, 20–2.

29 Brust, M., Walker, M., Bethell, D., Schiffrin, D.J. and Whyman, R. (1994) Synthesis of thiol-derivatized gold nanoparticles in a two-phase liquid-liquid system. *Journal of the Chemical Society D: Chemical Communications*, 801–2.

30 Neveu, S., Bee, A., Robineau, M. and Talbot, D. (2002) Size-selective chemical synthesis of tartrate stabilized cobalt ferrite ionic magnetic fluid. *Journal of Colloid and Interface Science*, **255**, 293–8.

31 Kang, Y.S., Risbud, S., Rabolt, J.F. and Stroeve, P. (1996) Synthesis and characterization of nanometer-size Fe_3O_4

and γ-Fe_2O_3 particles. *Chemistry of Materials*, **8**, 2209–11.

32 Hong, R., Fischer, N.O., Emrick, T. and Rotello, V.M. (2005) Surface PEGylation and ligand exchange chemistry of FePt nanoparticles for biological applications. *Chemistry of Materials*, **17**, 4617–21.

33 West, A.R. (1988) *Basic Solid State Chemistry*, John Wiley & Sons, Inc., New York, pp. 356–9.

34 Zeng, H., Rice, P.M., Wang, S.X. and Sun, S. (2004) Shape-controlled synthesis and shape-induced texture of $MnFe_2O_4$ nanoparticles. *Journal of the American Chemical Society*, **126**, 11458–9.

35 Seo, W.S., Jo, H.H., Lee, K., Kim, B., Oh, S.J. and Park, J.T. (2004) Size-dependent magnetic properties of colloidal Mn_3O_4 and MnO nanoparticles. *Angewandte Chemie, International Edition in English*, **43**, 1115–17.

36 Sun, S. and Murray, C.B. (1999) Synthesis of monodisperse cobalt nanocrystals and their assembly into magnetic superlattices. *Journal of Applied Physics*, **85**, 4325–30.

37 Park, J., Kang, E., Son, S.U., Park, H.M., Lee, M.K., Kim, J., Kim, K.W., Noh, H.J., Park, J.H., Bae, C.J., Park, J.G. and Hyeon, T. (2005) Monodisperse nanoparticles of Ni and NiO: synthesis, characterization, self-assembled superlattices, and catalytic applications in the Suzuki coupling reaction. *Advanced Materials*, **17**, 429–34.

38 Chen, M. and Nikles, D.E. (2002) Synthesis of spherical FePd and CoPt nanoparticles. *Journal of Applied Physics*, **91**, 8477–9.

39 Latham, A.H. and Williams, M.E. (2007) Controlling transport and chemical functionality of magnetic nanoparticles. *Accounts of Chemical Research*, **41**, 411–20.

40 Lu, A.-H., Salabas, E.L. and Shüeth, F. (2007) Magnetic nanoparticles: synthesis. protection, functionalization, and application. *Angewandte Chemie, International Edition in English*, **46**, 1222–44.

41 Sun, S. (2006) Recent advances in chemical synthesis, self-assembly, and applications of FePt nanoparticles. *Advanced Materials*, **18**, 393–403.

42 (a) Nuzzo, R.G. and Allara, D.L. (1983) Adsorption of bifunctional organic disulfides on gold surface. *Journal of the American Chemical Society*, **105**, 4481–3; (b) Allara, D.L. and Nuzzo, R.G. (1985) Spontaneously organized molecular assemblies. 1. Formation, dynamics, and physical properties of n-alkanoic acids adsorbed from solution on an oxidized aluminum surface. *Langmuir*, **1**, 45–52; (c) Bain, C.D. and Whitesides, G.M. (1988) Formation of two-component surfaces by the spontaneous assembly of monolayers on gold from solutions containing mixtures of organic thiols. *Journal of the American Chemical Society*, **110**, 6560–1.

43 (a) Storhoff, J.J., Elghanian, R., Mucic, R.C., Mirkin, C.A. and Letsinger, R.L. (1998) One-pot colorimetric differentiation of polynucleotides with single base imperfections using gold nanoparticle probes. *Journal of the American Chemical Society*, **120**, 1959–64; (b) Keating, C.D., Kovaleski, K.M. and Natan, M.J. (1998) Protein: colloid conjugates for surface enhanced Raman scattering: stability and control of protein orientation. *The Journal of Physical Chemistry B*, **102**, 9404–13.

44 (a) Sun, J., Zhou, S., Hou, P., Yang, Y., Weng, J., Li, X. and Li, M. (2007) Synthesis and characterization of biocompatible Fe_3O_4 nanoparticles. *Journal of Biomedical Materials Research. Part A*, **80A**, 333–41; (b) Kataby, G., Cojocaru, M., Prozorov, R. and Gedanken, A. (1999) Coating carboxylic acids on amorphous iron nanoparticles. *Langmuir*, **15**, 1703–8.

45 Daou, T.J., Begin-Colin, S., Grenèche, J.M., Thomas, F., Derory, A., Bernhardt, P., Legaré, P. and Pourroy, G. (2007) Phosphate adsorption properties of magnetite-based nanoparticles. *Chemistry of Materials*, **19**, 4494–505.

46 (a) Li, W., Xing, J., Li, Y., Xiong, X., Li, X. and Liu, H. (2008) Desulfurization and bio-regeneration of adsorbents with magnetic *P. delafieldii* R-8 cells. *Catalysis Communications*, **9**, 376–80;

(b) Li, J., Zhao, X., Shi, Y., Cai, Y., Mou, S. and Jiang, G. (2008) Mixed and hemimicelles solid-phase extraction based on cetyltrimethylammonium bromide-coated nano-magnets Fe_3O_4 for the determination of chlorophenols in environmental water samples coupled with liquid chromatography/spectrophotometry detection. *Journal of Chromatography A*, **1180**, 24–31.

47 Kataby, G., Ulman, A., Prozorov, R. and Gedanken, A. (1998) Coating of amorphous iron nanoparticles by long-chain alcohols. *Langmuir*, **14**, 1512–15.

48 Kataby, G., Prozorov, T., Koltypin, Y., Cohen, H., Sukenik, C.N., Ulman, A. and Gedanken, A. (1997) Self-assembled monolayer coatings on amorphous iron and iron oxide nanoparticles: thermal stability and chemical reactivity studies. *Langmuir*, **13**, 6151–8.

49 Lucas, I.T., Durand-Vidal, S., Dubois, E., Chevalet, J. and Turq, P. (2007) Surface charge density of maghemite nanoparticles: role of electrostatics in the proton exchange. *The Journal of Physical Chemistry C*, **111**, 18568–76.

50 Wilhelm, C. and Gazeau, F. (2008) Universal cell labeling with anionic magnetic nanoparticles. *Biomaterials*, **29**, 3161–74.

51 Choi, J., Lee, J.I., Lee, Y.B., Hong, J.H., Kim, I.S., Park, Y.K. and Hur, N.H. (2006) Immobilization of biomolecules on biotinylated magnetic ferrite nanoparticles. *Chemical Physics Letters*, **428**, 125–9.

52 Wan, S., Huang, J., Guo, M., Zhang, H., Cao, Y., Yan, H. and Liu, K. (2007) Biocompatible superparamagnetic iron oxide nanoparticle dispersions stabilized with poly(ethylene glycol)-oligo(aspartic acid) hybrids. *Journal of Biomedical Materials Research. Part A*, **80A**, 946–54.

53 Samanta, B., Yan, H., Fischer, N.O., Shi, J., Jerry, D.J. and Rotello, V.M. (2008) Protein-passivated Fe_3O_4 nanoparticles: low toxicity and rapid heating for thermal therapy. *Journal of Materials Chemistry*, **18**, 1204–8.

54 Kinsella, J.M., Shalaev, M.V. and Ivanisevic, A. (2007) Ligation of nanoparticle coated DNA cleaved with restriction enzymes. *Chemistry of Materials*, **19**, 3586–8.

55 Li, Y., Xu, X., Deng, C., Yang, P. and Zhang, X. (2007) Immobilization of trypsin on superparamagnetic nanoparticles for rapid and effective proteolysis. *Journal of Proteome Research*, **6**, 3849–55.

56 Nicewarner-Peña, S.R., Carado, A.J., Shale, K.E. and Keating, C.D. (2003) Barcoded metal nanowires optical reflectivity and patterned fluorescence. *The Journal of Physical Chemistry B*, **107**, 7360–7.

57 Fond, A.M., Birenbaum, N.S., Felton, E.J., Reich, D.H. and Meyer, G.J. (2007) Preferential noncovalent immunoglobulin G adsorption onto hydrophobic segments of multi-functional metallic nanowires. *Journal of Photochemistry and Photobiology A*, **186**, 57–64.

58 Laibinis, P.E., Fox, M.A., Folkers, J.P. and Whitesides, G.M. (1991) Comparisons of self-assembled monolayers on silver and gold: mixed monolayers derived from $HS(CH_2)_{21}X$ and $HS(SH_2)_{10}Y$ (X,Y = CH_3, CH_2OH) have similar properties. *Langmuir*, **7**, 3167–73.

59 (a) Templeton, A.C., Hostetler, M.J., Warmoth, E.K., Chen, S., Hartshorn, C.M., Krishnamurthy, V.M., Forbes, M.D.E. and Murray, R.W. (1998) Gateway reactions to diverse, polyfunctional monolayer-protected gold clusters. *Journal of the American Chemical Society*, **120**, 4845–9;
(b) Hostetler, M.J., Templeton, A.C. and Murray, R.W. (1999) Dynamics of place-exchange reactions on monolayer-protected gold cluster molecules. *Langmuir*, **15**, 3782–9.

60 (a) White, M.A., Johnson, J.A., Koberstein, J.T. and Turro, N.J. (2006) Toward the synthesis of universal ligands for metal oxide surfaces: controlling surface functionality through click chemistry. *Journal of the American Chemical Society*, **128**, 11356–7;
(b) Willis, A.L., Turro, N.J. and O'Brien, S. (2005) Spectroscopic characterization

of the surface of iron oxide nanocrystals. *Chemistry of Materials*, **17**, 5970–5.

61 Boal, A.K., Das, K., Gray, M. and Rotello, V.M. (2002) Monolayer exchange chemistry of γ-Fe_2O_3 nanoparticles. *Chemistry of Materials*, **14**, 2628–36.

62 (a) Xu, C., Xu, K., Gu, H., Zheng, R., Liu, H., Zhang, X., Guo, Z. and Xu, B. (2004) Dopamine as a robust anchor to immobilize functional molecules on the iron oxide shell of magnetic nanoparticles. *Journal of the American Chemical Society*, **126** (32), 9938–9;
(b) Gu, H., Yang, Z., Gao, J., Chang, C.K. and Xu, B. (2005) Heterodimers of nanoparticles: formation at a liquid-liquid interface and particle-specific surface modification by functional molecules. *Journal of the American Chemical Society*, **127**, 34–5.

63 (a) Xie, J., Xu, C., Xu, Z., Hou, Y., Young, K.L., Wang, S.X., Pourmand, N. and Sun, S. (2006) Linking hydrophilic macromolecules to monodisperse magnetite (Fe_3O_4) nanoparticles via trichloro-s-triazine. *Chemistry of Materials*, **18**, 5401–3.
(b) Xie, J., Xu, C., Kohler, N., Hou, Y. and Sun, S. (2007) Controlled PEGylation of monodisperse Fe_3O_4 nanoparticles for reduced non-specific uptake by macrophage cells. *Advanced Materials*, **19**, 3163–6;
(c) Wang, L., Yang, Z., Gao, J., Xu, K., Gu, H., Zhang, B., Zhang, X. and Xu, B. (2006) A biocompatible method of decorporation: bisphosphonate-modified magnetite nanoparticles to remove uranyl ions from blood. *Journal of the American Chemical Society*, **128** (41), 13358–9;
(d) Somaskandan, K., Veres, T., Niewczas, M. and Simard, B. (2008) Surface protected and modified iron based core-shell nanoparticles for biological applications. *New Journal of Chemistry*, **32**, 201–9.

64 Guin, D., Baruwati, B. and Manorama, S.V. (2007) Pd on amine-terminated ferrite nanoparticles: a complete magnetically recoverable facile catalyst for hydrogenation reactions. *Organic Letters*, **9**, 1419–21.

65 Gao, J., Li, L., Ho, P.-L., Mak, G.C., Gu, H. and Xu, B. (2006) Combining fluorescent probes and biofunctional magnetic nanoparticles for rapid detection of bacteria in human blood. *Advanced Materials*, **18**, 3145–8.

66 Shultz, M.D., Reveles, J.U., Khanna, S.N. and Carpenter, E.E. (2007) Reactive nature of dopamine as a surface functionalization agent in iron oxide nanoparticles. *Journal of the American Chemical Society*, **129**, 2482–7.

67 Lattuada, M. and Hatton, T.A. (2007) Functionalization of monodisperse magnetic nanoparticles. *Langmuir*, **23**, 2158–68.

68 Maenosono, S., Suzuki, T. and Saita, S. (2008) Superparamagnetic FePt nanoparticles as excellent MRI contrast agents. *Journal of Magnetism and Magnetic Materials*, 320, L79–83.

69 Jia, X., Chen, D., Jiao, X., He, T., Wang, H. and Jiang, W. (2008) Monodispersed Co, Ni-Ferrite nanoparticles with tunable sizes: controlled synthesis magnetic properties, and surface modification. *The Journal of Physical Chemistry C*, **112**, 911–17.

70 Lattuada, M. and Hatton, T.A. (2007) Preparation and controlled self-assembly of janus magnetic nanoparticles. *Journal of the American Chemical Society*, **129**, 12878–89.

71 Folkers, J.P., Gorman, C.B., Laibinis, P.E., Buchholz, S., Whitesides, G.M. and Nuzzo, R.G. (1995) Self-assembled monolayers of long-chain hydroxamic acids on the native oxide of metals. *Langmuir*, **11**, 813–24.

72 Baldi, G., Bonacchi, D., Comes Franchini, M., Gentili, D., Lorenzi, G., Ricci, A. and Ravagli, C. (2007) Synthesis and coating of cobalt ferrite nanoparticles: a first step toward the obtainment of new magnetic nanocarriers. *Langmuir*, **23**, 4026–8.

73 Bagaria, H.G., Ada, E.T., Shamsuzzoha, M., Nikles, D.E. and Johnson, D.T. (2006) Understanding mercapto ligand exchange on the surface of FePt nanoparticles. *Langmuir*, **22**, 7732–7.

74 Latham, A.H. and Williams, M.E. (2006) Versatile routes toward functional,

water-soluble nanoparticles via trifluoroethylester-PEG-thiol ligands. *Langmuir*, **22**, 4319–26.

75 Arumugam, P., Patra, D., Samanta, B., Agasti, S.S., Subramani, C. and Rotello, V.M. (2008) Self-assembly and cross-linking of FePt nanoparticles at planar and colloidal liquid-liquid interfaces. *Journal of the American Chemical Society*, **130**, 10046–7.

76 Srivastava, S., Samanta, B., Jordan, B.J., Hong, R., Xiao, Q., Tuominen, M.T. and Rotello, V.M. (2007) Integrated magnetic bionanocomposites through nanoparticle-mediated assembly of ferritin. *Journal of the American Chemical Society*, **129**, 11776–80.

77 Srivastava, S., Samanta, B., Arumugam, P., Han, G. and Rotello, V.M. (2007) DNA-mediated assembly of iron platinum (FePt) Nanoparticles. *Journal of Materials Chemistry*, **17**, 52–5.

78 Ofir, Y., Samanta, B., Arumugam, P. and Rotello, V.M. (2007) Controlled fluorination of FePt nanoparticles: hydrophobic to superhydrophobic surfaces. *Advanced Materials*, **19**, 4075–9.

79 Huh, Y.-M., Lee, E.-S., Lee, J.-H., Jun, Y.-W., Kim, P.-H., Yun, C.-O., Kim, J.-H., Suh, J.-S. and Cheon, J. (2007) Hybrid nanoparticles for magnetic resonance imaging of target-specific viral gene delivery. *Advanced Materials*, **19**, 3109–12.

80 Tanaka, Y. and Maenosono, S. (2008) Amine-terminated water-dispersible FePt nanoparticles. *Journal of Magnetism and Magnetic Materials.*, **320**, L121–4.

81 Chiang, P.-C., Hung, D.-S., Wang, J.-W., Ho, C.-S. and Yao, Y.-D. (2007) Engineering water-dispersible FePt nanoparticles for biomedical applications. *IEEE Transactions on Magnetics*, **43**, 2445–7.

82 (a) Ma, Y.-J. and Gu, H.-C. (2007) Study on the endocytosis and the internalization mechanism of aminosilane-coated Fe_3O_4 nanoparticles in vitro. *Journal of Materials Science. Materials in Medicine*, **18**, 2145–9;
(b) Liang, S., Wang, Y., Yu, J., Zhang, C., Xia, J. and Yin, D. (2007) Surface modified superparamagnetic iron oxide nanoparticles: as a new carrier for bio-magnetically targeted therapy. *Journal of Materials Science. Materials in Medicine*, **18**, 2297–302;
(c) Zhang, Y., Sun, C., Kohler, N. and Zhang, M. (2004) Self-assembled coating on individual monodisperse magnetic nanoparticles for efficient intracellular uptake. *Biomedical Microdevices*, **6**, 33–40;
(d) Shaw, S.-Y., Chen, Y.-J., Ou, J.-J. and Ho, L. (2006) Preparation and characterization of *Pseudomonas putida* esterase immobilized on magnetic nanoparticles. *Enzyme and Microbial Technology*, **39**, 1089–95;
(e) Hung, C.-W., Holoman, T.R.P., Kofinas, P. and Bentley, W.E. (2008) Towards oriented assembly of proteins onto magnetic nanoparticles. *Biochemical Engineering Journal*, **38**, 164–70.

83 Rossi, L.M., Quach, A.D. and Rosenzweig, Z. (2004) Glucose oxidase-magnetic nanoparticle bioconjugate for glucose sensing. *Analytical and Bioanalytical Chemistry*, **380**, 606–13.

84 De Palma, R., Peeters, S., Van Bael, M.J., Van den Rul, H., Bonroy, K., Laureyn, W., Mullens, J., Borghs, G. and Maes, G. (2007) Silane ligand exchange to make hydrophobic superparamagnetic nanoparticles water-dispersible. *Chemistry of Materials*, **19**, 1821–31.

85 Shen, H.-Y., Zhu, Y., Wen, X.-E. and Zhuang, Y.-M. (2007) Preparation of Fe_3O_4-C_{18} nano-magnetic composite materials and their cleanup properties for organophosphorous pesticides. *Analytical and Bioanalytical Chemistry*, **387**, 2227–37.

86 Vasilyev, S., Pita, M. and Katz, E. (2008) Logic gates based on magnetic nanoparticles functionalized with a bioelectrocatalytic system. *Electroanalysis*, **20**, 22–9.

87 Koh, I., Wang, X., Varughese, B., Isaacs, L., Ehrman, S.H. and English, D.S. (2006) Magnetic iron oxide nanoparticles for biorecognition evaluation of surface coverage and activity. *The Journal of Physical Chemistry B*, **110**, 1553–8.

88 Kawamura, M. and Sato, K. (2007) Magnetic nanoparticle-supported crown

ethers. *Chemical Communications (Cambridge, England)*, **32**, 3404–5.
89 Zheng, Y., Stevens, P.D. and Gao, Y. (2006) Magnetic nanoparticles as an orthogonal support of polymer resins: applications to solid-phase Suzuki cross-coupling reactions. *Journal of Organic Chemistry*, **71**, 537–42.
90 Templeton, A.C., Hostetler, M.J., Kraft, C.T. and Murray, R.W. (1998) Reactivity of monolayer-protected gold cluster molecules: steric effects. *Journal of the American Chemical Society*, **120**, 1906–11.
91 Tan, H., Zhan, T. and Fan, W.Y. (2006) Direct functionalization of the hydroxyl group of the 6-Mercapto-1-hexanol (MCH) ligand attached to gold nanoclusters. *The Journal of Physical Chemistry B*, **110**, 21690–3.
92 (a) Thode, C. and Williams, M.E. (2008) Grignard functionalization of Weinreb amide-modified Au nanoparticles. *Langmuir*, **24**, 5988–90;
(b) Fleming, D.A., Thode, C.J. and Williams, M.E. (2006) Triazole cycloaddition as a general route for functionalization of Au nanoparticles. *Chemistry of Materials*, **18**, 2327–34.
93 (a) O'Reilly, R.K., Joralemon, M.J., Wooley, K.L. and Hawker, C.J. (2005) Functionalization of micelles and shell cross-linked nanoparticles using click chemistry. *Chemistry of Materials*, **17**, 5976–88;
(b) O'Reilly, R.K., Joralemon, M.J., Hawker, C.J. and Wooley, K.L. (2006) Fluorogenic 1,3-dipolar cycloaddition within the hydrophobic core of a shell cross-linked nanoparticle. *Chemistry – A European Journal*, **12**, 6776–86.
94 Sun, E.Y., Josephson, L. and Weissleder, R. (2006) "Clickable" nanoparticles for targeted imaging. *Molecular Imaging*, **5**, 122–8.
95 Binder, W.H. and Weinstabl, H.C. (2007) Surface-modified superparamagnetic iron-oxide nanoparticles. *Monatshefte fur Chemie*, **138**, 315–20.
96 Mondini, S., Cenedese, S., Marinoni, G., Molteni, G., Santo, N., Bianchi, C.L. and Ponti, A. (2008) One-step synthesis and functionalization of hydroxyl-decorated magnetic nanoparticles. *Journal of Colloid and Interface Science*, **322**, 173–9.
97 Gravano, S.M., Dumas, R., Liu, K. and Patten, T.E. (2005) Methods for the surface functionalization of γ-Fe_2O_3 nanoparticles with initiators for atom transfer radical polymerization and the formation of core-shell inorganic-polymer structures. *Journal of Polymer Science. Part A-1, Polymer Chemistry*, **43**, 3675–88.
98 Lin, P.-C., Ueng, S.-H., Yu, S.-C., Jan, M.-D., Adak, A.K., Yu, C.-C. and Lin, C.-C. (2007) Surface modification of magnetic nanoparticle via Cu(I)-catalyzed alkyne-azide [2 + 3] cycloaddition. *Organic Letters*, **9**, 2131–4.
99 Stöber, W., Fink, A. and Bohn, E. (1968) Controlled growth of monodisperse silica spheres in the micron size range. *Journal of Colloid and Interface Science*, **26**, 62–9.
100 Lu, Z., Wang, G., Zhuang, J. and Yang, W. (2006) Effects of the concentration of tetramethylammonium hydroxide peptizer on the synthesis of Fe_3O_4/SiO_2 core/shell nanoparticles. *Colloids and Surfaces A*, **278**, 140–3.
101 Lee, D.C., Mikulec, F.V., Pelaez, J.M., Koo, B. and Korgel, B.A. (2006) *The Journal of Physical Chemistry B*, **110**, 11160–6.
102 Jacinto, M.J., Kiyohara, P.K., Masunaga, S.H., Jardim, R.F. and Rossi, L.M. (2008) Recoverable rhodium nanoparticles: synthesis, characterization and catalytic performance in hydrogenation reactions. *Applied Catalysis A*, **338**, 52–7.
103 Stjerndahl, M., Andersson, M., Hall, H.E., Pajerowski, D.M., Meisel, M.W. and Duran, R.S. (2008) Superparamagnetic Fe_3O_4/SiO_2 nanocomposites: enabling the tuning of both the iron oxide load and the size of the nanoparticles. *Langmuir*, **24**, 3532–6.
104 (a) Liz-Marzán, L.M., Giersig, M. and Mulvaney, P. (1996) Synthesis of nanosized gold-silica core-shell particles. *Langmuir*, **12**, 4329–35;
(b) Mulvaney, P., Liz-Marzán, L.M., Giersig, M. and Ung, T. (2000) Silica encapsulation of quantum dots and

metal clusters. *Journal of Materials Chemistry*, **10**, 1259–70;
(c) Yang, Y., Hori, M., Hayakawa, T. and Nogami, M. (2005) Self assembled 3-Dimensional arrays of Au@SiO_2 core-shell nanoparticles of enhanced optical nonlinearities. *Surface Science*, **579**, 215–24.

105 Aslam, M., Li, S. and Dravid, V.P. (2007) Controlled synthesis and stability of Co@SiO_2 aqueous colloids. *Journal of the American Ceramic Society*, **90**, 950–6.

106 Yu, S.-Y., Zhang, H.-J., Yu, J.-B., Wang, C., Sun, L.-N. and Shi, W.-D. (2007) Bifunctional magnetic-Optical nanocomposites: grafting lanthanide complex onto core-shell magnetic silica nanoarchitecture. *Langmuir*, **23**, 7836–40.

107 (a) Shaw, S.-Y., Chen, Y.-J., Ou, J.-J. and Ho, L. (2006) Preparation and characterization of *Pseudomonas putida* esterase immobilized on magnetic nanoparticles. *Enzyme and Microbial Technology*, **39**, 1089–95;
(b) Sharma, A., Qiang, Y., Antony, J., Meyer, D., Kornacki, P. and Paszczynski, A. (2007) Dramatic increase in stability and longevity of enzymes attached to monodispersive iron nanoparticles. *IEEE Transactions on Magnetics*, **43** (6), 2418–20;
(c) Rossi, L.M., Quach, A.D. and Rosenzweig, Z. (2004) Glucose oxidase-magnetite bioconjugate for glucose sensing. *Analytical and Bioanalytical Chemistry*, **380**, 606–13.

108 (a) Lai, C.W., Wang, Y.-H., Lai, C.-H., Yang, M.-J., Chen, C.-Y., Chou, P.-T., Chan, C.-S., Chen, Y.-C. and Hsiao, J.-K. (2008) Iridium-complex-functionalized Fe_3O_4/SiO_2 core/shell nanoparticles: a facile three-in-one system in magnetic resonance imaging, luminescence imaging, and photodynamic therapy. *Small*, **4**, 218–24;
(b) Li, M.-J., Chen, Z., Yam, V.W.-W. and Zu, Y. (2008) Multifunctional ruthenium (II) polypyridine complex-based core-shell magnetic silica nanocomposites: magnetism, luminescence, and electrochemiluminescence. *ACS Nano*, **2**, 905–12.

109 Chen, W.-Y. and Chen, Y.-C. (2007) MALDI MS analysis of oligonucleotides desalting by functional magnetite beads using microwave-assisted extraction. *Analytical Chemistry*, **79**, 8061–6.

110 Li, L., Choo, E.S.G., Liu, Z., Ding, J. and Xue, J. (2008) Double-layer silica core-shell nanospheres with superparamagnetic and fluorescent functionalities. *Chemical Physics Letters*, **461**, 114–17.

111 Chen, W.-J., Tsai, P.-J. and Chen, Y.-C. (2008) Functional Fe_3O_4/TiO_2 core/shell magnetic nanoparticles as photokilling agents for pathogenic bacteria. *Small*, **4**, 485–91.

112 Sunkara, B.K. and Misra, R.D.K. (2008) Enhanced antibactericidal function of W^{4+}-doped titania-coated nickel ferrite composite nanoparticles: a biomaterial system. *Acta Biomaterialia*, **4**, 273–83.

113 Zhang, M., Shi, S., Meng, J., Wang, X., Fan, H., Zhu, Y., Wang, X. and Qian, Y. (2008) Preparation and characterization of near-infrared luminescent bifunctional core/shell nanocomposites. *The Journal of Physical Chemistry C*, **112**, 2825–30.

114 (a) Chen, C.-T., Chen, W.-Y., Tsai, P.-J., Chien, K.-Y., Yu, J.-S. and Chen, Y.-C. (2007) Rapid enrichment of phosphopeptides and phosphoproteins from complex samples using magnetic particles coated with alumina as the concentrating probes for MALDI MS analysis. *Journal of Proteome Research*, **6**, 316–25;
(b) Liu, J.-C., Tsai, P.-J., Lee, Y.C. and Chen, Y.-C. (2008) Affinity capture of uropathogenic *Escherichia coli* using pigeon ovalbumin-bound Fe_3O_4@Al_2O_3 magnetic nanoparticles. *Analytical Chemistry*, **80**, 5425–32.

115 Brown, K.R., Walter, D.G. and Natan, M.J. (2000) Seeding of colloidal Au nanoparticle solutions. 2. Improved control of particle size and shape. *Chemistry of Materials*, **12**, 306–13.

116 Lyon, J.L., Fleming, D.A., Stone, M.B., Schiffer, P. and Williams, M.E. (2004) Synthesis of Fe oxide core/Au shell

nanoparticles by iterative hydroxylamine seeding. *Nano Letters*, **4**, 719–23.

117 Oliva, B.L., Pradhan, A., Caruntu, D., O'Connor, C.J. and Tarr, M.A. (2006) Formation of gold-coated magnetic nanoparticles using TiO_2 as a bridging material. *Journal of Materials Research*, **21**, 1312–16.

118 Mikhaylova, M., Kim, D.K., Bobrysheva, N., Osmolowsky, M., Semenov, V., Tsakalakos, T. and Muhammed, M. (2004) Superparamagnetism of magnetite nanoparticles: dependence on surface modification. *Langmuir*, **20**, 2472–7.

119 (a) Mandal, M., Kundu, S., Ghosh, S.K., Panigrahi, S., Sau, T.K., Yusuf, S.M. and Pal, T. (2005) Magnetite nanoparticles with tunable gold or silver shell. *Journal of Colloid and Interface Science*, **286**, 187–94;
(b) Tang, D., Yuan, R. and Chai, Y. (2006) Direct electrochemical immunoassay based on immobilization of protein-magnetic nanoparticle composites on to magnetic electrode surfaces by sterically enhanced magnetic field force. *Biotechnology Letters*, **28**, 559–65.

120 Xu, Z., Huo, Y. and Sun, S. (2007) Magnetic core/shell Fe_3O_4/Au and Fe_3O_4/Au/Ag nanoparticles with tunable plasmonic properties. *Journal of the American Chemical Society*, **129**, 8689–99.

121 Lim, J., Tilton, R.D., Eggeman, A. and Majetich, S.A. (2007) Design and synthesis of plasmonic magnetic, nanoparticles. *Journal of Magnetism and Magnetic Materials*, **311**, 78–83.

122 Park, H.-Y., Schadt, M.J., Wang, L., Lim, I.-I.S., Njoki, P.N., Kim, S.H., Jang, M.-Y., Luo, J. and Zhong, C.-J. (2007) Fabrication of magnetic core@shell Fe oxide@Au nanoparticles for interfacial bioactivity and bio-separation. *Langmuir*, **23**, 9050–6.

123 Wang, L., Park, H.-Y., Lim, S.I.-I., Schadt, M.J., Mott, D., Luo, J., Wang, X. and Zhong, C.-J. (2008) Core@shell nanomaterials: gold-coated magnetic oxide nanoparticles. *Journal of Materials Chemistry*, **18**, 2629–35.

124 Wei, D.H., Hung, D.S., Ho, C.S., Wang, J.W. and Yao, Y.D. (2007) Fabrication of monodisperse FePt@Au core-shell nanoparticles. *Physica Status Solidi C*, **4**, 4421–4.

125 (a) Bai, J. and Wang, J.-P. (2005) High-magnetic-moment Core-Shell-Type FeCo-Au/Ag nanoparticles. *Applied Physics Letters*, **87**, 152502-1–152502-3;
(b) Xu, Y.H., Bai, J. and Wang, J.-P. (2007) High-magnetic-moment multifunctional nanoparticles for nanomedicine applications. *Journal of Magnetism and Magnetic Materials*, **311**, 131–4.

126 Mandal, S. and Krishnan, K.M. (2007) Co core Au shell nanoparticles evolution of magnetic properties in displacement reaction. *Journal of Materials Chemistry*, **17**, 372–6.

127 Iglesias-Silva, E., Rivas, J., León Isidro, L.M. and López-Quintela, M.A. (2007) Synthesis of silver-coated magnetite nanoparticles. *Journal of Non-Crystalline Solids*, **353**, 829–31.

128 Poddar, P., Srinath, S., Gass, J., Prasad, B.L.V. and Srikanth, H. (2007) Magnetic transition and large magnetocaloric effect associated with surface spin disorder in Co and Co core Ag shell nanoparticles. *The Journal of Physical Chemistry C*, **111**, 14060–6.

129 Park, J.-I. and Cheon, J. (2001) Synthesis of "solid solution" and "core-shell" type cobalt-platinum magnetic nanoparticles via transmetalation reactions. *Journal of the American Chemical Society*, **123**, 5743–6.

130 Jun, C.-H., Park, Y.J., Yeon, Y.-R., Choi, J.-R., Lee, W.-R., Ko, S.-J. and Cheon, J. (2006) Demonstration of a magnetic and catalytic Co@Pt nanoparticle as a dual-functional nanoplatform. *Chemical Communications (Cambridge, England)*, 1619–21.

131 Chen, Y., Yang, F., Dai, Y., Wang, W. and Chen, S. (2008) Ni@Pt core-shell nanoparticles synthesis, structural and electrochemical properties. *The Journal of Physical Chemistry C*, **112**, 1645–9.

132 (a) Peng, X., Schlamp, M.C., Kadavanich, A.V. and Alivisatos, A.P. (1997) Epitaxial growth of highly luminescent CdSe/CdS

core/shell nanocrystals with photostability and electronic accessibility. *Journal of the American Chemical Society*, **119**, 7019–29;
(b) Hines, M.A. and Guyot-Sionnest, P. (1996) Synthesis and characterization of strongly luminescing ZnS-capped CdSe, nanocrystals. *The Journal of Physical Chemistry*, **100**, 468–71;
(c) Dabbousi, B.O., Rodriguez-Viejo, J., Mikulec, F.V., Heine, J.R., Mattoussi, H., Ober, R., Jensen, K.F. and Bawendi, M.G. (1997) (CdSe)ZnS core-shell quantum dots: synthesis and characterization of a size series of highly luminescent nanocrystallites. *The Journal of Physical Chemistry B*, **101**, 9463–75;
(d) Cao, Y.-W. and Banin, U. (1999) Synthesis and characterization of InAs/InP and InAs/CdSe Core/Shell nanocrystals, *Angewandte Chemie, International Edition in English*, **38**, 3692–4;
(e) Blackman, B., Battaglia, D. and Peng, X. (2008) Bright and water-soluble near IR-emitting CdSe/CdTe/ZnSe typeII/type-I nanocrystals, tuning the efficiency and stability by growth. *Chemistry of Materials*, **20**, 4847–53;
(f) Blackman, B., Battaglia, D.M., Mishima, T.D., Johnson, M.B. and Peng, X. (2007) Control of the morphology of complex semiconductor nanocrystals with a type II heterojunction, dots vs. peanuts, by thermal cycling. *Chemistry of Materials*, **19** (15), 3815–21;
(g) Kim, S., Fisher, B., Eisler, H.-J. and Bawendi, M. (2003) Type-II quantum dots: CdTe/CdSe(core/shell) and CdSe/ZnTe(core/shell) heterostructures. *Journal of the American Chemical Society*, **125**, 11466–7.

133 (a) Kim, B.-S. and Taton, T.A. (2007) Multicomponent nanoparticles via self-assembly with cross-linked block copolymer surfactants. *Langmuir*, **23**, 2198–202;
(b) Beaune, G., Dubertret, B., Clément, O., Vayssettes, C., Cabuil, V. and Ménager, C. (2007) Giant vesicles containing magnetic nanoparticles and quantum dots: feasibility and tracking by fiber confocal fluorescence microscopy, *Angewandte Chemie, International Edition in English*, **46**, 5421–4.

134 Gao, J., Zhang, B., Gao, Y., Pan, Y., Zhang, X. and Xu, B. (2007) Fluorescent magnetic nanocrystals by sequential addition of reagents in a one-pot reaction: a simple preparation for multifunctional nanostructures. *Journal of the American Chemical Society*, **129**, 11928–35.

135 Zanella, M., Falqui, A., Kudera, S., Manna, L., Casula, M.F. and Parak, W.J. (2008) Growth of colloidal nanoparticles of group II-VI and IV-VI semiconductors on top of magnetic iron-platinum nanocrystals. *Journal of Materials Chemistry*, **18**, 4311–17.

136 Jiang, W., Yang, H.C., Yang, S.Y., Horng, H.E., Hung, J.C., Chen, Y.C. and Hong, C.-Y. (2004) Preparation and properties of superparamagnetic nanoparticles with narrow size distribution and biocompatible. *Journal of Magnetism and Magnetic Materials*, **283**, 210–14.

137 Fuentes, M., Mateo, C., Rodriguez, A., Casqueiro, M., Tercero, J.C., Riese, H.H., Fernández-Lafuente, R. and Guisán, J.M. (2006) Detecting minimal traces of DNA using DNA covalently attached to superparamagnetic nanoparticles and direct PCR-ELISA. *Biosensors and Bioelectronics*, **21**, 1574–80.

138 Liang, Y.-Y., Zhang, L.-M., Li, W. and Chen, R.-F. (2007) Polysaccharide-modified iron oxide nanoparticles as an effective magnetic affinity adsorbent for bovine serum albumin. *Colloid and Polymer Science*, **285**, 1193–9.

139 Liang, Y.-Y. and Zhang, L.-M. (2007) Bioconjugation of papain on superparamagnetic nanoparticles decorated with carboxymethylated chitosan. *BioMacromol*, **8**, 1480–6.

140 Li, G.Y., Haung, K.L., Jiang, Y.R., Yang, D.L. and Ding, P. (2008) Preparation and characterization of *Saccharomyces cerevisiae* alcohol dehydrogenase immobilized on magnetic nanoparticles. *International Journal of Biological Macromolecules*, **42**, 405–12.

141 Zhu, A., Yuan, L. and Dai, S. (2008) Preparation of well-dispersed

superparamagnetic iron oxide nanoparticles in aqueous solution with biocompatible N-succinyl-O-carboxymethylchitosan. *The Journal of Physical Chemistry C*, **112**, 5432–8.

142 Aurich, K., Schwalbe, M., Clement, J.H., Weitschies, W. and Buske, N. (2007) Polyaspartate coated magnetite nanoparticles for biomedical, applications. *Journal of Magnetism and Magnetic Materials*, **311**, 1–5.

143 Ma, H.-L., Qi, X.-R., Maitani, Y. and Nagai, T. (2007) Preparation and characterization of superparamagnetic iron oxide nanoparticles stabilized by alginate. *International Journal of Pharmaceutics*, **333**, 177–86.

144 Magnin, D., Callegari, V., Mátéfi-Tempfli, S., Mátéfi-Tempfli, M., Glinel, K., Jonas, A.M. and Demoustier-Champagne, S. (2008) Functionalization of magnetic nanowires by charged biopolymers. *Biomacromolecules*, **9**, 2517–22.

145 Shukoor, M.I., Natalio, F., Metz, N., Glube, N., Tahir, M.N., Therese, H.A., Ksenofontov, V., Theato, P., Langguth, P., Boissel, J.-P., Schröder, H.C., Müller, W.E.G. and Tremel, W. (2008) dsRNA-functionalized multifunctional γ-Fe_2O_3 nanocrystals: a tool for targeting cell surface receptors, *Angewandte Chemie, International Edition in English*, **47**, 4748–52.

146 Hong, J., Gong, P., Xu, D., Sun, H. and Yao, S. (2007) Synthesis and characterization of carboxyl-functionalized magnetic nanogel via "green" photochemical method. *Journal of Applied Polymer Science*, **105**, 1882–7.

147 Gelbrich, T., Feyen, M. and Schmidt, A.M. (2006) Magnetic thermoresponsive core-shell nanoparticles. *Macromolecules*, **39**, 3469–72.

148 Gürler, C., Feyen, M., Behrens, S., Matoussevitch, N. and Schmidt, A.M. (2008) One-step synthesis of functional Co nanoparticles for surface-initiated polymerization. *Polymer*, **49** (9), 2211–16.

149 Kobayashi, M., Matsuno, R., Otsuka, H. and Takahara, A. (2006) Precise surface structure control of inorganic solid and metal and oxide nanoparticles through surface-initiated radical polymerization. *Science and Technology Advanced Materials*, **7**, 617–28.

150 (a) Makhluf, S.B.-D., Qasem, R., Rubinstein, S., Gedanken, A., Breitbart, H. and Magnetic, L. (2006) Nanoparticles into sperm cells does not affect their functionality. *Langmuir*, **22**, 9480–2; (b) Makhluf, S.B.-D., Abu-Mukh, R., Rubinstein, S., Breitbart, H. and Gedanken, A. (2008) Modified PVA-Fe_3O_4 nanoparticles as protein carriers into sperm cells. *Small*, **4** (9), 1453–8.

151 Bhattacharya, S., Eckert, F., Volodymyr, B. and Pich, A. (2007) Temperature-, pH-, and magnetic-field-sensitive hybrid microgels. *Small*, **3**, 650–7.

152 Kim, B.-S., Qui, J.-M., Wang, J.-P. and Taton, T.A. (2005) Magnetomicelles composite nanostructures from magnetic nanoparticles and cross-linked amphiphilic block copolymers. *Nano Letters*, **5**, 1987–91.

153 Keng, P.Y., Shim, I., Korth, B.D., Douglas, J.F. and Pyun, J. (2007) Synthesis and self-assembly of polymer-coated ferromagnetic nanoparticles. *ACS Nano*, **1**, 279–92.

154 Song, H.M., Kim, Y.J. and Park, J.H. (2008) Three-dimensional hierarchically organized magnetic nanoparticle polymer composites achievement of monodispersity and enhanced tensile strength. *The Journal of Physical Chemistry C*, **112**, 5397–404.

155 Nasongkla, N., Bey, E., Ren, J., Ai, H., Khemtong, C., Guthi, J.S., Chin, S.-F., Sherry, A.D., Boothman, D.A. and Gao, J. (2006) Multifunctional polymeric micelles as cancer-targeted, MRI-ultrasensitive drug delivery systems. *Nano Letters*, **6**, 2427–30.

156 Belfield, K.D. and Zhang, L. (2006) Norbornene-functionalized diblock copolymers via ring-opening metathesis polymerization for magnetic nanoparticle stabilization. *Chemistry of Materials*, **18**, 5929–36.

157 Shtykova, E.V., Huang, X., Gao, X., Dyke, J.C., Schmucker, A.L., Dragnea, B., Remmes, N., Baxter, D.V., Stein, B., Konarev, P.V., Svergun, D.I. and Brostein, L.M. (2008) Hydrophilic

monodisperse magnetic nanoparticles protected by an amphiphilic alternating copolymer. *The Journal of Physical Chemistry C*, **112**, 16809–17.

158 Tasis, D., Tagmatarchis, N., Bianco, A. and Prato, M. (2006) Chemistry of carbon nanotubes. *Chemical Reviews*, **106**, 1105–36.

159 Ma, Y., Hu, Z., Yu, L., Hu, Y., Yue, B., Wang, X., Chen, Y., Lu, Y., Liu, Y. and Hu, J. (2006) Chemical functionalization of magnetic carbon-encapsulated nanoparticles based on acid oxidation. *The Journal of Physical Chemistry B*, **110**, 20118–22.

160 Ma, Y., Yue, B., Yu, L., Wang, X., Hu, Z., Fan, Y., Chen, Y., Lin, W., Lu, Y. and Hu, J. (2008) Artificial construction of the magnetically separable nanocatalyst by anchoring pt nanoparticles on functionalized carbon-encapsulated nickel nanoparticles. *The Journal of Physical Chemistry C*, **112**, 472–5.

161 Zhu, G.-X., Wei, X.-W. and Jiang, S.A. (2007) Facile route to carbon-coated nickel-based metal nanoparticles. *Journal of Materials Chemistry*, **17**, 2301–6.

162 Williams, D.N., Gold, K.A., Pulliam Holoman, T.R., Ehrman, S.H. and Willison, O.C., Jr (2006) Surface modification of magnetic nanoparticles using gum arabic. *Journal of Nanoparticle Research*, **8**, 749–53.

163 Jiang, L., Sun, W. and Kim, J. (2007) Preparation and characterization of ω-functionalized polystyrene-magnetite nanocomposites. *Materials Chemistry and Physics*, **101**, 291–6.

164 Sangermano, M., Priola, A., Kortaberria, G., Jimeno, A., Garcia, I., Mondragon, I. and Rizza, G. (2007) Photopolymerization of epoxy coatings containing iron-oxide nanoparticles. *Macromolecular Materials and Engineering*, **292**, 956–61.

165 Yánez-Flores, I.G., Betancourt-Galindo, R., Matutes Aquino, J.A. and Rodríguez-Fernández, O. (2007) Preparation and characterization of magnetic and PVC nanocomposites. *Journal of Non-Crystalline Solids*, **353**, 799–801.

166 Lee, H., Yu, M.K., Park, S., Moon, S., Min, J.J., Jeong, Y.Y., Kang, H.-W. and Jon, S. (2007) Thermally cross-linked superparamagnetic iron oxide nanoparticles synthesis and application as a dual imaging probe for cancer in vivo. *Journal of the American Chemical Society*, **129**, 12739–45.

167 García, I., Tercjak, A., Zafeiropoulos, N.E., Stamm, M. and Mondragon, I. (2007) Self-assembling nanomaterials using magnetic nanoparticles modified with polystyrene brushes. *Macromolecular Rapid Communications*, **28**, 2361–5.

168 Hong, J., Gong, P., Xu, D., Dong, L. and Yao, S. (2007) Stabilization of α-chymotrypsin by covalent immobilization on Amine-functionalized superparamagnetic nanogel. *Journal of Biotechnology*, **128**, 597–605.

169 Wilson, O.C., Jr, Blair, E., Kennedy, S., Rivera, G. and Mehl, P. (2008) Surface modification of magnetic nanoparticles with oleylamine and gum arabic. *Materials Science and Engineering C*, **28**, 438–42.

170 Shamim, N., Hong, L., Hidajat, K. and Uddin, M.S. (2007) Thermosensitive polymer (N-isopropylacrylamide) coated nanomagnetic particles: preparation and characterization. *Colloids Surface B*, **55**, 51–8.

171 Mefford, O.T., Vadala, M.L., Goff, J.D., Carroll, M.R.J., Mejia-Ariza, R., Caba, B.L., St Pierre, T.G., Woodward, R.C., Davis, R.M. and Riffle, J.S. (2008) Stability of polydimethylsiloxane-magnetite nanoparticle dispersions against flocculation: interparticle interactions of polydisperse materials. *Langmuir*, **24**, 5060–9.

172 Hong, J., Xu, D., Gong, P., Ma, H., Dong, L. and Yao, S. (2007) Conjugation of enzyme on superparamagnetic nanogels covered with carboxyl groups. *Journal of Chromatography*, **850**, 499–506.

173 Lee, H.Y., Lim, N.H., Seo, J.A., Yuk, S.H., Kwak, B.K., Khang, G., Lee, H.B. and Cho, S.H. (2006) Preparation and magnetic resonance imaging effect of polyvinylpyrrolidone-coated iron oxide nanoparticles. *Journal of Biomedical*

Materials Research. Part B, Applied Biomaterials, **79B**, 142-50.

174 Bromberg, L. and Hatton, T.A. (2007) Decomposition of toxic environmental contaminants by recyclable catalytic, superparamagnetic nanoparticles. *Industrial and Engineering Chemistry Research*, **46**, 3296–303.

175 Zhang, J., Srivastava, R.S. and Mirsa, R.D.K. (2007) Core-shell magnetite nanoparticles surface encapsulated with smart stimuli-responsive polymer synthesis, characterization, and LCST of viable drug-targeting delivery system. *Langmuir*, **23**, 6342–51.

176 Mangeney, C., Fertani, M., Bousalem, S., Zhicai, M., Ammar, S., Herbst, F., Beaunier, P., Elaissari, A. and Chehimi, M.M. (2007) Magnetic Fe_2O_3-Polystyrene/Ppy core/shell particles: bioreactivity and self-assembly. *Langmuir*, **23**, 10940–9.

177 Lai, J.J., Hoffman, J.M., Ebara, M., Hoffman, A.S., Estournès, C., Wattiaux, A. and Stayton, P.S. (2007) Dual magnetic-/temperature-responsive nanoparticles for microfluidic separations and assays. *Langmuir*, **23**, 7385–91.

178 (a) Mahdavian, A.R., Sehri, Y. and Salehi-Mobarakeh, H. (2008) Nanocomposite particles with core-shell morphology II. An investigation into the affecting parameters on preparation of Fe_3O_4-poly(butyl acrylate-styrene) particles via miniemulsion polymerization. *European Polymer Journal*, **44**, 2482–8;
(b) Mahdavian, A.R., Ashjari, M. and Mobarakeh, H.S. (2008) Nanocomposite particles with core-shell morphology I. Preparation and characterization of Fe_3O_4-poly(butyl acrylate-styrene) particles via miniemulsion polymerization. *Journal of Applied Polymer Science*, **110**, 1242–9.

179 Binder, W.H., Petraru, L., Roth, T., Groh, P.W., Pálfi, V., Keki, S. and Ivan, B. (2007) Magnetic and temperature-sensitive and release gels from supramolecular polymers. *Advanced Functional Materials*, **17**, 1317–26.

180 Zhang, F., Su, Z., We, F. and Li, F. (2008) Synthesis and characterization of polystyrene-grafted magnetite nanoparticles. *Colloid and Polymer Science*, **286**, 837–41.

181 Liang, Y., Xia, X., Luo, Y. and Jia, Z. (2007) Synthesis and performances of Fe_2O_3/PA-6 nanocomposite fiber. *Materials Letters*, **61**, 3269–72.

182 Arias, J.L., Gallardo, V., Ruiz, M.A. and Delgado, A.V. (2008) Magnetite/poly(alkylcyanoacrylate) (core/shell) nanoparticles as 5-fluorouracil delivery systems for active targeting. *European Journal of Pharmaceutics and Biopharmaceutics*, **69**, 54–63.

183 Robinson, I., Alexander, C., Lu, L.T., Tung, L.D., Fernig, D.G. and Thanh, N.T.K. (2007) One-step synthesis of monodisperse water-soluble "dual-responsive" magnetic nanoparticles. *Chemical Communications (Cambridge, England)*, **44**, 4602–4.

184 Herdt, A.R., Kim, B.-S. and Taton, T.A. (2007) Encapsulated magnetic nanoparticles as supports for proteins and recyclable biocatalysts. *Bioconjugate Chemistry*, **18**, 183–9.

185 Joumaa, N., Toussay, P., Lansalot, M. and Elaissari, A. (2008) Surface modification of iron oxide nanoparticles by a phosphate-based macromonomer and further encapsulation into submicrometer polystyrene particles by miniemulsion polymerization. *Journal of Polymer Science. Part A-1, Polymer Chemistry*, **46**, 327–40.

186 Chemin, N., Rozes, L., Chanéac, C., Cassaignon, S., Le Bourhis, E., Jolivet, J.-P., Spalla, O., Barthel, E. and Sanchez, C. (2008) Structure and mechanical properties of mesostructured functional hybrid coatings based on anisotropic nanoparticles dispersed in poly(hydroxylethyl methacrylate). *Chemistry of Materials*, **20**, 4602–11.

187 Zhang, D.-H., Li, G.-D., Li, J.-X. and Chen, J.-S. (2008) One-pot synthesis of Ag-Fe_3O_4 nanocomposite: a magnetically recyclable and efficient catalyst for epoxidation of styrene. *Chemistry Communications*, **29**, 3414–16.

188 Berre, J.-F., Schonbeck, N., Gazeau, F., Kharrat, D.E., Sandre, O., Vacher, A. and Airiau, M. (2006) Controlled clustering of superparamagnetic nanoparticles using block copolymers: design of new contrast agents for magnetic resonance imaging. *Journal of the American Chemical Society*, **128**, 1755–61.

189 Wuang, S.C., Neoh, K.G., Kang, E.-T., Pack, D.W. and Leckband, D.E. (2008) HER-2-mediated endocytosis of magnetic nanospheres and the implications in cell targeting and particle magnetization. *Biomaterials*, **29**, 2270–9.

190 Manuel, J., Kim, J.-K., Ahn, J.-H., Cheruvally, G., Chauhan, G.S., Choi, J.-W. and Kim, K.-W. (2008) Surface-modified maghemite as the cathode material for lithium batteries. *Journal of Power Sources*, **184**, 527–31.

191 Hong, S., Chen, H., Wang, L. and Wang, L. (2008) Luminescent and magnetic Fe_3O_4/Py/PAM nanocomposites for the Chromium(VI) determination. *Spectrochimica Acta Part A–Molecular and Biomolecular Spectroscopy*, **70**, 449–53.

192 Ho, K.M. and Li, P. (2008) Design and synthesis of novel magnetic core-shell polymeric particles. *Langmuir*, **24**, 1801–7.

193 Mahmoudi, M., Simchi, A., Imani, M., Milani, A.S. and Stroeve, P. (2008) Optimal design and characterization of superparamagnetic iron oxide nanoparticles coated with polyvinyl alcohol for targeted delivery and imaging. *The Journal of Physical Chemistry B.*, **112**, 14470–81.

194 Park, I.-K., Ng, C.-P., Wang, J., Chu, B., Yuan, C., Zhang, S. and Pun, S.H. (2008) Determination of nanoparticles vehicle unpackaging by MR imaging of a T2 magnetic relaxation switch. *Biomaterials*, **29**, 724–32.

195 Cheng, Z., Liu, S., Gao, H., Tremel, W., Ding, N., Liu, R., Beines, P.W. and Knoll, W.A. (2008) Facile approach for transferring hydrophobic magnetic nanoparticles into water-soluble particles. *Macromolecular Chemistry and Physics*, **209**, 1145–51.

196 Boguslavsky, Y. and Margel, S. (2008) Synthesis and characterization of Poly(divinylbenzene)-coated magnetic iron oxide nanoparticles as precursor for the formation of air-stable carbon-coated iron crystalline nanoparticles. *Journal of Colloid and Interface Science*, **317**, 101–14.

197 (a) Wang, L., Bai, J., Li, Y. and Huang, Y. (2008) Multifunctional nanoparticles displaying magnetization and near-IR absorption. *Angewandte Chemie, International Edition in English*, **47**, 2439–42;
(b) Tan, C.J., Chua, H.G., Ker, K.H. and Tong, Y.W. (2008) Preparation of bovine serum albumin surface-imprinted submicrometer particles with magnetic susceptibility through core-shell miniemulsion polymerization. *Analytical Chemistry*, **80**, 683–92.

198 Sacanna, S. and Philipse, A.P. (2006) Preparation and properties of monodisperse latex spheres with controlled magnetic moment for field-induced colloidal crystallization and (dipolar) chain formation. *Langmuir*, **22**, 10209–16.

199 Ren, J., Hong, H., Ren, T. and Teng, X. (2006) Preparation and characterization of magnetic PLA-PEG composite nanoparticles for drug targeting. *Reactive and Functional Polymers*, **66**, 944–51.

200 Li, A., Tan, B., Allix, M., Cooper, A.I. and Rosseinsky, M.J. (2008) Direct coprecipitation route to monodisperse dual-functionalized magnetic iron oxide nanocrystals without size selection. *Small*, **4** (2), 231–9.

201 Wang, W.-C., Neoh, K.-G. and Kang, E.-T. (2006) Surface Functionalization of Fe_3O_4 magnetic nanoparticles via RAFT-mediated graft polymerization. *Macromolecular Rapid Communications*, **27**, 1665–9.

202 Guo, Z., Chen, Y., Zhou, W., Haung, Z., Hu, Y., Wan, M. and Bai, F. (2008) Facilely dispersible magnetic nanoparticles prepared by a surface-initiated atom transfer radical polymerization. *Materials Letters*, **62**, 4542–4.

203 Aqil, A., Vasseur, S., Duguet, E., Passirani, C., Benoît, J.P., Jérôme, R.

and Jérôme, C. (2008) Magnetic nanoparticles coated by temperature responsive copolymers for hyperthermia. *Journal of Materials Chemistry*, **18**, 3352–60.

204 Zhang, B., Cheng, J., Gong, X., Dong, X., Liu, X., Ma, G. and Chang, J. (2008) Facile fabrication of multi-colors high fluorescent/superparamagnetic nanoparticles. *Journal of Colloid and Interface Science*, **322**, 485–90.

205 Yang, X., Chen, Y., Yuan, R., Chen, G., Blanco, E., Gao, J. and Shuai, X. (2008) Folate-Encoded and Fe_3O_4-loaded polymeric micelles for dual targeting of cancer cells. *Polymer*, **49**, 3477–85.

206 Sun, H., Yu, J., Gong, P., Xu, D., Hong, J., Zhang, C. and Yao, S. (2006) Novel core-shell magnetic nanogels synthesized in an emulsion-free aqueous system under UV irradiation for potential targeted radiopharmaceutical applications. *International Journal of Nanoscience*, **5**, 253–8.

207 Makhluf, S.B.-D., Qasem, R., Rubinstein, S., Gedanken, A. and Breitbart, H. (2006) Loading magnetic nanoparticles into sperm cells does not affect their functionality. *Langmuir*, **22**, 9480–2.

208 Sheparovych, R., Sahoo, Y., Motornov, M., Wang, S., Luo, H., Prasad, P.N., Sokolov, I. and Minko, S. (2006) Polyelectrolyte stabilized nanowires from Fe_3O_4 nanoparticles via magnetic field induced self-assembly. *Chemistry of Materials*, **18**, 591–3.

209 Korth, B.D., Keng, P., Shim, I., Bowles, S.E., Tang, C., Kowalewski, T., Nebesny, K.W. and Pyun, J. (2006) Polymer-coated ferromagnetic colloids from well-defined macromolecular surfactants and assembly into nanoparticle chains. *Journal of the American Chemical Society*, **128**, 6562–3.

210 Shamim, N., Hong, L., Hidajat, K. and Uddin, M.S. (2006) Thermosensitive-polymer-coated magnetic nanoparticles adsorption and desorption of bovine serum albumin. *Journal of Colloid and Interface Science*, **304**, 1–8.

211 Hu, F.X., Neoh, K.G. and Kang, E.T. (2006) Synthesis and in vitro anti-cancer evaluation of tamoxifen-loaded magnetite/PLLA composite nanoparticles. *Biomaterials*, **27**, 5725–33.

212 Bowles, S.E., Wu, W., Kowalewski, T., Schalnat, M.C., Davis, R.J., Pemberton, J.E., Shim, I., Korth, B.D. and Pyun, J. (2007) Magnetic assembly and pyrolysis of functional ferromagnetic colloids into one-dimensional carbon nanostructures. *Journal of the American Chemical Society*, **129**, 8694–5.

213 Sayar, F., Güven, G. and Pişkin, E. (2006) Magnetically loaded poly(methyl methacrylate-*co*-acrylic acid) nanoparticles. *Colloid and Polymer Science*, **284**, 965–78.

214 Lu, S., Ramos, J. and Forcada, J. (2007) Self-stabilized and magnetic polymeric composite nanoparticles by emulsifier-free miniemulsion polymerization. *Langmuir*, **23**, 12893–900.

215 Shin, S. and Jang, J. (2007) Thiol containing polymer encapsulated magnetic nanoparticles as reusable and efficiently separable adsorbent for heavy metal ions. *Chemistry Communications*, **41**, 4230–2.

216 Zhang, Q., Thompson, M.S., Carmichael-Baranauskas, A.Y., Caba, B.L., Zalich, M.A., Lin, Y.-N., Mefford, O.T., Davis, R.M. and Riffle, J.S. (2007) Aqueous dispersions of magnetite nanoparticles complexed with copolyether dispersants: experiments and theory. *Langmuir*, **23**, 6927–36.

217 Wang, S.C., Neoh, K.G., Kang, E.-T., Pack, D.W. and Leckband, D.E. (2007) Polypyrrole nanospheres with magnetic and cell-targeting capabilities. *Macromolecular Rapid Communications*, **28**, 816–21.

218 Ding, H., Liu, X.-M., Wan, M. and Fu, S.-Y. (2008) Electromagnetic functionalized cage-like polyaniline composite nanostructures. *The Journal of Physical Chemistry B*, **112**, 9289–94.

219 Fan, Q.-L., Neoh, K.-G., Kang, E.-T., Shuter, B. and Wang, S.-C. (2007) Solvent-free atom transfer radical polymerization for the preparation of poly(poly(ethyleneglycol) monomethacrylate)-grafted Fe_3O_4 nanoparticles: synthesis,

characterization, and cellular uptake. *Biomaterials*, **28**, 5426–36.

220 Narain, R., Gonzales, M., Hoffman, A.S., Stayton, P.S. and Krishnan, K.M. (2007) Synthesis of monodisperse biotinylated p(NIPAAm)-coated iron oxide magnetic nanoparticles and their bioconjugation to streptavidin. *Langmuir*, **23**, 6299–304.

221 (a) Avanti® Polar Lipids, Inc., http://avantilipids.com (accessed September 2008);
(b) Invitrogen™ Corp., http://invitrogen.com/site/us/en/home.htm (accessed September 2008).

222 (a) Dubertret, B., Skourides, P., Norris, D.J., Noireaux, V., Brivanlou, A.H. and Libchaber, A. (2002) In vivo imaging of quantum dots encapsulated in phospholipid micelles. *Science*, **298**, 1759–62;
(b) Grancharov, S.G., Zeng, H., Sun, S., Wang, S.X., O'Brien, S., Murray, C.B., Kirtley, J.R. and Held, G.A. (2005) Bio-functionalization of monodisperse magnetic nanoparticles and their use as biomolecular labels in a magnetic tunnel junction based sensor. *The Journal of Physical Chemistry B*, **109**, 13030–5.

223 Mulder, W.J.M., Strijkers, G.J., van Tilborg, G.A.F., Griffioen, A.W. and Nicolay, K. (2006) Lipid-based nanoparticles for contrast-enhanced MRI and molecular imaging. *NMR in Biomedicine*, **19**, 142–64.

224 Lim, Y.T., Lee, K. and Chung, B.H. (2006) Immobilization of histidine-tagged proteins by magnetic nanoparticles encapsulated with nitrilotriacetic acid (NTA)-phospholipids micelle. *Biochemical and Biophysical Research Communications*, **344**, 926–30.

225 Conti, M., Falini, G. and Samori, B. (2000) How strong is the coordination bond between a histidine tag and Ni-nitrilotriacetate? An experiment of mechanochemistry on single molecules. *Angewandte Chemie, International Edition in English*, **39**, 215–18.

226 Ito, A., Fujioka, M., Yoshida, T., Wakamatsu, K., Ito, S., Yamashita, T., Jimbow, K. and Honda, H. (2007) 4-*S*-Cysteaminylphenol-loaded magnetite cationic liposomes for combination therapy of hyperthermia with chemotherapy against malignant melanoma. *Cancer Science*, **98**, 424–30.

227 (a) Hutchins, B.M., Platt, M., Hancock, W.O. and Williams, M.E. (2007) Directing transport of $CoFe_2O_4$-functionalized microtubules with magnetic fields. *Small*, **3**, 126–31;
(b) Platt, M., Muthukrishnan, G., Hancock, W.O. and Williams, M.E. (2005) Millimeter scale alignment of magnetic nanoparticle functionalized microtubules in magnetic fields. *Journal of the American Chemical Society*, **127**, 15686–7;

228 Tomalia, D.A. (1994) Starburst/cascade dendrimers: fundamental building blocks for a new nanoscopic chemistry set. *Advanced Materials*, **6**, 529–39.

229 Boas, U. and Heegaard, P.M.H. (2004) Dendrimers in drug research. *Chemical Society Reviews*, **33**, 43–63.

230 (a) Knecht, M.R., Garcia-Martinez, J.C. and Crooks, R.M. (2006) Synthesis, characterization, and magnetic properties of dendrimer-encapsulated nickel nanoparticles containing <150 Atoms. *Chemistry of Materials*, **18**, 5039–44;
(b) Scott, R.W.J., Datye, A.K. and Crooks, R.M. (2003) Bimetallic palladium-platinum dendrimer-encapsulated catalysts. *Journal of the American Chemical Society*, **125**, 3708–9;
(c) Scott, R.W.J., Wilson, O.M. and Crooks, R.M. (2005) Synthesis characterization, and applications of dendrimer-encapsulated nanoparticles. *The Journal of Physical Chemistry B*, **109**, 692–704.

231 Atwater, J.E., Akse, J.R. and Holtsnider, J.T. (2008) Cobalt-poly(amido amine) superparamagnetic nanocomposites. *Materials Letters*, **62**, 3131–4.

232 Auten, B.J., Hahn, B.P., Vijayaraghavan, G., Stevenson, K.J. and Chandler, B.D. (2008) Preparation and characterization of 3 nm magnetic NiAu nanoparticles. *The Journal of Physical Chemistry C*, **112**, 5365–72.

233 Shi, X., Thomas, T.P., Myc, L.A., Kotylar, A. and Baker, J.R., Jr (2007) Synthesis, characterization, and intracellular uptake

of carboxyl-terminated poly(amidoamine) dendrimer-stabilized iron oxide nanoparticles. *Physical Chemistry Chemical Physics*, **9**, 5712–20.

234 Landmark, K.J., DiMaggio, S., Ward, J., Kelly, C., Vogt, S., Hong, S., Kotylar, A., Myc, A., Thomas, T.P., Penner-Hahn, J.E., Baker, J.R., Jr, Banaszak Holl, M.M. and Orr, B.G. (2008) Synthesis, characterization, and in vitro testing of superparamagnetic iron oxide nanoparticles targeted using folic acid-conjugated dendrimers. *ACS Nano*, **2** (4), 773–83.

Keywords

nanoparticle; magnetic; encapsulation; monolayer; functionalization; ligand substitution; synthesis

15
Characterization of Magnetic Nanoparticles Using Magnetic Force Microscopy

Gunjan Agarwal

15.1
Introduction

The aim of this chapter is to provide an overview of the magnetic force microscopy (MFM) technique and its application for the characterization of magnetic nanoparticles (MNPs). The chapter also serves as a user's guide to MFM, without unnecessary repetition of previously published information, and without excessive mathematical detail. The reader is introduced to physical principals of MFM, the properties of MFM probes, probe calibration, methods of MFM detection, and application of MFM for MNPs. The goal is not to provide a detailed overview of MFM and hardware design, as several excellent texts (cited in the references) are available for this purpose. Rather, the special considerations and challenges required for MFM studies of MNPs, especially in biological samples, are highlighted. The chapter concludes with some details of the recent developments and future trends in MFM of MNPs for the life sciences.

15.2
Development of MFM

Understanding the nature of magnetism at the nanometer-length scale is of interest from a fundamental perspective, as well as for the development of next generation of MNPs for the life sciences. The study of MNPs involves special challenges since, below a critical dimension, the competition between magnetostatic energy and exchange energy is predicted to suppress magnetic domain formation, leading to single-domain structures. These single-domain MNPs not only possess low magnetization values, as compared to bulk material, but may also have lower coercivity or a superparamagnetic character at temperatures conducive to living systems. Thus, specialized techniques are needed to understand and characterize the magnetic nature of MNPs.

Nanomaterials for the Life Sciences Vol. 4: Magnetic Nanomaterials. Edited by Challa S. S. R. Kumar

ISBN: 978-3-527-32154-4

Magnetic force microscopy is used widely for investigating magnetic systems. The ease of use, a large number of commercially available models, and a low cost of operation make the magnetic force microscope an instrument of choice for many scientists studying magnetic systems. The technique of MFM has evolved from atomic force microscopy (AFM) as a special method of studying magnetic materials and their properties [1]. MFM is a scanned probe technique based the mechanical detection of the magnetostatic interaction of the microscope probe and the magnetic sample (Figure 15.1). During the MFM experiment, magnetic material in the sample interacts, through magnetic dipolar interaction, with the apex of the cantilever tip (or probe) coated with a magnetic material. As for most scanning probe microscopes, the signals in MFM are governed by the probe characteristics, the tip–sample interaction, and the detection system used.

Martin and Wickramasinghe [3] were the first to build a magnetic force microscope, by using a 25 μm-diameter iron wire as the cantilever with its end as the magnetic tip. The tip was formed by electrochemically etching the end of the iron wire down to a 50 nm radius. The wire was bent at a sharp right-angle near its end, such that the tip axis was aligned perpendicular to the cantilever (the rest of the wire). These authors measured the deflection of the cantilever, and therefore the force exerted on it, with an optical interferometer. Saenz *et al.* developed another early magnetic force microscope by using tunneling to measure the deflection of a thin nickel foil used as a cantilever and tip [4]. The lateral resolution of these first instruments was 100 nm – a substantial improvement over any magnetic imaging technique available at that time.

Since its inception, the MFM technique has undergone several improvements to make it a widely used procedure that is available on modern AFM machines.

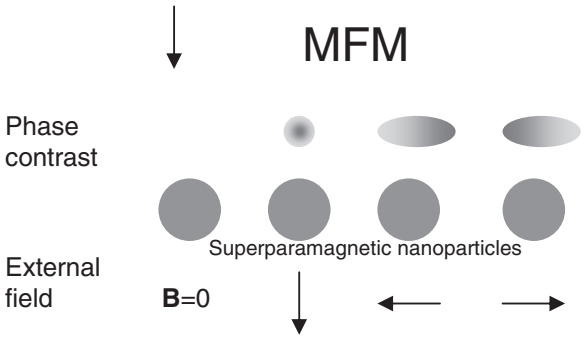

Figure 15.1 Detecting nanomagnets by MFM [2]. Using external magnetic fields and magnetic atomic force microscope tips, it is possible to characterize the dipolar nature of magnetic nanoparticles in ambient air. These approaches could help localize magnetic nanoparticles in biological samples. Reproduced with permission from Ref. [2].

These include the use of thin-film-coated MFM probes with a wide variety of magnetic and mechanical properties (see Section 15.6.2), the use of split photodiodes to detect cantilever deflection [5–7], and the use of dynamic mode AFM to enhance the force sensitivity of the MFM technique (see Section 15.4.2). As a result, in recent years a spatial resolution of 20–30 nm has been achieved with MFM, making it an attractive technique for the characterization of MNPs. With further advances in the field, it is envisaged that MFM may achieve its theoretical limit of resolution (5–10 nm).

MFM has found numerous applications in fundamental research and in the data storage industry. MFM serves as a useful tool for disk-failure analysis, and to analyze magneto-optical media and corresponding read/write processes, which usually require a micron-scale spatial resolution. More recent, nonstandard applications of MFM include magnetic dissipation imaging [8] to investigate magnetization dynamics through studying the energy transfer between the cantilever and the magnetic sample, and low-temperature measurements to investigate magnetic vortices [9] or local variations in the magnetic penetration length in superconductors and colossal magnetoresistance materials [10]. The application of MFM to characterize nanoscale magnetic domains has not yet been completely explored, mainly because special considerations need to be given to MFM experimental conditions, sample preparation and probe characterization to enable the qualitative and quantitative detection of MNPs.

15.3 Comparison of MFM to Other Techniques

Despite the emerging interest of the life sciences community in the use of MNPs, there is a clear absence of a detection technique for their localization and characterization at the single-particle level. The techniques currently being used to detect MNPs can broadly be classified as invasive or noninvasive. The limitation in resolution and/or sensitivity of these techniques as compared to MFM is discussed here.

15.3.1 Invasive Imaging

Superconducting quantum interference device (SQUID) magnetometry is conventionally used to characterize the bulk magnetic properties of materials, including samples of MNPs with masses of several micrograms. In the recently developed scanning SQUID microscopy technique, the pick-up coil is scanned over the surface of the sample where it picks up the stray magnetic field of the magnetic moments in the sample [11]. As a result, the spatial resolution of the method is defined by the dimensions of this coil. The highest demonstrated resolution to date is approximately 10 μm which is insufficient for studying systems of MNPs [12]. Similarly, the scanning Hall probe microscope (SHPM) suffers from low

spatial resolution (>1 μm) as compared to MFM, and requires the use of very low temperatures (typically liquid helium) [13]. However, like the magnetic force microscope, both the scanning SQUID microscope and the SHPM are capable of obtaining information from below the surface due to the long-range aspect of magnetic interactions. In recent years, arrays of SQUID sensors have been used to probe the fields generated by the human heart or brain [14]. However, these applications have been limited to a macroscopic scale.

Conventional *in vitro* microscopic analyses can provide enhanced spatial resolution. However, unlike the magnetic force microscope, SQUID or SHPM, these instruments cannot characterize magnetic behavior but only provide an insight into the presence of elements, such as iron. For instance, Perl's iron staining technique is popularly used in histology to identify the presence of iron at a spatial resolution limited to ~200 nm. High-resolution techniques, such as transmission electron microscopy (TEM) coupled with X-ray diffraction (XRD) microanalysis can enable the localization of iron deposits and nanoparticles which are <100 nm in size. However, very limited reports exist on the use of TEM/XRD for ultrastructural studies of iron deposits in diseased tissues at the subcellular level [15–17], possibly due to the involved sample preparation, the sophisticated instrumentation, and the damage caused to the tissue in XRD. Recently, off-axis electron holography has been demonstrated to provide insight into magnetic phenomena on the nanoscale [18]. Compared to electron beam techniques, such as electron holography, Lorentz microscopy, scanning electron microscopy with polarization analysis (SEMPA) and X-ray photoelectron microscopy (XPEEM) [19], MFM has the advantages of simpler sample preparation, ease of operation, easier access to low temperatures, and lower cost. Furthermore, a fundamental advantage of MFM over electron beam techniques is that, with MFM, one can apply much larger fields *in situ*, which is very important for the study of those samples with a paramagnetic character.

15.3.2 Noninvasive Imaging

Among the noninvasive techniques, the well-developed magnetic resonance imaging (MRI) relies on the indirect detection of MNPs through their effect on the proton relaxation time in the vicinity of MNPs (T_2^* effects) visible as a negative contrast [20–22]. This effect, however, is not easily quantifiable and cannot be used to qualify or quantify iron content with any degree of certainty. Other imaging techniques such as synchrotron-based micro-computed tomography (CT) imaging (with a voxel resolution of 2 μm), synchrotron-based X-ray fluorescence microscopy (XRF) [23] and position emission tomography (PET) [24], have been used to localize, identify, and quantitate iron deposits and regions of intraplaque hemorrhage in mouse tissue. In general, however, these studies lack spatial resolution and ability to speciate iron at a level below approximately 5.6×10^{-18} g mm^{-2} corresponding to a spatial resolution of 0.5 μm.

15.3.3
Magnetic Resonance Force Microscopy

Among the upcoming techniques which may match the capabilities of MFM, magnetic resonance force microscopy (MRFM) is the most promising scanned probe technique based on the mechanical detection of magnetic resonance. MRFM was proposed as a method to overcome the sensitivity limitations of inductively detected MRI, and to push the spatial resolution of MRI into the nanometer and, ultimately, the atomic scale. MRFM methods have steadily improved since the first demonstrations, with significant advances in both electron spin and nuclear spin detection. Recently, the detection of magnetic resonance on a single electron spin has been demonstrated [25]. MRFM uses a magnetic tip and an ultrasensitive cantilever to sense the dipolar magnetic force between the tip and spins in a sample. In this sense, the MRFM arrangement is similar to that of MFM, and in fact the MRFM and MFM data are collected simultaneously in a MRFM experiment. Unlike MFM, where the static magnetic force is detected, the sensitivity of MRFM is enhanced through dynamic manipulation of the sample magnetic moments at the mechanical resonant frequency of the MRFM cantilever. In general, due to the detection of a dynamic magnetic force, MRFM can deliver sensitivity greater than that of MFM. For example, it has recently been demonstrated that MRFM is capable of two-dimensional (2-D) nuclear magnetic resonance (NMR) imaging with 90 nm spatial resolution [26]. However, MRFM relies on the capability to manipulate magnetic moments in the sample, which in turn is heavily dependent on the sample magnetic properties such as the shape, saturation magnetization, ferromagnetic resonance linewidth, and so on, which would make interpretation of the obtained results more difficult. Whilst the MRFM technique holds great promise for the investigation of individual nanoparticles, it is still a work-in progress and requires sophisticated and specialized equipment and experimental conditions – unlike the MFM technique, which is available on most commercial atomic force microscopes.

15.4
Physical Principals of MFM

15.4.1
Static Mode

For a magnetic force microscope cantilever, the force F (which is experienced normal to the cantilever) can result in a static deflection x of the cantilever, in accordance with Hooke's law, given by:

$$F = -kx \tag{15.1}$$

where k is the spring constant of the magnetic force microscope cantilever. It is evident from Equation 15.1 that stiffer cantilevers (with higher k-values) would result in a smaller cantilever deflection as compared to softer cantilevers. The minimum force detectable by the magnetic force microscope cantilever is also dependent on the sensitivity of the deflection sensor used (i.e., Δx is typically 0.01 nm), which is usually ascertained using AFM force spectroscopy. For a magnetic force microscope cantilever with k ranging from 0.1 to 1 N m^{-1}, the minimum detectable force is in the piconewton (pN) range, or higher. For long-range weak forces, such as in MFM, and $F <$ pN, the cantilever deflection ($<10^{-4}$ nm) is below the deflection sensitivity of most sensors [27]. Therefore, the dynamic method involving measurement of force gradients instead of forces acting on the cantilever is more in-vogue for MFM.

15.4.2 Dynamic Mode

An alternate, and more commonly used, method to measure long-range forces as in MFM is by oscillating the cantilever at its resonant frequency, ω_c, given by:

$$\omega_c = \sqrt{k/m} \tag{15.2}$$

where m is the mass of the cantilever. As the probe is scanned in a 2-D spatial raster pattern over the sample surface, the force gradient F' experienced by the cantilever normal to its plane, modifies the effective spring constant (k_{eff}) of the cantilever. This results in a shift, $\delta\omega$, in the cantilever resonant frequency given by:

$$\delta\omega = \omega_c \frac{F'}{2k} \tag{15.3}$$

For most MFM experiments, the cantilever is almost parallel to the sample surface and, assuming that the magnetic interaction is primarily along the vertical z direction, then $F' = \mathrm{d}F_z/\mathrm{d}z$. It is worth noting that, in this dynamic mode, the cantilevers used are with much higher k-values as compared to the static mode (Table 15.1), and therefore the cantilever deflection for MFM is usually negligible.

Magnetic data can be recorded either as variations in amplitude, phase, or frequency of the cantilever oscillation [27]. Amplitude modulation (AM) is the method more commonly available on commercial equipments to estimate F', where the change in amplitude or phase of the vibrating cantilever is measured at a fixed *drive* frequency ω_D. The drive frequency is selected as the frequency where the amplitude A of the cantilever has the steepest slope, and is given by:

$$\omega_D = \omega_c\left(1 \pm 1/\sqrt{8Q}\right) \tag{15.4}$$

Table 15.1 Examples of commercially available magnetic force microscope cantilevers/probes used in dynamic mode.

Probe name	Company	H_c (Oe)	k (N m^{-1})	Magnetic coating
NSC18	MicroMasch	240–310	3.5	Co–Cr (60 nm)
MFMR	Nanoworld and nanosensors	300–400	1–5	Cobalt alloy (40 nm)
MESP	Veeco	<10 to 400	2–3	Co–Cr alloy of various thickness
–	Seiko instruments	650	20	Cobalt–platinum–chromium alloy
ASYMFM	Asylum	<10 to >5000	1–2	30 nm permalloy to Co-alloys of various thickness

where Q is the quality factor of the cantilever. Under this condition, the amplitude change δA, at ω_D arising due to change in resonance frequency is given by:

$$\delta A = \left(\frac{2A_0Q}{3\sqrt{3k}}\right)F' \tag{15.5}$$

and the change in phase is given by:

$$\delta\Phi = \frac{Q}{k}F' \tag{15.6}$$

where A_o is the amplitude of the cantilever when $\omega_c = \omega_D$ (in Equation 15.5). Figure 15.2 shows the MFM amplitude and phase images of a magnetic tape acquired using the AM technique on a commercial magnetic force microscope [28]. One of the limitations of the AM method is that changes in amplitude do not occur instantaneously with a change in the tip–sample interactions, but rather on a time scale of $t_{AM} < 2Q/\omega_c$ [7].

An alternative method to estimate F' is to directly measure $\delta\omega$ via the frequency modulation (FM) technique [27]. This involves changes in the instrument design to incorporate a phase-lock loop and a frequency counter. Additionally, the amplitude of the cantilever is kept constant by means of an amplifier with automatic gain control and positive feedback loop using the signal from the cantilever deflection. The FM technique has the advantage that very high-Q cantilevers can

(a)

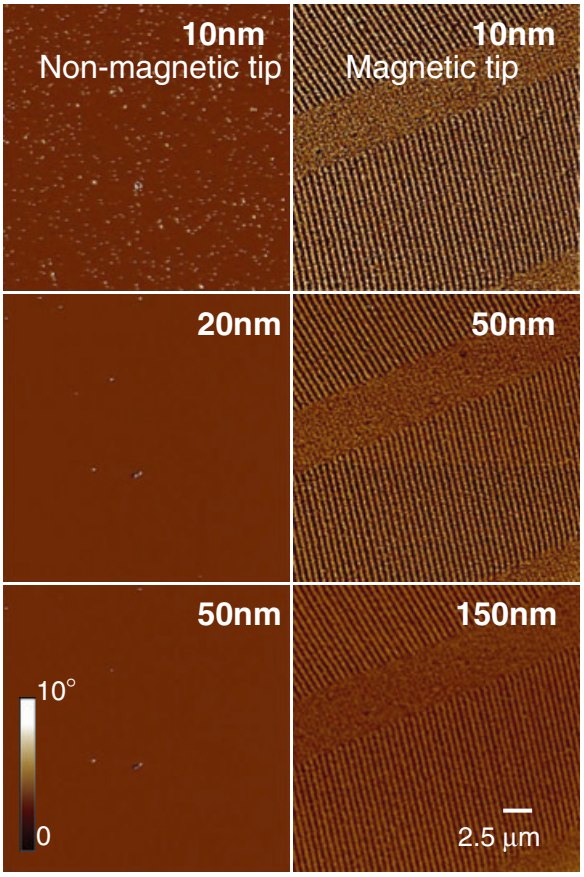

(b)

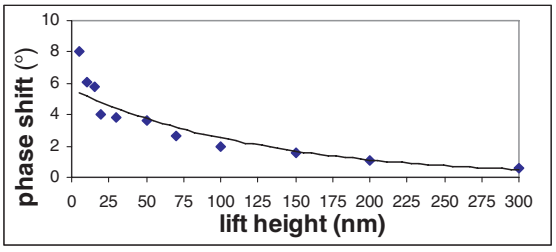

Figure 15.2 Identification of bit patterns in a magnetic tape using MFM [28]. (a) Phase-contrast images in lift-mode on a magnetic tape sample using (left) a nonmagnetic and (right) a magnetic atomic force microscope tip. The lift-heights for each image are indicated at the top right. Only images obtained using a magnetic tip show contrast in the written bit pattern, even at a lift-height of 150 nm. The scale bar applies to all images; (b) Plot of phase angle (Φ°) versus lift-height (nm) for a section of magnetic tape using a magnetic atomic force microscope tip, showing an exponential decay. Reproduced with permission from Ref. [28].

be used to achieve high sensitivity, and therefore is especially useful for MFM in a vacuum. Additionally, in this method the delay in detecting changes in F' can be reduced to $t_{FM} < 1/\omega_c$ [7, 29]. Phase detection and FM produce the best results, giving good contrast even when the amplitude signal fails to show detailed information.

15.4.3 Forces Due to Magnetic Interaction

For a point–dipole tip, the force F acting on the tip by a magnetic sample is given by:

$$F = (m_t, \nabla)H_s \tag{15.7}$$

where m_t is the magnetic moment of the tip and H_s is the field from the sample. As is evident from Equation 15.7, F will be greater at those points where the gradient of the magnetic field is higher, such as at magnetic poles or at regions where the magnetization is changing rapidly. In other words, the magnetic force microscope cannot sense homogeneous magnetic fields, but can only detect gradients in magnetic fields.

For MNPs, which generally possess a single magnetic domain, the magnetic field at the tip experienced due to a small sample magnetic particle, m_s at a distance r from the tip is given by [27]:

$$H_s(r) = \frac{3r(r \cdot m_s) - m_s}{r^3} \tag{15.8}$$

Therefore the force F experienced by the magnetic force microscope tip is given by:

$$F = \nabla\left(\frac{3\left(m_t \cdot \hat{r}\right)\left(m_s \cdot \hat{r}\right) - m_t.m_s}{r^3}\right) \tag{15.9}$$

If both the dipoles (m_s and m_t) point in the z-direction and r is also in the z-direction, then:

$$F = -6m_t m_s / z^4 \tag{15.10}$$

and the force gradient F' is given by [27, 30]:

$$F' = \partial F / \partial z = 24 m_t m_s / z^5 \tag{15.11}$$

which can also be valid for multidomain magnetic particles, provided that all the domains are oriented along the z-direction.

15.5 Noise in MFM

15.5.1 Thermal Noise

The force gradient detection in MFM is limited by the noise sources in the detection system. These include noise from the deflection sensor, acoustic noise, and thermal oscillations of the cantilever. For cantilevers with small spring constants, noise from the deflection sensor is usually negligible. Acoustic noise can often be blocked out or filtered out from MFM images. The predominant limitation is the rms amplitude arising from thermal oscillations, given by (in accordance with equipartition theorem) [27]:

$$A_T = \sqrt{k_B T / k} \tag{15.12}$$

where T is the temperature and k_B is Boltzmann's constant. However, when the deflection of the cantilever as measured by an optical beam deflection system is taken into account, the cantilever measures a change in inclination instead of a vertical movement. Butt and Jaschke [31] showed that the mean "virtual" vertical deflection of a free cantilever, when measured using beam deflection, is given by:

$$A_T = \sqrt{4k_B T / 3k} \tag{15.13}$$

which at a temperature of 22 °C amounts to:

$$A_T = 0.074\,nm/\sqrt{k} \quad \text{(for diving board cantilever)} \tag{15.14}$$

$$\text{and} \quad A_T = 0.056\,nm/\sqrt{k} \quad \text{(for V-shaped board cantilever)} \tag{15.15}$$

Thus, although V-shaped cantilevers are predicted to have a lower thermal oscillation amplitude as compared to diving board cantilevers, the spring constant of V-shaped cantilevers is generally much lower, resulting in higher values for A_T. Further, it can be seen that for the static mode of MFM, where the use of V-shaped cantilevers is more common, deflection due to thermal oscillation can be much larger than that due to magnetic interaction.

It is mainly in the dynamic or noncontact mode, where the cantilever is driven at amplitudes much larger than A_T, that the changes in amplitude, and so on, arising due to magnetic interactions can be ascertained. The force sensitivity in MFM is thus defined as the minimum detectable force gradient despite the thermal oscillations and other noise. The force sensitivity has been derived from force spectral density (probability distribution of force noise over a range of frequencies) as [29]:

$$F'_{\min} = \frac{1}{A}\sqrt{\frac{2kk_B TB}{w_c Q}} \quad \text{for AM} \tag{15.16}$$

where A is the mean-square amplitude of the driven cantilever vibration and B is the detection bandwidth [30]. In FM mode, the force sensitivity is limited not only by the cantilever thermal motion, but may also be affected by electronic noise arising from the cantilever deflection sensor, photodiode shot noise, and Johnson noise.

Thus, we can see that the spring constant of a cantilever is a critical factor in determining how sensitive a cantilever is – that is, how small a force can be measured. Interatomic force constants in solids are in the range from 10 to about $100\,\mathrm{N\,m^{-1}}$, and in biological samples they can be as small as $0.1\,\mathrm{N\,m^{-1}}$. Thus, typical values for k in the static mode [33] are 0.01 to $5\,\mathrm{N\,m^{-1}}$. In the dynamic mode, if the cantilever is soft (small k), the point at which the gradient of the interaction force becomes equal to k is reached earlier than for a stiff cantilever. At that point, the tip jumps into contact to the sample surface (called "snap-down"), and the deflection of the cantilever is coupled to its deformation. Thus, the useful range of k for MFM is restricted to $>0.1\,\mathrm{N\,m^{-1}}$ (Table 15.1). On the other hand, it is also necessary to maintain a high resonant frequency to decrease sensitivity to mechanical disturbances and track the sample surface more rapidly in dynamic mode. These conflicting requirements are generally solved by reducing the mass of the cantilever (m), so that the ratio k/m is as large as possible. Further, as discussed above in dynamic mode, a high quality factor of the cantilever Q is preferred to reduce thermal noise. While increasing Q reduces the cantilever's sensitivity and reduces the noise [34], it also increases the response time t_{AM} and thus restricts the bandwidth of the system.

15.5.2
Magnetic Versus Topographic Signals

Besides thermal noise, various probe–sample interactions such as electrostatic forces (proportional to $1/z^2$), van der Waals forces (proportional to $1/z^7$), damping and capillary forces can contribute to the force derivative. These nonmagnetic interactions are also present in topographic AFM imaging, and can give rise to changes in cantilever deflection (in static mode) or amplitude, phase and frequency changes in the vibrating cantilever (in dynamic mode). In MFM, it is important to separate the long-range magnetostatic coupling between probe and sample from the contribution of other (topographic) interactions. This is especially important when the tip is brought very close to the sample (in order to improve MFM resolution), as the nonmagnetic forces become increasingly stronger. A number of factors in cantilever design and/or selection and in experimental conditions are employed to distinguish between MFM and topographic imaging.

The primary solution to this problem is to keep the topography influence constant by letting the tip follow the sample height profile at a user-specified distance above the sample, commonly called the "lift height" [27]. This mode is typically called the "constant distance mode", and involves measuring the topography on

each scan line in a first scan, and then performing the second scan of the same line at the specified lift-height. During the second (magnetic) scan line, the feedback is turned off. In theory, the topographic contributions should be eliminated in the second image. This method, although widely used, places higher demands on instrument stability, because it is sensitive to drift, especially with increasing lift heights.

Another verification for distinguishing between topographic or magnetic features (especially for MNPs) is to vary the strength of the magnetic interaction. This can be achieved by either changing the polarity of tip-magnetization or by using nonmagnetic tips. By using nonmagnetic cantilevers with a similar spring constant, Q and probe geometry as magnetic cantilevers, one can – to a close approximation – estimate the contributions of nonmagnetic probe–sample interactions as a function of lift height. These can then be subtracted from the signals obtained using magnetic cantilevers to delineate the magnetic versus topographic signals. By using well-calibrated magnetic cantilevers, it is also possible to ascertain, quantitatively, the sample magnetization (see Section 15.7). Alternatively, the sample magnetic properties may also be varied, especially for superparamagnetic or paramagnetic samples, by the use and manipulation of external magnetic fields. However, in these cases one would need to carefully understand if – and how – the magnetic properties of the magnetic force microscope would be affected by an application of the external magnetic fields. More specialized techniques, such as the application of a sinusoidal voltage to the magnetic force microscope tip or eddy-current MFM [35], have also been employed to distinguish between topography and magnetic signals.

15.6 MFM Cantilevers and Probes

As in AFM imaging, the mechanical characteristics of the cantilever and magnetic properties of the probe have a large impact on the tip–sample interaction, and play an important role in contrast formation due to the long-range nature of magnetic forces. As described above, the cantilever properties important for the magnetic force microscope are its quality factor Q, resonance frequency, and the spring constant, which can be determined experimentally using the thermal tuning or other methods [36, 37], often available on modern AFM instruments. The ideal MFM probe would consist of the minimum probe size, but have sufficient m_t to detect tip–sample magnetic interactions. Magnetic force microscope probes have evolved from simple wire apexes to commercially available thin-film-coated silicon probes. Highly specialized probes, achieved by focused ion beam (FIB) milling or attaching fullerene carbon multiwalled nanotubes to microfabricated Si cantilever tips, have improved MFM resolution to less than 20 nm. The batch fabrication and calibration of such advanced magnetic force microscope probes, however, are not within easy reach.

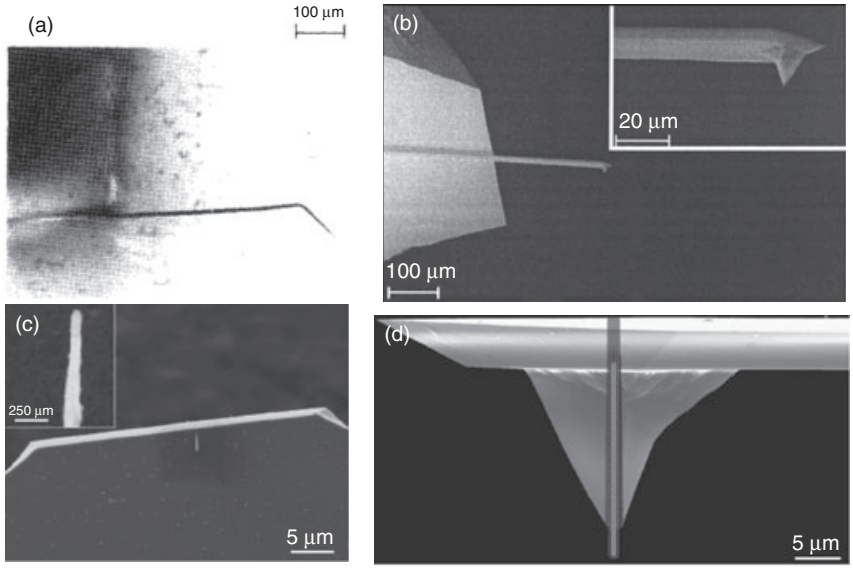

Figure 15.3 Evolution of magnetic force microscope probes. (a) Optical micrograph of a Ni cantilever/probe used in early magnetic force microscopes [38] ; (b) Electron microscope image of a modern MESP-type magnetic force microscope tip, displaying the small flexible cantilever of about 200 mm length and the actual tip, which is shown further magnified within the upper-right section [39]; (c) SEM image of a single as-grown carbon-nano-cap (CNC) probe on a tipless cantilever. Inset: high-magnification SEM image of the CNC tip [40]; (d) SEM image of a cross-section of a conical hole produced by focused ion beam milling with a nanotube attached inside the hole [41]. Reproduced with permission from Refs [38–41], as indicated.

15.6.1
Wire Probes

The early magnetic force microscope probes were composed of solid metallic wires with tapered ends (Figure 15.3a) [38]. For MFM studies in ambient air, Ni wires have been preferred as Fe wires can become oxidized. Such tips yield a larger tip-volume and hence a larger tip magnetic moment m_t; this in turn will result in a larger tip–sample interaction signal, but compromise on spatial resolution. Furthermore, each probe must be calibrated individually, and the reproducibility of an identical probe is difficult.

15.6.2
Thin-Film-Coated Si Probes

Due to the widespread use of AFM, cantilevers with integrated sharp tips are fabricated today in large numbers from silicon-based materials. A typical magnetic

force microscope probe consists of a micromechanical cantilever with a conical or pyramidal tip at its end (Figure 15.3b) [39]. These probes, with a well-defined physical geometry, resonance frequency and *Q*-factor, are then coated with a thin (typically 60–100 nm) layer of magnetic material for the purpose of MFM observations. The probes are then magnetized by use of an external magnetic field. Integrated magnetic force microscope tips have a much lower stray field arising from the tip (H_z) as compared to wire tips, because of their smaller magnetic volume (confined to the tip apex) leading to less total magnetic moment. Although this small stray field is advantageous in MFM applications, the force gradient sensitivity ($^2H_z/\partial z^2$) of the integrated magnetic force microscope tips is slightly lower than that of wire tips. Thin-film tips offer the flexibility of tailoring their magnetic properties by changing the probe and cantilever geometry, thickness, and/or the magnetic material used for coating. The saturation magnetization and coercivity of the material used for tip-coating influences the ultimate magnetic properties of the magnetic force microscope probe. The different types of magnetic coating for probes have been recently reviewed by Yacoot *et al*. [7]; these include coating with conventional high-coercivity materials such as CoCr and CoPtCr, or low-coercivity ferromagnetic materials such as Co, NiFe, or iron. Other nonconventional coatings include superparamagnetic granular Fe(SiO_2) films, diamagnetic platinum, and antiferromagnetic (CoCrPt/Ru/CoCrPt) or multilayer coatings of ferromagnetic materials [7].

15.6.3 FIB Probes

Focused ion beam (FIB) milled probes can be produced from conventional probes consisting of a standard cantilever with a probe coated with a 50–100 nm-thick magnetic film. The cantilever is transferred into a scanning electron microscope and the electron beam is focused onto the tip apex. Due to cracking of the residual hydrocarbons by the electron beam, a tiny carbon probe is deposited right at the tip apex. This carbon tip is then used as an etch mask during the ArC iron milling of the probe. The etching time and ion flux are adjusted such that the exposed magnetic material is completely removed from the probe while the carbon tip is not completely etched away. This prevents the magnetic coating underneath the carbon tip from being attacked. The result of the whole procedure is a cantilever that exposes a tiny magnetic particle at the probe's apex, rather than the complete magnetic coating [42]. The lower limit for the dimension of magnetic particle arises as an ultra-small particle becomes superparamagnetic.

Occasionally, a high-aspect ratio magnetic structure is fabricated onto a non-magnetic tip to result in what is known as a "monopole magnetic tip". For instance, instead of coating the probe with a thin magnetic film, a high-moment magnetic particle may be attached directly to the cantilever tip (or to a tipless cantilever). Typically, this is achieved by gluing a magnetic material onto the atomic force microscope probe, and then etching off the excess material by FIB milling. Fer-

romagnetic particles (NdFeB) attached to commercial cantilevers [43] offer the strongest sensitivity, as these particles have both a high magnetization and high coercivity values. The magnetic field emanating from the particle on the magnetic force microscope probe can therefore be very strong (>400 G m^{-1}). These tips have an advantage in imaging paramagnetic particles, as they can have a high force sensitivity of the detection cantilever and can maximize the magnetic force between the tip and the sample. However, the physical dimensions of these probes are generally several hundreds of nanometers, which limits their spatial resolution. FIB-milled probes are generally difficult to replicate identically, and/or to mass produce.

15.6.4 CNT Probes

Carbon nanocone (CNC) [40] tips (Figure 15.3c) or carbon nanotube (CNT) [41] probes (Figure 15.3d) offer a higher resolution because the magnetic material on the CNT probe (Figure 15.3d) is contained within a narrow cylinder, in contrast to standard pyramidal probes [44]. The smaller volume of magnetic material that contributes to the signal results in a higher spatial resolution (<20 nm). The sharper tip radius of the CNT also allows a better topographic scan, which yields a more accurate height profile for the tip to follow. CNT probes are less invasive than commercially available probes, because a smaller amount of magnetic material is brought into close proximity with the sample. Finally, the magnetic material is distributed on the probe along an easy-to-model straight cylinder, a feature which may help in more quantitative MFM studies. For studying MFM in biological samples which usually have low coercivity, CNT MFM probes offer a useful alternative.

15.7 Probe Calibration

Although the physical dimensions of the probe can be ascertained using scanning electron microscopy (SEM), the characterization and calibration of its magnetic properties requires special considerations. These include the tip hysteresis loop and coercivity, as well as the magnetization distribution of the tip. In particular for the latter, one does not know how this differs from tip to tip, and how much magnetic material of the tip-coating is used in the imaging process, even when considering the simplest possible homogeneous magnetization distribution of the tip. Sophisticated techniques such as electron holography [45] or vibrating cantilever magnetometry [44] have been used to characterize the magnetic force microscope tips through both theoretical and analytical models. Use of the magnetic force microscope as a microscopic magnetometer to calibrate the tips remains the most popular method. A quick method of verifying (qualitatively) the tips is to image magnetic tapes. These samples usually have a longitudinal magnetic

recording – that is, the magnetization is parallel to the sample surface. In MFM images, the magnetic transitions appear as dark or bright stripes corresponding to attractive or repulsive phase gradients (Figure 15.2). However, a quantitative characterization of the magnetic force microscope probe is especially desirable when there is a need to ascertain the magnetic properties of the sample.

15.7.1 Quantitative Calibration of the Magnetic Force Microscope Probe

Several calibration functions have been defined using the magnetic force microscope, with differences in variables such as probe properties, measurement mode, stray-field geometry, and so on. Among the theoretical models, we [2] and others [46] have developed a model for the spatial distribution of a magnetic force microscope tip. Transfer-function approaches have also been used to calculate the force on a tip exerted by a sample with perpendicular magnetization [47, 48]. In numerous experimental studies, the rather simple point probe model [49] has proven to be quite successful in the understanding of MFM image formation. The point–probe approximation idealizes a more or less complicated tip magnetization distribution by either an effective magnetic dipole moment **m**, or a magnetic monopole moment **q**, located at an imaginary position δ from the apex of the atomic force microscope tip (Figure 15.4) [39]. For an oscillating cantilever, the phase shift $\Delta\Phi$ is proportional to the force gradient acting on the tip (Equation 15.6), which results from the first and second derivatives of the magnetic field felt by the tip (Equations 15.7 and 15.9). Based on experimental validation by SQUID [50], in almost all models of tip calibration, it is considered that the easy axis of magnetization of the magnetic coating lies within the plane of the coating. Thus, for a pyramidal-shaped tip, the tip primarily has a magnetization in the z-direction with only a small (10%) y-component, resulting in $m_x = m_y = 0$ and [39]:

$$\Delta\Phi = \mu_0 \frac{Q}{k}\left[-q\frac{\partial H_z}{\partial z} + m_z \frac{\partial^2 H_z}{\partial H^2}\right] \tag{15.17}$$

which can be used to determine the tip dipole moment q or the monopole moment m_z from experimentally measured phase shifts, once the analytical expression for the stray field of the calibration sample are known. For a phase shift measured in degrees:

$$\Delta\Phi_{dipole} = -\mu_0 \frac{180}{\pi}\frac{Q}{k}\left[m_z \frac{\partial^2 H_z}{\partial z^2}\right] \tag{15.18}$$

and

$$\Delta\Phi_{monopole} = -\mu_0 \frac{180}{\pi}\frac{Q}{k}\left[-q\frac{\partial H_z}{\partial z}\right] \tag{15.19}$$

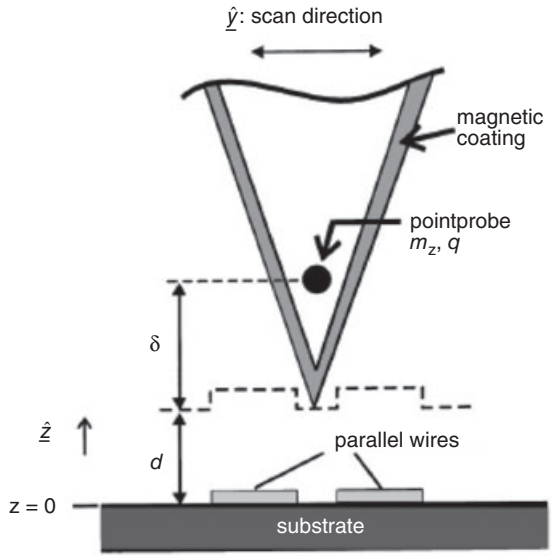

Figure 15.4 Calibration of magnetic force microscope tip using the point-probe model [39]. Schematic representation of the cross-section of a set of parallel wires and a magnetic force microscope tip, which is located above the parallel wires. The tip is idealized within the point-probe approximation by an imaginary point-dipole with dipole moment **m**, or by an imaginary point-monopole with monopole-moment **q**, where the point probe is located at some position within the real tip at a distance *d* measured from the tip apex or, respectively, at a position $z = d + \delta$ measured from the substrate plane. *d* is the experimentally controllable tip lift-height. Reproduced with permission from Ref. [39].

By treating the magnetic force microscope tip as a point probe, the analysis of the image contrast as a function of both the magnetic field strength and the tip lift-height allows one to quantitatively determine the effective magnetic dipole and monopole moments of the tip, as well as their imaginary locations within the real physical tip. The fit to experimental data is expected to lead to identical results with either the monopole or the dipole description of the tip [39]. For commercially available tips arising from the same wafer, the values for m_z, q, δm or δq have been found to deviate by approximately 20% from average values [39].

15.7.2 Calibration Samples

The use of a calibrated magnetic force microscope tip for sample magnetometry is often restricted to samples which have the same stray field geometry as the calibration sample. Samples with various stray field geometries such as hard disk transitions, current strips, current rings and magnetotactic bacteria, have been used to characterize tips (for a review, see Ref. [39]). Kebe and Carl [39] used

various geometrical configurations of current-carrying parallel wires to analyze the resulting magnetic contrast by MFM at various lift-heights. This calibration produces detailed information, such as the magnetization loop of the tip and its coercivity. Gomez *et al.* [51] demonstrated a method that yielded a quantitative value of the magnetic moment of the tip using a combination of electrostatic and magnetic forces between the tip and a current-carrying conductor.

For MNP studies, it is desirable to calibrate the magnetic force microscope tips with a stray field geometry similar to that of MNPs, such as are found in current-carrying rings or artificially patterned hard magnetic films [52] or permalloy dots [53]. Both, current-carrying rings and single-domain dots of radius R, have been found to reveal the same characteristic decay length ξ of the magnetic field in z-direction; that is, $\xi = R$ is valid and results in the calibration [53]:

$$m_z = 1.7 \times 10^{-2} \cdot R^2 \tag{15.20}$$

$$\text{and} \quad \delta = 7.65 \times 10^{-1} \cdot R \tag{15.21}$$

Finally, it is also possible to characterize the response of the tip in the presence of an external magnetic field. Babcock *et al.* [54] used a current strip in conjunction with an applied field to measure the hysteretic properties of a series of magnetic force microscope tips. Such an approach may be especially desirable when analyzing superparamagnetic samples (such as MNPs) by MFM, where an external magnetic field is required to induce sample magnetization.

15.8 Resolution in MFM

The spatial resolution in MFM is related to both the magnetized part of the probe, which is exposed to the sample stray field, and to the probe–sample distance. In order to improve the resolution, it is necessary to decrease the magnetically sensitive part of the probe to the smallest possible size and geometry, and to operate the probe in close proximity to the sample surface.

15.8.1 Lateral Resolution

The lateral resolution in MFM can be characterized by either its "point response" in real space or by its spatial frequency response in Fourier space. Various simulation approaches using point spread functions have confirmed that the cylindrical tip with a spheroidal tip-end having a large ellipticity is ideal for high-resolution MFM imaging [55]. Further lower tip-heights are preferred, as the effective tip volume will be increased by lowering the tip [39]. It is also important to consider the single- versus multidomain magnetic nature of the magnetic force microscope

tip. Ideally, the tip should consist of a single-domain magnetic particle/layer with a high magnetic moment. The presence of multiple domains can lead to fine structures in MFM traces which can make image interpretation more complex. The resolution in MFM is also dependent on the spatial confinement of the sample stray field. The theoretical limit for MFM resolution in ambient air is 5–10 nm; however, experimentally in recent years a resolution of only 20–30 nm has been achieved. Further improvement in MFM resolution can only be made by exploiting the short-range magnetic exchange forces, as is used in the MRFM technique.

15.8.2
Vertical Resolution

The vertical resolution in MFM is dependent on the tip–sample interaction force (F or F'), the tip–sample distance (z), and the signal-to-noise ratio. The decay of long-range interactions such as magnetic forces can be estimated using an exponential approximation [56], where:

$$F'(z) \propto e^{(-z/\Lambda)} \tag{15.22}$$

where Λ is the decay length of the interaction, and can be estimated using Equation 15.11 and the force sensitivity of the magnetic force microscope. For a change in δz in the tip position, $F'(z)$ will change to $F'(z + \delta z)$, resulting in:

$$\delta z = \Lambda \ln\left(\frac{1}{1-s}\right) \tag{15.23}$$

where $s = F'_{\min}/F'(z)$. Therefore, a high vertical resolution (low δz) in MFM will depend on the decay length of the magnetic interaction and the force sensitivity of the magnetic force microscope.

15.9
MFM for Magnetic Nanoparticles

MFM has proved to be a useful technique to localize and characterize macroscale magnetic domains in materials and, more recently, also for ferromagnetic nanoparticles. A number of studies have been reported on the MFM imaging and analysis of nanoscale magnetic materials of diameters ranging from few tens of nanometers to millimeter and of thicknesses less than 50 nm (Table 15.2). The magnetic materials studied range from ferromagnetics such as Co and iron dots [57–63], to superparamagnetic nanoparticles [2, 28] or MNPs isolated from biological systems [46, 64]. Whilst MFM can reliably detect the presence of nanoscale magnetic domains, it capability to quantitatively analyze a particle's magnetic moment and agglomeration status remains to be determined.

Table 15.2 Dynamic mode MFM studies in ambient air performed on magnetic nanomaterials.

Sample type	Sample dimensions	Reference
Ferromagnetics		
Permalloy dots	1 mm diameter with 50 nm thickness	[57]
$La_{0.7}Sr_{0.3}MnO_3$ (LSMO) grown on $SrTiO_3$ surfaces	500 nm diameter patterned islands	[58]
γ-Fe_2O_3 particles	Prolate ellipsoids, 300 nm × 65 nm	[59]
Co dots	140 × 250 nm laterally with 7 nm thickness	[60]
Fe dots	40–120 nm in diameter, with 40 nm thickness	[61]
α-MnAs quantum dots	Single-domain ferromagnets ~50 nm in diameter	[62]
ε-Co	12 nm particles	[63]
Superparamagnetic/ biological MNPs		
MNPs from bacteria	Chain of 10 particles, each 70 nm in size	[64]
Magnetostatic bacteria	17.5 nm in diameter with 50 nm thickness	[46]
EPR spin probe	Prolate ellipsoids, 1 μm × 100 nm	[28]
Iron oxide particles	10 nm iron-oxide cores, surrounded by dextran matrix	[2]

EPR = electron paramagnetic resonance.

15.9.1 Ferromagnetic Nanoparticles

MFM has been used to study the domain structure of 500 nm islands of $La_{0.7}Sr_{0.3}MnO_3$ (LSMO) grown on $SrTiO_3$ surfaces [58]. For structures with in-plane magnetization, these stray fields emanate from the domain walls, instead of the domains themselves. MFM images demonstrate that, for LSMO islands on (110)-oriented $SrTiO_3$ substrates, the domain pattern varies depending on the shape of the island (Figure 15.5A). Calculations based on the magnetostatic energy, the anisotropy energy, and the domain wall energy, support these findings and predict that for diameters >50 nm the flux closure or vortex domain is the energeti-

cally favorable configuration for all shapes studied. Thus, MFM has been used to show how ferromagnetic domain patterns can be controlled by varying the shape and size of the islands, the film thickness, and the relative magnitudes of the magnetocrystalline and magnetoelastic energies.

In another study, individual ferromagnetic quantum dots (QDs) of α-MnAs which were approximately 50 nm in size have been imaged using MFM in ambient air [62]. The MFM studies revealed that a magnetic field as low as 60 Oe could switch the polarization of the magnetic domain in these dots (Figure 15.5B). Low-moment, Co-coated magnetic force microscope probes were used for this study so as to minimize perturbation of the sample by the magnetic field of the tip. The analysis of the MFM signal, along with electron microscopy studies, could be utilized to ascertain that the remanant magnetization of the QD was perpendicular to its NW [0001] growth axis. Additionally, variable-temperature MFM studies were conducted to analyze the temperature dependence of the α-MnAs QDs and to establish the Curie temperature T_c of the QDs (Figure 15.5C). The MFM images were acquired at temperature increments of 5 K. While the magnetic contrast in the MFM images remained constant up to 308 K, it disappeared abruptly at 313 K and remained absent at higher temperatures. Upon returning the sample temperature to room temperature, the magnetic contrast reappeared. The T_c determined using these MFM studies was between 308 to 313 K, which is very close to the T_c of bulk α-MnAs at 318 K.

One of the smallest particles analyzed using MFM has been the 12 nm ε-cobalt nanoparticles, by Puntes *et al*. [63]. These authors compared the absolute value of the average magnetic moment as a function of particle density by using high-magnetic moment (thicker CoCr coating) magnetic force microscope tips and samples consisting of noninteracting monodisperse particles or small particle agglomerates (Figure 15.5D). In these samples, the individual particles are not resolved and the agglomerates behave as single dipoles. As expected for single dipoles, the magnetic signal consists of two blobs of opposite sign, localized at the extremities, and with no magnetic structure in between. The agglomerates point roughly in the same direction, possibly because they are magnetized by the tip during the AFM scan. Initially, an increase in magnetic moment with particle density was observed, after which the magnetic signal started to decreasing as the dipolar interactions brought the magnetic dipoles in-plane. A change in the slope indicated the concentration when the dipolar interaction between particles began to compete successfully with the tip interaction. It is understood that in disordered systems, such as an agglomeration of nanoparticles, dipolar interactions would tend to reduce the coercivity [59].

15.9.2
Superparamagnetic or Paramagnetic Nanoparticles

One of the key challenges in detecting superparamagnetic particles by MFM is that these particles will possess a magnetic moment only in the presence of a magnetic field. Another factor to consider when studying MNPs is that, in most

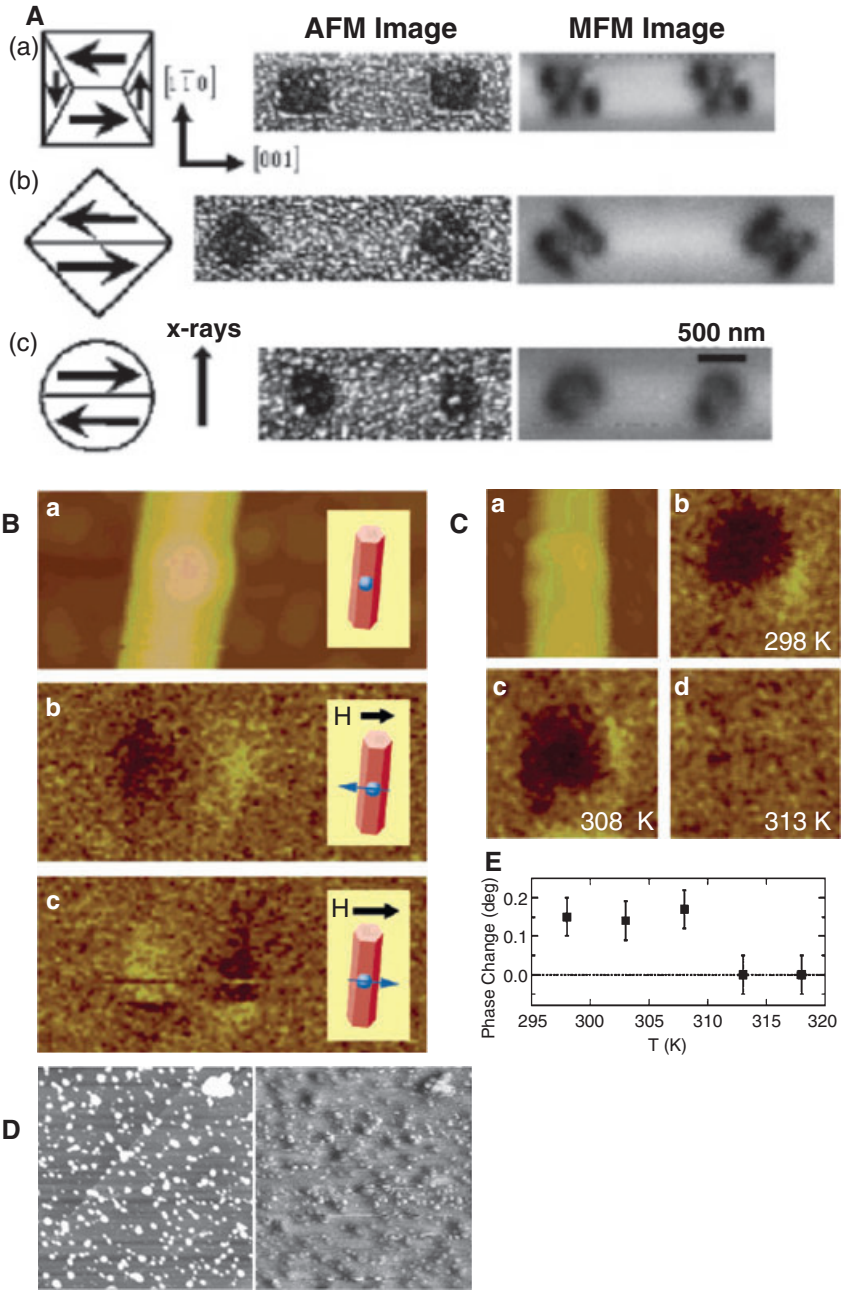
A
(a)
AFM Image
MFM Image
[1 $\bar{1}$ 0]
[001]
(b)
x-rays
(c)
500 nm
B
a
b
H
c
H
C
a
b
298 K
c
308 K
d
313 K
E
Phase Change (deg)
0.2
0.1
0.0
295
300
305
310
315
320
T (K)
D

cases, the MNPs are soft magnetic materials – namely, that they have low remanent magnetization and low coercivity. As a result, the tip or sample stray fields (H_T or H_S) may be mutually affected if the stray field exceeds the anisotropy fields (H_K). For nondestructive MFM imaging [27]:

$$H_T < H_K^S \quad \text{and} \quad H_S < H_K^T$$

One way to minimize this effect is to use a large tip–sample separation distance (though this may limit lateral resolution) and a careful selection of the magnetic force microscope probe.

In recent studies [2, 28], we have demonstrated the feasibility of detecting superparamagnetic MNPs via the MFM technique in ambient air. The SQUID studies confirmed the superparamagnetic nature of the MNPs, and revealed that an external magnetic field of a few tens of milliTesla is sufficient to induce a stable magnetic dipole in MNPs, even at room temperature [2]. As a result, a perpendicular or in-plane magnetic field of this magnitude range was applied to the sample at room temperature to induce a stable magnetic moment in MNPs. The MFM experiments revealed that the presence of an external magnetic field and a magnetic probe was essential to detect and distinguish an MFM signal from MNPs. By applying a magnetic field perpendicular to the sample (Figure 15.6a), monopoles of MNPs were detected as a negative phase contrast dependent on lift-height, and by applying an in-plane magnetic field (Figure 15.6b) the in-plane dipole moment of MNPs was seen as a combination of a positive and negative phase contrast. It is interesting to note that some particles in the AFM images did not show any MFM phase contrast at all, suggesting that the particle composition in

Figure 15.5 MFM of ferromagnetic nanoparticles. (A) Schematic of the domain pattern, AFM image and MFM image of 500 nm-diameter islands on (110)-oriented STO substrates with (a) square, (b) diamond, and (c) circular shapes. The $La_{0.7}Sr_{0.3}MnO_3$ (LSMO) films have been aligned with the magnetically easy [001] direction pointing horizontally [58]; (B) Single QD (~50 nm) switching in an external magnetic field [62]. (a) Topography image; (b) MFM image of the MnAs QD in an applied field of 40 Oe that opposes the QD magnetization. Thus, the QD magnetization is stable at small opposing fields; (c) MFM image of the switched QD. The streaks in the image indicate that the stray field of the tip competes with the applied field, causing the QD to switch back for some tip–sample configurations. All images are $400 \times 185\,nm^2$ in size; (C) Variable-temperature MFM determination of the QD Curie temperature [62]. (a) Topography image of MnAs/InAs-QD/NW; (b–d) MFM phase images of the QD at the indicated temperatures, showing that the magnetic field-dependent phase contrast is approximately constant between 298 and 308 K, and the contrast disappears at 313 K; (e) The phase, which is approximately proportional to the magnetization, is plotted as a function of temperature. The phase drops abruptly to zero around the bulk Curie temperature of 313 K, consistent with a first-order phase transformation, as is seen in bulk MnAs. All images are $300 \times 300\,nm^2$ in size;. (D) Topography and magnetic structure of 12-nm Co nanoparticle islands [63]. (a) AFM and (b) MFM images of scan sizes $3 \times 3\,\mu m$. Vertical scales: 20 nm and 2° respectively. Reproduced with permission from Refs [58, 62, 63], as indicated.

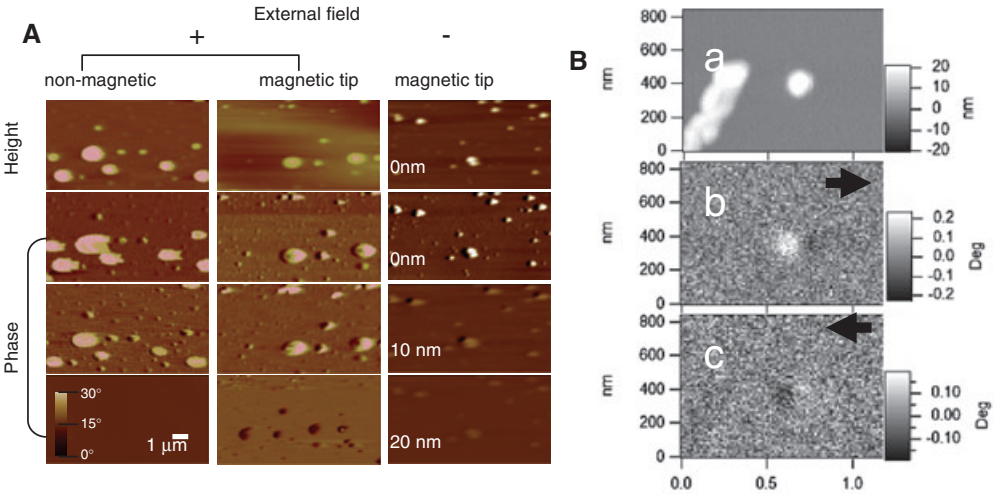

Figure 15.6 MFM of superparamagnetic nanoparticles [2]. (A) Tapping mode height (first row) and phase images (rows 2 to 4) of MNPs consisting of 10 nm iron oxide cores, obtained in lift-mode using a nonmagnetic or magnetic atomic force microscope probe with/without the presence of an externally applied vertical magnetic field, as indicated. In each series of images the amplitude of cantilever oscillations was kept constant for various lift-heights. The lift-height for each row of images is indicated at top left in column 3. The grayscale for phase values and scale bar for image size is shown as inset in bottom left, and applies to all panels; (b) MFM experiment on MNPs using an external, in-plane magnetic field; (B) A topographic AFM image of MNPs on mica; (b) MFM phase image when the same region was scanned using a horizontal field. Note the location of a bright phase contrast on the left and a dark phase on the right of each particle; (c) When the direction of the external field is reversed, the phase contrast also reverses. The nonmagnetic contaminant in the lower left corner shows no magnetic contrast. Reproduced with permission from Ref. [2].

these cases may be partially or completely nonmagnetic in nature. This is explicable, as the MNPs used in this study are known to be coated with a dextran matrix, which is nonmagnetic in nature. Some of the particulate material on the samples might have arisen from the disintegrated dextran matrix.

An analysis of the phase shifts for the MFM data (Figure 15.7) revealed that the probe–sample interaction follows the interaction of single-domain magnetic particle(s) with a magnetic force microscope probe magnet, as defined in Equation 15.11. By using this equation, the magnetic moment of the MNPs analyzed in the MFM experiments was estimated at $3.7 \times 10^{-17}\,\mathrm{Am}^2$, which suggested that the observed MFM signals were arising from an agglomerate of approximately 150 individual MNPs each 10 nm in diameter. It is interesting to note that electron microscopy imaging of MNP samples prepared in a similar manner as for AFM, revealed that the majority of MNPs were clusters of several tens of 10 nm iron oxide cores. The numerical simulations further (Figure 15.8) confirmed that superparamagnetic iron oxide particles of sizes >20 nm are readily detectable using

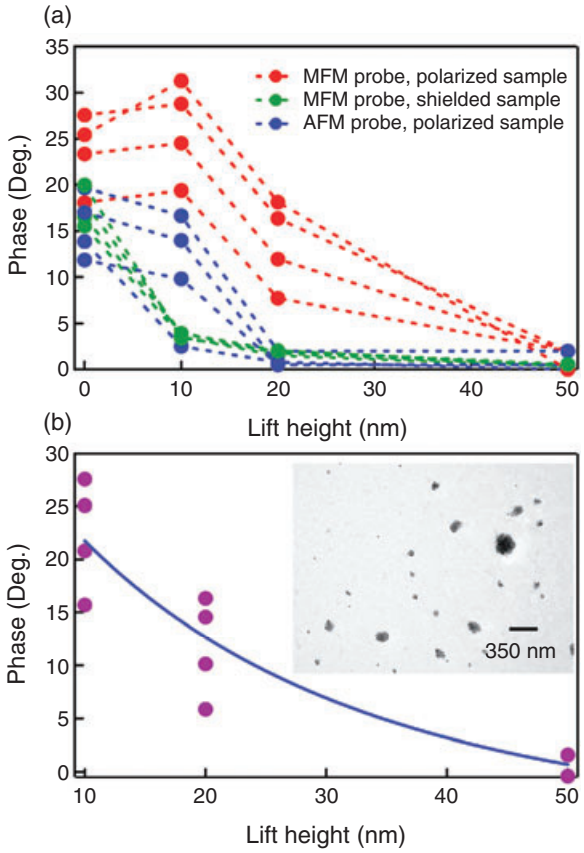

Figure 15.7 Quantitative analysis of MFM data [2]. Phase-shift values obtained in MFM experiments on MNPs as described in Figure 15.6. (a) Phase shift versus lift-height values for the three experimental conditions, as indicated. The strength of the probe–sample interaction (and therefore the phase shift) is largest when the magnetic force microscope probe interacts with polarized MNPs (kept in the presence of an external magnetic field). At lift heights ~20 nm, only the probe with polarized MNPs shows significant phase-contrast values, while interaction of the probe with unpolarized particles is similar to that of a nonmagnetic probe; (b) Plot of phase-shift data as a function of lift-height for the experiment with a magnetic force microscope probe and polarized MNPs (same as in panel a) of average height ~20.0 nm, corrected for phase shift due to background interaction obtained as an average phase shift observed at a given lift-height in the experiment with the magnetic force microscope probe on unpolarized particles. The fit of these data (solid line) using Equation 15.11 gives an effective magnetic moment of the particles studied as $m_s = 3.7 \times 10^{-17}\,Am^2$; (inset in (b)) A TEM image of MNP samples show that the majority of the particles are clusters or aggregates of several 10 nm iron oxide nanoparticles. Reproduced with permission from Ref. [2].

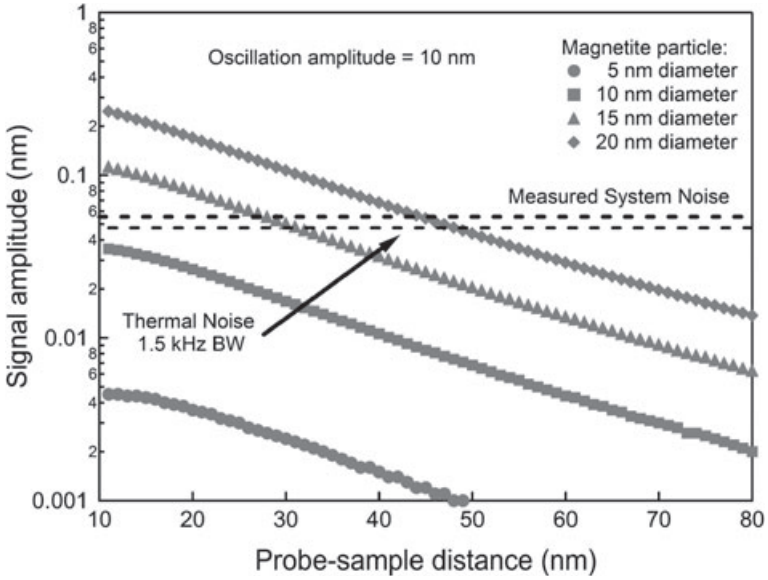

Figure 15.8 Estimation of force sensitivity of MFM [2]. Simulated amplitude shifts, δA (in nm), as a function of probe sample distance (lift-height, in nm) resulting from a magnetic probe interacting with four different-sized MNPs (5, 10, 15, and 20 nm diameter) when polarized in the presence of an external magnetic field. The flat lines indicate the noise floor (A_n) arising due to thermally induced cantilever oscillations for a bandwidth of 1.5 kHz or the experimental phase noise, as described by Equation 15.16. Reproduced with permission from Ref. [2].

MFM in ambient air with commercially available magnetic force microscope probes at lift-heights of 20–40 nm, while the force gradient falls below the thermal noise for particles of size <10 nm. However, particles of sizes 10 nm or less may be detectable using MFM for cases when m_t or m_s are significantly higher. Other groups have carried out similar analyses, and reported that particles <15 nm in size may be below the detection limit of MFM in ambient air, when using commercially available thin-film probes [30]. In another report, MFM has been utilized to distinguish magnetic versus gold–nanoparticle conjugates to DNA strands [65]. Consistent with our results, in this study MFM was unable to show contrast for lift-heights greater than 30 nm in detecting MNPs in ambient air. Thus, under appropriate experimental conditions, the MFM technique can detect and identify the magnetic interaction of superparamagnetic MNPs with the magnetic force microscope probe in ambient air.

15.10
The Application of MFM in the Life Sciences

The magnetic particles that occur naturally in living systems are understood to be nanoscale paramagnetic or superparamagnetic particles, composed mostly of mag-

netite. A diverse range of particle sizes for magnetite have been reported in biological systems, from single particles of <50 nm to clumps of 50–100 nm, or larger particles between 200 and 600 nm [2]. The magnetic moment for a magnetotactic bacterium containing 22 magnetite particles, each 50 nm in diameter, was reported as 1.3×10^{-15} Am^2. This value is consistent with the material magnetite, which has a saturation magnetization of 4.8×10^5 A m^{-1} [66]. Bacterial magnetic particles are also reported to be single nanocrystals (50–100 nm) having a single magnetic domain, and exhibiting a ferrimagnetic character with excellent dispersion in aqueous solutions imparted by the lipid membrane covering them [67]. The magnetic deposits in mammalian tissue are more complex, consisting of a mixture of ferromagnetic, superparamagnetic, and paramagnetic particles. For instance, the human brain is estimated to contain at least 5×10^6 single-domain iron crystals per gram of tissue, in clumps of between 50 to 100 particles [68]. Understanding the particle size and magnetic nature of these nanocrystals requires specialized techniques that combine high spatial resolution with optimal force sensitivity.

A number of investigations using MFM have been conducted aimed at the qualitative detection of such particles in biological systems. These include the detection of iron compounds in neurological disorders [69], magnetic domains in magnetotactic bacteria [46], and iron deposits in hepatitis B-diseased livers [70]. The technique has also been used to detect endogenously occurring nanoscale magnetic domains present in trout tissues [71] (Figure 15.9). Limited studies have also been performed on localizing and detecting MNPs in cell-based systems, such as antisense oligonucleotide (ASO)-coupled silica-coated magnetic iron oxide nanoparticles (SMNPs) internalized into human leukemia (HL-60) cells [72]. Bacterial MNPs conjugated to biotin have also been used as magnetic markers for detecting bound streptavidin, using MFM, but without the application of external magnetic fields [73]. In this study, magnetic force microscope tips with lower coercivity in ambient air enabled the identification of monopoles, while higher-coercivity tips in a vacuum enabled the detection of magnetic dipoles in individual MNPs.

15.11 Limitations in MFM

A true quantitative interpretation of MFM images is still difficult, and may only be achieved in special cases after careful calibration of the magnetic force microscope tip and understanding the sample stray fields. The main weakness of this AFM-based technique is that the point at which motion is detected by the detection system is not the point that probes the surface. The length of the tip, which could be between 6 and 10 μm, and its movement, which includes rotation due to torsion and bending due to lateral forces as well as unknown change of the length by tip wear, is beyond our present measurement capabilities. It is important to point out that, at the present state of development, a typical commercial MFM instrument is capable of providing mostly qualitative information about the sample under investigation. The resulting image provides information about the existence of the

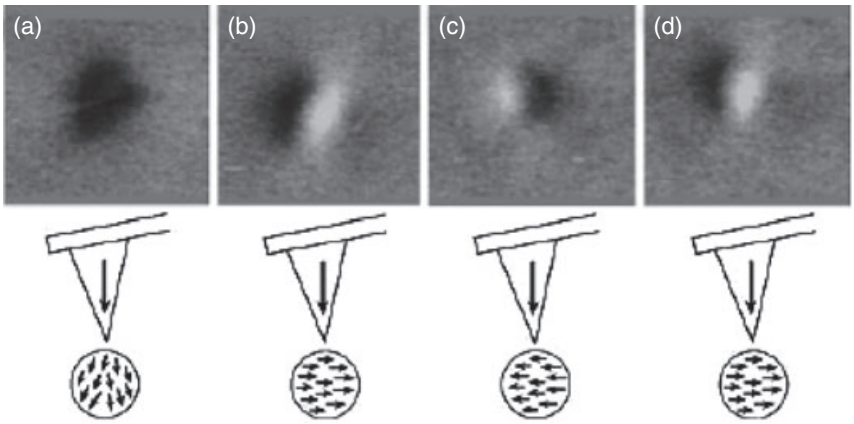

Figure 15.9 MFM of MNP in a biological system [71]. The MFM images show the response of a putative single magnetic particle (within trout tissue) in the presence of an applied field. The magnetic field applied in the plane of the sample was +1.4, +150, –150, and +130 mT for images (a) to (d), respectively. MFM images (75 nm squares) are shown above, with a representation of the magnetic force microscope tip and magnetization of the particle underneath. The tip (inverted triangle) is permanently magnetized with a coercivity of +500 mT at right-angles (arrow in inverted triangle) to the applied field. The small arrows within each circle under the tip represent the alignment of the individual magnetic dipole moments that might act as the field source. (a) The image shows a dark patch at the location of the particle, which indicates an attractive reaction between the tip and sample, consistent with the magnetic field from the magnetic force microscope tip weakly magnetizing the particle and causing an attractive interaction. (b–d) MFM images showing the near-dipolar responses of the magnetic particle under a strong applied magnetic field. These are consistent with an MFM image of a single-domain particle magnetized along the direction of the applied field. Note that the reversal of the field and dipolar response in (c) are consistent with the particle magnetization flipping in the reversed applied field. In images (b) to (d), the applied field was large enough to completely align the magnetic moment of the crystals within the field. Reproduced with permission from Ref. [71].

magnetic moments in the sample, but does not supply enough information for a convenient quantitative analysis of the data with the purpose of characterizing the magnetic properties of MNPs. The quantitative MFM analysis of MNPs forms an active area of current research by several groups.

15.12
Recent Developments in MFM

15.12.1
Non-Optical Methods for Cantilever Detection

Non-optical methods to detect the deflection of the cantilever are based on self-sensing capabilities of the cantilever, and do not require alignment and reflection

of a laser beam from the reverse side of the cantilever. This is a particularly attractive approach when the MFM instrument is operated in a vacuum environment, especially at low temperatures, where optical adjustments are difficult. Among the non-optical methods for MFM are piezoresistive cantilevers [74, 75], piezoelectric cantilevers [76, 77], and tuning fork-based cantilevers. In the latter case, a commercial magnetic cantilever tip can be attached to one prong of the tuning fork to realize shear-mode MFM operation [78]. While the resonance frequency of a tuning fork is similar to that of a cantilever, the quality factor Q and the spring constant k of a tuning fork are typically 102- and 104-fold larger than those of the cantilever, respectively. Hence, the force sensitivity of tuning fork-based MFM is less than that of cantilever-based MFM by a factor of 10. In another advancement, a scanning magnetoresistance microscope (SMRM) has been developed, that is equipped with a microfabricated cantilever on which a spin-valve (SV) -type MR sensor element is mounted [79]. These non-optical cantilevers lend themselves well to multiple cantilever applications. However, further challenges lie ahead with the need to servo control all of the cantilevers independently.

15.12.2
Application of External Magnetic Fields

When examining MNPs with MFM, innovative techniques must be selected and developed to apply external magnetic fields to the sample, while minimally affecting the magnetic moment of the magnetic force microscope probe. One configuration for application of magnetic field is by placing an electromagnet (e.g., a Helmholtz coil) very close to the sample. This technique can be used to apply fields of up to a few hundred Oe. Increasing the field beyond this value is known to heat the sample and cause drifts in the probe. Another technique for applying a higher magnetic field to the sample, without sample heating, relies on a rare-earth magnet mounted on a rotating cylinder [80]. In this case, flux from the magnet is shunted through either the sample or the cylinder faces, depending on the angular position of the rotating armature. In recent years, hardware accessories to enable the application of external magnetic fields have become available for commercial AFM instrumentation.

15.12.3
Technique Developments for MFM

High-frequency MFM (HF-MFM) is one of the most promising current developments in MFM. In this procedure, the cantilever is oscillated by the piezoelement *and* the HF magnetic field applied to the sample, leading to an overlap of the two oscillations. This technique ensures HF-MFM images also in situations where the standard amplitude modulation technique fails [81], and offers several parameters to increase the achieved HF-MFM signal strength. Moreover, recent model calculations [82] have shown that the HF-MFM technique indeed measures the emerging stray fields, and not the field gradients as in conventional MFM. The HF-MFM

technique has been used mainly to study hard disk write heads. By using supersharp tips, Koblishcka *et al.* [83], have shown that HF-MFM enables a higher resolution (20 nm) than standard MFM. As with conventional MFM, the selection of probe parameters such as thickness and the type of magnetic coating for HF-MFM requires special consideration [84, 85].

Other upcoming MFM techniques include magnetic exchange force microscopy, which has been proposed to achieve atomic resolution by revealing the arrangement of both surface atoms and their spins simultaneously, using an external magnetic field to align the magnetic polarization at the tip apex [86]. In recent advances, individual atoms have been chemically identified using AFM [87]. Another novel method proposes the combination of three-dimensional electron spin resonance imaging by magnetic resonance force microscopy (MRFM) and topographic imaging of the sample surface by surface force magnetometry [88]. Eddy current microscopy may also be developed to serve as another alternative for the high-resolution imaging of MNPs [89].

15.13 Summary and Future Perspectives

The scope for MFM lies in detecting the presence of magnetic particles and/or spatially localizing magnetic dipoles in naturally occurring superparamagnetic or ferromagnetic particles, especially when these are of nanoscale dimensions. In biological samples, it is likely that such magnetic nanoparticles occur in clusters or aggregates, are embedded in a biological matrix to different depths, and are surrounded by biomolecules of heterogeneous composition. The localization of such embedded nanoparticles would also involve a careful understanding of the "shielding" effect of the biological matrices. Even greater challenges lie in developing MFM for the detection of magnetic particles in fluids, as the damping forces on the cantilever are several-fold greater in a fluid environment. Nevertheless, the development and application of MFM for detecting superparamagnetic nanoparticles holds great promise in biology for several applications, including the study of biomagnetism, the use of MNPs for labeling cells and tissues, and for the detection of endogenous magnetic deposits in tissues. An ability to spatially localize magnetic plaques at nanometer resolution under ambient atmospheric conditions will provide a better understanding of the mechanism of nanoparticle and iron uptake by cells and tissues.

References

1 Hartmann, U. (1999) Magnetic force microscopy. *Annual Review of Materials Science*, **29**, 53–87.

2 Schreiber, S., Savla, M., Pelekhov, D.V., Iscru, D.F., Selcu, C., Hammel, P.C. and Agarwal, G. (2008) Magnetic force microscopy of superparamagnetic nanoparticles. *Small*, **4** (2), 270–8.

3 Martin, Y. and Wickramasinghe, H.K. (1987) Magnetic imaging by "force

microscopy" with 1000 A-ring resolution. *Applied Physics Letters*, **50**, 1455–7.
4 Saenz, J.J., Garcia, N., Grütter, P., Meyer, E., Heinzelmann, H., Wiesendanger, R., Rosenthaler, L., Hidber, H.R. and Güntherodt, H.G. (1987) Observation of magnetic forces by the atomic force microscope. *Journal of Applied Physics*, **62**, 4293–1496.
5 Fukuma, T., Kimura, M., Kobayashi, K., Kazumi, M. and Yamada, H. (2005) Development of low noise cantilever deflection sensor for multienvironment frequency-modulation atomic force microscopy. *Review of Scientific Instruments*, **76**, 126110–13.
6 Huang, Q.X., Fei, Y.T., Gond, S., Misumi, I., Sato, O., Keem, T. and Kurosawa, T. (2006) The interference effect in an optical beam deflection detection system of a dynamic mode AFM. *Measurement Science and Technology*, **17**, 1417–23.
7 Yacoot, A. and Koenders, L. (2008) Aspects of scanning force microscope probes and their effects on dimensional measurement. *Journal of Physics D: Applied Physics*, **41**, 103001–5.
8 Stipe, B.C., Mamin, H.J., Stowe, T.D., Kenny, T.W. and Rugar, D. (2001) Magnetic dissipation and fluctuations in individual nanomagnets measured by ultrasensitive cantilever magnetometry. *Physical Review Letters*, **86** (13), 2874–7.
9 de Lozanne, A. (2006) Application of magnetic force microscopy in nanomaterials characterization. *Microscopy Research and Technique*, **69** (7), 550–62.
10 Fritzsche, J., Moshchalkov, V.V., Eitel, H., Koelle, D., Kleiner, R. and Szymczak, R. (2006) Local observation of reverse-domain superconductivity in a superconductor-ferromagnet hybrid. *Physical Review Letters*, **96** (24), 247003–6.
11 Kirtley, J.R., Tsuei, C.C., Rupp, M., Sun, J.Z., Yu-Jahnes, L.S., Gupta, A., Ketchen, M.B., Moler, K.A. and Bhushan, M. (1996) Direct imaging of integer and half-integer Josephson vortices in high-Tc grain boundaries. *Physical Review Letters*, **76** (8), 1336–9.
12 Grossman, H., Myers, W., Vreeland, V., Bruehl, R., Alper, M., Bertozzi, C. and Clarke, J. (2004) Detection of bacteria in suspension by using a superconducting quantum interference device. *Proceedings of the National Academy of Sciences of the United States of America*, **101**, 129–34.
13 Dede, M., Urkmen, K., Giri en, O., Atabak, M., Oral, A., Farrer, I. and Ritchie, D. (2008) Scanning Hall probe microscopy (SHPM) using quartz crystal AFM feedback. *Journal of Nanoscience and Nanotechnology*, **2**, 619–22.
14 Vrba, J. and Robinson, S.E. (2002) SQUID sensor array configurations for magnetoencephalography applications. *Superconductor Science and Technology*, **15**, R51–89.
15 Lee, F., Lee, T., Pan, C., Huang, A. and Chau, L. (1998) Colocalization of iron and ceroid in human atherosclerotic lesions. *Atherosclerosis*, **138**, 281–8.
16 Zhou, J., Leuschner, C., Kumar, C., Hormes, J. and Soboyejo, W. (2006) Colocalization of iron and ceroid in human atherosclerotic lesions. *Biomaterials*, **9**, 2001–8.
17 Mahmoudi, M., Simchi, A., Imani, M., Milani, A.S. and Stroeve, P. (2008) Optimal design and characterization of superparamagnetic iron oxide nanoparticles coated with polyvinyl alcohol for targeted delivery and imaging. *The Journal of Physical Chemistry, B*, **112** (46), 14470–81.
18 Thomas, J.M., Simpson, E.T., Kasama, T. and Dunin-Borkowski, R.E. (2008) Electron holography for the study of magnetic nanomaterials. *Accounts of Chemical Research*, **41** (5), 665–74.
19 Locatelli, A., Mentes, T.O., Aballe, L., Mikhailov, A. and Kiskinova, M. (2006) Formation of regular surface-supported mesostructures with periodicity controlled by chemical reaction rate. *The Journal of Physical Chemistry B*, **110** (39), 19108–11.
20 Nitz, W.R. and Reimer, P. (1999) Contrast mechanisms in MR imaging. *European Radiology*, **9**, 1032–46.
21 Ruehm, S.G., Corot, C., Vogt, P., Kolb, S. and Debatin, J.F. (2001) Magnetic resonance imaging of atherosclerotic plaque with ultrasmall superparamagnetic particles of iron oxide in hyperlipidemic rabbits. *Circulation*, **103**, 415–22.
22 Wang, Y., Hussain, S. and Krestin, G. (2001) Superparamagnetic iron oxide contrast agents: physicochemical

characteristics and applications in MR imaging. *European Radiology*, **11** (11), 2319–31.
23 Langheinrich, A.C., Michniewicz, A., Sedding, D.G., Lai, B., Jorgensen, S.M., Bohle, R.M. and Ritman, E.L. (2007) Quantitative X-ray imaging of intraplaque hemorrhage in aortas of apoE(−/−)/LDL(−/−) double knockout mice. *Investigative Radiology*, **42** (5), 263–73.
24 Warburton, L. and Gillard, J. (2006) Functional imaging of carotid atheromatous plaques. *Journal of Neuroimaging*, **16** (4), 293–301.
25 Rugar, D., Budakian, R., Mamin, H.J. and Chui, B.W. (2004) Single spin detection by magnetic resonance force microscopy. *Nature*, **430**, 329–32.
26 Mamin, H.J., Poggio, M., Degen, C.L. and Rugar, D. (2007) Nuclear magnetic resonance imaging with 90-nm resolution. *Nature Nanotechnology*, **2** (5), 301–6.
27 Wiesendanger, R. and Guntherodt, H.J. (1992) *Scanning Tunneling Microscopy II, Springer Series in Surface Sciences*, Vol. **28**, Springer.
28 Savla, M., Pandian, R., Kuppusamy, P. and Agarwal, G. (2008) Magnetic force microscopy of an oxygen-sensing probe. *Israel Journal of Chemistry*, **48** (1), 33–8.
29 Albrecht, T.R., Grütter, R., Horne, D. and Rugar, D. (1991) Frequency modulation detection using high-Q cantilevers for enhanced force microscope sensitivity. *Journal of Applied Physics*, **69**, 668–73.
30 Rasa, M., Kuipers, B.W.M. and Philipse, A.P. (2002) Atomic force microscopy and magnetic force microscopy study of model colloids. *Journal of Colloid and Interface Science*, **250**, 303–15.
31 Butt, H.J. and Jaschke, M. (1995) Calculation of thermal noise in atomic force microscopy. *Nanotechnology*, **6**, 1–7.
32 Stark, R.W., Drobek, T. and Heckl, W.M. (2001) Thermomechanical noise of a free V-shaped cantilever for atomic force microscopy. *Ultramicroscopy*, **86**, 207–15.
33 Giessibl, F.J. (2003) Advances in atomic force microscopy. *Reviews of Modern Physics*, **75**, 949–83.
34 Giessibl, F.J. (2002) *Principles of Non Contact Atomic Force Microscopy* (eds S. Morita *et al.*), Springer, Berlin, pp. 11–46.
35 Hoffmann, B., Houbertz, R. and Hartmann, U. (1998) Eddy current microscopy. *Applied Physics A: Materials Science and Processing*, **66**, S409.
36 Burnham, N., Chen, X., Hodges, C.S., Matei, G.A., Thoreson, E.J., Roberts, C.J., Davies, M.C. and Tendler, S.J.B. (2003) Comparison of calibration methods for AFM cantilevers. *Nanotechnology*, **14**, 1–6.
37 Clifford, C.A. and Seah, M.P. (2005) The determination of atomic force microscope cantilever spring constants via dimensional methods for nanomechanical analysis. *Nanotechnology*, **16**, 1666–80.
38 Rugar, D., Mamin, H.J., Guethner, P., Lambert, S.E., Stern, J.E., McFadyen, I. and Yogi, T. (1990) Magnetic force microscopy: general principles and application to longitudinal recording media. *Journal of Applied Physics*, **68** (3), 1169–73.
39 Kebe, T. and Carl, A. (2004) Calibration of magnetic force microscopy tips by using nanoscale current-carrying parallel wires. *Applied Physics Reviews*, **95** (3), 775–92.
40 Chen, C., Chen, H.L., Gapin, A., Jin, S., Yuan, L. and Liou, H.S. (2008) Iron–platinum-coated carbon nanocone probes on tipless cantilevers for high resolution magnetic force imaging. *Nanotechnology*, **19** (7), 075501.
41 Winkler, A., Mühl, T., Menzel, S., Kozhuharova-Koseva, R., Hampel, S., Leonhardt, A. and Büchner, B. (2006) Magnetic force microscopy sensors using iron-filled carbon nanotubes. *Journal of Applied Physics*, **99**, 104905–5.
42 Phillips, G.N., Siekman, M., Abelmann, L. and Lodder, J.C. (2002) High resolution magnetic force microscopy using focused ion beam modified tips. *Applied Physics Letters*, **81**, 865–7.
43 Fong, K.C., Lee, I.H., Banerjee, P., Che, Y., Obukhov, Yu., Pelekhov, D.V. and Hammel, P.C. (2006) Using high coercivity magnet particle for high sensitivity magnetic resonance force microscopy (abstract). Meeting of The American Physical Society, March, 2006.
44 Stipe, B.C., Mamin, H.J., Stowe, T.D., Kenny, T.W. and Rugar, D. (2001)

Magnetic dissipation and fluctuations in individual nanomagnets measured by ultrasensitive cantilever magnetometry. *Physical Review Letters*, **86**, 2874–7.

45 Matteucci, G., Frost, B.G. and Medina, F.F. (2004) Study of the field around magnetic force microscopy probes using electron holography. *Ultramicroscopy*, **99** (2–3), 95–102.

46 Proksch, R.B., Schäffer, T.E., Moskowitz, B.M., Dahlberg, E.D., Bazylinski, D.A. and Frankel, R.B. (1995) Magnetic force microscopy of the submicron magnetic assembly in a magnetotactic bacterium. *Applied Physics Letters*, **66**, 2582–4.

47 Hans, J.H., Stiefel, B., van Schendel, P., Moser, A., Hofer, R., Martin, S., Güntherodt, H.J., Porthun, S. *et al.* (1998) Quantitative magnetic force microscopy on perpendicularly magnetized samples. *Journal of Applied Physics*, **83**, 5609–20.

48 van Schendel, P.J.A., Hug, H.J., Stiefel, B., Martin, S. and Güntherodt, H.J. (2000) A method for the calibration of magnetic force microscopy tips. *Journal of Applied Physics*, **88**, 435–45.

49 Hartmann, U. (1989) The point dipole approximation in magnetic force microscopy. *Physics Letters. A*, **137**, 475–8.

50 Lohau, C.J., Kirsch, S. and Wassermann, E.F. (2001) Magnetization reversal and coercivity of magnetic-force microscopy tips. *Journal of Applied Physics*, **89**, 6098–104.

51 Gomez, R.D., Pak, A.O., Anderson, A.J., Burke, E.R., Leyendecker, A.J. and Mayergoyz, I.D. (1998) Quantification of magnetic force microscopy images using combined electrostatic and magnetostatic imaging. *Journal of Applied Physics*, **83**, 6226–8.

52 Dreyer, S., Norpoth, J., Jooss, C., Sievers, S., Neu, V. and Johansen, T. (2007) Quantitative imaging of stray fields and magnetization distributions in hard magnetic element arrays. *Journal of Applied Physics*, **101**, 083905–5.

53 Hehn, M., Ounadjela, K., Bucher, J.P., Rousseaux, F., Decanini, D., Bartenlian, B. and Chappert, C. (1996) Nanoscale magnetic domains in mesoscopic magnets. *Science*, **272** (5269), 1782–5.

54 Babcock, K.L., Elings, V.B., Shi, J., Awschalom, D.D. and Dugas, M. (1996) Field dependence of microscopic probes in magnetic force microscopy. *Applied Physics Letters*, **69**, 705–7.

55 Saito, H., Rheem, Y.W. and Ishio, S. (2005) Simulation of high-resolution MFM tips for high-density magnetic recording media with low bit aspect ratio. *Journal of Magnetism and Magnetic Materials*, **287**, 102–6.

56 Morita, S. (2002) *Introduction in Noncontact Atomic Force Microscopy* (eds S. Morita *et al.*), Springer, Berlin, pp. 1–10.

57 Shinjo, T., Okuno, T., Hassdorf, R., Shigeto, K. and Ono, T. (2000) Magnetic vortex core observation in circular dots of permalloy. *Science*, **289** (5481), 930–2.

58 Takamura, Y., Chopdekar, R.V., Scholl, A., Doran, A., Liddle, A.J., Harteneck, B. and Suzuki, Y. (2006) Tuning magnetic domain structure in nanoscale $La_{0.7}Sr_{0.3}MnO_3$ islands. *Nano Letters*, **6** (6), 1287–91.

59 Lederman, M., Fredkin, D.R., O'Barr, R., Schultz, S. and Ozaki, M. (1994) Measurement of thermal switching of the magnetization of single domain particles (invited). *Journal of Applied Physics*, **75**, 6217–22.

60 Kleiber, M. *et al.* (1998) Magnetization switching of submicrometer Co dots induced by a magnetic force microscope tip. *Physical Review B*, **58**, 5563–7.

61 Gider, S., Shi, J., Awschalom, D.D., Hopkins, P.F., Campman, K.L., Gossard, A.C., Kent, A.D. and von Molnár, S. (1996) Imaging and magnetometry of switching in nanometer-scale iron particles. *Applied Physics Letters*, **69**, 3269–71.

62 Ramlan, D.G., May, S.J., Zheng, J.G., Allen, J.E., Wessels, B.W. and Lauhon, L.J. (2006) Ferromagnetic self-assembled quantum dots on semiconductor nanowires. *Nano Letters*, **6**, 50–4.

63 Puntes, V.S., Gorostiza, P., Aruguete, D.M., Bastus, N.G. and Alivisatos, A.P. (2004) Collective behaviour in two-dimensional cobalt nanoparticle assemblies observed by magnetic force microscopy. *Nature Materials*, **3**, 263–8.

64 Suzuki, H., Tanaka, T., Sasaki, T., Nakamura, N., Matsunaga, T. and Mashiko, S. (1998) High-resolution magnetic force microscope images of a magnetic particle chain extracted from magnetic bacteria AMB-1. *Japanese Journal of Applied Physics*, **37**, 1343–5.

65 Kinsella, J.M. and Ivanisevic, A. (2008) Fabrication of ordered metallic and magnetic heterostructured DNA-Nanoparticle hybrids. *Colloids and Surfaces B: Biointerfaces*, **63**, 296–300.

66 Mann, S., Sparks, N.H., Walker, M.M. and Kirschvink, J.L. (1988) Ultrastructure, morphology and organization of biogenic magnetite from sockeye salmon, *Oncorhynchus nerka*: implications for magnetoreception. *The Journal of Experimental Biology*, **140**, 35–49.

67 Nakamura, N. and Matsunaga, T. (1993) Highly sensitive detection of allergen using bacterial magnetic particles. *Analytica Chimica Acta*, **281**, 585–9.

68 Kirschvink, J.L., Kobayashi, K.A. and Woodford, B.J. (1992) Magnetite biomineralization in the human brain. *Proceedings of the National Academy of Sciences of the United States of America*, **89**, 7683–987.

69 Dobson, J. (2001) Nanoscale biogenic iron oxides and neurodegenerative disease. *FEBS Letters*, **496** (1), 1–5.

70 Martinelli, A.L., Filho, A.B., Franco, R.F., Tavella, M.H., Ramalho, L.N., Zucoloto, S., Rodrigues, S.S. and Zago, M.A. (2004) Liver iron deposits in hepatitis B patients: association with severity of liver disease but not with hemochromatosis gene mutations. *Journal of Gastroenterology and Hepatology*, **9**, 1036–41.

71 Diebel, C.E., Proksch, R., Green, C.R., Neilson, P. and Walker, M.M. (2000) Magnetite defines a vertebrate magnetoreceptor. *Nature*, **406**, 299–302.

72 Shen, H.B., Long, D.H., Zhu, L.Z., Li, X.Y., Dong, Y.M., Jia, N.Q., Zhou, H.Q., Xin, X. and Sun, Y. (2006) Magnetic force microscopy analysis of apoptosis of HL-60 cells induced by complex of antisense oligonucleotides and magnetic nanoparticles. *Biophysical Chemistry*, **122** (1), 1–4.

73 Amemiya, Y., Tanaka, T., Yoza, B. and Matsunaga, T. (2005) Novel detection system for biomolecules using nano-sized bacterial magnetic particles and magnetic force microscopy. *Journal of Biotechnology*, **120**, 308–14.

74 Takahashi, H., Ando, K. and Sgirakawabe, Y. (2002) Self-sensing piezoresistive cantilever and its magnetic force microscopy applications. *Ultramicroscopy*, **91**, 63–72.

75 Kohout, S., Roos, J. and Keller, H. (2007) Novel sensor design for torque magnetometry. *Review of Scientific Instruments*, **8** (1), 013903–6.

76 Peter, F., Rüdiger, A., Szot, K., Waser, R. and Reichenberg, B. (2006) Sample-tip interaction of piezoresponse force microscopy in ferroelectric nanostructures. *IEEE Transactions on Ultrasonics, Ferroelectrics, and Frequency Control*, **53** (12), 2253–60.

77 Kalinin, S.V., Rar, A. and Jesse, S. (2006) A decade of piezoresponse force microscopy: progress, challenges, and opportunities. *IEEE Transactions on Ultrasonics, Ferroelectrics, and Frequency Control*, **53** (12), 2226–52.

78 Kim, K., Seo, Y., Jang, H., Chang, S., Hong, M.-H. and Jhe, W. (2006) Shear-mode magnetic force microscopy with a quartz tuning fork in ambient conditions. *Nanotechnology*, **17**, S201–4.

79 Takezaki, T. and Sueoka, K. (2008) Quantitative current measurements using scanning magnetoresistance microscopy. *Ultramicroscopy*, **108** (9), 970–4.

80 Proksch, R., Runge, E., Hansma, P.K., Foss, S. and Walsh, B. (1995) High field magnetic force microscopy. *Journal of Applied Physics*, **78**, 3303–7.

81 Li, S., Stokes, S., Liu, Y., Foss-Schrader, S., Zhu, W. *et al.* (2002) Dual vibrational magnetic force microscopy. *Journal of Applied Physics*, **91**, 7346–8.

82 Nazarov, A.V., Plumer, M.L. and Pant, B.B. (2005) High-frequency magnetic force microscopy characterization of magnetic recording writer poles. *Journal of Applied Physics*, **97**, 10N902–3.

83 Koblischa, M.R., Wei, J.D., Richter, C., Sulzbach, T. and Hartman, U. (2008) Advanced cantilevers for magnetic force

microscopy and high frequency magnetic force microscopy. *Scanning*, **30**, 27–34.

84 Koblischka, M.R., Kirsch, M., Wei, J.D. and Hartmann, U. (2007) Preparation of ferrite-coated MFM cantilevers. *Journal of Magnetism and Magnetic Materials*, **316**, e666–9.

85 Kaiser, U., Schwarz, A. and Wiesendanger, R. (2007) Magnetic exchange force microscopy with atomic resolution. *Nature*, **446** (7135), 522–5.

86 Sugimoto, Y., Pou, P., Abe, M., Jelinek, P., Pérez, R., Morita, S. and Custance, O. (2007) Chemical identification of individual surface atoms by atomic force microscopy. *Nature*, **446** (7131), 64–7.

87 Tsuji, S., Yoshinari, Y., Kawai, E., Nakajima, K., Park, H.S. and Shindo, D. (2007) Magnetic resonance force microscopy combined with surface topography. *Journal of Magnetic Resonance*, **188** (2), 380–6.

88 Balasubramanian, G., Chan, I.Y., Kolesov, R., Al-Hamoud, M., Tisler, J., Shin, C., Kim, C., Wojcik, A., Hemmer, P.R., Krueger, A., Hanke, T., Leitenstorfer, A., Bratschitsch, R., Jelezko, F. and Wrachtrup, J. (2008) Nanoscale imaging magnetometry with diamond spins under ambient conditions. *Nature*, **455** (7213), 648–51.

89 Nalladega, V., Sathish, S., Jata, K.V. and Blodgett, M.P. (2008) Development of eddy current microscopy for high resolution electrical conductivity imaging using atomic force microscopy. *Review of Scientific Instruments*, **79** (7), 073705–9.

Keywords

superparamagnetic; ferromagnetic; magnetic nanoparticles; atomic force microscopy; magnetic force microscopy; life sciences

16
Cobalt Nanomaterials: Synthesis and Characterization

Zhihua Zhang, Tiejun Zhou, Meihua Lu, Allen Wei Choong Poh, and Seidikkurippu N. Piramanayagam

16.1
Introduction

Magnetic materials encompass a wide variety of materials, which have a diversity of applications. Based on their compositional nature, magnetic materials can be categorized as three major groups: (i) metal and metal alloys, such as Fe, Co, Ni, FePt, FeCo, and NdFeB; (ii) metal ferrites, such as $CoFe_2O_4$ and Fe_3O_4; and (iii) dilute magnetic semiconductor (DMS), such as ZnO or TiO_2 doped with Mn, Fe, and Co. These materials have paramount applications including data storage devices, in the generation of electricity, as electronic devices, and spintronics – indeed, it is difficult to imagine a world without magnetic materials! The telecommunications and integrated circuits (IC) industries are constantly striving for faster data transmission and miniaturization of devices, both of which require the revolution of new advanced magnetic materials [1].

With the advent of burgeoning developments in nanoscience and nanotechnology during the past decade, extensive research into the synthesis and applications of myriad types of magnetic nanomaterials, with dimensions at least in the nanometer range, has been a major trust area hitherto. In the near future, nanoscale magnetic particles will clearly become the key components in the "nanotechnology revolution" for magnetic recording, biologics, electronics, and catalysis.

In the nanometer-sized regime, the small particles possess short-range structures that mimic their counterpart bulk materials. However, compared to bulk materials, nanoscale materials exhibit distinct thermal, optical, mechanical, magnetic and electronic properties due to their small size and high surface-to-volume ratio. In the case of magnetic particles, fine-particle systems are composed of a collection of different-sized single-domain particles. As the particle size decreases towards a critical particle diameter, the formation of domain walls becomes energetically unfavorable and the particles become single domain. However, as the particle size continues to decrease below the single-domain value, the spins are increasingly affected by thermal fluctuations and the system becomes superparamagnetic when the temperature is above the blocking temperature. Such

Nanomaterials for the Life Sciences Vol. 4: Magnetic Nanomaterials. Edited by Challa S. S. R. Kumar

ISBN: 978-3-527-32154-4

individual nanoparticles have a large constant magnetic moment and behave like a giant paramagnetic atom with a fast response to applied magnetic fields and negligible residual magnetism and coercivity [2].

In this chapter, we will discuss the magnetic properties and synthesis of cobalt-based nanoparticles, and also provide a brief summary of the characterization techniques commonly involved in the study of nanoparticles. An exhaustive review on synthesis of cobalt-based nanoparticles is then provided, together with a discussion and summary of the magnetic properties of cobalt-based nanoparticles.

16.2
The Characterization of Co Nanoparticles

Nanoparticles – and in particular magnetic nanoparticles such Co-based nanoparticles – have been characterized by a variety of techniques. The shape, size, and microstructure of the Co-based nanoparticles can be monitored using both transmission electron microscopy (TEM) and scanning electron microscopy (SEM), while the crystalline structure can be determined using X-ray diffraction (XRD) and selected area electron diffraction (SAED) in conjunction with TEM. The bulk magnetic properties may be measured using alternating gradient magnetometry (AGM), vibrating sample magnetometry (VSM) and superconducting quantum interference device (SQUID) magnetometry. The particle morphology can be determined using scanning probe microscopy (SPM), including atomic force microscopy (AFM), while the oxidation or chemical states of the nanoparticles may be investigated using X-ray photoelectron spectroscopy (XPS), which is also referred to as electron spectroscopy for chemical analysis (ESCA). In some research studies on the chemical synthesis of nanoparticles, Fourier-transform infrared (FTIR) spectroscopy may also be used to verify the presence of molecules of specific functional groups by monitoring the vibration frequencies of the functional groups in the FTIR spectrum. Although, in addition to the above-mentioned techniques, many other methods are currently also used to characterize Co-based nanoparticles, only the more frequently used techniques will be highlighted here.

16.2.1
Shape, Size, and Microstructure

16.2.1.1 Transmission Electron Microscopy

The transmission electron microscope operates on the same basic principles as the light microscope, but uses electrons instead of light as a "light source". Consequently, the much lower wavelength of electrons makes it possible to achieve a resolution which is 1000-fold better than with a light microscope (in the order of a few Ångstroms).

In the transmission electron microscope, a field emission gun at the top of the microscope emits electrons which travel through a vacuum in the column of the microscope. In the same way that a light microscope uses glass lenses for focusing,

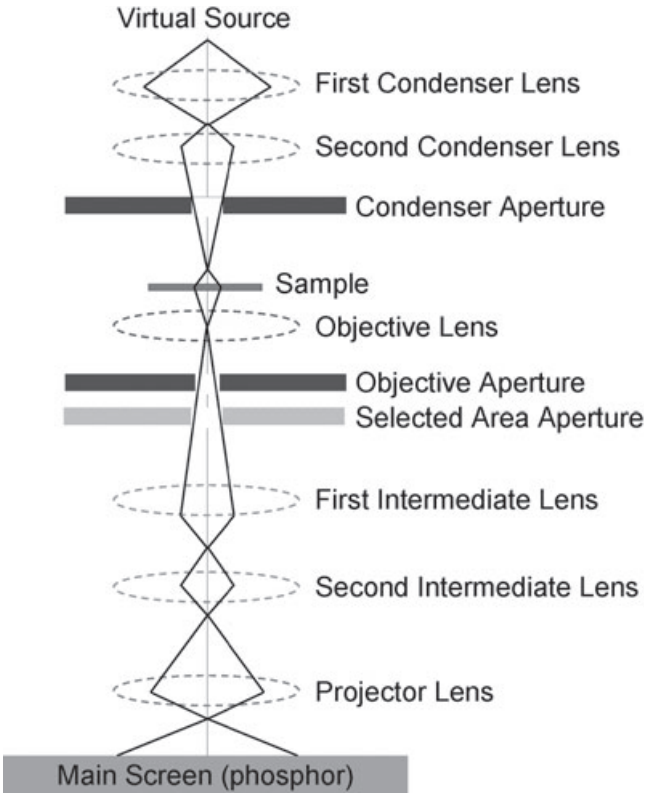

Figure 16.1 The schematic diagram of a transmission electron microscope.

the transmission electron microscope uses various electromagnetic lenses to focus the electrons into a very fine beam (as shown in Figure 16.1). The electron beam then travels through the specimen under investigation. Depending on the density of the material present, some of the electrons are scattered and disappear from the path of beam. At the bottom of the microscope, the unscattered electrons hit a fluorescent screen, which give rise to a "shadow image" of the specimen, with the different parts being displayed in varied darkness according to their density. The image can be studied directly by the operator using a phosphor screen, or photographed with a camera. The darker areas of the image represent those areas of the sample that fewer electrons were transmitted through (i.e., they are thicker or denser), whereas the lighter areas represent those areas of the sample that more electrons were transmitted through (i.e., they are thinner or less dense).

Other than imaging, the transmission electron microscope is also used to carry out SAED. This is achieved by adjusting the magnetic lenses such that, when the back focal plane of the lens is placed on the imaging apparatus, a diffraction pattern can be generated. For crystalline samples, this produces an image that consists of a series of dots in the case of a single crystal, or a series of rings in the

case of a polycrystalline material. For the single crystal case, the diffraction pattern is dependent upon the orientation of the specimen, and the resultant image is a lattice image. This image provides the operator with information about the space group symmetries in the crystal and its orientation to the beam path; however, this is typically done without utilizing any information, but the position at which the diffraction spots appear. Any further analysis of this image is complex, as the image is sensitive to a number of factors including the specimen thickness and orientation, objective lens defocus, and spherical and chromatic aberration. Although quantitative interpretation of the contrast shown in lattice images is possible, it is inherently complicated and may require extensive computer simulation and analysis.

16.2.1.2 **Scanning Electron Microscopy**

In the scanning electron microscope, a field emission "gun" at the top of the microscope emits electrons which travel through vacuum with energies from 10^2 eV to 10^4 eV. The gun is focused at the surface of the specimen and scanned across it in a "raster" pattern (see Figure 16.2). A number of phenomena occur at the surface under the impact of electron beam, and a "signal" or radiation can be collected for every position of the incident electron beam.

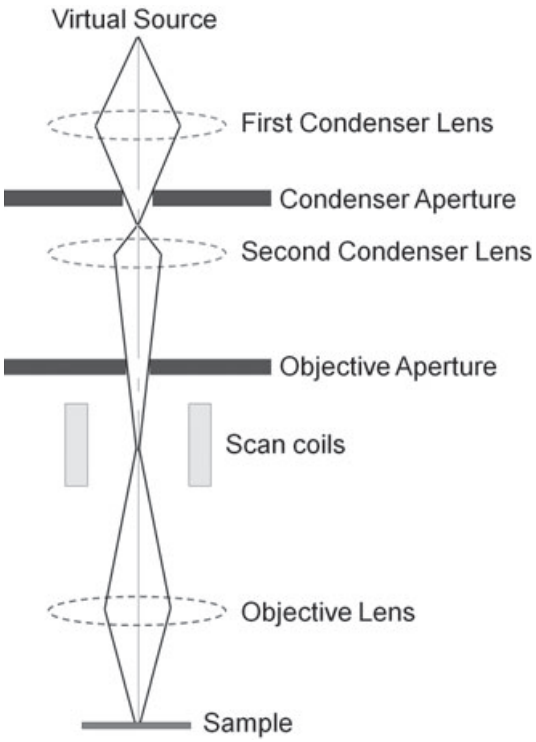

Figure 16.2 The schematic diagram of a scanning electron microscope.

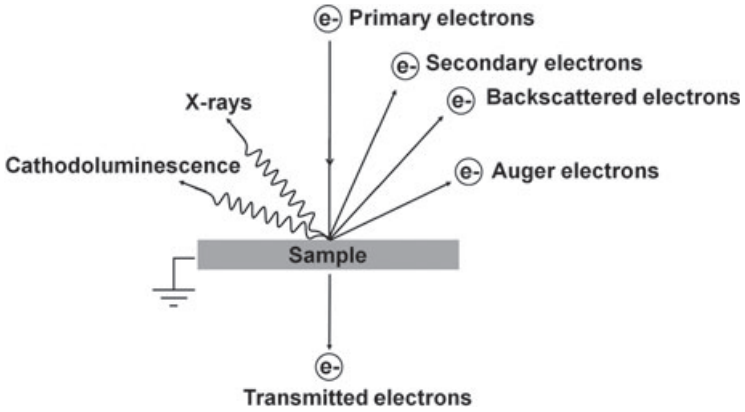

Figure 16.3 Schematic diagram showing the various types of electrons and photons emitting from the sample upon irradiation with an electron beam.

When accelerated electrons enter a sample, they are scattered both elastically (by electronic static interaction with atomic nuclei) and inelastically (by interaction with atomic electrons). The various types of electrons and photons emitted as a result of the incident electron beam interacting with the sample are shown in Figure 16.3.

The backscattered electrons are caused by an incident electron colliding with an atom in the specimen which is nearly normal to the incident's path. The incident electron is then scattered "backwards" by 180°. The production of backscattered electrons varies directly with the specimen's atomic number; this differing production rate causes higher atomic number elements to appear brighter than lower atomic number elements. This interaction is utilized in SEM to differentiate parts of the specimen that have a different average atomic number, and hence is able to show variations in the chemical composition of a specimen.

On the other hand, the secondary electrons are caused by an incident electron passing "near" an atom in the specimen – that is, near enough to impart some of its energy to a lower energy electron (usually in the K-shell). This causes a slight energy loss and path change in the incident electron and ionization of the electron in the specimen atom. This ionized electron then leaves the atom with a very small kinetic energy of about 5 eV; this is then termed a "secondary electron". Each incident electron can produce several secondary electrons. The production of secondary electrons is highly topography-related. Due to their low energy (5 eV), only secondary electrons that are very near the surface (typically <10 nm) can exit the sample and be examined. Any changes in topography in the sample that are larger than this sampling depth will change the yield of secondary electrons due to collection efficiencies. Hence, they are used in SEM to derive the properties of the surface structure (topography) of the specimen rather than any underlying structures.

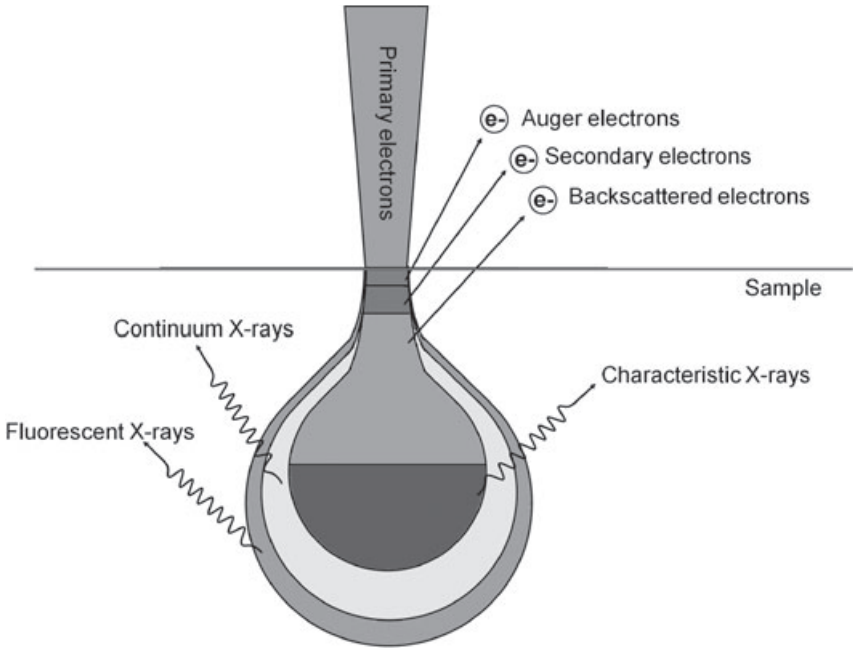

Figure 16.4 Schematic diagram showing the regions in the interaction volume from which various types of electrons and photons originate upon irradiation with an electron beam.

Auger electrons are caused by the de-excitation of the specimen atom after a secondary electron is produced (Figure 16.4). As a lower-energy (usually K-shell) electron was emitted from the atom during the secondary electron process, an inner (lower energy) shell now has a vacancy. A higher energy electron from the same atom can "fall" to a lower energy, filling the vacancy, and this creates an energy surplus in the atom which can be corrected by emitting an outer (lower energy) electron; this is known as an Auger electron. Auger electrons have a characteristic energy which is unique to each element from which the electron was emitted. The Auger electrons are collected and sorted according to energy to provide compositional information about the specimen. A more extensive discussion on Auger electrons is provided in later section.

X-rays are caused by de-excitation of the specimen atom after a secondary electron has been produced. As a lower-energy (usually K-shell) electron was emitted from the atom during the secondary electron process, an inner (lower energy) shell now has a vacancy. A higher-energy electron can "fall" into the lower energy shell, filling the vacancy. As the electron "falls" it emits energy, usually in the form of X-rays to balance the total energy of the atom. X-rays or light emitted from the atom will have a characteristic energy which is unique to the element from which it originated.

16.2.2 Magnetic Properties

The magnetic properties (bulk) of the Co-based nanoparticles are usually characterized using VSM or AGM. In AGM (see Figure 16.5a), the sample is mounted on a piezoelectric transducer which oscillates when the sample is subjected to an alternating magnetic field gradient superimposed on the direct current (DC) field of an electromagnet. The force exerted on the magnetized sample in a magnetic field gradient can be measured. The AGM has a low noise floor of 10^{-8} emu, and the piezoelectric reed sample holder of the magnetometer must be operated at the resonance frequency of the sample holder, which depends on the mass of the sample/substrate combination. Hence, every new sample requires re-tuning to its

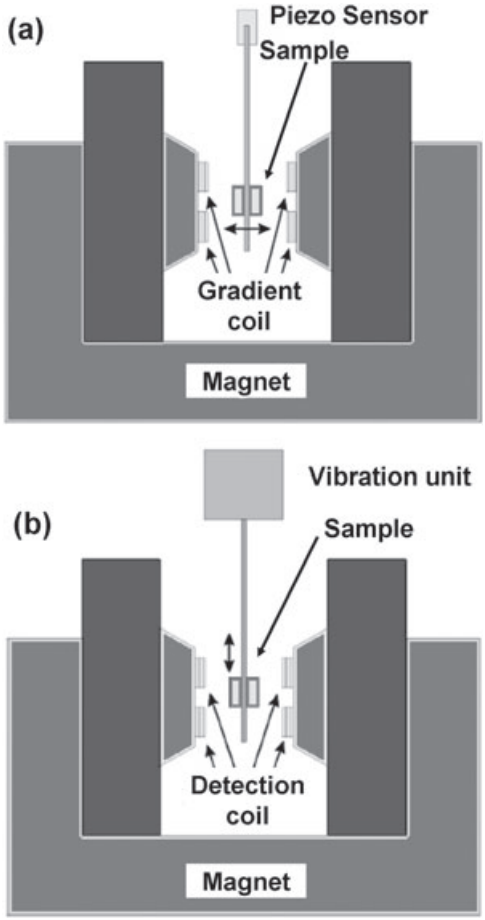

Figure 16.5 Schematic diagrams of (a) an alternating gradient magnetometer and (b) a vibrating sample magnetometer.

resonance frequency. If its magnetic moment is low, automatic tuning will be ineffective and manual tuning will be required. As a result of the involvement of human judgment in tuning, even with careful manual tuning of a low moment sample the saturation moment was found to vary by more than ±5% over 10 consecutive measurements. This limits the use of AGM to low-moment samples. In addition, the measured moment is very sensitive to sample placement due to the gradient field, and therefore care must be taken to ensure that the sample and the calibration standard are identical in mass and size in order to obtain a calibrated reading. When measuring low-coercivity samples (~100 Oe or smaller), it is necessary to reduce the magnitude of the gradient field in order to maintain accuracy. This, in turn, in reduces the sensitivity of the AGM procedure (compared to VSM) and also severely limits the suitability of AGM for measuring low coercivities, as the alternating field cycles through part of the hysteresis loop. Similarly, the gradient field limits the accuracy of remanence measurements, as the field is cycling through a minor loop around remanence.

In VSM (Figure 16.5b), the sample is vibrated in the magnetic field using a vibrator mechanism. The magnetizing field (DC) is provided by an electromagnet driven by a DC bipolar power supply, while the signal voltage is generated in the detection coils due to the changing flux emanating from the vibrating sample. The output measurement displays the magnetic moment (M) as a function of the field (H). In this stepped-field mode, the magnetic field was changed in selected step sizes and the magnetic moment measured with the field held stationary. The advantage of the stepped-field system is that the field between measurement points can be changed at a very high rate (>2 kOe s^{-1}), and consequently passing through all the field points does not take very much time. In fact, more time is spent at each measurement field to measure the signal several times and average the result (digital signal averaging), which leads to a significant noise reduction if the noise is uncorrelated. However, the noise floor for VSM is 10^{-6} emu, which is two orders of magnitude higher than that for AGM. In addition to AGM and VSM, SQUID magnetometry is also frequently used to determine the magnetic properties of Co-based nanoparticles, and in particular low-temperature studies of magnetic nanoparticles. However, details of this technique will not be provided at this point.

16.2.3 Morphology

Atomic force microscopy is commonly used to study the morphology of materials. The atomic force microscope consists of a microscale cantilever with a sharp tip (probe) at its end that is used to scan the specimen surface (see Figure 16.6). The cantilever is typically silicon or silicon nitride, and has a tip radius of curvature on the order of nanometers. When the tip is brought into the proximity of a sample surface, forces between the tip and the sample lead to a deflection of the cantilever, according to Hooke's law. Depending on the situation, the forces measured in AFM include mechanical contact force, van der Waals forces, capillary forces, chemical bonding, electrostatic forces, magnetic forces (see magnetic force micros-

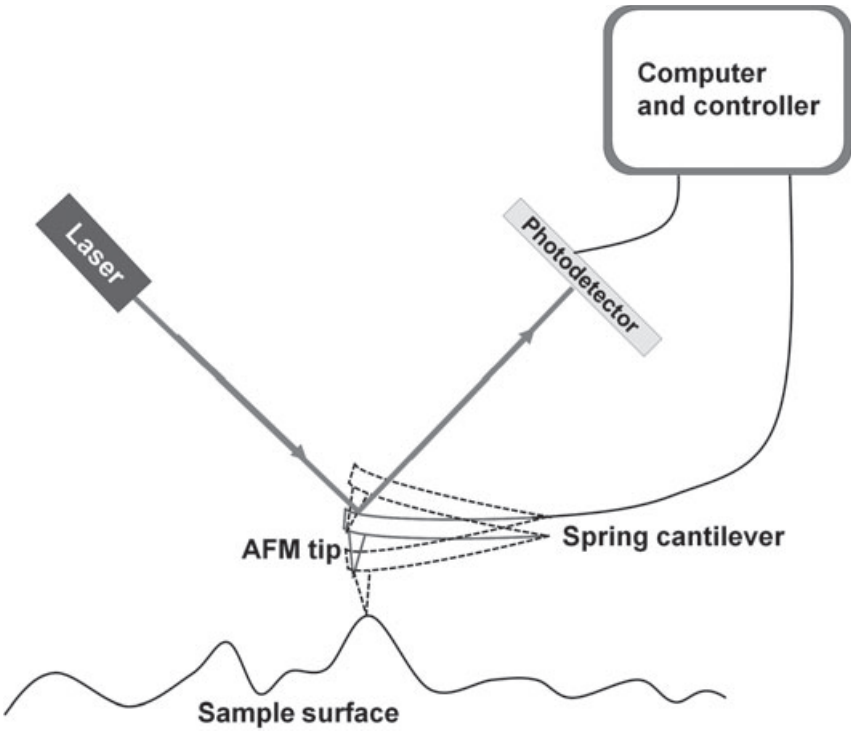

Figure 16.6 Schematic diagram showing details of the atomic force microscope.

copy; MFM), Casimir forces, and solvation forces. As well as force, additional quantities may simultaneously be measured through the use of specialized types of probe. Typically, the deflection is measured using a laser spot which is reflected from the top of the cantilever into an array of photodiodes. A plot of the laser deflection versus tip position on the sample surface provides the resolution of the "hills" and "valleys" that constitute the topography of the surface. The atomic force microscope can function in two ways: (i) with the tip touching the sample ("contact mode"); or (ii) with the tip tapping across the surface ("tapping mode").

The two main advantages of AFM over SEM is that the atomic force microscope can function in ambient air or a liquid environment, whereas the electron microscope requires that all probes be undertaken in a vacuum. In addition, in AFM a three-dimensional (3-D) image is plotted, whereas in SEM only a two-dimensional (2-D) image or projection of a sample is provided.

A major drawback of the atomic force microscope, however, is the limited area that it can scan and the image resolution that it can generate; typically, an electron microscope can scan an area measured in millimeters, but an atomic force microscope can scan only micrometers. From this perspective, it is easy to see why an electron microscope can scan a wider area faster than can an atomic force microscope.

16.2.4
Elemental and Chemical Analysis

16.2.4.1 Auger Electron Spectroscopy

Auger electron spectroscopy (AES) is an analytical technique which is based on measurement of the kinetic energy of electrons ejected from an atom, usually following the bombardment of that atom by high-energy electrons. When an atom is struck by a high-energy electron (typically in the range 1 to 25 keV), there is some probability of a core-level electron being ejected. The atom is then in an energetic ionic state with an electron missing from a core level. One mechanism by which the atom can relax into a lower energy state is for another electron, from the same atom, to fill the core level hole with the release of energy. This energy can then cause the emission of another electron (the Auger electron) (Figure 16.7a). AES may be used to determine the type of elements present in magnetic nanoparticles, the relative quantity of each element, and also occasionally the chemical state of the elements present.

16.2.4.2 X-Ray Photoelectron Spectroscopy (XPS)

XPS is based upon a "single photon in and an electron out" process and, in many ways the underlying process is a much simpler phenomenon than the Auger process described previously. The energy of an X-ray photon is given by the Einstein relationship:

$$E = h\nu \tag{16.1}$$

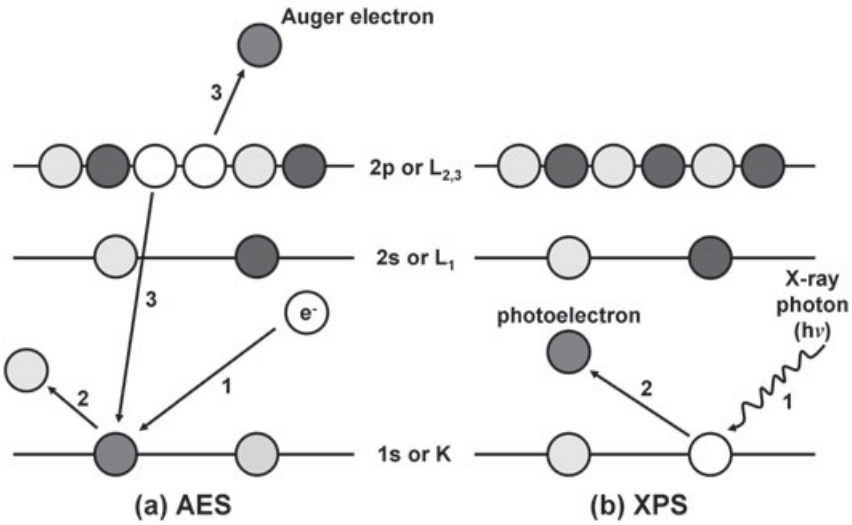

Figure 16.7 Schematic diagrams showing mechanisms of (a) Auger electron spectroscopy (AES) and (b) X-ray photoelectron spectroscopy (XPS).

where h is the Planck's constant (6.62×10^{-34} J) and ν is frequency (Hz) of the radiation.

In XPS, the X-ray photon is absorbed by an atom in a molecule or solid, leading to ionization and the emission of a core (inner shell) electron or photoelectron (Figure 16.7b). The kinetic energy distribution of the emitted photoelectrons (i.e., the number of emitted photoelectrons as a function of their kinetic energy) can be measured using any appropriate electron energy analyzer, and a photoelectron spectrum can thus be recorded. As the electron's energy is present solely as kinetic energy (KE), this can be rearranged to give the following expression for the KE of the photoelectron:

$$\mathrm{KE} = h\nu - (E(A+) - E(A)) \tag{16.2}$$

Here, the $(E(A+) - E(A))$ term represents the difference in energy between the ionized and neutral atoms, and is generally known as the binding energy (BE) of the electron; this then leads to the following commonly quoted equation:

$$\mathrm{KE} = h\nu - \mathrm{BE} \tag{16.3}$$

$$\mathrm{BE} = h\nu - \mathrm{KE} \tag{16.4}$$

Equation 16.4 is obtained by rearrangement of Equation 16.3.

Hence, with XPS analysis, the oxidation state or chemical state of the element in the magnetic nanoparticles can be determined. This is very useful, especially to determine if the magnetic material of the magnetic nanoparticles has undergone oxidation (which will degrade the nanoparticles' magnetic properties).

16.2.5
Fourier Transform Infrared (FTIR) Spectroscopy

Infrared spectroscopy exploits the fact that molecules have specific frequencies at which they rotate or vibrate corresponding to discrete energy levels (vibrational modes). These resonant frequencies are determined by the shape of the molecular potential energy surfaces, the masses of the atoms, and by the associated vibronic coupling. In order for a vibrational mode in a molecule to be infra-red (IR) active, it must be associated with changes in the permanent dipole. Simple diatomic molecules have only one bond, which may stretch, whereas more complex molecules have many bonds and the vibrations can be conjugated, leading to IR absorptions at characteristic frequencies that may be related to chemical groups.

The IR spectrum of a sample is collected by passing a beam of IR light through it; a subsequent examination of the transmitted light reveals how much energy was absorbed at each wavelength. This can be achieved using a monochromatic beam, which changes in wavelength over time, or by using a Fourier transform instrument to measure all wavelengths at once. From this, a transmittance or absorbance spectrum can be produced, showing at which IR wavelengths the

sample absorbs. An analysis of these absorption characteristics then reveals details about the molecular structure of the sample.

16.2.6
The Crystal Structure: X-Ray Diffraction (XRD)

X-ray diffraction, which is a form of X-ray crystallography, is a method for determining the arrangement of atoms within a crystal. In this process a beam of X-rays strikes a crystal and scatters into many different directions; based on the angles and intensities of the scattered beams, a crystallographer can then produce a 3-D picture of the density of electrons within the crystal. From this electron density, the mean positions of the atoms in the crystal can be determined, as well as their chemical bonds, their disorder, and other information.

Powder diffraction XRD is a technique used to characterize the crystallographic structure, crystallite size (grain size), and preferred orientation in polycrystalline or powdered solid samples. Powder diffraction is commonly used to identify unknown substances, by comparing diffraction data against a database. It may also be used to characterize heterogeneous solid mixtures to determine the relative abundance of crystalline compounds. Powder diffraction is also commonly used to determine strains in crystalline materials. Alternative techniques such as thin film diffraction and grazing incidence X-ray diffraction may also be used to characterize the crystallographic structure and preferred orientation of substrate-anchored thin films. X-ray rocking curve analysis is used to quantify grain size and mosaic spread in crystalline materials.

In the XRD set-up, the sample is mounted on a goniometer and gradually rotated while being bombarded with X-rays; this produces a diffraction pattern of regularly spaced spots known as “reflections”. The 2-D images taken at different rotations are converted into a 3-D model of the density of electrons within the crystal by using the mathematical method of Fourier transforms, combined with chemical data known for the sample.

16.3
Synthesis of Cobalt-Based Nanoparticles

16.3.1
Introduction

In this section, the synthesis of cobalt-based nanomaterials will be outlined, based on their notable magnetic characteristics compared to Fe and Ni, as indicated in Table 16.1. Recently, cobalt nanocrystal has received more attention than Fe and Ni due to its unique properties and stronger oxidation-resistance. In addition to its magnetic use, cobalt nanoparticles can be used in a variety of applications, including as the catalyst for the Fischer–Tropsch reaction, as functional coatings, for electroplating, and for biomedical assays. In terms of its crystal structure, cobalt

Table 16.1 Magnetic properties of ferromagnetic elements of Co, Fe and Ni.

Element	n_B	σ_s at 0 K (Am^2kg^{-1})	σ_s at 293 K (Am^2kg^{-1})	T_c (K)
Co	1.72	162	161	1388
Fe	2.22	222	218	1043
Ni	0.62	57	54	627

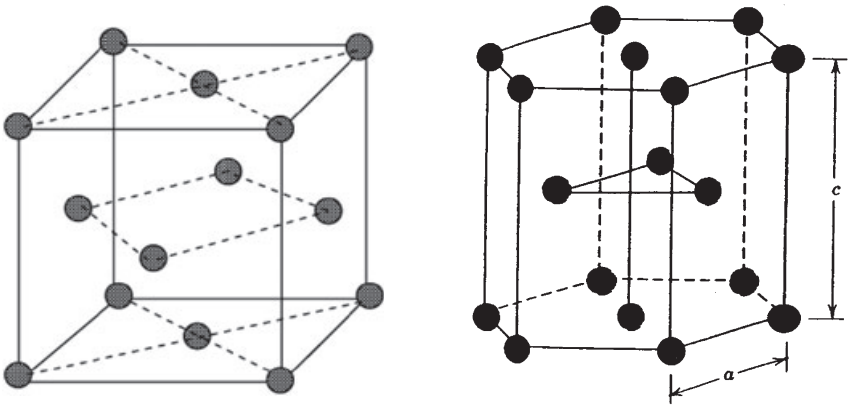

Figure 16.8 The cobalt crystal structures of the fcc and hcp phases.

is known to have two crystal phases: hexagonal close-packed (hcp) and face-centered cubic (fcc) (see Figure 16.8). Although both phases can coexist at room temperature, the fcc structure is thermodynamically preferred above 450 °C while the hcp phase is favored at lower temperatures. More recently, a new metastable ε-phase cobalt, which is less dense than both the hcp and fcc structures, was discovered by Dinge and Banwendi during the synthetic process of cobalt nanoparticles [3]. This structure is cubic (space group $P4_132$) with a unit cell parameter a = 6.097 Å. The unit cell structure is similar to that of b-manganese (a high-temperature phase of manganese). It contains 20 cobalt atoms, which are divided into two types: 12 atoms of Type I and eight atoms of Type II. Generally, this cobalt phase has only been generated by solution-phase approaches instead of other common techniques, such as varying temperature and pressure.

16.3.2
Stabilization of Nanomaterials

The nanosized metallic cobalt particle can bring about superior and facilitating properties due to its very high surface-to-volume ratio. On the other hand, this special hallmark could induce an unfavorable tendency for nanoparticles to

agglomerate together, which would lead to decrease or even loss of any associated properties. Therefore, an understanding of the colloidal stabilization mechanism is crucial to the design and synthesis of these nanoparticles in a well-defined way. The preservation of long-term stability, without agglomeration or precipitation, would be the primary prerequisite for any application related to magnetic nanoparticles.

Derjaguin, Landau, Verwey, and Overbeek developed the DLVO theory in 1940s to explain the stability mechanism of colloids in suspension. Their theory suggested that the balance between two opposing forces – that is, electrostatic repulsion and van der Waals attraction – would determine whether the particles agglomerated together or were separated from each other. This theory is also extendable for the interpretation and formulation of nanosized nanoparticles. In general, three major approaches have been discussed for the stabilization of nanoparticles in terms of the stabilizers used: (i) electrostatic repulsion; (ii) steric stabilization; and (iii) electrosteric stabilization. The scheme is shown in Figure 16.9.

Nanoparticles dispersed in an aqueous solution are able to generate an electrostatic repulsion due to the positively or negatively charged surfaces, while uncharged particles are free to form colloids and to aggregate. In solution, the presence of a net charge on a particle will affect the distribution of ions surrounding that particle, and result in an electrical stern layer and diffuse double-layer around the particles. When a particle moves due to either gravity or to an applied electric field, ions within the boundary will move with it accordingly. However, a boundary remains where ions do not travel with the particle – this is termed the "surface of hydrodynamic shear" or the "slipping plane". The potential that exists at this boundary is known as the "zeta potential"; this is a critical parameter to determine the stability of a colloidal suspension. When all of the particles have a large negative or positive potential, they will repel each other to keep suspension stable, whereas flocculation happens with a low potential value. The ionic strength, temperature, pH value, or the addition of an electrolyte would each affect the zeta potential and, in turn, the stability of the particles.

In the case of steric stabilization, bulky functional organic molecules or polymers are adsorbed onto the particle surface so as to form a protective layer among nanoparticles, and thus prevent the particle surfaces from coming into close

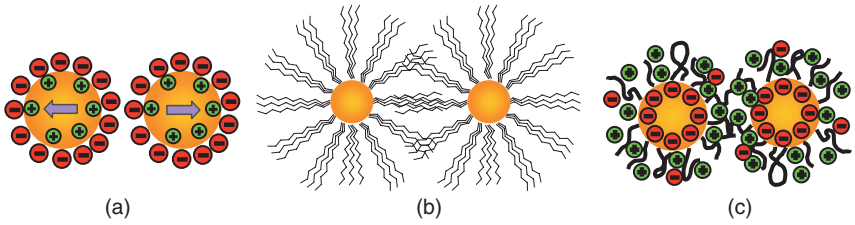

Figure 16.9 Schematic representation of (a) electrostatic repulsion; (b) steric stabilization; and (c) electrosteric stabilization of colloidal nanoparticles.

contact with each other. The thickness of the coating was sufficient to keep particles separated by steric repulsions between the organic molecules or polymer layers, and the van der Waals attract forces were too weak to cause the particles to adhere at this stage. In contrast to electrostatic repulsion in aqueous media, this type of stabilization could be extended both in organic media and aqueous solution [4]. With regards to the electrosteric stabilization (which is in combination of electrostatic and steric stabilization), ionic surfactants containing ionizable groups such as polycarboxylic acid, zwitterionic molecules or polyelectrolyte have been widely investigated for this process [5]. These dispersants are able to be adsorbed onto the surface of nanoparticles with opposite charges so as to generate an electric repulsive and steric layer. The electrosteric stabilization can be also achieved with polymetaloxoanions such as the couple ammonium $Bu_4N^+/P_2W_{15}Nb_3O_{62}^{9-}$ [6]. Whilst not directly indicated in the following section, these stabilization methods have been effectively utilized to guide the controlled synthesis of cobalt nanoparticles.

16.3.3
Synthesis of Cobalt Nanomaterials

The preparation of well-defined nanoparticles with sizes ranging from 1 to 100 nm is essential in order to conduct studies capable of distinguishing truly novel properties inherent to nanoscale structures from those associated with structural heterogeneities or polydispersity. To date, many comprehensive reviews have been prepared on the synthesis, characterization, and application of myriad nanoparticles [7], and so in this chapter attention will be focused specifically on the synthesis of cobalt nanomaterials. Based on the conversion process used, the synthetic methodologies can be categorized as physical methods, chemical vapor deposition (CVD), and liquid-phase chemical precipitations.

16.3.3.1 Physical Methods

Traditionally, molecular beam epitaxy (MBE) growth, sputtering and laser irradiation methods are commonly used to deposit cobalt nanoparticle and films at desired substrates. MBE was developed during the early 1970s as a means of growing high-purity epitaxial layers of semiconductor compounds, since when it has been further extended to fabrication of different types of material. The most important feature of MBE is its slow deposition rate (on the order of a few $Å\,s^{-1}$), which allows the films to grow epitaxially. It is critical that the material sources should be extremely pure and the entire process carried out in an ultra-high vacuum (10^{-8} Pa) environment in order to produce high-purity layers. Single cobalt atoms and nanoparticles were deposited in ultra-high vacuum by MBE on a Pt (111) single crystal surface. Isolated adatoms were obtained by depositing minute amounts of Co, while 2-D and monlayer larger particles were obtained by statistical growth and diffusion-controlled aggregation. Those atoms and particles showed giant magnetic anisotropy energy, which was found to be dependent on single-atom coordination changes [8].

Sputtering is another widely employed process for thin film deposition and IC technology, whereby atoms are ejected from a solid target material due to bombardment of the target by energetic ions. The fabrication of individual cobalt nanoparticles on different substrates such as SiO_2/Si (001) [9], AlN [10], and silicon nitride [11], have been realized by sputtering technology. The particle growth kinetic, topographic and magnetic properties were studied, while the magnetic behavior was seen to depend significantly on the Co layer thickness. In addition, a nanosized PtCo alloy with $L1_0$ phase has been prepared via a two-stage fabrication process by combining conventional sputtering and thermal processing technologies. This method can be used for ultra-high-density perpendicular magnetic recording [12]. Very recently, Xu and Wang demonstrated a general method for the direct gas-phase synthesis of multicomponent nanoparticles with distinctively different heterostructures via magnetron sputtering. The relationship between the composition distribution in the nanoparticles and their thermal history in the nanocluster source enabled the control and design of heterostructures in the gas phase. Au coated with a cobalt shell and a cobalt core coated with a multilayered shell could be readily obtained by optimizing the experimental conditions [13].

Laser irradiation represents an efficient approach to produce cobalt nanoparticle for magnetic applications. Here, nonvolatile memory devices have been fabricated by embedding ~5 nm cobalt nanoparticles into a metal/oxide/semiconductor (MOS) capacitor through a laser irradiation approach. Capacitance–voltage electrical measurements of the fabricated device indicated charging and discharging behavior in MOS structure due to the charging effect in the Co nanoparticles. Furthermore, a structural analysis confirmed the deposition of cobalt nanoparticles inside the gate oxide [14]. These promising results have demonstrated that the laser irradiation process might represent a potential candidate for the fabrication of nanocrystal memory devices.

16.3.3.2 **Chemical Vapor Deposition**

Chemical vapor deposition is a chemical process which transforms a volatile precursor into thin film or powder on the surface of a wafer substrate. In a typical CVD process, precursors are introduced into CVD chamber by carrier gases, which either decompose on their own or react with other gases/vapors on the substrate surface at elevated temperature. The CVD process consists of three steps: (i) the mass transport of reactants by diffusion from the location where gases are supplied to the surface where deposition must occur; (ii) the chemical reactions on the growth surface; and (iii) the removal of volatile byproducts by gas flow through the reaction chamber.

Different volatile cobalt complexes have been exploited as sources for the deposition of cobalt thin films on solid substrates. Cobalt carbonyl, cobalt (II, III) acetylacetonate, cobaltocene and $Co(C_5H_5)(CO)_2$ and $Co(CO)_3(NO)$ have each indicated their feasibilities as precursors for the generation of Co films, and typical spherical nanoparticles were produced in most cases. Unfortunately, several serious drawbacks were apparent, such as complicated reaction pathways in the gas phase, a low thermal stability, a low vapor pressure, a high deposition temperature, or

contaminated films [15]. Volatile and thermally stable cobalt (I) hydride complexes HCo $[P(OR)_3]_4$ (where R = methyl, ethyl, *iso*-propyl, or *n*-propyl) were synthesized and used as precursors in CVD, and smooth and dense cobalt thin films with variable grain size were fabricated on Si at temperatures as low as 300 °C without employing hydrogen [16]. In addition, a highly conformal pure Co film was deposited on either SiO_2-coated or trench-patterned wafers by using $Co_2(CO)_8$ or $C_{12}H_{10}O_6(Co)_2$ (dicobalt hexacarbonyl *tert*-butylacetylene) as the Co precursor, which would be quite promising for the production of advanced electronic devices [17]. Recently, pulsed-spray evaporation CVD has been adopted to grow metallic cobalt and Co_2C films on solid substrates. For this, alcoholic solutions of cobalt acetylacetonate were loaded as a liquid feedstock, in which alcohol acted as both solvent and reducing agent. Different types of alcohols, pulse width and frequency, and starting concentrations of the loading precursor determined the growth rate, size, crystallinity, and thickness of metallic films [18].

16.3.3.3 **Liquid-Phase Chemical Precipitation**

16.3.3.3.1 **Microemulsion Approach** Microemulsions are thermodynamically stable, isotropic dispersions of oil and water with a thin film of surfactant molecules adsorbed at the water/oil interface. Surfactants are amphiphilic molecules which have a polar hydrophilic (water-loving) "head" and a nonpolar hydrophobic (water-hating) "tail". By varying the hydrophile–lipophile balance (HLB) value of the surfactants and the continuous/dispersed phase, both oil-in-water (direct or water-borne) microemulsions and water-in-oil microemulsions can be produced. The latter type, which is also referred to as an "inversed microemulsion", is generally exploited in the preparation of inorganic oxide, semiconductor and metal nanoparticles, and so on.

Typically, surfactants may be classified as: (i) anionic, such as sodium bis(2-ethylhexyl)sulfosuccinate, usually called AOT; (ii) cationic, such as tetra-alkyl quaternary ammoniums; and (iii) nonionic, such as *tert*-octylphenoxy-polyethoxyethanol (Triton X-100). The inverse micelle is explained in terms of the water-surfactant molar ratio w $[H_2O]/[\text{surfactant}]$, which determines the droplet size. Due to its small dispersion sizes (which usually are 5–20 nm in diameter), the microemulsion will be either transparent or translucent. In contrast to the colloidal approach, the micellar reagent may act as a physical boundary rather than as a true surface-capping agent. Besides its variable size, cylindrical, lamellar and hexagonal shapes of droplets can be obtained by adding cosurfactants together with normal surfactants; thus, the final nanostructure was dependent on the micellar morphology [7c, 19].

Pileni and coworkers reported the synthesis of monodispersed cobalt nanoparticles by using AOT as surfactant and Co $(AOT)_2$ as the starting materials. The diameter of the droplets was controlled by the volume of water, and varied from 0.5 to 18 nm [20]. The uniform cobalt nanoparticles could be self-organized into either 2-D [21, 22] or 3-D superlattices [23] by extracting cobalt nanoparticle with lauric acid or triphosphine oxide from reverse micelles, and then re-dispersed into

pyridine or other nonpolar solvents such as hexane. These 2-D and 3-D superlattices of cobalt nanocrystals coated with lauric acid chains were found to be highly stable, with samples exposed to air appearing not to be oxidized even after a period of several weeks.

Furthermore, ordered fcc "supercrytals" or disordered 3-D assemblies consisting of 7.5 nm cobalt nanoparticles were produced by the slow evaporation of a colloidal solution on a highly oriented pyrolitic graphite (HOPG) substrate and optimization of the substrate temperature and evaporation rate [24, 25]. Grazing incidence small-angle X-ray scattering (GISAXS) diffractograms were used to study the difference between the ordered and disordered structures and magnetic properties of well-characterized disordered and fcc-ordered 3-D assemblies were also investigated. Significant differences were seen to arise from the mesoscopic order, due to the differences in anisotropy and distribution of dipolar interaction energies in the two systems. Moreover, the soft annealing of fcc cobalt nanoparticles at 125 °C induced the structural transition into ferromagnetic hcp cobalt nanocrystals without changing the size, size distribution, and passivating layer [26].

In addition to anionic AOT-assisted surfactant, the control of cobalt nanoparticle production of sizes ranging about 4 nm to 9 nm has been achieved using a germ-growth method during inverse micelle synthesis with the cationic surfactant, didodecyldimethylammonium bromide [27]. Mixed platinum–cobalt nanoparticles with an average size of 3–4 nm were prepared by using nonionic Triton X-100 as surfactant and 2-propanol as cosurfactant [28]. Haeiwa *et al.* reported an approach to encapsulate Co nanoparticles with SiO_2 capsule based on a reverse micellar technique. For this, cationic tetra-alkyl ammonium bromide (CTAB) was used as the surfactant to prepare cobalt ion micelles, after which the reductant was added to form cobalt nanoparticles, followed by the addition of tetraethylorthosilicate (TEOS). The hydrolysis and polymerization of silane occurred in water droplets and then formed a hollow silica shell. The water content was shown to affect the reduction of cobalt salt as well as the hydrolysis rate of TEOS, and thus to control the thickness of the shell [29]. Ganguli *et al.* prepared cobalt oxalate nanorods by first using a reverse micellar process, and then decomposing the rods thermally to cobalt in a H_2 atmosphere [30].

16.3.3.3.2 **Chemical Reduction in Aqueous Solution** The reduction of inorganic cobalt salts in aqueous solution with powerful reducing reagents (e.g., borohydrides, such as $NaBH_4$ or KBH_4) is a simple, convenient and cost-effective approach for the preparation of cobalt nanoparticles. For this, cobalt ions were reduced to metallic cobalt by borohydride, according to the following two-step reaction:

$$2\,Co^{2+} + 4\,BH_4^- + 9\,H_2O \rightarrow Co_2B + 12.5\,H_2 + 3\,B(OH)_3$$

$$4\,Co_2B + 3\,O_2 \rightarrow 8\,Co + 2\,B_2O_3$$

When cobalt salts (e.g., cobalt chloride) were mixed rapidly with $NaBH_4$, ultrafine particles of Co_2B would first be formed, and these would react further with

oxygen; thus, the boron would be oxidized and the cobalt is reduced to its desirable metallic form [31]. The challenge of this method would be first, to avoid the generation of unwanted cobalt byproducts, and second, to prevent the oxidation in open air of the as-formed cobalt nanoparticles after the reaction.

Recently, a homogeneous silica shell was coated onto as-prepared amorphous cobalt nanoparticle by combining a normal reduction and the Stöber synthesis. In this reaction, citrate ions were added to the whole solution, as this considered to prevent further growth through a double-layer repulsion between the negatively charged cobalt nanoparticles. The cobalt/silica core–shell particles formed had a tunable shell thickness, and could subsequently be transformed into independent and crystalline nanoparticles after annealing; these were stable in air for long periods of time [32]. A similar approach was investigated for the preparation of silica-coated cobalt nanoparticles which could be assembled to form one-dimensional (1-D) structures, with the reaction being driven by a weak external magnetic field and strong dipole–dipole magnetic interactions. The opposite structures of cobalt-coated silica spheres were also prepared by using the layer-by-layer self-assembly technique [33]. The mechanism of self-assembly into 1-D and magnetic pearl necklaces was stimulated by molecular dynamics simulation [34]. Furthermore, the synthesis of larger cobalt nanoparticle with an average size of 95 nm and with a thin layer of silica has been demonstrated, where the core–shell nanostructure showed superparamagnetic behavior as the uniform cobalt core nanospheres were composed of many metallic Co nanoclusters [35]. Alternatively, Co nanoparticles of 1–2 nm diameter were synthesized and located inside the supercages of faujasite zeolite or in the mesopores generated during the reduction process, and exhibited higher catalytic activities in Fischer–Tropsch syntheses [36]. Most recently, waterborne-synthesized cobalt nanoparticles were exploited as sacrificial templates in the generation of gold nanotubes [37] or for forming a protective layer on gold surfaces to improve surface-enhanced Raman scattering (SERS) effects [38].

$Co_{30}Fe_{70}$ nanoparticles with mean particle size of approximately 8 nm were successfully synthesized by the chemical reduction of cobalt chloride and iron chloride, with borohydride as a reducing agent, in aqueous solution. Here, the uniform $Co_{30}Fe_{70}$ nanoparticles exhibited an excellent soft magnetic behavior, such as high permeability, negligible coercivity, and a high saturation magnetization similar to that of the $Co_{30}Fe_{70}$ bulk [39]. In a series of similar experiments, mesoporous silicates containing PtCo nanoparticles with size of 2–3 nm [40] and silica-coated CoPt nanoparticles have also been investigated [41]. For this, the particles were immobilized inside the porous walls or cavities and prevented from coalescence during calcinations. The replacement of water with different types of polar solvent, such as alcohol [42] and dimethylformamide [43] has also attracted more attention for the synthesis of well-dispersed Co nanoparticles via an analogous chemical reduction technology.

16.3.3.3.3 **Polymer-Assisted Approach** Due to its advantages of superior mechanical properties and excellent ability to form thin films, polymers have been pro-

actively employed as efficient stabilizers for the controlled synthesis of cobalt nanoparticles. The as-synthesized polymer nanocomposites consisting of inorganic nanoparticles and organic polymers, often exhibit a host of mechanical, electrical, optical and magnetic properties, which are far superior to those of the individual components. These desirable properties are derived from a synergistic and hybrid interaction between the inorganic and organic interfaces that separate the building blocks. Many reviews have been produced describing the role of polymer stabilizers and polymer-supported magnetic nanocomposites [44].

Currently, the *in situ* synthesis of cobalt nanostructures in polymer matrix has been widely utilized, where the polymer material and cobalt source are mixed in solution, after which a reducing agent is added to reduce the cobalt ions to metallic cobalt. A seminal study reported the synthesis of well-defined cobalt colloids by using random poly(methyl methacrylate–ethyl acrylate–*N*-vinyl-pyrrolidone) terpolymers as stabilizers, with Co_2CO_8 being decomposed in refluxing toluene and the particle size readily controlled by varying the cobalt to surfactant loading ratio [45]. Subsequently, a variety of polymers with functional groups such as –COOH, $–NH_2$ and $–SO_3H$ have been used to produce polymer-supported cobalt nanocomposites. As an example, a perfluorinated sulfo-cation membrane (MF-4SK), prepared using an ion-exchange method, was used to create superparamagnetic, self-aggregated cobalt nanoparticles, the magnetic properties of which indicated that such nanoparticles exhibited superparamagnetic properties above the blocking temperature (T_B) [46]. Most recently, water-soluble cobalt spherical nanoparticles and nanorods have been produced using alkyl thioether end-functionalized poly(methacrylic acid) as ligands, where the dispersion was stable for approximately two months and could, potentially, be used for biomolecular conjugation due to its carboxylic functional groups [47]. Polymers spheres such as polystyrene were used as sacrificial templates for other air-stable cobalt nanoparticles where, through a single-step swelling process, the cobalt precursors diffused into uniform polystyrene microspheres, followed by a decomposition of the polymer-encapsulated metal complexes under an inert atmosphere at 600 °C. Ultimately, the carbon and metal oxide formed a thin shell which protected the core of the cobalt nanoparticles against further oxidation [48].

Pyun and coworkers have recently prepared phosphine oxide and amine-functionalized styrenic polymers, and used these as surfactants to mediate the growth of ferromagnetic cobalt nanoparticles [49]. The polymer moiety was capable of encapsulating the nanoparticle to form a shell, and of imparting long-term colloidal stability to the magnetic dispersions in solution, such that the 1-D structure of the assembled nanoparticles could be formed in the solid state. In addition, functionalized cobalt nanoparticles have been used as the macroinitiators for surface-initiated polymerizations when preparing magnetic polymer brush shells with an adjustable thickness [50].

Most recently, polyvinyl pyrrolidone (PVP) has been demonstrated as one of the most effective stabilizers and modifiers to prevent the agglomeration of metal nanoparticles, and to provide an elaborate control of the growth of metal nanocrystals in chemical solution synthesis, such as Ag [51], Au [52], Pd [53], and

Pt [54]. In chemical terms, the metal–PVP complex would form a coordinative bonding between the metal ions and the amide functional group in PVP. Schaaek *et al.* were the first to describe a one-pot synthesis of superparamagnetic CoPt hollow spheres when using PVP as template, and also studied the kinetic growth of hollow spheres. These hollow nanospheres, which had average diameters ranging from 10 to 50 nm, displayed single-phase fcc structures and were thermally stable up to 300 °C on a copper grid. Subsequent SQUID magnetometry measurements demonstrated ferromagnetic properties with a hysteresis loop at 5 K and with a coercivity of 980 Oe. Higher-temperature magnetic measurements indicated superparamagnetism, which was consistent with the small size of the individual nanoparticles that comprised the hollow nanostructures [55].

Guo and colleagues reported a straightforward synthesis to produce magnetic cobalt chains of hollow spheres in solution by using PVP as both a stabilizer as well as a template to direct the self-assembly of hollow spheres in solution. In the absence of PVP, only solid Co microspheres were obtained without a hollow chain structure, while the PVP adsorbed onto the surfaces of the nanoparticles prevented further aggregation and ensured a hollow structure formation [56]. The concentration and type of reducing agent used were also shown to affect the final morphology of as-obtained cobalt nanoparticles. For example, Chen and coworkers presented a unique 1-D legume-like structure of cobalt nanoparticles by using a simple, magnetic-field-induced assembly approach with the assistance of PVP [57]. Without an applied magnetic field, it was possible to produce uniform and well-distributed polymer-stabilized cobalt nanoparticles. A 1-D legume-like structure of cobalt nanoparticles was also formed via a magnetic-field-induced assembly method, in which cobalt nanoparticles were arranged along the lines of magnetic force in a head-to-tail configuration, such that the PVP molecules permanently linked the ordered 1-D structure through the interpenetration and bridging of the PVP molecule layers. Submicrometer to nanometer-sized cubic FeCo alloys with varying chemical compositions have also been prepared by refluxing iron and cobalt salt with PVP as the capping agent and ethylene glycol (EG) as the solvent and reductant [58].

Well-defined block copolymers have been widely used both in solution as micellar assemblies, or in microphase-separated thin films as templates for nanoparticle formation. Meanwhile, the uniformity of the micellar assemblies would ensure the narrow distribution of the as-obtained nanoparticles. The spatial distribution of cobalt nanocluster in PS_{25300}-b-$PMMA_{25900}$ block copolymer was investigated by performing the nucleation and growth of the metal clusters and the phase separation of the block copolymers in a homogeneous solution [59]. Due to the relatively stronger interaction of the poly(methyl methacrylate) (PMMA) block towards the cobalt metal fragments, the incorporation of the cobalt nanoclusters into the PMMA block had the effect of immobilizing the micellar structure, thus preventing the expected phase transformation to the expected lamellar morphology upon removal of the solvent, which caused the selective phase separation. Antonietti *et al.* [60] used polystyrene-block-poly(4-vinylpyridine) (PS-*b*-4VP) to produce a

bimodal distribution of both smaller superparamagnetic and larger ferromagnetic Co nanoparticles, which was attributed to the nucleation and growth of particles both inside and outside the PS-*b*-PVP micelles. Subsequently, inverse PS-*b*-2VP micelles [61] and polyacrylic acid-*b*-PS [62] have also been used to prepare well-dispersed and uniform cobalt nanoparticles, with different cobalt phases being obtained by varying the tuning process conditions. Riffle *et al*. synthesized block copolymers such as polysiloxane and polystyrene with a nitrile (–CN) group via anionic polymerization, and used this type of polymer to produce monodispersed spherical cobalt superparamagnetic and ferromagnetic cobalt nanoparticles encased in the copolymers [63]. Pierre described the synthesis of a stable cobalt colloid in the presence of a PDMS-*b*-(PMVS-*co*-PMTMS) dispersion, and subsequently calcined polymer-coated cobalt nanocomposites to form siliceous shells on the cobalt surfaces for an oxidation protection of the core [64].

16.3.3.3.4 **Hydrothermal/Solvothermal Synthesis** Hydrothermal synthesis refers to chemical reactions in aqueous solution under elevated temperatures and pressures. In a typical synthesis, the precursors and reagents are placed in a certain amount of water phase, and the mixture then heated to high temperature in an autoclave to initiate the reaction. Autoclaves with Teflon inserts are commercially available, and can be used at temperatures of up to several hundreds of degrees Centigrade, and pressures of several bar. Teflon-constructed vessels have proved to be the ideal containers under these conditions, as they are inert to both hydrofluoric acid and alkaline media, in contrast to glass and quartz. The particle size and morphogenesis can be adjusted by altering the experimental conditions, such as temperature, pH, and pressure.

Highly stable subnanometer-sized cobalt particles with an average size of 0.8 nm have been synthesized in the confined spaces within the nanopores of crystalline molecular sieves. These metallic cobalt clusters were estimated to comprise approximately 50 cobalt atoms, and to exhibit an extremely low ferromagnetic ordering temperature [65]. Besides the preparation of spherical nanoparticles, the hydrothermal approach could be used to produce a myriad of amazing nanostructures in the same way. For example, 1-D cobalt nanorods, nanowires and nanobelts have each been fabricated via this chemical route. In contrast, the cationic surfactant CTAB favored the formation of nanorods, and subsequently formed 2-D, square-shaped frames or dense multilayer nanosquares, due to the presence of a magnetic field [66]. Qian and coworkers described a sodium dodecyl benzenesulfonate-assisted hydrothermal approach to obtain single crystalline hcp-phase cobalt nanobelts [67]. Elsewhere, the introduction of citrate salts as a complexing reagent and shape modifier led to the production of single crystalline Co nanowires, under the same conditions [68]. Both, nanobelts and nanowires indicated a ferromagnetic characteristic and an enhanced coercivity value compared to the bulk Co. Nest-shaped, hollow core–shell cobalt [69], snowflake-like [70], and flower-like cobalt nanostructures [71] have all been obtained via a similar approach with an optimal modification of reductant, concentration of base, and reaction temperature. These 3-D cobalt architectures were stacked and assembled

by small hexagonal nanosheets or nanorods generated during the hydrothermal process, with the mechanism of formation being proposed rationally.

Recently, a solvothermal method has been developed in which the reaction was carried out in organic media such as alcohols, amines and ionic liquids, instead of an aqueous solution. When using organic complexes such as a metal carbonyl and acetylacetonate as feedstocks, the solvothermal method demonstrates clear advantages over its hydrothermal counterpart, as these compounds are either insoluble or are decomposed in water, with the result being an unsuccessful reaction. Similar 3-D, flowerlike Co hierarchical microspheres were obtained in ethylene glycol solution with either CTAB [72] or PVP as stabilizer [73]. The microspheres produced consisted of nanoplatelets of approximately 20 nm and 50 nm in thickness, respectively. By using Ru as heterogeneous seeds, and dual-function 1,2-propanediol as the solvent and reducing agent, a straightforward approach has been explored to synthesize 1-D Co nanostructures such as nanowires, nanorods, and nanonails in the presence of steric acid [74]. Meanwhile, 1-D CoPt nanowires have been prepared in high yields by using $Co_2(CO)_8$ and $Pt(AcAc)_2$ as the starting materials. In this case ethylene diamine, when used as the solvent, may act as a bidentate ligand and play a key role in directing the growth of CoPt nanowires at the minimum required high temperature [75]. Later, Yu *et al*. demonstrated a novel solvothermal approach for preparing stable, bracelet-like Ni–Co magnetic alloy flux-closure nanorings with tunable dimensions and lengths. Here, a high concentration of PVP could be used to stabilize the intermediate short Ni–Co nanochains, while magnetic dipole interaction favored self-assembly of the final nanorings and chains [76].

16.3.3.3.5 **Nonhydrolytic Organometallic Thermolysis** In 1993, Bawendi and coworkers demonstrated a nonhydrolytic liquid phase method for preparing semiconductor nanocrystallites, in which the organometallic precursors and other reagents were injected into high-boiling point solvent under an inert atmosphere and over a temperature range of 120 to 300 °C [77]. The as-obtained semiconductor quantum dots (QDs) had advantages over other synthetic methods, such as a high monodispersity and a good surface quality. Since that time, tremendous efforts have been made to utilize this approach in the synthesis of myriad types of nanocrystal, including as metal chalcogenides [78], metal oxides [79], and metals [80]. The sizes and morphologies of the final nanocrystals were determined by the monomer concentration, the nucleation ratio, and the crystallographic phase of the material and capping agents [81].

A new crystal ε-phase of cobalt nanoparticle was discovered following the thermal decomposition of octacarbonyldicobalt $Co_2(CO)_8$ at 110 °C in solution, and in the presence of trioctylphosphane oxide (TOPO) as coordinating ligand [3]. XRD studies indicated different patterns compared to the standard fcc and hcp structures. Typically, the ligands and surfactants could be shown to play a critical role in determining the resultant structure of the cobalt nanocrystals grown in solution at low temperatures. In 2001, Alivosatos and coworkers reported an elaborate, shape-controlled synthesis of cobalt nanocrystals via the rapid injection of $Co_2(CO)_8$

into a hot mixture of coordinating solvent containing oleic acid and TOPO. Both the hcp and ε-phases, as well as various morphologies of cobalt nanocrystals (e.g., spheres, anisotropic nanocrystals, ribbons) were successfully obtained by controlling the reaction time and the surfactant concentration [82]. Two types of surfactant that were adsorbed differentially to the nanocrystal crystallographic faces were crucial for the oriented growth of different cobalt nanocrystals. As extension of these studies, the same group further explored the synthesis of hcp Co disk-shaped nanocrystals in the presence of a linear amine, which was found to enable the easier formations of disk and also a higher yield [83]. In order to acquire some mechanistic insight into the decomposition process of $Co_2(CO)_8$ to final cobalt nanocrystals, an *in situ* ATR-FTIR study was carried out very recently. Subsequently, several intermediate carbonylated species have been detected and a tentative mechanism has been proposed for the formation of cobalt colloids from the homogeneous molecular precursors. It was shown that the surfactant could influence the decarbonylation rate, and also participate as a ligand in transient cobalt species to produce the final cobalt nanoparticles [84]. Moreover, when the influence of the surfactants was investigated in determining the size and shape of cobalt nanoparticles, the results showed that amine surfactant led to the preferential formation of flat or spherical particle shapes, while TOPO led to the production of monodispersed particles [85].

Alternative cobalt sources have also been monitored for the production of high-quality cobalt nanoparticles via a nonhydrolytic approach. For this, $CoCl_2$ [86], CoI_2 [87], $Co(Ac)_2$ [88] and $Co(AcAc)_3$ [89] have each been reduced with lithium, superhydride, or long-chain 1,2-alkyldiols in the presence of fatty acid and trialkylphosphine stabilizers, and resulting in the production of monodisperse cobalt nanocrystals with tunable size, crystal structures, and morphologies. Dumestre *et al*. reported the preparation of uniform cobalt nanoparticles, nanorods, and nanowires via the thermal decomposition of $[Co(\eta^3\text{-}C_8H_{13})(\eta^4\text{-}C_8H_{12})]$ in a hydrogen atmosphere [90]. Kumar's group also investigated the influence of alkyne-bridged $Co_2(CO)_8$ (ADH) on the formation of cobalt nanoparticles, compared to the standard $Co_2(CO)_8$ [91]. The results showed that cobalt nanoparticles obtained via ADH were larger in size, had a low polydispersity, with an fcc structure and good anti-oxidant properties, whereas those produced with standard $Co_2(CO)_8$ had a hcp structure, a high polydispersity and were less stable against oxidation. Very recently, the same group conducted a series of systematic studies regarding the new role of surfactants in influencing the reaction pathways for the formation of cobalt nanoparticles prior to nucleation. Varying the nature of the surfactants led to differences in both the reaction pathways and the reaction intermediates, so as to produce Co nanoparticles with very different properties [92].

The structural effects, thermal stability, and magnetic properties of colloidal cobalt nanoparticles have been investigated intensely via the self-assembly of spherical cobalt nanoparticles on different flat substrates, such as silicon nitride, silicon oxide and silicon, through the slow evaporation of a colloidal solution [93–95] or via magnetic field-induced assemblies [96]. These orderly patterned cobalt nanoparticles showed not only stability against oxidation at room

temperature but also improved magnetic properties compared to those of the cobalt nanoparticles when powder-compacted into a capsule or diluted with wax. The group of Wei demonstrated the formation of bracelet-like rings from resorcinarene-stabilized cobalt nanoparticles via a dipole-directed self-assembly and an evaporation-driven hole formation in viscous wetting layers. Both, chain and bracelet formation were shown to be directed by cooperative dipolar interactions, which would compete with nondirectional van der Waals interactions at close range [97]. When the phase transfer from nonpolar solvent to polar media was studied, the Co nanoparticle prepared via an organometallic approach was generally hydrophobic and readily dispersible in nonpolar solvent, rather than in polar media such as water or alcohol. Krishnan *et al.* demonstrated a means of transferring this hydrophobic nanoparticle into the water phase, without changing the particle size. For this, tetramethylammonium hydroxide pentahydrate acted as the phase transfer agent, while 12-aminododecanoic acid was used as a stabilizing agent to enrich the nanoparticle surfaces with negative COO^- groups, which stabilize the particle in water by electrosteric repulsion [98]. Amphiphilic polymers could also be exploited for the aqueous phase transfer of as-synthesized Co nanoparticles, the existence of which has already been proven in other nanocrystals prototypes [99].

Cobalt nanocomposites, including metal or semiconductor structures, have been likewise extensively investigated by using an efficient thermolysis approach. Well-defined Co–Pt nanoalloys with solid solution and core–shell type were produced via transmetalation reactions between $Co_2(CO)_8$ and $Pt(hfac)_2$ precursors. The simultaneous reaction of cobalt and platinum sources resulted in the formation of "solid-solution"-type alloys such as $CoPt_3$ and CoPt nanoparticles, while the reaction of presynthesized Co nanoparticles with $Pt(hfac)_2$ produced "Co_{core}–Pt_{shell}"-type nanoalloys [100, 101]. Highly monodisperse crystalline $CoPt_3$ nanoparticles via the reduction of $Co_2(CO)_8$ and $Pt(AcAc)_2$ have been synthesized in the presence of 1-adamantanecarboxylic acid, which provided a superior stabilization of Co–Pt alloy nanocrystals than did other, more conventional capping agents [102]. A slow evaporation of the colloidal dispersion led to the creation of a multilayered, self-assembled, AB_5-type superlattice with two different particle sizes and microsized facetted colloidal crystals consisting of monodisperse $CoPt_3$ nanocrystals. Furthermore, rational studies of the effects of different reaction conditions on the final particle size have disclosed that the size might be precisely tuned and reproduced without an Ostwald ripening stage by controlling the balance between the rates of nucleation and growth [103]. Ligand exchange with these nanocrystals may cause changes in stoichiometry and morphologies, due to the preferential dissolution of one metal part [104]. CoPt nanorods prepared in ionic liquids [105], 3-D ferromagnetic CoPt polypod-like nanostructures [106] and novel nanostructures composed of Co nanocrystals coated with QDs (CdSe) with bifunctional magnetic and optical properties, have also been reported [107].

Notably, at the same time, new and versatile technologies for Co nanoparticle synthesis have been explored, such as electrochemical [108] or sonochemical [109] microwave-assisted [110], microfluidic [111], and electrospinning [112]. Although

these methods have been less widely studied than the aforementioned major approaches, they provide not only alternative pathways but also certain advantages in terms of the potential scale-up of production and streamlining of the processes.

16.3.4 Summary and Outlook

The aim of this section was to outline the ongoing research activities with cobalt nanoparticles, focusing in particular on the synthetic processes. At present, many synthetic approaches have been developed for the preparation of cobalt nanomaterials, with orderly assembled cobalt nanostructures with diameter in the range of one to tens of nanometers and well-controlled dimensions being realized via currently available synthetic technologies. A stable cobalt nanoparticle dispersion could be produced either via a fast reduction or a rapid thermal decomposition of metal precursors in the presence of stabilizing agents, which would control the growth of nanoparticles and avoid the formation of cobalt aggregates. In addition to individual cobalt nanoparticle synthesis, multicomponent cobalt-related nanocomposites have been fabricated in order to improve cobalt stability, to import new functions/features or to enhance the performance of cobalt-based system. The surfactant type, stabilizer concentration, molar ratio, pH value, loading sequence, reaction temperature and solvent media are paramount parameters for determining the particle size, crystal phase, composition and morphologies of as-synthesized nanoparticles. Although the commercial applications of cobalt nanoparticles are still limited, significant progress has been made during the past few years, such that industrial applications of this powerful and fascinating nanomaterial will undoubtedly emerge during the near future.

16.4 Magnetic Properties of Co Nanoparticles

16.4.1 Introduction

An understanding of the magnetic properties of nanometer-scale particles is a very important issue for both fundamental research and many technical applications [2, 113, 114]. Magnetic nanoparticles have been investigated for potential applications as the active components of ferrofluids, recording tapes, recording media, hard/soft-coupled permanent magnets, nanocrystalline soft magnets, as biomedical materials such as drug-carriers, and also as catalysts [115–120]. Whilst these diverse technological applications have formed the focus of extensive research investigations, it is also important to appreciate that magnetic nanoparticles are themselves also used as research tools in areas of materials physics, geology, biology, and medicine.

The properties of materials composed of magnetic nanoparticles result from both the intrinsic properties of the particles and the interactions between them [121, 122]. The intrinsic magnetic properties of nanoparticles are heavily influenced by the finite size and surface effects, the relevance of which increases as the particle sizes decrease. Finite size effects are due to the nanometer size of the particles, which permits particles to change from multidomain to single domain, such that the ferromagnetic particle will behave like a paramagnet. Such finite size effects even permit nanoparticles to demonstrate macro-scope quantum tunneling of magnetization if the particle size is sufficiently small. A variety of finite size effects occur in magnetic materials [121]. Surface effects are related to the symmetry breaking of the crystal structure at the boundary of each particle. Hence, as the particle size decreases, the surface atoms will become a very large proportion of a nanoparticle, which in turn implies that the surface and interface effects become increasingly important. For example, for fcc cobalt with a diameter of approximately 1.6 nm, about 60% of the total number of spins are surface spins [123]. Yet, because of the large surface atoms/bulk atoms ratio of the nanoparticles, the surface spins make an important contribution to the magnetization. The local breaking of symmetry may lead to changes in the band structure, lattice constant or/and atom coordination. Indeed, under these conditions some surface- and/or interface-related effects may occur, such as enhanced anisotropy, increased moment and, under certain conditions, core–surface exchange anisotropy. Because the surface effect is due to the local symmetry break and/or any change of the local atom coordination in nanoparticles, the coating of nanoparticles with metals or other materials may alter not only the anisotropy energy but also the magnetic moment.

The finite size and surface effects (intrinsic effects) and interaction in nanometer particles may manifest through a wide variety of anomalous magnetic properties with respect to those of bulk materials, and these will be discussed in detail in the following sections. First, we will review the intrinsic effects starting from the finite size effect – how size changes the particle from multidomain to single domain, how the single-domain particle reverse under magnetic field, why small nanoparticles show superparamagnetic behavior, and how to probe such behavior. The surface effects will then be discussed – how the surface atoms alter the particle anisotropy and magnetic moments, and how a cover layer can further modify the anisotropy energy and magnetic moment. Details of exchange coupling between the core and the oxide shell of nanoparticles will also be discussed.

16.4.2 Finite Size Effects

16.4.2.1 Size-Dependent Crystalline Structure

Cobalt nanoparticles may occur in multiple crystal phases, and this can result in large differences in the magnetic moment and crystalline anisotropy. This appears to be a size effect which is related to the balance of surface and bulk free energies

for the different possible crystal structures, and therefore depends on the particle size and matrix material. Cobalt nanoparticles generated by high-pressure sputtering have been shown [124] to undergo a transition from hcp to fcc below about 300 Å. The bulk equilibrium phase at room temperature is hcp-Co, whereas fcc-Co is a high-temperature phase that is stable above 695 K. Kitakami *et al.* [124] argued that the hcp-Co to fcc-Co transition as a function of size is due to the lower surface energy of the fcc-Co phase. In support of the size effect hypothesis, these authors showed that annealing above the bulk phase transition temperature and slow cooling does not convert the nanoparticles to hcp-Co. As the moment of the two Co phases differs by only about 2%, the principal effect on the magnetic behavior should be a much smaller magnetocrystalline anisotropy for the fcc-Co phase. This would be an important consideration when using Co nanoparticles in a permanent magnet material or recording media, as the anisotropy fields for fcc-Co and hcp-Co are approximately 500 Oe and 10 kOe, respectively. Michels *et al.* reported mixed phases of hcp-Co and fcc-Co nanocubes with an average cube-edge of approximately 50 nm [125], whereas others have shown that when the Co particle size is <20 nm, only fcc-Co phase were found [65, 82, 83, 126–128]. These results further support the size-dependent crystalline structure effects.

16.4.2.2 Size-Dependent Magnetic Domain Structure and the Reversal of Co Nanoparticles

It is known that the magnetization behavior of a magnetic material is highly size-dependent. When a large magnetic particle, which contains mobile domain walls, is subjected to a magnetic field, its domain walls will move to minimize the free energy of the system and the magnetization reversal proceeds via domain-wall displacement. For domain motion, the switching field H_{SW} is angle-dependent and follows the following equation: $H_{SW} = H_0/\cos(\theta_H)$ (where θ_H is the applied field angle respective to the direction of magnetization). When the size of the particle decreases below a critical size $-d_c$, the domain wall disappears and the particles become single domain due to the fact that the energy cost to produce a domain wall is greater than the corresponding reduction in the magnetostatic energy. The critical size depends on the saturated magnetization, anisotropy energy and exchange interaction between the individual spins, which can be estimated by $d_c = 18\dfrac{(AK_u)^{1/2}}{\mu_0 M_S^2}$ (large K_u) and $d_c = \sqrt{\dfrac{36A}{\mu_0 M_S^2}\left[\ln\left(\dfrac{d_c}{a}\right)-1\right]}$ (small K_u) (K_u is the anisotropy constant, M_S is saturated magnetization, and A is the exchange coupling constant). For smaller anisotropy FCC-Co particles (K_u~7×10^4 J m^{-3}), the critical size of the single domain is 30 nm, while for the larger anisotropy HCP-Co particles (K_u~4.5×10^5 J m^{-3}), the critical size is 65 nm. Therefore, the magnetic nanoparticles normally investigated are single-domain in nature. The magnetic reversal of such particles with a single domain had been described by the Stoner–Wohlfarth (S–W) model in a very simple theory, namely the uniform rotation model. When investigating experimentally the magnetic reversal of magnetic nanoparticles, the angle dependence of magnetic reversal are often used.

16.4.2.3 Thermal-Activation Effect on the Moment and Coercivity

The S–W model does not cover thermally activated behavior. In fact, the magnetic moment of single-domain ferromagnetic particles will decay towards thermal equilibrium under the effect of thermal energy. For a single-domain ferromagnetic particles with uniaxial anisotropy at zero applied field and a certain temperature (T), there are two minimum energy states separated by a energy barrier: $E_B = \frac{K_u V}{k_B T}$, where k_B is Boltzmann's constant. When a magnetic field H is applied to the nanoparticles, E_B can be approximated by the following expression:

$$E_B = \frac{K_u V}{k_B T}\left(1 - \frac{H}{H_0}\right)^n \tag{16.5}$$

$$\text{with} \quad H_0 = 2xK_u/M_S \tag{16.6}$$

The field H_0 is defined simply as the field at which the energy barrier is zero. The external applied field will decrease the energy barrier until switching occurs, and thus H_0 is also called the "switching field", H_{SW}. Therefore, x can be expressed by:

$$x = \left(\sin^{\frac{2}{3}}\theta + \cos^{\frac{2}{3}}\theta\right)^{-\frac{3}{2}} \tag{16.7}$$

Preiffer has shown that the S–W model yields the approximation for n: [129]

$$n = 0.86 + 1.14x \tag{16.8}$$

When H is along the anisotropy axis of the particles, $x = 1$ and $n = 2$. For an assembly of noninteraction particles, the anisotropy axis is 2-D randomly oriented, which corresponds to $\theta = 30$–$35°$; $n = 1.43$. Victora has reported the theoretical calculation that, with the field not aligned with the anisotropy axis, n would be expected to be 1.5 for every general anisotropy, even including interaction [130]. Generally, the exponent $n = 1.5$ is used to evaluate thermal fluctuation for the nanoparticle with H not aligned with its anisotropy axis [131].

The probability of crossing the energy barrier per unit time can be expressed by:

$$\frac{1}{\tau} = f_0 \exp\left(-\frac{E_B}{k_B T}\right) \tag{16.9}$$

where τ is known as the "characteristic relaxation time". The moment $M(t)$ of the noninteracting particles assembly then decays exponentially with time from the initial saturated moment M_0 as:

$$M(t) = M_0\left[2\exp\left(-\frac{t}{\tau}\right) - 1\right] \tag{16.10}$$

Due to thermal activation effects, the coercivity of a nanoparticle is dependent on the measuring time. Sharock [131] pointed out that the coercivity as function of time t, where t is the time elapsed to cause switching half of the moments, can be expressed as:

$$H_C(t) = H_0\left\{1-\left[\frac{k_BT}{K_uV}\ln\left(\frac{f_0t}{\ln 2}\right)\right]^{1/n}\right\} \tag{16.11}$$

It can be seen from Equation 16.11 that $H_C(t)$ decreases with increasing t and the smaller (K_uV/k_BT), the higher rate of $H_C(t)$ decreases with increasing t.

16.4.2.4 Superparamagnetism in Co Nanoparticle System and its Direct Investigation

According to Equation 16.9, when the energy barrier of the particle is decreased to certain value, the magnetization of the particle is free to align with the field at a given temperature and certain measuring time window. This state is referred to as "superparamagnetic" because the particle behaves similarly to the paramagnetic spin but with a much larger magnetic moment. For example, if an arbitrary measurement time is taken as be $\tau = 100\,\mathrm{s}$ and $f_0 = 10^9\,\mathrm{s}^{-1}$, then the condition for superparamagnetism is

$$K_uV = 25k_BT \tag{16.12}$$

However, if the particles of a certain size were cooled below a critical temperature, the spins of the particles would be blocked (they would not relax during the time of measurement), and thus hysteresis would appear and superparamagnetism disappear. This critical temperature is termed the "blocking temperature" (T_B), and is defined as:

$$T_B = \frac{K_uV}{25k_B} \tag{16.13}$$

The magnetization of a particle, $M(B,T)$ is described by the Langevin function:

$$\begin{aligned} M(H,T) &= M_S(T)\left[\coth\left(\frac{M_S(T)VH}{k_BT}\right)-\frac{k_BT}{M_S(T)VH}\right] \\ &= M_S(T)L\left(\frac{M_S(T)VH}{k_BT}\right) \end{aligned} \tag{16.14}$$

where $M_S(T)$ is the spontaneous magnetization with temperature. The magnetization curves at different temperatures fall into a single function when the magnetization is plotted against the applied magnetic field divided by temperature (H/T).

An imperfect H/T superposition can result from a broad distribution of particles size, changes in the spontaneous magnetization of the particles as a function of temperature, or anisotropy effects [132]. The magnetization of superparamagnetic particles may be used to determine the mean particle size and width of the size distribution when a distribution form of the particles was given [133, 134].

The temperature-dependent magnetization, $M(T)$, of a particle with given size exhibits a peak in the zero-field-cooled (ZFC) magnetization at T_B, but exhibits a gradual decrease in the field-cooled (FC) magnetization. In particles assembly, the distribution of particle size may also cause a distribution of the blocking temperature [135–137]. Other than the ZFC and FC curve characterizations of superparamagnetism, some direct investigations of superparamagnetism have also been proposed [94]. Woods *et al*. suggested the direct probing of superparamagnetism in films of self-assembled cobalt nanoparticles by measuring the spontaneous magnetic noise arising from these films as a function of temperature [94]. Nanoparticle spin flips, induced by thermal energy, are directly sensed by a micro-SQUID technique, providing statistical information on the magnetic properties of millions of particles in the array. In this way, not only can the average anisotropy energy and width be determined, but the entire magnetic anisotropy energy distribution can also be extracted. This technique is a complete "magnetic fingerprint".

For superparamagnetic particles without interparticle interaction and having a simple bistable state, the magnetic noise power measured at temperature T, cyclic frequency ω, and distance d away, using a micro-SQUID method, is [138, 139]:

$$S_B(\omega, T) = \left(\frac{\mu_0}{4\pi}\frac{MV}{d^3}\right)^2 \frac{\tau}{1+\omega^2\tau^2} \tag{16.15}$$

where M is the particle magnetization, V is the particle volume, and τ is the average cyclic flipping time for the moment.

For a distribution $D(U)$ of particle anisotropy energies, one finds for the noise power (approximating with use of an average prefactor to the Lorentzian in Equation 16.15):

$$S_B(\omega, T) \propto \int_0^\infty \frac{\tau_0 e^{U/k_BT}}{1+\omega^2\tau_0^2 e^{2U/k_BT}} D(U)dU \tag{16.16}$$

Based on Equation 16.16, the noise power is a function of cyclic frequency and temperature. It was found from a plot of noise power as a function of frequency from a film of 5 nm Co nanoparticles at various temperatures, that the noise decreases monotonically in the frequency window for each particular temperature, having an approximate form of $S_B \sim f^{-\alpha}$.

Based on Equation 16.16, the anisotropy energy distribution of Co nanoparticles can be found from the noise power according to:

$$D(-k_BT\log(\omega\tau_0)) \propto \frac{2\omega}{\pi k_BT} S_B(\omega, T) \tag{16.17}$$

The noise power data as a function of temperature for both the 3 nm and 5 nm samples were used to derive their anisotropy energy distributions. At each frequency, the distribution was calculated and normalized to make the total probability under the distribution equal to unity. It was found from these data that the distribution for the 3 nm particles reached a peak at 4.35×10^{-21} J, and had a full-width half maximum (FWHM) of approximately 110%, and a tail at high energies. For the 5 nm particles, the distribution was more symmetric, with a peak at 1.22×10^{-20} J, and a FWHM of approximately 64%. If it was assumed that the energy peak for each sample was that of a single-domain, spherical nanoparticle of nominal diameter, then $K_{3nm} = 3.08 \times 10^5\,J\,m^{-3}$ and $K_{5nm} = 1.87 \times 10^5\,J\,m^{-3}$, which was in general agreement with other values derived for mt-fcc Co nanoparticles [140, 141].

16.4.3 Surface Effects of Co Nanoparticles

16.4.3.1 Moment Enhancement of Surface Atoms

The effects of the coordination numbers and local environment of Fe, Co, Ni atoms on magnetic moments were investigated by confining the Fe, Co, Ni atoms to various structures such as chains, surface, layers and crystals, and introducing impurities, vacancies and vacancy complexes using *ab-initio* tight-binding theory [142]. Liu *et al*. found that the magnetic moment per atom increased as the number of magnetic atoms in the near-neighbor shell (coordination number) decreased, this being due to the decrease in the overlap of nearby atomic orbitals as the coordination numbers decreased. The effect of vacancies on the nearest-neighbor magnetic atom tended to enhance this magnetic moment, again due to a decrease in the coordination number. The magnetism of free Fe, Co, Ni clusters consisting of several atoms to several hundreds of atoms was investigated using the Stern–Gerlach deflection technique. These clusters show typical superparamagnetic behavior [143–145]. The magnetic moment per atom increases with the applied field and cluster size and is higher than the bulk value.

Respaud *et al*. studied the magnetic moment enhancement of Co nanoparticles of sizes 1.5 nm and 2.0 nm [146]. The monodispersed nanoparticles of cobalt were prepared by an original method, using the decomposition under hydrogen of an organometallic precursor in the presence of a stabilizing polymer [147]. Two colloids (Coll-I and Coll-II) were obtained by changing the organometallic concentration in the polymer. Observations with high-resolution transmission electronic microscopy (HRTEM) showed the Co particles to be well isolated and regularly dispersed in the polymer, but with a very narrow size distribution centered around 1.5 nm (Coll-I) and 2 nm (Coll-II) diameter. These particles were superparamagnetic above the T_B of 9 K (Coll-I) and 13.5 K (Coll-II). In order to precisely determine the values of $<\mu_{Co}>$, magnetization loops of up to 5 T were measured, while for temperatures below T_B [148] a hysteristic behavior was observed. In order to confirm that saturation was indeed achieved, an initial magnetization curve up to 35 T at 4.2 K was measured, with the results being analyzed by considering

the law of approach to saturation of an assembly of particles with uniaxial anisotropy:

$$M(B) = M_S(T)\left\{1 - \frac{k_B T}{M_S(T)\nu B} - \frac{4}{15}\left[\frac{K_a}{M_S(T)B}\right]^2\right\} \tag{16.18}$$

The authors attempted to fit the magnetization curves up to 35 T with Equation 16.18, and included in Equation 16.18 a variation of the magnetic moment with the applied magnetic field $M_S(B)$. By this, the average magnetic moment per cobalt ($<\mu_{Co}(B)>$) atom could be deduced. $<\mu_{Co}(B)>$ presented a variation in two stages for the two samples: a rapid stage in fields up to 3–4 T, and a quasilinear stage in fields up to 35 T. These increases were more significant for the smallest particles (Coll-I with diameter of 1.5 nm).

16.4.3.2 Anisotropy Enhancement of Co Nanoparticles

It has long been discussed that the isotropic magnetic moment of a free atom is shown to develop giant magnetic anisotropy energy, due to symmetry reduction at an atomically ordered surface. Single cobalt atoms, when deposited onto platinum (111), are found to have a magnetic anisotropy energy of 9 millielectron volts (meV) per atom arising from the combination of unquenched orbital moments (1.1 Bohr magnetons) and strong spin–orbit coupling induced by the platinum substrate [8]. By assembling cobalt nanoparticles containing up to 40 atoms, the magnetic anisotropy energy is further shown to be dependent on single-atom coordination changes.

Gambardella *et al*. deposited the Co atoms and particles in ultrahigh vacuum by using MBE on a clean Pt(111) surface. When the size effects on the magnetic anisotropy energy were studied, it was found that a clear increase in the angular moment, *L*, and magnetic anisotropy energy (MAE), *K*, was observed as the particle size was reduced. The enhancement of MAE was mainly due to the unquenched angular moment and the strong coupling between the spin moment and the angular moment. A strong enhancement of magnetic anisotropy perpendicular to the film plane was also observed in very thin Co films, which results from similar effects [8]. These have also been observed by many other research groups [149–152].

It has been shown above that, for very small clusters, the magnetic properties become dominated by the properties of the surface atoms [152]. It is logical then, that *K* is affected by the interaction of these atoms with their surroundings. This effect has been observed for thin films, the anisotropy and magnetization of which depend heavily on the type of substrate on which they grow [153, 154]. For clusters, the magnetic properties would be modified by the surroundings, such as a metal capping layer [155]. Such modification of magnetic properties by metal capping layers has been demonstrated by Luis *et al*. [155], who prepared nanometer-sized Co clusters by sequential sputter deposition of Al_2O_3 and Co layers on a Si substrate. The capped clusters were easily prepared by depositing a 1.5 nm-thick layer of a noble metal M (Cu or Au) onto the preformed clusters [156, 157]. In order to

obtain good signal quality, the samples were usually made by piling up a number (N) of these Co/Al_2O_3 or $Co/M/Al_2O_3$ repetition units. It was found from the hysteresis loops that the capping process makes the loops significantly broader: for $D = 1.8$ nm, the coercive field $\mu_0 H_c$ was found to increase from 50 mT for clusters in alumina to 73 mT for Cu-capped clusters, and to 320 mT for Au-capped clusters. These data indicated that capping with a noble metal makes the clusters magnetically harder; the same trend was observed for samples with varying cluster size D.

The K_u of uncapped and capped clusters has also been studied as a function of D. In agreement with previous results [153], K_u largely exceeds the bulk value for fcc Co and increases as D decreases; this size dependence indicates that K_u is enhanced at the cluster surface. A separation between the surface and core atoms has proven useful in our understanding of the electronic structure of Co and other fcc metal (Au, Pt) clusters. Within this simple core–shell picture, K_u is described by

$$K_u = f \times K_{surface} + (1 - f) K_{bulk}, \tag{16.19}$$

where $K_{surface}$ refers to surface atoms, $K_{bulk} = 7 \times 10^4$ J m^{-3} is the contribution arising from the bulk anisotropy of fcc Co [152], and $f \approx 1 - (1 - a/D)$, where $a = 0.4$ nm and is the fraction of surface atoms in a fcc cluster. For the smallest clusters (1 nm), almost 80% of the atoms (of order 55) lie at the cluster's interface with the surrounding matrix. This simple model enables us to obtain an estimate for $K_{surface}$ and to study how it is modified by the capping. For uncapped clusters, $K_{surface} \approx 25\, K_{bulk}$, while for Cu-capped clusters $K_{surface} \approx 40\, K_{bulk}$, that is, about 60% larger than for clusters in pure alumina, whereas capping with Au makes it almost three times larger ($K_{surface} \sim 70\, K_{bulk}$).

16.4.3.3 Exchange Bias Between the Core and the Oxidized Surface in Co Nanoparticles

Exchange bias refers to the unidirectional pinning of a ferromagnetic (FM) layer by an adjacent antiferromagnetic (AF) layer. The exchange coupling of ferromagnetic and antiferromagnetic films across their common interface causes a shift in the hysteresis loop. Unidirectional anisotropy and exchange bias can be qualitatively understood by assuming an exchange interaction at the AF/FM interface [158]. When materials with FM/AF interfaces are cooled through the Néel temperature (T_N) of the AF, an anisotropy is induced in the FM [159, 160] (with the Curie temperature of the FM, T_C, larger than T_N).When a field is applied in the temperature range $T_N < T < T_C$, the FM spins align with the field, while the AF spins remain random. When cooling to $T < T_N$, in the presence of the field, the AF spins next to the FM align ferromagnetically to those of the FM due to the interaction at the interface (assuming ferromagnetic interaction). The other spin planes in the AF "follow" the AFM order so as to produce zero net magnetization. When the field is reversed, the FM spins start to rotate. However, for sufficiently large AF anisotropy, the AF spins remain unchanged. Therefore, the FM/AF interfacial interaction tries to align the FM spins with the AF spins at the interface

and keep them in their original position. Because an extra field is needed to overcome the interfacial coupling, the field needed to completely reverse an FM layer will be larger. Therefore, the FM spins have one single stable configuration – that is, the anisotropy is unidirectional. However, once the field is rotated back to its original direction, the FM spins will start to rotate at a smaller field, due to the ferromagnetic interaction with the AF spins. The material behaves as if there was an extra (internal) biasing field. Therefore, the FM hysteresis loop is shifted in the field axis – that is, exchange bias. This phenomenon was first discovered in partially oxidized Co particles in 1956 by Meiklejohn and Bean [161], and subsequently investigated by many other research groups [162–164].

16.4.4 Summary

In this section, we have attempted to review some of the magnetic properties of Co nanoparticles and their assembly, including finite size effects and surface effects. Due to there being too many aspects of magnetic nanoparticles, it was not possible to cover the topic in an exhaustive manner, and a selection of the most important properties was thus chosen to provide information to the reader. Nonetheless, it is hoped that the stimulating conjunctures in this chapter will encourage further exploration of this exciting area.

16.5 Summary and Outlook

In this chapter, an overview on the synthesis and characterization of cobalt-based nanoparticles has been provided. Various techniques used to characterize the nanoparticles have been presented, together with details of their synthesis and a discussion of their magnetic properties. As the field of nanotechnology continues to gather momentum on a daily basis, the potential applications of these materials will clearly lead to intensive research being conducted in this area for many years to come. Although, at present the full potential of these nanoparticles may not yet have been realized (e.g., as data storage media), it is strongly believed that areas such as biotechnology will, in time, utilize these nanoparticles in a highly effective manner.

References

1 Kronmüller, H. and Parkin, S. (2007) *Handbook of Magnetism and Advanced Magnetic Materials*, John Wiley & Sons, Ltd, Chichester.

2 Lu, A.H., Salabas, E.L. and Schüth, F. (2007) Magnetic nanoparticles: synthesis, protection, functionalization, and application. *Angewandte Chemie, International Edition in English*, **46** (8), 1222–44.

3 Dinega, D.P. and Bawendi, M.G. (1999) A solution-phase chemical approach to

a new crystal structure of cobalt. *Angewandte Chemie, International Edition in English*, **38** (12), 1788–91.

4 Napper, D.H. (1983) *Polymeric Stabilization of Colloidal Dispersions*, Academic Press, London.

5 (a) Hackley, V.A., Somasundaran, P. and Lewis, J.A. (2002) *Polymers in Particulate System*, Marcel Dekker, New York; (b) Hui, C.L., Li, X.G. and Hsing, I.M. (2005) Well-dispersed surfactant-stabilized Pt/C nanocatalysts for fuel cell application: dispersion control and surfactant removal. *Electrochimica Acta*, **51**, 711–19.

6 Lin, Y. and Finke, R.G. (1994) Novel polyoxoanion- and Bu_4N^+-stabilized, isolable, and redissolvable, 20–30-ANG Ir300–900 nanoclusters: the kinetically controlled synthesis, characterization, and mechanism of formation of organic solvent-soluble, reproducible size, and reproducible catalytic activity metal nanoclusters. *Journal of the American Chemical Society*, **116** (18), 8335–53.

7 (a) Roucoux, A., Schulz, J. and Patin, H. (2002) Reduced transition metal colloids: a novel family of reusable catalysts? *Chemical Reviews*, **102** (10), 3757–78; (b) Cushing, B.L., Kolesnichenko, V.L. and O'Connor, C.J. (2004) Recent advances in the liquid-phase syntheses of inorganic nanoparticles. *Chemical Reviews*, **104** (9), 3893–946; (c) Burda, C., Chen, X.B., Narayanan, R. and El-Sayed, M.A. (2005) Chemistry and properties of nanocrystals of different shapes. *Chemical Reviews*, **105** (4), 1025–102.

8 Gambardella, P., Rusponi, S., Veronese, M., Dhesi, S.S., Grazioli, C., Dallmeyer, A., Cabria, I., Zeller, R., Dederichs, P.H., Kern, K., Carbone, C. and Brune, H. (2003) Giant magnetic anisotropy of single cobalt atoms and nanoparticles. *Science*, **300**, 1130–3.

9 Chung, B.X. and Liu, C.P. (2004) Synthesis of cobalt nanoparticles by DC magnetron sputtering and the effects of electron bombardment. *Material Letters*, **58** (9), 1437–40.

10 Ciriaa, M., Arnaudasa, J.I., Huttel, Y., Gomezb, H., Cebolladab, A. and Armellesand, G. (2007) Magnetic and topographic correlations in Co nanoparticles. *Journal of Magnetism and Magnetic Materials*, **316** (2), e787–90.

11 Presaa, B., Matarranz, R., Clavero, C. and Garcia-Martin, J.M. (2007) Morphological and magnetic properties of Co nanoparticle thin films grown on Si_3N_4. *Journal of Applied Physics*, **102** (5), 053901–7.

12 Newman, D.M., Wears, M.L., Jollie, M. and Choo, D. (2007) Fabrication and characterization of nano-particulate PtCo media for ultra-high density perpendicular magnetic recording. *Nanotechnology*, **18** (20), 205301.

13 Xu, Y.H. and Wang, J.P. (2008) Direct gas-phase synthesis of heterostructured nanoparticles through phase separation and surface segregation. *Advanced Materials*, **20** (5), 994–9.

14 Yang, J.Y., Yoon, K.S., Choi, W.J., Do, Y.H., Kim, J.H., Kim, C.O. and Hong, J.P. (2007) Cobalt metal nanoparticles embedded in SiO_2 dielectric layer for the application of nonvolatile memory. *Current Applied Physics*, **7** (2), 147–50.

15 (a) Gross, M.E., Kranz, K.S., Brasen, D. and Luftman, H. (1988) Organometallic chemical vapor deposition of cobalt and formation of cobalt disilicide. *Journal of Vacuum Science Technology B*, **6** (5), 1548–52; (b) Dormans, G.J.M., Meekes, G.J. and Staring, E.G.J. (1991) OMCVD of cobalt and cobalt silicide. *Journal of Crystal Growth*, **114** (3), 364–72; (c) Longergan, A.R., Nuesca, G., Goldberg, C., Peterson, G., Kaloyeros, A.E., Arkles, B. and Sullivan, J.J. (2001) Interlayer mediated epitaxy of cobalt silicide on silicon (100) from low temperature chemical vapor deposition of cobalt formation mechanisms and associated properties. *Journal of the Electrochemical Society*, **148** (1), C21–7.

16 Choi, H. and Park, S. (2003) Liquid cobalt (I) hydride complexes as precursors for chemical vapor deposition. *Chemistry of Materials*, **15**, 3121–4.

17 (a) Lee, J., Yang, H.J., Lee, J.H., Kim, J.Y., Nam, W.J., Shin, H.J., Ko, Y.K., Lee, J.G., Lee, E.G. and Kim, C.S. (2006) Highly conformal deposition of pure Co

films by MOCVD using $Co_2(CO)_8$ as a precursor. *Journal of the Electrochemical Society*, **153** (6), G539–42; (b) Lee, K., Park, T., Lee, J., Kim, J., Kwak, N., Yeom, S. and Jeon, H. (2008) Characteristics of cobalt films deposited by metal organic chemical vapor deposition method using dicobalt hexacarbonyl *tert*-butylacetylene. *Japanese Journal of Applied Physics*, **47**, 5396–9.

18 (a) Premkumar, P.A., Turchanin, A. and Bahlawane, N. (2007) Effect of solvent on the growth of Co and Co_2C using pulsed-spray evaporation chemical vapor deposition. *Chemistry of Materials*, **19** (25), 6206–11; (b) Premkumar, P.A., Bahlawane, N. and Hoinghaus, K.K. (2007) CVD of metals using alcohols and metal acetylacetonates, Part I: optimization of process parameters and electrical characterization of synthesized films. *Chemical Vapor Deposition*, **13** (5), 219–26.

19 Eastoe, J., Hollamby, M.J. and Hudson, L. (2006) Recent advances in nanoparticle synthesis with reversed micelles. *Advances in Colloid and Interface Science*, **128–130**, 5–15.

20 Petit, C. and Pileni, M.P. (1997) Nanosize cobalt boride particles: control of the size and properties. *Journal of Magnetism and Magnetic Materials*, **166** (1–2), 82–90.

21 Petit, C., Taleb, A. and Pileni, M.P. (1998) Self-Organization of magnetic nanosized cobalt particles. *Advanced Materials*, **10** (3), 259–61.

22 Petit, C., Taleb, A. and Pileni, M.P. (1999) Cobalt nanosized particles organized in a 2D superlattice: synthesis, characterization, and magnetic properties. *The Journal of Physical Chemistry B*, **103** (11), 1805–10.

23 Lisiecki, I., Albouy, P.A. and Pileni, M.P. (2003) Face-centered-cubic supracrystals of cobalt nanocrystals. *Advanced Materials*, **15** (9), 712–16.

24 Lisiecki, I., Albouy, P.A. and Pileni, M.P. (2004) "Supra" crystal: control of the ordering of self-organization of cobalt nanocrystals at the mesoscopic scale. *The Journal of Physical Chemistry B*, **108** (52), 20050–5.

25 Lisiecki, I., Parker, D., Salzemann, C. and Pileni, M.P. (2007) Face-centered cubic supra-crystals and disordered three-dimensional assemblies of 7.5 nm cobalt nanocrystals: influence of the mesoscopic ordering on the magnetic properties. *Chemistry of Materials*, **19** (16), 4030–6.

26 Petit, C., Wang, Z.L. and Pileni, M.P. (2007) Ferromagnetic cobalt nanocrystals achieved by soft annealing approach–from individual behavior to mesoscopic organized properties. *Journal of Magnetism and Magnetic Materials*, **312** (2), 390–9.

27 Lin, X.M., Sorensen, C.M. and Klabunde, K.J. (1999) Control of cobalt nanoparticle size by the germ-growth method in inverse micelle system: size dependent magnetic properties. *Journal of Materials Research*, **14**, 1542–7.

28 Zhang, X. and Chan, K.Y. (2002) Microemulsion synthesis and electrocatalytic properties of platinum–cobalt nanoparticles. *Journal of Materials Chemistry*, **12**, 1203.

29 Haeiwa, T., Segawa, K. and Konishi, K. (2007) Magnetic properties of isolated Co nanoparticles in SiO_2 capsule prepared with reversed micelle. *Journal of Magnetism and Magnetic Materials*, **310** (2), e809–11.

30 Ahmed, J., Ahmad, T., Ramanujachary, K.V., Lofland, S.E. and Ganguli, A.K. (2008) Development of a microemulsion-based process for synthesis of cobalt (Co) and cobalt oxide (Co_3O_4) nanoparticles from submicrometer rods of cobalt oxalate. *Journal of Colloid and Interface Science*, **321** (2), 434–41.

31 Glavee, G.N., Klabunde, K.J., Sorensen, C.M. and Hadjipanayis, G.C. (1992) Borohydride reductions of metal ions. A new understanding of the chemistry leading to nanoscale particles of metals, borides, and metal borates. *Langmuir*, **8** (3), 771–3.

32 Kobayashi, Y., Horie, M., Konno, M., Rodriguez-Gonzalez, B. and Liz-Marzán, L.M. (2003) Preparation and properties of silica-coated cobalt nanoparticles. *The Journal of Physical Chemistry B*, **107** (30), 7420–5.

33 Salgueirino-Maceira, V. and Correa-Duarte, M.A. (2006) Cobalt and silica based core–shell structured nanospheres. *Journal of Materials Chemistry*, **16**, 3593.

34 Salgueirino-Maceira, V., Correa-Duarte, M.A., Hucht, A. and Farle, M. (2006) One-dimensional assemblies of silica-coated cobalt nanoparticles: magnetic pearl necklaces. *Journal of Magnetism and Magnetic Materials*, **303** (1), 163–6.

35 Salgueirino-Maceira, V., Correa-Duarte, M.A., Farle, M., Lopez-Quintela, M.A., Sieradzki, K. and Diaz, R. (2006) Synthesis and characterization of large colloidal cobalt particles. *Langmuir*, **22** (4), 1455–8.

36 Wang, Y., Wu, H.L., Zhang, Q.H. and Tang, Q.H. (2005) Cobalt nanoparticles prepared in faujasite zeolites by borohydride reduction. *Microporous Mesoporous Materials*, **86** (1–3), 38–49.

37 Schwartzberg, A.M., Olson, T.Y., Talley, C.E. and Zhang, J.Z. (2007) Gold nanotubes synthesized via magnetic alignment of cobalt nanoparticles as templates. *The Journal of Physical Chemistry C*, **111** (44), 16080–2.

38 Bao, F., Li, J.F., Ren, B., Yao, J.L., Gu, R.A. and Tian, Z.Q. (2008) Synthesis and characterization of Au@Co and Au@Ni core–shell nanoparticles and their applications in surface-enhanced Raman spectroscopy. *The Journal of Physical Chemistry C*, **112** (2), 345–50.

39 Kim, C.W., Kim, Y.H., Cha, H.G., Kwon, H.W. and Kang, S.Y. (2006) Synthesis and characterization of highly magnetized nanocrystalline $Co_{30}Fe_{70}$ alloy by chemical reduction. *The Journal of Physical Chemistry B*, **110** (48), 24418–23.

40 King, N.C., Blackley, R.A., Wears, M.L., Newman, D.M., Zhou, W.Z. and Bruce, D.W. (2006) The synthesis of mesoporous silicates containing bimetallic nanoparticles and magnetic properties of PtCo nanoparticles in silica. *Chemical Communications*, **32**, 3414.

41 Kobayashi, Y., Kakinuma, H., Nagao, D., Ando, Y., Miyazaki, T. and Konno, M. (2008) Synthesis and properties of Co–Pt alloy silica core-shell particles. *Journal of Sol-Gel Science and Technology*, **47** (1), 16–22.

42 Zhao, Y.W., Zheng, R.K., Zhang, X.X. and Xiao, J.Q. (2003) A simple method to prepare uniform Co nanoparticles. *IEEE Transactions on Magnetics*, **39**, 2764–6.

43 Zhang, Z.J., Chen, X.Y., Zhang, X.F. and Shi, C.W. (2006) Synthesis and magnetic properties of nickel and cobalt nanoparticles obtained in DMF solution. *Solid State Communications*, **139** (8), 403–5.

44 (a) Pyun, J. (2007) Nanocomposite materials from functional polymers and magnetic colloids. *Polymer Reviews*, **47** (2), 231–63; (b) Grubbs, R.B. (2007) Roles of polymer ligands in nanoparticle stabilization. *Polymer Reviews*, **47** (2), 197–215; (c) Rodriguez, H.J., Checot, F., Gnanou, Y. and Lecommandoux, S. (2005) Toward "smart" nano-objects by self-assembly of block copolymers in solution. *Progress in Polymer Science*, **30** (7), 691.

45 Thomas, J.R. (1966) Preparation and magnetic properties of colloidal cobalt particles. *Journal of Applied Physics*, **37** (7), 2914.

46 Park, I.W., Yoon, M., Kim, Y.M., Kim, Y., Yoon, H., Song, H.J., Volkov, V., Avilov, A. and Park, Y. (2003) Magnetic properties and microstructure of cobalt nanoparticles in a polymer film. *Solid State Communications*, **126** (7), 385–9.

47 Lu, L.T., Tung, L.D., Robinson, I., Ung, D., Tan, B., Long, J., Cooper, A.I., Fernigde, D.G. and Thanh, N.T.G. (2008) Size and shape control for water-soluble magnetic cobalt nanoparticles using polymer ligands. *Journal of Materials Chemistry*, **18**, 2453.

48 Shpaisman, N. and Margel, S. (2007) Air-stable Fe and Co crystalline nanocomposite particles prepared by a single-step swelling of metal precursors within polystyrene microspheres of narrow size distribution. *New Journal of Chemistry*, **31**, 1507.

49 Korth, B.D., Keng, P., Shim, I., Bowles, S.E., Tang, C., Kowalewski, T., Nebesny, K.W. and Pyun, J. (2006) Polymer-coated

ferromagnetic colloids from well-defined macromolecular surfactants and assembly into nanoparticle chains. *Journal of the American Chemical Society*, **128** (20), 6562–3.

50 Güerler, C., Feyen, M., Behrens, S., Matoussevitch, N. and Schmidt, A.M. (2008) One-step synthesis of functional Co nanoparticles for surface-initiated polymerization. *Polymer*, **49** (9), 2211–16.

51 Washio, I., Xiong, Y.J., Yin, Y.D. and Xia, Y.N. (2006) Reduction by the end groups of poly(vinyl pyrrolidone): a new and versatile route to the kinetically controlled synthesis of Ag triangular nanoplates. *Advanced Materials*, **18** (13), 1745–9.

52 Sun, Y.G. and Xia, Y.N. (2002) Shape-controlled synthesis of gold and silver nanoparticles. *Science*, **298**, 2176–9.

53 Narayanan, R. and El-Sayed, M.A. (2003) Effect of catalysis on the stability of metallic nanoparticles: Suzuki reaction catalyzed by PVP-palladium nanoparticles. *Journal of the American Chemical Society*, **125** (2), 8340–7.

54 Chen, W.X., Lee, J.Y. and Liu, Z.L. (2002) Microwave-assisted synthesis of carbon supported Pt nanoparticles for fuel cell applications. *Chemical Communications*, **21**, 2588.

55 Vasquez, Y., Sra, A.K. and Schaak, R.E. (2005) One-pot synthesis of hollow superparamagnetic CoPt nanospheres. *Journal of the American Chemical Society*, **127** (36), 12504–5.

56 Guo, L., Liang, F., Wen, X.G., Yang, S.H., He, L., Zheng, W.Z., Chen, C.P. and Zhong, Q.P. (2007) Uniform magnetic chains of hollow cobalt mesospheres from one-pot synthesis and their assembly in solution. *Advanced Functional Materials*, **17** (3), 425–30.

57 Xiong, Y., Chen, Q.W., Tao, N., Ye, J., Tang, Y., Feng, J.S. and Gu, X.Y. (2007) The formation of legume-like structures of Co nanoparticles through a polymer-assisted magnetic-field-induced assembly. *Nanotechnology*, **18** (34), 345301.

58 Kodama, D., Shinoda, K., Sato, K., Konno, Y., Joseyphus, R.J., Motomiya, K., Takahashi, H., Matsumoto, T., Sato, Y., Tohji, K. and Jeyadevan, B. (2006) Chemical synthesis of sub-micrometer- to nanometer-sized magnetic FeCo dice. *Advanced Materials*, **18** (23), 3154–9.

59 Tadd, E.H., Bradley, J. and Tannenbaum, R. (2002) Spatial distribution of cobalt nanoclusters in block copolymers. *Langmuir*, **18** (6), 2378–84.

60 Platonova, O.A., Bronstein, L.M., Solodovnikov, S.P., Yanovskaya, I.M., Obolonkova, E.S., Valetsky, P.M., Wenz, E. and Antonietti, M. (1997) Cobalt nanoparticles in block copolymer micelles: preparation and properties. *Colloid and Polymer Science*, **275** (5), 426.

61 Diana, F.S., Lee, S.H., Petroff, P.M. and Kramer, E.J. (2003) Fabrication of hcp-Co nanocrystals via rapid pyrolysis in inverse PS-b-PVP micelles and thermal annealing. *Nano Letters*, **3** (7), 891–5.

62 Liu, G., Yan, X., Lu, Z., Curda, S.A. and Lal, J. (2005) One-pot synthesis of block copolymer coated cobalt nanocrystals. *Chemistry of Materials*, **17** (20), 4985–91.

63 (a) Rutnakornpituk, M., Thompson, M.S., Harris, L.A., Farmer, K.E., Esker, A.R., Riffle, J.S., Connolly, J. and Pierre, T.G. (2002) Formation of cobalt nanoparticle dispersions in the presence of polysiloxane block copolymers. *Polymer*, **43** (8), 2337–48; (b) Baranauskas, V.V., III, Zalich, M.A., Saunders, M., St Pierre, T.G., and Riffle, J.S. (2005) Poly(styrene-b-4-vinylphenoxyphthalonitrile)–cobalt complexes and their conversion to oxidatively stable cobalt nanoparticles. *Chemistry of Materials*, **17**, 5246–54.

64 Zalich, M.A., Vadala, M.L., Riffle, J.S., Saunders, M. and St Pierre, T.G. (2007) Structural and magnetic properties of cobalt nanoparticles encased in siliceous shells. *Chemistry of Materials*, **19**, 6597–604.

65 Barea, E., Batlle, X., Bourges, P., Corma, A., Fornés, V., Labarta, A. and Puntes, V.F. (2005) Synthesis and characterization of stabilized subnanometric cobalt metal particles.

Journal of the American Chemical Society, **127** (51), 18026–30.

66 Liu, W., Zhong, W., Wu, X.L., Tang, N.J. and Du, Y.W. (2005) Hydrothermal microemulsion synthesis of cobalt nanorods and self-assembly into square-shaped nanostructures. *Journal of Crystal Growth*, **284** (3–4), 446–52.

67 Xie, Q., Dai, Z., Huang, W., Liang, J.B., Jiang, C.L. and Qian, Y.T. (2005) Synthesis of ferromagnetic single-crystalline cobalt nanobelts via a surfactant-assisted hydrothermal reduction process. *Nanotechnology*, **16** (12), 2958.

68 Xie, Q., Qian, Y.T., Zhang, S.Y., Fu, S.Q. and Yu, W.C. (2006) A hydrothermal reduction route to single-crystalline hexagonal cobalt nanowires. *European Journal of Inorganic Chemistry*, **12**, 2454–9.

69 Zhang, J., Dai, Z., Bao, J., Zhang, N. and Lopez-Quintela, M.A. (2007) Self-assembly of Co-based nanosheets into novel nest-shaped nanostructures: synthesis and characterization. *Journal of Colloid and Interface Science*, **305** (2), 339–44.

70 Liu, X.H., Yi, R., Wang, Y.T., Qiu, G.Z., Zhang, N. and Li, X.G. (2007) Highly ordered snowflakelike metallic cobalt microcrystals. *The Journal of Physical Chemistry C*, **111** (1), 163–7.

71 Zhang, Y.J., Zhang, Y., Wang, Z.H., Li, D., Cui, T.Y., Liu, W. and Zhang, Z.D. (2008) Controlled synthesis of cobalt flowerlike architectures by a facile hydrothermal route. *European Journal of Inorganic Chemistry*, **17**, 2733–8.

72 Zhu, L.P., Zhang, W.D., Xiao, H.M., Yang, Y. and Fu, S.Y. (2008) Facile synthesis of metallic Co hierarchical nanostructured microspheres by a simple solvothermal process. *The Journal of Physical Chemistry C*, **112** (27), 10073–8.

73 Zhang, Y.J., Yao, Q., Zhang, Y., Cui, T.Y., Li, D., Liu, W., Lawrence, W. and Zhang, Z.D. (2008) Solvothermal synthesis of magnetic chains self-assembled by flowerlike cobalt submicrospheres. *Crystal Growth and Design*, **8** (9), 3206–12.

74 Liu, Q.Y., Guo, X.H., Chen, J.L., Li, J., Song, W. and Shen, W.J. (2008) Cobalt nanowires prepared by heterogeneous nucleation in propanediol and their catalytic properties. *Nanotechnology*, **19**, 365608.

75 Zhang, Z.T., Blom, D.A., Gai, Z., Thompson, J.R., Shen, J. and Dai, S. (2003) High-yield solvothermal formation of magnetic CoPt alloy nanowires. *Journal of the American Chemical Society*, **125** (25), 7528–9.

76 Hu, M.J., Lu, Y., Zhang, S., Guo, S.R., Lin, B., Zhang, M. and Yu, S.H. (2008) High yield synthesis of bracelet-like hydrophilic Ni–Co magnetic alloy flux-closure nanorings. *Journal of the American Chemical Society*, **130** (35), 11606–7.

77 Murray, C.B., Norris, D.J. and Bawendi, M.G. (1993) Synthesis and characterization of nearly monodisperse CdE (E = sulfur, selenium, tellurium) semiconductor nanocrystallites. *Journal of the American Chemical Society*, **115** (19), 8706–15.

78 (a) Talapin, D.V., Rogach, A.L., Kornowski, A., Haase, M. and Weller, H. (2001) Highly luminescent monodisperse CdSe and CdSe/ZnS nanocrystals synthesized in a hexadecylamine–trioctylphosphine oxide–trioctylphosphine mixture. *Nano Letters*, **4**, 207–11; (b) Peng, Z.A. and Peng, X.G. (2001) Formation of high-quality CdTe, CdSe, and CdS nanocrystals using CdO as precursor. *Journal of the American Chemical Society*, **123** (1), 183–4.

79 Rockenberger, J., Scher, E.C. and Alivisatos, A.P. (1999) New nonhydrolytic single-precursor approach to surfactant-capped nanocrystals of transition metal oxides. *Journal of the American Chemical Society*, **121** (49), 11595–6.

80 (a) Sun, S.H., Murray, C.B., Weller, D., Folks, L. and Moser, A. (2000) Monodisperse FePt nanoparticles and ferromagnetic FePt nanocrystal superlattices. *Science*, **287**, 1989–92; (b) Dumestre, F., Chaudret, B., Amiens, C., Renaud, P. and Fejes, P. (2004)

Superlattices of iron nanocubes synthesized from Fe $[N(SiMe_3)_2]_2$. *Science*, **303**, 821–3; (c) Green, M. (2005) Organometallic based strategies for metal nanocrystal synthesis. *Chemical Communications*, **24**, 3002.

81 Jun, Y.W., Choi, J.S. and Cheon, J.W. (2006) Shape control of semiconductor and metal oxide nanocrystals through nonhydrolytic colloidal routes. *Angewandte Chemie, International Edition in English*, **45** (21), 3414–39.

82 Puntes, V.F., Krishnan, K.M. and Alivisatos, A.P. (2001) Colloidal nanocrystal shape and size control: the case of cobalt. *Science*, **291**, 2115–17.

83 Puntes, V.F., Zanchet, D., Erdonmez, C.K. and Alivisatos, A.P. (2002) Synthesis of hcp-Co nanodisks. *Journal of the American Chemical Society*, **124** (43), 12874–80.

84 Lagunas, A., Jimeno, C., Font, D., Solà, L. and Pericas, M.A. (2006) Mechanistic studies on the conversion of dicobalt octacarbonyl into colloidal cobalt nanoparticles. *Langmuir*, **22** (8), 3823–9.

85 Shukla, N., Svedberg, E.B., Ell, J. and Roy, A.J. (2006) Surfactant effects on the shapes of cobalt nanoparticles. *Material Letters*, **60** (16), 1950–5.

86 Sun, S.H. and Murry, C.B. (1999) Synthesis of monodisperse cobalt nanocrystals and their assembly into magnetic superlattices (invited). *Journal of Applied Physics*, **85** (8), 4325.

87 Leslie-Pelecky, D.L., Bonder, M., Martin, T., Kirkpatrick, E.M., Liu, Y., Zhang, X.Q., Kim, S.H. and Rieke, R.D. (1998) Using high-temperature chemical synthesis to produce metastable nanostructured cobalt. *Chemistry of Materials*, **10** (11), 3732–6.

88 Wu, N., Fu, L., Su, M., Aslam, M., Wong, K.C. and Dravid, V.P. (2004) Interaction of fatty acid monolayers with cobalt nanoparticles. *Nano Letters*, **4** (2), 383–6.

89 Cha, S.I., Chan, B.M., Kim, K.T. and Hong, S.H. (2005) Ferromagnetic cobalt nanodots, nanorices, nanowires and nanoflowers by polyol process. *Journal of Materials Research*, **20**, 2148–53.

90 Dumestre, F., Chaudret, B., Amiens, C., Fromen, M.C., Casanove, M.J., Renaud, P. and Zurcher, P. (2002) Shape control of thermodynamically stable cobalt nanorods through organometallic chemistry. *Angewandte Chemie, International Edition in English*, **41** (22), 4286–9.

91 de Silva, R.M., Palshin, V., Fronczek, F.R., Hormes, J. and Kumar, C.S.S.R. (2007) Investigation of the influence of organometallic precursors on the formation of cobalt nanoparticles. *The Journal of Physical Chemistry C*, **111** (28), 10320–8.

92 de Silva, R.M., Palshin, V., de Silva, K.M.N., Henry, L.L. and Kumar, C.S.S.R. (2008) A new role for surfactants in the formation of cobalt nanoparticles. *Journal of Materials Chemistry*, **18**, 738.

93 Chitu, L., Chushkin, Y., Luby, S., Majkova, E., Satka, A., Ivan, J., Smrcok, L., Buchal, A., Giersig, M. and Hilgendorff, M. (2007) Structure and self-assembling of Co nanoparticles. *Materials Science and Engineering: C*, **27** (1), 23–8.

94 Woods, S.I., Kirtley, J.R., Sun, S.H. and Koch, R.H. (2001) Direct investigation of superparamagnetism in Co nanoparticle Films. *Physical Review Letters*, **87** (13), 137205–8.

95 Yang, H.T., Shen, C.M., Su, Y.K., Yang, T.Z., Gao, H.J. and Wang, Y.G. (2003) Self-assembly and magnetic properties of cobalt nanoparticles. *Applied Physics Letters*, **82**, 4729.

96 Cheng, G.J., Romero, D., Fraser, G.T. and Walker, A.R.H. (2005) Magnetic-field-induced assemblies of cobalt nanoparticles. *Langmuir*, **21** (26), 12055–9.

97 Tripp, S.L., Pusztay, S.V., Ribbe, A.E. and Wei, A. (2002) Self-assembly of cobalt nanoparticle rings. *Journal of the American Chemical Society*, **124** (2), 7914–15.

98 Bao, Y., Pakhomov, A.B. and Krishnan, K.M. (2006) Brownian magnetic relaxation of water-based cobalt nanoparticle ferrofluids. *Journal of Applied Physics*, **99** (8), 08H107.

99 Pellegrino, T., Manna, L., Kudera, S., Liedl, T., Koktysh, D., Rogach, A.L., Keller, S., Radler, J., Natile, G. and Parak, W.J. (2004) Hydrophobic nanocrystals coated with an amphiphilic polymer shell: a general route to water soluble nanocrystals. *Nano Letters*, **4** (4), 703–7.

100 Park, J.I. and Cheon, J. (2001) Synthesis of "solid solution" and "core-shell" type cobalt–platinum magnetic nanoparticles via transmetalation reactions. *Journal of the American Chemical Society*, **123** (24), 5743–6.

101 Park, J.I., Kim, M.G., Jun, Y.W., Lee, J.S., Lee, W.R. and Cheon, J. (2004) Characterization of superparamagnetic "core–shell" nanoparticles and monitoring their anisotropic phase transition to ferromagnetic "solid solution" nanoalloys. *Journal of the American Chemical Society*, **126** (29), 9072–8.

102 Shevchenko, E.V., Talapin, D.V., Rogach, A.L., Kornowski, A., Haase, M. and Weller, H. (2002) Colloidal synthesis and self-assembly of $CoPt_3$ nanocrystals. *Journal of the American Chemical Society*, **124** (38), 11480–5.

103 Shevchenko, E.V., Talapin, D.V., Schnablegger, H., Kornowski, A., Festin, O., Svedlindh, P., Haase, M. and Weller, H. (2003) Study of nucleation and growth in the organometallic synthesis of magnetic alloy nanocrystals: the role of nucleation rate in size control of $CoPt_3$ nanocrystals. *Journal of the American Chemical Society*, **125** (30), 9090–101.

104 Gehl, B., Aleksandrovic, V., Erbacher, M., Juergens, B., Schurenberg, M., Kornowski, A., Weller, H. and Baumer, M. (2008) Ligand exchange with thiols: effects on composition and morphology of colloidal CoPt nanoparticles. *ChemPhysChem*, **9**, 821.

105 Wang, Y. and Yang, H. (2005) Synthesis of CoPt nanorods in ionic liquids. *Journal of the American Chemical Society*, **127** (15), 5316–17.

106 Tzitzios, V., Niarchos, D., Gjoka, M., Boukos, N. and Petridis, D. (2005) Synthesis and characterization of 3D CoPt nanostructures. *Journal of the American Chemical Society*, **127** (40), 13756–7.

107 Kim, H., Achermann, M., Balet, L.P., Hollingsworth, J.A. and Klimov, V.I. (2005) Synthesis and characterization of Co/CdSe core/shell nanocomposites: bifunctional magnetic-optical nanocrystals. *Journal of the American Chemical Society*, **127** (2), 544–6.

108 Ledo-Suarez, A., Rodriguez-Sanchez, L., Blanco, M.C. and Lopez-Quintelaor, M.A. (2006) Electrochemical synthesis and stabilization of cobalt nanoparticles. *Physica Status Solidi*, **203**, 1234–40.

109 Nikitenko, S.I., Koltypin, Y., Palchik, O., Felner, I., Xu, X.N. and Gedanken, A. (2001) Synthesis of highly magnetic, air-stable iron-iron carbide nanocrystalline particles by using power ultrasound. *Angewandte Chemie, International Edition in English*, **40** (23), 4447–9.

110 Chau, J.L.K., Hsu, M.K. and Kao, C.C. (2006) Microwave plasma synthesis of Co and SiC-coated Co nanopowders. *Material Letters*, **60** (7), 947–51.

111 Song, Y.J., Modrow, H., Henry, L.L., Saw, C.K., Doomes, E.E., Palshin, V., Hormes, J. and Kumar, C.S.S.R. (2006) Microfluidic synthesis of cobalt nanoparticles. *Chemistry of Materials*, **18** (12), 2817–27.

112 Wu, H., Zhang, R., Liu, X.X., Lin, D.D. and Pan, W. (2007) Electrospinning of Fe, Co, and Ni nanofibers: synthesis, assembly, and magnetic properties. *Chemistry of Materials*, **19** (14), 3506–11.

113 Billas, I.M.L., Châtelain, A. and de Heer, W.A. (1994) Magnetism from the atom to the bulk in iron, cobalt, and nickel clusters. *Science*, **265**, 1682–4.

114 Kodama, R.H., Berkowitz, A.E., McNiff, E.J., Jr and Foner, S. (1996) Surface spin disorder in $NiFe_2O_4$ nanoparticles. *Physical Review Letters*, **77** (2), 394–7.

115 Chikazumi, S., Taketomi, S., Ukita, M., Mizukami, M., Miyajima, H., Setogawa, M. and Kurihara, Y. (1987) Physics of magnetic fluids. *Journal of Magnetism and Magnetic Materials*, **65** (2–3), 245–51.

116 Lu, A.H., Schmidt, W., Matoussevitch, N., Bönnemann, H., Spliethoff, B.,

Tesche, B., Bill, E., Kiefer, W. and Schüth, F. (2004) Nanoengineering of a magnetically separable hydrogenation catalyst. *Angewandte Chemie, International Edition in English*, **43** (33), 4303–6.

117 Tsang, S.C., Caps, V., Paraskevas, I., Chadwick, D. and Thompsett, D. (2004) Magnetically separable, carbon-supported nanocatalysts for the manufacture of fine chemicals. *Angewandte Chemie, International Edition in English*, **43** (42), 5645–9.

118 Gupta, A.K. and Gupta, M. (2005) Synthesis and surface engineering of iron oxide nanoparticles for biomedical applications. *Biomaterials*, **26** (18), 3995–4021.

119 Mornet, S., Vasseur, S., Grasset, F., Verveka, P., Goglio, G., Demourgues, A., Portier, J., Pollert, E. and Duguet, E. (2006) Magnetic nanoparticle design for medical applications. *Progress in Solid State Chemistry*, **34** (2–4), 237–47.

120 Li, Z., Wei, L., Gao, M.Y. and Lei, H. (2005) One-pot reaction to synthesize biocompatible magnetite nanoparticles. *Advanced Materials*, **17** (8), 1001–5.

121 Lu, A.H., Slabas, E.L. and Schüth, F. (2007) Magnetic nanoparticles: synthesis, protection, functionalization, and application. *Angewandte Chemie, International Edition in English*, **46**, 1222–44.

122 Sun, S.H. and Zeng, H. (2002) Size-controlled synthesis of magnetite nanoparticles. *Journal of the American Chemical Society*, **124** (28), 8204–5.

123 Batlle, X. and Labarta, A. (2002) Finite-size effects in fine particles: magnetic and transport properties. *Journal of Physics D*, **35**, R15.

124 Kitakami, O., Sato, H., Shimada, Y., Sato, F. and Tanaka, M. (1998) Size effect on the crystal phase of cobalt fine particles. *Physical Review B*, **56**, 13849–54.

125 Graf, C.P., Birringer, R. and Michels, A. (2006) Synthesis and magnetic properties of cobalt nanocubes. *Physical Review B*, **73**, 212401–4.

126 Wen, G.H., Zheng, R.K., Fung, K.K. and Zhang, X.X. (2004) Microstructural and magnetic properties of passivated Co nanoparticle films. *Journal of Magnetism and Magnetic Materials*, **270** (3), 407–12.

127 Li, H. and Liao, S.J. (2008) Organic colloid method to prepare ultrafine cobalt nanoparticles with the size of 2 nm. *Solid State Communications*, **145** (3), 118–21.

128 Waddell, J., Inderhees, S., Aronson, M.C. and Dierker, S.B. (2006) Magnetization of cobalt nanodiscs. *Journal of Magnetism and Magnetic Materials*, **297** (1), 54–9.

129 Pfeiffer, H. (1990) Influence of thermal fluctuations on the magnetic properties of particle assemblies. *Physica Status Solidi A*, **122** (1), 377–89.

130 Victora, R.H. (1989) Predicted time dependence of the switching field for magnetic materials. *Physical Review Letters*, **63** (4), 457–60.

131 Sharrock, M.P. (1994) Time dependence of switching fields in magnetic recording media (invited). *Journal of Applied Physics*, **76** (10), 6413.

132 Pelecky, D.L.L. and Rieke, R.D. (1996) Magnetic properties of nanostructured materials. *Chemistry of Materials*, **8** (8), 1770–83.

133 Wiekhorst, F., Shevchenko, E., Weller, H. and Kötzler, J. (2003) Anisotropic superparamagnetism of monodispersive cobalt-platinum nanocrystals. *Physical Review B*, **67**, 224416–26.

134 Binns, C., Trohidou, K.N., Bansmann, J., Baker, S.H., Blackman, J., Bucher, J.P., Kechrakos, D., Kleibert, A., Louch, S., Meiwes-Broer, K.H., Pastor, G.P., Perez, A. and Xie, Y. (2005) The behaviour of nanostructured magnetic materials produced by depositing gas-phase nanoparticles. *Journal of Physics D: Applied Physics*, **38** (22), R357.

135 Respaud, M., Broto, J.M., Rakoto, H., Fert, A.R., Thomas, L., Barhara, B., Verelst, M., Snoeck, E., Lecante, P., Mosset, A., Osuna, J., Ely, T.O., Amiens, C. and Chaudret, B. (1998) Surface effects on the magnetic properties of ultrafine cobalt particles. *Physical Review B*, **57**, 2925–35.

136 Denardin, J.C., Brabdl, A.L., Knobel, M., Panissod, P., Pakhomov, A.B.,

Liu, H. and Zhang, X.X. (2002) Thermoremanence and zero-field-cooled/field-cooled magnetization study of $Co_x(SiO_2)_{1-x}$ granular films. *Physical Review B*, **65**, 064422–9.

137 Parker, D., Lisiecki, I., Salzemann, C. and Pileni, M.P. (2007) Emergence of new collective properties of cobalt nanocrystals ordered in fcc supracrystals: II, magnetic investigation. *The Journal of Physical Chemistry C*, **111** (34), 12632–8.

138 Kogan, S. (1996) *Electronic Noise and Fluctuations in Solids*, Cambridge University Press, New York, p. 33.

139 Buckingham, M.J. (1983) *Noise in Electronic Devices and Systems*, Ellis Horwood Limited, New York, p. 33.

140 Chen, J.P., Sorensen, C.M., Klabunde, K.J. and Hadjipanayis, G.C. (1995) Enhanced magnetization of nanoscale colloidal cobalt particles. *Physical Review B*, **51**, 11–527.

141 Jamet, M., Wernsdorfer, W., Thirion, C., Mailly, D., Dupuis, V., Mélinon, P. and Pérez, A. (2001) Magnetic anisotropy of a single cobalt nanocluster. *Physical Review Letters*, **86**, 4676–9.

142 Liu, F., Press, M.R., Khanna, S.N. and Jena, P. (1989) Magnetism and local order: *Ab initio* tight-binding theory. *Physical Review B*, **39**, 6914–24.

143 Bucher, J.P., Douglass, D.C. and Bloomfield, L.A. (1991) Magnetic properties of free cobalt clusters. *Physical Review Letters*, **66**, 3052–5.

144 Louderback, J.G., Cox, A.J., Lising, L.J., Douglass, D.C. and Bloomfield, L.A.Z. (1993) Magnetic properties of nickel clusters. *Zeitschrift fur Physik D*, **26**, 301.

145 Billas, I.M.L., Châtelain, A. and de Heer, W.A. (1994) Magnetism from the atom to the bulk in iron, cobalt, and nickel clusters. *Science*, **265**, 1682–4.

146 Respaud, M., Broto, J.M., Rakoto, H., Fert, A.R., Thomas, L., Barbara, B., Verelst, M., Snoeck, E., Lecante, P., Mosset, A., Osuna, J., Ould Ely, T., Amiens, C. and Chaudret, B. (1998) Surface effects on the magnetic properties of ultrafine cobalt particles. *Physical Review B*, **57**, 2925–35.

147 Osuna, J., de Caro, D., Amiens, C., Chaudret Etienne, B., Respaud, S.M., Broto, J.M. and Fert, A.R. (1996) Synthesis, characterization, and magnetic properties of cobalt nanoparticles from an organometallic precursor. *The Journal of Physical Chemistry*, **100** (35), 14571–4.

148 Bean, C.P. and Livingston, J.D. (1959) Superparamagnetism. *Journal of Applied Physics*, **30**, S120.

149 Bruno, P. (1989) Tight-binding approach to the orbital magnetic-moment and magnetocrystalline anisotropy of transition-metal monolayers. *Physical Review B*, **39**, 865.

150 Rusponi, S., Cren, T., Weiss, N., Epple, M., Buluschek, P., Claude, L. and Brune, H. (2003) The remarkable difference between surface and step atoms in the magnetic anisotropy of two-dimensional nanostructures. *Nature Materials*, **2** (8), 546–51.

151 Paulus, P.M., Goossens, A., Thiel, R., Van Der Kraan, A., Schmid, G. and De Jongh, L. (2001) Surface and quantum-size effects in Pt and Au nanoparticles probed by ^{197}Au Mössbauer spectroscopy. *Physical Review B*, **64**, 205418–35.

152 Luis, F., Torres, J.M., García, L.M., Bartolomé, J., Stankiewicz, J., Petroff, F., Fettar, F., Maurice, J.L. and Vaurès, A. (2002) Enhancement of the magnetic anisotropy of nanometer-sized Co clusters: influence of the surface and of interparticle interactions. *Physical Review B*, **65**, 094409–18.

153 den Broerer, F.J.A., Hoving, W. and Bloemen, P.H.J. (1991) Magnetic anisotropy of multilayers. *Journal of Magnetism and Magnetic Materials*, **93**, 562–70.

154 Wilhelm, F., Bovensiepen, U., Scherz, A., Poulopoulos, P., Ney, A., Wende, H., Ceballos, G. and Baberschke, K. (2000) Manipulation of the curie temperature and the magnetic moments of ultrathin Ni and Co films by Cu-capping. *Journal of Magnetism and Magnetic Materials*, **222** (1–2), 163–7.

155 Luis, F., Bartolomé, F., Petroff, F., Bartolomé, J., García, L.M., Deranlot, C., Jaffrès, H., Martínez, M.J., Bencok, P., Wilhelm, F., Rogalev, A. and Brookes, N.B. (2006) Tuning the magnetic

anisotropy of nanoparticles by metal capping. *Europhysics Letters*, **76**, 142–8.

156 Maurice, J.L., Briatico, J., Carrey, J., Petroff, F., Schelp, L.F. and Vaures, A. (1999) Clusters obtained by sputter deposition of cobalt atoms on alumina. *Philosophical Magazine A*, **79** (12), 2921–34.

157 Briatico, J., Maurice, J.L., Carrey, J., Imhoff, D., Petroff, F. and Vaures, A. (1999) Structure of cobalt cluster films obtained by sputter deposition on alumina. *The European Physical Journal D*, **9**, 517.

158 Nogués, J. and Schuller, I.K. (1999) Exchange bias. *Journal of Magnetism and Magnetic Materials*, **192** (2), 203–32.

159 Meiklejohn, W.H. (1962) Exchange anisotropy – a review. *Journal of Applied Physics*, **33** (3), 1328.

160 Meiklejohn, W.H. and Bean, C.P. (1957) New magnetic anisotropy. *Physical Review*, **105**, 904–13.

161 Meiklejohn, W.H. and Bean, C.P. (1956) New magnetic anisotropy. *Physical Review*, **102**, 1413–14.

162 Gangopadhyay, S., Hadjipanayis, G.C., Sorensen, C.M. and Klabunde, K.J. (1993) Exchange anisotropy in oxide passivated Co fine particles. *Journal of Applied Physics*, **73** (10), 6964.

163 Löffler, J., Wagner, W., van Swygenhoven, H., Meier, J., Doudin, B. and Ansermet, J.P. (1997) Magnetic properties of nanostructured ferromagnetic metals. *Materials Science Forum*, **235–238**, 699–704.

164 Löffler, J., van Swygenhoven, H., Wagner, W., Meier, J., Doubin, B. and Ansermet, J.P. (1997) Influence of grain size and oxidation on the magnetic properties of nanostructured Fe and Ni. *Nanostructured Materials*, **9** (1–8), 523–6.

Keywords

magnetic nanoparticles; superparamagnetism; size effects; biomagnetics; nanostructures; nanomagnets

Index

Nanomaterials for the Life Sciences Vol. 4: Magnetic Nanomaterials. Edited by Challa S. S. R. Kumar

ISBN: 978-3-527-32154-4